

# **ENGINEERING MECHANICS 2011**

**17<sup>th</sup> INTERNATIONAL CONFERENCE**

**MAY 9 - 12, 2011, SVRATKA, CZECH REPUBLIC**



## **BOOK OF FULL TEXTS**

**Editor: Vladimír Fuis**

---

**Association for Engineering Mechanics**

**Institute of Thermomechanics,  
Academy of Sciences of the Czech Republic, v.v.i. – branch Brno**

**Institute of Solid Mechanics, Mechatronics and Biomechanics,  
Faculty of Mechanical Engineering, Brno University of Technology**

**Institute of Theoretical and Applied Mechanics,  
Academy of Sciences of the Czech Republic, v.v.i.**

**ŽDAS Inc., Žďár nad Sázavou**

**Czech Society for Mechanics**

**IFTToMM Member Committee of Czech Republic**

**Text may be copied and used freely, but credit should be given to this Proceedings.**

**Copyright © 2011    Institute of Thermomechanics  
Academy of Sciences of the Czech Republic, v.v.i., Prague**

**1<sup>st</sup> edition, 2011**

**Editor © Vladimír Fuis, 2011**

**ISBN    978-80-87012-33-8**

**ISSN    1805-8248 (printed)**

**ISSN    1805-8256 (electronic)**



**All the papers were reviewed by members of the international scientific committee.**

### **SCIENTIFIC COMMITTEE**

<b>Prof. Ján Benčat, PhD.</b>	<b>University of Žilina, SK</b>
<b>Prof. Radim Čajka, PhD.</b>	<b>VSB - Technical University of Ostrava, CZ</b>
<b>Assoc. Prof. Vladimír Čech, PhD.</b>	<b>OPROX a.s., Brno, CZ</b>
<b>Prof. Miloš Drdáký, DSc.</b>	<b>ITAM AS CR, Prague, CZ</b>
<b>Assoc. Prof. Karel Frydryšek, PhD.</b>	<b>VSB - Technical University of Ostrava, CZ</b>
<b>Vladimír Fuis, PhD. (chairman)</b>	<b>Inst. of Thermomechanics AS CR, Brno, CZ</b>
<b>Prof. Ardeshir Guran, PhD.</b>	<b>Institute of Structronics, Ottawa, CA</b>
<b>Prof. Dr. Bodo Heimann</b>	<b>University of Hannover, GE</b>
<b>Jaromír Horáček, DSc.</b>	<b>Inst. of Thermomechanics AS CR, Prague, CZ</b>
<b>Assoc. Prof. L. Ilieva-Mitutsova, PhD.</b>	<b>Bulgarian Academy of Sciences, Sofia, BG</b>
<b>Prof. Ryszard Jablonski</b>	<b>Warsaw Univ. of Techn, PL</b>
<b>Prof. Přemysl Janíček, DSc., FEng.</b>	<b>Brno University of Technology, CZ</b>
<b>Prof. Zbyněk Jaňour, DSc.</b>	<b>Inst. of Thermomechanics AS CR, Prague, CZ</b>
<b>Prof. Miroslav Jícha, PhD.</b>	<b>Brno University of Technology, CZ</b>
<b>Prof. Milan Jirásek, DSc.</b>	<b>Czech Technical University in Prague, CZ</b>
<b>Assoc. Prof. Jiří Kala, PhD.</b>	<b>Brno University of Technology, CZ</b>
<b>Prof. Zdeněk Kala, PhD.</b>	<b>Brno University of Technology, CZ</b>
<b>Prof. Zdeněk Knésl, PhD.</b>	<b>Inst. of Physics of Materials AS CR, Brno, CZ</b>
<b>Prof. Alena Kohoutková, PhD.</b>	<b>Czech Technical University in Prague, CZ</b>
<b>Prof. Ctirad Kratochvíl, DSc.</b>	<b>Inst. of Thermomechanics AS CR, Brno, CZ</b>
<b>Prof. Anne-Maria Laukkanen, PhD.</b>	<b>University of Tampere, FI</b>
<b>Prof. Eduard Malenovský, DSc.</b>	<b>Brno University of Technology, CZ</b>
<b>Prof. František Maršík, DSc.</b>	<b>Inst. of Thermomechanics AS CR, Prague, CZ</b>
<b>Prof. Arkadiusz Meżyk</b>	<b>Silesian University of Technology, Gliwice, PL</b>
<b>Jiří Minster, DSc.</b>	<b>ITAM AS CR, Prague, CZ</b>
<b>Jiří Náprstek, DSc.</b>	<b>ITAM AS CR, Prague, CZ</b>
<b>Prof. Dr. Bořek Patzák</b>	<b>Czech Technical University in Prague, CZ</b>
<b>Prof. Michail V. Pavlenko</b>	<b>Moscow State Mining University, RU</b>
<b>Prof. Kazimierz Peszynski, PhD.</b>	<b>Univ. of Technol. and Life Science, Bydgoszcz, PL</b>
<b>Prof. Jindřich Petruška, PhD.</b>	<b>Brno University of Technology, CZ</b>
<b>Prof. Jaromír Příhoda, PhD., FEng.</b>	<b>Inst. of Thermomechanics AS CR, Prague, CZ</b>
<b>Ladislav Půst, DSc.</b>	<b>Inst. of Thermomechanics AS CR, Prague, CZ</b>
<b>Prof. Eugeniusz Ratajczyk</b>	<b>Warsaw University of Technology, PL</b>
<b>Prof. Janusz Sempruch, MSc.</b>	<b>Univ. of Technol. and Life Science, Bydgoszcz, PL</b>
<b>Prof. Olga V. Skopintseva</b>	<b>Moscow State Mining University, RU</b>
<b>Prof. Ján Sládek, DSc.</b>	<b>ICA, SAS, Bratislava, SK</b>

<b>Prof. Vladimír Sládek, DSc.</b>	<b>ICA, SAS, Bratislava, SK</b>
<b>Prof. Eugeniusz Switonski</b>	<b>Silesian University of Technology, Gliwice, PL</b>
<b>Prof. Pavel Šafařík, PhD.</b>	<b>Inst. of Thermomechanics AS CR, Prague, CZ</b>
<b>Prof. Michal Šejnoha, DSc.</b>	<b>Czech Technical University in Prague, CZ</b>
<b>Prof. Alexander Tesár, DSc,</b>	<b>ICA, SAS, Bratislava, SK</b>
<b>Prof. Václav Tesař, PhD.</b>	<b>Inst. of Thermomechanics AS CR, Prague, CZ</b>
<b>Prof. Tomasz Topoliński</b>	<b>Univ. of Technol. and Life Science, Bydgoszcz, PL</b>
<b>Prof. Michael Valášek, DSc.</b>	<b>Czech Technical University in Prague, CZ</b>
<b>Assoc. Prof. Jan Valíček, PhD.</b>	<b>VSB-Technical University of Ostrava, CZ</b>
<b>Prof. Pavel Vlasák, DSc.</b>	<b>Institute of Hydrodynamics AS CR, Prague CZ</b>
<b>Prof. Jaroslav Zapoměl, DSc.</b>	<b>Inst. of Thermomechanics AS CR, Ostrava, CZ</b>
<b>Prof. Vladimír Zeman, DSc.</b>	<b>University of West Bohemia in Pilsen, CZ</b>
<b>Prof. Rudolf Žitný, PhD.</b>	<b>Czech Technical University in Prague, CZ</b>
<b>Prof. Milan Žmindák, PhD.</b>	<b>University of Žilina, SK</b>

## **HONOURARY COMMITTEE**

**Ing. Miroslav Šabart - Managing Director of ŽŽAS, a.s.**

**František Mládek - Mayor of Svratka**

## **ORGANIZATION COMMITTEE**

**Ing. Vladimír Fuis, PhD. (chairman)**

**Ing. Jiří Krejsa, PhD.**

**Ing. Tomáš Návrat, PhD.**

**The Conference is hosted by the hotel ŽŽAS at Svratka.**

## **Main Headings**

<b>Table of Contents .....</b>	<b>6</b>
<b>Keynote Lectures .....</b>	<b>17</b>
<b>Papers .....</b>	<b>43</b>
<b>Authors Index .....</b>	<b>707</b>

### **List of sections:**

<b>KEY</b>	<b>Keynote Lectures</b>
<b>BIO</b>	<b>Biomechanics</b>
<b>DYN</b>	<b>Dynamics and Kinematics</b>
<b>FLU</b>	<b>Fluid Mechanics</b>
<b>FRA</b>	<b>Fracture Mechanics</b>
<b>MCT</b>	<b>Mechatronics</b>
<b>REL</b>	<b>Reliability</b>
<b>SOL</b>	<b>Mechanics of Solids</b>
<b>TER</b>	<b>Termomechanics</b>
<b>POS</b>	<b>Posters</b>

# Table of Contents

## KEYNOTE LECTURES

<b>Guran A.:</b> <i>THE CONTRIBUTIONS OF CZECHOSLOVAKIAN ENGINEERS AND SCIENTISTS TO MODERNIZATION OF IRAN (1851-1938): A HISTORICAL REVIEW AND APPRAISAL</i> .....	17
<b>Janíček P., Burša J.:</b> <i>CHARACTERISTICS OF SCIENCE AND SCIENTIFIC ACTIVITIES; CONSIDERATIONS ABOUT WHAT IS AND WHAT IS NOT SCIENTIFIC</i> .....	25
<b>Šklíba J., Svoboda R.:</b> <i>DEVELOPMENT OF MATHEMATICAL MODEL OF THE HYDRAULIC DAMPER</i> .....	33

## PAPERS

<b>Bednář L., Tajč L., Jirka L.:</b> <i>CALCULATION STUDY OF STEAM FLOW THROUGH A CONTROL VALVE</i> .....	43
<b>Benčat J., Koňár J., Papán D.:</b> <i>DYNAMIC MODELLING AND TESTING OF NEW BRIDGE CROSSING DANUBE IN BRATISLAVA</i> .....	47
<b>Benkovský P., Starek L.:</b> <i>OPTIMAL NUMBER AND LOCATION OF PIEZOCERAMIC ACTUATORS AND SENSORS FOR VIBRATION SUPPRESSION OF TWO-DIMENSIONAL SYSTEMS</i> .....	51
<b>Blekta J., Petříček J., Mevald J., Lufinka A.:</b> <i>ADJUSTMENT OF SEAT SUSPENSION DAMPING</i> .....	55
<b>Bouřil V., Vorel J., Šejnoha M.:</b> <i>AIR VOIDS IN MATRIX BASED TEXTILE COMPOSITES</i> .....	59
<b>Brouček M., Kuklík P.:</b> <i>THE IMPACT OF GROUNDWATER ON ARTIFICIALLY COMPACTED SOILS</i> .....	63
<b>Březina L., Březina T.:</b> <i>UNCERTAIN MODELING OF MECHATRONIC SYSTEMS</i> .....	67
<b>Byrtus M.:</b> <i>USAGE OF NONLINEAR NORMAL MODES IN DYNAMICS</i> .....	71
<b>Cech V., Jevicky J.:</b> <i>GENERATOR OF BASIC COMMAND SIGNALS FOR QUALITY TESTING OF PAN AND TILT DEVICES SERVOMECHANISMS</i> .....	75
<b>Cichański A.:</b> <i>INFLUENCE OF FINITE ELEMENT ORDER ON SCF PRECISION FOR U-SHAPED NOTCHES IN FLAT BARS UNDER TENSION</i> .....	79

<b>Civín A., Vlk M., Navrátil P., M. Matug M.:</b> <i>RING-CORE RESIDUAL STRESS MEASUREMENT: ANALYSIS OF DEPTH INCREMENT DISTRIBUTION FOR INTEGRAL EQUATION METHOD</i> .....	83
<b>Čada Z., Hradil P., Kala J., Kanický V., Salajka V.:</b> <i>ASSESSMENT OF TANKS WITH FLUIDS SUBJECTED TO SEISMIC EXCITATION</i> .....	87
<b>Čada Z., Hradil P., Mrózek M., Salajka V.:</b> <i>PARAMETRIC STUDY ON DYNAMIC BEHAVIOUR OF A MULTI-STOREY BUILDING INCLUDING SOIL-STRUCTURE INTERACTION</i> .....	91
<b>Čajka R., Matečková P.:</b> <i>TEMPERATURE DISTRIBUTION OF SLIDE JOINT IN REINFORCED CONCRETE FOUNDATION STRUCTURES</i> .....	95
<b>Čečrdle J.:</b> <i>LANDING SHOCK AEROELASTIC RESPONSE ANALYSIS OF UTILITY AIRCRAFT</i> .....	99
<b>Damborský P., Profant T., Kotoul M.:</b> <i>STRESS SINGULARITY ANALYSIS OF CRACKS LYING ON THE INTERFACE BETWEEN TWO ORTHOTROPIC MATERIALS</i> .....	103
<b>Dančová P., Vít T., Kotek M.:</b> <i>EXPERIMENTAL INVESTIGATION OF SYNTHETIC JET ARRAY</i> .....	107
<b>Dániel V., Jamróz T., Had J.:</b> <i>FEM NONLINEAR CONTACT VIBRATION ANALYSIS OF A DISC ADAPTER</i> .....	111
<b>Doktor T., Valach J., Kytýř D., Jiroušek O.:</b> <i>PORE SIZE DISTRIBUTION OF HUMAN TRABECULAR BONE – COMPARISON OF INTRUSION MEASUREMENTS WITH IMAGE ANALYSIS</i> .....	115
<b>Donát M.:</b> <i>ASSESSMENT OF THE INFLUENCE OF THE ELECTROMECHANICAL INTERACTION ON ROTORDYNAMIC INSTABILITY IN ELECTRIC MACHINES</i> ..	119
<b>Dušek D.:</b> <i>POSSIBILITIES OF USING OF MECHANICAL ANALYZER FOR DECOMPOSITION OF NON-STATIONARY SIGNALS</i> .....	123
<b>Dvořák J.:</b> <i>REPLACEMENT OF THE MECHANICAL PLANISHING SYSTEM OF THE FORGING PRESS IHI 800 JAPAN</i> .....	127
<b>Eliáš J., Le J.-L.:</b> <i>MODELING OF FATIGUE CRACK GROWTH IN CERAMICS UNDER COMPRESSIVE CYCLING</i> .....	131
<b>Fischer C.:</b> <i>GPU COMPUTATION IN ENGINEERING PRACTICE</i> .....	135
<b>Foglar M., Křístek V.:</b> <i>ANALYTICAL APPROACH TO CENTRE-LINE OPTIMIZATION OF BURIED ARCH BRIDGES AND ITS BOUNDARIES</i> .....	139
<b>Foglar M., Sochorová E., Kohoutková A.:</b> <i>FIELD TESTS OF BLAST PERFORMANCE OF REINFORCED CONCRETE AND FIBER REINFORCED CONCRETE SPECIMENS</i> .....	143
<b>Frantík P., Veselý V.:</b> <i>SIMULATION OF THE FRACTURE PROCESS IN QUASI-BRITTLE MATERIALS USING A SPRING NETWORK MODEL</i> .....	147
<b>Frydryšek K.:</b> <i>PROBABILISTIC APPROACHES APPLIED IN THE SOLUTION OF PROBLEMS IN MINING AND BIOMECHANICS</i> .....	151

<b>Fuis V., Málek M., Janíček P.:</b> <i>PROBABILITY OF DESTRUCTIONS OF CERAMICS USING WEIBULL'S THEORY</i> .....	155
<b>Gottvald J.:</b> <i>ANALYSIS OF STEEL STRUCTURE VIBRATIONS OF THE BUCKET WHEEL EXCAVATOR SCHRS 1320</i> .....	159
<b>Guran A., Vahidi-Shams A.:</b> <i>AN ENHANCED APPROACH IN MOTION DETECTION OF HUMAN MOVEMENTS</i> .....	163
<b>Hadas Z., Singule V.:</b> <i>ENERGY HARVESTING – OPPORTUNITY FOR FUTURE REMOTE APPLICATIONS</i> .....	167
<b>Hájková A., Padevět P., Plachý T., Tesárek P.:</b> <i>RECYCLING OF FLUE GAS DESULPHURIZATION GYPSUM AT LABORATORY CONDITIONS</i> .....	171
<b>Hajžman M., Šašek J., Byrtus M., Zeman V.:</b> <i>DYNAMIC LOADING OF A SQUIRREL CAGE MOTOR FOR VARIOUS VEHICLES</i> .....	175
<b>Havelka J., Sýkora J., Kučerová A.:</b> <i>FAST EVALUATION OF LINEAL PATH FUNCTION USING GRAPHICS PROCESSING UNIT</i> .....	179
<b>Hladík O., Uruba V.:</b> <i>ON TURBULENT BOUNDARY LAYER DYNAMICS</i> .....	183
<b>Hlaváček P., Šmilauer V., Patzák B.:</b> <i>EASY GENERATION OF MODELS/MESHES USING AN OPEN-SOURCE SOFTWARE SALOME</i> .....	187
<b>Hlavatý M., Starek L.:</b> <i>THE DETECTION OF DEFECTS OF MECHANICAL STRUCTURES USING SURFACE ACOUSTIC WAVES (SAW)</i> .....	191
<b>Horák M., Jirásek M.:</b> <i>COMPARISON OF NONLOCAL AND GRADIENT-ENHANCED DAMAGE-PLASTICITY MODEL</i> .....	195
<b>Horný L., Kronek J., Chlup H., Gultová E., Heller L., Žitný R., Vokoun D.:</b> <i>INFLATION-EXTENSION TEST OF SILICON RUBBER TUBE REINFORCED BY NITI WIRES</i> .....	199
<b>Hortel M., Škuderová A.:</b> <i>NON-LINEAR TIME HETERONYMOUS DAMPING IN NON-LINEAR PARAMETRIC PLANETARY SYSTEMS</i> .....	203
<b>Hotař V., Salač P.:</b> <i>EEE – METHOD BASED ON FRACTAL DIMENSION FOR ANALYSIS OF TIME SERIES</i> .....	207
<b>Hrbáček J., Hrbáček R., Věchet S.:</b> <i>MODULAR CONTROL SYSTEM ARCHITECTURE FOR A MOBILE ROBOT</i> .....	211
<b>Hromádka D., Žitný R., Horný L., Chlup H., Veselý J., Kronek J., Gultová E.:</b> <i>IDENTIFICATION OF CONSTITUTIVE MODEL BLOOD VESSEL WALL FROM WATER HAMMER EXPERIMENT</i> .....	215
<b>Hubová O.:</b> <i>AEROELASTIC INSTABILITIES ON THE HEIGHT RISE BUILDINGS</i> .....	219
<b>Hynek M., Votapek P.:</b> <i>THERMAL ANALYSIS OF TYRE CURING PROCESS</i> .....	223
<b>Chalupa M., Veverka J., Vlach R.:</b> <i>DYNAMIC LOADING OF VEHICLE TRACK SIMULATION</i> .....	227
<b>Ilieva-Mitutsova L., Chavdarov I., Vitkov V., Yaroshevsky V.:</b> <i>MODELLING OF A MECHATRONIC MODULE FOR FOOT RECEPTOR ACTIVATION</i> .....	231

<b>Janíček P., Schmidová E., Navrátil P., Jandora R.:</b> <i>PREDICTING THE DIRECTION OF CRACK PROPAGATION ALONG THE CIRCUMFERENCE OF A MODEL RAILWAY CARRIAGE UNDER VARIOUS OPERATING CONDITIONS</i> .....	235
<b>Janouchová E., Kučerová A.:</b> <i>COMPARISON OF SPACE-FILLING DESIGNS IN DISCRETE DOMAINS</i> .....	239
<b>Jirouš F., Stárek K., Kupsa V.:</b> <i>THE COMPLEMENT TO TUBE-SYSTEM DESIGN</i> .....	243
<b>Jiroušek O., Zlámál P.:</b> <i>MICROSTRUCTURAL MODELS OF TRABECULAR BONE - COMPARISON OF CT-BASED FE MODELS</i> .....	247
<b>Jonáš J., Pokorný Z., Ficek F.:</b> <i>XRK 2-180 STRAIGHTENING MACHINE MODERNIZATION</i> .....	251
<b>Jurenka J., Španiel M., Kuželka J.:</b> <i>SIMULATION OF FATIGUE CRACK PROPAGATION UNDER CONTACT LOADING CONDITIONS</i> .....	255
<b>Kabeláč J.:</b> <i>SHEAR STRESS ON ARBITRARY CROSS SECTION INCLUDING PLASTICITY</i> .....	259
<b>Kadlec M.:</b> <i>FAILURE MECHANISM AND STRAIN FIELDS ON A CARBON/EPOXY COMPOSITE SUBJECTED TO COMPRESSION AFTER IMPACT</i> .....	263
<b>Kala J., Hradil P., Salajka V.:</b> <i>MEASURES WHICH CAN BE USED TO PREDICT, PREVENT AND RESOLVE THE PROBLEMS OF LIVELINESS IN FOOTBRIDGES</i> .....	267
<b>Kala Z., Kala J.:</b> <i>SENSITIVITY ANALYSIS OF STABILITY PROBLEMS OF STEEL COLUMNS USING SHELL FINITE ELEMENTS AND NONLINEAR COMPUTATION METHODS</i> .....	271
<b>Karczmarzyk S.:</b> <i>ACOUSTIC CHARACTERISTICS OF PLANE MULTILAYERED SANDWICH INFINITE-INFINITE STRUCTURES</i> .....	275
<b>Kharlamova I. S. Kharlamov A. A., Chára Z., Vlasák P.:</b> <i>MODELLING OF BED IN PROCESS OF PARTICLE SALTATION IN CHANNEL</i> .....	279
<b>Kirchner J., Mrkos J.:</b> <i>QKK 50 MANIPULATOR TONGS CALCULATION</i> .....	283
<b>Klapka M., Mazurek I., Strecker Z.:</b> <i>THE ANALYSIS OF THE AUTOMOTIVE DIFFERENTIAL VIBRATIONS BY MEANS OF BIFURCATION DIAGRAMS</i> .....	287
<b>Klich J., Valíček J., Sitek L., Foldyna J., Harničárová M., Hlaváček P.:</b> <i>STUDY OF SURFACE TOPOGRAPHY GENERATED BY THE ACTION OF PULSATING WATER JET</i> .....	291
<b>Knotek S., Jícha M.:</b> <i>CFD SIMULATION OF FLOW OVER A WAVY SURFACE</i> .....	295
<b>Kolařík F., Patzák B.:</b> <i>COMPARISON OF P1P1 AND Q1P0 “TAYLOR-HOOD ELEMENTS” IN FLOW PROBLEMS</i> .....	299
<b>Kotek M., Jašíková D., Kopecký V.:</b> <i>EXPERIMENTAL STUDY OF THE FLOW FIELD IN T-JUNCTION MODEL USING PIV METHOD</i> .....	303
<b>Koudelka P.:</b> <i>VARIABILITY OF BEARING RESISTANCE PROPERTIES OF SOILS</i> .....	307
<b>Králík J., Králík J. jr.:</b> <i>DETERMINISTIC AND PROBABILITY ANALYSIS OF THE STEEL CHIMNEY UNDER WIND LOADS</i> .....	311

<b>Králík V., Němeček J.:</b> <i>NANOINDENTATION BASED EVALUATION OF EFFECTIVE ELASTIC PROPERTIES OF METAL FOAM</i> .....	<b>315</b>
<b>Kratochvíl C., Švéda P., Houfek M., Houfek L.:</b> <i>PROBLEM OF IDENTIFICATION OF DETERMINISTIC CHAOS IN THE INTERACTIVE DRIVE SYSTEMS</i> .....	<b>319</b>
<b>Kratochvíl O., Křižan J.:</b> <i>ANALYSIS OF SLENDER BRIDGE STRUCTURE</i> .....	<b>323</b>
<b>Krejša J., Věchet S.:</b> <i>MOBILE ROBOT MOTION PLANNER VIA NEURAL NETWORK</i> ..	<b>327</b>
<b>Krybus D., Patzák B.:</b> <i>PARALLELIZATION OF THE DELAUNAY TRIANGULATION</i> ....	<b>331</b>
<b>Křivý V., Čajka R.:</b> <i>DESIGN AND RELIABILITY ASSESSMENT OF ROOF STRUCTURAL ELEMENTS USING THE NEW DIGITAL GROUND SNOW LOAD MAP OF THE CZECH REPUBLIC</i> .....	<b>335</b>
<b>Kubík P., Petruška J., Hůlka J.:</b> <i>DUCTILE FRACTURE CRITERIA IN PREDICTION OF CHEVRON CRACKS</i> .....	<b>339</b>
<b>Kubis A., Navrátil P.:</b> <i>INFLUENCE OF ECCENTRICITY ON THE AXIAL FLOW IN LEAKAGE JOINTS</i> .....	<b>343</b>
<b>Kušnerová M., Čep R., Valíček J., Harničárová M., Zelenák M., Hlaváček P., Kaplonek W., Židlík P., Haluzíková B.:</b> <i>USE OF RESONANCE IN WATERJET TECHNOLOGY</i> .....	<b>347</b>
<b>Kuželka J., Nesládek M., Růžička J., Jurenka J., Španiel M.:</b> <i>EXPERIMENTAL DETERMINATION OF RELATIVE SLIPPING DURING FRETTING FATIGUE TESTS</i> .....	<b>351</b>
<b>Kytýř D., Valach J., Doktor T., Jiroušek O.:</b> <i>ASSESSMENT OF C/PPS COMPOSITES DEGRADATION INDICATORS USING ACOUSTIC MEASUREMENT</i> .....	<b>355</b>
<b>Lehký D., Frantík P.:</b> <i>CHANGE OF MODAL PROPERTIES DUE TO DAMAGE IN BEAM BUCKLING PROBLEM</i> .....	<b>359</b>
<b>Lokaj A., Vavrušová K.:</b> <i>CONTRIBUTION TO THE PROBABILISTIC APPROACH OF THE IMPACT STRENGTH OF WOOD</i> .....	<b>363</b>
<b>Lošák P., Malenovský E.:</b> <i>OPTIMIZATION OF BLADED DISK PASSIVE DAMPING ELEMENT</i> .....	<b>367</b>
<b>Lukerchenko N., Keita I., Kvurt Y., Miles J.:</b> <i>INFLUENCE OF THE SPHEROID PROLONGATION ON THE DRAG FORCE</i> .....	<b>371</b>
<b>Makovička D., Makovička D. jr.:</b> <i>EFFECT OF VIBRO-INSULATION ON RESTRICTION OF VIBRATION TRANSFER FROM SUBSOIL INTO THE BUILDING</i> .....	<b>375</b>
<b>Marcián P., Borák L., Valášek J., Krpalek D., Řehák K., Navrátil P.:</b> <i>CREATION OF COMPUTATIONAL MODELS OF CANCELLOUS BONE</i> .....	<b>379</b>
<b>Matějka L., Pěnčík J.:</b> <i>ANALYSIS OF LONG-TERM BEHAVIOR OF AN INSULATION BLOCK FROM RECYCLED HDPE BY COMRESS LOADING</i> .....	<b>383</b>
<b>Matějka M., Hyhlík T., Pick P.:</b> <i>COMPARISON OF NUMERICAL AND EXPERIMENTAL METHODS OF SOLUTION OF THE FLOW FIELD OF HUMP</i> .	<b>387</b>



<b>Matug M., Vašek M., Mišun V., Navrátil P., Cívín A., Řehák K.: ANALYSIS OF INFLUENCE OF VOCAL FOLD –VOCAL TRACT MODELS CONNECTION BY USING FEM .....</b>	<b>391</b>
<b>Mrkos J., Omes J.: OPTIMIZATION OF THE PRESS FRAME LKDS 800.....</b>	<b>395</b>
<b>Myšáková E., Lepš M.: COMPARISON OF SPACE-FILLING DESIGN STRATEGIES....</b>	<b>399</b>
<b>Náprstek J., Fischer C., Pirner M.: DYNAMICS OF A VIBRATION DAMPERWORKING ON A PRINCIPLE OF A HEAVY BALL ROLLING INSIDE A SPHERICAL DISH.....</b>	<b>403</b>
<b>Navrátil P., Janíček P., Brabenec L., Marcián P., Matug M., Cívín A.: IMPACT BEHAVIOUR OF A NEWLY DESIGNED RAILROAD WHEEL.....</b>	<b>407</b>
<b>Němcová H., Plachý T., Ťoupek R., Tesárek P., Polák M.: INFLUENCE OF MOISTURE TO MECHANICAL PROPERTIES OF MATERIALS .....</b>	<b>411</b>
<b>Němec I., Juráňová M., Frantík P., Ševčík I.: DYNAMIC ANALYSIS OF COLLAPSE OF A HIGH BUILDING.....</b>	<b>415</b>
<b>Němec I., Weis L.: A THEORETICALLY CORRECT ALGORITHM FOR NONLINEAR CONSTITUTIVE MATRIX OF A SHELL .....</b>	<b>419</b>
<b>Němec L.: HYDROSTATIC SYSTEMS OF WIND MILLS .....</b>	<b>423</b>
<b>Nesládek M., Španiel M.: FEM ANALYSES FOR DESIGN VERIFICATION OF AIRCRAFT ENGINE PARTS.....</b>	<b>427</b>
<b>Nevařil A., Hradil P., Mrózek M.: SELECTED APPROACHES TO MATHEMATIC MODELING OF RAIN-WIND INDUCED VIBRATIONS.....</b>	<b>431</b>
<b>Nikiforov A.: SIMULATION OF VIBROIMPACT ROTOR-SEALING RING SYSTEM.....</b>	<b>435</b>
<b>Novotný P., Vít T., Dančová P.: NUMERICAL SIMULATIONS OF RECOVERY HEAT EXCHANGERS.....</b>	<b>439</b>
<b>Omishore A.: VERIFICATION OF THE DESIGN RELIABILITY OF STEEL STRUCTURES.....</b>	<b>443</b>
<b>Padevět P., Bittnar P.: HIGH TEMPERATURE AND ITS INFLUENCE ON THE CREEP OF CEMENT PASTE FROM CEM II.....</b>	<b>447</b>
<b>Pásek M., Šimurda J.: A NEW QUANTITATIVE DESCRIPTION OF INTRACELLULAR <math>Ca^{2+}</math> DYNAMICS IN THE MODEL OF RAT VENTRICULAR MYOCYTE.....</b>	<b>451</b>
<b>Pavlenko M. V.: VIBRATORY STIMULATION OF FLUID FLOWS IN POROUSMEDIUM OF COAL SEAM.....</b>	<b>455</b>
<b>Pečínka L., Švrček M.: APPLICATION OF THE SIMULATION BASED RELIABILITY ANALYSIS ON THE ASSESSMENT OF THE CRITICAL THROUGH WALL CRACK STABILITY .....</b>	<b>459</b>
<b>Plachý T., Němcová H., Tesárek P., Polák M.: DYNAMIC MODULUS OF ELASTICITY OF DENTAL GYPSUM .....</b>	<b>463</b>
<b>Podešva J.: THE DOMAIN DECOMPOSITION WITH THE CONTACT PROBLEM.....</b>	<b>467</b>

<b>Pohanka L., Malenovský E.: ADDED MASS AND DAMPING OF INCOMPRESSIBLE VISCOUS FLUID .....</b>	<b>471</b>
<b>Polach P., Hajžman M.: INVESTIGATION OF VERTICAL DYNAMICS OF A HYDROGEN FUEL BUS.....</b>	<b>475</b>
<b>Poruba Z., Szweda J., Sikora R.: REALIZATION OF GEOMETRIC NONLINEARITIES IN THE DETERMINATION OF EIGEN FREQUENCIES AND SHAPES BY FINITE ELEMENT METHOD.....</b>	<b>479</b>
<b>Pospíšil S., Král R., Náprstek J.: MULTIPURPOSE EXPERIMENTAL RIG FOR AEROELASTIC TESTS ON BRIDGE GIRDERS AND SLENDER BEAMS.....</b>	<b>483</b>
<b>Potěšil A.: NON-STATIONARY HEATING OF SHELL MOULDS IN THE PROCESS OF MANUFACTURE OF ARTIFICIAL LEATHERS .....</b>	<b>487</b>
<b>Profant T., Klusák J., Kotoul M.: THE ANALYSIS OF THE CRACK INITIATED FROM THE ORTHOTROPIC BI-MATERIAL SHARP NOTCH.....</b>	<b>491</b>
<b>Příhoda J., Zubík P., Šulc J., Sedlář M.: MODELLING OF SUPERCRITICAL TURBULENT FLOW OVER AN INCLINED BACKWARD-FACING STEP IN A OPEN CHANNEL.....</b>	<b>495</b>
<b>Puklický L.: PROBABILISTIC ANALYSIS FOR DESIGN ASSESSMENT OF COMPOSITE STEEL-AND-CONCRETE COMPRESSION MEMBERS .....</b>	<b>499</b>
<b>Půst L., Pešek L.: EXCITATION OF ROTATING DISK BY STATIONARY PERMANENT MAGNETS .....</b>	<b>503</b>
<b>Radolf V., Laukkanen A. M., Havlík R., Horáček J.: NUMERICAL SIMULATION OF ACOUSTIC CHARACTERISTICS OF PROFESSIONAL VOICE BASED ON MRI AND ACOUSTIC MEASUREMENTS.....</b>	<b>507</b>
<b>Rendlová Z., Zeman V.: ANALYSIS OF THE EFFECT OF HYDRODYNAMIC BEARINGS AND DAMPING ON ROTOR STABILITY.....</b>	<b>511</b>
<b>Ripel T., Hrbáček J., Krejsa J.: DESIGN OF THE FRAME FOR AUTONOMOUS MOBILE ROBOT WITH ACKERMAN PLATFORM.....</b>	<b>515</b>
<b>Roupec J., Mazurek I., Strecker Z.: CHANGING THE BEHAVIOR OF MR FLUIDS DURING LONG TERM OPERATION .....</b>	<b>519</b>
<b>Řehák K., Florian Z., Marcián P., Valášek J., Krpalek D., Matug M.: STRESS ANALYSIS OF BURCH-SCHNEIDER CAGE.....</b>	<b>523</b>
<b>Sant Z., Casha A., Cilia J.: CAN THE FOAM MODEL SIMULATE THE BONE BEHAVIOUR? .....</b>	<b>527</b>
<b>Sempruch J., Strzelecki P.: ERROR OF FATIGUE LIFE DETERMINATED ACCORDING TO THE FITNET METHOD.....</b>	<b>531</b>
<b>Sikora R., Poruba Z., Szweda J.: INFLUENCE OF PERTURBATION ON OILWHIRL PHENOMENON GENESIS .....</b>	<b>535</b>
<b>Skarolek A., Pustka M., Pomp N.: HDL MODEL OF MACHINE TOOL SLIDEWAY.....</b>	<b>539</b>
<b>Skopintseva O. V.: THE SORPTION OF HYDROCARBONS IN THE CONDITIONS OF COAL MOISTENING .....</b>	<b>543</b>

<b>Sloupenský Z., Pochylý F.: IMPELLER BLADE DESIGN BASED ON THE DIFFERENTIAL GEOMETRY .....</b>	<b>547</b>
<b>Sobotka J.: ON APPLICATIONS OF GENERALIZED FUNCTIONS TO CALCULATION OF THIN CYLINDRICAL SHELLS .....</b>	<b>551</b>
<b>Sochorová E., Foglar M., Křístek V., Kohoutková A.: LOADING TO STRUCTURES BY REMOTE EXPLOSION.....</b>	<b>555</b>
<b>Spano M., Stara V.: TURBULENCE MODELS FOR SIMULATION OF FLOW OVER WEIRS.....</b>	<b>559</b>
<b>Staňák P., Sládek J., Sládek V.: APPLICATION OF MESHLESS MLPG METHOD FOR TRANSIENT ANALYSIS OF AXISYMMETRIC CIRCULAR PLATE BENDING PROBLEM .....</b>	<b>563</b>
<b>Stein G. J., Darula R., Chmúrny R.: A CLAMPED-CLAMPED BEAM STATIC SAG LIMITS UNDER PERPENDICULAR MAGNETIC FORCE.....</b>	<b>567</b>
<b>Stránský J., Jirásek M.: MODELING OF DYNAMIC FRAGMENTATION: ONE-DIMENSIONAL CASE.....</b>	<b>571</b>
<b>Striz B., Vysanska M.: MECHANICS OF FLAT TEXTILE FABRICS – THEORY .....</b>	<b>575</b>
<b>Szarková V., Valíček J., Řepka M., Harničárová M., Spurný M., Kawulok P., Rokosz K., Kuběna V.: NEW APPROACH FOR EVALUATING THE SURFACE TOPOGRAPHY OF ROLLED SHEETS .....</b>	<b>579</b>
<b>Szweda J., Poruba Z., Sikora R.: APPROACH FOR DYNAMIC PROPERTIES ADJUSTMENT OF STEEL STRUCTURE FEM MODELS.....</b>	<b>583</b>
<b>Šašek J., Zeman V., Kellner J.: MODAL ANALYSIS OF THE IMPERFECT BLADED DISK WITH FRICTION ELEMENTS.....</b>	<b>587</b>
<b>Šedek J.: FE-MODELING OF STIFFNESS EQUIVALENT RIVETED JOINTS .....</b>	<b>591</b>
<b>Šimonová H., Keršner Z., Seidl S.: CORRECTION OF FATIGUE PARAMETER VALUES OF CONCRETE USING APPROXIMATION OF MECHANICAL-FRACTURE PARAMETER VALUES IN TIME.....</b>	<b>595</b>
<b>Štěrba P.: TOTAL FLUID MANAGEMENT FOR HYDRAULIC LIQUIDS.....</b>	<b>599</b>
<b>Štigler J., Haluza M., Bílek M.: PRELIMINARY DESIGN OF BASIC PARAMETERS OF THE AERATOR .....</b>	<b>603</b>
<b>Štigler J., Šperka O., Klas R.: A MATHEMATICAL MODEL OF THE FLUID FLOW IN THE TEE-JUNCTION. THE COMPARISON OF THE CFD COMPUTATION AND THE MEASUREMENTS. ....</b>	<b>607</b>
<b>Tesár A.: SHEAR LAG EFFECT IN RESPONSE OF BOX BRIDGES.....</b>	<b>611</b>
<b>Tesárek P., Hájková A., Plachý T.: EFFECT OF A WATER-GYPSUM RATIO ON MECHANICAL PROPERTIES OF GYPSUM .....</b>	<b>615</b>
<b>Tesař V.: HYBRID-SYNTHETIC IMPINGING JETS .....</b>	<b>619</b>
<b>Tlustoš J.: HYDRAULIC SYSTEMS FOR THE FUTURE .....</b>	<b>623</b>

<b>Topoliński T., Cichański A., Mazurkiewicz A., Nowicki K., Jung S.:</b> <i>RELATIONS BETWEEN FRACTAL DIMENSION AND VOLUME OF TRABECULAR BONE AND ITS BEHAVIOUR UNDER LOADING</i> .....	627
<b>Uruba V.:</b> <i>INDEPENDENT MODES IN A BOUNDARY LAYER SEPARATION REGION</i> . 631	
<b>Valášek J., Marcián P., Krpalek D., Řehák K., Manek F., Florian Z.:</b> <i>STRESS-STRAIN ANALYSIS OF RESTORED FIRST MOLAR WITH CAVITY OF CLASS I...</i> 635	
<b>Valášek R.:</b> <i>TUNING OF SHOCK ABSORBERS ON VEHICLE</i> .....	639
<b>Vaverka M., Zapletal L., Šamánek O., Vrbka M.:</b> <i>INFLUENCE OF SURFACE DENTS ON ELASTOHYDRODYNAMIC AND MIXED LUBRICATION</i> .....	643
<b>Věchet S., Krejsa J.:</b> <i>CONCURRENT MAPPING AND LOCALIZATION BASED ON POTENTIAL FIELDS</i> .....	647
<b>Veseliny M., Židek K., Líška O.:</b> <i>APPLICATION OF ADVANCED TECHNOLOGIES IN REHABILITATION PROCESS</i> .....	651
<b>Vítek K.:</b> <i>OPTIMIZATION OF THE HOLE DRILLING METHOD FOR THE STRESS STATE IDENTIFICATION</i> .....	655
<b>Vlasák P., Kysela B., Chára Z.:</b> <i>COARSE-PARTICLES CONVEYING IN PIPES</i> .....	659
<b>Volavý J., Forman M., Jícha M.:</b> <i>THE EFFECT OF TURBULENCE ANISOTROPY ON PARTICLE DEPOSITION IN PARTICLE-LADEN CHANNEL FLOW</i> .....	663
<b>Vorel J., Kučerová A., Šmilauer V., Bittnar Z.:</b> <i>VIRTUAL TESTING OF CONCRETE</i> ..	667
<b>Yun K., Jůza Z., Hoznedl M., Bednář L., Tajč L.:</b> <i>EFFECT OF EQUALIZING GAPS ON THE FLOW IN THE TURBINE STAGES</i> .....	671
<b>Zahradník R., Kvapil J.:</b> <i>ALGORITHM FOR CALCULATION OF HEAT TRANSFER COEFFICIENT OF CYLINDRICAL BAR BLOWN BY HOT AIR</i> .....	675
<b>Zapoměl J., Ferfecki P.:</b> <i>A COMPUTATIONAL ANALYSIS OF THE STEADY STATE LATERAL VIBRATION OF A FLEXIBLY SUPPORTED RIGID UNBALANCED ROTOR ATTENUATED BY SQUEEZING THE THIN FILMS OF CLASSICAL AND MAGNETORHEOLOGICAL LIQUIDS</i> .....	679
<b>Zeneli E., Jirouš F.:</b> <i>SEAWATER DESALINATION PLANT – A CASE STUDY</i> .....	683
<b>Židek R., Brdečko L.:</b> <i>DEFLECTION OF REINFORCED CONCRETE STRUCTURES ACCORDING TO EC2: COMPARISON OF METHODS</i> .....	687
<b>Zobal O., Padevět P.:</b> <i>INFLUENCE OF INCREASING TEMPERATURE ON THE MECHANICAL PROPERTIES OF CEMENT PASTE MADE OF CEM I AND CEM II</i> .....	691
<b>Židek K., Maxim V.:</b> <i>TESTING OF REHABILITATION DEVICE WITH INDUSTRIAL ROBOT</i> .....	695
<b>Žmindák M., Novák P., Eisner I.:</b> <i>MODELING OF STRENGTH OF ELASTIC REINFORCED COMPOSITES BY FIBER INCLUSIONS</i> .....	699
<b>Župa T., Židek K., Líška O.:</b> <i>DESIGN OF THE CONTROL SYSTEM FOR REHABILITATION DEVICE OF UPPER ARM</i> .....	703

# **KEYNOTE LECTURES**



## **CONTRIBUTIONS OF CZECHOSLOVAKIAN ENGINEERS AND SCIENTISTS TO MODERNIZATION OF IRAN (1851-1938): A HISTORICAL REVIEW AND APPRAISAL**

**A. Guran\***

**Abstract:** *Contributions of Czechoslovakian engineers and scientists to the development of industry and education in Iran goes back to the year 1851, when August Karel Kříž (1814-1886) from Tábor and Jakub Eduard Polak (1820-1880) from Velká Mořina at Karlštejn were sent to Tehran to teach in the first Iranian technical school of European style (Dar al-Funun). During the two world wars Czech companies like Škoda Work and ČKD built parts of trans-Iranian railway, as well as numerous buildings, bridges, power plants, glass factories, sugar factories, palaces and theater halls in Iran. Working with Iran was so important during the first republic (1918-1938) that Charles University built one of the most prestigious departments of Persian studies in the world and many prominent researchers in the Oriental Institute of the Czech Academy of Sciences in Prague were involved in Iranian studies.*

**Keywords:** *History of science and technology, Czech engineers and scientists, first map of Tehran, Vresk Bridge, Dar al-Funun.*

### **1. Introduction**

Today, all nations of the world seek to achieve through development of their resources greater material welfare and higher standards of living that science and engineering have brought to our modern world.

The pathways of the present, it is said, lead out of the past. Study of the past might reveal elements that would aid in clarifying the present problems (Guran and Youssouf, 2000; Guran, 2004).

While, the Persian literature is quite known in Czech lands today (Shaki, 1967; Rypka, 1968; Guran, 2005), very little is known, in open literature, about the contributions of Czechoslovakian engineers and scientists to modernization of Iran.

In this short article we give a brief historical review and appraisal of the past activities. The aim of the presentation is to revisit some parts of, the almost forgotten, history of engineering mechanics before the Second World War.

### **2. Karel August Kříž (1814-1886) and Dar al-Funun**

Despite the fact that Tehran is very often in the media these days, only few people know that the first map of this capital city of an ancient oriental country was created, in the second half of the 19<sup>th</sup> century, by a native of Tábor, Karel August Kříž. It occurred under very interesting circumstances. It is worth to remembering his stay in not very well known Persia of that time. This almost forgotten Engineer came to Iran in connection with his cartographic enterprise. This last January was the 125<sup>th</sup> anniversary of his death.

In his youth Kříž served in the Austrian army and as an artillery officer he participated in the Italian campaign of marshal Radecky, 1848-1849. After this campaign he was adjourned to Vídeňské Nové Město, where he was raised to hetman. In 1851 his promising career as an army officer was interrupted. The military success of Radecky had public acceptance also abroad far away from the borders of the empire. His glory came even to the distant Persia, to the court of shah Násereddin. The king's

---

\* Prof. Dr. Ardeshir Guran, Ph.D.: Institute of Structronics, 275 Slater Street, 9th Floor, Ottawa, Canada; Institut für Mathematik und Rechneranwendung Universität der Bundeswehr München, Germany. e-mail: Ardeshir.guran@mail.mcgill.ca

counselor grand vezier Mírza Tagichán came up with the idea of the reorganizing Persian army according to the European standards. The Austrian emperor was asked to offer some experts, who would undertake the task. Vienna, even without official Persian diplomatic relations, willingly met the wishes of Mírza Tagichán Amir Kabir. Kříž was appointed as the head of the group of experts, because of his background, and rich experiences. All of the participants had to leave the army. The reason was the lack of official diplomatic relations. Because the task was not considered government business, it was assumed a private enterprise for each participant.

The expedition set off in August 1851. Besides Kříž and his wife, there were two medical doctors, Polak and Hëntzch, together with a geologist, Czarnotta. The core of the expedition consisted of military experts; hetman Zatti, then an infantry officer, and lieutenant Nemiro. They arrived in Tehran after four months long of rather difficult journey, which cost them a lot of psychological and physical stresses during which all of them fight against various health problems. Besides all these, the circumstances at the Persian court had changed fundamentally, In spite of many intricacies - the pressure from British ambassador also included - the young shah continued in his plan to establish military academy, and this way the so called Austrian experts could undertake their tasks.

Teaching at Dar al-Funun, Kříž wrote the first Persian textbooks of mathematics, artillery, fortification, and algebra (Gurney and Nabavi, 1993). (See Fig. 1)



*Fig. 1: Eastern gate of Dar al-Funun in the Naser Khosrow Street, Tehran (Guran, 2011).*

He introduced the first telephone line in Tehran and together with his students he prepared the first map of Tehran and its surroundings, published as lithography (Fig. 2).





*Fig. 2: The first map of Tehran (Rozhoň, 2006).*

The King awarded Kříž the rank of brigadier general (Sartip) in the Persian army for his merits in the school and other activities. Kříž referred to this after his return to Czech lands and published his memoirs in Czech periodicals (Bečka et al., 1990; Ekhtiyar, 1994; Bečka et al., 2001; Rozhoň, 2005; Rozhoň, 2006). Polak, a physician, became the king's personal doctor and taught surgery and anatomy at Dar al-Funun. He returned to Vienna in 1860 and published a significant work containing numerous reports about Iran (Polak, 1865). The important role of these two scientists in Iran-Czech cultural relations and in the founding of Dar al-Funun is elaborated by Dr. Jiří Bečka and published recently (Shaki, 1967; Bečka et al., 1990).

Despite the difficulties, within a few months a curriculum had been established and a structure of examinations and grades created. The curriculum was based on the respective specialties of the foreign instructors, students in each discipline wearing uniforms of a specified color. Preliminary subjects like mathematics, geography, history, and French were taught by Europeans. By the beginning of the second year, 1852-53, a system of levels had been introduced for each major subject, each level theoretically lasting three years before an examination to qualify for a higher level; the full cycle of instruction was designed to last twelve years. At each level copper, silver, silver-gilt, and gold medals were awarded for superior performance, though it was also possible for those with outstanding ability to be accepted into higher levels or to move more rapidly through the system.

The number of students in the first year reflects the immediate popularity of Dar al-Funun. About 105 students had enrolled in the seven main subjects, though this figure may include some overlap. The breakdown reveals the emphasis placed on the military sciences: infantry 30, cavalry 5, artillery 26, and engineering 12. On the other hand, in medicine there were 20, in pharmacy 7, and in mining 5. In addition, subjects like French and swordsmanship could be studied. Military officers not formally enrolled at Dar al-Funun could benefit from participation in daily infantry and cavalry maneuvers held by the European instructors outside the city walls. Because of the division into levels, classes were usually small, which placed considerable demand on the foreign instructors' time. The more able and experienced students served as teaching assistants at the lower levels.

The roster of subjects, student names, and examination results from August 1858 reveals how quickly the core curriculum of Dar al-Funun had become established. Since the first year the number of students had remained relatively constant, and the subjects taught were similar, the military sciences predominating. The main difference was the larger number of those studying languages. In 858 thirty-five students were learning French and twelve English or Russian (Yaghmaee, 1969-71).

In the first years of the Europeans' service, Dar al-Funun had developed not only a core curriculum, but also an academic routine and administrative framework strong enough to survive the vicissitudes that affected most new initiatives in Nāṣer-al-Dīn Shah's reign. The daily schedule and the pattern of

holidays, punishments, and regular examinations, as well as the administrative posts, were all determined in this first phase. A sense of tradition and some guarantee of respectable academic achievement were created. Much of the credit was also due to the dedication and ability of the instructors and translators. Despite the problems of teaching at widely varied levels, they were still able to produce excellent results. For example, within a few years Polak had trained a number of students who were admitted to medical schools in Paris and completed important research (Polak, 1865). Some returned to teach at Dar al-Funun, establishing a tradition in which the best students remained attached to the institutions (Gurney and Nabavi, 1993; Yaghmaee, 1969-71).



Fig. 3: Jakub Eduard Polak photographed by Julie Hafner. Nationalbibliothek, Vienna, Austria.



Fig. 4: Jakub Eduard Polak, photograph of drawing. Nationalbibliothek, Vienna, Austria.

### 3. Railways, Buildings, Palaces, Bridges, and Armoured vehicles

After the First World War and soon after the creation of Czechoslovakia, the new republic felt an urgent need for a financial base that would facilitate the transformation of the armament factories of the former Austro-Hungarian Empire into a peace-oriented manufacturing concern. Some steps to that end had already been taken before the end of the war when Škoda Works in Pilsen (Plzeň) started production of steam locomotives. Fig. 5 shows a photo of the power plant with steam aggregates built in Tehran. Many palaces were built in Tehran by Czechoslovakian firms decorated by Bohemian crystals. Reza Shah's palace (now made accessible to public) has crystal chandeliers the size of icebergs in the dining room.



Fig. 5: Power plant with steam aggregates built in Tehran (Rypka, 1946).

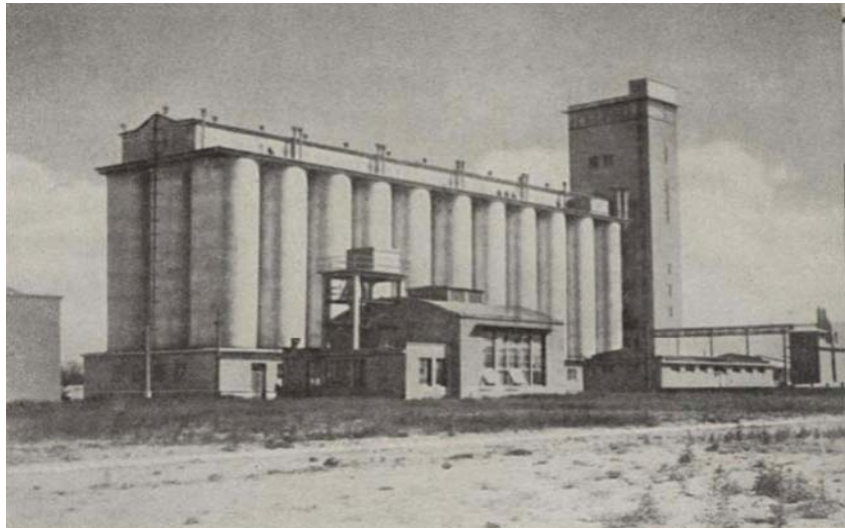


*Fig. 6: Silo for storage of cotton seeds built in Tabriz (Rypka, 1946).*

During the years 1929-31 Škoda did not export anything to Iran. The following year it received orders amount to 7.9 K millions (which was about 2% of the all its orders). The year 1932 was not particularly successful for Škoda. The only growing export was that to South America and the only a new potential market discovered in Iran. In the year 1933 it was already 92 K millions which was 14.25% of all the orders, except production of car, mining, and Iron factories. From this year the Persian market became one of the most important markets for Škoda.

The Czechoslovakian firms were part of the consortium committed itself to finish the Northern railway line, planned to reach Tehran no later than mid-1937. The first one hundred and fifteen of which were to pass through Talar River Valley and make a steady ascent into the Elburz mountains to reach Gaduk, the highest-placed railway station of the line, at 2,100 m above sea level. Obligated to follow a circuitous route in order to navigate the natural obstacles of the landscape and tackle the steep rise of the highlands, the intervening distance and line of track running to the peak was deemed to rival the famed St. Gothard railway in Switzerland, as to the beauty of its scenery and the boldness of its concept. Such asserted parallels were warranted by the complexities of the construction project that required the building of seventy-five tunnels; many partly spiraled as the line cut its way up through the mountains, and at one point boring a passage more than 3 km long. Hundreds of bridges were similarly needed to carry the line across rivers and gorges. The most notable of these structures was the Vresk Bridge whose 66 m wide masonry arch spanned a deep river valley and, by the time of the Northern line's completion in 1937, would stand as the tallest rail bridge in the world at 120 m. Fig. 7 shows a close view of Vresk Bridge in *Savadkuh* county. Fig. 8 shows the Bridge photographed by Professor Jan Rypka.

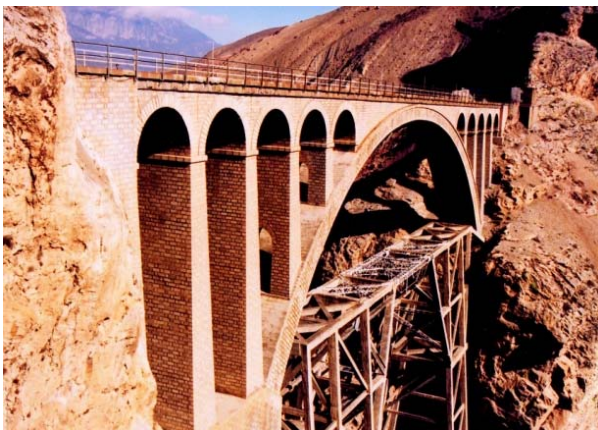


*Fig. 7: Vresk Bridge viewed having Orim and Arfeku in the background (Guran, 2011).*

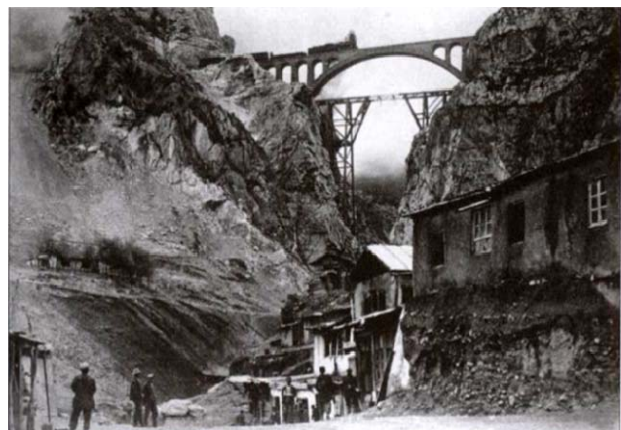


*Fig. 8: Vresk Bridge in Northern line railway (Rypka, 1946).*



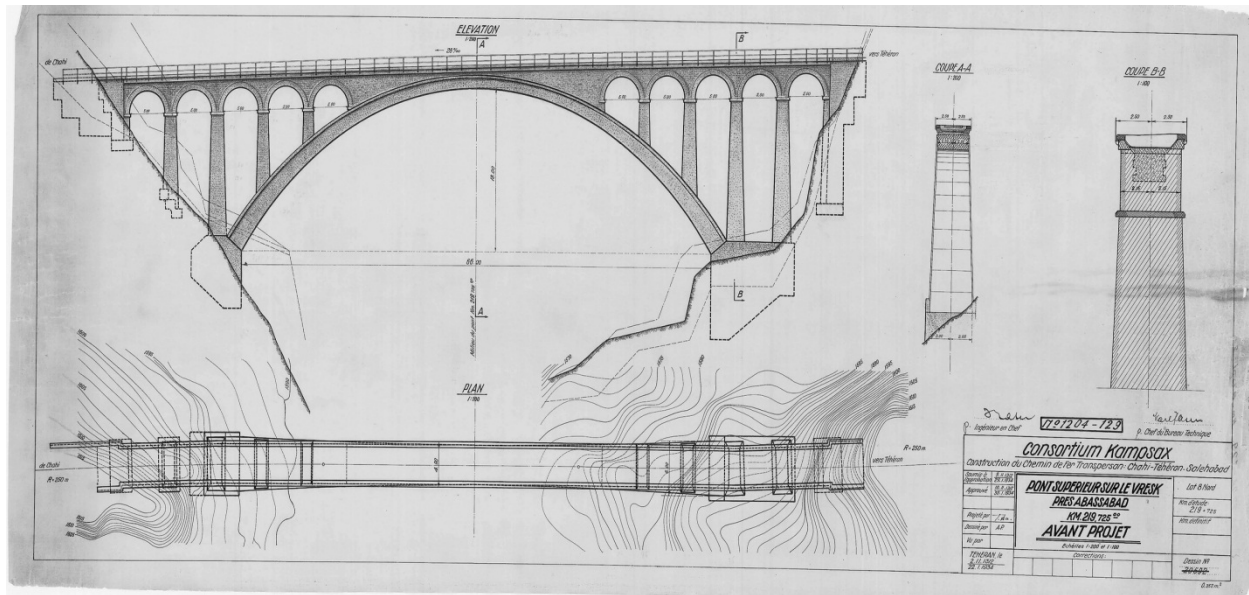


Fig. 9: Vresk bridge: Plan and Elevation, Designed and drawn in 22.1.1934 (Courtesy Consortium KAMPSAX).

During World War II, the Vresk bridge was known as the bridge of victory. The Vresk bridge honored by appearing on the face of a Persian postage stamp. There are enough of this stamp around today that collectors are still able to find them (Fig. 10).



Fig. 10: Fig: 1942-46 Vresk Bridge post stamp (Face value 10 dinars).



Fig. 11: An old bridge replaced by Skoda in Mazandaran (Rypka, 1946).

The porous soil, saturated with moisture from the persistent rainfall of the North, also presented the engineers with a great challenge as extensive drainage works and protective, artificial tunnels were needed to prevent and protect against mud slides. Fig. 11 shows a picture of a bridge constructed by Škoda.

Actively building up its army between the two world wars, Iran needed armored vehicles. Between 1931- 41, Iran purchased over 300,000 rifles, some 6,000 light and heavy machine guns, and about 350 cannons of various types. As for armored vehicles, the Czech CKD AH-IV and the TNH was selected. The Iranian order was initially for 50 TNH light tanks. Purchased on August 17 1936, the TNH light tanks were delivered to Iran in 1937. Fifty of these tanks and fifty of AH-IV tankettes equipped the First and Second divisions of the Imperial Iranian Ground Forces, twenty five of each type per division. These tanks were on active duty up until 1947.

In closing the author would like to mention some very modest collaborations with his Czech colleagues (Guran and Valášek, 2004; Guran and Nekvasilova, 2011; Guran, 2011). Of course, these are nothing when compared with the past glories. Nevertheless, it is hoped that readers will gain an understanding of this almost forgotten technical and cultural exchange, and maybe encouraged to carry out research work of their own on this subject under history of science and technology. The main purpose of this paper is met if this hope is realized.



Fig. 12: 3<sup>rd</sup> International Congress on Mechatronics edited by A. Guran and M. Valášek, ČVUT v Praze 2004.



Fig. 13: Institute for Theoretical and Applied Mechanics, Academy of Sciences of the Czech Republic 9<sup>th</sup>, March 2005.



Fig. 14: Dr. Věra Kubičková Orientální ústav, Akademie věd ČR (1918-2009). Drawn by Dr. Mansour Shaki in 1955.

## Acknowledgement

Many conversations with Drs. Věra Kubičková, Jiří Bečka, Jan Marek, Mansour Shaki, and Yaroslav Foltá were useful in preparation of this article.

I would also like to thank the staff at the Archive of the Czech Academy of Sciences in Prague, the Škoda Museum in Písek, and the Technical Museum in Prague allowing me access to their sites. The work was completed during my visit to the Institute for Theoretical and Applied Mechanics, Academy of Sciences of the Czech Republic during 2004-2005, and House of Uranus (1921-1994), a private

archive for history of technical science and medicine, in Vresk village (Iran), during 2007-2008. I am indebted to my colleagues at ITAM, in particular Prof. Ondřej Fischer, Prof. Ladislav Fryba, and Prof. Miroslav Škaloud for their friendship and kind hospitality during the preparation of this work.

The paper is dedicated to memory of our wonderful colleague Dr. Věra Kubíčková (1918-2009) to honor her monumental contributions in Persian literature, poetry, and Iran-Czech cultural relations.

## References

- Bečka, J. (1990) Perský generál August Karel Kříž (1814-1886), In: Slovanské historické studie, 17, 1990, pp. 110-127.
- Bečka, J. (2001) Dva z Čech budovali školu v Teheránu. In: Dobré dílo českých rukou. Praha : Kontinenty : Dar Ibn Rushd, pp. 6–9.
- Ekhtiyar, M. (1994) The Dar al-Funun: Educational Reform and Cultural Development in Quajar Iran, Ph.D. Dissertation (New York University).
- Fryba, L. (1972) Vibration of solids and structures under moving loads, Academia, Prague, (Translated into Farsi by A. Guran, (2011).
- Guran, A. & Yousouf, D. I. (2000) Principle of least action: history of a long controversy. Transactions of the Canadian Society for Mechanical Engineering, Vol. 24, No. 1, pp. 285-294.
- Guran, A. (2004) Ernst Mach and Peter Salcher: the development of nonlinear wave mechanics during the period 1850–1950, in: Proceedings of International Symposium Peter Salcher and Ernst Mach: A successful Teamwork, Rijeka, Croatia, 23-25 September.
- Guran, A. & Valášek, M. (Eds). (2004) 3rd International Congress on Mechatronics (MECH2K4), Czech Technical University Press, Prague.
- Guran, A. (2005) Perská literatura v Čechách a česká literatura v Íránu, III. kongresu světové literárněvědné bohemistiky, Czech Academy of Science, Institute of Czech Literature, Czech Academy of Science, Prague.
- Guran, A. & Nekvasilova J. (2011) Treni jako nelinearní jev dynamice- historicky prehled (in press).
- Guran, A. (2011) History of Modern Science and Technology in Iran, Cuvillier Verlag, Göttingen, Germany.
- Gurney, J. & Nabavi, N. (1993) Dar al-Funun," Encyclopedia Iranica, Vol. 6, pp. 662-668.
- Polak, J. E. (1865) Persien. Das Land und seine Bewohner. Ethnographische Schilderungen. Brockhaus, Leipzig.
- Rozhoň, V. (2005) Čeští cestovatelé a obraz zámorí v české společnosti. Praha : Skřivan. 31 p.
- Rozhoň, V. (2006) První mapa Teheránu, Military Geographic Review 2, pp 34-36.
- Rypka, J. (1946) Iransky Poutník, Družstevní práce, 433 pages, Praha.
- Rypka, J. (1968) History of Iranian literature. Written in collaboration with Otakar klíma, Věra Kubíčková, Felix Taure, Jiří Bečka, Jiří Cejpek, Jan Marek, I. Hrbek and J. T. P. de Bruijn., 928 pp., front., map. Dordrecht: D. Reidel Publishing Co., Guilders 130.
- Shaki, M. (1967) Modern Persian Poetry, in Yádnáme-ye Jan Rypka, Prague.
- Yaghmaee (1969-71) Madrasa-ye Dār al-fonūn, Yağmā 22, 1969-70, pp. 21-27, 78-82, 143-49, 220-23, 322-25, 403-06, 517-21, 592-98; 23, 1970-71, pp. 233-38, 361-66, and 423-26.



## **CHARACTERISTICS OF SCIENCE AND SCIENTIFIC ACTIVITIES; CONSIDERATIONS ABOUT WHAT IS AND WHAT IS NOT SCIENTIFIC**

**P. Janíček\*, J. Burša\***

**Abstract:** *The paper deals with non-traditional, but highly needed issues: to formulate the criteria of scientific activity. It is really unbelievable that in the period of information and scientific society there is a lack of such criteria and the assessment of scientific activities is totally voluntary. In the presented paper the authors have tried to propose the attributes of scientific activities.*

**Keywords:** *Characteristics of science, basic scientific fields and branches, scientific activities, non-scientific activities, systemic methodology.*

### **1. Introduction**

Definitions of science, scientific activities, or a scientist as a person can be formulated at various levels of knowledge, in dependence on the person dealing with these notions. In everyday life most people do not need to deal with their definitions at all. In a general meaning, the science is understood as something connected with some hardly understandable theories, activities related to these theories are scientific activities, and a person dealing with science is called scientist.

Another situation exists in the professional community of scientists who are frequently confronted with these notions because of various reasons. Either they „practice“ the science as a professional activity or they judge the results of a scientific work of someone else.

In any case they need to have a certain opinion concerning the notions scientific activity and science. There are someones who think everything to be clear, and any discussion dealing with these terms to be unnecessary, or even audacious and provocative. For „more contemplative“ scientists, thinking about the discussed notions may bring problems, growing sometimes to a stressing, traumatizing or even frustrating situation. A responsible answer to the questions what is the science or what is a scientific activity requires a complex of informational, creative, evaluating and decision-making activities (Janíček, 2007).

What was the motivation of the authors to write this paper? First, a personal one: they found out that the answer is not unique and unambiguous in literature sources and also the interviewed scientist were not able to formulate clear and satisfactory answers. Second, there is an objective reason: if there is a tendency to unify anything throughout the EU, a unification in such an important field like decision (judging) whether a certain activity is really scientific or not is highly needed. Shortly, also the rules in the field of the science should be unified, not only in Europe but in all the world.

The authors express their opinion that these reasons are sufficient for an attempt trying to fill this lack and to formulate some criteria for activities to be „scientific“, with the aim to make possible an objective decision what is and what is not scientific. The authors base their paper on a systemic approach, it means they started with a literature search about science, they evaluated a number of facts concerning science, they selected their substantial features and in this way they formulated attributes of science and scientific activities. Their effort aimed at achieving objectivity of their decisions.

---

\* prof. Ing. Přemysl Janíček, DrSc. and assoc. prof. Ing. Jiří Burša, Ph.D.: Institute of Solid Mechanics, Mechatronics and Biomechanics, Brno University of Technology, 602 00 Brno, Czech Republic, e-mails: janicek@fme.vutbr.cz, bursa@fme.vutbr.cz

## 2. Comprehensive characteristics of science

A solution to the problematic situation requires informational, creative, evaluating or decision-making and executive activities. In other words, first it is necessary to collect information about what is considered to be a science nowadays, then it is necessary to process this information and to make a decision in a creative way about how a comprehensive characteristic of the science could be formulated on their basis.

As an representative example of various definitions of the science let's cite M. Spala, (2006) „*Science is a systemic observation of natural effects and states with the aim to find out the characteristic facts and, consequently, to formulate laws and principles based on these facts.*“ It is evident that the author is natural scientist and science in this definition is limited to this field. And what about the other scientific fields?

On the basis of comprehensive analyses of actual definitions of science and from analyses of the philosophy of science (Feyerabend, 1980; Spala, 2006; Fajkus, 2005; Marshack, 1972) it was shown the following notions are used in these definitions: a durable and critical effort, an activity, a veritable and general cognition, a compilation of true pieces of knowledge, truthfulness, accuracy, possibility to be verified, structured, proved and systemic investigation of something novel, application of scientific methods, unavoidable role of the ethical community of scientists (the concept used and defined in (smolin, 2006)), applicability, etc. Consequently the following characteristics have been summarized:

### Science is a human activity with the following characteristics:

- ❶ Science is a durable, targeted, creative, structured, organized and mostly collective **activity of persons (scientists)** having a form of investigation and cognition and a character of real as well as abstract and **mutually interconnected processes**; they start by formulation of hypotheses, continue through their testing (transformation of hypotheses into theories), and may be concluded by participation in applications of the results of these activities.
- ❷ The objective of science is a durable acquiring of **primary novel scientific pieces of knowledge** about everything being part of the known Universe, i.e. all entities either natural or man-made; this fact defines the science as a **multi-element system** with various fields and branches.
- ❸ The science applies the scientific methodology in its cognitive processes, as a summation and intersection of various **scientific methods**, theories, approaches and algorithms.
- ❹ The scientist aims at the **verity of the scientific pieces of knowledge** and they do their best in the investigation process to ensure this in the terminal phase of the scientific cognition.
- ❺ The science verifies the **validity of scientific hypotheses** and **credibility of scientific pieces of knowledge** in two different ways:
  - ❶ by suitable, specific branch oriented **testing processes** (testing of statistical hypotheses, verification, falsification),
  - ❷ the opinion of the **ethical community of scientists** about the content, methodology, methods, algorithms and results of the scientific investigation.
- ❻ The decisive arbiter for judging what activity is accepted as scientific is the opinion of the **ethical community of scientists**, under consideration of all their specific features.

It holds that there is no limitation concerning the specific **field of human activity**, in which the scientific investigation is carried out in the sense of the above characteristics of science. Also the **grade of practical applicability** of scientific pieces of knowledge is no characteristic of the science and can be very different. However, a practical application of the scientific pieces of knowledge is considered to be positive, because it represents an objective benefit ensuring a development of the society.



### 3. Scientific methodology

In general, the **methodology** is defined as a discipline dealing with **methods** (a coherent set of rules and descriptions of verified procedures how a certain problem can be solved with certain SW and HW instruments) and **method algorithms** for a certain field of human activities. **Scientific methodology** uses to be understood as a theory of scientific methods and algorithms. It develops the methods of formulations of scientific problems, their multifactorial analyses, verification of hypotheses, creation of theories, ways of solutions to scientific problems, realization of cognitive processes, etc. According to the authors' meaning, the following equation can be formulated:

$$\textit{Scientific methodology} = \textit{systemic methodology}.$$

To formulate such an equation is one thing but the problem is how to substantiate its validity. Let's make an attempt to do it. The systemic methodology is a generalized, it means interdisciplinary?? methodology for any real or abstract system. It is a methodology of the theory of systems, which can be defined as follows (details (Janicek, 2007)):

*The systemic methodology is and abstract subject, the structure of which is created of systemic approach and thinking, systemic methods and algorithms.*

Since the time of its birth, i. e. approx. the year 1950, nobody has disputed against the theory of systems as a component part of scientific cognition. In other words, the community of scientists has accepted this theory as scientific. Consequently, the systemic methodology can be considered to be scientific as well.

The systemic methodology is based on the **systemic approach** ((Janicek, 2007, p. 12). This approach is actually considered to be a generalized creative (inventive) methodology of thinking and activities, applicable on abstract as well as real entities, with systemic attributes being its fundamentals. However, the actual situation in relation to the systemic approach is more proclamative than user-oriented; it is seldom really applied. Everybody is speaking about it, somebody is thinking to apply it; in fact, however, there is a lack of its full-valued applications.

The **systemic methods** can be overviewed as follows: ① system of logical methods, created by intersection of these paarwise methods: induction – deduction, analysis – synthesis, abstraction – concretization, ② experimental methods, ③ modelling (in its material or abstract forms), ④ statistical methods. These methods are scientific, it means appreciated (accepted) by the community of scientists.

### 4. Truthfulness of the scientific pieces of knowledge

The philosophical cathegory „**truthfulness**“ is a component part of nearly all partial definitions of the science. Commonly it is used in the sense of identity between the results of the cognitive process and the objective reality (see the term testing procedures).

**Important note:** If we insist on the above statement on „truth in the science“, then an „excommunication“ of some scientists (or their groups) would be a necessary consequence, namely of those trying to find evidences of truth of their hypotheses but having not yet managed it. As a particular example, this is the case of all the scientist dealing with the so called **theory of strings**. They have created a hypothesis the elementary particles of matter are not point-like objects, but their essence is „string-like“; it means their shape becomes more elongated if their energy increases and they shorten when their energy is decreasing. The ambition of the theory of strings is (in the case this hypothesis will be verified experimentally) to unify the quantum theory, gravitational theory and physics of elementary particles. The scientific community, however, have not acknowledged (confirmed) this hypothesis as a theory. Lee Smolin writes in his book (Smolin, 2006): „*String theory either is or is not the culmination of the scientific revolution that Einstein began in 1905. This kind of assessment cannot be based on unrealized hypotheses or unproved conjectures, or on the hopes of the theory's adherents. This is science, and the truth of a theory can be assessed based only on results that have been published in the scientific literature; thus we must be careful to distinguish between conjecture, evidence, and proof.*“

The community of scientists considers also creation and elaboration of **scientific hypotheses** to be a scientific process, under condition they comprehend a methodology how their verity can be proven.

This fact, however, excludes the truthfulness as an explicit characteristic of the science. In other words, also those cognitive processes, which have not proven their truthfulness yet, can be considered as scientific, if an evident effort is shown to prove their verity. Therefore the par. ④ of the above characteristics of the science cannot be formulated more strictly.



*Photo : Cornelia Firsching, ČTK.*

## 5. Community of scientists

Community of scientists it is a non-organized, voluntary group of individuals, scattered throughout the territory, which is dealing with scientific activities and representing „professing“ fidelity to the ethical codex; the main idea of this codex is a rational analysis of arguments concerning credibility and verity of the scientific hypotheses and pieces of knowledge, a certain agreement with a new piece of knowledge, giving him a hallmark of a „collective credibility“ or „collective correctness“ (Janicek, 2007).

Note: The community of scientists is the only one relevant human arbiter of the science. This exclusivity does not mean they cannot fail; some short-term failures can occur in the following cases:

- A scientific piece of knowledge is revolutionary – a scientist presents a novel piece of knowledge, fully unknown and hardly believable to the others, so that they are not able to consider it to be a scientific benefit. This fact can be illustrated by the discovery of chemical oscillators at the beginning of the past century by Morgan and Bray, which was refused by the scientific community as a nonsense. The case of the Belousov's chemical oscillator (1951) is rather similar, he was waiting for a general acknowledgement for 17 years until Zabolotinsky carried out the same experiment with another chemical system. Both of them became then famous scientists (Janicek, 2007, p. 1071).
- A syndrome of a collective (groupwise) thinking can occur in the community of scientists (or especially in its substantial but relatively closed part), so that some scientific pieces of knowledge are refused even when being correct. Such a situation can occur in the scientific practise (separation of the supporters of the hypothesis of strings and their refusal of the classical physics of elementary particles (Smolin, 2006), as well as in the reviewers teams of certain scientific journals.

On the basis of (Smolin, 2006) we can express the following statement:

***Science** is able to function effectively **if and only if** the scientists create a community constrained and sustained by fidelity to the generally accepted ethic rules.*

The basic ethic principles of the scientific community can be expressed shortly as follows (from (Smolin, 2006)):

**1st principle:** If the disputation can be decided by scientists „in good faith (bona fide)“ on the basis of rational arguments applied on facts known and accessible in public, then it must be considered carefully and decided in this way.

**2nd principle:** If the rational arguments applied on facts known and accessible in public do not induce identical meaning of the scientists „in good faith“, then the individuals must be allowed or even encouraged by the community to deduce their own conclusions.

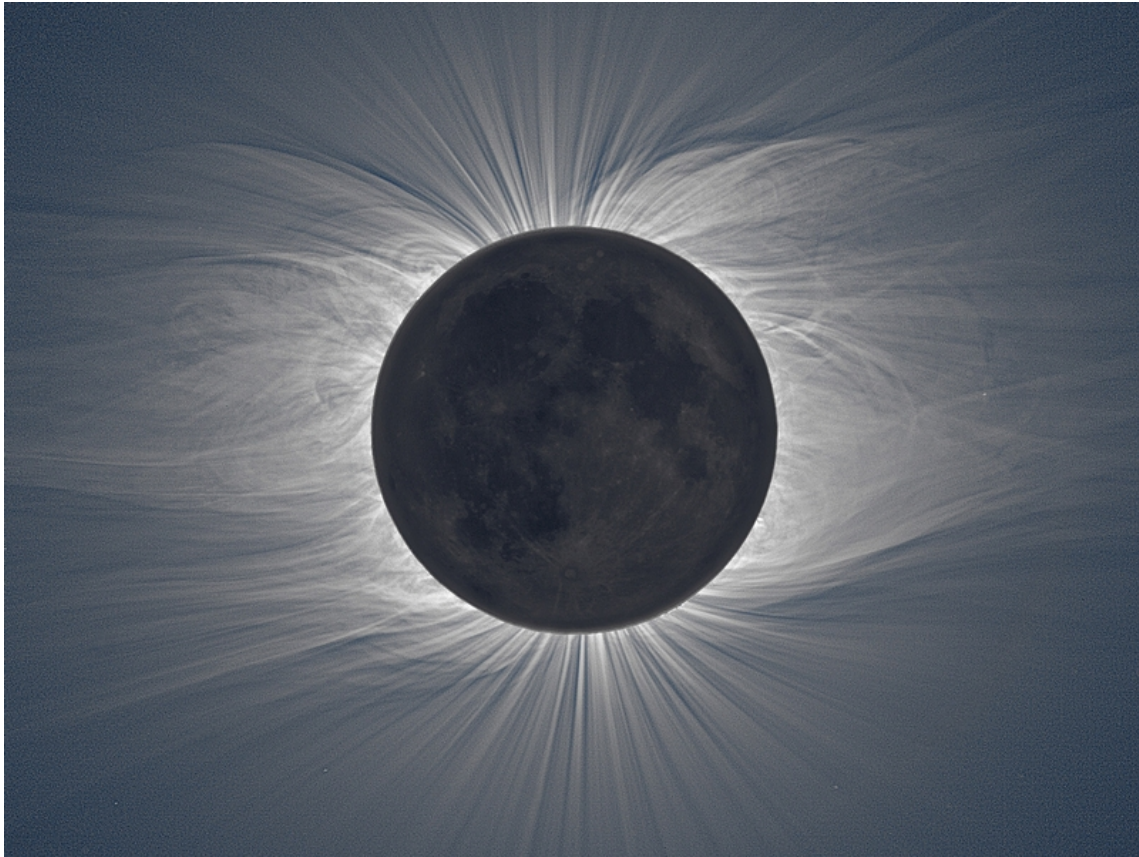


*Photo : Miloslav Druckmüller.*

## **6. Systemization of scientific fields and branches**

The systemization of science into fields and branches can be based on various criteria, e.g., on the principle, method and object of the investigation, used in seeking for new pieces of knowledge. Here the ***criterion of the object of investigation*** is used. The authors have divided the scientific fields as follows: basic scientific fields (natural sciences), man-constituted sciences, humanities, and social, formal and complementary sciences. The grade of novelty is rather different among these fields, the first two fields aim strictly at discovering something novel, while supporting and complementary sciences contribute to discovering (however, also in these fields discoveries are possible).

### **6.1. Basic scientific fields**

Cognitive activities are realized here with entities born and existing independently of humans. This entities are natural in the most general sense of this word. They can be divided into non-living (non-living nature) and living (living nature comprehending all organisms from bacterias up to humans). The basic scientific branches are commonly denoted as **natural sciences**.

- ① *Non-living entities* – can be represented by all the dead matter in the surroundings of humans, which originated without their contribution (humans have not contributed to its existence or modified it directly). By means of their creative activities, humans have constituted the following scientific branches dealing with the non-living nature: physics (astronomy), geology, chemistry and material sciences. Some of them were enhanced later to the living nature in the form of biophysics, biochemistry, biomaterial sciences, etc.

- ② *Living entities* – comprehend all the animated nature with a traditional division into fauna, flora and humans. The scientific fields belonging here are as follows:
- + biology (botanics, zoology, biology of human),
  - + biochemistry, biophysics, organic chemistry,
  - + medical sciences, as intersection of biological and social sciences, they deal with anatomical and functional changes in the human organism as a consequence of diseases, including their prevention and therapeutics.

## 6.2. Man-constituted scientific fields

In these fields the entities made by humans are investigated, namely these fields bring knowledge on the „second nature“. Humans realize their cognitive activities within the framework of technology (technical objects) and various technological processes (production and other processes, technical as well as non-technical ones, e.g. biological processes). This has brought many specific branches into existence (agriculture, forestry). The market with various products initiated the birth of economy.

The number of these scientific branches is increasing strongly nowadays; we can mention not only all the traditional technical, technological, agricultural and economical sciences, but also bioengineering ((Janicek, 2007, p.82), e.g. bionics, biorobotics, biomechanics, genetic engineering, etc.).

It is evident that many man-constituted scientific branches apply the knowledge of the basic scientific fields to discover new facts and patterns within themselves.

*Note: Those, who feel the notion “man-constituted scientific fields“ to be a forced newspeak, can replace this notion by the more common „engineering sciences“; it corresponds to the original meaning of the word „engineer“ (lat. „ingenium“ means creation, creativity). Then engineering scientific branches are those used in creation of the second nature and to solve its problems.*

## 6.3. Humanities and social sciences

These scientific fields deal with human beings and their society. Philosophy as well as philology plays a general role among these sciences. For illustration, social sciences comprehend sociology, psychology, politology, demography, economy, etc. Also cultural sciences belong to this category, such as archeology, ethnography, anthropology, aesthetics, linguistics, etc.

## 6.4. Formal scientific fields

The title „formal“ relates to the fact these fields use formal language (symbols, icons) in their expressions. They belong to supporting fields in the sense they support cognitive activities in the basic as well as in man-constituted branches; these scientific fields are general, applicable in all branches. This category comprehends mathematics (the language of natural and social sciences) and logics (the language of all sciences, but especially humanities). Mathematics and logics are also denoted as abstract sciences. Philosophy plays also the role of a supporting science partially, it can be understood as a methodological and critical basis of the other fields or as integration of all specialized fields and branches (theory of science).

## 6.5. Complementary scientific fields

These scientific fields complement not only the above mentioned categories of sciences, but various other professional activities as well. The following scientific branches can be included into this group: geodesy and cartography, environmentalism, technology of measuring and illumination, information systems, technical cybernetics, forensic engineering, technology of wood processing, amelioration of waters (flood protection, morphology and regulation of rivers, lakes).

Naturally, the grade of importance and scientific significance  $m_v$  of new pieces of knowledge acquired in all the listed branches is very different, higher or lower. It is extremely difficult to define the scale between more and less scientific, the authors have no ambition to be arbiters in this sense. A strict division by an exactly defined boundary line is probably even not possible.

All of the listed scientific fields, basic ones as well as man-constituted, formal and complementary, belong to concrete scientific branches.

## 7. Characteristics of scientific activities – what is scientific?

The comprehensive characteristic of science presented in chapter 3 has been created with the following aims:

- ① To offer an understandable characteristic of science, formulated with a commonly used terminology, to most individuals from all of the above scientific branches, except for „philosophers of science“.
- ② To formulate general characteristics of scientific activities. They are important for making decisions what activities and corresponding branches can be considered to be scientific. And similarly, what of them are not scientific.
- ③ To formulate characteristics of scientific pieces of knowledge. They are important for making decisions whether a certain paper (a written description of methods and results of some cognitive processes) can be considered to be scientific or not.

### 7.1. Characteristics of scientific activities

The characteristics of scientific activities (processes) defined below are based on the definition of the science in chapter 3. These characteristics can represent „*attributes of scientific activities*“:

#### Basic characteristics of a scientific activity

- ① A scientific activity is a predominantly durable, targeted, structured, organized, individual or collective activity, having a form of investigation and cognition.
- ② A necessary condition of a scientific activity is its **actual novelty** in the sense of:
  - + acquiring of a **novel piece of knowledge** (a primary piece of knowledge at the given time)
  - + **completion** of an existing knowledge with **new facts**.
- ③ **Targeted motivation** for a creative seeking for new pieces of knowledge.
- ④ Application of the **scientific methodology** in the investigation; this can be the systemic methodology.
- ⑤ **Verity** of the acquired piece of knowledge confirmed by testing processes, or a scientific hypothesis including ideas about testing procedures and ways of their realization.
- ⑥ **Reproducibility** of the results of cognitive process.
- ⑦ **Approval of the** (scientific-ethic and imaginative) **community of scientists** that the investigative processes or their results in the form of pieces of knowledge can be considered to be scientific.

### 7.2. What is not a scientific activity

It is extremely important to answer this question because persons being in positions of reviewers of any scientific papers, theses, projects or other written outputs need to deal with it; it concerns proposals of grant projects, evaluation of their partial or terminal reports, as well as dissertation, doctoral or habilitation theses.

A general answer to the question in the headline is very simple:

**A sufficient condition for an activity not to be scientific is violence of anyone of the characteristics of the scientific activities.**

In the end, the individual „attributes of non-scientific activities“ should be defined exactly. This has been done by negating the „attributes of scientific activities“ in the previous chapter:



### Attributes of non-scientific activities

- ① The activity does **not contain the element** of „actual novelty“, namely it does not develop the existing knowledge in any way.
- ② There is **no targeted motivation of seeking for „something novel“**; seek for novel pieces of knowledge is not the primary goal of the activity.
- ③ **Scientific methodology is not used** in the activities.
- ④ The activities **do not aim at verification** of the achieved results; either the hypothesis does not contain the way how to verify them or the piece of knowledge is not verified at all.
- ⑤ **Activities are non-reproducible.**
- ⑥ The „**community of scientist does not consider**“ the concerned activities to be scientific.

*Note: Consiously the first paragraph of the characteristics of scientific activities was not negated. It describes their properties, that these activities are durable, targeted, structured, organized, etc. However, it cannot be excluded that a knew piece of knowledge may be acquired by an impulsive one time cognitive activity; also this activity need not to be targeted in respect to the new piece of knowledge, because this may be acquired within the framework of a differently targeted activity as well.*

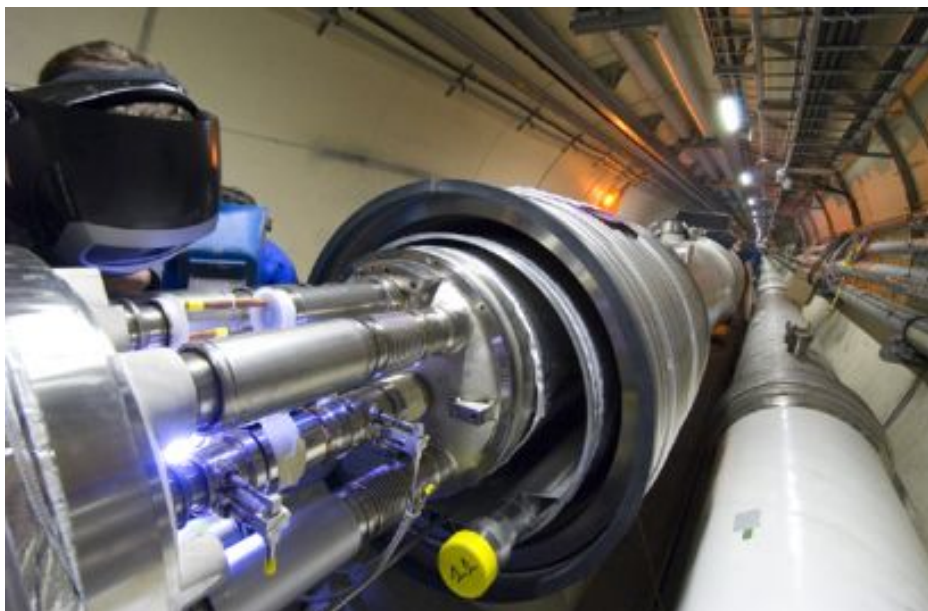


Photo : LHC in CERN ([www.ct24.cz](http://www.ct24.cz)).

## 8. Conclusion

The proposed attributes of scientific activities should not be considered as complete in terms of content and precise scientific terminology. This paper should be considered as an opening of discussion on the issues of scientific activities.

## References

- Smolin, L. (2006) The Trouble with Physics, Spin Networks, Ltd.
- Feyerabend, P. K. (1980) Against method. Verso, London.
- Špála, M. (2006) O vědě a výzkumu do začátku studia. Univerzita Karlova, 1. L.F., Prague (in Czech).
- Fajkus, B. (2005) Filosofie a metodologie vědy. Academia, Prague (in Czech).
- Marshack, A. (1972) The Roots of Civilisation. Weidenfeld and Nicolson.
- Janiček, P. (2007) Systémové pojetí vybraných oborů pro techniky; hledání souvislostí, I. a II. díl, CERM, VUTIU, Brno, (in Czech).

## DEVELOPMENT OF MATHEMATICAL MODEL OF THE HYDRAULIC DAMPER

J. Šklíba<sup>\*</sup>, R. Svoboda<sup>\*\*</sup>

**Abstract:** *The physical model of two cylinder hydraulic damper is composed from several groups of equations, which describe: a) the dynamic equilibrium of the forces loading the valves, b) the dynamic equilibrium of volume flows in the working spaces of the damper, c) equation of the state of the air in the accumulator, d) the dependencies of discharge coefficient on Reynolds number, e) the dependency of hydraulic capacity on the concentration of free air in the working liquid. According to a number of places in which is the pleasure concentrated, we have models with three, five or seven pressures. It is described and commented the development of physical model and its precising.*

**Keywords:** *Hydraulic damper, damper valves, free air in working liquid, volume flow, discharge coefficient.*

### 1. Introduction

At present types of dampers with a two-phase working liquid consisting of oil and air with the possibility of developing steam and gas cavern located under and above the piston are used on a regular basis. These types reflect reality much better. The original assumption of an ideal oil-based working liquid with no other ingredients surely did not correspond with reality as there is always at least minimal amount of air present, and can therefore be released from as well as dissolved in the liquid. Some working liquids create so called steam cavern during the work cycle. This means that in case of drop of pressure to the value of saturated vapor  $P_n$  a bar of saturated vapor is created while the pressure remains constant. If afterwards the pressure has a tendency to increase, first the vapor is condensed at pressure  $P = P_n$ , and only after its condensation will the pressure increase. Other working liquids, such as Czech damper oils, do not develop a steam cavern; however, under certain conditions, they can release dissolved air in form of bubbles of different sizes. This is also the case of working liquid becoming lacteous immediately after the beginning of a working cycle.

As a matter of fact, the concentration of air dissolved in oil changes dramatically (especially upon the flow through valves) during the whole working cycle, which comparatively alters the physical parameters of the working medium. Depending on actual operational conditions, especially pressure and temperature, the air in some areas of the damper dissolves and is released from the oil at the same time. It is not yet possible to describe this dynamic process of gradual dissolving and re-release of air from the oil at full length.

For these reasons, the dynamic process of dissolving and releasing air in oil is at least approximately replaced with the assumption of constant level of air concentration stabilized after certain time of the damper operation. A model of damper specified like this works similarly as the original model with the only difference that instead of ideal one-time liquid as the working medium, the two-phase liquid with invariable ratio of oil and dissolved air is used, which resembles the reality much more. Nonetheless, it was not possible to accept the calculation processes and equations derived from the original models without any change, only with specified physical parameters of the mixture instead of pure oil. It was necessary to modify them with regards to retaining the physical principles valid for the intended working medium; in addition, it was necessary to include the description of dynamics (of development and disappearance) of the steam and air cavern.

---

<sup>\*</sup> prof. RNDr. Jan Šklíba, CSc.: Faculty of Mechanical Engineering, Technical University of Liberec, Studentská 2; 461 17, Liberec; CZ, e-mail: jan.skliba@tul.cz

<sup>\*\*</sup> RNDr. Rudolf Svoboda, CSc.: Techlab s.r.o.; Sokolovská 207; 190 00, Praha 9; CZ, e-mail: svobodaru@techlab.cz

## 2. Two-phase working liquid with constant air concentration in oil

As it has already been stated, the real working liquid (oil) always contains certain amount of air, either in form of bubbles, or air dissolved in liquid. As the amount and form of air contained in oil changes the physical qualities of the working medium fundamentally, it is not possible to neglect this fact during the construction of the dasher model (Šklíba, 2007). In equations of the model of dasher, compressibility plays a crucial role. While the compressibility of mixture depends mainly on the volume of free air contained in oil in form of bubbles, air dissolved in oil (i.e. air bound to the molecules of oil) changes the compressibility only minimally.

Unfortunately, the ratio of free and bound air in oil does not remain stable, but it changes dynamically during the whole working cycle. Depending on actual operational conditions, namely pressure and temperature, the air keeps dissolving as well as releasing from oil continuously in areas of damper. The most significant changes are located in areas with the biggest pressure and temperature gradients, especially when flowing through valves and other constricting elements. That means that the concentration of air is time- and space-dependent within individual areas of the damper, and it is different in each area of the damper.

In case of a mixture with non-zero concentrations of free air, the equilibrium of volume flows cannot be used to deduce the total of volume flow. The mixture of oil and air is compressible, the density depends on the pressure, and the incoming volumetric stream flowing through a constricting element to the area with lower pressure is increasing to outgoing stream (the bubbles contained in oil expand in an area with lower pressure). Therefore, it is necessary to replace the equilibrium of volume flows with the condition of equilibrium of mass flows, which now expresses the principle of matter conservation:

„The sum of all mass flows between areas of the damper is equal to zero“. To be specific, it means that we deduct the mass flow flowing from area  $y$  to area  $k$  from the total mass of medium contained in area  $j$ -X, and we add the same value to the mass of medium  $i$  area  $k$ . As for the oil without air bubbles, i.e. with zero concentration  $K_m = 0$ , the condition of equilibrium of mass flows is equivalent to the condition of equilibrium of volume flows, and the equation of equilibrium operating with mass flows of mixture  $Q_m$  can be replaced by the original equation of a damper with oil filling.

The present standard dynamic model of hydraulic damper deals with pressures concentrated into three regions ( regions above the piston, under the piston and the accumulator). This model consists of systems of differential equations describing equations of motion of valves, dynamic balance of flows in the damper, evolving and dissolving of columns of saturated vapors and algebraic equations describing dependence of discharge coefficients of flows on corresponding Reynolds numbers.

The precise model of hydraulic damper deals with pressures concentrated into seven regions. In this model the flows through valves are modeled more precisely and pressure gradients in supply channels are respected for all four valves.

For both standard and precise models the flows among regions of the damper are supposed to be one-dimensional, the liquid is compressible, in the state of unsaturated solution (it does not contain free air), viscose. The columns of liquid are described by concentric parameters.

## 3. Dynamic model of the double-tube car damper

System of equations of hydraulic damper model (Šklíba, 2006) with pressures concentrated into three regions represents:

### *a) Dynamic balance of streams in the regions of damper (for three-pressure model)*

Let  $W_i$ ,  $i = 1, 2, 3$  designates volume flows and changes of volume caused by movements of piston, outer cylinder and valve (index 1, 2, 3 corresponds to the regions above the piston, under the piston and in the accumulator). For  $W_i > 0$  the stream flows into the region resp. volume of the region decreases, for  $W_i < 0$  the stream flows out of the region resp. volume of the region grows.

When no column of saturated vapor exists (the region is full of liquid) and the pressure does not fall under the level of saturated vapor pressure  $P_{np}$ , it holds



$$C_i \cdot \dot{P}_i = W_i, \quad \dot{V}_{pi} = 0, \quad i = 1, 2, \quad P_i \geq P_{np} \text{ and } V_{pi} = 0. \quad (1)$$

When the pressure falls down the level of saturated vapor pressure or the column of saturated vapor is developed, the pressure remains constant and the volume of column of saturated vapors changes:

$$\dot{P}_i = 0, \quad \dot{V}_{pi} = -W_i, \quad i = 1, 2, \quad P_i < P_{np} \text{ or } V_{pi} > 0. \quad (2)$$

The pressure  $P_3$  in the accumulator is given by equation

$$(C_3 + V_{V3} / P_3) \cdot \dot{P}_3 = W_3, \quad (3)$$

where  $V_{B3}$  is volume of the air in the accumulator. Hydraulic capacities  $C_{ki}$  are given by relations

$$C_{k1} = -(V_{10} - (S - S_0) \cdot y(t)) \cdot (E_k + E_{kp} P_1)^{-1} \quad (4)$$

$$C_{k2} = -(V_{20} - S \cdot y(t)) \cdot (E_k + E_{kp} P_2)^{-1} \quad (5)$$

$$C_{k3} = V_{30} \cdot (E_k + E_{kp} P_3)^{-1}$$

and resulting volume flows  $W_i$  by formulas

$$\begin{aligned} W_1 &= Q_{12} - Q_{21} + Q_{13} - (S - S_0) \cdot \dot{y}(t) - S_{21} \dot{x}_2 + S_{11} \dot{x}_1, \\ W_2 &= -Q_{12} + Q_{21} - Q_{23} + Q_{32} + S \cdot \dot{y}(t) - S_3 \dot{x}_3 - S_{11} \dot{x}_1 + S_4 \dot{x}_4 + S_{21} \dot{x}_2 \\ W_3 &= Q_{23} - Q_{32} + Q_{13} - S_4 \dot{x}_4 + S_3 \dot{x}_3 - S_a \dot{x}_6 \end{aligned} \quad (6)$$

when the working liquid is a mixture of oil and of a free air, we introduce  $V_{Vi}$  stands for volumes of the free air in the mixture.

$$\begin{aligned} \left( C_{ki} + \frac{V_{Vi}}{P_i} \right) \dot{P}_i &= W_i, \quad i = 1, 2 \\ \left( C_{k3} + \frac{V_{V3} + V_{B3}}{P_3} \right) \dot{P}_3 &= W_3 \end{aligned} \quad (7)$$

Quantity  $Q_{ij}(i \neq j)$  represents the total stream flowing from  $i$ -th to  $j$ -th region. The resulting flows  $Q_{ij}$  are further branched to the single flows through valves, calibrated orifices and parasitic flows through different leaks, for instance

$K(P_i - P_j)$  parasitic flow through the piston in the working cylinder,

$\alpha_0 K_1 \sqrt{P_1 - P_2}$  or  $\alpha'_0 K_1 \sqrt{P_2 - P_1}$  flow through the calibrated valve orifices,

$\alpha_1 k_1 x_1 \sqrt{P_1 - P_2}$  or  $\alpha_2 k_2 x_2 \sqrt{P_2 - P_1}$  flow through the valve gaps, and so on.

For instance the resulting flow  $\tilde{Q}_{21}$  flowing through the discharge valve is given by relations

$$\begin{aligned} \tilde{Q}_{21} &= 0, & P_2 &\leq P_1 \\ &= K(P_2 - P_1) + \alpha'_0 K_1 \sqrt{P_2 - P_1}, & P_2 &> P_1, \quad x_2 < 0 \\ &= K(P_2 - P_1) + (\alpha'_0 K_1 + k_2 \alpha_2 x_2) \sqrt{P_2 - P_1}, & P_2 &> P_1, \quad 0 \leq x_2 \leq x_{2\alpha} \\ &= K(P_2 - P_1) + (\alpha'_0 K_1 + k_2 \alpha_2 x_{2\alpha}) \sqrt{P_2 - P_1}, & P_2 &> P_1, \quad x_2 > x_{2\alpha} \end{aligned} \quad (8)$$

Similar equations hold for remaining three valves.

#### **b) State equation of the gas in the accumulator**

$$V_b = (V_{0a} - V_{30} - F_a x_b) = \Phi(n, P_3, T) \quad (9)$$

**c) Dependence of discharge coefficients of flows** (Šklíba, 2005, 2004) through valves  $\alpha_i$  ( $i=1, \dots, 4$ ) and calibrated piston orifices  $\alpha_5, \alpha_6$  on corresponding Reynolds numbers

$$\alpha_i = \alpha_{i00} + \alpha_{i0}(1 - \exp(-\alpha_{li} \text{Re}_i)), \quad \text{where} \quad \text{Re}_i = \frac{2Q_{vi}}{\pi d_{Hi} \nu} \quad (10)$$

and  $Q_{Vi}$  represent flows through valves or calibrated orifices with hydraulic diameter  $b_{Vi}$

**d) Dynamic balance of forces on valves** (see Figs. 1 and 2)

$$m_k (\ddot{x}_k - \ddot{y}(t)) \cdot (-1)^{k+1} + \delta_k \dot{x}_k + c_k (x_k + x_{kp}) + \tilde{Z}_k = (F_{k1} P_1 - F_{k2} P_2) \cdot (-1)^{k+1} \quad (11)$$

$$\tilde{Z}_k = \tilde{Z}_k(x_k, \dot{x}_k, \ddot{x}_k, \alpha_k, (P_1 - P_2) \cdot (-1)^{k+1}, L_k), \quad k=1,2, \quad x_k \geq 0 \quad (12)$$

$$\tilde{Z}_k = \delta_{0k} \dot{x}_k + c_k^* x_k, \quad k=1,2, \quad x_k < 0 \quad (13)$$

$$m_k \ddot{x}_k + \delta_k \dot{x}_k + c_k (x_k + x_{kp}) + \tilde{Z}_k = (F_{k1} P_3 - F_{k2} P_2) \cdot (-1)^{k+1} \quad (14)$$

$$\tilde{Z}_k = \tilde{Z}_k(x_k, \dot{x}_k, \ddot{x}_k, \alpha_k, (P_3 - P_2) \cdot (-1)^{k+1}, L_k), \quad k=3,4, \quad x_k \geq 0 \quad (15)$$

$$\tilde{Z}_k = \delta_{0k} \dot{x}_k + c_k^* x_k, \quad m_k = m_{kv} + 0.33 \cdot m_{prk} + \rho S_k L_k, \quad k=3,4, \quad x_k < 0 \quad (16)$$

where  $\tilde{Z}_i, i=1,...,4$  represent the hydrodynamic forces in case of open valve and the resistance valve seat forces in case of closed valve. Starting from the general relation and substituting relation for the space flow through the throttled valve slot we obtain the following expression for the hydrodynamic force (often called the Bernoulli force too) which acts on the plate valve (other types of valves are usually not used for hydraulic dampers - see Šklíba, 2004)

$$\tilde{Z} = \alpha^2 \sum_{i=1}^2 \sigma_{i0} x^i \cdot \Delta P + \alpha \sum_{i=0}^1 \gamma_{i0} x^i (\Delta P)^{\frac{1}{2}} \cdot \dot{x} + \rho S L \ddot{x} \quad (17)$$

where  $\alpha$  is discharge flow coefficient,  $x$  is valve stroke,  $S$  sign front area of the valve. The first member in the relation represents the stationary force component acting as a non-linear reverse spring, the second represents a non-stationary component acting as a non-linear damping force and the third member represents inertia forces of the mass of liquid included in so called ‘damping space’ – this mass is added to the mass of the valve and to the reduced mass of the valve spring.

The standard dynamic model of hydraulic damper consists therefore of four non-linear differential equations of the second order and five non-linear differential equations of the first order, completed with seven algebraic equations. The system is of thirteenth order.

Differential equations for each valve, which describe pressure and flow through the supply channels, are added to the precise model. The state vector of the precise model consists therefore of twenty one components.

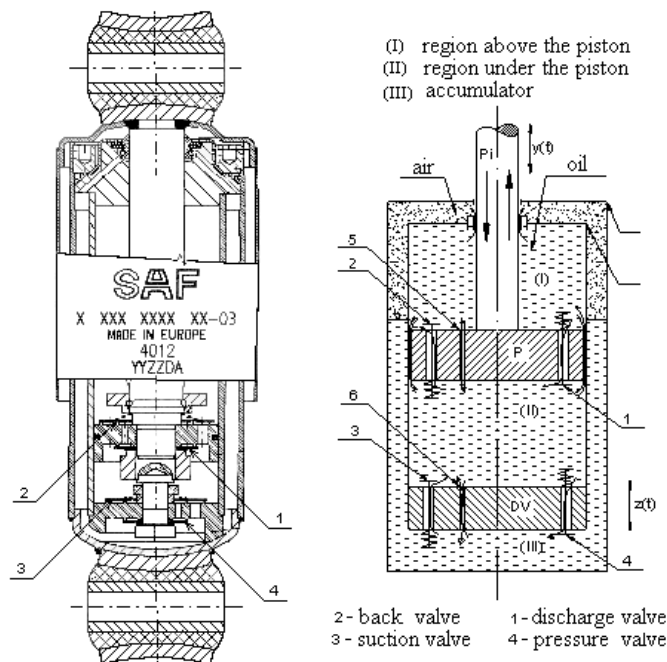


Fig. 1: Scheme of two-cylinder hydraulic damper.

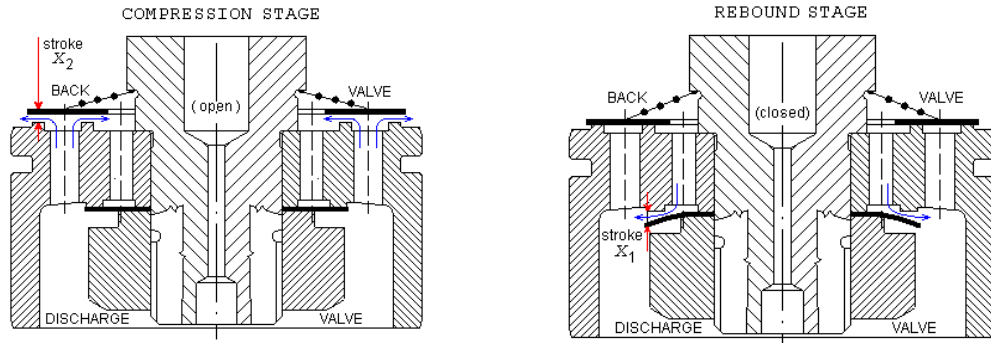


Fig. 2: Function of the valves in the piston – compression (left) and rebound (right).

As it has been stated above, we imagine the mixture in the areas above and under the piston as formally divided in liquid and gas component. The mass concentration of the mixture  $K_m$  remains the same, so there will be the same mass ratio of oil and air in areas above and under the piston regardless of the current values of pressure and volume of the mixture; the only thing that changes in dependence on pressure is the ratio of oil and air volumes in these areas. The situation in an accumulator is rather more difficult, as there is not only a stable bar of free air (that is considered neither to dissolve in oil nor to pass from other areas of the damper), but also a bar of bound air in the mixture, which has already been in the accumulator, or which has entered through two valves in the bottom of the cylinder.

During the working cycle both the oil volumes and the volumes of air contained in the mixture change dynamically in areas above and under the piston. As for the damper with oil filling, the change of pressures was calculated from the total change of volumes and volume flows and from the hydraulic capacity of oil in a given area. However, we must also take into account the changes of air volumes in the area for the damper with mixture of oil. The pressures in areas above and under the piston will therefore be determined by the equations where the term in the denominator represents a sort of „hydraulic capacity“ of the mixture in the given area.

The relief and discharge valve are not considered as separate components as in the quasistatic model; they are rather considered as compound hydraulic components created by the combination of parallel and serial intake canals, calibrated orifices, and a volume of the pre-stressed springs, that is the elementary hydraulic components forming the valve set between two areas of the damper.

#### 4. Issues of stability of the dynamic model of the damper

Fig. 3 shows calculated characteristics of one valve set of a damper with different (initial) volume concentrations of free air in oil. It is evident that with increasing concentration of free air, the rate of the power growth (initially jump) is decreasing significantly in both areas of transitions of the compression and expansion phases. At higher concentrations, however, the characteristics appear to be influenced negatively by the self-excited oscillation.

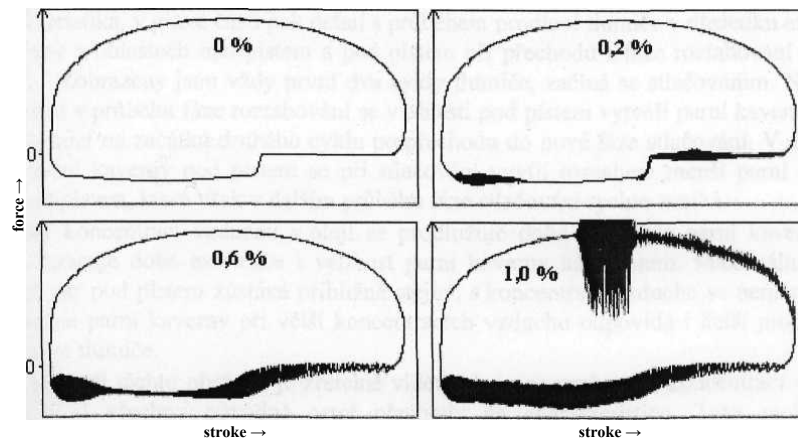


Fig. 3: Characteristics of the damper at different volume concentrations of air in oil.

There can be three kinds of origin of the self-excited oscillation (Šklíba, 2005) on the calculated characteristics:

- It is a fictitious self-excited oscillation caused by faulty numerical integration of the damper equations; then, it is necessary to find a more suitable integration method.
- Self-excited oscillation is a feature of the mathematical model of the damper, but in fact it does not happen; then, it is necessary to adjust/generalize the model of the damper.
- Self-excited oscillation really happens in an existing damper.

Along with numerical integration (and independently on it), complex proper values of linearized system of equations of the damper are calculated (real part of the proper value represents the damping, imaginary part indicates natural frequency).

As it is known from the theory of differential equations, the system is stable if all proper values are damped, i.e. if their real parts are negative. If at least one proper value has a positive real part, the system is unstable, and self-excited oscillation will occur with a frequency corresponding to the frequency of the unstable proper value. This situation agrees with the numerical calculations of self-excited oscillation of the damper exactly. The self-excited oscillation starts to evolve/disappear on the characteristics at the moment when the damping of the proper value changes the sign from negative to positive values, respectively from positive to negative. At that, the natural frequency, deducted from the calculated development of self-excited oscillation, matches the calculated natural frequency – imaginary part of the proper value exactly.

The formulas imply high dependence of stable qualities of the valve subsystem on the modulus of elasticity of the working medium. It is not possible to describe the damper as a whole analytically; however, it is reasonable to assume that a quantity that has a significant impact on the properties of all four valves as basic subsystems of the damper will have a vital influence on the dynamics of the damper as a whole. Exactly the same situation occurs at the calculations of a damper with two-phase liquid with constant concentration of air in oil. Because of the volume of free air in oil, the compressibility of the mixture increases sharply, i.e. its modulus of elasticity  $E$  decreases. The result is a dramatic deterioration of the stability properties, the higher is the concentration of air in oil, the worse are the stability properties of the model. The damping effects of the flows from the valves motion are not sufficient to compensate for the negative impact of significantly higher compressibility of oil with free air added.

Data for “whistling” dampers, in which the self-excited oscillation occurs during operation, could not be gained, so for this reason, there is no comparison with the calculation. So far, all previous experience with calculations of K50 damper (see Figs. 4a and 4b) and dampers of other types suggests that the origin of calculated self-excited oscillation is to be found in the imperfections of the existing dynamic model of damper, especially in the description (model) of the real working fluid mixed with air.

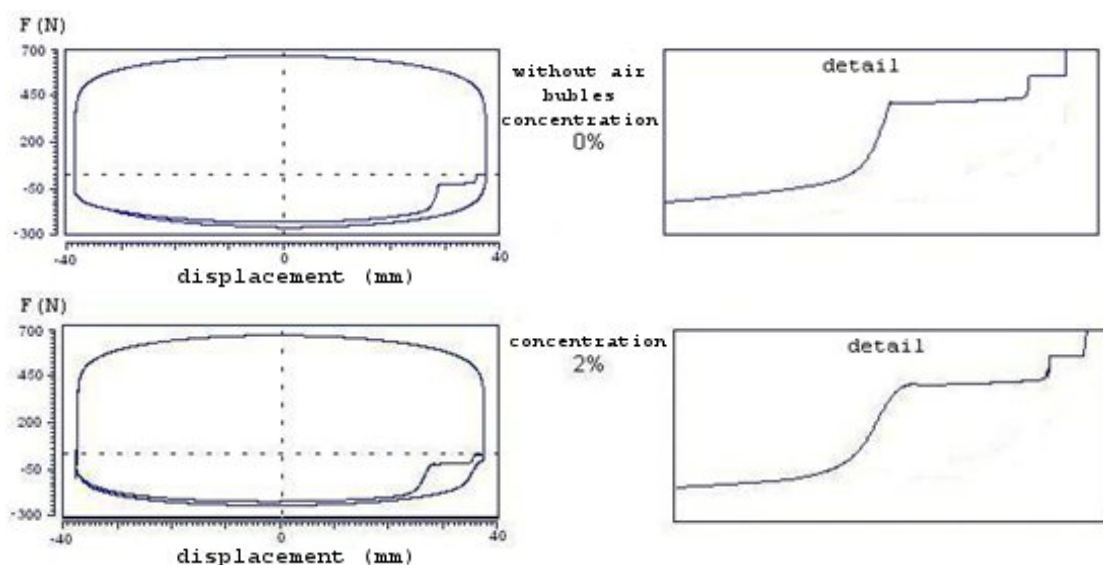


Fig 4a: The influence of the concentration of free air in the working liquid.

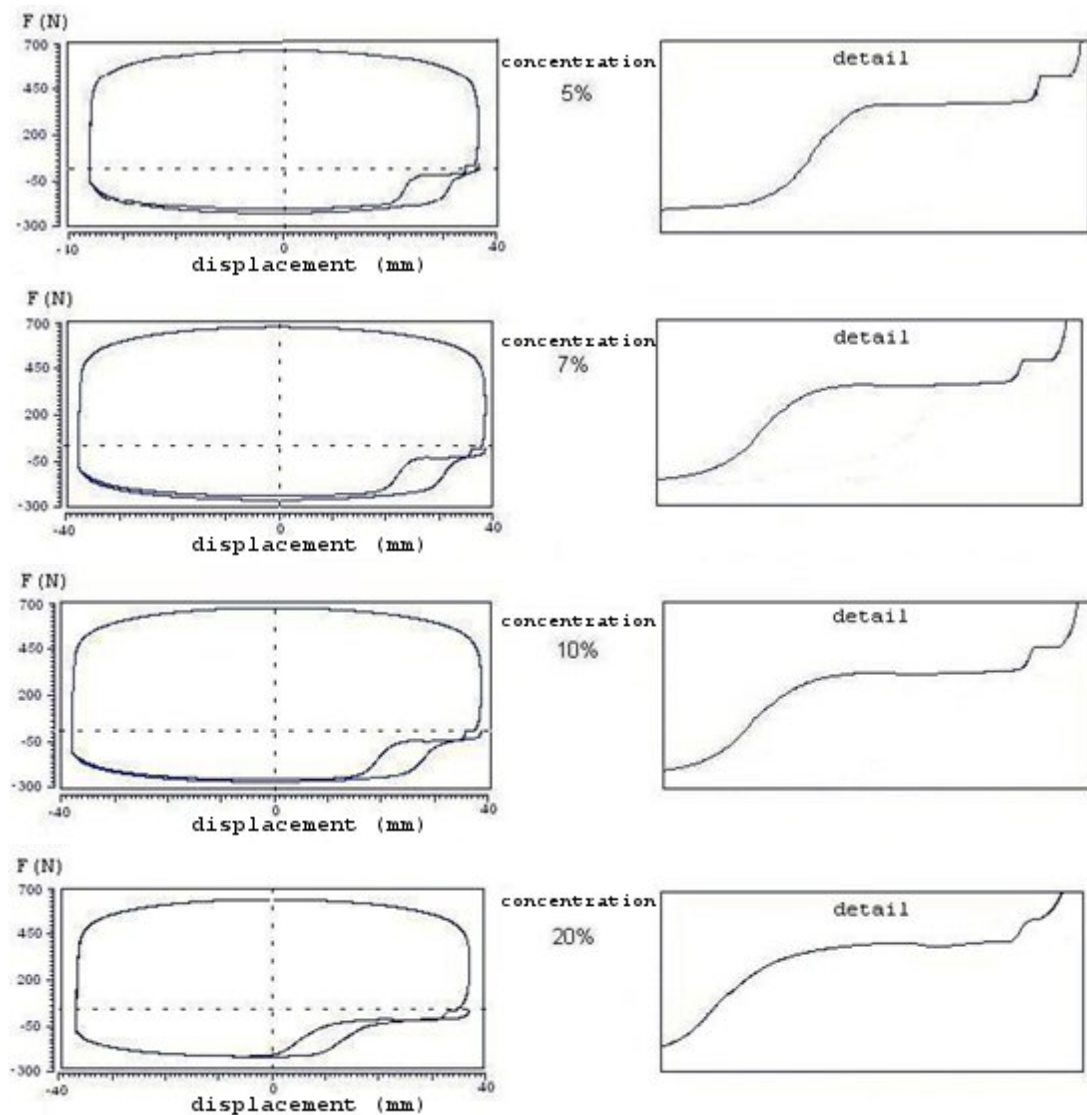


Fig. 4b: The influence of the concentration of free air in the working liquid.

## 5. Preparation of the model with a variable concentration of free air

The research will cover either the theoretic or the experimental part: the researchers' workplace is equipped with a system capable to detect either cavitation cores or dynamic impacts of cavitation directly. Cavitation is detected by ABS (Acoustic bubble spectrometer), which is an acoustic apparatus permitting by means of two piezoelectric converters to evaluate the quantity and size of cavitation bubbles in the volume between the two converters.

Apertures situated on the low-pressure part also allow to detect cavitation optically. The lighting is realized through ND-Yag continuous laser. The chamber is also adapted to install a PVDF hydrophone, which permits the detection of acoustic manifestations.

The results from measuring the quantity and size of bubbles at various work cycles (the rate of flow, the pressure at the entrance and the setting of the choke element will be modified) will be handed over to the Institute of Thermomechanics of the Academy of Sciences of the Czech Republic.

The expansion and compression velocity are then the guiding parameters capable to determine the real elastic and viscose properties of such mixture. The results will be handed over to Technical University of Liberec, where at the end; they will be included into a mathematic model of a damper.

As first approach the state behaviour may be interpolated as a mixture of liquid substances (oils) at the equilibrium with properties resembling oily foams. Then to depict the meta-steady behaviour of air saturated oil is necessary to know its state behaviour at the equilibrium. To describe this interaction,

chemical potential would be the primary dimension. Considering that a real liquid (oil) is taken in account, it will be necessary to know the activity, or the fugacity coefficients. These coefficients put real measured values and concentration in relation to values of pressures-fugacity as well as concentration-activity to define the chemical potential. The so defined chemical potential may be utilized for serious thermodynamic analysis. The fugacity and activity are mainly influenced by gases solubility, i.e. a precise value of Henry's constant and liquid surface tension. Utilizing the 1<sup>st</sup> transition theory of phase taking into account the high dependence of Henry's constant to temperature and the surface tension influenced by temperature and chemical composition (the so called Gibbs isotherm) it is possible to formulate the thermo-physical properties of two-phase mixtures in meta-stable state either.

The given project assumes that to measure gases solubility (precisely air) in hydraulic oils, in the range of at least 10 to 80°C and pressure between 0.1 – 5 MPa, equipment should be assembled. Such device is assumed to be more or less universal and with subtle modifications would allow measurements based on saturation or extraction principles, to determine the amount of dissolved gas at constant pressure as well as volume. It is also assumed that in the future this apparatus allows studying gases solubility in new materials such as ion liquids, which properties (thermal stability, non-flammability, and volatility) might be potentially suitable as hydraulic liquids. The results from measuring steady states, relevant Henry's constants, coefficients of activity and fugacity, elaborated in Institute of Chemical Technology Prague will be handed over to the Institute of Thermomechanics of the Academy of Sciences of the Czech Republic.

## 6. Conclusions

From the analyze of the executed models it follows that the prepared model with variable concentration of free air in the working liquid represents a qualitative improvement. The introduction of global and local temperatures will be necessary. This model will be multidisciplinary and its composition claims a cooperation of several research workplaces.

## Acknowledgement

The research has been supported by project MSM 4674788501 "Optimalizace vlastností strojů v interakci s pracovními procesy a člověkem".

## References

- Šklíba, J. & Svoboda, R. (2006) Model hydraulického tlumiče se vzduchovými a parními kavernami. Proc. Of Conference Engineering Mechanics 2006, Svratka, pp. 342-343.
- Šklíba, J. & Svoboda, R. (2007) On the problem of dependence of damper force on the concentration of free air in working liquid. Springer proceedings in physics, Vibrations problems.
- Šklíba, J. & Svoboda, R. (2005) Self-excited valve oscillations in a model of hydraulic damper. Vibroengineering 2006, proceedings of the 6th international conference, Lithuania, pp. 230-233.
- Šklíba, J., Svoboda, R. & Matějec, R. (2005) Specification of flow conditions in the mathematical model of hydraulic damper. Vibrations problems ICOVP 2005, pp. 455-461.
- Šklíba, J., Zúbek, T. & Matějec, R. (2004) Specification Experimentální výzkum charakteristik odlehčovacího ventilu teleskopického tlumiče včetně přírodních kanálů. Interakce a zpětné vazby, Praha, pp. 79-86.

# P A P E R S





## CALCULATION STUDY OF STEAM FLOW THROUGH A CONTROL VALVE

L. Bednář<sup>\*</sup>, L. Tajč<sup>\*</sup>, L. Jirka<sup>\*</sup>

**Abstract:** Outcomes of a numerical simulation of flow through an unbalanced control valve during the turbine's operational modes. A 2D as well as a 3D calculation study is considered. Effect of a protective screen on aerodynamic conditions inside the valve is modeled. Distribution of velocity and pressures in the diffuser is determined. Pressures affecting the valve cone are described.

**Keywords:** Steam turbine, control valve.

### 1. Introduction

Control valves adjust the required output of the turbine by means of the mass flow and admission steam pressure before the turbine. Unbalanced valves have been adequately tested in practical applications. In the course of time, a flat-bottomed valve cone has become established. A valve of this type, however, has never been used for turbines because of the supercritical steam parameters. The calculation study is to evaluate aerodynamic characteristics affecting the valve cone and the output pipe under extreme temperatures and pressures. An effect of the screen and the entry angle of flow rotation on distribution of the velocity and pressures in the space under the valve cone can also be considered. This presentation summarizes outcomes of a numerical simulation of steam flow through the valve (Jirka, 2007).

### 2. Calculation model of the control valve

A cross-section of the control valve is illustrated in Fig. 1. The valve is equipped with a protective screen of a cylindrical shape made of metal sheeting, perforated with approximately one thousand small round apertures. In its bottom section, channels are milled under 45°. These apertures spin a part of the admission steam. It is supposed that the rotation of the flow helps stabilize the flow under the valve cone and equalize pressure fields, thus reducing the pipe's vibrations. The valve stem is terminated with a flat-bottomed cone and a punch. The input section consists of a cone with the apex angle of  $\alpha = 60^\circ$ , the output diffuser has a 7° enlargement. The cone, together with the cone seating, forms a nozzle with jump enlargement. The sudden enlargement of the profile stabilizes the flow-separation effect from the cone's surface. This conception is required especially when the valve is only partly open and the pressure ratios are high. Step changes of pressure in impact waves then occur in lower Mach number values. The total pressure on the input  $p_{1c} = 27.18$  MPa and the total temperature on the input  $T_{1c} = 868.15$  K. The extent of the calculated alternatives is illustrated in Tab. 1.

Tab. 1: The extent of the calculated alternatives.

Name	Marking	Extent			
Relative lift	$\bar{h} = h/D$	0.15	0.3	0.4; 0.45	$h \dots$ the cone's lift
Pressure ratio	$\varepsilon = p_3/p_{1c}$	0.955 ÷ 0.965	0.88 ÷ 0.99	0.98 ÷ 0.999	$D \dots$ diffuser's throat diameter
					$p_3 \dots$ pressure behind the diffuser

<sup>\*</sup> Ing. Lukáš Bednář, Ing. Ladislav Jirka and Ing. Ladislav Tajč, CSc.: ŠKODA POWER s. r. o., Tylova 1/57, 301 28 Plzeň; CZ, e-mails: lukas.bednar@doosan.com, ladislav.jirka@doosan.com, ladislav.tajc@doosan.com

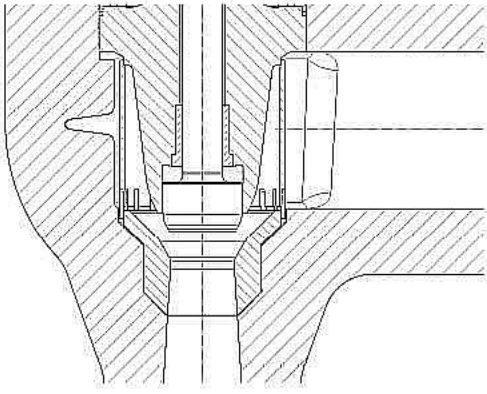


*Fig. 1: Cross-section detail of the control valve.*

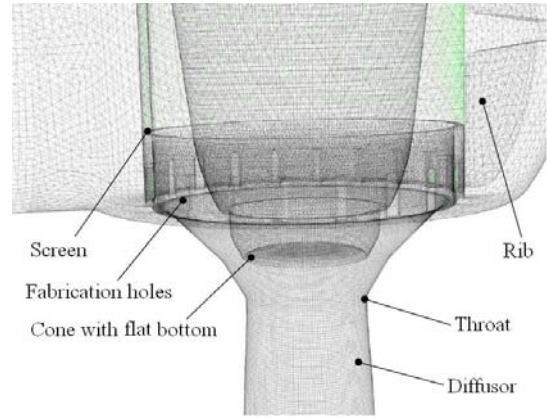


*Fig. 2: Detail of important sections of the valve in a 3D model.*

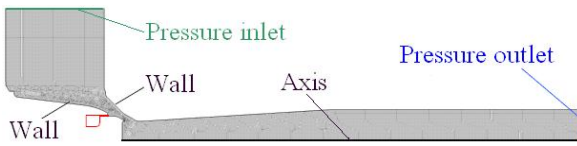


*Fig. 3: 2D grid of the axially symmetric model with specified boundary conditions.*



*Fig. 4: 2D grid of the axially symmetric model with specified boundary condition on the input.*

Two grid alternatives were used for the 2D calculation. They are illustrated in Figures 3 and 4. In the first grid alternative, the protective screen was not modeled. The flow rotation was specified for the entire input diameter. Four deviations from the radial direction were selected, i.e.  $0^\circ$ ,  $15^\circ$ ,  $30^\circ$  and  $45^\circ$ . The second 2D grid (Fig. 4) contains the protective screen. The input section of the calculation grid was removed because the rotation adjustment for a porous boundary condition under the specified angle could not be preset. This is why the entry is moved to the screen area and is divided into two parts – the top section (pressure input 1) with radially drilled holes and the bottom (pressure input 2) with apertures for steam entry under different angles. Basic simplification of both grids regards axially symmetrical flow.

In creation of the 3D grid illustrated in Fig. 2, attention was paid to the highest possible shape identity with a real valve. Only the protective screen, which contains about one thousand perforations, was not modeled directly, but by means of a porous medium. This concerns an area where the pressure resistance of the medium flow increases. The bottom directional apertures were created directly. For the 3D model, only a calculation with relative lift was performed  $\bar{h} = 0.3$ . In the calculations, non-dimensional mass flow was considered  $q = \dot{m} / \dot{m}_{tkr}$ . The calculated mass flow  $\dot{m}$  refers to the critical mass flow  $\dot{m}_{tkr}$ . It is calculated for the flow area inside the diffuser throat.

### 3. Simulation on 2D axially symmetrical models

On the first 2D grid, stationary and non-stationary calculations with  $0^\circ$  diversions from the radial entry and stationary calculations with  $15^\circ$ ,  $30^\circ$  and  $45^\circ$  diversions from the radial entry were simulated. For the first mentioned alternative, a calculation both by application of ideal gas modification and the UDF function of Redlich-Kwong's equation was considered. On the second grid, only stationary calculations were simulated for the deviations of  $0^\circ$ ,  $15^\circ$ ,  $30^\circ$  and  $45^\circ$  from the radial entry on input 2. The flow characteristics for alternatives on the first grid are illustrated in Fig. 5 and for the second grid in Fig. 6.

It becomes clear that both grid alternatives show almost identical values. Pressure loss in the protective screen is negligible. Deviation of flow from the radial direction does not show visible differences in mass flows through the valve. It does not matter whether the rotation concerns the entire input area or just its section. Modeling of the real gas properties leads to a slight increase of steam

flow through the valve. Within the turbine's operational modes ( $\bar{h} = 0.3$  a  $q = 0.3$ ) this change will practically take no effect. At the turbine's full output, the pressure loss in the valve is lower than two percent. The simulation also proved that the stationary calculation practically does not differ from the non-stationary calculation. These findings, however, may not be true for short lifts of the valve cone, i.e. when transonic flow takes effect. This, however, was not tested in this case.

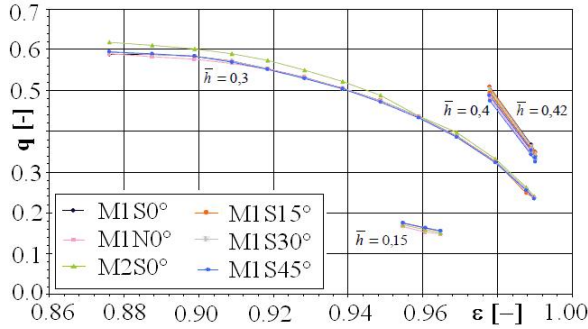


Fig. 5: Flow characteristics for options on the first 2D grid.

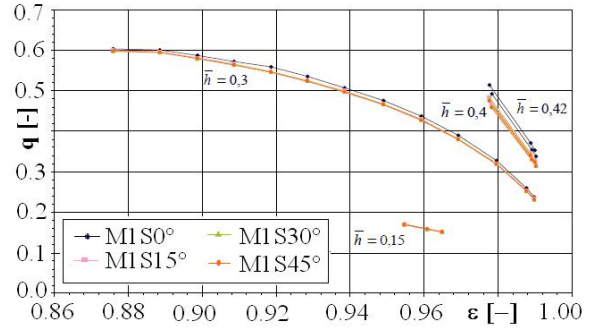


Fig. 6: Flow characteristics for options on the second 2D grid.

Fig. 7 illustrates velocity vectors in the diffuser under the valve cone. There is an area with back-flow immediately under the cone. The maximum velocity in the diffuser occurs in the vicinity of its wall. Alongside the flow, however, the velocity profile gradually becomes equalized (Fig. 8).

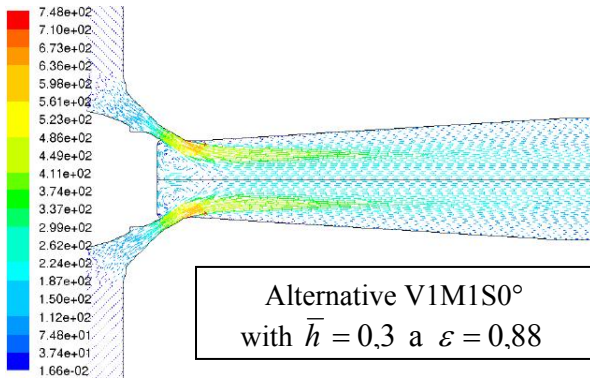


Fig. 7: Velocity vectors.

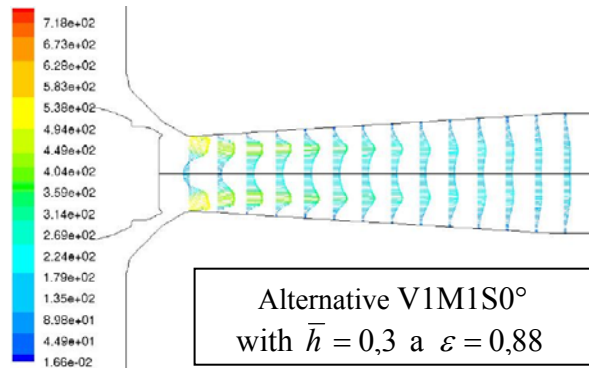


Fig. 8: Velocity profiles alongside the diffuser.

#### 4. Simulation on a 3D model

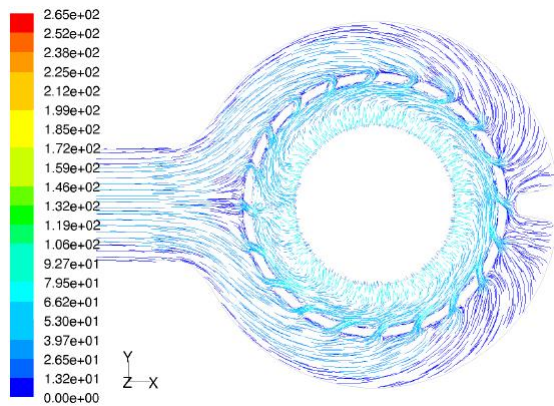


Fig. 9: Flow field in the half-point of the apertures' height;  $\varepsilon = 0.98$ .

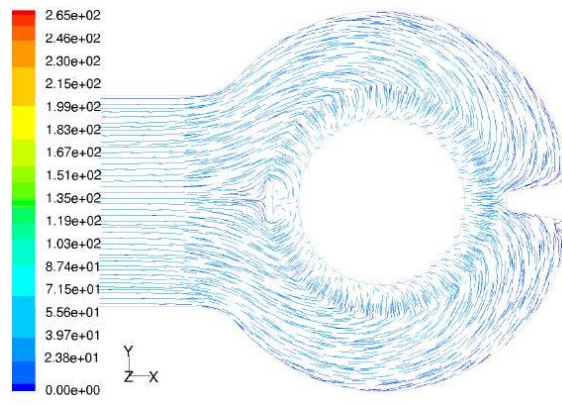


Fig. 10: Flow field in the area of circular apertures;  $\varepsilon = 0.98$ .

The model was created for the valve's relative lift  $\bar{h} = 0.3$  and stationary simulation for three pressure ratios 0.97, 0.98 and 0.99. For the 3D model, the relative mass flow through the valve results in a

lower value. This is caused by steam entry in one direction. It means that there are unbalanced conditions for steam entry through the directional apertures on the protective screen. The calculations prove that 79.5 per cent of the total mass flow runs through the porous zone of the screen in all the tested models. The rest flows through the directional apertures. An analysis of a flow field of the horizontal cross-section (Fig. 9) which is performed in the half-point of the apertures' height documents that re-distribution of the mass flow is caused by the direction of the apertures. It is favorable for the steam flow in the right section of the screen, in contrast to the other side. This Fig. 9 also documents a correct operation of the directional apertures, i.e. spinning of the steam. The stream-lines that are the closest to the internal circle belong to the steam which passed through the top apertures of the screen and flows down vertically. The flow field in the area of circular apertures is illustrated in Fig. 10. There are better conditions for steam entry in the front section of the screen than on the lateral sides. A rib on the opposite side enables a better balancing of the steam flow.

A curve at the maximal Mach numbers has a similar progression for the 3D model as for the 2D axially symmetric models, as it is documented in Fig. 11. However, it is moved by a certain amount to lower values. The pressure distribution on the cone is similar, with identical conclusions as with the 2D models, as it is documented in Fig. 12.

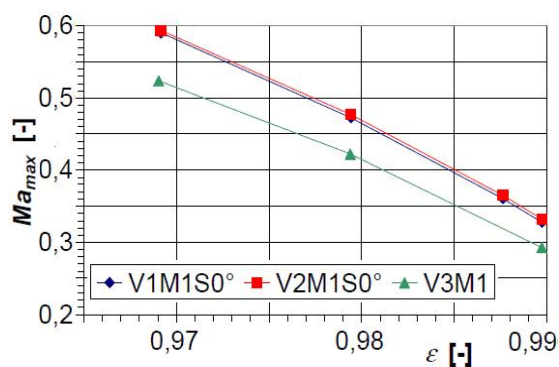


Fig. 11: Comparison of the maximal Mach numbers.

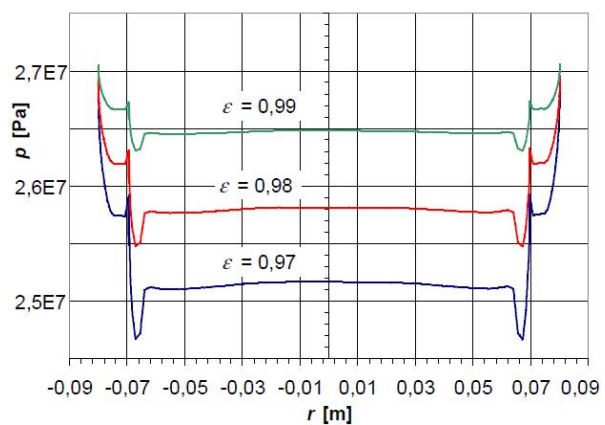


Fig. 12: Pressure distribution on the cone surface.

## 5. Conclusions

The 2D calculation grid of the symmetrical model simplifies the process of numerical simulation of a flow through the valve. However, it does not guarantee obtaining a reliable figure of the situation inside the valves. There are no significant differences between findings regarding the 2D and the 3D models for operational pressure conditions.

A varied angle of the flow's deviation from the radial direction on the entry into the valve has no effect on the passage of the mass flow through the valve. It is mainly affected by the geometry of the flow section of the valve and the pressure ratio.

A non-stationary calculation for operational pressure ratios on the valve does not produce visible alterations with regard to the stationary valve.

There is a backflow in the area immediately under the flat-bottomed punched cone.

Directional apertures on the protective screen cause unbalanced distribution of the mass flow around the screen's perimeter.

The pressure affecting the bottom of the cone is practically identical in operational modes of the turbine.

## References

Jirka, L. (2007) Výpočtová studie proudění páry regulačním ventilem, Thesis, University of West Bohemia, Plzeň, Czech Republic.



## **DYNAMIC MODELLING AND TESTING OF NEW BRIDGE CROSSING DANUBE IN BRATISLAVA**

**J. Benčat<sup>\*</sup>, J. Koňár<sup>\*</sup>, D. Papán<sup>\*</sup>**

**Abstract:** *The cable-stayed bridges are usually built for long span and are subjected to dead and moving loads, seismic motions of supports to wind forces, temperature and many other forces. The dynamic study of the suspended and cable-stayed bridges was initiated by collapse of the well-known Tacoma Bridge in the USA. The paper deals with the vibration of suspended bridge subjected to the action of moving loads during the regular dynamic tests of the bridge and to point out on the discrepancy that may occur between finite element modelling (FEM) and on-site strain and displacements and acceleration amplitude measurements.*

**Keywords:** *Structural response, structures dynamic diagnostics, FEM analysis, bridge dynamic loading tests, natural frequencies and modes.*

### **1. Introduction**

The aim of the paper is based on practical experience from the assessment of the New Bridge crossing Danube in Bratislava, Slovakia, a 431.8 m long with skew pylon 90 m high. The length of the main span crossing Danube is 303.0 m and total width of the bridge deck is 21.0 m. The FE modelling is described and typical problems are outlined. From the regular tests of the bridge results it follows that the assessment results in the ultimate limit state and especially in the fatigue limit state are very sensitive to precise finite element modelling, see the papers (Baťa et al., 1994; Benčat, 2008; Benčat, 2009; Benčat et al., 2009; Ozakan et al., 2003; Troitsky, 1988). Also, a reliable FE-model is a necessary basis for applying more advances assessments such as plastic analysis, fracture mechanic, seismic analysis, etc.

### **2. FEM analysis**

The relevant combination of a detailed and comprehensive finite element modelling, sensitivity analysis, on-site measurements and model updating is crucial for the assessment in order to provide a solid decision basis for the necessary actions to be taken. Despite both the complex structural layout of the bridge (Fig. 1) and simplifying assumptions of the FE model *IDA Nexis* software (Fig. 2), results showed good agreement for all identified frequencies in the basic frequency range 0 – 5 Hz (Fig. 4).

### **3. Bridge dynamic loading test**

The dynamic response tested two spans of the bridge was induced by passing load vehicle *SCANIA* with weight of 15 900 kg in the both directions with various speed. The operating dynamic loading test (DLT) started with a load speed of  $c = 5$  km/h (crawling speed) which increased up to the maximum achievable speed  $c = 62$  km/h.

A computer – based measurement system (CBMS) was used to record the dynamic response of the bridge excitations induced by testing vehicle over DLT period. The investigated vibration acceleration amplitudes were recorded at selected points with maximum calculated deflection in each of the investigated two spans (Fig. 1).

---

<sup>\*</sup> prof. Ing. Ján Benčat, PhD., Ing. Juraj Koňár and Ing. Daniel Papán, PhD.: Department of Structural Mechanics, Faculty of Civil Engineering University of Žilina; Univerzitná 8215/1; 010 26 Žilina; Slovakia, e-mails: jan.bencat@fstav.uniza.sk, juraj.konar@fstav.uniza.sk, daniel.papan@fstav.uniza.sk

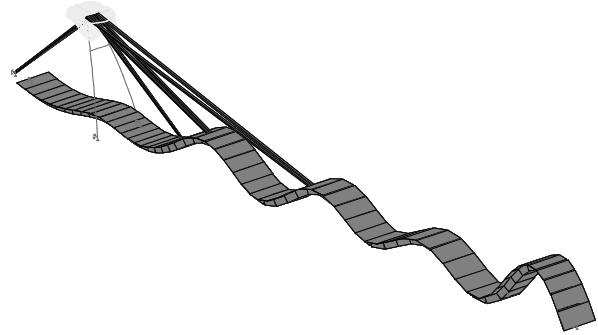


Fig. 2: Natural mode example.

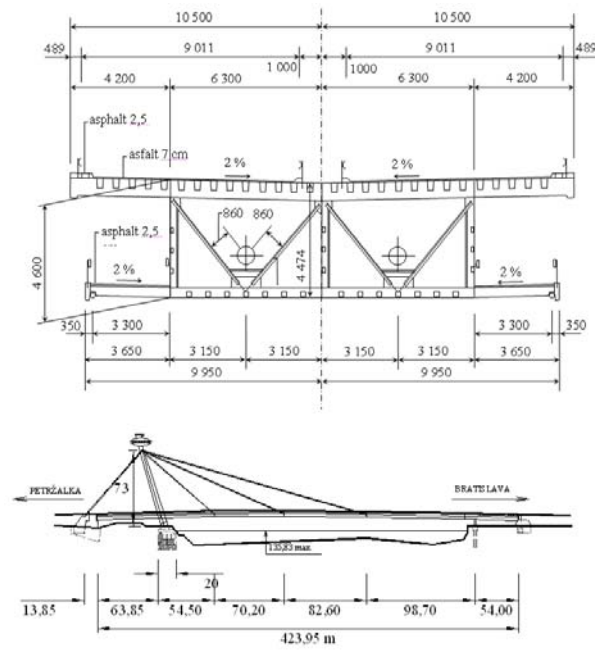


Fig. 1: New Bridge over the Danube in Bratislava.

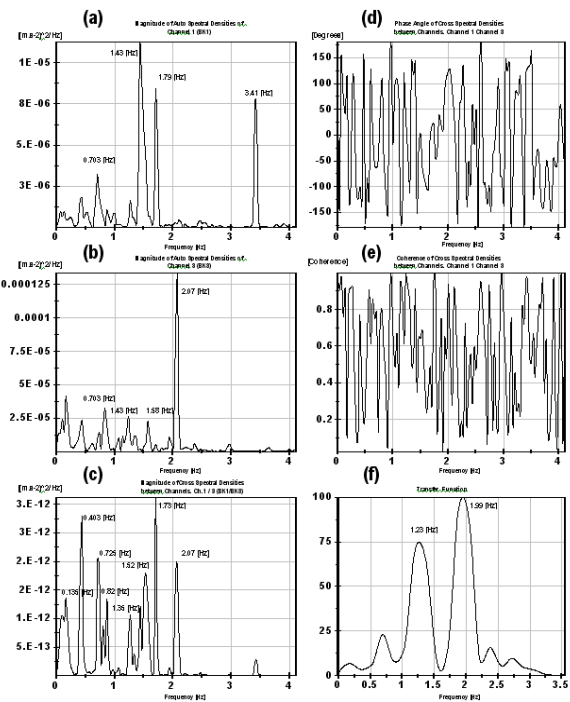


Fig. 3: Spectral analysis procedure functions.

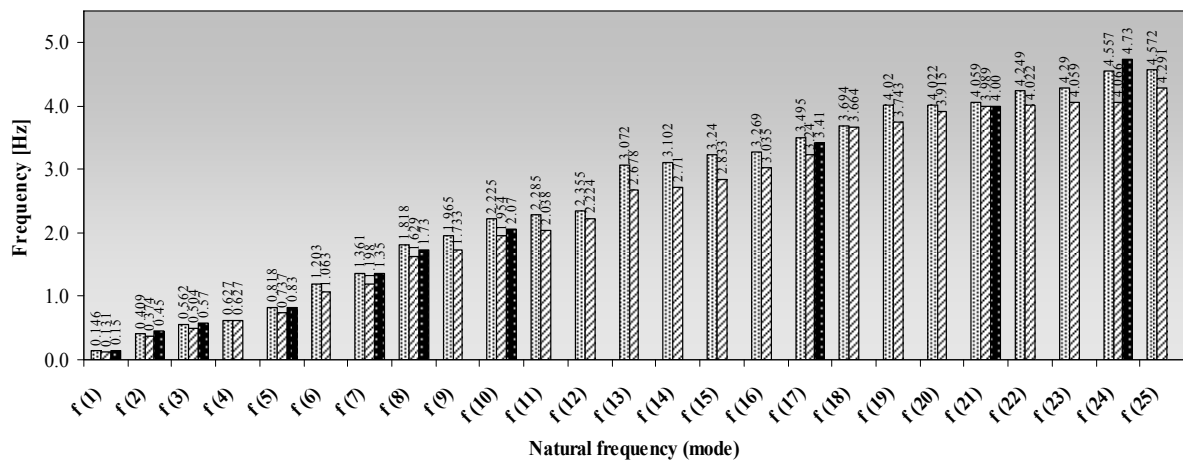


Fig. 4: Calculated and experimental natural bridge frequencies comparison.



In the same points the vibration amplitudes in both vertical and horizontal direction respectively were recorded, by accelerometers *Brüel-Kjaer BK 8306 (BK1...BK4)* with the amplifiers *BK 2635*. In the same points were installed the tensometers *Kistler 9232A* with the amplifiers *Kistler 5011 (K1, BK2)* and in the 1st span of the bridge inductive displacement transducers (relative sensors) *Bosh (R1...R4)* were installed, too. Output signals from the all sensors (accelerometers, tensometers and transducers) were preamplified and recorded on two PC facilities with A/D converters of the software packages *NI LabVIEW* and *DISYS* in the central measuring station *KSM – UZ*.

#### 4. The off - line experimental analysis

Analysis has been carried out in the *Laboratory of the Department of Structural Mechanics, University of Žilina*. *Natural frequencies* were obtained using spectral analysis of the recorded bridge response dynamic components of the structure vibration, which are considered ergodic and stationary. The vibration *ambient ability* has been investigated by means of the correlation and spectral analysis in order to obtain *cross correlation functions*  $R_{xy}(t)$  and *coherence function*  $\gamma_{xy}^2(f)$ . *Spectral analysis*, for example paper (Bendat et al., 1993; Brownjohn et al., 2008; Brownjohn et al., 2010), was performed via *National Instruments* software package *NI LabVIEW*. As an example, Fig. 3 shows a part of the spectral analysis procedure results of the dynamic vertical components structure vibration from the bridge DLT.

The experimental analysis of the bridge dynamic response caused by moving load made it possible to *identify eight basic modes of bridge vibration*. These frequencies have been received by analysis of small amplitude vibration and so the analysis corresponds to linear vibration. From the tests vibration time histories it was possible to predict the *damping characteristics* according to test and monitoring results (Benčat, 2008; Benčat, 2009) by using logarithmic decrement –  $\nu$ . The evaluation of the *logarithmic decrement* has been done using the bridge free vibration records due to the vehicle moving after their bridge passing. The logarithmic decrement corresponding to the *first* and *second* modes of the bridge vibrations varies in range  $\nu = 0.024 \div 0.049$ .

#### 5. Conclusions

Theoretical and experimental investigation dynamic response of the *New Bridge over the Danube in Bratislava* is described in the paper. The following conclusions can be drawn:

- The predicted dynamic behavior of the bridge by a simplified *FEM* analysis calculation was compared to the measured one. Despite both the complex structural layout of the bridge (Fig. 1) and simplifying assumptions of the model (Fig. 4), results showed good agreement for all identified frequencies in the basic frequency range 0 – 5 Hz.
- The experimental analysis of the bridge dynamic response caused by moving load made it possible to identify 8 *basic modes of bridge vibration*. These frequencies have been received by analysis of small amplitude vibration and so the analysis corresponds to linear vibration.
- The experimentally achieved *dynamic load factor (DLF)* shows that real stiffness of structure is fully comparable with the corresponding value for  $\delta \approx 1,10$  obtained by computation according to *Slovak standard* prescriptions.
- Many different formulas were suggested to evaluate the *DLF* from the experimental data obtained under traffic loading. More recently, researchers have used the ratio of *maximum dynamic response over the maximum filtered response* (used in this analysis) as a definition of the *DLF*. A response range approach was also suggested for *fatigue considerations*.
- Filtering techniques used to extract the static component from displacement or strain signals, obtained from dynamic testing under traffic loading, can have a considerable influence on the *DLF*. Proper filter characteristic should be used, and the static component should be compared with crawling speed test or static deflection from *SLT*, which was performed before *DLT* in this tests.
- This computational model will be applied for the bridge fatigue and seismic analysis before starting a decision making process regarding to the bridge strengthening.
- The results of the correlation and spectral analysis of the time histories of the bridge dynamic response proved ambient ability of the bridge vibration.

## Acknowledgement

We kindly acknowledge the research project *VEGA, Nr.1/0756/09* granted by *Scientific Grant Agency of the Slovak Republic Ministry of Education*. We should also like to thank the *Civil Engineering Faculty – University of Žilina* for additional feed in this field research activity.

## References

- Baťa, M., Plachý, V., Sýkora, J., Bílý, V., Polák, M. (1994) Static and dynamic tests of bridges, Proceedings of Czech – US Bridge Conference, Praha.
- Benčat, J. (2008) Report on static and dynamic test results of the New Bridge over the Danube in Bratislava, SvF/08, UZ / Žilina.
- Benčat, J. (2009) Report on dynamic monitoring results of the New Bridge over the Danube in Bratislava, SvF/09, UZ / Žilina.
- Benčat, J., Papánová, Z. & Papán, D. (2009) Assesment, Measurement and Monitoring of the New Bridge crossing the Danube in Bratislava, in Civil, Structural and Environmetal Engineering Computing, Civil–Comp Press, Stirlingshire, UK 2009, CSEE, 1– 4 Sept. 2009, Madeira, Portugal.
- Bendat, J. S., Piersol, A. G. (1993) Engineering applications of correlation and spectral analysis, (2nd edt.), Wiley Interscience, New York.
- Brownjohn, J. M. W., Reynolds, P. & Pavic, A. (2008) Advances in dynamic testing methods for in–situ civil engineering structures. Seventh European Conference on Dynamics EUROLYN 2008, Southampton, UK, 7– 9 July 2008
- Brownjohn, J.M.W., Reynders, E., de Roeck, G. (2010) Dynamic testing of constructed facilities. ASCE Congress 2010, Orlando, Florida, USA, 12–15 May 2010.
- Ozakan, E., Main, J., Jones, P. (2003) Long – term measurement on a cable – stayed bridge, Proc. of IMAC XXI – Conference, Orlando, Florida.
- Slovak Standard No.73 6209 – Loading test of bridges.
- Slovak Standard No.73 6203 – Loading of bridges.
- Troitsky, M. S. (1988) Cable – stayed bridges, (2nd edt.), BSP Professional Books.

## **OPTIMAL NUMBER AND LOCATION OF PIEZOCERAMIC ACTUATORS AND SENSORS FOR VIBRATION SUPPRESSION OF TWO-DIMENSIONAL SYSTEMS**

**P. Benkovský\*, L. Starek\***

**Abstract:** *This paper deals with the development of process for finding the optimal number and location of piezoceramic actuators and sensors to suppress the vibration of 2D systems. This choice must satisfy the condition of maximum possible system observability and controllability and is independent of the choice of control algorithm. Controllability and observability of the system is expressed via grammians of controllability and observability, respectively as product of these two items. The problem is solved by the optimization process in MATLAB program using a combination of library functions as well as its own created function and a set of input data from system model from program package ANSYS. Comparing the matrix product of grammians in the optimization process, serves as the main benchmark and its result is a set of indicia location of piezoceramic members.*

**Keywords:** *Grammians, 2D systems, optimization, MATLAB, ANSYS.*

### **1. Introduction**

Active vibration suppression is no new concept, but many studies are still concerned with the theoretical description of the problem and are solving problems of specific boundary conditions. The aim of this work is to take advantage of already known theoretical principles to solve more general issues, namely, the systems with non-constant thickness, complex boundary conditions, etc. The main objective is to design optimization algorithm and subroutine that will process the input data. This can expand capabilities of solvers for 1D and 3D systems in future. Creation of a virtual model was realized by FEM in program ANSYS. Next, the output data from ANSYS were transferred to MATLAB for further use. This transfer is realized by set subroutines, which provide all necessary information like mass, stiffness matrix, geometry, indexing of nodes and so on. These subroutines also solve the problem of mixed or missing nodes due matrix reduction. Maximization of observability and controllability grammians was chosen as main condition for this optimization problem. For maintaining simplicity, sensors and actuators are considered collocated. So calculation of grammians can be realized in state-space balanced representation, which guarantees that observability and controllability grammians will be diagonal and the same. Finally, solving the optimization problem for selected modes will return node indexes, if they satisfy the criteria adopted.

In chapter 2 a whole process of solution is described. An example of pinned plate without damping is shown in chapter 2.1.

### **2. Process of solution**

In general, we obtain nodal model from FEM, which will be implemented into our MATLAB solver:

$$M\ddot{q} + Kq = 0 \quad (1)$$

It's a system without inputs and outputs with  $n_d$  degrees of freedom.  $M$ ,  $K$  are mass and stiffness matrices with dimensions  $(n_d \times n_d)$ .  $q$  and their second derivatives are displacement vector and acceleration vector with dimensions  $(n_d \times 1)$ . Using prescribed subroutines we will transform this

---

\* Ing. Peter Benkovský and prof. Ing. Ladislav Starek, CSc.: Institute applied mechanics and mechatronics, Slovak Technical University in Bratislava, Námestie Slobody 17; 812 31 Bratislava 1; SK, e-mails: peter.benkovsky@stuba.sk, ladislav.starek@stuba.sk

system to state space and at the same time we will create inputs and outputs of the system (Gawronsky, 2004).

$$x = \begin{Bmatrix} x_1 \\ x_2 \end{Bmatrix} = \begin{Bmatrix} q \\ \dot{q} \end{Bmatrix}$$

$$\dot{x}_1 = x_2$$

$$\dot{x}_2 = \mathbf{M}^{-1}\mathbf{K}x_1 + \mathbf{M}^{-1}\mathbf{B}_0u$$

$$y = \mathbf{C}_{oq}x_1 + \mathbf{C}_{ov}x_2 \quad (2)$$

Where  $x$  is state vector and a  $\mathbf{B}_0$ ,  $\mathbf{C}_{oq}$ ,  $\mathbf{C}_{ov}$  are input matrix, output displacement and velocity matrices in a nodal form. *Their dimensions are  $(2 \times nd \times 1)$ ,  $(nd \times s)$ ,  $(r \times nd)$  and  $(r \times nd)$ , where  $s$  and  $r$  represent the number of inputs and outputs of the system.*

Now we can calculate observability and controllability grammians  $\mathbf{W}_o$  and  $\mathbf{W}_c$  using Lyapunov equation:

$$\mathbf{A}\mathbf{W}_c + \mathbf{W}_c\mathbf{A}^T + \mathbf{B}\mathbf{B}^T = 0$$

$$\mathbf{A}^T\mathbf{W}_o + \mathbf{W}_o\mathbf{A} + \mathbf{C}^T\mathbf{C} = 0 \quad (3)$$

Using information about balanced representation we can obtain both grammians, that will be diagonal and equal (Starek, 2009, Moore):

$$\mathbf{W}_o = \mathbf{W}_c = \mathbf{\Gamma}$$

$$\mathbf{\Gamma} = \text{diag}(\gamma_1, \dots, \gamma_{2n})$$

$$\gamma_i \geq 0, i = 1, \dots, 2n \quad (4)$$

So now we can define grammians as functions of  $i$ -th location of inputs and outputs on structure and the degree of observability and controllability for each mode (or mode  $m$ ) by:

$$\Gamma_m = f_m(i) \quad (5)$$

$$M_m = \frac{\Gamma_m(i)}{\max(\Gamma_m)} * 100\% \quad (6)$$

Similarly we can define the degree of observability and controllability on the whole structure for all selected modes,

$$S = \frac{\sum Q_m \Gamma_m(i)}{\max \sum(\Gamma_m)} * 100\% \quad (7)$$

as summation of functions  $\Gamma_m$  of selected modes in  $i$ -th location, divided by maximum of this summarized functions. Where  $Q_m$  is weighting function for each mode (inspired by Halim and Moheimani, 2003).

## 2.1. Example

Plate with these attributes has been modelled:

Dimension: 1 x 1 meter

Thickness: 0.01 meter

Material - Aluminum

Density: 2700 kg/m<sup>3</sup>

Young modulus: 70 GPa

First three natural frequencies for transverse vibration in ANSYS are:

- 17.828 Hz
- 38.883 Hz (2 symmetric modes)
- 48.261 Hz

Pinned at nodes: 1, 2, 12, and 22 (Fig. 1).

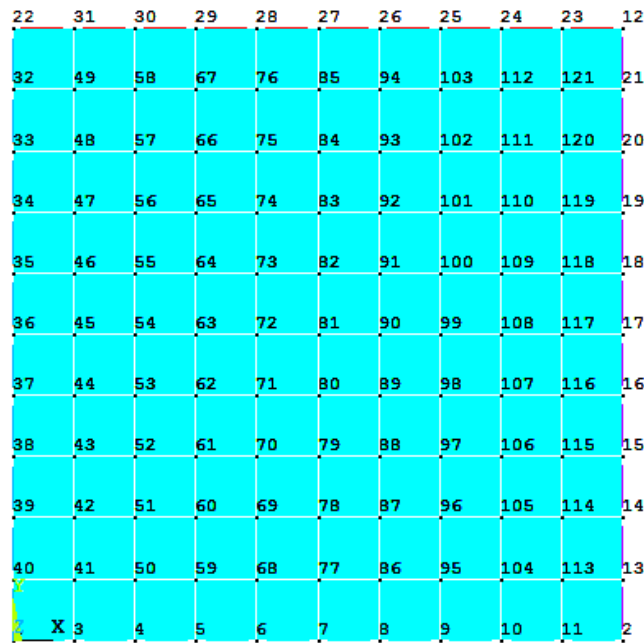


Fig. 1: Plate with map of nodes.

Using created subroutines we will try to find optimal placement for 1, 2 and 4 collocated sensors and actuators for three independent modes.

Tab. 1: Node numbers in dependence of mode and quantity of inputs/outputs.

Number of S/A	Mode 1	Mode 2	Mode 4
1	[81]		
2	[72 81]	[45 117],[7 27]	
4	[72 80 82 90]	[6 8 26 28]	[7 17 36 27]

### 3. Conclusions

Additional research is needed to verify these results experimentally. The algorithm is working quite well for independent modes, but needs proper weighting function when it is solving a set of modes. Also, with too many combinations, computational time is increasing significantly, which can be remedied by optimizing subroutine for input/output combinations generation. Algorithm was also tested on beam structure with variable thickness over its length, with similar properties. Good solution for independent modes were obtained; and relatively inaccurate results for a set of modes, yet with a better computational time, when the weighting function was not defined properly.

### Acknowledgements

The authors gratefully acknowledge the support of the Slovak Ministry of Education Grant Agency VEGA # 1/0744/10.

## References

- Gawronsky, W. K. (2004) Advanced structural dynamics and active control of structures, Mechanical engineering series, Springer Verlag New York Inc.
- Halim, D and Moheimani, S O R (2003) An optimization approach to optimal placement of collocated piezoelectric actuators and sensors on a thin plate, Mechatronics 13 27–47.
- Moor, B.C. (1981) Principal Component Analysis in Lienear Systems, Controllability, Observability and Model Reduction, IEEE Transactions on Automatic Control, Vol. 26, pp. 17-32.
- Starek, L. (2009) Kmitanie s riadením , Vydala Slovenská technická univerzita v BA v Nakladateľstve STU, Edícia vysokoškolských učebníc, ISBN 978-80-227-3227-7.



## ADJUSTMENT OF SEAT SUSPENSION DAMPING

**J. Blekta<sup>\*</sup>, J. Petříček<sup>\*</sup>, J. Mevald<sup>\*</sup>, A. Lufinka<sup>\*\*</sup>**

**Abstract:** *Now a day, many types of seat used in working machines are constructed for vibroizolation in vertical direction. Seat vibrations in longitudinal and lateral directions are very unsuitable, because seat mechanism is not designed for this type of excitation. This paper shows one of the suitable seat suspension to horizontal seat vibrations minimizing and seat motion damping adjusting.*

**Keywords:** *Vibrations, damping, optimization, simulation, multibody.*

### 1. Introduction

Thanks horizontal vibrations, seat mechanism contact parts are abraded after some time and clearances in guide ways come up. The lateral vibrations increase passive resistance of mechanism also. This is very unpleasant, because in dependence of excitation intensity, passive resistances are changing and damping of whole seat mechanism is changing together.

### 2. Seat measurement

To verify expectations mentioned above, laboratory measurement with real seat was realized in Hydrodynamic laboratory of Technical University of Liberec. Seat Actimo M by Grammer company was measured - see Fig. 1.

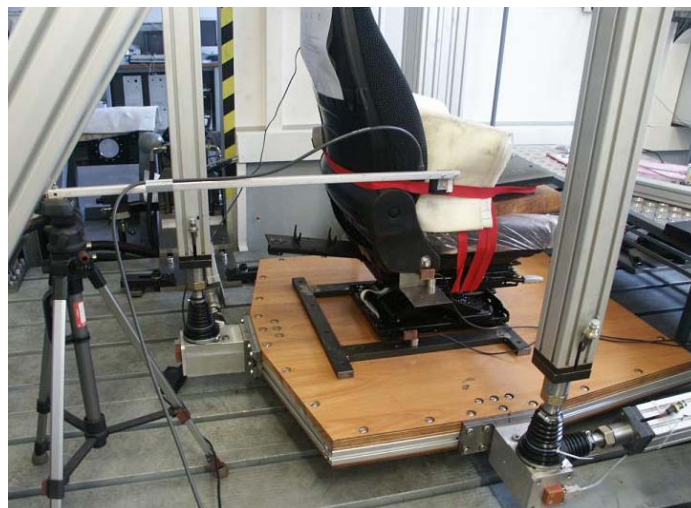


*Fig. 1: Seat measurement.*

Seat were excited by three signals of 5 mm, 10 mm and 15 mm amplitude. Each of these signals contain harmonics sub-signals of 0.5 Hz, 0.75 Hz, 1 Hz, 1.25 Hz, 1.5 Hz, 2 Hz, 2.5 Hz, 3 Hz, 3.5 Hz, 4 Hz and 5 Hz frequencies. Each frequency was represented by 10 cycles. Seat was excited by this signal triads in longitudinal (x), lateral (y) and vertical (z) direction separately. Measurement was realized with passive mass of 40 kg, 60 kg and 80 kg weight and also with active mass - human of 80

---

<sup>\*</sup> Ing. Jiří Blekta, Ph.D., Ing. Jiří Petříček and assoc. prof. Ing. Josef Mevald, CSc.: Department of Applied Mechanics, Technical University of Liberec, Studentská 2; 461 00, Liberec; CZ, e-mails: jiri.blekta@tul.cz, jiri.petricek@tul.cz, josef.mevald@tul.cz

<sup>\*\*</sup> Ing. Aleš Lufinka, Ph.D.: Department of Design of Machines Elements and Mechanisms, Technical University of Liberec, Studentská 2; 461 00, Liberec; CZ, e-mail: ales.lufinka@tul.cz

kg weight. In this case, only signal of 5 mm amplitude was used, because norm limits for test with human body have not to be exceeded.

Seat squab position in relevant direction was measured by laser sensor. Position of platform board desk was measured by LVDT sensors built in hydraulic motors. On seat squab and platform desk accelerometers were mounted to measure of acceleration of these parts.

In the Figs. 2, 3 and 4 bellow dependence of transmission ratios of seat squab displacements in  $x$ ,  $y$  and  $z$  directions for 80 kg passive weight on excitation frequency are shown. Figs. 5, 6 and 7 show the same dependence for active weight.

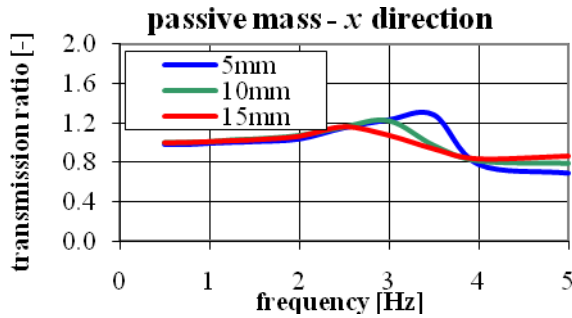


Fig. 2: Trans. ratios - passive mass, x direct.

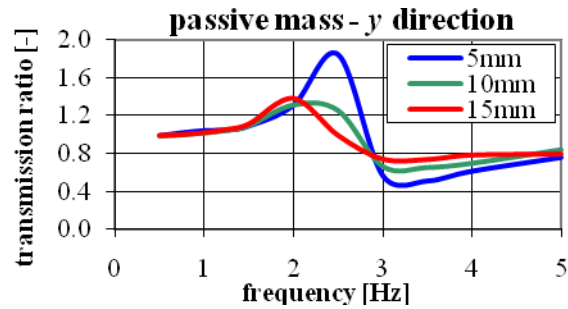


Fig. 3: Trans. ratios - passive mass, y direct.

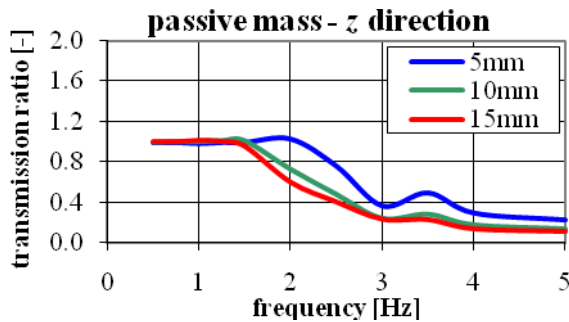


Fig. 4: Trans. ratios - passive mass, z direct.

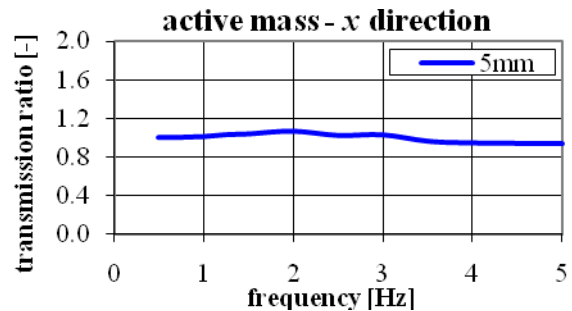


Fig. 5: Trans. ratios - active mass, x direct.

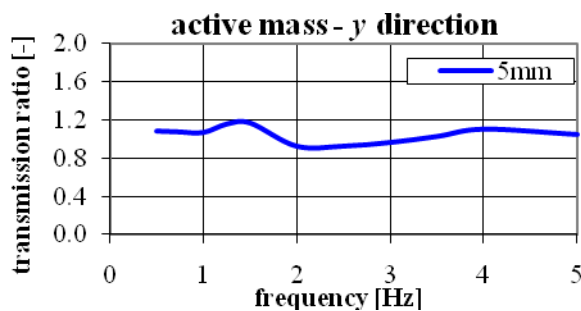


Fig. 6: Trans. ratios - active mass, y direct.

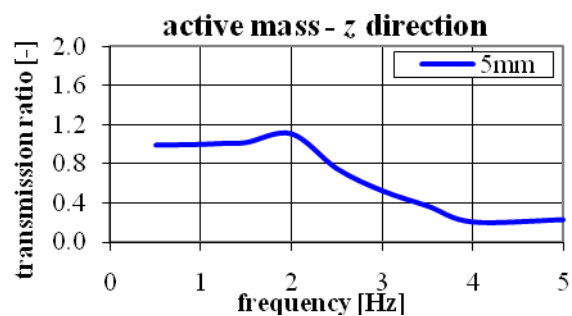


Fig. 7: Trans. ratios - active mass, z direct.

From figures above follows, that exciting signal is reduced for most of frequencies in case of vertical direction. This can't to be said for  $x$  and  $y$  directions however. Vibration transfer in  $x$  direction is a little bit better than in  $y$  one (better stiffness of seat mechanism in  $x$  direction). Peak of 5 mm curve in Fig. 3 is done by comparable value of exciting signal amplitude and seat mechanism clearances.

From reasons mentioned above is very suitable to minimize seat vibrations in horizontal directions. One possibility how to do it is thinking about a proper seat suspension.

Suitable seat suspension can be realized by mechanism of parallelogram type. It can be e.g. desk hanged by three arms on a frame of working machine. This is shown in Fig. 8. Desk with mounted seat has 3 degrees of freedom - translational movement in longitudinal and lateral direction and rotation about vertical axis. By proper parameters setting (length of arms, desk movement damping) a good vibroizolation in horizontal directions can be achieved.

### 3. Application of parallelogram seat suspension

This type of seat suspension was applied in Doly Nástup Tušimice, where vibroizolation of colliery machine driver was requested (Blekta et al., 2010). Cabin with driver seat is placed inside of cabin frame. Cabin frame is excited by motion in general direction (by mining of bucket wheel). Originally, cabin was mounted to frame by rigid joints. These results in the very intensive driver vibrations, root mean square values (RMS) of seat acceleration in horizontal directions were measured about 0.1 g during c. 50 s of measured data.

A new conception of cabin suspension is shown in Fig. 9. This conception is based on cabin motion unlocking in two horizontal direction (x and y) and one cabin torsion motion.

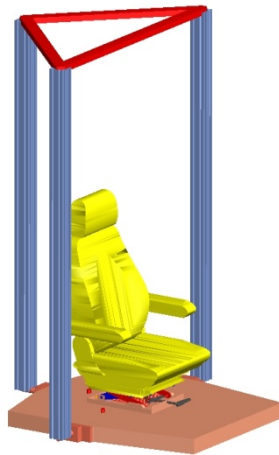


Fig. 8: A new conception of seat suspension.

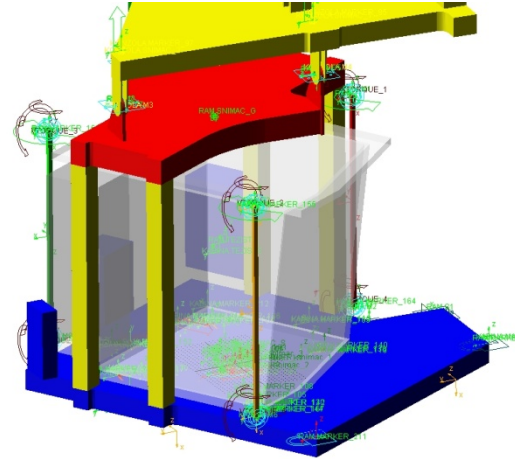


Fig. 9: A new cabin suspension.

### 4. Optimal cabin motion damping

Ideally, cabin movement could not be damped. Damping makes worse vibration transmission between cabin and cabin frame. In other side, zero damping makes unpleasant cabin pitching when driver get on the cabin floor. Another unpleasant pitching makes random impulses, when bucket-wheel mines in hard subsoil.

From reasons mentioned above there was constructed friction damper (between cabin frame and cabin floor). This damper is shown in Fig. 10. One of the most important advantage of friction damper is damping value independent upon cabin position in the cabin frame (in the cases, that machine don't work in ideally horizontal position). Damper is made from a friction disk pressed by spring to the cabin floor. By spring preload friction force value can be changed. Spring preload can be easily set by four screws.

Optimal cabin motion damping was computed from model in MSC.ADAMS software. It was set on the base of the seat squab acceleration RMS value. Model was excited by signal measured on real machine. In Fig. 11 dependence between seat squab acceleration RMS value and spring preload is shown.



Fig. 10: Friction damper.

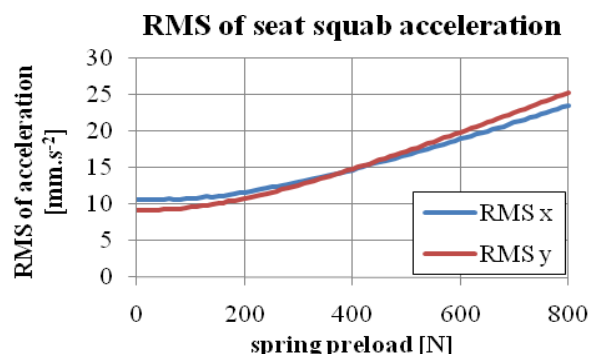


Fig. 11: RMS of seat squab acceleration vs. preload.

For driver getting on board simulation we used force impulse of  $T = 0.5$  s duration. The value of force is done by momentum, which is passed to cabin. For human weight  $m = 80$  kg and his velocity  $v = 2.5$  m.s<sup>-2</sup> resultant force is

$$F = \frac{m \cdot v}{T} = \frac{80 \cdot 2.5}{0.5} = 400 [N] \quad (1)$$

From a lot of simulations value of optimal spring preload was set to 400 N. Criteria for value setting was chosen by maximum signal oscillations during transient condition excited by above mentioned force impulse and random kinematic impulse, which was inserted in exciting signal measured on real machine (at time 15 s) in lateral and longitudinal direction. Result seat center of mass displacement is shown in Figs. 12 and 13.

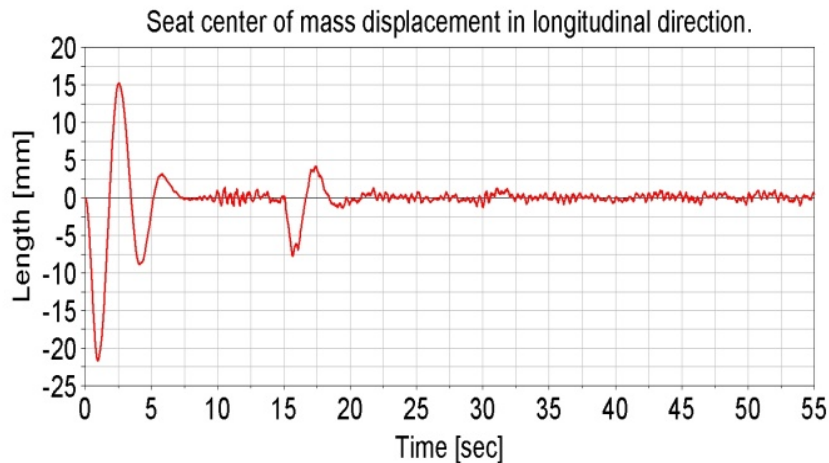


Fig. 12: Seat squab displacement - x.

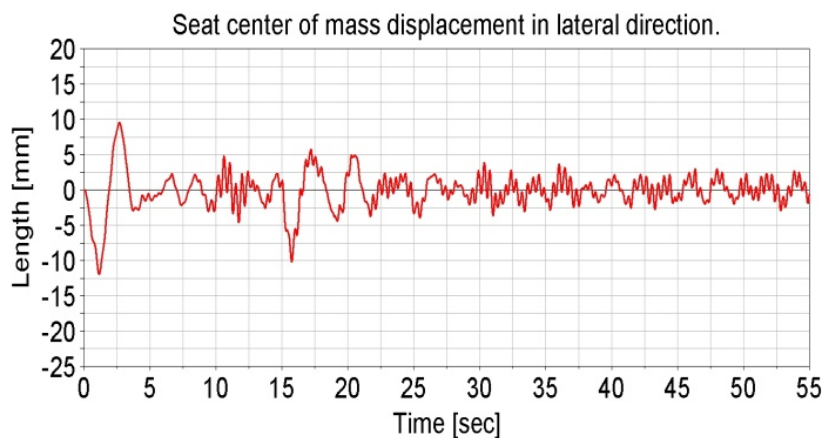


Fig. 13: Seat squab displacement - y.

## 5. Conclusions

Finally, spring preload was set to 400 N. After one month of machine running RMS of horizontal acceleration of seat central mass was measured c. 0.01 g. It is tenth of origin value.

## Acknowledgement

This paper was supported by the subvention from Ministry of Education of the Czech Republic under Contract Code MSM 4674788501.

## Reference

Blekta, J., Petříček, J., Mevald, J., Bocko, P., Sivčák, M. (2010) A new cab and seat mount of bucket wheel excavator Schrs 1320, in: Proc. 12th Int. Conf. Applied Mechanics 2010, Technical University of Liberec, Liberec, pp. 13-16.

## AIR VOIDS IN MATRIX BASED TEXTILE COMPOSITES

V. Bouřil\*, J. Vorel\*, M. Šejnoha\*

**Abstract:** *A two-layer statistically equivalent periodic unit cell with air voids is offered to predict a macroscopic response of plain weave multilayer textile composites. Two different approximations of air voids are considered to properly describe the given material system in accordance with the X-ray microtomography. Numerical predictions of both the effective thermal conductivities and elastic stiffnesses and their comparison with available laboratory data are presented and their limitations are discussed.*

**Keywords:** *Textile composites, finite element method, air voids, homogenization.*

### 1. Introduction

In the last decade, composites have been attracting great attention of many engineers due to the irreplaceable position in a variety of engineering spheres including building, aeronautic, space and automobile industry. Applications range from rehabilitation and repair of concrete and masonry structures to the design of biocompatible medical implants. Nowadays, an increasing number of fiber reinforced composite components are being fabricated with load-carrying fibers, which are woven to form a fabric. This reinforcement system has advantages with respect to fabrication as well as mechanical properties. The weaving and interlacing of the fiber tows produces a self-supporting system that can be manipulated to form complex shapes.

Although woven composites are frequently used in practice, an accurate and reliable thermomechanical analysis of these material systems still presents a non-trivial challenge due to their complex geometry and imperfections displayed at several length scales, e.g. yarn waviness and misalignment of individual tows, porosity of woven composite, etc. In plain weave composites at least three different length scales are recognize, i.e. micro-scale (tow = fiber-matrix-void interaction), meso-scale (individual plies) and macro-scale (sample, component), see Fig. 1. To obtain the macroscopic material properties of such complicated material system the coupled (Sýkora, 2010) or uncoupled (Vorel & Šejnoha, 2009, Sýkora et al., 2010) homogenization technics can be employed.

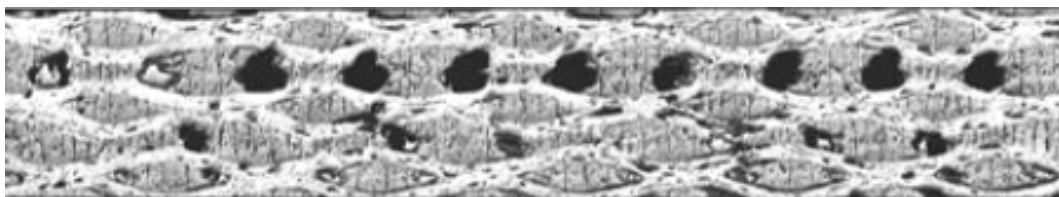


*Fig. 1: Real composite system.*

Here, the meso-scale level of uncoupled homogenization approach is assumed. In particular, the comparison of influence of pore shape discretization on the effective thermal coefficients and the effective stiffness matrices by means of finite element (FE) simulations is presented. The selection of mechanical and heat conduction problems is promoted not only by available experimental measurements but also by their formal similarity. To support the proposed approach the numerically obtained results for carbon-carbon composites are compared with experimental data.

---

\* Bc. Václav Bouřil, Ing. Jan Vorel, Ph.D. and prof. Ing. Michal Šejnoha, Ph.D., DSc.: Czech Technical University in Prague, Faculty of Civil Engineering, Thákurova 7; 166 29, Prague; CZ, e-mails: vaclav.bouril@gmail.com, jan.vorel@fsv.cvut.cz, sejnomo@fsv.cvut.cz



## 2. Numerical approach

The effective properties of a multilayered carbon-carbon (C/C) plain weave composite including the porous phase are derived in this section. The geometrical model of the corresponding representative volume element, here given in terms of the statistically equivalent periodic unit cell (SEPUC), is displayed in Fig. 2. Although the FE analysis is computationally demanding it is adopted in this study as it provides more accurate results and allows an incorporation of various intrinsic imperfections of composites.

Suppose that the homogenized effective conductivities of the yarn are already known from an independent micromechanical analysis performed on the level of individual fibers, see (Vorel & Šejnoha, 2009). The objective now is to find effective parameters on the mesoscopic level for a multilayered composite. The concept of statistically equivalent periodic unit cell for random or imperfect microstructures is utilized. A lucid presentation of individual steps enabling the substitution of real microstructures by their simplified artificial representatives - the SEPUCs – is available, e.g. in (Zeman & Šejnoha 2007). The three-dimensional structure of SEPUC, shown in Fig 2, is formed by two identical one-layer blocks, relatively shifted in all directions. Afterwards the air voids (inclusions) are introduced into the created unit cell using two different approximations which are in coincidence with the X-ray microtomography presented in Fig. 3:

- Ellipsoidal voids – with the higher level of simplification the air voids on the meso-scale can be seen as the ellipsoidal inclusions placed between the fabric reinforcements, see Fig. 2a. The relative ratio of spheroid axes is chosen as high as possible to fill the space between the tows.
- Distorted voids – this approach follows the real manufacturing process in the sense that the each tow is coated with a layer of matrix of a specific thickness. The resulting inclusions between the layers are then considered as the air voids, see Fig. 2b.

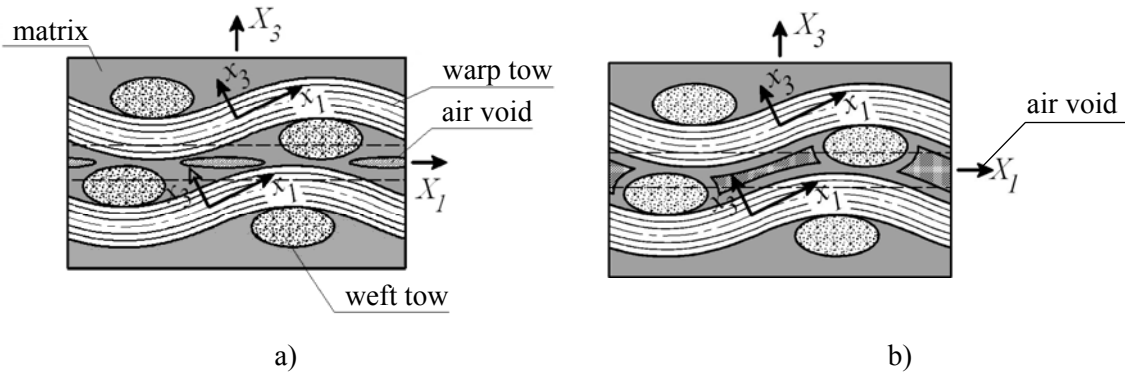


Fig. 2: Geometrical model of two-layer SEPUC: a) Ellipsoidal, b) distorted voids.

The above mentioned computational models are subsequently used for the finite element based homogenization. This technique implies the use of conforming finite element meshes easily enabling the implementation of periodic boundary conditions, see (Kouznetsova et al., 2001; Michel et al., 1999) for additional details. This might seem daunting in that it requires not only incorporation of an arbitrary shift of the two layers of fabric reinforcement, but also an independent introduction of voids. In the present study these obstacles are overcome by employing the volumetric modeling capacities of the ANSYS package (ANSYS, 2005).

In order to ensure the symmetry of the resulting FEM mesh, a primitive block of the tow is modeled first. Subsequently, using mirroring, copying and merging operations, the whole volume of one reinforcement layer is generated. The second fabric is created by a copying and shifting of the previous layer.



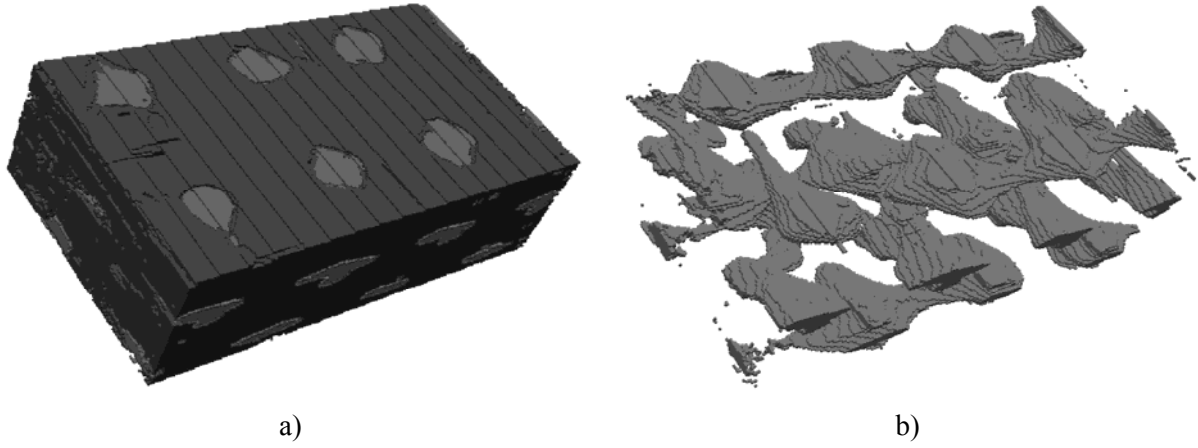


Fig. 3: X-ray microtomography: a) Interior distribution and shape of large vacuoles, b) three-dimensional view of the porous composite structure.

The porous phase is introduced next being represented by four identical oblate spheroids or irregular volumes as already mentioned. Their location is assumed to mimic the distribution of large vacuoles that typically appear, as also seen in Fig. 3, in the location of tow crossing.

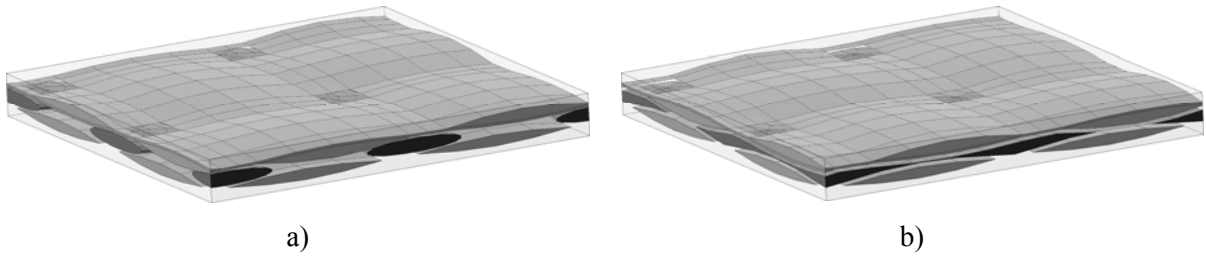


Fig. 4: 3D view of the geometry of a two-layer unit cell model with: a) Ellipsoidal, b) distorted voids.

The volume of pores equal to 5.5% is assumed. Note that this value corresponds to the percentage determined by the image analysis (Tomková & Košková, 2004). Details regarding the construction of the SEPUC from the solution of a certain optimization problem are provided in (Vorel et al., 2010). This step is quite complex and this is also the reason why the porous phase was excluded from the minimization problem and introduced subsequently to address the influence of shape of pores as the main objective of this paper.

Tab. 1: Effective elastic properties and thermal conductivities. Comparison of numerical results and experimental data (Černý et al., 1989; Boháč, 2005).

<i>Parameter</i>	<i>FEM</i>		<i>Experiment</i>
	<i>Ellipsoidal voids</i>	<i>Distorted voids</i>	
$E_{\text{warp, weft}}$ [GPa]	60.3	60.1	65
$G_{\text{warp, weft}}$ [GPa]	8.1	4.1	6
$\chi_{\text{warp, weft}}$ [W/mK]	9.03	9.00	10
$\chi_{\text{trans}}$ [W/mK]	1.89	1.49	1.6

This goal is achieved by comparing the effective conductivity coefficients  $\chi$  and elastic moduli of the two geometrical models in Fig. 4. The results are stored in Tab. 1 suggesting reasonable accuracy of Fem predictions when compared to experimental data.

### 3. Conclusions

In order to realistically model complex plain weave textile laminates with three-dimensional, generally non-uniform texture of the reinforcements and significant amount of porosity on the mesoscopic level, we advocate the use of SEPUC weakened by air voids. Both approaches presented in this paper provide a reasonable agreement with experimental data, see Tab. 1. Each one of the introduced approximations has intrinsic limits which are related to their shapes. The substitution of air voids by ellipsoidal inclusions has mainly the restriction in the limited volume of pores phase introduced in such a manner. This problem is caused by the nonflexible shape of inclusions and the capability to place them between the reinforcement fabrics. On the other hand the distorted pores provide us with higher possibility to grasp the correct volume of pores, but in some cases deliver lower estimates for an in-plane shear modulus because of the separation of layers by the inclusions.

### Acknowledgement

The financial support provided by the GAČR grants No. 106/08/1379 and P105/11/0224 and partially also by the research project CEZ MSM 6840770003 is gratefully acknowledged.

### References

- ANSYS (2009) Documentation for ANSYS. ANSYS, Inc. Home page: <http://www.ansys.com>.
- Boháč, V. (2005) Measurement of thermophysical properties of C/C composite. Technical report, Slovak Academy of Science, Bratislava.
- Černý, M., Glogar, P. & Machota, L. (2000) Resonant frequency study of tensile and shear elasticity moduli of carbon fibre reinforced composites (CFRC). *Carbon*, 38, pp. 2139-2149.
- Kouznetsova, V., Brekelmans, W.A.M. & Baaijens, P.T. (2001) An approach to micro-macro modeling of heterogeneous materials. *Computational Mechanics*, 27, 1, pp. 37-48.
- Michel, J.C., Moulinec, H. & Suquet, P. (1999) Effective properties of composite materials with periodic microstructure: A computational approach. *Computer Methods in Applied Mechanics and Engineering*, 172, 1, pp. 109-143.
- Sýkora, J. (2010) Multiscale modeling of transport processes in masonry structures. Ph.D. thesis, CTU in Prague.
- Sýkora, J., Vorel, J., Krejčí, T., Šejnoha, M. & Šejnoha, J. (2009) Analysis of coupled heat and moisture transfer in masonry structures. *Materials and Structures*. 42, 8, pp. 1153-1167.
- Tomková, B. & Košková, B. (2004). The porosity of plain weave C/C composite as an input parameter for evaluation of material properties. In *Proc.: International Conference Carbon 2004*, Providence, USA, p. 50.
- Vorel, J. & Šejnoha, M. (2009) Evaluation of homogenized thermal conductivities of imperfect carbon-carbon textile composites using the Mori-Tanaka method. *Structural Engineering and Mechanics*, 33, 4, pp. 429-446.
- Vorel, J., Zeman, J., Šejnoha, M. & Tomková, B. (2010) Homogenization of plain weave composites with imperfect microstructure: Part II-Analysis of real-world materials. Submitted for publication.
- Zeman, J. & Šejnoha, M. (2007) From random microstructures to representative volume elements. *Modelling and Simulation in Materials Science and Engineering*, 15, 4, pp. 325-335.

## THE IMPACT OF GROUNDWATER ON ARTIFICIALLY COMPACTED SOILS

M. Brouček<sup>\*</sup>, P. Kuklík<sup>\*\*</sup>

**Abstract:** *The paper presents analysis of laboratory experiments on soils that are usually classified as coarse grained soils and are often used as backfill for trenches from pipes and conduits. The reason for selecting coarse grained soil is a generally accepted fact that fine soils suffer with soil structure collapse when the matric suction is cancelled while for coarser soils such as sands or gravel this problem is frequently neglected. The main aim is to show the effect of rising and varying groundwater to the settlement of the foundation structure. Experiments are carried out on large soil specimens created in the laboratory using compactors. The effect of compaction and moisture inside the specimen to the settlement is taken into account.*

**Keywords:** *Settlement, groundwater table variation, structure collapse, particles redistribution, matric suction.*

### 1. Introduction

Recently reported increasing number of damaged structures built on artificially compacted soils such as pavements, roads, etc. caused raised interest in evaluation of effect the groundwater has on the compacted soils. Similar problems have been reported in structures built on soils that have not experienced significant contact with groundwater.

The idea of the influence of groundwater on the mechanical behaviour of soils, in natural or changed state, is not innovative when considering the idea itself. However the research effort was in the past mainly focused on avoiding difficulties in the area of hydraulic structures and deep excavations. The aim was to formulate empirical recommendations which would ensure certain conditions inside the soil or dam body. For civil engineering structure purposes the whole area is being neglected apart from foundations on clays. Current standards do not take the influence of the groundwater table variations into the account neither for the design purposes of newly built structures nor for back analysis of the damage of the already built.

### 2. Experiments and tested soils

The governing idea of the implemented experiments is to provide set of laboratory results for different artificially compacted soil that are often used as backfill for trenches. Additionally the results obtained should allow for comparison with the in-situ results. The aim is to describe the soil behaviour under the semi-constant load, which could represent an upper structure, while vary the groundwater table position. For similar load and settlement values measured in situ on the appropriate type of the soil we can evaluate the influence of the probable groundwater change to the upper structure in advance without complicated and expensive large scale in-situ experiments. This will allow us to improve the standards for newly constructed soil structures in areas where groundwater table variation potentially occurs. Another use of the results presented is improvement of the loss functions used for evaluation of flood damage (Kang, Su and Chang, 2005).

---

<sup>\*</sup> Ing. Miroslav Brouček: Department of Hydraulic Structures, Faculty of Civil Engineering, Czech Technical University in Prague; Thákurova 7; 166 29, Prague; CZ, e-mail: miroslav.broucek@fsv.cvut.cz

<sup>\*\*</sup> doc. Pavel Kuklík, CSc.: Department of Mechanics, Faculty of Civil Engineering, Czech Technical University in Prague; Thákurova 7; 166 29, Prague; CZ, e-mail: kuklikpa@fsv.cvut.cz

With a general classification of the structures based on the changes in subsoil it is easy to present an improved risk analysis of the flood areas which is an impartial, not place dependent and useful tool for any cost-effective analysis of suggested protective measures.

The experiments have been prepared with use of experience gathered from small scale inundation experiments recently carried out.

## 2.1. Description of the experiments

The soil sample's stand is a reinforced concrete box without the top covering part. The bottom part contains a system of pipes 12.5 mm in diameter that is connected to the large water storage tank. The box is horizontally constricted by steel beams in two levels. Steel frame is attached to the box to take the reaction force and additional small frame presents an inertial body to which the deformations are measured. The inside size of the box are 1 x 1 x 1 m.

The test itself is similar to static plate load test which is described in standards and is often used in practice so no special arrangements are needed for comparison with in-situ tests. Load is applied through a hydraulic jack to the steel plate 2 cm thick and 30 cm in diameter. The load is measured in the hydraulic system and once more in the pressure cell between the reaction frame and the hydraulic jack. Two settlement sensors which are used for measuring the settlement are installed on the plate and have guaranteed accuracy 0.01 mm. An a) part of Fig. 1 shows a scheme of the experiment while b) part shows the experiment in reality ready for testing.

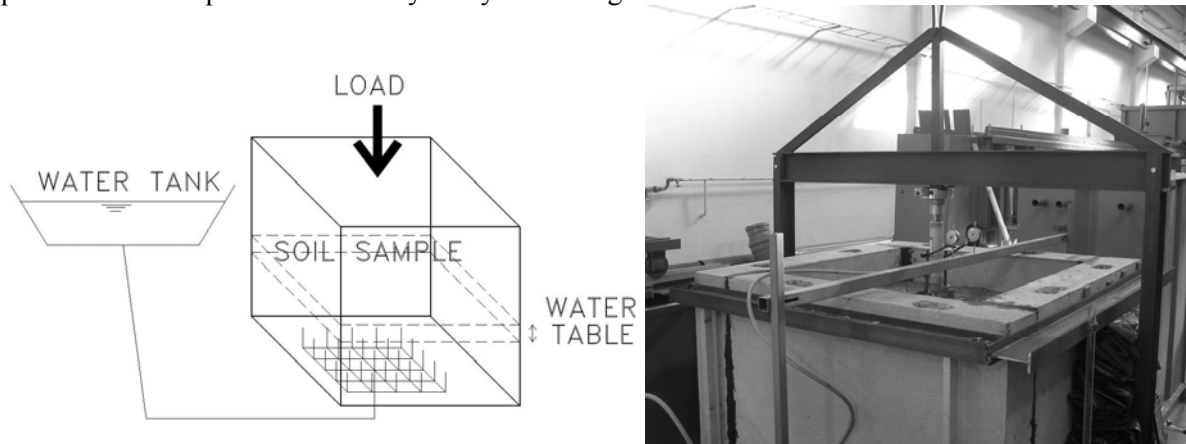


*Fig. 1: Experiment - a) scheme; b) photo.*

The soil is inserted into the concrete box by layers 15 – 20 cm thick. Each layer is compacted by vibrating plate. Compacting experiment is carried in advance so that the time of vibration is known. The soil contains natural amount of moisture as it is kept in plastic covers after being removed from the site. The time of storage is as short as possible. The moisture content is also tested on small samples.

## 2.1. Selected results

Results from the experiments are sets of load-displacement curves or time-displacement curves. For the purpose of this paper we selected results from one series of experiments on one soil.

### 2.2.1. Tested soil characteristics

The presented results were obtained on soil specimen classified as poorly grained gravel, i.e. G2 – GP. The portion of particles larger than 60 mm was 17.3% of the weight. The optimal moisture content and maximal dry soil density was evaluated using standard Proctor test and the compacting experiment prescribed 25 minutes duration of compaction with vibrating plate for each 20 cm thick layer.

This particular soil was obtained from excavation in the central area of the Prague city. In this part of the city the soil is experiencing large groundwater movement especially due to engineering activity linked with lowering water table for foundation work.

This soil has also proved its predisposition for internal erosion and collapse when exposed to high hydraulic gradient or flow pressure. Several road and building accidents were reported regarding this matter.

### 2.2.2 Results from dry load tests

Following figures show first and third loading tests on dry sample – natural water content. The SM1 and SM2 abbreviations in the charts stand for settlement measurement point 1 and 2. As the plate is instrumented with the joint that allows differential settlement of the plate at least 2 measuring points are necessary.

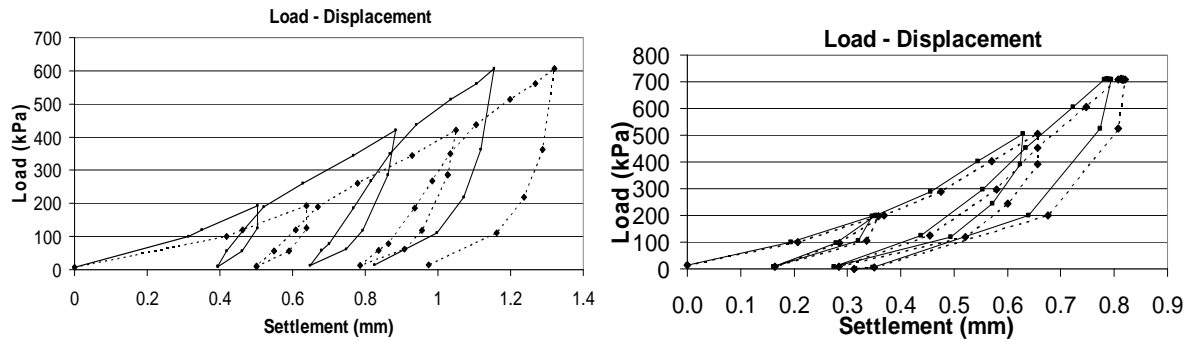


Fig. 2: Loading test nr. 1 and nr. 3 – dry.

Three facts can be nicely observed on the left part of Fig. 3 (Experiment nr. 1). First is the characteristic loop in the unloading/reloading path. As the elastic hysteresis is generally load rate dependant it is quite interesting observation when the load steps were no shorter than 5 minutes each.

Second it is the unloading/reloading path that has different slope than primary loading path. This phenomenon of structural strength vs. void ratio was described in the past (Terzaghi, 1996).

Third important fact observed is small hardening of the material.

The third test proved small creep behaviour of the soil even without the presence of water. Creep was observed in sandy soils in the past (Hsiung, 2008). The important aspects are the magnitude of the creep and the duration. The whole creep behaviour last approximately 1 hour but more than 80% of the creep deformation was reached after first 15 minutes. Following figure shows the results from first loading experiment with water entering the specimen.

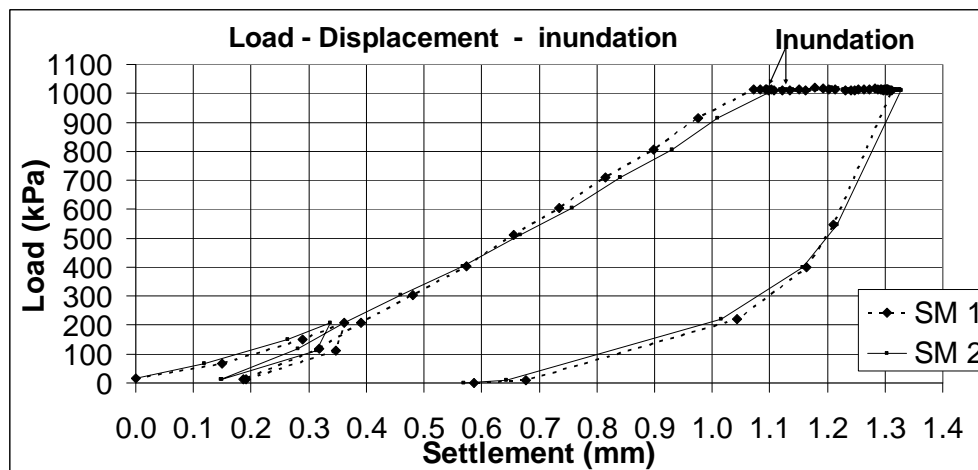


Fig. 3: Loading test nr. 4 – wet.

Before the inundation took place the load was kept constant for a time necessary to eliminate the effect of dry creep. It is important to point out that the highest position of the water table was 40 cm below the surface of the specimen. The inundation caused increase in settlement from 1.1 mm to 1.32 mm in average, i.e. increase by 20%. Although the observed volume change (less than 0.1%) was very low when compared to finer soils, for example 2.5% to 5.8% for sandy silt observed by Jia (Jia et al., 2009), and Fredlund (Fredlund Rahardjo, 1993), (Fredlund and Morgenstern, 1977) or 1.1% for

Mississippi silt observed by Tadepalli (Tadepalli, Rahardjo, Fredlund, 1992) the relative increase in settlement is very high.

When considering the influence zone below the plate we would expect that until the groundwater table reaches the border of the zone no effect on the settlement should be observed. During the first inundation the zone was very close to the bottom and so the change in behaviour took place immediately.

When running dry experiments after the inundation experiments the first response of the sample was very similar to the last loading curve although when doing the same procedure with dry-dry experiment we observe significantly stiffer response. Leaving the specimen to “rest for a long time will cause a small decrease in overconsolidation. Result obtained from the same specimen after 3 months were similar to second loading test on this specimen.

### **3. Conclusions**

The presented experimental results show that coarse soils such as gravel suffers a weak form of particles redistribution due to wetting process and although the volumetric deformation is not as high as in case of finer soils it still presents a great increase in settlement with respect to the applied load and deformation without ground water

The drop in the pore pressure due to drawdown of the water table did not show any significant deformations. This may due to the fact that the increase in an effective pressure due to the drawdown is not high enough when compared with the other involved stresses.

The tested sample also proved creep behaviour in the dry state but the magnitude of the settlement is significantly smaller compared to one caused by the inundation.

The behaviour of the sample also shows better agreement with the critical state constitutive models rather than plasticity models (Sejnoha and Janda, 2006).

### **Acknowledgement**

The authors would like to acknowledge the financial support provided within research projects MSM6840770001, MSM6840770002 and VG20102014056.

### **References**

- Fredlund, D.G., Morgenstern, N.R. (1977) Stress state variables for unsaturated soils. J. Geotech. Eng. Div., ASCE 103(GT5), 447-466.
- Fredlund, D.G., Rahardjo, H. (1993) Soil mechanics for unsaturated soils, Wiley-IEEE.
- Hsiung, B-CH.B. (2008). A case study on the behaviour of a deep excavation in sand. Computers and Geotechnics 36: 665–675.
- Jia, G.W., Zhan, L.T., Chen, Y.M. and Fredlund, D.G. (2009). Performance of a large-scale slope model subjected to rising and lowering water levels, Engineering Geology 106: 92-103.
- Kang, J-L., Su, M-D., Chang, L-F. (2005) Loss Functions and Framework for Regional Flood Damage Estimation in Residential Area, J. Mar. Sci. Tech., 13(3), 193-199.
- Sejnoha, M., and Janda, T. (2006) Formulation of generalized Cam clay model; Engineering Mechanics, vol. 13, no. 5, pp. 367-384.
- Tadepalli, R., Rahardjo, H., Fredlund, D.G. (1992) Measurements of matric suction and volume changes during inundation of collapsible soils. Geotechnical Testing Journal, ASTM, 15(2): 115–122.
- Terzaghi, K., Peck, R.B., Mesri, G. (1996) Soil Mechanics in Engineering Practice, Wiley-Interscience.

## UNCERTAIN MODELING OF MECHATRONIC SYSTEMS

L. Březina<sup>\*</sup>, T. Březina<sup>\*\*</sup>

**Abstract:** The paper proposes an approach to modeling of systems with a parametric uncertainty. The approach is based on use of upper linear fractional transformation which is commonly used for the modeling of the uncertain systems. The main difference between the classical methods and the proposed one is that the proposed method describes the uncertainty as a difference between values of corresponding matrices elements of nominal and perturbed state-space model of the described system. This result into a general analytic description of the uncertain model which may be easily used for building of an uncertain model based on a nominal and perturbed state-space model of any system. The obtained uncertain model respects the form for a robust controller design. The approach is presented on simple mass-damper-spring system.

**Keywords:** Parametric uncertainty, uncertain model, mass-damper-spring.

### 1. Introduction

The present tendencies in the area of modeling of the mechatronic systems are mostly concentrated on building of a model as precise as possible. However building of a precise model is not always possible. This might be caused by change of some of system parameters during the action of the system or just simply by inaccurate or incomplete information about the system, neglected nonlinearities, etc. These inaccuracies or deviations from the reality may be described by introducing an uncertainty to the model. Such a model is then established by its nominal parameters which may vary within a certain range given by the uncertainty.

The standard methods of the parametric uncertainty modeling (Petkov et al., 2002, 2008) are typically based on  $\mathbf{M} - \Delta$  configuration (Fig. 1). The  $\mathbf{M}$  matrix represents the augmented model obtained by the upper linear fractional transformation (ULFT) (Safonov, 1982) and  $\Delta$  matrix represents a diagonal perturbation matrix.

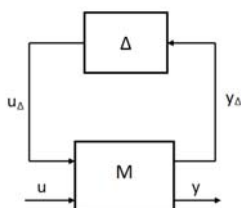


Fig. 1: The standard  $\mathbf{M} - \Delta$  configuration for a model with a parametric uncertainty.

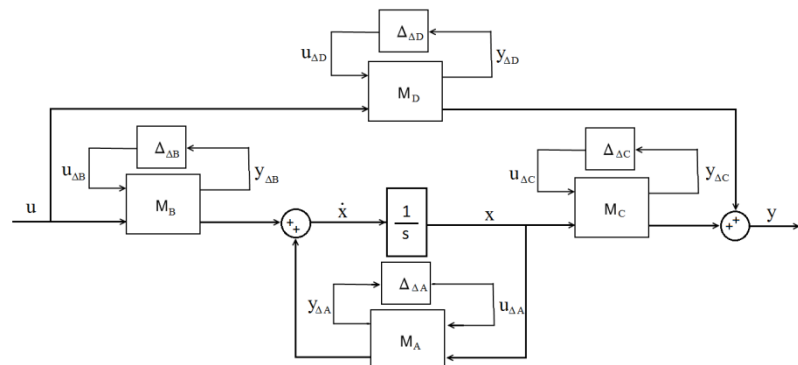


Fig. 2: Scheme of particular transfer function matrices.

The matrix  $\mathbf{M}$  is typically constructed individually for every uncertain parameter in the model (Gu, 2005). Let's note that the ULFT must be then also used individually. The obtained matrices are then

<sup>\*</sup> Ing. Lukáš Březina, Ph.D.: Institute of Solid Mechanics, Mechatronics and Biomechanics, Brno University of Technology, Technická 2, 616 69, Brno; CZ, e-mail: brezina.l@fme.vutbr.cz

<sup>\*\*</sup> doc. RNDr. Ing. Tomáš Březina, CSc.: Institute of Automation and Computer Science, Brno University of Technology, Technická 2, 616 69 Brno; CZ, e-mail: brezina@fme.vutbr.cz



combined into a compact uncertain model. This is very uncomfortable in cases where is needed a high number of uncertain parameters in the model. The advantage of the proposed approach is that the uncertain model is constructed analytically in the most general form. Such a general description may be consequently easily used for building of an uncertain model of any system without need for precedent design steps typical for constructing of uncertain models (ULFT, etc.).

The possibility of the uncertain modeling is also offered by commercially available tool Robust Control Toolbox in Matlab with functions ‘ureal’, ‘umat’ and ‘uss’. The crucial disadvantage of these functions is that even the application of one of them transforms the standard ‘ss’ (state-space) Matlab model into an ‘uss’ (uncertain state-space) form. Such a transformed model is suitable for simulations but it is impossible to use it for a robust controller design (e.g. ‘hinfyn’ function in Matlab).

It was already mentioned that proposed method leads to a general form of the uncertain model in the analytic form. The modeling of the system as uncertain then requires the knowledge of the nominal and perturbed model in state-space form only. The advantage of the method is the possibility of its application to models of high orders where modeling of the uncertainty individually for desired parameters might be demanding or for models where the inner structure of the model is not exactly known (for example models obtained by identification). Obtained model also respects the form for a robust controller design in Matlab.

## 2. Modeling of a system with parametric uncertainty

The approach to the modeling of the Stewart platform with a parametric uncertainty based on state-space models of the system was described in (Březina, L. & Březina, T., 2010). Now the more general approach will be presented. The basic idea is to determine the difference between particular values of state matrices elements of a nominal system and a maximally perturbed system. Then the uncertain model is obtained by upper linear fractional transformation.

The nominal system is described as

$$\begin{aligned}\dot{\mathbf{x}} &= \bar{\mathbf{A}}\mathbf{x} + \bar{\mathbf{B}}\mathbf{u} \\ \mathbf{y} &= \bar{\mathbf{C}}\mathbf{x} + \bar{\mathbf{D}}\mathbf{u}\end{aligned}\quad (1)$$

and the maximally perturbed system as

$$\begin{aligned}\dot{\mathbf{x}} &= \mathbf{A}\mathbf{x} + \mathbf{B}\mathbf{u} \\ \mathbf{y} &= \mathbf{C}\mathbf{x} + \mathbf{D}\mathbf{u}\end{aligned}\quad (2)$$

The meaning of the particular terms is following:

$\mathbf{x}$  represents the vector of states,  $\dot{\mathbf{x}}$  represents the vector of the time derivations of the states,  $\mathbf{u}$  is the vector of inputs,  $\mathbf{y}$  is the vector of outputs, matrices  $\bar{\mathbf{A}}, \bar{\mathbf{B}}, \bar{\mathbf{C}}, \bar{\mathbf{D}}$  represent state matrices of the nominal system and finally  $\mathbf{A}, \mathbf{B}, \mathbf{C}, \mathbf{D}$  represent the state matrices of the perturbed system.

State matrices of the perturbed system (2) may be also defined as

$$\mathbf{A} = \bar{\mathbf{A}} + \mathbf{A}_\Delta, \quad (3)$$

the uncertainty contribution is then  $\mathbf{A}_\Delta = \mathbf{A} - \bar{\mathbf{A}}$ . There are similarly derived  $\mathbf{B}_\Delta$ ,  $\mathbf{C}_\Delta$  and  $\mathbf{D}_\Delta$ .

The upper linear fractional transformation is described as

$$\mathbf{F}_u(\mathbf{M}, \Delta_u) = \mathbf{M}_{22} + \mathbf{M}_{21}\Delta_u(\mathbf{I} - \mathbf{M}_{11}\Delta_u)^{-1}\mathbf{M}_{12}. \quad (4)$$

It is then obtained  $\mathbf{M}_{21}\mathbf{M}_{12} = \mathbf{A}_\Delta$ ,  $\mathbf{M}_{11} = \mathbf{0}$ ,  $\mathbf{M}_{12} = \mathbf{I}$ ,  $\mathbf{M}_{21} = \mathbf{A}_\Delta$  and  $\mathbf{M}_{22} = \bar{\mathbf{A}}$  by comparing (4) with (3). The approach is same also for other state matrices.

The interconnection transfer function matrix is then  $\mathbf{M} = \begin{bmatrix} \mathbf{M}_{11} & \mathbf{M}_{12} \\ \mathbf{M}_{21} & \mathbf{M}_{22} \end{bmatrix}$ .

Consequently, according to the scheme of the system containing particular transfer function matrices (Fig. 2), it is obtained

$$\begin{bmatrix} \mathbf{y}_{\Delta A} \\ \dot{\mathbf{x}} \end{bmatrix} = \begin{bmatrix} \mathbf{0} & \mathbf{I} \\ \mathbf{A}_{\Delta} & \bar{\mathbf{A}} \end{bmatrix} \begin{bmatrix} \mathbf{u}_{\Delta A} \\ \mathbf{x} \end{bmatrix}, \begin{bmatrix} \mathbf{y}_{\Delta B} \\ \dot{\mathbf{x}} \end{bmatrix} = \begin{bmatrix} \mathbf{0} & \mathbf{I} \\ \mathbf{B}_{\Delta} & \bar{\mathbf{B}} \end{bmatrix} \begin{bmatrix} \mathbf{u}_{\Delta B} \\ \mathbf{u} \end{bmatrix}, \quad (5)$$

$$\begin{bmatrix} \mathbf{y}_{\Delta C} \\ \mathbf{y} \end{bmatrix} = \begin{bmatrix} \mathbf{0} & \mathbf{I} \\ \mathbf{C}_{\Delta} & \bar{\mathbf{C}} \end{bmatrix} \begin{bmatrix} \mathbf{u}_{\Delta C} \\ \mathbf{x} \end{bmatrix}, \begin{bmatrix} \mathbf{y}_{\Delta D} \\ \mathbf{y} \end{bmatrix} = \begin{bmatrix} \mathbf{0} & \mathbf{I} \\ \mathbf{D}_{\Delta} & \bar{\mathbf{D}} \end{bmatrix} \begin{bmatrix} \mathbf{u}_{\Delta D} \\ \mathbf{u} \end{bmatrix}, \quad (6)$$

where  $\mathbf{u}_{\Delta A}, \mathbf{u}_{\Delta B}, \mathbf{u}_{\Delta C}, \mathbf{u}_{\Delta D}$  represents inputs to the perturbation matrices  $\Delta_{\Delta A}, \Delta_{\Delta B}, \Delta_{\Delta C}, \Delta_{\Delta D}$ ,  $\mathbf{y}_{\Delta A}, \mathbf{y}_{\Delta B}, \mathbf{y}_{\Delta C}, \mathbf{y}_{\Delta D}$  are then outputs from the perturbation matrices.

The compact form of the matrix representation of the general uncertain model with the global perturbation matrix is then

$$\begin{bmatrix} \dot{\mathbf{x}} \\ \mathbf{y}_{\Delta A} \\ \mathbf{y}_{\Delta B} \\ \mathbf{y}_{\Delta C} \\ \mathbf{y}_{\Delta D} \\ \mathbf{y} \end{bmatrix} = \begin{bmatrix} \bar{\mathbf{A}} & \mathbf{A}_{\Delta} & \mathbf{B}_{\Delta} & \mathbf{0} & \mathbf{0} & \bar{\mathbf{B}} \\ \mathbf{I} & \mathbf{0} & \mathbf{0} & \mathbf{0} & \mathbf{0} & \mathbf{0} \\ \mathbf{0} & \mathbf{0} & \mathbf{0} & \mathbf{0} & \mathbf{0} & \mathbf{I} \\ \mathbf{I} & \mathbf{0} & \mathbf{0} & \mathbf{0} & \mathbf{0} & \mathbf{0} \\ \mathbf{0} & \mathbf{0} & \mathbf{0} & \mathbf{0} & \mathbf{0} & \mathbf{I} \\ \bar{\mathbf{C}} & \mathbf{0} & \mathbf{0} & \mathbf{C}_{\Delta} & \mathbf{D}_{\Delta} & \bar{\mathbf{D}} \end{bmatrix} \begin{bmatrix} \mathbf{x} \\ \mathbf{u}_{\Delta A} \\ \mathbf{u}_{\Delta B} \\ \mathbf{u}_{\Delta C} \\ \mathbf{u}_{\Delta D} \\ \mathbf{u} \end{bmatrix}, \begin{bmatrix} \mathbf{u}_{\Delta A} \\ \mathbf{u}_{\Delta B} \\ \mathbf{u}_{\Delta C} \\ \mathbf{u}_{\Delta D} \end{bmatrix} = \begin{bmatrix} \Delta_{\Delta A} & \mathbf{0} & \mathbf{0} & \mathbf{0} \\ \mathbf{0} & \Delta_{\Delta B} & \mathbf{0} & \mathbf{0} \\ \mathbf{0} & \mathbf{0} & \Delta_{\Delta C} & \mathbf{0} \\ \mathbf{0} & \mathbf{0} & \mathbf{0} & \Delta_{\Delta D} \end{bmatrix} \begin{bmatrix} \mathbf{y}_{\Delta A} \\ \mathbf{y}_{\Delta B} \\ \mathbf{y}_{\Delta C} \\ \mathbf{y}_{\Delta D} \end{bmatrix}. \quad (7), (8)$$

Let's note that  $-\mathbf{I} \leq \Delta_{\Delta A, \Delta B, \Delta C, \Delta D} \leq \mathbf{I}$  for the symmetrical +/- perturbation of the uncertainty around the nominal value.

The typical form of an uncertain model for a robust controller design is according to (Gu, 2005) following

$$\mathbf{G} = \begin{bmatrix} \mathbf{A}_v & \mathbf{B}_{v1} & \mathbf{B}_{v2} \\ \mathbf{C}_{v1} & \mathbf{D}_{v11} & \mathbf{D}_{v12} \\ \mathbf{C}_{v2} & \mathbf{D}_{v21} & \mathbf{D}_{v22} \end{bmatrix}. \quad (9)$$

The form (9) corresponds with (7) for  $\mathbf{A}_v = \bar{\mathbf{A}}$ ,  $\mathbf{B}_{v1} = [\mathbf{A}_{\Delta} \quad \mathbf{B}_{\Delta} \quad \mathbf{0} \quad \mathbf{0}]$ ,  $\mathbf{B}_{v2} = \bar{\mathbf{B}}$ ,  $\mathbf{C}_{v1} = [\mathbf{I} \quad \mathbf{0} \quad \mathbf{I} \quad \mathbf{0}]^T$ ,  $\mathbf{C}_{v2} = \bar{\mathbf{C}}$ ,  $\mathbf{D}_{v11} = [\mathbf{0}]$ ,  $\mathbf{D}_{v12} = [\mathbf{0} \quad \mathbf{I} \quad \mathbf{0} \quad \mathbf{I}]^T$ ,  $\mathbf{D}_{v21} = [\mathbf{0} \quad \mathbf{0} \quad \mathbf{C}_{\Delta} \quad \mathbf{D}_{\Delta}]$ .

### 3. Example – Mass-Damper-Spring system

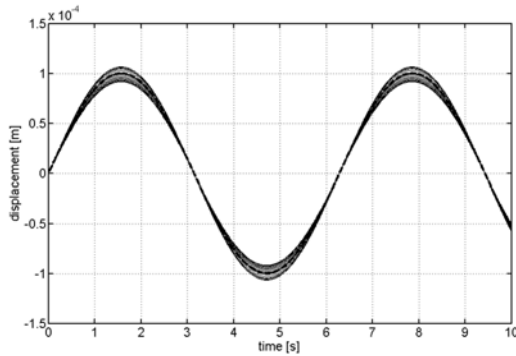
The example represents simple mass – damper – spring system which is in the nominal state-space form for  $x_1 = x$  and  $x_2 = \dot{x}$  described by matrices  $\bar{\mathbf{A}}, \bar{\mathbf{B}}, \bar{\mathbf{C}}, \bar{\mathbf{D}}$  as

$$\frac{d}{dt} \begin{bmatrix} x_1 \\ x_2 \end{bmatrix} = \begin{bmatrix} 0 & 1 \\ -\frac{\bar{k}}{\bar{m}} & -\frac{\bar{b}}{\bar{m}} \end{bmatrix} \begin{bmatrix} x_1 \\ x_2 \end{bmatrix} + \begin{bmatrix} 0 \\ 1 \\ \bar{m} \end{bmatrix} f, y = [1 \quad 0] \begin{bmatrix} x_1 \\ x_2 \end{bmatrix} + [0] f. \quad (10)$$

The perturbed model defined by matrices  $\mathbf{A}, \mathbf{B}, \mathbf{C}, \mathbf{D}$  then contains parameters  $m = \bar{m}(1 + \delta_m)$ ,  $b = \bar{b}(1 + \delta_b)$ ,  $k = \bar{k}(1 + \delta_k)$  substituted to (10) instead of nominal parameters. There are consequently obtained matrices  $\mathbf{A}_{\Delta}$ ,  $\mathbf{B}_{\Delta}$ ,  $\mathbf{C}_{\Delta}$  and  $\mathbf{D}_{\Delta}$  according to (3). The compact uncertain model of the system and the perturbation matrix are then obtained according to (7) and (8).

The following results of the uncertain model behavior were obtained for the values of the nominal parameters  $\bar{m} = 1 \text{ kg}$ ,  $\bar{b} = 100 \text{ Ns/m}$ ,  $\bar{k} = 1.10^5 \text{ N/m}$ . The perturbed model was obtained for the uncertainty 10% of each of the nominal values, i.e.  $\delta_m, \delta_b, \delta_k = 0,1$ . There were done twenty random

samples of the model (i.e.  $-\mathbf{I} \leq \Delta_{\Delta A, \Delta B, \Delta C, \Delta D} \leq \mathbf{I}$ ) for the input force  $f = F_0 \sin(\omega t)$ ,  $F_0 = 10\text{ N}$  and  $\omega = 1\text{ rad/s}$ .



*Dashed line for the nominal model, solid line for the uncertain model realizations.*  
**Fig. 3:** Random outputs from the uncertain model for the given output.

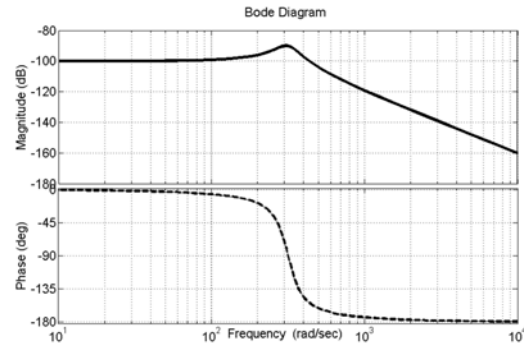


**Fig. 4:** Bode diagrams for the random realizations of the uncertain model.

It may be easily determined that initial difference 10% of the nominal parameters causes for  $\Delta_{\Delta A, \Delta B, \Delta C, \Delta D} = \pm \mathbf{I}$  approximate maximal difference  $\pm 6.6\%$  of the nominal output, Fig. 3. There is no significant change in the behavior in the frequency domain, Fig. 4.

#### 4. Conclusions

The paper proposes a method for constructing of uncertain models which is based on obtaining of general uncertain model description in the analytic form. Once the general model is obtained by standard methods for modeling with the parametric uncertainty it may be used for constructing of any state-space model as uncertain. It is required knowledge of the nominal and perturbed model only. The method is suitable for models of high orders where modeling of the uncertainty for individual parameters might be very demanding or models with not precisely known structure (e.g. obtained from the identification). The advantage is its high versatility and the fact that obtained uncertain model respects the form for a robust controller design which might be a problem for commercial tools. The disadvantage of the method may be slightly wider uncertainty zone than necessary. This is for systems with nonsymmetrical balancing of matrices elements values in perturbed systems (with maximal and minimal uncertainty) around the corresponding values in the nominal system. The method was presented for sake of simplicity on a mass-damper-spring system.

#### Acknowledgement

This work is supported from research plan MSM 0021630518 Simulation modelling of mechatronic systems.

#### References

- Březina, L. & Březina, T. (2010) Stewart Platform Model with Uncertain Parameters. Solid state phenomena, 164, 2010, pp.177 – 182.
- Gu, D.W., Petrov, P.H. & Konstantinov, M.M. (2005) Robust Control Design with Matlab. Springer, London.
- Petkov, P.H., Gu, D.W. & Konstantinov, M.M. (2002) Robust mu-design of a disk drive servo system, in: Proc. IEEE International Symposium on Computer Aided Control System Design, IEEE, New York, pp. 57-62.
- Petkov, P.H., Yonchev, A.S. & Christov, N.D., et al. (2008) Numerical methods for robust control, in: Proc. 6th International Conference on Large-Scale Scientific Computing, Springer, Berlin, pp.350-357.
- Safonov, M.G. (1982) Stability margins of diagonally perturbed multivariable feedback systems. Control theory and applications, 129, 6, 1982, pp. 251–256.

## USAGE OF NONLINEAR NORMAL MODES IN DYNAMICS

M. Byrtus<sup>\*</sup>

**Abstract:** *The paper summarizes the method of nonlinear normal modes (NNMs) which has gained importance in nonlinear dynamics. Two main definitions of NNMs are discussed: Rosenberg's definition and Shaw and Pierre definition based on geometric arguments and inspired by the centre manifold technique. Fundamental properties of NNMs like frequency-energy dependence, modal interactions and mode bifurcations and stability are introduced. To compute the NNMs analytical and numerical approaches are used and compared. The NNMs approach to nonlinear dynamics is clearly demonstrated and compared with linear normal modes (LNMs) using a smooth nonlinear mechanical system.*

**Keywords:** *Nonlinear normal modes, mode bifurcation, stability, modal analysis.*

### 1. Introduction

The concept of normal modes is central in the theory of linear vibrating systems. The linear normal modes (LNMs) have interesting mathematical properties. They can be used to decouple the governing equations of motion, where a linear system vibrates as if it were made of independent oscillators governed by the eigensolutions. Moreover, free and forced oscillations can be expressed as linear combination of individual LNM motions. LNMs are relevant dynamical features that can be exploited for various purposes.

In real-life applications, nonlinearity is a frequent occurrence. Typical nonlinearities include backlash and friction in control surface, hardening nonlinearities, saturation effects, etc. Further, for instance, structural behaviour of materials made of composites is deviating significantly from linearity too. Any attempt to apply traditional linear analysis to nonlinear systems results at best in suboptimal design. In this context, NNMs offer a solid theoretical and mathematical tool for interpreting wide class of nonlinear dynamical phenomena, yet they have a clear and simple conceptual relation to the LNMs. Moreover, they can be advantageously used for the reduction of nonlinear models (Gabale & Sinha, 2011). The objective of the present paper is to describe and illustrate in a simple manner fundamental properties of NNMs for conservative nonlinear systems.

### 2. Basic definitions of NNMs

There exist two main definitions of the NNMs in the literature, due to Rosenberg and Shaw and Pierre (Kerschen et al., 2009). Historically, Lyapunov's and Poincaré's contributions served as the cornerstone of the NNMs development. Lyapunov showed that there exist at least  $n$  different families of periodic solutions around the stable equilibrium point of  $n$ -DOF conservative systems with no internal resonances. At low energy, the periodic solutions of each family are in the neighbourhood of a LNM of corresponding linearized system. These  $n$  families define  $n$  NNMs that can be regarded as nonlinear extensions of the  $n$  LNMs of the corresponding linear system (Vakakis et al., 1996).

During the normal mode motion of a linear conservative system, each system component moves with the same frequency and with a fixed ratio amongst displacements of the components. Targeting a straightforward nonlinear extension of the LNM concept, Rosenberg defined a NNM as a *vibration in unison* of the system (i.e. synchronous oscillation). This definition requires that all points of the system reach their extreme values and pass through zero simultaneously and allows all displacements to be expressed in terms of a single reference displacement.

---

<sup>\*</sup> Ing. Miroslav Byrtus, Ph.D.: Department of Mechanics, University of West Bohemia, Univerzitni 8, 306 14 Plzen, CZ, e-mail: mbyrtus@kme.zcu.cz

Shaw and Pierre proposed a generalization of Rosenberg's definition that provides a direct extension of the NNMs concept to damped systems. Based on geometric arguments and inspired by the center manifold technique, they defined a NNM as two dimensional invariant manifold in phase space. Such a manifold is invariant under the flow, which extends the invariance property of LNM to nonlinear systems (Shaw & Pierre, 1993).

### 3. Fundamental properties of NNMs

NNMs have intrinsic properties that are fundamentally different from those of LNM. They are reviewed and some of them are illustrated in this chapter.

#### 3.1. Frequency-energy dependence

One typical dynamical feature of nonlinear systems is the *frequency-energy dependence* of their oscillations. Let us consider a 2-DOF conservative system with a cubic stiffness, which is governed by the equations

$$\begin{aligned}\ddot{q}_1 + (2q_1 - q_2) + 0.5q_1^3 &= 0, \\ \ddot{q}_2 + (2q_2 - q_1) &= 0.\end{aligned}\tag{1}$$

To solve the system (1), harmonic balance method can be applied. This method expresses the periodic motion of a system by means of finite Fourier series (Nayfeh, 1996). The solution can be expressed as two cosine functions with different amplitudes for each coordinate, respectively. Substituting the solution into (1), one can obtain the unknown amplitudes in dependence on frequency of the periodic motion. Based on this, total energy of the system can be calculated. Due to the frequency-energy dependence, the representation of NNMs in a frequency-energy plot (FEP) is used (Peeters et al., 2009). A NNM motion is represented by a point in the FEP which is drawn at a frequency corresponding to the minimal period of the periodic motion and at energy equal to the conserved total energy during the motion. Each branch represents a family of NNM motion with the same qualitative features (Fig. 1).

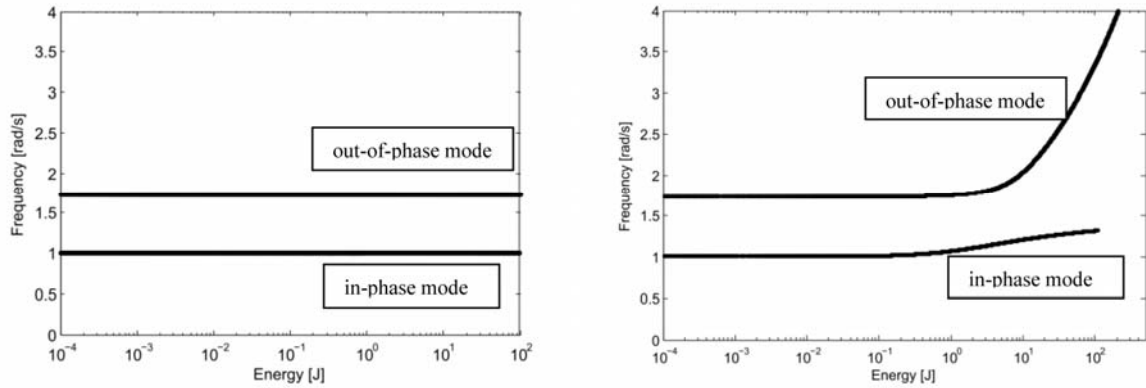


Fig. 1: Frequency-energy plot of system (1), (left – LNM, right – NNM).

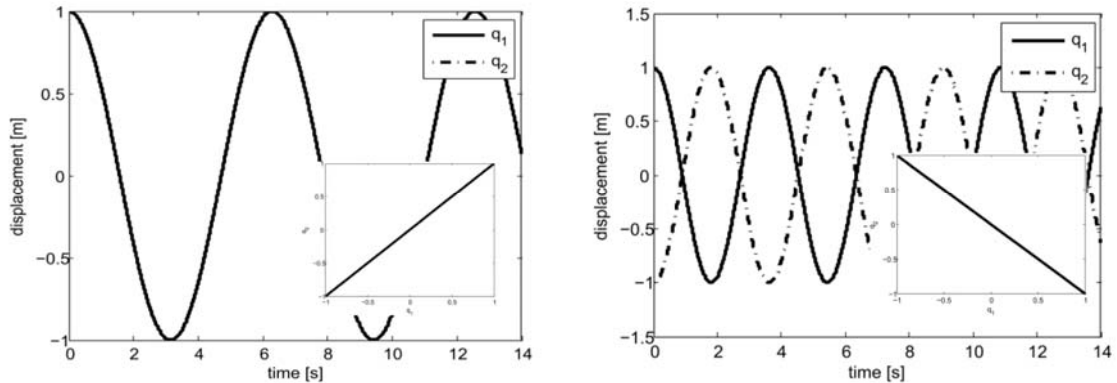


Fig. 2: Time series and motion in configuration space of LNM; (left: in-phase mode  $T = 6.238$  s, right: out-of-phase mode,  $T = 3.627$  s).

Two representations of both LNMs and NNMS are shown in Fig. 2 and 3. Nonlinear normal modes can be represented by time series of coordinates of the system or they can be viewed in configuration space. The LNMs are represented by a straight line in configuration space and NNMs by a general curve. Fig. 2 shows linear normal modes of linearized system (1) while Fig. 3 displays a periodic solution (NNMs) of the nonlinear system (2), which corresponds to free vibration excited by nonzero initial conditions. It can be clearly seen that the nonlinear system can exhibit other periodic solution with different behaviour and time period of motion than those presented in Fig. 2. The periodic solution was found by shooting method combined with Newton-Raphson method. To ensure the convergence of this method, initial conditions have to be very close to existing solution to ensure the sufficient convergence.

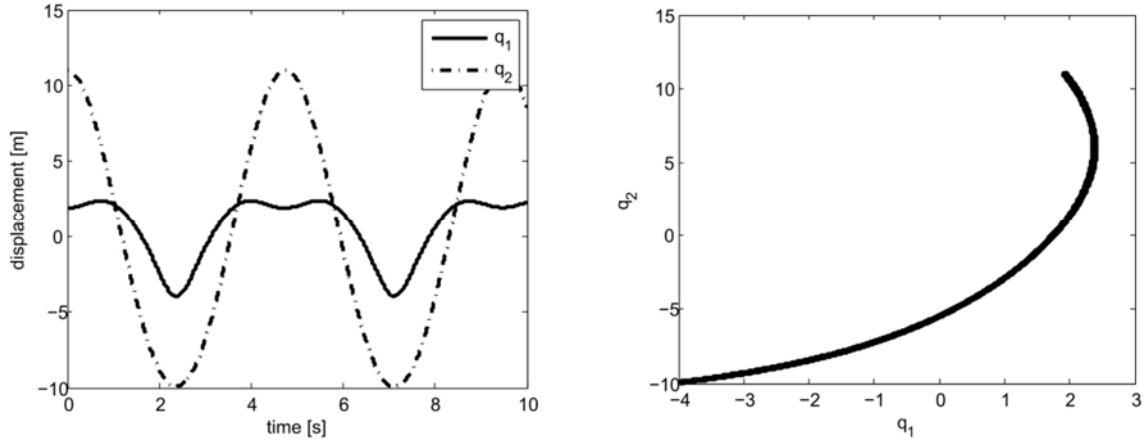


Fig. 3: Time series of NNM motions of system (2) – left, NNM motions in configuration space – right; in-phase NNM for  $[q_1(0), q_2(0), \dot{q}_1(0), \dot{q}_2(0)] = [1.9, 11, 0, 0]$ ,  $T = 4.75$  s.

### 3.2. Modal interaction

Another salient feature of nonlinear systems is that NNMs may interact during a general motion of the system. A case of particular interest is when the linear natural frequencies are commensurate or nearly commensurate. An energy exchange between the different modes employed may therefore be observed during the internal resonance. For instance, exciting a high frequency mode may produce a large amplitude response in a low frequency mode. Dynamical interaction of an elastic system and nonlinear absorber exploiting these energy transfers has been studied by Mikhlin & Reshetnikova (2005).

### 3.3. Mode bifurcations and stability

A third fundamental property of NNMs is that their number may exceed the number of DOFs of the system. Due to mode bifurcation, not all NNMs can be regarded as nonlinear continuation of normal modes of linear system (Kerschen et al., 2009). Internally resonant NNMs are one example, another possible example corresponds to the NNM bifurcation of the system

$$\begin{aligned}\ddot{q}_1 + q_1 + q_1^3 + K(q_1 - q_2)^3 &= 0, \\ \ddot{q}_2 + q_2 + q_2^3 + K(q_2 - q_1)^3 &= 0\end{aligned}\quad (2)$$

for variations of the parameters  $K$ . This system possesses similar NNMs that obey to the relation  $q_2(t) = cq_1(t)$ . Eliminating  $q_2(t)$  from Eqs. (2), one obtains two equations for  $q_1(t)$  which must lead to the same solution. Therefore, after some modifications, it follows

$$K(1+c)(c-1)^3 = c(1-c^2), \quad c \neq 0. \quad (3)$$

Eq. (3) means that system (2) always possesses two modes characterized by  $c = \pm 1$  which are direct extension of the LNMs. However, this system can possess two additional similar NNMs which cannot be captured using linearization procedures. At  $K=0.25$ , these NNMs bifurcate from the out-of-phase mode (see Fig. 4) (Kerschen et al., 2009).

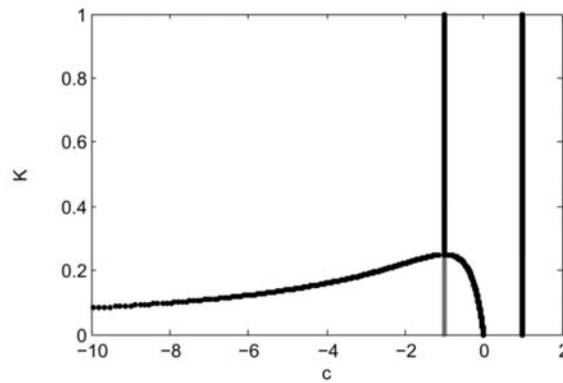


Fig. 4: NNM bifurcation of system (2) (black – stable NNMs, grey – unstable NNM).

#### 4. Computation of NNMs

Numerical calculation is based on the fact that the NNMs are a continuation of LNMS. Therefore, continuation methods are often employed (Peeters et al, 2009). The simplest and most intuitive continuation technique is the sequential continuation method, which uses the shooting method to find the periodic solution for given time period. But this method has some drawbacks. The convergence depends critically on the closeness of the initial guess to the actual solution and it is unable to deal with so called turning points. For better performance, a continuation algorithm uses a more sophisticated prediction than the last computed solution. In addition, corrections of the period have to be considered. The sequential continuation method was used to calculate presented results.

#### 5. Conclusions

This paper deals with nonlinear normal modes (NNMs) as a useful theoretical and mathematical tool for nonlinear system investigation. Nonlinear normal modes represent a continuation of linear normal modes (LNMs) in cases when the linearized models cannot be used. The NNMs introduce a periodic motion and therefore numerical methods for finding periodic solutions can be advantageously employed. This paper serves as a brief summary of basic NNMs definitions and introduces fundamental properties of NNMs regarding conservative nonlinear systems and shows how the NNMs differ from LNMs. The NNMs approach will be extended to damped nonlinear systems and in the future it will be used for dynamical analysis of mechanical systems with clearances in general.

#### Acknowledgement

This work was supported by project No. P101/11/P457 "Modelling, analysis and optimisation of vibro-impact oscillation in large rotating coupled systems" of the Czech Science Foundation.

#### References

- Gabale, A. P. & Sinha, S. C. (2011) *Model reduction of nonlinear systems with periodic excitation via construction of invariant manifolds*. Journal of Sound and Vibration. doi:10.1016/j.jsv.2010.12.013.
- Kerschen, G., Peeters, M., Golinval, J. C. & Vakakis, A. F. (2009) *Nonlinear normal modes, Part I: A useful framework for the structural dynamicist*. Mechanical Systems and Signal Processing 23, 170-194.
- Mikhlin, Y. V. & Reshetnikova, S. N. (2005) *Dynamical interaction of an elastic system and essentially nonlinear absorber*. Journal of Sound and Vibration 283, 91-120.
- Nayfeh, A. H. (1995) *Applied Nonlinear Dynamics (Analytical, Computational and Experimental Methods)*. John Wiley & Sons, Inc.
- Peeters, M., Vigu  , R., S  randour, G., Kerschen, G. & Golinval, J. C. (2009) *Nonlinear normal modes, Part II: Towards a practical computation using numerical continuation techniques*. Mechanical Systems and Signal Processing 23, 195-216.
- Shaw, S. W. & Pierre, C. (1993) *Normal modes for non-linear vibratory systems*. Journal of Sound and Vibration 164(1), 85-124.
- Vakakis, A. F., Manewitch L. I., Mikhlin, Y. V., Pilipchuk, V. N & Zevin A. A. (1996) *Normal modes and localization in nonlinear systems*. John Wiley & Sons, Inc.



## GENERATOR OF BASIC COMMAND SIGNALS FOR QUALITY TESTING OF PAN AND TILT DEVICES SERVOMECHANISMS

V. Cech<sup>\*</sup>, J. Jevicky<sup>\*\*</sup>

**Abstract:** *The pan and tilt devices (P&TD) are often used for placement of camera and antenna systems which must track moving objects (targets) precisely and speedily in many applications. For the basic testing of the adjustment and the quality of their positioning servomechanisms, the unit step functions of position or velocity are used as command signals. We have developed the program SNBP for the complex testing. The algorithms description of its foregoer EFG was published in the conference Engineering Mechanics 2004. As time goes on, it has shown the necessity to develop a connecting link – the generator of only basic command signals necessary in the middle phase during servos testing. We have utilized the traditional model of a target movement, i.e. the hypothesis about its uniform straight-line motion. This model is not able to generate a correct command signal for the elevation motion control in the range greater than  $\pm 90^\circ$ . At present, P&TDs are made with substantially greater elevation ranges. Therefore we have remade completely the model. The simulation model, which we present now, is able to generate the command signal for the unlimited traverse motion and for the elevation motion, too.*

**Keywords:** *Pan and tilt device, positional servomechanism, basic command signals generator (simulator).*

### 1. Target movement model

A basic clarification of the simulation target movement model is in Fig. 1 and 2. A pan and tilt device (P&TD) is placed in the point *B* (Fig. 1). Its traverse (pan) axis is perpendicular to the horizontal plane and it intersects the elevation (tilt) axis just in the point *B*. Due to simplicity, we assume that the Line-of-Sight (LOS) of the camera objective passes through the same point and that the LOS is directed precisely to the target point *T*, which represents the target. Consequently, the target point *T* is identical to the aiming point. The non-simplified description of the configuration is adduced in Cech, V. & Jevicky, J. (2004).

The target is moving uniformly rectilinearly and so its trajectory is determined explicitly by the ground speed vector  $\mathbf{vT} = (vT, \alpha T, \lambda T)$ . The movement proceeds in the vertical target course over ground plane (track plane) (Fig. 2 – a set of *T*-points, specially *T*<sub>0</sub>, *T*<sub>H</sub>, *T*<sub>A</sub>, *T*). The target course over ground is given by the unit vector of its speed, consequently by the angles  $(\alpha T, \lambda T)$ , where  $\alpha T$  is the actual track bearing (azimuth),  $\lambda T$  is the angle of course pitch over ground ( $\lambda T = 0$  – „constant altitude“,  $\lambda T > 0$  – pitching angle,  $\lambda T < 0$  – diving angle).

The shortest horizontal range *dTB* from the point *B* to the track plane (the line segment *BPC*) is denoted as (azimuthal) course (track) parameter  $|pA| = \min dTB$ . If  $pA = 0$ , then it is called as “coming course (track)”; if  $pA \neq 0$ , then it is called as “crossing course (track)”. It is presumed traditionally, that  $pA \geq 0$ . For simplification of calculations, we will assume that  $pA$  is a real number.

Vertically over the point *PC* there is lying so-called midpoint *TA* of the target path. Actual path *sA* is contractually equal to zero in this point, i.e.  $sA(TA) = 0$ . It is valid contractually that  $sA = vT \cdot tA$ , where *tA* is contractual time of the target motion. The half-line is denoted as “approaching leg” for  $t_A < 0$  and as “receding leg” for  $t_A > 0$ . In calculations there is used the actual horizontal path  $x_A = s_A \cdot \cos \lambda_T$ , which lies in the target horizontal course (track). The horizontal increments of topographical coordinates of the system UTM relative to the point *B* are

---

<sup>\*</sup> assoc. prof. Ing. Vladimír Čech, CSc.: OPROX, a.s., Brno, Kulkova 8, 615 00 Brno, CZ, e-mail: cech-vladimir@volny.cz

<sup>\*\*</sup> assoc. prof. RNDr. Jiří Jevický, CSc.: University of Defence, Kounicova 65, 602 00 Brno; CZ, e-mail: jiri.jevicky@centrum.cz

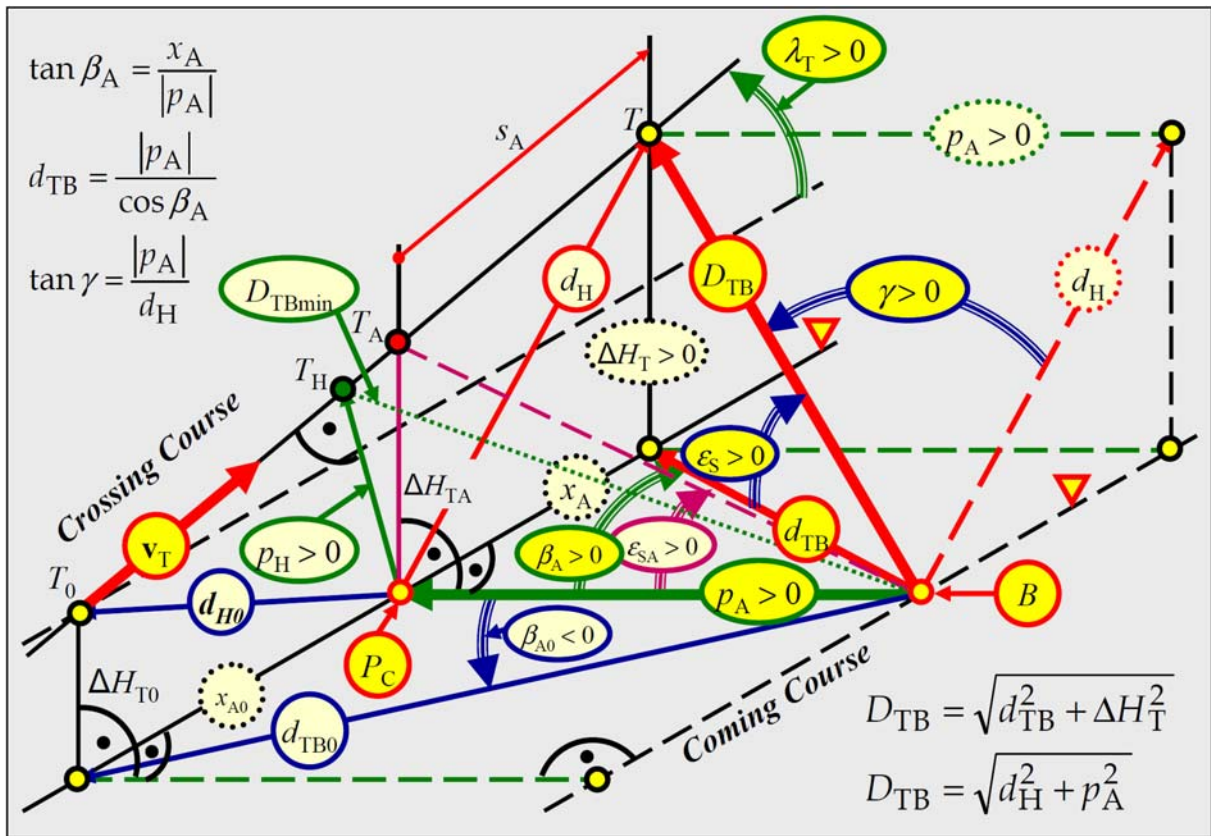


Fig. 1: The first scheme for clarification of geometric relations.

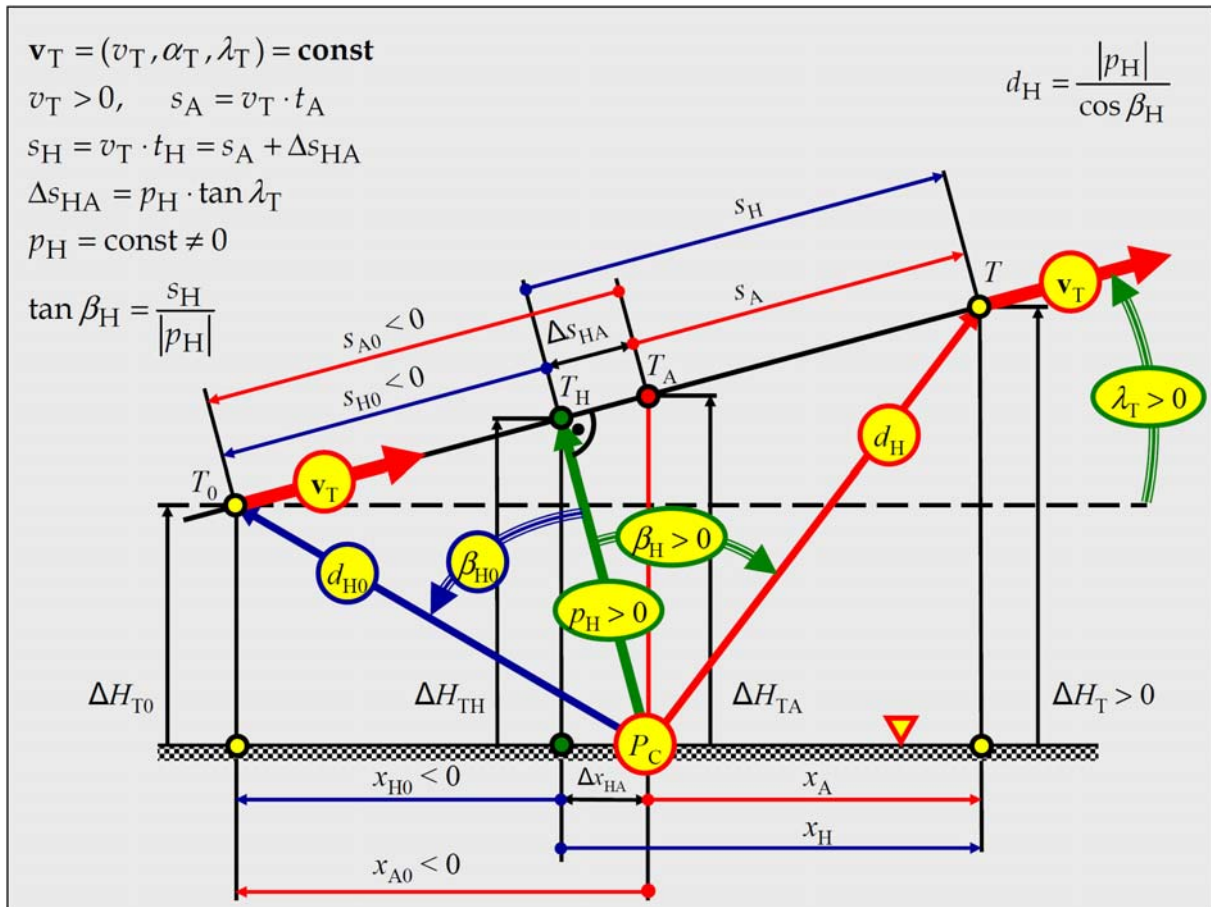


Fig. 2: The second scheme for clarification of geometric relations.

$$\begin{aligned}\Delta E_T &= x_A \cdot \sin \alpha_T + p_A \cdot \sin(\alpha_T + 270^\circ), \\ \Delta N_T &= x_A \cdot \cos \alpha_T + p_A \cdot \cos(\alpha_T + 270^\circ).\end{aligned}\quad (1)$$

In contrast to traditional procedures, we will use the slant range  $d_H$  of the point  $T$  to the point  $P_C$ . We denote its minimal size as the elevation course (track) parameter  $|p_H| = \min d_H$  (the line segment  $T_H P_C$ ). For simplification of calculations, we will assume that  $p_H$  is a real number,  $p_H \neq 0$ . It is valid for the altitude of the target point  $T$

$$\Delta H_T = \Delta H_{TA} + s_A \cdot \sin \lambda_T, \quad \Delta H_{TA} = p_H / \cos \lambda_T. \quad (2)$$

This introduction of the parameter  $p_H \neq 0$  and the slant range  $d_H$  allows to use the universal relation for the slant range to target point  $T$

$$D_{TB} = \sqrt{d_H^2 + p_A^2}, \quad d_H = |p_H| / \cos \beta_H. \quad (3)$$

## 2. Usage of model of target movement for generating command signals $\varepsilon_S$ , $\psi_a$

An instantaneous position of the target point  $T$  is determined by the pair of angles  $\beta_A \in \langle -90^\circ; +90^\circ \rangle$ ,  $\beta_H \in \langle -90^\circ; +90^\circ \rangle$  (Figs. 1, 2). Their sizes can be calculated easily from values  $(v_T, \lambda_T, p_H, p_A)$ , which determine simulated movement of the target, and from the chosen time  $t_A$ . It can be determined consequently with the use of angles  $\beta_A$ ,  $\beta_H$ :

a) Traditional value of the bearing (azimuth) of the target point  $T$

$$\alpha_{TB} = \begin{cases} (\alpha_T + 270^\circ) + \beta_{AE0} & \text{if } p_A = 0, \\ (\alpha_T + 180^\circ) + (\beta_A + 90^\circ) \cdot \text{sgn}(p_A) & \text{otherwise,} \end{cases} \quad \alpha_{TB} \in \langle 0^\circ, 360^\circ \rangle, \quad (4)$$

where  $\beta_{AE0}$  is defined below in (9).

b) The absolute traverse (pan) angle

$$\psi_a = (\alpha_{TB} - \alpha_{MD}) \in \langle 0^\circ, 360^\circ \rangle, \quad (5)$$

where  $\alpha_{MD}$  is the bearing (azimuth) of main direction of pan and tilt device (its orientation is towards the north in the horizontal plane). It must be for simulations  $\psi_a \in (-\infty, +\infty)$ .

c) The angular height of the target point  $T$  angle detected by an elevation (tilt) angle sensor

$$\varepsilon_S = \begin{cases} [\beta_H + (90^\circ - \lambda_T)] \cdot \text{sgn}(p_H) & \text{if } p_A = 0, \\ \arctan\left(\frac{\Delta H_T}{d_{TB}}\right) & \text{otherwise,} \end{cases} \quad \varepsilon_S \in \langle -180^\circ, +180^\circ \rangle, \quad d_{TB} = |p_A| / \cos \beta_A. \quad (6)$$

d) Traditional angular height of the target point  $T$

$$\varepsilon_{TB} = \begin{cases} \arcsin(\sin \varepsilon_S) & \text{if } p_A = 0, \\ \varepsilon_S & \text{otherwise,} \end{cases} \quad \varepsilon_{TB} \in \langle -90^\circ, +90^\circ \rangle. \quad (7)$$

e) Hereafter, it is valid for  $p_A = 0$ :

$$\begin{aligned}\dot{\varepsilon}_S &= \dot{\beta}_H \cdot \text{sgn}(p_H), & \dot{\varepsilon}_{TB} &= -\dot{\varepsilon}_S \cdot \text{sgn}(\beta_H - \lambda_T), \\ \ddot{\varepsilon}_S &= \ddot{\beta}_H \cdot \text{sgn}(p_H), & \ddot{\varepsilon}_{TB} &= [\ddot{\beta}_H - \delta(\beta_H - \lambda_T)] \cdot \text{sgn}(p_H),\end{aligned}\quad (8)$$

where  $\delta(\beta_H)$  is the Dirac delta function.

The definition of the angle  $\beta_A$  is extended for the case of  $p_A = 0$  by the value

$$\beta_{AE0} = \begin{cases} 90^\circ \cdot \text{sgn}(\beta_H - \lambda_T) & \text{in the traditional model (limited elevation, see } \varepsilon_{TB0} \text{ in Fig. 3),} \\ -90^\circ & \text{in the new model (unlimited elevation, see } \varepsilon_{S0} \text{ in Fig. 3).} \end{cases} \quad (9)$$

The instantaneous size of angle

$$\gamma = \arctan\left(\frac{|p_A|}{d_H}\right) \in \langle -90^\circ, +90^\circ \rangle \quad (10)$$

is important for the choice of control strategy of elevation and traverse movement. We will clarify this problem on some of consequential conferences together with problems of the choice of the target point  $T_0$  initial position (the choice of  $t_{A0}$ ) for simulations of positional servomechanisms behavior. The work with the time  $t_{Asim} = t_A - t_{A0}$  is possible during simulations.

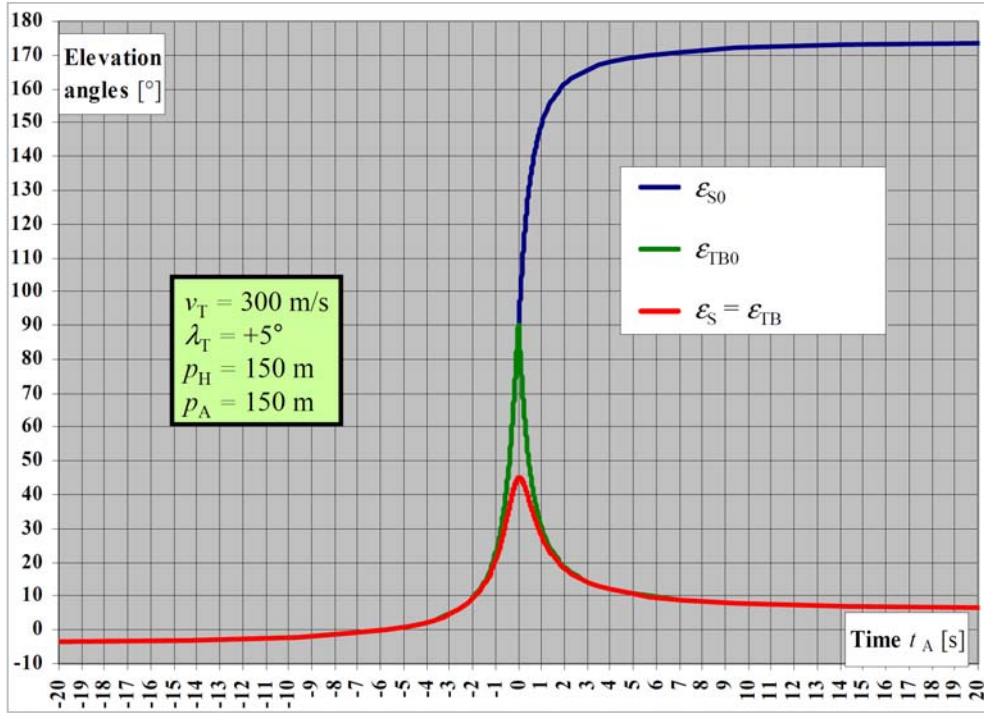


Fig. 3: Courses of angles  $\varepsilon_{S0}$ ,  $\varepsilon_{TB0}$  for  $p_A = 0$  and  $\varepsilon_S = \varepsilon_{TB}$  for  $p_A \neq 0$ .

### 3. Conclusions

The traditional model had been developed gradually since the end of 19<sup>th</sup> century and it was finalized in the second half of 1930s (Pchelnikov, N. I. (1940), Curti, P. (1945), Locke, A. S. (1955)). The model does not differentiate between angles  $\varepsilon_S$  and  $\varepsilon_{TB}$ . As it is obvious from relations (6), (7), (8) and from the graph in Fig. 3, this simplification represents a serious defect, which fully takes effect during simulations of elevation motions in systems with unlimited elevation. Our asset consists in recognition of this problem and its elimination.

### Acknowledgement

This work has originated under the support of financial means from the industrial research project of the Ministry of Industry and Trade of the Czech Republic – project code FR – TI 1/195: “Research and development of technologies for intelligent optical tracking systems”.

### References

- Cech, V. & Jevicky, J. (2004) The Problem of the Exitation Functions Generation for the Model of the Special Positional Servomechanism of the Rangefinder. In Book of Extended Abstracts of Engineering Mechanics 2004 and Proceedings on CD-ROM, Svratka, May 2004, p. 61- 62, ISBN 80-85918-88-9.
- Curti, P. (1945) Einführung in die Äussere Ballistik. Frauenfeld (Schweiz), Verlag Huber and Co. Aktiengesellschaft 1945, 408 p.
- Locke, A. S. (1955) Guidance. D. Van Nostrand Company, Princeton, NJ, USA 1955.
- Pchelnikov, N. I. (1940) Pribory Upravleniya Artillerijskim Zenitnym Ognem (PUAZO). Kniga pervaja, Moskva, Gosudarstvennoye voyennoye izdatelstvo NARKOMATA oborony SSSR 1940, 352 pages, (Anti-Aircraft Fire-Control Equipment).

## INFLUENCE OF FINITE ELEMENT ORDER ON SCF PRECISION FOR U-SHAPED NOTCHES IN FLAT BARS UNDER TENSION

A. Cichański\*

**Abstract:** *The paper presents results of research on precision of stress concentration factor for flat bars with opposite U-shaped notches under tension. The calculations were performed with the use of the finite element method with utilization of elements of various approximating polynomials orders. Each type of element underwent tests for different characteristic size of element. Precision of numerical calculations for stress concentration factor  $K_t$  was compared to errors of analytical calculations performed with employment of various approximate methods. The results gained in the work allow to indicate optimal mesh size and type of finite element providing precise  $K_t$  value with minimal DOF number.*

**Keywords:** *Notch, local approach, stress concentration factor, finite element method.*

### 1. Introduction

Determination of fatigue live of elements with notch still employs a local approach. This kind of solution assumes that the magnitude of fatigue damage of an element is determined by the stress at notch root  $\sigma$ . Its value is determined according to nominal net stress  $S$  and stress concentration factor  $K_t$ , as well as material constants  $E$ ,  $n'$ ,  $K'$ . The calculation models, representing the local approach, among others (Stephens et al., 2001) include the Neuber's hypothesis (1) and Glinka-Molski strain energy density method (2):

$$\frac{\sigma^2}{E} + \sigma \left( \frac{\sigma}{K'} \right)^{1/n'} = \frac{(K_t S)^2}{E} \quad (1)$$

$$\frac{\sigma^2}{E} + 2 \frac{1}{1+n'} \sigma \left( \frac{\sigma}{K'} \right)^{1/n'} = \frac{(K_t S)^2}{E} \quad (2)$$

The tests results present conservatism of fatigue life calculations performed with the use of the Neuber's hypothesis (Boroński, 2007) and underestimation of the values for stresses determined with the use of the strain energy density method (Łagoda & Macha, 1998). In order to reduce the above mentioned errors, various types of notation modifications (1) and (2) are proposed. One of them is implementation of power density of stresses parameter (Łagoda & Macha, 1998) to the strain energy density method, which leads to the following notation (3):

$$\frac{\sigma^2}{E} + 2 \frac{1-n'}{1+n'} \sigma \left( \frac{\sigma}{K'} \right)^{1/n'} = \frac{(K_t S)^2}{E} \quad (3)$$

Analysis of dependencies (1) ÷ (3) indicate a considerable influence of stress concentration factor on precision of  $\sigma$  calculations with respect to presence of the factor  $K_t$  in the second power. For purposes of fatigue live engineering calculations, the values of  $K_t$  factor for various notch types and sizes were presented in diagrams or described by the simplified dependence (Pilkey & Pilkey, 2008).

The paper presents results of research on precision of stress concentration factor for flat bars with opposite U-shaped notches under tension. The estimation were performed with the use of the finite element method with utilization of elements of various approximating polynomials orders. Each type of element underwent tests for different characteristic size of element. Error of numerical calculations

---

\* Dr.Eng. Artur Cichański: University of Technology and Live Sciences in Bydgoszcz, Mechanical Engineering Faculty, Kaliskiego 7; 85-769, Bydgoszcz; PL, e-mail: artur.cichanski@utp.edu.pl



stress concentration  $K_t$  factor was compared to errors of analytical calculations performed with employment of various approximate methods.

## 2. Analytical methods

One of the most commonly used analytical approximate dependency for determination of the values of stress concentration factor is the Neuber's trigonometric formula (Pilkey & Pilkey, 2008). It is a combination of  $K_{tE}$  and  $K_{tH}$  values as presented below (4).

$$K_t = \frac{(K_{tE} - 1)(K_{tH} - 1)}{\sqrt{(K_{tE} - 1)^2 + (K_{tH} - 1)^2}} + 1 \quad (4)$$

The  $K_{tE}$  describes the stress concentration factor for shallow elliptical notch in semi-infinitely wide member. The  $K_{tH}$  describes the stress concentration factor for deep hyperbolic notch in infinitely wide member. The Neuber's formula provides  $K_t$  values determined with 10% precision with respect to the exact solution. Similar precision is characteristic of the method proposed by Pilkey (Pilkey & Pilkey, 2008). It allows direct reading of  $K_t$  value from the diagram or to calculate the value from analytical dependence (5). In the dependence the  $t$  refers to notch depth in a specimen with  $W$  width, and  $C1 \div C4$  values depend on the  $t$  depth and notch radius  $\rho$ .

$$K_m = C_1 + C_2 \left( \frac{2t}{W} \right) + C_3 \left( \frac{2t}{W} \right)^2 + C_4 \left( \frac{2t}{W} \right)^3 \quad (5)$$

An exact solution to the issue of flat bar with opposite U-shaped notches was performed by Nisitani with the use of body force method (Nisitani & Noda, 1986). Due to considerable complexity of such solution Nisitani provided the table of results appointed to notches of selected geometrical dimensions. In order to achieve precise approaches for notches of any geometry Noda (Noda et al., 1995) proposed a wide range of notations based on Neuber dependence modification. Such formulated dependencies allow to determine, in a wide range of uses,  $K_t$  values with 1% precision with respect to the exact solution.

## 3. Numerical solution

### 3.1. Calculation conditions

The analyses were performed in plane stress state for tension of flat bars with opposite U-shaped notches specimens (Fig. 1) with geometry according to the work (Fatemi et al., 2004). Two notch radius  $R$  were tested. The bigger one generating stress concentration factors in tension  $K_t = 1.757$  (Noda et al., 1995) was marked as shallow notch. The smaller one generating stress concentration factors in tension  $K_t = 2.715$  was marked as sharp notch. Geometrical dimensions of specimens shown in Fig. 1 are presented in Tab. 1.

Tab. 1: Nominal dimensions of analysed specimens.

	H	R
shallow notch, $K_t = 1.757$	41.12 mm	9.128 mm
sharp notch, $K_t = 2.715$	35.56 mm	2.778 mm

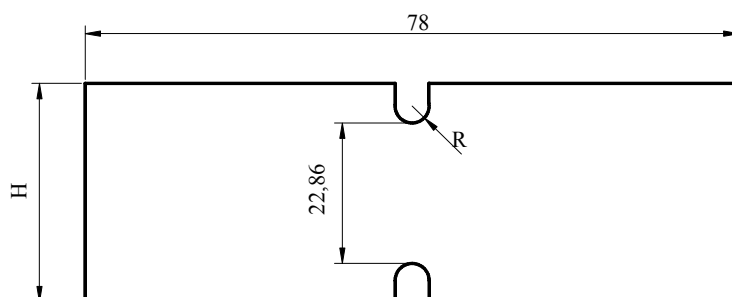


Fig. 1: Specimens for analyses.

Linear FEM analyses performed in ANSYS were of two-dimensional character. For the purpose of the calculations the free meshing was used (Cichański, 2010). The analyses used four-node finite elements with approximating polynomials of the order from the first to sixth. Due to dual symmetry, in geometric shape and boundary conditions, the analyses employed a quarter of specimen. Rejection of specimen parts located on other sides of symmetry plane was considered via adequate defining of symmetrical boundary conditions on edges of division.

### 3.2. Analyses results

For selected orders of finite elements approximating polynomials, a numbers of calculations with various characteristic dimension of mesh were every time performed. As the mesh size decrease, the number of finite elements essential for division of specimen Fig. 1 increase. Along with the number of elements, the number of degrees of freedom for the analysed issue increase as well. Based on such prepared mesh a stress distribution was determined. According to the stress values at the notch root the value of stress concentration factor was appointed. The  $K_t$  values determined for the sharp notch with respect to the number of degrees of freedom for meshes of various sizes are presented in Fig. 2a. The analyses results for shallow notches are similarly presented on Fig. 2b. Every line presented on the Fig. 2 was determined with the use of elements of defined approximating polynomial order.

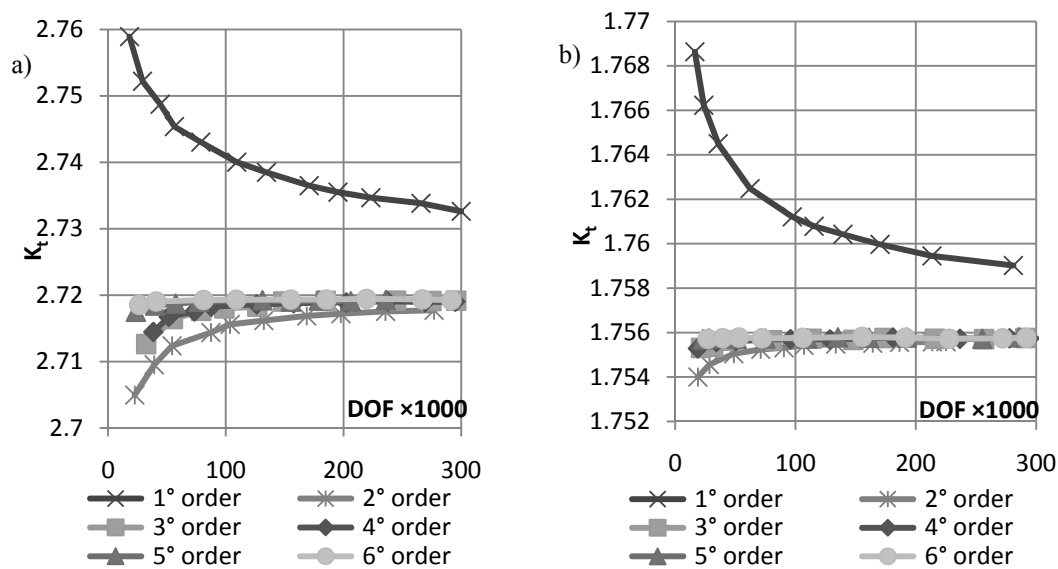


Fig. 2: Analyses results: sharp notches a) shallow notches b).

Charts presented in Fig. 2 indicate that for both types of notches the precision of calculations rises with the increase of finite element order. Additional charts processing were performed in order to determine what size of a model can provide  $K_t$  with constant precision for different approximating polynomial order. As a measure of the analysis accuracy was taken percent error  $\delta_{ord}$  with the reference value  $K_t$  determined with the use of sixth order elements. The DOF numbers with respect to the order of approximating polynomial for percent error  $\delta_{ord}$  less than 0.02% for all elements orders are presented in Tab. 2 and for elements orders 2° to 6° in Fig. 3.

Tab. 2: Problem size and  $\delta_{ord}$  for sharp and shallow notch.

		approximating polynomial order					
		1°	2°	3°	4°	5°	6°
sharp notch	element size	0.036 mm	0.063 mm	0.18 mm	0.22 mm	0.4 mm	0.9 mm
	DOF	955 170	817 488	172 200	188 540	90 645	45 124
	$\delta_{ord}$	0.319%	0.012%	-0.001%	-0.01%	-0.002%	0%
shallow notch	element size	0.04 mm	0.2 mm	0.6 mm	0.7 mm	1.5 mm	3 mm
	DOF	957 716	107 854	21 289	25 556	8 702	3 098
	$\delta_{ord}$	0.126%	-0.004%	0.004%	-0.002%	0%	0%

In the next step calculations were performed to compare the numerical and selected analytical methods. The  $K_t$  value determined with the use of Noda method was taken as a reference value for  $\delta_{met}$



percent errors (Noda et al., 1995). The values of errors for Neuber method were determined using the dependency (4) and values of errors for Pilkey method were determined using the dependency (5). The values of errors for Finite Element Method were determined using the sixth order of approximating polynomial. Results of methods comparison are presented in Fig. 4.

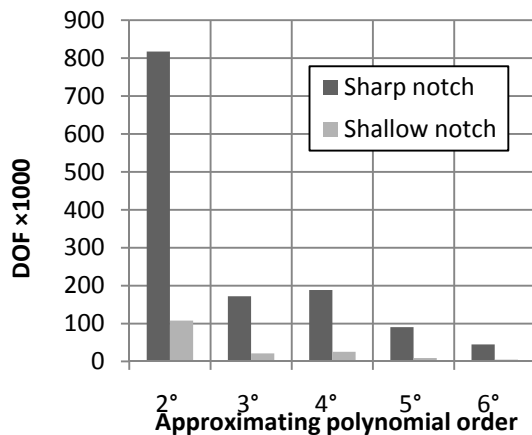


Fig. 3: DOF number for  $\delta_{ord} < 0.02\%$ .

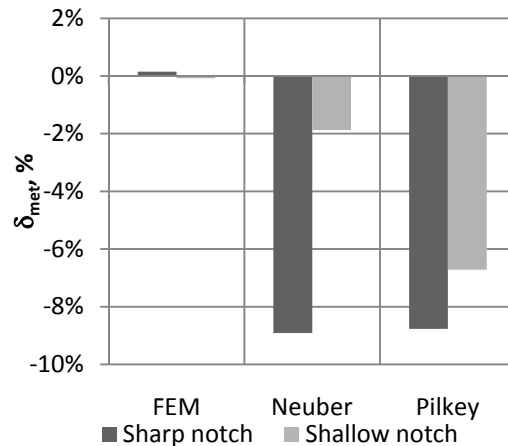


Fig. 4: Comparison of calculation performed with different methods.

First order elements analysis even with size above 1 mln DOF calculates  $K_t$  with error  $\delta_{ord}$  much more bigger than elements with second and higher orders of approximating polynomial. The mesh composed of second order finite elements allows to determine stress concentration factor precisely with five times more degrees of freedom in contrast to elements of third order Fig. 3. For elements with orders higher than third DOF number continuously decrease. The FEM analyses of elements with notches allow to increase precision of calculation for stress concentration factor by ten times if compared to approximate analytical methods Fig. 4. Additional advantage of numerical method is the ability to determine stress and strain distributions around the notch.

#### 4. Conclusions

The work results allow to indicate optimal size of the mesh and the type of the finite element which shall allow obtaining high precision of calculations for stress concentration factor with controlled number of the problem DOF. The mesh composed of sixth order elements allows the most precision FEM determination stress concentration factor. The FEM analysis allow significantly decrease of  $K_t$  calculations error if compared to approximate analytical methods.

In order to perform further reduction in the number of DOF for first order elements without the loss of precision in calculation of stress concentration factor, one shall indicate a method for refine the mesh around the notch root.

#### References

- Boroński, D. (2007) Metody badań odkształceń i naprężeń w zmęczeniu materiałów i konstrukcji. Wydawnictwo Instytutu Technologii Eksploatacji, Radom.
- Cichański, A. (2010) Influence of mesh morphology near the notch on precision of SCF determination. Journal of Polish CIMAC, 5, 2, Gdańsk, pp.65-71.
- Fatemi, A., Zeng, Z. & Plaseied, A. (2004) Fatigue behaviour and life predictions of notched specimens made of QT and forged microalloyed steels. International Journal of Fatigue, 26, pp.663-672.
- Łagoda, T. & Macha, E. (1998) Energy solution to fatigue under combined cyclic bending with torsion of smooth and notched specimens. Materials Science, 34, 5, pp.630-639.
- Nisitani, H. & Noda, N. (1986) Stress concentration of a strip with double edge notches under tension or in-plane bending. Engineering Fracture Mechanics, 23, 6, pp.1051-1065.
- Noda, N.A., Sera, M. & Takase, Y. (1995) Stress concentration factors for round and flat specimens with notches. International Journal of Fatigue, 17, 3, pp.163-178.
- Pilkey, W.D. & Pilkey D.F. (2008) Peterson's stress concentration factors. John Wiley & Sons, Inc.
- Stephens, R.I., Fatemi, A., Stephens, R.R. & Fuchs H.O. (2001) Metal Fatigue in Engineering, 2nd Edition. John Wiley&Sons, Inc.

## **RING-CORE RESIDUAL STRESS MEASUREMENT: ANALYSIS OF DEPTH INCREMENT DISTRIBUTION FOR INTEGRAL EQUATION METHOD**

**A. Cívín<sup>\*</sup>, M. Vlk<sup>\*</sup>, P. Navrátil<sup>\*</sup>, M. Matug<sup>\*</sup>**

**Abstract:** *The ring-core method is the semi-destructive experimental method. Correctly determined and properly used calibration or relaxation factors for the residual stress measurement by the ring-core method are essential. Knowledge of their dependence on the geometric changes of the ring-groove and on the disposition of the residual state of stress through the depth of metallic material gives results, correspond of theirs appropriate application. This paper is focused on the evaluation of calibration factors  $a_{ij}$  and  $b_{ij}$ , necessary for the residual state of stress determination by the integral equation method. The finite element method is used for simulation of the residual state of stress and to calculate relieved strains on the top of the core. Three types of the depth increment distribution are studied, i.e. constant, increasing and optimized depth increment distribution, which is commonly used.*

**Keywords:** *Ring-core method, integral method, calibration factors, residual stress, strain gauge.*

### **1. Introduction**

The ring-core method (RCM) is a semi-destructive experimental method used for the evaluation of homogeneous and non-homogeneous residual stresses, acting over the depth of drilled core. Therefore, the specimen is not totally destroyed during measurement and it could be used for further application in many cases.

In this paper, the most suitable mathematical theory to evaluate non-uniform residual stress fields, which is the integral equation method (IEM), is discussed. This method overcomes typical drawbacks of the incremental strain method (ISM), which lead to incorrect results, where a steep gradient of residual state of stress occurs. The incremental strain method assumes that the measured deformations  $d\varepsilon_a$ ,  $d\varepsilon_b$ , and  $d\varepsilon_c$  are functions only of the residual stresses, acting in the current depth  $z$  of the drilled groove and they do not depend on the previous increments  $dz$ , including another residual stresses. More information about the ISM could be found in papers Cívín & Vlk (2010). Anyway, relieved strains do not depend only on the stress acting within the drilled layer and its position, but also on the geometric changes of the ring groove during deepening. These two factors are taken into account by the integral equation method, which has been particularly developed for the practical use by Schajer.

The IEM assumes that strain relaxation, correspond to the particular depth of drilled groove, is superposition of all deformations caused by partial residual stresses, acting within every drilled layer of all depth increments, see Figs. 1 and 2.

Papers made by Ajovalasit et al., (1996); Zuccarello, (1996) generally describe the IEM like a method, with a high sensitivity to the measurement errors due to the numerical ill-conditioning of the equation set. Strain gauges on the top of the core are not enough sensitive to the strains, relieved in the deeper layers of the drilled groove. Therefore, influence of the strain measurement errors on the calculated residual stress depends particularly on the number and magnitude of the depth increment distributions  $\Delta z_i$  and consequently on the maximum depth  $H$  of the groove. Influence of the step distribution on the determination of calibration factors  $a_{ij}$ ,  $b_{ij}$  and on the subsequent residual stress state determination has been investigated for three different types of depth increment distribution. Total depth of drilled groove  $H = 5 \text{ mm}$  has been made by  $n = 8$  constant, increasing and optimized (Ajovalasit et al.,

---

<sup>\*</sup> Ing. Adam Cívín, assoc. prof. Ing. Miloš Vlk, CSc., Ing. Petr Navrátil and Ing. Michal Matug: Institute of Solid Mechanics, Mechatronics and Biomechanics, Brno University of Technology, Technická 2896/2; 616 69, Brno; CZ, e-mails: civin.adam@seznam.cz, vlk@fme.vutbr.cz, ynavra26@stud.fme.vutbr.cz, ymatug01@stud.fme.vutbr.cz

(1989); Zuccarello, (1996)) depth increments. Optimum depth increment distribution should minimize error sensitivity of the experimental measurement and considerably improves the numerical conditioning.

This paper describes how application of the ring-core method with theory of the IEM and the finite element method (FEM) could be used for a numerical simulation and determination of uniform or non-uniform residual state of stress. The numerical simulation is used for the measurement of relieved residual strains on the top of the model's core at real positions of the strain gauge rosette's measuring grids. Calibration factors' matrices  $\mathbf{a}$  and  $\mathbf{b}$ , which are lower triangular, need to be calculated first to describe uniform and non-uniform residual state of stress by the integral equation method.

## 2. Integral equation method

Like each method, the IEM has its own theoretical background to define certain relations between known and unknown parameters. The integral of the infinitesimal strain relaxation components caused by the residual stresses at all depths, relaxed in the range  $(0 \leq z \leq H)$ , is described by Eq. (1):

$$\varepsilon_{k(H)} = \frac{1}{E} \int_0^H \left\{ \left[ A_{(H,z)} \cdot (\sigma_{1(z)} + \sigma_{2(z)}) + B_{(H,z)} \cdot (\sigma_{1(z)} - \sigma_{2(z)}) \right] \cdot \cos 2\alpha_{k(z)} \right\} dz \quad k = a, b, c \quad (1)$$

where  $\varepsilon_{a(H)}$ ,  $\varepsilon_{b(H)}$ ,  $\varepsilon_{c(H)}$  are strains, measured by the strain gauge rosette on the top of the core's surface after milling a groove having depth  $H$ ,  $\sigma_{1(z)}$  and  $\sigma_{2(z)}$  are the unknown residual stresses acting at current depth  $z$ ,  $\alpha_{k(z)}$  is the angle between the maximum principal stress  $\sigma_{1(z)}$  and the direction of the strain gauge's measuring grid  $k=a, b, c$  and  $A_{(H,z)}$ ,  $B_{(H,z)}$  are calibration functions, dependent on the shape and geometry of the ring-groove (Fig. 1). Using a three-grid rosette, Eq. (1) leads to a three linear equation set from which the principal residual stresses and their orientation can be evaluated too.

For  $i = 1, \dots, n$  finite depth increments Eq. (1) can be written as:

$$\varepsilon_{ki} = \sum_{j=1}^i \varepsilon_{kij} \quad k = a, b, c \quad (2)$$

where the strain  $\varepsilon_{kij}$  depends only on the stress existing in the  $j^{\text{th}}$  layer by means of Eq. (3).

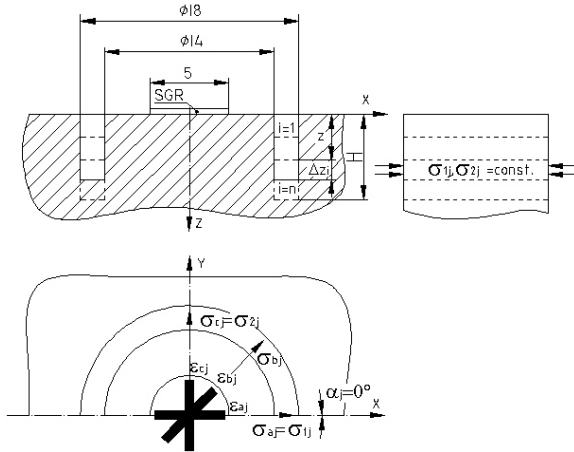


Fig. 1: Ring-core method: geometry and general notation.

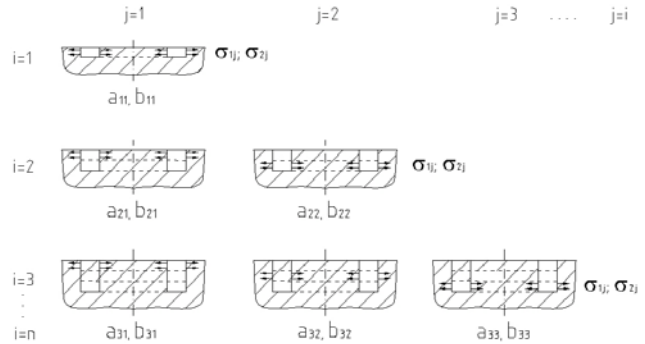


Fig. 2: Loading cases based on theory of the integral equation method.

Consequently, it is necessary to divide the maximum depth  $H$  into  $n$  intervals with the depth increment of  $\Delta z_i$  and to approximate the function of the principal residual stresses  $\sigma_{1(z)}$  and  $\sigma_{2(z)}$  in each interval with uniform distribution (Fig. 2). Therefore, considering  $i$  finite depth increments, Eq. (1) can be written as:

$$\varepsilon_{kij} = \frac{a_{ij}}{E} (\sigma_{1j} + \sigma_{2j}) + \frac{b_{ij}}{E} (\sigma_{1j} - \sigma_{2j}) \cos 2\alpha_{kj} \quad (3)$$

in which  $\varepsilon_{kij}$  is the strain component, relaxed on the surface solely due to the stress acting in the  $j^{\text{th}}$  layer, when  $i^{\text{th}}$  depth increments have been achieved,  $a_{ij}$  and  $b_{ij}$  are calibration factors and  $\sigma_{1j}$ ,  $\sigma_{2j}$  are stresses acting within the  $j^{\text{th}}$  layer.

Calibration factors  $a_{ij}$  and  $b_{ij}$  of the lower triangular matrices  $\mathbf{a}$  and  $\mathbf{b}$  cannot be determined by calibration coefficients  $K_1$  and  $K_2$  used for the IEM and described in papers Civín & Vlk (2010). They can be possibly obtained only by the finite element simulation.

### 3. FEM simulation

A prerequisite for correct and accurate measurement of residual strains on the top of the core is to use the finite element simulation. The ANSYS analysis system is used for the subsequent FE-simulation.

FE-analysis is based on a specimen volume with dimensions of  $a \times a = 50 \text{ mm}$  and thickness of  $t = 50 \text{ mm}$ . Due to symmetry, only a quarter of the model has been modelled with centre of the core on the surface as the origin. The shape of the model is simply represented by a block with planar faces with a quarter of the annular groove drilled away (Figs. 3 and 4). The annular groove has been made by  $n = 8$  increments with the different step's size  $\Delta z_i$  (Tab. 1). The maximum depth of drilled groove is  $H = 5 \text{ mm}$ . Dimension of outer diameter is  $D = 2r_i = 18 \text{ mm}$  and groove width is  $h = 2 \text{ mm}$ .

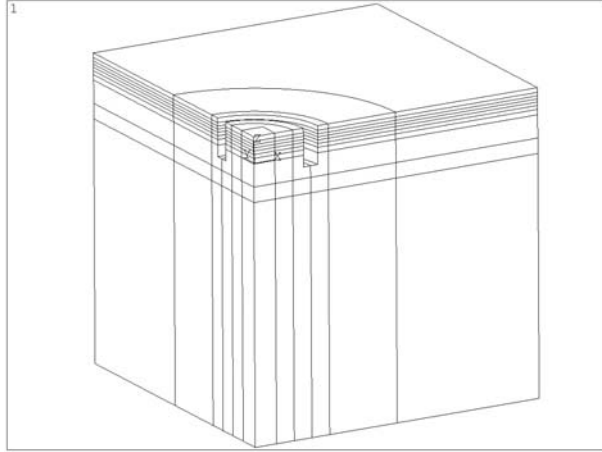


Fig. 3: Quarter of global solid model.

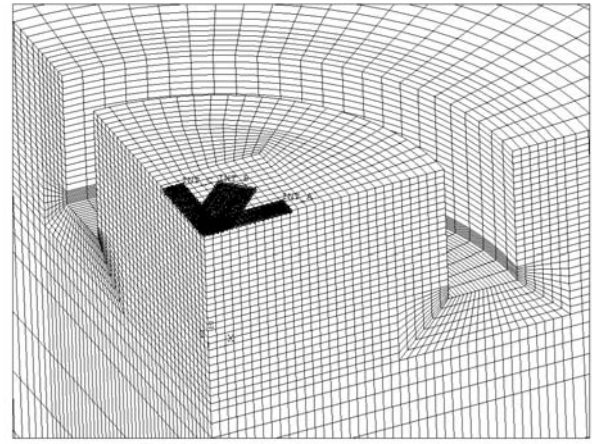


Fig. 4: Detail of core with finite element mesh.

Linear, elastic and isotropic material model is used with material properties of Young's modulus  $E = 210 \text{ GPa}$  and Poisson's ratio  $\mu = 0.3$ . Length and width of each measuring grid is  $l = 5 \text{ mm}$  and  $w = 1.9 \text{ mm}$  respectively. In case of known directions of principal residual stresses, placing of the three-element strain gauge rosette on the top of the ring-core is shown in Fig. 2. Strain measurement on the top of the core is made by integration across rosettes' measuring grid surface.

Tab. 1: Distribution of the depth  $n = 8$  increments  $\Delta z_i$  for a total depth of  $H = 5 \text{ mm}$ .

Depth distribution:	Depth increment $\Delta z_i$ [mm]:							
	$\Delta z_1$	$\Delta z_2$	$\Delta z_3$	$\Delta z_4$	$\Delta z_5$	$\Delta z_6$	$\Delta z_7$	$\Delta z_8$
Constant	0.5	0.5	0.5	0.5	0.5	0.5	1.0	1.0
Increasing	0.1	0.25	0.4	0.55	0.7	0.85	1.0	1.15
Optimized <sup>1)</sup>	0.6	0.45	0.4	0.4	0.45	0.5	0.7	1.5

<sup>1)</sup> proposed in papers by Ajovalasit et al., (1996); Zuccarello, (1996)

### 4. Calibration factors determination

For correct determination of depth-varying principal residual stresses  $\sigma_{1j}$ ,  $\sigma_{2j}$  by the IEM, it is necessary to determine calibration factors  $a_{ij}$ ,  $A_{ij}$  and  $b_{ij}$ ,  $B_{ij}$  for each depth increment distribution.

In order to determine factors  $a_{ij}$  and  $A_{ij}$  it is necessary to consider for Eq. (3) biaxial state of uniform stress with  $\sigma_{1j} = \sigma_{2j} = 1 \text{ MPa}$ , where  $\varepsilon_{aij} = \varepsilon_{bij} = \varepsilon_{cij} = \varepsilon_{ij}$ :

$$a_{ij} = \frac{E\varepsilon_{ij}}{2\sigma_{1j}} ; A_{ij} = \frac{a_{ij}}{E} = \frac{\varepsilon_{ij}}{2\sigma_{1j}} \quad (4, 5)$$

To evaluate factors  $b_{ij}$  and  $B_{ij}$  it is necessary to consider for Eq. (3) a pure shear state of uniform stress with  $\sigma_{1j} = -\sigma_{2j} = 1 \text{ MPa}$ , and for  $\alpha_{aj} = 0^\circ$ :

$$b_{ij} = \frac{E\varepsilon_{aij}}{2\sigma_{1j}} ; B_{ij} = \frac{b_{ij}}{E} = \frac{\varepsilon_{aij}}{2\sigma_{1j}} \quad (6, 7)$$

Finally, particular principal residual stresses  $\sigma_{1j}$ ,  $\sigma_{2j}$ , acting in  $j^{\text{th}}$  layer of drilled groove with  $i = 1, \dots, n$  depth increments, can be determined by using Eq. (5) and Eq. (7):

$$\sigma_{1j} = \frac{1}{4} \left[ \frac{\varepsilon_{aij} + \varepsilon_{cij}}{A_{ij}} + \frac{\varepsilon_{aij} - \varepsilon_{cij}}{B_{ij}} \right] ; \sigma_{2j} = \frac{1}{4} \left[ \frac{\varepsilon_{aij} + \varepsilon_{cij}}{A_{ij}} - \frac{\varepsilon_{aij} - \varepsilon_{cij}}{B_{ij}} \right] \quad (8, 9)$$

For considered depth of ring-groove  $H = 5 \text{ mm}$  are calibration factors  $a_{ij}$  and  $b_{ij}$ , determined for each type of depth increment distribution (see Tab. 1), written in Tab. 2 ÷ 4.

*Tab. 2a: Constant depth increment.*

$a_{ij}[1]$	$j=1$	2	3	4	5	6	7	8
$i=1$	-0,0238							
2	-0,0426	-0,0291						
3	-0,0570	-0,0459	-0,0295					
4	-0,0679	-0,0573	-0,0444	-0,0270				
5	-0,0755	-0,0652	-0,0533	-0,0396	-0,0228			
6	-0,0807	-0,0705	-0,0591	-0,0465	-0,0331	-0,0180		
7	-0,0859	-0,0759	-0,0649	-0,0531	-0,0412	-0,0298	-0,0283	
8	-0,0876	-0,0778	-0,0669	-0,0553	-0,0438	-0,0329	-0,0383	-0,0111

*Tab. 2b: Constant depth increment.*

$b_{ij}[1]$	$j=1$	2	3	4	5	6	7	8
$i=1$	-0,0219							
2	-0,0424	-0,0296						
3	-0,0580	-0,0488	-0,0326					
4	-0,0700	-0,0621	-0,0509	-0,0329				
5	-0,0793	-0,0721	-0,0626	-0,0500	-0,0315			
6	-0,0864	-0,0795	-0,0709	-0,0602	-0,0469	-0,0290		
7	-0,0955	-0,0891	-0,0812	-0,0719	-0,0614	-0,0500	-0,0606	
8	-0,1004	-0,0942	-0,0866	-0,0776	-0,0678	-0,0577	-0,0857	-0,0451

*Tab. 3a: Linearly increasing depth increment.*

$a_{ij}[1]$	$j=1$	2	3	4	5	6	7	8
$i=1$	-0,0024							
2	-0,0045	-0,0093						
3	-0,0077	-0,0174	-0,0207					
4	-0,0112	-0,0263	-0,0365	-0,0341				
5	-0,0144	-0,0344	-0,0497	-0,0560	-0,0433			
6	-0,0167	-0,0402	-0,0591	-0,0698	-0,0669	-0,0429		
7	-0,0180	-0,0432	-0,0641	-0,0771	-0,0775	-0,0624	-0,0316	
8	-0,0184	-0,0443	-0,0659	-0,0797	-0,0814	-0,0684	-0,0435	-0,0147

*Tab. 3b: Linearly increasing depth increment.*

$b_{ij}[1]$	$j=1$	2	3	4	5	6	7	8
$i=1$	-0,0013							
2	-0,0040	-0,0077						
3	-0,0074	-0,0169	-0,0201					
4	-0,0111	-0,0264	-0,0376	-0,0362				
5	-0,0146	-0,0352	-0,0524	-0,0621	-0,0516			
6	-0,0174	-0,0424	-0,0644	-0,0802	-0,0838	-0,0619		
7	-0,0194	-0,0474	-0,0727	-0,0923	-0,1016	-0,0949	-0,0630	
8	-0,0205	-0,0504	-0,0776	-0,0993	-0,1112	-0,1092	-0,0915	-0,0554

*Tab. 4a: Optimized depth increment.*

$a_{ij}[1]$	$j=1$	2	3	4	5	6	7	8
$i=1$	-0,0318							
2	-0,0519	-0,0257						
3	-0,0659	-0,0384	-0,0222					
4	-0,0770	-0,0474	-0,0329	-0,0208				
5	-0,0864	-0,0548	-0,0403	-0,0312	-0,0213			
6	-0,0937	-0,0605	-0,0458	-0,0376	-0,0317	-0,0200		
7	-0,0998	-0,0652	-0,0503	-0,0426	-0,0384	-0,0310	-0,0223	
8	-0,1042	-0,0688	-0,0537	-0,0463	-0,0431	-0,0372	-0,0352	-0,0261

*Tab. 4b: Optimized depth increment.*

$b_{ij}[1]$	$j=1$	2	3	4	5	6	7	8
$i=1$	-0,0300							
2	-0,0520	-0,0263						
3	-0,0670	-0,0410	-0,0244					
4	-0,0793	-0,0515	-0,0374	-0,0247				
5	-0,0903	-0,0605	-0,0469	-0,0383	-0,0280			
6	-0,0998	-0,0681	-0,0544	-0,0473	-0,0429	-0,0301		
7	-0,1092	-0,0756	-0,0616	-0,0554	-0,0539	-0,0481	-0,0414	
8	-0,1198	-0,0839	-0,0693	-0,0636	-0,0641	-0,0617	-0,0696	-0,0830

## 5. Conclusion

This paper provided basic information about the integral equation method, used particularly for the non-uniform residual stress determination by the experimental ring-core method. To determine important calibration factors  $a_{ij}$ ,  $b_{ij}$  of lower triangular matrices  $\mathbf{a}$  and  $\mathbf{b}$ , appropriate equations and the FE-model have been used. Application of optimized step distribution increases the spatial resolution without a significant increase of the error sensitivity and for a given number of steps it allows to minimize sensitivity of the strain measurement errors.

## Acknowledgement

This work has been supported by the specific research FSI-S-11-11/1190.

## References

- Ajovalasit, A. et al. (1996) Determination of Nonuniform Residual Stresses Using the Ring-Core Method Transactions of the ASME – Journal of Engineering Materials and Technology, vol. 118, no. 2, pp. 224-228.
- Civín, A. & Vlk, M. (2010) Assessment of Incremental Strain Method Used for Residual Stress Measurement by Ring-Core Method, in: 48<sup>th</sup> Int. Conference Experimental Stress Analysis 2010, Velké Losiny, pp. 27-34.
- Civín, A. & Vlk, M. (2010) Ring-Core Residual Stress Measurement: Analysis of Calibration Coefficients for Incremental Strain Method. Bulletin of Applied Mechanics, Vol. 6, No. 24, pp. 77-82.
- Zuccarello, B. (1996) Optimization of Depth Increment Distribution in the Ring-Core Method, Journal of Strain Analysis for Engineering Design, vol. 31, no. 4, pp. 251-258.

## ASSESSMENT OF TANKS WITH FLUIDS SUBJECTED TO SEISMIC EXCITATION

Z. Čada<sup>\*</sup>, P. Hradil<sup>\*</sup>, J. Kala<sup>\*</sup>, V. Kanický<sup>\*</sup>, V. Salajka<sup>\*</sup>

**Abstract:** *Checking analyses of large steel tanks with fluid have been carried out within the frame of the project of completion of Units 3 a 4 of the nuclear power plant Mochovce. The calculations have been carried out in accordance with the regulations NTD A.S.I. The calculations include the assessment of the tank resistance to seismic loads. The seismic analysis is based on the specified level of ground acceleration, for which the necessary floor response spectra have been generated. Problems have appeared with computation of responses of tanks with fluid. The applied ANSYS program package does not allow (for the time being) a correct response spectrum analysis with the use of FLUID30 finite elements. The application of FLUID80 elements is questionable, yet acceptable with cross-checking solution using FLUID30 elements. The paper contains procedure applied for the calculation of the convective mode frequency and the respective fluid pressure field. The resultant seismic responses of analyzed tanks have been combined with responses to static loads. Consequently, parameters of marginal seismic resistance of tanks have been computed.*

**Keywords:** *Fluid structure interaction, ANSYS, steel tank, nuclear power plant, seismic analysis, acoustic-fluid element.*

### 1. Introduction

In order to complete the construction of Units 3 and 4 of the nuclear power plant in Mochovce the assessment of the seismic resistance is being carried out. Among the equipment assessed, there are also thin-walled steel tanks containing fluid. In seismic response calculations, fluid inertial effects must be taken into account. This paper deals with the application of the ANSYS program system (SAS IP, Inc., 2009) to determine the response of fluid filled tanks to seismic action. The response analysis of a tank must be correct so that it could serve as a reliable input to predict the tank behavior. The required response characteristic needed to assess the limit states of the tank bearing capacity and serviceability are displacements and stresses (Directive NTD ASI 2001). To evaluate the tank response to seismic loading, a rational method based on the analysis of hydrodynamic equations with corresponding boundary conditions must be used (ENEL, 2009, ASME QME-1-2007). The analysis must consider fluid movement as well as tank shell deformation due to interaction with fluid. Natural frequencies and vibration modes of the tank interacting with fluid must be determined. When using the finite element method, the structure and the modeled fluid region are discretized. When using the Lagrange approach, the fluid is modeled as a solid with negligible shear modulus and the movement of fluid particles is described using equations of motion. The disadvantage of this approach consists in the fact that within the range of significant lower natural frequencies are to be found very high numbers of frequencies of insignificant vibration of mostly fluid domain. When using the Euler method, the fluid particle movement is not considered. In the fluid domain the variables are pressures or velocities at nodes. The fluid structure interaction is characterized at the boundary by a normal component of the acceleration. In the ANSYS program system finite elements are implemented to solve the fluid structure interaction directly. The elements suitable for fluid modeling by the Lagrange approach are FLUID80 3-D Contained Fluid eight-node isoparametric finite elements. These elements are modified 3D elements for elastic solid analysis. The elements suitable for fluid modeling by Euler

---

<sup>\*</sup> Ing. Zdeněk Čada, Ing. Petr Hradil, Ph.D., doc. Ing. Jiří Kala, Ph.D., doc. Ing. Viktor Kanický, CSc. and doc. Ing. Vlastislav Salajka, CSc.: Institute of Structural Mechanics, Faculty of Civil Engineering, Brno University of Technology, Veveří 331/95; 602 00, Brno; CZ, e-mails: cada.z@fce.vutbr.cz, hradil.p@fce.vutbr.cz, kala.j@fce.vutbr.cz, kanicky.v@fce.vutbr.cz, salajka.v@fce.vutbr.cz

approach are FLUID30 3-D Acoustic Fluid eight-node isoparametric finite elements. The approach according to Euler is based on the Helmholtz acoustic (Kinsler, L. E. & Frey, A. R., 1962).

## **2. Testing computations**

### **2.1. Computation models**

Several computations have been carried out to test the optimum procedure of the modal analysis of the tank containing fluid. Two computation models have been used in order to analyze the effects of the choice of the type, shape and size of finite elements:

**Model A** - vertical cylindrical steel tank with fluid. The model has been used to analyze the effects of changing the following characteristics: tank diameter, tank height, shell thickness, element mesh density, type and formulation of elements, shape of elements.

**Model B** - vertical cylindrical thin-walled fluid containing steel tank with heavy roof supported by a central column. The model has been used to analyze the effects of changing the type and formulation of elements.

### **2.2. Convective type of the fluid vibration**

The tank base seismic vibrations excite vibration of the fluid content. Vibration nodes characterized by fluid surface local level variations (fluid sloshing, convective mode vibrations) result in substantial increase of the fluid hydrodynamic pressure at the upper part of the tank shell. Using several alternatives of the model A, lowest natural frequencies of convective mode vibrations have been computed. Results have been compared with data given in Eurocode 8 (ČSN EN 1998-5, 2006). Differences up to 5 % have been found. Using FLUID30 elements, convective mode natural frequencies and corresponding pressure fields have been readily computed. No effects of shapes of elements have been observed. The application of FLUID80 element offers same advantages, e.g. direct computation of displacements. However, it has been concluded, that the only acceptable shape of the FLUID80 element for reliable computations is a shape close to cube. When computing the first sloshing vibration mode, shift of the frequency spectrum must be applied.

### **2.3. Impulsive type of vibration of fluid interacting with the structure**

Impulsive type vibration of the fluid content interacting with the structure has been analyzed at the model A, using both FLUID30 and FLUID80 elements with various sizes and shapes. For a selected mode (e. g. tank first bending node), when decreasing the size of elements, the computed frequencies converge to the same frequency. The frequency value at FLUID30 elements converges smoothly and the rate of convergence is higher. Consequently, with a given mesh, FLUID30 elements provide natural frequencies with a higher accuracy, than FLUID80 elements. Modal analysis of two variants of the model B has been carried out, using formulations (settings) of both FLUID30 and FLUID80 elements available in the ANSYS program. The values of the first bending frequency of the tank have been computed and compared. However, no reliable conclusion about the optimum choice of the element setting have been obtained.

### **2.4. Impulsive mode response analysis of the tank with fluid**

The response analysis in the time domain has been carried out, using model B variants described in par. 2.3, A third variant based on the added mass concept has been analyzed, too. The model has been tuned to the first bending frequency. The acceleration of the tank base has been described using a quasi harmonic function with frequency varying with time so, that during the considered time interval the dominant tank bending mode vibration has been excited. Using the same models, response spectrum analysis has been carried out. The response spectrum has been generated using the above mentioned excitation function. Maximum response displacements obtained by direct integration have been compared with those obtained using the response spectrum analysis. The model with FLUID80 elements has shown satisfactory coincidence. The model with added mass properly tuned to the dominant natural frequency has shown satisfactory results, too. The application of the model with FLUID30 elements has not shown generally reliable results.



### 3. Seismic response of a selected tank for the nuclear power plant Mochovce

#### 3.1. Computation model of the tank with fluid

Seismic response analysis of the vertical cylindrical steel tank storing 550 m<sup>3</sup> of active concentrate in the NPP Mochovce has served as a case problem. The computation model of the tank ( $d = 10$  m) is shown in Fig. 1. For modeling the tank structure, mostly SHELL43 elements have been used. Two variants of the fluid domain modeling have been applied. The response spectrum analysis has been carried out using FLUD80 elements. With respect to the complexity of the structure, the fluid domain mesh differs from the structure mesh the fluid-structure interaction ensure CONTA174 and TARGE170 elements. The model with FLUID30 elements has been used for the modal analysis verification.

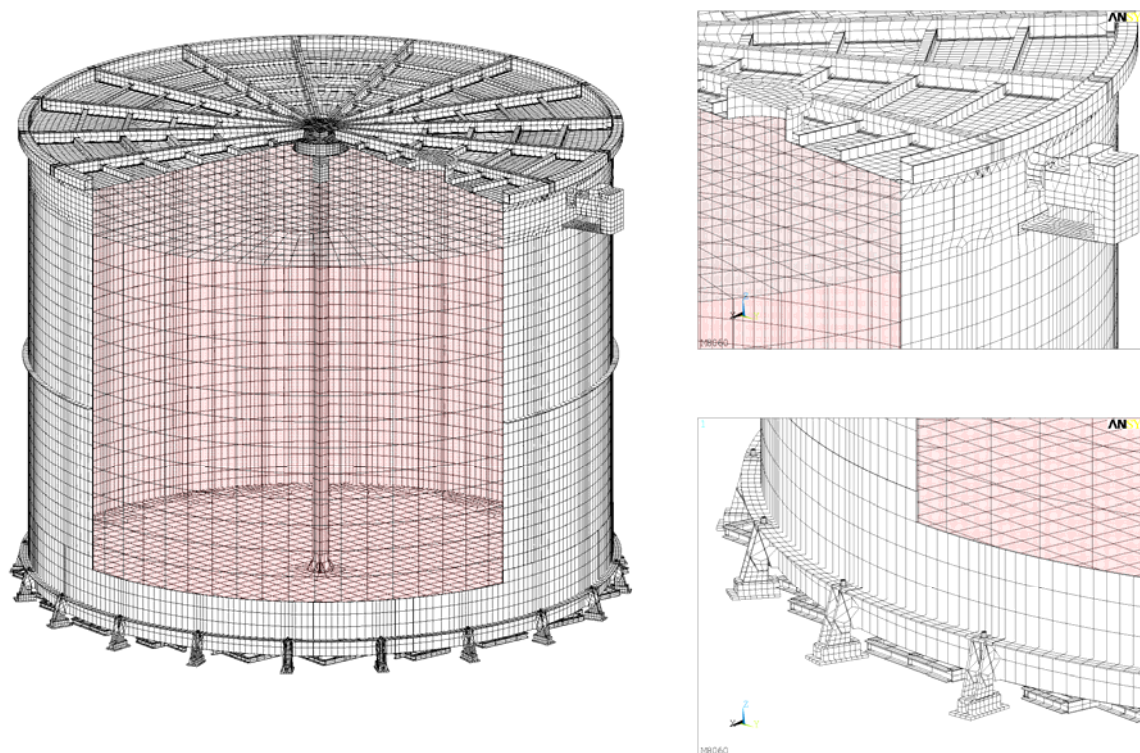
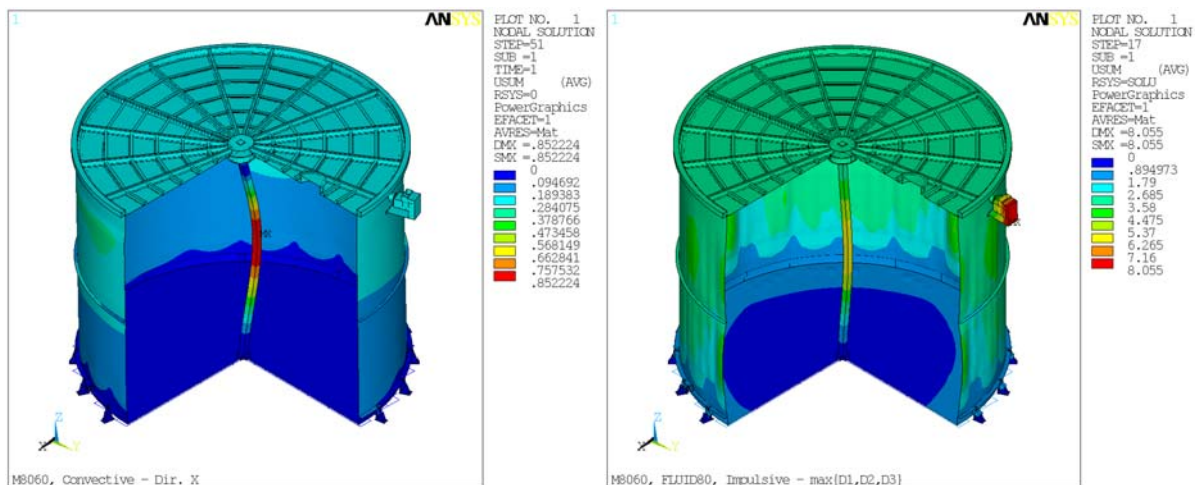


*Fig. 1: Tank computational model.*

#### 3.2. Seismic response analysis

Seismic response analysis has been performed using the elastic response spectrum method. Design spectra for two earthquake levels have been used. For the design earthquake level (SL-1), damping ratio 2 % has been considered, whereas for the maximum computational earthquake (SL-2) damping ratio of 3 % has been used (with impulsive fluid vibration modes). For convective fluid vibration modes damping ratio 0.5 % has been used. Seismic responses in both displacements and stresses have been computed for three orthogonal directions ( $x$ ,  $y$  and  $z$ ). Modal responses have been combined using Complete Quadratic Combination rule (except simply added convective mode responses). Subsequently, directional response effects have been combined using factored addition rule. For the final limit state assessments, addition rule has been applied to combine the maximum seismic effects with static loads at current operation conditions. For illustration, separated resultant responses to convective and impulsive excitation are shown in Fig. 2a and Fig. 2b, respectively.



a) Response of convective fluid motion

b) Response of impulsive fluid/structure motion

Fig. 2: Resultant responses.

#### 4. Conclusions

Verification seismic analyses of several tanks with fluid designed for the Nuclear Power Plant Mochovce have been carried out using the finite element method implemented in the ANSYS program. Particular attention has been devoted to assess correctly the seismic resistance level of tanks sensitive to fluid-structure interactions. The applications of fluid elements of the ANSYS program have been thoroughly tested. It can be stated, that for the time being, direct response analysis of the tank with fluid using elements based on the Euler approach (FLUIF30 elements) cannot be performed. The analysis using elements based on the Lagrange approach (FLUIF80 elements) can be carried out, however with great caution. Modal analyses using fluid elements can be routinely performed.

#### Acknowledgement

This contribution has been prepared in the frame of grant project GACzR No. 103/09/2007 The effect of technical and natural seismicity on structural reliability of and achievement in project MSM0021630519 Progressive reliable and durable civil engineering structures.

#### References

- ASME QME-1-2007, Qualification of Active Mechanical Equipment Used in Nuclear Power Plants. ASME [American Society of Mechanical Engineers], New York, Revision of ASME QME-1-2002, November 2007.
- Methodology for Elaboration and Updating of Proof Documentation of MO34 Mechanical Equipment, ENEL Slovenské elektrárne 2009.
- ENEL, Requirements Evaluation of Seismic Resistance of Structures Systems and Components of Mochovce NPP, ENEL Slovenské elektrárne 2009.
- Directive NTD ASI 2001, section III: Assessment of the VVER Nuclear Power Plant equipment and pipe strength was opted for, ASI [Mechanical Engineers Association], Prague, Brno, May 2001.
- SAS IP, Inc., ANSYS Release 12.1 Documentation, SAS IP, Inc., 2009.
- Kinsler, L. E. & Frey, A. R. (1962) Fundamentals of Acoustics, John Wiley & Sons, Inc..
- ČSN EN 1998-5, Eurocode 8: Design of Structures of Earthquake Resistance Part 4; Silos, Tanks and Pipelines. 2006.

## PARAMETRIC STUDY ON DYNAMIC BEHAVIOUR OF A MULTI-STOREY BUILDING INCLUDING SOIL-STRUCTURE INTERACTION

Z. Čada<sup>\*</sup>, P. Hradil<sup>\*</sup>, M. Mrózek<sup>\*</sup>, V. Salajka<sup>\*</sup>

**Abstract:** *The paper deals of a with the parametric study of the dynamic behavior multistorey panel building applying an advanced computation model developed using finite element library of the ANSYS program package. Variations of parameters determining dynamic behavior of both building and subsoil motion have been considered. Response of the building to seismic motion of the subsoil has been analyzed. The method of elastic response spectra has been used for computing the building response. The decisive input data have been parameterized. Subsequently, a deterministic type sensitivity analysis has been carried out, applying the LHS (Latin Hypercube Sampling) method. Computations have been performed using the program "optiSlang", designed for optimization and probabilistic analyses.*

**Keywords:** *Seismic analysis, dynamic response, response spectra, deterministic sensitivity analysis, parametric study, multi-story panel building, Latin Hypercube Sampling, ANSYS, OptiSlang.*

### 1. Introduction

Calculation of maximum possible building structure response to given seismic motion of object foundations (e.g. record of measured velocities by geotechnical station), has been applied on numerical finite element method. Subsequently the solution of dynamic response has been solved by direct integration of the equation of motion or mode superposition method and spectral analysis consequently. In both cases resultant maximum response (in time domain) depends on frequency characteristics of computational model.

In the case, that a natural frequency of the model occurs close to a sharp local peak or concavity in the response spectrum curve, the response can vary considerably even due to small changes of structure input parameters. Then the resultant response can vary at small change of input parameters. Due to seismic excitation calculated by response spectra method dynamic response strongly depends on natural frequency of computational model. For example, if a natural frequency of a model is about 3.5 Hz (Fig. 1, Čada et al., 2010), than small change of model frequency can cause for significant change of dynamic response. In practice, small change of frequency can be caused by different modelling techniques depended on individual engineering approach.

### 2. Description of mathematical model and analysis of parameters

Dynamic behaviour of panel structure (Fig. 2) depending on input parameter has been analysed using computational model assembled in system ANSYS (ANSYS Release 13.0, 2010). Superstructure has been modelled using finite element SHELL43 and subsoil has been modelled using SOLID187 elements.

#### 2.1. Modulus of elasticity, mass distribution, thickness of panels

Modulus of elasticity of concrete has been considered with high variation. Value of modulus of elasticity is generally influenced by many factors (such as age of concrete, range of micro-cracks ...) with different probability distribution. Value of modulus of elasticity represents the stiffness of entire

---

<sup>\*</sup> Ing. Zdeněk Čada, Ing. Petr Hradil, Ph.D., Ing. Michal Mrózek and doc. Ing. Vlastislav Salajka, CSc.: Institute of Structural Mechanics, Faculty of Civil Engineering, Brno University of Technology, Veveří 331/95; 602 00, Brno; CZ, e-mails: cada.z@fce.vutbr.cz, hradil.p@fce.vutbr.cz, mrozek.m@fce.vutbr.cz, salajka.v@fce.vutbr.cz

construction (finishing of panel joints, weak stiffness of minor not-modelled construction parts, viscous behaviour of concrete ...)

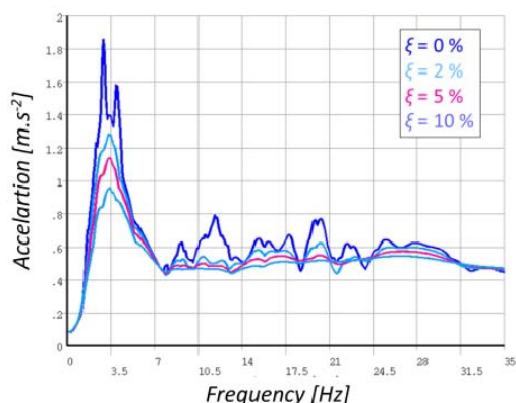


*Fig. 1: Ground response spectra of a seismic action.*

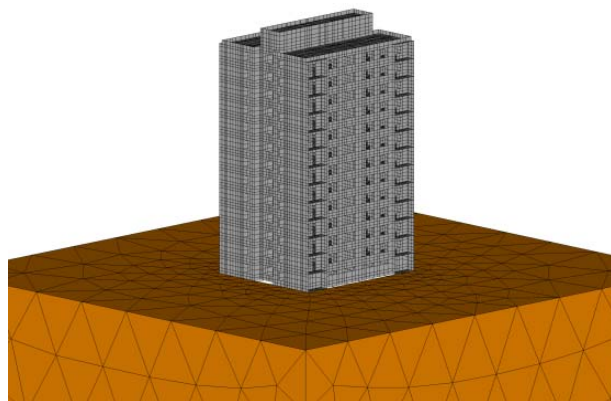


*Fig. 2: Computational model.*

Total mass of building structure is determined as a sum of self-weight (load bearing and non-bearing construction members) and mass of persons and accessories that varies in time of building structure utilization. Total mass of the building structure is determined as the sum of the proper mass of the structure (including both load bearing and non-bearing parts) and the mass that varies within the building utilization time (e.g. mass of accessories, persons, etc.). The mass of the load bearing structural parts is derived from the panel thickness and the concrete density. Time varying component of object mass has been modelled as added mass uniformly distributed over the ceilings. Variances of concrete density takes into account its uncertainty which changes due to the moisture and the reinforcement ratio etc. Uncertainty of non-bearing construction members is further taken into account.

Manufacturing tolerances of a panel thickness are expected small. Despite this fact formerly mentioned property variation has been included in computation in order to model the change of wall and bending stiffness ratio. Panels have been divided into 4 groups: ceiling panels, transverse wall panels, lateral wall panels, roofing construction. For each of this groups have been prescribed one parameter of thickness ratio. This includes the presumption of soft change of transverse, lateral and vertical stiffness ratio.

## 2.2. Model of subsoil

Within this case study the spatial computational model of subsoil consisting of solid elements has been implemented. Region of solid elements models elastic massless subsoil. Size of modelled subsoil and elements has been parameterized. In case of modelling massless subsoil the mass of soil moving with the subsoil zone during the dynamic action is neglected. This simplification facilitates the computation (necessary amount of calculated mode shapes) and evaluation (searching for dominant mode shapes). Dynamic modulus of elasticity of soil has been set as a linear function of the depth. Input parameters are the modulus of elasticity at the ground surface and the gradient of elasticity modulus (change corresponding to 1 m depth). Used range of soil modulus of elasticity has been stated with assumption of considerable uncertainty during the soil profile determination in situ.

## 2.3. Computation of natural frequencies and mode shapes

Natural frequencies and mode shapes have been obtained using Block Lanczos method. Ten lowest frequencies have been investigated.

## 2.4. Output parameters

Output parameters correspond to response characteristics of the model. It concerns three natural frequencies at which the participation factor takes the maximum value in directions  $x$ ,  $y$  and  $z$ . These participation factors are recorded too. The response to the unit spectrum of acceleration for three directions of excitation ( $S_{a,x} = 1 \text{ m.s}^{-2}$ ,  $S_{a,y} = 1 \text{ m.s}^{-2}$ ,  $S_{a,z} = 1 \text{ m.s}^{-2}$ ) has been solved. SRSS method has



been used for calculating only for internal forces at different floors and displacement of the top floor. Then the formula for single internal force (direction x) evaluation is:

$$F_{x,SRSS}(z) = \sqrt{\sum_N \left( \frac{F_{x,i}(z)p_x S_{a,x}}{(2\pi f_i)^2} \right)^2 + \sum_N \left( \frac{F_{x,i}(z)p_y S_{a,y}}{(2\pi f_i)^2} \right)^2 + \sum_N \left( \frac{F_{x,i}(z)p_z S_{a,z}}{(2\pi f_i)^2} \right)^2} \quad (1)$$

Internal forces (e.g.  $F_{x,i}$ ) at different floors have been obtained as a sum of node forces at horizontal section of building structure model. Displacement of the top floor has been obtained as an average value of four displacement values at roof corners. Resulting parameter of internal forces is then the extreme value of internal forces distribution.

Tab. 1: Input and output parameters.

	Variable	Unit	Limits		Description
			Bot.	Top	
u	1				
	$sirka\_m$	[m]	2	40	Size of subsoil region surrounding building.
	$hloubka\_m$	[m]	3	80	Depth of subsoil
	$es\_1\_m$	[m]	1	5	Size of finite elements bellow the building
	$es\_2\_m$	[m]	2	15	Size of finite elements at the interface of building and subsoil
	$E0\_MPa$	[MPa]	35	75	Modulus of elasticity of subsoil at level 0
	$E1\_MPa$	[MPa.m <sup>-1</sup> ]	10	25	Linear part elasticity modulus of subsoil raises with depth
	$DENS\_beton\_kgm3$	[kg.m <sup>-3</sup> ]	2100	2500	Density of concrete structure components
	$r\_pricne$	[-]	0.95	1.05	Thickness ration of transverse panels to designed thickness
	$r\_podelne$	[-]	0.95	1.05	Thickness ration of lateral panels to designed thickness
	$r\_stropy$	[-]	0.95	1.05	Thickness ration of floor panels to designed thickness
	$r\_strecha$	[-]	0.95	1.05	Thickness ration of roof panels to designed thickness
	$prid\_hmota\_kgm2$	[kg.m <sup>-2</sup> ]	25	100	Additional mass in floors
	$r\_EX$	[-]	0.80	1.30	Ratio of concrete modulus of elasticity to designed modulus
z	2				
	$px\_max$	[m <sup>0.5</sup> ]	1994	2449	Maximal participation factor in x direction
	$py\_max$	[m <sup>0.5</sup> ]	1992	2462	Maximal participation factor in y direction
	$pz\_max$	[m <sup>0.5</sup> ]	1836	2660	Maximal participation factor in z direction
	$Fx\_max\_MN$	[MN]	3.997	5.804	Maximal shear force (SRSS) over building cross-section
	$Fy\_max\_MN$	[MN]	4.000	5.696	Maximal shear force (SRSS) over building cross-section
	$Fz\_max\_MN$	[MN]	4.100	6.341	Maximal normal force (SRSS) over building cross-section
	$Mx\_max\_MNm$	[MNm]	91.71	124.43	Maximal bending moment (SRSS) over building cross-section
	$My\_max\_MNm$	[MNm]	93.26	126.38	Maximal bending moment (SRSS) over building cross-section
	$Mz\_max\_MNm$	[MNm]	2.518	3.994	Maximal torsional moment (SRSS) over building cross-section
	$ux\_mm$	[mm]	7.469	25.428	Maximum displacement of roof (SRSS) in x direction
	$uy\_mm$	[mm]	7.854	21.570	Maximum displacement of roof (SRSS) in y direction
	$uz\_mm$	[mm]	0.322	1.697	Maximum displacement of roof (SRSS) in z direction
	$usum\_mm$	[mm]	9.842	32.937	Maximum total displacement of roof (SRSS)
	$mass\_t$	[10 <sup>3</sup> t]	5.323	7.101	Total mass of structure and additional load
	$fx\_Hz$	[Hz]	1.276	2.316	Frequency at maximum participation factor in x direction
	$fy\_Hz$	[Hz]	1.169	2.167	Frequency at maximum participation factor in y direction
	$fz\_Hz$	[Hz]	3.890	9.191	Frequency at maximum participation factor in z direction

### 3. Deterministic sensitivity analysis

Deterministic sensitivity analysis of parametric model has been carried out using LHS method (Latin Hypercube Sampling) which is included in software optiSlang (optiSlang 3.1.4, 2010). In case of deterministic sensitivity analysis the individual parameters are defined by equal distribution. Adopting deterministic approach compared to stochastic there is no need to know the statistic distribution of each parameter. Input parameters and equal distribution intervals are stated in Tab. 1. Total count of simulation has been one thousand which overreaches recommendation given by the sum multiplied by two of input and output parameters.

Sensitivity of chosen input parameters to input parameters are shown in Fig. 3. Sensitivity has been calculated based on the linear correlation coefficient of two parameters. Output parameters represent the response magnitude. Behaviour is similar for the other directions.

## 4. Conclusions

Dependence between input and output parameters is proved by the study carried out on the numerical model of the panel building interacting with subsoil.

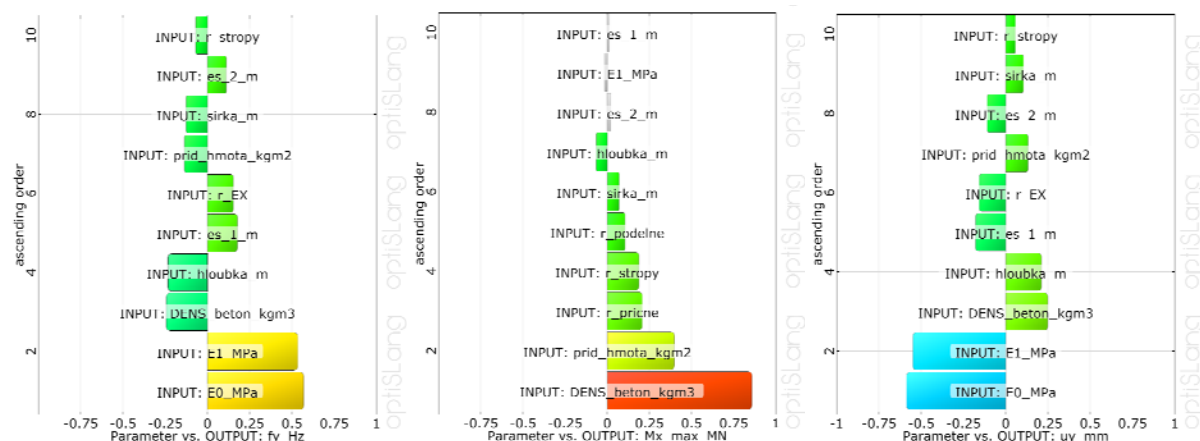


Fig. 3: Linear correlation coefficient  $f_y$ \_Hz,  $M_{x\_max\_MN}$  and  $u_y$ \_mm parameters.

Deterministically unfavourable values of parameters are probably supposed to be chosen by the engineer. Decreasing the subsoil stiffness and increasing the mass of construction can result in lower dominant natural frequency and increase of bending moment and shear force. On condition of approximately constant spectrum of acceleration such choice of parameters results in conservative results. In other cases the inaccuracy of the response strongly depends on spectral values so that the resulting response can be undervalued (non-conservative).

Resulting response spectra determined by the measurements or calculated as floor response spectra should be modified so that the user obtain conservative results without the need of performing model parametric studies. Modification of response spectra is deal with in ASCE 4-98 (2000) and Regulatory Guide 1.122 (1978). Modification reduces values peaks by 15% and extends frequency zone about 15%. Modification of response spectra must depend on probabilistic distribution of parameters with respect to ultimate limit states according (Eurocode 8, 2008).

## Acknowledgement

This contribution has been prepared in the frame of grant project GACzR No. 103/09/2007 The effect of technical and natural seismicity on structural reliability of and achievement in project MSM0021630519 Progressive reliable and durable civil engineering structures.

## References

- Čada, Z. & Salajka, V. & Hradil, P. & Kanický, V. (2010) Effects of Natural and Technical Seismicity on Building Structures in Czech Republic. Transactions of the VŠB – Technical University of Ostrava, Civil Engineering Series. Ostrava 2010, ISSN 1213-1962.
- ANSYS Release 13.0 (2010), Documentation, SAS IP, Inc.
- OptiSlang 3.1.4 (2010), Documentation, Dynardo GMBH.
- ASCE 4-98 (2000) Seismic Analysis of Safety-Related Nuclear Structures and Commentary. ASCE [American Society of Civil Engineers]. Reston. 2000.
- Regulatory Guide 1.122. (1978) Development of floor design response spectra for seismic design of floor-supported equipment or components. U.S. NRC [Nuclear Regulatory Commission]. Washington DC, Revision 1, February 1978.
- Eurocode 8 (2008) Design of structures of earthquake resistance.

## TEMPERATURE DISTRIBUTION OF SLIDE JOINT IN REINFORCED CONCRETE FOUNDATION STRUCTURES

R. Čajka<sup>\*</sup>, P. Matečková<sup>\*</sup>

**Abstract:** In the paper temperature distribution in foundation structure is analyzed for different temperature regime of environment. Temperature distribution is analyzed numerically using Nonstac computer program. Nonstac computer program solves one dimensional temperature distribution and it is possible to input appropriate thermal characteristics as a function of temperature and to take into account heat of hydration development, variation of environment temperature and if needed in special cases e.g. purposeful warming of the foundation structure. Calculated temperatures will be used in future research for strain analysis in footing bottom with slide joint and consequently stress and strain of foundation structure.

**Keywords:** Slide joint, foundation structure, temperature distribution.

### 1. Introduction

Slide joints are used for elimination of friction in footing bottom caused by deformation of foundation structure owing to shrinkage, creep, pre-stressing and temperature variation or by subsoil deformation, owing to e.g. undermining, Fig. 1.

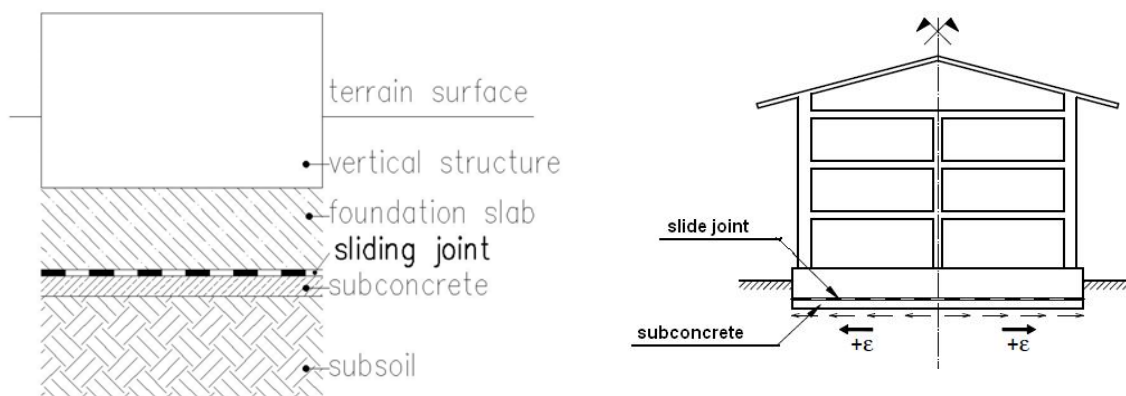


Fig. 1: Schematic drawing of slide joint.

Original slide joint design method dates from the eighties of last century and was primary focused on foundations on undermined area, material of slide joint was mainly asphalt belt. Currently number of new and potentially suitable material for slide joint is at disposal. Rheological shear characteristics of selected materials were tested at Faculty laboratory, VSB –TU Ostrava, some of the results are introduced in doctoral thesis (Maňásek,P., 2008).

One of the important factors, which affect the rheological shear resistance of slide joint, is the temperature. For that reason research and laboratory testing of selected materials continues and rheological shear characteristics are tested in dependence on temperature in air conditioned room. Experiments are in testing the operation, Fig. 2. Air-conditioned room with dimensions 1000 x 2500 x 2200 mm is made of polyurethane foam, thickness 125 mm. Temperature limit is from -20°C to +40°C, cooling is provided through cooling unit with vaporizer, heating through electric heater with

---

<sup>\*</sup> prof. Ing. Radim Čajka, CSc.and Ing. Pavlina Mateckova, Ph.D.: Department of Building Structures, Faculty of Civil Engineering, VSB – Technical University of Ostrava, L. Podeste 1875/17; 708 33, Ostrava; CZ, e-mails: radim.cajka@vsb.cz, pavlina.mateckova@vsb.cz



centrifugal fan. Experimentally appointed function of slide joint resistance versus temperature should contribute to design optimization of slide joint and consequently also foundation structure.



Fig. 2: Testing rheological shear characteristics in air conditioned room.

## 2. Thermal actions

Analysis of temperature distribution in foundation structure enable estimating of temperatures, expected in slide joints for different temperature regimes, eventually with heat of hydration taking into account.

### 2.1. Environmental temperature

Temperature variation in building structures is given in ČSN EN 1991-1-5 (2005). Thermal action is expressed with maximal temperature  $T_{\max}$  in summer and minimal temperature  $T_{\min}$  in winter. Appropriate temperatures are for Ostrava region  $T_{\max} = 37^{\circ}\text{C}$  and  $T_{\min} = -33^{\circ}\text{C}$ . With considering solar radiation the temperature of the structure could be in summer up to  $T_{\max} = 67^{\circ}\text{C}$ . Environmental average month temperatures are available also in standards for thermal protection of buildings.

It is also possible to make use of published measured temperatures in subsoil, e.g. average temperatures of environment at the depth 0.5 m and 1.0 m for different above see levels (Halachya, M., Sobotka, P., 1988), Fig. 2. Experiments with temperature measuring in subsoil are planed also at Department of Constructional Surrounding at Faculty of civil Engineering VSB-TU Ostrava.

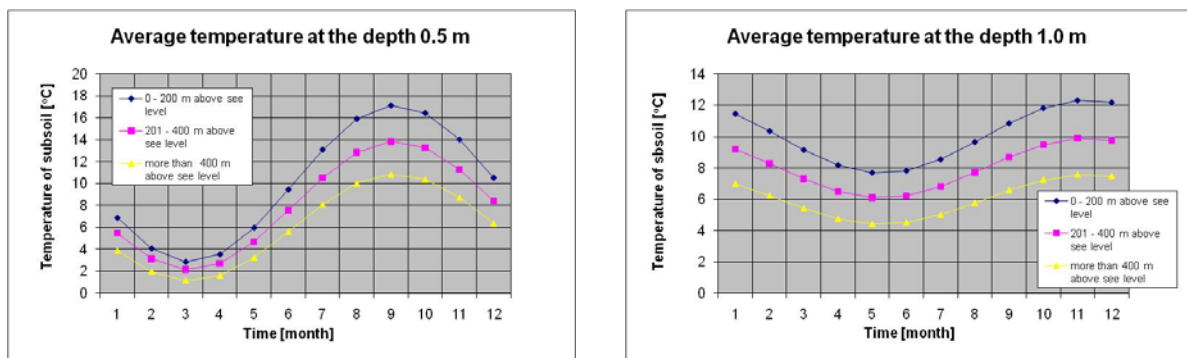


Fig. 3: Measured temperatures in subsoil, (Halachya, M., Sobotka, P., 1988).

Description of temperature variation through the day is given e.g. in textbook (Halachya, M. 1970). Temperature variation is expressed as sinus function (1):

$$T_e(t) = T_{med} + A_e \cdot \sin \frac{\pi}{12} \cdot (t + t_o + t_p) \quad (1)$$

where  $T_{med}$  is average daily temperature,  $A_e$  is temperature amplitude,  $t$  is time. Average daily temperature and temperature amplitude is considered in summer  $T_{med, \text{sum}} = 20.5^{\circ}\text{C}$ ,  $A_{e, \text{sum}} = 6.7^{\circ}\text{C}$ , in winter  $T_{med, \text{win}} = 5.0^{\circ}\text{C}$ ,  $A_{e, \text{win}} = 6.0^{\circ}\text{C}$ . In summer solar radiation has to be taken into consideration.

Influence of solar radiation is expressed through solar radiation intensity  $E_e$  which is defined similarly to temperature as sinus function. Result heat flow is determined by multiplying the radiation intensity with absorbing capacity for radiation.

## 2.2. Heat of hydration

Number of dependences was derived for the development of the heat of hydration in time. In this paper the development according to ČSN 731208 (2010) is used. Temperature variation  $\Delta T_a(t)$  is considered according to exponential function (2):

$$\Delta T_a(t) = \Delta T_a (1 - e^{-\beta t}) \quad (2)$$

$$\Delta T_a = \frac{m \cdot Q_h}{c \cdot \rho} \quad (3)$$

$$\beta = \beta_{10} \cdot 2^{\frac{T_{or} - 10}{10}} \quad (4)$$

where  $m$  is weight of cement in  $1 \text{ m}^3$  of concrete,  $c$  is specific heat of concrete,  $\rho$  is density of concrete,  $Q_h$  is heat of hydration assigned by laboratory experiment or according to data in ČSN 731208 (2010),  $T_{or}$  original temperature of concrete,  $\beta_{10}$  basic value of coefficient for  $T_{or} = 10^\circ\text{C}$ .

For the temperature distribution analysis it is important to get intensity of heat generation which is derivation of temperature variation (2), (5):

$$q(t) = c \cdot \rho \cdot \frac{\partial T}{\partial t} = c \cdot \rho \cdot \Delta T_a (0 + \beta \cdot e^{-\beta t}) = c \cdot \rho \cdot \Delta T_a \cdot \beta \cdot e^{-\beta t} \quad (5)$$

## 3. Temperature distribution – foundation slab

Computer program Nonstac solves numerically Fourier differential equation of one dimensional transient temperature distribution (6), Čajka (2010). It is possible to input appropriate thermal characteristics as a function of temperature, heat generation and variant environmental temperatures.

$$\frac{\partial T}{\partial t} = \frac{\lambda}{c \cdot \rho} \cdot \frac{\partial^2 T}{\partial x^2} + \frac{q}{c \cdot \rho} \quad (6)$$

where  $T$  is temperature,  $t$  is time,  $\lambda$  is heat conductivity,  $\rho$  is density,  $c$  is specific heat,  $q$  is heat generation, e.g. heat of hydration.

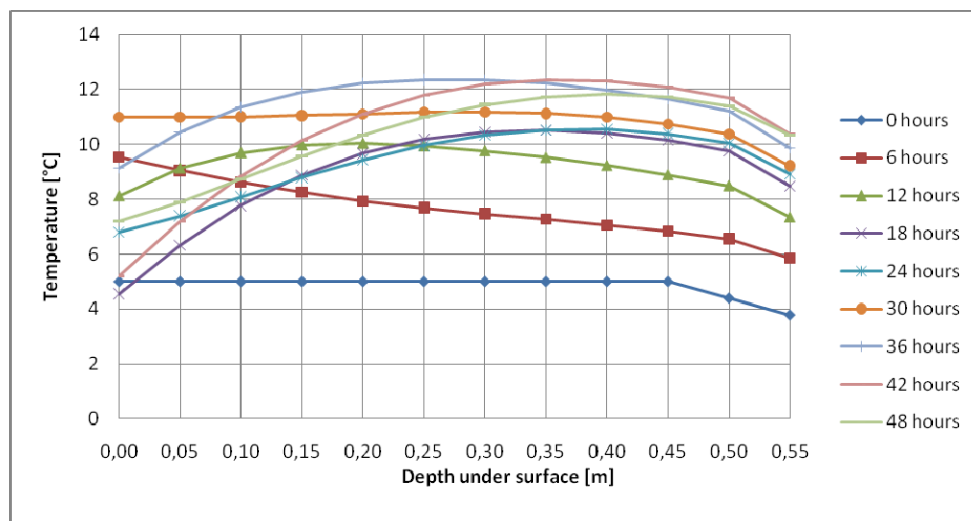


Fig. 4: Temperatures in foundation slab – concreting in winter time.

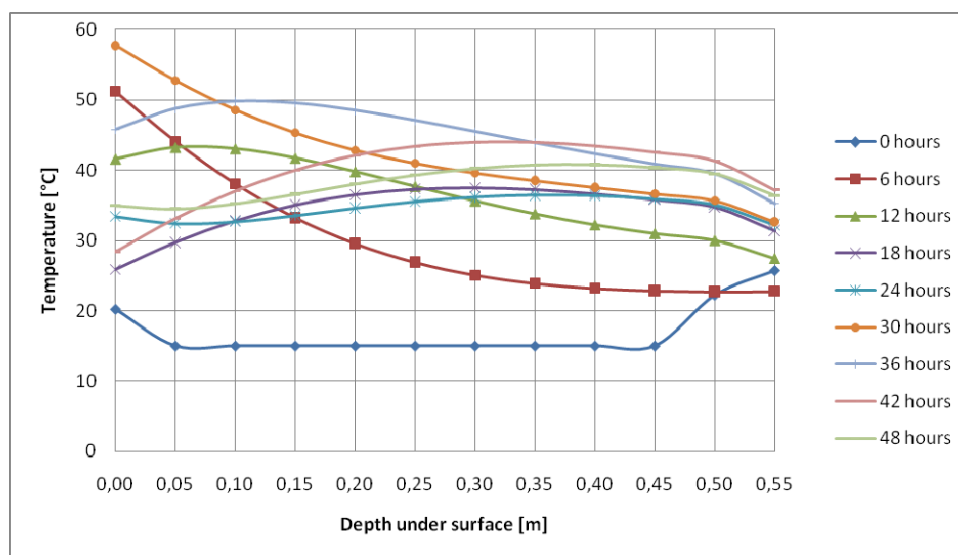


Fig. 5: Temperatures in foundation slab – concreting in summer time.

In the study example temperature distribution in foundation slab with thickness 550 mm is analyzed for 48 hours from concreting. Temperature distribution is considered as one-dimensional, environmental temperature varies for concreting in winter time, Fig. 4, and in summer time according to (1) Fig. 5. In summer time the intensity of solar radiation is taken into consideration.

#### 4. Conclusions

In the paper the temperature distribution in foundation slab is analyzed using Nonstac computer program. Nonstac solves numerically one dimensional temperature array, enable to input appropriate thermal characteristics as a function of temperature, heat generation and variant environmental temperatures. Temperatures in foundation slab are analyzed for concreting in summer time and in winter time. Analysis of temperature distribution in foundation slab enable estimating of temperatures, expected in slide joints. Particular temperature is one of the significant factors, which affects rheological shear characteristics of slide joint material. Experiment of rheological shear characteristics as a function of temperature are in testing the operation. Experimentally appointed function of slide joint resistance versus temperature should contribute to design optimization of slide joint and consequently also foundation structure.

#### Acknowledgement

This outcome has been achieved with the financial support of the Ministry of Industry and Trade of the Czech Republic, program TIP, project No. FR-TI2/746 Rheological sliding joint with thermo-controlled viscoelastic properties.

#### References

- Čajka, R. (2002) Influence of friction in the subsoil to strain of foundation structures. Inaugural dissertation, VSB-Technical university of Ostrava. (In Czech).
- Čajka, R. (2010) Analysis of computer numerical solution of transient temperature distribution with temperature dependant material properties. (In Czech).
- ČSN EN 1991-1-5 Eurocode 1(2005) Action on structures – Part 1-5: General actions – Thermal actions. ČNI Prague.
- ČSN 731208 (2010) The design of waterworks concrete structures. UNMZ Prague. (In Czech).
- Halahyja, M. (1970) Heat engineering, lighting, acoustic. ALFA Bratislava. (In Slovak).
- Halahyja, M., Sobotka, P. (1988) Analysis of factors which affect the long-time temperature variation in subsoil. In journal Sanitary Engineering and air conditioning, volume 31, nb 6. Prague. (In Slovak).
- Maňásek, P. (2008) Foundation structures with slide joint. Doctoral thesis, VSB-Technical university of Ostrava. (In Czech).

## LANDING SHOCK AEROELASTIC RESPONSE ANALYSIS OF UTILITY AIRCRAFT

J. Čečrdle<sup>\*</sup>

**Abstract:** *The paper deals with the aircraft landing shock aeroelastic response analysis. The analysis was performed as a part of the aircraft certification in order to fulfill the CS / FAR 23 § 23.479(d) regulation requirement. The FE model used for the former flutter analyses was utilized. The excitation force was based on the landing gear drop test results. The airflow parameters were set according the aircraft flight envelope and the regulation statements. The modal transient aeroelastic response solution was employed. The structure response was evaluated at the engine center of gravity and the selected points on the wing.*

**Keywords:** *Aeroelasticity, aeroelastic response, landing shock response, EV-55 aircraft.*

### 1. Introduction

EV-55 aircraft is a high-wing utility aircraft for 9 - 14 passengers certified according the CS 23 airworthiness regulations at the normal category. The wingspan is 16.1 m; the maximal take-off weight is 4600 kg; the aeroelastic certification altitude is 3100 m and the maximal level flight velocity is 452 km.h<sup>-1</sup>.

According the mentioned regulation, the aircraft with the significant overlapping masses (e.g. wing mounted engines) must be designed with respect to the dynamic forces for the level landing conditions defined by the regulation (CS 23 §23.479(d)). Therefore it is mandatory to perform the analysis of the load factor at the engine centre of gravity for the defined landing conditions.

### 2. Analytical Model and Used Methods

Respecting the demand to minimize the analysis effort and the available input data we decided to utilize the aeroelastic computational model used for the former flutter analyses (see Čečrdle, Maleček & Černý (2011)). Note that the ordinarily used approach of the aircraft landing response analysis is to use the multi-body simulation including the landing gear characteristics (stiffness and damping) and the aircraft global dynamic model.

The structural model (see Fig. 1) is a beam-like model, the aerodynamic model (see Fig. 1) is based on the Wing - Body Interference unsteady aerodynamic theory. Both models are interpolated by means of beam splines. Model is prepared as a half-span model with the appropriate boundary condition at the plane of symmetry (symmetric, antisymmetric).

For the landing shock response analyses, the former model was adapted. The mass model was adjusted for the landing gear down configuration and additional auxiliary nodes (excitation and response acquisition points) were included. The excitation force is based on the main landing gear drop test with the expected descent velocity of  $V_y = 3.048 \text{ m.s}^{-1}$ . The excitation signal was included in the time domain. The landing level flight velocity was expected  $V_{TD} = 148 \text{ km.h}^{-1}$ . The analysis was performed by means of the NASTRAN program system, the aeroelastic transient response solution was employed. This solution relies on the Fourier transform technique. It is separated into three phases: Firstly, the loads (defined in the time domain) are transformed into the frequency domain. Then the responses are computed in the frequency domain and finally the responses are transformed back to the time domain. The theoretical background of the used solution is given by Rodden and Johnson (1994).

---

<sup>\*</sup> Ing. Jiří Čečrdle, Ph.D.: Strength of Structures Dept., Aeronautical Research and Test Institute (VZLU), Beranovych 130; 199 05, Praha - Letnany; CZ, e-mail: cecrdle@vzlu.cz

The aerodynamic model included no correction for the compressibility ( $M = 0$ ), the dynamic pressure of  $q = 1035.57 \text{ Pa}$  was given from the  $V_{TD}$  and the altitude of  $H = 0$ . For the structural damping, the viscous model was used. The damping ratio was considered either as conservative estimation (1%) or as the maximal value accepted by the regulation (2%). The analyses were performed for the two mass configurations of the model. The mass configurations were realized as a compromise between the regulation specifications and the mass configurations available at the existing model:

- 1) wing fuel loading of 100%; average fuselage loading; total weight of 4700 kg;
- 2) wing fuel loading of 0 %; maximal cargo fuselage loading; total weight of 4654 kg.

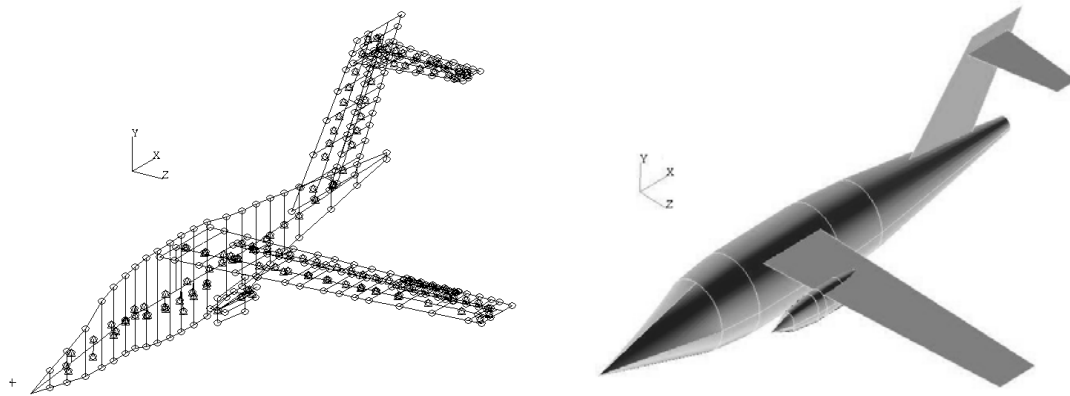


*Fig. 1: Structural and Aerodynamic Model.*

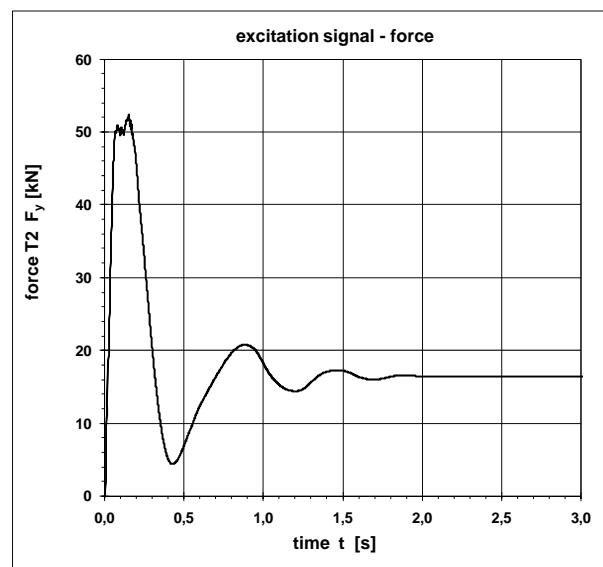


*Fig. 2: Excitation force.*

### 3. Analyses and Results

The excitation signal (see Fig. 2) was applied to the main gear point, the structure response was acquired at the engine centre of gravity and the selected points on the wing (see Fig. 3). The structure response, it means displacement, velocity and acceleration in the vertical direction for the structural damping ratio of 1% and the mass configuration nr.1 is presented in Figs. 4 - 6. The maximal acceleration at the engine centre of gravity was  $5.62 \text{ m.s}^{-2}$ ; at the wing tip point (W4) it was  $56.05 \text{ m.s}^{-2}$ .

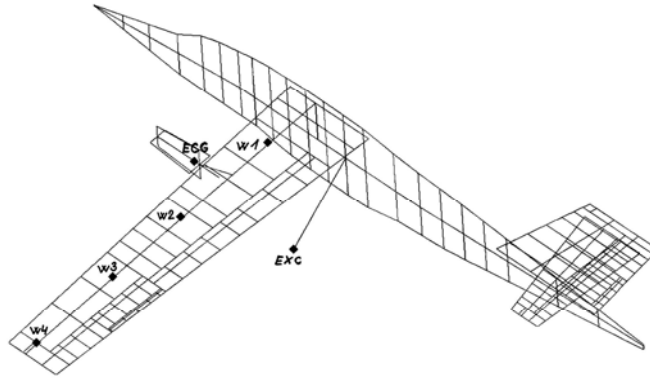


Fig. 3: Excitation and response acquisition points.

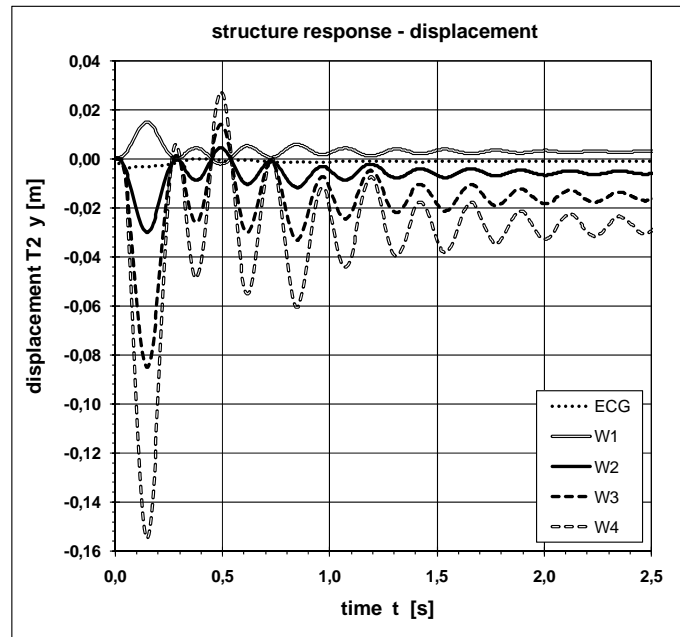


Fig. 4: Structure response - displacement.

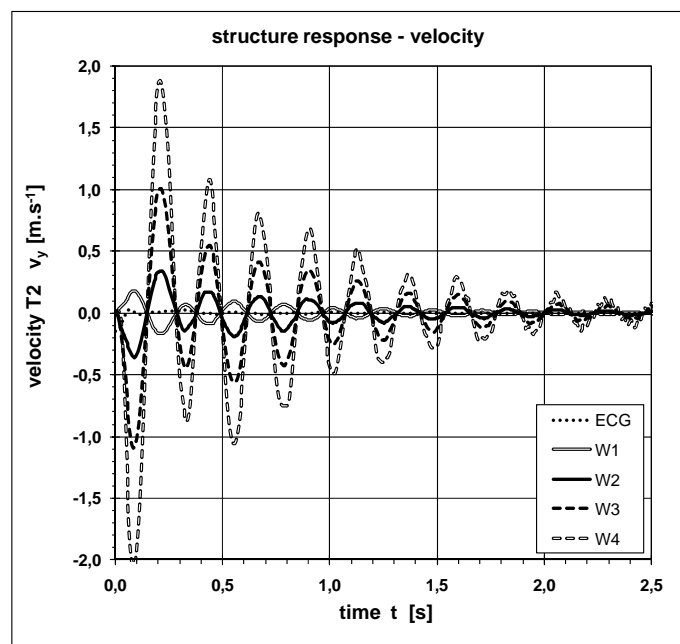


Fig. 5: Structure response - velocity.

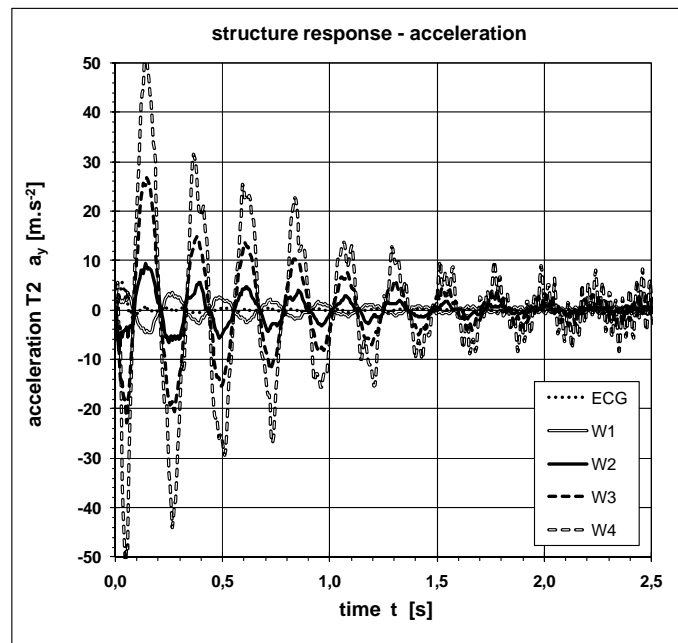


Fig. 6: Structure response - acceleration.

#### 4. Conclusion

The paper describes the landing shock aeroelastic response analyses of the utility aircraft. There were utilized the results of the main landing gear drop test and the analytical model used for the former flutter analyses. The response was acquired at the engine centre of gravity and the selected points along the wingspan. The results will be used for the aircraft certification - it fulfill the requirements of the CS 23 §23.479(d) regulation. It will be also utilized as the input data for the follow-on fatigue analyses.

#### References

- Čečrdle, J., Maleček, J. & Černý, O. (2011) Aeroelastic Analysis of Twin Turboprop Utility Aircraft, Proceedings of the Institution of Mechanical Engineers, Part G: Journal of Aerospace Engineering, ISSN 0954-4100, Sage Publications, UK, accepted for publication.
- Rodden, W.P. & Johnson, E.H. (1994) MSC/NASTRAN Aeroelastic Analysis, The Mac-Neal Schwendler Corporation, Los Angeles, CA, USA.



## STRESS SINGULARITY ANALYSIS OF CRACKS LYING ON THE INTERFACE BETWEEN TWO ORTHOTROPIC MATERIALS

P. Damborský\*, T. Profant\*, M. Kotoul\*

**Abstract:** *This article deal with problems of cracks in bodies with bimaterial interface. The stress and displacement near the front of crack located at the interface between two orthotropic materials is analyzed both analytically and numerically using FEM. Analytical description of the singular stress field and displacements is obtained using the anisotropic generalized complex potentials of plane elasticity.*

**Keywords:** *Orthotropic bimaterials, interface crack, conservative integrals, stress intensity.*

### 1. Introduction

The problem of a crack propagating along an interface between two materials is of great importance to industry. With increasing application of composite materials consisting of long fibre reinforced composite layers in different directions there is growing interest into the understanding of interface fracture between two orthotropic materials. To this end, accurate and efficient methods are required for determining the stress and displacement fields in the neighbourhood of crack tip. Before proceeding, relevant concepts related to interface cracks in orthotropic bimaterials are presented.

### 2. Fracture mechanics of interface cracks between two orthotropic materials in plane strain

Plane strain deformation can be treated by a change of compliances of an orthotropic material  $s_{ij}$  as

$$s'_{ij} = s_{ij} - \frac{s_{i3}s_{3j}}{s_{33}}, \quad i, j = 1, 2, 6. \quad (1)$$

Using the newly defined material parameter  $s_{\pm} = \sqrt{s'_{11}s'_{22} \pm (s'_{12} + s'_{66}/2)}$ , the real Barnett-Lothe tensors  $\mathbf{L}$  and  $\mathbf{S}$  can be expressed following Ting (1996) such as

$$\mathbf{L}^{-1} = \sqrt{2}s + \begin{bmatrix} \sqrt{s'_{11}} & 0 \\ 0 & \sqrt{s'_{22}} \end{bmatrix}, \quad \mathbf{S}\mathbf{L}^{-1} = (\sqrt{s'_{11}s'_{22}} + s'_{12}) \begin{bmatrix} 0 & -1 \\ 1 & 0 \end{bmatrix}. \quad (2)$$

Further, it is convenient to introduce a symmetric, positive definite matrix  $\mathbf{D}$  and a symmetric matrix  $\mathbf{W}$  defined by

$$\mathbf{D} = \begin{bmatrix} D_{11} & 0 \\ 0 & D_{22} \end{bmatrix} = \mathbf{L}_1^{-1} + \mathbf{L}_2^{-1}, \quad \mathbf{W} = \begin{bmatrix} + & -w \\ w & 0 \end{bmatrix} = \mathbf{S}_1\mathbf{L}_1^{-1} - \mathbf{S}_2\mathbf{L}_2^{-1}, \quad (3)$$

where subscripts 1 and 2 refer to the material 1 and 2 respectively.

The in-plane stresses in the neighbourhood of a crack tip at an interface are given by

$$\sigma_{ij} = \frac{1}{\sqrt{2\pi r}} \left[ \operatorname{Re}(Kr^{i\varepsilon}) \Sigma_{ij}^{(1)}(\theta, \varepsilon) + \operatorname{Im}(Kr^{i\varepsilon}) \Sigma_{ij}^{(\varepsilon)}(\theta, \varepsilon) \right], \quad (4)$$

---

\* Ing. Petr Damborský, Ing. Tomáš Profant, Ph.D. and prof. RNDr. Michal Kotoul, DrSc.: Faculty of Mechanical Engineering, Brno University of Technology, Technická 2, 616 69 Brno, CZ, e-mails: damborsky.petr@gmail.com, profant@fme.vutbr.cz, kotoul@fme.vutbr.cz

where  $i,j=1,2$ , the complex stress intensity factor  $K=K_1+iK_2$  and the superscript (1) and (2) are related to the real and imaginary parts of  $Kr^{j\varepsilon}$ .  $\varepsilon$  is referred to as the oscillatory index defined by

$$\varepsilon = 1/2\pi \ln(1 + \beta/1 - \beta), \quad (5)$$

where  $\beta$  is the generalised Dundurs parameter  $\beta = -w/\sqrt{D_{11}D_{22}}$ . The complex stress intensity factor  $K$  in Eq. (4) exhibits three principal drawbacks—it contains the logarithm of length, its physical dimension depends on  $\varepsilon$  and the phase angle  $\arg(K)$  depends on the used length unit. To remove these drawbacks a reference length  $l$  is usually introduced which defines the new complex stress intensity factor  $\hat{K} = Kl^{1\varepsilon}$ . The subsequent description of the singular elastic field employs the dimensionless matrix  $R(c)$  which is defined as a function of complex number  $c$  (see Mantic (2004))

$$\mathbf{R}[c] - \text{Re}[c]\mathbf{I} + \beta^{-1} \text{Im}[c]\mathbf{D}^{-1}\mathbf{W} = \begin{bmatrix} \text{Re}[c] & \text{Im}[c]\sqrt{D_{22}/D_{11}} \\ -\text{Im}[c]\sqrt{D_{11}/D_{22}} & \text{Re}[c] \end{bmatrix} \quad (6)$$

and the traction ahead of crack along the interface are expressed for  $r \rightarrow 0$  as:

$$\begin{bmatrix} \sigma_{xy} \\ \sigma_{yy} \end{bmatrix}(r, 0) = \begin{bmatrix} \sigma_{xy}^{sing} \\ \sigma_{yy}^{sing} \end{bmatrix}(r, 0) + O(1) = \frac{1}{\sqrt{2\pi r}} \mathbf{R} \left[ \left( \frac{r}{l} \right)^{i\varepsilon} \right] \hat{\mathbf{K}} + O(1), \text{ for } r \rightarrow 0, \quad \hat{\mathbf{K}} = \begin{bmatrix} \hat{K}_2 \\ \hat{K}_1 \end{bmatrix}, \quad (7)$$

while the crack face displacements in the vicinity of the crack tip are found to be

$$\begin{bmatrix} \Delta u_x \\ \Delta u_y \end{bmatrix}(r) = \begin{bmatrix} \Delta u_x^{sing} \\ \Delta u_y^{sing} \end{bmatrix}(r) + O(1) = \sqrt{\frac{r}{2\pi}} \frac{2\mathbf{D}}{\cosh \pi\varepsilon} \mathbf{R} \left[ \frac{1}{1+2i\varepsilon} \left( \frac{r}{l} \right)^{i\varepsilon} \right] \hat{\mathbf{K}} + O(r), \quad r \rightarrow 0. \quad (8)$$

The phase angle of mode mixity  $\psi$  is defined as follows:

$$\psi = \arg(\hat{K}_1 + i\sqrt{D_{11}/D_{22}}\hat{K}_2) = \arg(\sqrt{D_{11}/D_{22}} \sigma_{xy}^{sing} / \sigma_{yy}^{sing}(l, 0)). \quad (9)$$

### 3. Conservative integral

The reciprocal theorem of elastostatics states that in the absence of body forces and residual stresses the following integral is path independent

$$\Psi(\mathbf{u}, \mathbf{u}') = \int_{\Gamma} (\sigma_{ij}(\mathbf{u}) \cdot n_i u'_j - \sigma_{ij}(\mathbf{u}') \cdot n_i u_j) ds, \quad (10)$$

where  $\Gamma$  is any contour surrounding the crack tip and  $\mathbf{u}, \mathbf{u}'$  are two admissible displacement fields and  $\sigma_{ij}(\mathbf{u}), \sigma_{ij}(\mathbf{u}')$  are the corresponding stress fields. Hence

$$\int_{\Gamma_1} (\sigma_{ij}(\mathbf{u}) \cdot n_i u'_j - \sigma_{ij}(\mathbf{u}') \cdot n_i u_j) ds = \int_{\Gamma_2} (\sigma_{ij}(\mathbf{u}) \cdot n_i u'_j - \sigma_{ij}(\mathbf{u}') \cdot n_i u_j) ds. \quad (11)$$

For the path far from the crack tip, the unprimed field is obtained from solution to the problem numerically by FE, for example. Along the vanishingly small path, the unprimed field is the singular eigensolution to the crack problem given in Eq.(7) and (8). The primed solution is chosen so that this integral identically yields the sought stress intensity factor. The primed solution (the auxiliary solution) corresponds to the singular eigensolution with the eigenvalue  $-1/2-i\varepsilon$  for the displacement field. It has unbounded energy near the crack tip and thus corresponds to some concentrated source at the crack tip. It is a mathematical tool which allows extracting asymptotic coefficient terms from the complete exact solution. The generic form of the auxiliary traction vector  $\mathbf{t}'$  acting along the contour  $\Gamma$  was derived as follows

$$\mathbf{t}'(z) = \left( \mathbf{I} + \overline{\mathbf{H}}^{-1} \mathbf{H} \right) \frac{e^{-\pi\varepsilon} k_1 \mathbf{w}' z^{-i\varepsilon} + e^{\pi\varepsilon} \overline{k_1 \mathbf{w}' z^{i\varepsilon}}}{z^{\frac{3}{2}} e^{-\pi\varepsilon}} \quad (12)$$

where  $\mathbf{I}$  stands for unit matrix,  $z = x + \mu y$ , where  $\mu$  is a complex characteristic material number with positive imaginary part,  $\mathbf{w}'$  is the complex eigenvector,  $k_1$  is a complex constant, and  $\mathbf{H}$  is the bimaterial matrix for two orthotropic materials with aligned principal axes

$$\mathbf{H} = \begin{bmatrix} H_{11} & -i\beta(H_{11}H_{22})^{1/2} \\ i\beta(H_{11}H_{22})^{1/2} & H_{22} \end{bmatrix} \quad (13)$$

whose components can be found in Suo (1990).

#### 4. Numerical results

Bimaterial orthotropic strip subjected to tensile loading along the boundary parallel to the interface with an edge interface crack was modelled by FE with the system ANSYS. The material properties are listed in the Tab. 1. The phase angle of mode mixity  $\psi_k$  was calculated from Eq. (9) for  $l = 1$  mm providing the value  $\psi_k = -0.178$  rad. The angular dependence of analytically obtained singular field along a circular contour surrounding the crack tip was compared with the numerically obtained field at  $r = 1$  mm using a very fine mesh.

Tab. 1: Elastic properties of the orthotropic bimaterial strip and corresponding values of Dundurs' parameters  $\alpha$ ,  $\beta$ .

	$E_L$ [GPa]	$E_T$ [GPa]	$E_Z$ [GPa]	$\nu_{TZ}$	$\nu_{ZL}$	$\nu_{TL}$	$G_{TZ}$ [GPa]	$G_{ZL}$ [GPa]	$G_{TL}$ [GPa]	$\alpha$	$\beta$
Mat 1	200	80	80	0.3	0.3	0.3	30	30	30	-	0.1024
Mat 2	50	150	150	0.3	0.3	0.3	30	30	30	0.1193	

The angular parts of the asymptotic stress-displacement field are plotted as functions of the polar angle  $\theta$  for several values of the phase angle of mode mixity in Figs. 1 - 5.

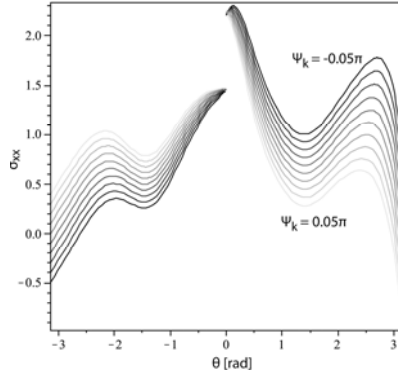


Fig. 1: Asymptotic stress  $\sigma_{xx}$  along the circular path for several values of the phase angle  $\psi_k$ .

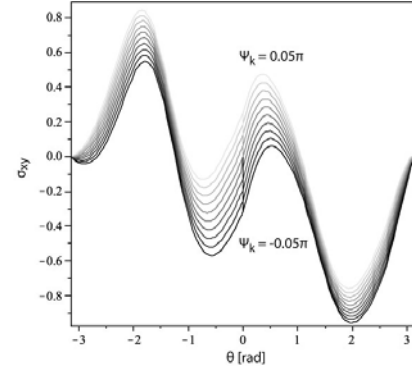


Fig. 2: Asymptotic stress  $\sigma_{yy}$  along the circular path for several values of the phase angle  $\psi_k$ .

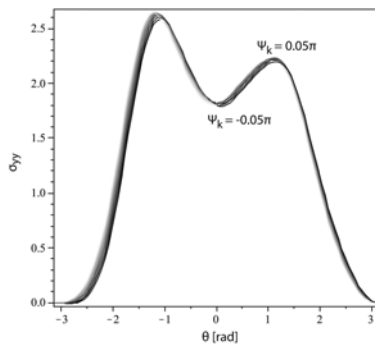


Fig. 3: Asymptotic stress  $\sigma_{xy}$  along the circular path for several values of the phase angle  $\psi_k$ .

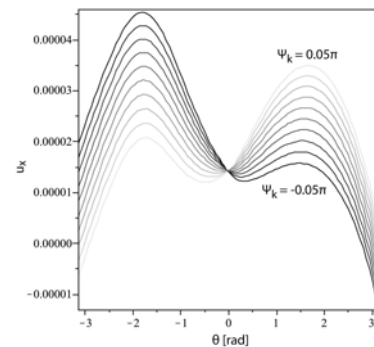


Fig. 4: Asymptotic displacement  $u_x$  for several values of the phase angle  $\psi_k$ .

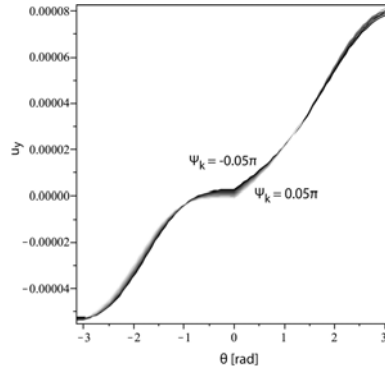


Fig. 5: Asymptotic displacement  $u_y$  for several values of the phase angle  $\psi_k$ .

It is clearly seen that the stress components  $\sigma_{yy}$  and the displacement components  $u_y$  depend only very little on the phase angle.

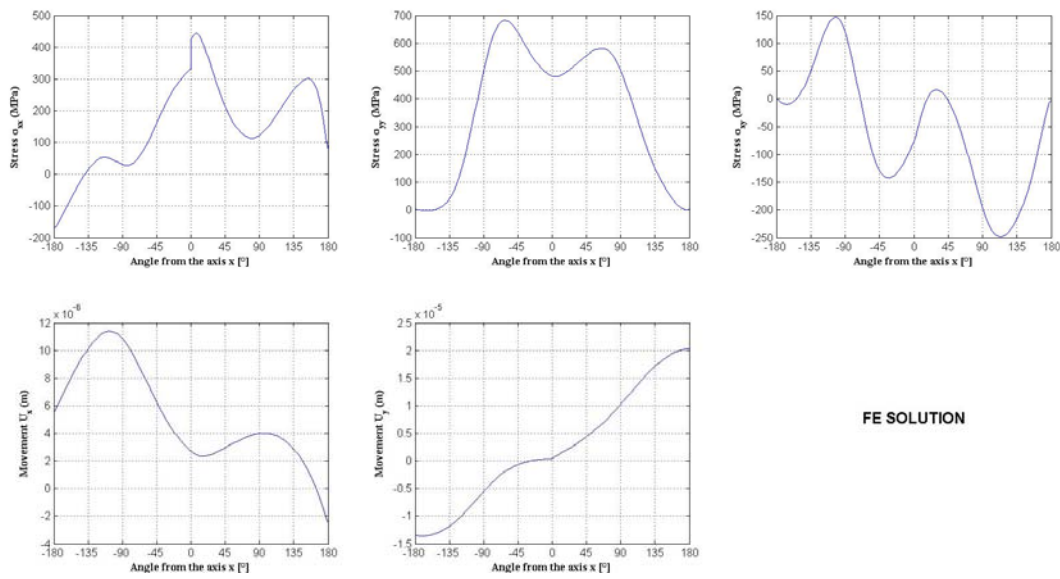


Fig. 6: FE solution to the stress-displacement field near the crack tip.

## 5. Conclusion

The stress field and the displacement field, calculated by FEM at the distance  $r = 1$  mm from the crack tip is shown in Fig. 6. Observe that angular dependences of all quantities perfectly match with the analytical singular solutions. It means that the domain of dominance of the singular solution is of order of 1 mm for the examined specimen/crack configuration. The auxiliary solution defined in Eq. (12) was also evaluated and substituted into the conservative integral in Eq. (10), which enables us to calculate the real and imaginary part of the complex stress intensity factor. Further results will be presented at the conference.

## Acknowledgement

The authors gratefully acknowledge a financial support of the Czech Science Foundation under the Projects No. 101/09/1821 and the Specified Research Grant No. FSI-S-10-12.

## References

- Ting, T.C.T. (1996) Anisotropic Elasticity, Theory and Applications, Oxford University Press, Oxford.
- Mantić, V. & Paris, F. (2004) Relation between SIF and ERR based measures of fracture mode mixity in interface cracks. Int. J. Fracture. 130, pp. 557-569.
- Suo, Z. (1990) Singularities, interfaces and cracks in dissimilar anisotropic media. Proc. R. Soc. Lond. A., 427, pp.331-358.

## EXPERIMENTAL INVESTIGATION OF SYNTHETIC JET ARRAY

P. Dančová<sup>\*</sup>, T. Vít<sup>\*</sup>, M. Kotek<sup>\*\*</sup>

**Abstract:** *Paper deals on an experimental investigation of a synthetic jet array. This investigation focuses on a partial problem of the general task “a synthetic jet array interacting with a channel flow”. The experiments have been performed with water as a working fluid using hot-wire anemometry, laser Doppler vibrometry and particle image velocimetry methods.*

**Keywords:** *Synthetic jet array, actuator, piezoelectric membrane, heat transfer, particle image velocimetry.*

### 1. Introduction

Experimental setup is made from a channel and a synthetic jet (SJ) array. SJ is generated by the periodic motion of an actuator oscillating membrane. It is synthesized by the interactions within a train of vortices. The time-mean mass flux in SJ orifice is zero; hence the other common expression is zero-net-mass-flux (ZNMF) jet (Smith and Glezer, 1998, Glezer and Amitay, 2002, and Cater and Soria 2002). The arrangement for general task “a synthetic jet array interacting with a channel flow” can be useful in many micro-scale applications, such as cooling of micro-electronics or the detection of various (biological, biomedical or chemical) species. The flow regime in micro-scale is usually laminar with very small Reynolds numbers. Therefore, the transfer processes such as mixing and cooling are typically based on gradient diffusion (Timchenko *et al.*, 2007, Dančová *et al.*, 2009).

### 2. Experimental investigation

#### 2.1. Problem parameterization

SJ is characterized by several independent parameters. Considering the plug flow model (one-dimensional piston like flow in the actuator orifice), the main parameters are: the actuator orifice diameter  $D$ , the time-mean orifice velocity  $U_0$ , the “stroke length”  $L_0$ , the Reynolds number of SJ and the Strouhal number. All parameters are defined e.g. in (Smith and Glezer, 1998, Glezer and Amitay, 2002, or Dančová *et al.*, 2009).

#### 2.2. Experimental setup

The experimental setup is made out from plexiglass (Fig. 1a), internal dimensions are (200 x 200 x 40) mm, length x width x high. The upper wall is bolted with four screws – this connection enables to take off this wall. SJ array is made from four SJ actuators, for dimensions see Fig. 1b. SJ actuator consists of a sealed cavity (diameter  $D_D = 36$  mm), which is equipped with an emitting orifice (diameter  $D = 3.0$  mm) and with an actuating piezoelectric membrane (KINGSTATE KPS-100). The piezoelectric membrane (PM) was used because it has many significant advantages, e.g. applicability in different fluids, in broad temperature ranges, and in heavy-duty facilities. Other advantages of PM are long an operational lifetime and low power consumption.

---

<sup>\*</sup> Ing. Petra Dančová and doc. Ing. Tomáš Vít, Ph.D.: Institute of Thermomechanics AS CR, v.v.i.; Dolejškova 1402/5; 182 00, Prague 8; CZ, e-mails: petra.dancova@tul.cz, e-mail: tomas.vit@tul.cz

<sup>\*\*</sup> Ing. Michal Kotek: Institute of Systems Control and Reliability Management, Technical University of Liberec; Studentská 2; 461 17, Liberec 1; CZ, e-mail: michal.kotek@tul.cz

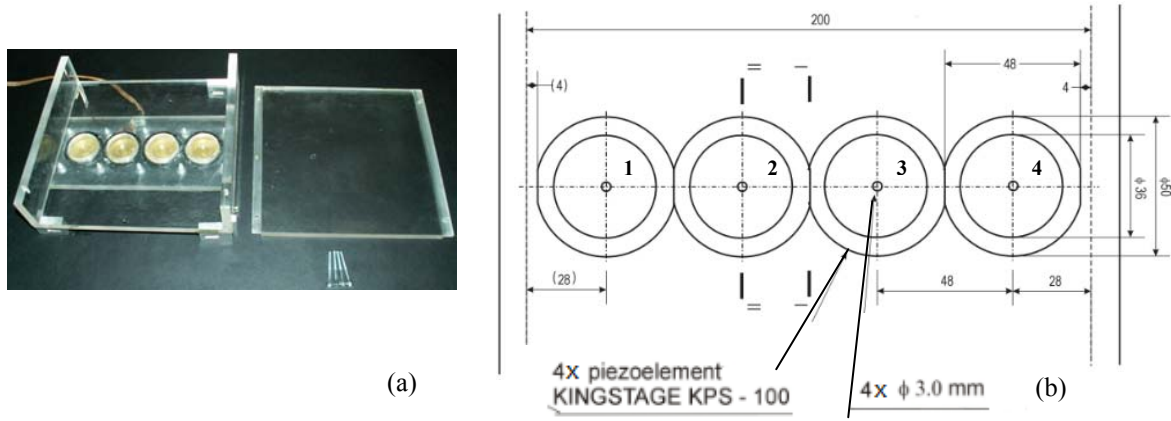


*Fig. 1: SJ array equipment*  
*(a) disassembled device, (b) detailed view of the SJ array of actuators (bottom view).*

### 2.3. Experimental methods

Three different experimental methods were used. For SJ actuator frequency characteristic a hot wire anemometry (HWA) was used in regime of constant temperature. The sampling frequency and number of samples were 7 kHz and 32768, respectively. For data analysis the commercial software StreamWare version 3.03 and Excel was used.

The actuator piezoelectric membrane centre displacement and velocity was measured using laser Doppler vibrometry (LDV). Measurement is based on the Doppler effect, and the portable digital vibrometer Ometron VH-1000-D B&K 8338 was used. The main parameters: frequency range 0.5 Hz ÷ 22 kHz; measurement ranges (full scale (peak- peak)) 20 mm/s, 100 mm/s, 500 mm/s; spurious free dynamic range (SFDR): > 90dB; and best resolution: 0.02  $\mu\text{m/s/Hz}^{0.5}$ . The response of a PM to a harmonic driving signal for frequency  $f = 15$  Hz was measured. The LabView software was used to acquire and analyze the signal obtained from the Ometron vibrometer. Software Excel was used for additional calculations and analysis.

Behavior and flow field of SJ array was measured using particle image velocimetry (PIV). Seeding particles for the PIV experiments were polyamide balls with diameter 20  $\mu\text{m}$ , which density is comparable to water. The particles were illuminated by a double pulse laser with maximum 125 mJ per 10 ns pulse and repetition rate 2 x 15 Hz. The typical delay time between two pulses was 5 ms. The laser beam was expanded into a light sheet of about 1 mm thick. The image pairs were acquired using the camera (HiSense model MKI, DANTEC) with a spatial resolution of 1280 x 1024 pixels. The resulting vector maps were averaged over 100 PIV records. Velocity vectors were determined by adaptive correlation over interrogation windows 32 x 32 pixels at a 25 % overlap. Data processing used the commercial software DynamicStudio version 2.21 (DANTEC).

## 3. Results

The SJ array actuators were fed with sinusoidal current. The input electrical voltage and current were about 19 V<sub>effective</sub> and about 3 mA (rms).

### 3.1. Hot wire anemometry

It is known that SJ actuators work very well near their resonance/natural frequencies. Following this fact, the frequency characteristic of the SJ actuator is the first step of the experiments. If the actuator works with the natural frequency, it has the highest power and velocity. Fig. 2 shows the frequency characteristic. Frequency was measured in range of (10-60) Hz. Fig. 2 shows that SJ actuator works with the highest voltage, velocity respectively, on 15 Hz, which is the working frequency of SJ array. The far from natural frequency, the more velocity  $U_0$  values decrease (Fig. 2a). SJ actuator has also the second resonance, which follows the Helmholtz resonator frequency (see Kinsler *et al.*, 2000).

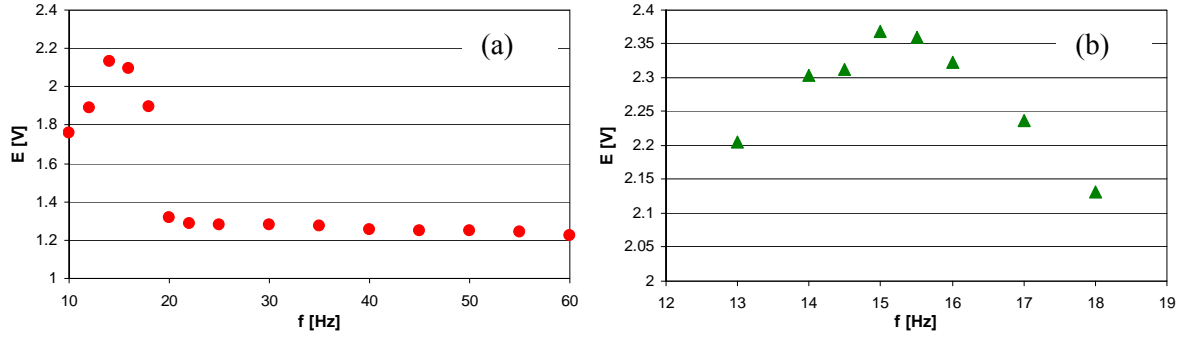


Fig. 2: (a) Frequency characteristic of SJ actuator, (b) detailed view.

### 3.2. Laser Doppler vibrometry

Figs. 3a and 3b show the results from LDV measurement. The sampling rate for this measurement was 3000 Hz. The period starts with the leading edge of the TTL signal. TTL signal has the same frequency (15 Hz) as the frequency of SJ actuators driving signal from the signal generator. Fig. 3a shows measurement of the membrane centers velocities in time (colored curves), blue curve is TTL signal. There is a visible phase shift between TTL signal and the response of the membrane. Here is also shown, that the SJ actuators work without phase shift, which is important for the general task of SJ array with affection of channel flow. Fig. 3b shows the membrane centre displacement in time compared with TTL. Velocities are measured with laser Doppler vibrometer and displacements are calculated from measured values. This is the reason why curves in Fig. 3a have not smooth character.

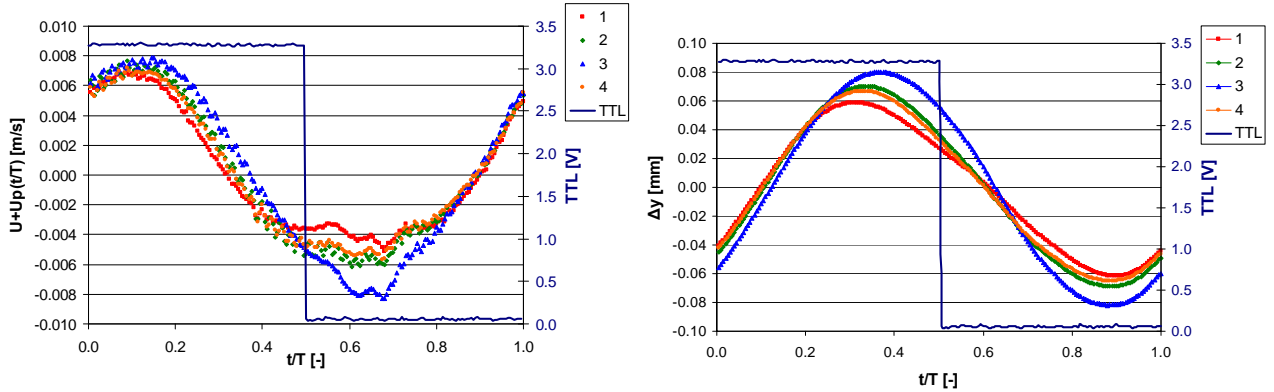


Fig. 3: SJ array: (a) membrane centers velocity, (b) membrane centers displacement.

### 3.3. Particle image velocimetry

First step of PIV experiments is the synchronization of SJ actuators with laser and camera system. Synchronization procedure is described e.g. in (Kotek and Kopecký, 2009). Experiments were performed with and without the upper wall of the equipment (Fig. 1a). Experimental results on Fig. 4a show whole SJ array in time of full extrusion from the actuators cavities with the upper wall of the equipment in form of velocity magnitude vectors. Monitored plane was aligned to the collective center line of all orifices. It demonstrates the influence of particular SJs. On Fig. 4b is seen SJ array in the same time as Fig. 4a, but the view is displaced 10 mm from the orifice axes. Fig. 5 represents the SJ array in time of full extrusion without the equipment upper wall. There is visible a small influence between SJs in form of outer SJ bending.

## 4. Conclusions

This paper brings results of HWA, LVD and PIV experimental research of the synthetic jet array. This part of investigation is important to understand how SJ array behavior is influenced by basic parameters – cavity dimensions, natural frequency of particular actuators, displacement and velocity of the actuator membranes. This knowledge is applied into research of a channel flow which is affected by a synthetic jet array with emphasis on low Reynolds numbers.



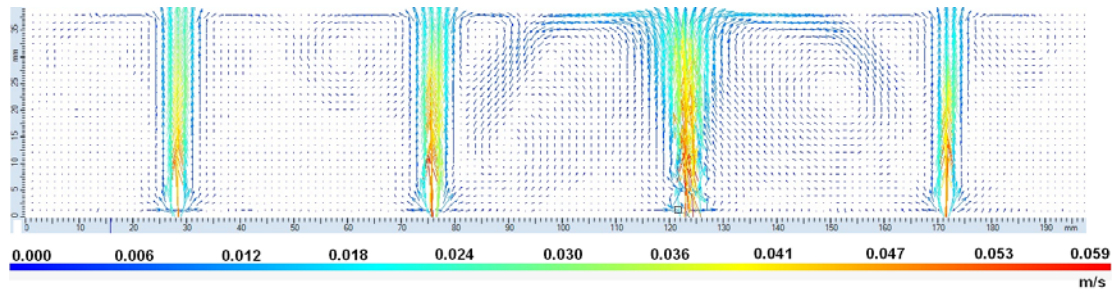


Fig. 4a: SJ array focused on the orifice axes (in form of velocity magnitude vectors).

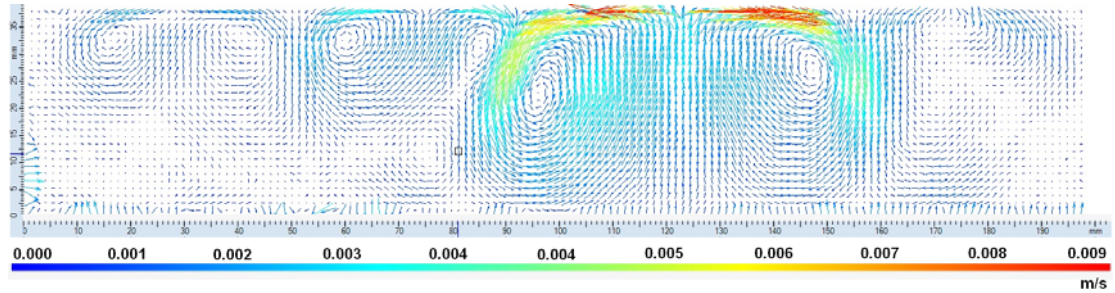


Fig. 4b: SJ array displaced 10 mm from the orifice axes (in form of velocity magnitude vectors).

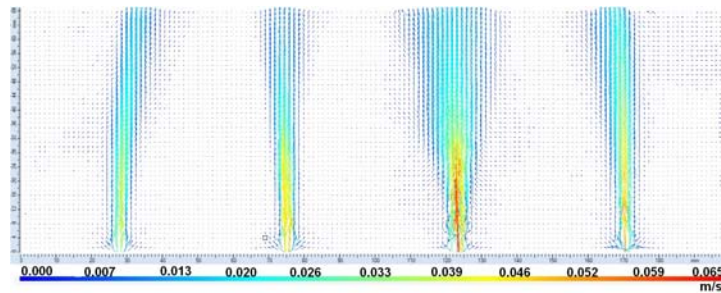


Fig. 5: SJ array without the equipment upper wall (in form of velocity magnitude vectors).

## Acknowledgement

We gratefully acknowledge the support of the Grant Agency AS CR (Project IAA200760801) and GA CR (P101/11J019/1).

## References

- Cater, J.E., Soria, J. (2002) The evolution of round zero-net-mass-flux jets, in: J. Fluid Mechanics 472, pp. 167-200.
- Dančová, P., Vít, T., Trávníček, Z. (2007) Analysis of SJ piezo-ceramic pulsation generator, in: Developments in Machinery Design and Control, pp. 15-16.
- Dančová, P., de Lange, H. C., Vít, T., Šponiar, D., Trávníček, Z. (2009a) Laminar channel flow effected by synthetic jets – Experimental and numerical studies, in: Proc. 7th World Conference on Experimental Heat Transfer, Fluid Mechanics and Thermodynamics ExHFT-7, Krakow, Poland, pp. 967–974.
- Dančová, P., de Lange, H. C., Vít, T., Šponiar, D., Trávníček, Z. (2009b) Channel flow controlled by synthetic jet array, in: Proc. 6th International Symposium on Turbulence, Heat and Mass Transfer THMT'09, Rome, Italy, pp. 935–938.
- Glezer, A., Amitay M. (2002) Synthetic jets, in: Annu. Rev. Fluid Mech. 34, pp. 503-529.
- Kinsler, L. E., Frey, A. R., Coppens, A. B., Sanders J. V. (2000) Fundamentals of Acoustics, 4th Ed., Wiley & Sons, Inc., New York.
- Kotek, M., Kopecký, V. (2009) Application of laser anemometric and visualization methods on research of weft propulsion mechanism, in: Proc. of In. conference Experimental Fluid Mechanics 2009, Liberec, Czech Republic, pp. 128-135.
- Smith, B.L., Glezer, A. (1998) The formation and evolution of synthetic jet, in: Phys. Fluids 10, pp. 2281-2297.
- Timchenko, V., Reizes, J.A., Leonardi, E.: (2007) An evaluation of synthetic jets for heat transfer enhancement in air cooled micro-channels, in: Int. J. Numer. Methods Heat Fluid Flow, 17(3), pp. 263-283.

## FEM NONLINEAR CONTACT VIBRATION ANALYSIS OF A DISC ADAPTER

V. Dániel<sup>\*</sup>, T. Jamrůz<sup>\*</sup>, J. Had<sup>\*</sup>

**Abstract:** *In order to simulate a launch, all space instruments undergo a vibration tests. Due to the fixing points in vibrating machines being different, adapters are used for each space instrument. In random environments the load is defined as stochastic data. Only linear analysis can be used. This article describes the method for FE modeling of nonlinear contact transient analysis. The load is defined as random stochastic data depicted as a graph versus time and applied to space instruments. For base excitation, the large-mass method was used. The contact is formed by GAP elements. From the results, the PSD (Power Spectral Density) spectrum and  $g_{RMS}$  values of vibration are computed and evaluated.*

**Keywords:** *Vibration, space instrument, contact, FEM.*

### 1. Introduction

To simulate a launch in space, all space instruments are tested by vibration test equipment. Because the fixing points on the vibration machine are in a different position than that of the space instrument, adapters are used. In the micro-accelerometer (MAC) of the SWARM mission a disc adapter was used. The required adapter is required to have minimum variation of transmissibility between test item and mounting points. A random spectrum is defined for each instrument itself. In the MAC, the random spectrum range is from 20 Hz to 2000 Hz. The overall random  $g_{RMS}$  variation is maximally  $\pm 10\%$ . This imposes a high demand on the vibration machine. The machine facilities under heavy acceleration are limited by the maximum weight of measuring instrument and adapter. In our case the adapter's maximum weight was set to 10 kg. The transmissibility variation shall not exceed a change of +3 dB between 5 to 500 Hz and +6 dB between 500 to 2000 Hz. During test, the disc adapter and the vibration machine equipment are not constantly in contact, this being the reason why the nonlinear contact analysis must be used.

### 2. Design

Three designs were modeled. The first a disc adapter with a 25 mm thickness and a 450 mm diameter connected to the vibration machine by 8 screws in a circular formation, radius of which is 203.2 mm. The second a disc adapter with a 35 mm thickness and a diameter of 350 mm. Due to the position of the MAC on the adapter prohibiting the use of 8 screws, 6 screws were used instead in a circular pattern with radius 152.4 mm. The last design used countersunk screw heads, 12 screws can be used, 8 with a radius of 152.4 mm and 4 with a radius of 101.6 mm.

The FE model is computed by NASTRAN software. The disc adapter is modeled as a 3D solid, the vibration machine as a 2D surface on the base. For base excitation, the large-mass method (Leftheris, 2006) was used. The 2D surface on the base was connected with point mass (CONM2) by a rigid RBE2 element. The disc adapter is fixed to the vibration machine by screws in a circular pattern. The screws are modeled as a rigid RBE2 element. The contact is formed by GAP elements with nonlinear behavior (CGAP) not forming classical gap contact as defined in Laursen, 2003. The element is in continuous contact time as node-to-node contact element (Wriggers, 2002). The advantage of node-to-node contact in comparison to slave-master contact is it being a fast solution without iteration. The different properties in compression and tension are defined as nonlinear stiffness material property.

---

<sup>\*</sup> Ing. Vladimír Dániel, Ph.D., Ing. Tomáš Jamrůz and Ing. Jiří Had: Aeronautical research and test institute, Aerospace Research Centre, Beranových 130; 199 05, Prague; CZ, e-mails : daniel@vzlu.cz, jamroz@vzlu.cz, had@vzlu.cz

GAP tension - open stiffness is 100MPa, compression - close stiffness is 45000MPa. The close stiffness corresponds to material stiffness of Electron (vibration test machine material (magnesium alloy)). Material properties of used material are shown in Tab. 1.

Tab. 1: Material properties of disc plate (duralumin) and vibration test machine plate (Electron).

no.	Description	Material	$E_{11}$ [MPa]	$G_{44}$ [MPa]	$\nu$ [1]	$\rho$ [kg/m <sup>3</sup> ]	Damping G
<u>1</u>	Duralumin	7075 T651 (Al alloy)	71700.	26900	0.33	2810	0.005
<u>2</u>	Electron	Electron A8 (EN 1753 MC21110)	45000	17000	0.34	1800	

### 3. Methods

Firstly, a modal analysis (SOL 103) was made. The frequency range of interest is from 20 Hz to 2000 Hz. The first mode was a calculated circle mode (0,0) on frequency 1119 Hz and a second bending mode (1,0) on frequency 2063 Hz. Next the nonlinear transient analysis (SOL129) was used. The overall acceleration of a random test is 15.23  $G_{RMS}$  (root mean square value multiple by gravitational acceleration) having stochastic character. The maximum PSD of vibrations between 100 and 300 Hz are 0.405  $G^2/Hz$ . Between 20 Hz and 100 Hz, the +3 dB/Oct rate is defined. Between 300Hz and 2000Hz, the -5dB/Oct rate is defined. The defined spectrum is shown in Fig. 3. Instead of acceleration, a force load is applied at the large-mass point. The sensitivity analysis of the large mass value was made. It has exponential effect on the  $g_{RMS}$  value. Over the value  $10^6 * m_0$ , the  $g_{RMS}$  value doesn't change. Due to limitations for large-mass being only in numeric overflow, the value of  $10^7 * m_0$  was used (recommended value by NASTRAN software is  $10^6 * m_0$ ).

The transfer of stochastic spectra to deterministic values of acceleration versus time by the time averaging was used in (Ariaratnam, 1988). In our case the random load spectra is transferred to acceleration versus time data using MATLAB software. White noise was filtered according to the required spectrum properties using a band pass filter. The final time history load has a greater  $g_{RMS}$  (value of 20 G). A greater value is necessary for a conserved solution. The workflow for computing the random behaviour in nonlinear transient analysis is depicted in Fig. 1.



Fig. 1: Workflow for transient analysis with stochastic load.

A 0.05s overall time was used in  $5e^{-5}s$  intervals. According to Umashankar, material damping  $\xi_{Al}$  measured 0.0025 using  $f_{resonance}$  of 383Hz ( $GE = 0.005$ ,  $W4 = 2406$ ). The material damping constant of  $G_E$  and  $W4$  are used by NASTRAN software in a damping matrix [B]. Random vibration with symmetric geometric nonlinearities is described in (Roberts, 1990). In our case, the GAP element forms asymmetric geometric nonlinearity. The equation of motion is given as:

$$[M]\ddot{u} + \frac{G_{Al}}{W4}[K]\dot{u} + [K]u = m\{a\} \quad (1)$$

Using a free system, the general displacement  $u$  does not correspond to the vibration between the disc adapter and a rigid platform. The vibration displacement  $u'$  is defined as:

$$u'(t) = u_{adapter}(t) - u_{ground}(t) \quad (2)$$

### 4. Results

From transient nonlinear analysis, acceleration and displacement at each point was computed. The results for the displacement of the vibration  $u'$  for the above-described designs is shown in Fig. 2. The actual value of  $u'$  varies greatly in time. The lowest vibration is shown with the model having a 35 mm thickness and 12 screws.

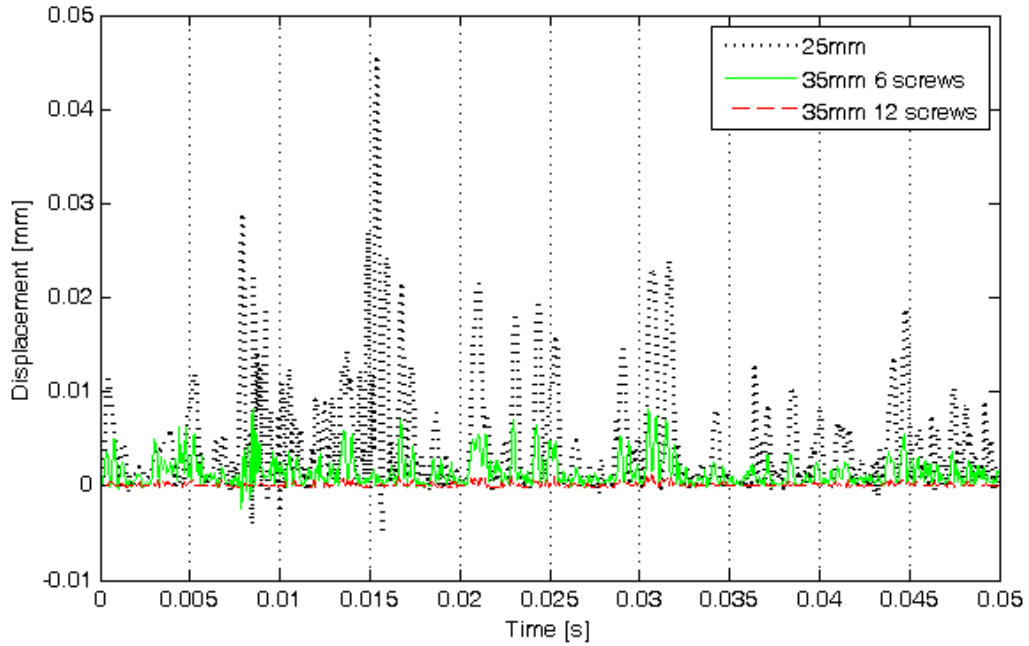


Fig. 2: Computed displacement  $u'(t)$  between adapter and ground with nonlinear transient response (legend describes the thickness of the disc adapter).

We change the stochastic data to a graph. Due to this, we cannot evaluate the deterministic values; and must use a stochastic estimation. One such estimation is the root mean square (RMS) value (Lalanne, 2002). The RMS values of acceleration with the most intense vibration point  $g_{RMS}$  are shown in Tab. 1. From a spectral analysis of transient record, we can determine the resonance frequency (Reddy, 2004). The nonlinear parameters of the GAP element in contact with a rigid ground forms local surface deformation comparable with a non-rigid platform. In low frequency dynamics, the local surface deformation can significantly affect the results (Laursen, 2003). We can compute the mean value 2.345 as the ratio between nonlinear contact resonance and model resonance.

Tab. 1: Calculated modes, nonlinear resonances and effective values of acceleration  $g_{RMS}$ .

	Mass [kg]	Mode no.1 [Hz]	Mode no.2 [Hz]	Nonlinear resonance no.1 [Hz]	Nonlinear resonance no.2 [Hz]	$g_{RMS}$ [g]
Random load						15.2
Transient load						20
25 mm $\varnothing_{450}$	10.326	1119	2061	2600	4720	86.4
35 mm $\varnothing_{350}$ 6screws	8.689	1914	2267	4400	5620	38.3
35 mm $\varnothing_{350}$ 12screws	8.689	5161	5857	over 10000	over 10000	21.4

The disc adapter with a 35 mm thickness and a diameter of 350 mm was manufactured and tested. For the random vibration test, a vibration machine LDS V850-22kN was used. The difference between 6 and 12 fixing screws were investigated. The measured spectrum of 6 screws crosses the tolerance of +6 dB at frequency 1400 Hz. The 12 screw design withstood to the defined requirements. The PSD of vibration are shown in Fig. 3. Because of our 0.05 s interval record, we have no results below 100 Hz (with respect to 5 points being a minimum to evaluate the sinusoidal behavior).

Three designs of disc adapters widely change the transferred spectrums when compared with load. The 25 mm thickness adapter changes the spectral density of +3 dB from 480 Hz onwards. The overall  $g_{RMS}$  value was 86.4 g because the first resonance of the disc around 2600 Hz. The 35 mm thickness adapter with 6 screws changes the spectral density of +3 dB at 1560 Hz with the experiment showing the limit at frequency 1170 Hz. The 35 mm thick adapter with 12 screws does not change the spectral density +3 dB from 2420 Hz, the experiment shows a frequency of 1500 Hz. Even the experiment shows +3 dB at 1500 Hz, +6 dB don't come until 2000 Hz. The overall  $g_{RMS}$  value is 21.4 g. The variation value (+7%) is in accordance with the requirements. The design with 12 screws is acceptable for use in a random vibration test.

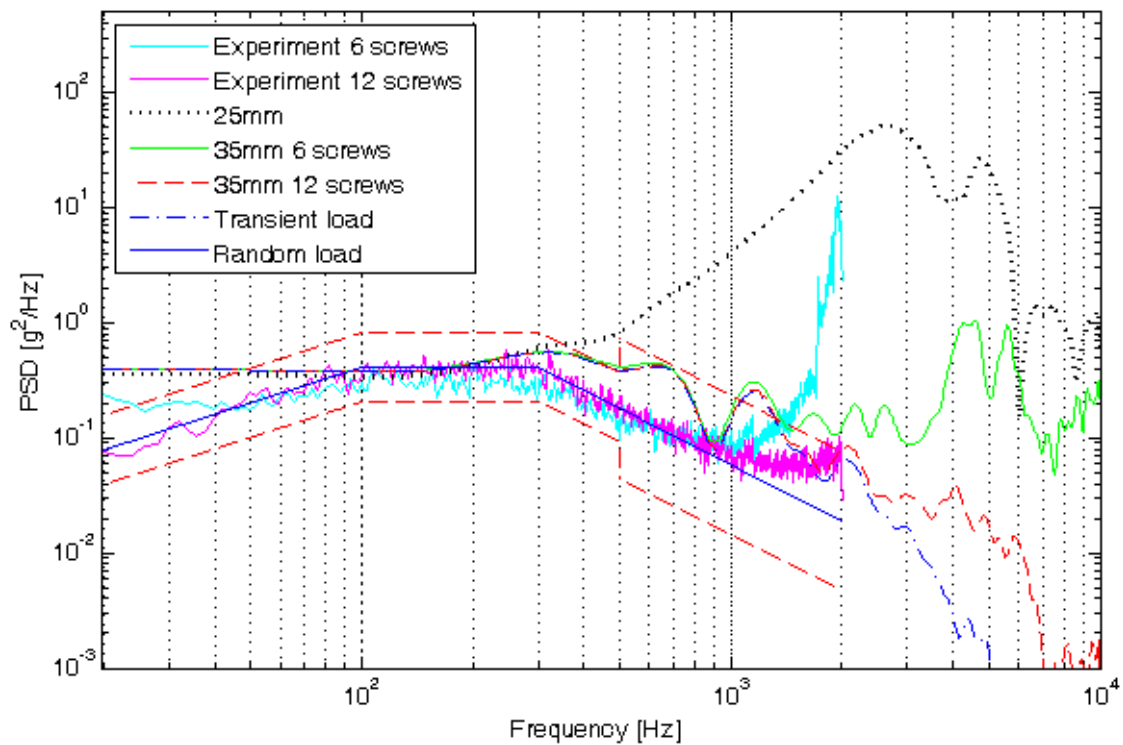


Fig. 3: Measured spectrums (Experiment) and computed spectrums of the 3 designs of a disc adapter.

## 5. Conclusions

The work describes the FE nonlinear contact random analysis. The process was demonstrated on the three adapter designs for vibration testing. For random vibration, a wide range of frequencies, between 20 Hz and 2000 Hz were used. The only acceptable adapter in this range is the one with 350 mm diameter and 35 mm thickness with 12 mounting screws. To analyze the spectrum, nonlinear transient contact analysis must be used with a sufficient time length and sampling rate. To evaluate the result defined by stochastic behavior, only the stochastic estimated results shall be used. The  $g_{RMS}$  and PSD values were used. Nevertheless, to calculate the results we need to view the load as a graph versus time data. The MATLAB software was used for that by filtering white noise. The results were verified by vibration experiments.

## Acknowledgement

This work was supported by the Czech Ministry of Education, Youth and Sports, by the Grant No. 1M0501.

## References

- Ariaratnam, S. T., Schuëller, G.I., Elishakoff, I. (1988) Stochastic structural dynamics: progress in theory and applications. Elsevier applied science publishers Ltd, pp. 63-89.
- Lalanne, Ch. (2002) Mechanical vibration and shock: Random vibration. Taylor & Francis Books, Inc, New York.
- Laursen, A. (2003) Computational Contact and Impact Mechanics, Fundamentals of Modeling Interfacial Phenomena in Nonlinear Finite Element Analysis. Springer-Verlag, Berlin, pp. 113-116.
- Leftheris, B.P., Stavroulaki, M.E., Sapounaki, A.C., Stavroulakis, G.E. (2006) Computational Mechanics for Heritage Structures. WIT Press 2006, Great Britain, pp. 105-107.
- Reddy, J. N. (2004) An introduction to nonlinear finite element analysis. Oxford university press, Grea Britain.
- Roberts, J. B., Spanos, P. D. (1990) Random vibration and statistical linearization. John Wiley& Sons Ltd, pp. 37-39.
- Umashankar K. S., Abhinav Alva, Gangadharan K. V. and Vijay Desai (2009) Damping behaviour of cast and sintered aluminium. ARPN Journal of Engineering and Applied Sciences, Vol. 4 No. 6.
- Wriggers, P. (2002) Computational contact Mechanics. John Wiley& Sons Ltd, England, pp. 166-171.



## **PORE SIZE DISTRIBUTION OF HUMAN TRABECULAR BONE – COMPARISON OF INTRUSION MEASUREMENTS WITH IMAGE ANALYSIS**

**T. Doktor<sup>\*</sup>, J. Valach<sup>\*</sup>, D. Kytýř<sup>\*</sup>, O. Jiroušek<sup>\*\*</sup>**

**Abstract:** *This paper deals with pore size distribution assessment in trabecular structure of human proximal femur. Two different approaches for estimation of histograms of pore size distribution are tested, mercury intrusion porosimetry and image analysis. For the image analysis two-dimensional images of cross-sections of the specimens were used and the pore size distribution was estimated using a stereological calculation method based on the geometrical properties of an idealized pore. Comparison of the results of both methods is presented. Suitability of both methods for biological materials is discussed regarding to mechanical properties of these materials, characteristics of pores and range of pore sizes present in the structure.*

**Keywords:** *Pore size distribution, image analysis, trabecular bone, mercury intrusion porosimetry.*

### **1. Introduction**

Description of heterogeneous materials using a representative volume element is a way to simplify the analysis of their mechanical behaviour. Information about the inner structure required for the development of the representative volume element of the trabecular bone can be obtained in the form of histogram of pore size distribution. Measurements of pore size distribution in the trabecular structure of human proximal femur are described in the paper.

### **2. Materials and methods**

#### **2.1. Specimens**

Two sets of specimens were used for the tests, both harvested from human proximal femur (male donor, 72 years old). The first set, three cylindrical specimens (diameter 5mm, height 10mm), was used for MIP measurements (Washburn, 1921). The specimens were dried using a hot air dryer at temperature 40° C for 15 hours. The second set, three slices of dimensions 20x30mm and thickness 2.5mm, was used for pore size distribution assessment using image analysis. The slices were cut using a precise saw Buehler Isomet 1000 (Buehler, Ltd., Düsseldorf, Germany) and the cylinders were prepared using a diamond hollow drill bit (Narex, s.r.o., Česká Lípa, Czech rep.). The specimens were delipidated using an ultrasonic cleaner Polsonic SONIC 3 (Polsonic Palczyński Sp. J., Warsaw, Poland) and a detergent solution Alconox (Alconox, Inc., White Plains, USA).

#### **2.2. Mercury intrusion porosimetry**

MIP measurements were performed using PoreMaster 60 GT device (Quantachrome Instruments, Inc, Boynton Beach, USA). Pressure of mercury up to  $413.6 \cdot 10^6$  Pa was used, mercury surface tension was  $0.48 \text{ N} \cdot \text{m}^{-1}$  and mercury contact angle was 140°.

---

<sup>\*</sup> Bc. Tomáš Doktor, Ing. Jaroslav Valach, Ph.D. and Ing. Daniel Kytýř : Department of Mechanics and Materials, Czech Technical University in Prague, Faculty of Transportation Sciences, Na Florenci 25; 110 00, Prague; CZ, e-mails: {xdoktor, valach, xkytyr}@fd.cvut.cz

<sup>\*\*</sup> Doc. Ing. Ondřej Jiroušek, Ph.D.: Institute of Theoretical and Applied Mechanics, Academy of Sciences of the Czech Republic, Prosecká 76, 190 00; Prague; CZ, e-mail:jirousek@itam.cas.cz

### 2.3. Image analysis

Images of the slices were acquired using a high resolution flatbed scanner EPSON Perfection V350 (Seiko Epson Corporation, Owa, Japan). Resolution 4800dpi was used (1px corresponds to 5μm). The process of identification of cross-section of pores was performed in three main steps: segmentation of the captured image, calculation of the cross-section areas and estimation of the pore size distribution. All these procedures were implemented in the Matlab computational environment (Mathworks, Inc., Natick, USA) based on functions described in Gonzales (2004). First, the images were segmented using thresholding to convert the gray-scale image into a binary form and using a concatenation of morphological operations (dilatation and erosion) to separate cross-sections of the connected pores.

In the second step, sizes of all cross-sections of the pores present in the captured image were calculated using a two-pass algorithm for connected component analysis (Shapiro & Stockman, 2001). In the third step, obtained frequencies of differently sized cross-sections of pores were converted into the histogram of pore sizes using a stereological calculation method described in (Xu & Pitot, 2003). The method is based on the geometric properties of a sphere and on the probability of affiliation of the cross-section to differently sized spheres (depicted in Fig. 1).

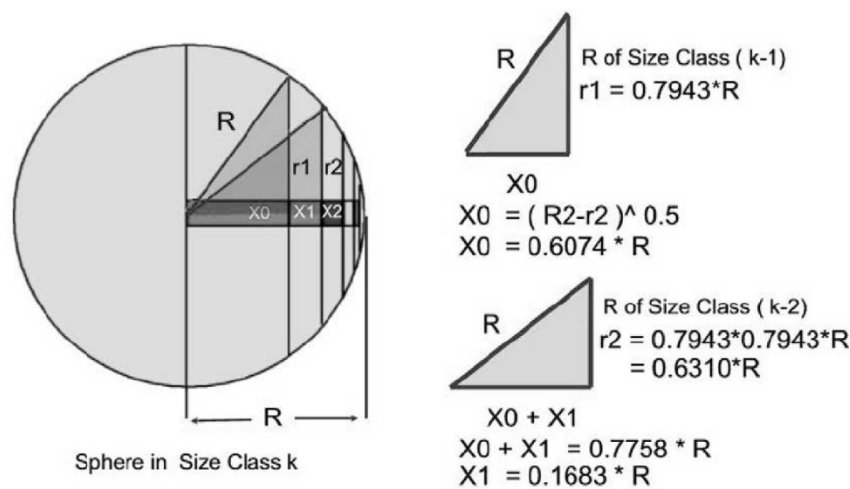


Fig. 1: Principle of the stereologic calculation (Xu & Pitot, 2003).

### 3. Results

Results of MIP measurements are depicted in Fig. 2. For comparison of the results of MIP with the image analysis the histogram obtained by MIP was converted into 25 size classes corresponding with the arrangement of the results of the image analysis (depicted in Fig. 3). Pore size distribution obtained by the image analysis is depicted in Fig. 4. Porosity ratios obtained by both methods are listed in Tab. 1.

Tab. 1: Comparison of volume porosity ratio obtained by MIP and by the image analysis.

<i>Mercury intrusion porosimetry</i>		<i>Image analysis</i>	
<i>Sample No.</i>	<i>Porosity [%]</i>	<i>Sample No.</i>	<i>Porosity [%]</i>
<b>1</b>	<b>69.8</b>	<b>4</b>	<b>62.8</b>
<b>2</b>	<b>68.7</b>	<b>5</b>	<b>59.3</b>
<b>3</b>	<b>45.3</b>	<b>6</b>	<b>61.7</b>



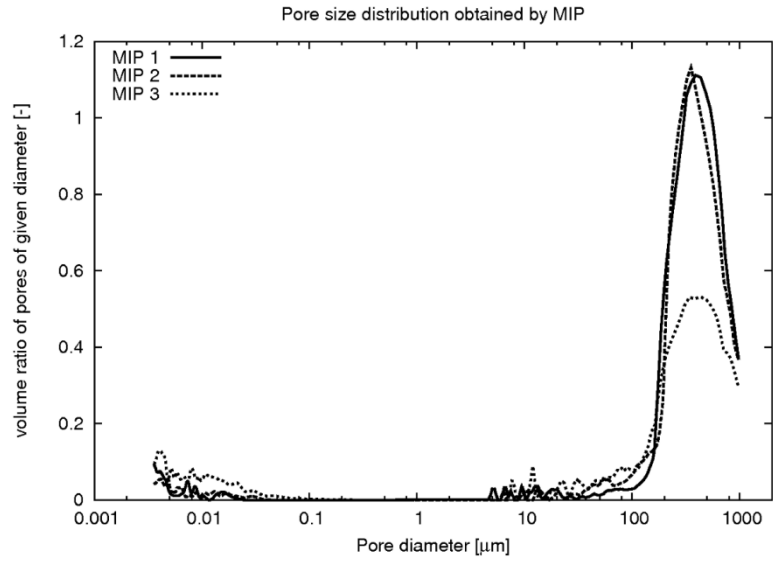


Fig. 2: Results of MIP measurements.

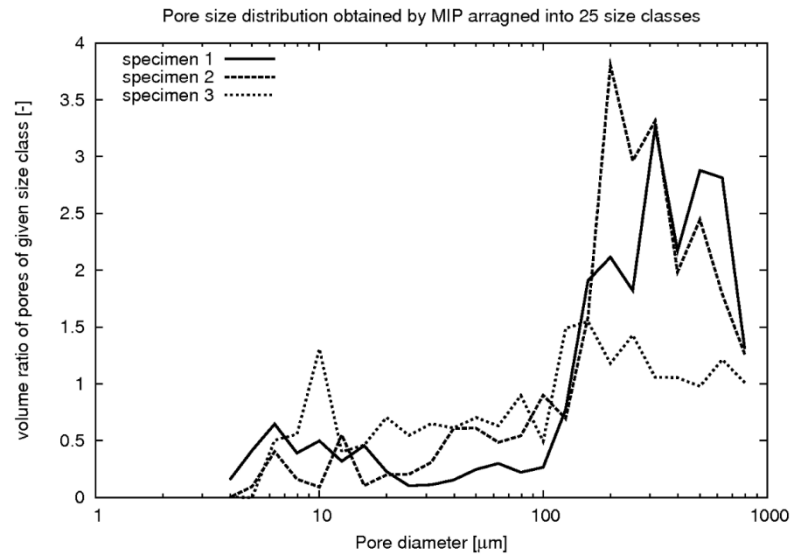


Fig. 3: Results of MIP measurements arranged into 25 size classes for a better comparison with the image analysis.

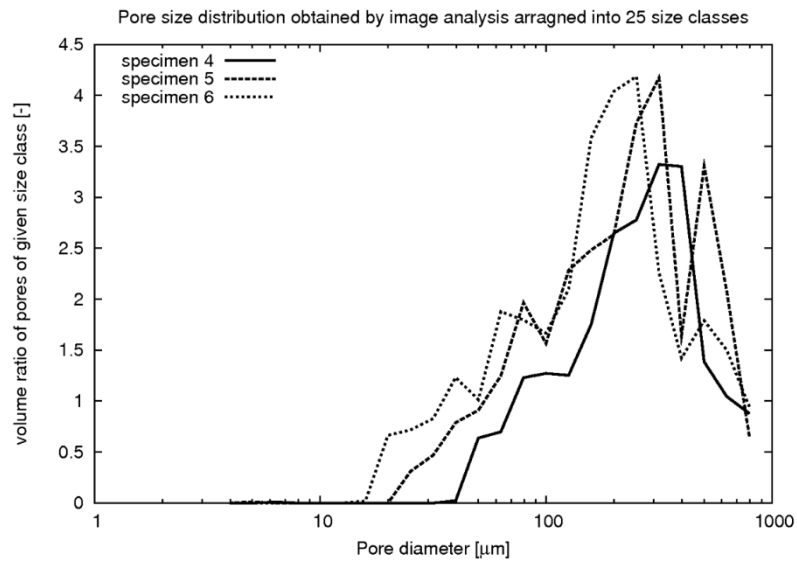


Fig. 4: Results of image analysis.

#### 4. Discussion

By MIP two main types of porosity distinguished by Cowin (2001) were detected. The pore size up to  $0.1\ \mu\text{m}$  is associated with spaces between mineral crystallites and collagen. Voids detected in range from  $5\ \mu\text{m}$  to  $9.50 \cdot 10^3\ \mu\text{m}$  belong to intertrabecular porosity.

Lower porosity ratio and lower frequency of pores of large size in case of the specimen No. 3 was caused by the previous use of this specimen in a loading test. The test had required to equip the specimen with epoxy resin reinforcement on the top and bottom bases. Therefore a part of the voids were filled by the resin and were not able to be filled by mercury.

Differences between porosity ratios obtained by MIP and image analysis are caused by the lower limit of the pore size registered by the image analysis (pores smaller than  $20\ \mu\text{m}$  were omitted).

MIP provides histograms of pore-sizes in range from  $3.50 \cdot 10^{-3}\ \mu\text{m}$  to  $9.50 \cdot 10^3\ \mu\text{m}$ . The range of the pore sizes registered using the image analysis is limited by the resolution and the dimensions of the captured images and by the used stereological calculation method. The method used in this work allows to register pores in 25 size classes with the ratio between the smallest and largest size-class equal to 250 (determined by the scale factor between size classes).

Suitability of MIP for biological tissues is limited due to high mercury pressure applied by the measurement and due to the requirements for the specimens – sample volume up to  $6.6\ \text{cm}^3$  and low humidity. The limited dimensions of the specimens make the measurements impossible for materials with high frequency of large voids. For some biologic materials (e. g. fungi) the intrusion measurements are impossible because of the requirement on the low specimen humidity or due to the high pressure applied during the intrusion measurement (both can cause undesirable changes of the inner structure).

#### 5. Conclusions

In this study pore size distribution in trabecular structure of human proximal femur was estimated using MIP and using image analysis. Both methods show in a good agreement the largest frequency of pore size in range from  $200\ \mu\text{m}$  to  $300\ \mu\text{m}$ . Comparison of suitability of both methods for assessment of pore size distribution in biological materials was discussed. The main advantages of MIP are in a wide range of registered pore sizes and a high resolution. The image analysis provides the possibility of pore size distribution assessment also for materials with a high frequency of large voids (over  $1000\ \mu\text{m}$ ) or with closed voids or materials with unfavorable mechanical properties.

The main limitation of the presented image analysis method is founded in the idealization of the voids by spheres. The used algorithm for connected component analysis provides also information about shape of pore cross-sections and therefore the analysis can be extended by estimation of predominant orientation of pores to allow estimation of anisotropic properties of the bone structure.

#### Acknowledgement

The research has been supported by Grant Agency of the Czech Technical University in Prague (grant No. SGS10/218/OHK2/2T/16), by the Grant Agency of the Czech Republic (grant No. P105/10/2305), research plan of the Academy of Sciences of the Czech Republic AV0Z20710524 and by research plan of the Ministry of Education, Youth and Sports MSM6840770043.

#### References

- Cowin, S. C. (2001) Bone mechanics handbook, CRC Press, Florida, pp. 23(6-7).
- Gonzales, R. C. (2004) Digital image processing using MATLAB, Upper Saddle River, Pearson.
- Shapiro, L. & Stockman, G. (2001) Computer Vision, Prentice Hall.
- Washburn, E. W. (1921) Note on a Method for Determining the Distribution of Pore Sizes in a Porous Material, Proceedings of National Academy of Sciences.
- Xu, Y. H. & Pitot, H. C. (2003) An improved stereologic method for three-dimensional estimation of particle size distribution from observations in two dimensions and its application. Computer Methods and Programs in Biomedicine.

## ASSESSMENT OF THE INFLUENCE OF THE ELECTROMECHANICAL INTERACTION ON ROTORDYNAMIC INSTABILITY IN ELECTRIC MACHINES

**M. Donát\***

**Abstract:** *The electromechanical interaction in rotating electric machines induces additional forces between the rotor and the stator. A simple electromechanical computational model, which was developed by Holopainen et al., was used for study of this problem. Dependence of the eigenfrequencies of the rotor on shaft stiffness and load level of the motor is results of this work.*

**Keywords:** *Electric, machines, rotor, magnetic pull.*

### 1. Introduction

Rotating electrical machines are composed from two main parts, the stator and the rotor. The magnetic fields in the air gap between the stator and the rotor induce electromagnetic forces, which acting on the machine structure. If the stiffness of the air gap is constant along whole circumference, that means the rotor and the stator have an ideal cylindrical shape and they are ideally concentric, the magnitude of the electromagnetic forces is zero. If the stiffness of the air gap is not constant, the magnitude of the electromagnetic forces is nonzero and is called as unbalanced magnetic pull (UMP). UMP induces two eccentricity harmonics of the magnetic fields in the air gap, which affect dynamic behavior of the rotor.

### 2. Methods

Holopainen et al. (2002) created a simple eletromechanical computational model for assessment of the influence of the electromechanical interaction on rotordynamic behavior of the rotating electrical machines. Initial assumptions of this computational model are:

- the rotor and the stator have an ideal cylindrical shape,
- axis of rotation of the rotor makes whirling motion around axis of the stator,
- a whirling radius is constant,
- a damping of the surrounding medium is viscous type.

This model is a combination of the de Laval rotor, which describes mechanical behavior of the rotor and the simple parametric model of the electromagnetic forces, which operates between the stator and the rotor, presented by Arkio et al. (2000) This model can by written as follow

$$\begin{bmatrix} 1 & 0 & 0 & 0 \\ 0 & 1 & 0 & 0 \\ 0 & 0 & 1 & 0 \\ 0 & 0 & 0 & 1 \end{bmatrix} \cdot \begin{bmatrix} z \\ \dot{z} \\ q_{p-1} \\ q_{p+1} \end{bmatrix} + \begin{bmatrix} 0 & -1 & 0 & 0 \\ k_e/m & b/m & -1/m & -1/m \\ -k_{p-1} & 0 & -a_{p-1} & 0 \\ -k_{p+1} & 0 & 0 & -a_{p+1} \end{bmatrix} \cdot \begin{bmatrix} z \\ \dot{z} \\ q_{p-1} \\ q_{p+1} \end{bmatrix} = \begin{bmatrix} 0 \\ f(t)/m \\ 0 \\ 0 \end{bmatrix} \quad (1)$$

Where  $m$  is the mass of the rotor,  $b$  is the mechanical damping coefficient,  $f$  is the excitation force,  $k_e$  is the effective stiffness of the rotor, which is calculated as  $k_e = k - k_0$ ,  $k$  is the shaft stiffness

---

\* Ing. Martin Donát: Institute of Solid Mechanics, Mechatronics and Biomechanics, University of Technology, Technická 2896/2; 616 69, Brno; CZ, e-mail: Donat.Martin@email.cz

coefficient,  $k_0$ ,  $k_{p\pm 1}$ ,  $a_{p\pm 1}$  are the parameters of the resulting electromagnetic force, the unknown  $z$  is a complex number, that describes the position of the centre of gravity of the rotor,  $z(t) = x(t) + iy(t)$ ,  $x$  and  $y$  are the Cartesian coordinates of the position of the centre of gravity of the rotor and the unknown  $q_{p\pm 1}$  are variables related to the eccentricity harmonics of the magnetic fields, that are called as quasi-displacements.

Notice:

$k_0$ ,  $k_{p\pm 1}$  are real parameters proportional to the square of the fundamental flux density in the air gap.

$a_{p\pm 1}$  are complex parameters,  $a_{p\pm 1, \text{Im}}$  refer to whirling frequencies at which the splits of the two eccentricity harmonics become zero,  $a_{p\pm 1, \text{Re}}$  depend on the dimensions of the machines.

The subscripts of the parameters  $p + 1$  and  $p - 1$  refer to the respective eccentricity harmonics of the electromagnetic fields.  $p$  denotes number of pole pairs of the machine.

Value of the parameters  $k_0$ ,  $k_{p\pm 1}$ ,  $a_{p\pm 1}$  are determined by the finite element method. In this approach the effects of core saturation in the model were included.

Equation (1) can be easily written as

$$\begin{aligned} \overline{\mathbf{M}}\dot{\mathbf{x}} + \overline{\mathbf{K}}\mathbf{x} &= \overline{\mathbf{f}} \\ \mathbf{E}\dot{\mathbf{x}} + \overline{\mathbf{K}}\mathbf{x} &= \overline{\mathbf{f}} \end{aligned} \quad (2)$$

Where  $\overline{\mathbf{M}} = \mathbf{E}$  is the augmented matrix of the mass,  $\overline{\mathbf{K}}$  is the augmented matrix of the stiffness,  $\overline{\mathbf{f}}$  is the augmented vector of the excitation and  $\mathbf{x}$  is the augmented vector of the unknowns.

The homogenous part of the solution of the equation (2) comprises the eigenvalue problem.

$$(\mathbf{K} + \lambda \mathbf{E})\mathbf{u} = \mathbf{0} \quad (3)$$

### 3. Results

#### 3.1. Assessment of the influence of the shaft stiffness and load level on the eigenfrequencies of the rotor

The assessment was performed for three load level of the four-pole cage induction motor about performance 15 kW. Essential mechanical properties are: mass of the rotor  $m = 30 \text{ kg}$ , mechanical damping coefficient  $b = 2 \cdot 10^3 \frac{\text{kg}}{\text{s}}$  and shaft stiffness coefficient  $k \in \langle 0,5 \div 23 \rangle \cdot 10^6 \frac{\text{N}}{\text{m}}$ . Parameters of the electromagnetic forces are listed in Tab. 1.

Tab. 1: Parameters of the electromechanical forces.

Parameter	$k_0$ [MN/m]	$k_{p-1}$ [MNrad/ms]	$k_{p+1}$ [MNrad/ms]	$a_{p-1}$ [rad/s]	$a_{p+1}$ [rad/s]
No load motor	4.37	8.37	94.7	$(-0.59 + 25i) \cdot 2\pi$	$(-1.7 + 25i) \cdot 2\pi$
50% load	4.89	9.1	102.5	$(-0.42 + 25.4i) \cdot 2\pi$	$(-2.09 + 23.8i) \cdot 2\pi$
100% load	6.22	15.7	74.9	$(-0.50 + 25.8i) \cdot 2\pi$	$(-1.68 + 22.6i) \cdot 2\pi$

The imaginary parts of the eigenvalues of the matrix  $\overline{\mathbf{K}}$  correspond with eigenfrequencies of the rotor. The two higher eigenfrequencies are associated with the forward (FW) and the backward (BW) whirling modes of the rotor. The two lowest eigenfrequencies are associated with the eccentricity harmonics of the electromagnetic fields ( $p + 1$  and  $p - 1$ ). The Fig. 1 shows eigenfrequencies as the function of the load of the motor and shaft stiffness. These dependencies show, as the shaft stiffness is

decreased, the whirling modes and electromagnetic modes interact strongly with each other's. The influence of the electromagnetic modes is stronger at full load, therefore further is analyzed this case.

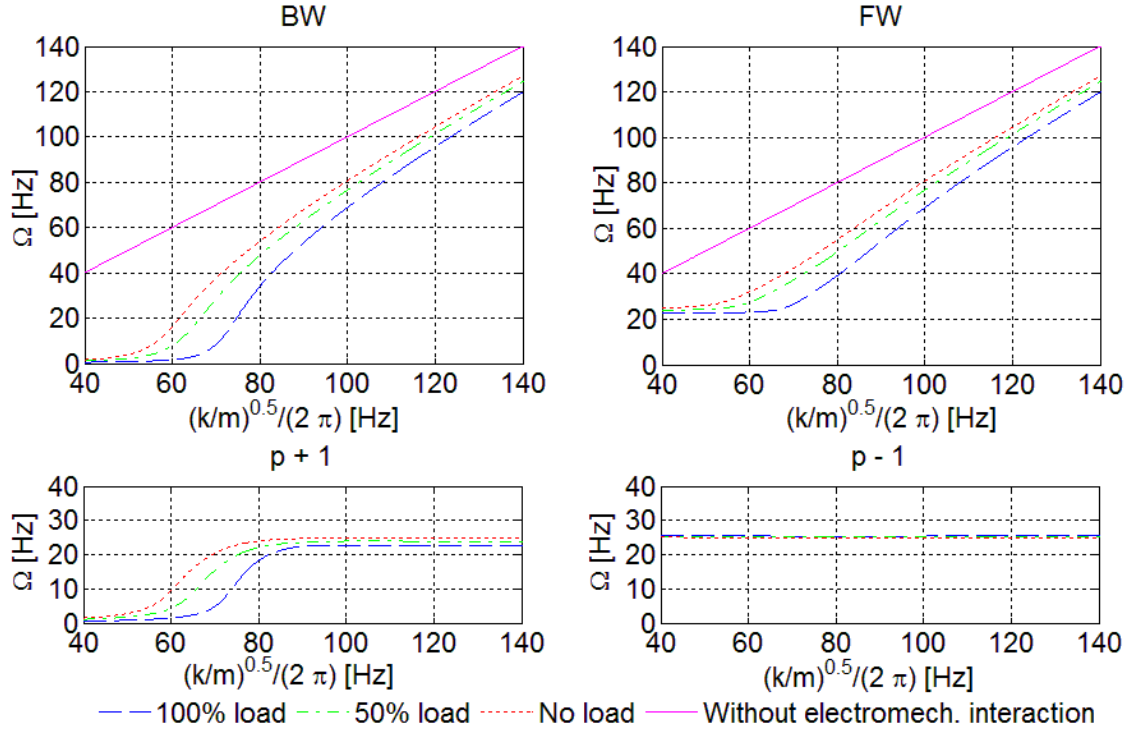


Fig. 1: Eigenfrequencies as function of the shaft stiffness and load level of the motor.

The real parts of the eigenvalues of the matrix  $\bar{\mathbf{K}}$  correspond with decay constants. The Fig. 2 shows the decay constants as the function of the shaft stiffness of the full load motor. These dependencies show, that the UMP causes inside of the motor additional damping. Under the certain conditions can be decay constant of the  $p+1$  mode positive and thus the motion of the rotor can be instable. Therefore in the next is assessed the influence of the parameters of the electromagnetic force on the rotor dynamics stability.

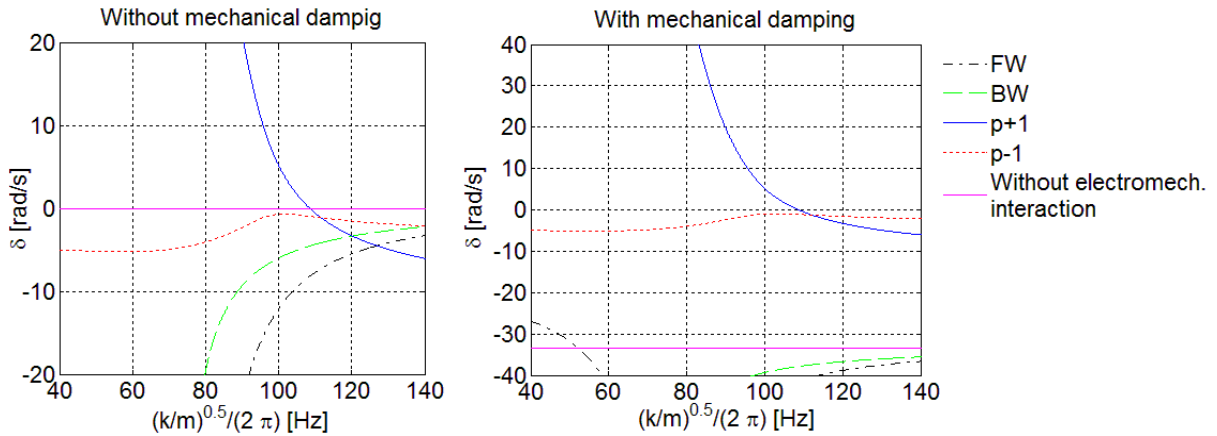


Fig. 2: Decay constants as function of the shaft stiffness.

### 3.2. Rotor dynamic stability

Figs. 3 - 6 show stability charts. This figures show following: if the value of the effective stiffness increases the stability of the system increases too. In addition an increase of parameters  $k_{p\pm 1}$  and a decrease of parameters  $a_{p\pm 1, \text{Re}}$  may destabilize the system.

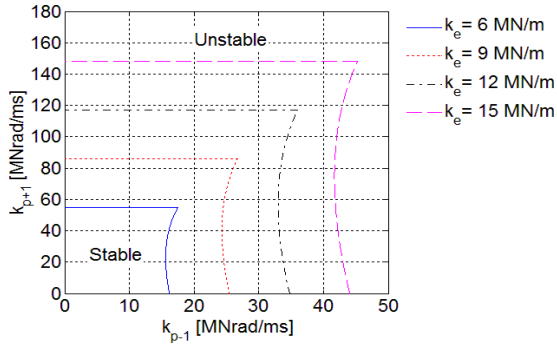


Fig. 3: Stability chart 1.

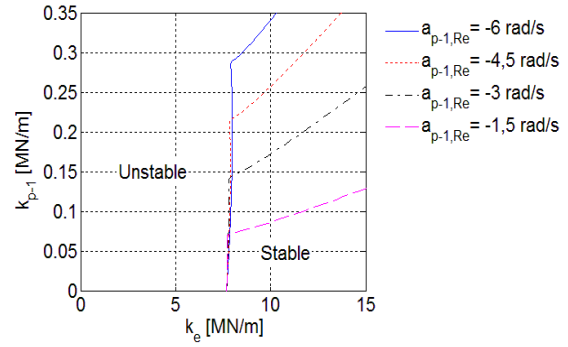


Fig. 5: Stability chart 3.

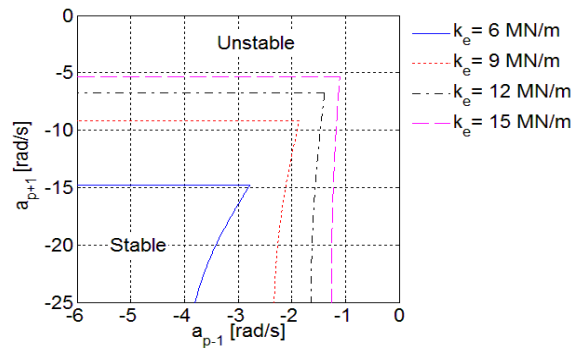


Fig. 4: Stability chart 2.

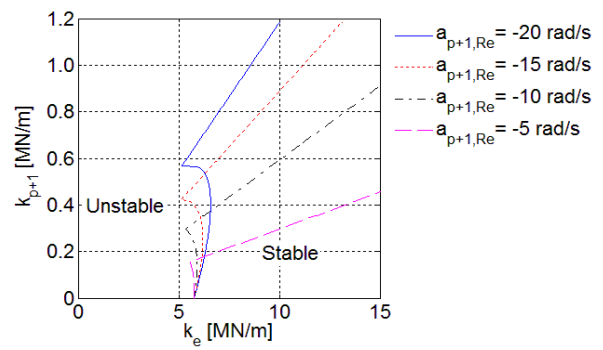


Fig. 6: Stability chart 4.

#### 4. Conclusion

The results showed that electromagnetic interaction in rotating electrical machines leads to decreasing of the critical speed of rotor and to increasing of damping of the rotor.

The goal of this work was verification of the mathematical model described by Holopainen et al. first and next step will be modification of the model for calculation with the non-linear unbalanced magnetic pull and inclusion of the non-linear bearings. This non-linear model should be presented in the conference.

#### Acknowledgement

This paper was written with support by the EU, project no.: CZ.1.07/2.4.00/12.0030.

#### References

- Holopainen, TP., Tenhunen, A. & Arkkio A. (2002) Electromagnetic circulatory forces and rotordynamic instability in electric machines, in: Proc. 6th Int. Conf. On Rotor Dynamics, University of New South Wales, Sydney, pp. 446-463.
- Arkkio, A., Antila, M., Pokki, K., Simon, A. & Lantto, E. (2000) Electromagnetic force on a whirling cage motor. IEE Proc. Electric Power Applications, 147, 5, pp.353-360.
- Belmans, R., Vandenput, A. & Geysen, W. (1987) Calculation of the flux density and the unbalanced pull in two pole induction machines. Arch. für Elektrotechnik, 70, 3, 151-161.
- Gash, R. & Pfützner, H. (1980) Rotor dynamics, SNTL, Prague.

## POSSIBILITIES OF USING OF MECHANICAL ANALYZER FOR DECOMPOSITION OF NON-STATIONARY SIGNALS

D. Dušek \*

**Abstract:** *This paper deal with possibilities of using of an array of resonators for decomposition of any non-stationary signals. A basic mathematical model composed from resonators with mutually connection and basic principle of signal decomposition is described first. Then a basic shape of simple resonant beams which can be produced by MEMS technology is described. Finally possible areas of using of the MEMS array of resonators are presented.*

**Keywords:** *MEMS, signal, decomposition, cochlea.*

### 1. Introduction

The idea of using of a mechanical analyzer for decomposition of non-stationary signals is inspired by function of the mammalian inner ear, concretely by function of cochlea. The cochlea is perhaps the most important part of the human ear because a transmission of mechanical signals into electrical signals is done there. Very interesting behavior of the cochlea is not only the transmission of the signals from electric into mechanical but simultaneously decomposition of the whatever non-stationary signal into simple frequency components. These decomposed electrical signals are consequently transferred by hearing nerves into the brain.

The cochlea is compound basically from three fluid spaces (scala vestibuli, scala tympani and scala media). These three fluid spaces are divided by two membranes (Reissner's membrane and basilar membrane where a hear sense cells are located) whereas the scala vestibule and scala tympani are connected by small hole which is called helicotrema. The fluid spaces together with membranes are coiled into spiral shape which looks similar like snail shell.

Decomposition of the non-stationary signals into simple frequency components is fully mechanical process. Acoustic pressure incoming from outer ear space excites ossicular chain (it is middle ear bones- malleus, incus and stapes) and through stapes is transmitted into fluid space of scala vestibuli. Consequently the pressure waves in the scala vestibule excite bending traveling waves on the basilar membrane. It is important that maximum amplitude of the traveling waves on the basilar membrane is frequency dependent. High frequencies excite the basilar membrane on its basal end and low frequencies excite the basilar membrane on its apical end. The basilar membrane has this property thanks to its special shape because the basilar membrane has different width and thickness along its length. Maximum thickness of the basilar membrane is on its basal end and minimum on its apical end whereas maximum width of the basilar membrane is on its apical end and minimum width on its basal end.

The basic cochlear mechanics was described already by Békésy (1960) He like first on the world observed the traveling waves running on the basilar membrane and for his work on mechanics of hearing was honored by the Nobel Prize in the year 1961. Today we known that big difference between mechanics of cadaver and live cochlea exist (the cadaver basilar membrane has linear mechanical properties while the live cochlea is high non-linear system with active mechanism) but the basic principle of the signal decomposition based on the mechanical resonance of the basilar membrane is valid and today generally accepted.

---

\* Ing. Daniel Dušek, Ph.D.: Institute of Solid Mechanics, Mechatronics and Biomechanics, Brno University of Technology, Technická 2896/2; 616 69, Brno; CZ, e-mail: dusek@fme.vutbr.cz



Today technologies of miniaturization like Micro Electro Mechanical System (MEMS) (Gag-El-Hak 2006) which could be able to produce the artificial cochlea in very small dimensions are on the increase. This technology utilizes similar procedure for production of mechanical parts like procedures used in production of electronics microchips. Today a few scientists on the world try to design the MEMS artificial cochlea in the form of membrane similar to real cochlea (Chen et al, 2006, Shintaku et al. 2010, White et al. 2002, Tianying 2002). Another possibility is using of an array of resonators (Xu et al. 2004, Bachman et al. 2006).

## 2. Mathematical model

A basic scheme of the principle of the signal decomposition by the array of resonators is shown in the Fig. 1. In this case an input signal is compound from two frequency components. If the array of resonators is actuated by this signal so only those two resonators will start to resonate which eigenfrequencies are equal to the two frequency components in the input signal.

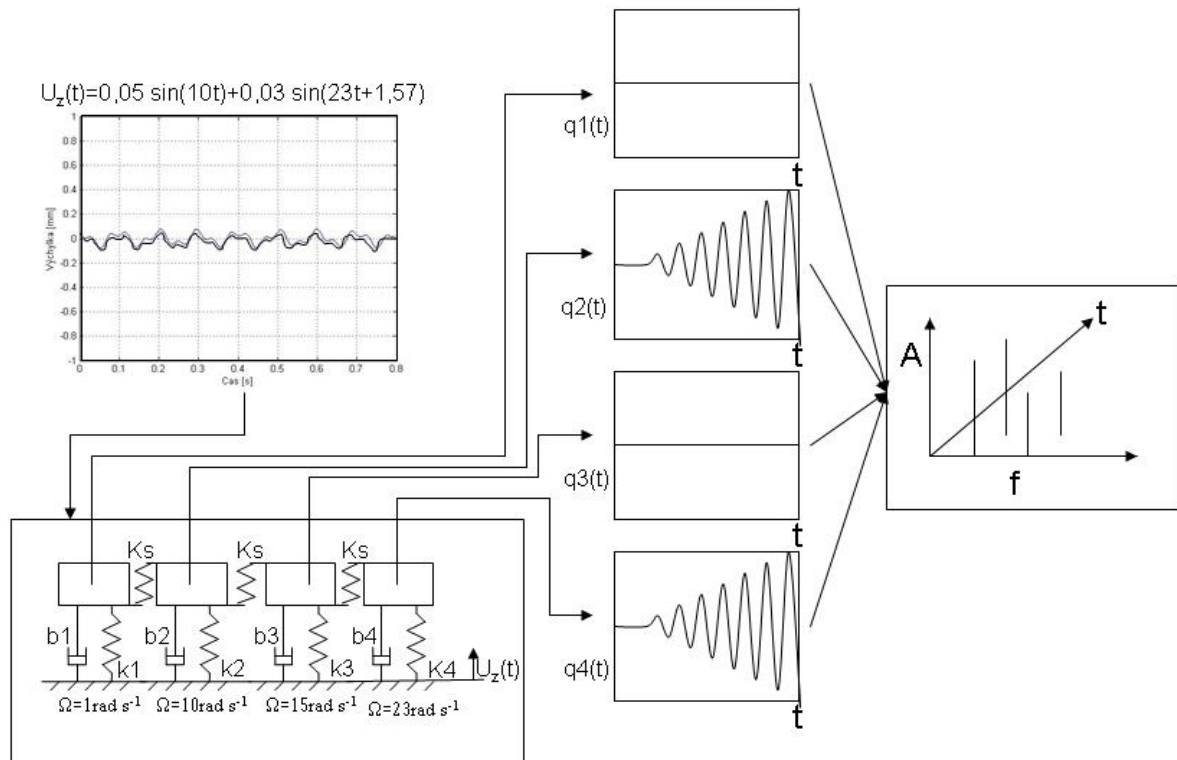


Fig. 1: Diagram of a basic principle of signal decomposition by a simple mathematical model composed from an array of mechanical resonators.

The mathematical model described in the Fig. 1 can be expressed by following matrix form of differential equations of motion:

$$\mathbf{M} \ddot{\mathbf{q}} + \mathbf{B} \dot{\mathbf{q}} + \mathbf{K} \mathbf{q} = \mathbf{q}_z' \mathbf{B} + \mathbf{q}_z \mathbf{K} + \mathbf{K}_{s1} \mathbf{q} + \mathbf{K}_{s2} \mathbf{q} \quad (1)$$

In equation 1  $\mathbf{q}_z$  is a vector of displacement of kinematical actuation,  $\mathbf{q}_z'$  is a vector of velocity of the kinematical actuation,  $\mathbf{q}$  is a vectors of displacement,  $\dot{\mathbf{q}}$  is a vector of velocity and  $\ddot{\mathbf{q}}$  is a vector of acceleration of the resonators.  $\mathbf{M}$  is a matrix of mass of resonators,  $\mathbf{B}$  is a matrix of viscous damping of resonators,  $\mathbf{K}$  is a matrix of stiffness of resonators and  $\mathbf{K}_{s1}$  and  $\mathbf{K}_{s2}$  are matrixes of stiffness of connection springs between neighbour resonators.

Calculations for different value of viscous damping of the resonators and different values of the stiffness of connection springs were done. It means the matrix  $\mathbf{M}$  and  $\mathbf{K}$  which define eigenfrequencies of the resonators were constant for all calculations but matrixes  $\mathbf{B}$  and  $\mathbf{K}_{s1}$  and  $\mathbf{K}_{s2}$  were different for the calculations. The results of these calculations are in more detail described in the author's paper *Mathematical Model of an Artificial Cochlea Based on an Array of Resonators* (Dušek, 2009).

Results gained from this simple mathematical model showed that for correct signal decomposition is very important mainly value of viscous damping of the resonators and also value of stiffness of connection springs between neighbor resonators. The results showed that it is need to use quite high value of viscous damping of the resonators for correct non-stationary signal decomposition. Low value of the viscous damping leads to long transient effects which evoke smudging of gained spectrograms in frequency domain. The results also showed that for correct signal decomposition using of very low or zero stiffness of connection springs is need. The higher value of stiffness of connection springs leads to vibration of neighbor resonators and this effect leads to creation of false frequency components in the spectrogram (Dušek, 2009).

On the grounds of the results gained from simple mathematical model a shape of resonators was chosen. For a reason of easy production by any of MEMS technologies a two layer beam was chosen without any mutually connection between neighbor beams (It corresponds to array of resonators with zero stiffness of connection springs calculated by simple mathematical model.). The value of the viscous damping of the resonant beams depends mainly on fluid medium where the beams will located. As the fluid medium is supposed to use a silicone oil. The silicone oil is produced in very wide range of kinematic viscosity (from 0.65 cSt. to 20 000 000cSt. - Clearco Products, 2011) and the silicone oil is also used by other scientist in his artificial cochlea (Shintaku et al., 2010, White et al., 2002).

The two layer beam is schematically shown in the Fig. 2. The layer T1 represents a spring of the resonator and layer T2 represents a mass o the resonator. It is supposed to use an array composed from these resonant beams which all have same thickness of layer T1 and T2. The different eigenfrequencies of the resonators should be effected through different length of the resonant beams.



*Fig. 2: Shape of resonant beams.*

### **3. Possible applications**

#### **3.1. Artificial full implantable cochlea**

The most useful application of the MEMS array of resonators should be the artificial full implantable cochlea which could replace injured and functionless human cochlea. Today used cochlear implant is fully electronic device which is composed from two parts- internal (this part is permanently implanted in human head) with electrodes and external (this part is placed out of the human head) with microphone and speech processor. Both parts communicated thru skin by an electromagnetic induction coil (Rubinstein 2004, Wikipedia 2011). Although development of the cochlear implants is very significant there are not full implantable cochlear implants today. The full electronic cochlear implants are still too high consumption of energy and they have quite large dimensions. It is supposed that the MEMS artificial cochlea should be much more effective with the energy source and together with any energy harvesting systems (energy gained from warm of human body or from heart or human moving vibration) it should be full implantable. For example artificial MEMS cochlea developed by Shintaku et al., 2010 do not need any external sources because they use a piezoelectric effect for generating of the electric pulses.

### 3.2. Technical vibro diagnostics

Another possibility of using of the array of resonators is area of the technical vibro-diagnostics. The technical vibro-diagnostics is based in absolute majority cases in analyzing of the FFT spectrums. Classical measurement chain is composed from mechanical sensor, amplifier, anti-aliasing filter and any powerful processor for calculation of the FFT. The advantage of the MEMS array of resonator is reduction of the measurement chain only into the mechanical sensor, because filtering of the signal would be made mechanically. Another advantage is also decomposition of the signal by the array of resonators in real time and this can be used for on-line monitoring and controlling of the machines (there is not a problem to integrated the mechanical parts together with electrical controlling part on one chip).

### 4. Conclusions

This paper deals with possibilities of using of the MEMS array of mechanical resonator for decomposition of the non-stationary signals. Basic mathematical model of the array of resonator shown that it is need to use quite high value of viscous damping of the resonators and to use preferably separated resonators without mutually connection. With a view to easy production by any of MEMS technology a two layer beam was chosen like optimal shape of the resonators. Areas of using of the MEMS mechanical analyzer should be mainly full implantable cochlear implants and sensors used in vibro diagnostics.

### Acknowledgement

The paper was written with the support by the Grant Agency of AS CR - Project No.: KJB201730802 and by the EU project No.: CZ.1.07/2.2.00/07.0406.

### References

- Bachman M., Zeng F.G., Xu T. & Li G.P. (2006) Micromechanical resonator array for an implantable bionic ear, *Audiol Neurotol*, 11, 2, pp. 95-103.
- Békésy G. von, (1960) *Experiments in hearing*, McGraw-Hill, New York.
- Dušek, D. (2009) A Mathematical Model of an Artificial Cochlea Based on an Array of Resonators. DAAAM International Scientific Book, Vienna, Austria: DAAAM International, pp. 273-280.
- Dušek D. (2010) Design of a MEMS artificial cochlea like an array of resonators. In *Annals of DAAAM for 2010 and Proceedings of the 21th International DAAAM Symposium*. DAAAM International Vienna,
- Gag-El-Hak M. (2006) *The MEMS handbook*, CRC Press, Boca Raton.
- Rubinstein, J. T., (2004) How cochlear implants encode speech, *Current Opinion in Otolaryngology & Head and Neck Surgery* 2004, Volume 12.
- Shintaku H., Nakagawa T., Kitagawa D., Tanujaya H., Kawano S. & Ito J. (2010) Development of piezoelectric acoustic sensor with frequency selectivity for artificial cochlea, *Sensors and Actuators A: Physical*, Vol. 158, Issue 2, March 2010, pp. 183-192.
- Tianying R. (2002) Longitudinal pattern of basilar membrane vibration in the sensitive cochlea, *Proceeding of the National Academy of Science of the United States of America*, 99, No. 26.
- White R.D. & Grosh K. (2002) Design and characterization of MEMS piezoresistive cochlear-like acoustic sensor, *Proceedings of international mechanical engineering congress and exposition*, New Orleans, USA.
- Wikipedia, The Free Encyclopedia (accessed: 7.2.2011) [http://en.wikipedia.org/wiki/Cochlear\\_implant](http://en.wikipedia.org/wiki/Cochlear_implant).
- Clearco Products (accessed: 10.3.2011) <http://www.clearcoproducts.com/>.

## **REPLACEMENT OF THE MECHANICAL PLANISHING SYSTEM OF THE FORGING PRESS IHI 800 JAPAN**

**J. Dvořák\***

**Abstract:** *Replacement of the mechanical planishing system of the forging press IHI 800 Japan. Realization of new progressive hydraulic solution. The survey of conventional and advanced drives and control systems.*

**Keywords:** *Planishing, forging press, hydraulics.*

### **1. Introduction**

More than two years ago, our company Žďas a.s., which is the leading manufacturer of forging presses with more than fifty-year experience, has been asked by a Japanese customer to prepare a technical offer for the reconstruction of an 800 t capacity pull-down forging press of Japanese make. The customer expected meeting the following requirements due to reconstruction:

- removal of the press mechanical drive
- increase in the number of planishing strokes
- forming speed increase

During a visit to a customer's place it was found that the year of production of the press is 1988. In the year 1992, a Japanese company carried out a reconstruction of the hydraulic drive. Unfortunately they had at their disposal a minimum of supporting drawings. When the company obtained finally the necessary drawings, there were not included last modifications made during the reconstruction. During the inspection visit, the measurements needed to connect new manifolds were carried out on the existing subassemblies.

### **2. Existing equipment description**

The main motion of the press was carried out using two principles:

- For forging, when high working strokes (over 40 mm) are required, the hydraulic drive has been applied
- For forging, especially for finishing operations – strokes under 40 mm, the mechanical drive has been applied

#### **2.1. Original hydraulic drive description**

The installed hydraulic drive was composed of four pump units consisting of hydraulic high-pressure piston axial-flow pumps (Japanese make), which were connected via the flexible coupling to the electric motor. The deliveries of hydraulic pumps were connected to a common unloading manifold. A part of the drive was the tank with a capacity of 10 m<sup>3</sup> of working fluid. Mounted on the tank was the pre-filling hydraulic pump. A part of the tank was also the filtering and cooling circuit. Close to the press there were control manifolds for the press cylinder (Fig. 1), return and hold cylinders. The pressure pre-filling tank also belonged to the hydraulic station.

---

\* Jiří Dvořák, Bc.: Žďas a.s., Strojírenská 6; P.O.BOX 145; 59171 Žďár nad Sázavou; phone: +420.566642333, fax: +420.566642817, e-mail: jiri.dvorak@zdas.cz

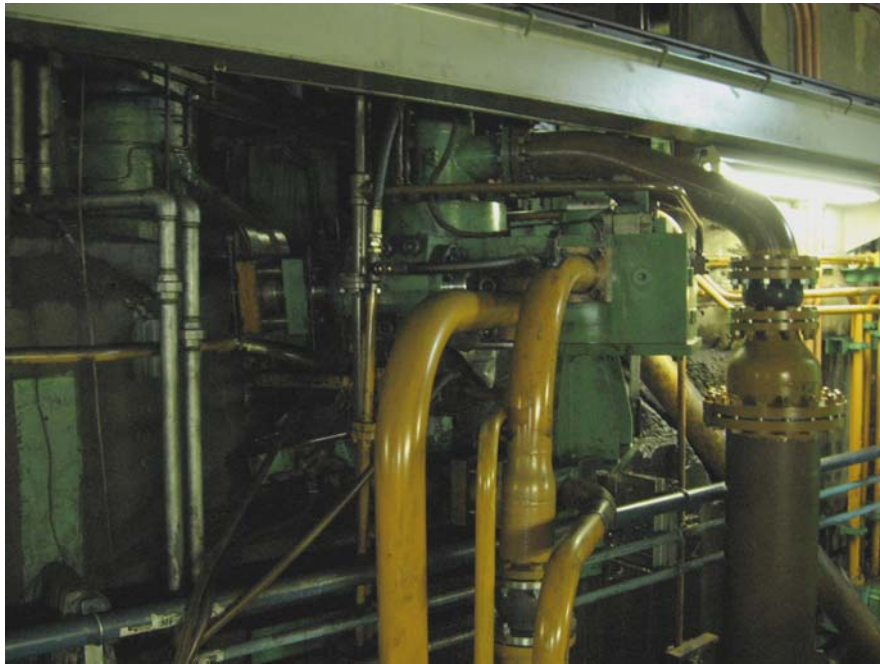


*Fig. 1: Existing hydraulic manifold for press cylinder control.*

## **2.2. Original mechanical drive description**

The existing mechanical drive of the forging press (Fig. 3) was composed of the electric motor (1) of 800 kW output, the gearbox (2) and the eccentric shaft (3) to which the press cylinder (5) was pulled by means of hold cylinders (4). The electric motor revolutions were reduced by means of the gearbox (2) so that the press could reach 80 strokes at a constant path of 40 mm. The disadvantage of this solution was the impossibility to change the height of stroke during forging by means of mechanical drive and high energy demands.

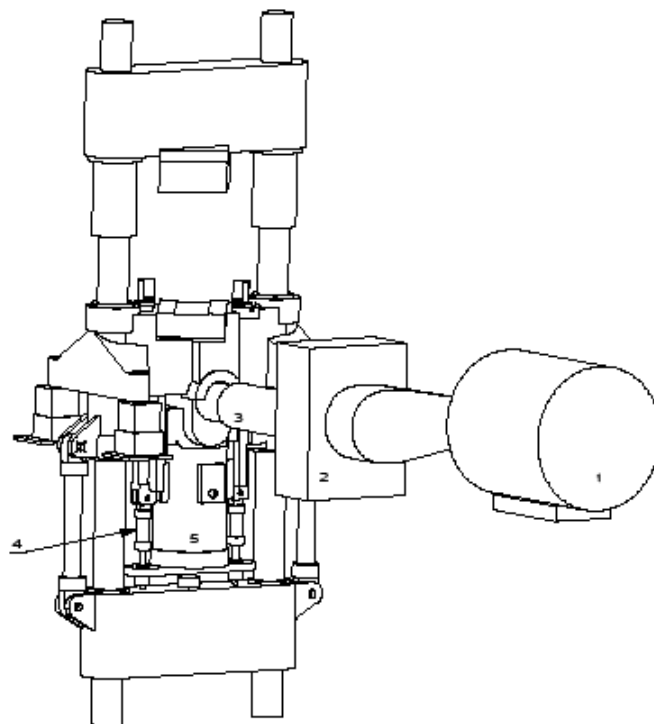


*Fig. 2: Eccentric-shaft press drawing.*



*Fig. 3: Existing mechanical drive of the forging press.*

### **3. Advanced solution proposed**

The proposed advanced control of the drive is based on the idea of not changing the direction of fluid flow between the source – main pump unit and the press ram using the existing constant-displacement pumps. For this solution, the permanent connection of the return cylinders to the pressure source, i.e. to the accumulator station, has been applied, because it is an easy control of the press. The operation of the press is controlled only by one valve, i.e. by the forge valve installed close by the press ram. Under this control mode, the forging press can reach 120 strokes at a 10 mm height of stroke.

#### **3.1. Press control principle using the forge valve (Fig. 4)**

The working fluid is supplied by the main pump units (1) to the press cylinder (5) which is connected via the forge valve (7) with the pre-filling tank (12). When the forge valve is fully closed, the press is capable of forging at a maximum forming force, which is directly proportional to the main-pump delivery. At the moment of reversing command, the forge valve starts continuous opening due to a smooth course of decompression, thus finishing the downward motion of the press. The next opening of the forge valve results in flowing-off of working fluid into the pre-filling tank and then via the safety valve to the main tank. Due to the action of return cylinders (6), the press moves to the top dead centre. Before reaching the top dead centre of the press, the valve will close again and the whole cycle is repeated.

Return cylinders are permanently connected to the accumulators (7), which are refilled by means of the hydraulic unit (9) via the non-return valve (10). The return cylinder circuit is provided with a safety valve (8).

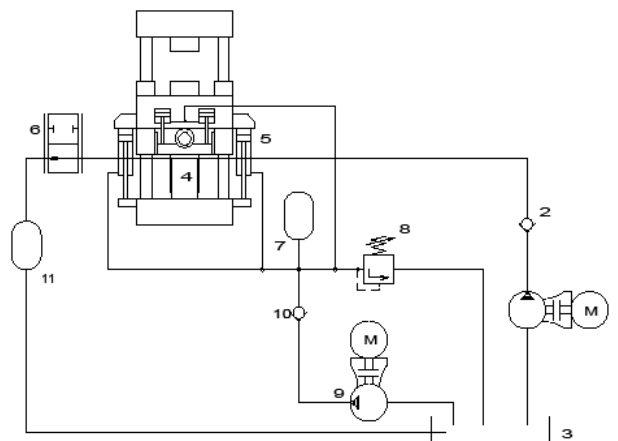


*Fig. 4: Press control principle using forge valve.*



To increase the forming speed, it was necessary to install a new constant-delivery pump unit Kawasaki LXV260 with pump-unloading manifold (Fig. 5). Because of new pump installation it was needful to solve the filling hydraulic pump. After performing the calculations, the existing filling hydraulic pump was proved to be unsatisfactory because of a small delivery of working fluid for the main hydraulic pumps. So a new filling hydraulic pump was necessary to be designed.



*Fig. 5: New control manifold of new pump unit.*

For the proposed solution, a problem had occurred concerning the location of control components for return cylinders – accumulator station and control manifold. This problem has been solved using design software Unigraphics NX3. By means of this system, the 3D design with the placement of individual components and their interconnection was created completely. This design was successfully presented to the customer and executed during the period of 10-12/2010 by the customer's approval. In the commissioning, a high speed of the press, i.e. 125 strokes per 10 mm path, has been achieved.

At present, the forging press under reconstruction has been in a test operation.

#### **4. Conclusions**

In the case of replacement of the mechanical planishing operation by the hydraulic one by means of advanced solution, a significant high speed of the press has been attained; this was one of the most important requirements of the client.

In the case of adjustment of the hydraulic drive, the value of 125 strokes per 10 mm path has been achieved compared to 80 strokes per 40 mm path in the original mechanical drive.

Another main feature of the hydraulic system is the option of operator to select the height of press stroke by means of automated system during finishing operations; this was not possible before.

The hydraulic solution of the quick-forging system is a full substitution for the same mechanical solutions. The hydraulic solution offers more advantages and higher flexibility.

#### **References**

Catalogue of the forging presses – ŽĎAS a.s. (2007).



## MODELING OF FATIGUE CRACK GROWTH IN CERAMICS UNDER COMPRESSIVE CYCLING

J. Eliáš<sup>\*</sup>, J.-L. Le<sup>\*\*</sup>

**Abstract:** *This contribution presents a simple numerical model for crack growth under mode-I compressive fatigue loading. Residual tensile stress at the crack tip, which is responsible for crack advance, is simulated by the plastic-like behavior in compression. Tensile part of the constitutive law accommodates a phenomenological hysteresis behavior. This constitutive law is implemented into an implicit discrete 2D numerical model. The model is used to simulate the compression-compression fatigue fracturing of ceramics, particularly polycrystalline alumina. It is shown that the model is capable of capturing trends observed in experimentally obtained crack growth behavior.*

**Keywords:** *Compression-compression fatigue, discrete model, hysteresis, crack arrest.*

### 1. Introduction

Fatigue crack propagation, which determines the durability of structural elements, is of importance in most civil and mechanical engineering applications. The fatigue crack can propagate under periodic loads that are much lower than monotonic strengths. A simple and useful predictive tool was given in Paris & Erdogan (1963), who proposed a power law equation relating the crack growth rate ( $da/dN$ ) to the stress intensity factor difference ( $\Delta K$ ). So called Paris-Erdogan law,  $da/dN = C\Delta K^m$ , has two parameters,  $C$  and  $m$ , which need to be found by matching experimental results.

Numerical modeling is often used in regimes beyond validity of the analytical formula (e.g. variable  $\Delta K$  or short cracks). Key feature of fatigue numerical model is hysteresis, which has been mostly prescribed phenomenologically, i.e. directly in constitutive law (for instance Desmorat et al., 2006; Nguyen et al., 2001; Roe & Siegmund, 2003). Recently, the phenomenology of hysteresis has been overcome by meso-level model – no hysteresis at the level of constitutive models resulted in combination with a material mesostructure to hysteretic loops in overall specimen response (Grassl & Rempling, 2008). Though such simulations provide useful insights into mechanisms leading to loading-unloading hysteresis, they are computationally extremely demanding.

This study focuses on one particular case, where Paris-Erdogan law is not directly applicable, i.e. the compression-compression mode-I fatigue. Traditionally, an attention has been paid to metallic materials (e.g. Fleck et al., 1985; Reid et al., 1979) but many experiments were done also on ceramics (Ewart & Suresh, 1986; Subhash et al., 1999). The crack propagates, because residual tensile stresses develop at the notch tip at the end of each loading cycle. The local and global stress intensity factors differ from each other. What is important for the crack propagation is the local one. This local stress intensity factor evolves during crack propagation and it might be hard to estimate it and use it with the Paris-Erdogan law. Instead of making analytical attempts, we developed a simple numerical model, which accommodates both (i) tensile damage-like hysteretic behavior to describe damage accumulation due to cycling according to Nguyen et al. (2001) and (ii) compressive plastic law, which produces residual tensile stresses. The model is applied to simulation of crack propagation in polycrystalline alumina in a specimen with stress concentrator. These results are compared with experimental observations published in Ewart & Suresh (1986).

---

<sup>\*</sup> Jan Eliáš, Ph.D.: Institute of Structural Mechanics, Brno University of Technology, Brno, Veveří 331/95, 602 00, Brno, Czech Republic; e-mail: elias.j@fce.vutbr.cz

<sup>\*\*</sup> Jia-Liang Le, Ph.D.: Department of Civil Engineering, University of Minnesota, 500 Pillsbury Drive S.E., Minneapolis, Minnesota, USA; e-mail: jle@umn.edu

## 2. Kinematics and statics overview

Instead of usual finite elements, material is replaced by a 2D assembly of rigid bodies (cells). These are interconnected by springs (normal, shear and rotational, Fig. 1a). Every cell has three degrees of freedom. Displacement jumps determining spring extensions are calculated through the rigid body motion (Bolander & Saito, 1998). Geometry of the cells is irregular, given by Voronoi tessellation on pseudorandom set of points with a restricted minimal mutual distance (Bolander et al., 2000). The tessellation procedure enables to increase mesh density around the notch tip and along the crack path – see Fig. 1c. So far, we focused our effort to develop only 1D constitutive behavior described further. For this reason, we eliminated shear as much as possible and thus a straight crack path is predefined in the model – see Fig. 1b. The discrete model is chosen here for the sake of simplicity, the usual finite elements could be used as well. However, the discrete model can also reflect material inhomogeneity, because the size of the discrete cells was set approximately to the real size of the grains.

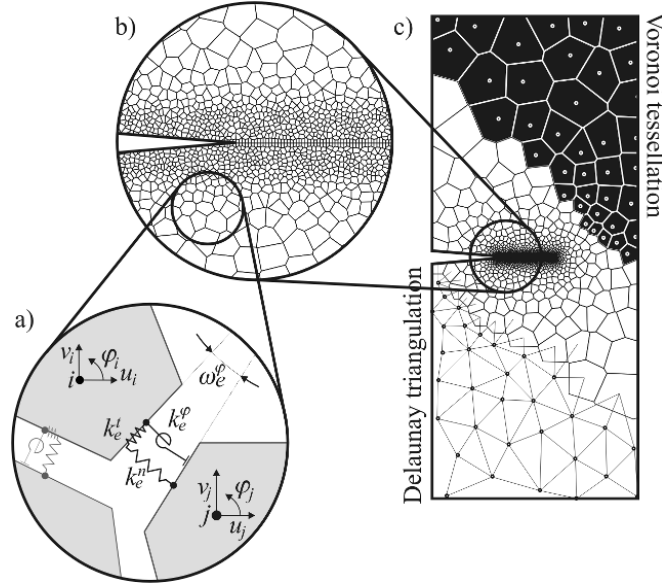


Fig. 1: Schematic explanation of the discrete model: a) mesh of irregular geometry given by Voronoi tessellation; b) predefined crack path; c) spring contact between rigid bodies.

## 3. Constitutive model

We lump the entire nonlinear phenomenon at the crack tip into one layer of spring contacts, where the crack may occur. The nonlinear behavior of these spring sets is represented by damage variable  $d$  (determined solely by normal spring) and plastic strains  $\epsilon^p$  (nonzero only in the normal direction):  $\sigma = [(1-hd)\mathbf{D}_n + (1-d)\mathbf{D}_{sr}](\epsilon - \epsilon^p)$ .  $\mathbf{D}$  is matrix of material elastic constants ( $n$  for the normal spring and  $sr$  for the shear and the rotational spring),  $\epsilon$  and  $\epsilon^p$  is the total and the plastic strain vector and  $h$  is a parameter controlling a portion of the stiffness recovered in compression similarly to Desmorat et al. (2006). In tension,  $h$  equals 1. In compression,  $h$  might lie between 0 and 1. In this work, we assume  $h$  equals 0.999. Damage variable,  $d$ , is calculated from normal stress,  $\sigma$ , and normal strain,  $\epsilon$ , (stress and strain in normal spring)  $d = (1 - \sigma/E(\epsilon - \epsilon^p))/h$ ;  $E$  is elastic modulus for plain stress.

What remains is to determine functions returning stress  $\sigma$  for arbitrary value of strain  $\epsilon$  in normal spring. The model combines damage-like approach with plasticity. Change of normal spring extension,  $\Delta\delta$ , in a spring of length  $t$  results into change of strain  $\Delta\epsilon = \Delta\delta/t$ . The strain change is decomposed into three components: elastic  $\Delta\epsilon^e$ , plastic  $\Delta\epsilon^p$  and fracture/opening  $\Delta\epsilon^o$ . In compression, the fracture component equals zero and the plastic part changes (increases) only when the descending linear softening branch is reached – see Fig. 2b.

On the contrary, the tensile part does not have any plastic increment. The strain increment is divided only into the elastic and the fracture component, so that both return the same stress: elastic part from 1D elasticity and fracture part from the traction-separation law sketched in Fig. 2a. Traction ( $T = \sigma A$ ) is related to separation ( $\delta^o = \epsilon^o t$ ) through following differential equations (Nguyen et al., 2001).

$$\dot{T} = \begin{cases} K^+ \dot{\delta}^o & \text{if } \dot{\delta}^o > 0 \\ K^- \dot{\delta}^o & \text{if } \dot{\delta}^o < 0 \end{cases} \quad (1)$$

$$\dot{K}^+ = \begin{cases} -K^+ \dot{\delta}^o / \delta_f & \text{if } \dot{\delta}^o > 0 \\ (K^+ - K^-) \dot{\delta}^o / \delta_f & \text{if } \dot{\delta}^o < 0 \end{cases} \quad (2)$$

Parameter  $\delta_f$  governs a cumulation of the damage due to cycling. State variables  $K^+$  and  $K^-$  are tangent stiffnesses in  $T$ - $\delta^o$  relation – see Fig. 2a;  $K^+$  is used for positive increments, whereas  $K^-$  for negative increments of the opening. Unloading always takes direction to the origin. Traction  $T$  cannot exceed the linear softening boundary – Fig. 2a; when this happens, the stress is dictated by the standard crack band model (Bažant and Oh, 1983) and both  $K^+$  and  $K^-$  are set to point to the origin. Though we simulate cycle by cycle, it is not possible to calculate experimentally performed 300000 cycles. Thus, the simulation of one “effective” cycle is understood to correspond with many experimental cycles.

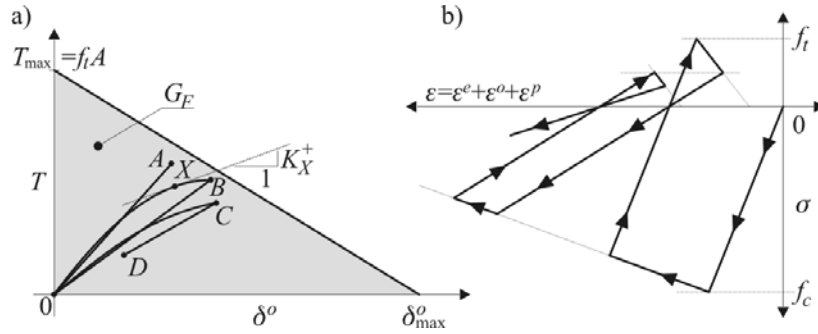


Fig. 2: a) Hysteresis according to Nguyen et al. (2001); b) coupling plasticity and damage.

#### 4. Matching experimental data

The authors attempted to match experiments performed on polycrystalline alumina in Ewart & Suresh (1986). The loading was performed as sketched in Fig. 3a, the maximal stress was -29.8 MPa and the minimal one -298 MPa (11% of compressive strength). Specimen geometry is shown in Fig. 2b ( $D = 15.9$  mm,  $a_0 = 6.3$  mm,  $l = 37$  mm, thickness 9.4 mm).

The minimal distance between points of discrete model was set to 13  $\mu$ m. This produces an average cell size about 18  $\mu$ m, which is approximately the real grain size in polycrystalline alumina. Following material parameters were used in simulation: tensile strength 260 MPa, compressive strength 2620 MPa, Elastic modulus 372 GPa, fracture energy in tension 35 J/m<sup>2</sup>, fracture energy in compression 10000 J/m<sup>2</sup> (almost horizontal softening line compared to the rest). Parameter  $\delta_f$  was determined by “trial and error” method to be approximately 1E-6 m. Stiffness recovery in compression was suppressed ( $h = 0.999$ ), because in the experiment the crack was cleaned ultrasonically every 5000 cycles.

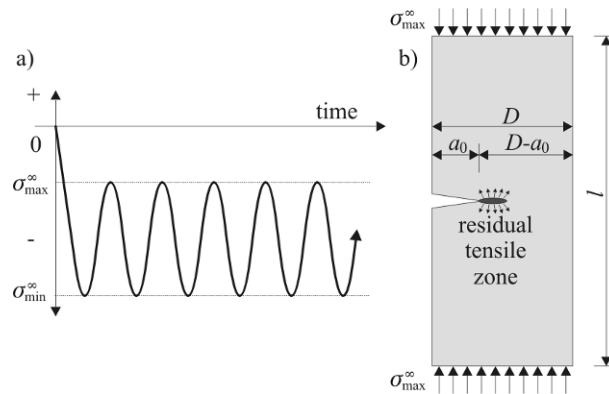


Fig. 3: a) Performed cycling scheme; b) development of the residual tensile zone (Subhash et al., 1999).

## 5. Results and Conclusions

Fig. 4 shows the simulated and the experimentally observed crack growth rate. An overall trend in crack propagation with cycles is well captured. However, large differences still remain. Mainly, the crack arrest occurs too early and it is too sudden. Moreover, the initial crack growth rate is too large. Both these issues should be suppressed; otherwise a predictive capability of such a model would be useless.

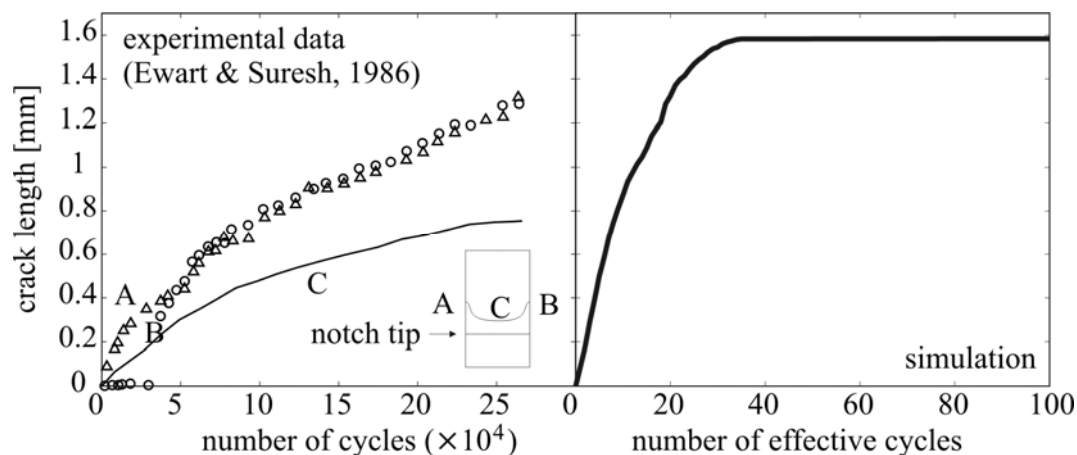


Fig. 4: Comparison of model results to experimental observation.

## Acknowledgement

This outcome has been achieved with the financial support of (i) the Czech Science Foundation under projects no. P105/11/P055 and (ii) the Ministry of Education, Youth and Sports of the Czech Republic under project no. ME10030. The support is gratefully acknowledged.

## References

- Bazant, Z.P. & Oh, B.-H. (1983) Crack band theory for fracture of concrete. *Materials and Structures*, 16, pp. 155-177.
- Bolander, J. E., Hong, G. S. & Yoshitake, K. (2000) Structural concrete analysis using rigid-body-spring networks. *Computer-Aided Civil and Infrastructure Engineering*, 15, pp. 120-133.
- Bolander, J. E. & Saito, S. (1998) Fracture analyses using spring networks with random geometry. *Engineering Fracture Mechanics*, 61, pp. 569-591.
- Desmorat, R., Ragueneau, F. & Pham, H. (2006) Continuum damage mechanics for hysteresis and fatigue of quasi-brittle materials and structures. *International Journal for Numerical and Analytical Methods in Geomechanics*, 31, 2, pp. 307-329.
- Ewart, L. & Suresh, S. (1986) Dynamic fatigue crack growth in polycrystalline alumina under cyclic compression. *Journal of Materials Science Letters*, 5, 8, 774-778.
- Fleck, N.A., Shin, C.S. & Smith, R.A. (1985) Fatigue crack growth under compressive loading. *Engineering Fracture Mechanics*, 21, 1, pp. 173-185.
- Grassl, P. & Rempling, R. (2008) A damage-plasticity interface approach to the meso-scale modelling of concrete subjected to cyclic compressive loading. *Engineering Fracture Mechanics*, 75, pp. 4804-4818.
- Nguyen, O., Repetto, E.A., Ortiz, M. & Radovitzky, R.A. (2001) A cohesive model of fatigue crack growth. *International Journal of Fracture*, 110, 4, pp. 351-369.
- Paris, P.C. & Erdogan, F. (1963) A critical analysis of crack propagation laws. *Journal of Basic Engineering*, 85, 4, pp. 528-534.
- Reid, C.N., Williams, K. & Hermann, R. (1979) Fatigue in compression. *Fatigue & Fracture of Engineering Materials & Structures*, 1, 2, pp. 267-270.
- Roe, K.L. & Siegmund, T. (2003) An irreversible cohesive zone model for interface fatigue crack growth simulations. *Engineering Fracture Mechanics*, 70, pp. 209-232.
- Subhash, G., Beesley, S.M., Govila, R.K. & Rafenillo, W. (1999) Fatigue crack propagation in aluminum nitride ceramics under cyclic compression. *Journal of Materials Science*, 34, pp. 4645-4652.

## GPU COMPUTATION IN ENGINEERING PRACTICE

C. Fischer<sup>\*</sup>

**Abstract:** *In many research fields the numerical problems demand extremely large computational power. As a consequence, researchers are constantly demanding new and more powerful computers. Recently, the graphics chip producer NVIDIA launched the CUDA parallel computing architecture, which enables scientists to utilize the extreme power available on modern and relatively cheap Graphical Processor Units (GPUs). Necessity to change the common approach together with significant difference in the GPU architecture prevents the wide usage of the graphics hardware. A flexible programming interface to GPU has been recently implemented in numerical packages like Mathematica™ or Matlab®. Such an interface does not hide the differences completely, but greatly simplifies the development of the optimized code. The contribution presents simple examples of GPU utilization in a real engineering environment.*

**Keywords:** *Numerical computation, GPU, CUDA.*

### 1. Introduction

It is widely respected fact, that the progress in computer hardware development is driven mainly by entertainment industry. Unceasing demand of better and more realistic games and wide spread of the personal computers makes the powerful hardware cheaper and cheaper. It is no doubt, that developing of the specialized computational equipment only for the scientific purposes would be very expensive. It has already appeared in the past, that the scientist have adopted devices developed for home entertainment and used them in their serious work, like powerful clusters based on cheap XBOXes (Microsoft) or PS3 (Sony) game consoles (see [PS3]). Recently, similar effect came to light with GPU computation. However, there is one significant difference between approaches of companies producing game consoles and GPU producers. While Microsoft and Sony tried hard to disable any other usage of their products than pure entertainment, ATI (AMD) and NVIDIA support the great success of the general purpose computing on their graphics hardware.

Is GPU computing really profitable or is it only hype? As everything in the real world, it depends on the circumstances. The modern GPU serve as a powerful graphics engine thanks to its highly parallel programmable processor. As a parallel device it features peak arithmetic and memory bandwidth that substantially outpaces its CPU counterpart. Contemporary graphics processors thus operate as co-processors within the host computer. This means that each GPU is considered to have its own memory and processing elements that are separate from the host computer. In contrast to contemporary CPUs, which have 1-8 fast computational cores, the recent GPUs are equipped by several hundreds of simple yet powerful cores. From that fact one can deduce the typical field of application of the GPUs. The appropriate task should be able to exploit a high number of available cores. Typical examples are various simulation procedures (chemistry, electro, biology, etc.), CFD, Monte Carlo methods and others.

The acronym CUDA (see [CUDA]) stands for Compute Unified Device Architecture. Being developed, maintained and distributed by NVIDIA, it offers unified programming approach to all recent NVIDIA GPUs. Access to the ATI's GPUs is provided using the OpenCL standard (see [OpenCL]). Open Computing Language (OpenCL) is a framework for writing programs that execute across heterogeneous platforms consisting of CPUs, GPUs, and other processors. CUDA, as well as OpenCL use C language as the main programming tool. Although OpenCL standard can be used for NVIDIA devices too, we will restrict ourselves to the CUDA programming interface in this paper.

---

<sup>\*</sup> RNDr. Cyril Fischer, PhD.: Institute of Theoretical and Applied Mechanics AS CR, v.v.i., Prosecká 76, Prague 9, Czech Republic, e-mail FischerC@itam.cas.cz

Tab. 1: Selected representatives of the NVIDIA graphics cards.

Graphics Card Product	Cores	Memory	Price
Quadro 6000 (Fermi)	448	6.0GB ECC, 384-bit, 144GB/s	3 200 €
Quadro 5000 (Fermi)	352	2.5GB ECC, 320-bit, 120GB/s	1 800 €
Quadro 4000 (Fermi)	256	2.0GB, 256-bit, 89.6GB/s	800 €
Quadro 2000 (Fermi)	192	1.0GB, 128-bit, 41.6GB/s	500 €
Quadro 600 (Fermi)	96	1.0GB, 128-bit, 25.6GB/s	180 €
GeForce GT 430	96	1.0GB, 128-bit, 25.6GB/s	70 €
GeForce GT 330M (mobile)	48	1.0GB, 128-bit, ??GB/s	

## 2. Main differences

Although the presented contribution attempts to show that the usage of graphics hardware can be straightforward, it is necessary to point out the main differences between CPU and GPU programming. These differences could be named as “dedicated and complicated memory”, “compute capabilities”, “parallel algorithms”.

- Dedicated memory. The graphics cards are usually equipped with a certain amount of a very fast graphics memory, connected to the main memory of the computer via relatively slow bus (PCIe). All data have to pass this bottleneck.
- Complicated memory. Memory architecture of the graphics devices is rather complicated. However, the high level interface unifies (up to certain limit) memory access. For details see e.g. [CUDA2].
- Compute capabilities and precision. Although CUDA recognizes several categories of the GPUs, the end-user interested in scientific computation distinguishes only two categories: Prior version 1.3, which does not use double precision floating point numbers, and version 1.3 and newer, which is able to perform double precision arithmetic. From this point of view, situation is quite similar to the early computational era, when the cost of double precision operations was twice the single precision. Performance of the recent GPUs, which are capable double precision operations, suffers similar handicap. In contradistinction to the Intel based FPU, which uses internally 80bit precision and several types of rounding, the double precision computations of NVIDIA GPUs use 64bit even for the intermediate results. There are some additional deviations from the IEEE 754 standard, see [CUDA] and (Goldberg, 1991). The trigonometric functions implemented in the hardware are not very accurate, (with error up to several “ULP, unit in the last place”), but CUDA programming toolkit provides less powerful but accurate math library.
- Parallel algorithms. Graphics processors are built as SMID (single instruction, multiple data) devices. This means, that the code (instruction) is always preformed on a predefined set of data. The minimum size of the data processed in SIMD fashion by a CUDA multiprocessor is a group of 32 threads (so called warp). However, instead of manipulating warps directly, programmers work with blocks that can contain 64 to 1024 threads.

## 3. Programming examples

As we are working with graphics cards, let us start with a famous graphics example, Mandelbrot set. It is defined by the relation:

$$\mathbb{M} = \{c \in \mathbb{C} : \exists s \in \mathbb{R}, \forall n \in \mathbb{N}, |P_c^n(0)| \leq s\}$$

where  $P_c: z \mapsto z^2 + c$ .

The sample code is listed in Fig. 1. Arguments of the functions are as follows: Scalar return vector ANS, dimension of the desired image, complex constant c, scale of the image r and maximal allowed number of iterations. The code looks out tangled,

```

1 __global__ void mandelset(int * ANS, int n,
2 Real_t c0RE, Real_t c0IM, Real_t r, int lim) {
3 int index=threadIdx.x+blockIdx.x*blockDim.x;
4 if (index<n*n){
5 Real_t dx = r/(n - 1), dy = r/(n - 1);
6 Real_t zRE, zIM, cRE, cIM, tmp;
7 int i=(int)(index/n), j=(int)(index%n), k=0;
8 zRE = 0; cRE = c0RE + (2*i - 1 - n)*dx;
9 zIM = 0; cIM = c0IM + (2*j - 1 - n)*dy;
10 while (hypot (zRE, zIM) < 2 && k++ < lim){
11 tmp = 2*zRE*zIM + cIM;
12 zRE = zRE*zRE - zIM*zIM + cRE;
13 zIM = tmp;}
14 ANS[index]=k;
15 }

```

Fig. 1: C code for generating Mandelbrot Set.

but it is only due to lack of complex arithmetic in C language. Having the code ready (e.g. in the form of text string `src`), a Mathematica function can be prepared using a simple command:

```
Needs["CUDALink`"];
CudaMandel = CUDAFunctionLoad[src, "mandelset", {{_Integer, _, "InputOutput"}, (1)
    _Integer, _Real, _Real, _Real, _Integer}, blockdim];
```

Resulting function can be used in the same manner like any other standard or user defined function.

```
n = 999; zzz = ConstantArray[1, {n*n}];
ans = CudaMandel[zzz, n, .37, .1, 0.005, 255];
```

There are several constructions in the example, which is worth to emphasize. First, type specification `Real_T` stands for a general floating point type. Compiler substitutes single or double precision type according to available hardware. Second, let us look at the 3<sup>rd</sup> line of code in Fig. 1:

```
int index=threadIdx.x+blockIdx.x*blockDim.x;
```

Variables `threadIdx`, `blockIdx`, and `blockDim` are part of the standard CUDA toolkit, see [CUDA3]. They identify individual threads and help to access the corresponding data for a particular part of computation. Third, see the line 4 in the code. As the program is executed in wraps, each thread has to check if it operates on the valid data. The last remark belongs so the parameter `blockdim` in (1). This value depends not only on the particular hardware, but also on memory demands of the code. It is bounded by hardware parameters: maximum block dimension, maximum threads per block and maximum number of registers per block. Typical values of the mentioned parameters can be 512, 512 and 8096 respectively. Especially number of registers can be limiting for a complicated code.

As a second example, let try us check precision of the build-in trigonometric functions. To show the basic access to the memory on the graphics card, the procedure will be following:

1. Allocate input and output arrays on the graphics card, lines 15 – 17, Fig. 2.
2. Fill the input array  $\varepsilon \cdot \square$  for integers  $i$ :  $0 \leq i < N$  (function `fill`, lines 5 – 9),  $\varepsilon$  is ULP or the machine epsilon – line 18. It is computed using the local procedure (resident on GPU), lines 1 – 4.
3. For each value  $x$  from the input array call the built-in instruction `__sinf(x)`, line 19, function is defined 20 – 14.
4. Read and check the result, lines 21 – 24.

Due size limitation of a single block of GPU memory, the interval  $(0, 2\pi)$  has to be divided to several parts of length  $N$  and computation has to repeat. It appears, that the greatest error is about  $10\varepsilon$  for arguments close to  $2\pi$ .

```
src="
1 __device__ float gpuEps(void) {
2 float x=2.0; int k=0,lim=10000;
3 while ((1.0+x)>1.0 && k++<(lim))x=x/2.0;
4 return x;}
5 __global__ void fill(Real_t * A, int length) {
6 int index=threadIdx.x + blockIdx.x*blockDim.x;
7 if (index < length) A[index]=index*gpuEps();
8 }";
filleps = CUDAFunctionLoad[src, "fill",
    {{_Real}, _Integer}, 512];
src = "
10 __global__ void ts(float *A, float *B, int N){
11 int index=threadIdx.x + blockIdx.x*blockDim.x;
12 if (index < N) A[index]=__sinf(B[index]);
13 }";
testsin = CUDAFunctionLoad[src, "ts",
    {{_Real}, {_Real}, _Integer}, 512];

15 n = 10000000;
16 mem1 = CUDAMemoryAllocate[Real, {n}];
17 mem2 = CUDAMemoryAllocate[Real, {n}];
18 filleps[mem1, n];
19 testsin[mem2, mem1, n];
20 var1= CUDAMemoryGet[mem1];
21 var2= CUDAMemoryGet[mem2];
22 GPUEPS = var1[[2]];
23 Maximum=Max[Abs[var2 - Sin[var1]]/GPUEPS]
```

Fig. 2: Program for checking the accuracy of `__sinf`.

As the last example of usage GPU computing, let us try to apply the described approach to the analysis of experimental data, obtained in UTAM in 2010. The resonance properties of the pendulum have been measured. Pendulum was supported by Cardan joint and excited in one direction only by a shaker, see Pospíšil (2010). Movement of the pendulum was recorded in the both directions by a pair of identical high-speed rotary magnetic encoders. They have a frictionless design and provide 8192 counts per revolution. The natural frequency of the pendulum was about 0.6 Hz, sampling frequency of the data acquisition setup was 200 samples per second. Length of the records varied, starting from 6 minutes up to several hours. It has appeared that the instantaneous frequency of the response was noticeably dependent on the actual amplitude, which has varied quite quickly in the resonance region. Moreover, as the resonance frequency interval for this setup was rather narrow, less than one Hertz, the data analysis had to be performed with exceptional care. To obtain accurate values of the instantaneous frequency and amplitude, the response had to be divided into individual periods



(response was almost harmonic). Each section of data was then approximated by a trigonometric function, whose parameters provided most accurate data.

Performing this computation using just simple Mathematica's function FindFit took for a single data almost an hour. On the other hand, fitting a sinus function through almost harmonic data, especially when the very good initial approximation from FFT analysis is available is a task, which can be easily programmed and then parallelized massively on the GPU.

Data fitting consists in minimization of a function  $Z(a, b, c) = \sum_{i=1}^n (data_i - a \sin(b t_i + c))^2$ . If the gradient vector and Hessian matrix of this function are available, the standard Newton method can be used to find a zero point of the grad  $Z$ . Implementation of the Newton method was taken from Numerical Recipes (Press et al., 1992). The main part of the CUDA program is shown in the listing in Fig. 3. To understand it, let us denote `nans` number of analyzed periods and `ndata` number of samples used in each period of data. Vector `ANS` has dimension  $(3 \text{ nans})$  — 3 parameters for each period. Vectors `t` and `data` have dimension  $(ndata * nans)$ . Initial approximation is stored in triples in `ANS` on input; resulting values are in the same places of `ANS` on output. From the code in Fig. 3 let us emphasize the line 7, where the input/output data vectors are distributed according to thread index. To each instance of `newt` procedure, the addresses of the appropriate parts of the arrays are passed.

```
src=" ...
1 __global__ void fpars(Real_t *ANS, int nans,
2 Real_t *data, Real_t *t, int ndata) {
3   int index=threadIdx.x + blockIdx.x*blockDim.x;
4   int n=3;
5   Real_t tolX=1e-5, tolF=1e-5;
6   if (index<nans)
7     newt(&(ANS[index*n]), n, tolX, tolF,
          &(data[index*ndata]),
          &(t[index*ndata]), ndata);
8 }";
Needs["CUDALink`"]
CudaNewt=CUDAFunctionLoad[src,
  "fpars", {{_Real, _, "InputOutput"}, _Integer,
            {_Real, _, "Input"}, {_Real, _, "Input"},
            _Integer}, 128];
```

Fig. 3: Driver for the procedure `newt`.

#### 4. Conclusions

It is always difficult to reasonably balance the time, which is necessary for certain task, between long computation and tedious programming. Great success of high level programming packages like Matlab and Mathematica is based on ease of use, which is redeemed by reduced computation speed. We have shown, that at little extra effort certain numerical problems can be speeded up noticeably.

#### Acknowledgement

The support of the Grant Agency of the AS CR No. IAA200710805 and AV0Z20710524 research plan are gratefully acknowledged.

#### References

- Goldberg, D. (1991) What every scientist should know about floating-point arithmetic, Journal ACM Computing Surveys (CSUR), Volume 23 Issue 1.
- Pospíšil S., Fischer C., Náprstek J. (2010) Experimental and theoretical stability analysis of damped auto-parametric pendulum, In Engineering Mechanics 2010. Book of extended abstracts. Praha, Institute of Thermomechanics AS CR, v. v. i., pp. 111-123.
- Press, W.H., Teukolsky, S.A., Vetterling, W.T., Flannery, B.P. (1992) Numerical Recipes in C, second edition, Cambridge University Press.
- [CUDA] <http://en.wikipedia.org/wiki/CUDA>.
- [CUDA2] <http://ixbtlabs.com/articles3/video/cuda-1-p5.html>.
- [CUDA3] [http://developer.download.nvidia.com/compute/cuda/1\\_0/](http://developer.download.nvidia.com/compute/cuda/1_0/)  
NVIDIA\_CUDA\_Programming\_Guide\_1.0.pdf.
- [OpenCL] <http://en.wikipedia.org/wiki/OpenCL>.
- [PS3] <http://www.ps3cluster.umassd.edu/>.

## **ANALYTICAL APPROACH TO CENTRE-LINE OPTIMIZATION OF BURIED ARCH BRIDGES AND ITS BOUNDARIES**

**M. Foglar<sup>\*</sup>, V. Křístek<sup>\*</sup>**

**Abstract:** *An arch is one of the oldest structural shapes that mankind has invented. The Roman Empire constructed a large number of stone arch bridges on roads or aqueducts, many of which exist to the present. Arch bridges were constructed throughout medieval times; some of them represent masterpieces of the world's cultural heritage. Buried arch bridges are built on both roads and railways, both as underbridges or overbridges. Due to low construction costs, great durability and endurance, they are favored by contractors and investors. Buried arch bridges are built with spans ranging from 2 m up to 40 m. This paper discusses the structure-soil interaction of buried arch bridges. With the use of an analytical derivation, a method of centre-line optimization of buried arch bridges is proposed and the limitations of this approach discussed.*

**Keywords:** *Buried structures, arch, structure-soil interaction.*

### **1. Introduction**

An arch is one of the oldest structural shapes mankind has invented. The Romans constructed a large number of stone arch bridges on roads or aqueducts, many of which exist in present day.

Buried arch bridges are built on both roads and railways, both as underbridges or overbridges. Due to low construction costs, great durability and endurance, they are favored by contractors and investors. Buried arch bridges are built spanning from 2 m up to 40 m.

This paper discusses the structure-soil interaction of buried arch bridges. Utilizing an analytical derivation, a method of centre-line optimization of buried arch bridges is proposed and the limitations of this approach discussed.

### **2. Loading of buried arch bridges**

Buried structures are vertically selfloaded, by impact of the fill, by weight of the fill and in addition due to surface traffic of the buried structure (usually a carriageway). Lateral loading of buried structures is caused mainly by structure-soil interactions, i.e. lateral loading due to compaction of backfill, earth pressure at rest (or active/ passive earth pressure depending on deflection of the structure) and lateral loading due to excess weight.

On frame bridges, the definition of loading is elementary. With buried arch bridges, the load-analysis is complicated by the fact that the horizontal and vertical loads act on the plane of projection of the centre line, see Fig. 1.

An elementary segment of the arch is loaded, according to Fig. 1, by vertical loading  $p$  /kN/m/ from the fill defined as

$$p = (h + y) \gamma \quad (1)$$

and lateral loading  $s$  /kN/m/ defined as

$$s = k (h + y) \gamma \quad (2)$$

---

<sup>\*</sup> Ing. Marek Foglar, Ph.D. and prof. Ing. Vladimír Křístek, DrSc.: Department of concrete and masonry structures, Czech Technical University, Thákurova 7; 166 29, Prague; CZ, e-mails: marek.foglar@fsv.cvut.cz, kristek@fsv.cvut.cz

where  $h$  /m/ is the height of the fill,  $\gamma$  /kN/m<sup>3</sup>/ is the volumetric mass of the fill,  $y$  /m/ is the vertical coordinate from the arch crown and  $k$  /-/ is the parameter determining the lateral earth pressure. Simplified, the excess vertical and horizontal by traffic can be substituted by increasing the height of the fill.

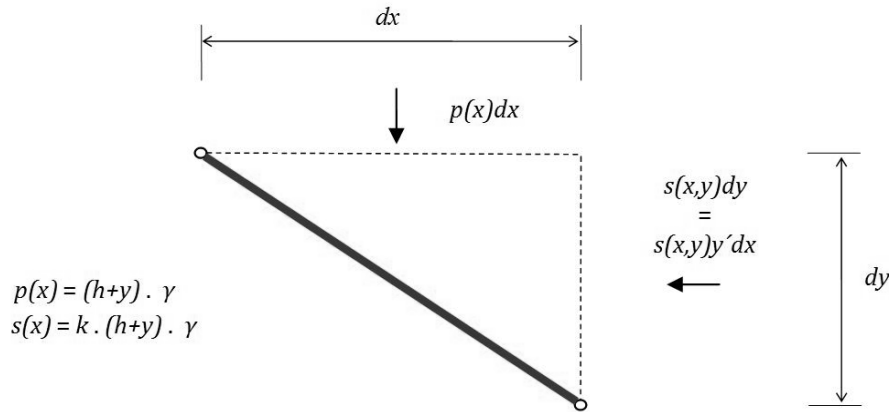


Fig. 1: Loading of an elementary arch segment.

The loading causes deflections of the structure, which changes the initial loading by earth pressure. Fig. 2 shows typical loading and deflection of a buried arch bridge in operation.

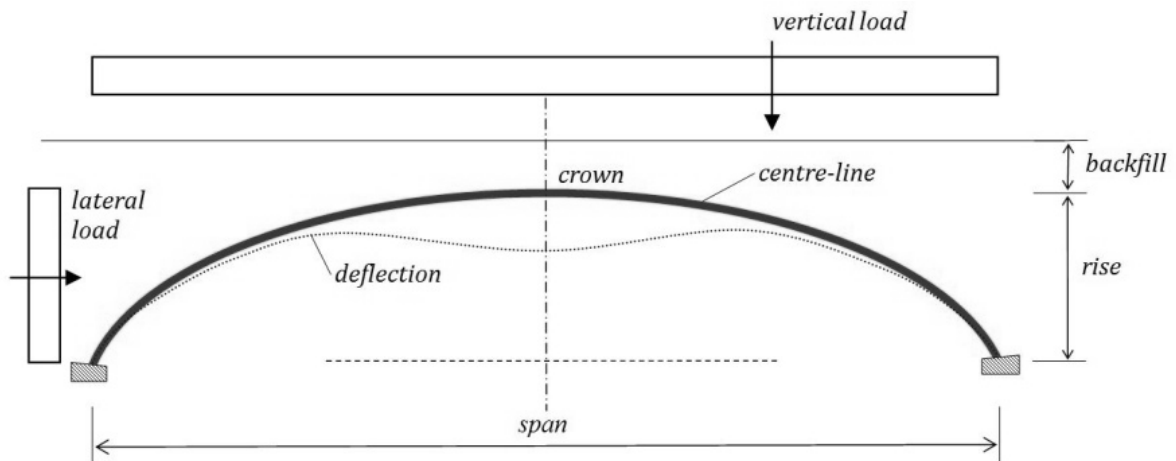


Fig. 2: Buried arch bridge loading.

### 3. Centre-line optimization of buried arch bridges

The process of centre-line optimization of buried arch bridges leads to a centre-line which is a resultant of forces affecting the structure, thus no perceivable bending moments are present. The optimization results into negligible flexural stresses, therefore almost no bending reinforcement is required thus decreasing the construction time. This topic is discussed in detail in referenced articles.

The shape of the optimized centre-line is defined by a field of loadings affecting the arch. The arch is divided into a finite number of segments; to each of them an interaction vector is attributed. As previously noted and plotted in Fig. 1, the vertical loading is introduced as  $p(x,y)$ , the vertical as  $s(x,y)$ .

The shape of the optimized centre-line  $y(x)$  is derived on an elementary segment; the axial force in the arch  $H$  /kN/ is dissociated into its horizontal part  $H(x)$  and vertical part  $V(x)$ , see Fig. 3.

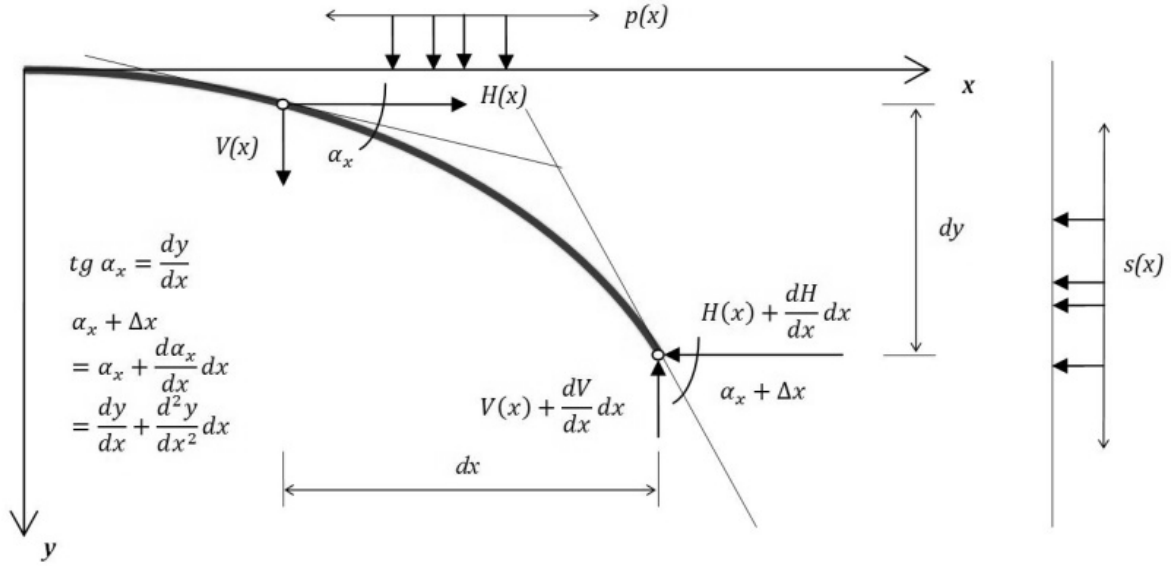


Fig. 3: Derivation of an optimal centre-line.

Horizontal and vertical conditions of equilibrium must be fulfilled:

- horizontally:

$$H(x) - s \cdot dy - H(x) - \frac{dH}{dx} dx = 0 \quad (3)$$

$$\frac{dH}{dx} = s \cdot \frac{dy}{dx} \quad (4)$$

$$H' + s y' = 0 \quad (5)$$

- vertically:

$$V(x) = H(x) \cdot \operatorname{tg} \alpha_x \quad (6)$$

$$H(x) \cdot \operatorname{tg} \alpha_x + p \cdot dx - \left( H(x) + \frac{dH}{dx} dx \right) \cdot \operatorname{tg} \alpha_x = 0 \quad (7)$$

The angle  $\alpha_x$  is substituted by the expression noted in Fig. 2, the product

$$-\frac{dH}{dx} dx \cdot \frac{d^2 y}{dx^2} \cdot dx$$

is neglected:

$$H(x) \cdot \frac{d^2 y}{dx^2} + \frac{dH}{dx} \cdot \frac{dy}{dx} - p = 0 \quad (7)$$

$$H y'' + H' y' - p = 0 \quad (8)$$

Substituting (5) to (8):

$$H y'' + s (y')^2 - p = 0 \quad (9)$$

Introducing  $y' = z(x)$ :

$$H z' + s z^2 = p \quad (10)$$

Substituting (1) to (8) and (2) to (5):

$$H y'' + H' y' - \gamma y = h \gamma \quad (11)$$

$$H' + k \gamma y y' + k h \gamma y' = 0 \quad (12)$$

The Equations (11) and (12) can be solved in a closed form only under special boundary conditions; therefore a numerical solution is necessary in most cases. The most suitable method for the solution is the pre process of the vector synthesis. For the process of vector creation, the centre line is divided

into equal horizontal segments. For each segment, the interaction vector is defined. The numerical application of vector synthesis is fast and robust for all possible loading arrangements.

The method was applied on existing bridges (Foglar et al. 2010), great reductions of bending moments were achieved, see Fig. 4. Though great reductions (from 1400 kNm to less than 200 kNm at the restraint), the ideal state, i.e. total reduction of bending moments, was not achieved.

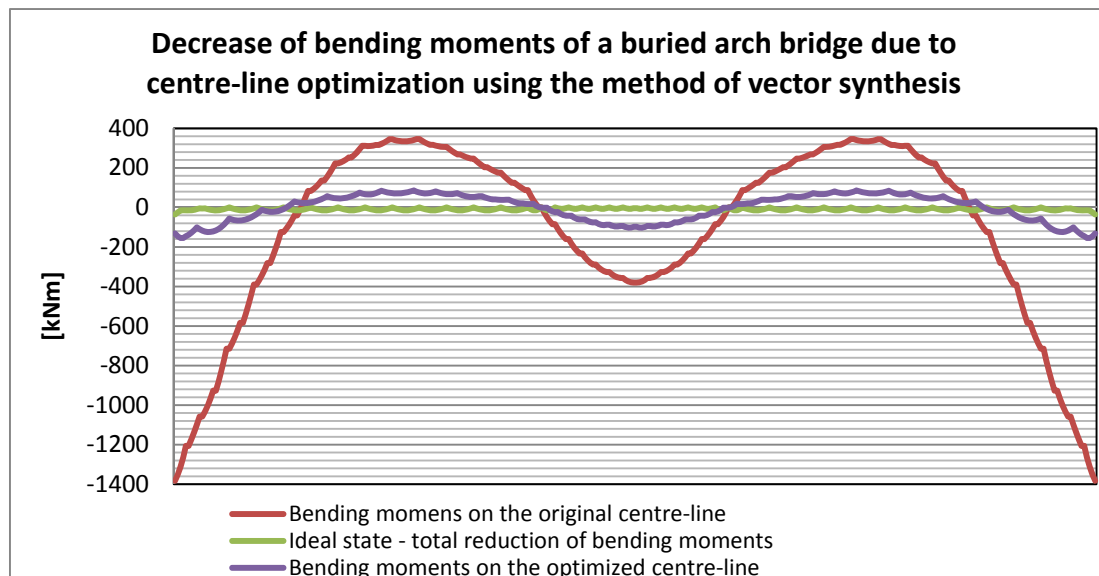


*Fig. 4: Reduction of bending moments due to centre-line optimization.*

This problem is attributed to the slip between soil and the structure. In FEM modeling, the slip is modeled by contact elements with a friction coefficient, whose value is derived empirically. The analytical approach must be modified to incorporate this phenomenon.

#### 4. Conclusions

This paper discussed the structure-soil interaction of buried arch bridges. With the basis of an analytical derivation, a method of centre-line optimization of buried arch bridges was described and its boundaries discussed. Further research is outlined.

#### Acknowledgement

This text presents outcomes of the projects supported by the Czech Science Foundation, project No. 103/09/2071 and Czech Ministry of Education project MSM 6840770005.

#### References

- Foglar, M. & al. (2010) The use of fiber reinforced concrete in buried arch bridges (in Czech). *Beton TKS*, 10, 2, pp. 92-95.
- Foglar, M. & Kristek, V. (2010) Structure-soil interaction of buried arch bridges, in: Frydrysek & Nikodym (ed.), *Beams and frames on elastic foundation 3*, Ostrava – VSB – Technical University of Ostrava, Ostrava, pp. 303-319.

## **FIELD TESTS OF BLAST PERFORMANCE OF REINFORCED CONCRETE AND FIBER REINFORCED CONCRETE SPECIMENS**

**M. Foglar<sup>\*</sup>, E. Sochorová<sup>\*</sup>, A. Kohoutková<sup>\*</sup>**

**Abstract:** According to recent publications, from 2005 to 2008 there were more than 13000 terrorist attacks around the world which took more than 73000 human lives. The attacks were targeted mainly on the technical and civic infrastructure, like governmental buildings, bridges, etc. Due to improved ductility, fibre-reinforced concrete (FRC) shows better performance under blast and impact loading than conventionally reinforced concrete. Field tests of FRC and reinforced concrete specimens were performed in cooperation with the Czech Army corps and Police of the Czech Republic in the military training area Boletice. The tests were performed using real scale precast slabs and 25 kg of TNT charges placed in distance from the slab for better simulation of real in-situ conditions. The paper presents primary results of the tests.

**Keywords:** Blast loading, fiber concrete, reinforced concrete.

### **1. Introduction**

Recent terrorist attacks in Moscow (2011), Stockholm (2010), London (2005), Madrid (2004), etc. show great vulnerability of civil and transport infrastructure to this kind of threat. Attacks on structures like airports, railway and subway stations, bridges and governmental building can cause great casualties. These casualties multiply when the explosion causes collapse of the entire structure.

One of the ways of improving the blast performance of civil and transport infrastructure is the use of progressive materials like fiber reinforced polymer composites (Buchan & Chen, 2007). In case of building new structures, the needed ductility can be achieved by using plastic fibers in the concrete mix. Even bigger increase of blast and impact performance can be achieved by the use of ultra high performance fiber-reinforced concrete or engineered cementitious composites (Millard & al., 2010).

This paper presents the primary results of field tests of blast performance of reinforced concrete and reinforced concrete specimens with plastic fibers. The tests were performed in cooperation with the Czech Army corps and Police of the Czech Republic at the military training area Boletice using real scale precast slabs and 25 kg of TNT charges placed in distance from the slab for better simulation of real in-situ conditions.

### **2. Field tests of blast performance of reinforced concrete and reinforced concrete specimens with plastic fibres**

#### **2.1. Specimens**

Dimensions of the specimens were designed in real scale of a small span bridge in as concrete slabs, 6 m long, 1.5 m wide and 0.3 m thick.

The specimens were made of C30/37-X0 concrete. Both specimens were reinforced by conventional reinforcement (B500B according to EN 1992-1-1 design code) at both surfaces, longitudinally by 11Ø16 mm reinforcing bars (every 140 mm), transversely by Ø10 mm (every 150 mm). The shear reinforcement was provided by Ø8 mm links (9 pcs/m<sup>2</sup>).

---

<sup>\*</sup> Ing. Marek Foglar, Ph.D., Ing. Eva Sochorová and prof. Ing. Alena Kohoutková, CSc.: Department of concrete and masonry structures, Czech Technical University, Thákurova 7; 166 29, Prague; CZ, e-mails: marek.foglar@fsv.cvut.cz, eva.sochorova@fsv.cvut.cz, akohout@fsv.cvut.cz

Polypropylene 54 mm long synthetic fibers at  $4.5 \text{ kg/m}^3$  were used in the second specimen. The dosage of the fibers was kept low as it can be achieved on-site.

## 2.2. Layout of the experiments

The experiments were carried out at the military training area Boletice in cooperation the Czech Army corps and Police of the Czech Republic. The blasts were performed on former artillery practice target area (900 m above sea level) which is now used for dismantling obsolete ammunition and ammunition from WW2 which is still found in the Czech Republic during construction works.

The slabs were placed on timber posts which were fixed in position by steel tubes. The ground under the slabs was removed; 5 m in diameter and 1 m deep excavation was prepared under the slabs so the results of the experiments would not be influenced by rebound of the pressure wave.

The 25 kg TNT charges were placed on steel “chairs” (3Ø10 mm links, 3 mm thick S235 plate) in the middle of the slabs. The “chairs” provided off stand of 450 mm from the slab. This value was chosen as the most usual height of car trunk.

The charges were covered by a woolen blanket. According to the cooperating pyrotechnist, the blanket would concentrate the blast wave by 10-20%. The woolen blanket represents the camouflage, as the charge would not be discovered by routine police road check.

Layout of the experiments can be seen in Fig. 1.



*Fig. 1: Layout of the experiments.*

The charges were fired remotely by radio impulse.

The overpressure in the blast wave was recorded by four pressure sensors PCB<sup>®</sup>-type ICP 137A23, the signal was converted on a four-channel oscilloscope Tektronix<sup>®</sup>-type TDS3014B; the bus was located c.60 m far in a former gun bank. The sensors were dug in to the ground level, in order to minimize the possibility of damage by flying debris, but keeping the reading optimal. The sensors were placed on a helix with center at the location of the charge in distances 15, 20, 25 and 30 m.



## 2.2. Results of the experiments

The experiments showed the beneficiary effect of added fibers on blast performance of the specimens. The differences in puncture and spalling of concrete on the soffit of the slabs can be found in Tab. 1. The different effect of the blast on the surface closer to the explosion can be seen in Fig. 2 and 3.

*Tab. 1: Comparison of blast performance of RC and RC with plastic fibers.*

<i>Damage</i>	<i>RC specimen</i>	<i>RC with plastic fibers</i>	<i>RC with fibers / RC</i>
<i>Puncture – top surface</i>	<i>0.43 m<sup>2</sup></i>	<i>0.26 m<sup>2</sup></i>	<i>60%</i>
<i>Permanent deflection</i>	<i>0.31 m</i>	<i>0.378 m</i>	<i>122%</i>
<i>Concrete spalling (soffit) - &lt; concrete cover</i>	<i>2.35 m<sup>2</sup></i>	<i>1.89 m<sup>2</sup></i>	<i>80%</i>
<i>Concrete spalling (soffit) - &gt; concrete cover</i>	<i>1.71 m<sup>2</sup></i>	<i>1.09 m<sup>2</sup></i>	<i>64%</i>
<i>Concrete spalling (left side) - &lt; concrete cover</i>	<i>0.35 m<sup>2</sup></i>	<i>0</i>	<i>-</i>
<i>Concrete spalling (left side) - &gt; concrete cover</i>	<i>0.52 m<sup>2</sup></i>	<i>0.05 m<sup>2</sup></i>	<i>10%</i>
<i>Concrete spalling (right side) - &lt; concrete cover</i>	<i>0.23 m<sup>2</sup></i>	<i>0.11 m<sup>2</sup></i>	<i>48%</i>
<i>Concrete spalling (right side) - &gt; concrete cover</i>	<i>0.34 m<sup>2</sup></i>	<i>0.16 m<sup>2</sup></i>	<i>47%</i>

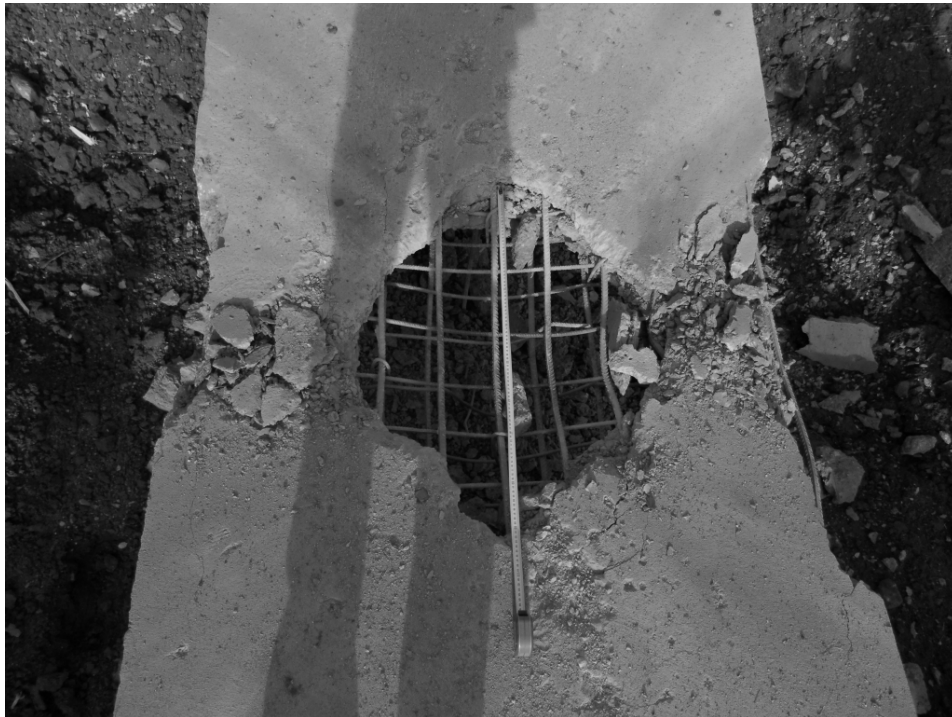


*Fig. 2: Top surface of the RC specimen after the blast.*

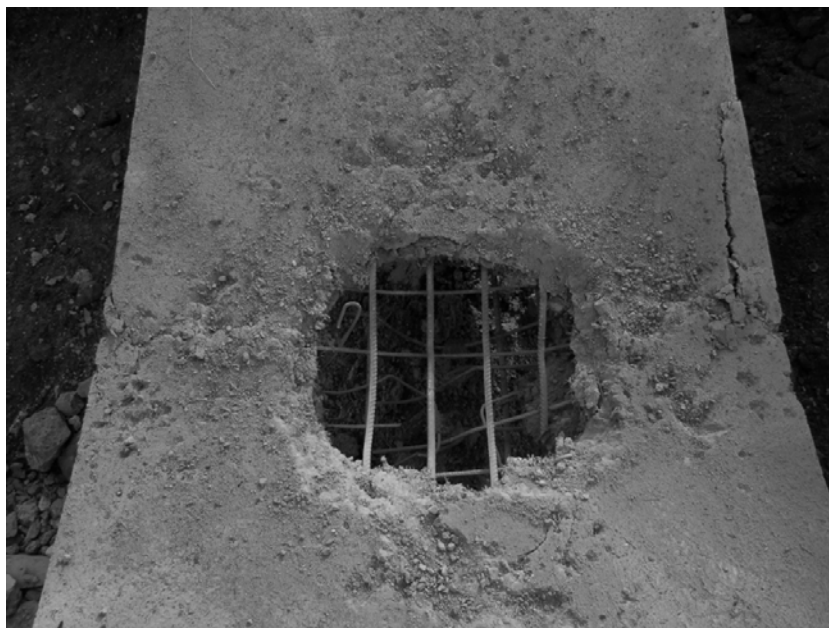


*Fig. 3: Top surface of the RC specimen with plastic fibers after the blast.*

In both cases, one longitudinal rebar and two transverse bars were torn by the explosion. The links did not show any effect on the shear capacity of the specimens; they were dislocated and remained hanging at the reinforcement or fell in the debris under the specimen.

### 3. Conclusions

The paper presented primary results of the field experiments targeted on comparison of blast performance of reinforced concrete and reinforced concrete with plastic fibers. The tests were performed using real scale precast slabs (0.3 x 1.5 x 6 m) and 25 kg of TNT charges placed in distance from the slab for better simulation of real in-situ conditions.

The results proved the beneficiary effect of added fibers on blast performance of the specimens. The puncture on the surface closer to the charge was reduced by 40% in area, the concrete spalling at the soffit of the specimen by 20% in area.

### Acknowledgement

This paper was supported by the Czech Science Foundation, project No. 103/09/2071 and Czech Ministry of Education project MSM 6840770005.

### References

- Buchan, P.A. & Chen, J.F. (2007) Blast resistance of FRP composites and polymer strengthened concrete and masonry structures – A state-of-the-art review. *Composites: Part B* 38, pp. 509-522.
- Coughlin, A.M. & al. (2010) Behavior of portable fiber reinforced concrete vehicle barriers subject to blasts from contact charges. *International Journal of Impact Engineering*, 37, 5, pp. 521-529.
- Foglar, M. & al. (2011) Blast performance of reinforced concrete and fiber-reinforced concrete specimens (in Czech). *Natural hazards (optimalisation of protection, interaction with structures)*. CTU Press, Prague, pp. 155-162.
- Foglar, M. & al. (2010) The use of fibre reinforced concrete in blast and impact design (in Czech). *Beton TKS*, 10, 2, pp. 71-73.
- Millard, S.G. & al. (2010) Dynamic enhancement of blast resistant ultra high performance fiber-reinforced concrete under flexural and shear loading. *International Journal of Impact Engineering*, 37, 4, pp. 405-413.
- Schenker, A. & al. (2008) Full-scale field tests of concrete slabs subjected to blast loads. *International Journal of Impact Engineering*, 35, 3, pp. 184-198.
- Wu, C. & al. (2009) Blast testing of ultra-high performance fibre and FRP-retrofitted concrete slabs. *Engineering Structures*, 31, 9, pp. 2060-2069.

## **SIMULATION OF THE FRACTURE PROCESS IN QUASI-BRITTLE MATERIALS USING A SPRING NETWORK MODEL**

**P. Frantík<sup>\*</sup>, V. Veselý<sup>\*</sup>**

**Abstract:** *This paper deals with numerical simulation of the fracture process in cementitious composite specimens. A technique based on physical discretization of continuum is employed. The study supplements the verification of a technique for estimation of the extent (size and shape) of the fracture process zone in quasi-brittle silicate-based specimens/structures during tensile failure. The analysis presented in the paper shows that the extent of the cumulative failure zone simulated by the considered model agrees very well with experimental results reported in the literature.*

**Keywords:** *Quasi-brittle fracture, physical discretization, nonlinear dynamic system, process zone.*

### **1. Introduction**

Today, numerical simulations are often used to investigate failure processes in quasi-brittle cementitious composites. In order to better understand and verify the fundamental issues involved, numerous simulation techniques have been proposed based on different approaches (for a review see e.g. Bažant and Planas, 1998, Jirásek, 2009). In this paper, simulations by means of the physical discretization of continuum technique (Frantík, 2007) are presented. This discretization technique, described in detail later below and successfully applied in e.g. Frantík et al. (2009), is similar to lattice modelling and uses a procedure developed for rigid body spring networks (RBSN) (Bolander et al., 1999). The computational code developed for the simulations by the authors is based on a nonlinear dynamical description of the problem. The results of such numerical dynamical simulations are considered to answer questions regarding the evolution of the fracture process zone (FPZ), the amount of energy dissipated within it, etc.

### **2. Numerical simulation of experiments**

Several experimental techniques which deal with the estimation of the zone of tensile failure in quasi-brittle cementitious composites are reported in the literature (summarized in e.g. van Mier 1997, Shah et al. 1995). The simulations presented in this paper are compared to records of experimental techniques based on acoustic emission scanning (AES). This technique was considered here under the assumption that the sources of AE phenomena are similar in nature to the failure mechanisms simulated within the used model and also because AES is the method most widely employed in such research.

Mihashi & Nomura (1996) tested two sets of wedge-splitting test (WST) specimens made of concrete and mortar differing in strength and aggregate size. The experimental set-up with an indication of the specimens' dimensions is depicted in Fig. 2 left. Two specimens (marked as C10 and C20) were selected for simulation of the fracture process since the results of the AE scanning of fracture phenomena (i.e. the extent of the damage zone) were also reported in the paper.

#### **2.1. Numerical modelling via the physical discretization of continuum approach**

The modelled specimen is substituted by a set of mass points with the given coordinates  $(x_i, y_i)$  in Cartesian space, mutually connected by simple translational springs. The springs can be generally

---

<sup>\*</sup> Ing. Petr Frantík, Ph.D. and Ing. Václav Veselý, Ph.D.: Institute of Structural Mechanics, Faculty of Civil Engineering, Brno University of Technology, Veveří 331/95; 602 00, Brno; CZ, e-mail: kitnarf@centrum.cz, vesely.v1@fce.vutbr.cz

defined as fully nonlinear and their inertial properties are neglected (concentrated at the mass points). The model is defined as a nonlinear dynamical system described by the following equations:

$$\begin{aligned}\frac{dx_i}{dt} &= v_{xi}, & \frac{dv_{xi}}{dt} &= (R_{xi} - c_1 m_i v_{xi} (1 + c_2 |v_{xi}| (1 + c_3 v_{xi}))), \\ \frac{dy_i}{dt} &= v_{yi}, & \frac{dv_{yi}}{dt} &= (R_{yi} - c_1 m_i v_{yi} (1 + c_2 |v_{yi}| (1 + c_3 v_{yi}))),\end{aligned}\quad (1)$$

where  $v_{xi}$  and  $v_{yi}$  are the velocity vector components of the mass point with index  $i$ ,  $m_i$  is its mass,  $c_1$ ,  $c_2$ ,  $c_3$  are coefficients of nonlinear viscous damping and  $R_{xi}$ ,  $R_{yi}$  are vector components of the resultant force  $R_i$  caused by connected translational springs. A single translational spring with indices  $ij$  loads the mass points  $i$  and  $j$  via the force  $F_{ij} = f_{ij}(u_{ij})$ , where  $f_{ij}$  is the stress function shown in Fig. 1 left. This function is described using four parameters: stiffness  $k_{ij}$ , initial critical tensile elongation  $u_{crit,0ij}$ , initial ‘zero’ elongation  $u_{zero,0ij}$  (i.e. the value of the tensile elongation for which the value of the carrying force drops to zero), and initial ‘flac’ elongation  $u_{flac,0ij}$  (i.e. the value of the compressive, negative elongation for which the value of the carrying force reaches a constant value).

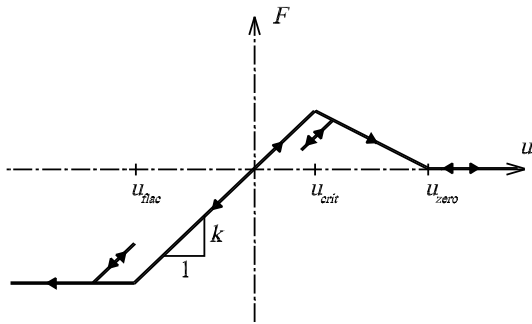


Fig. 1: Scheme of the stress function used within the FyDiK simulation technique.

As was mentioned above, the discretization technique used here is based on a procedure developed for the RBSN model (Bolander et al. 1999). This means that the mass of the mass points and the parameters of the translational springs are computed based on Delaunay triangulation and Voronoi tessellation. Mass points are generated to cover an area larger than that of the specimen. This area serves as a virgin material from which the specimen area is cut. The generation of mass points is provided in equilateral triangular mesh of size  $s$  (triangle side length) with an added random ‘noise’ vector of size  $0.8rs$ , where  $r$  is a random number

from the rectangular distribution over an interval of unit length. Every mass point has its own Voronoi cell, which specifies its mass according to cell area, material density  $\rho$  and thickness  $b$ . Similarly, every translational spring has an edge of a Voronoi cell which specifies its ‘cross-sectional’ area. This area,  $A_{ij}$ , is then used for calculation of the spring parameters (more details in Frantik et al., 2011).

The FyDiK model enables simulation of the progress of failure of the selected WST specimen. The numerical model of the test was created from a homogeneous elastic isotropic material with parameters corresponding to the concrete tested by Mihashi & Nomura (1996), i.e. specific gravity  $\rho = 2400 \text{ kg/m}^3$ , modulus of elasticity  $E = 33.01 \text{ GPa}$ , tensile strength  $f_t = 2.8 \text{ MPa}$ , and compressive strength  $f_c = 31.45 \text{ MPa}$ . The specimen was modelled free of any boundary conditions except the fixation of the velocities of two points, which ensures loading. An illustrative example of the discretization of a WST specimen is shown in Fig. 2. Dynamical effects were regulated by nonlinear viscous damping optimized for this loading speed by the coefficients:  $c_1 = 1000 \text{ Nskg}^{-1}\text{m}^{-1}$ ,  $c_2 = 0$ ,  $c_3 = 100$ . Loading was stopped after reaching the time  $t = 0.5 \text{ s}$ .

## 2.2. Results

During the simulation, the amount of dissipated energy caused by exceeding the critical elongation of the individual translational springs was recorded, see Fig. 3 and 4. The locations of the individual failure events are indicated by spots in the images and coloured according to the amount of dissipated energy. The size of the spots corresponds with the length of the associated spring (where the energy is dissipated). The term ‘dissipated energy’ refers to the energy released by the failure of particles (being at the softening branch of the stress function, see Fig. 1) creating the model in this paper. The evolution of a simulation of the FPZ is depicted via a sequence of six stages of the fracture process in Fig. 4. The FPZ is represented here as a union of failure events which took place during the 0.01 s preceding the time step when the FPZ was evaluated and depicted. The considered stages of the simulated failure are emphasized on the corresponding loading curve in the graph in Fig. 2 right.

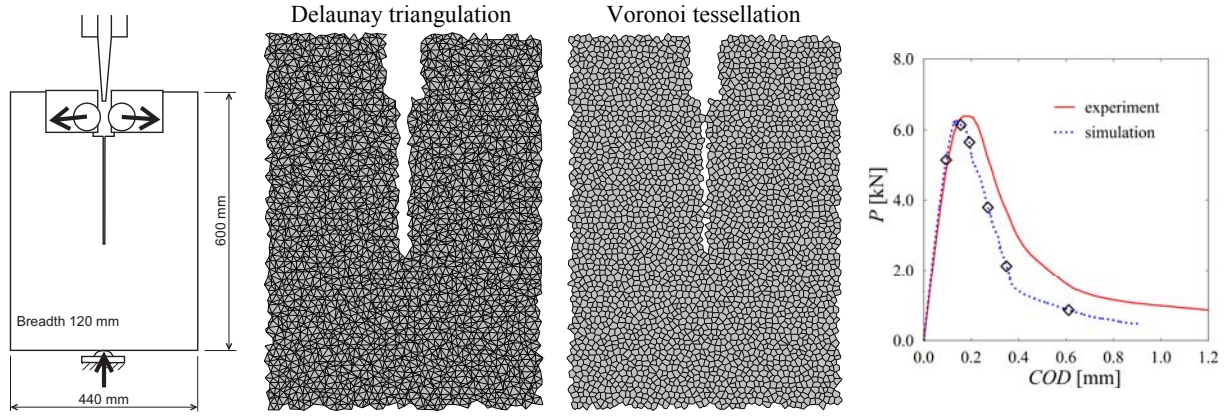


Fig. 2: Experimental set-up and dimensions of a selected WST specimen (after Mihashi & Nomura 1996) (left); an illustrative example of the FyDiK model showing triangulation and tessellation; load–crack opening displacement ( $P$ –COD) diagrams from the experiment and FyDiK simulations (right).

### 3. Discussion of results and conclusions

A comparison of the considered numerical approach to the experimental estimation of the FPZ extent (particularly its cumulative representation) is performed for the stage corresponding to the peak load and for the end of the fracture in Fig. 3 left and right, respectively. The region where the acoustic-emission-like events are located that was provided by the FyDiK fracture model is in good agreement with the considered experimental example taken from Mihashi & Nomura (1996). However, a more detailed experiment is necessary for a comparison of the intensities of energy dissipation. Due to the lack of sound and complete experimental data available in the literature the authors are planning to conduct its own AE experiments.

The paper presents a numerical study of the formation and evolution of failure zones at propagating crack tips during the fracture testing of concrete WST specimens. This analysis was motivated by the need for verification and validation of the (semi-)analytical technique for estimation of the extent (size and shape) of the fracture process zone in quasi-brittle silicate-based composites during tensile failure which has been recently developed by the authors (termed the ReFraPro technique, Veselý & Frantík, 2008, Veselý & Frantík, 2010). The author's own implementation of the computational model based on the physical discretization of continuum was successfully employed for a partial verification of the developed ReFraPro method. The used FyDiK model provided a fairly good approximation of a volume where AE events have been localized experimentally. Moreover, it also enabled the investigation of the energy consumption of such events. Therefore, the results of the simulations can serve as a significant source of new knowledge which can be obtained regarding the energy dissipation mechanisms in the fracture process zone in the case of quasi-brittle materials.

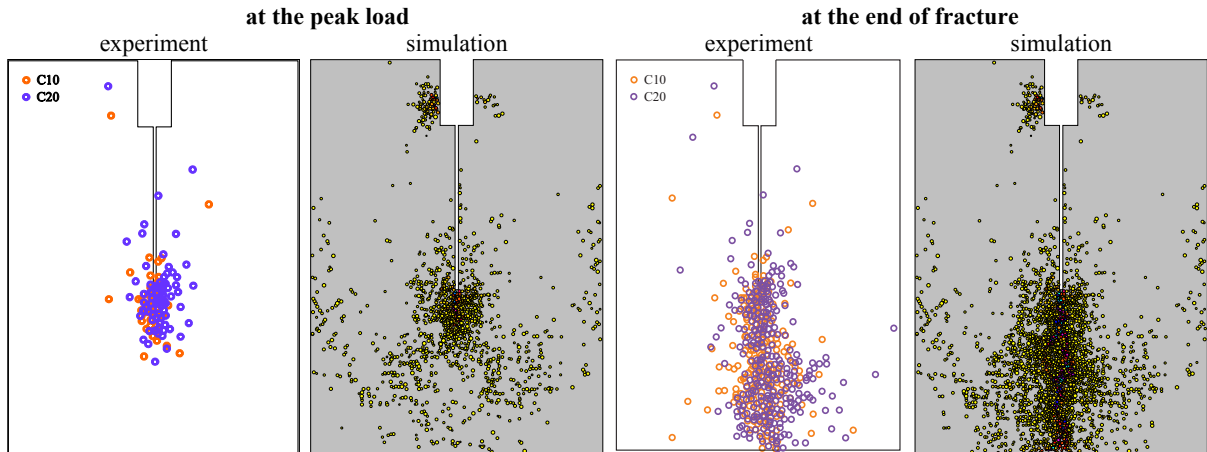


Fig. 3: A comparison of the cumulative damage zone extents for two stages of the fracture estimated experimentally using AES (Mihashi & Nomura, 1996), and numerically using the FyDiK model.

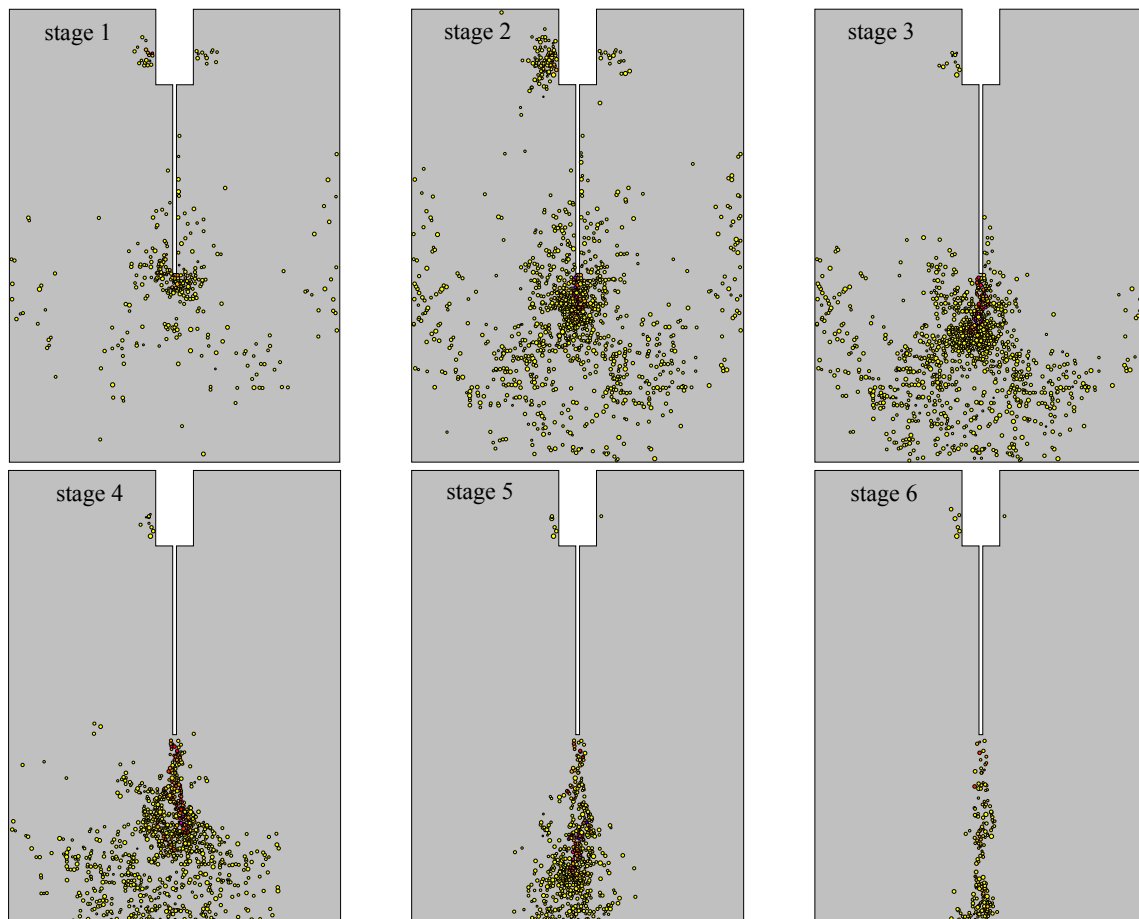


Fig. 4: A WST specimen with a depiction of the evolution of the FPZ extent with an indication of the energy dissipation intensity (from light – low intensity – to dark – high intensity) simulated by the *FyDiK* model for selected stages of the fracture process (see the *P-COD* diagram in Fig. 2 right).

## Acknowledgement

Financial support from the Ministry of Education, Youth and Sports, project No. 1M0579, and the Czech Scientific Foundation, project No. P105/11/1551, is gratefully acknowledged.

## References

- Bažant, Z. P. & Planas, J. (1998) Fracture and size effect in concrete and other quasi-brittle materials. CRC Press, Boca Raton.
- Bolander, J. E., Yoshitake, K. & Thomure, J. (1999) Stress analysis using elastically uniform rigid-body-spring networks. *J. Struct. Mech. Earthquake Eng.*, 633, 125-132.
- Frantik, P. (2007) *FyDiK* application, <http://www.kitnarf.cz/fydik>, 2007-2011.
- Frantik, P., Keršner, Z., Veselý, V. & Řoutil, L. (2009) Fractality of simulated fracture. *Key Eng. Mat.*, Vol. 409.
- Frantik, P., Veselý, V. & Keršner, Z. (2011) Efficient lattice modelling of the fracture process zone extent in cementitious composites. *Proc. of the 2nd Int. Conf. on Parallel, Distributed, Grid and Cloud Computing for Engineering* (B.H.V. Topping and P. Iványi eds.), Civil-Comp Press, Stirlingshire, Scotland. In print.
- Jirásek, M. (2009) Modeling of localized inelastic deformation – lecture notes. Czech Techn. Univ., Prague.
- Mihashi, H. & Nomura, N. (1996) Correlation between characteristics of fracture process zone and tension-softening properties of concrete. *Nuclear Engineering and Design*, 165, 359-376.
- Shah, S. P., Swartz, S. E. & Ouyang, C. (1995) Fracture mechanics of structural concrete: applications of fracture mechanics to concrete, rock, and other quasi-brittle materials. John Wiley & Sons, New York.
- van Mier, J. G. M. (1997) Fracture processes of concrete: assessment of material parameters for fracture models. CRC Press, Boca Raton.
- Veselý, V. & Frantik, P. (2008) *ReFraPro* – Reconstruction of Fracture Process, Java application, 2008-2011.
- Veselý, V. & Frantik, P. (2010) Reconstruction of a fracture process zone during tensile failure of quasi-brittle materials. *Applied and Computational Mechanics*, 4, 237-250.



## PROBABILISTIC APPROACHES APPLIED IN THE SOLUTION OF PROBLEMS IN MINING AND BIOMECHANICS

K. Frydryšek \*

**Abstract:** *This paper focuses on the probabilistic numerical solution of the problems in mining and biomechanics. Theory and applications of the Simulation-Based Reliability Assessment (SBRA) method are presented in the solution of a hard rock (ore) disintegration process (i.e. the bit moves into the ore and subsequently disintegrates it, the results are compared with experiments, new design of excavation tool is proposed) and in the solution of designing of the external fixators applied in traumatology and orthopaedics (these fixators can be applied for the treatment of open and unstable fractures or for lengthening human or animal bones etc.). Application of the SBRA method connected with FEM in these areas is a new and innovative trend.*

**Keywords:** *SBRA method, hard rock (ore) disintegration, rock mechanics, traumatology, external fixators, biomechanics.*

### 1. Introduction

In structural reliability assessment, the concept of a limit state separating a multidimensional domain of random (stochastic) variables into “safe” and “unsafe” domains has been generally accepted, see references Frydryšek1 (2009), Halдар & Mahadevan (2001), Marek & Brozzetti (2003) and Marek & Guštar (1995). Let us consider the Simulation-Based Reliability

Assessment (SBRA) Method, a probabilistic direct Monte Carlo approach, in which all inputs are given by bounded histograms. Bounded histograms include the real variability of the inputs. Application of the SBRA method is a modern and innovative trend in mechanics. Using SBRA method, the probability of failure (i.e. the probability of undesirable situation) is obtained mainly by analyzing the reliability function  $RF = RV - S$ , see Fig. 1. Where  $RV$  is the reference (allowable) value and  $S$  is a variable representing the load effect combination. The probability of failure is the probability that  $S$  exceeds  $RV$  (i.e.  $P(RF \leq 0)$ ). The probability of failure is a relative value depending on the definition of  $RV$  and it usually does not reflect an absolute value of the risk of failure (for example, it usually does not correspond to a “total” collapse).

Hence, this paper focuses on the probabilistic numerical solution of the problems in mining and biomechanics. Application of the SBRA method connected with FEM in these areas is a new and innovative trend.

### 2. Solution of a hard rock disintegration process

The provision of sufficient quantities of raw materials for the metallurgy is the main limiting factor of further development. It is therefore very important to understand the ore disintegration process, including an analysis of the bit (i.e. excavation tool) used in mining operations. The main focus is on

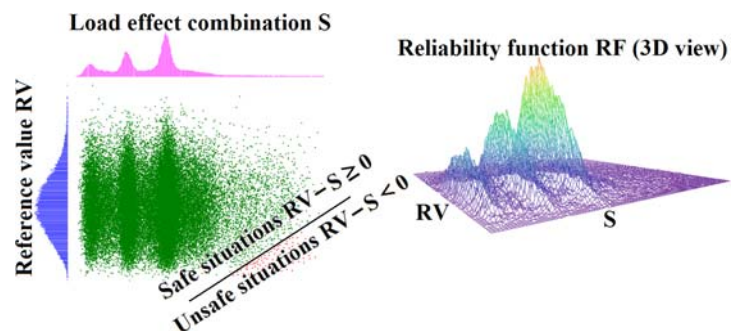


Fig. 1: Reliability function  $RF$  (SBRA method).

\* assoc. prof., M.Sc. Karel Frydryšek, Ph.D., ING-PAED IGIP: Department of Mechanics of Materials, Faculty of Mechanical Engineering, VŠB – Technical University of Ostrava, 17. listopadu 15/2172; 708 33, Ostrava; CZ, e-mail: karel.frydrysek@vsb.cz



modelling of the mechanical contact between the bit and the platinum ore and its evaluation (i.e. practical application in the mining technology), see Fig. 2. However, material properties of the ore have a large stochastic variability. Hence, the stochastic approach (i.e. SBRA Method in combination with FEM is applied). MSC.Marc/Mentat software was used in modelling this problem.

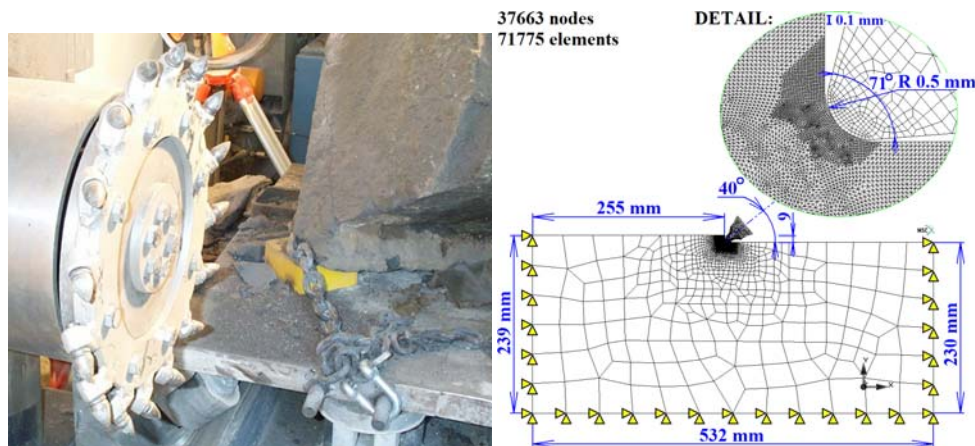


Fig. 2: Typical example of mechanical interaction between bits and hard rock (ore disintegration process) and its solution via FEM.

The bit moves into the ore with the prescribed time dependent function and subsequently disintegrates it. When the bit moves into the ore (i.e. a mechanical contact occurs between the bit and the ore) the stresses (i.e. the equivalent von Mises stresses) in the ore increase. When the equivalent stress is greater than the tensile strength in some elements of the ore, then these elements break off. Hence, a part of the ore disintegrates. This is done by deactivating the elements, see Fig. 3.

The ore material is elasto-plastic with isotropic hardening rule. The probabilistic inputs, i.e. elastic properties (Modulus of elasticity  $E$  and Poisson's ratio  $\mu$ ) and plastic properties (yield stress  $R_p$  and fracture stress  $R_m$ ) are described by bounded histograms, see Fig. 4.

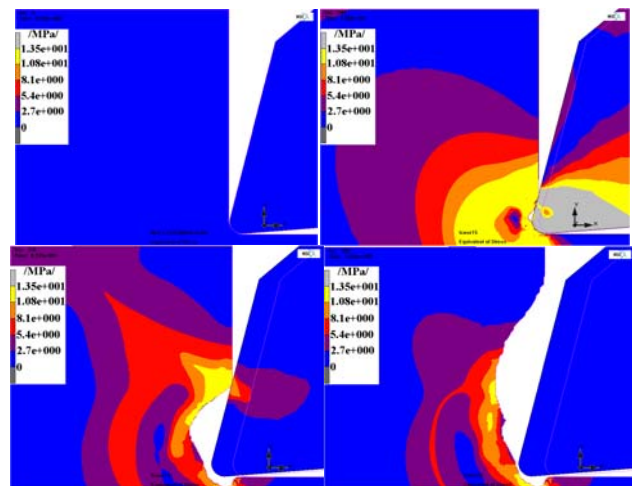


Fig. 3: Disintegration of the ore and movement of the bit (equivalent von Mises stresses distributions).

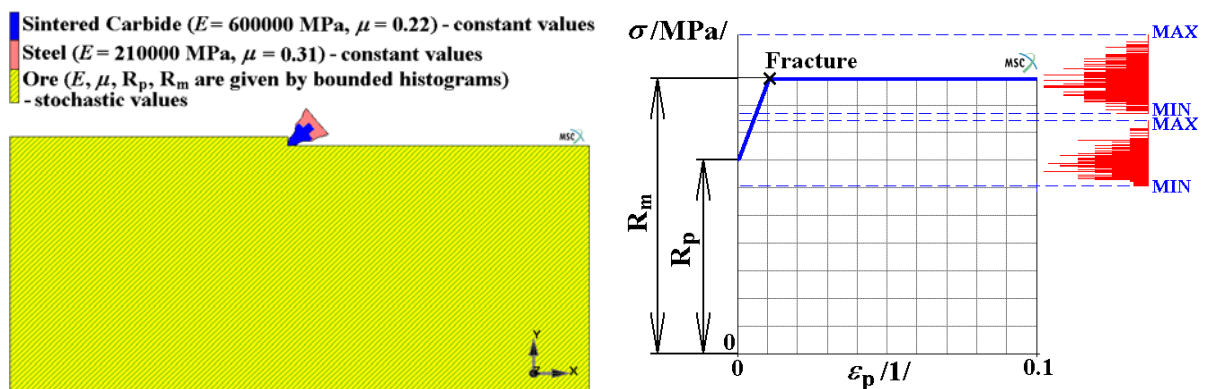


Fig. 4: Material properties (probabilistic inputs).

The results (acquired by SBRA method in combination with FEM) were subsequently statistically evaluated (Anthill, MSC.Marc/Mentat and Mathcad software were used). Because of the material non-linearities, the mechanical contacts with friction, the large number of elements, many iteration steps,

and the choice of 500 Monte Carlo simulations, four parallel computers (with 26 CPU) were used to handle the large computational requirements for this problem.

From the results, the reaction forces can be calculated. These forces act in the bit, see Fig. 5 (distribution of the total reaction forces acquired from 500 Monte Carlo simulations - stochastic result, i.e. print of 500 curves). The calculated maximum forces (i.e. SBRA-FEM solutions, see Fig. 5a) can be compared with the experimental measurements (i.e. compared with a part of Fig. 5b). However, the experimental results also have large variability due to the anisotropic and stochastic properties of the material and due to the large variability of the reaction forces.

All the results presented here were applied for optimizing and redesigning of the cutting bit (excavation tool), see Fig. 6. For more information see references Frydryšek (2009a), Frydryšek (2009b) and Frydryšek (2009c).

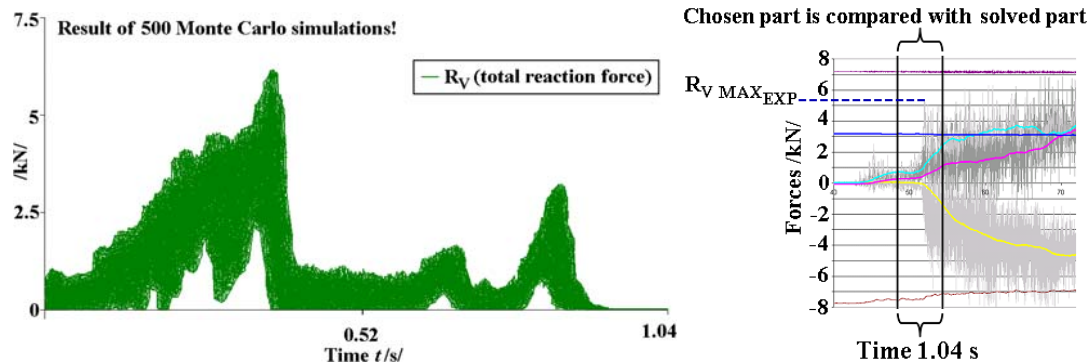


Fig. 5: Calculated reaction forces in the bit (probabilistic approach) and their measurements.

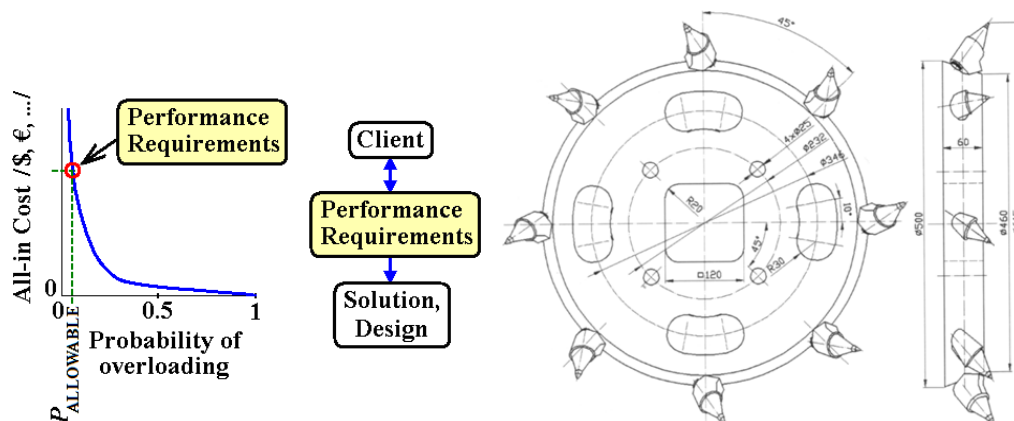


Fig. 6: Definition of the acceptable probability of overloading and final shape of excavation tool for platinum ore disintegration process.

### 3. Designing of external fixators applied for the treatment of open and unstable fractures

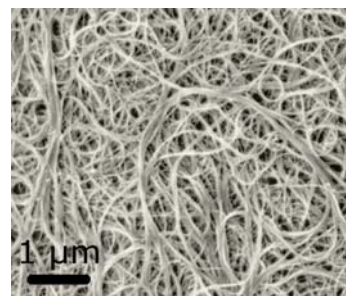
According to the current studies and research, performed at VŠB – Technical University of Ostrava and Traumatology Centre of the University Hospital of Ostrava (Ostrava, Czech Republic), for example see references Frydryšek & Pleva (2010), Madeja & Pleva (2009), Pleva (1999) and Rozum (2008), the current design of external fixators must be modified, see Fig. 7. Fixators can be applied in traumatology, surgery and orthopaedics. Such as treatment of open and unstable (complicated) fractures, limb lengthening, deformity correction, consequences of poliomyelitis, foot deformities, hip reconstructions, for treatment of humans and animals etc. However, there are real needs to make a modern design of fixators which satisfy new trends and demands in medicine, see Frydryšek & Pleva (2010). These demands, which are mutually



Fig. 7: Design of external fixators a) based on metals - current design, heavier, expensive, etc. b) based on reinforced polymers - new design, lighter, cheap, more friendly etc.).

connected, should be solved by:

1. Applications of new smart materials (The outer parts of fixators must be x-ray invisible - which leads to shortening the operating time and reducing the radiation exposure of patients and surgeons. Antibacterial protection - application of nanotechnologies on the surface of the outer parts of the fixators to prevent or reduce possible infection. Weight optimization).
2. New design (according to shape, ecological perspective, patient's comfort, reducing the time of the operation, reducing the overall cost, "friendly-looking design").
3. Measuring of the real loadings (strain gauges etc.).
4. Numerical modelling and experiments (i.e. SBRA application, FEM etc., to avoid the overloading).



*Fig. 8: CNT bundles.*

It is possible to satisfy all these demands by a new composite materials using proper polymers reinforced by the carbon nanotubes (CNT), because some current solutions based on light metals (aluminium, titanium etc.) are heavy and visible in x-ray diagnostic, see Fig. 7 and 8. New proposed design cannot be more specified here. The reason for this are the business secrets.

#### 4. Conclusions

Application of the SBRA Method in the area of rock mechanics (hard rock disintegration process - design of excavation tool) and biomechanics (design of external fixators in traumatology) were reported. Application of the SBRA method is a modern and innovative trend in engineering.

#### Acknowledgement

This work was supported by the Ministry of Industry and Trade of the Czech Republic as the part of project № MPO FR-TI3/818 named "External Fixation".

#### References

- Frydryšek, K. (2009a) Application of Probabilistic SBRA Method in the Scientific and Technical Practice, inaugural dissertation in the branch of Applied Mechanics, written in Czech language, Faculty of Mechanical Engineering, VŠB-Technical University of Ostrava, Ostrava, Czech Republic, pp.144.
- Frydryšek, K. (2009b) Simulation-Based Reliability Assessment Method and FEM Applied for the Platinum Ore Disintegration Process, In: Applied Simulation and Modelling, Palma de Mallorca, Spain, CD-ROM, ISBN: 978-0-88986-808-3, pp.148-153.
- Frydryšek, K. (2009c) Stochastic Solution and Evaluation of the Ore Disintegration Process, In: Proceedings of the 2009 International Conference on Scientific Computing CSC2009, ISBN: 1-60132-098-1, CSREA Press, Las Vegas, USA, pp.40-46.
- Frydryšek, K., Pleva, L., Košťál, P. (2010) New Ways for Designing External Fixators Intended for the Treatment of Open and Unstable Fractures, In: "Applied Mechanics 2010" 12<sup>th</sup> International Scientific Conference (Proceedings), Department of Applied Mechanics, Faculty of Mechanical Engineering, Technical University of Liberec, Liberec, Czech Republic, ISBN 978-80-7372-586-0, pp.43-47.
- Haldar, A., Mahadevan, S. (2001) Probability, Reliability and Statistical Methods in Engineering Design, John Wiley & Sons, Inc, ISBN 0-471-33119-8, New York, USA.
- Madeja, R., Pleva, L., Vávrová, P. (2009) Navigation in Traumatology, Úraz. chir. 17, 2009, no. 3, pp.1-6.
- Marek, P., Brozzetti, J., Guštar, M., Tikalsky, P. (2003) Probabilistic Assessment of Structures Using Monte Carlo Simulation Background, Exercises and Software, (2nd extended edition), ISBN 80-86246-19-1, ITAM CAS, Prague, Czech Republic.
- Marek, P., Guštar, M., Anagnos, T. (1995) Simulation-Based Reliability Assessment For Structural Engineers, CRC Press, Boca Raton, USA, ISBN 0-8493-8286-6.
- Pleva, L. (1999) External Fixator for Treatment of Acetabulum Fractures, final report of the project IGA MZ ČR, reg. č. 3522-4, written in Czech language, FNŠP – Ostrava-Poruba, Czech Republic, pp.77.
- Rozum, K. (2008) External Fixators for the Treatment Open Unstable Fractures, inaugural work written in Czech language, Faculty of Mechanical Engineering, VŠB – Technical University of Ostrava, Czech Republic, ISBN 978-80-248-1670-8, pp.43.



## PROBABILITY OF DESTRUCTIONS OF CERAMICS USING WEIBULL'S THEORY

V. Fuis<sup>\*</sup>, M. Málek<sup>\*\*</sup>, P. Janíček<sup>\*\*</sup>

**Abstract:** *The probability calculation using two variants of Weibull weakest-link theory is presented in this article. The first variant assumed only one tensile stress (the first principal stress  $\sigma_1$ ) and the second variant assumed all three principal stresses in the ceramic component.*

**Keywords:** *Computational modeling, ceramic head, in vivo destructions, hip joint endoprosthesis, Weibull theory.*

### 1. Introduction

Fracturing of metal materials in a fragile condition is assessed by fragile fracture based on the condition of fragile strength. It states that the limit condition of fragile strength occurs when reduced stress, corresponding to the condition at hand, equals the fragile strength limit. Such concept can be perceived as the first level of assessment of its fragile fracture for the ceramics. Higher levels of assessment involve taking into account non-homogeneity of ceramic structure in the sense that it contains numerous micro-failures (pores, cavities and cracks) that increase susceptibility to fragile fracturing. For assessment of fracturing of ceramics cohesion we must use probability approach respecting stochastic division of micro-fractures in the ceramics body volume. This approach describes origination of the limit condition of fragile fracture the so-called „probability of destruction“. This is a statistic approach to destruction of ceramics. There are various statistic reliability approaches. One is the Weibull's weakest-link theory (Weibull, 1939), based on a very simplified assumption that a reliability-assessed ceramics body is perceived as a system consisting of many elements (Andreasen, 1994), (Bush, 1993). If in any elements of the body there originates a stress that causes, under existing physical properties of the ceramics, uncontrolled spreading of a fragile fracture in the element, it usually results in a fragile destruction to the entire body. The issue of ceramics body reliability in view of destruction of its integrity was thus converted to the determination of probability of destruction  $P_f$  regarding individual elements of the body. Due to the accidental distribution of defects in the volume of bodies made of ceramic materials, physical properties of individual micro-volumes of these materials differ and thus various micro-volumes have different real fragile strength. It is being proved that statistical distribution of the probability of ceramic materials destructions is of Weibull's type. More micro-volumes in the body increase probability that the body contains a „weak link“, in which the fragile destruction is initiated. Probability of failure of ceramic bodies in the form of fragile destruction is the function of all micro-volumes in the body with various stresses. From the aforementioned facts, W. Weibull (Weibull, 1939) deduced mathematical formulae governing the probability of destruction in ceramic bodies for various „stress levels“ originating in bodies as a result of external load. In the simpler model, he considered only 1-axis tensile stress, on the higher level he worked with real 3-axis stress.

---

<sup>\*</sup> Ing. Vladimír Fuis, Ph.D.: Centre of Mechatronics – Institute of Thermomechanics and Faculty of Mechanical Engineering, Brno University of Technology, Technická 2, 616 69, Brno, CZ, e-mail: fuis@fme.vutbr.cz

<sup>\*\*</sup> Ing. Michal Málek and prof. Ing. Přemysl Janíček, DrSc.: Institute of Solid Mechanics, Mechatronics and Biomechanics, Faculty of Mechanical Engineering, Brno University of Technology, Technická 2, 616 69 Brno, CZ, e-mail: ymalek04@stud.fme.vutbr.cz, janicek@fme.vutbr.cz

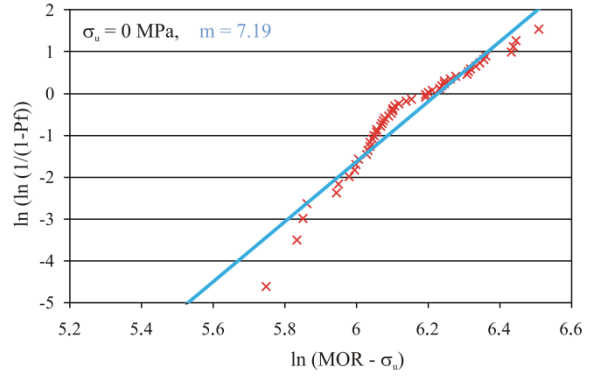
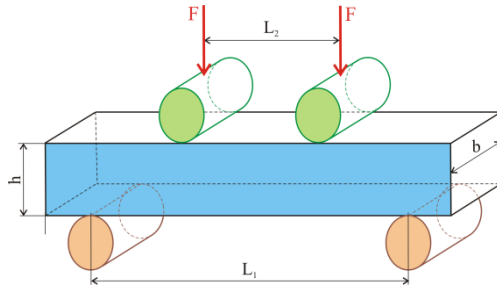
## 2. Weibull's model of destruction probability for a 1-axis tensile stress

This model has been elaborated for two modifications of Weibull's theory: three-parametric (contains three ceramics material parameters) and two-parametric (with two parameters). The original Weibull's formulae for destruction probability  $P_f$  were deduced in integral shape (Bush, 1993). Since stress, one of the input quantities in the Weibull's theory, is determined using the finite elements method, Weibull's formulae are quoted in the differential shape here. Three-parametric Weibull's formula is as follows:

$$P_f = 1 - e^{-\sum_{i=1}^n \left( \frac{\sigma_i - \sigma_u}{\sigma_0} \right)^m \Delta V_i}, \sigma_i > \sigma_u \quad (1)$$

where  $n$  number of elements in the body,  $\sigma_i$  first principal stress in the  $i$ -th body element,  $\Delta V_i$  volume of the  $i$ -th body element,  $\sigma_u$  is stress [MPa], under which material is not disrupted,  $\sigma_0$  is normalized material strength [MPa.m<sup>3/m</sup>] of the material volume unit,  $m$  Weibull's modulus.

Quantities  $\sigma_u$ ,  $\sigma_0$ ,  $m$  can be considered material properties of ceramics. For two-parametric Weibull's approach,  $\sigma_u = 0$ , which means that material destruction is possible for any tensile (positive) values of the first principal stress (Bush, 1993). Two-parametric analysis is used more frequently, because it provides more conservative results than the three-parametric analysis. Note to the Weibull's modulus  $m$ : The modulus expresses the measure of dispersion of the ceramic material strength. It is defined as a slope of the regression line in Fig. 2 for real 3-point bending experiments ( $h = b = 2.5$  mm,  $L_1 = 10$



mm,  $L_2 = 0$  mm) (Fuis, 2007):

$$\ln\left(\ln \frac{1}{1-P_f}\right) \quad \text{versus} \quad \ln(\text{MOR}), \quad \text{where} \quad \text{MOR} = \frac{3(L_1 - L_2)F}{2h^2b}. \quad (2)$$

Fig. 1: Modulus of rupture test dimensions.

Fig. 2: Weibull plot of the normalized MOR data.

The MOR (Modulus of Rupture) quantity is the maximum flexural stress under which destruction occurs in four-point bending (Fig. 1). Measuring to determine  $m$  is realized on many samples (at least 35). Method of  $P_f$  probability determination is shown in (Bush, 1993).

## 3. Weibull's model of destruction probability for a 3-axis general stress

Apart from the aforementioned two and three-parametric analysis of ceramics destruction probability for 1-axis stress, Weibull also designed a modification of destruction probability valid for general spatial (three-axis) stress. He proceeded from the hypothesis that in spherical pores in ceramics, maximum stress around the pore is independent of its size (Andreasen, 1994). He also assumed that destruction of ceramics is caused by a combination of normal stress  $\sigma_n$  (impacting fractures perpendicularly and resulting in the 1<sup>st</sup> fracture mode) and maximum shear stress  $\tau$  (acting in the fracture plane and resulting in 2<sup>nd</sup> fracture mode). Both these stresses are the functions of principal stresses  $\sigma_1$ ,  $\sigma_2$ ,  $\sigma_3$ . This is standard approach for many physical conditions.

In the final version proposed by Weibull to analyze ceramics destruction probability, he neglected the impact of shear stress on the destruction (Weibull, 1939). Yet the aforementioned method is used frequently. He proposed the following formula to respect the impact of general spatial stress on the probability of destruction:

$$P_f = 1 - e^{-\int_V \left\{ \frac{2m+1}{2\pi\sigma_0^m} \int_0^{2\pi} \int_0^{\pi/2} \left[ \cos^2 \Phi (\sigma_1 \cos^2 \Psi + \sigma_2 \sin^2 \Psi) + \sigma_3 \sin^2 \Phi \right]^m \cos \Phi d\Phi d\Psi \right\} dV} \quad (3)$$

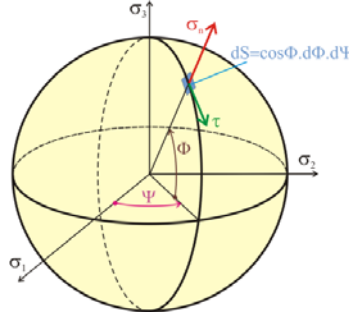


Fig. 3: Unit radius sphere representing all possible flaw/crack orientations.

#### 4. Comparative analyses of Weibull's model for 1-axis and 3-axis stress

Comparative analyses were carried out for the following material characteristics: Weibull's modulus  $m = 7.19$  (Fig. 2), normalized material strength of material volume unit  $\sigma_0 = 473,8 \text{ [MPa.m}^{3/7.19}]$  (Fuis, 2007). Determination of destruction probability according to Weibull's formulae (1) or (3) always requires integration via a corresponding body. For Weibull's model for 3-axis stress, it is integration in the relation (3), which is time-consuming with the current algorithms. To simplify the testing we chose a  $10 \times 10 \times 10 \text{ mm}$  cube-shaped model body (Figs. 4 – 6 – (Málek, 2010)).

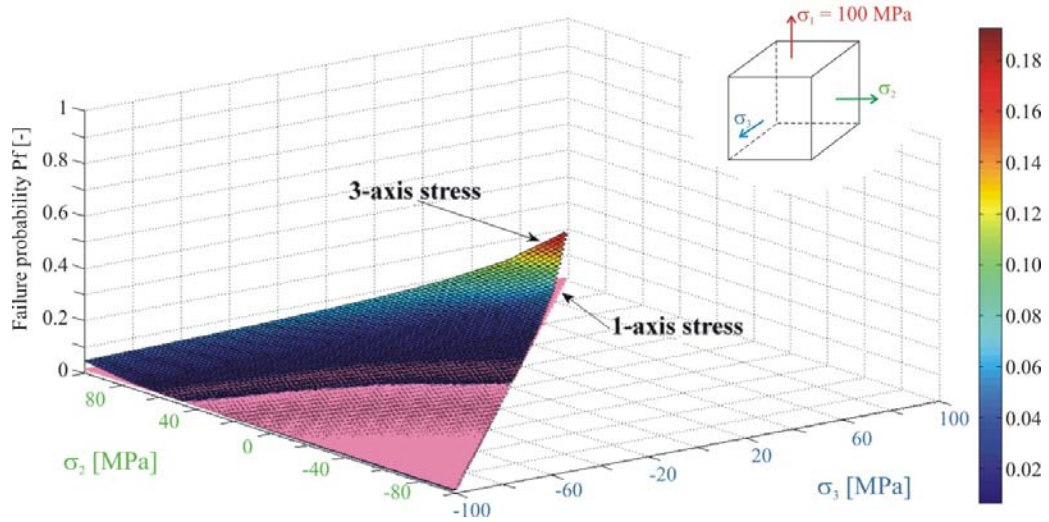


Fig. 4: Surfaces of failure probability in Weibull's model for 3-axis stress ( $\sigma_1 = 100 \text{ MPa}$ ).

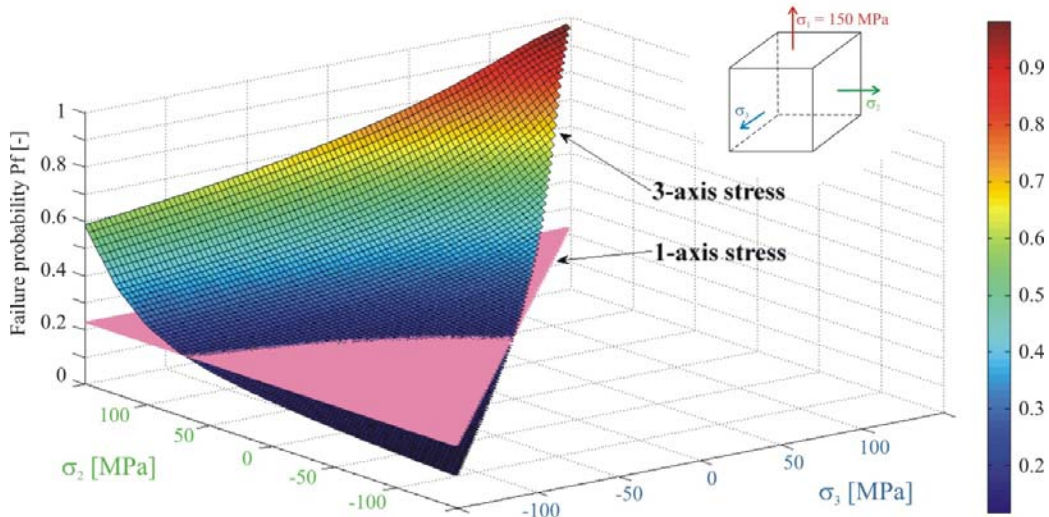


Fig. 5: Surfaces of failure probability in Weibull's model for 3-axis stress ( $\sigma_1 = 150 \text{ MPa}$ ).

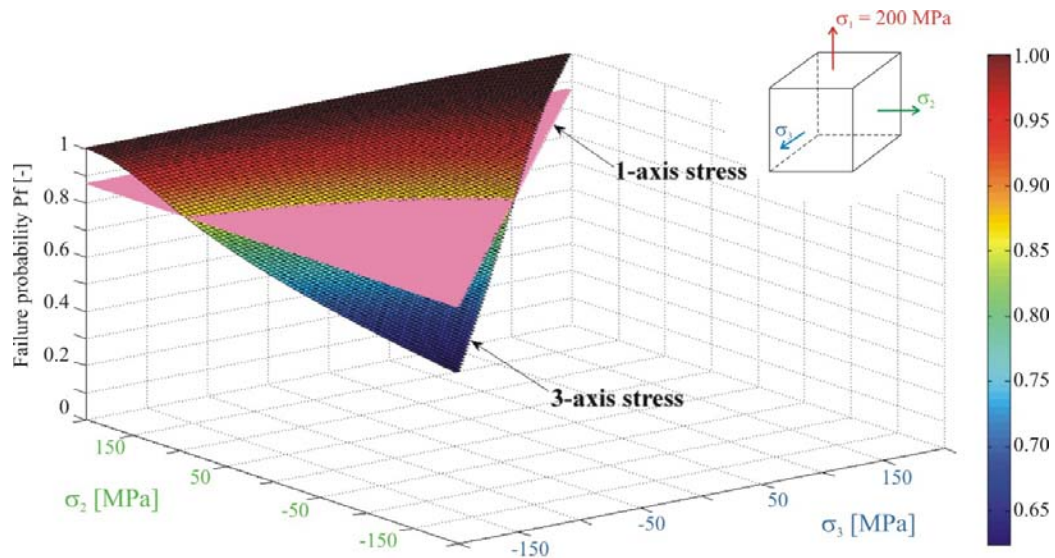


Fig. 6: Surfaces of failure probability in Weibull's model for 3-axis stress ( $\sigma_1 = 200$  MPa).

We analyzed the following three stress variants (with different first principal stresses (Málek, 2010)):

- the first principal stress  $\sigma_1 = 100$  MPa, another principal stresses  $\sigma_2$  and  $\sigma_3$  are taken the value ( $-100$  MPa to  $+100$  MPa) – Fig. 4,
- the first principal stress  $\sigma_1 = 150$  MPa, another principal stresses  $\sigma_2$  and  $\sigma_3$  are taken the value ( $-150$  MPa to  $+150$  MPa) – Fig. 5,
- the first principal stress  $\sigma_1 = 200$  MPa, another principal stresses  $\sigma_2$  and  $\sigma_3$  are taken the value ( $-200$  MPa to  $+200$  MPa) – Fig. 6.

This covered all types of stresses: 3-axis general ( $\sigma_1 \neq \sigma_2 \neq \sigma_3 \neq 0$ ), 3-axis semi-even ( $\sigma_1 = \sigma_2 \neq \sigma_3 \neq 0$ ), 3-axis even tensile ( $\sigma_1 = \sigma_2 = \sigma_3 \neq 0$ ), 2-axis general ( $\sigma_1 \neq \sigma_2 \neq 0, \sigma_3 = 0$ ), 2-axis even tensile ( $\sigma_1 = \sigma_2 \neq 0, \sigma_3 = 0$ ), shear ( $\sigma_1 \neq 0, \sigma_3 = -\sigma_1, \sigma_2 = 0$ ) that were homogenous in the entire cube.

Owing to identical volumes and homogenous stress in all cube elements it sufficed to determine destruction probability in a single element and its multiplication by the total number of cube elements gave us the destruction probability for the entire cube.

Dependences of destruction probability of the model cube on stresses  $\sigma_1, \sigma_2, \sigma_3$  for 1<sup>st</sup> to 3<sup>rd</sup> version (i.e. for Weibull's 3-axis stress model) are shown in Figs. 4 - 6. These graphs also show dependence of model cube destruction probability for the two-parameter model for 1-axis stress, i.e. for the first principal tensile stress (Eq. (1) with  $\sigma_u = 0$ ). Figs. 4 - 6 reveal that the second and third stresses substantially affect destruction probability in three-axis stress when all three principal stresses are tensile (positive).

## Acknowledgement

This paper was prepared with the support of the project AV0Z20760514.

## References

- Andreasen, J.H. (1994) Reliability-based design of ceramics. *Materials and Design*. Vol. 15, Nr. 1, p. 3-13.
- Bush, D.R. (1993) Designing ceramic components for structural applications. *Journal of Materials Engineering and Performance*. Vol. 2 (6), 1993, p. 851-862.
- Fuis V, Navrat T, Hlavon P, et al. (2007) Reliability of the Ceramic Head of the Total Hip Joint Endoprosthesis Using Weibull's Weakest-link Theory. *IFMBE Proc*. Vol. 14, Congress on Medical Physics and Biomedical Engineering, Seoul, South Korea, 2006, pp 2941-2944.
- Málek, M. (2010) Reliability analysis of the hip point endoprosthesis ceramic head. Diploma work, Brno University of Technology, Faculty of Mechanical Engineering, 2010, 75 pages, (in Czech).
- Weibull, W. (1939) A statistical theory of the strength of material. *R. Swedish Acad. Eng. Sci. Proc.*, No. 151, p. 1-45.



## **ANALYSIS OF STEEL STRUCTURE VIBRATIONS OF THE BUCKET WHEEL EXCAVATOR SCHRS 1320**

**J. Gottvald\***

**Abstract:** *In case of bucket wheel excavators (BWE) the digging forces are dominant sources of vibrations. The influence of digging forces on steel structures of upper part of BWE depends on position of terrace. Structural configuration of BWE is different while cutting terrace on the ground level or higher level. It causes changes of stiffness of steel structure and changes of natural frequencies of BWE. More over location of the resultant of digging forces changes too. Huge measurement of vibrations of the steel structure of upper part of BWE SchRs 1320 was made during operation. The paper deals with the influence of changes in locations of the bucket wheel boom to vibrations of the steel structure of upper part of BWE SchRs 1320.*

**Keywords:** *Bucket wheel excavator, Natural frequency, Vibrations, Accelerometer, Fourier transform, Frequency, Amplitude, Measuring, Time-frequency transform.*

### **1. Introduction**

Machines for surface mining such as bucket wheel excavators (BWE) are heavily dynamically loaded during operating. Their steel structures and steel components are continually loaded dependently on geological situations during surface mining, requirements of plans of mining i.e. maximum usage of machine. The material from which the machines or their components are made is damaged by fatigue. The fatigue damage can cause failure of the machines or of some of their significant components, see e.g. (Bošnjak et al., 2010; Savković et al., 2011).

It is of a great importance to the operator of mining machines to their machines were in use as long as possible, they would also like to avoid machines failures which are connected with enormous economical loss and in the worst cases with losses of human lives. Their aim is also to avoid ecological losses. Dominant factors that influence life time of structures can be studied by methods of uncertainty and sensitivity analysis see e.g. (Kala 2009; Melcher et al., 2009). We can expect some influence of higher order interaction effects of input factors on carrying capacity (Kala, 2010). Results of these studies provide data, which are significant to decision-making about control services see, e.g. (Kala et al., 2010). In general priority should be given to controls and consequently to predictions of residual life times of significant components of structures (Kala 2008) as well as whole structures see e.g. (Vujic et al., 2010).

In case of bucket wheel excavators the digging forces are the dominant source of vibrations. It is desirable to investigate the influence of digging forces on steel structure of BWE and on any significant components. Progress of digging forces depends on geological profile of block. Occurrences of stone bands have undesirable influence on steel structure vibrations and depreciation of machine. It is possible to predict this occurrence and to optimize the working process. Another aspect that has significant influence on dynamical response of steel structure of BWE is their structural setting. BWEs are machines that change the structural setting during their working process. They change locations of bucket wheel boom what is of influence on situations of terraces in working block as well as on location of the resultant of the digging forces.

---

\* Ing. Jakub Gottvald: VÍTKOVICE ÚAM a.s., Mezírka 775/1; 602 00, Brno; CZ, e-mail: jakub@gottvald.eu

## 2. Measuring of vibrations of bucket wheel excavator SchRs 1320

On the BWE SchRs 1320 vibrations of upper part of steel structure were continuously measured. Measuring was made during one mining cycle of the whole block, which was mined by terrace cutting method. The block was 20.5 m high and was divided into four terraces. The first terrace was 7.2 m high, the second was 4.9 m high, the third was 5.2 m high, and the last, the forth, was 3.2 m high. These dimensions were computed from the record of locations of the bucket wheel boom, which were measured for operator with other data; details about measuring are described in (Fries et al., 2010). The whole measured signal was divided into individual benches in terrace and directions of slewing of vibrations were differentiated, too. For evaluation of measuring FFT analysis with combination of time-frequency (wavelet) method were used, which gave us useful information about changes of frequencies in time. Figs. 2 - 17 show obtained results. On Fig. 1 and others we can see changes of some frequency peaks that are dependent on geometrical changes of mined benches and of some geological anomaly, too. Fig. 4 and subsequent others show results of FTT analysis, these results are more convenient for description of peaks values, however information on time dependence is lost. On figures below are data that were measured by accelerometer A\_06z, which was situated in right bearing of bucket wheel shaft, see scheme on Fig. 1, for details of other measured places see (Fries et al., 2010; Gottvald, 2010).

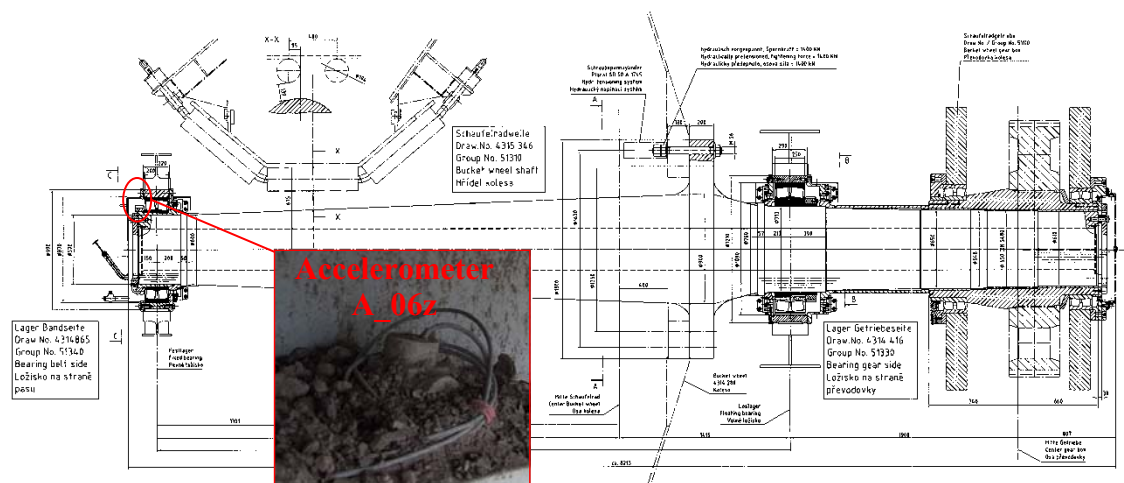


Fig. 1: Scheme of bucket wheel shaft with accelerometer A\_06z.

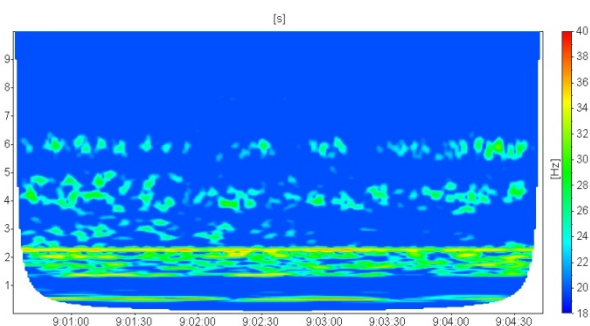
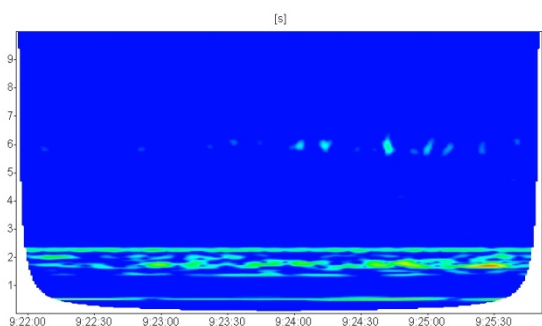


Fig. 2: 1<sup>st</sup> terrace – slewing to the left (1<sup>st</sup> bench). Fig. 3: 1<sup>st</sup> terrace – slewing to the right (2<sup>nd</sup> bench).

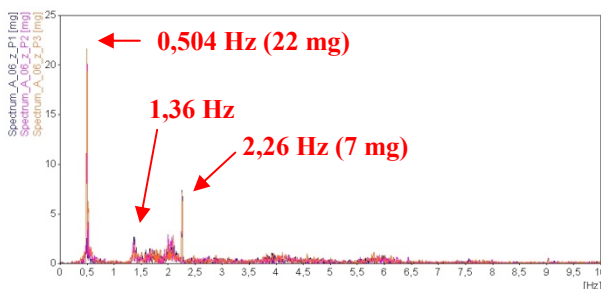
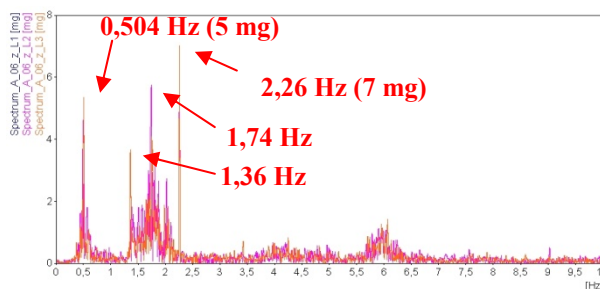


Fig. 4: Frequency spectrum – 1<sup>st</sup> terrace, slewing to the left.

Fig. 5: Frequency spectrum – 1<sup>st</sup> terrace, slewing to the right.

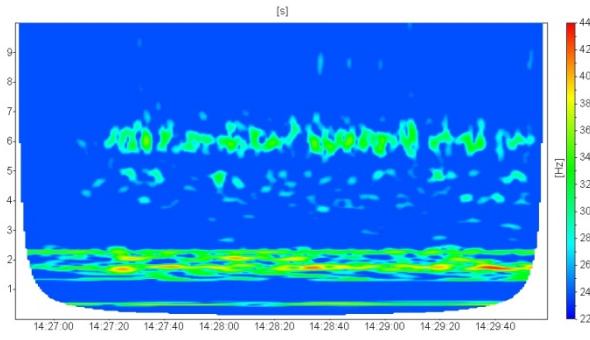


Fig. 6: 2<sup>nd</sup> terrace, slewing to the left (1<sup>st</sup> bench).

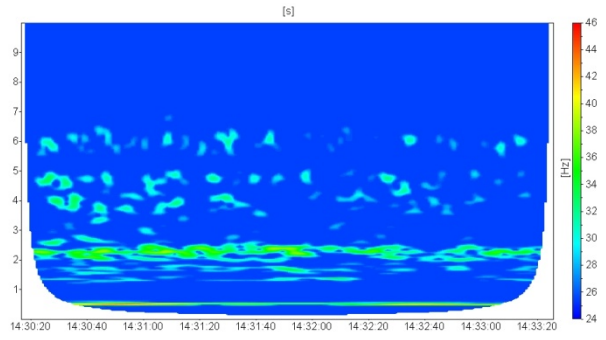


Fig. 7: 2<sup>nd</sup> terrace, slewing to the right (2<sup>nd</sup> bench).

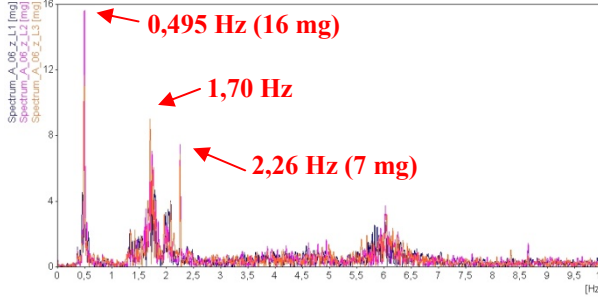


Fig. 8: Frequency spectrum – 2<sup>nd</sup> terrace, slewing to the left.

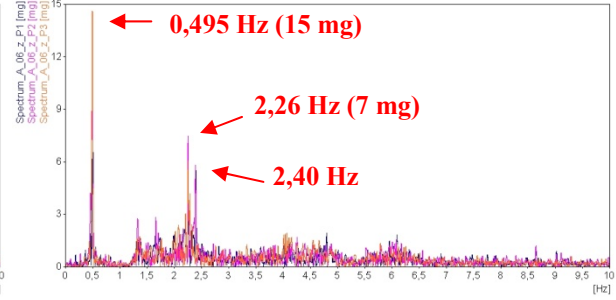


Fig. 9: Frequency spectrum – 2<sup>nd</sup> terrace, slewing to the right.

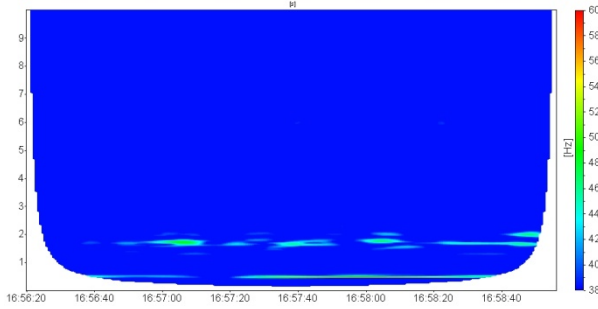


Fig. 10: 3<sup>rd</sup> terrace, slewing to the left (1<sup>st</sup> bench.)

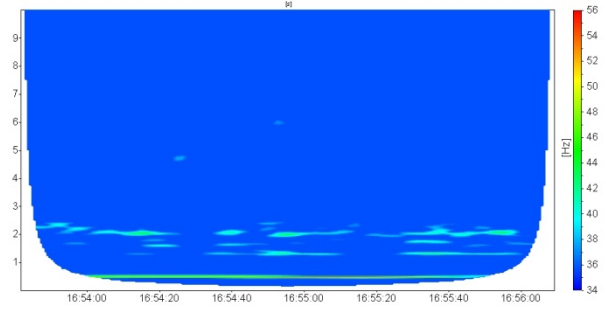


Fig. 11: 3<sup>rd</sup> terrace, slewing to the right (2<sup>nd</sup> bench).

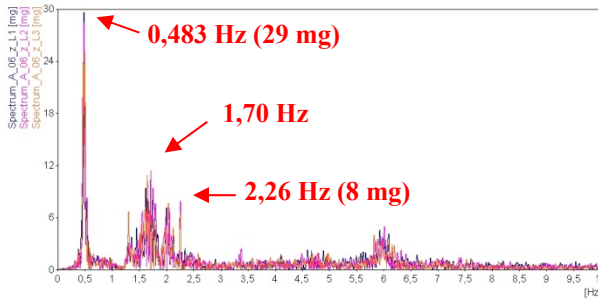


Fig. 12: Frequency spectrum – 3<sup>rd</sup> terrace, slewing to the left.

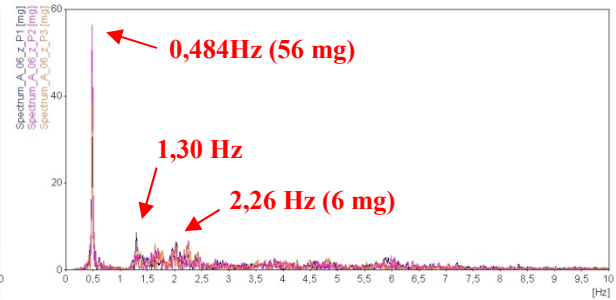


Fig. 13: Frequency spectrum – 3<sup>rd</sup> terrace, slewing to the right.

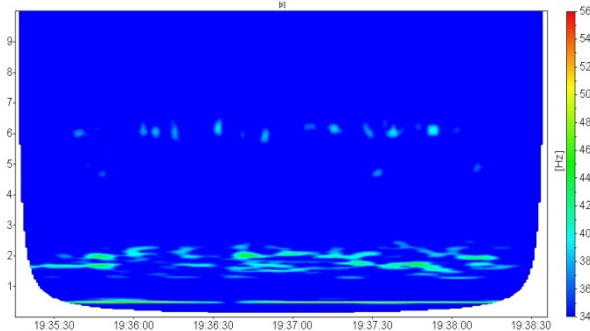


Fig. 14: 4<sup>th</sup> terrace, slewing to the left (1<sup>st</sup> bench).

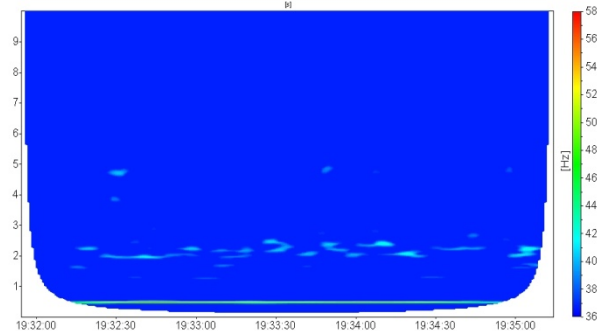


Fig. 15: 4<sup>th</sup> terrace, slewing to the right (2<sup>nd</sup> bench).

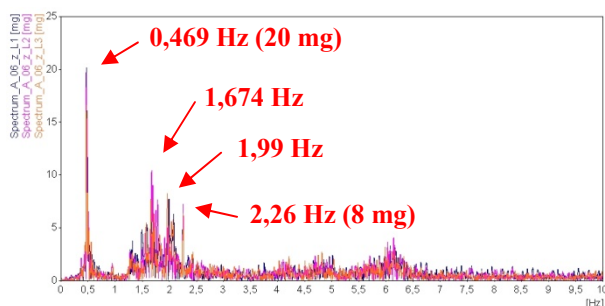


Fig. 16: Frequency spectrum – 4<sup>th</sup> terrace, slewing to the left.

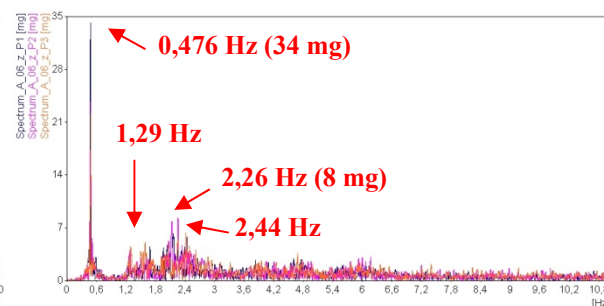


Fig. 17: Frequency spectrum – 4<sup>th</sup> terrace, slewing to the right.

### 3. Conclusions

On the basis of evaluation of measuring it could be said that first natural frequency of BWE SchRs 1320 in the first terrace is 0.504 Hz, in the second terrace is 0.495 Hz, in the third terrace is 0.483 Hz, and in the fourth terrace is 0.469 Hz. The values of measured natural frequencies correspond with previous measuring and computing of natural frequencies presented in (Gottvald, 2010). Declining trend of natural frequencies acknowledges simulations presented in (Fries et al., 2010). From frequency spectrums it appears that amplitude has opposite tendency and significantly decreases. This situation corresponds with resonant curves presented in (Fries et al., 2010).

In measured signals frequency 2.26 Hz was inducted. This was rotational frequency of 26 buckets on the wheel during mining. The frequency had constant amplitude c. 8 mg ( $1 \text{ mg} = 9.81 \times 10^{-3} \text{ m.s}^{-2}$ ). Character of these frequency spectra we can see e.g. on Fig. 4 by FTT analysis, and e.g. on Fig. 2 by time-frequency analysis. The calculated spectrums show domination of the first natural frequency of the BWE SchRs 1320 and confirm the previous results of measuring of the natural frequencies of BWE SchRs 1320, see (Gottvald, 2010).

### Acknowledgement

The author gratefully acknowledges the partial support provided by the Grant Agency of the Academy of Sciences of the CR within the project of AVČR IAA201720901 and support provided by the Ministry of Industry and Trade of the Czech Republic within the project FT-TA4/018.

### References

- Bošnjak, S., Petković, Z., Zrnić, N., Pantelić, M., Obradović, A. (2010) Failure analysis and redesign of the bucket wheel excavator two-wheel bogie, *Engineering Failure Analysis* 17: 473–485, doi:10.1016/j.engfailanal.2009.09.007.
- Fries, J., Gottvald, J., Helebrant, F., Jurman, J., Vejvoda, S. (2010) Selected problems from the operation of bucket wheel excavators. Ostrava: Publishing Centre of Technical University of Ostrava. 210 p. ISBN 978-80-248-2359-1 (in Czech).
- Gottvald, J. (2010) The calculation and measurement of the natural frequencies of the bucket wheel excavator SchRs 1320/4x30, *Transport* 25(3): 269–277, doi: 10.3846 / transport.2010.33.
- Kala, Z. (2009) Sensitivity assessment of steel members under compression, *Engineering Structures*, 31, 6, pp.1344–1348, doi:10.1016/j.engstruct.2008.04.001.
- Kala, Z., Puklický, L., Omishore, A., Karmazínová, M. & Melcher, J. (2010) Stability problems of steel-concrete members composed of high strength materials. *Journal of Civil Engineering and Management*, 16, 3, pp.352–362, doi: 10.3846/jcem.2010.40.
- Kala, Z. (2010) Sensitivity analysis of stability problems of steel plane frames, *Thin-Walled Structures*, 49, 5, pp.645–651, doi:10.1016/j.tws.2010.09.006.
- Melcher, J., Škaloud, M., Kala, Z. & Karmazínová, M. (2009) Sensitivity and statistical analysis within the elaboration of steel plated girder resistance. *Advanced Steel Construction*, 5, 2, pp.120–126.
- Savković, M., Gašić, M., Arsić, M., Petrović, R. (2011) Analysis of the axle fracture of the bucket wheel excavator, *Engineering Failure Analysis* 18: 433–44, doi:10.1016/j.engfailanal.2010.09.031.
- Vujic, S., Miljanovic, I., Maksimovic, S., Milutinovic, A., Benovic, T., Hudej, M., Dimitrijevic, B., Cebasek, V., Gajic, G. (2010) Optimal dynamic management of exploration life of the mining machinery: models with undefined interval, *Journal of Mining Science*, Vol. 46, No. 4, doi: 10.1007/s10913-010-0053-2.



## AN ENHANCED APPROACH IN MOTION DETECTION OF HUMAN MOVEMENTS

A. Guran<sup>\*</sup>, A. Vahidi-Shams<sup>\*</sup>

**Abstract:** *In this paper, we will present a robust and fast motion detection approach, which can localize and keeps track an object in motion under hard real-time constraints. To eliminate the undesirable problems such as lighting and Shadows we used some techniques. The enhanced digital image is very closer to the scene perceived by the human visual system. Furthermore, we could decrease the effect of little and Periodic movement in back ground such as the leaves move in the wind, Moving shadow or Sea wave in Presence or absence of the movement objects. Experiment results to certify this efficiency showed desirable process time and performed with high accuracy. Introduced Model might be advantageous in various tasks of object tracking such as Analysis of Fundamental Human Movements.*

**Keywords:** *Computer vision, human detection, motion detection, human movements.*

### 1. Introduction

Currently, motion detection and human interaction detection is one of the most active research topics in machine vision (Azad et al., 2007, Bandouch and Beetz, 2009), which used in wide spectrum of applications in many areas such as human-robot interaction, smart surveillance, virtual reality and perceptual-interface (Krüger et al., 2007; Kulic et al., 2008). An extensive literature exists regarding motion analysis in video streams using fixed camera. There are various numbers of approaches involving statistical analysis of motion suggested over the years. Some publications discuss the effect of camera, light-setting and the color spaces have in the process (Blostein and Huang, 1991, Deutscher and Reid, 2005). Various techniques for moving object detection have been proposed. Commonly three approaches are background subtraction, temporal differencing and optical flow. Background subtraction is the most commonly used approach in presence of still cameras. The principle of this approach is to use a background model and compare the current frame with a reference. The foreground objects present in the scene are detected in this way. The statistical model based on the background subtraction is flexible and fast, but in this method the background scene and the camera are required to be stationary well (Schuldt et al., 2004). Temporal differencing is based on frames difference that attempts to detect moving regions by making use of the difference of consecutive two frames in a video sequence. This approach is very adaptive to dynamic environments, but in general performs a poor job of extracting the complete forms of certain types of moving objects (Bobick and Davis, 2001). The other approach is the optical flow which is an approximation of the local image movement and specifies how much each frame pixel moves between adjacent images. According to the smoothness constraint, the corresponding points in the two successive frames should not move more than a few pixels. For an uncertain environment, this means that the camera motion or background changing should be relatively small. The optical flow based methods are complex, but it can detect the motion accurately even without knowing the background (Yun et al., 2005). Edwin Land coined “Retinex” word for his model of human color vision, combining the retina of the eye and the cerebral cortex of the brain. The retinex Image Enhancement Algorithm is an automatic image enhancement method that enhances a digital image in terms of dynamic range compression, color independence from the spectral distribution of the scene illuminant, and color/lightness rendition. The digital image enhanced by the retinex Image Enhancement Algorithm is much closer to the scene perceived by the human visual system, under all kinds and levels of lighting variations, than the digital image enhanced by any other method. Although retinex models are still widely used in computer

---

<sup>\*</sup> prof. Dr. Ardeshir Guran, Ph.D. and Ing. Afra Vahidi Shams, M.Sc: Institute of Structronics, 275 Slater Street, 9th Floor, Ottawa Canada; e-mails: ardeshir.guran@mail.mcgill.ca, afra.vahidishams@gmail.com

vision, they have been shown not to accurately model human color perception (Land and Mccann, 1971). Periodic motion is ubiquitous in the natural world, with instances ranging from the simple harmonic movement, which could appear in the background of our scene. Also shadows' movement beside motion of targets can decrease accuracy of MDS (motion detector systems). Furthermore, because of our main aim to implement it in embedded DSP(digital signal processor), we needed more robust algorithm that is fairly simple to compute, has the potential to run in real-time, and is relatively immune to noise. Here, we present the modified and developed to eliminate the effects of these undesirable problems. The principal idea in this study is to integrate the benefits of these three above approaches and a robust Model is represented. The principal goal of this algorithmic rule is to separate the background interference and foreground information effectively and discover the moving object accurately.

## 2. Overview of the Method

System presented here was done according to following principles:

- The aim of the system is robust and fast motion detection and tracking for surveillance systems.
- Images are received from a stable or non stable video camera.
- System is localizing movement object on the bases of motion picture analysis in camera view.
- System is designed to work in real time (now on standard PC class computer).

### 2.1. Algorithm Flow

The proposed algorithm consists of seven stages for image acquisition, preprocessing, characteristic extraction and motion detection. Fig. 1 shows the process flow of the proposed robust motion detection algorithm. Each of these stages will be described in detail in the next Section (Shams and Guran, 2011).

## 3. Detailed Algorithm Description

**Step1.** Each image frame is taken from signal source. Since we are analyzing color pictures we got three brightness difference values for each base color (RGB).at this stage, input image is enhanced based on retinex method.

**Step2.** At this stage image is pre-processed. The main aim of it is to make image properties better for generating objects data. Removing shadow improves the accuracy, According to this fact and to do this, we first convert pixel information from the RGB (Red/Green/Blue) color space to the HSV (Hue-Saturation-Value) color space. HSV color space corresponds closely to the human perception of color (Hurlbert, and Wolf, 2002) and it has revealed more accuracy to distinguish shadows. Then, it tries to estimate how the occlusion due to shadow changes the value of H, S and V. The rationale is that cast shadow's occlusion darkens the background pixel and saturate its color.

**Step3.** In this step we needs binary image for entry the next layer, to achieve this goal, all pixels with values below the threshold are set to 0, all those above are set to 1. This is a simple way to remove the effects of any non-linearity in the contrast in the frame. However, the threshold value must be defined. It could be achieved by calculating the threshold based on a histogram of a given differential image. And again filtration is performed, this time using logic or median filters. Threshold can be described by the following equation:

$$Th = \left( \frac{\sum_{x=1}^n \sum_{y=1}^m (x, y)}{n \times m} \right) - \sum_{i=1}^{n \times m} P_i \cdot (img_i - \mu)^2 / 2, \mu = \sum_{i=1}^{n \times m} P_i \cdot img_i \text{ where } n \text{ and } m \text{ are size of image (img)} \quad (1)$$

**Step4.** Differential image is calculated as difference between current frame and current background (in our case last frame). For the first read frame the calculation is not performed, since at this moment the background bitmap is not available.

**Step5.** The aim of this phase to find association between objects form following levels (objects from two following frames of motion picture) and label the object as a movement one, not identified or as matched to some object form the previous level. At first, similar pixels are rejected. Next, for each pixel on current frame list the different pixel from the previous list is selected with the highest value.

**Step6.** Last layer is the background update. The background is then used in this step and updated recurrently. The idea of background generating is based on integration of information inserted by every new frame with background. It is suitable for inhibiting the little periodic movement effects. We repeated for 4 times each as one layer and then repeated for each layer.

**Step7.** At last, Comparison between two layers which shown in Fig. 1 leads to detection of movement objects and area of motion is shown with colorful rectangles. Steps are depicted in Fig. 2.

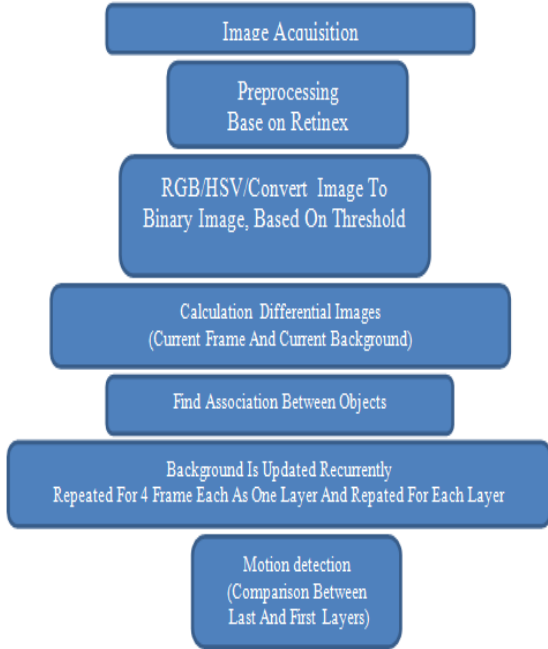


Fig. 1: The flow of algorithm.

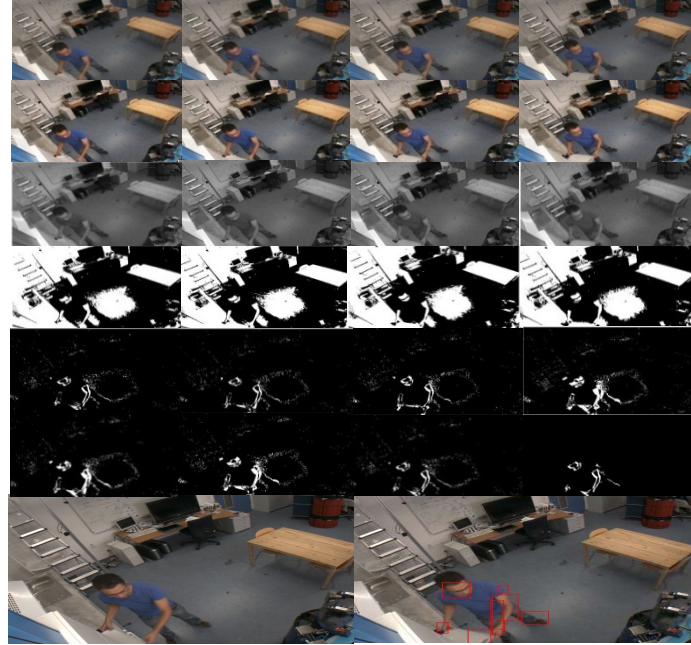


Fig. 2: Four frames and results of steps are depicted from top: a) frame 1 to 4 of each cycle b) enhanced image (Based on Retinex) c) gray value images d) binary images based on threshold e) differential between frames(L1: 1,2 & L2: 2,3 & L3: 3,4 & L4: L1,L2 & L5: L2,L3 & L6: L4,L5).

## 4. Experimental Setup and Results

### 4.1. Experiment 1: human motion detection

We design first experiment to detect human movement. To evaluate our system, we performed several experiments on the TUM kitchen data. The algorithm is implemented in Matlab2010a program. The size of the input video image is 320×240 pixels and the sample rate is about 25 frames per second. In our experiment each cycle just takes about 120 ms time (each 4 frames).

### 4.2. Dataset

The TUM Kitchen Data Set has been recorded in the TUM kitchen (Tenorthet A1, 2009). The recorded (synchronized) data consists of calibrated videos, motion capture data and recordings from the sensor network, and is well-suited for evaluating approaches for motion tracking as well as for activity recognition. In particular, the following modalities are provided: Video data (25 Hz) from four static overhead cameras (Fig. 1) provided as 384x288 pixel RGB color image sequences (JPEG) or compressed video files (AVI). Additionally, full resolution (780x582 pixels) raw Bayer pattern video files are available.

### 4.3. Experiment 2: motion detection under hard real-time constraints

In experiment 1, we saw that the method yielded the best results, which is completely consistent with our expected results. We employed this method to solve motion detection under hard real-time constraints problem. To be able to compare the robustness of this method to solve the little and \periodic movement problem, we repeated the first experiment but with different set of data (Several video frequencies in sea surface as experimental video frequencies). In this experiment we used a video which one Jockey was riding a horse at the beach. Also the robustness to outdoor lighting changes was investigated. The results are relative ideal. Detection of moving targets in different sea surfaces is shown in Fig. 3.





Fig. 3: Human motion detection (top), motion detection under hard real-time constraints (bottom).

## 5. Conclusion

This paper introduces a robust and comparatively accurate method for detecting moving targets, especially for human motion detection, under hard real-time constraints. The particular advantage of the proposed method is that it can be applied to complex scenes, when does not rely on camera stabilization. The results show that it can detect moving targets correctly and be robust even for the noise of shadows and ocean wave. Experiments results show that the method detecting moving targets high efficiency and high accuracy. Also when two or more moving objects are superimposed together, it can detect them as different moving object. Second, because of our aim and with this proposed method this is easily usable for real-time detection. Third, in the condition of complex background, it can detect small targets as well as common targets. However, there are still something need to improve. We believe these problems are important issues in motion detection and more comprehensive study is required to investigate. In the future work, we are going to investigate these complications with more details and also ways of minimizing their effects should be considered in future.

## References

- Azad, P., Ude, A., Asfour, T. & Dillman, R. (2007) Toward an Unified Representation for Imitation of Human Motion on Humanoids, In IEEE International Conference on Robotics and Automation (ICRA). Rome, Italien, April, pp. 2558-2563.
- Bandouch, J. & Beetz, M. (2009) Tracking humans interacting with the environment using efficient hierarchical sampling and layered observation models, IEEE Int. Workshop on Human-Computer Interaction. In conjunction with ICCV2009. Sept. 27 Oct. 4, pp. 2040–2047.
- Bobick, A. F. & Davis, W. (2001) The recognition of human movement using temporal templates. IEEE Transactions on Pattern Analysis and Machine Intelligence, 23(3): pp. 257–267.
- Blostein, S & Huang, T. (1991) Detecting small, moving objects in image sequences using sequential hypothesis testing. IEEE Transactions on Signal Processing, 39(7):pp. 1611–1629.
- Deutscher, J. & Reid, I. (2005) Articulated body motion capture by stochastic search. International Journal of Computer Vision (IJCV), 61(2):pp. 185–205.
- Hurlbert, A. & Wolf, K. (2002) The contribution of local and global cone-contrasts to colour appearance: a Retinex-like model. In B.E. Rogowitz and T.N. Pappas Human Vision and Electronic Imaging VII. Proc. of SPIE 4662, pp. 286-297.
- Kulic, D., Takano, W. & Nakamura, Y. (2008) Incremental learning, clustering and hierarchy formation of whole body motion patterns using adaptive hidden markov chains, International Journal of Robotics Research, 27(7):pp. 761–784.
- Krüger, V., Kragic, D., Ude, A. & Geib, C. (2007) The meaning of action: a review on action recognition and mapping. Advanced Robotics, 21(13):pp. 1473–1501.
- Land, H. E. & McCann, J. J. (1971) "Lightness and Retinex Theory," J. Opt. Soc. Am. 61, pp.1-11.
- Schuldt, C., Laptev, I. & Caputo, B. (2004) Recognizing human actions: a local svm approach. In 17th International Conference on Pattern Recognition (ICPR 2004), volume 3, pp. 32–36.
- Tenorth, M., Bandouch, J. & Beetz, M. (2009) The TUM kitchen data set of everyday manipulation activities for motion tracking and action recognition, in IEEE Int. Workshop on Tracking Humans for the Evaluation of their Motion in Image Sequences (THEMIS) at ICCV, pp. 1089 - 1096 .
- Vahidi-Shams, A. & Guran, A (2011) A Robust And Fast Motion Detection And Tracking Method For Video Surveillance Systems Accepted in The Eighth IASTED International Conference on Biomedical Engineering (Biomed 2011) February.16-18, Innsbruck, Austria.
- Yun, J., Yan, D. & Ze-ping, L. (2005) Study on improved arithmetic of image segmentation, Optical technique, pp. 155-157.

## **ENERGY HARVESTING – OPPORTUNITY FOR FUTURE REMOTE APPLICATIONS**

**Z. Hadas<sup>\*</sup>, V. Singule<sup>\*\*</sup>**

**Abstract:** *This paper deals with energy harvesting principles, current and future applications of these devices. The paper critically evaluates opportunity of such power supplies for future remote applications (wireless sensing, autonomous electronics, mobile technologies etc.) and makes an effort to describe advantages of energy harvesters against traditional power supplies. The definition of energy harvesting describes these technologies as the use of an ambient energy to provide electrical power for small electronic and electrical devices making them self-sufficient. The technologies employed variously convert human power, body fluids, heat differences, vibration or other movement, ultraviolet, visible light or infrared to electricity and there are more options coming along. The progress in wireless technologies on start of new millennium made demands on inexhaustible power source for wireless applications and the ambient energy seems like the suitable power source. The surrounding of most engineering systems contains some form of an ambient energy. Currently most of energy harvesting applications is tested in the laboratory and practical applications of some energy harvesting technologies (photovoltaic, thermoelectric generators, vibration energy harvesters etc.) have been used in several engineering applications. The aim of this paper is brief state of art and review of these technologies.*

**Keywords:** *Energy harvesting, mechatronics, generator, electro-mechanical system.*

### **1. Introduction**

This paper deals with energy harvesting principles, current and future applications of these devices. Energy harvesting technologies have emerged as a prominent research area and it continue to grow at rapid pace (Belleville et al., 2010). A wide range of applications are targeted for the harvesters, including wireless sensor nodes for structural health monitoring, embedded and implanted sensor nodes for medical applications, monitoring of mechatronic systems (e.g. tire pressure in automobiles), recharging the batteries of large systems or running security systems in household conditions (Poulin et al., 2004; Paradiso and Starner, 2005). Recent development includes the components and devices at micro–macro scales covering materials, electrodynamic (thermal, solar etc.) conversion systems, electronics, and integration. The growing demand for energy harvesting systems (Niyato et al., 2007) has motivated this paper to present the current state of art in this field.

**Definition of energy harvesting system** (Mateu and Moll, 2005): An energy harvesting device generates electric energy from its surroundings using some energy conversion method. Therefore, the energy harvesting devices here considered do not consume any fuel or substance. On the other hand the environment energy levels are very low (at least for today's electronic devices requirements).

### **2. Development in Energy Harvesting Field**

The current electronic circuits and applications are capable to operate at microwatt power levels (Chao et al., 2007; Vullers et al., 2009) and it is feasible to power them from non-traditional energy sources. This leads to use energy harvesting technologies, which provide power to charge, supplement or replace batteries in systems where battery use is inconvenient, impractical, expensive or dangerous (Mateu and Moll, 2005). Power requirements of small electronic products including Wireless Sensor

---

<sup>\*</sup> Ing. Zdeněk Hadaš, Ph.D.: Institute of Solid Mechanics, Mechatronics and Biomechanics, Faculty of Mechanical Engineering, Brno University of Technology, Technická 2896/2; 616 69, Brno; CZ, e-mail: hadas@fme.vutbr.cz

<sup>\*\*</sup> assoc. prof. Ing. Vladislav Singule, CSc.: Institute of Production Machines, Systems and Robotics, Faculty of Mechanical Engineering, Brno University of Technology, Technická 2896/2; 616 69, Brno; CZ, e-mail: singule@fme.vutbr.cz

Types of harvesting providing power without external charger

Energy harvesting becomes more capable

Rotary electrodynamic

BUT generators

Photovoltaic or thermoelectric

Vibration harvester (electrodynamic or piezo)

RF beam

Miniature photovoltaic or linear electrodynamic

Standby

10 nW

100 nW

1 μW

10 μW

100 μW

1 mW

10 mW

100 mW

1 W

10 W

100 W

Electronic devices become less power hungry

AAA AA Large rechargeable

Passive RFID (no battery)

Hearing aid

Miniature FM Receiver

Advanced WSN / Active RFID

Transceiver Bluetooth

PALM, MP3

LED indicator light

Conventional WSN transmit

Small LCD & OLED displays

GSM & Mobile phone

Bicycle lighting

ac electroluminescent display

μP laptop

μP desktop

Source IDTechEx

### 3. Potential Energy Harvesting Applications

Tab. 1: Review of energy harvesting applications.

The energy harvesting technologies can be useful in aeronautic and automotive applications, as source for portable devices and source for wireless sensor networks for intelligent monitoring and diagnostic of mechatronic systems. So far, the majority of work on energy harvesting development has been concerned with photovoltaics (Nasiri et al., 2009). Most of these applications have benefitted from huge investment in photovoltaics as renewable energy of which energy harvesting i.e. power for small

devices, is a minor part. Further energy harvesting devices employ variously converting of human power, body fluids, heat differences, vibration or other random movement. The surrounding of most engineering systems contains some form of such ambient energy.

The development in field energy harvesting from vibration started on the end of previous millennium (Williams and Yates, 1996). The energy harvesting field can be divided into micro and macro scale devices. The micro scale energy harvesting technologies (Peano and Tambosso, 2005; Liu et al., 2008) include development of micromechanical electromagnetic systems (MEMS), SMART materials (Guyomar et al., 2005) and nanotechnologies (smart dust or embedded battery-less sensors) (Vijayaraghavan and Rajamani, 2010). The development of macro scale energy harvesting systems is focused on sources for wireless sensor networks (Gungor and Hancke, 2009) and remote electronics with power consumption several milliwatts.

#### 4. Energy Harvesting at Brno University of Technology

The energy harvesting development of our team has started in 2004 and it is focused on macro scale energy harvesting from mechanical energy of vibrations (Hadas et al., 2007). Several vibration power generators were developed for powering of wireless sensors for aeronautic application (Hadas et al., 2008). Our development is focused on energy harvesting from very low level of vibrations in engineering applications (Hadas et al., 2010). The improved generator operates correctly in 0.1 g level of vibrations and with operating frequency 17-18 Hz and output power 7 mW (5 V). The harvested output power (voltage) grows with level of vibrations. The measurement of this generator is shown in Fig. 2. The picture of this very sensitive BUT generator is included in Fig. 1. It demonstrates potential applications of this technology and our development as source for industrial wireless sensors in a modern diagnostic system. The very sensitive generator presents opportunity for energy harvesting from random movement too.

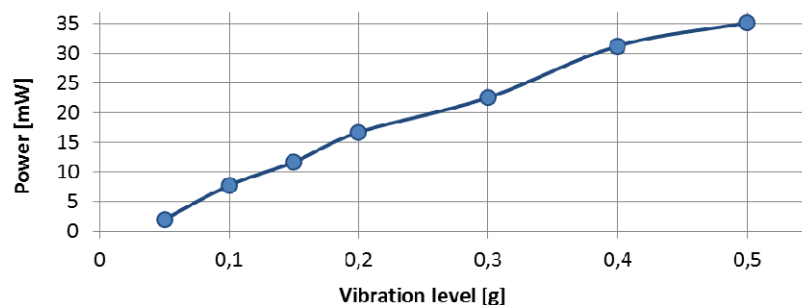


Fig. 2: Measurement of BUT generator, harvested power vs. vibration level.

#### 5. Successful Energy Harvesting Applications

Currently, the most of energy harvesting applications is tested in the laboratory and practical applications of some energy harvesting technologies have been used in several engineering applications. Main players in energy harvesting fields are companies: AdaptivEnergy, EnOcean, Holst Centre, Lumedyne, MEMS@Mit, Micropelt, Microstrain, Morgan Electro Ceramics, Piezo TAG, Perpetuum, Thermo Life, TPL Micropower, Transense Technology, Visietyre. In total, there are about 500 organizations working on energy harvesting and about half of them being academic.

There is already a large number of successful energy harvesting applications, particularly those using technology harvesting electricity from light, human movement and heat. Photovoltaic conversion of light is the most popular, being used from road furniture to satellites, with solar powered phones, torches, lanterns, radios, wristwatches and other devices increasingly seen. Partly, this is because photovoltaic has no moving parts and is therefore unusually long lived and reliable and partly it delivers high power per unit of volume and is rapidly improving in affordability, size, weight, spectral response and other parameters. No other forms of energy harvesting has all these credentials but alternatively are also needed because a high proportion of devices using energy harvesting will be embedded in future, where light is not available.

## 6. Conclusions

Energy harvesting has been successful in several engineering (aeronautic, automotive, military and civil engineering). The first really high volume of industrial applications is wireless sensor networks which are rising to at least billions of devices per year. Other consumer goods such as mobile phones and laptops will become significant; however, generated power of energy harvesting devices is very low for these consumer goods. Energy harvesting technologies are enabling the commercial progress of next-generation ultra-low-power electronic devices and systems. These devices are being deployed for wireless as well as wired systems such as mesh networks, sensor and control systems, micro-electro-mechanical systems (MEMS), radio frequency identification (RFID) devices, and so on.

The aim of this paper was briefly reviewed energy harvesting technologies and their opportunity for future wireless and remote applications.

## Acknowledgement

Published results were acquired using the subsidization of the Ministry of Education, Youth and Sports of the Czech Republic, MSM 0021630518 "Simulation modeling of mechatronic systems".

## References

- Belleville, M., Fanet, H., Fiorini, P., Nicole, P., Pelgrom, M. J. M., Piguet, C., Hahn, R., Van Hoof, C., Vullers, R., Tartagni, M. and Cantatore, E. (2010) 'Energy autonomous sensor systems: Towards a ubiquitous sensor technology', *Microelectronics Journal*, 41(11), 740-745.
- Chao, L., Tsui, C. Y., Ki, W. H. and Acm (2007) Vibration Energy Scavenging and Management for Ultra Low Power Applications, *Islped'07: Proceedings of the 2007 Inter. Symp. on Low Power Electronics and Design*.
- Gungor, V. C. and Hancke, G. P. (2009) 'Industrial Wireless Sensor Networks: Challenges, Design Principles, and Technical Approaches', *Ieee Transactions on Industrial Electronics*, 56(10), 4258-4265.
- Guyomar, D., Badel, A., Lefeuvre, E. and Richard, C. (2005) 'Toward energy harvesting using active materials and conversion improvement by nonlinear processing', *Ieee Transactions on Ultrasonics Ferroelectrics and Frequency Control*, 52(4), 584-595.
- Hadas, Z., Kluge, M., Singule, V. and Ondrusek, C. (2007) Electromagnetic vibration power generator, 2007 *Ieee International Symposium on Diagnostics for Electric Machines, Power Electronics & Drives*.
- Hadas, Z., Ondrusek, C. and Singule, V. (2010) 'Power sensitivity of vibration energy harvester', *Microsystem Technologies-Micro-and Nanosystems-Information Storage and Processing Systems*, 16(5), 691-702.
- James, E. P., Tudor, M. J., Beeby, S. P., Harris, N. R., Glynn-Jones, P., Ross, J. N. and White, N. M. (2004) 'An investigation of self-powered systems for condition monitoring applications', *Sensors and Actuators a-Physical*, 110(1-3), 171-176.
- Liu, J. Q., Fang, H. B., Xu, Z. Y., Mao, X. H., Shen, X. C., Chen, D., Liao, H. and Cai, B. C. (2008) 'A MEMS-based piezoelectric power generator array for energy harvesting', *Microelectronics Journal*, 39(5), 802-806.
- Mateu, L. and Moll, F. (2005) Review of Energy Harvesting Techniques and Applications for Microelectronics, *Proceedings of the SPIE Microtechnologies for the New Millenium*.
- Nasiri, A., Zabalawi, S. A. and Mandic, G. (2009) 'Indoor Power Harvesting Using Photovoltaic Cells for Low-Power Applications', *Ieee Transactions on Industrial Electronics*, 56(11), 4502-4509.
- Niyato, D., Hossain, E., Rashid, M. M. and Bhargava, V. K. (2007) 'Wireless sensor networks with energy harvesting technologies: A game-theoretic approach to optimal energy management', *Ieee Wireless Communications*, 14(4), 90-96.
- Paradiso, J. A. and Starner, T. (2005) 'Energy scavenging for mobile and wireless electronics', *Ieee Pervasive Computing*, 4(1), 18-27.
- Peano, F. and Tambosso, T. (2005) 'Design and optimization of a MEMS electret-based capacitive energy scavenger', *Journal of Microelectromechanical Systems*, 14(3), 429-435.
- Poulin, G., Sarraute, E. and Costa, F. (2004) 'Generation of electrical energy for portable devices Comparative study of an electromagnetic and a piezoelectric system', *Sensors and Actuators a-Physical*, 116(3), 461-471.
- Vijayaraghavan, K. and Rajamani, R. (2010) 'Novel Batteryless Wireless Sensor for Traffic-Flow Measurement', *Ieee Transactions on Vehicular Technology*, 59(7), 3249-3260.
- Vullers, R. J. M., van Schaijk, R., Doms, I., Van Hoof, C. and Mertens, R. (2009) 'Micropower energy harvesting', *Solid-State Electronics*, 53(7), 684-693.
- Williams, C. B. and Yates, R. B. (1996) Analysis of a micro-electric generator for microsystems, *Sensors and Actuators, A: Physical*, A52(1), 8-11.



## RECYCLING OF FLUE GAS DESULPHURIZATION GYPSUM AT LABORATORY CONDITIONS

A. Hájková\*, P. Padevět\*, T. Plachý\*, P. Tesárek\*

**Abstract:** *The main point of this research was to determine the practical and theoretical level of possibilities of the recycling gypsum binder and to characterize the recycling gypsum binder according to the only available Czech standard for gypsum binders – ČSN 72 2301. Therefore, the laboratory experiment of the recycling process was conducted and then the recycled gypsum binder was tested by the tests specified in this standard. Finally, comparison between starting compound, which was subjected to the process of recycling, with recycled gypsum binder was carried out. Specialty of the recycled gypsum in this case, which has undergone the process of recycling, is its age – 5 years, and also the fact that during this period it was exhibited as the gypsum block in the building envelope with no protective features and was exposed to exterior conditions as sun, wind, snow, rain etc.*

**Keywords:** *Flue gas desulphurization gypsum, mechanical properties, recycling, compressive strength.*

### 1. Introduction

Recycling of building waste is nothing new today. In recent years beginning to emerge in the world different recycling processes of building waste, it is a way how environmentally friendly disposal with the building waste which was previously unthinkable (Ahmed and Ugai, 2010). If we talk about recycling of gypsum, we can say that the process is relatively efficient, recycled gypsum can be used as full-valued materials, not only in the building industry (Vranken and Laethem, 2000). The actual recycling is necessary to comply with certain criteria for the recycling process as well as ensure the quality of the feedstock (Wirsching, 1983). The gypsum binder classified according to ČSN 72 2301 as G-13 B III (ČSN 72 2301, 1978) was selected for the laboratory experiment of the recycled hardened gypsum. The binder was subjected to standard tests and was subsequently used for making the gypsum block that has been located in the building envelope without the protective elements for 5 years (a facade rendering, an insulation, etc.) – Fig. 1. After 5 years, the gypsum block was cut, crushed and used for production of a new recycled gypsum binder.



*Fig. 1: The gypsum blocks (left – the interior side, right – the exterior side).*

\* Ing. Andrea Hájková, Ing. Pavel Padevět, Ph.D., Ing. Tomáš Plachý, Ph.D. and Ing. Pavel Tesárek, Ph.D.: Czech Technical University in Prague, Faculty of Civil Engineering, Department of Mechanics; Thákurova 7, 166 29 Prague 6 - Dejvice, Czech Republic, emails: andrea.hajkova@fsv.cvut.cz, pavel.padevet@fsv.cvut.cz, plachy@fsv.cvut.cz, tesarek@fsv.cvut.cz



## 2. Process of recycling

The recycling process was carried out in several points, which are summarized in Tab. 1, where they are listed with description of each applied process:

Tab. 1: Processes of gypsum recycling at laboratory conditions.

Processes	Description
Hard crushing	Hard crushing of the gypsum block by the press machine WPM 100 kN
Predrying	Predrying in the laboratory conditions during the temperature $20\text{ }^{\circ}\text{C} \pm 1\text{ }^{\circ}\text{C}$
Gentle crushing	Crushing by the metal hammer (weight 3 kg) to elements $< 1\text{ cm}$
Milling	Milling on the equipment RETSCH PM 400 to elements $< 2\text{ mm}$
Screening	Elimination of elements $> 2\text{ mm}$
Calcination	Calcination proceeded during 10 days with the temperature $110\text{ }^{\circ}\text{C} \pm 3\text{ }^{\circ}\text{C}$ in the drying machine by the amount of $500\text{ g} \pm 100\text{ g}$

After the recycling processes, the recycled gypsum binder was placed in a container to prevent degradation of moisture and dirt. The isolated recycled gypsum binder was cooled to a laboratory temperature of  $20\text{ }^{\circ}\text{C} \pm 1\text{ }^{\circ}\text{C}$ . After reaching a laboratory temperature, the following tests were carried out on recycled gypsum binder according to the standard ČSN 72 2301:

- fineness of grinding,
- determining of the normal consistency,
- determining of the start and end of setting,
- compressive strength after 2 hours,
- bending strength after 2 hours.

Further parameters were determined too: cleanness of the recycled gypsum binder, bulk density and total open porosity. Based on described tests and additional parameters it was possible to compare the original gypsum binder and the recycled one according to the standard ČSN 72 2301.

## 3. Tests

### 3.1. Fineness of grinding

Fineness is the only test, which can affect the “end” feature recycled binders. Milling was carried out on a machine RETSCH PM 400 in a container of 500 ml – weight of every shot was  $200\text{ g} \pm 10\text{ g}$ , to achieve the desired fineness. Then the powdered gypsum binder was sifted through a sieve of a mesh diameter 2 mm. Particles remaining on the screen were removed from the gypsum binder. The result was similar grinding of these tested gypsum binders. Both mixtures can be classified in category III – finely ground – by the standard ČSN 72 2301.

### 3.2. Determining the normal consistency

The amount of water in the mixture (water-gypsum ratio) is the basic criterion for determining of the gypsum binder properties (Chandara et al. 2009). In determining of the normal consistencies is necessary to follow the procedure set out in the standard and determine the appropriate ratio of water and mixture. For the original mixture, it was chosen water-gypsum ratio 1 : 0.627, for the recycled mixture water-gypsum ratio of 1 : 1.020. The dependence on a water standard spillage over the water-gypsum ratio is shown in Fig. 2. Results could be dependent on the spillage  $l_r$  [mm] and the water-gypsum ratio  $v$  [-] expressed by the equation of a line:

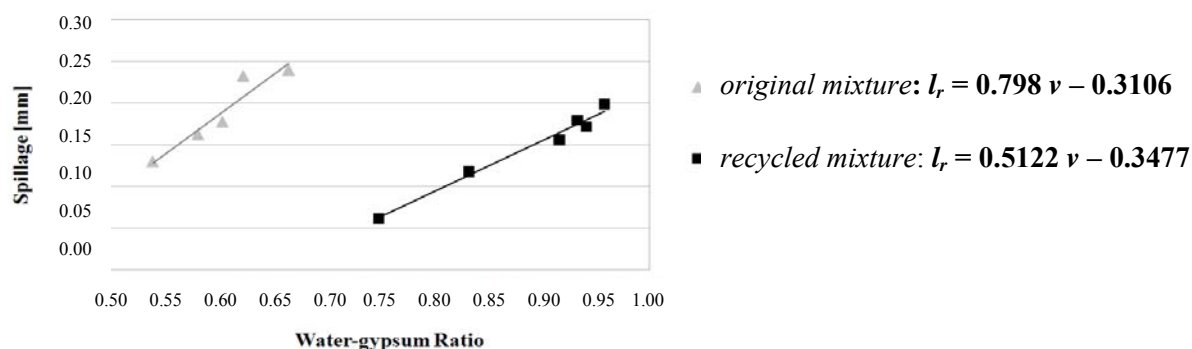


Fig. 2: The Dependence of the gypsum spillage on the water-gypsum ratio.

### 3.3. Determining of start and end of setting

For this test, it is always necessary to use a mixture of a normal consistency, therefore mixtures with the above-mentioned water-gypsum ratio. The Vicat device was used for determining of start and end of gypsum mixture setting. Results for the both compounds are listed in Tab. 2.

Tab. 2 shows the different values for beginning and for the overall setting time. The process of recycling accelerated values of the beginning and the end of solidification of the recycled gypsum binder approximately about ½ times.

Tab. 2: Determining the start and the end of setting.

Sample	Measurement	Start of setting [min]	End of setting [min]
Original binder	1	9	14
	2	9	12
	3	9	13
	Average	9	13
Recycled binder	1	4.5	6
	2	4.5	8
	3	4.5	7
	Average	4.5	7

### 3.4. Compressive strength after 2 hours

A compressive strength test was performed on the samples 40×40×160 mm. The samples were made from the original and the recycled gypsum binders. A pressure testing was performed 2 hours after mixing the gypsum with water at a laboratory temperature 20 °C ± 1 °C by the press machine WPM 100 kN. The calculated values are shown in Fig. 3:

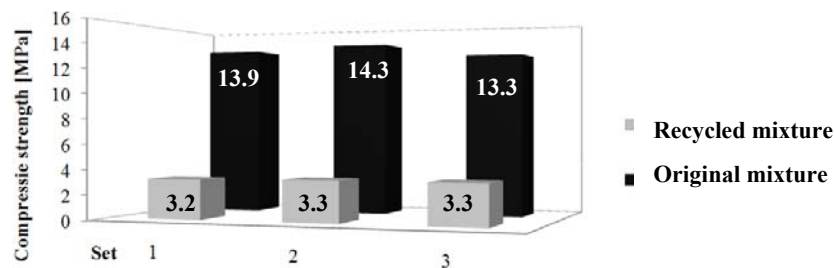


Fig. 3: Compressive strength.

In the Fig. 4 it can be seen a big drop in 2 hour compressive strength and it is approximately 76 %. Decrease in the compressive strength may be large due to almost double water ratio used for making the set of the samples from the recycled gypsum binder.

The bending strength is not a standard test for the classification of gypsum binders, but is an integral part of this experiment (as a complete mechanical parameter). Fig. 4 shows the results of the experiment. Presented values of the bending and compressive strengths showed effect of the recycling process, in this case – decreased significantly strength values.

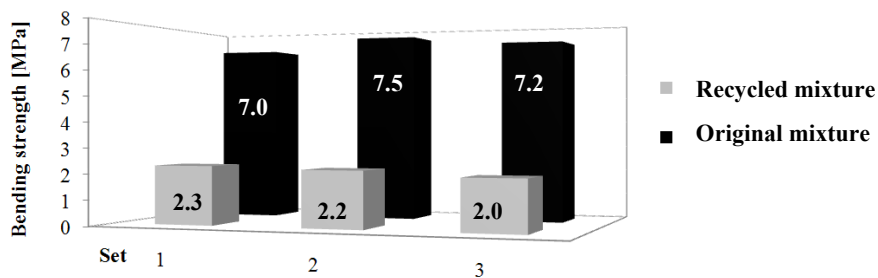


Fig. 4: Bending strength.

### 3.5. Cleanliness of the recycled gypsum binder

Purity of the recycled gypsum mixture was calculated after calcination process. During calcination the weight loss of the gypsum binder were measured, calcination was stopped, when the weight was stabilized. Weight was stable after 10 days of drying at temperature 110 °C. For the known values of molecular masses of individual molecules and the values of purity of the original gypsum binder mixture specified by the manufacturer, it was mathematically determined the resulting purity of the recycled gypsum binder (Thormark, 2001). The original gypsum binder reached 98 % of purity (indicated by the manufacturer), our measured value of purity for the recycled gypsum binder was  $96.6 \pm 1.8$  °C %.

### 3.6. Bulk density and total open porosity

Bulk density of the gypsum samples was calculated from the weight and the volume of the tested samples; the resulting value of recycled gypsum binder is  $850 \text{ kg/m}^3$  and it is different from the value of the original gypsum binder –  $1170 \text{ kg/m}^3$ . Total open porosity was determined using the known matrix density of the original mixture. This value is 54 % for the original gypsum binder and 66 % for the recycled gypsum binder.

## 4. Conclusions

From the obtained dates of the laboratory experiments on the recycled gypsum binder (Table 3) according to ČSN 72 2301 was ones classified as the gypsum binder G-3 AIII, the original gypsum binder was classified as the gypsum binder G-13 BIII. Furthermore, we can say that quality of the recycled gypsum binder is affected by recycling, calcination, the selected grinding fineness and quality of the feedstock (Hájková, A., 2010). Recycled materials can be considered as full-valued with a wide range of application and despite the fact that there was a significant decrease in strength.

Tab. 3: Measured data according to the standard ČSN 72 230.

Description	Water-gypsum ratio	Absolute setting-up	Fineness of grinding	Compressive strength after 2 hours [MPa]	Bulk density [ $\text{kg/m}^3$ ]	Total open porosity [%]
Original binder	0.627	Normal setting-up	Finely ground	13.8	1170	54
Recycled binder	1.020	Quick setting-up	Finely ground	3.3	850	66

## Acknowledgement

This project was supported by CTU in Prague under the project Advanced experimental methods SGS10/136/OHK1/2T/11.

## References

- ČSN 72 2301 (1978) Sádrová pojiva. Klasifikace. Všeobecné technické požadavky. Zkušební metody. Prague: Czechoslovak standardization institutions, pp. 17.
- Hájková, A. (2010) Energosádra a možnosti její recyklace s ohledem na mechanické vlastnosti, Prague, Thesis, Czech Technical University in Prague, pp. 93.
- Wirshing, F. (1983) Calcium Sulfate, In: Ullmanns Encyclopedia of Industrial Chemistry, Volume 6, Weinheim, Wiley-VCH Verlag, pp. 90 – 94.
- Vranken, K. C., Laethem, B. (2000) Recycling Options for Gypsum from Construction and Demolition Waste, Waste Management Series, Volume 1, Waste Materials in Construction Wascon 2000 - Proceedings of the International Conference on the Science and Engineering of Recycling for Environmental Protection, Harrogate, England 31 May, pp. 325 – 331.
- Ahmed, A., Ugai, K. (2010) Environmental Effects on Durability of Soil Stabilized with Recycled Gypsum, Cold Regions Science and Technology, 2010 (Accepted manuscript).
- Thormark, C. (2001) Conservation of Energy and Natural Resources by Recycling Building Waste, Resources, Conservation and Recycling, Volume 33, Issue 2, pp. 113 – 130.
- Chandara, Ch., Azizli, K. A. M., Ahmad, Z. A., Sakai, E. (2009) Use of Waste Gypsum to Replace Natural Gypsum as Set Retarders in Portland Cement, Waste Management, Volume 29, Issue 5, pp. 1975 – 1679.

## DYNAMIC LOADING OF A SQUIRREL CAGE MOTOR FOR VARIOUS VEHICLES

M. Hajžman<sup>\*</sup>, J. Šašek<sup>\*</sup>, M. Byrtus<sup>\*</sup>, V. Zeman<sup>\*</sup>

**Abstract:** Squirrel cage induction motors are employed in various machines and means of transport mostly as traction motors. The usage of this type of motors in vehicles can be connected with possible fatigue problems because of non-stationary loading and changing operational conditions. The complex dynamic model of an electro-motor rotor is described in this paper. It is based on solid and beam finite elements, on rigid bodies and on special couplings derived in a rotating coordinate system. The loading conditions and states are summarized and each dynamic excitation caused mainly by electro-magnetic field fluctuations and or track irregularities is described. The whole methodology was supported by experimental measurements and it was applied to a real motor.

**Keywords:** Vibrations, electromotor, rotor dynamics, finite element method, steady state response.

### 1. Introduction

An important example of rotating systems is a squirrel cage induction motor which is used in various machines and means of transport mainly as a traction motor. The operation of this type of motor in vehicles can be connected with possible fatigue problems because of non-stationary loading and changing operational conditions and therefore it is necessary to analyze dynamic response of the rotor.

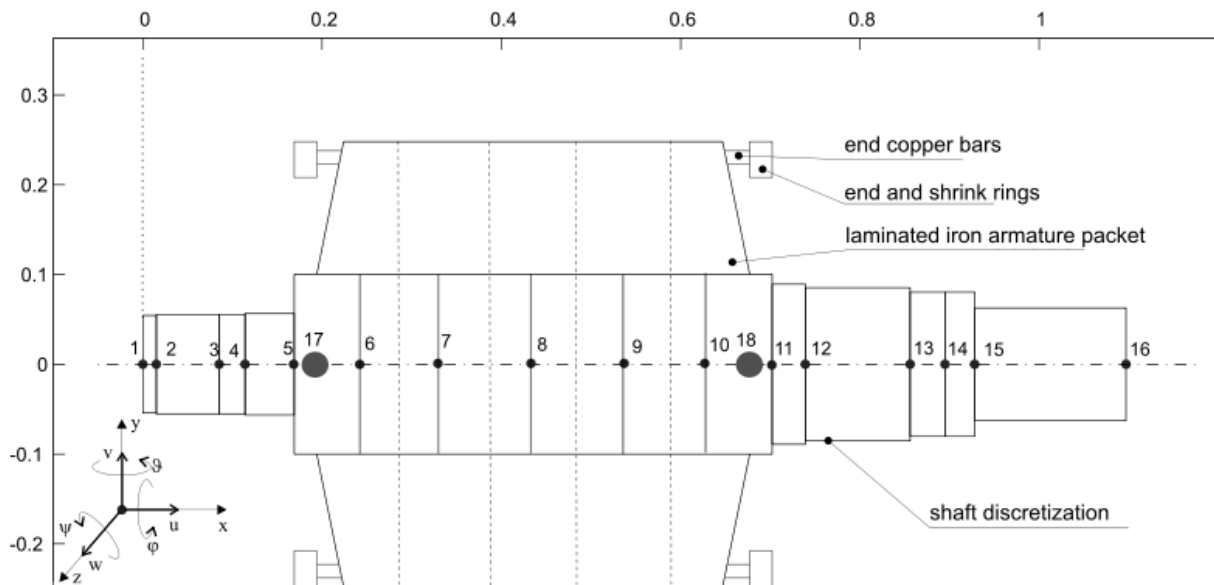


Fig. 1: Scheme of a rotor of a squirrel cage motor.

The scheme of the rotor of this studied type of electric motor is shown in Fig. 1. The rotor consists of a rotor shaft with laminated iron armature mounted in the middle shaft part. Laminations have the form of thin sheet metals with holes. The squirrel cage is composed of rotor bars (usually made of copper) passing through the laminations and joined by end rings on both ends (also made of copper). The end rings can be constricted by shrink rings made of certain more stiff material and mounted with initial

<sup>\*</sup> Ing. Michal Hajžman, Ph.D., Ing. Jakub Šašek, Ph.D., Ing. Miroslav Byrtus, Ph.D. and prof. Ing. Vladimír Zeman, DrSc.: Department of Mechanics, Faculty of Applied Science, University of West Bohemia, Univerzitní 22; 306 14, Plzeň; CZ, e-mails: mhajzman@kme.zcu.cz, jsasek@kme.zcu.cz, mbyrtus@kme.zcu.cz, zemanv@kme.zcu.cz

tension. The short end pieces of rotor bars extruded from the armature are deformed during the rotor operation due to rings inertia and electromagnetic forces. Fatigue problems can be characterized by ruptures of the end ring and rotor bar connections.

This paper describes an advanced dynamic model of the rotor and summarizes the possible excitation modes. According to the literature review, e.g. Caruso et al. (2008) or Enge & Maisser (2005), the usage of such complex models of squirrel cage motor rotors is very unique.

## 2. Advanced dynamic model of a rotor of a squirrel cage motor

The originally developed complex dynamic model of the rotor of the squirrel cage motor is described in this section. The advanced model is characterized by the end and shrink rings considered as flexible bodies and copper bars end modelled as a set of beams revolved by defined radius. This model is intended for high-frequency and comprehensive dynamic analyses. The flexible shaft with the mounted laminated armature is modelled by the same way as in the basic dynamic model (see Hajžman et al., 2010a). The basic dynamic model was introduced in Hajžman et al. (2010b) and was characterized by considering ideally rigid end and shrink rings.

The end and shrink rings in the advanced dynamic model are considered to be 3D continuum and therefore they are modelled by solid finite elements derived in the rotating coordinate system, similarly as the shaft finite elements in Hajžman et al. (2009) and Šašek (2010). The eight-node rotating solid finite element with three translational displacements in each node is described in more detail e.g. in Šašek (2010).

The end and shrink rings (left denoted by subscript  $L$ , right denoted by subscript  $R$ ) are represented in the advanced dynamic model by the mass matrices  $\mathbf{M}_{L1}$ ,  $\mathbf{M}_{R1}$ , matrices of gyroscopic effects  $\omega_0 \mathbf{G}_{L1}$ ,  $\omega_0 \mathbf{G}_{R1}$  ( $\omega_0$  is the rotor angular velocity), stiffness matrices  $\mathbf{K}_{L1}$ ,  $\mathbf{K}_{R1}$  and spin softening matrices  $\omega_0^2 \mathbf{K}_{dL1}$ ,  $\omega_0^2 \mathbf{K}_{dR1}$ . The order of these matrices is given by the number of degrees of freedom of the discretized rings and they are composed of particular element matrices. The model should be also extended by the vectors of centrifugal forces  $\omega_0^2 \mathbf{f}_{L1}$  and  $\omega_0^2 \mathbf{f}_{R1}$  (see Hajžman et al., 2009). The model of the end and shrink rings can be written in the form

$$\mathbf{M}_{L1} \ddot{\mathbf{q}}_{L1}(t) + (\mathbf{B}_{L1} + \omega_0 \mathbf{G}_{L1}) \dot{\mathbf{q}}_{L1}(t) + (\mathbf{K}_{L1} - \omega_0^2 \mathbf{K}_{dL1}) \mathbf{q}_{L1}(t) = \omega_0^2 \mathbf{f}_{L1} , \quad (1)$$

$$\mathbf{M}_{R1} \ddot{\mathbf{q}}_{R1}(t) + (\mathbf{B}_{R1} + \omega_0 \mathbf{G}_{R1}) \dot{\mathbf{q}}_{R1}(t) + (\mathbf{K}_{R1} - \omega_0^2 \mathbf{K}_{dR1}) \mathbf{q}_{R1}(t) = \omega_0^2 \mathbf{f}_{R1} , \quad (2)$$

where  $\mathbf{B}_{L1}$  and  $\mathbf{B}_{R1}$  denote material damping matrices.

End parts of flexible bars connecting end rings and laminated armature (see Fig. 1) are considered to be 1D continuum. Special beam finite elements which are rotating with defined radius were developed for this purpose (Šašek, 2010) and their model ( $L$  for left,  $R$  for right) is of the form

$$\mathbf{M}_{L2} \ddot{\mathbf{q}}_{L2}(t) + (\mathbf{B}_{L2} + \omega_0 \mathbf{G}_{L2}) \dot{\mathbf{q}}_{L2}(t) + (\mathbf{K}_{L2} - \omega_0^2 \mathbf{K}_{dL2}) \mathbf{q}_{L2}(t) = \omega_0^2 \mathbf{f}_{L2} , \quad (3)$$

$$\mathbf{M}_{R2} \ddot{\mathbf{q}}_{R2}(t) + (\mathbf{B}_{R2} + \omega_0 \mathbf{G}_{R2}) \dot{\mathbf{q}}_{R2}(t) + (\mathbf{K}_{R2} - \omega_0^2 \mathbf{K}_{dR2}) \mathbf{q}_{R2}(t) = \omega_0^2 \mathbf{f}_{R2} , \quad (4)$$

where the corresponding matrices is of the same meaning as in the previous case of rings but are derived for rotating beam finite elements.

The remaining part of the rotor is the shaft with the mounted laminated armature that is modelled using rotating shaft finite elements (see Hajžman et al., 2009) with defined rigid bodies of the discretized armature packet and defined elastic properties of the packet. The shaft and armature model can be written as

$$\begin{aligned} & (\mathbf{M}_S + \mathbf{M}_A) \ddot{\mathbf{q}}_S(t) + (\mathbf{B}_S + \mathbf{B}_A + \omega_0 \mathbf{G}_S + \omega_0 \mathbf{G}_A) \dot{\mathbf{q}}_S(t) + \\ & + (\mathbf{K}_S + \mathbf{K}_A - \omega_0^2 \mathbf{K}_S - \omega_0^2 \mathbf{K}_A) \mathbf{q}_S(t) = \mathbf{0} \end{aligned} \quad (5)$$

and is created from the matrices representing the flexible shaft (subscript  $S$ ) and the discretized armature with its elastic properties (subscript  $A$ ). Bearing characteristics are included in damping matrix  $\mathbf{B}_S$  and stiffness matrix  $\mathbf{K}_S$ .

The motion equations (1) to (5) belong to the uncoupled rotor subsystems. In order to obtain the whole rotor model, the transformation between generalized coordinates of the particular subsystems should be derived (e.g. the last nodes of the flexible bars in (3) and (4) should be connected with the appropriate nodes of the end rings in (1) and (2)). The whole transformation defined by transformation matrix  $\mathbf{T}_R$  between original uncoupled general coordinates  $\mathbf{q}(t)$  and new coupled general coordinates  $\tilde{\mathbf{q}}(t)$  is  $\mathbf{q}(t) = \mathbf{T}_R \tilde{\mathbf{q}}(t)$ . Then the whole rotor model is (see Šašek, 2010) of the form

$$\tilde{\mathbf{M}}\ddot{\tilde{\mathbf{q}}}(t) + (\tilde{\mathbf{B}} + \omega_0 \tilde{\mathbf{G}})\dot{\tilde{\mathbf{q}}}(t) + (\tilde{\mathbf{K}} - \omega_0^2 \tilde{\mathbf{K}}_d)\tilde{\mathbf{q}}(t) = \omega_0^2 \tilde{\mathbf{f}} + \tilde{\mathbf{f}}(t), \quad (6)$$

where the general excitation vector  $\tilde{\mathbf{f}}(t)$  was added. The parameter identification in the case of a real application is discussed in Hajžman et al. (2010b). The experimental modal analysis was employed in order to tune the proper eigenfrequencies of the numerical model. The illustration of the chosen tuned eigenmode characterized by dominant torsional deformation and higher eigenmode characterized by dominant deformation of the ring is in Fig. 2.

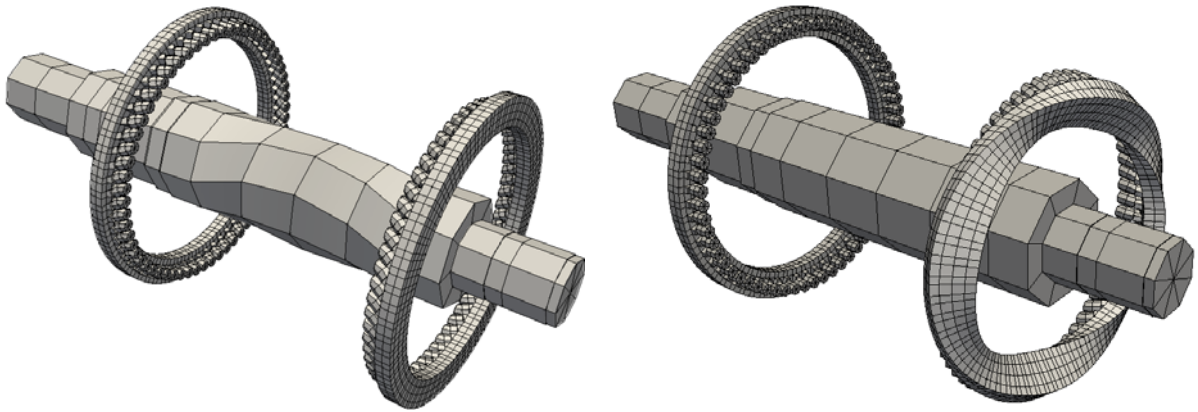


Fig. 2: Illustration of rotor eigenmodes (the laminated armature is not visualized).

### 3. Loading of a squirrel cage motor

The rotor of the squirrel cage motor can be loaded in various situations by various ways. The main excitation types are summarized in this chapter. It is considered that the motor is used as a traction motor in a rail vehicle. The definition of a motor loading is a principal step of dynamic analysis of the rotor of a squirrel cage induction motor.

The first possible excitation, which is rather static then dynamic one, is the centrifugal force loading represented by vector  $\omega_0^2 \tilde{\mathbf{f}}$ . The analysis of a centrifugal response was presented in Šašek (2010). For the accurate and realistic solution of the rotor response to the static centrifugal excitation, it is necessary to solve detailed contact problem of the shrink and end short-circuit rings considering initial tension. This task is not the subject of this paper and should be performed by means of commercial software tools based on the finite element method.

One of the most common and most often loadings is the excitation by pulsating electro-magnetic torques which are excited by the electro-magnetic field of the motor. The detailed calculation of these torques for the real studied induction motor was shown in Bartoš & Janda (2008). The results of the electro-magnetic field analysis are the Fourier series of the pulsating electro-magnetic torques that can be understood as steady polyharmonic excitation. In this case, the rotor dynamic response can be also considered by polyharmonic one and due to the linearity of the model (6) each harmonic part can be solved separately. The solution of this problem together with preliminary analysis of stresses in the rotor bars is presented in Šašek (2010).



Another important type of excitations, which can arise during the standard motor operation, is the excitation in the course of driving through the curved track. Since the curves for the rail vehicles are not too aggressive as in case of road vehicles, the dynamic response is not so significant. However, the effect on the fatigue and service life can be evaluated. The gyroscopic torques for the particular curve was derived in dependency on the vehicle velocity, curve radius, moments of inertia of the end and shrink ring and drive gear ratio. These torques are acting on the end and shrink rings and are causing the dynamic loading because of the rotor rotation.

Similarly small vibration effects are caused by the kinematic excitation in the course of driving on the uneven rails in both horizontal and vertical directions. Byrtus et al. (2009) presents the possible method for such excitation determination.

The last considered excitation type is the electro-magnetic excitation due to the short circuit. Several types of short-circuit faults can be recognized. After electromagnetic field analysis (Bartoš, 2008), the excitation can be defined by time histories of short-circuit torques. The rotor model (6) can be solved by means of numerical integration in order to obtain the time histories of mechanical variables.

#### 4. Conclusions

This paper presents the advanced dynamic model of the rotor of the squirrel cage electromotor. The model is characterized by the flexible end and shrink rings and therefore it is suitable for high-frequency analysis, where bending and torsional behaviour of the rings as well as of the shaft can be dominant.

The created computational model can be used for many types of dynamical analyses. The most important ones are modal analysis, steady-state response analysis and non-stationary time integration of motion equations. The excitation types in case of rail vehicles were summarized in the paper. It can be defined mainly on the basis of electromagnetic field calculation and track irregularities definition. Future work will be aimed at detail calculations of the response to these excitation types and successive output for stress and fatigue investigation.

#### Acknowledgement

This work was supported by the research project MSM4977751303 of the Ministry of Education, Youth and Sports of the Czech Republic.

#### References

- Bartoš, V. (2008) Pulzační momenty asynchronního stroje v poruchových stavech. Research report 22160-12-08. Department of Electromechanics and Power Electronics, University of West Bohemia, Plzeň.
- Bartoš, V. & Janda, M. (2008) Pulzační momenty asynchronního stroje při neharmonickém napájení, část 2. Research report 22160-04-08. Department of Electromechanics and Power Electronics, University of West Bohemia, Plzeň.
- Byrtus, M., Skála, O. & Zeman, V. (2009) Modelling and behaviour of a bogie on irregular track, in: Proc. Nat. Conf. with Int. Part. Engineering Mechanics 2009 (J. Náprstek & C. Fischer eds), Svratka, pp.159-174.
- Caruso G. et al. (2008) Torsional eigenfrequency identification of squirrel cage rotors of induction motors, in: Proc. Int. Symposium on Power Electronics, Electrical Drives, Automation and Motion, IEEE, Ischia, pp.1271-1275.
- Enge, O. & Maisser, P. (2005) Modelling Electromechanical Systems with Electrical Switching Components Using the Linear Complementarity Problem. *Multibody System Dynamics*, 13, 421-445.
- Hajžman, M., Byrtus, M., Šašek, J. & Zeman, V. (2010a) Modelling and analysis of dynamics of electric motor rotor, in: Proc. Joint Int. Conf. on Multibody System Dynamics 2010 (A. Mikkola ed.), Lappeenranta.
- Hajžman, M., Byrtus, M. & Zeman, V. (2010b) Development of the basic dynamical model of a squirrel cage motor. *Engineering Mechanics*, 3/4, 17, pp.225-235.
- Hajžman, M., Šašek, J. & Zeman, V. (2009) Modelling of flexible rotor vibrations in the rotating coordinate system, in: *Modelling, Simulation and Control of Nonlinear Engineering Dynamical Systems. State-of-the-Art, Perspectives and Applications* (J. Awrejcewicz ed.), Springer, Berlin, pp. 277-288.
- Šašek, J. (2010) Dynamika rotorových soustav s poddajnými disky. Ph.D. thesis, University of West Bohemia, Plzeň.

## FAST EVALUATION OF LINEAL PATH FUNCTION USING GRAPHICS PROCESSING UNIT

J. Havelka\*, J. Sýkora\*, A. Kučerová\*

**Abstract:** Homogenization methods are becoming the most popular approach to modelling of heterogeneous materials. The main principle is to represent the heterogeneous microstructure with an equivalent homogeneous material. When dealing complex random microstructures, the unit cell representing exactly periodic morphology needs to be replaced by a statistically equivalent periodic unit cell (SEPUC) preserving the important material properties in the statistical manner. One of the statistical descriptors suitable for SEPUC definition is the lineal path function. It is a low-order descriptor capable of capturing certain information about the phase connectedness. Its main disadvantage is the computational cost. In this contribution, we present the reformulation of the sequential C code for evaluation of the lineal path function into the parallel C code with Compute Unified Device Architecture (CUDA) extensions enabling the usage of computational potential of the NVIDIA graphics processing unit (GPU).

**Keywords:** Lineal path function, homogenization, statistically equivalent periodic unit cell, graphics processing unit.

### 1. Introduction

Modelling of random heterogeneous materials is a multi-disciplinary problem with a wide range of relevant engineering applications. The unifying theoretical framework is provided by homogenization theories, which aim at the replacement of the heterogeneous microstructure with an equivalent homogeneous material, e.g. (Torquato, 2002). Currently, two main approaches are available: (i) computational homogenization and (ii) effective media theories. While the first class of methods studies the distribution of local fields within a typical heterogeneity pattern using a numerical method, the second group estimates the response analytically on the basis of limited geometrical information (e.g. the volume fractions of constituents) of the analysed medium.

It is generally accepted that detailed discretization techniques, and the Finite Element Method (FEM) in particular, remain the most powerful and flexible tools available. Despite of the tedious computation time, it provides us details of local stress and strain fields. Moreover, it is convenient to characterize the material heterogeneity by introducing the concept of a Periodic Unit Cell (PUC) (Vorel, 2009) or Statistically Equivalent Periodic Unit Cell (SEPUC), see (Zeman & Šejnoha, 2007; Vorel et al., 2011) for more details. On the other hand, if only the overall (macroscopic) response is demanded variable, it is sufficient to introduce structural imperfections in a cumulative sense using one of the averaging schemes, e.g. the Mori-Tanaka method (Vorel & Šejnoha, 2009).

If the effective material parameters of complex microstructure (see Fig. 1) are demanded, the homogenization technique based on the SEPUC can be utilized. Furthermore, this approach allows us to reduce the computation cost by generating smaller unit cell describing the real structure. The generation of the SEPUC is based on optimization of an appropriate statistical descriptor. The most commonly used group of descriptors embodies a set of general  $n$ -point probability functions, applicable to an arbitrary two-phase composite (Torquato, 2002). A different statistical function deserves attention when phase connectivity information is to be captured in more detail, as e.g. for medium at Figure 1. Therefore we focus here on usage of the lineal path function. The principal drawback concerns its evaluation, which is non-negligible time-consuming, especially when evaluated

---

\* Jan Havelka, Ing. Jan Sýkora, Ph.D. and Ing. Anna Kučerová, Ph.D.: Faculty of Civil Engineering, Czech Technical University in Prague, Thákurova 7/2077; 166 29, Prague; CZ, e-mails: jan.havelka.1@fsv.cvut.cz, jan.sykora.1@fsv.cvut.cz, anicka@cml.fsv.cvut.cz

many times within the optimization process. Hence, we present an accelerated implementation of the lineal path function on the GPU.



Fig. 1: Three cuts through trabecular bone microstructure obtained by micro Computed Tomography (Jiroušek et al., 2008), courtesy of O. Jiroušek, Institute of theoretical and applied mechanics.

The following section contains the definition of the lineal path function. The Section 3 discusses its algorithmic formulation and Section 4 presents the resulting speed-up obtained at GPU in comparison with the sequential CPU formulation together with concluding remarks.

## 2. Lineal path function

The lineal path function (Lu & Torquato, 1992) is one of the low-order microstructural descriptors based on a more complex fundamental function which contains more detailed information about phase connectedness and hence certain information about long-range orders (Zeman, 2003).

The fundamental function can be defined as

$$\lambda_r(\mathbf{x}_1, \mathbf{x}_2, \alpha) = \begin{cases} 1, & \text{if } \mathbf{x}_1\mathbf{x}_2 \subset D_r(\alpha), \\ 0, & \text{otherwise,} \end{cases} \quad (1)$$

i.e., a function which equals to 1 when the segment  $\mathbf{x}_1\mathbf{x}_2$  is contained in the phase  $r$  for the sample  $\alpha$  and zero otherwise. The lineal path function, denoting the probability that the  $\mathbf{x}_1\mathbf{x}_2$  segment lies in the phase  $r$ , then follows directly from the ensemble averaging of this function

$$L_r(\mathbf{x}_1, \mathbf{x}_2) = \overline{\lambda_r(\mathbf{x}_1, \mathbf{x}_2, \alpha)}. \quad (2)$$

Under the assumptions of statistical homogeneity and isotropy, the function simplifies to

$$L_r(\mathbf{x}_1, \mathbf{x}_2) = L_r(\mathbf{x}_1 - \mathbf{x}_2) = L_r(\|\mathbf{x}_1 - \mathbf{x}_2\|). \quad (3)$$

Obviously, if the points  $\mathbf{x}_1$  and  $\mathbf{x}_2$  coincide, the lineal path function takes the value of volume fraction of the phase  $r$ . On the other hand, for points  $\mathbf{x}_1$  and  $\mathbf{x}_2$  that are far apart the lineal path function vanishes.

## 3. Algorithmic formulation

The generation of SEPUC is usually based on digital images, which are discretized representation of a studied medium. The segments are then defined as a set of pixels connecting two pixels  $\mathbf{p}_1$  and  $\mathbf{p}_2$  with the coordinates within the image  $\mathbf{p}_i = (w, h)$ ,  $w \in (1, W)$  and  $h \in (1, H)$ , where  $W$  and  $H$  are the dimensions of the image (see Fig. 2). The sets of pixels for segments starting in  $\mathbf{p}_1 = (1, 1)$  and ending in  $\mathbf{p}_2 = (w, h)$  are obtained by algorithm given in (Bresenham, 1965). The group of segments is complemented by the ones starting in  $\mathbf{p}_1 = (1, H)$  and ending in  $\mathbf{p}_2 = (w, h)$  to cover all possible lengths and orientations within the image. Once having the defined segments, the computation of lineal path function involve simple translations of each segment throughout the image and the comparison whether all pixels of the segment at a given position correspond to image pixels with the value representing the investigated phase.



that for very small images, the usage of CPU outperforms the GPU because of additional time spent by copying the data from main memory RAM to GPU memory. Nevertheless, the parallelism of GPU gains for images larger than  $50 \times 50$  px and the time savings increase exponentially.

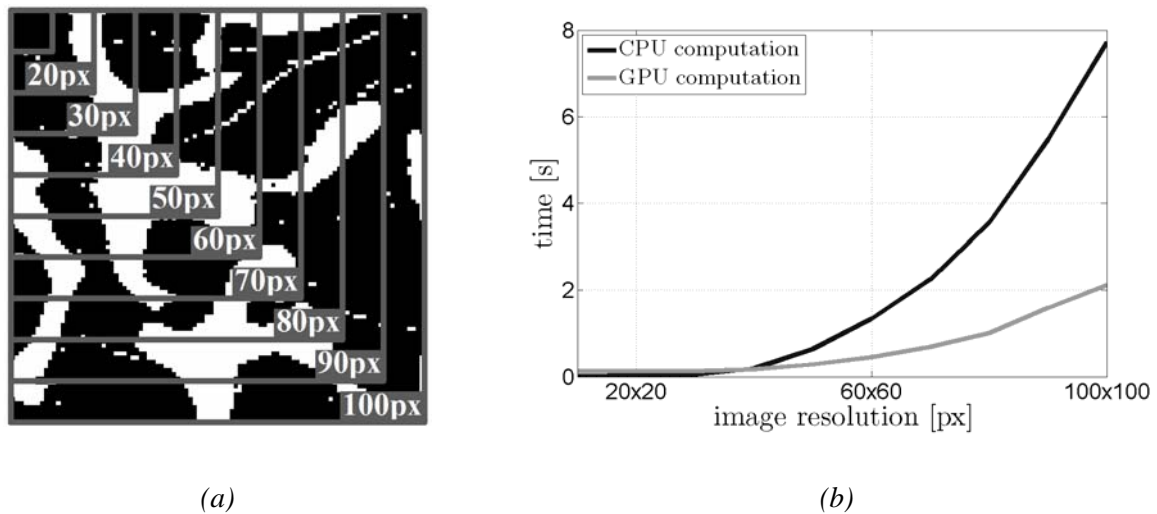


Fig. 5: (a) Testing images; (b) Comparison of CPU and GPU performance.

### Acknowledgement

The financial support of this work by the Czech Science Foundation (projects No. 105/11/0411 and 105/11/P370) is gratefully acknowledged.

### References

- Bresenham, J.E. (1965) Algorithm for computer control of a digital plotter. IBM System journal, 4, 1, pp. 25-30.
- Jiroušek, O., Vavřík, D., Jakůbek, J. & Dammer, J. (2008) Correlation of trabecular bone mechanical properties to its microstructure using  $\mu$ CT-based FE modeling, in: Proc. Engineering Mechanics, Institute of Thermomechanics AS CR, Prague.
- Lu, B. & Torquato, S. (1992) Lineal-path function for random heterogeneous materials, Physical Review E, 45, 2, pp. 922-929.
- NVIDIA Corporation (www) 2701 San Tomas Expressway Santa Clara, CA 95050, USA. <http://developer.nvidia.com/page/home.html>
- Torquato, S. (2002) Random heterogeneous materials. Springer-Verlag, New York.
- Vorel, J. (2009) Multi-scale modeling of composite materials. Ph.D. thesis, CTU in Prague, Prague.
- Vorel, J. & Šejnoha, M. (2009) Evaluation of homogenized thermal conductivities of imperfect carbon-carbon textile composites using the Mori-Tanaka method. Structural Engineering and Mechanics, 33, 4, pp. 429-446.
- Vorel, J., Zeman, J., Šejnoha, M. & Tomková, B. (2011) Homogenization of plain weave composites with imperfect microstructure: Part II-Analysis of real-world materials, submitted for publication.
- Zeman, J. (2003) Analysis of Composite Materials with Random Microstructure. Ph.D. thesis, CTU Reports, 7, 3 CTU Press, Prague.
- Zeman, J., Šejnoha, M. (2007) From random microstructures to representative volume elements. Modelling and Simulation in Materials Science and Engineering, 15, 4, S325-S335.

## ON TURBULENT BOUNDARY LAYER DYNAMICS

O. Hladík\*, V. Uruba\*

**Abstract:** *Results of experiments on fully developed turbulent boundary layer are presented. The boundary layer was generated on a smooth flat wall forming one side of the channel of rectangular cross section.*

**Keywords:** *Turbulent boundary layer, dynamics, time resolved PIV.*

### 1. Introduction

The stereo PIV method applied to the plains parallel to the wall has been used for study of the transitional boundary layer structure. This method was suggested for the first time in Longmire et al. (2003). They demonstrated the method in which the flow structure is described by planar fields of three-dimensional velocity vectors and can be effectively visualized in a single plot. In addition to local velocity values, the fields also contain information on in-plane velocity gradients. For the turbulent boundary layer examined, vorticity, swirl strength, instantaneous Reynolds shear stress, and streamwise velocity were considered as useful quantities to visualize. In combination they can be used to identify and characterize packets of hairpin vortices as shown recently in Volino et al. (2007).

### 2. Experimental setup

Experiments have been carried out on the blow-down facility in channel of cross section  $250 \times 100 \text{ mm}^2$  and 3 m in length. The inner surface of the channel with dimension 250 mm have been used as a wall for development the boundary layer. The Cartesian coordinate system have been introduced with  $x$  axis in the channel axis,  $y$  perpendicular to the wall and  $z$  direction parallel to the wall and perpendicular to the channel axis. Mean velocity in the channel core of about 4.5 m/s have been set and the boundary layer on the smooth wall in distance 2000 mm from the channel inlet, where the boundary layer starts its development. The Reynolds number based on  $x$  distance was about  $6 \cdot 10^5$ .

The flow-field measurements were acquired using time-resolved PIV technique. Streamwise-wall normal ( $x, y$ ) plane were acquired at the spanwise centerline of the test section to evaluate the boundary layer characteristics. The main experiments were performed in streamwise-spanwise ( $x, z$ ) planes were acquired at  $y$  equal approx. 2 mm, this corresponds to approximately 0.08 of the boundary layer conventional thickness.

The time-resolved PIV method was used to resolve the instantaneous velocity fields. The measuring system DANTEC consists of laser with cylindrical optics and CMOS camera. Laser New Wave Pegasus Nd:YLF, double head, wavelength 527 nm, maximal frequency 10 kHz, a shot energy is 10 mJ for 1 kHz (corresponding power  $2 \times 10 \text{ W}$ ). Camera NanoSense MkIII, maximal resolution  $1280 \times 1024$  pixels and corresponding maximal frequency 500 double-snaps per second. The camera internal memory 4 GB represents 1635 full resolution double-snaps. The maximal working frequency of the camera is limited by data rate, so it could be augmented by reducing its resolution. In the experiments we used reduced resolution with maximal possible frequency, 1600 consecutive snaps were acquired and evaluated representing 3.2 s in real time. As tracing particles the SAFEX smoke was applied. The software Dynamics Studio ver.3 was used for both data acquisition and velocity-fields evaluation by application of the adaptive correlation method.

---

\* Ing. Ondřej Hladík and assoc. prof. Ing. Václav Uruba, CSc.: Institute of Thermomechanics, AS CR, v.v.i., Dolejškova 5, 182 00 Praha 8; CZ, e-mails: hladik@it.cas.cz, uruba@it.cas.cz



### 3. Results

The boundary layer was of well-developed turbulent structure. The profiles of mean longitudinal velocity component  $U$  and variances of both velocity  $\text{var}U$  and  $\text{var}V$  components are shown in Fig. 1. The mean velocity profile shows well developed logarithmic part. Please note that the points close to the wall are of informative meaning, because the size of the interrogation area (i.e. measuring point) was about 1 mm.

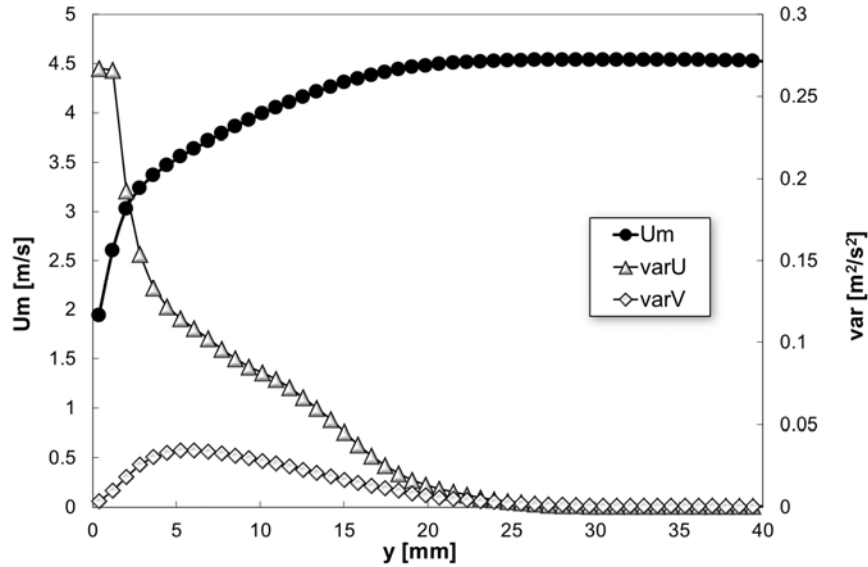


*Fig. 1: Boundary layer mean velocity profile and variances of both velocity components.*

The boundary layer thickness has been estimated to approx. 25 mm. The distance of measuring plane ( $x, z$ ) in  $y$  was approx. 2 mm, this corresponds to 0.08 of the boundary layer conventional thickness. The mean velocity was about 2.9 m/s and was approximately constant in the measuring plane with dimension 82 mm streamwise and 65 mm spanwise.

The mean velocity was subtracted from all instantaneous vector fields. The flow-field in the snap number 110 has been chosen in a random way and its vector field is shown in Fig. 2. The typical structure of the in-plane velocity vector components is visible. The vortices are moving in the mean flow direction and the structure is subjected to changes. However the character is not changing significantly.

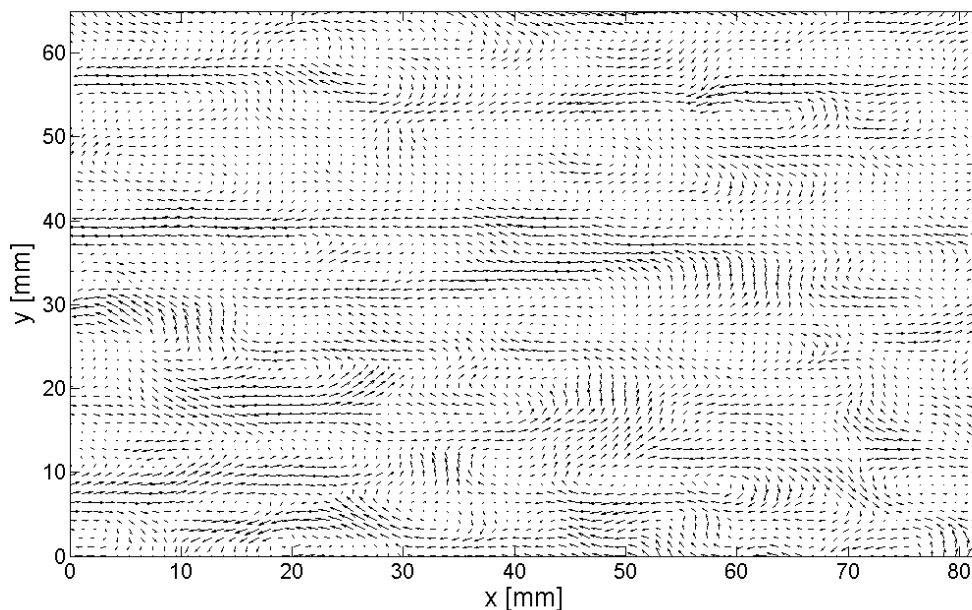


*Fig. 2: Distribution of instantaneous velocity vectors.*

In Fig. 3 distribution of instantaneous streamwise velocity fluctuations is depicted. The low velocity streaks can be identified in the flow-field and in Fig. 3 are represented by dark color.

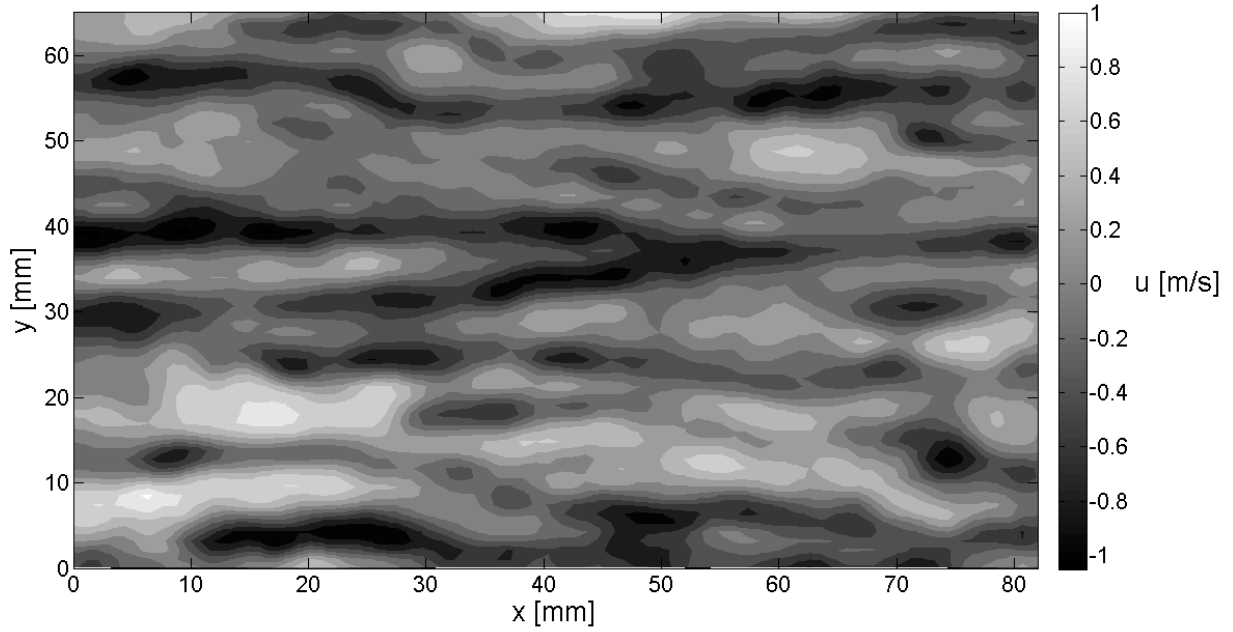


*Fig. 3: Distribution of instantaneous longitudinal velocity component.*

Distribution of vorticity component perpendicular to the measuring plane is shown in Fig. 4. Light parts represent positive vorticity (anticlockwise direction) while dark parts indicate negative vorticity (clockwise direction).

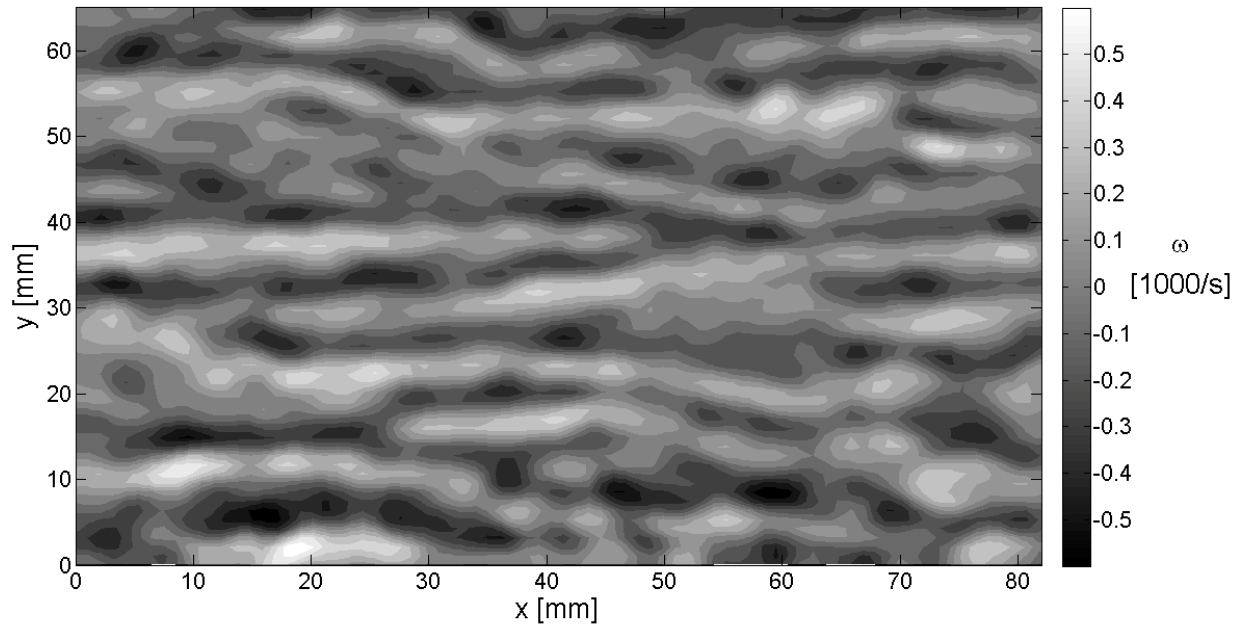


*Fig. 4: Distribution of instantaneous vorticity.*

#### 4. Conclusions

The fully developed turbulent boundary layer was subjected to experiments using time-resolved PIV technique. The profiles of mean longitudinal velocity of this boundary layer were evaluated from acquired set of data. The velocity fields in plane parallel to the wall close to it were evaluated in time sequences. The time evolution of the vector fields will be subjected to further analysis.

## **Acknowledgement**

This work has been supported by the Grant Agency of the Czech Republic, projects Nos. 101/08/1112 and P101/10/1230.

## **References**

- Longmire, E.K., Ganapathisubramani, B., Marusic, I., Urness, T., and Interrante, V. (2003) Effective visualization of stereo PIV vector fields of a turbulent boundary layer. *Journal of Turbulence*, No. 23, Vol. 4, pp. 1468–5248.
- Volino, R.J. Schultz, M.P. & Flack, K.A. (2007) Turbulence structure in rough- and smooth-wall boundary layers, *Journal of Fluid Mechanics*, Vol. 592, pp. 263-293.

## **EASY GENERATION OF MODELS/MESHES USING AN OPEN-SOURCE SOFTWARE SALOME**

**P. Hlaváček<sup>\*</sup>, V. Šmilauer<sup>\*</sup>, B. Patzák<sup>\*</sup>**

**Abstract:** *Computer-aided engineering (CAE) represents the broad usage of computers for engineering problems. It includes computer-aided design (CAD) or computer-aided analysis (CAA) to prepare representation of physical object, to discretize the object, to run analysis and to plot the results. Commercial software have often integrated modeler/mesher/solver/post-processor into one big package. These include ATENA, ABAQUS, ANSYS, SCIA, MARC to mention a few. The open-source CAE has been dropping behind in terms of user friendliness and efficiency. The situation is changing dramatically now since commercial companies support development of open-source. Salome presents a nice platform for pre/post-processing, released under the terms of the GNU LGPL license. This paper will demonstrate application of Salome modeler/mesher for various engineering analyses: steel buckling and multiscale heat analysis. Generation of appropriate mesh is easy and very efficient and can be exported to several computational codes, such as an object-oriented OOFEM. Post-processing can be carried out via VTK data format, for example in Paraview open-source post-processor. Python language can easily glue all components into one package, using advantages of control/modification/verification stages in each data transfer process.*

**Keywords:** *CAE, CAD, Salome, OOFEM.*

### **1. Introduction**

Computer Aided Engineering (CAE) represents a broad computer software support in engineering tasks, covering, e.g., Computer Aided Design (CAD) or Computer Aided Analysis (CAA). This paper elucidates CAE design in integration with finite element package used for civil engineering purposes.

The open-source platform Salome is a pre/post-processing environment for numerical simulations. In the presented paper the pre-processing, which includes creation of model, meshing and input data converting, for analysis in in-house package OOFEM is carried out. The OOFEM (Object Oriented Finite Element Solver) is an in-house open-source package for solving of multiphysics problems (Patzák, 2011). The python-based unv2oofem converter efficiently integrates pre-processing software with computationally-based OOFEM. For example, after the modeling and meshing in Salome platform, the mesh could be exported as UNV data-file. The unv2oofem converter then exports the data to OOFEM-readable input file. Unv2oofem reads the mesh geometry from UNV data set assembles material properties and node/boundary conditions defined in extra file and writes the OOFEM input file in native format.

### **2. Selected open-source tools for CAE**

The Salome is an open-source platform for numerical simulations (Open CASCADE, 2011). It is developed by Open Cascade (France) and LGPL licensed, meaning the source could be modified and redistributed. The Salome is primarily designed as a platform for integration of external codes. The main feature of Salome represents the link between CAD modeling and computational software in terms of CAA. The Salome, as distributed, allows a simple and fast creation of various geometry models and sophisticated meshing.

---

<sup>\*</sup> Ing. Petr Hlaváček, doc. Ing. Vít Šmilauer, Ph.D. and prof. Dr. Ing. Bořek Patzák: Faculty of Civil Engineering, Czech Technical University in Prague; Thákurova 7; 166 29, Prague; CZ, e-mails: petr.hlavacek@fsv.cvut.cz, vit.smilauer@fsv.cvut.cz, borek.patzak@fsv.cvut.cz

The OOFEM is an open-source finite element solver with object oriented architecture developed at the Faculty of Civil Engineering in Prague by B. Patzák *et al.* (Patzák & Bittnar, 2001). The OOFEM is released under the GNU General Public License (GPL) and could be used for solving of multiphysics tasks as mechanical, transport or fluid mechanics problems (Patzák, 2011). The OOFEM input file has an open ASCII format and generally can be written/modified in any text software. The output from OOFEM can be exported to VTK data set, for example.

The ParaView is an open-source data visualization application, which allows to build fast visualizations for data analysis using qualitative and quantitative techniques (Kitware, 2011). The data exploration can be done interactively in 3D. The ParaView supports input file in the VTK format.

### 3. Application of CAE/CAD tools to engineering problems

Two selected engineering problems solved by above mentioned software are presented in this section. The mechanical problem of steel structure buckling and the heat transport problem during concrete casting of a highway bridge are described.

#### 3.1. Steel plasticity with buckling

This example demonstrates analysis of a structural detail, where a girder beam crosses a column. A welded pair of U profiles 300 mm creates both cross-sections of the beam and the column. The geometry was meshed into 10 383 nodes and 30 786 linear tetrahedral elements.

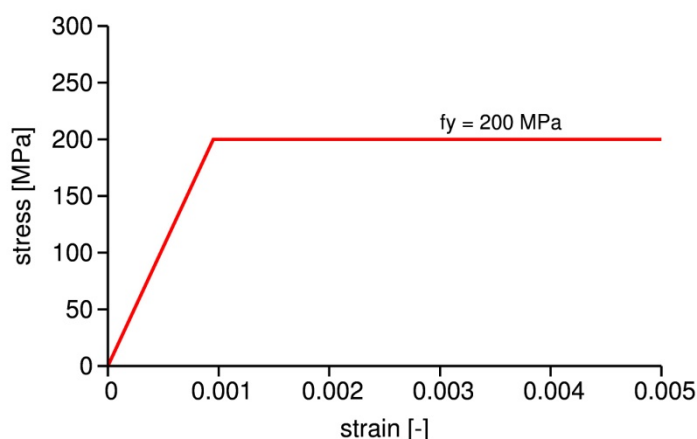


Fig. 1: Stress–strain curve for ideal elasto-plastic material.

Perfectly plastic material is assigned to steel with the yield strength of 200 MPa (Fig.1), which roughly corresponds to the steel grade S235. Updated Lagrangian formulation ensured updating nodal position after each time increment thus facilitating second-order theory and equilibrium on deformed shapes assuming small strains in constitutive laws (Eq. 1) (Jirásek & Bažant, 2002).

$$\boldsymbol{\sigma} = \mathbf{D} : (\boldsymbol{\varepsilon} - \boldsymbol{\varepsilon}_{pl}) \quad (1)$$

Fig. 2 shows the mesh created in Salome package; also the stresses and the displacement vector immediately before collapse are depicted. The maximum axial force 1.58 MN applied on the vertical column leads to collapse in plastic/buckling mode. The computation took 11.5 min in eight loading steps. The whole analysis, including construction of geometry, meshing, computation, post-processing and interpretation took less than one hour of work.

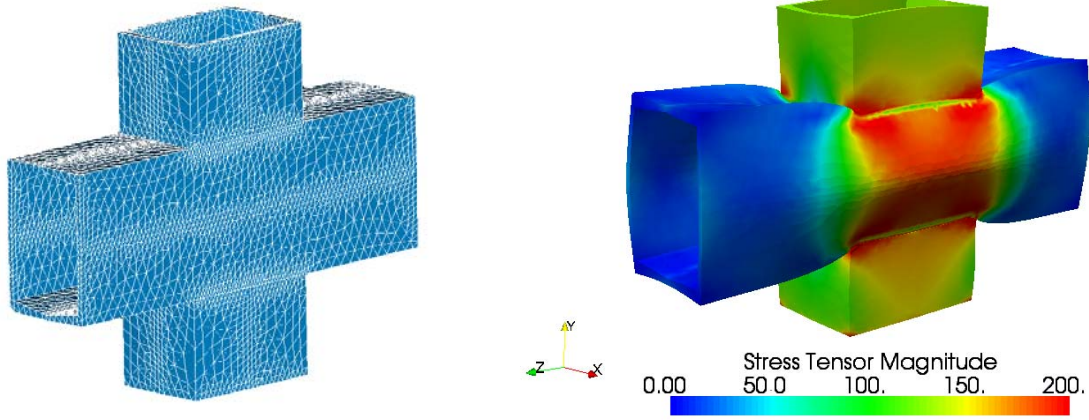


Fig. 2: Detail of a joint with the mesh and computed stress magnitude.

### 3.2. Multiscale heat transport analysis

The second example shows the simulation of heat transport during hardening of concrete in Oparno highway bridge. Hydrating concrete produces significant amount of hydration heat, which causes several problems in massive concrete elements. Multiscale simulation helped to find an optimal position of cooling pipes and cooling regime on the bridge arch. The well-known non-stationary heat conduction equation, mentioned for example by Bao-Lin Wang *et al.* (Bao-Lin Wang & Yiu-Wing Mai, 2005), reads:

$$-\frac{\partial q(\mathbf{x},t)}{\partial x} + \bar{Q}(\mathbf{x},t) = \rho(\mathbf{x},t)c(\mathbf{x},t)\frac{\partial T(\mathbf{x},t)}{\partial t} \quad (2)$$

The simulation runs on the left symmetric part of the arch cross-section. The model and mesh were created in Salome platform, the 2D triangular finite elements were oriented in directions of supposed temperature gradients and refined in the region of cooling pipes, see Fig. 3.

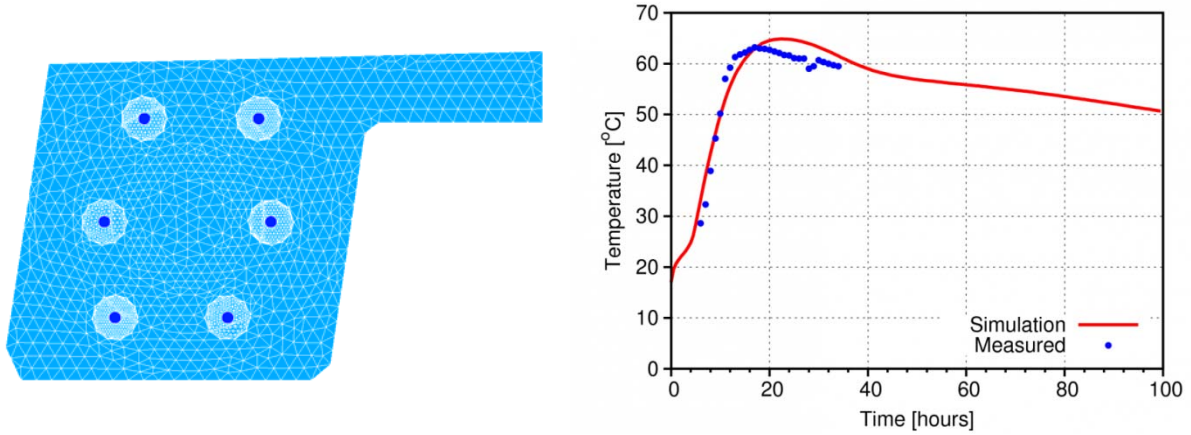
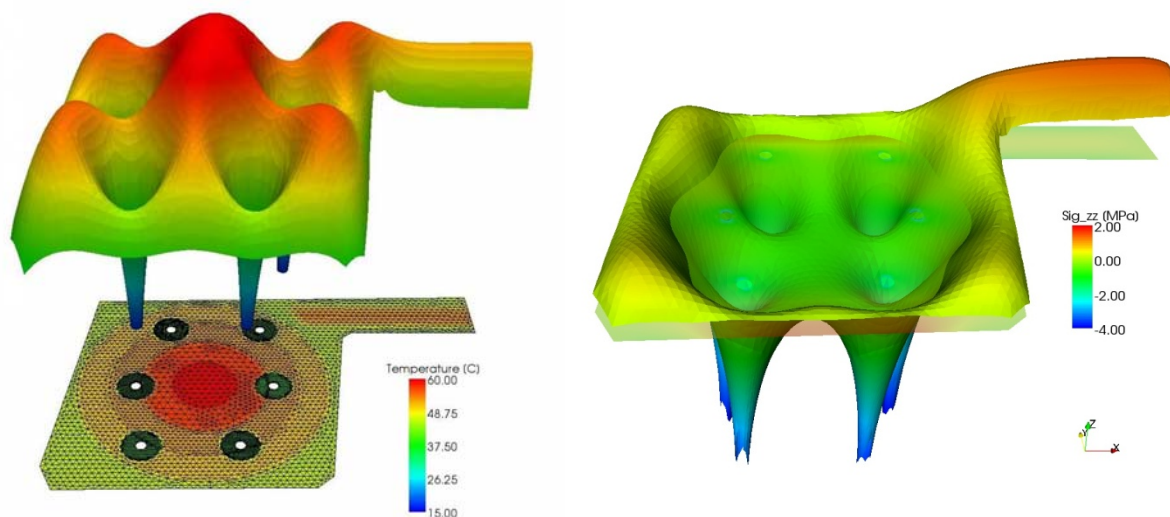


Fig. 3: Left: Mesh of Oparno bridge cross-section, Right: Validation of simulation with measured temperatures in the core of beam.

Fig. 4 shows the temperature evolution during concrete hardening and induced out-of-plane stress when considering B3 model for concrete creep. Optimal position of cooling pipes is apparent. Note that the cooling turns off after several hours which detaches natural Dirichlet's boundary conditions and changes number of equations. The flat bottom subfigure shows the 2D triangular mesh and the assignment of hydration models to groups of finite elements on the cross-section. Fig. 2 also validates the multiscale simulation with the temperature in the core of the beam. Temperature remained below 65°C during summer casting, which was found acceptable.





*Fig. 4: Temperature and stress field during concrete hardening.*

#### 4. Conclusions

With the development of open-source software, CAE/CAD analysis can be easily integrated with other computational software. This facilitates necessary step for the creation of a user-friendly platform, which is required in the majority of modeling steps. The Salome platform as a pre-processor in the combination with the OOFEM as a solver and with the ParaView as a post-processor present an open-source alternative to the commercial computational programs. The assessment of a steel joint and the design of cooling pipes proved the excellent features of the presented software.

#### Acknowledgement

Financial support from the Grant Agency of the Czech Technical University in Prague, grant No. SGS10/135/OHK1/2T/11 and from the Czech Science Foundation GA ĆR103/09/H078 are gratefully acknowledged.

#### References

- Kitware (2011) ParaView application home page, <http://www.paraview.org>.
- Open CASCADE (2011) Salome platform home page, <http://www.salome-platform.org>.
- Patzák B. (2011) OOFEM project home page, <http://www.oofem.org>.
- Patzák B. & Bittnar Z. (2001) Design of object oriented finite element code. *Advances in Engineering Software*, 32(10-11):759--767.
- Šmilauer, V. et al. (2011) Multiscale simulation of fracture of braided composites via repetitive unit cells. *Engineering Fracture Mechanics*, in press.
- Jirásek M. & Bažant Z. P. (2002) *Inelastic Analysis of Structures*, Book, John Willey & Sons, Ltd, ISBN 0-471-98716-6
- Bao-Lin Wang & Yiu-Wing Mai (2005) Transient one-dimensional heat conduction problems solved by finite element. *International Journal of Mechanical Sciences*, 47(2):303-317.

## THE DETECTION OF DEFECTS OF MECHANICAL STRUCTURES USING SURFACE ACOUSTIC WAVES (SAW)

M. Hlavatý\*, L. Starek\*

**Abstract:** *The article gives the general view to the detection of defects (rather the cracks) of mechanical structures through initializing and receiving so-called Rayleigh waves, which have value over 1 MHz (ultrasonic). The detection of cracks in solids using ultrasound is known for several decades, but as a method continuous monitoring (on-line) of cracks during operation of structures is being developed only a few years. Main physical properties SAW are; waves may be created and propagated only at surface materials (with small dissipation) and ability surface waves to penetrate into the certain depth under surface. In addition, depth of penetration depended of wave frequency. In conjunction with the fact, that the surface-breaking crack behaves as a low-pass filter, the SAW have a perspective in detection of cracks. This is the subject of analysis. In addition, attention focus to selection potential appropriate parameters for detection, which would detect cracks effective and also monitor ones propagate in the material.*

**Keywords:** *Nondestructive testing, surface acoustic waves, on-line method, cracks.*

### 1. Introduction

Properly on-line nondestructive testing method of detection of surface-breaking cracks for mechanical structures must satisfy several criteria:

- Method must use the smallest sensors and equipment because crack is being created often in difficult to access place.
- Method should not be calibrated for individual case of structural monitoring.
- The detection of crack must have un-ambiguous results.
- On-line monitoring system must be robust towards environmental noise and varying conditions of mechanical structures.
- Crack should be detected as soon as possible.
- Easy in terms of interpret and computational time.

Many articles, which were published in conferences and journals showed that on-line method, which use ultrasonic surface waves, may satisfy criteria presented above. This method use small and powerful sensors and measuring equipments with high sensitivity. Due the high frequency transducers robustness of method towards environmental noise can be attained. The inverse proportional between penetrate depth  $d$  and wave frequency  $f$  cause high sensitivity of method. Even, this method reaches better sensitivity than for example optical or gage method. Indeed, SAW or Rayleigh waves penetrate approximately one wavelength  $\lambda$  into the material (Vanlanduit et al., 2003). Up to 95 % wave energy transmits in this penetration depth. Rayleigh wave velocity is  $c$  (for steel is  $c = 3240 \text{ m.s}^{-1}$ ).

$$f = \frac{c}{\lambda} = \frac{c}{d} \quad (1)$$

The penetration depth in function of its frequency is showed in figure 1. We can use this property of SAW to the cracks detection, because discontinuities cause reflection of surface waves. Therefore, the surface-breaking crack causes complete scattering (reflection) of spectral part of the signal, which is formed SAW having wavelengths smaller than crack length. Unfortunately, this theorem doesn't true quite. Waves scattering depend on the stress-state of place with crack. In other words, when the crack

---

\* Ing. Michal Hlavatý and prof. Ing. Ladislav Starek, PhD.: Institute of applied mechanics and mechatronics, Faculty of Mechanical engineering, Slovak University of Technology in Bratislava; Námetie Slobody 17; 812 31; Bratislava 1; Slovakia, e-mails: [michal.hlavaty@stuba.sk](mailto:michal.hlavaty@stuba.sk), [ladislav.starek@stuba.sk](mailto:ladislav.starek@stuba.sk)

is closed (e.g. caused by bending beam), through crack is transmitted full signal energy without reflection. Thus, statistic parameters must use for detection and monitoring of cracks.

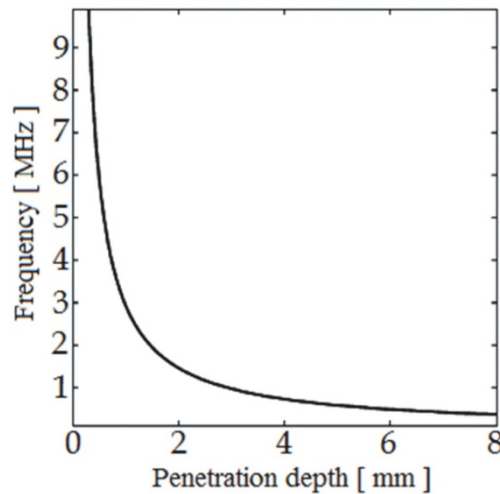


*Fig. 1: Penetration depth versus its frequency.*

## 2. The describe of the potential appropriate parameters

Proposed the on-line methods of cracks detection use information about transmitted (there are two sensors, crack is between the; pitch-catch mode) or reflected (there are one sensor; pulse-echo mode) signals in time and frequency domains. Firstly, attention to possible transmission of signal through tightly closed crack is given.

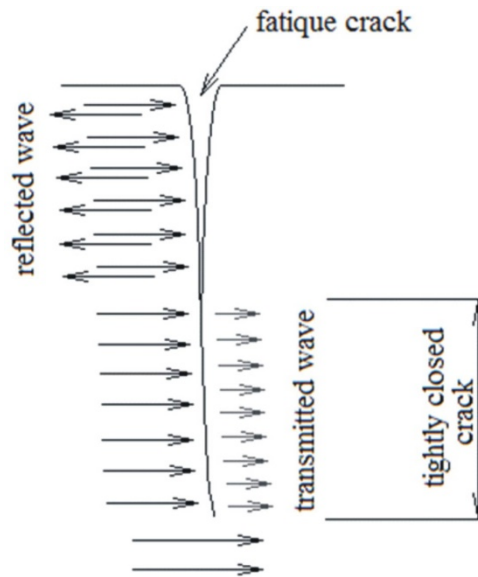


*Fig. 2: The different interactions of crack with SAW.*

The different interaction of surface waves with tightly closed crack is given in Fig. 2. Roughly half of energy SAW is transmitted through crack, because crack is partially closed (crack areas are touching). This state may cause bad detection of crack, i.e. underestimating of size of a crack and suppression of detection of small cracks (Harri et al., 2006). Therefore, statistical parameters must be used in evaluation of crack monitoring, when load cause opening and closing of fatigue crack. Satisfactory experimental results of fatigue cracks detection was achieved sensing of the receiving signal amplitude (especially in frequency domain). Crack can be either open or close, when mechanical system is subjected operating load. Then, if surface waves from transducer are transmitted (with greater frequency as the load) through crack, amplitudes of received waves have varying values. Of course, crack length must be larger than wavelength, also frequency of waves sending must be higher than the load frequency. So-called effect the breathing crack causes varying the amplitude values. Therefore,

minimum amplitude may be satisfactory experimental parameter. The experimental results (amplitude of transmitted spectral component) for crack detection are showed in Fig. 3 (Harri et al., 2006). The dispersion of the amplitude components (2 and 5 MHz) started to grow in certain moment. Effect the breathing crack caused decrease of the minimum amplitude. Because the maximum amplitude of transmitted signal remained constant, the dispersion of the amplitude (the difference between maximum and minimum amplitude) increased proportionally with the number of load cycles (number of measurements).

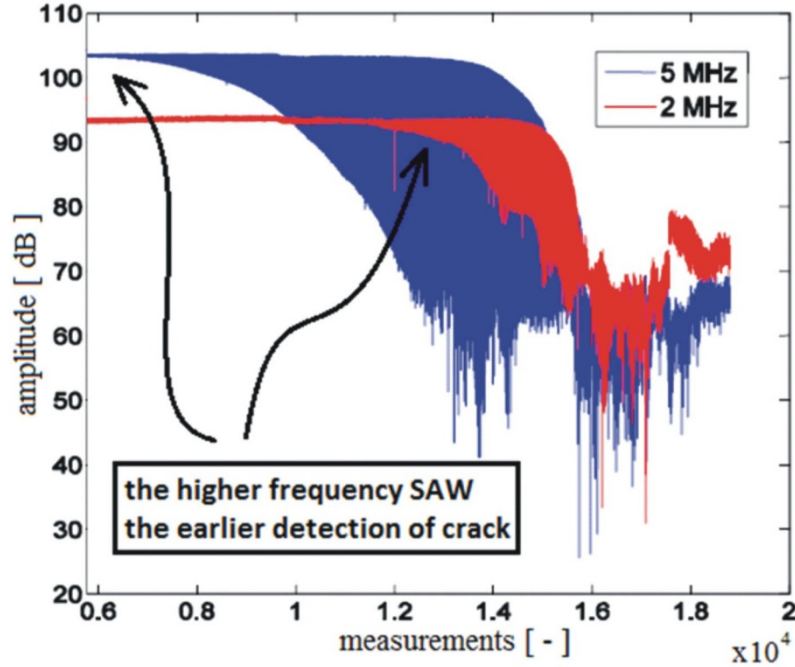


Fig. 3: Amplitude of the 2 and 5 MHz spectral components.

The minimal amplitude of 5 MHz spectral components started to grow in earlier moment than minimal amplitude of 2 MHz component. Then, amplitude of the SAW can be used to monitor crack depth and to estimate its length in the material. Note that plastic deformation of the crack root causes decrease of the maximal amplitude. This is due to the fact that the crack is not closed.

The phase indicator is also good statistical parameter for the detection of the crack (only pulse excitation). The creation of the crack causes stiffness decrease of the mechanical systems. Thus the greater depth of the crack the smaller stiffness of mechanical system. If distance between the sensors (pitch-catch mode) is  $l$  and phase difference of the SAW is  $\Phi = 180^\circ$ , the spatial difference can be computed from equation (2)

$$\delta l = \frac{c}{2f} \quad (2)$$

$$\varepsilon = \frac{\delta l}{l} \quad (3)$$

and the strain  $\varepsilon$  can be computed from equation (3). Therefore, if there is a sudden increase in the strain, crack was created very probably. The phase indicators versus a crack length is given in Fig. 4 (Vanlanduit et al., 2003). Better sensitivity than for the amplitude indicators is showed (the crack was detected for its length about 0.17 mm, i.e. improvement toward previous indicator is 15%; this case).

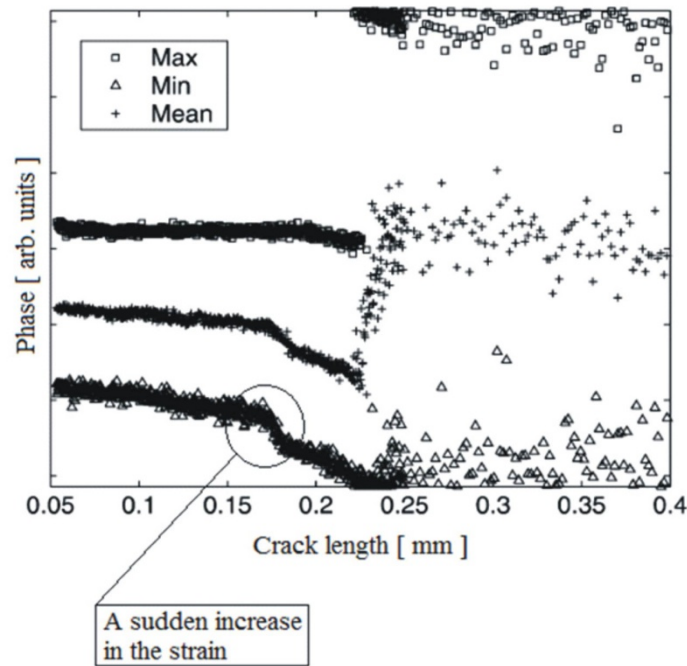


Fig. 4: Phase indicators in function a crack length.

Unfortunately, the monitoring of crack occurs impossible for larger one length, when signal-to-noise ratio has small value. Consequently, the phase indicator is good statistical parameter for detection of small crack.

### 3. Conclusions

The method of surface acoustic waves (Rayleigh waves) for detection of crack was presented. Firstly, several important criteria for on-line detection of crack and fundamentals of method were explained. Secondly, the appropriate statistical indicators of method were designed - minimum amplitude and phase of SAW. Experiments showed that the minimum amplitude is very good indicator of detection, because we can detect and monitor crack using this parameter quite reliably. The phase indicator is better parameter than minimum amplitude, but one is appropriate only for detection of small cracks, because small value of signal-to-noise ratio attains for larger crack length.

### Acknowledgments

The author gratefully acknowledges the support of the Slovak Ministry of Education Grant Agency VEGA # 1/0744/10.

### References

- Harri, K., Guillaume, P., Vanlanduit, S. (2006) On-line monitoring of cracks using ultrasonic "multisine" surface waves. ECNDT, Th.1.5.3, pp.1-7.
- Cook, D.A., Berthelot, Y.H. (2001) Detection of small surface-breaking fatigue cracks in steel using scattering of Rayleigh waves. NDT&E international, 34, pp. 483-492.
- Vanlanduit, S., Guillaume, P., Van Der Linden, G. (2003) On-line monitoring of fatigue cracks using ultrasonic surface waves. NDT&E international, 36, pp. 601-607.
- Jeong, K.N., Blackshire, J.L. (2010) Interaction of Rayleigh surface waves with a tightly closed fatigue crack. NDT&E international, 43, pp. 432-439.
- Masserey, B., Fromme, P. (2009) Surface defect detection in stiffened plate structures using Rayleigh-like waves. NDT&E international, 42, pp. 564-572.

## COMPARISON OF NONLOCAL AND GRADIENT-ENHANCED DAMAGE-PLASTICITY MODEL

M. Horák<sup>\*</sup>, M. Jirásek<sup>\*</sup>

**Abstract:** *This paper deals with a damage-plasticity model combining Mises plasticity with isotropic damage. Due to softening induced by damage growth, the governing differential equations lose ellipticity, which leads to an ill-posed boundary value problem. From the numerical point of view, ill-posedness is manifested by pathological sensitivity of the results to the size of finite elements. To avoid this undesired behavior, the model is regularized by a nonlocal integral formulation or, alternatively, by an implicit gradient formulation. The difference between the formulations is discussed and the behavior of both regularized models is illustrated by a numerical example.*

**Keywords:** *Nonlocal continua, damage-plasticity model, finite elements.*

### 1. Introduction

This paper presents a coupled damage-plasticity model. Continuum damage mechanics is suitable for the description of stiffness degradation due to the growth of defects such as micro-voids and micro-cracks, while plasticity theory describes permanent deformations of a material induced e.g. by slip mechanisms. However, standard damage-plasticity models with softening would lead to physically meaningless results. In this contribution, two methods that can provide an objective description of localized inelastic processes are described. Both can be classified as strongly nonlocal (Bažant and Jirásek, (2002)) and introduce a new material parameter with the dimension of length.

### 2. Constitutive model

In this section, the constitutive model combining the classical Mises plasticity with isotropic damage is described. We restrict our attention to the small strain theory, thus the kinematic framework is based on the additive decomposition of strain into the elastic part and the plastic part,

$$\boldsymbol{\varepsilon} = \boldsymbol{\varepsilon}_e + \boldsymbol{\varepsilon}_p. \quad (1)$$

The stress-strain law has the form

$$\boldsymbol{\sigma} = (1 - \omega)\bar{\boldsymbol{\sigma}} = (1 - \omega)\mathbf{D} : \boldsymbol{\varepsilon}_e, \quad (2)$$

where  $\boldsymbol{\sigma}$  is the nominal stress tensor,  $\bar{\boldsymbol{\sigma}}$  is the effective stress tensor,  $\mathbf{D}$  is the fourth-order stiffness tensor and  $\omega$  denotes a scalar damage variable. The yield condition is formulated in terms of the effective stress, and so the Mises yield function is written as

$$f(\bar{\boldsymbol{\sigma}}, \kappa) = \sqrt{\frac{3}{2} \bar{\mathbf{s}} : \bar{\mathbf{s}}} - \sigma_Y(\kappa), \quad (3)$$

where  $\bar{\mathbf{s}}$  is the deviatoric part of effective stress.

The loading-unloading conditions are expressed in the usual form

$$f(\bar{\boldsymbol{\sigma}}, \kappa) \leq 0 \quad \dot{\lambda} \geq 0 \quad \dot{\lambda} f(\bar{\boldsymbol{\sigma}}, \kappa) = 0. \quad (4)$$

---

<sup>\*</sup> Ing. Martin Horák and prof. Ing. Milan Jirásek, DrSc.: Katedra mechaniky, Stavební fakulta ČVUT v Praze, Thákurova 7/2077, 166 29 Praha 6; CZ, e-mails: martin.horak@fsv.cvut.cz, milan.jirasek@fsv.cvut.cz



The yield function (3) incorporates the isotropic linear hardening rule

$$\sigma_Y(\kappa) = \sigma_0 + H\kappa. \quad (5)$$

where  $H$  denotes the hardening modulus and  $\kappa$  is the cumulated plastic strain defined by the evolution law

$$\dot{\kappa} = \sqrt{\dot{\boldsymbol{\varepsilon}}_p : \dot{\boldsymbol{\varepsilon}}_p}. \quad (6)$$

The associative flow rule is considered,

$$\dot{\boldsymbol{\varepsilon}}_p = \dot{\lambda} \frac{\partial f(\bar{\boldsymbol{\sigma}}, \kappa)}{\partial \bar{\boldsymbol{\sigma}}}. \quad (7)$$

The growth of damage is driven by the cumulated plastic strain and is described by the exponential law

$$\omega(\kappa) = \omega_c \left(1 - e^{-a\kappa}\right). \quad (8)$$

In the equation above,  $\omega_c$  is the critical damage and  $a$  is a positive dimensionless parameter that controls the softening part of the stress-strain diagram.

### 3. Regularization techniques

The local model cannot be used after loss of ellipticity of the governing equation, because of the resulting pathological sensitivity of the numerical results with respect to the size and orientation of the finite element mesh. The present model is regularized by the integral or gradient formulation. In both approaches, the damage variable is computed from the over-nonlocal cumulated plastic strain while the plastic part of the model remains local. The over-nonlocal cumulated plastic strain is computed as

$$\hat{\kappa} = (1 - m)\kappa + m\bar{\kappa}, \quad (9)$$

where  $\bar{\kappa}$  is the nonlocal cumulated plastic strain and  $m$  is a model parameter. Full regularization can be achieved only if parameter  $m$  is greater than 1 (Jirásek and Rolshoven, 2003). Evaluation of the nonlocal cumulated plastic strain follows a different procedure for the integral formulation and for the gradient formulation.

#### 3.1. Integral-type nonlocal formulation

The integral nonlocal formulation is based on weighted spatial averaging of the cumulated plastic strain:

$$\bar{\kappa}(x) = \int_V \alpha(x, s) \kappa(s) ds, \quad (10)$$

with the nonlocal weight function  $\alpha(x, s)$  defined as

$$\alpha(x, s) = \frac{\alpha_0(\|x - s\|)}{\int_V \alpha_0(\|x - t\|) dt}. \quad (11)$$

Here,

$$\alpha_0(r) = \left(1 - \frac{r^2}{R^2}\right)^2. \quad (12)$$

is a monotonically decreasing function for  $r < R$  and vanishes if the distance  $r$  exceeds the nonlocal interaction radius  $R$ .

### 3.2. Gradient-enhanced formulation

The gradient formulation can be conceived as the differential counterpart to the integral formulation. Here we focus on the implicit gradient formulation, which is more robust than the explicit one and requires only  $C^0$  continuous finite element approximation. Instead of evaluation of the integral in (10), the nonlocal cumulated plastic strain is computed from a Helmholtz-type differential equation

$$\bar{\kappa} - l^2 \nabla^2 \bar{\kappa} = \kappa, \quad (13)$$

with homogeneous Neumann boundary condition. In (13),  $l$  is the length scale parameter and  $\nabla^2$  is the Laplace operator. It can be shown that the implicit gradient formulation is equivalent to the integral one with a special weight function, but the numerical implementation is quite different.

### 4. Numerical implementation

The numerical implementation of the local version of the model consists of the classical radial return algorithm followed by an explicit evaluation of damage. In the integral theory, nonlocal cumulated plastic strain is evaluated from the integral (10), which is in the numerical implementation replaced by the finite sum

$$\bar{\kappa}_k = \sum_{l=1}^{N_{GP}} w_l J_l \alpha_{kl} \kappa_l, \quad (14)$$

where  $w_l$  is the integration weight,  $J_l$  is the Jacobian of the isoparametric transformation, and

$$\alpha_{kl} = \frac{\alpha_0 (\|x_k - x_l\|)}{\sum_{n=1}^{N_{GP}} w_n J_n \alpha_0 (\|x_k - x_n\|)} \quad (15)$$

is the weight of interaction between points  $k$  and  $l$ .  $\alpha_{kl}$  vanishes if the distance between points  $k$  and  $l$  is larger than the nonlocal integration radius  $R$ , so the sum can be evaluated only for Gauss points  $l$  inside the circle radius  $R$  centered at Gauss point  $k$ .

Implementation of the implicit gradient approach leads to a coupled problem. The Helmholtz equation (13) is coupled with the standard equilibrium equation, and new degrees of freedom (which correspond to nodal values of the nonlocal variable) are introduced. It is shown in (Simone et al., 2003) that using the same order for the interpolation functions for the displacement and for the nonlocal cumulated plastic strain could lead to spurious oscillations in the stress field. To suppress such oscillations, a quadratic approximation of displacement and a linear approximation of nonlocal cumulated plastic strain are used in the simulation.

One advantage of the integral formulation is that the kinematic and equilibrium equations remain standard and the strain and stress keep their usual form, but the computational cost is increasing since the profile of nonzero elements of the nonlocal consistent algorithmic tangent stiffness is growing during the simulation due to the nonlocal interaction between Gauss points; see Jirásek & Patzák (2004) and (Horák et al., 2011) for derivation and other numerical aspects of the consistent nonlocal algorithmic tangent stiffness. The main disadvantage of the implicit formulation consists in the introduction of new nonlocal degrees of freedom with non-straightforward physical meaning; on the other hand the computational cost does not depend on the internal length.

### 5. Numerical simulation

Both nonlocal models were implemented into OOFEM, an object-oriented finite element code (Patzák, & Bittnar, 2001; Patzák, Rypel & Bittnar, 2001). To show that the models remove pathological sensitivity to the size of finite elements, a simple uniaxial tensile test of the bar clamped at one end and loaded by a prescribed displacement incrementally applied at the free end is simulated. The yield stress in the central part of the bar is reduced by 10% to trigger localization. The following geometrical and material parameters were selected: bar length  $L = 100$  cm, cross-sectional area

$A = 1 \text{ cm}^2$ , Young's modulus  $E = 40\,000 \text{ MPa}$ , initial yield stress  $\sigma_Y = 100 \text{ MPa}$ , hardening modulus  $H = 0 \text{ MPa}$ , damage parameters  $\omega_C = 0.7$ ,  $a = 60$  and nonlocal parameter  $m = 1.5$ , internal length for nonlocal model  $R = 2 \text{ cm}$  and internal length for gradient model  $l = 2 \text{ cm}$ . The finite element mesh and the development of damage along the bar are plotted in Fig. 1. The size of localization zone for the local version of the model is dictated by the element size. The gradient and integral models lead to meaningful results with a localization band extending over several elements. The width of the band depends on the choice of the length scale parameters.

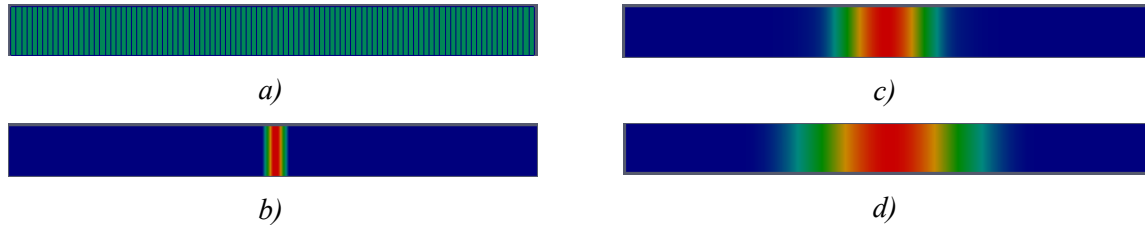


Fig. 1: a) Finite element mesh, b) damage distribution for the local model, c) damage distribution for the gradient formulation, d) damage distribution for the integral formulation.

## 6. Conclusions

We have presented a model that combines Mises plasticity with isotropic damage mechanics, and introduced two remedies which lead to an objective description of localized failure processes. Further research will focus on the comparison of the computational efficiency of both models in two-dimensional and three-dimensional large-scale problems, and on extensions of the gradient regularization to more general yield conditions.

## Acknowledgement

Financial support received from the Czech Science Foundation under project GAČR P108/11/1243 is gratefully acknowledged.

## References

- Horák, M., Jirásek, M., Charlebois, M. & Zysset, P.K. (2011) Nonlocal tangent operator for damage-plasticity model, in Programs and Algorithms of Numerical Mathematics, to appear.
- Patzák, B. & Jirásek, M. (2004) Consistent tangent stiffness for nonlocal damage models, in Computers and Structures, 80, pp. 1279-1293.
- Bazant, Z.P. & Jirásek, M. (2002) Nonlocal integral formulations of plasticity and damage: Survey of progress, in Journal of Engineering Mechanics ASCE, 128, pp. 1119-1149.
- Jirásek, M. & Rolshoven, S. (2003) Comparison of integral-type nonlocal plasticity models for strain-softening materials, in International Journal of Engineering Science, 41, pp. 1553-1602.
- Peerlings, R. H. J., de Borst, R., Brekelmans, W. A. M., de Vree J. H. P. (1996) Gradient-enhanced damage for quasi-brittle materials, in International Journal for Numerical Methods in Engineering, 39, pp. 3391-3403.
- Simone, A., Askes, H., Peerlings, R.H.J., Sluys, L.J. (2003) Interpolation requirements for implicit gradient-enhanced continuum damage models, Communications in Numerical Methods in Engineering, 19, pp. 563-572.
- Patzák, B. & Bittnar, Z. (2001) Design of object oriented finite element code, Advances in Engineering Software, 32, pp.759-767.
- Patzák, B., Rypl D. & Bittnar, Z. (2001) Parallel explicit finite element dynamics with nonlocal constitutive models. Computers and Structures, 79, pp. 2287-2297.

## INFLATION-EXTENSION TEST OF SILICON RUBBER TUBE REINFORCED BY NITI WIRES

L. Horný\*, J. Kronek\*, H. Chlup\*, E. Gultová\*, L. Heller\*\*, R. Žitný\*, D. Vokoun\*\*

**Abstract:** *The composite tube fabricated from elastomer matrix reinforced with NiTi wires was tested within simultaneous inflation and extension. Four different longitudinal weights were applied ( $m = 41$  g; 188 g; 488 g; and 785 g). The inflation was induced with repeating pressurization up to 200 kPa. No significant hysteresis and material instability, typical for elastomeric tubes, were observed. Simplified model, assuming the tube to be anisotropic hyperelastic continuum, was adopted in order to estimate material parameters by analytical model of the thick-walled vessel. This model was only successful in fitting the data corresponding to the smallest longitudinal weight. It was concluded that NiTi reinforcement reduces elastomer viscoelasticity in macroscopic response, which can not be fully described with the model considering the effect of wires only as the introduction of anisotropy.*

**Keywords:** *Anisotropy, hyperelasticity, inflation-extension test, nitinol, silicon rubber.*

### 1. Introduction

Structures based on thin NiTi wires, due to shape memory, superelasticity and biocompatibility, have become increasingly utilized in biomedical engineering. So-called self-expandable stents, which are used upon revascularization treatments in stenotic arteries, are frequently made of nitinol wires (Stoeckel et al., 2004). Such wires can be designed in 2D and 3D structures using standard textile production methods (weaving, knitting, and braiding). Generally, the shape memory allows these materials to be programmed by means of metallurgical treatment. Such products can afterward be employed as mechanical controlling units. On the other hand, rather large recoverable strains (in comparison with metals) of nitinol can be utilized in a design of actuators. Combining above mentioned and considering hydraulic systems nonconventional pumps or ventilators may be constructed.

The aim of the present study is to investigate mechanical response of elastomeric tube reinforced with thin NiTi wires. Pressure-diameter and longitudinal extension-force relationships were obtained within the inflation-extension test with the silicon rubber tube with implemented wires. This is only the pilot study which can not report final conclusions and constitutive model of the structure which is composite in its nature. Nevertheless, preliminary results will direct us at suitable computational model.

### 2. Methods

#### 2.1. Sample preparation

NiTi wire with a diameter 100  $\mu\text{m}$  used in this study was purchased from Fort Wayne Metals (Indiana, USA). Tubular sample of silicon elastomer-NiTi wire composite was fabricated at the Institute of Physics of the Czech Academy of Sciences. Metallic part of the final composite was fabricated as fenestrated cylindrical shell (braided structure of NiTi fibers) with 36 helically coiled wires. Wires were wound around in two families of helices symmetrically disposed along the longitudinal axis of

---

\* Ing. Lukáš Horný, Ing. Jakub Kronek, Ing. Hynek Chlup, Ing. Eva Gultová and prof. Ing. Rudolf Žitný, CSc.: Faculty of Mechanical Engineering, Czech Technical University in Prague, Technická 4; 166 07, Prague; CZ, e-mails: Lukas.Horny@fs.cvut.cz, Jakub.Kronek@fs.cvut.cz, Hynek.Chlup@fs.cvut.cz, Eva.Gultova@fs.cvut.cz, Rudolf.Zitny@fs.cvut.cz

\*\* Ing. Luděk Heller, PhD. and Ing. David Vokoun, PhD.: Institute of Physics, Academy of Sciences of the Czech Republic, Na Slovance 2; 182 21, Prague; CZ, e-mails: heller@fzu.cz, vokoun@fzu.cz

the cylinder with the pitch angle approximately  $\pm 58^\circ$  (circumferential axes-helix). Tubular NiTi structure was subsequently annealed at  $450^\circ\text{C}$  for 30 minute. Mechanical properties of the wires are summarized in Table 1. For detailed description of the mechanical behavior of nitinol wires see Heller et al. (2008).

Used polymer matrix belongs to the group of silicon elastomers (trademark Sylgard 160) obtained as mixture of soft and hard phase. NiTi textile-polymer composite sample was prepared by infiltration of braided structure laid in a mold with the polymer and hybridizing it by curing at room temperature. Final composite vessel had outer and inner radius equal to  $R_o = 3.025$  mm, and  $R_i = 1.25$  mm, respectively.

*Tab. 1: Composite tube summary.*

<b>NiTi wire</b>	
<i>Young modulus of austenite</i>	<i>46.2 GPa</i>
<i>Young modulus of martensite</i>	<i>18.0 GPa</i>
<i>Transformation yield stress of austenite at room temperature</i>	<i>553 MPa</i>
<i>Maximum recoverable transformation strain</i>	<i>5.23 %</i>
<i>Thickness</i>	<i>100 <math>\mu\text{m}</math></i>
<i>Number</i>	<i>36</i>
<i>Heat treatment</i>	<i>450°C for 30 min.</i>
<i>Reference radius of the helices</i>	<i>1.75 mm</i>
<b>Composite structure</b>	
<i>Cylindrical tube with silicon elastomer matrix reinforced with NiTi wires</i>	
<i>Reference outer radius</i>	<i>3.025 mm</i>
<i>Reference inner radius</i>	<i>1.250 mm</i>
<i>Helix angle (between circumferential axis)</i>	<i><math>\pm 58^\circ</math></i>
<i>Reference length of the tube</i>	<i>5 cm</i>

## 2.2. Experiment

In order to obtain mechanical response of the sample to external load the inflation-extension test was carried out at the Laboratory of Human Biomechanics, Faculty of Mechanical Engineering of the Czech Technical University in Prague. Within the inflation-extension test the sample is loaded by internal pressure and axial force. The force is originated by the pressure which is applied to the end of the tube (closed tube configuration) and with additional weight. The experimental setup is documented in Fig. 1. The pressurization was carried out manually by a syringe. Four different weights were consecutively applied to induce longitudinal prestrain;  $m = 41$  g; 188 g; 488 g; and 782 g (this is the total mass of longitudinal load under zero transmural pressure). Four pressurization cycles were repeated with each weight.

Displacements of the inflated tube were recorded by point optical probes Chrocodile M4 (Precitec Group, Germany). Two of these sensors were involved in longitudinal displacement and torsion angle measurement. The change of the diameter was recorded with the laser scanner ScanControl LLT 2800-25 (Micro-epsilon, Germany). The internal pressure was monitored with the pressure transducer Kulite XLT-123B-190M-3.5BAR-D (Kulite Semiconductor Products, USA). All quantities were recorded into a PC for further post-processing.

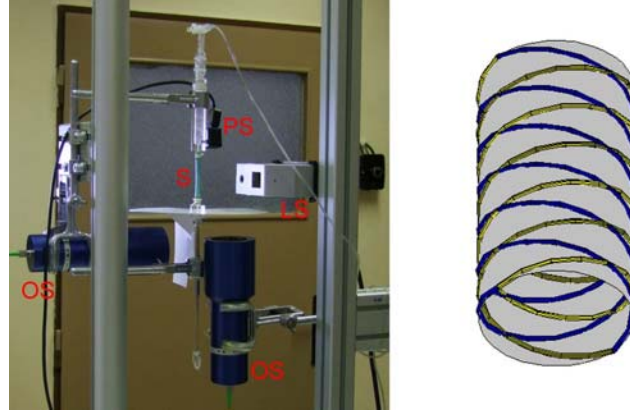


Fig. 1: The experimental setup (left) and the sketch of the composite structure. The letters on the left side denote: OS – optical sensor Chrocodile M4; LS – laser scanner ScanControl; PS – pressure transducer Kulite; and S – sample.

### 2.3. Model

Several assumptions were made in order to keep simplicity necessary for analytical treatment of the problem. The material of the final structure was homogenized. It means that reinforcement wires were considered to define preferred directions in hyperelastic continuum. Thus, their influence was reduced to originating anisotropy. Both families of wires were presumed to be mechanically equivalent. It results in so-called locally orthotropic material (Holzapfel, 2000, ch. 6). Viscoelastic properties of the silicon rubber were neglected due to the reinforcement with the stiff elastic fibers. The strain energy density function  $W$  was considered to be decoupled into isotropic part (Mooney-Rivlin; elastomer contribution) and anisotropic part (contribution of the wires).  $W$  is defined in (1).

$$W = \frac{\mu}{2}(I_1 - 3) + \frac{\nu}{2}(I_2 - 3) + c(I_4 - 1)^2, \quad (1)$$

where  $\mu$ ,  $\nu$ , and  $c$  denote stress-like material parameters.  $I_1$  and  $I_2$  are first and second principal invariants of the right Cauchy-Green strain tensor  $\mathbf{C}$ . It can be written as  $\mathbf{C} = \mathbf{F}^T \mathbf{F}$ , where  $\mathbf{F}$  is the deformation gradient.  $I_4$  denotes additional invariant generated by anisotropy of the continuum. Considering simultaneous extension (uniform) and inflation of incompressible tube (due to rubbery matrix)  $\mathbf{F}$  is obtained as  $\mathbf{F} = \text{diag}[RL/(rl), r/R, l/L] = \text{diag}[\lambda_R, \lambda_T, \lambda_Z]$ . Here  $R$  and  $L$  denote radius and length in the reference configuration. Lowercase letters indicate spatial configuration. It results in  $I_4 = \lambda_T^2 \cos^2(\beta) + \lambda_Z^2 \sin^2(\beta)$ . Mention that mechanical equivalency of two families of reinforcing fibers implies that one helical family is disposed under  $\beta$  and second one under  $-\beta$ ; here considered as the declination from circumferential direction. Details of this approach can be found in Holzapfel et al. (2000), and Ogden (2009). Also equilibrium equations for inflated and extended thick-walled cylindrical tube were adopted from the latter. Observed internal pressure,  $p$ , and longitudinal load,  $F$ , can be predicted in such a way.

### 3. Results

Data sample intended for parameters estimation was collected from the last pressurization cycle of each longitudinal load. It is shown in Fig. 2. Pressure-circumferential stretch relationships suggest that macroscopic response of the sample holds the response typical for inflated polymer tube (concave curve). No material instability (non-uniform bulge), however, was observed. Implemented wired structure probably prevents the tube from it. Observed small torsions (0-2.5°/5cm) were not considered to be materially intrinsic.

Material parameters were estimated using weighted least square optimization in Maple 13 (Maplesoft, Canada). They are listed in the caption of Fig. 2. However, it has to be said that the model failed in the prediction of entire range of the experiment. Only data for the first longitudinal weight were fitted successfully. Especially longitudinal load was dramatically underestimated (error reached up to  $\approx 5.5$  N at the peak value). It suggested to fit data corresponding to the first weight ( $m = 41$  g) separately. This result is depicted with continuous curves in Fig. 2.



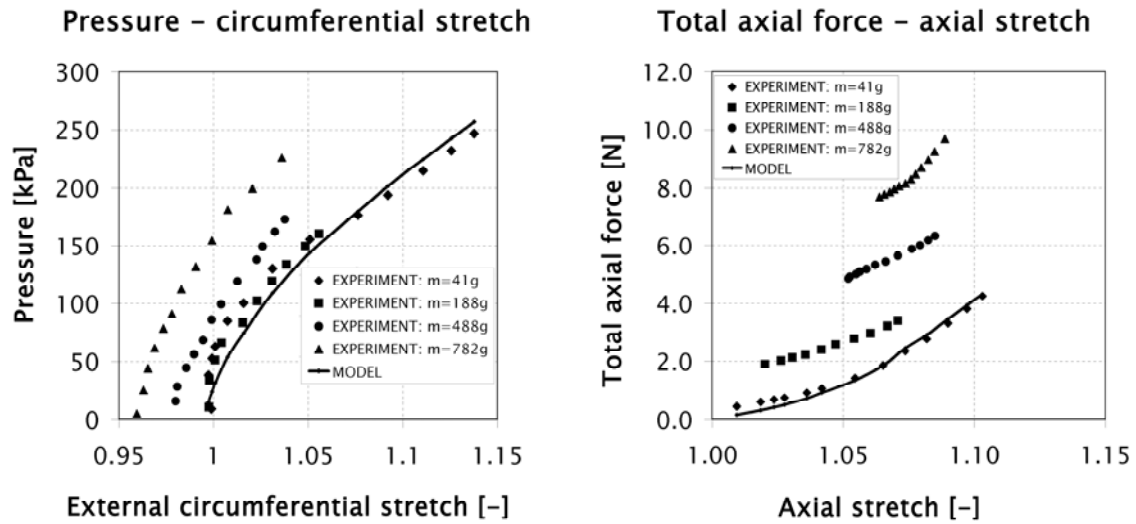


Fig. 2: Comparison of the model predictions (first weight only) and experimental data. Parameters involved in (1) were estimated as  $\mu=-18.37\text{kPa}$ ;  $\nu=220.9\text{kPa}$ ;  $c=34.62\text{kPa}$ ; and  $\beta=0$ . Total axial force means the force generated by hanged weight and by the pressure acting on the end of the tube.

#### 4. Discussion and Conclusions

It was concluded that NiTi reinforcement reduces elastomer viscoelasticity in macroscopic response, which can not be fully described with the model considering the effect of wires only as the introduction of anisotropy. It should also be noted that the best fit model predicts parameter  $\beta$  to be zero, which is not in accordance with the fabricated structure. It suggests that the reinforcement is the most propagated as the stiffening in the circumferential direction.

This is only the pilot study. It clearly shows, however, that the structural model, probably based on non-affine deformation of the elastomeric tube and NiTi wires, is needed. In other words – any model for elastomer-wire kinematic interaction; because the present model presumes the same strains sustained by both components and it seems to be the weak point. Similar effect might be obtained incorporating bending stiffness of wires. But, development of such models should be accompanied with advancing of experimental techniques. Involving of x-ray tomography in future experiments is of our concern.

#### Acknowledgement

This work has been supported by projects of Ministry of Education MSM6840770012 and Czech Science Foundation P108/10/1296.

#### References

- Duerig, T.W., Tolomeo, D.E., & Wholey, M. (2000) An overview of superelastic stent design. *Minimally Invasive Therapy and Allied Technologies*, 9, 3-4, pp.235-246.
- Heller, L., Kujawa, A., Šittner, P., Landa, M., Sedlák, P. & Pilch, J. (2008) Quasistatic and dynamic functional properties of thin superelastic NiTi wires. *European Physical Journal: Special Topics*, 158, 1, pp.7-14.
- Heller, L., Vokoun, D., Majtás, D., & Šittner, P. (2008) Thermomechanical characterization of shape memory alloy tubular composite structures. *Advances in Science and Technology*, 59, pp.150-155.
- Holzappel, G.A. (2000) *Nonlinear solid mechanics*. John Wiley and Sons, Chichester.
- Holzappel, G.A., Gasser, T.C., & Ogden R.W. (2000) A new constitutive framework for arterial wall mechanics and a comparative study of material models. *Journal of Elasticity*, 61, 1-3, pp.1-48.
- Stoeckel, D., Pelton, A. & Duerig, T. (2004) Self-expanding nitinol stents: material and design considerations. *European Radiology*, 14, 2, pp.292-301.
- Ogden, R.W. (2009) Anisotropy and nonlinear elasticity in arterial wall mechanics, in: *Biomechanical Modelling at the Molecular, Cellular and Tissue Levels* (G.A. Holzappel & R.W. Ogden eds), Springer, Wien, pp.179-258.

## NON-LINEAR TIME HETERONYMOUS DAMPING IN NON-LINEAR PARAMETRIC PLANETARY SYSTEMS

M. Hortel\*, A. Škuderová\*

**Abstract:** *The analysis of dynamics of time heteronymous weakly and strongly non-linear planetary transmission systems with kinematic couplings – gears constitutes a study of complicated function of many parameters including the gearing material damping properties and damping viscous properties of lubricating oil film in gear mesh. The structures with lightening holes in cog wheel discs are characterized then by time variable damping in gear meshes. The following contribution deals with this time heteronymous non-linear damping.*

**Keywords:** *Non-linear dynamics, time variable damping, planetary systems.*

### 1. Introduction

The presenting study concurs the works (Hortel & Škuderová, 2010; 2011) that deals with matters of linear and non-linear damping of motions in gear mesh of kinematic pairs with constant damping coefficients and with time variable one.

The world development of transmission systems especially in mobile machines leads to high-power high-speed constructions with minimum dimensions and masses. Deep basic research in the area of internal dynamics of weakly and strongly non-linear time heteronymous deterministic systems is focused to the area of complicated planetary, i.e. differential, and pseudoplanetary systems with split power flows. The research here is motivated primarily by whole series of pending issues in the area of dynamic phenomena that influence and closely relate to the safety and dependability of such systems. The issue and existence of these phenomena in many cases of such complicated systems is not still wholly known in term of both theoretical and experimental.

By light high-speed drive systems occur often in discs of the cog wheels the lightening holes for example by the speed reducers of turbines onto propellers, which cause the speed heteronomy in the damping properties of cog wheel discs. The lightening disc holes as well as the forms of discs can have generally according to the functional requirements the different forms. Consequently the *radial* stiffnesses – masses and the damping characteristics that result of these properties, can have the complicated functional relations that depend on the revolutions of appropriate wheels.

### 2. Mathematical – physical model and analysis of influence of time variable damping by lightening holes in cog wheels

The time variance of disc stiffness – mass depends on the size, number and location of lightening holes along the wheel circumference. It follows from above mentioned, that a real damping in a gear mesh is a complicated time variable i.e. heteronymous function which can influence not only by its quantitatively but mainly by qualitatively properties for example the phase shifts of the amplitude of relative motion in the gear mesh towards the amplitude of the modified resulting stiffness function of gearing and can influence that way the dynamics i.e. the dynamic forces in these systems.

Such time damping function of a disc  $k_d(t) = k_d(t+T)$  of a cog wheel with the period  $T = 2\pi/\omega$  in the interval  $\langle 0; T \rangle$ , which fulfils the conditions of an uniqueness and finiteness, with a finite number

---

\* Ing. Milan Hortel, DrSc. and Ing. Alena Škuderová, Ph.D.: Institute of Thermomechanics ASCR, v.v.i., Dolejškova 5, 182 00 Prague 8, CZ, e-mails: hortel@it.cas.cz, skuder@it.cas.cz

of maximums and minimums and discreteness (Dirichlet's conditions) can be expressed into a convergent series of the form

$$k_d(t) = k_d(t+T) = \frac{1}{2T} \int_0^{2T} k_d(t) dt + \sum_{m=1}^{\infty} \left\{ \left[ \frac{2}{T} \int_0^T k_d(t) \cos p m \omega t dt \right] \cos p m \omega t + \left[ \frac{2}{T} \int_0^T k_d(t) \sin p m \omega t dt \right] \sin p m \omega t \right\}, \quad (1)$$

where  $\omega = \pi / 30$  is the angular velocity of cog wheel,  $n \dots$  the number of the cog wheel revolutions,  $p \dots$  the number of the lightening holes in the gear disc or generally the number of the periods of the courses of the damping who are caused by the inhomogeneity of the wheel disc

By reason that are not yet experimentally developed the functional damping relation will be applied in the following studies, in the "zero" approximation, instead of (2) the simplified function

$$k_d(t) = k_{d0} + k_d \sin p \omega t, \quad (2)$$

where  $p = 1, 2, 3, \dots$  and  $k_{d0}, k_d$  are the constant damping coefficients.

If we introduce the time heteronomous function (2) into the system of the motion equations of the substitutive mathematical – physical model of one branch of power flow of the pseudoplanetary system from Fig.2 (Hortel & Škuderová, 2010) i.e. the sun gear 2 and one satellite 3, we obtain the system of the ordinary differential equations with time variable coefficients in the form (Hortel & Škuderová, 2010)

$$\begin{aligned} \mathbf{M} \mathbf{v}'' + [{}_1 \mathbf{K}(\beta, \delta_i, H) + {}_1 \mathbf{k}_d(t)] \mathbf{v}' + \sum_{K_1 > 1} [{}_K \mathbf{K}(D, D_i, H) + {}_{K_1} \mathbf{k}_d(t)] \|\mathbf{w}'(\mathbf{v}')\|^{K_1} \text{sgn}(\mathbf{w}'(\mathbf{v}')) \\ + {}_1 \mathbf{C}(\varepsilon, \kappa, Y_n, U_n, V_n, H, t) \mathbf{v} + \sum_K \mathbf{C}(\varepsilon, \kappa, I_n, H, t) \mathbf{w}^K(\mathbf{v}) = \mathbf{F}(a_n, b_n, \bar{\varphi}, H, t), \end{aligned} \quad (3)$$

where  $\mathbf{v}$  means here generally the 6-dimensional vector of displacement of system vibration,  $\mathbf{w}^K(\mathbf{v})$  is the  $K$ -th power of vector  $\mathbf{v}$ , which is defined by expression  $\mathbf{w}^K(\mathbf{v}) = \mathbf{D}(\mathbf{w}(\mathbf{v})) \mathbf{w}^{K-1}(\mathbf{v})$ .  $\mathbf{D}(\mathbf{w}(\mathbf{v}))$  means the diagonal matrix, whose elements at the main diagonal are comprised by elements of vector  $\mathbf{w}(\mathbf{v}) \equiv \mathbf{v}$ . Furthermore  $\mathbf{M}$  is the matrix of mass and inertia forces,  ${}_1 \mathbf{K}, {}_1 \mathbf{k}_d(t)$  and  ${}_K \mathbf{K}, {}_{K_1} \mathbf{k}_d(t)$  are the matrices of linear and non-linear constant and time variable damping forces,  ${}_1 \mathbf{C}$  and  ${}_K \mathbf{C}$  are the matrices of linear and non-linear reversible forces and  $\mathbf{F}(t)$  is the vector of non-potential external excitation with components  $a_n, b_n$  and the phase angle  $\bar{\varphi}$ .  $H$  is the Heaviside's function, which allows to describe the motions – contact bounces – due to strongly non-analytical non-linearities, for example due to technological tooth backlash  $s(t)$ . Corresponding constant linear and non-linear coefficients of damping are denoted by  $\beta, \delta_i$  or  $D, D_i$ , whereas  $\beta(k_1, k_{1m}, H)$ , where  $k_1, k_{1m}$  are the linear coefficients of material of viscous damping in gear mesh\*,  $D(k_{2,3}, k_{2,3m}, H)$ , where  $k_{2,3}, k_{2,3m}$  are the non-linear (2 – quadratic, 3 - cubic) coefficients of the material or viscous damping in the gear mesh. The linear parametric stiffness functions are denoted by the symbols  $Y_n, U_n, V_n$  and non-linear parametric functions, so-called parametric non-linearities, by the symbol  $I_n$ .  $\varepsilon$  and  $\kappa$  are the coefficients of the mesh duration and the amplitude modulation of the stiffness function  ${}_1 \mathbf{C}(t)$ ,  $t$  is the time.

The resonance characteristics of linear as well as non-linear systems with constant coefficients with the typical overhangs of the solidifying or softening resonance characteristics are markedly elaborated. This can not be fully declared about the resonance characteristics of linear or non-linear parametric systems with impact effects, where all the phenomena of linear or non-linear systems including the influence of the time variable damping  ${}_1 k_d(t)$ ,  ${}_K k_d(t)$  and the changes of the stiffness level – the parametric functions – and the phase shifts of the amplitude of relative motions  $y(t)$  in gear mesh in

---

\*) The subscript  $m$  is for the tooth backlash.

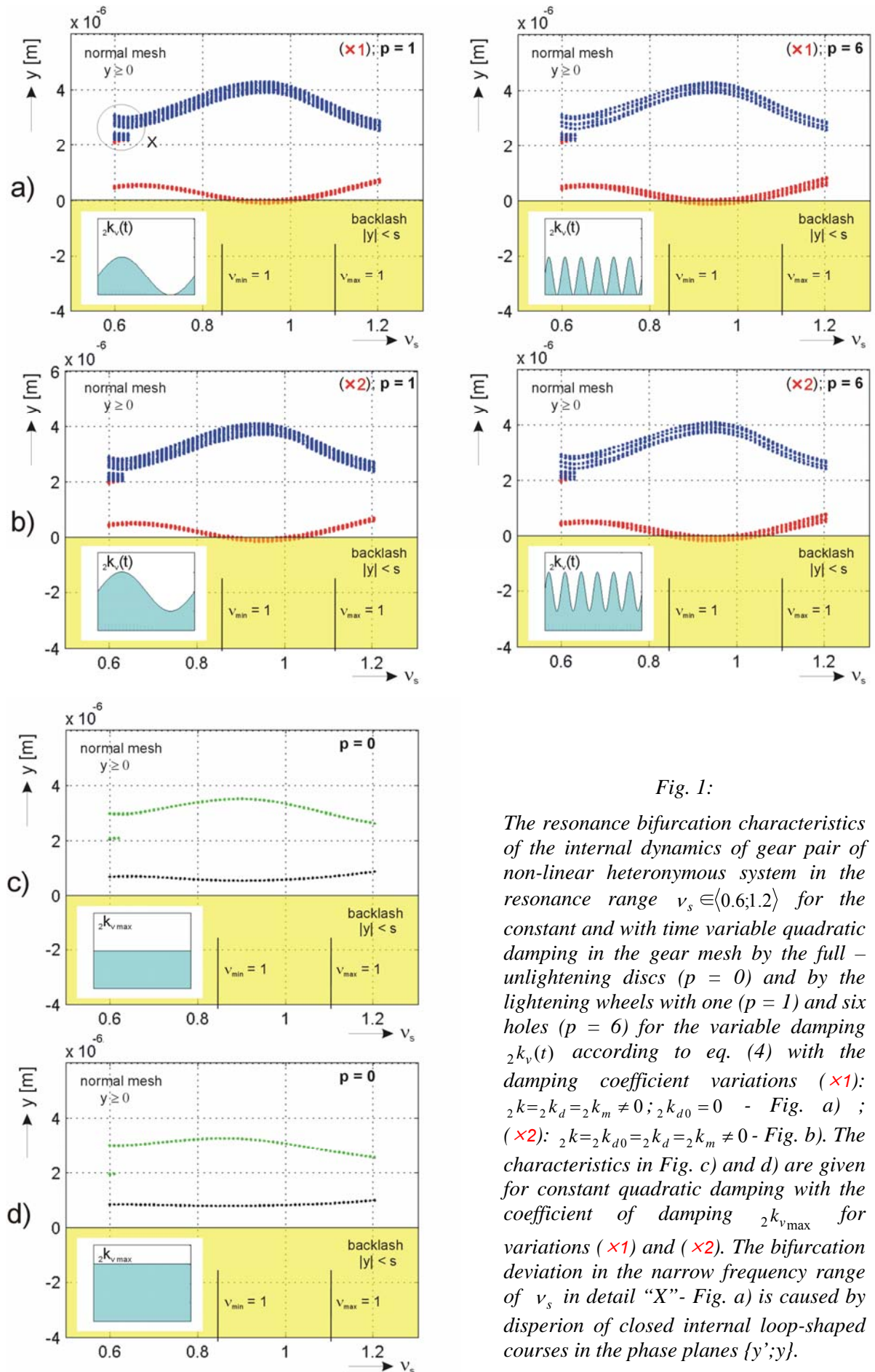


Fig. 1:

The resonance bifurcation characteristics of the internal dynamics of gear pair of non-linear heteronomous system in the resonance range  $v_s \in (0.6; 1.2)$  for the constant and with time variable quadratic damping in the gear mesh by the full – unlightening discs ( $p = 0$ ) and by the lightening wheels with one ( $p = 1$ ) and six holes ( $p = 6$ ) for the variable damping  ${}_2k_v(t)$  according to eq. (4) with the damping coefficient variations (x1):  ${}_2k = {}_2k_d = {}_2k_m \neq 0; {}_2k_{d0} = 0$  - Fig. a) ; (x2):  ${}_2k = {}_2k_{d0} = {}_2k_d = {}_2k_m \neq 0$  - Fig. b). The characteristics in Fig. c) and d) are given for constant quadratic damping with the coefficient of damping  ${}_2k_{vmax}$  for variations (x1) and (x2). The bifurcation deviation in the narrow frequency range of  $v_s$  in detail “X”- Fig. a) is caused by disperion of closed internal loop-shaped courses in the phase planes  $\{y'; y\}$ .

consequence of action of damping forces towards the parametric excited function  $C(t)$ .

With regard to limited paper size we illustrate further in brief only the influence of two variations of non-linear – quadratic with time variable damping on internal dynamics of solid system (3). For the whole field of gear mesh, i.e. normal, phase of contact bounces – impact of tooth faces and inverse mesh then results from (2) and (3) the general term for damping

$${}_2k_v(t) = [{}_2k + {}_2k_{d0} + {}_2k_d \sin p\omega t](H1 + H2) + {}_2k_m[1 - (H1 + H2)], \quad (4)$$

where  $H1 = H(y)$  is the Heaviside's function for the normal gear mesh  $y \geq 0$ ,  $H2 = H(-y - s)$  is the Heaviside's function for inverse mesh  $|y| > s$ .

The values for variation quadratic damping are

$$(\times 1): {}_2k = {}_2k_d = {}_2k_m \neq 0; {}_2k_{d0} = 0, (\times 2): {}_2k = {}_2k_{d0} = {}_2k_d = {}_2k_m \neq 0.$$

These variations ( $\times 1$ ), ( $\times 2$ ) will be theoretically compared for the number of lightening holes of wheel discs  $p=1$  and  $p=6$ . The quantitative parameter values of analysed system with six degree of freedom are presented in (Hortel & Škuderová, 2010). By reason that the non-conservative system with constant damping leads for all the given damping variations on the steady or quasi-steady vibration already at the fifth revolution of gear set, for a comparison the all amplitude-frequency characteristics of system with time variable damping will be displayed for these fifth revolution.

The purpose of this study is to educe the methodology that make possible to analyse the influence of all parameter variations in the area of linear, non-linear, (see (3)) with constant and time variable damping on internal dynamics of here studied complicated system.

In Fig. 1 are given resonance bifurcation characteristics in coordinates  $\{\nu_s; y\}$  for the solution variations a) ( $\times 1$ ), b) ( $\times 2$ ) for the number of lightening holes in cog wheels  $p=1$  and  $p=6$  with time variable quadratic damping  ${}_2k_v(t)$ , where  $\nu_s$  is frequency relative to the mean value of the resulting stiffness function  $C(t)$  in gear mesh. The figures c), d) represent the resonance bifurcation characteristics for the full – unlightening ( $p=0$ ) discs of cog wheels with constant quadratic damping  ${}_2k_v(t) = {}_2k_{v_{\max}} = konst$ , where  ${}_2k_{v_{\max}}$  are the maximum values of corresponding damping courses of variations a), b). The time courses of damping are marked in the individual figures

### 3. Conclusion

The influences of all possible variations and combinations of linear and non-linear constant and the time variable damping forces will be subjected to deeper qualitative and quantitative analysis in the next studies so that the summary damping characteristics obtained by experimental methods could be simulated and approximated by means of theoretically modified damping characteristics of solved systems.

### Acknowledgement

This study has been elaborated in the frame of research project AV0Z20760514 in the Institute of Thermomechanics AS CR, v.v.i..

### References

- Hortel M. & Škuderová A. (2010) To the time heteronymous damping in a non-linear parametric planetary systems. Proceedings of Engineering Mechanics 2010, pp. 45-46.
- Hortel M. & Škuderová A. (2010) The influence of lightening disc holes of cog wheels on dynamic properties of their mesh by high-speed light transmission systems. Monograph Deterioration, Dependability, Diagnostics. University of Defense Brno, pp. 105-117.
- Hortel M. & Škuderová A. (2011) Vliv proměnlivého diskového tlumení ozubených kol na kvalitativní vlastnosti dynamiky nelineárních parametrických soustav. Proceedings of Dynamics of Machines 2011, pp. 43-42.

## EEE – METHOD BASED ON FRACTAL DIMENSION FOR ANALYSIS OF TIME SERIES

V. Hotař\*, P. Salač\*\*

**Abstract:** *In our research we have developed a new analysis of topological one-dimensional objects (especially time series or dividing lines): Evaluation of length changes with Elimination of insignificant Extremes. The method, useful for complex data, stems from an estimation of the fractal dimension, so it measures changes of lengths in sequential steps. The EEE method does not use a “ruler” for measurement, but the line is defined by local extremes (maxima and minima). The extremes are eliminated and the length of the function, which is linear by parts, is measured. The lengths are plotted in relation to the number of all steps and the plot is evaluated. Mathematically generated functions (e.g. based on the Hurst coefficient), time series from real production processes and dividing lines (surface profiles and surface roughness) were used for the first experiment. The results show good potential for applications in measurement in off-line evaluations of data sets and on-line monitoring and control.*

**Keywords:** *Fractal dimension, time series, dividing line, Hurst coefficient.*

### 1. Introduction

Evaluation of signals (time series) from experiments, monitoring or production control are standard part of analyses. The choice of the analyses used for the monitoring should correspond with the character of the data obtained. The fractal dimension (describes in books e. g. Mandelbrot, 1982 and Peitgen et al., 1992) and a combination of statistical tools were used experimentally and are interesting and powerful tools for complex data quantification, for poor quality troubleshooting, production optimalization and non-stability of systems troubleshooting in laboratories and in industrial applications (e.g. paper A. Hotař et al., 2009, V. Hotař, 2008).

Our research team developed a new method for describing complexity with a modified technique of an estimated fractal dimension: Evaluation of length changes with Elimination of insignificant Extremes (EEE). The method brings benefits in describing data complexity and results are 2 parameters, one estimate complexity and the second is connected with statistics.

### 2. Methodology of EEE

The method is based on length evaluation of a curve (a time series). The curve is defined by measured values and they are isolated points - local extremes (maxima and minima). On the curve, unnecessary extremes are classified with a defined rule and a new simplified function is defined by the remaining points. The new function is used for the next classification. An example of a function defined by points and connected into the linear by parts function  $f$  is in Fig. 1. In the first step the function  $f$  is purged of points which are not local extremes (the local extremes are black points in the Fig. 1). First and last points are added to the extremes. The simplified function  $g$  is generated from such received points, Fig. 2.

A relative length of the function  $g$ , is computed and the result is saved. The relative length is evaluated from the absolute length of the function from point to point and divided by the length of its projection onto the x axis. The procedure for the elimination of insignificant extremes is applied to the simplified

---

\* Ing. Vlastimil Hotař, Ph.D.: Department of Glass Producing Machines and Robotics, Technical University of Liberec, Studentská 2; 461 17, Liberec; CZ, e-mail: vlastimil.hotar@tul.cz

\*\* RNDr. Petr Salač, CS.c.: Department of Mathematics and Didactics of Mathematics, University of Liberec, Studentská 2; 461 17, Liberec; CZ, e-mail: petr.salac@tul.cz



function  $g$ . The rule of the procedure uses functions formed from maxima and minima of the function  $g$ , Fig. 3, the functions  $g_{max}$  and  $g_{min}$  extended with the first and last points of the function  $g$ . The function  $g_{max}$  is generated from the maxima of the function  $g$  and in this function local maxima are found (black dots in Fig. 3). The function  $g_{min}$  is generated from minima and the local minima are found.

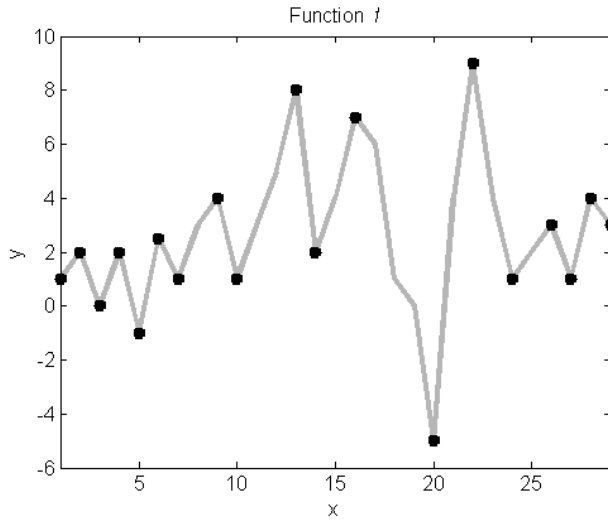


Fig. 1: Function  $f$  and its local extremes.

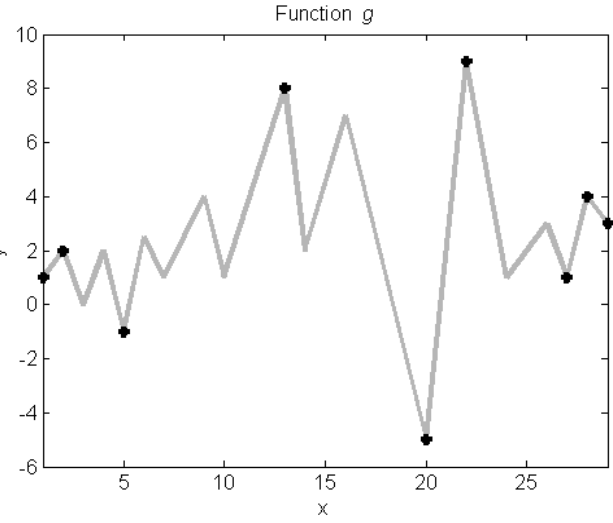


Fig. 2: Simplified function  $g$  and its local extremes.

The local maxima and minima of the functions  $g_{max}$  and  $g_{min}$  are used for the generation of the function  $g_{red}$ , Fig. 4. In this function again local maxima and minima are defined (Fig. 4, black dots). These final local extremes of the function  $g$  (Fig. 2, black dots) and the first and last points from the function  $h$ , Fig. 5. The relative length of function  $h$  is computed and the result is saved.

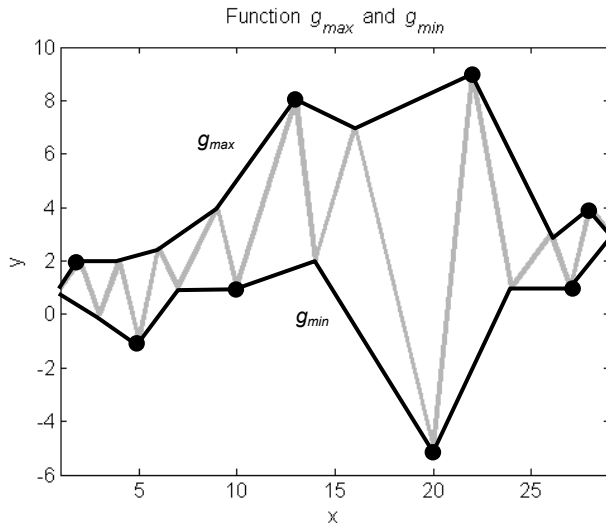


Fig. 3: Functions  $g_{max}$  and  $g_{min}$  generated from local extremes of function  $g$ .

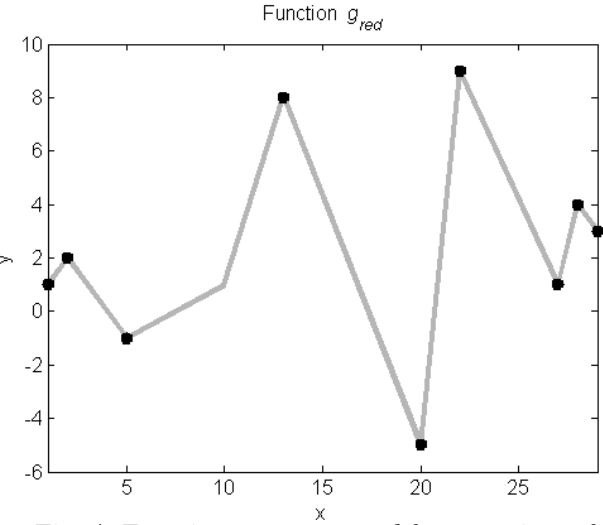


Fig. 4: Function  $g_{red}$  generated from maxima of function  $g_{max}$  and from minima of function  $g_{min}$ .

The same procedure is used for the new simplified function  $h$  and its global extremes and the first and last point (Fig. 5, black dots) define the function  $k$ . The function is formed from the global maximum and minimum of all functions ( $f$ ,  $g$ ,  $h$ ), therefore the analysis is stopped. All functions are depicted in Fig. 6.

The steps of the analysis are plotted versus the computed relative lengths of functions  $g$ ,  $h$ ,  $k$ , Fig. 7. The relation between the relative lengths and the steps of elimination are evaluated by a sufficient regression function that can be: a regression line (Fig. 7), a quadratic function or a hyperbolic function. The parameters of the regression functions are used for the evaluation of the function  $f$ .

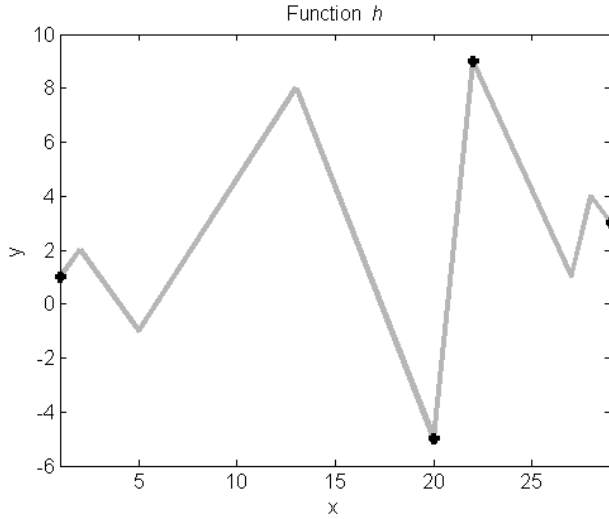


Fig. 5: Simplified function **h** and its local extremes.

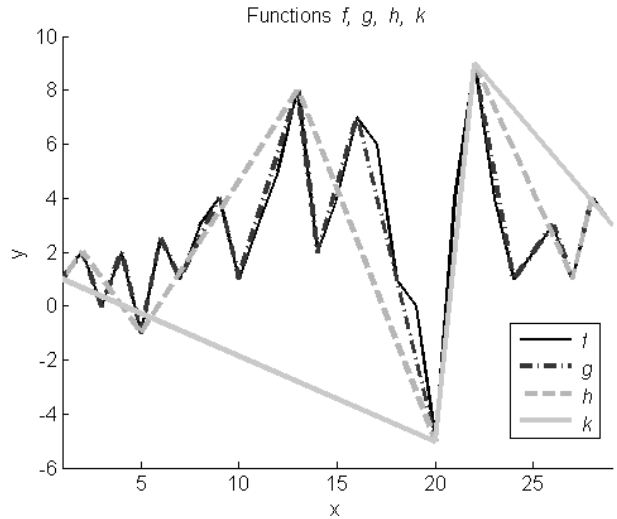


Fig. 6: Function **f** and simplified functions **g**, **h**, **k**.

### 3. Experimentation with mathematically generated functions

Time series obtained from simulation of fractional Brownian motion using Cholesky-Factorization of the related covariance matrix (FBM) were used to test of the developed method. An example of testing time series is in Fig. 8 and is generated using the input Hurst coefficient  $H = 0.4$ . The coefficient represents the character of time series and can be between value 0 and 1 (higher coefficients generate smoother functions, more information can be found in Evertsz 1996, Peitgen et al., 1992). The dependence between the relative lengths and the steps of elimination is in Fig. 9.

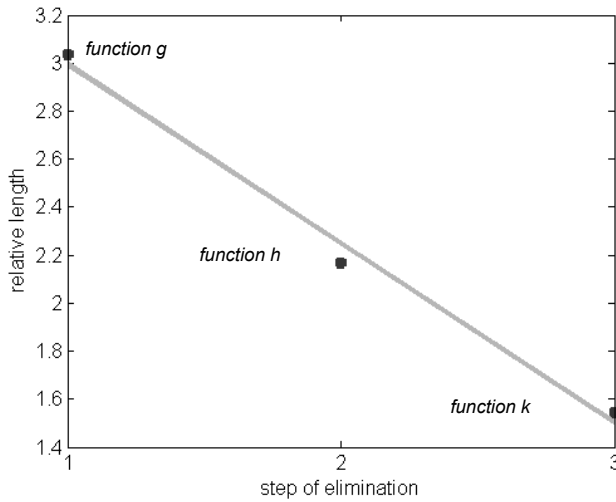


Fig. 7: Plot of the relation between steps of analysis and relative length, regression line.

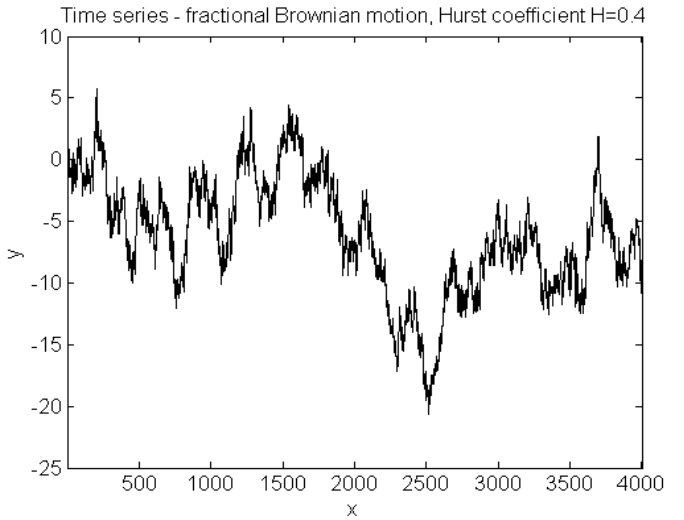


Fig. 8: Simulation of time series using fractional Brownian motion.

The relation between the steps and the lengths is hyperbolic:

$$y = \frac{d}{x+a} + b \quad (1)$$

It can be evaluated by parameters  $d$  and  $a$ . The parameter  $b$  is always  $b = 1$ . The parameter  $a$  has to be computed numerically using an error function.

900 simulated time series from FBM were used for an evaluation of the method EEE with a Hurst coefficient between 0.1 and 0.95. Fig. 10 shows the dependence between Hurst coefficients and the average value of parameters  $a$  and  $d$ .

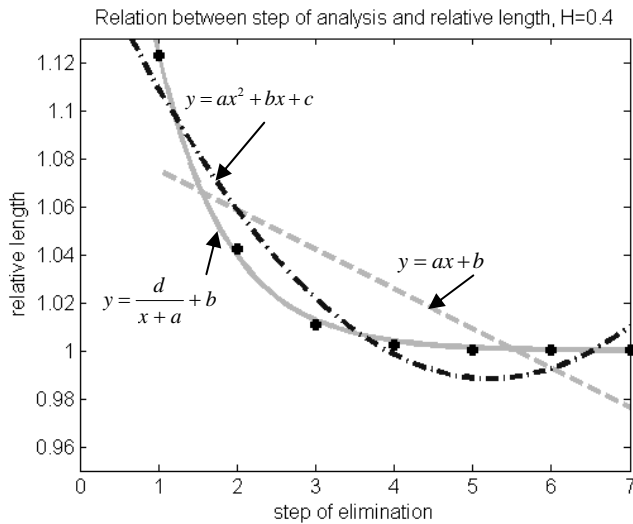


Fig. 9: Relation between step of analysis and relative length for time series FBM,  $H = 0.4$ .

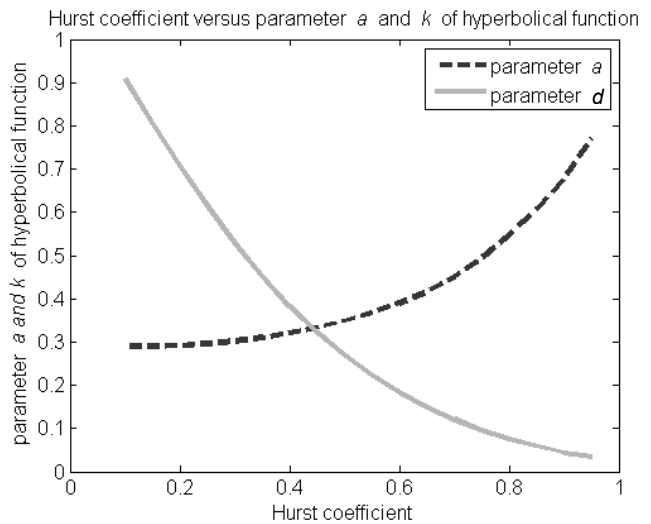


Fig. 10: Hurst coefficient versus average value of parameters **a** and **d** of hyperbolic function.

#### 4. Conclusion

The method EEE describes the character of curves and can be used to classify their complexity. Currently, tests with real topological one-dimensional curves are being conducted. Time series from measurement, real production processes and the dividing line between two materials are being used. The results of the tests will be compared with parameters of statistical tools, fractal dimensions and spectral analysis. Although some specific problems in higher frequencies of record characteristic have to be solving, the first results have been promising.

#### Acknowledgement

This work was supported by the research project No. MSM 4674788501, which is financed by the Ministry of Education of the Czech Republic.

#### References

- Evertsz, C.J.G., Peitgen, H.O. and Voss, R.F. (1996) Fractal Geometry and Analysis. Singapore: World Scientific Publishing Co.Pte. Ltd.
- Hotař, A. – Kratochvíl, P. - Hotař, V. (2009) The Corrosion Resistance of Fe<sub>3</sub>Al Based Iron Aluminides in Molten Glasses. Kovové Materiály - METALLIC MATERIALS, p. 247-252.
- Hotař, V. (2008) Monitoring of Glass Production Using Vision Systems. In: 9<sup>th</sup> ESG Conference, Slovak Republic. Zurich: Trans Tech Publications Ltd. p. 511-516. ISBN: 0-87849-387-5.
- Mandelbrot, B. B. (1982) The fractal geometry of nature. New York: W. H. Freeman and Co.
- Peitgen, H.O., Juergens, H. and Saupe, D. (1992) Chaos and Fractals: New Frontiers of Science. New York; Berlin; Heidelberg: Springer-Verlag.

## **MODULAR CONTROL SYSTEM ARCHITECTURE FOR A MOBILE ROBOT**

**J. Hrbáček<sup>\*</sup>, R. Hrbáček<sup>\*\*</sup>, S. Věchet<sup>\*\*\*</sup>**

**Abstract:** *The paper presents both hardware and software means used to develop a scalable low/middle level control system for the autonomous mobile robot Advée. Brief description of chosen hardware resources is given and use of a Linux-based operating system as a foundation of a soft real-time control system is discussed as well as the choice of other vital software components, e.g. inter-process communication mechanism. Described system has been fully implemented and successfully exploited in operation.*

**Keywords:** *Robotics, real-time systems, inter-process communication.*

### **1. Introduction**

Developing any new technical work brings many conceptual decisions – especially when the work is an autonomous mobile robot. But only a few of these dilemmas can be solved at the beginning of development – and design of the “brain”, the control system, is not an exception. It is therefore very important to find the right trade-off between abstraction and concreteness in design that determines proportion between the ease of initial development and possibility of future modifications. Modularity mentioned in paper title is one of parameters that strongly influence adaptability of the system to unexpected eventualities. In the case of described control system it is achieved in terms of both hardware and software means – hardware components are interconnected using shared busses that allow for adding and replacing individual components as long as defined communication interface is abided. The principle of software modularity is exactly the same – the modules can be added or reimplemented on condition of maintaining of specified interfaces.

A rich variety of control system designs can be found in the field of mobile robotics – ranging from simpler libraries aimed mainly on communication among individual components of the system to complex frameworks including a lot more. To the former group we can count for example IPC (Simmons & James, 2001) or LCM (Huang et al., 2010) that provide purely module interconnection and do not constrain any other aspect of the system architecture. On the other side, frameworks like Player/Stage (Gerkey et al., 2003) or MRDS (Microsoft, 2011) offer much more than just communication (e.g. a complete simulation environment including an artificial 3D world model) but also force the system to more predetermined shape. The system designers must then decide whether the complex frameworks bring more benefits than limitations and eventually exploit one of simpler packages – as this paper shows.

### **2. Hardware systems**

The described control platform hardware consists of two main parts – the master single-board computer (SBC) and the slave components including sensors, actuators and auxiliary devices (power units etc.). A basic structure of hardware means in conjunction with software modules is in Fig. 1.

---

<sup>\*</sup> Bc. Jan Hrbáček: Institute of Solid Mechanics, Mechatronics and Biomechanics, Faculty of Mechanical Engineering, Brno University of Technology, Technická 2896/2, 616 69 Brno; CZ, e-mail: jan@hrbacek.info

<sup>\*\*</sup> Radek Hrbáček: Department of Telecommunications, Faculty of Electrical Engineering and Communication, Brno University of Technology, Purkyňova 118, 612 00 Brno; CZ, e-mail: radek@hrbacek.info

<sup>\*\*\*</sup> Ing. Stanislav Věchet Ph.D.: Institute of Automation and Computer Science, Faculty of Mechanical Engineering, Brno University of Technology, Technická 2896/2, 616 69 Brno; CZ, e-mail: vechet.s@fme.vutbr.cz

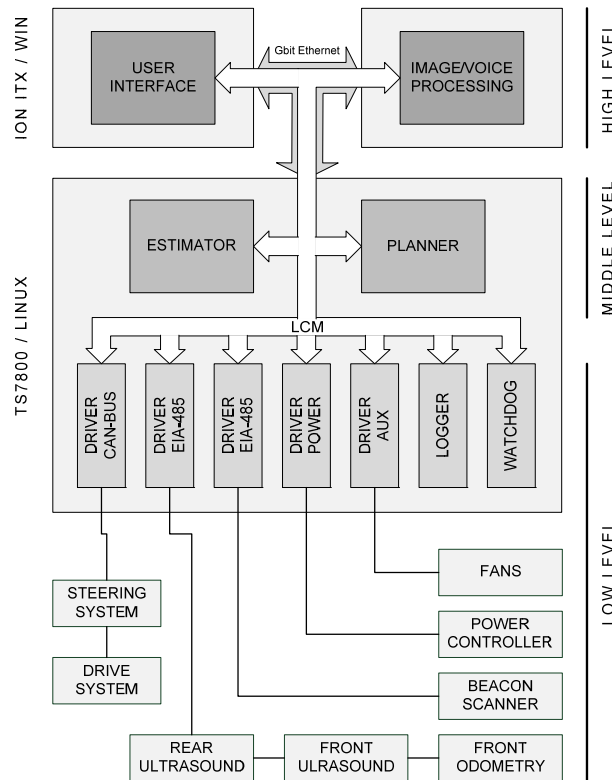


Fig. 1: Simplified hardware and software modules scheme.

### 2.1. Master computer

There were several aspects essential in the master computer selection process:

- industrial-grade *ruggedness* needed to lay solid foundations of overall control system reliability and robustness in harsh conditions,
- *communication busses* support necessary to interface peripheral devices (CAN-bus, EIA-485 etc.),
- sufficient *computational power* to run simple low-level data manipulation modules as well as more complex middle-level data processing.

All these features are implemented by the Technologic Systems' TS-7800 single-board computer which has been chosen to host low- and middle-level software equipment.

### 2.2. Sensors and actuators, auxiliary systems

Hardware components other than computers are a mixture of industrially used devices and custom developed modules. The sensory equipment is formed by sixteen ultrasonic range finders providing information on near surrounding of the robot and incremental rotary encoders for odometry. Sensors are polled for data using EIA-485 communication bus. Motion of the robot is handled by a driving motor and a steering motor, both industrially graded and controlled over CAN-bus. Last but not least, there is a system of power supply and switch modules that provide power to individual components of the robot. Control over these hardware modules (and thereby boot-up and halting sequence of the whole robot) is taken by a separate module communicating with the Linux SBC through EIA-422 link.

### 3. Low- and middle-level software means

Overall software equipment of the robot is divided into three layers:

- the *low level* provides interaction with hardware devices described in previous chapters – basically it translates device-specific data into standard inter-modular messages and vice versa,
- the *middle level* implements robot state estimation and path planning,
- the *high level* cares handles user interaction.

This paper deals with the two lower layers. Both these layers are hosted on the Linux single-board computer although thanks to used inter-module communication mechanism can be run on separate computers and even under different operating systems without any change of communication-related code. The use of Linux-based operating system was clear from the beginning – due to its high modularity it can be run in a variety of forms ranging from small embedded applications to multiprocessor supercomputers. The TS-7800 SBC is primarily designed to operate in conjunction with Linux and the source code of almost all custom hardware drivers is published by the manufacturer which leads to simple adaptability to concrete needs of the application and feasibility of fixing potential errors in implementation (own experience – problems with 9-bit serial port mode).

Every piece of developed software functionality is a part of some *module* – an independent process communicating with other modules using hereinafter described mechanisms.

### 3.1. Inter-module communication

Inter-module communication mechanism (or generally inter-process communication, IPC) belongs to the most important parts of the system. There are several roles that such mechanism should be playing:

- define *unambiguous interface* between modules
- provide *high-throughput* and *minimal-latency* communication channel
- support *multiple platforms* – at least Linux and Windows, C and C#.NET

A number of systems that solve these requirements exist – differing in the basic paradigm (client-server vs. publisher-subscriber), complexity (encapsulating more IPC methods, data marshalling<sup>1</sup> etc.) or operating system/programming language support. A good comparison of several popular IPC libraries targeted for use in robotics is provided in (Huang et al., 2009).

As already stated, whole software equipment of the robot is spread over minimally two computers. This fact disqualifies many traditional IPC methods as for example shared memory, files or pipes. The computers are interconnected through Ethernet and solution based on the standard TCP/IP protocol suite seems to fit well. The next decision after filtering out unsuitable mechanisms is conceptual – choosing the paradigm. Considering that most of the data flowing through the robot is of periodic nature, the publisher-subscriber model suits better. It can be implemented as “push” or “pull” – the “push” mechanism delivers data instantly while the “pull” method uses clients asking periodically for any new data. To ensure lowest possible latency, “push” method has to be used. Unambiguity of the communication between different interface implementations is best achievable using dedicated message definition files and programming language specific generators of message-related code (marshalling, un-marshalling, publishing etc.).

Having all these demands in mind, minimalistic yet powerful LCM (Huang et al., 2009; Huang et al., 2010) has been chosen as an optimal mechanism for message passing in Advee.

#### 3.1.1. LCM: Lightweight Communications and Marshalling

LCM is a set of libraries developed originally by the MIT DARPA Urban Challenge Team for their autonomous vehicle Talos. It covered all requirements except for the .NET framework support – this minor flaw was solved by creating the *lcm-dotnet* port which has been added to the project. There is now a binding for C/C++, Java, Python, MATLAB and C# what makes it extremely flexible – users can for example test production code in C/C++ or Java in MATLAB simulation environment. LCM is composed of three main functional blocks:

- *message definition* using a C-like definition language that can be compiled into language-native message support files using the *lcm-gen* tool
- *message marshalling/un-marshalling* – conversion between native and byte representation with defined endianness and runtime type safety checking
- *communication itself* based on UDP multicast

---

<sup>1</sup> marshalling means encoding the message into a byte array sendable over the network



### 3.1.2. Standard module interface

On the top of LCM there are a few standard messages defined that each module has to implement – an error reporting message and module state setting and reporting messages. State of the module can take one of globally defined states (INIT, RUN, PAUSE, STOP, ERROR and TERMINATE) that form a state machine common to all modules. This allows using a watchdog module that guards other modules from misbehavior (it can e.g. restart an unresponsive module).

### 3.2. Remote diagnostics and simulation support

Inherent feature of the LCM's transport layer (UDP multicast) is that virtually unlimited number of recipients can subscribe to messages from outside of the system without any negative impact upon the system. It is then easy to implement a non-obtrusive diagnostic tool that can monitor system modules and visualize important data. Currently there are three separate diagnostic applications: for Linux console, Android OS and Windows/.NET, each with slightly different usage. A communication logger is also implemented simply by listening to all messages and writing them to a file.

It is possible to replace any module by its simulation equivalent with the same interface without letting know the rest of the system. This is used to emulate outer environment of the robot by replacing the low layer (both software and hardware) by a SIMLIB-based (Peringer, 2010) chassis simulator that runs a dynamic model of the robot in a given artificial world.

## 4. Practical experiences from robot operation

In general, presented control system architecture together with custom diagnostic tools proved to be flexible enough to allow software reorganizations during Advée's development and highly reliable in operation enabling commercial utilization of the robot. LCM as the backbone of the system fits the demands very well, although there are some difficulties related to UDP multicast implementation on Android OS (but this is related to diagnostics only). Communication latencies are imperceptible.

## 5. Conclusions

Unified modular architecture with shared communication mechanism brings many benefits including simple system monitoring/diagnostics, simulation and testing using unmodified production code. Scalability is given both by the ease to add more modules (for example interfacing a new sensor) and by the ability to spread individual modules to more computers without changing single line of code. Because every module runs as a separate process, the robustness of the whole system is not threatened by individual module instability. The qualities of presented approach were verified during over 100 hours of production operation.

## Acknowledgements

Published results were acquired with the support of the Ministry of Education, Youth and Sports of the Czech Republic, research plan MSM 0021630518 "Simulation modeling of mechatronic systems".

## References

- Gerkey, B.P., Vaughan R.T. & Howard, A. (2003) The Player/Stage Project: Tools for Multi-Robot and Distributed Sensor Systems. Proceedings of the International Conference on Advanced Robotics (ICAR 2003), Coimbra, Portugal, pp. 317-323.
- Huang, A.S., Olson, E. & Moore, D.C. (2010) LCM: Lightweight Communications and Marshalling. Proceedings of the International Conference on Intelligent Robots and Systems (IROS), Taipei, Taiwan.
- Huang, A.S., Olson, E. & Moore, D.C. (2009) Lightweight Communications and Marshalling for Low-Latency Interprocess Communication. Technical Report MIT-CSAIL-TR-2009-041, Cambridge, USA.
- Microsoft Corporation (2011). Microsoft Robotics Developer Studio. <<http://www.microsoft.com/robotics/>>.
- Peringer, P. (2010) SIMLIB Home Page. <<http://www.fit.vutbr.cz/~peringer/SIMLIB/>>.
- Simmons, R. & James, D. (2001) Inter-Process Communication: A Reference Manual. Pittsburgh, USA.

## IDENTIFICATION OF CONSTITUTIVE MODEL BLOOD VESSEL WALL FROM WATER HAMMER EXPERIMENT

D. Hromádka<sup>\*</sup>, R. Žitný<sup>\*</sup>, L. Horný<sup>\*</sup>, H. Chlup<sup>\*</sup>, J. Veselý<sup>\*</sup>, J. Kronek<sup>\*</sup>, E. Gultová<sup>\*</sup>

**Abstract:** *This paper presents a water hammer experiment performed on an physical model of blood vessel. Physical model of blood vessel was manufactured from latex tubes textile rubber bands and elastic matrix. Latex tube outer surface was covered by elastic matrix. Textile rubber bands were wound on elastic matrix and they imitated reinforcing effect of collagen fibers. Mathematical model describes pulsation of pressure after instantaneous closing of valve at outlet of pipeline a part of which is a short elastic tested tube. Constitutive viscoelastic model was used to describe the behavior of blood vessel wall.*

**Keywords:** *Water hammer, constitutive model, blood vessel, pressure pulsation, oscillations.*

### 1. Introduction

The water hammer phenomenon was studied for more than one hundred years. This phenomenon is usually explained by considering an ideal reservoir – pipe – valve system in which a steady flow of fluid is almost instantaneously stopped by a valve closure. Water hammer theory is based upon Joukovsky's, momentum and continuity equations (Ghidaoui et al., 2005) which must be solved numerically. Hybrid models are usually solved by method of characteristics for the water hammer equation and by FEM for the solid (compressible) structure. Kochupillai (Kochupillai et al., 2004) presented finite element formulation based on fluid velocity of flow. Other methods for solving water hammer equation are presented in (Ghidaoui 2005). Bessems (Bessems et al., 2008) in his paper focused on modeling the linear viscoelastic behavior of blood vessel wall during dynamic loading.

In this paper we are focused on water hammer experiment on physical model of blood vessel. Mathematical model formulation is simplified by the fact that only a small part of system boundary is flexible (tested section of elastic tube is very short comparing with a long rigid piping in experimental setup). Thus the effect of a moving pulse wave can be neglected and the whole system can be approximated by the 'windkessel' model that is by a system of ordinary differential equations. One specimen of elastic tubes was tested: a simple tube having a composite structure as a human blood vessel. And this is the primary aim: development and manufacturing of reproducible and uniform physical model of blood vessel having a structure of intima, media and adventitia layers, layers reinforced by oriented collagen fibers with a limited extensibility (tested bands have the limiting extensibility 2). The connection between layers was performed by using a silicone matrix. It is believed that the water hammer tests could be useful in further development of these physical model of blood vessels.

### 2. Methods

Experiments were carried out using the experimental setup shown schematically in Fig. 1. Water flows from a reservoir through a vertical pipe and elbow to the tested section closed by a valve (stop cock). Pressure at the water level in the reservoir and at the valve outlet is atmospheric, therefore the only driving force is gravity (height  $H$ ). The tested elastic pipe has approximately the same initial inner radius ( $R=10$  mm) as the connected piping and the valve, the length of tested elastic section is about

---

<sup>\*</sup> Ing. David Hromádka, prof. Ing. Rudolf Žitný, CSc., Ing. Lukáš Horný, Ing. Hynek Chlup, Ing. Jan Veselý, Ing. Jakub Kronek and Ing. Eva Gultová: CTU in Prague; Technická 4; 160 07, Prague; CZ, e-mails: david.hromadka@fs.cvut.cz, rudolf.zitny@fs.cvut.cz, lukas.horny@fs.cvut.cz, hynek.chlup@fs.cvut.cz, jan.vesely@fs.cvut.cz, jakub.kronek@fs.cvut.cz, david.hromadka@fs.cvut.cz

10% of the connected rigid pipes (of the length  $L$ ). Parameters of water hammer experiment are presented in Tab. 1.

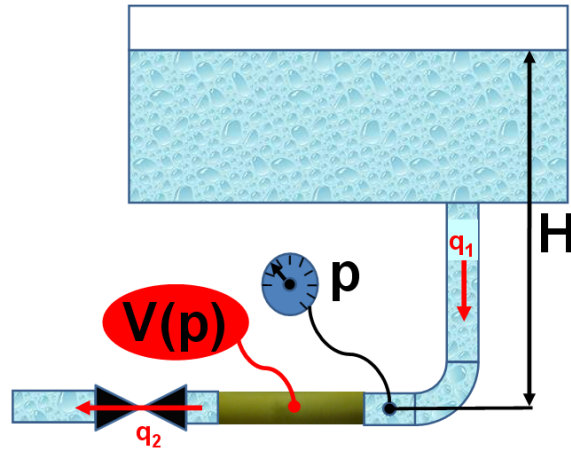


Fig. 1: Scheme of experimental setup with reservoir.

Tab. 1: Water hammer experiment parameters.

Specimen	Value
Inner diameter	0.0174 mm
Wall thickness	0.0024 mm
Length	0.1450 mm
Setup	Value
Inner pipe diameter	0.02 m
Wall thickenss of pipe	0.0028m
Water level	1 m

## 2.1. Model

Mathematical model is reduced only to 3 ordinary differential equations for pressure  $p(t)$  in the viscoelastic pipe and the flow rate  $q_1(t)$  in the rigid piping (and at inlet to the elastic section) and the flow rate  $q_2(t)$  through valve. However this is not enough, the simplified model assumes either uniform or parabolic velocity profile

The final form of differential equations is continuity equation (1), balance momentum equation (2) where  $\lambda$  is friction factor calculated as  $64/\text{Re}$  in laminar and as  $0.316/\text{Re}^{0.25}$  in the turbulent flow regime. Coefficient  $\zeta$  determines local pressure losses in elbow and at inlet from reservoir. Function  $f(t)$  in Eq. (2) is a function decreasing from 1 to 0 and describes the time course of gradual closing the valve at outlet.

$$\frac{dV}{dt} = q_1 - q_2 \quad (1)$$

$$q_2 = q_1 f(t) \quad (2)$$

$$L\rho \frac{dq_1}{dt} = \pi R^2 (\rho g H + p_a - p) - \frac{\rho}{\pi R^2} \left( \frac{\lambda L}{4R} + \frac{\xi}{2} \right) q |q| \quad (3)$$

$$\frac{dp}{dt} = \frac{\partial G}{\partial V} (q_1 - q_2) + \frac{\partial G}{\partial \dot{V}} \left( \frac{dq_1}{dt} - \frac{dq_2}{dt} \right) \quad (4)$$

$$p = G(V, \dot{V}) = \frac{h_0 \eta_3}{\left(\frac{V}{V_0}\right)^{0.5} r_0 2V} \frac{dV}{dt} - \frac{V_0 h_0}{V r_0} \sum_{i=1}^3 \mu_i \left( \left(\frac{V}{V_0}\right)^{-0.5\alpha_i} - \left(\frac{V}{V_0}\right)^{0.5\alpha_i} \right) \quad (5)$$

The Eqs. (4, 5) describe relationship between pressure, volume and rate of volume change of the viscoelastic section. The elastic part is determined experimentally from inflation tests. Ogden's constitutive equation (hyperelastic spring) combined with parallel dashpot are used for description of inflated axisymmetric membrane (artificial blood vessel). Initial conditions for system (1) (2) (3) and (4) are zero pressure (in fact overpressure), volumetric flow rate and the volume corresponding to the steady state and fully opened valve. Fully implicit numerical solution was implemented in a simple Fortran program.

### 2.1.1. Elastic response

The inflation test of the physical model of blood vessel revealed nonlinear pressure-volume relationship, see Fig. 3. Thus hyperelastic model has been adopted describing pure elastic contribution. Ogden's model of the strain energy density  $W$ , proposed originally for elastic response of polymer materials, fit experimental data successfully. Its mathematical form is given by equation (6). Here  $\mu_k$  denote stress-like material parameters and  $\alpha_k$  are dimensionless. Experimentally identified values from static tests are listed in Table 2.

$$W = \sum_{k=1}^3 \frac{\mu_k}{\alpha_k} \left( \lambda_T^{\alpha_k} + \lambda_Z^{\alpha_k} + \lambda_R^{\alpha_k} - 3 \right) \quad (6)$$

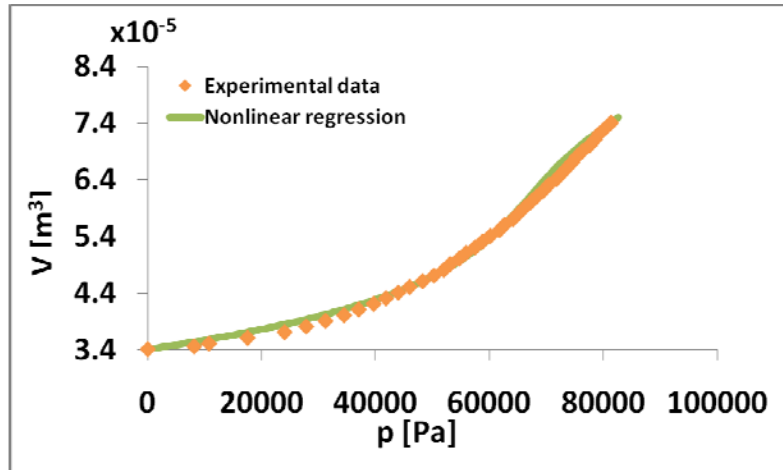


Fig. 3: Nonlinear pressure-volume relationship fitted by Ogden model.

Tab. 2: Estimated material parameters for elastic contribution.

Parameter	Value
$\mu_1$	1.219 MPa
$\mu_2$	-3.355 MPa
$\mu_3$	0.3449 MPa
$\alpha_1$	-4.211
$\alpha_2$	-1.153
$\alpha_3$	6.028

### 2.1.2. Dynamic response

Results from experiment and simulation are shown in Fig. 4 (points represent recorded pressure from water hammer experiment and the green line is numerical prediction for parameters in Tab. 2. In simulation was used constant viscosity  $\eta_3 = 3 \text{ Pa}\cdot\text{s}$

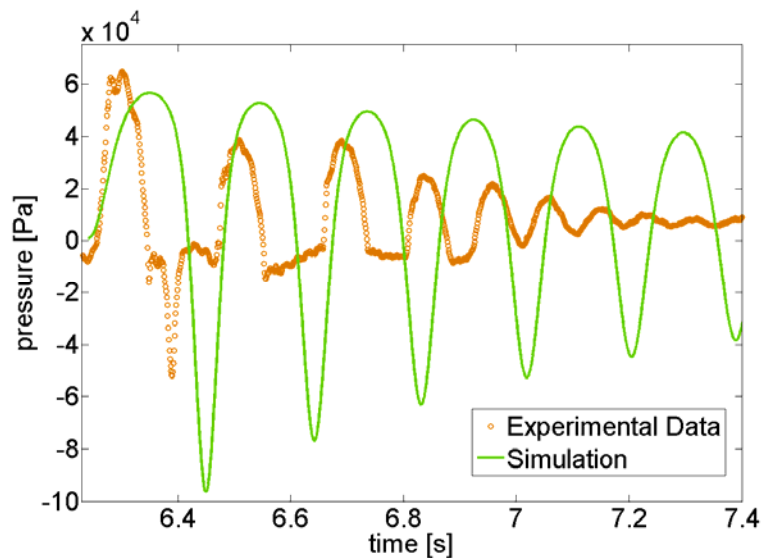


Fig. 4: Pressure responses after almost instantaneously closed valve.

## 3. Conclusions

Calculated natural frequency is little bit lower than the measured. Discrepancy of the response shape is caused first of all by the fact that the inflation test was performed only with inner overpressure (behavior of elastic section at negative pressure obviously cannot be extrapolated from Fig. 3). The second problem concerns the damping constant – this value was not optimized, and it seems that the single linear dashpot model is not suitable. Experiments did not confirmed the hypothesis that the initial frequency of oscillations will be higher due to increased stiffness at large deformation (effect of limited extensibility) and that the frequency will be gradually decreasing at an attenuated response tail.

## Acknowledgement

This work has been supported by Institutional research plan MSM6840770012-Transdisciplinary Research in the Field of Biomedical Engineering II and by Project GA106/08/0557 - Material properties of veins and their remodelling.

## References

- Bessemers, D. 2008 Experimental validation of a time-domain-based wave propagation model of blood flow in viscoelastic vessels. *Journal of Biomechanics*, 41, pp. 284–291.
- Ghidaoui, S. M. 2005. A review a water hammer theory and practice. *Applied mechanics reviews*, Jan. 2005, vol. 58, no 1-6, p. 49-75.
- Kochupillai, J. 2004 A new finite element formulation based on the velocity of flow for water hammer problems, *International Journal of Pressure Vessels and Piping*, 2005, vol. 82, p. 1-14.

## AEROELASTIC INSTABILITIES ON THE HEIGHT RISE BUILDINGS

**O. Hubová\***

**Abstract:** *The wind action on structures may be represented by peak velocity pressures, in conditions of strong wind, or by the basic stochastic descriptors of the velocity fluctuation, i.e. turbulence intensity, power spectral density and correlation between velocities at different points of the structures and probability distribution. The energy of turbulent fluctuations is distributed over a range of frequencies and the turbulence intensity is changing with height and terrain category. The resonance response due to gust wind takes into account also motion of the structures itself. Application examples will be given for the multi storey concrete and steel buildings.*

**Keywords:** *Wind velocity, intensity of turbulence, power spectral density function, stochastic response.*

### 1. Introduction

Wind load is the fundamental type of action especially on slender structures. The mean part of the wind pressure – static type is associated with mean wind speed. The fluctuating part is weakly stationary random process with respect time  $t$  and homogeneous random process with  $z$ . The wind action is represented as random field in time and place. It is assumed linear elastic behavior of structures, the response can be obtained by superposition of the response due to mean wind and than due to fluctuating part  $v(z, t)$ . The intensity of turbulence is defined as the variance of fluctuating part to the mean wind velocity and depends on height  $z$  and orography factor and roughness length, it should be between 5 - 30 %. The energy of turbulence (gustiness) is distributed over a range of frequencies. The effect of the wind on the structures as well as the response of the slender structures depends on the size, shape and dynamic properties of the structures.

### 2. Wind forces

The wind velocity and the velocity pressure and force are composed of a mean and a fluctuating component. The aerodynamic wind force for the area  $A$  at height  $z$  is:

$$F(z, t) = c_D \frac{1}{2} \rho (v_m(z) + v(z, t))^2 \cdot A \cong c_D \left[ \frac{1}{2} \rho \cdot v_m(z)^2 + \rho \cdot v_m(z) \cdot v(z, t) \right] \cdot A \quad (1)$$

The fluctuating part of wind pressure  $c_d \cdot \rho \cdot v_m(z) \cdot v(z, t)$  is distributed non-simultaneously on the on building; therefore we can use for autocorrelation function expression (2).

$$R_{FF}(\tau) = \lim_{T \rightarrow \infty} \int_{-T/2}^{T/2} F(z, t) \cdot F(z, t + \tau) dt = c_D^2 \cdot \rho^2 \cdot v_m(z)^2 \cdot A^2 \cdot \overline{v(z, t) \cdot v(z, t + \tau)} \quad (2)$$

Wind distribution over frequencies can be expressed by the power spectral density function of along wind turbulence. For the natural wind at height  $z = 10$  m over the ground we can use according (Pirner et al, 2003) expression (3) or by (Davenport, 1962) expression (4):

$$S_v(n) = \frac{1}{3} \frac{v_{m,10}^2}{n} \cdot \frac{(1800n / v_{m,10})^2}{[1 + (1800n / v_{m,10})^2]^{4/3}} \quad (3)$$

\* assoc. prof. Ing. Olga Hubová, PhD.: Slovak University of Technology, Department of Structural Mechanics, Radlinského 11; 813 68, Bratislava; SK, e-mail: olga.hubova@stuba.sk



$$S_v(n) = 4K \frac{v_{m,10}^2}{n} \cdot \frac{\left(1200n/v_{m,10}\right)^2}{\left[1 + \left(1200n/v_{m,10}\right)^2\right]^{4/3}} \quad (4)$$

Where  $K$  is terrain roughness factor (open country  $K = 0.005$ ; city  $K = 0.025$ ) and  $v_{m,10}$  is the reference wind velocity at height 10 m. The similar distribution over frequencies (see EN 1991-1-4, 2005) is expressed by the non-dimensional power spectral density function  $S_L(z, n)$ :

$$S_L(z, n) = \frac{n \cdot S_v(z, n)}{\sigma_v^2} \quad (5)$$

The along wind spectral density for horizontal excitation for symmetrical geometrical shape and stiffness or mass distribution:

$$S_{y,direction}(n, z) = \sum_{i=1}^{\infty} |H_i(z, n)|^2 \cdot \iint_A \phi_{i,y}(z_1) \cdot \phi_{i,y}(z_2) \cdot S_{p1p2}(n, z_1, z_2) \cdot dA_1 dA_2 \quad (6)$$

where  $|H_i(z, n)|$  frequency characteristic of the structure according to harmonic impulse  $Dir(z - z_k) \cdot e^{i2\pi nt}$  at the point  $k$

$S_{p1p2}(n, z_1, z_2)$  is the power spectral density of the wind pressure at different points.

$\phi_{i,y}(z)$  is the natural frequency of along wind vibration of the mode “ $i$ ”

According to experimental measurements is possible to express relationship between spectral density of wind pressure and power spectral density of wind velocity.

$$S_p(n) = 4 \left( \frac{q_{m,10}}{v_{m,10}} \right)^2 \cdot S_v(n) \quad (7)$$

Using aerodynamic admittance coefficient we can obtain for horizontal excitation at the top of structure expression:

$$S_{y,direction}(n) = |H(n)|^2 \cdot \frac{4 \cdot q_m^2(z=h)}{v_m^2(z=h)} S_v(n) \cdot A^2 \chi^2 \quad (8)$$

The coefficient of aerodynamic admittance  $\chi^2$  depends on roughness and dimensions of building.

The standard deviation of the horizontal displacement for the symmetrical structures:

$$\sigma_v^2 = \frac{4 \cdot q_m^2(z=h)}{v_m^2(z=h)} \int_0^{\infty} |H(n)|^2 \chi^2 S_v(n) \cdot A^2 dn \quad (9)$$

where

$$H(n) = \frac{1}{M_1 \cdot (n_{1,y}^2 - n^2 + 2i \cdot n_b \cdot n) 4\pi^2} \quad (10)$$

### 3. Numerical Analysis

#### 3.1. Response of height steel building

We can find the maximal dynamic displacement for the 150 m tall steel building, system of 36 steel columns and cross-beams forming a space frame with stiff joints on rectangular plan 35 x 35 m (see Fig. 1) in terrain category III. The equivalent mass per unit  $m(z) = 245 \cdot 10^3$  kg/m.

Equivalent vibrating mass:

$$M_I = \int_0^{150} \left( \frac{z}{h} \right)^2 \cdot m(z) dz = 1.225 \cdot 10^7 \text{ kg},$$

$$C = \omega^2 M_I = 3.79 \cdot 10^7 \text{ Nm}^{-1}, \quad A = 150 \times 35 = 5250 \text{ m}^2$$

The fundamental flexural frequencies  $n = n_{1,y} = 0.28$  Hz. Mean velocity at the top of building:

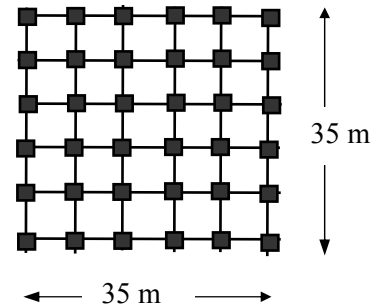


Fig. 1: Rectangular plan.

$$v_m(z=h) = c_r(z) \cdot c_o(z) \cdot v_{m,10} = 1 \cdot 0.19 \left( \frac{z_o}{z_{o,II}} \right)^{0.07} \ln \left( \frac{z}{z_o} \right) \cdot v_{m,10}$$

Mean wind pressure:

$$q_m(z) = \frac{1}{2} \cdot \rho \cdot c_D \cdot v_m(z)^2 \cdot b = \frac{1}{2} \cdot 1.25 \cdot 1.5 \cdot 35 \cdot v_m(z)^2 = 32.81 \cdot v_m(z)^2$$

The logarithmic decrement of structural damping for steel building (EN 1991-1-4, 2005):

$$\delta_y \cong 2\pi \cdot \xi = 0.05$$

For fundamental flexural mode  $\phi_1(z) = (z/h)^\xi$  and  $n = n_{1,y}$  we can obtain standard deviation of the horizontal displacement for the symmetrical structures: according to (9) and (10):

$$\sigma_v^2 = \frac{4 \cdot q_m^2(z=h)}{v_m^2(z=h)} \chi^2 S_v(n_{1,y}) \cdot A^2 \frac{\pi^2 \cdot n_{1,y}}{C^2 \cdot \delta^2} \quad (11)$$

Aerodynamic admittance functions for the 1<sup>st</sup> flexural mode:  $\chi^2 = 0.0516$

The power spectral density function for  $n = n_{1,y}$  is:  $S_v(n) = 135.33$

Response according to random vibration approach:

According to (11) we can obtain standard deviation of the horizontal displacement for the symmetrical structures:

$$\sigma_{y,direction}^2 = 4.712 \cdot 10^{-3} \quad \sigma_{y,direction} = 0.0686 \text{ m}$$

For the maximal non harmonic horizontal displacement due to mean and fluctuating part of wind we can write:

$$y_{\max}(z=150) = y_m(z=150) + \sigma_{y,direction} = 0.077675 + 0.0686 = 0.1463 \text{ m}$$

Deflection due to mean wind velocity for slender steel building is:

$$y_m(z) = \frac{\int_0^h q_m(z) \cdot \phi_1(z) dz}{4\pi^2 n_{1,y}^2 \cdot M_1} \phi_1(z) = \frac{1/2 \cdot \rho \cdot c_D \cdot b \int_0^h \left( 0.19 \left( \frac{z_o}{z_{o,II}} \right)^{0.07} \ln \left( \frac{z}{z_o} \right) \cdot v_r \right)^2 \phi_1(z) dz}{4\pi^2 n_{1,y}^2 \cdot M_1} \phi_1(z) = 0.07765 \text{ m}$$

Conventional mixing model due to EN 1991-14, (Hubová et al., 2000) and (Hubová, 2007) with detail method of structural factor:

The drag wind force  $F_w$  in wind direction is defined by:

$$F_w = c_s c_d \cdot c_f \cdot q_p(z_e) \cdot A_{ref} \quad (12)$$

$$c_s c_d = \frac{1 + 2 \cdot k_p \cdot I_v(z_e) \cdot \sqrt{B^2 + R^2}}{1 + 7 \cdot I_v(z_e)} \quad (13)$$

$$q_p(z) = [1 + 7 I_v(z)] \cdot 1/2 \cdot \rho \cdot v_m^2(z) \text{ is peak velocity pressure} \quad (14)$$

The resonance response factor:

$$R^2 = \frac{\pi^2}{2 \cdot \delta} \cdot S_L(z_e, n_{1,x}) \cdot R_h(\eta_h) \cdot R_b(\eta_b) \quad (15)$$

The aerodynamic admittance functions for fundamental mode:

$$\begin{aligned} R_h(\eta_h) &= \frac{1}{\eta_h} - \frac{1}{2\eta_h^2} (1 - e^{-2\eta_h}) & \eta_h &= \frac{4,6 \cdot h}{L(z_e)} \cdot f_L(z_e, n_{1,y}) \\ R_b(\eta_b) &= \frac{1}{\eta_b} - \frac{1}{2\eta_b^2} (1 - e^{-2\eta_b}) & \eta_b &= \frac{4,6 \cdot b}{L(z_e)} \cdot f_L(z_e, n_{1,y}) \end{aligned} \quad (16)$$

Response according to the (EN 1991-1-4, 2005) is obtained from Eq. (12) – (16):

$$y_{\max}(z=150) = 0.1624 \text{ m}$$

### 3.2. Response of height concrete building

We can find the maximal dynamic displacement for the concrete building (see Hubová, 2010) in terrain category III using equations (4) and (6) - (11).

$$M_I = \int_0^{76.42} \left( \frac{z}{h} \right)^2 \cdot \frac{m_b}{h} dz = 1.2056 \cdot 10^7 \text{ kg}, C = \omega^2 M_I = 2.2 \cdot 10^8, A = 3530.6 \text{ m}^2$$

$$v_m(z=h) = 33.41 \text{ m/s}, v_{m,10} = 28 \text{ m/s}, n = n_{1,y} = 0.68 \text{ Hz}, n_{2,y} = 3.311 \text{ Hz}$$

$$\xi_y = 0.01, \delta_y \cong 2\pi \cdot \xi = 0.0628 \text{ is logarithmic decrement of structural damping}$$

$$q_m(z) = \frac{1}{2} 1.25 \cdot 1.5 \cdot 46.2 \cdot v_m(z)^2 = 43.31 \cdot v_m(z)^2, \chi^2 = 0.0151$$

$$S_v(n) = \frac{1}{3} \frac{v_{m,10}^2}{n} \cdot \frac{(1800n/v_{m,10})^2}{[1 + (1800n/v_{m,10})^2]^{4/3}} = 30.969$$

$$\sigma_{y,direction}^2 = 3.55 \cdot 10^{-5}$$

Horizontal response due to mean wind load and contribution of the fluctuating component is:

$$y_{max}(z=76.42) = y_m + y_f = 0.01005 + 0.013685 = 0.0237 \text{ m.}$$

Maximal deflections for concrete building with rectangular plan and with regular distribution of mass 473 279 kg/m according to the EN 1991-1-4 is:

$$y_{max}(z=76.42) = 0.048 \text{ m.}$$

#### 4. Conclusions

Displacements on the top of buildings according two different calculations give us different values. The simplified method according to EN is conservative and based on peak pressures. The separation of turbulence intensity can get better understand of the wind effect on structures. The random vibration procedure presents full dynamical evaluation of response of sensitive height rise structures and it is significant for engineer. Results and conclusion in this height buildings show that is necessary to take into account stochastic and resonance effect of turbulence intensity. Fluctuating part of wind load can be obtained using random process simulation with different power spectral density function.

#### Acknowledgement

The presented results were achieved under sponsorship of the Grand Agency VEGA of the Slovak Republic.

#### References

- Background document of ENV 1991-2-4, (1996) Wind Action, Draft.
- Davenport, A.G. (1962) The response of slender, line like structures to a gusty wind, Proc. Inst. Civil. Eng., 6610, p.23/III.
- EN 1991-1-4: Euro code 1: Action on structures – Part 1-4: General actions-Wind actions, 2005.
- Hubová, O. & Prekop, L. (2000) Wind excited response of a line slender structures, in: Proc. Int. Conf. Dynamics of Civil Engineering and transport Structures and Wind Engineering, Vyhne, pp. 41-44.
- Hubová, O. (2007) The effect of the wind on the structure, Slovak Journal of Civil Engineering 2007/3, Volume XV, ISSN 1210-3896.
- Hubová, O. (2010) Simplified approach for assessing building wind response. Proc. 10 th Int. Scientific conference VSU' 2010, Sofia 3-4 June 2010, ISBN 1314-071X.
- Chmielewski, T & Górski, P. (1998) Along Wind Response of the TV Tower, in: Proc of 2<sup>nd</sup> East European Conference EECWE'98, Prague, pp.105- 112.
- Koloušek, V. & Pirner, M. & Fischer, O. & Náprstek, J.(1983) Wind effects on Civil Engineering Structures, Academia Praha, Elsevier, koed. London 1984.
- Petersen, Ch. (1996) Dynamik der Baukonstruktionen, Braunschweig/Wiesbaden. Friedrich Vieweg & Sohn Verlag-gesellschaft mbH, ISBN 3-528-08123-6.
- Pirner, M. & Fischer, O. (2003) Zatížení staveb vetrem, ČKAIT Praha.

## THERMAL ANALYSIS OF TYRE CURING PROCESS

M. Hynek<sup>\*</sup>, P. Votapek<sup>\*</sup>

**Abstract:** *The manufacturing of tyres requires mastering the control of curing process which has a significant effect of the thermal and mechanical behavior of the formed part. Basically, curing analysis can be considered as thermal-mechanical coupled phenomena with heat consuming character and significant dependence of physical properties on temperature. Quite a number of papers deal with chemical aspects of rubber curing, compare numerous cure reaction kinetic models, discuss various mathematical models for the simulation of the vulcanization and demonstrate the interaction between temperature distribution fields and curing degree fields (Bafnec, 2007). The main goal of this paper is to focus on the understanding of the heat transfer in a cure press with respect to the used heating procedure and the designs of the cure mold. Moreover, a comparison between the effectiveness of steam dome and heating plate cure presses is made. The findings can be used for the optimization of curing cycles and thus for increasing the quality of the final product as well as for the potential energy consumption reduction.*

**Keywords:** *Cure press, mold heating, energy consumption reduction.*

### 1. Introduction

There are currently used two concepts of building a cure press – steam dome and heating plates (see Fig. 1). Although the steam dome concept is more energy consuming it is still preferred in the production of large tyres as a more uniform temperature distribution in the curing mold is achieved (Ghoreishy, 2005). This argument can be confirmed by thermovision measurement of the curing mold (Honner, 2002). However, the effect of the mold heating concept on the time history in thick parts of the cured tyre is not significant (especially, if additional heating channels are exploited) as shown later in this paper.

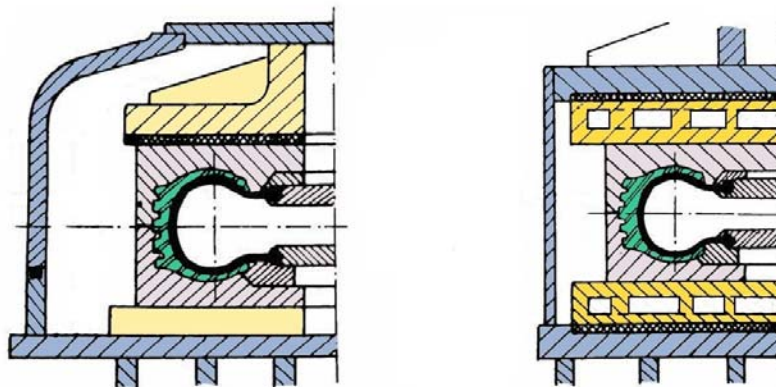


Fig. 1: EM 2011 logo Tyre curing press concepts – steam dome (left), heating plates (right).

### 2. CAD and FEM Model

Although a 3D CAD model of a real tractor tyre (see Fig. 2) was created it was decided to analyze the problem as axisymmetric.

---

<sup>\*</sup> assoc. prof. Ing. Martin Hynek, Ph.D. and Ing. Petr Votapek: Department of Machine Design, Faculty of Mechanical Engineering, University of West Bohemia, Univerzitni 22; 306 14, Pilsen; CZ, e-mails: hynek@kks.zcu.cz, pvotapek@kks.zcu.cz

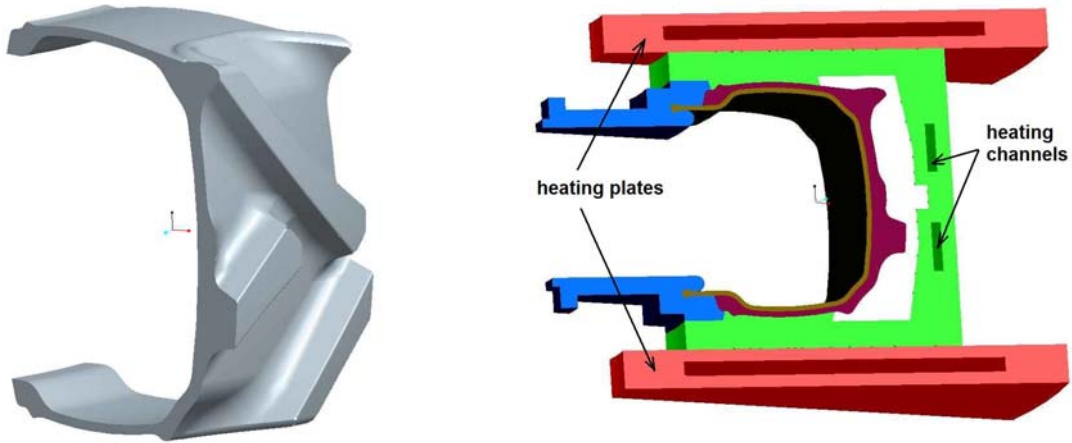


Fig. 2: CAD model – tyre segment (left), mold segment (right).

In the first stage, four variants of cure press were analyzed (see Tab. 1) and temperature histories in four locations (see Fig. 3) were compared.

Tab. 1: Solved variants.

Variant name	Brief specification
plates + channel	plates and heating channels (hot steam), membrane (hot water), aluminum insert
only plates	plates (hot steam), no channels, membrane (hot water), aluminum insert
steam dome	steam dome (hot steam), membrane (hot water), aluminum insert
steam dome, steel	steam dome (hot steam), membrane (hot water), complete mold made of steel

Boundary conditions for steam dome variants were defined in accordance with thermocouple measurements by definition of time histories of heat transfer coefficients and temperatures measured on the real steam dome cure press. The ambient temperature close to the press was 120°C, the temperature of the heating water in the membrane reached 170°C and steam temperature in the steam dome reached 165°C.

The boundary conditions for the heating plate variant without heating channels were adopted from measurements conducted on a similar cure press with heating plates. Steam temperature in the heating plates and heating channels reached again up to 165°C.

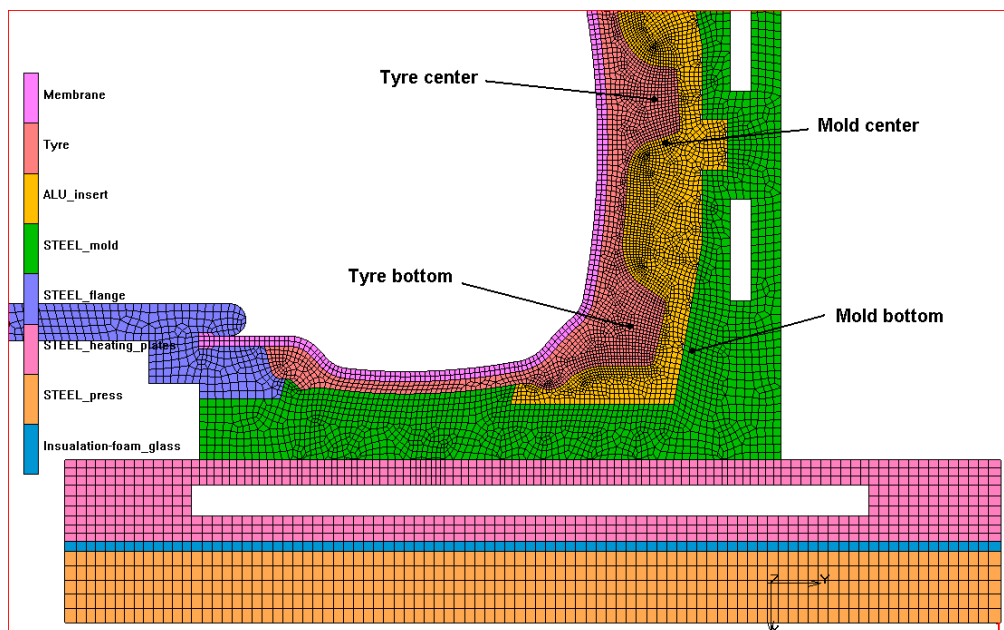


Fig. 3: Mesh of the axisymmetric FEM model with four locations for temperature history comparison.

### 3. Results

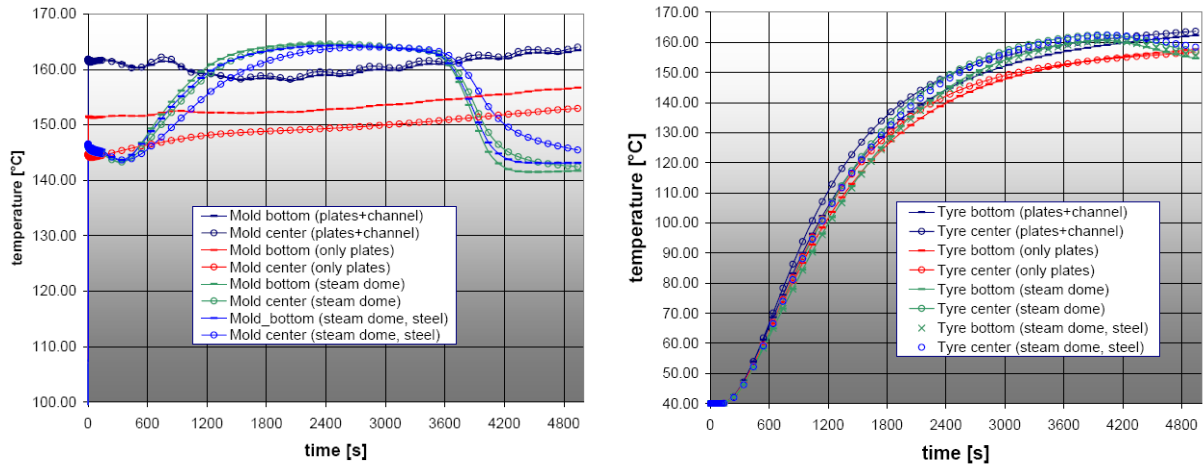


Fig. 4: Temperature histories in mold (left) and tyre (right) for all four variants.

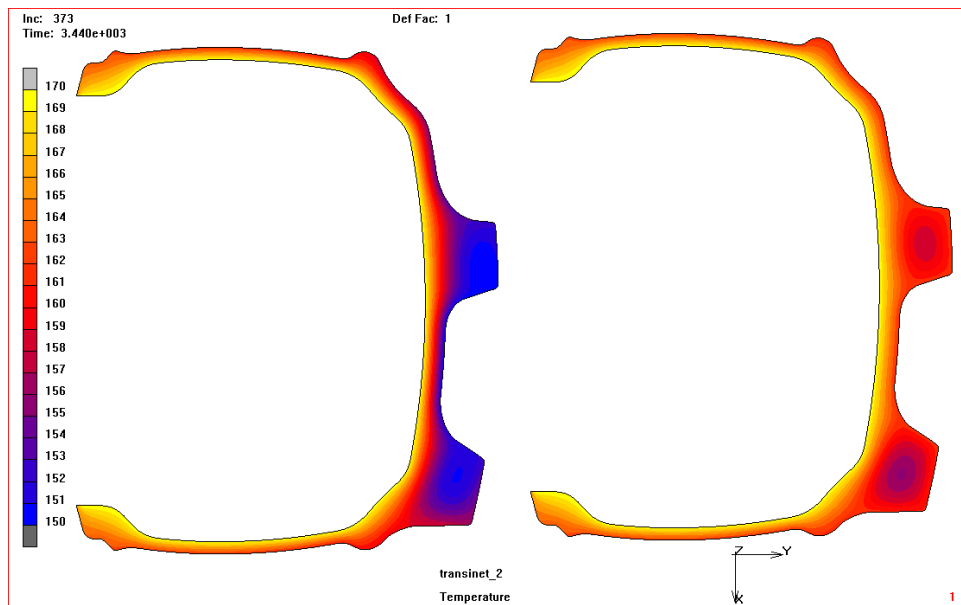


Fig. 5: Thermal field [°C] in tyre in time 57min20s – “only plates” (left), “plates+channel” (right).

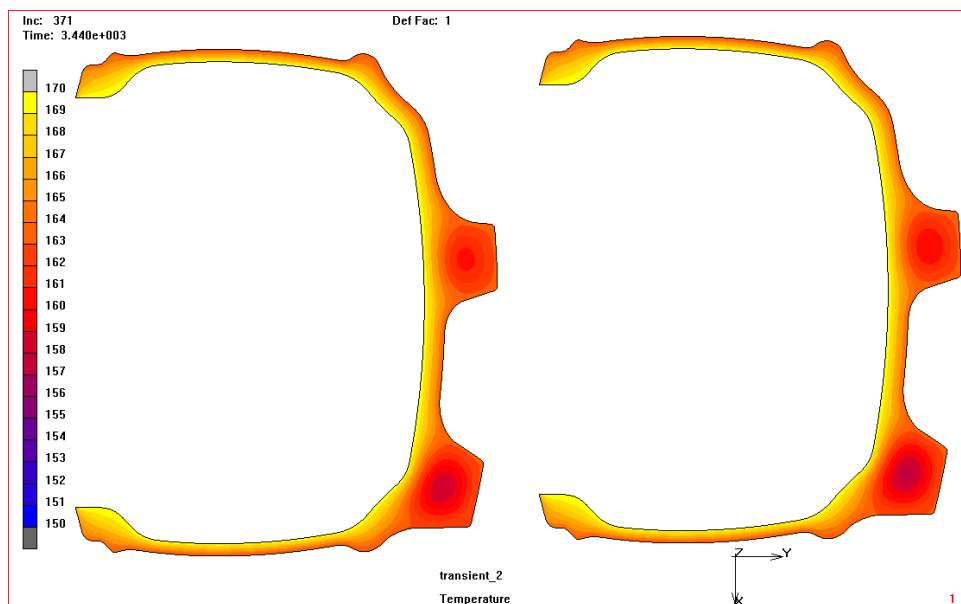


Fig. 6: Thermal field [°C] in tyre in time 57min20s – “steam dome” (left), “steam dome, steel” (right).

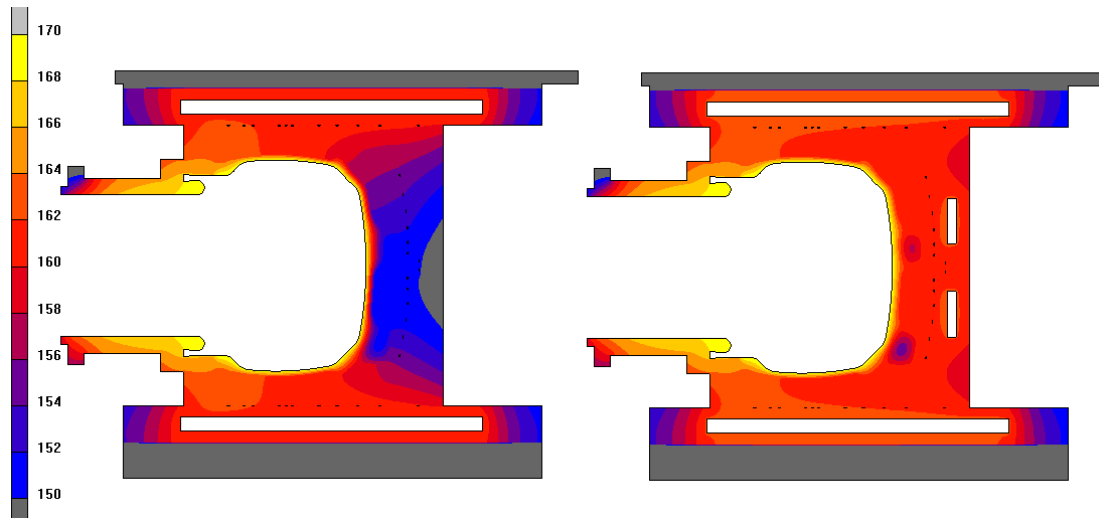


Fig. 7: Thermal field [°C] in mold in 57min20s – “only plates“ (left), “plates+channel” (right).

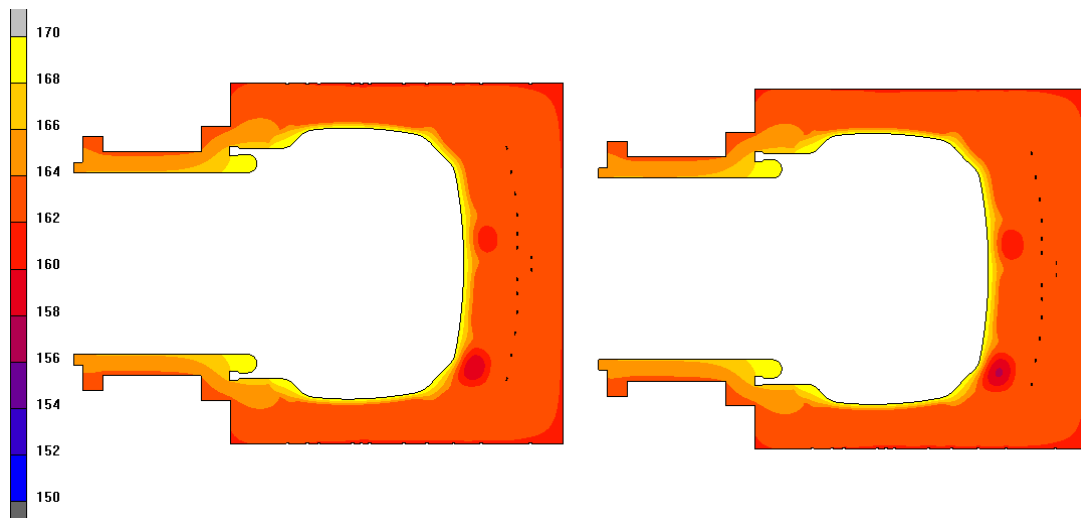


Fig. 8: Thermal field [°C] in mold in 57min20s – “steam dome“ (left), “steam dome, steel” (right).

#### 4. Conclusions

The effect of the mold heating concept (steam dome vs. heating plates) on the time history in thick parts of the cured tyre is significant despite the indisputable differences in thermal fields in molds heated with plates or steam. Heating plates in combination with properly designed heating channels (preferably with independent heating control) seem to a promising alternative to the steam dome concept. However, it should be pointed out that development of a new curing mold should be always accompanied by detailed thermal measurement with thermocouples placed in both mold and tyre to provide necessary setup data for FEM analyses.

From thermal point of view, the influence of insert material (aluminum or steel) on thermal fields in tyre and mold (and therefore on the cure process) is negligible and only manufacturing aspects can prevail.

#### References

- Bafnec, M. & Haydary, J. (2007) Chemical Engineering Aspects of Tire Curing Simulation, Konstruktion und Simulation, pp. 308-311.
- Ghoreishy, M. & Naderi, G. (2005) Three Dimensional Finite Element Modelling of Truck Tyre Curing Process in Mould, Iranian Polymer Journal 14 (8), pp. 735-743.
- Honner, M. & Litos, P. (2002) Thermovision measurement of curing press mold, Repot Nr. NTC 04-02/11.



## DYNAMIC LOADING OF VEHICLE TRACK SIMULATION

M. Chalupa<sup>\*</sup>, J. Veverka<sup>\*\*</sup>, R. Vlach<sup>\*\*\*</sup>

**Abstract:** *The article describes design of vehicle track computation model and basic testing step of dynamic loading simulation of the track. The model is built for computational simulating system MSC. ADAMS, TVT. Computational model intended for MSC computational system is built from geometrical and contact computational part. The aim of the simulating calculation is the determination of change influence of specific vehicle track constructive parameters (curve track geometry or track preloading) on changes of examined qualities of the vehicle track link (reaction force against motion, minimal track link speed and medium track speed). The results of simulating calculations are given by using of mentioned model. The full model consists of all parts of real vehicle undercarriage design. The computing result sample comes out as one of many possible cases. The influence of changes of all parameters on the needed torque changes of driving sprocket is displayed in the article. Further research plans are described in the article as well.*

**Keywords:** *Dynamic properties, testing, computational simulation.*

### 1. Introduction

The paper is introducing possible modeling method of selected type of vehicle track (Vlach, 2001) and some results of simulating computer modeling of dynamic loading of vehicle track by vehicle running (Vlach, 2003).

The work described in the article has been performed in order to solve the requirement for analyzing the problem of not good course holding of specific track vehicle when driven at a speed exceeding  $65 \text{ km} \cdot \text{h}^{-1}$  (Chalupa, 2007). It is possible to find out the reasons of this effect and propose possibilities of its elimination. It would be useful to propose possible design changes, which would make safe improvement maximum vehicle speed at the same time (Chalupa, 2009).

Main task of the work now is to define main possibilities of track vehicle course holding improvement by simultaneous increase of maximum speed vehicle. As a first step, the simulation is used for collecting of undercarriage design parameters under influence of different vehicle course holding conditions and increasing maximum speed. The basic simulating calculations are done already in this part of work. The purpose of these preliminary simulations is to monitor the influence of changes in supporting axes reaction forces in relation with changes of track links weight and initial tension of track. Such changes can influence vehicle course holding. It is well known that design parameters have relevant influence on dynamic loading of some undercarriage parts. The complete calculation of this influence is subject of the second part presented work.

### 2. Computational model and simulating results description

The PC computational system MSC.ADAMS.AVT, version 8.0 (Adams, 2003) is used for the computational modelling. This system can be used for the analysis and synthesis of kinetic and dynamic characteristics of the modelling mechanic system and its animation.

Computational model intended for MSC computational system is built from two basic parts. They are geometrical and contact computational parts of model.

---

<sup>\*</sup> assoc. prof. Ing. Milan Chalupa, CSc.: UO Brno, Kounicova 65, 612 00 Brno, e-mail: milan.chalupa@unob.cz

<sup>\*\*</sup> Ing. Josef Veverka, Ph.D., MSC.Software s.r.o., Příkop 4, 602 00 Brno, e-mail: josef.veverka@mscsoftware.com

<sup>\*\*\*</sup> Ing. Radek Vlach : Ústav mechaniky těles, FSI VUT Brno; Technická 2, 619 69 Brno; e- mail: vlach@fec.vutbr.cz

## 2.1. Geometrical part of computational model

Geometrical computational model consists of basic parts of vehicle undercarriage, movable parts and the main parts of the track link. These parts are defined by components with right geometrical shape. The critical aspect at this point is to keep flat contact.

The parts of suspension are defined as simplified shape components, such as without contact components. This type of components is generated from offer of universal track vehicles undercarriage components. They are defined by input data as basic design dimensions, weight, moment of inertia, stiffness, absorbing and number of parts.

## 2.2. Contact part of computational model

Contact computational model consists of impact and frictional forces system. To guarantee the highest accuracy and practicality, the impact and frictional forces of individual undercarriage parts are defined in such way, that the whole model resembles the reality as much as possible. These contact forces are described in Adams System by impact force:

$$F = -k (q - q_0)^n - c \dot{q} \quad (1)$$

where:  $q - q_0$ ...penetration of bodies in contact,  
 $k$  ... contact stiffness,  
 $c$  ... absorbing,  
 $\dot{q}$  ...sliding velocity of bodies in contact,  
 $n$  ... exponent  $n = 1.5$  by using of Hertz theory.

Contact model is described by characteristic of influence sliding velocity on friction coefficient as well.

## 2.3. Simulating calculation description

The aim of the simulating calculation is the determination of change influence of specific vehicle track constructive parameters (curve track geometry or track preloading) on changes of examined qualities of the vehicle track link (reaction force against motion, minimal track link speed and medium track speed). These are determined especially by intensity changes of the reaction force of the carrying elements of track links bodies.

It is evident that the results of simulation computations have proven the assumption that by means of changes in constructional parameters of undercarriage parts it is possible to improve dynamic behaviour of some parts of track vehicle undercarriage and optimize dynamic properties of the vehicle in motion.

## 2.4. Implementation of simulating calculations

Simulating calculation is quantifying the influence of ten parameters on needed torque of driving sprocket on supporting rollers axes reaction forces.

The ten parameters tested are:

1. Radius of driving wheel,
2. Radius of tightening wheels,
3. Initial tension track,
4. Track link weight,
5. Stiffness of connection plugs track link,
6. Resistance against turning of clutches plugs track link,
7. Geometry of the driving rib,
8. Bearing rollers weight,
9. Radiuses of bearing roller,
- 10 Stiffness of assessment base in bearing rollers.

The input data and information for simulations and general influence quantifying: vehicle of 40 km/h, horizontal plane -  $0^\circ$ , geometry of model for ADAMS/AVT.

Simulation calculations were realized with use of computation model displayed in Fig. 1.

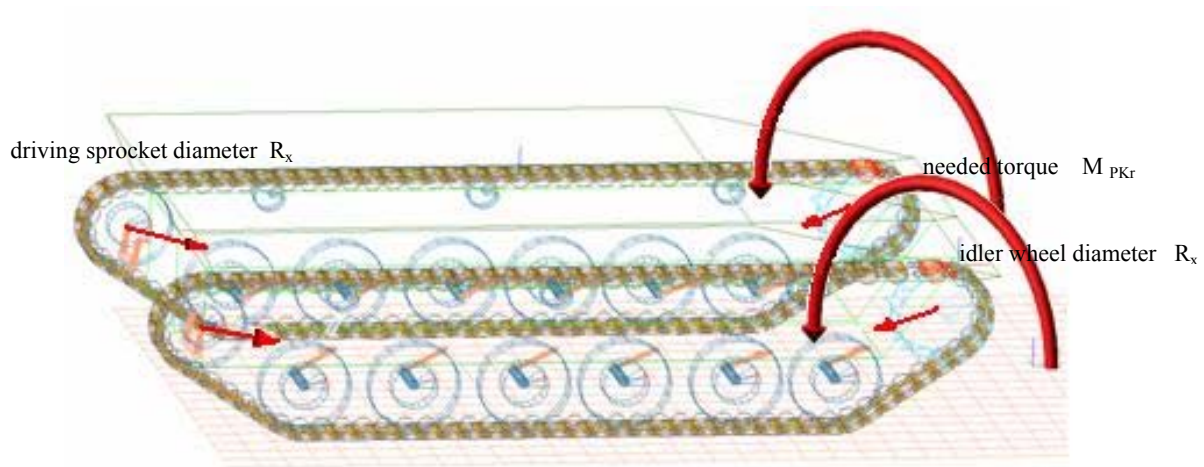


*Fig. 1: Geometrical model for testing of influence of all parameters.*

## 2.5. Results of simulating calculations

The results of performed basic simulating calculations shown the big influences of changes of

- Track links weight,
- Initial tension of track,
- Radius of driving wheel,
- Geometry of grip rib of track link

on supporting rollers axes reaction forces. It is clear that these design parameters have big influence on dynamic loading of some undercarriage parts and therefore a maximum speed of vehicle. The same influences of changes of needed torque on sprocket wheel in relation with changes of driving sprocket diameter were approved as well. This parameter influences vehicle course holding and improves maximum speed of the vehicle. This phenomenon will be the subject of our forthcoming research when full calculation will be performed.

## 3. Further research plans

Application of second-rate simulation collection will be performed hereafter to assemble of approximation relation  $y_0$  of influence monitored parameters  $R_x$ ,  $F_{pr}$ ,  $k_p$ , and  $m_x$ . This further research plan consists of three steps:

1. Composite plan simulations assembly for four parameters,
2. Implementation of 24 simulations calculations, and
3. Assessment of regression function.

## 4. Conclusion

The paper describes one of the possible ways of design and creating the computational model of real track vehicle movement mechanism in software environment MSC.ADAMS.AVT. Vehicle track design and recommendation for upgrading simulating mathematical model is emphasized. The objective is to create computation simulation for the purpose of finding the basic information on track component parts and undercarriage performance of moving track vehicle.

It is obvious from the contents of the article that our research conducted and described up to now is an introduction only to problems of vehicle track dynamic properties computational modelling, which seems to be the only viable way of track dynamic properties analysis of moving track vehicle. On the grounds of these analysis outcomes it will be possible to state which constructional changes will lead to objective accomplishment.

This objective can be defined as a track vehicle directional improvement by simultaneous maximum speed increase, simulated apart from other factors, not only on optimization of track construction, but also on the whole track kinetic and suspension arrangement of track vehicle undercarriage mechanism.

### Acknowledgement

The paper was written with the support of Research plan 0000401 of Faculty of Military Technologies of University of Defense in Brno.

### References

- ADAMS/MSC/Tracked Vehicle Toolkit version 2003.0, Documentation, MSC Software, Sweden.
- Chalupa, M., Kratochvíl, C., Kotek, V., Heriban, P. (2007) : Computer Method of Analysis of Driving System Dynamic Properties. In: "AT & P Journal Plus". Bratislava: HMH s.r.o., Tavarikova osada 39, 841 02 Bratislava 42, 2007, ISSN 1336-5010.
- Chalupa, M.: (2007) Simulation Method of Analysis of Driving System Dynamic Properties. In: Proceedings of the International conference "48<sup>th</sup> International conference of Departments of Mechanical Engineering", Smolenice 12.-14.9.2007, STU v Bratislavě, Slovensko 2007, ISBN 978-80-227-2708-2.
- Chalupa, Milan, Veverka, Josef. (2009) „Vehicle track dynamic loading simulation“. In *Sborník přednášek národní konference s mezinárodní účastí Inženýrská mechanika 2009*. Svratka: 2009, s. 501-510. ISBN 978-80-87012-11-6.
- Vlach, R., Kotek, V. (2001) Analysis of Behaviour ski for skiing along grass area. In: Proceedings of the International conference „Engineering mechanics 2001“, 14.-17.5.2001, Svratka, ČR.
- Vlach, R., Grepl, R., Chalupa, M., Ondrůšek, Č. (2003) Modeling of Dynamical Properties of Track Vehicle, In: Proceedings of the International conference „Computational mechanics 2003.“ 3.-5. 11. 2003, Nečtiny, ČR.

## **MODELLING OF A MECHATRONIC MODULE FOR FOOT RECEPTOR ACTIVATION**

**L. Ilieva-Mitutsova<sup>\*</sup>, I. Chavdarov<sup>\*\*</sup>, V. Vitkov<sup>\*</sup>, V. Yaroshevsky<sup>\*\*\*</sup>**

**Abstract:** *The module is developed like executive mechanism of a biomechatronic system for a rehabilitation of patients – paraplegics and patients during the period of continuous immovability. It must ensure according to the assignment: basing and fixation of the patient's leg; basing of a measuring sensor and a mechanism for acupressure, and also gives the possibility for their connection to various foot points for the programme performance of the procedures. The next stage of the development was optimisation of the module by size and weight and its transformation into independent portable device with insurance for vertical position in the bed of the immovable patients. The models of four variants of constructive design of the module are analysed and discussed. The choice of the most suitable variant is performed for the functional assignment presented in this report. A 3D model of the module is presented. Simulation of the treatment procedure and measuring on the patient's foot via the virtual prototype of the specialized mechatronic module is performed.*

**Keywords:** *Mechatronic module, rehabilitation, receptor activation, modelling.*

### **1. Introduction**

The mechatronic module is designed for a applicable in the rehabilitation of patients in the early post-traumatic stage after the occurrence of a spinal cord trauma or poli-trauma, and in the rehabilitation of patients suffering from durable immobilization in a lying position (Platonov et al., 2008). The carried out preliminary scientific and experimental investigations show clearly the effectiveness of this approach not only for the recreation of the functions of the supporting and locomotion human system, but also for the organ function stimulation, projected on the supporting foot surface by the nervous tips.

### **2. Methods**

Developed mechatronic module can ensure treatment procedures on method of acupressure at specific foot acupressure points, receptor activation along specific trajectory or affects foot reflex areas. It operates according to a previously prescribed program. Thus, functioning of the internal organs of patients suffering from durable immobilization (in lying position) is activated.

The module can ensure control measure the bioelectrical resistance by means of a specialized sensor. Such a sensor is needed to design a high-spatial resolution map of acupuncture points of a patient's foot, and the map should be used to analyze the results of the treatment. The sensor measuring both the initial (pre-treatment) foot skin electro-conductivity, as well as the current one operating during the process of medical treatment, is of essential importance for the successful stimulation of patient's foot.

Product *Mechanical Desktop 2005* is applied for the creation of a virtual 3D model of the module.

The program “MSC.visualNastran 4D 2002” for computer simulation is applied on the 3D model.

---

<sup>\*</sup> assoc. prof. Lidia Ilieva-Mitutsova, Ph.D. and assist. prof. Vladimir Vitkov: Institute of Mechanics, Bulgarian Academy of Sciences, Acad. G. Bonchev str., bl. 4, 1113 Sofia, e-mails: lidia@imbm.bas.bg, vitkov@imbm.bas.bg

<sup>\*\*</sup> assoc. prof. Ivan Chavdarov, Ph.D., Central Laboratory of Mechatronics and Instrumentation, Bulgarian Academy of Sciences, Acad. G. Bonchev str., bl. 1, 1113 Sofia, e-mail: ivan\_chavdarov@dir.bg

<sup>\*\*\*</sup> prof. assoc. prof. Viktor.Yaroshevsky, Ph.D., Keldysh Institute of Applied Mathematics, 4 Miusskaya Sq., 125047 Moscow, e-mail: yarosh@keldysh.ru

### 3. Requirements to technical module design

The designed module must meet the following requirements:

1. Sustainable basing the patient's leg, which is in a reclining or sitting position.
2. An accessibility to be ensured to maximum number of points on the foot with the aim to measure the bioelectrical resistance by means of a specialized sensor.
3. Accessibility to maximum number of points on the foot for automatic acupressure performance according to a programme assignment, individually for each patient.
4. Discomfort must not be created to the patient, and also not to influence the precision of the carried out measurements.
5. Basing to be possible at different patient's feet sizes.
6. Safety of the patients to be ensured of the device activity at arising programme or mechanical reasons.

### 4. Technical module design - variants

Four variants of the module for founding of patient leg, measuring and acupressure are developed and modelled and they are presented in Fig. 1.

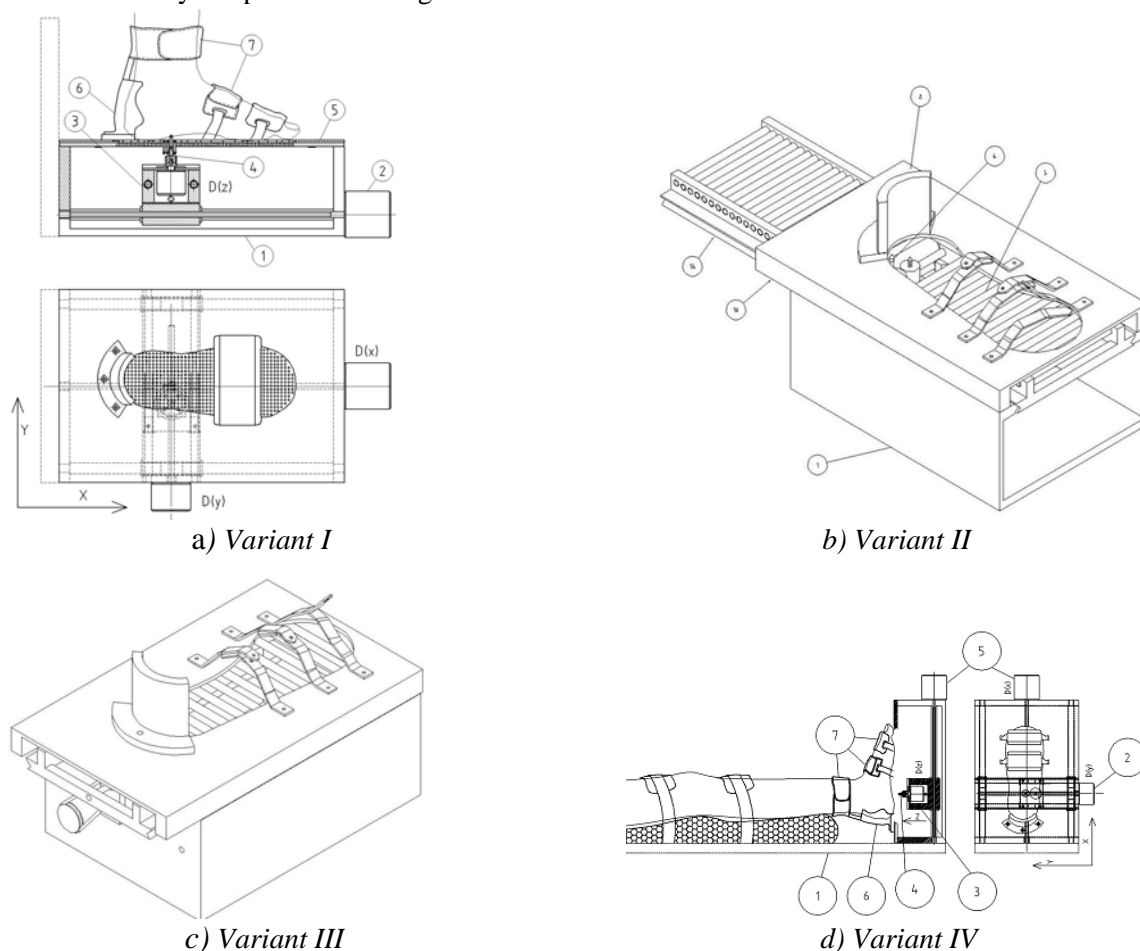


Fig. 1: Module- shoe for founding of patient leg, measuring and acupressure – variants.

Variant I was developed mostly and on a patent level and was registered as a Bulgarian patent BG 109266 A which was developed as a stationary variant of a biomechatronic system for rehabilitation of paraplegics. The next stage of the development was optimisation of module by size and weight and its transformation into independent portable device with insurance for vertical position in the bed of the immovable patients. The study describing the realization of Variant I is close to the cited in literature Japanese patent, registered in Europe as EP 0 372 114 A1. The objective of the work presented in this paper is a modelling of Variant IV, being the most suitable one for a portable device for application in a patient's bed when the patient being stationary.



#### 4.1. View of the device

The developed module includes the following component, (Fig. 2): 1- base, 2 - translation linear drive along axis Y, 3 - combined module-carriage, 4 - executive mechanism for acupressure, 5 - translation linear drive along axis X, 6 - heel support, 7 - foot fixations.

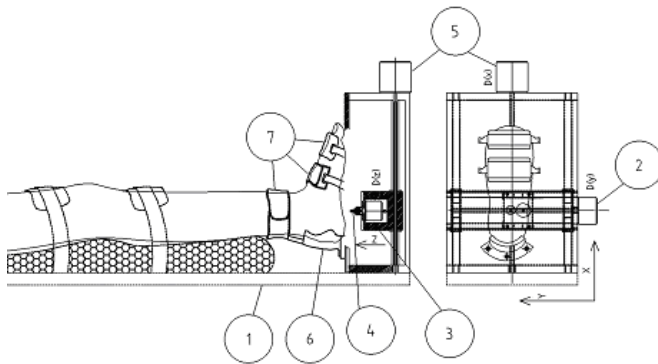


Fig. 2: General view of the device.

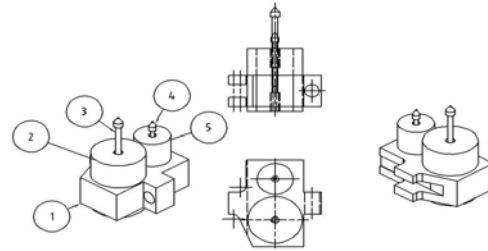


Fig. 3: Combined module-carriage.

The foot is based at support 6; leg is fixed above the ankle joint and in the front part of the foot is prepared fixations 7, which place is regulated longitudinally according to the foot size. The surface of the foot remains uncovered for a direct contact to each point for measurement of the skin electrical resistance and acupressure. Combined module - carriage (Fig. 3) comprises carriage 1, to it is immovably attached module for acupressure 2 and a measuring module 5.

In the modules joints are included respectively two linear drives, by means of which a translation along axis Z is realised. The respective useful contact pressure of an electrode for measurement 4 is achieved by means of drive control and the external force (acupressure) is regulated by means of the executive mechanism 3.

#### 4.2. 3D model of the module for founding of patient leg, measuring and acupressure

Module functions simulation is performed on the derived 3D model of the module for basing of the leg, measuring and acupressure.

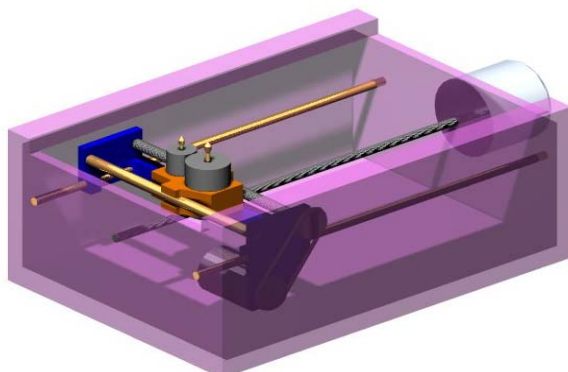


Fig. 4: A mechanism for a plane motion and positioning for measurement and acupuncture.

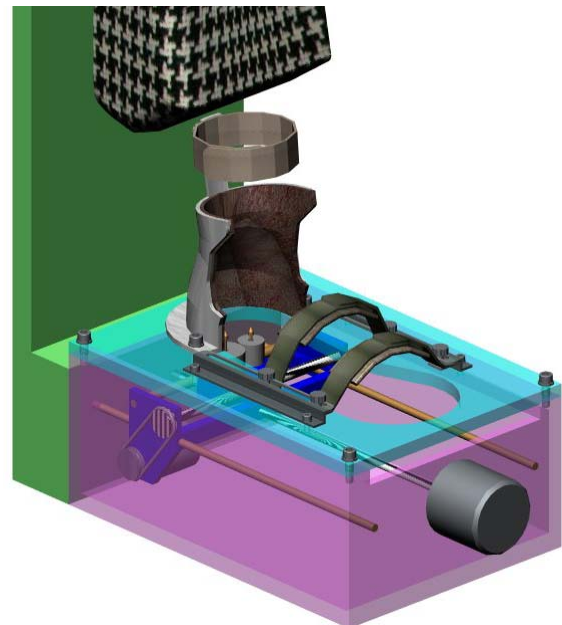


Fig. 5: 3D model of the mechatronic module



## 5. Conclusions

The conclusions derived after modelling and simulation help the successful realization of the prototype of the portable module for procedures with supporting and healing effect of patients in the early stage after the occurrence of a spinal cord trauma or politrauma.

The following scientific and application results are expected:

- Measuring of the bioelectrical resistance to be performed in the foot points for each individual patient by means of a specialized sensor “*Skin Touch*”. An individual chart of the acupuncture foot points of the patient is build up.
- Planning and performing of treatments (acupresura) in definite points, along a defined trajectory or an area on the foot.
- Performing of a periodical estimation and control of the treatment results by means of measuring of the bioelectrical resistance in definite foot points. The healing programme undergoes a consecutive variation if necessary.

The mechatronic module can be applied in the clinic practice after performing technical, laboratory and clinical experiments.

## Acknowledgement

This work was supported by a Bi-lateral project of BAS and RAS “Technical and clinical investigations of the model of biomechatronic system for foot receptor activation and investigation of the rehabilitation of spinal patients” and Institutional Research Plan of Institute of Mechanics of BAS.

## References

- Platonov, A., Ilieva-Mitutsova, L., Yaroshevsky, V., Serbenjuk, N., (2008) Development of Mechatronic-Biomechanical Complex for Locomotion Therapy, In: Proc.of 12<sup>th</sup> Inter. Conf. on Developments in Machinery Design and Control „ Nowogrod 2008“ (K.Peszynsky eds) on CD, ISBN 978-83-87982-08-9, pp.55-64.
- EP 0 372 114 A1 European Patent, Application Number: 88120465.5, Date of Patent: Jun.13, 1990 Bulletin 90/24, Massage device, Inventor: Nishiguchi, Hidetsugu, 561, Meiwa-cho oaza Uninaka Taki-gun Mie 515-03(JP).
- BG 109266 A Bulgarian patent, Application Number: 65876, Date of Patent: Jun.09, 2010, Bulletin A 61 H 39/04 92006.01), Device for acupresura, Inventor: Ilieva-Mitutsova, Vitkov et al., IMECH of BAS, Acad. G. Bonchev str., bl. 4, 1113 Sofia (BG).

## **PREDICTING THE DIRECTION OF CRACK PROPAGATION ALONG THE CIRCUMFERENCE OF A MODEL RAILWAY CARRIAGE UNDER VARIOUS OPERATING CONDITIONS**

**P. Janíček<sup>\*</sup>, E. Schmidová<sup>\*\*</sup>, P. Navrátil<sup>\*</sup>, R. Jandora<sup>\*\*\*</sup>**

**Abstract:** *This contribution deals with reliability of railway wheels as influenced by the occurrence of impaired limiting material strength. Results are presented of material investigation, experimental and computational modelling of crack propagation. The presented computational prediction of the direction of propagation of primary cracks differing in their length and position under various operation conditions is entirely original.*

**Keywords:** *Railway wheel, fatigue failure, experimental and computational modeling, fracture mechanics, prediction of crack propagation direction.*

### **1. Introduction**

Reliability of railway wheels is an essential factor affecting railway traffic reliability. Railway wheels reliability depends on attainment of their limit states, primarily the limit states of wheel material failure, more specifically the occurrence of topologically different cracks. The problem remains topical as the requirements imposed on the strength of materials continue to grow as the train speeds continue to rise. The essentials of limit states initiation, fatigue failure and their modifications have been investigated along several directions using various types of modelling: (1) Examination of the occurrence of limit states and their analysis for railway wheels in operation (the resulting knowledge underlying knowledge modelling). (2) Experimental modelling on special testers that simulate operating conditions, using different wheel materials and different heat treatments. (3) Computational, computer-assisted simulation of crack initiation and prediction of crack propagation, always using continuum mechanics and fracture mechanics. (4) Material investigation as a part of material and technology engineering (investigation of the effect of structure on fracture resistance of the material concerned).

### **2. Methods**

The contribution presents the approaches employed and the results of experimental and computational modelling of impaired strength of railway wheel materials.

#### **2.1. Experimental material investigation and modelling using a tester**

The strength of railway wheels is adversely affected by fatigue processes that take place in the material concerned. The affected locations appear in parts of the material subject to recurring plastic deformation. Both conditions apply to railway wheels (the wheel rotates, locations subject to plastic deformation exist) and, accordingly, fatigue-related cracks will definitely occur. It is always just a matter of time when surface cracks appear. The time until crack initiation depends on the properties and behaviour of the material concerned and on the character of the operating conditions.

---

<sup>\*</sup> prof. Ing. Přemysl Janíček, DrSc. and Ing. Petr Navrátil: Institute of Solid Mechanics, Mechatronics and Biomechanics, Brno University of Technology, 602 00 Brno, Czech Republic, e-mails: janicek@fme.vutbr.cz, ynavra26@stud.fme.vutbr.cz

<sup>\*\*</sup> doc. Ing. Eva Schmidová, Ph.D.: Department of Mechanics, Materials and Machine Parts, Jan Perner Transport Faculty, University of Pardubice, Studentská 95, 532 10 Pardubice; Czech Republic, e-mail:eva.schmidova@upce.cz

<sup>\*\*\*</sup> Ing. Radek Jandora: Honeywell, spol. s r.o. HTS CZ o.z., Turanka 98c, 627 00 Brno, Czech Republic, e-mail: radek.jandora@honeywell.com

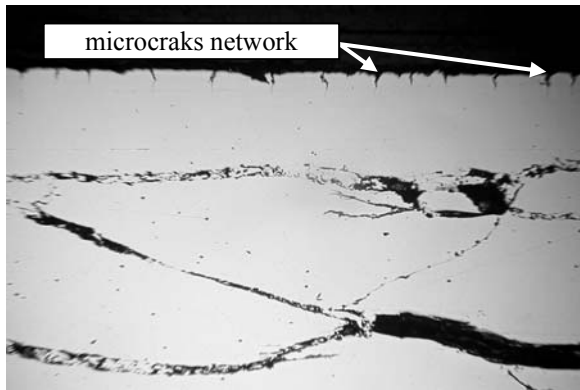


*Fig. 1: Network of microcracks perpendicular to the contact surface.*

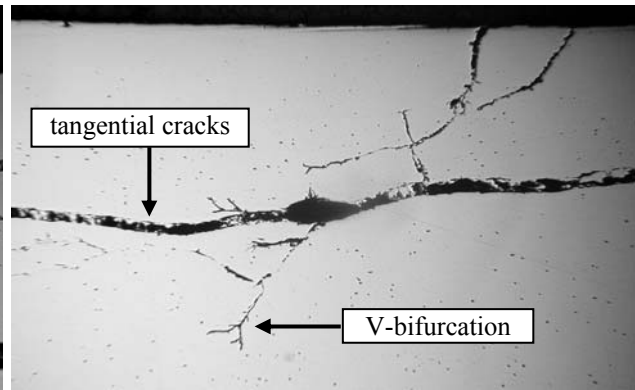


*Fig. 2: Network of tangential cracks beneath a hardened surface layer.*



*Fig. 3: Part of railway wheel perimeter crumbled away.*

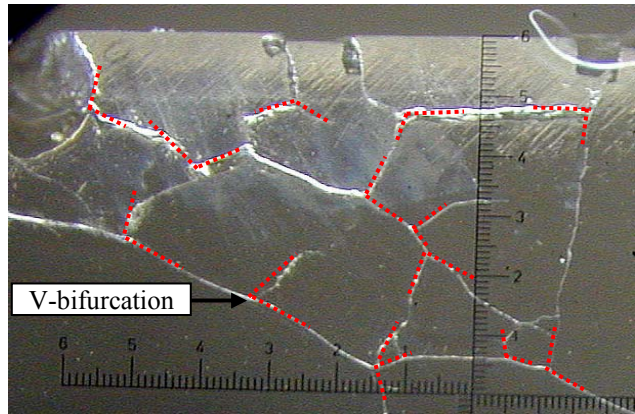


*Fig. 4: "V-bifurcation" of cracks beneath a railway wheel contact surface.*

The following facts are presented here: Standard materials of railway wheels exhibit a ferritic-pearlitic structure with carbon content up to 0.56 %. Higher values of strength (in particular the fatigue-strength limit) are achieved by suppressing the content of structurally free ferrite and refining the structure (by reducing the interlamellar perlite spacing) through appropriate heat treatment of the surface layers.

With increasing carbon content "sensitivity" of the material to the adverse effect of temperature also increases. Once the limit adhesion is exceeded at the point of contact railway wheel/rail, temperature rises above the phase transition temperature, resulting in formation of high-carbon twinned martensite that constitutes one of several typical initiating effects that lead to crumbling away of the contact surface (Fig. 3). A trend exists towards a phase transition at a given rate of cooling so that conditions underlying anisothermal decomposition of austenite are satisfied. Surface cracks are then initiated as network of microcracks perpendicular to the contact surface (Fig. 1). Outside the hardened layer cracks bend along typical transition zones after partial austenitisation. This structural effect on orientation of the cracks is thus restricted by the range of the phase transitions up to a depth of 2 to 3 mm. The above reason underlying crack initiation results from a certain "non-standard operating operation" - brake action.

Contact-fatigue material damage represents another mechanism underlying crack formation in railway wheels. Inside a layer up to 0.2 mm thick a mechanism of cumulative plasticity depletion has been revealed, resulting in initiation of surface cracks. Within the range of the deformation field subsequent damage is then oriented along the direction of plastic flow of the steel.

The two mechanisms of damage initiation are important inside a certain domain close to the wheel tread. Cracks however propagate also outside that domain and branch in the shape of a very open letter V. The present authors suggest the name V-bifurcation for this type of crack splitting (Fig. 2 and Fig. 4). This phenomenon has not been systematically analysed yet. Most instances of experimental and computational modelling focus on crack initiation, where a surface without any cracks represents the starting model of the wheel tread.

To study the phenomenon of V-bifurcation one has to use a different geometrical model; one must start with a tread containing primary cracks and investigate, using the methods of fracture mechanics, how the cracks - depending on their geometrical parameters (shape, length, angle) - behave when subject to various operating conditions (start, braking, steady drive). Computational (computer-assisted) modelling is the preferred approach.

## 2.2. Computational modelling - behaviour of cracks under various operating conditions

Problem to be solved: "A primary, straight crack - of length  $L$  and at angle  $\alpha$  with regard to the perimeter tangent - exists at the wheel perimeter. The direction of its propagation is to be predicted under various operating conditions (start, braking, steady drive) and for various positions of cracks".

Input data for the algorithm: Wheel:  $R = 460$  mm,  $G = 10^4$  kg, material:  $E = 2.1 \times 10^5$  MPa,  $\mu = 0.3$ . Partial calculation models of the wheel have been developed: model "rotary desk of constant thickness" - Fig. 5; model of relations (contact wheel perimeter - rail); model of load (rotation and load imposed on the axle); model of the material (homogeneous, isotropic); model of deformation (small deformation); model of stress (plain strain). Crack length: between 2 mm and 70 mm; crack angle:  $10^\circ$  to  $90^\circ$ . Discretization of the crack surroundings is apparent from Fig. 6. Operating conditions investigated are shown in Fig. 7.

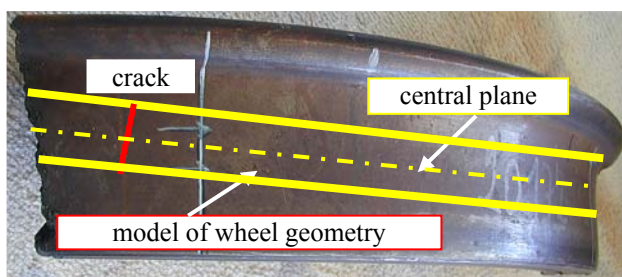


Fig. 5: Railway wheel tread and model geometry.

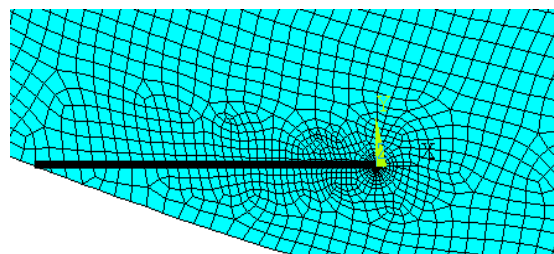


Fig. 6: Discretization of railway wheel crack surroundings.

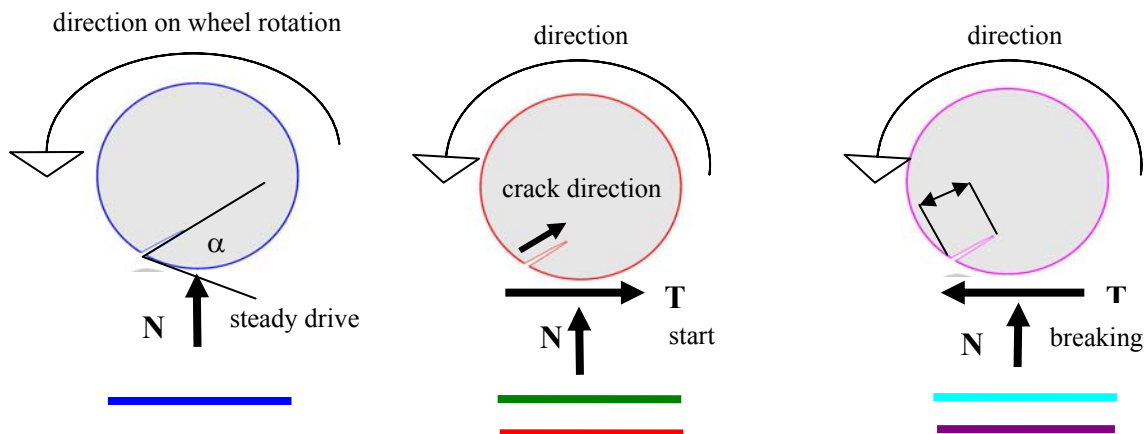


Fig. 7: Operating conditions of wheel - crack propagation.

Output from the algorithm: Stress, first mode  $K_I$ , second mode  $K_{II}$ , effective stress coefficient  $K_{ef}$ , predicted direction of crack propagation from its root - angle  $\Omega$  - is calculated from the maximum tangential stress using the formula

$$\Omega = \arccos \frac{3K_{II}^2 + K_I \sqrt{K_I^2 + 8K_{II}^2}}{K_I^2 + 9K_{II}^2}. \quad (1)$$

The sign of angle  $\Omega$  is determined from the ratio  $K_I/K_{II}$ ; since  $K_I > 0$  the sign of angle  $\Omega$  is given by the sign of  $K_{II}$ : if  $K_{II} < 0$   $\Omega < 0$  as well, in other words, the predicted direction of crack propagation is towards the wheel perimeter. If  $K_{II} > 0$  the predicted direction is towards the wheel centre.

The sign of angle  $\Omega$  is determined from the ratio  $K_I/K_{II}$ ; since  $K_I > 0$  the sign of angle  $\Omega$  is given by the sign of  $K_{II}$ : if  $K_{II} < 0$   $\Omega < 0$  as well, in other words, the predicted direction of crack propagation is towards the wheel perimeter. If  $K_{II} > 0$  the predicted direction of crack towards the wheel centre.

The results of computational modelling are plotted in Fig. 8 as dependencies of  $K_I$ ,  $K_{II}$ ,  $K_{ef}$  and  $\Omega$  on the place of stress (the place of the crack tip with regard to the place of contact wheel/rail) for the various operating conditions investigated. The results of computational modelling lead to the following conclusions: **❶** The first mode stress coefficient  $K_I$  is significantly smaller than the second mode stress coefficient  $K_{II}$ . **❷** The sign of the second mode stress coefficient  $K_{II}$  differs for start and braking; accordingly, depending on the sign the crack slews towards the wheel perimeter or towards the wheel centre: during one rotation a V-bifurcation thus originates with an angle of around  $135^\circ$ . **❸** For cracks of small length (1.5 to 3 mm) and small angles of the primary crack (between  $10^\circ$  and  $20^\circ$ ) the crack propagates predominantly towards the perimeter. **❹** For longer cracks (starting at around 50 mm) and higher angles of the primary crack the crack propagates predominantly towards the wheel centre, regardless of the operating conditions.

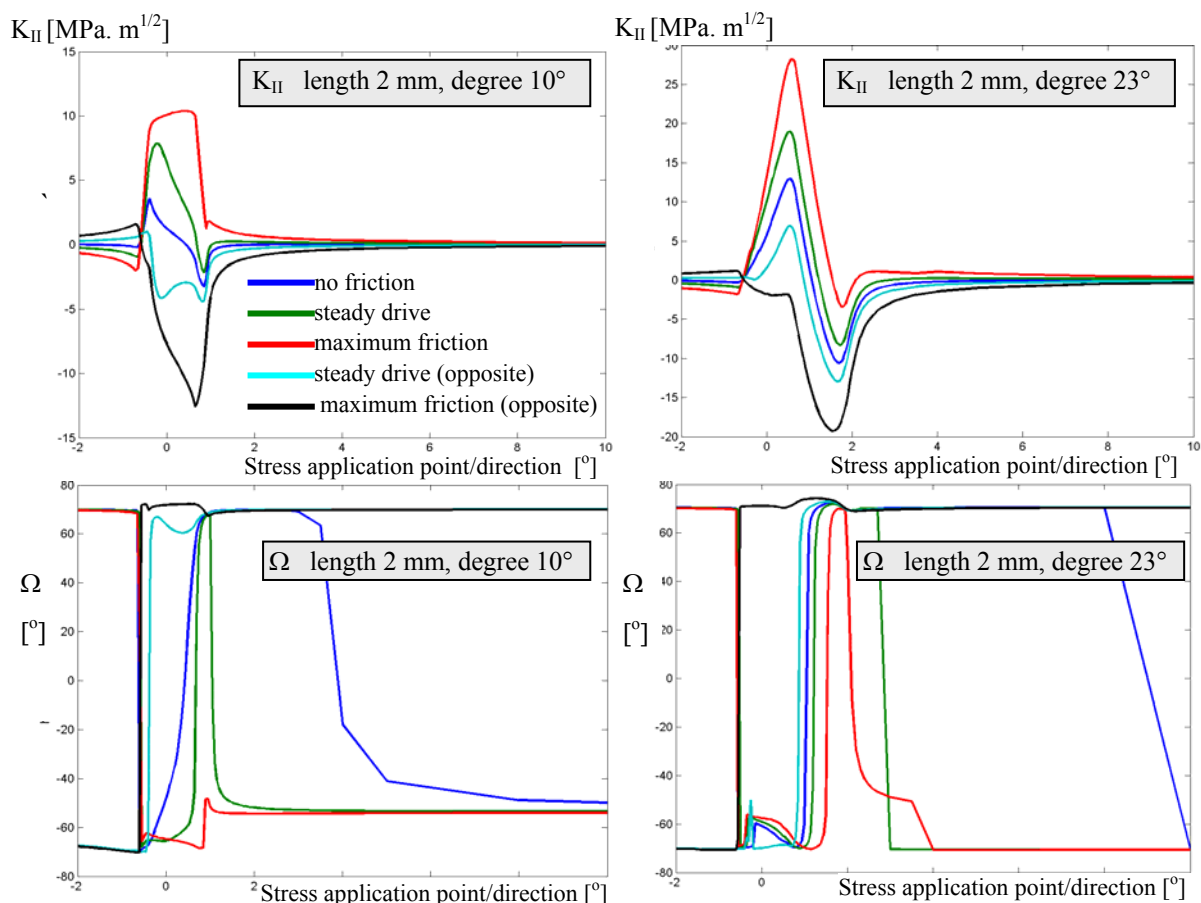


Fig. 8: Results of computational modelling - behaviour of cracks in railway wheel.  
From top to bottom: stress coefficient  $K_{II}$ , predicted angle of crack propagation  $\Omega$ .

### 3. Conclusions

The results of computational modelling agree with the facts observed for actual railway wheels - computational modelling thus provides plausible results.

### Acknowledgement

This work was supported by the Research Centrum of Railway Vehicles under sponsorship of the Ministry of Education, Youth and Sports of Czech Republic, project No. 1M0519.



## COMPARISON OF SPACE-FILLING DESIGNS IN DISCRETE DOMAINS

E. Janouchová<sup>\*</sup>, A. Kučerová<sup>\*</sup>

**Abstract:** *In order to properly explore response of a model, one needs to perform simulations for a set of design points. When dealing complex non-linear models, the simulations are usually very time-consuming, hence the number of simulations performed within a limited time is rather low. Randomly chosen design points do not ensure the observed properties will be captured properly. Therefore, the design points must be chosen carefully. The motivation of the presented contribution is to investigate methods, which are suitable for generating designs in discrete parameter space, where each parameter can attain different number of levels, because commonly used software based on Latin Hypercube Sampling fails in solving such a situation. Hence, we compare here several well-known metrics for assessing optimal designs as for instance the Euclidean maximin distance, the maximum pairwise correlation or the D-optimal criterion. The resulting optimal designs are consequently employed for the evaluation of the stochastic sensitivity analysis so as to investigate their ability in prediction of the 'parameter-response' correlations.*

**Keywords:** *Design of experiments, discrete domains, space-filling, orthogonality, stochastic sensitivity analysis.*

### 1. Introduction

The increasing complexity of numerical models makes the exploration of a model response an important area of investigation. To minimize the number of time-exhaustive simulations, reliable meta-models are usually constructed (Simpson et al., 2001). The meta-models represent the approximation/interpolation of a model response over the domain of model parameters called the design space. They are usually obtained by minimization of their error in a set of design points. The predictability of the resulting meta-model is in such setting driven by the choice of the design points being often called as the design of experiments.

The following section reviews several common metrics for assessing optimal designs and explores their properties when applied to discrete design spaces. Each metric defines a different optimal design. It is shown that the design optimal with respect to one metric does not reach the optimum for other metrics. After introducing the space-filling algorithms, in Section 3, we present their mutual comparison with emphasis on discrete domains. This is complemented with the optimal LHS algorithm due to Iman & Conover (1980), which is available in many engineering software packages. The ability of the optimal designs to capture the impact of model parameters to model responses is then critically assessed in Section 4. Finally, Section 5 gives conclusions and suggests directions for future work.

### 2. Metrics for assessing optimal designs

Let us recall several metrics commonly used for the determination of a suitable design of experiments.

*Audze-Eglais objective function (AE)* proposed by Audze & Eglais (1977) is based on a potential energy among design points. The points are distributed as uniformly as possible when the potential energy proportional to the inverse of the squared distance between points is minimized, i.e.

---

<sup>\*</sup> Eliška Janouchová and Ing. Anna Kučerová, Ph.D.: Faculty of Civil Engineering, Czech Technical University in Prague, Thákurova 7/2077; 166 29, Prague; CZ, e-mails: eliska.janouchova@fsv.cvut.cz, anicka@cml.fsv.cvut.cz

$$\min AE = \min \sum_{i=1}^n \sum_{j=i+1}^n \frac{1}{L_{ij}^2}, \quad (1)$$

where  $n$  is the number of points and  $L_{ij}$  is the Euclidean distance between points  $i$  and  $j$ .

*Euclidean maximin distance (EMM)* is another metric preferring uniform designs. For a given design, the Euclidean maximin distance is defined as a minimal distance among all distances  $L_{ij}$ . A larger value is better, so we minimize the negative value of the minimal distance.

*Pearson product-moment correlation coefficient (PMCC)* can be used as a metric, which does not prefer uniformity, but leads to orthogonal designs. A correlation among design points can induce spurious correlation among coefficients of linear meta-models and can affect other meta-model-based estimates (Cioppa & Lucas, 2007). The simplest metric computes the absolute value of a correlation for each pair of variables. The goal is then to minimize the obtained maximal correlation.

*Spearman's rank correlation coefficient (SRCC)* is considered to be more general than PMCC, because the PMCC reveals only the linear dependence between two variables. Here, the correlation is not computed between coordinates of points, but these coordinates are ordered and the correlation is computed between the resulting ranks.

*D-optimality (Dopt)* is a metric formulated for maximization of entropy. The goal is to maximize the determinant of the information matrix  $\mathbf{A}$ . Here we employ a Bayesian modification to the information matrix proposed by Hofwing & Strömberg (2010) in order to eliminate duplicates in the final D-optimal design. As we assume a minimization process, we minimize  $Dopt = -\det \mathbf{A}$ .

When determining the optimal design of experiments, the criteria described above are supposed to be minimized by an optimization algorithm. Therefore, one aspect is the difficulty of its minimization. As the first study, we considered two-dimensional square domain with the fixed position of three points placed into the corners (top-right, bottom-right and bottom-left). Then, we were searching for an optimal position of the fourth point. Fig. 1 shows the value of particular metrics as a function of the fourth point position.

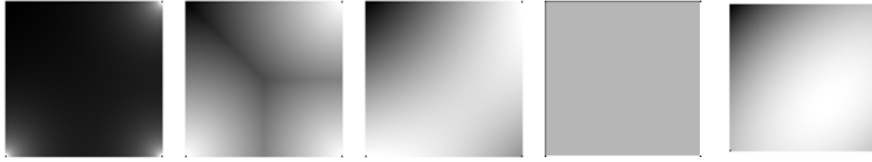


Fig. 1: Shape of different metrics for varying position of the 4<sup>th</sup> point. Black is the desired minimum, white is the maximum. From left: AE, EMM, PMCC, SRCC, Dopt.

Regarding the obtained shapes, we can conclude that the AE, EMM and SRCC metrics have one clear optimum in the fourth (top-left) corner. The value of the AE metric steeply decreases with increasing distance from the three occupied corners, but there is a large slowly decreasing valley towards the fourth corner. The EMM metric decreases more rapidly, but its shape is not smooth. The SRCC metric is constant over almost the whole domain except boundary, which can make the optimization unfeasible for gradient-based algorithms. Finally, the metrics PMCC and Dopt are smooth but have local extremes at occupied corners. Therefore, we conclude that the AE metric seems to be easiest for the minimization.

### 3. Tournaments of metrics

When generating large designs including a high number of points, the optimization of the described metrics becomes a complex task. Therefore, packages with the optimal Latin Hypercube Sampling method are often used for this purpose. LHS defines constraints to the designs which significantly reduce the design space and simplifies the following optimization. The main idea is to divide the interval of each variable to a number of levels equal the number of design points. Unfortunately, such an approach is not applicable for discrete variables as each may attain different number of values. Hence, we focus on the optimal designs not suffering the LHS restrictions.



To examine the quality of optimal designs with respect to different metrics, we have studied three different situations with 7, 10 and 13 design points to be placed into the two-dimensional square discrete domain with 10 levels in both dimensions. Since the designs are not excessively complex, a Simulated Annealing method with a sufficient number of iterations was applied to find the global optimum on each metric. While AE and Dopt metrics both define only one optimal design, other metrics lead to several designs with the same optimal value. Hence, the results in all following tables present the worst case scenario – the values correspond to the worst (optimal valued) design. In each row of Tabs. 1 – 3, one metric was optimized and the obtained optimal design was evaluated by other metrics. In Tab. 2, one row for optimal LHS is added, since only in such a scenario, the number of design points is equal to the number of levels in both dimensions. In particular, oLHS optimized with respect to SRCC were obtained by software SPERM 2.0 (Novák, www).

Tab. 1: Values and ranks (#) of metrics optimized for placing 7 points into the domain  $10 \times 10$ .

<b>Metric</b>	<b>AE</b>		<b>EMM</b>		<b>PMCC</b>		<b>SRCC</b>		<b>Dopt</b>		<b>Average #</b>
	<i>value</i>	#	<i>value</i>	#	<i>value</i>	#	<i>value</i>	#	<i>value</i>	#	
<b>AE</b>	0.485	1	-4.00	2	0.018	2	0.000	1	$-2.10^{13}$	2	<b>1.6</b>
<b>EMM</b>	0.587	3	-4.47	1	0.271	4	0.198	3	$-5.10^{12}$	3	<b>2.8</b>
<b>PMCC</b>	4.609	4	-1.00	3	0.000	1	0.372	4	$-1.10^7$	4	<b>3.2</b>
<b>SRCC</b>	4.784	5	-1.00	3	0.474	5	0.000	1	$-1.10^6$	5	<b>3.8</b>
<b>Dopt</b>	0.514	2	-4.00	2	0.019	3	0.049	2	$-3.10^{13}$	1	<b>2</b>

Tab. 2: Values and ranks (#) of metrics optimized for placing 10 points into the domain  $10 \times 10$ .

<b>Metric</b>	<b>AE</b>		<b>EMM</b>		<b>PMCC</b>		<b>SRCC</b>		<b>Dopt</b>		<b>Average #</b>
	<i>value</i>	#	<i>value</i>	#	<i>value</i>	#	<i>value</i>	#	<i>value</i>	#	
<b>AE</b>	1.375	1	-3.00	2	0.015	3	0.020	3	$7.10^{15}$	6	<b>3.0</b>
<b>EMM</b>	1.801	3	-3.61	1	0.153	4	0.142	5	$-1.10^{27}$	2	<b>3.0</b>
<b>PMCC</b>	8.092	5	-1.00	5	0.000	1	0.227	6	$-1.10^{16}$	4	<b>4.2</b>
<b>SRCC</b>	9.408	6	-1.00	5	0.241	5	0.000	1	$-7.10^{15}$	5	<b>4.4</b>
<b>Dopt</b>	1.450	2	-2.83	3	0.015	3	0.026	4	$-7.10^{28}$	1	<b>2.6</b>
<b>oLHS</b>	3.555	4	-1.42	4	0.006	2	0.006	2	$-3.10^{20}$	3	<b>3.0</b>

Tab. 3: Values and ranks (#) of metrics optimized for placing 13 points into the domain  $10 \times 10$ .

<b>Metric</b>	<b>AE</b>		<b>EMM</b>		<b>PMCC</b>		<b>SRCC</b>		<b>Dopt</b>		<b>Average #</b>
	<i>value</i>	#	<i>value</i>	#	<i>value</i>	#	<i>value</i>	#	<i>value</i>	#	
<b>AE</b>	2.83	1	-3.00	1	0.015	2	0.017	2	$-1.10^{36}$	2	<b>1.6</b>
<b>EMM</b>	3.20	2	-3.00	1	0.153	3	0.186	5	$-6.10^{28}$	3	<b>2.8</b>
<b>PMCC</b>	16.04	5	-1.00	3	0.000	1	0.180	4	$-2.10^{21}$	5	<b>3.6</b>
<b>SRCC</b>	14.50	4	-1.00	3	0.241	4	0.000	1	$-2.10^{25}$	4	<b>3.2</b>
<b>Dopt</b>	3.42	3	-1.42	2	0.015	2	0.056	3	$-6.10^{42}$	1	<b>2.2</b>

#### 4. Prediction of correlation between model inputs and outputs: illustrative examples

Among the first steps of meta-model formulation is the determination of important model parameters with high impact on model response. This is usually done by stochastic sensitivity analysis.

Tab. 4: Prediction of input-output correlation for model  $z = x + y$ .

<b>Design</b>	<b>Full</b>	<b>AE</b>	<b>EMM</b>	<b>PMCC</b>	<b>SRCC</b>	<b>Dopt</b>	<b>oLHS</b>
<b>corr (x, z)</b>	0.700	0.699	0.813	0.236	0.975	0.694	0.835
<b>corr (y, z)</b>	0.700	0.686	0.566	0.840	0.161	0.673	0.530
<b>Sum of errors</b>		0.016	0.247	0.604	0.814	0.033	0.305
<b>Rank (#)</b>		<b>1</b>	<b>3</b>	<b>5</b>	<b>6</b>	<b>2</b>	<b>4</b>

Therefore, we studied the ability of optimal designs to predict the SRCC between each parameter and the model response. For the sake of clarity, we considered two simple models, linear and non-linear, both along with two discrete parameters  $x$  and  $y$ , each having 10 levels. The real parameter-response correlation can be obtained for a *full* design comprising all 100 samples. One design with 10 points was optimized for each metric and we evaluated the corresponding estimate of the parameter-response correlation. The results are summarized in Tabs. 4 and 5.

Tab. 5: Prediction of input-output correlation for model  $z = x^2 + y^2$ .

<i>Design</i>	<i>Full</i>	<i>AE</i>	<i>EMM</i>	<i>PMCC</i>	<i>SRCC</i>	<i>Dopt</i>	<i>oLHS</i>
<i>corr</i> ( $x, z$ )	0.686	0.699	0.419	0.195	0.948	0.698	0.827
<i>corr</i> ( $y, z$ )	0.686	0.686	0.875	0.914	0.160	0.669	0.450
<i>Sum of errors</i>		0.013	0.456	0.719	0.788	0.029	0.377
<i>Rank</i> (#)		<b>1</b>	<b>4</b>	<b>5</b>	<b>6</b>	<b>2</b>	<b>3</b>

## 5. Conclusions

The goal of this contribution was to compare different metrics determining design of experiments suitable for construction of a meta-model. In Section 2, it was shown that the AE metric is superior to other metrics from an optimization point of view. Section 3 then examines designs optimized for one metric with respect to other metrics. The results have shown that the AE metric defines nearly orthogonal designs with very good uniformity. Also the Dopt metric provide the nearly orthogonal designs with good uniformity, but their overall quality is a little bit worse than the quality of AE designs. Finally, Section 4 presents two examples of design-based estimation of the parameter-response correlation. Also here, the AE and Dopt metrics exceed the remaining ones. We should also point out that the commonly used oLHS generated by the SPERM software can produce an estimate with non-negligible error. Nevertheless, its widespread usage is driven by its uncontested ability to quickly generate reasonably good and very complex designs and especially designs for non-uniformly distributed parameters. Unfortunately, oLHS is useless in case of discrete domains with different number of parameter levels. Hence, we focus our future work on development of an optimization algorithm capable to minimize the AE metric even for more complex designs in discrete space.

## Acknowledgement

The financial support of this work by the Czech Science Foundation (projects No. 105/11/0411 and 105/11/P370) is gratefully acknowledged.

## References

- Audze P. & Eglais V. (1977) New approach for planning out of experiments. Problems of Dynamics and Strengths, 35, pp. 104-107. Zinatne Publishing House.
- Cioppa, T.M. & Lucas, T.W. (2007) Efficient nearly orthogonal and space-filling latin hypercubes. Technometrics, 49, 1, pp. 45-55.
- Hofwing, M. & Strömberg, N. (2010) D-optimality of non-regular design spaces by using a Bayesian modification and a hybrid method. Structural and Multidisciplinary Optimization, 42, 1, pp. 73–88.
- Iman, R.L. & Conover, W.J. (1980) Small sample sensitivity analysis techniques for computer models, with an application to risk assessment, Communications in Statistics, Part A. Theory and Methods, 17, pp.1749-1842.
- Johnson, M., Moore, L. & Ylvisaker, D. (1990) Minimax and maximin distance designs. Journal of Statistical Planning and Inference, 26, 2, pp. 131-148.
- Novák, J. (www) Generator of optimal LHS designs SPERM 2.0, www: [http://www.cideas.cz/ke\\_stazeni/sperm/index.htm](http://www.cideas.cz/ke_stazeni/sperm/index.htm).
- Shewry, M.C. & Wynn, H.P. (1987) Maximum entropy sampling. Journal of Applied Statistics, 14, 2, pp. 165-170.
- Simpson, T.W., Poplinski, J.D., Koch, P.N. & Allen, J.K. (2001) Metamodels for Computer-based Engineering Design: Survey and recommendations. Engineering with Computers, 17, 2, pp. 129-150.

## THE COMPLEMENT TO TUBE-SYSTEM DESIGN

F. Jirouš<sup>\*</sup>, K. Stárek<sup>\*\*</sup>, V. Kupsa<sup>\*\*</sup>

**Abstract:** It is shown that a system with counter-current in- and outflow (U-type flow) in heat exchangers can lead to an even distribution in branched systems with given high temperature. The irregularity of flow distribution in branched systems can be reduced by optimization of the feeder and header diameters. The computation formulas for the feeder and header diameters are given.

**Keywords:** Heat exchanger, U-type flow system, even flow distribution, optimization of diameters.

### 1. Optimal design of feeder and leader diameters

For the high-temperature heat exchanger is proposed a U-type flow system and optimal diameter of feeder and header looked out. The simplest form of a mechanical energy balance Bernoulli's equation for vertical feeder – Jirouš (2002), Jirouš (2010). Fig. 1, is defined

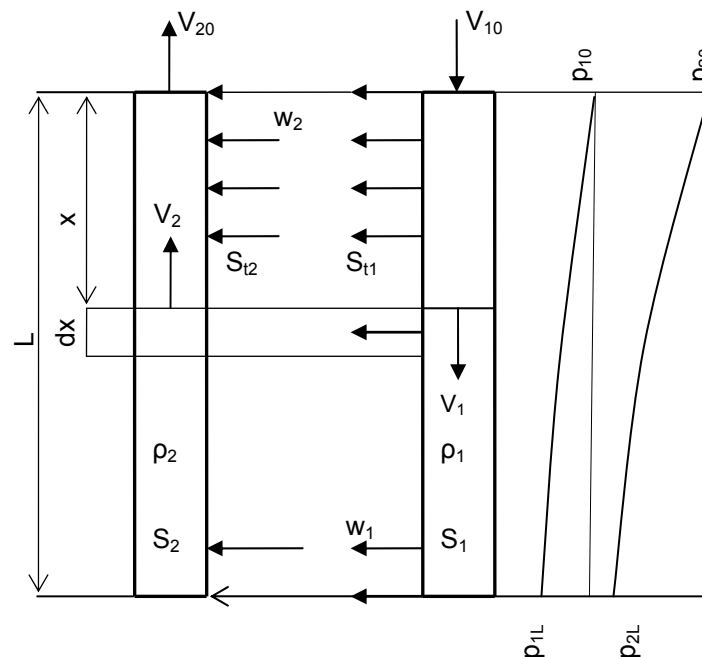


Fig. 1: U-type flow system.

$$\frac{dp_1}{dx} = -E \cdot \rho_1 \cdot V_1 \cdot \frac{dV_1}{dx} + g \cdot \rho_1 \quad (1)$$

with E factor of pressure gradient in the feeder, for vertical header:

$$\frac{dp_2}{dx} = -A \cdot \rho_2 \cdot V_2 \cdot \frac{dV_2}{dx} + g \cdot \rho_2 \quad (2)$$

<sup>\*</sup> prof. Ing. František Jirouš, DrSc.: ČVUT v Praze, Fakulta strojní, Technická 4, 166 07, Praha 6; CZ, e-mail: Frantisek.Jirous@fs.cvut.cz

<sup>\*\*</sup> Ing. Kamil Stárek, Ph.D. and Ing. Vladimír Kupsa: VÍTKOVICE POWER ENGINEERING a.s. Ruská 1142/30, 706 00, Ostrava - Vítkovice; CZ, e-mail: kamil.starek@vitkovice.cz, vladimir.kupsa@vitkovice.cz

with A factor of pressure gradient in header. Pressure difference of fluid flowing in the tube becomes:

$$p_1 - p_2 = \zeta_v \cdot \frac{\rho_1}{2} \cdot w_1^2 \quad (3)$$

The pressure difference between pressure  $p_{10}$  and pressure  $p_1(x)$  in feeder is:

$$\Delta p_1 = p_1(x) - p_{10} \quad (4)$$

Integrating (1) between points  $x = 0$  and  $x$ :

$$\Delta p_1 = E \cdot \frac{\rho_1}{2} (V_{10}^2 - V_1^2) + g \cdot \rho_1 \cdot x \quad (5)$$

The pressure difference between pressure  $p_{20}$  and pressure  $p_2(x)$  in header is:

$$\Delta p_2 = p_2(x) - p_{20} \quad (6)$$

and integrating (2) between points  $x = 0$  and  $x$ :

$$\Delta p_2 = A \cdot \frac{\rho_2}{2} (V_{20}^2 - V_2^2) + g \cdot \rho_2 \cdot x \quad (7)$$

Under conditions of

1. The pressure in feeder  $p_1 = \text{constant}$  and in header  $p_2 = \text{constant}$
2. Fluid velocities from feeder in a tube and from tube in header are constant velocity of fluid:

$$\bar{w} = \frac{m}{S_t \cdot \rho} \quad (8)$$

3. Flow cross-section of tubes  $S_t$  is replaced by a crevice with the length  $L$  and latitude:

$$b = \frac{S_t}{L} \quad (9)$$

Mass balance in feeder element yields:

$$S_1 \cdot V_1 \cdot \rho_1 - b_1 \cdot dx \cdot \bar{w}_1 \rho_1 = [S_1 \cdot V_1 + d(S_1 \cdot V_1)] \rho_1 \quad (10)$$

therefore the fluid velocity in tubes is:

$$\bar{w}_1 = -\frac{L_1}{S_{t1}} \cdot \frac{d(S_1 \cdot V_1)}{dx} \quad (11)$$

This equation shows that:

$$d(S_1 \cdot V_1) = -\frac{m}{L_1 \cdot \rho_1} dx \quad (12)$$

The integration gives:

$$S_1 \cdot V_1 = \frac{m}{\rho_1} \left( 1 - \frac{x}{L_1} \right) \quad (13)$$

if for  $x = 0$ :

$$S_1 \cdot V_1 = S_{10} \cdot V_{10} \quad (14)$$

Hence both:

$$\frac{dp_1}{dx} = \frac{dp_2}{dx} = 0 \quad (15)$$

From (1) is given:

$$V_1 \cdot dV_1 = \frac{g}{E} dx \quad (16)$$

The integration yields, if for  $x = 0$   $V_1 = V_{10}$ :

$$V_1 = \sqrt{\frac{2g}{E} \cdot x + V_{10}^2} \quad (17)$$

By substitution in equation (13) the optimal cross-section of feeder is:

$$S_{1OPT} = \frac{m}{\rho_1} \left(1 - \frac{x}{L_1}\right) \cdot \frac{1}{\sqrt{\frac{2g}{E} \cdot x + V_{10}^2}} \quad (18)$$

for horizontal feeder:

$$S_{1OPT} = \frac{m}{\rho_1 \cdot V_{10}} \left(1 - \frac{x}{L_1}\right) \quad (19)$$

Mass balance in header element yields:

$$S_2 \cdot V_2 \cdot \rho_2 = S_2 \cdot V_2 \cdot \rho_2 + d(S_2 \cdot V_2) \cdot \rho_2 + \frac{S_{t2}}{L_2} \cdot \rho_2 \cdot \bar{w}_2 dx \quad (20)$$

Analogous advancement as by feeder for the optimal cross-section of header yields:

$$S_{2OPT} = \frac{m}{\rho_2} \frac{1 - \frac{x}{L_2}}{\sqrt{\frac{2g}{A} \cdot x + V_{20}^2}} \quad (21)$$

and for horizontal header:

$$S_{2OPT} = \frac{m}{\rho_2 \cdot V_{20}} \left(1 - \frac{x}{L_2}\right) \quad (22)$$

## 2. Verification of analytical model and design calculation of distributing and collecting chamber of steam-air mixture heater

Steam-air mixture heater is a special high temperature radiation - convection heat exchanger used for heating of steam-air mixture to a temperature of about 835 °C, by flue gas of inlet temperature of about 1100 °C.

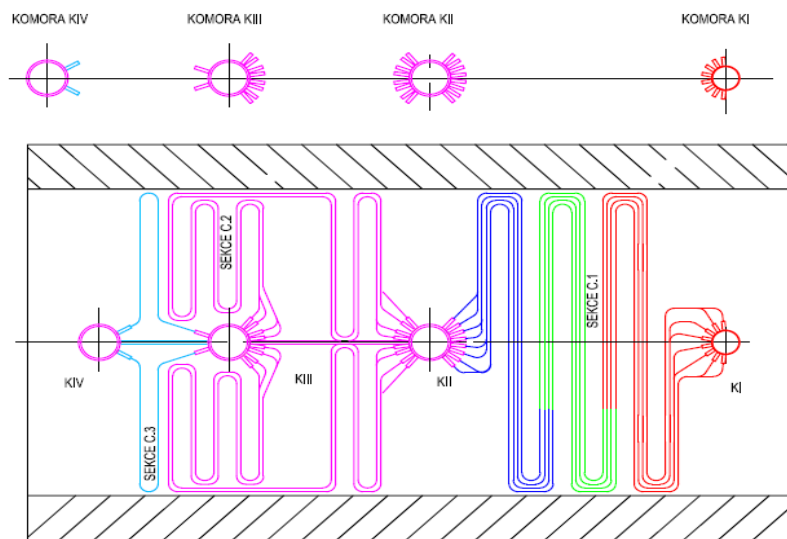


Fig. 2: Heat exchanger for heating steam – air mixture.

Due to the high temperature flue gas is necessary to ensure a high degree of hydraulic uniformity of steam-air mixture flowing in the tube system and at the same time ensuring of maximum allowable

temperature of chamber walls KIV insulated with Sibril. For this purpose, the mathematical model was created in ANSYS CFX software. First, it was done a calculation of general type of chamber KIV (Fig. 3), which served to verify of the analytical mathematical model (Fig. 4) and to determine the maximum surface temperature of the chamber wall. The results of the change process in static pressure along the chamber confirmed a high degree of congruence between the two models.

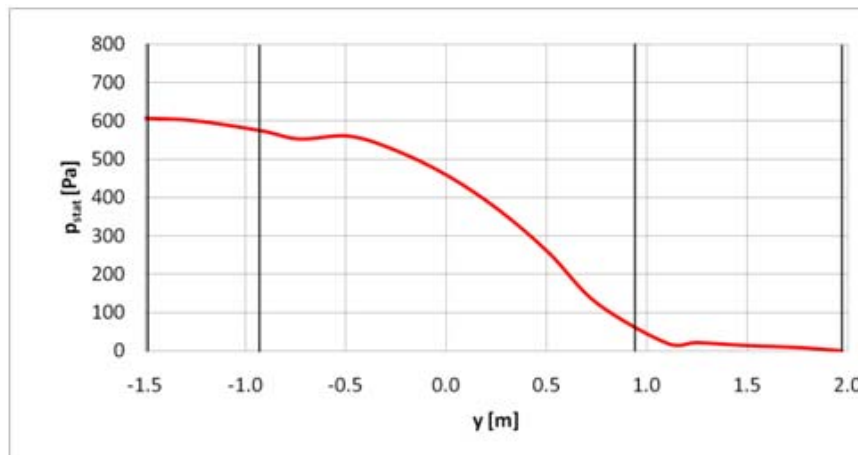


Fig. 3: Process of difference of static pressure with CFD method.

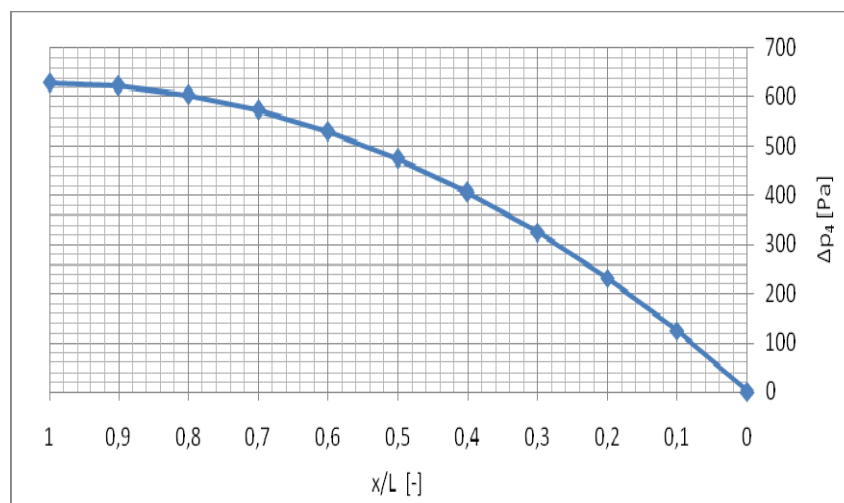


Fig. 4: Difference of static pressure of analytical calculation with A factor 2.2.

### 3. Conclusion

With regard to the observed surface temperature of the chamber it was abandoned for the general type variation and through a series of calculations using CFD methods (Computational Fluid Dynamics) it has been proposed optimal geometry of KIV chamber, which serve to modify of flowing and thus increase the heat removal from the chamber. Due to the increase in value of difference of static pressure in the length of the collecting chamber KIV compared to general type variation of chamber it was made a calculation of new section of distributing chamber KI by analytical model in order to maintain the same degree of hydraulic uniformity of flowing in the tube system as in the option of general type variation of chambers. This calculation was necessary with regard to maintaining of the same internal diameter of the chamber KIV.

### References

- Jirouš, F. (2010) Applied heat and mass transfer. CTU Press, Prague, (in Czech).
- Jirouš, F. (2002) The equations of flow distribution in header systems of steam boilers: Proc. 8th Int. Conf. on Engineering mechanics 2002. Svratka, Czech Republic 13-16 May, 2002, (in Czech).

## MICROSTRUCTURAL MODELS OF TRABECULAR BONE - COMPARISON OF CT-BASED FE MODELS

O. Jiroušek<sup>\*</sup>, P. Zlámal<sup>\*</sup>

**Abstract:** *In the article a detailed comparison of techniques used to develop detailed FE models of trabecular bone microstructure is presented. The FE models are built using a stack of microtomographic images of trabecular bone of 35 $\mu\text{m}^3$  spatial resolution. Compression test of a cylindrical sample taken from human proximal femur is virtually performed using FE models developed using different procedures. Effect of improper segmentation (deficiency/excess of bone volume), mesh smoothing, mesh density, use of hexahedral/tetrahedral elements, linear/quadratic shape functions is evaluated in a parametric study. Material model used in the study is based on results from nanoindentation. Obtained elastic properties of the sample are compared to experimental results from compression test.*

**Keywords:** *Microstructural FE model, mesh quality, segmentation, trabecular bone.*

### 1. Introduction

Precise measurement of bone quality in vivo is important for early diagnosis of osteoporosis and other bone diseases that lead to increase of fracture risk. One of the traditional and widely used methods of diagnosis of osteoporosis is DEXA (Dual-energy X-ray absorptiometry). Although DEXA is the most widely used technique for clinical bone quality measurements, the method itself has serious limitations and it has been shown to be inaccurate. DEXA is not an accurate measurement of true bone mineral density, it is rather a measurement that reflects bone area. Therefore DEXA can overestimate the bone mineral density for taller subjects and underestimate the bone mineral density of smaller subjects. Moreover, bone strength is not influenced only by the density of the tissue, but also by the spatial arrangement of the individual trabeculae and the quality of their interconnections.

It has been shown (Verhulp et al., 2008, Bourne et al., 2004) that accurate micro-FE models of trabecular bone structure are a promising technique that accounts for the spatial arrangement of trabeculae and the quality of their interconnection and can be used for precise bone quality assessment. The ability of the microstructural models to predict the overall mechanical properties is influenced by several factors, namely the tissue material model and precision of the techniques used in the process of development of the FE model. This article aims at investigation of the influence of segmentation methods, methods used to develop the micro-FE models, used finite elements, quality of the FE mesh on resulting overall mechanical properties as a measure of bone quality.

### 2. Materials and methods

The FE models were developed based on a sample of human trabecular bone scanned in a micro computed tomography ( $\mu\text{CT}$ ) scanner. A cylindrical trabecular bone specimen (5 mm diameter, 10 mm length) was drilled from a human femoral head (70 year old male) and then cleaned of marrow by washing in ultrasonic cleaner (Bandelin Sonorex Digitex, Berlin, Germany). Ends of the sample were impregnated with epoxy resin. The sample was fixed in a special micro loading devices with a frame made of a material with very low X-ray absorption. The loading device with the mounted sample was placed on a rotating table in a shielded case of  $\mu\text{CT}$  device. Tomographic scanning was performed using X-ray tungsten microfocus tube with divergent cone beam and a hybrid silicon pixel detector

---

<sup>\*</sup> assoc. prof. Ing. Ondřej Jiroušek, PhD. and Ing. Petr Zlámal: Department of Biomechanics, Institute of Theoretical and Applied Mechanics Academy of Sciences of the Czech Republic, v.v.i, Prosecká 809/76; 190 00, Prague; CZ, e-mails: {jirousek, zlamal}@itam.cas.cz



(Medipix-2). For the measurement a 80  $\mu$ A tube current and 45 kV acceleration voltage were used. Tomography of the undeformed specimen was acquired with 0.5° increments up to total 360° rotation.

After the first tomography the sample was loaded up to 4% overall strain in 0.5% increments. Between the strain increments the specimen was allowed to relax for 20 min. Applied force was measured during the whole experiment using a 100 N load cell (U9B, HBM GmbH, Darmstadt (Germany)). Every strain increment has been tomographically captured using 180 projections in 1° increments.

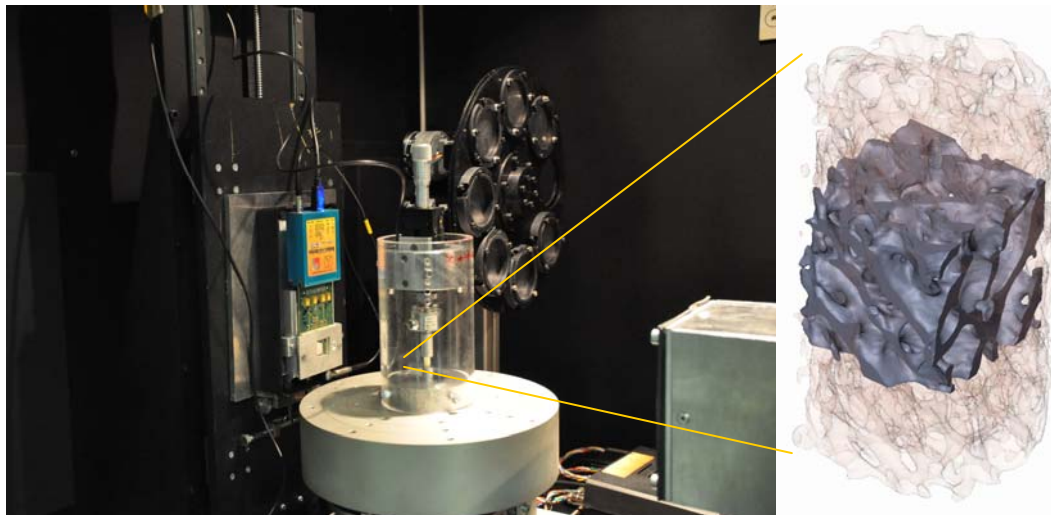


*Fig. 1: Experimental setup in the micro-CT and developed FE model of the microstructure.*

Stress-strain curve of the experiment has been developed. Stress has been calculated as the applied force divided by the full-size cross-sectional area and strain has been assessed from the displacement of the loading platens computed from the X-ray projections. From the stress-strain curve Young's modulus of elasticity in the direction of the applied load has been computed:  $E_{z,meas} = 2.102$  GPa.

## 2.1. Influence of excessive tissue segmentation

Apart from the modulus of elasticity at the tissue level, segmentation plays an important role on resulting mechanical properties of the sample. As a reference, properly segmented images (half-maximum height protocol and the automatic and adaptive iterative thresholding procedure) were taken. As improperly segmented images the binary images containing the properly segmented tissue were volumetrically grown to make the total TB/TV ratio larger. Three increments were tested to give four FE models (base, grow1, grow2, grow3). The difference in the volume of the FE models is depicted in Fig. 2.

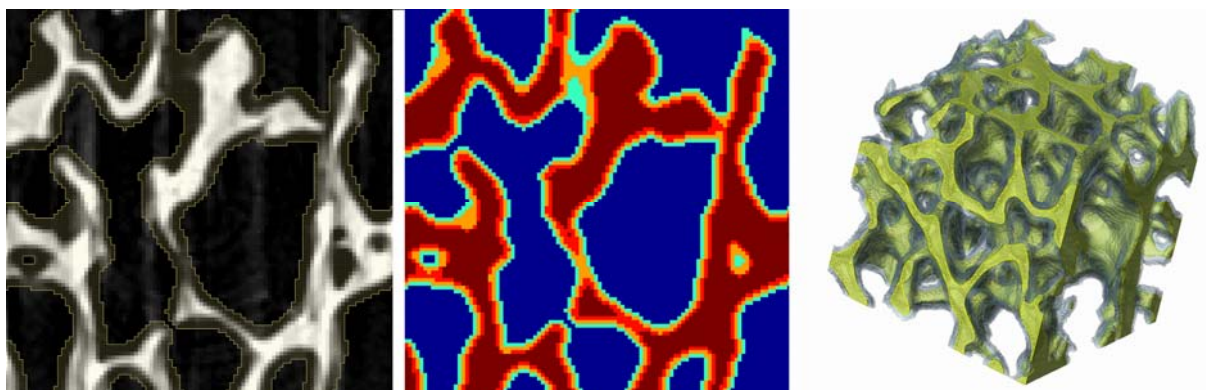


*Fig. 2: Effect of inaccurate segmentation shown in a selected micro-CT image and resulting model.*

## 2.2. Tetrahedral vs hexahedral models

The properly segmented images were taken as the base for development of all the FE models. To compare hexahedral and tetrahedral elements used to fill the volume of the sample four voxel models with different size of the voxels (1x1x1, 2x2x2, 4x4x4 and 8x8x8 pixels were used to define a single voxel) and five tetrahedral models with different density of the FE mesh (total number of nodes

65938, 83122, 150183, 222071, 321748). Apart from the linear tetrahedral elements, models discretized using quadratic tetrahedral elements were tested (total number of nodes 449853, 559125, 980689, 1510082, 2194965).

### 2.3. Small deformation vs large deformation analysis

Selected models (voxel\_1x1x1, lin\_tetra\_222071, quad\_tetra\_559125) were compared in both small deformation and large deformation analysis. Since the material properties at the tissue level were considered linear elastic, small deformation analyses were computed in one load step.

### 2.4. Comparative simulation

To assess the influence of the abovementioned parameters on the ability of the resulting FE models to predict the overall elastic material properties of the trabecular bone a virtual compression test of the micro-FE models have been carried out. Young's modulus of the trabecular bone tissue (15 GPa) was assessed previously by nanoindentation. The sample was loaded in three perpendicular directions to assess the orthotropic elastic constants. The z-direction was assumed to be the direction of loading, y-axis was in the direction of the X-ray beam and x-direction was perpendicular to the direction of the X-ray beam.

The bottom side of the specimen was fixed in all spatial directions and the upper side was prescribed a uniform displacement in z-direction. Magnitude of the applied strain was 1%. Elastic properties were calculated as the applied force (calculated as the sum of reactions at the fixed end) divided by the cross-sectional area of the sample.

Apart from the orthotropic elastic properties ( $E_x$ ,  $E_y$ ,  $E_z$ ) also the maximal values of principal stresses were compared for all the load cases.

## 3. Results

As the most appropriate model the most dense tetrahedral model with quadratic shape based on the original image data (no downsampling) was taken. The orthotropic material properties were computed using the reaction forces computed in the constrained part of the sample. Resulting Young's modulus of elasticity in the direction of applied load was computed for this reference model as  $E_{z,FEM}=1.925$  GPa (SD=.0.177 GPa). The elastic constants predicted by the voxel models were in good correspondence with the experimentally assessed value in case of the voxel model with no downsampling used. The base model underestimates the Young's modulus ( $E_{z,voxel}=1.858$  GPa, SD = 0.244 GPa). All FE models give good results for estimation of elastic properties up to 4x4x4 downsampling of the original volumetric image data.

Tab. 1: Overall material properties for selected FE models.

<i>Model name</i>	<i><math>E_x</math> [GPa]</i>	<i><math>E_y</math> [GPa]</i>	<i><math>E_z</math> [GPa]</i>	<i><math>\sigma_{1,max}</math> [MPa]</i>	<i><math>\sigma_{3,min}</math> [MPa]</i>
<i>voxel shrink</i>	<i>0.6328</i>	<i>1.286</i>	<i>1.225</i>	<i>98.657</i>	<i>-49.154</i>
<i>voxel base</i>	<i>1.063</i>	<i>1.971</i>	<b><i>1.858</i></b>	<i>76.142</i>	<i>-44.113</i>
<i>voxel grow 2x2x2</i>	<i>1.615</i>	<i>2.268</i>	<i>2.530</i>	<i>42.173</i>	<i>-39.628</i>
<i>voxel grow 4x4x4</i>	<i>1.902</i>	<i>2.840</i>	<i>3.178</i>	<i>34.123</i>	<i>-33.143</i>
<i>150183 linear tetra</i>	<i>1.160</i>	<i>2.221</i>	<i>1.911</i>	<i>118.576</i>	<i>-64.154</i>
<i>980689 quadratic tetra</i>	<i>1.167</i>	<i>2.231</i>	<i>1.813</i>	<i>125.225</i>	<i>-77.321</i>
<i>222071 linear tetra</i>	<i>1.186</i>	<i>2.267</i>	<i>1.931</i>	<i>124.341</i>	<i>-77.123</i>
<b><i>1510082_quadratic tetra</i></b>	<b><i>1.153</i></b>	<b><i>2.231</i></b>	<b><i>1.925</i></b>	<b><i>128.875</i></b>	<b><i>-79.342</i></b>

Stresses predicted by the FE models varies more significantly that the predicted elastic properties. To make the postprocessing easier to compare only the central part of the FE model was taken into account and stresses were computed at the same trabecula. Taking as the reference model again the

largest tetrahedral model with quadratic shape functions we can see that the voxel models significantly underestimate the stresses in the trabecular structure.

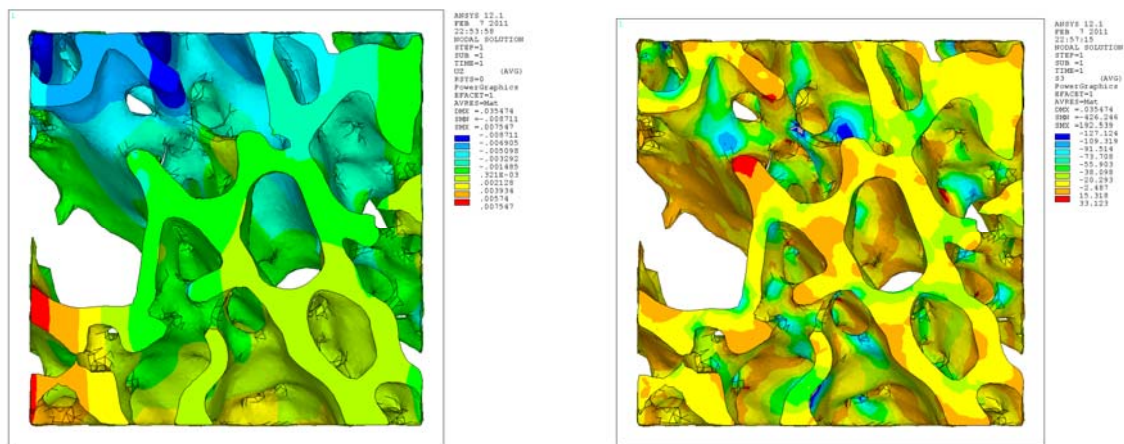


Fig. 3: Exemplary results of  $\mu$ FE analysis – linear tetrahedral model (150183 nodes) showing displacements in the vertical direction and third principal stresses in medial plane of the cubic sample.

#### 4. Conclusions

Microstructural FE models provide an excellent tool for prediction of elastic properties of trabecular bone. This study shows that effective elastic modulus of trabecular bone can be predicted using micro-FE models with tissue properties obtained from nanoindentation. Also the deformed mesh for the tetrahedral elements showed a good correspondence with the reconstructed CT scans with the same applied deformation.

As the best predictor of the deformation behavior of trabecular bone, FE models developed using tetrahedral elements with quadratic shape function should be considered. The density of the FE mesh should be evaluated first in a parametric study. The voxel models provide good results for orthotropic elastic properties, however, a great care must be paid to proper segmentation. Under or over segmentation can affect the results significantly.

On the other hand, for estimation of the elastic properties only, the models can be developed based on downsampled images. However, if stresses and strains in the microstructure are to be evaluated this downsampling is not desirable. In this case, again, the quadratic tetrahedral elements give the best results.

#### Acknowledgement

Support of the Grant Agency of the Czech Republic (grant No. P105/10/2305) as well as research plan of the Academy of Sciences of the Czech Republic AV0Z20710524 is gratefully acknowledged. This work was carried out in frame of the Medipix Collaboration and has been supported by the Project LC06041.

#### References

- Verhulp, E., van Rietbergen, B., Müller, R., Huiskes R. (2008) Indirect determination of trabecular bone effective tissue failure properties using micro-finite element simulations, *Journal of Biomechanics*, 41(7), pp.1479-1485.
- Bourne, B.C., van der Meulen, M.C.H. (2004) Finite element models predict cancellous apparent modulus when tissue modulus is scaled from specimen CT-attenuation, *Journal of Biomechanics*, 37(5) pp. 613-621.
- Medipix collaboration at: <http://medipix.web.cern.ch/MEDIPIX>.

## **XRK 2-180 STRAIGHTENING MACHINE MODERNIZATION**

**J. Jonáš<sup>\*</sup>, Z. Pokorný<sup>\*</sup>, F. Ficek<sup>\*\*</sup>**

**Abstract:** *The manufacturing program of ZDAS, a.s. includes the straightening machine of XRK type. The XRK 2-180 straightening machine is an energy-intensive one. Within the framework of the innovation of this type of the straightening machine we have made its new design so as to improve the machine parameters, to reduce the prices and the energy-demand factor. The designed straightening machine XRK 2-180 was computer-simulated and checked for strength using the program MSC.MARC. The features of the innovated straightening machine are as follows: increase of speed by 20%, reduction of the energy-demand factor by 27.3%, reduction of weight by 7.4%, decrease in cost by 8.6%, and the average improvement by 11.2% as to the parameters of the range of products to be straightened.*

**Keywords:** *Straightening machines, two-roll oblique straightening machine, production costs.*

### **1. Introduction**

Straightening machines produced at ŽDAS a.s. are of roller, section and oblique type. Roll straightening machine are designed for cold or hot straightening of sheets. Section straightening machines are designed to straighten sections. Oblique straightening machines are intended for straightening of circular rods and pipes and are divided according to the number of straightening rolls, as follows: XRK 6 with two rolls, XRK 9 with nine rolls, XRK 10 having ten rolls and special-purpose ones.

The task was to create a new design of the XRK 2-180 straightening machine to meet the set parameters:

- for rounds to be straightened - maximum diameter 180 mm at yield strength of Re 1000 MPa,
- maximum straightening speed 18 m/min,
- maximum decrease in weight,
- maximum price reduction.

### **2. Machine description**

The straightening machine (Fig. 1) is an oblique two-roll one with straightening rolls mounted one over the other; both rolls are driven. In the pre-stressed frame consisting of the upper and lower crossbeams and four columns there are the other mechanisms. Fastened in the upper crossbeam is the guide for the upper work roll being adjustable in height and at an angle. Vertical adjustment is done by means of the nut and the screw which is rotated by the gearbox with electromotor. Setting at an angle is done by means of the hydraulic cylinder. The lower crossbeam comprises the guide-way for the lower work roll which is hydraulically spring-loaded and set to an angle by means of hydraulic cylinder. To guide bars between the work rolls, the guide-gibs are provided there. Each work roll has its own drive fastened to the foundation frame into concrete. The drive consists of the electric motor, coupling, gearbox and propeller shaft.

---

<sup>\*</sup> Ing. Jiří Jonáš, Ing. Zdeněk Pokorný: advance designer – „Rolling mill equipment“: ŽDAS, a.s., Strojírenská 6, 591 01 Žďár nad Sázavou; e-mails: jiri.jonas@zdas.cz, zdenek.pokorny@zdas.cz

<sup>\*\*</sup> Ing. František Ficek: advance designer - „Technical calculations“: ŽDAS, a.s., Strojírenská 6, 591 01 Žďár nad Sázavou.; e-mail: frantisek.ficek@zdas.cz

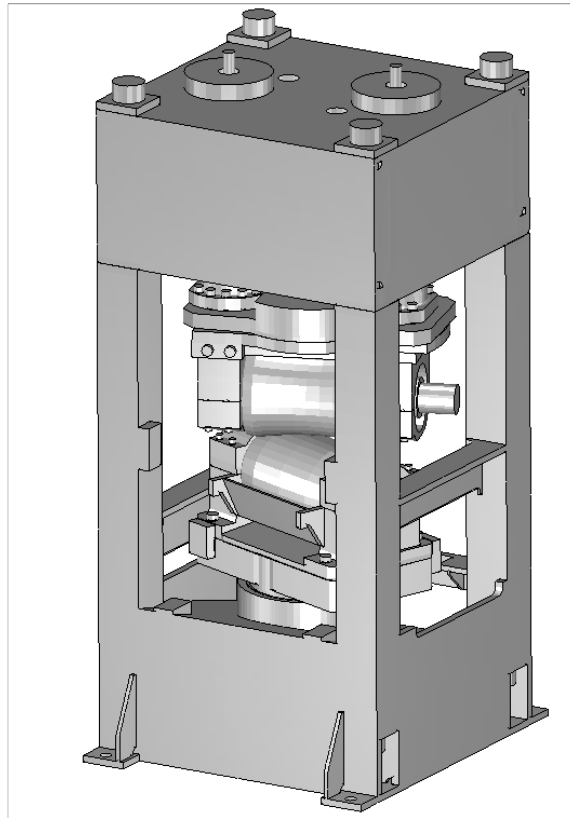


*Fig. 1: Machine description.*

## **2.1. New straightening machine design**

When designing the construction of the XRK 2-180 straightening machine we came out mainly from the construction of series of newer straightening machines (Fig. 2) ranging from the size XRK 2-80 up to XRK 2-150, and from energy-force calculations acc. to the required parameters. We also solved the production technology with respect to the cost.

The work roll diameter was determined, according to the calculation, to be 680 mm for the lower roll and 630 mm for the upper roll. The work-roll diameters of the XRK 2-180 straightening machine from the year 1979 were 730 mm for the lower roll and 670 mm for the upper roll. According to the calculation, the work-roll body length has been determined to be 960 mm. The work roll body length of the XRK 2-180 from the year 1979 was 1350 mm. A shorter length of the work roll body will positively affect the width and weight of the straightening machine; the disadvantage, however, is a greater straightening force, which will result in greater stress of the straightening machine and increase of height of the cross-beams. The lower work roll mounting was designed for the roll diameter of 670 mm, body length of 960 mm and for double-row spherical-roller bearings 24164 determined by calculation. The upper work roll mounting was designed for the roll diameter of 630 mm, body length of 960 mm and double-row spherical-roller bearings determined by the calculation.

When designing of the lower part of the straightening machine we came out from the XRK 2-150 straightening machine frame drawing. The roll holder, which serves to hold the chock and rotates in the slide bearings mounted in the lower crossbeam, was designed as a casting and also as a weldment. When designing the lower crossbeam we came out from the XKR 2-150 straightening machine lower crossbeam drawing; the lower crossbeam was designed as a casting and also as a weldment.

When designing the upper part of the straightening machine we came out from the XKR 2-150 straightening machine upper adjustment drawing. The upper crossbeam was designed as a casting and as a weldment, too. Further, we also designed columns, anchors and nuts.

Critical parts were designed as castings and weldments. We compared both variants and chosen the preferable one.



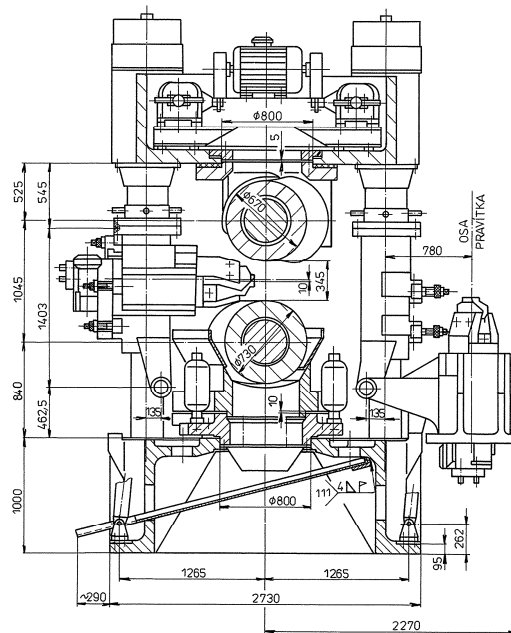
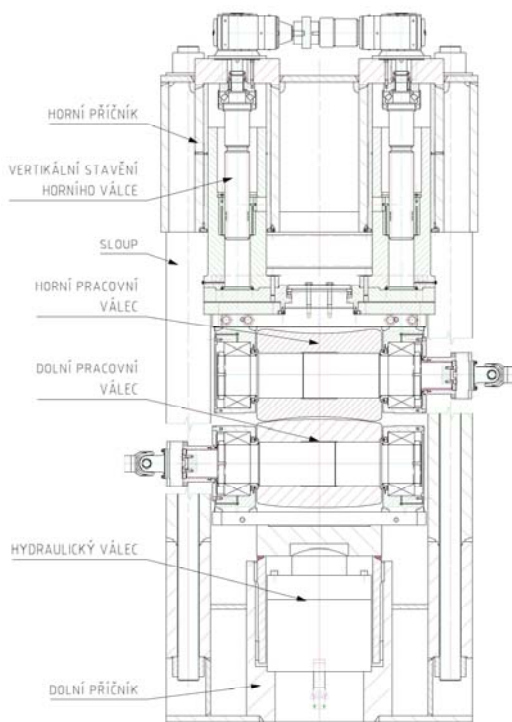


*Fig. 2: New straightening machine design.*

*Fig. 3: Old straightening machine design.*

## 2.2. Old straightening machine design

This is an oblique two-roll straightening machine having rolls mounted one over the other (Fig. 3). Both rolls are driven. The frame is the structural part of the machine. The main part is the lower crossbeam in which four columns are mounted and secured by nuts. Swing-mounted in the centre of the lower crossbeam is the support plate on which the lower-roll chock is fit. This chock is supported on four hydraulic jacks. The upper crossbeam transmits the straightening force onto columns with lower crossbeam and it moves using a nut and a worm gear along columns of the frame. The upper-roll chock is centered on the upper crossbeam, mounted via the carrier ring using four bolts and balanced by Belleville springs. To guide the rods between the work rolls, the guide-gib mechanism is used. Each work roll has its self-contained drive attached to a foundation frame embedded in concrete. The drive consists of the electric motor, coupling, gearbox and propeller shaft.

### 2.3. Straightening machine load

This design model was created by František Fícek using the program MSC. MARC. To load the work rolls of the model, the straightening force  $F_r = 7301.1$  kN was applied (Fig. 3). To load the frame, the straightening forces were applied, which act on the guide gibs while the bar passes through the straightening machine. The mechanism of the guide gibs was not designed for the time being. The frame of the straightening machine was loaded at the expected point of clamping of the guide-gib mechanism.

The comparison of parameters of XRK 2-180 straightening machines is shown in Tab. 1.

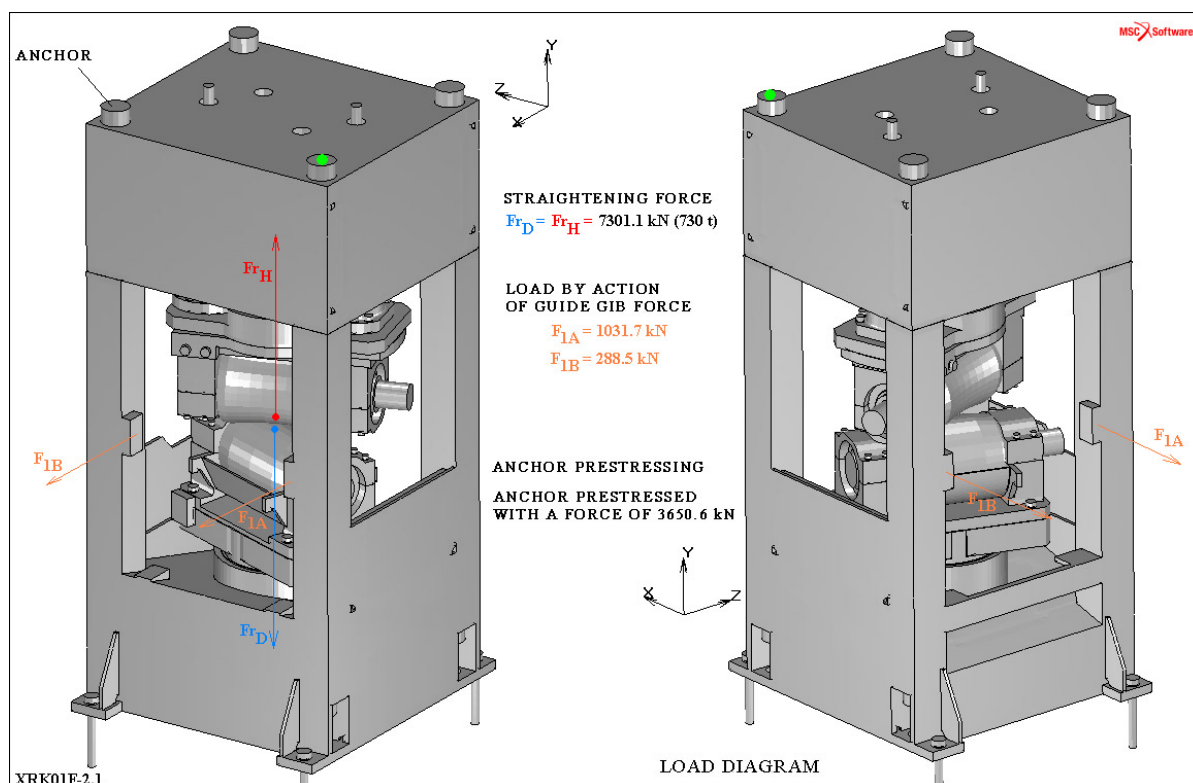


Fig. 4: Straightening machine load.

Tab. 1: Comparison of straightening machine parameters.

	Straight ening speed [m/min]	Maximal diameter [mm] up to Re				Drive motor input [kW]	Straight. machine weight [kg]	Prod. costs [mil. CZK]
		Re=1000 MPa	Re=900 MPa	Re=800 MPa	Re=600 MPa			
Old straightening machine	7.5 and 15	165	175	180	190	220	95109.1	19.637
New straightening machine	5÷18	180	190	200	220	160	88063.6	17.941
Difference [%]	+20	+9.1	+8.6	+11.1	+15.8	-27.3	-7.4	-8.6

### 3. Conclusion

As regards the XRK 2-180 straightening machine designed in this way, we have managed to achieve a decrease in cost by 8.6% and a reduction of weight by 7.4% compared to the straightening machine from the year 1979.

Main features of the designed straightening machine:

- decrease in speed by 20%,
- for rounds to be straightened, increase of maximum diameter by 11.2%,
- reduction of energy demands by 27.3%.

### Reference

Ficek, F. (2009) Supplement 1., ŽDAS a.s.



## **SIMULATION OF FATIGUE CRACK PROPAGATION UNDER CONTACT LOADING CONDITIONS**

**J. Jurenka<sup>\*</sup>, M. Španiel<sup>\*</sup>, J. Kuželka<sup>\*</sup>**

**Abstract:** *The article is a contribution to numerical simulations of pitting arise phenomena on the gear teeth. The basic assumption of the presented simulations was that pitting (pits) is a result of fatigue crack propagation under (rolling) contact loading conditions. The solution approach consisted of numerical simulations of fatigue cracks growth in the FEM framework and a comparison of numerical and experimental results. An acceptable agreement of the numerical and experimental results confirms (not proves) that fatigue crack propagation can present a true damage mechanism of the pitting wear rise. A theoretical basis of the presented simulations is an approximation of fatigue crack growth description by the so called Paris law in conjunction with FEA of crack tip loading conditions and fracture criteria evaluation. This allows, at the given crack geometry and loading amplitude in each simulated loading cycle, to estimate the crack growth rate and extension increment direction, and to model its increment by which the crack was lengthened in the following simulation. The simulations were performed under the ABAQUS CAE FEM programme which enables to create in-house codes using the Python scripting language and which is the basis of all FEA including the simulation of the crack growth.*

**Keywords:** *Gears, pitting, FEM simulation, crack propagation.*

### **1. Introduction**

Pitting phenomena belong to a contact fatigue problem area, which rise under rolling contact conditions especially. The published approaches to the numerical simulation of pitting damage rise process can be divided into two main domains. The basic assumption of the first group is that a pressured fluid lubricant penetrates into cracks and influences its growth. This approach can be represented e.g. by Fajdiga et al. (2004), who simulate fatigue crack growth from a surface initial crack and contact loading approximated by pressure distribution corresponding to the EHD lubrication theory. In the second group of approaches other possible damage mechanisms of pitting rise are assumed. E.g. Ding et al. (2003) simulate pitting rise from subsurface initial cracks.

The presented article belongs to the first group of the above mentioned approaches. The fatigue crack growth is simulated from the surface initial crack. The contact conditions between real gear teeth near the pitting crack mouth were computed and the pressured fluid lubricant penetration into pitting crack was assumed.

### **2. Applied phenomenological crack growth theories**

Validity of the small scale yielding conditions is the basic assumption of the presented crack growth simulations. The phenomenological theory of fatigue crack propagation – the Paris law – applied in this work supposes that the initial cracks are so long that all parts could be modelled as an isotropic continuum and a dimension of crack tip plastic zone is negligible compared to the crack length.

The crack growth predictions were based on the computation and evaluation of fracture mechanics J-integral criterion. J-integral was used for both calculating fatigue crack growth rate according to the Paris law (1), where  $C$  and  $m$  are material parameters and  $\Delta J$  is a J-integral amplitude, and evaluating the fatigue crack growth direction, which corresponds to the direction in which the maximum of the J-

---

<sup>\*</sup> Ing. Josef Jurenka, assoc. prof. Miroslav Španiel, CSc. and Ing. Jiří Kuželka: CTU in Prague, Technická 4; 166 07, Prague 6; CZ, e-mails: josef.jurenka@fs.cvut.cz, miroslav.spaniel@fs.cvut.cz, jiri.kuzelka@fs.cvut.cz

integral value was calculated. This criterion is equivalent to the maximal tangential stress criterion in terms of linear elastic fracture mechanics conditions.

$$\frac{da}{dN} = C(\Delta J)^m \quad (1)$$

### 3. Experimental works

Experimental works were performed at two levels. Firstly, simple so called CT test specimens were employed to provide data for validation of the crack growth prediction models. Secondly, a setup of gearing testing machine was debugged and fatigue tests of the real gearing were carried out.

#### 3.1. CT specimens testing

The main goal of the CT specimens testing was both the Paris law parameters identification used for the crack growth rate prediction and verification of the implemented approach to crack growth direction prediction (maximum of J-integral) according to observing the crack growth under mixed mode loading conditions (Španiel et al., 2008). The CT specimens were manufactured from the 18CrNiMo7-6 material, which is normally used for gears and shafts. After heat finishing, the following characteristics of the material can be mentioned: Young's modulus 210 000 MPa, yield stress 1100 MPa, strength 1250 MPa. The estimated Paris law parameters are the following:  $C = 1.42e-5 \text{ mm}/[\text{cycle} \cdot (\text{N} \cdot \text{mm})^{1.3}]$  and  $m = 1.3$ .

#### 3.2. Gearing testing

The main goal of the gearing testing was to obtain experimental data for subsequent verification of the numerical model of the fatigue crack growth under contact loading conditions. Verification criteria of numerical models were both the geometrical parameters of pits and the assessment of the number of the loading cycles, which are necessary for the pits rise. Parameters of tested gearing are listed in Tab. 1.

Tab. 1: Basic geometrical parameters of the tested gearing.

Geometrical parameters of tested gearing		
Gearing ratio	$i_{\text{mp}}$	3.2
Modulus	$m$	5 mm
Axis distance	$a_w$	160 mm
	Pinion	Gear
Teeth number	15	48
Gear thickness	17 mm	12 mm
Loading time/loading cycles	68 hours/5.9e6 cycles	
Torque moment	400 Nm	

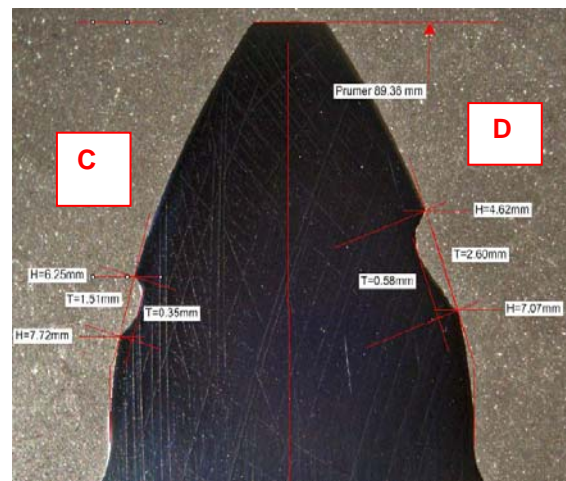


Fig. 1: Pits location (pitting).

In order to perform the gearing tests in real time, a short testing mode was chosen. The experimental test stand was designed as the so called Niemann's close torque chain, which normally consists of two connected gear boxes (experimental and technological). The required test torque is induced by a leverage mechanism.

The pits geometry and pitting cracks in various propagation stages were analyzed using suitable material cuts and metallographic samples of the most damaged gear teeth, Fig. 1. It can be derived from the metallographic samples that the fatigue cracks are initiated along the whole contact surface. In the tooth heel domain the cracks are initiated in the direction of the tooth head and in the tooth head domain in the direction of the tooth heel. The results of the experimental tests show that pitting cracks propagate especially in the so called one tooth contact condition area, thus the pitting damage is concentrated in this area.

## 4. Numerical simulations

The pitting rise investigation mentioned in this article is based on the simulations of the gearing contact conditions, which induce boundary conditions for subsequent fatigue crack growth computational predictions. Basic mechanical quantities defining contact conditions are: contact pressure, shear stress, relative slip range and rate. Actually these quantities could be affected by both properties of fluid lubricant used and contact surface roughness. In the FEA models the tribological relations are approximated by friction coefficient  $f$ , whose value can be in the range of 0.05 - 0.15. Simple linear isotropic material model was assumed according to the material properties.

According to both published works and own experiences the penetration of pressured fluid lubricant into pitting cracks should be considered in simulations, because the pressured lubricant can cause crack opening during contact rolling around the cracked region. A simple cavity model was used to include pressured fluid lubricant penetration in the FEA models. The pressure of the lubricant closed in the crack is assumed to be equal to the actual contact pressure near the crack mouth.

### 4.1. Numerical models

Simulation programs were created using developmental interface of the commercial ABAQUS CAE FEM programme, which provides both a function for stress intensity factors, T-stress, J-integral evaluation and a Python language interface for in-house programme codes submit. FE analyses are quasistatic and planar considering plane strain conditions. The schedule of complex pitting crack growth simulation is shown in Fig. 2.

- At first the simulation of contact conditions around the future crack mouth location (pinion without initial crack) is performed to estimate the relevant contact pressure distribution.

- Subsequently the simulations of pitting crack growth are carried out. The initial crack is included in the first computational step. In the next computational steps the crack is incrementally extended by a relatively small length increment in the given direction. Each computational step consists of a contact rolling simulation around the crack region (2.1, Fig. 2), J-integral amplitude ( $\Delta J$ ), crack growth direction, the number of loading cycles calculation (2.2, Fig. 2) and the pitting crack geometry modification (2.3, Fig. 2).

Influence of the pressured fluid lubricant closed inside the crack is included in the FE models using special elements, which allow simulating charging resp. discharging of deformable cavities by incompressible fluid.

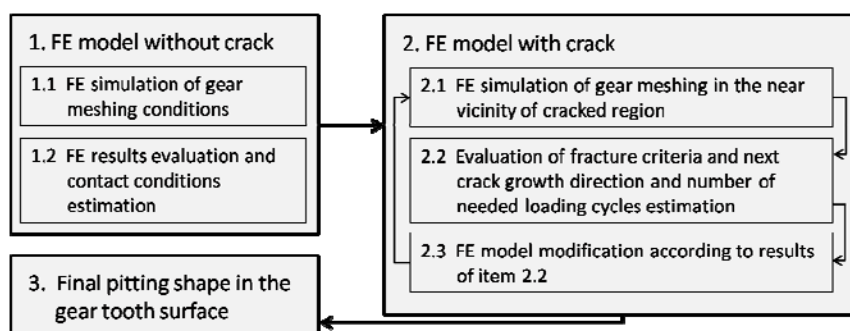


Fig. 2: Pitting crack growth simulation schedule.

### 4.2. Results

The main goal of the above mentioned simulations was the numerical model verification. A sensitivity study of the influence of the model parameters (friction coefficient, initial crack inclination to the contact surface, length of the crack increment etc.) on the pitting crack growth behaviour was performed. The FEA model of pinion with the final crack (predicted pit shape) after the crack growth simulation is shown in Fig. 3. Estimation of the number of loading cycles was based on the J-integral amplitude calculation in each simulation step. The crack length increment  $\Delta a$  was every time equal to 0.015mm. The predicted number of loading cycles required for the pit rise according to Fig. 3 is approximately equal to 740 000. Neither the first nor the last simulation step, resp. crack extension,

was included in the final number of the loading cycles. The J-integral amplitudes in these steps correspond to the initiation, resp. fracture stage of crack behavior.

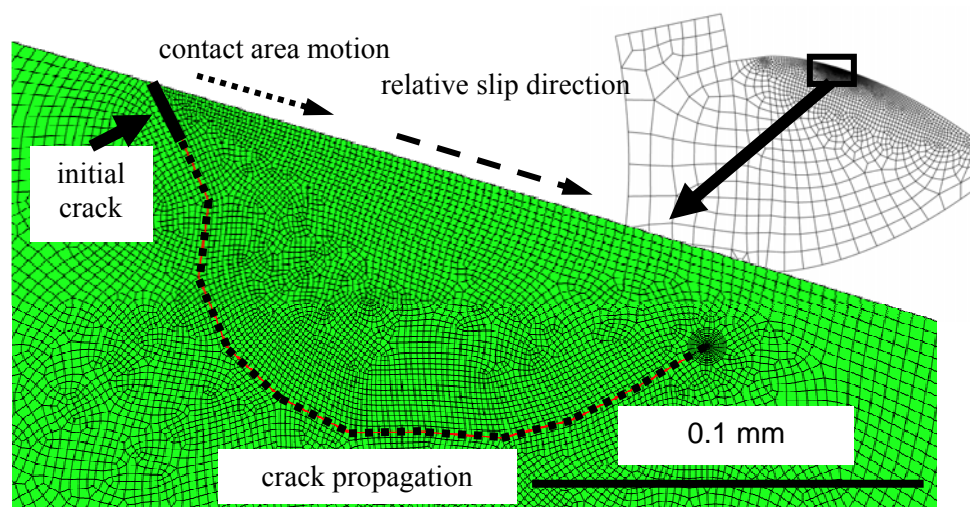


Fig. 3: Final crack resp. pit shape after simulation – pitting.

Tab. 2: Pitting rise prediction according to Fig. 3.

<i>Crack length [mm]</i>	<i>J-integral value [Nmm]</i>	<i>Number of loading cycles [-]</i>	<i>Crack length [mm]</i>	<i>J-integral value [Nmm]</i>	<i>Number of loading cycles [-]</i>
0.015 ini.	-	-	0.135	0.08093	3.71E+04
0.035	0.004179	1.75E+06	0.155	0.082998	3.59E+04
0.055	0.026429	1.59E+05	0.175	0.105771	2.62E+04
0.075	0.019907	2.30E+05	0.195	0.085879	3.43E+04
0.095	0.042368	8.60E+04	0.215	0.064731	4.96E+04
0.115	0.044134	8.16E+04	fracture	0.113319	

## 5. Conclusion

The main result of the above mentioned simulation is confirmation that the Paris law can be a relevant mathematical model to describe the pitting crack growth under rolling contact conditions. The complex parametrical FE model of real gearing was created using the Python programming language. This FE model simulates both the contact conditions of real gears including pressured fluid lubricant penetration into crack during contact rolling and the incremental crack propagation. Both the dimensions of the final pit (Fig. 3) and the predicted number of loading cycles are approximately 10x smaller than the experimental results. These differences could be caused by a simple cavity model, in which is supposed, that the fluid lubricant can flow towards and outwards the crack tip according to the actual contact pressure in the vicinity of the crack mouth. This simplified approximation will be replaced by a more sophisticated one within the future work. New cavity model will be based on the numerical simulation of the lubricant flow between teeth during gearing meshing and which will include so called lubricant closure inside the crack.

## Acknowledgement

This research was supported by the Czech Science Foundation (no.101/06/1427) and Josef Božek Research Center of Engine and Automotive Engineering.

## References

- Ding, Y., Rieber, N., F. (2003) Spalling formation mechanism for gears, *Wear* 254.
- Fajdiga, G., Flašker, J., Glodež, S. (2004) The Influence of different parameters on surface pitting of contacting mechanical elements, *Engineering Fracture Mechanics* 71.
- Španiel, M. - Jurenka, J. - Kuželka, J. (2008) Verification of FE model of fatigue crack propagation under mixed mode conditions, In: *MECCANICA*, Vol. 43, ISSN 1572-9648.

## **SHEAR STRESS ON ARBITRARY CROSS SECTION INCLUDING PLASTICITY**

**J. Kabeláč\***

**Abstract:** *In this paper a method for determination of shear stress distribution over arbitrary cross section is described. Cross section is loaded by any combination of shear and torsion. Other inner forces are not considered at this presented method. PDE are formulated for this problem, which are transformed by variational principle to the deformational variant of the finite element method. The solution of overall internal forces and stiffness characteristic of cross section including plasticity for using in a beam element model is suggested in this paper.*

**Keywords:** *Cross section, finite element method, plasticity, shear stress.*

### **1. Introduction**

The motivation for the presented work is development of beam element with material nonlinearity. At the present time, a beam element with material nonlinearity for uniaxial stress is implemented in many of commercial FEM softwares. Its formulation is simple. Cross section is divided into particular tensile fibers with plasticity conditions. This element well describes plastic properties of cross section at tension and bending, but it does not respect the effect of shear and torsion. But in case of short or twisted beam it cannot be omitted in respect to their real plasticity behavior.

Formulation of beam element is based on stress distribution over the cross section and subsequent behavior of the cross section in response to beam deformation. Only nonlinear material behavior of cross section in response to a twist and skewness is assumed and condition of free warping is supposed. Other loads components are not considered. This simplified formulation is presented in this paper.

Deformation variant of FEM is used for solution of behavior of shear stress over cross section. The arguments of this use are discussed at the end of the paper. The primary function that is investigated is cross section warping and this problem is transformed by variational methods on solution by finite element method. The method is founded on the article by Gruttmann & Wagner (2001), where cross sections plasticity capacity in torsion is discussed. This method is extended to general combination of shear loading of cross section with possibility of finding out tangential stiffness of cross section including plasticity.

### **2. Method**

For solution of shear loading of cross section the following simplifying assumptions are accepted:

- Beam is straight, prismatic and it is loaded only by shear and torsion.
- Overall rotations about y and z axis and displacement of cross section in beam axis x are zeros.
- On the basis of the assumptions 1. and 2. it can be stated that there are only shear strains  $\gamma_{xy}$ ,  $\gamma_{xz}$  and thus there is shear stress  $\tau_{xy}$ ,  $\tau_{xz}$  in the cross section. The other members of stress and strain tensors are zeros.
- Cross section warping is free.
- Deformations are small.

---

\* Ing. Jaromír Kabeláč: FEM Consulting, Veveří 331/94; 602 00, Brno, CZ, e-mail: jaromir.kabelac@seznam.cz



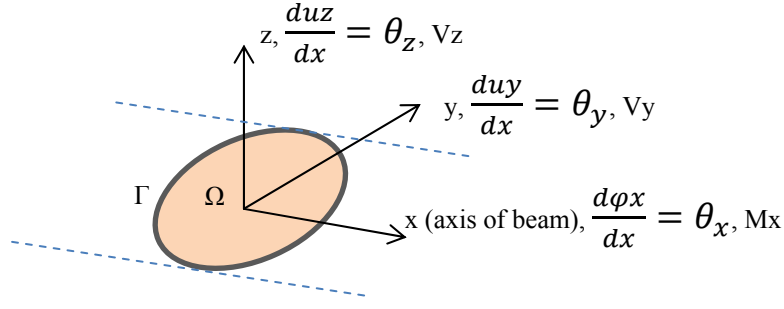


Fig. 1: Axis convention.

On the basis of the abovementioned assumptions, kinematic conditions for cross section deformation could be written as follows:

$$\begin{aligned} u_x(y, z) &= w(y, z) \\ u_y(y, z) &= \theta_z \cdot x - z \cdot \theta_x \cdot x + \Phi_y(y, z) \\ u_z(y, z) &= -\theta_y \cdot x + y \cdot \theta_x \cdot x + \Phi_z(y, z) \end{aligned} \quad (1)$$

Where  $w(y, z)$  is the primarily searched warping function and functions  $\Phi_y(y, z)$ ,  $\Phi_z(y, z)$  are the functions of transversal contraction, which are caused by a axial stress. For shear strains over cross section it is valid:

$$\boldsymbol{\gamma} = \begin{bmatrix} \gamma_{xy} \\ \gamma_{xz} \end{bmatrix} = \begin{bmatrix} \frac{\partial u_x}{\partial y} + \frac{\partial u_y}{\partial x} \\ \frac{\partial u_x}{\partial z} + \frac{\partial u_z}{\partial x} \end{bmatrix} = \begin{bmatrix} \frac{\partial w}{\partial y} + \theta_z - z \cdot \theta_x + \frac{\partial \Phi_y}{\partial x} \\ \frac{\partial w}{\partial z} - \theta_y + y \cdot \theta_x + \frac{\partial \Phi_z}{\partial x} \end{bmatrix} \quad (2)$$

Because relation between bending moment and shear force is  $dM/dx = V$ , derivations of functions  $\Phi_y(y, z)$ ,  $\Phi_z(y, z)$  for real materials will be always nonzero. The impact of this effect on shear stress distribution for linear material is discussed for example in Gruttmann, Sauer & Wagner (1999). This effect is not considered in the presented method and the following assumption is accepted:

$$\frac{\partial \Phi_y}{\partial x} = 0; \frac{\partial \Phi_z}{\partial x} = 0 \quad (3)$$

As further assumption the following constrains for overall rotation and displacement are accepted:

$$\begin{aligned} U_x &= \int_{\Omega} u_x \cdot d\Omega = 0 \\ \varphi_y &= \int_{\Omega} z \cdot u_x \cdot d\Omega = 0 \\ \varphi_z &= \int_{\Omega} -y \cdot u_x \cdot d\Omega = 0 \end{aligned} \quad (4)$$

Equilibrium equations have to be satisfied at every point of the cross section. Since external load does not have influence on the cross section, shear stresses have to be tangent to cross section boundary. In respect of assumption of the other zero elements of stress tensor the following boundary problem can be formulated.

$$\begin{aligned} \frac{\partial \tau_{xy}}{\partial y} + \frac{\partial \tau_{xz}}{\partial z} &= 0 \quad \text{on } \Omega \\ \tau_{xy} \cdot n_y + \tau_{xz} \cdot n_z &= 0 \quad \text{on } \Gamma \end{aligned} \quad (5)$$

Variational principle is used and the equation (5) is multiplied by test function and integrated across the area of the cross section  $\Omega$ : The result has to be equal to zero in respect of variational principle.

$$a(w, \delta w) = \int_{\Omega} \left( \frac{\partial \tau_{xy}}{\partial y} + \frac{\partial \tau_{xz}}{\partial z} \right) \cdot \delta w \cdot d\Omega = 0 \quad (6)$$

Equation (6) is integrated by parts.

$$a(w, \delta w) = - \int_{\Omega} \left( \tau_{xy} \cdot \frac{\partial \delta w}{\partial y} + \tau_{xz} \cdot \frac{\partial \delta w}{\partial z} \right) \cdot d\Omega + \oint_{\Gamma} (\tau_{xy} \cdot n_y + \tau_{xz} \cdot n_z) \cdot \delta w \cdot d\Gamma = 0 \quad (7)$$

From the boundary condition (5) it is obvious that the value of the line closed integral in (7) is zero and final integral equation can be written:

$$\int_{\Omega} \delta \boldsymbol{\gamma}^T \cdot \boldsymbol{\tau} \cdot d\Omega = 0 \quad \text{where} \quad \boldsymbol{\tau} = \begin{bmatrix} \tau_{xy} \\ \tau_{xz} \end{bmatrix}, \delta \boldsymbol{\gamma} = \begin{bmatrix} \frac{\partial \delta w}{\partial y} \\ \frac{\partial \delta w}{\partial z} \end{bmatrix} \quad (8)$$

According to classic formulation of finite element method, the test function is assumed equal to the base function of finite element. In the following examples linear triangle elements and isoparametric elements are used. Formation of element and methods of integration are not described here, but they can be found for example in Némec et al. (2010) or Zienkiewicz & Taylor (2005).

$$\delta \mathbf{w} = \sum_i^{elem} \mathbf{N}_i \cdot \delta \mathbf{w}_i = \left( \sum_i^{elem} \mathbf{N}_i \right) \cdot \mathbf{E} \quad (9)$$

$\mathbf{N}_i$  are base functions,  $\mathbf{E}$  is unit matrix and  $\mathbf{w}_i$  are values of warping function at a grid of the mesh. From (9) it can be written:

$$\delta \boldsymbol{\gamma} = \sum_i^{elem} \begin{bmatrix} \frac{\partial \mathbf{N}_i}{\partial y} \\ \frac{\partial \mathbf{N}_i}{\partial z} \end{bmatrix} \cdot \delta \mathbf{w}_i = \left( \sum_i^{elem} \mathbf{B}_i \right) \cdot \mathbf{E} \quad (10)$$

Shear strains on elements can be formulated on the basis of (2) :

$$\boldsymbol{\gamma}_i = \mathbf{B}_i \cdot \mathbf{w}_i + \begin{bmatrix} -\mathbf{N}_i \cdot \mathbf{z}_i & 0 & 1 \\ \mathbf{N}_i \cdot \mathbf{y}_i & -1 & 0 \end{bmatrix} \cdot \begin{bmatrix} \theta_x \\ \theta_y \\ \theta_z \end{bmatrix} = \mathbf{B}_i \cdot \mathbf{w}_i + \mathbf{G}_i \cdot \boldsymbol{\theta} \quad (11)$$

where  $\mathbf{y}_i$  and  $\mathbf{z}_i$  are coordinates of mesh grids. On the basis of this the problem (8) can be transformed into system of nonlinear equations  $\mathbf{F}$  with unknown values of warping  $\mathbf{w}_i$  at mesh grid.

$$\mathbf{F} = \sum_i^{elem} \int_{\Omega_i} \delta \boldsymbol{\gamma}^T \cdot \boldsymbol{\tau}(\boldsymbol{\gamma}_i) \cdot d\Omega_i = \sum_i^{elem} \int_{\Omega_i} \mathbf{B}_i^T \cdot \boldsymbol{\tau}(\mathbf{B}_i \cdot \mathbf{w}_i + \mathbf{G}_i \cdot \boldsymbol{\theta}) \cdot d\Omega_i = \mathbf{0} \quad (12)$$

A nonlinear relationship between shear stress and shear strain for isotropic material with HMH plastic condition is presented for example. However this is not a subject of this paper and using of the other formulations of plasticity is open and discussed for example in Chakrabarty (2006).

$$\boldsymbol{\tau}(\boldsymbol{\gamma}) = \mathbf{n} \cdot \frac{1}{\sqrt{3}} \sigma(\varepsilon) \quad \text{where} \quad \mathbf{n} = \frac{\boldsymbol{\gamma}}{\|\boldsymbol{\gamma}\|}, \quad \varepsilon = \sqrt{3} \cdot \|\boldsymbol{\gamma}\| \quad (13)$$

$$\mathbf{C}_{ij} = \frac{\partial \tau_{xi}}{\partial \gamma_{xj}} \quad (14)$$

Constraints (4) can be rewritten by using finite element formulation:

$$\int_{\Omega} \begin{bmatrix} w(y, z) \\ z \cdot w(y, z) \\ -y w(y, z) \end{bmatrix} \cdot d\Omega = \left( \sum_i^{elem} \int_{\Omega_i} \mathbf{N}_i^T \cdot [1 \quad z_i \quad -y_i] \cdot d\Omega_i \right)^T \cdot \mathbf{w}_i = \mathbf{R}^T \cdot \mathbf{w} = 0 \quad (15)$$

Newton method is used for solution of system of nonlinear equations (12). For this method it is necessary to determinate a tangent stiffness matrix:

$$\mathbf{K}_{ij} = \frac{\partial F_i}{\partial w_j} = \sum_i^{elem} \int_{\Omega_i} \mathbf{B}_i^T \cdot \mathbf{C}_i \cdot \mathbf{B}_i \cdot d\Omega_i \quad (16)$$

Final iteration method for finding of warping at mesh grid is following with respect of constraints (15):

$${}^{k+1} \mathbf{w} = {}^k \mathbf{w} + {}^k \Delta \mathbf{w} \quad (17)$$

$$\begin{bmatrix} {}^k \mathbf{K} & \mathbf{R} \\ \mathbf{R}^T & \mathbf{0} \end{bmatrix} \cdot \begin{bmatrix} {}^k \Delta \mathbf{w} \\ -{}^k \lambda \end{bmatrix} = \begin{bmatrix} {}^k \mathbf{F} \\ \mathbf{0} \end{bmatrix} \quad (18)$$

After this solution of warping function  $\mathbf{w}$  the last step remains. Resulting internal forces can be calculated in response to the deformations loading  $\boldsymbol{\theta}$ :

$$M_x = \int_{\Omega} (y \cdot \tau_{xz} - z \tau_{xy}) \cdot d\Omega; V_y = \int_{\Omega} \tau_{xy} \cdot d\Omega; V_z = \int_{\Omega} \tau_{xz} \cdot d\Omega \quad (19)$$

$$\mathbf{V} = \begin{bmatrix} M_x \\ V_y \\ V_z \end{bmatrix} = \sum_i^{elem} \int_{\Omega_i} \mathbf{G}_i^T \cdot \boldsymbol{\tau}(\mathbf{B}_i \cdot \mathbf{w}_i + \mathbf{G}_i \cdot \boldsymbol{\theta}) \cdot d\Omega_i \quad (20)$$



Tangential stiffness of cross section, which is necessary for formulation of beam element, is given by the following equation:

$$\mathbf{D}_t = \frac{\partial v_i}{\partial \theta_j} = \sum_i^{elem} \int_{\Omega_i} \mathbf{G}_i^T \cdot \mathbf{C}_i \cdot \mathbf{G}_i \cdot d\Omega_i \quad (21)$$

### 3. Example

The described method is illustrated by the following examples. Pure torsion of square cross section in plasticity state is shown in the left figure below. The color map shows intensity of shear stress and the vectors are directions of shear stress. Some combination of shear and torque of nonsymmetrical C profile is shown in the figure at the right side. This figure shows plastic strain as the color map and shear stress direction as vectors.

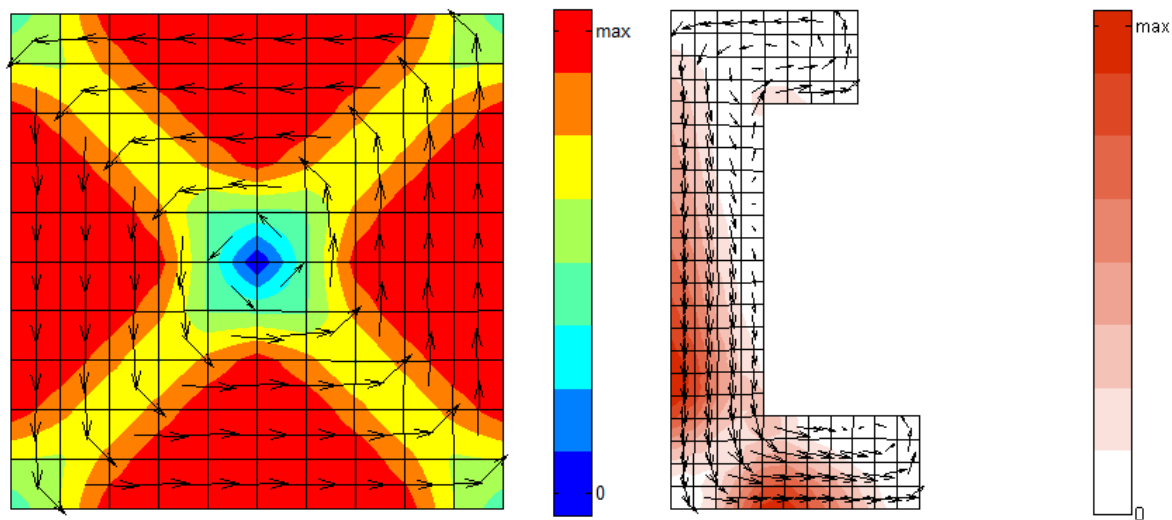


Fig. 2: Examples of solutions.

### 4. Conclusions

With regard to the use of deformation variant of the FEM it is not a problem to solve cross section with multiple internal loops without special constraints. Special conditions for the origin point of cross sections coordinate system are not required. The described method is directly applicable to simulation of plasticity free torsion. As it has already been discussed, shear does not occur without bending and due to this shear loading would be modeled with axial stress distribution. The condition of free warping is oversimplified for shear loading too. Nevertheless, this method is a contribution for formulation of a model of full plastic beam element.

### Acknowledgement

This contribution has been prepared with the financial support of the company FEM Consulting.

### References

- Chakrabarty, J. (2006) Theory of plasticity. Elsevier Butterworth-Heinemann, Oxford.
- Gruttmann, F. & Wagner, W. (2001) Finite Element Analysis of Saint-Venant Torsion Problem with Exact Integration of the Elastic-Plastic Constitutive Equations. Computer Methods in Applied Mechanics and Engineering, 190, pp. 3831-3848.
- Gruttmann, F., Sauer, M. & Wagner, W. (1999) Shear Stresses in Prismatic Beams with Arbitrary Cross-Sections. International Journal for Numerical Methods in Engineering, 45, 7, pp. 865-889.
- Němec, I. et al. (2010) Finite element analysis of structures. Shaker Verlag, Aachen.
- Zienkiewicz, O. C. & Taylor R. L. (2005) The Finite Element Method for Solid and Structural Mechanics, 6th edn. Elsevier Butterworth-Heinemann, Oxford.

## **FAILURE MECHANISM AND STRAIN FIELDS ON A CARBON/EPOXY COMPOSITE SUBJECTED TO COMPRESSION AFTER IMPACT**

**M. Kadlec\***

**Abstract:** *Polymer composite panels are widely used in aeronautic and aerospace structures due to their high strength vs. weight ratio. The objective of this study is to determine mechanisms of the failure of impacted composite laminates when subjected to compression. The other aim is to investigate using an optical strain measurement to detect impact damage in laminates subjected to loading. For this purpose a series of impact and compression after impact (CAI) tests were carried out on composites made of carbon fibre-reinforced epoxy resin matrix. First, impacted specimens were analyzed by an ultrasonic probe to assess delamination area around the impact site. Second, digital image correlation (DIC) measurement was performed to investigate the strain fields and the surface shape before and during loading. The full-field strain measurements showed a concentration band of a compressive strain near the impact where buckling occurred. The shear strain visualisation around the impact showed an area of heterogeneous deformation which was compared to the detected delamination area acquired by an ultrasonic technique. The results showed that the shear strain fields are able to identify the extension of impact damage and that the strain concentration factor can be a failure criterion to consider an ultimate load.*

**Keywords:** *Polymer composite, compression, strain field, impact damage, digital image correlation.*

### **1. Introduction**

Impact damage is serious damage mechanism in polymer composite laminates which limits its performance and reliability. It can occur during in-service or as a result of handling during manufacture. This can give rise to surface indentations and other damage below the surface such as matrix cracking, fibre breakage, delamination or disbonding. Under compressive loads, these failure mechanisms interact and compared to the undamaged state the impact-induced damage propagates to failure at significantly lower load levels (Cantwell, et al., 1986).

Paper (Freitas & Reis, 1998) described two buckling failure mechanisms (positive and negative impact site out-of-plane displacement) which are influenced more by the delamination area than by the stacking sequence. Sutherland et al. (2005) predicted the damage initiation threshold using two models, one based on the interlaminar fracture toughness of the composite and the second on the interlaminar shear strength ILSS. Yang, et al (2010) showed that the latter can successfully predict the relation of critical force to both target size and impactor geometry. The numerical results in the paper (Yan et al., 2010) denoted an extensive propagation of delamination with mode transition preceding sublaminate buckling. Initiation and propagation of matrix and fiber cracking, observed upon this buckling, is the cause of ultimate shear failure. The paper (Petit et al., 2007) presented CAI tests performed on composite laminate covered with a cork thermal shield. They investigated out-of-plane displacement field around the impacted zone by using two CCD cameras.

This paper deals with pure panels where are investigated not only the displacements, but also strains around the impacted zone by using photogrammetric system ARAMIS. The strain values before failure inside the impact zone are used for strain concentrations calculations. The second part of the results show visualizations of the shear strains in comparison with the ultrasound detected delamination areas.

---

\* Ing. Martin Kadlec: Aeronautical Research and Test Institute (VZLÚ, a.s.), Beranových 130; 199 05 Prague; CZ, e-mail: kadlec@vzlu.cz

## 2. Methods

Composite laminate specimens with dimensions 150 x 100 x 4 mm were manufactured by dry tows placement of IMA GS carbon fibres with areal weight of 140 g/m<sup>2</sup> and fibre volume of 57 %. The SDV32 resin system was introduced by injection. The lay-up configuration was [0/45/90/-45]<sub>4s</sub>.

All the 4 specimens were impacted by 16 mm diameter 5450 g mass impactor with energy 35 J. Fig. 1 shows an arrangement of an impact test including the clamp system which held the specimens. The impact machine prevented multiple hits on the specimen. Non-destructive detection of delaminations by Masterscan 340 ultrasound system with direct probe PRDT 2550, 5 Mhz was carried out after impacting and before loading. The delamination area was measured in 8 directions from the impact centre.

The antibuckling fixture (Fig. 2a) was used for loading according the AITM 1.0010 specification. The compressive loading was performed by SCHENCK 250 kN with constant displacement of 0.5 mm/min. ARAMIS HS system for full-field strain measurements is shown in Fig. 2b.

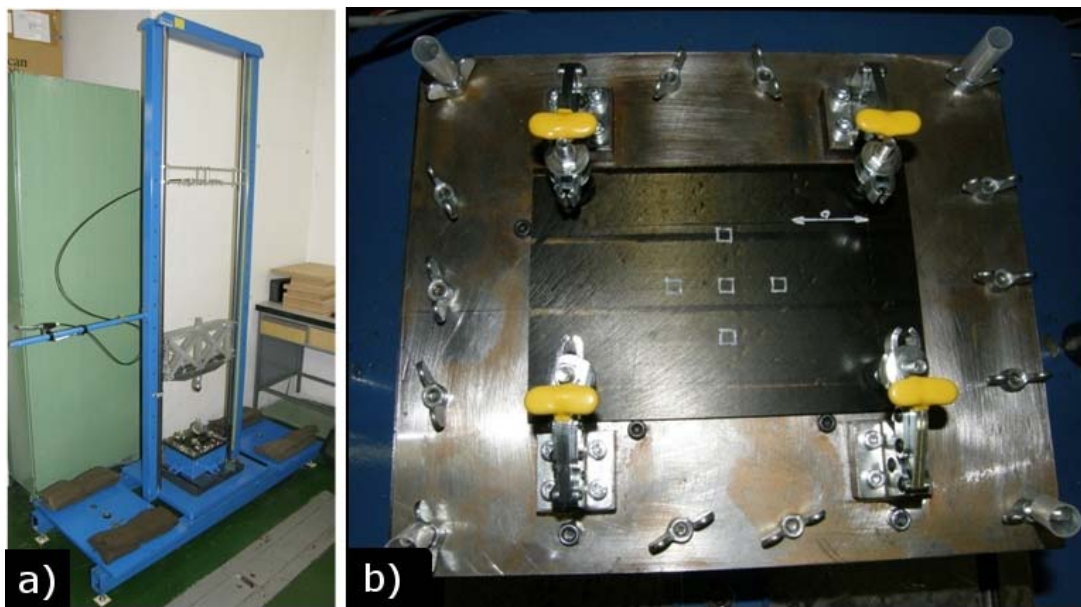


Fig. 1: a) Impact machine set up. b) Clamping device for impacting system with a specimen.

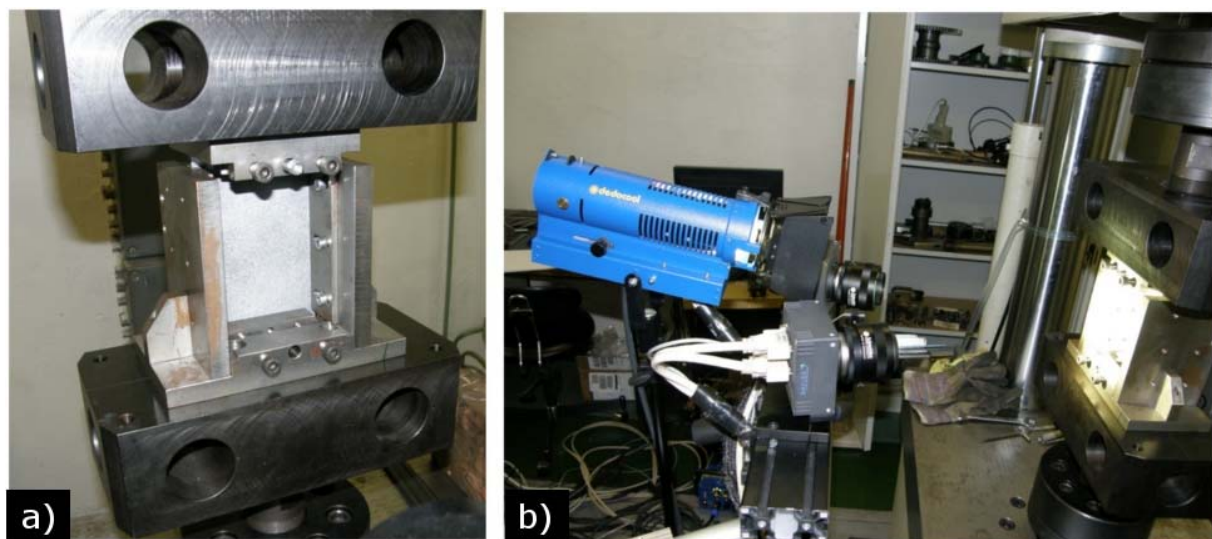


Fig. 2: a) CAI antibuckling fixture with a specimen sprayed by a black-white pattern.  
b) The ARAMIS cameras and a light aiming at a specimen.



### 3. Results

Impact dent depth and shape were measured by DIC and processed in MATLAB (Fig. 3). The mean depth value for the tested specimens was 0.29 mm.

Failure by loading was sudden without crack propagation. The fracture was observed in the plane perpendicular to the loading and passing through the impact dent where the compressive strain concentrations were dominant. The measured strain fields on specimen “A” before failure are shown in the following figures. Fig. 4a shows a field of strain in the loading direction with contraction of the impact depression and elongation of its borders. Fig. 4b represents shear strain in the specimen plane. The typical cross visualisation reveals the dent position and the affected area by the impact. Fig. 5a shows a field of von Mises strain which reveals also the cracks from impacting. Fig. 5b demonstrates the out-of-plane displacement and shows the further recessing of the dent during loading.

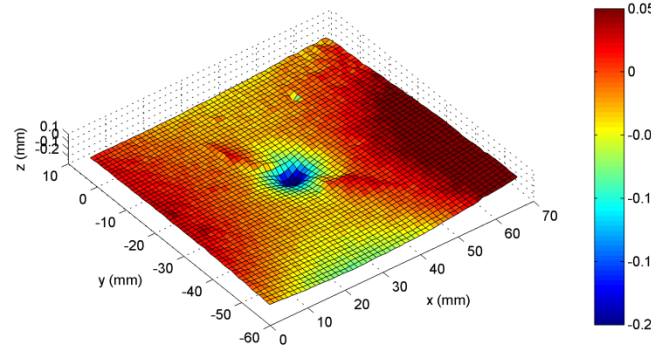


Fig. 3: The middle part of the specimen “A” surface after impact. Two diagonal cracks are visible. Z axis is 20 times scaled.

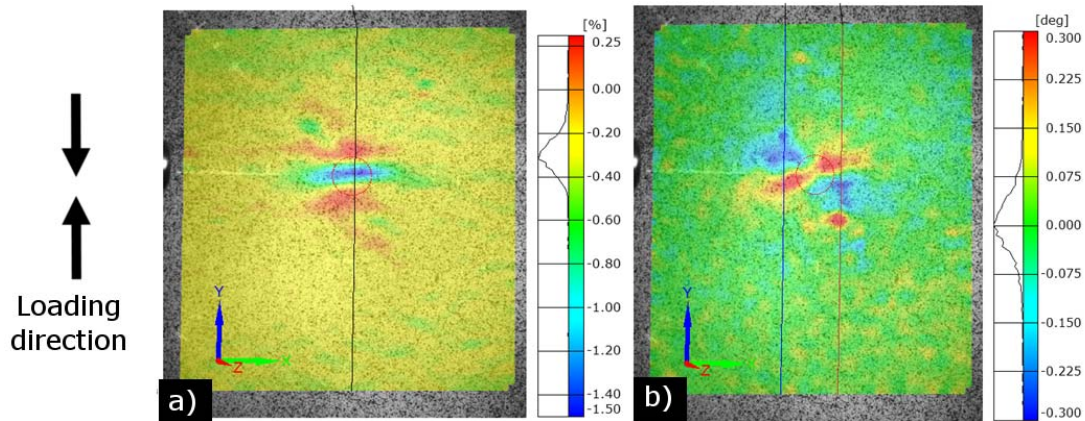


Fig. 4: a) Field of vertical strain  $\epsilon_y$  before failure. b) Field of shear angle before failure.

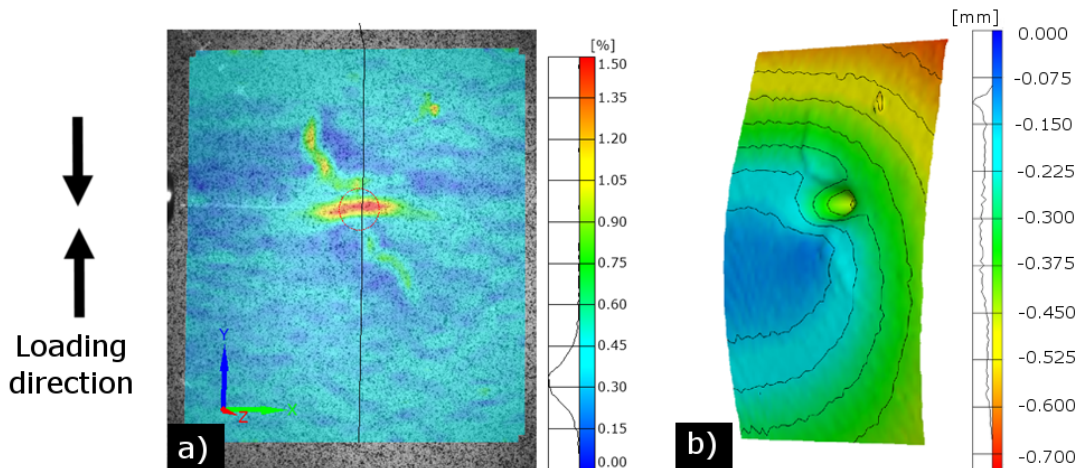


Fig. 5: a) Field of von Mises strain with visible cracks from impacting. b) Buckling visualized as out-of-plane displacement field scaled 10 times.

Compression strength  $\sigma_d$  was obtained by division of maximum force  $F_{\max}$  and specimen edge surface. Strain concentration factor was suggested as

$$\alpha_M = -\varepsilon_M/\varepsilon_A, \quad (1)$$

where  $\varepsilon_M$  is local von Mises strain at the impact centre and  $\varepsilon_A$  is averaged surface strain of the plate in the loading direction far from the impact. Both the strains were measured before failure. All the mentioned quantities are included in Tab. 1.

*Tab. 1: Strength, strain before failure and calculated strain concentration factors.*

Specimen	$F_{\max}$ (kN)	$\sigma_d$ (MPa)	$\varepsilon_A$ (%)	$\varepsilon_M$ (%)	$\alpha_M$ (1)
A	76.96	191.22	-0.30	1.95	6.5
B	78.42	193.62	-0.29	1.83	6.3
C	98.69	241.60	-0.36	2.15	6.0
D	102.38	256.32	-0.36	2.40	6.7

The shear strain visualisation was thresholded by the value of  $0.06^\circ$  to reveal the damage induced heterogeneity of the material. For comparison, the ultrasound detected delamination area border was overlaid to proof the fact, a delamination range can be detected by strain measurements (Fig. 6).

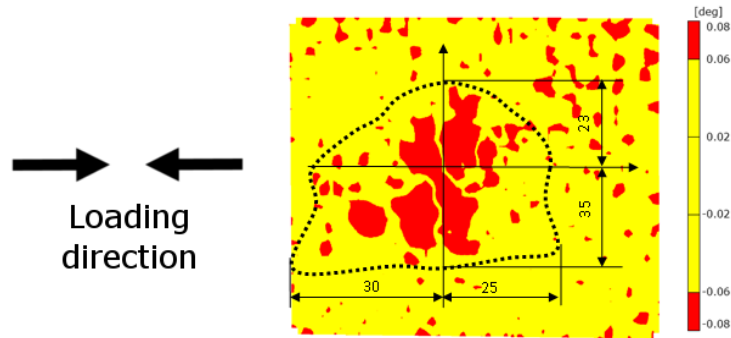


*Fig. 6: Thresholded field of shear strain with the overlaid border of ultrasound detected delamination.*

#### 4. Conclusions

The strain concentration coefficients are in a very good agreement in spite of the fact that the strengths are different which suggests it can be the failure criteria for compression after impact loading. The shear strain visualisation corresponds to a delamination extent in this composite material.

#### Acknowledgement

Financial support of grant MSM 0001066903 from the Czech Ministry of Education, Youth and Sport is gratefully acknowledged. The author also acknowledges Mr. Valerij Makarov for NDT measurements.

#### References

- Cantwell, W.J., Curtis, P. & Morton, J. (1986) An assessment of the impact performance of CFRP reinforced with high-strain carbon fibers. *Compos Sci Technol*, 25, pp.133–148.
- Freitas, M. & Reis, L. (1998) Failure mechanism on composite specimens subjected to compression after impact. *Composite Structures*, 42, pp.365–373.
- Petit, S., Bouvet, C., Bergerot, A. & Barrau, J. (2007) Impact and compression after impact experimental study of a composite laminate with a cork thermal shield. *Compos Sci Technol*, 6, pp.3286–3299.
- Sutherland L.S. & Guedes S.C. (2005) Contact indentation of marine composites. *Composite Structures*, 70, pp.287–94.
- Yan, H., Oskay, C., Krishnan, A. & Xu, L.R. (2010) Compression-after-impact response of woven fiber-reinforced composites. *Compos Sci Technol*, 70, pp.2128–2136.
- Yang, F.J. & Cantwell, W.J. (2010) Impact damage initiation in composite materials. *Compos Sci Technol*, 70, pp.336–342.

## MEASURES WHICH CAN BE USED TO PREDICT, PREVENT AND RESOLVE THE PROBLEMS OF LIVELINESS IN FOOTBRIDGES

J. Kala<sup>\*</sup>, P. Hradil<sup>\*</sup>, V. Salajka<sup>\*</sup>

**Abstract:** *There are several measures which can be used to predict, prevent and resolve the problems of liveliness in footbridges. The Frequency tuning means avoiding the critical frequency ranges for the fundamental modes. Detailed vibration response assessment is the basis of many contemporary design procedures. Measures to reduce vibration response mean (i) Restricting the use of the bridge; (ii) Increasing the damping (e.g. by adding extra damping devices such as viscous dampers or TMDs). Presented article is focused on possibilities of calculation and design of Tuned Mass Damper on light-weight footbridges.*

**Keywords:** *Footbridge, liveliness, damping devices, dynamic improvement, frequency tuning.*

### 1. Introduction

With the occurrence of the first problems related to the liveliness of footbridges, some early design recommendations, such as the one by (Walley, 1959), proposed that the fundamental vertical natural frequency of a structure below 2.7 Hz should be avoided. It is interesting to note that this corresponds to the upper limit of the range of the first walking harmonic, although at that time little was known about the actual nature of the walking force as no widely reported measurements of it existed. (Leonard, 1966) claimed that there was no need to avoid any frequency range if an appropriate damping and stiffness had been provided. For example, some footbridges are serviceable although their natural frequencies are inside the problematic ranges (Pimentel et. al., 2001) or the damping ratio is as low as 0.4% (Parker et. al., 2003). However, with modern trends towards slenderness in footbridge design, it happens that footbridges more and more frequently do not perform well in service as far as their vibration behavior is concerned. A list of examples of such problematic footbridges was compiled by (Pimentel, 1997). There are several measures which can be used to predict, prevent and resolve the problems of liveliness in footbridges (Bachmann and Amman, 1987):

- Frequency tuning: As previously mentioned, this measure means avoiding the critical frequency ranges for the fundamental modes. For vertical mode these are the frequencies of the first (1.6–2.4 Hz) and, for bridges with low damping, the second walking harmonic (3.5–4.5 Hz). Although (Bachmann and Amman, 1987) proposed the same provision for the lateral modes (namely, 0.8–1.2 Hz for the first and possibly 1.6–2.4 Hz for the second harmonic), it should be added that lower frequencies could be excited too, according to observations made on the Millennium Bridge, London where the frequency of the lowest mode excited was only 0.5 Hz (Dallard et. al., 2001). For the longitudinal direction, the first subharmonic and the first harmonic, with frequencies 0.8–1.2 Hz and 1.6–2.4 Hz, respectively, should be avoided. Excessive vibrations in this direction are very rare, but one case was reported by (Bachmann and Amman, 1987). It should be stressed that the designer can influence frequencies of the footbridge by choosing an appropriate layout of the structure (Pimentel, 1997) and by studying different options for distributing its stiffness and mass.

Structural frequency can, for example, be changed by stiffening the structure (installing stiffer handrails or adding tie-down cables); (Tilly et al., 1984) found that footbridges with stiffness in the middle of the main span which is lower than 8 kN/mm are likely to be prone to vibrations in the vertical direction.

---

<sup>\*</sup> assoc. prof. Ing. Jiří Kala, Ph.D., Ing. Petr Hradil, Ph.D. and assoc. prof. Ing. Vlastislav Salajka, CSc.: Institute of Structural Mechanics, Brno University of Technology, Veveří 95, 602 00, Brno, CZ, e-mails: kala.j@fce.vutbr.cz, hradil.p@fce.vutbr.cz, salajka.v@fce.vutbr.cz

- Detailed vibration response assessment: This is a measure which is the basis of many contemporary design procedures. However, it is underpinned by many uncertain modeling assumptions and its reliability is often questionable.
- Measures to reduce vibration response: These measures are:
  - Restricting the use of the bridge (for example, ban marching over the bridge);
  - Increasing the damping (e.g. by adding extra damping devices such as viscous dampers or TMDs).

It can be added here that warning and/or educating people to expect vibrations can help them to tolerate higher vibration levels than they would without an explanation that their safety is not in question. This is not surprising as safety is the main concern of the bridge users in case of excessive vibrations (Zivanovic et. al., 2005).

## **2. Improvement of dynamic behaviour**

The dynamic calculation described in next chapter exposed structure response over the comfort criteria limits given by (Eurocode 5, 2004). It wasn't possible to modify natural frequencies and moved them so that they are outside the resonance risk ranges in relation to excitation by the pedestrians, then attempts should be made to increase structural damping.

With an existing footbridge, it is also possible to try to modify its natural frequency vibrations. However, experience shows that it is generally cheaper to increase damping. Modification of vibration natural frequencies - a vibration natural frequency is always proportional to the square root of the stiffness and inversely proportional to the square root of the mass. The general aim is to try to increase vibration frequency. Therefore the stiffness of the structure needs to be increased. However, practice indicates that an increase in stiffness is frequently accompanied by an increase in mass, which produces an inverse result; this is a difficult problem to solve.

## **3. Increasing structural damping**

### **3.1. Natural structural damping of the structures**

The critical damping ratio is not an inherent fact of a material. Most experimental results suggest that dissipation forces are to all practical intents and purposes independent of frequency but rather depend on movement amplitude. The critical damping ratio also increases when vibration amplitude increases. It also depends on construction details that may dissipate energy to a greater or lesser extent (for instance, where steel is concerned, the difference between bolting and welding).

### **3.2. Damper implementation**

The use of dampers is another effective solution for reducing vibrations. Appendix 3 (SETRA, 2006) describes the different types of dampers that can be used and describes the operating and dimensioning principle of a selection of dampers. As a last resort, if the previous solutions do not work, damping systems can be installed, which will most usually be tuned mass dampers (these are the easiest to install: to work properly, viscous dampers often require the construction of complex devices to recreate major differential movement). A tuned mass damper consists of a mass connected to the construction using a spring, with a damper positioned in parallel. This device allows the vibrations in a construction to be reduced by a large amount in a given vibration mode, under the action of a periodic excitation of a frequency close to the natural frequency of this vibration mode of the construction. This shall only be considered as a last resort, as, despite the apparently attractive character of these solutions (substantial increase in damping at low cost), there are disadvantages. If tuned mass dampers are used, this is the most typical case:

- As many dampers are needed as there are frequencies of risk. For complex footbridges, which have many modes (bending, torsion, vertical, transversal, longitudinal modes, etc.) of risk, it may be very onerous to implement;



- The damper must be set (within about 2 - 3%) at a frequency of the construction that changes over time (deferred phenomena) or according to the number of pedestrians (modification of the mass). The reduction in effectiveness is appreciable;
- The addition of a damper degenerates, and thus doubles, the natural frequency under consideration: this complicates the overall dynamic behavior, and also the measurement of the natural frequencies;
- Even though manufacturers claim that dampers have a very long life-span, they do need a minimum level of routine maintenance: Owners must be made aware of this;
- Because of the added weight (approximately 3 to 5% of the modal mass of the mode under consideration), this solution will only work on an existing footbridge if it has sufficient spare design capacity. On a proposed footbridge, the designer may need to resize the construction;
- Preferably, 3% of guaranteed damping will be achieved: on very lightweight constructions (for which the ratio of the exciting force divided by the mass is high), it may not be sufficient. The Fig. 1 shows the lowering of amplitude response by increasing of damper relative mass. Frequency range (between peaks) where the damper is effective with increasing mass ratio is wider. Fig. 2 shows TMD – structure frequency ration influence on response.

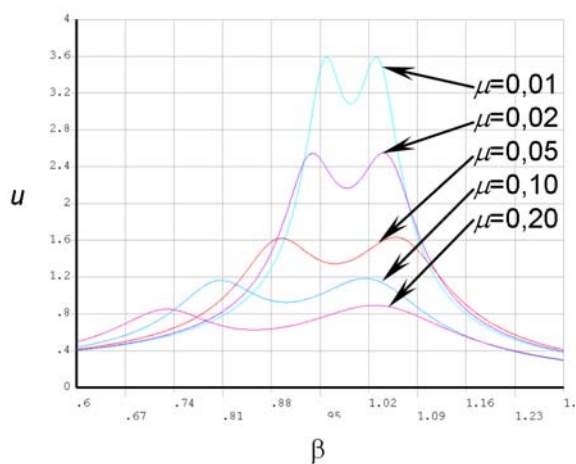


Fig. 1: Damper mass ratio influence.

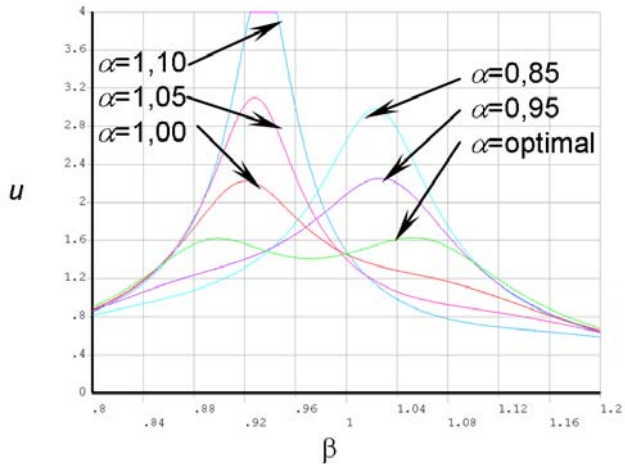


Fig. 2: Frequency ratio influence.

An important part of the computational bridge model assembly was the design of parameters for TMD. The vibration is provoked by the movement of a pedestrian on the bridge. The design of parameters consisted in the determination of the optimum damper position, mass, stiffness and damping force so that a maximum vertical vibration reduction was reached after the damper was placed into the bridge structure (Kala J. et. al., 2010b).

The first step for the design of damper parameters is the determination of its mass. TMD mass was determined as 1500 kg which approximately corresponds to 1/30 of moving structure mass in vertical direction. Subsequently, natural frequency and TMD damping ratio value were determined. In case study four variants of tuning TMD to minimize (a) displacement of empty and crowded structure, (b) acceleration of empty and crowded structure were analyzed (Kala J. et. al., 2010a).

#### 4. Conclusion

Footbridges with well-separated modes which have vibration serviceability problem respond mainly in one mode of vibration which is lightly damped. This means that, by using appropriate modal mass and stiffness, the excited mode can be represented as a SDOF system and the optimum TMD. In that case the parameter  $m$  becomes ratio of the absorber mass and modal (generalized) mass of the SDOF system. For a simple beam structure, the assumption that the relevant pedestrian harmonic does not move produces only small differences in the tuning parameters in comparison with a moving force. The effectiveness of the absorber is nevertheless lesser for the moving force case.

Generally, an optimization of absorber parameters (stiffness and damping) could be done for different types of excitation and considering different response parameters. A lot of work has been devoted to

this issue. Analyzed an undamped SDOF system under harmonic excitation but optimized response against displacement, velocity and acceleration of the main mass, and also against the force transmitted to the base. He also did optimization analysis for white noise excitation and harmonic base acceleration. They also pointed out the possibility to control the response in more than one structural mode by installation one TMD for each mode considered. Several TMDs can also be used for controlling SDOF system response due to wide-band random excitation.

In the case of footbridges, a single TMD for a dominant mode is usually considered. It is most effective to put the TMD at the point with maximum structural response that is at the antinode. This is a problem that has a lot of uncertain input factors. The effect of the influence of parameters on the mass and stiffness can be studied by methods of sensitivity analysis (Kala Z., 2009). Advanced is a method of global sensitivity analysis that allows us to analyze the higher order interaction effects (Kala Z., 2011).

## Acknowledgement

The article was elaborated within the framework of research project GACzR 104/11/0703, GACzR 103/09/1258 and project MSM0021630519.

## References

- Bachmann, H., Ammann, W. (1987) *Vibrations in Structures—Induced by Man and Machines*, Structural Engineering Documents, Vol. 3e, International Association of Bridge and Structural Engineering (IABSE), Zurich.
- Dallard, P., Fitzpatrick, A., Flint, A., Le Bourva, S., Low, A., Ridsdill-Smith, R.M., Willford, M. (2001) The London Millennium Footbridge, *Structural Engineer* 79 (22) 17–33.
- Eurocode 5, (2004) *Design of Timber Structures Part 2: Bridges*, EN1995- 2: 2004, European Committee for Standardization, Brussels, Belgium.
- Leonard, D.R. (1966) Human tolerance levels for bridge vibrations, TRRL Report No. 34, Road Research Laboratory.
- Jones, R. T., Pretlove, A.J. (1979) Vibration absorbers and bridges, *The Highway Engineer*.
- Kala, J., Hradil, P., Salajka, V. & Jutner, V., (2010a) Dynamic response of cable stayed steel bridge with tuned mass damper installed - numerical and experimental approach, In *proc. 10th International conference Modern building materials, Structures and techniques*, Vilnius, Lithuania, pp. 658-667, ISBN 978-9955-28-594-6.
- Kala, J., Hradil, P., Salajka, V., (2010b) Comfort criteria for suspension footbridge response on single pedestrian induced vibration analysis, In *proc. ESREL 2010 - Reliability, Risk and Safety*, Rhodes, Greece, pp. 1535-1540, ISBN 978-0-415-60427-7.
- Kala, Z. (2009) Sensitivity assessment of steel members under compression, *Engineering Structures*, 31, 6, pp.1344-1348
- Kala, Z. (2011) Sensitivity analysis of stability problems of steel plane frames, *Thin-Walled Structures*, 49, 5, pp.645-651.
- Parker, J.S., Hardwick, G. , Carroll, M. Nicholls, N.P. & Sandercock, D. (2003) Hungerford bridge millennium project-London, *Civil Engineering* 156 (2) 70–77.
- Pimentel, R.L. (1997) *Vibrational Performance of Pedestrian Bridges Due to Human-Induced Loads*, PhD Thesis, University of Sheffield, Sheffield, UK.
- Pimentel, R.L. , Pavic, A & Waldron, P. (2001) Evaluation of design requirements for footbridges excited by vertical forces from walking, *Canadian Journal of Civil Engineering* 28 (5) pp. 769–777.
- SETRA, (2006) *Footbridges: Assessment of vibrational behaviour of footbridges under pedestrian loading*, Technical guide SETRA, Paris, France.
- Walley, F. (1959) St James's park bridge, In *proceedings of the Institution of Civil Engineers* 12 (6257) pp. 217–222.
- Zivanovic, S., Pavic, A. & Reynolds, P. (2005) Vibration serviceability of footbridges under human-induced excitation: a literature review. *Journal of Sound and Vibration* 279. pp.1-71.

## **SENSITIVITY ANALYSIS OF STABILITY PROBLEMS OF STEEL COLUMNS USING SHELL FINITE ELEMENTS AND NONLINEAR COMPUTATION METHODS**

**Z. Kala<sup>\*</sup>, J. Kala<sup>\*</sup>**

**Abstract:** *The paper analyzes the influence of initial imperfections on the load-carrying capacity of a slender strut, applying the ANSYS programme. The geometrical and material nonlinear finite element method was applied for the theoretical analysis. Modelling of the steel structure was performed using SHELL elements. The effect of input imperfections on the load-carrying capacity is evaluated by Sobol' sensitivity analysis. The computation model elaborated is unique with regard to its numerically demanding character. The Latin Hypercube Sampling method was applied for the evaluation of sensitivity indices.*

**Keywords:** *Sensitivity analysis, shell elements, steel, stability, buckling.*

### **1. Introduction**

The sensitivity analysis is a study of how the variation in the output of a model (numerical or otherwise) can be apportioned, qualitatively or quantitatively, to different sources of variation, and how the given model depends upon the information fed into it (Saltelli et al., 2004). If we mean the computation models of building structures, the sensitivity analysis can be defined as a study of relationships between information flowing in and out of the model. Finite element models (FEM) of steel structures usual for the computation and analysis of output quantities necessary for an assessment of limit states of the structures mentioned, see, e.g., (Gottvald et al., 2010). The output quantities usually are load-carrying capacity, stress state, and deformation. The input quantities usually are material and geometrical characteristics of structures the histograms and statistic characteristics of which are determined by experimental research (Melcher et al., 2004; Kala et al., 2009; Kala et al., 2010). Let us note that not all the uncertainties are of stochastic character, see, e.g. (Kala, 2008). The epistemic uncertainty does not need to be studied in case that the input random quantities have been determined by experimental measurements including a considerable number of observations. Then there can be applied purely stochastic approaches. The stochastic sensitivity analysis determines which input random characteristics have the greatest influence on the random output. In general, there can be distinguished the local sensitivity analysis (Kala, 2005) and the global sensitivity analysis, see, e.g., (Kala, 2009). The local sensitivity analysis (e.g., correlation coefficients approach) does not provide any instruments for an analysis of the influence of higher order interaction effects which occur in systems consisting of more members (Kala, 2011a; Kala, 2011b0). In spite of this fact, it is applied to numerically demanding computation models, see, e.g., (Melcher et al., 2009). The global sensitivity analysis is much more demanding on the CPU time of the computer but in connection with nonlinear computational FEM, it provides importantly more information on the system studied. The detailed computation model is the basic prerequisite for obtaining exact results. The application of nonlinear FEM is necessary when, e.g., ultimate limit state of steel hot-rolled members is studied the load-carrying capacity of which is influenced by residual stress. The presented paper deals with the application of global sensitivity analysis to the study of influence of imperfections on load-carrying capacity of a steel hot-rolled member under compression. The results are unique because the influence of all the imperfections together with residual stress has been include into the solution.

---

<sup>\*</sup> prof. Ing. Zdeněk Kala, Ph.D. and assoc. prof. Ing. Jiří Kala, Ph.D.: Institute of Structural Mechanics, Brno University of Technology, Faculty of Civil Engineering, Veveří Street 95; 602 00, Brno; CZ, e-mails: kala.z@fce.vutbr.cz, kala.j@fce.vutbr.cz

## 2. Sensitivity analysis

Within the scope of modelling, the notion “sensitivity analysis” has different meaning to different people, see, e.g., (Okazawa et al., 2002). The sensitivity analysis enabling an analysis of the influence of arbitrary subgroups of input factors (doubles, triples, etc.) on the monitored output was worked out by the Russian mathematician Ilja M. Sobol (Sobol, 1993; Saltelli et al., 2004). The sensitivity analysis of load-carrying capacity (random output  $Y$ ) to input imperfections (random inputs  $X_i$ ) was performed in the presented study. Sobol’s first order sensitivity indices may be written in the form:

$$S_i = \frac{V(E(Y|X_i))}{V(Y)} \quad (1)$$

$S_i$  measures the first order (e.g., additive) effect (so-called main effect) of  $X_i$  on the model output  $Y$ . The second order sensitivity index  $S_{ij}$  is the interaction term (2) between factors  $X_i, X_j$ . Analogously, the second order sensitivity indices may be rewritten:

$$S_{ij} = \frac{V(E(Y|X_i, X_j))}{V(Y)} - S_i - S_j \quad (2)$$

Sensitivity index  $ij$  expresses the influence of doubles on the monitored output. Other Sobol’ sensitivity indices enabling the quantification of higher order interactions are expressed similarly.

$$\sum_i S_i + \sum_i \sum_{j>i} S_{ij} + \sum_i \sum_{j>i} \sum_{k>j} S_{ijk} + \dots + S_{123\dots M} = 1 \quad (3)$$

The number of members in (3) is  $2^M - 1$ , i.e., for  $M = 3$ , we obtain 7 sensitivity indices; for  $M = 10$ , 1023 sensitivity indices; it is excessively large for practical use. The main limitation in the determination of all members of (3) is the computational demanding character.

## 3. Computation model and input random variables

The strut was meshed in the programme ANSYS, being modelled of thin-walled elements, type SHELL 181. The symmetry was used with regard to the very demanding character of the problem solved. In the bar half in the symmetry plane, we supposed the translation fixed in all cross-section nodes in direction of axis  $X$ , and the rotation around axes  $Y$  and  $Z$ . On the second edge of the bar half solved, we fixed the translation of nodes in direction of the axis  $Y$  on the flange of profile IPE220. On the lower flange of that edge, we fixed the translations in the direction of axis  $Z$ . The upper flange was left free. The Euler method was applied, based on proportional loading in combination with the Newton-Raphson method in the geometrical and material non-linear FEM solution.

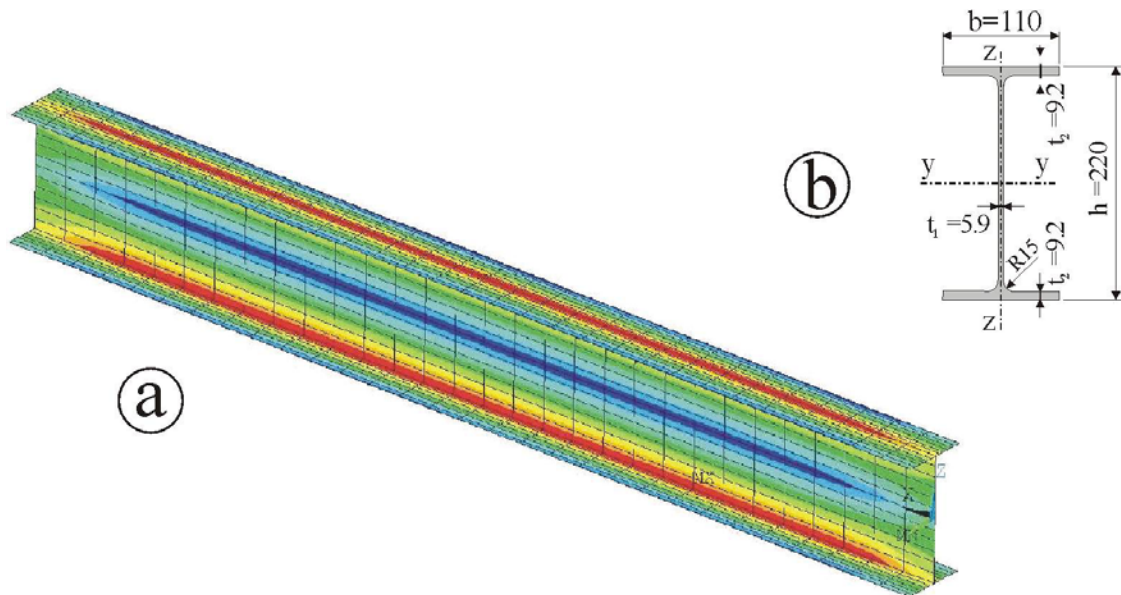


Fig. 1: a) Finite element shell model with residual stress distribution and b) Cross-section geometry.

The load-carrying capacity was determined as the loading constant during which the matrix determinant of tangential stiffness  $K_t$  of the structure would approach zero with certain accuracy. Since an accuracy of 0.1% was required for the determination of load-carrying capacity, it was necessary to use automatic control of the loading step with the Euler method. Bilinear kinematic material strengthening was assumed. We also assumed that the initial steel plasticization occurred when the Mises stress exceeded yield strength.

Theoretical models for expression of load carrying capacity should be always based on assumption that a real structure member contains various imperfections which influence the load carrying capacity. Generally, all input imperfections are of random character. Relatively sufficient information on material and geometrical characteristics of mass produced members of steel structures is available in comparison to other engineering structures (Soares, 1988; Melcher et al., 2004; Kala et al., 2009). Residual stress was introduced with mean value 80 MPa and standard deviation 40 MPa, with triangular distribution both on flanges and web. All the input random quantities were considered with the Gauss density function. All the input characteristics, synoptically given in Table 1, are statistically independent of one another.

Tab. 1: Input random quantities.

Random variables		Mean value	Standard deviation
Yield strength	$f_y$	297.3 MPa	16.8 MPa
Cross-sectional depth	$h$	220 mm	0.975 mm
Cross-sectional width	$b$	110 mm	1.093 mm
Web thickness	$t_1$	5.9 mm	0.247 mm
Flange thickness	$t_2$	9.2 mm	0.421 mm
Initial crookedness	$e_0$	0	0.00077 $L$
Young's modulus	$E$	210 GPa	12.6 GPa
Residual stress	$rs$	80 MPa	40 MPa

#### 4. Sensitivity analysis results and discussion

The LHS method was applied to calculation of sensitivity indices (McKey et al., 1979; Iman and Conover, 1980). The model output  $Y$  is the load-carrying capacity calculated in each run of the LHS method. The conditional random arithmetical mean  $E(Y|X_i)$  was evaluated for 3000 simulation runs; the variance  $V(E(Y|X_i))$  was calculated for 3000 simulation runs, as well. The variance  $V(Y)$  of load carrying capacity has been calculated for 10000 runs. The second-order sensitivity indices  $S_{ij}$  were calculated analogously. The influence of imperfections on the load carrying capacity changes with the strut increasing nondimensional slenderness, see Fig. 2.

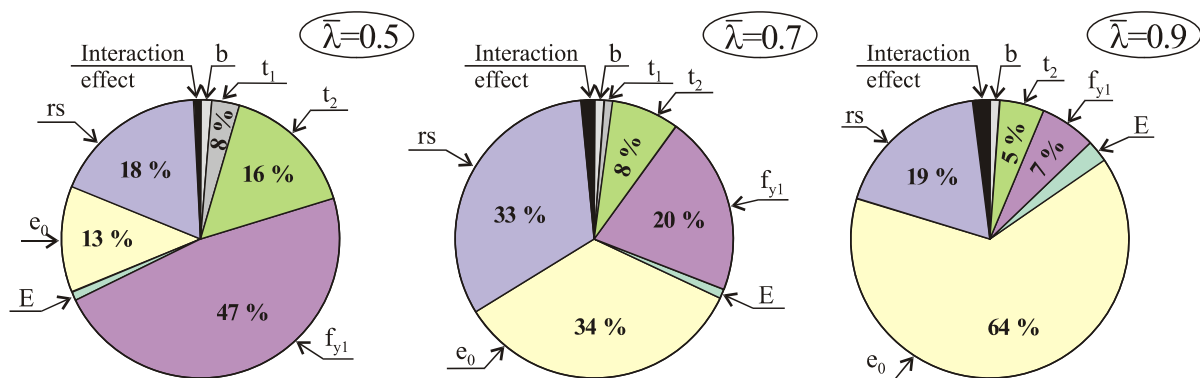


Fig. 2: Sensitivity analysis results.

## 5. Conclusions

The results presented in this paper quantify the influence of material and geometrical characteristics on the load-carrying capacity. The Sobol' sensitivity analysis in connection with nonlinear shell FEM enables to quantify the influence of residual stress, too. It is evident that the influence of residual stress is not the same as the influence of initial crookedness. From the point of view of standards for design of steel structures, it rises up the question whether the influence of residual stress can be reliably substituted by increase of the amplitude of bow imperfections. One of approaches how to answer this question is the elaboration of probabilistic reliability analyses of the ultimate limit state of steel members under compression (Kala, 2007). Further on, the results of the Sobol' sensitivity analysis have shown that the higher order interaction effects are relatively low.

## Acknowledgement

The article was elaborated within the framework of projects of AVČR IAA201720901, MSM0021630519 and P104/11/0703.

## References

- Gottvald, J. (2010) The calculation and measurement of the natural frequencies of the bucket wheel excavator SchRs 1320/4x30. *Transport*, 25, 3, pp.269-277.
- Iman, RC. & Conover, WJ. (1980) Small sample sensitivity analysis techniques for computer models with an application to risk assessment. *Communications in Statistics – Theory and Methods*, 9, 17, pp.1749–1842.
- Kala, Z. (2005) Sensitivity analysis of the stability problems of thin-walled structures. *Journal of Constructional Steel Research*, 61, 3, pp.415-422.
- Kala, Z. (2007) Stability problems of steel structures in the presence of stochastic and fuzzy uncertainty. *Thin-Walled Structures*, 45, 10-11, pp.861-865.
- Kala, Z. (2008) Fuzzy probability analysis of the fatigue resistance of steel structural members under bending. *Journal of Civil Engineering and Management*, 14, 1, pp.67-72.
- Kala, Z. (2009) Sensitivity assessment of steel members under compression, *Engineering Structures*, 31, 6, pp.1344-1348.
- Kala, Z., Melcher, J. & Puklický, L. (2009) Material and geometrical characteristics of structural steels based on statistical analysis of metallurgical products. *Journal of Civil Engineering and Management*, 15, 3, pp.299-307.
- Kala, Z., Puklický, L., Omishore, A., Karmazínová, M. & Melcher, J. (2010) Stability problems of steel-concrete members composed of high strength materials. *Journal of Civil Engineering and Management*, 16, 3, pp.352-362.
- Kala, Z. (2011a) Sensitivity analysis of stability problems of steel plane frames, *Thin-Walled Structures*, 49, 5, pp.645-651.
- Kala, Z. (2011b) Sensitivity analysis of steel plane frames with initial imperfections, *Engineering Structures*, (in print). ISSN: 0141-0296. doi:10.1016/j.engstruct.2011.04.007.
- McKey, MD, Conover, WJ, Beckman, & RJ. (1979) A comparison of the three methods of selecting values of input variables in the analysis of output from a computer code. *Technometrics*, 1, 2, pp.239-245.
- Melcher, J., Kala, Z., Holický, M., Fajkus, M. & Rozlívka, L. (2004) Design characteristics of structural steels based on statistical analysis of metallurgical products. *Journal of Constructional Steel Research*, 60, 3-5, pp.795-808.
- Melcher, J., Škaloud, M., Kala, Z. & Karmazínová, M. (2009) Sensitivity and statistical analysis within the elaboration of steel plated girder resistance. *Advanced Steel Construction*, 5, 2, pp.120-126.
- Okazawa, S., Oide, K., Ikeda, K. & Terada, K. (2002) Imperfection sensitivity and probabilistic variation of tensile strength of steel members. *International Journal of Solids and Structures*, 39, 6, pp.1651-1671.
- Saltelli A, Tarantola S, Campolongo F, Ratto M. *Sensitivity analysis in practice: A guide to assessing scientific models*. New York: John Wiley and Sons; 2004.
- Soares GC. (1988) Uncertainty modelling in plate buckling. *Structural Safety*, 5, 1, pp.17–34.
- Sobol', IM. (1993) Sensitivity analysis for non-linear mathematical models. *Mathematical Modelling and Computational Experiment*, 1, pp.407-414 [Translated from Russian. Sobol', IM. (1990) Sensitivity estimates for nonlinear mathematical models. *Matematicheskoe Modelirovanie*, 2, pp.112-118].



## ACOUSTIC CHARACTERISTICS OF PLANE MULTILAYERED SANDWICH INFINITE-INFINITE STRUCTURES

S. Karczmarzyk<sup>\*</sup>

**Abstract:** *An exact local model for computing the coincidence frequencies of multilayered sandwich panels and numerical results predicted by the model are presented in the paper. The model is derived within the local theory of linear elastodynamics without any simplifications concerning the structure. The coincidence frequencies for homogeneous panels and for five-layer and seven-layer sandwich panels are obtained and compared with corresponding results predicted by the models existing in the literature. Both flexural and breathing waves propagating in the sandwich structures are considered.*

**Keywords:** *Local model, flexural waves, breathing waves, coincidence frequencies, coincidence curve.*

### 1. Introduction

The plane continuous structures can be divided into three groups i.e., (1) infinite in two perpendicular directions, shortly infinite-infinite (I-I), panels, (2) finite-infinite (F-I) duct covers and (3) finite-finite (F-F) plates. Transmission loss (TL) is the basic characteristics of all the structures. In this paper however some other characteristics such as coincidence frequency and critical coincidence frequency of plane, multilayered sandwich panels are considered. The characteristics called here as 'coincidence curve' is defined as the ratio  $\omega_c/\omega_{cr} \equiv f_c/f_{cr}$ , where  $\omega_c$  denotes the coincidence frequency for an assumed incident angle  $\theta$  and  $\omega_{cr}$  is the critical coincidence frequency,  $\omega_{cr} = \omega_c(\theta = 90^\circ)$ .

All the coincidence characteristics are important for many reasons. In particular, the critical coincidence frequency  $\omega_{cr} \equiv 2\pi f_{cr}$ , is of special importance because of the following reasons (Bhattacharya et al., 1971). First, the critical coincidence frequency is the only frequency at which the transmission loss (TL) of a finite-finite (F-F) purely elastic plate equals to zero. Second, the critical coincidence frequency of the F-F plate is independent of the incident angle of the acoustic wave. Third, the critical coincidence frequency of the F-F simply supported plate equals to the critical coincidence frequency of the infinite-infinite (I-I) panel with the same cross-sectional parameters as the F-F plate. The third property is noted here as follows,  $(\omega_{cr})_{I-I} = (\omega_{cr})_{F-F}$ . Due to the third property the critical coincidence frequency can be computed either within the models (theories) for the F-F plates or within the corresponding models for the I-I panels. Obviously, the latter method is easier.

It is noted that more facts about importance of the critical coincidence frequency, when two-layer plasterboards and the sandwich structures are considered, one can find e.g. in the papers: (Matsumoto et al., 2006; Renji et al., 1997; Renji, 2005; Wang et al., 2005 and Zhou & Crocker, 2010). The main fact is that the acoustic transmission characteristics of the structures are highly dependent on whether the excitation frequency is below or above the critical coincidence frequency.

### 2. Statement of the problem

The structure considered in this paper is composed of  $p$  isotropic layers. It is infinite in directions  $x$ ,  $y$  and its thickness, being the sum of thicknesses of the layers, extends in direction  $z$ .

Statement of the acoustic problem for the multilayered structure contains the following Eqs: the kinematic assumptions (1) - satisfied individually for each layer, the wave Eqs (2) - satisfied individually for each layer, the Saint-Venant compatibility Eqs - satisfied individually for each layer,

---

<sup>\*</sup> Dr. Eng. Stanisław Karczmarzyk, DrSc.: Institute of Machine Design Fundamentals, Warsaw University of Technology, Narbutta 84; 02-524, Warsaw; PL, e-mail: karczmarzyk\_st@poczta.onet.pl

the calibration condition (3) - satisfied individually for each layer, the boundary conditions (4) - for the (outside) surfaces of the structure, the compatibility Eqs (5) between adjoining layers and the constitutive Eq (the Hooke law) - satisfied individually for each layer.

$$\underline{u} = \text{grad}\phi + \text{rot}\underline{\psi} \equiv u_k = \phi_{,k} + e_{klm}\psi_{m,l}, \quad \underline{u} = \{u_1 \ u_2 \ u_3\}, \quad k, l, m = 1, 2, 3. \quad (1)$$

$$[(\lambda + 2\mu)/\rho]\nabla^2\phi - \ddot{\phi} = 0, \quad (\mu/\rho)\nabla^2\psi_m - \ddot{\psi}_m = 0, \quad m = 1, 2, 3. \quad (2)$$

$$\psi_{k,k} \equiv \psi_{1,1} + \psi_{2,2} + \psi_{3,3} = 0. \quad (3)$$

$$\sigma_{33}(x, y, z = z_r) \equiv \sigma_{zz}(x, y, z = z_r) = q_r, \quad \sigma_{31}(x, y, z = z_r) \equiv \sigma_{zx}(x, y, z = z_r) = 0, \quad (4)$$

$$\sigma_{32}(x, y, z = z_r) \equiv \sigma_{yz}(x, y, z = z_r) = 0.$$

$$\sigma_{33(j)} = \sigma_{33(j+1)}, \quad \sigma_{31(j)} = \sigma_{31(j+1)}, \quad \sigma_{23(j)} = \sigma_{23(j+1)}, \quad (5)$$

$$u_{1(j)} = u_{1(j+1)}, \quad u_{2(j)} = u_{2(j+1)}, \quad u_{3(j)} = u_{3(j+1)}.$$

Symbols,  $u_k$ ,  $\lambda$  and  $\mu$ ,  $\rho$ ,  $\sigma_{lm}$ , appearing in (1)-(5), denote, displacement components, Lamé's parameters, material density and stresses, respectively. For a particular  $j^{\text{th}}$  layer the Lamé parameters  $\lambda$  and  $\mu$  as well as density  $\rho$ , appearing in the wave Eqs (2), should be replaced with  $\lambda_{(j)}$ ,  $\mu_{(j)}$  and  $\rho_{(j)}$ , respectively. Symbols  $q_r$  denote the normal acoustic loading acting on the surface denoted with  $r = 1, 2$ . If we assume that the subscript  $r$  equals to 1 ( $q_r = q_1$ ) for the top/left outside surface of the plate then  $r$  equals to 2 ( $q_r = q_2$ ) for the bottom/right outside surface of the structure, respectively. Symbol  $z_r$  in (4) denotes coordinates of the outside surfaces of the multilayered panel. It is noted that for the problem considered here the displacement field (1) can be simplified.

The acoustic loadings  $q_r$  are defined as follows (Renji, 2005; Wang et al., 2005),

$$q_1 = Z_{\text{air}}\dot{u}_z(z = -h/2), \quad q_2 = Z_{\text{air}}\dot{u}_z(z = +h/2), \quad Z_{\text{air}} = \rho_{\text{air}}c. \quad (6)$$

Symbols  $h$ ,  $\rho_{\text{air}}$ ,  $c$  denote thickness of the structure, air impedance and sound velocity in the air, respectively. The solution resulting from the above statement is called in the further text as the exact local model.

### 3. Numerical results

In order to show a broad applicability of the exact local model outlined in the paper the coincidence frequencies were computed for a homogeneous (one-layer) I-I panel, for a five-layer sandwich I-I panel and for a seven-layer sandwich I-I panel. To test the model and the computing program the results for the homogeneous structure are compared with the counterparts predicted by the Kirchhoff and Mindlin models. All the numerical results are presented in the Figs. 1 - 2 and in the Tables 1 - 3.

In Fig. 1 the coincidence curves and in Table 1 the coincidence frequencies for the flexural waves propagating in a homogeneous I-I panel of the following parameters,  $h_{(1)} = 25$  mm,  $E_{(1)} = 0.1 \cdot 10^{10}$  Pa,  $\nu_{(1)} = 0.16$ ,  $\rho_{(1)} = 1200$  kg/m<sup>3</sup>, are given. These input data are approximately parameters of the plasterboard. The (shear modulus)/density  $\equiv \mu_{(1)}/\rho_{(1)}$  ratio in the case equals to  $3.59 \cdot 10^5$ . Results denoted with the subscript SK are predicted by the local exact model, the counterparts denoted with subscripts K, M are predicted by the Kirchhoff and Mindlin model, respectively. It is seen that the coincidence curve resulting from the Kirchhoff theory is much below the curves predicted by the local and Mindlin models, within the range of the incident angle  $\eta \equiv \theta$  between 42 and 72 degrees.

Tab. 1: Flexural coincidence frequencies (Hz) for the plasterboard.

$\Theta$	42	48	54	60	66	72	78	84	90
$(f_c)_{SK}$	19465	10496	7450.4	5897.4	4987.9	4426.9	4084.7	3898.8	3839.7
$(f_c)_K$	6266.1	5080.1	4286.5	3740.7	3361.7	3101.7	2932.3	2836.5	2805.6
$(f_c)_M$	17801	9437.9	6771.8	5416.3	4617.7	4121.6	3817.5	3651.6	3598.8

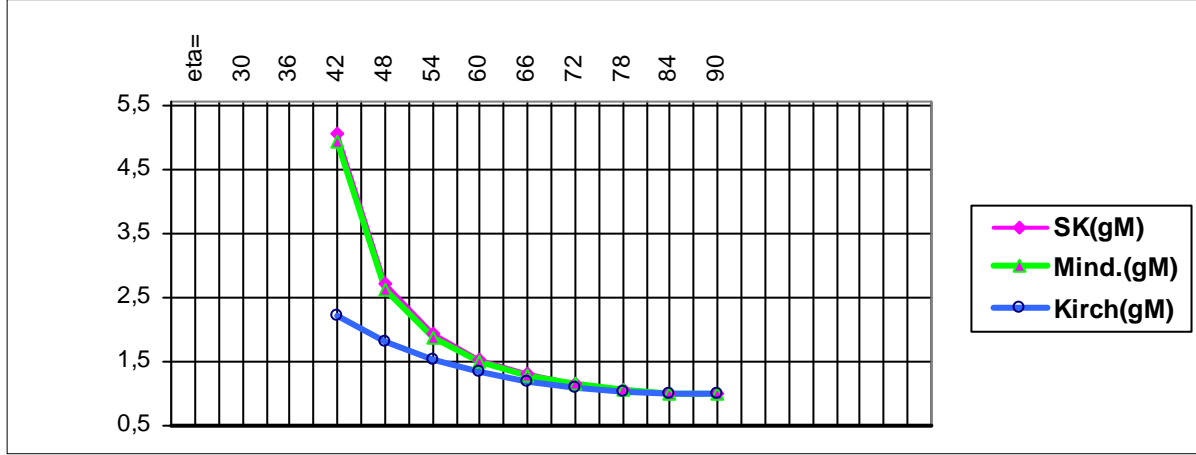


Fig. 1: Coincidence curves for the plasterboard.

In Fig. 2 the coincidence curves and in Tables 2 - 3 coincidence frequencies for a five-layer sandwich I-I panel and a seven-layer sandwich I-I panel are presented. Parameters of the five-layer structure are as follows:  $h_{(1)}=1$  mm,  $E_{(1)}=0.68910^{11}$  Pa,  $\nu_{(1)}=0.276$ ,  $\rho_{(1)}=2680$  kg/m<sup>3</sup>,  $h_{(2)}=0.5$  mm,  $E_{(2)}=0.39 \cdot 10^{10}$  Pa,  $\nu_{(2)}=0.08$ ,  $\rho_{(2)}=1175$  kg/m<sup>3</sup>,  $h_{(3)}=62$  mm,  $E_{(3)}=0.3059 \cdot 10^9$  Pa,  $\nu_{(3)}=0.85$ ,  $\rho_{(3)}=32.8$  kg/m<sup>3</sup>,  $h_{(2)}=h_{(4)}$ ,  $E_{(2)}=E_{(4)}$ ,  $\nu_{(2)}=\nu_{(4)}$ ,  $\rho_{(2)}=\rho_{(4)}$ ,  $h_{(1)}=h_{(5)}$ ,  $E_{(1)}=E_{(5)}$ ,  $\nu_{(1)}=\nu_{(5)}$ ,  $\rho_{(1)}=\rho_{(5)}$ . The layers 2, 4 may be for instance of the glue necessary to connect the outer aluminum layers and the middle honeycomb core. Parameters of the seven-layer structure are as follows:  $h_{(1)}=1$  mm,  $E_{(1)}=0.68910^{11}$  Pa,  $\nu_{(1)}=0.276$ ,  $\rho_{(1)}=2680$  kg/m<sup>3</sup>,  $h_{(2)}=0.5$  mm,  $E_{(2)}=0.39 \cdot 10^{10}$  Pa,  $\nu_{(2)}=0.08$ ,  $\rho_{(2)}=1175$  kg/m<sup>3</sup>,  $h_{(3)}=30$  mm,  $E_{(3)}=0.3059 \cdot 10^9$  Pa,  $\nu_{(3)}=0.85$ ,  $\rho_{(3)}=32.8$  kg/m<sup>3</sup>,  $h_{(4)}=2$  mm,  $E_{(4)}=0.925 \cdot 10^7$  Pa,  $\nu_{(4)}=0.25$ ,  $\rho_{(4)}=92.5$  kg/m<sup>3</sup>,  $h_{(2)}=h_{(5)}$ ,  $E_{(2)}=E_{(5)}$ ,  $\nu_{(2)}=\nu_{(5)}$ ,  $\rho_{(2)}=\rho_{(5)}$ ,  $h_{(1)}=h_{(7)}$ ,  $E_{(1)}=E_{(7)}$ ,  $\nu_{(1)}=\nu_{(7)}$ ,  $\rho_{(1)}=\rho_{(7)}$ . The layer 4 is of a cork conglomerate material. The results in Fig. 2 and in Tab. 2 refer to the flexural waves of the sandwich structures. In Tab. 3 the coincidence frequencies for the breathing waves are given.

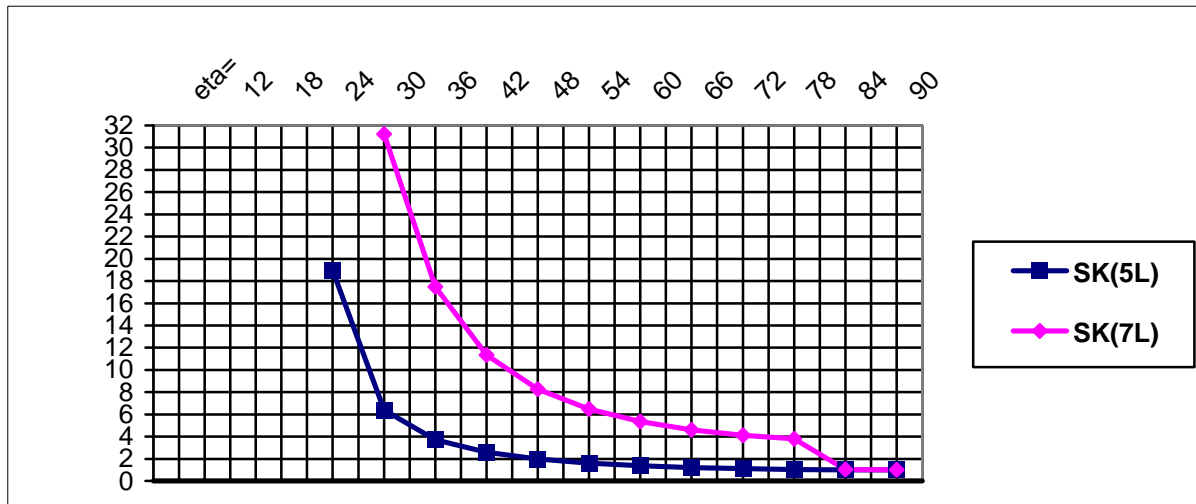


Fig. 2: Coincidence curves for the five-layer (5L) and seven-layer (7L) sandwich structures.

Symbol  $\Delta$  in Tab. 2 denotes the percentage differences between the coincidence frequencies.

*Tab. 2: Flexural coincidence frequencies (Hz) for the five-layer ( $f_{c5}$ ) and seven-layer ( $f_{c7}$ ) panel.*

$\Theta$	12	18	24	30	36	42	48	54	60	66	72	78	84	90
$(f_{c5})_{SK}$	51813	10400	2709.7	911.1	529.6	369.9	283.7	231.4	197.4	174.8	159.7	150.0	144.6	142.8
$(f_{c7})_{SK}$		87137	63686	4952.8	2770.7	1801.5	1311.4	1027.4	848.5	730.8	652.9	603.2	160.8	158.6
$\Delta$		737.86	2250.3	443.61	423.17	387.02	362.25	343.99	329.84	318.08	308.83	302.13	11.20	11.06

*Tab. 3: Breathing coincidence frequencies (Hz) for the five-layer ( $f_{c5}$ ) panel.*

$\Theta$	12	18	24	30	36	42	48	54	60	66	72	78	84	90
$(f_{c5})_{SK}$						27185	22218	19012	16857	15387	14390	13745	13382	13265

It is seen in Fig. 2 that the seven-layer panel seems to be much better for the acoustic purposes than the five-layer panel. The seven-layer structure is obtained by dividing the five-layer panel within the middle plane and inserting the layer of the cork material between the two symmetric parts.

#### 4. Conclusions

Coincidence frequencies and the coincidence curves for the homogeneous plasterboard and for two multilayered sandwich panels are obtained by applying the local exact model outlined in section 2. In order to test the model the characteristics for the homogeneous panel are compared with corresponding results predicted by the Kirchhoff and Mindlin models.

The comparison enables us to say that prediction of the coincidence frequencies by the Kirchhoff model is highly inaccurate, in particular for the lower values of the incident angle of the acoustic wave. The predictions of the Mindlin model and the local exact model are much closer.

Inserting of the compliant thin layer of cork material between two symmetric (about the middle plane) parts of the five-layer panel increases significantly the coincidence frequencies. It is also shown that the coincidence frequencies of the five-layer panel associated with the breathing acoustic waves propagating in the structure occur within the range of hearing by the human ear.

#### References

- Bhattacharya, M.C., Guy, R.W. & Crocker, M.J. (1971) Coincidence effect with sound waves in a finite plate, *Journal of Sound and Vibration* 18, 157-169.
- Matsumoto, T., Uchida, M., Sugaya, H. & Tachibana, H. (2006) Development of multiple drywall with high sound insulation performance, *Applied Acoustics* 67, 595-608.
- Renji, K., Nair, P.S. & Narayanan, S. (1997) Critical coincidence frequencies of flat panels, *Journal of Sound and Vibration* 205, 19-32.
- Renji, K. (2005) Sound transmission loss of unbounded panels in bending vibration concerning transverse shear deformation, *Journal of Sound and Vibration* 283, 478-486.
- Wang, T., Sokolinsky, V.S., Rajaram, S. & Nutt, S.R. (2005) Assessment of sandwich models for the prediction of sound transmission loss in unidirectional sandwich panels, *Applied Acoustics* 66, 245-262.
- Zhou, R., Crocker, M.J. (2010) Sound transmission loss of foam-filled honeycomb sandwich panels using statistical energy analysis and theoretical and measured dynamic properties, *Journal of Sound and Vibration* 329, 673-686.

## MODELLING OF BED IN PROCESS OF PARTICLE SALTATION IN CHANNEL

I. S. Kharlamova<sup>\*</sup>, A. A. Kharlamov<sup>\*</sup>, Z. Chára<sup>\*</sup>, P. Vlasák<sup>\*</sup>

**Abstract:** For numerical modelling particle saltation in channel with rough bed is important to define a bed configuration. The paper deals with the bed consisting of spherical particles of the different size than the saltating particle. In horizontal  $x$ - $z$  plane the particles are arranged hexagonally. In vertical direction the particles are distributed according to Gaussian distribution. Before each collision of the saltating particle with bed the bed is shifted on a random distance and it is rotated by a random angle, so there is uniform probability to find a bed particle in any point of the  $x$ - $z$  plane. The bed structure is chosen with aim to represent the natural bed as much as possible, thus the known information about distribution of the bed particles along  $y$ -direction is used and the location of bed particles in the  $x$ - $z$  plane is controlled by principles of equal probability and minimal dense packing.

**Keywords:** Bed structure, normal distribution, hexagonal packing.

### 1. Introduction

It is important to define the bed configuration for successful modelling of solid particles motion in a channel. Usually the modelling of the motion consists of two basic parts: the equations of motion and the bed structure (see for example Chára et al., 2010). The more accurate the expressions for forces are the more precise is the solution – the trajectories of the particles. The same is also valid for the bed structure: the closer to the nature the bed structure is the more exact the particle's trajectories are. Therefore, modelling of bed structure close to the nature is very important for the accurate modelling of particle saltation.

### 2. Bed structure

#### 2.1. Bed structure in model of Sekine and Kikkawa

The basis of present bed structure was taken from Sekine and Kikkawa (1992). They studied videotapes of saltation over an irregularly stacked bed composed of similar grains  $d_b$ . They experimentally found that bed grains are distributed with Gaussian distribution around mean bed level with standard deviation  $\sigma = d_b/3$ , see Fig. 1a. For modelling of saltation they used a cubing packing of bed grains in  $x$ - $z$  plane, see Fig. 1b.

#### 2.2. Bed structure in present model

In the model there is used the following bed arrangement. Bed consists of spherical particles; the size of bed particles  $d_b$  can be different from the size of saltating particles  $d_s$ . A small detached element of bed (bed sector) is created only in those areas where the saltating particle is going to collide with bed. The bed sector, which is created under saltating particle, consists of 19 or more particles packed hexagonally in  $x$ - $z$  plane, see Fig. 2. Along  $y$  axis bed particles are distributed with Gaussian distribution similarly to Sekine and Kikkawa (1992).

---

<sup>\*</sup> Mgr. Irina S. Kharlamova, Mgr. Alexander A. Kharlamov, Ing. Zdeněk Chára, CSc. and prof. Ing. Pavel Vlasák, DrSc.: Institute of Hydrodynamics ASCR, v. v. i.; Pod Patankou 30/5, 166 12, Prague 6, CZ, e-mails: ivanova@ih.cas.cz, kharlamov@ih.cas.cz, chara@ih.cas.cz, vlasak@ih.cas.cz

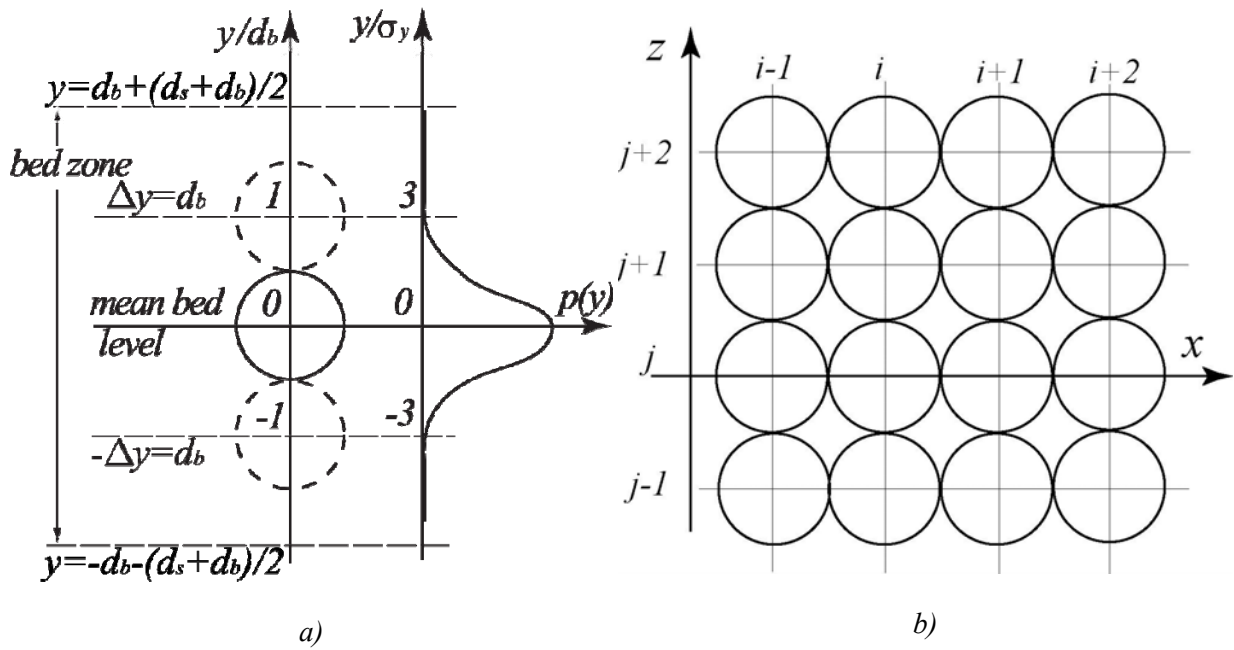


Fig. 1. Bed structure according to Sekine and Kikkawa (1992). a) Distribution of particles in  $y$ - $x$  plane and the bed zone; b) Distribution of particles in  $x$ - $z$  plane with cube grid:  $d_b \times d_b$ .

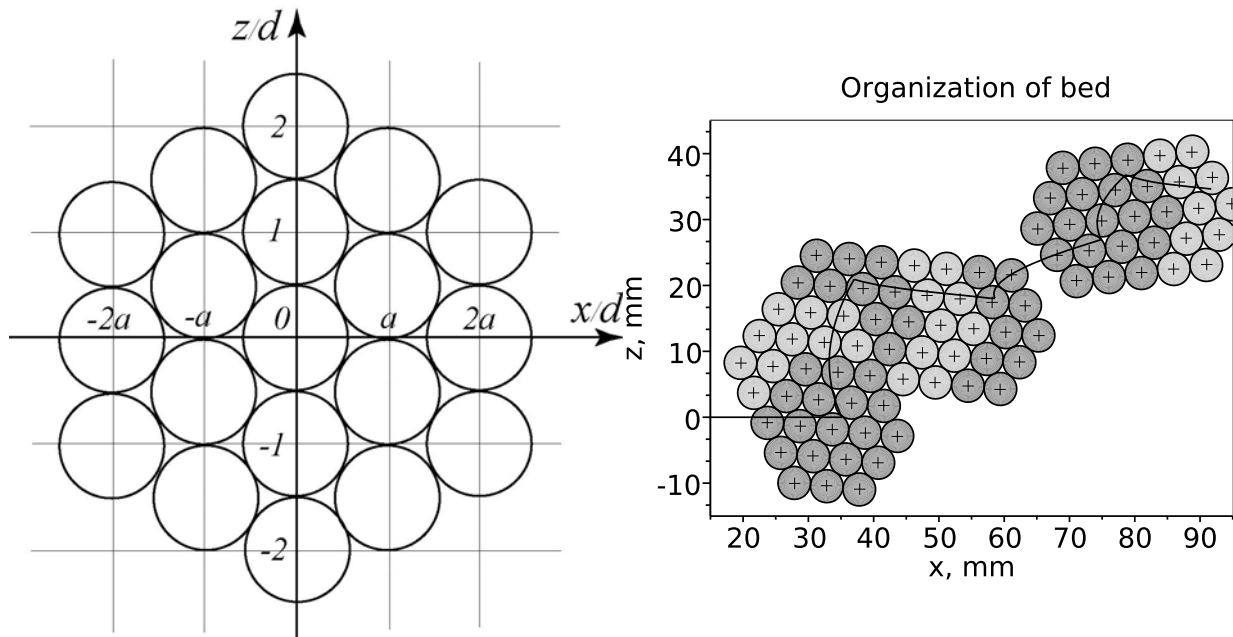


Fig. 2. Hexagonal arrangement of bed particles, present model. An element of grid has dimensions  $d_b \times a d_b$ ,  $a = \sqrt{3}/2$ .

Fig. 3. The example of bed sector extension: bed sector consists of 19 particles extending with 10 added particles in the direction of particle movement (black line).

### 2.3. The building of bed

The equations of motion of saltating particle are solved numerically until the saltating particle enters in a bed zone, i.e. the zone, where collision of saltating particle and bed particle is possible. (The upper bound of the bed zone  $y = d_b + (d_s + d_b)/2$ , see Fig. 1a.) Later bed sector of 19 particles is created in an anticipated point of the particle collision. From this time distances between centre of saltating particle and the bed particles start to be calculated. If the shortest distance becomes less than the sum  $(d_s + d_b)/2$ , than the collision between the saltating particle and the certain bed particle will be registered. Otherwise the equations of the saltating particle motion will be solved again, until the collision occurs. After the collision, while the saltating particle continues its motion within the bed



zone, distances between it and bed particles continue to be checked, that allows registering sequential collisions. If the saltating particle does not leave the bed zone, but leave the bed sector of 19 particles, than the additional 10 bed particles of the same organization will be added to extend the bed sector in the direction of the particle motion. It is repeated up to the moment, when saltating particle leaves the bed zone or sticks into the bed, see Fig. 3 and 4.

In order to avoid repeatability in mutual location of the saltating particle and the collided bed particle, the bed sector is shifted on a random distance and is turned by a random angle. The shift provides the uniform probability for finding a bed particle in whatever point of  $x$ - $z$  plane, whereas the turn makes uniform distribution in the directions of bed particles' paired orientations. Thus the mutual location of the saltating particle and bed particles changes for each bed sector.

When the saltating particle enters in the bed zone  $(-d_b-(d_s+d_b)/2; d_b+(d_s+d_b)/2)$  the following steps will be conducted for building of the bed structure.

1. The centre of bed sector ( $x_0$ -,  $z_0$ -coordinates) is situated to the anticipated point of the particle collision.
2. Around the centre of bed sector 19 particles are arranged in hexagonal distribution (see Fig. 2); the local  $x$ -,  $z$ -coordinates of 19 bed particles are determined with respect to  $x_0$ -,  $z_0$ -coordinates of bed sector centre.
3. The  $x_0$ -,  $z_0$ -coordinates of the centre of bed sector shift randomly in rectangle  $(1 \times \sqrt{3}/2) d_b$ ; and the bed sector is turn by a random angle in  $x$ - $z$  plane around its vertical axis, in order to make each impact unique, i.e. to avoid using the same bed organisation in the next bed sectors.
4. The  $y_0$ -coordinate of the centre of bed sector (mean bed level) is chosen within  $(-0.20 \div 0.20)d_b$  interval by uniform distribution. It was done in order to make possible slight vertical difference between individual bed structures.
5. The  $y$ -coordinates of centres of 19 bed particle are seated to their place by normal distribution  $f(y) = \frac{1}{\sqrt{2\pi\sigma^2}} \exp\left(-\frac{(y-y_0)^2}{2\sigma^2}\right)$  limited by  $(-3\sigma, 3\sigma)$  interval around  $y_0$ , where  $\sigma = d_b/3$ , according to Sekine and Kikkawa (1992).

These steps can create a rough bed like in nature condition. After the saltation particle leaves and then again enters the bed zone, the process of bed structure construction is repeated.

## 2.4. Sticking in the bed

The given bed structure has a parameter, which make possible to control the density of bed packing – i.e. the normal distribution parameter  $\sigma$ . The less  $\sigma$  the more consistent bed and the more difficult for saltating particle to penetrate through bed or even stick in it.

Using the parameter  $\sigma = d_b/3$ , which was defined experimentally (Sekine and Kikkawa, 1992), and small value of shear velocity  $u_*$  it is possible to get sticking a particle into bed, see Fig. 4. For various bed organisation the value of shear velocity  $u_*$ , at which particle sticks into bed, differs.

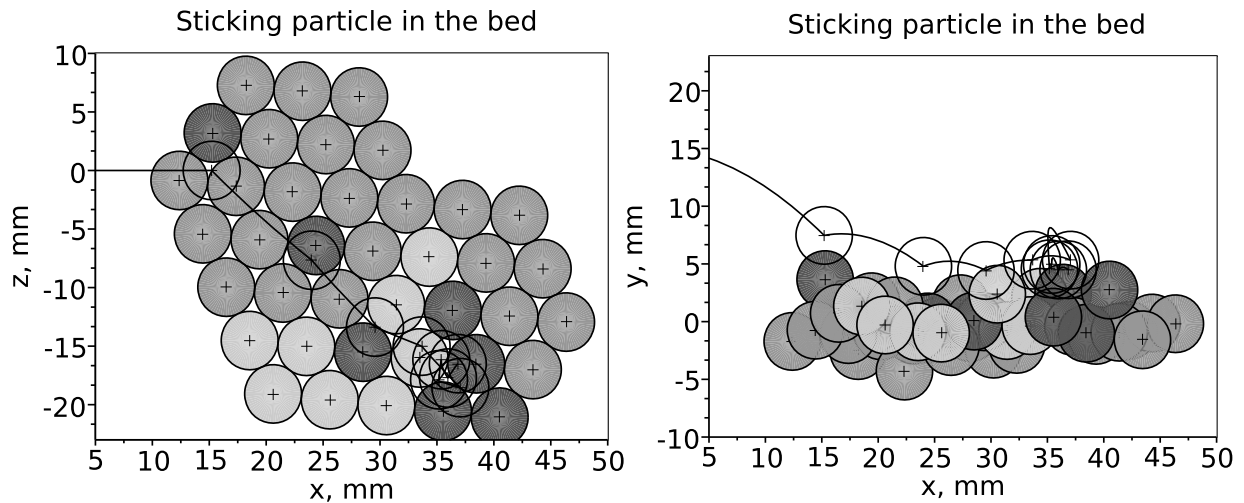


Fig. 4. Sticking saltating particle in the bed: saltating particle sticks in the bed at the 13th jump. Dark bed particles are the particles that take part in collision. Diameters of particles  $d_s = d_b = 5$  mm,  $\sigma = d_b/3$ , shear velocity  $u_* = 0.025$  m/s.

### 3. Conclusions

Reasonable bed structure is necessary for accurate modelling of saltation particles motion. Present model of bed structure uses the experimental investigation of bed particles distribution in vertical direction in natural channels (Sekine and Kikkawa, 1992). The distribution of bed particles in horizontal plane is based on principle of bed packing with minimal space between neighbour particles - hexagonal packing. During a process of calculation of a saltating particle motion the bed is created only on a small place of presumed particle's collision. Each new part of bed (bed sector) differs from the other. There is a uniform probability to find a bed particle in whatever point of horizontal plane. The model make possible to describe various behaviour of saltating particle during its collision with bed, namely it allows observing such events as sequential collision of the saltating particle with bed particles and sticking it in the bed.

### Acknowledgement

Support under the project No. 103/09/1718 of the Grant Agency of the Czech Republic and the Institutional Research Plan No. AV0Z20600510 of the Academy of Sciences of the Czech Republic are gratefully acknowledged.

### References

- Chára, Z., Kharlamov, A. A., Ivanova, I. S. & Vlasák, P. (2010) Trajectories of saltating particles over a rough channel bed, in: Int. Conf. on Numerical Analysis and Applied Mathematics (T.Simos, G.Psihoyios, C.Tsitouras eds.), Rhodes (GR), pp. 159-162.
- Sekine M., Kikkawa, H. (1992) Mechanics of saltating grains. J. Hydraul. Eng. ASCE, 118, 4, pp. 536-558.

## QKK 50 MANIPULATOR TONGS CALCULATION

J. Kirchner<sup>\*</sup>, J. Mrkos<sup>\*</sup>

**Abstract:** *This paper deals with the strength and deformation check of designed tongs assembly, tongs assembly with extensions and tongs axle for the QKK 50 manipulator according to the spatial image and drawings.*

**Keywords:** *QKK 50 manipulator, strength check.*

### 1. Introduction

ŽďAS forging manipulators are designed to handle a forging in the press working space. QKK rail manipulators (Figs. 1 and 2) represent the basic series and have a carrying capacity of 3, 5, 8, 12, 20 and 35 t. Manipulators with higher carrying capacities are designed and made individually according to the customer's specific requirements. The biggest manipulator manufactured up to now has a carrying capacity of 100 t.

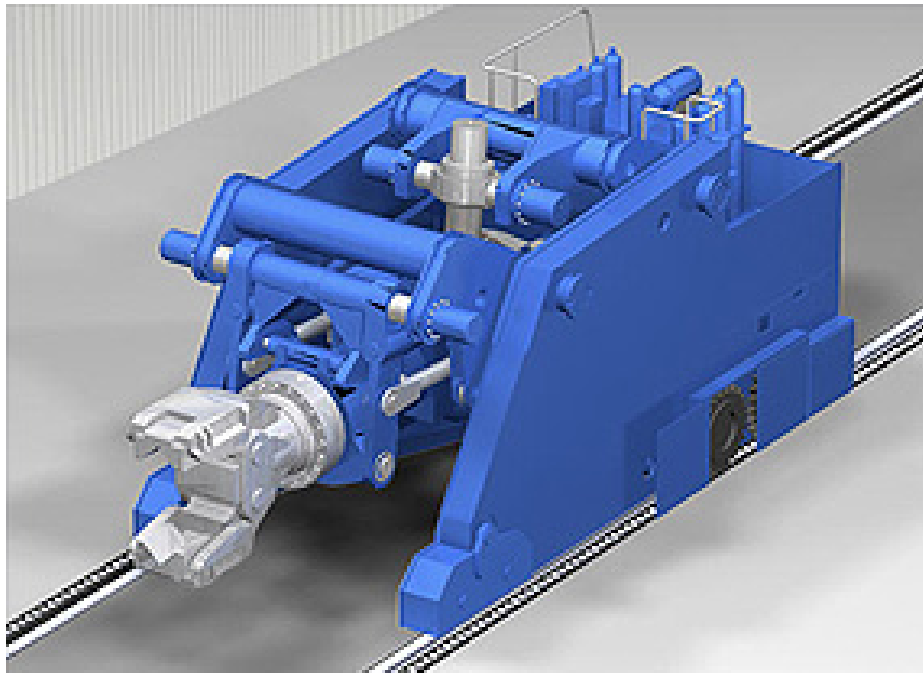


*Fig. 1: QKK 50 Manipulator (Mrkos, 2010).*

### 2. Computational model

Set parameters for calculation:

Material: material and heat-treatment values have been set for individual parts.

Working temperature: -5°C to +60°C, -5°C to +200°C

---

<sup>\*</sup> Ing. Jiri Kirchner and Ing. Josef Mrkos: ŽďAS, a.s., Strojírenská 6, 591 71, Žďár nad Sázavou, CZ, e-mails: jiri.kirchner@zdas.cz, josef.mrkos@zdas.cz

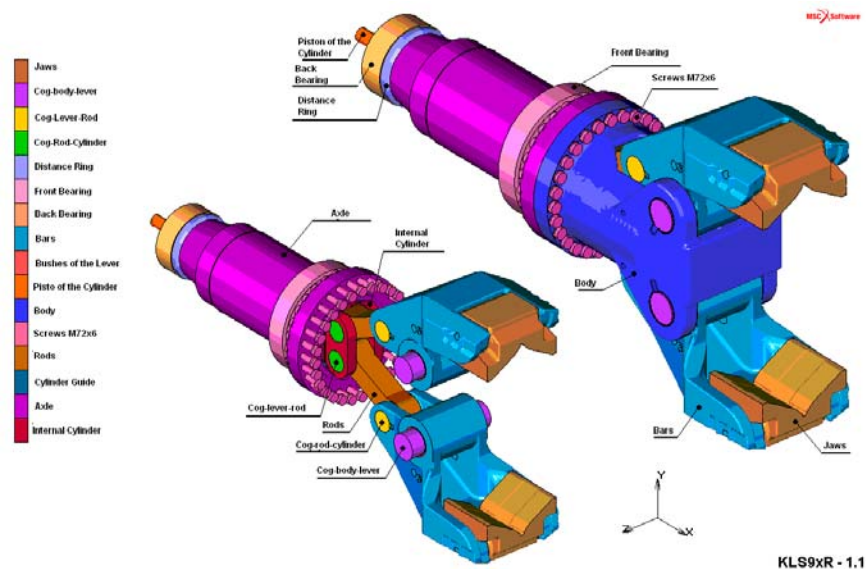


Fig. 2: Tongs of the QKK 50 Manipulator.

## 2.1. Example of the load

KLS91R - tongs-and-jaws assembly with use of contact between the interacting parts, including the simulation of the weight of transferred load, tongs opened - Z1 load (Fig. 3).

KLS92R - dtto KLS91R - Z2 load

KLS92R-1 - dtto KLS91R - Z2-1 load

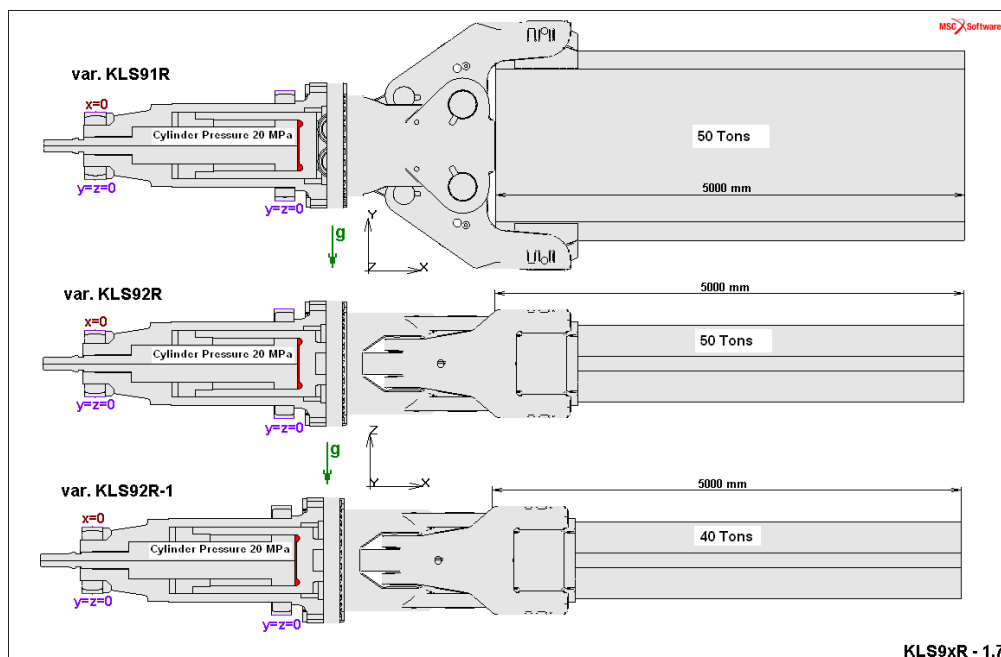


Fig. 3: Loads for KLS91R, KLS92R and KLS92R-1.

## 3. Methods

Elasticity calculation

Computing system: MARC – elastic field, spatial elements

Optimization: not performed

Calculation variants: description of the calculation-model geometry is shown in Figures KLS9xR-1.1 and for Tongs with Extensions.

- Load Z1: Loading with hydraulic-cylinder force  $F_x = 4\,567\text{ kN}$  ( 20 MPa ).  
 Loading with hydraulic-cylinder-piston force  $F_x = 4\,567\text{ kN}$  ( 20 MPa ).  
 Prestressing of bolts M72.  
 Simulation of the weight of transferred forging (50 tons) with tilting moment of 1250 kNm.  
 Dead tongs weight included.  
 Effects of gravitation are in the direction of the Y-axis of the system of coordinates.
- Load Z2: Loading with hydraulic-cylinder force  $F_x = 4\,567\text{ kN}$  ( 20 MPa ).  
 Loading with hydraulic-cylinder-piston force  $F_x = 4\,567\text{ kN}$  ( 20 MPa ).  
 Prestressing of bolts M72.  
 Simulation of the weight of transferred forging (50 tons) with tilting moment of 1250 kNm.  
 Dead tongs weight included.  
 Effects of gravity are in the direction of the Z-axis of the system of coordinates.
- Load Z2.1: Loading with hydraulic-cylinder force  $F_x = 4\,567\text{ kN}$  ( 20 MPa ).  
 Loading with hydraulic-cylinder-piston force  $F_x = 4\,567\text{ kN}$  ( 20 MPa ).  
 Prestressing of bolts M72.  
 Simulation of the weight of a forging being transferred (40tons) with tilting moment of 1000 kNm.  
 Dead tongs weight included.  
 Effects of gravitation are in the direction of the Z-axis of the system of coordinates.

The calculation has been performed for various load combinations.

For all loads, numerical, computational stability is ensured by introduction of homogenous edge conditions into some nodes.

Working load spectrum: The above-mentioned stationary loads have been evaluated for various spectra.

Number of loading cycles: Not specified

Required life:  $N_D > 1.0E7$  cycles (permanent)

Design assumptions:

- load is considered to be static,
- dead weight taken into account,
- geometrical non-linearity used,
- it is a non-linear calculation.

#### 4. Example of the outputs

Elasticity calculation results

Graphic outputs - deformations  $v_x$ ,  $v_z$  in the direction of global X-, Z-axes [mm], principal stress S1 (Fig. 4), design (reduced) stress SV acc. to HMH – [MPa].

##### **Strength evaluation:**

Ultimate state evaluation: Program system SKALA

Strength evaluation consists in the analysis of assumed critical sections and points in light of the possibility of occurrence of ductile, fatigue and sudden brittle fracture, including crack propagation.

The SKALA program fully utilizes the results of the strength solution using the system MARC in the linear field. To determine plastic deformation necessary to evaluate the life, generalized Neuber's principle has been applied widely.

Material characteristics: gained from the database SKALA (data acquired from CSN, CSN EN or other standards, from measurements, technical literature or from the expert estimate).

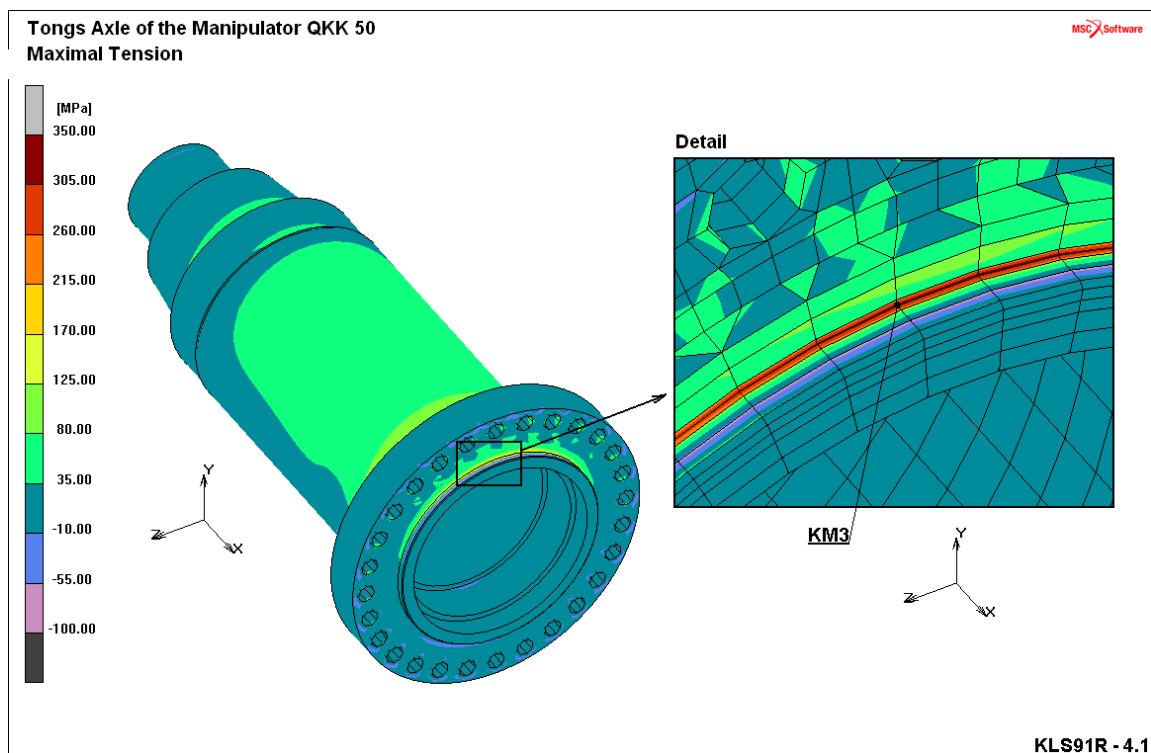


Fig. 4: QKK 50 manipulator tongs axle (load by a 50-t casting) - maximum principal stress  $S_1$ .

Type of loading: 1. Stationary amplitude of load (maximum operating one)

The ultimate states of ductile and sudden fracture are limited by maximum working or testing or emergency loads (if specified).

## 5. Conclusions

According to the results of the strength evaluation of the specified and final calculation variants of the tongs of the QKK 50 manipulator, it is possible to state the following:

- For the specified maximum operating load, the above mentioned materials and the working temperature range, the QKK 50 manipulator tongs comply in all critical points in terms of usually required safety both with the limit state of ductile fracture and with the limit state of sudden (brittle) fracture with a small up to a sufficient reserve.
- For the specified stationary maximum repetitive and/or alternating or pulsating operating loads, the above mentioned materials and the working temperature range, the QKK50 manipulator tongs comply in all critical points in terms of usually required safety with the fatigue limit state ( $N_D > 1.0E7$  cycles – permanent life) with a small up to sufficient reserve.
- For the specified non-stationary pulsating, repetitive or alternating working loads (see simulation spectra 1 through 4), the above mentioned materials and the working temperature range, the QKK50 manipulator tongs comply in terms of usually required safety with the required life of 19 years ( $N_D$  see point 2) with a sufficient reserve, even in all critical points as mentioned under point 2).
- Deformations of the QKK 50 manipulator tongs have also been analyzed.

## References

Mrkos J. (2010) Report V-007/10 QKK 50 Manipulator Tongs Calculation, Žďár nad Sázavou.



## THE ANALYSIS OF THE AUTOMOTIVE DIFFERENTIAL VIBRATIONS BY MEANS OF BIFURCATION DIAGRAM

M. Klapka<sup>\*</sup>, I. Mazůrek<sup>\*</sup>, Z. Strecker<sup>\*</sup>

**Abstract:** This article is concerned with capabilities of bifurcation and chaos analysis methods used for analysis of the automotive differential operation and noise. The purpose of the article is to give an overview of practical use of the above mentioned methods. The potential advantages, disadvantages are discussed as well as expected contributions of application of the bifurcation analysis to solving the automotive differential journal bearing noise problem.

**Keywords:** Automotive differential, sleeve bearing, chaos, bifurcation.

### 1. Introduction

Fighting the noise emitted by a running vehicle into the environment and into the passenger area is a long-lasting problem. The development department of the Škoda Auto manufacturer has dealt with this phenomenon recently. The automotive differential was identified as one of the noise sources. The stub shaft is inserted into the differential case through sleeve journal bearing which requires some radial clearance to be operational. Therefore, there is a mechanical looseness in the journal bearing which in combination with vibrations of the engine may result in an undesirable noise emission. The VW Group attempted to eliminate the problem by adjusting the radial clearance of the bearing with a tapered centring ring and an axial compression spring, see Fig. 1. However, new kinds of undesirable noises of the differential were observed under a different set of operating conditions compared to the previous case. The noise phenomenon related to the sleeve bearing arrangement without compression spring was labeled as “wummern” (perceived as drumming noise) and the noise of the bearing with the compression spring was labeled as “schnarren” (perceived as rough chattering noise). Brno University of technology was introduced to the problem. Our main goal was to identify the causes of the noise and to develop a method for identification of phenomena types. Therefore, an analytic method capable of determining the type of noise phenomenon was created by Mazůrek et. al (2009). The method processed measured values of the stub shaft center displacement relative to the center of the bearing. Although the described method proved as functional in practical applications we were looking for other ways to improve it or to perform even deeper analysis of the bearing operation. Thus, the analysis of the bifurcation diagrams and chaotic behavior of the bearing was suggested. Myers (1984)

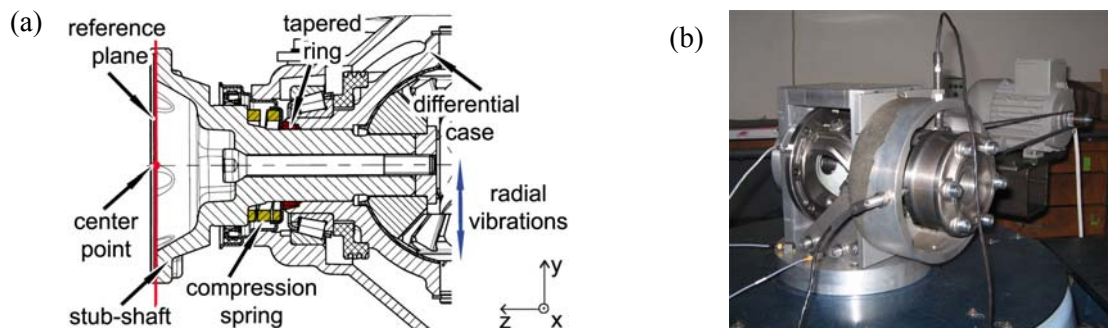


Fig. 1: a) Bearing arrangement with compression spring cut-away,  
 b) Test rig with differential in experimental box.

<sup>\*</sup> Ing. Milan Klapka, Ph.D., assoc. prof. Ing. Ivan Mazůrek, CSc. and Ing. Zbyněk Strecker: Institute of machine and industrial design, Brno University of technology, Faculty of mechanical engineering, Technická 2896/2; 616 69, Brno; CZ, e-mails: klapka.m@fme.vutbr.cz, mazurek@fme.vutbr.cz, y83216@stud.fme.vutbr.cz

applied Hopf bifurcation analysis to journal bearing stability problem. Addiletta et. al (1996) used methods of chaos analysis for examination of the system stability for rigid rotor with sleeve journal bearings. Some other applications of chaos and bifurcation analysis in solutions to journal bearing and rotor stability problems were described by Muszynska and Goldman (1995), Wang and Wang (2004), Laha and Kakoty (2010) or Wang (2010). The main goals of this article are: overview of the knowledge about applications of the bifurcation and chaos analysis methods to the automotive differential sleeve bearing with radial clearance, discussion of the results, and potential contributions to the solution process. Results acquired by means of bifurcation analysis are compared with results of the stub shaft displacement power summation analysis described by Mazurek (2009).

## 2. Examined bearing arrangements and operational conditions of the experiments

The bearing arrangement with adjustment of the radial clearance by tapered ring and compression spring (Fig. 1a) and an arrangement without the compression spring and tapered ring were experimentally examined.

The differential case was driven by controlled electromotor (see Fig. 1b) and was continuously slowed down from the speed of 3000 RPM to standstill. The speed of the differential case was proportional to the exciting vibrations which simulated vibrations of the vehicle engine. The exciting vibrations continuously decreased from 230 Hz to 10 Hz (corresponding to the maximum speed of 6900 RPM and the minimum speed of 300 RPM of the vehicle engine respectively, these values were also determined by technical parameters of the electrodynamic exciter). The amplitude of the exciting vibrations was 0.1 mm and the effect of decrease in excitation amplitude was observed with amplitude of 0.025 mm. The results of the experiments analyzed using the method of power summation of the stub shaft displacement are summarized in Tab. 1, where the greater value determines the type of noise emission.

Tab. 1: Parameters of the “wummern” and “schnarren” phenomena.

<i>Design of the bearing</i>	<i>wummern</i>	<i>schnarren</i>
<i>without compression spring, excitation amplitude 0.1 mm</i>	<i>0.474</i>	<i>0.357</i>
<i>without compression spring, excitation amplitude 0.025 mm</i>	<i>0.168</i>	<i>0.114</i>
<i>with compression spring, exciting amplitude 0.1 mm</i>	<i>0.222</i>	<i>0.553</i>
<i>with compression spring, exciting amplitude 0.025 mm</i>	<i>0.083</i>	<i>0.154</i>

## 3. Bifurcation diagrams

Bifurcation diagrams of the selected bearing designs with excitation amplitude of 0.1 mm and 0.025 mm are compared in Fig. 2. The frequency of the stub shaft center axis relative to displacement (in direction of exciting vibrations) passing through zero value as a function of the exciting vibrations frequency is depicted in the diagrams, the black line describes the ideal trajectory. The critical operating speeds are in the range from 2000 RPM to 6000 RPM. The difference between the bearing

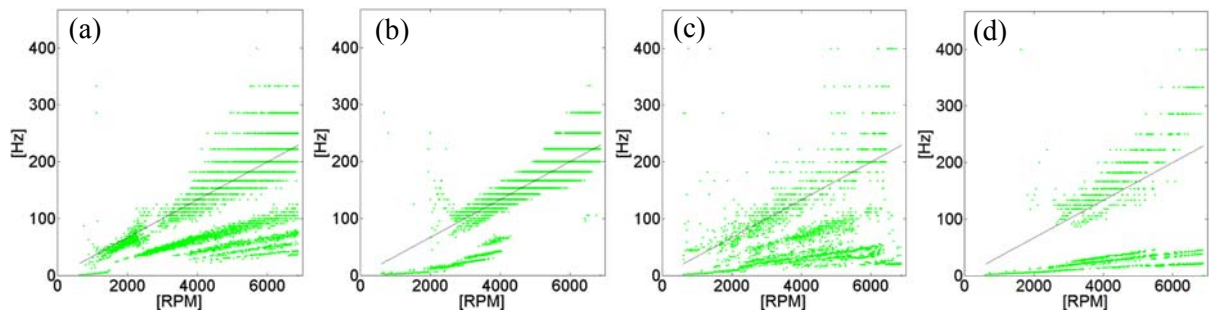


Fig. 2: The bifurcation diagrams of the bearing arrangement without compression spring (a), with the compression spring installed (b) both with exciting vibrations amplitude of 0.1 mm, and bearing arrangement without compression spring (c), with the compression spring installed (d) both with exciting vibrations amplitude of 0.025 mm.

design without compression spring and the one with the spring installed at the exciting vibrations amplitude of 0.1 mm is clearly visible from the comparison of the bifurcation diagrams, see Figs. 2a and 2b. There is a high amount of the bifurcations in the case of bearing without the spring. The sleeve bearing with radial clearance adjusted by the tapered ring and the compression spring has visibly lower bifurcation ratio and lower spread of points from the ideal trajectory of displacement frequency. Nonetheless, the behavior of stub shaft in the sleeve bearing is unstable in both of examined cases. It can, however, be claimed that the instability is somewhat lower in the case of bearing arrangement with compression spring. Interestingly, the resonance of the bearing at 4800 RPM has no significant effect on the bifurcation diagram pattern. The bifurcation diagrams of the stub shaft behavior loaded with 0.025 mm vibrations amplitude are shown in Figs. 2c and 2d. There are some significant changes in the pattern of the bifurcation diagrams, especially in the case of bearing design with compression spring. Observed differences between the diagrams arose most probably due to the reduced effect of exciting vibrations relatively to the effect of the differential case rotation and due to nonlinearity of the compression spring stiffness. From the results in Tab. 1 and bifurcation patterns in Fig. 2 it is possible to find that the higher amount of bifurcation (and spread of points from ideal trajectory) is characteristic for “wummern” type of noise. Lower amount of bifurcation (and spread of points from ideal trajectory) is characteristic for “schnarren” type of noise. Using subjective judgment it is possible to distinguish between the two observed types of noise. However, it would be more appropriate to find an objective criterion for this purpose. Therefore, an analysis of the phase trajectories was carried out.

#### 4. Phase-trajectory diagrams

Analysis of dependence of the stub shaft center displacement in the direction of the exciting vibrations on the displacement speed was performed and phase-trajectory diagrams of the center point radial vibrations (see Fig. 1) were created for every single revolution of the differential case. From the phase trajectories in Figs. 4, 5, 6 and 7 it is obvious that the bearing subjected to combination of exciting vibrations and rotation of differential case is unstable in the whole range of observed operational speeds irrespective of the bearing arrangement. Therefore, mostly chaotic attractors were observed. Only the bearing arrangement with compression spring tends to stable behavior for speeds above 4000 RPM and exciting vibrations amplitude of 0.1 mm (see Fig. 6). Such behavior could be related to the resonance of the bearing assembly at 4800 RPM. It seems that the effect of displacement in direction of the exciting vibrations is strengthened by resonance against the effect of rotation and the system tends to be more stable. However, there are more steel-on-steel impacts which result in undesirable noise emission. The phase-trajectory diagrams analysis seems to be unsuitable for the objective of distinguishing between examined noise phenomena because only chaotic phase trajectories were observed. No significant differences are noticeable between phase trajectories of the bearing without the compression spring and the bearing with the spring. Therefore no explicit criterion can be expressed for differentiation between “wummern” and “schnarren” noises.

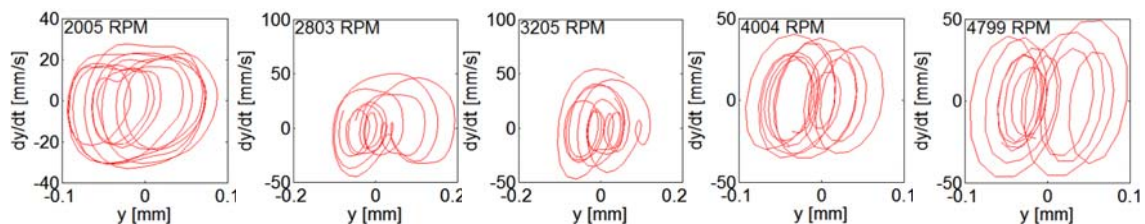


Fig. 4: Phase trajectories of the bearing arrangement without compression spring, amplitude 0.1 mm.

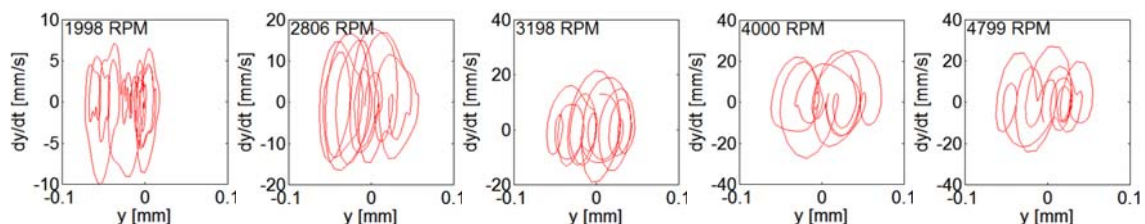


Fig. 5: Phase trajectories of the bearing arrangement without compression spring, amp. 0.025 mm.

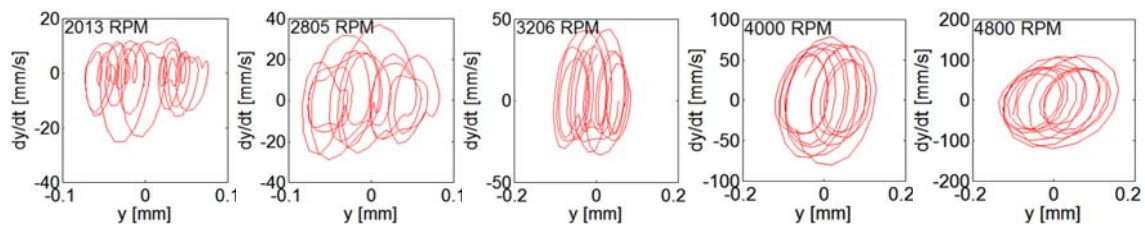


Fig. 6: Phase trajectories of the bearing arrangement with compression spring, amplitude 0.1 mm.

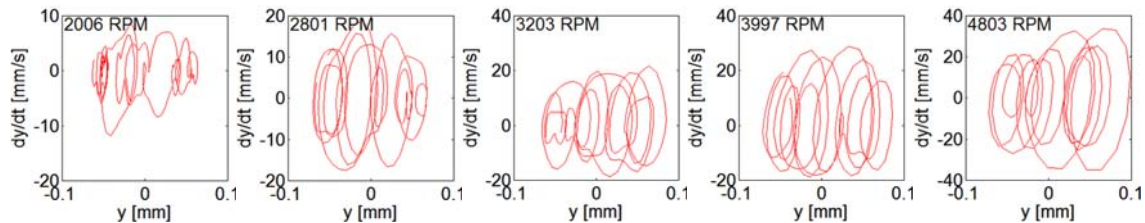


Fig. 7: Phase trajectories of the bearing arrangement with compression spring, amplitude 0.025 mm.

## 5. Conclusions

From the results of the bifurcation and phase diagrams analyses it is obvious that these methods can be used in combination with previously developed power summation analysis, mostly for better understanding of the bearing behavior. Generally, it is possible to subjectively differentiate the “wummern” and “schnarren” phenomena based on the bifurcation diagrams analysis (see Fig. 2), although no explicit criterion can be derived. The analysis of the phase-trajectory diagrams was carried out but the results were unsatisfactory. Neither objective nor subjective way of distinguishing between observed noises could be found from achieved results. Possibly, an estimate of the attractor dimension could be considered as an objective parameter if one assumes existence of explicit differences between attractor dimension values of the “schnarren” and “wummern” phenomena. Therefore, combined analysis using chaos and bifurcation methods could provide a lot of information about bearing behavior under various operating conditions. However, benefits of such complex data for design engineers in practical applications are questionable. Nonetheless, the combination of bifurcation and chaos analysis methods could be either valuable supplement of the stub shaft displacement power summation method or an alternative standalone analysis method for sleeve bearing behavior and noise assessment.

## Acknowledgement

These results were acquired with support of GACR 101/10/P429 and FSI-S-10-30.

## References

- Adiletta, G., Guido, AR., Rossi, C. (1996) Chaotic motion of rigid rotor in short journal bearing. *Nonlinear Dynamics*. 10, 3, pp. 251–69.
- Laha, S.K., Kakoty, S.K. (2011) Non-linear dynamic analysis of a flexible rotor supported on porous oil journal bearings. *Communications in Nonlinear Science and Numerical Simulation*. 16, 3, pp. 1617-1631.
- Mazurek, I. Klapka, M. Roupec, J. (2009) Noise Reduction of the Differential Sleeve Bearing. *Engineering Mechanics*. 16, 2, pp. 93 - 102.
- Muszynska, A. Goldman, P. (1995) Chaotic responses of unbalanced rotor/ bearing/stator systems with looseness or rubs. *Chaos, Solitons & Fractals*. 5, 9, pp. 1683-1704.
- Myers, C.J. (1984). Bifurcation Theory Applied to Oil Whirl in Plain Cylindrical Journal Bearings. *Journal of Applied Mechanics*. 51, 2, pp. 244 – 251.
- Wang, Ch. Ch. (2010) Bifurcation and nonlinear analysis of a flexible rotor supported by a relative short spherical gas previous bearing system. *Communications in Nonlinear Science and Numerical Simulation*. 15, 9, pp. 2659-2671.
- Wang, J.S., Wang, Ch. Ch (2005) Nonlinear dynamic and bifurcation analysis of short aerodynamic journal bearings. *Tribology International*. 38, 8, pp.740–748.



## STUDY OF SURFACE TOPOGRAPHY GENERATED BY THE ACTION OF PULSATING WATER JET

J. Klich <sup>\*</sup>, J. Valíček <sup>\*</sup>, L. Sitek <sup>\*</sup>, J. Foldyna <sup>\*</sup>, M. Harničárová <sup>\*\*</sup> P. Hlaváček <sup>\*</sup>

**Abstract:** *The paper is dealing with study of the surface topography created by the pulsating water jet. Topography is evaluated by height characteristics of the surface roughness (average roughness Ra and average maximum height of the profile Rz). The data obtained from surface texture are analyzed and interpreted in relation to the stand-off distance between the nozzle and the surface.*

**Keywords:** *Pulsating water jet, surface roughness, surface topography.*

### 1. Introduction

During more than 30 years of intensive development, high-speed water jet has gained a steady place in many fields of human activity. In addition to typical applications such as cutting of various materials by both water jet and abrasive water jet, removal of coatings and deposits from surfaces and utilisation of the jet in repair of concrete structures and buildings, the possibility of using of water-jet for surface treatment is investigated in recent years. The objective is to induce changes in surface topography (Borkowski, 2009; Frenzel, 1997; Toutanji & Ortiz, 2001) or to affect properties of surface layers e.g. by residual stress removal or peening (Colosimo & Monno, 1999; Gumkowski, 2003; Ju & Han, 2009).

Efficiency of conventional continuous jets can be significantly increased by using high-frequency pulsating water jets, which break up in air to separate water flow into water bunches (Foldyna et al., 2009). The impact pressure (so-called water-hammer pressure) generated by an impact of bunch of water on the target material is considerably higher than the stagnation pressure generated by corresponding continuous jet. In addition, the action of pulsating jet induces also fatigue and shear stresses in the target material due to the cyclic loading of the target surface and tangential high speed flow across the surface, respectively. Based on these effects one can expect even wider use of pulsating jets in surface treatment applications than in the case of conventional continuous ones.

The paper presents study of topography of surface created during experiments by the pulsating water jet impact on aluminum at different distances from the nozzle exit. Fan pulsating jet that enables to spread the jet energy to greater width (depending on inner geometry of the nozzle) was used in the experiments.

### 2. Material disintegration by pulsating water jet

Disintegration effects of the pulsating jet can be, depending on the stand-off distance from the nozzle, divided into three regions. In the first region the pulsating jet escapes from the nozzle as a continuous jet and due to uneven flow velocity it breaks up in air into separate bunches of water at some distance (in order of centimetres). In this region, the effects of the jet on material are similar to that of continuous one, i.e. insignificant when operating water pressure is of tens of MPa. The best performance of pulsed jet can be observed in the second region – after breaking up of the continuous jet to bunches. In this disintegration region, the jet easily disintegrates very hard materials (like metals,

---

<sup>\*</sup> Ing. Jiří Klich, assoc. prof. Ing. Jan Valíček, Ph.D., Ing. Libor Sitek, Ph.D., Ing. Josef Foldyna, CSc. and Ing. Petr Hlaváček: Institute of Geonics of the AS CR, v. v. i., Studentská 1768; 708 00, Ostrava; CZ, e-mails: jiri.klich@ugn.cas.cz, jan.valicek@ugn.cas.cz, libor.sitek@ugn.cas.cz, josef.foldyna@ugn.cas.cz, petr.hlavacek@ugn.cas.cz

<sup>\*\*</sup> Ing. Marta Harničárová: Faculty of Manufacturing Technologies of Technical University of Košice with a seat in Prešov, Bayerova 1, 080 01 Prešov, SK, e-mail: marta.harnicarova@tuke.sk

rocks, ceramics, etc.). The third, final region is characterized by breaking of bunches of water to small droplets at higher stand-off distances due to air friction (jet breakage region). The jet ability to disintegrate material significantly decreases, only droplet erosion occurs.

The surfaces of various materials exposed to the action of pulsating water jets are generally quite irregular and rough with larger true surface area compared to continuous jet. This is due to a combination of several failure mechanisms affecting the surface in disintegration region of the jet. Subsequent use of such surfaces could be interesting from the point of view of their friction characteristics and/or aesthetic appearance. However, they could be also used in applications where good adhesion of coating layer or new overlay material to substrate surface both in tension and shear is needed. Adequate macroscopic substrate roughness provides good mechanical locking and a large surface area for bonding. Thus, the overlay is properly mechanically linked with the substrate. Commonly used characteristics of the surface indicating the surface adhesion ability are roughness parameters  $Ra$  (average roughness) and  $Rz$  (average maximum height of the profile). Ratio of  $Ra/Rz$  then can provide information about properties of a new surface of the given material for application of specific coating.

In order to study even small disintegration effects of pulsating jet during the surface treatment, it was necessary to select appropriate material for testing. Aluminum appears to be one of suitable technical materials for these purposes due to its properties (soft, homogeneous and isotropic).

### 3. Experimental setup

Scheme of experimental arrangement for treatment of material surface by pulsating water jet is shown in Fig. 1. Test samples were prepared from 50 mm wide and 5 mm thick cold rolled aluminum strip (99.5% of aluminum). High-pressure water was supplied to the nozzle by a plunger pump; operating pressure was maintained at 30 MPa. High-pressure water was then fed into the acoustic generator of pressure pulsations equipped with fan nozzle (equivalent nozzle diameter of 2.05 mm, spraying angle of  $15^\circ$ ). Pressure pulses in high-pressure fluid were generated at frequency 20 kHz with amplitude of vibration  $3\text{ }\mu\text{m}$ . Pressure pulsations before the nozzle exit were changed to velocity pulsations in the nozzle and thus flat pulsating jet was created. The jet was moved over the test sample at feed rate of  $0.1\text{ m}\cdot\text{min}^{-1}$ . The stand-off distance  $L$  was progressively changed during the experiments ( $L = 30, 35, 40, 50, 60, 70, 80$  and  $90\text{ mm}$ ). Fig. 1 shows arrangement of experiments.

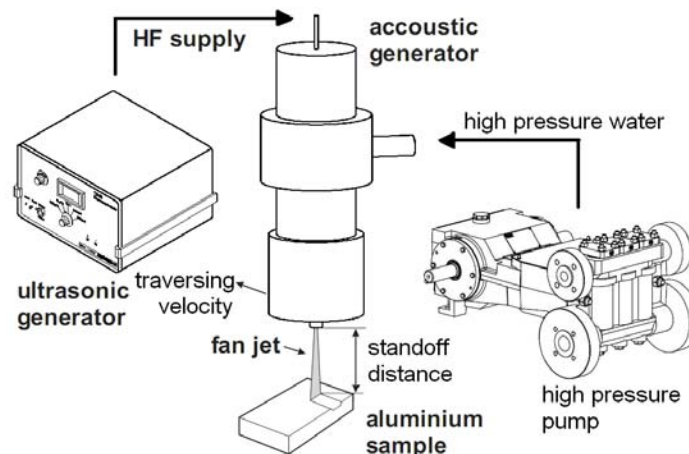


Fig. 1: Schematic diagram of experimental setup.

Slots created by the jet in the test aluminum sample were studied using optical profilometer FRT MicroProf (see example of slot reconstruction on Fig. 2). Ten profiles of the surface in the x-axis direction (perpendicular to the movement of the jet) and ten profiles in the y-axis direction (along the movement of the jet) were measured on the square area of  $5\times 5\text{ mm}$ . Measured data were processed using Mark III firmware and characteristics of surface roughness  $Ra$  and  $Rz$  were determined.



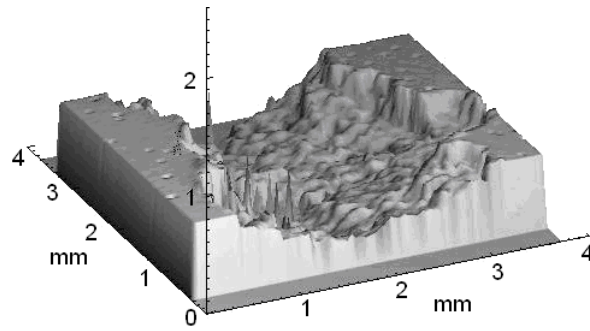


Fig. 2: 3D topography reconstruction of new surface created by the action of fan pulsating water jet.

#### 4. Results and discussion

The values of surface roughness ( $Ra$  and  $Rz$ ) in both directions ( $x$  and  $y$ ) obtained under the same working conditions were compared to each other. Statistical analysis proved that the surface created by pulsating jet is not influenced by the direction of motion of the jet above tested material (as in the case of many conventional machining methods).

Graphs of surface roughness parameters  $Ra$  and  $Rz$  in relation to the stand-off distance  $L$  are presented in Figs. 3 and 4. It can be seen that values of both  $Ra$  and  $Rz$  increase with increasing stand-off distance  $L$  up to approximately  $L = 80$  mm. At higher stand-off distances, values of  $Ra$  and  $Rz$  drop down significantly due to the fact that at the stand-off distance of approximately 90 mm the pulsating jet breaks up already into small droplets that do not have enough energy to erode aluminum surface (the stand-off distance is situated in the jet breakage region). The dependence of the roughness of surface treated by fan pulsating jet at stand-off distances from 30 to 80 mm (i.e. at disintegration region of the pulsating jet) can be roughly approximated by the regression line (shown in Figs. 3 and 4).

Next step was to determine the ratio of surface roughness parameters  $Ra/Rz$  (Fig. 5). The graph clearly shows that the stand-off distance has negligible effect to the ratio  $Ra/Rz$  and the ratio values are roughly the same in disintegration region. It can be stated that pulsating jet operating within the disintegration region creates surfaces with the same ability to mechanically lock paintings and other coatings applied to treated substrate. Another situation occurs in the jet breakage region, where the ratio  $Ra/Rz$  decreases significantly due to change in jet acting and thus also mechanism of material failure.

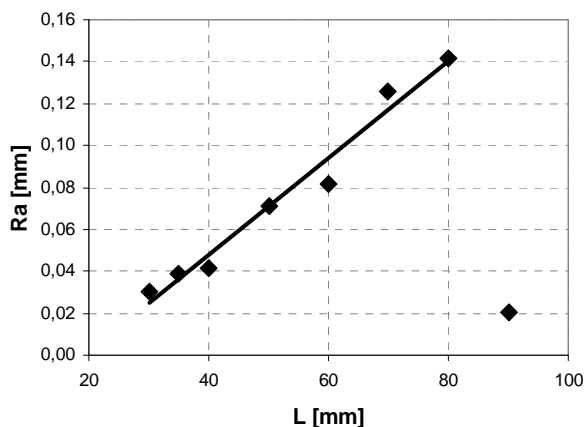


Fig. 3: Average roughness  $Ra$  depending on the stand-off distance  $L$  from the nozzle exit.

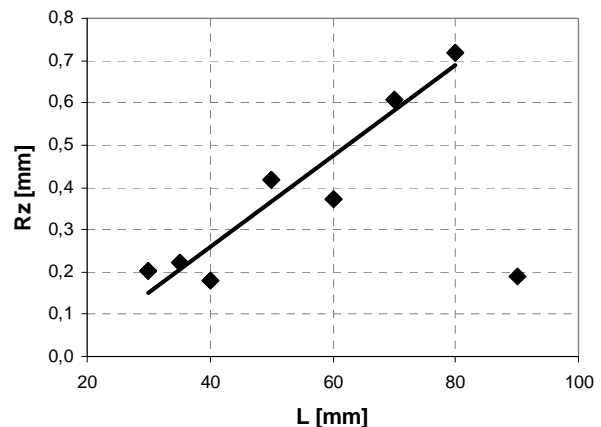


Fig. 4: Average maximum height of profile  $Rz$  depending on the stand-off distance  $L$  from the nozzle exit.

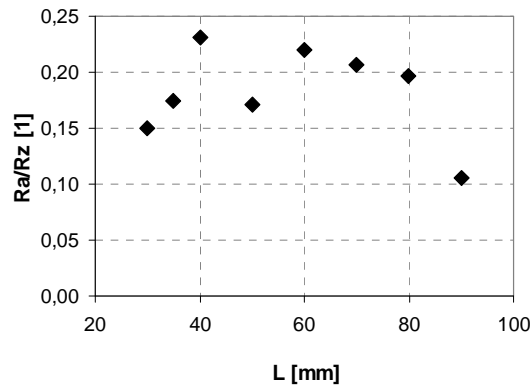


Fig. 5: Ratio  $Ra/Rz$  depending on the stand-off distance  $L$  from the nozzle exit.

## 5. Conclusions

This paper has focused attention on determination of basic surface profile parameters of aluminum surface newly created by pulsating water jet and their description. Surface profile parameters  $Ra$  and  $Rz$  were evaluated with respect to stand-off distance from the nozzle exit. In the disintegration region of pulsating jet both parameters  $Ra$  and  $Rz$  increase with increasing of stand-off distance, however, their ratio remains roughly constant. Because of change of failure mechanisms of material exposed to the pulsating jet in jet breakage region, not only decrease in  $Ra$  and  $Rz$  parameters but also decrease of their ratio can be observed.

The knowledge of surface description is very important in terms of adjustment of optimum technological parameters of pulsating water jet in relation to work-piece material and required quality of finished surface. Apart from stand-off distance, the ability of pulsating jet to disintegrate material may be influenced by many other parameters (such as water pressure, type, diameter and internal geometry of the nozzle, feed rate of the jet, frequency and amplitude of acoustic pulses, etc.). These factors will probably also affect the final texture of newly formed surface. Study of influence of these factors on surface texture will represent next step of our research.

## Acknowledgement

The work has been supported by project ASCR No. AV0Z30860518 and project Institute of clean technologies for mining and utilization of raw materials for energy use, reg. no. CZ.1.05/2.1.00/03.0082 supported by Research and Development for Innovations Operational Programme financed by Structural Funds of Europe Union and from the means of state budget of the Czech Republic.

## References

- Borkowski, P. (2009) Abrasive grains distribution in high-pressure abrasive-water jet used for surface treatment. Archives of Civil and Mechanical Engineering, Vol. 9, Iss. 3, pp. 5-16.
- Colosimo, B.M., Monno, M. (1999) Surface Strengthening by Water Jet Peening. Proceedings of the 5th International Conference on Advanced Manufacturing Systems and Technology, (Kuljanic ed.), Springer, Wien, pp. 627-634.
- Foldyna, J., Sitek, L., Ščučka, J., Martinec, P., Valíček, J. and Páleníková, K. (2009) Effects of pulsating water jet impact on aluminium surface. Journal of Materials Processing Technology Volume 209, Issue 20, Special Issue: 1st International Conference on Abrasive Processes, pp. 6174-6180.
- Frenzel, L. (1997) Continuous improvement initiatives of surface preparation with waterjetting. Proc. 9th. Amer. Waterjet Conf. (Hashish ed.), WJTA, St. Louis, pp 697-716.
- Gumkowski, S. (2003) Some aspects of surface cooling by impinging jets. Proceedings of the 4th Baltic Heat Transfer Conference (Sunden, Vilemas eds.), Begell House, Inc., New York, pp. 347-354.
- Ju, D.Y., Han, B. (2009) Investigation of water cavitation peening-induced microstructures in the near-surface layer of pure titanium. Journal of Materials Processing Technology. Vol. 209, Iss. 10, pp. 4789-4794.
- Toutanji, H., Ortiz, G. (2001) The effects of surface preparation on the bond interface between FRP sheets and concrete members. Composite Structures. Vol. 53, pp. 457-462.

## CFD SIMULATION OF FLOW OVER A WAVY SURFACE

S. Knotek<sup>\*</sup>, M. Jícha<sup>\*</sup>

**Abstract:** *The paper presents CFD simulation of flow over a wavy surface for selected geometric configurations and external flow velocities. The simulation characteristics and results are described in relation to the computational model whose assumptions are confirmed. The wall shear stress and pressure profile are investigated in dependence on the ratio of the wave amplitude to the wavelength.*

**Keywords:** *CFD, wavy surface.*

### 1. Introduction

The motivation of the general problem of gas flow over solid wavy surface can be seen in the efforts to propose computational models for prediction of hydrodynamic instabilities, which are generated by air flowing over the liquid film surface. Among a variety of approaches, the so-called quasi-static approach has its importance. It is based on the assumption that, for large ratios of fluid viscosities, the surface can be considered as static and solid. In the first step, the force effects of the gas flow acting on the solid surface defined by amplitude and wavelength are evaluated. These forces are then included in the calculations of the main problem of instability prediction.

As a crucial physical quantity for the instability occurrence, the shear and pressure forces acting on the wavy liquid surface have been identified (Hanratty, 1983). To calculate these quantities the approach based on the solution of the Orr-Sommerfeld equation modified by a specific turbulent model was proposed. The most used model is shown by (Abrams, 1984). Although the dimensionless wave number  $\alpha^*$  defined by (Abrams, 1984) is given in the range

$$0.0005 < \alpha^* = \frac{2\pi\nu}{\lambda u^*} < 0.01, \quad (1)$$

where  $u^*$  is friction velocity,  $\lambda$  wavelength and  $\nu$  kinematic viscosity, this model is validated only by experiments carried out for the selected ratio of wave amplitude to wavelength  $a/\lambda = 0.007$ . This fact, as well as the need to obtain data for models mentioned above, has motivated the validation of results and assumptions of this computational model for a larger number of ratios  $a/\lambda$  by a different methodology. Given the apparent complexity of real experiments, the approach of numerical experiments using CFD methods was chosen.

### 2. Characteristics of the CFD model

According to theoretical models based on the Kelvin-Helmholtz theory, the hydrodynamic instabilities grows at a speed of the gas flow around  $U = 7$  m/s (Hanratty, 1983). Therefore, the external flow velocity was set in the range  $U = 2$ -12 m/s. The range of ratios  $a/\lambda$  is based on the assumption that the instability arises from infinitesimal deviations of the surface from equilibrium level. The geometry of the waves was therefore defined by the scope of the ratio  $a/\lambda$  ranging from 0.005 to 0.05 covering also the experimental setup by (Abrams, 1984). The geometric model was created in software StarCCM+. The waves were modeled by a harmonic function with constant amplitude  $a = 0.5$  mm.

Due to the fact that the investigated physical parameters are affected by the growth of the boundary layer thickness, the computational domain was created in such a way that the area of measurement of physical quantities corresponds to the wave crest at the distance of 0.75 m from the leading edge. This

---

<sup>\*</sup> Ing. Stanislav Knotek and prof. Ing. Miroslav Jícha, CSc.: Energy Institute, Brno University of Technology, Technická 2896/2; 616 69, Brno; CZ, e-mails: knotek@fme.vutbr.cz, jicha@fme.vutbr.cz

geometrical configuration induces the same local Reynolds number  $Re_x$  for the same velocity of air flow, which allows the study of the influence of the ratio  $a/\lambda$  on the values of physical characteristics. Computational grid density was chosen so that, in the case of the shortest wavelength, the section of one wavelength in the direction of airflow is generated by 20 computational cells. Due to the influence of the velocity profile on the wall shear stress, 12 prismatic layers were created in the near-wall region to increase the accuracy of the model. Given the symmetrical nature of the problem, 2D geometry was used. The mesh in the case of the ratio  $a/\lambda = 0.025$  is shown in Fig. 1.

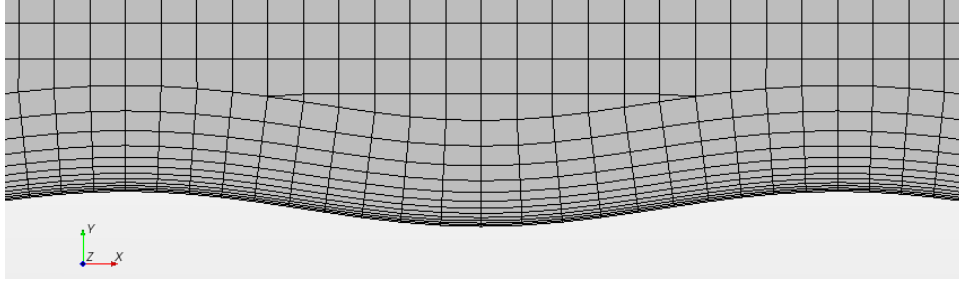


Fig. 1: The near-wall region mesh of the geometry model.

The height of the computational domain in all cases was set to  $h = 0.05$  m. On the upper side, the symmetry boundary condition corresponding to the flow over the flat plate was prescribed. Because of the unknown velocity profile above the wavy surface, the uniform velocity profile was set on the input located on the left-hand side of the computational area. The boundary layer thickness was along the entire length of the area in all cases less than  $h/2$ . Given the geometric configuration and the nature of the flow over the surface, the turbulence model  $k-\omega$  SST, see (Menter, 1994), was chosen.

### 3. Theoretical background

The paper (Abrams, 1984) presents a theoretical model of flow over a wavy surface that is defined by harmonic function

$$y = a \cos \alpha x, \quad (2)$$

where  $\alpha = 2\pi/\lambda$  is wavenumber corresponding to the wavelength  $\lambda$ . The model is based on the solution of the linearized Navier-Stokes equation for parallel flow with implemented turbulence model. The basic assumption of the model is the condition that the amplitude of the wave was small in comparison with the wavelength and the thickness of the boundary layer. Under these assumptions, the pressure and shear stress acting on the surface in the direction of the basic flow (x-direction) can be expressed by relations

$$\tau = \bar{\tau} + \tau' = \bar{\tau} + a\hat{\tau}e^{i\alpha x}, \quad (3)$$

$$P = \bar{P} + P' = \bar{P} + a\hat{P}e^{i\alpha x}, \quad (4)$$

where  $\hat{\tau}$  and  $\hat{P}$  are complex numbers

$$\hat{\tau} = \tau_{SR} + i\tau_{SI}, \quad (5)$$

$$\hat{P} = P_{SR} + iP_{SI}. \quad (6)$$

The shear stress and pressure fluctuations are therefore modeled by harmonic functions and described by formulas

$$\tau' = a(\tau_{SR} \cos \alpha x - \tau_{SI} \sin \alpha x), \quad (7)$$

$$P' = a(P_{SR} \cos \alpha x - P_{SI} \sin \alpha x), \quad (8)$$

where quantities  $\tau_{SR}$ ,  $\tau_{SI}$ ,  $P_{SR}$  and  $P_{SI}$  are dependent on the air velocity and on the wavenumber  $\alpha$ .

## 4. Results

### 4.1. Wall shear stress

From the formulas (3) and (7) follows that the wall shear stress fluctuation is modelled by harmonic function. The amplitude of this quantity and its phase shift against the wavy surface are defined by variables  $\tau_{SR}$  and  $\tau_{SI}$ . Simulations results, see Fig. 2, shows that the course of the average wall shear stress is harmonic for velocities lower than  $U = 12$  m/s if  $\lambda/a \geq 60$ . However, for shorter wavelengths, the back-flow occurs, see Fig. 3, for all velocities greater than 2 m/s and therefore the harmonic character is deformed.

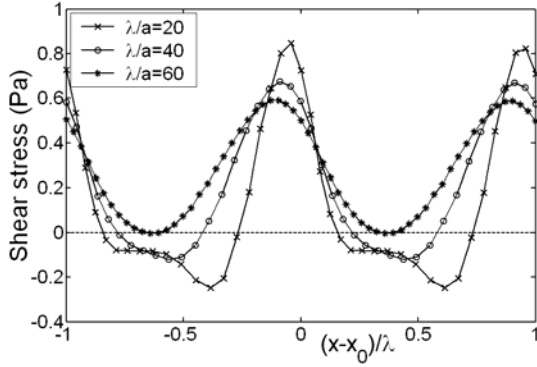


Fig. 2: The course of the shear stress for  $U=12$  m/s and  $\lambda=[0.01;0.02;0.03]$ m.

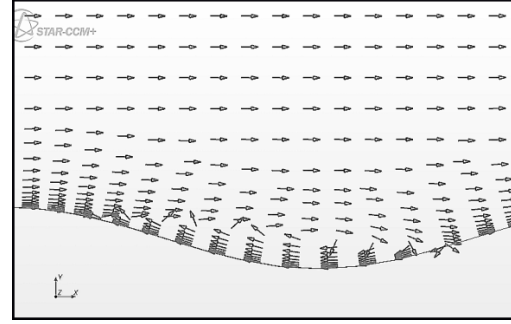


Fig. 3: Illustration of the back-flow for  $U=12$  m/s and  $\lambda=0.01$ m .

Fig. 2 indicates that the wavelength  $\lambda$  affects the amplitude and phase shift of the wall shear stress maximum to the wave crest. Recall that  $x_0=0$  in Fig. 2 corresponds to the wave crest at distance 0.75 m from the leading edge for all wavelengths. The dependency of the maximum values and phase shifts on the ratio  $\lambda/a$  shows Figs. 4 and 5 respectively.

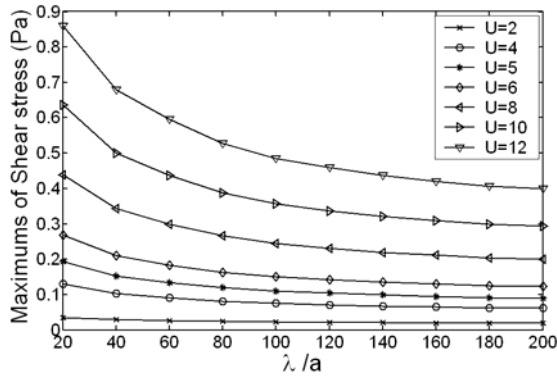


Fig. 4: Shear stress maximums in dependence on the ratio  $\lambda/a=20-200$  for  $U=2-12$  m/s.

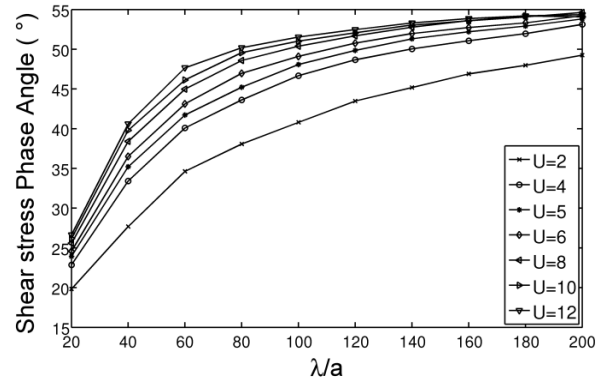


Fig. 5: Phase shift of the shear stress maximums in dependence on ratio  $\lambda/a$  for  $U=2-12$  m/s.

Fig. 4 illustrates that, for different flow velocities, the curves of the wall shear stress reduction in dependence on the growing ratio  $\lambda/a$  are mutually correlated. In contrast, the phase shifts of the wall shear stress to the wave crest do not show such a degree of correlation for different flow velocities, see Fig. 4. However, a clear increasing trend with increasing ratio  $\lambda/a$  is observed. Note that  $360^\circ$  degree phase shift corresponds to the  $\lambda$  shift of the wall shear stress maximum against the wave crest in Fig. 5.

### 4.2. Pressure

As in the case of the wall shear stress, simulations show that the pressure profile can be considered as harmonic if  $\lambda/a \geq 60$ . Fig. 6 illustrates the dependence of pressure minimums which are located near the wave crests and are important for the liquid film instabilities as well as the maximum values of the shear stress. From the figure can be further seen that minimums of the curves are located between  $\lambda/a = 40$  and  $\lambda/a = 60$ . From the simulations data does not follow a well-defined dependence of the

wave crests vs. pressure minimums phase shifts on the ratio  $\lambda/a$ . However all values of the shifts of the pressure minimums lie in the range from  $2^\circ$  to  $6^\circ$  for external flow velocities greater than 2 m/s.

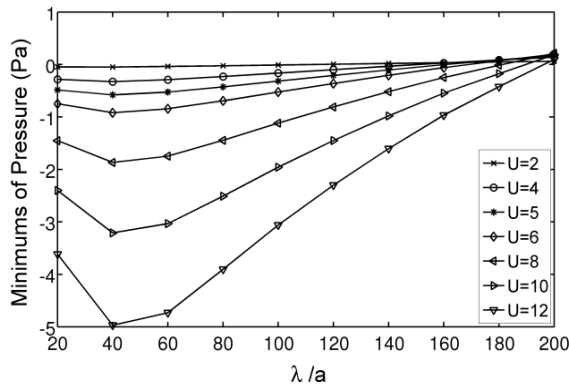


Fig. 6: The pressure minimums in dependence on  $\lambda/a$  for  $U=2-12$  m/s.

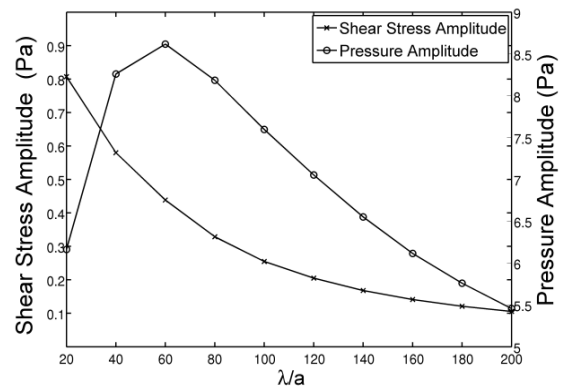


Fig. 7: The amplitudes of shear stress and pressure fluctuations for  $U=10$  m/s.

In the solution of the liquid film instability problem, the amplitudes of fluctuations  $|\tau'|$  and  $|P'|$  have its significance as well as average values of these quantities. The simulations shows that the amplitude of  $|\tau'|$  decreases with increasing  $\lambda/a$ , while the amplitude  $|P'|$  reaches its maximum in the neighborhood of the ratio  $\lambda/a = 60$ . Fig. 7 illustrates these quantities for  $U=10$  m/s.

## 5. Conclusions

This paper presents results of simulations of flow over a wavy solid surface described by a harmonic function and defined via the ratio of wavelength to the wave amplitude  $\lambda/a$  ranging from 20 to 200. The external flow velocity was set in the range from 2 to 12 m/s. With regard to the application of these results in the problem of the liquid film instability, the shear stress and pressure forces acting on the surface were studied. The aim of the research is primarily to assess the adequacy of computational models and their assumptions for selected geometrical and physical configuration. Subsequently, the issue is the possibility of using data obtained from CFD simulations as input parameters to the liquid film instability models.

The simulation results show that the assumptions of computational models are satisfied for  $\lambda/a \geq 60$  at least for the external flow velocity up to 12 m/s. In general, simulations confirm a considerable dependence of the physical quantities on the ratio  $\lambda/a$ . However, the computed values of friction velocity induce values of  $\alpha^*$  ranging from 0.0017 to 0.0574, which insufficiently cover the interval (1). Therefore, further simulations for greater external velocities are needed to detailed examination of the obtained data in comparison with computational models.

## Acknowledgement

The article was supported by the project of Czech Science Foundation GA101/08/0096.

## References

- Abrams, J. (1984) Turbulent flow over small amplitude solid waves, Ph.D. Dissertation, University of Illinois at Urbana-Champaign.
- Hanratty, T. J. (1983) Interfacial instabilities caused by air flow over a thin liquid layers, Waves on Fluid Interfaces (Edited by Meyer, R. E.), Academic Press, New York, pp. 221-259.
- Menter, F. R. (1994) Two-Equation Eddy-Viscosity Turbulence Models for Engineering Applications, AIAA Journal, vol. 32, pp. 269-289.



## COMPARISON OF P1P1 AND Q1P0 “TAYLOR-HOOD ELEMENTS” IN FLOW PROBLEMS

F. Kolařík\*, B. Patzák\*

**Abstract:** *This paper deals with comparison of two low-order finite elements used to describe homogenous incompressible flow in two dimensions with Eulerian description. The governing equations are presented as well as their discretized form obtained using traditional Galerkin method. Necessary stabilization techniques are discussed, allowing using interpolations violating LBB condition, application to convection-dominated problems, etc. The elements are compared on an example of lid cavity driven flow.*

**Keywords:** *Lid-driven, cavity, flow, stabilization, level set.*

### 1. Introduction

This paper is focused on comparison of different low-order elements used to model homogenous fluid flows. In the longer perspective, these elements will be used to simulate casting of fresh concrete. In present approach, the fluid is considered as homogenous continuous medium, the flow is described by Navier-Stokes equations and solved by the means of Finite element method. There are in principle three ways, how to describe motion of continuous medium. In Lagrangian description, motion of each point is described in framework of reference configuration. This approach is usually used in structural mechanics, for fluid dynamics is suitable only if discrete particle model is used. Otherwise, large deformations requires frequent remeshing. In Eulerian description, motion is connected to actual configuration and therefore, convective term is present. In this case, computation can be done on a fixed grid and no remeshing is needed. So called ALE formulation combines both and is proper in fluid-structure interaction. Further information can be found for example in (Donea & Huerta, 2003). In the present work, Eulerian formulation is used. Due to the presence of convective terms, an additional stabilization is needed. Two types of elements are used: Q1P0, a quadrilateral element with linear approximation of velocity and constant approximation of pressure and T1P1, a triangular element with linear approximation for both velocity and pressure fields. Either T1P1 or Q1P0 do not satisfy so called LBB stability condition, so proper pressure stabilization technique is necessary.

### 2. Governing equations, weak formulation and discretization

The flow of continuous Newtonian fluid is described by Navier-Stokes equation (1), which represents balance of momentum. Further, an incompressibility is assumed and therefore the velocity field must be divergence free (2):

$$\rho \frac{\partial \mathbf{u}}{\partial t} + \rho \mathbf{u} \cdot \nabla \mathbf{u} - \nabla \cdot \boldsymbol{\sigma} = \mathbf{b} \quad , \quad (\mathbf{x}, t) \in \Omega_t \quad (1)$$

$$\nabla \cdot \mathbf{u} = 0 \quad , \quad (\mathbf{x}, t) \in \Omega_t \quad (2)$$

Standard Dirichlet (3) and von Neumann (4) boundary condition are prescribed at the complementary parts of domain boundary:

$$\mathbf{u} = \mathbf{g} \quad , \quad \mathbf{x} \in \Gamma_g \quad (3)$$

---

\* Ing. Filip Kolařík and prof. Dr. Ing. Bořek Patzák: Department of Mechanics, Czech Technical University in Prague, Thákurova 7; 166 29, Prague; CZ, e-mails: filip.kolarik@fsv.cvut.cz, borek.patzak@fsv.cvut.cz

$$\mathbf{n} \cdot \boldsymbol{\sigma} = \mathbf{h}, \mathbf{x} \in \Gamma_h \quad (4)$$

In equations (1-4),  $\boldsymbol{\sigma}$  is stress tensor,  $\mathbf{u}$  is velocity field,  $\mathbf{b}$  vector of body forces and  $\rho$  is fluid density.

Weak formulation of problem (1-4) can be obtained using traditional Galerkin method. However, the standard Galerkin method is not very suitable for convection-dominated problems. In such case, non-physical oscillations are generated and computed solution is not realistic, as it is reported for example in (Donea & Huerta, 2003). Therefore, some stabilization technique to prevent the oscillations is needed. In this work, SUPG (Streamline Upwind – Petrov/Galerkin) and LSIC (Least squares on incompressibility constraint) stabilizations are used, but also different techniques are possible, for further references, see (Tezduyar, 2000), for example.

Another problem arising from numerical computations is due to treating incompressibility condition. Due to this assumption is not possible to compute pressure from any constitutive equation; pressure is another degree of freedom. In fact, pressure is a Lagrange multiplier on incompressibility constraint, and thus is determined by satisfying incompressibility condition. Function spaces for velocity and pressure are not independent, sufficient condition for convergence is so called LBB (Ladyzenska-Babuska-Brezzi) condition. This condition can be broken and realistic solutions can be obtained, but some other stabilization, for example PSPG (Pressure stabilizing-Petrov Galerkin) is needed.

After discretization, provided that proper finite element spaces are defined, stabilized finite element formulation of problem (1-4) can be stated as follows: find  $\mathbf{u}^h \in \mathbf{S}_u^h$  and  $p^h \in \mathbf{S}_p^h$  such that  $\forall \mathbf{w}^h \in \mathbf{V}_u^h$  and  $\forall q^h \in \mathbf{V}_p^h$  holds

$$\begin{aligned} & \int_{\Omega} \rho \mathbf{w}^h \cdot \frac{\partial \mathbf{u}^h}{\partial t} d\Omega + \int_{\Omega} \rho \mathbf{w}^h \cdot (\mathbf{u}^h \cdot \nabla \mathbf{u}^h) d\Omega + \int_{\Omega} \nabla \mathbf{w}^h : \boldsymbol{\tau}(\mathbf{u}^h) d\Omega - \int_{\Omega} \mathbf{w}^h \cdot \nabla p^h d\Omega \\ & - \int_{\Omega} \mathbf{w}^h \cdot \mathbf{b} d\Omega - \int_{\Gamma} \mathbf{w}^h \cdot \mathbf{h} d\Gamma + \int_{\Omega} q^h (\nabla \cdot \mathbf{u}^h) d\Omega \\ & + \sum_{el} \left[ \int_{\Omega_e} \tau_{SUPG} (\mathbf{u}^h \cdot \nabla \mathbf{w}^h) \cdot \left( \rho \frac{\partial \mathbf{u}^h}{\partial t} + \rho \mathbf{u}^h \cdot \nabla \mathbf{u}^h - \nabla \cdot \boldsymbol{\tau}(\mathbf{u}^h) + \nabla p^h - \mathbf{b} \right) d\Omega_e \right] \\ & + \sum_{el} \left[ \int_{\Omega_e} \tau_{PSPG} \frac{1}{\rho} \nabla q^h \cdot \left( \rho \frac{\partial \mathbf{u}^h}{\partial t} + \rho \mathbf{u}^h \cdot \nabla \mathbf{u}^h - \nabla \cdot \boldsymbol{\tau}(\mathbf{u}^h) + \nabla p^h - \mathbf{b} \right) d\Omega_e \right] \\ & + \sum_{el} \left[ \int_{\Omega_e} \tau_{LSIC} \nabla \cdot \mathbf{w}^h \rho \nabla \cdot \mathbf{u}^h d\Omega_e \right] = 0 \end{aligned} \quad (5)$$

Terms in the first two lines follow from standard Galerkin discretization, terms in the third line are due to SUPG stabilization, because of convective effects, terms in the fourth line provide PSPG stabilization (LBB condition is not satisfied), and last term provides additional stability for high velocities. Coefficients  $\tau_{SUPG}$ ,  $\tau_{PSPG}$  and  $\tau_{LSIC}$  can be computed as norm of certain terms of (5), as it is done in present work for Q1P0 element. In the case of T1P1 element, coefficients are computed in different way, using so called UGN-stabilization, which is based on characteristic element length, see (Tezduyar, 2000).

### 3. Numerical results

The performance of studied elements has been compared using lid driven cavity test, which is often used as a benchmark. The results are presented for solution corresponding to Reynolds number  $Re=100$ . In case of T1P1 element, results has been obtained at first as a solution to Stokes problem, where time dependent term is omitted and later also as a solution of a full Navier-Stokes problem. Used grid has 400 dofs and 722 elements. The results shown in Fig. 1 compare the velocity profiles along vertical line at the center of specimen. The response of both elements is compared to results obtained by T2P1 Taylor-Hood element with quadratic approximation of velocity and constant pressure (on the same grid, so that the number of velocity degrees of freedom is doubled), and reference solution from (Marchi et al., 2009) obtained on a fine grid of 1024x1024 nodes. The

pressure profiles are shown in Fig. 2, where the colors distinguish solutions obtained using different elements (red-Q1P0, green-T1P1 elements). The raw pressure profile for Q1P0 element exhibits spurious oscillations, but the post-processed profile (as shown in Fig. 2) shows a good agreement with other solutions.

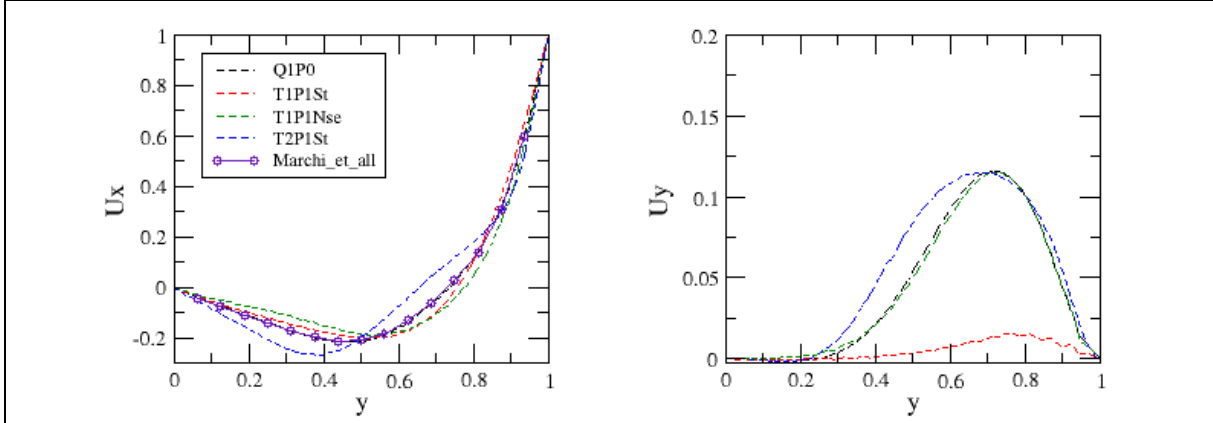


Fig. 1: Lid-driven cavity: velocity profiles along vertical line at specimen center for  $Re=100$ .

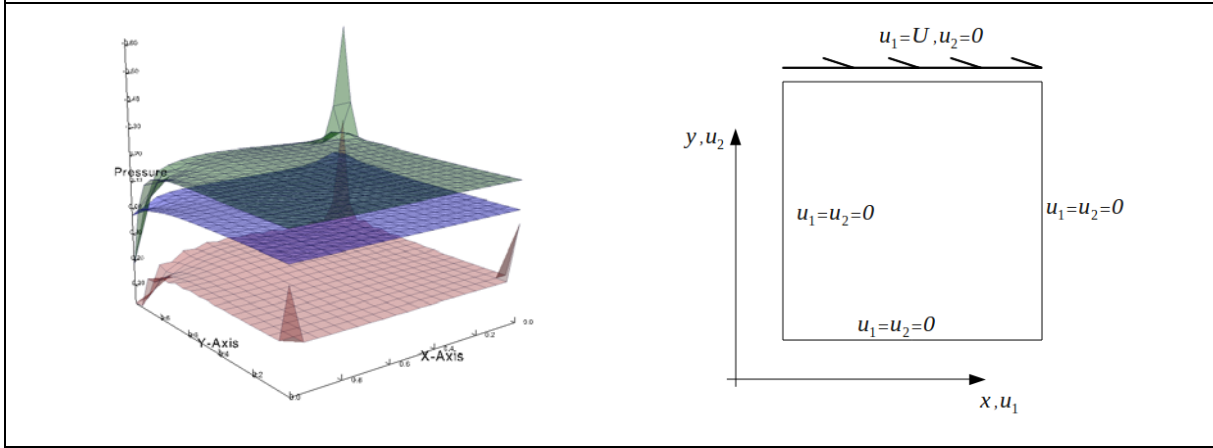


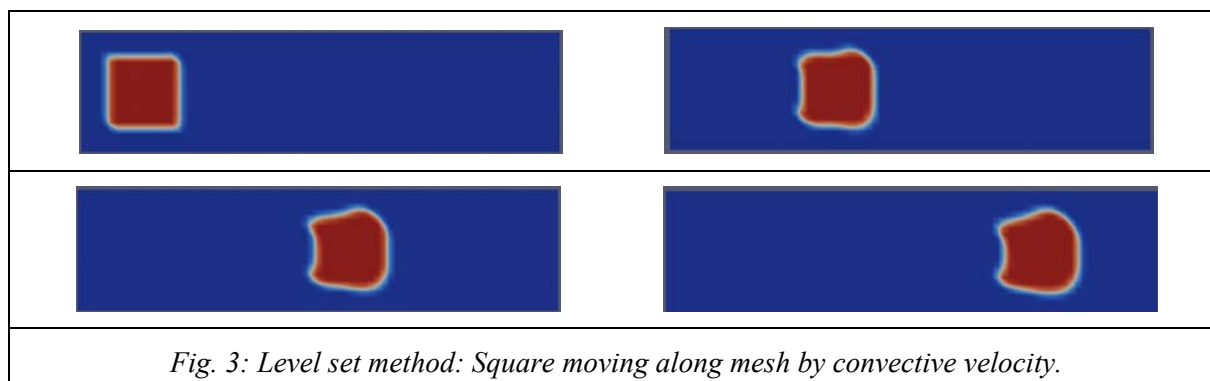
Fig. 2: Lid driven cavity: pressure profiles and lid driven test scheme.

#### 4. Level set method

In a longer perspective, results from this work will be used for modeling of flow with free surface. If governing equations of motion are formulated in Eulerian sense and computations are done on fixed domain (mesh), an interface-tracking technique is needed, see (Tezduyar 2006). In this work technique based on level set method is used. Main idea of this method is to represent interface as a zero level set of a suitable higher-dimensional function. Interface is then manipulated implicitly through this so called level set function. For further reference, see (Osher & Fedkiw 2001). The level set function is typically defined as a signed distance function of points from the interface. Governing equation for interface moving by convective velocity  $\mathbf{u}$  can be written as:

$$\frac{d\phi}{dt} = \frac{\partial\phi}{\partial t} + \mathbf{u} \cdot \nabla\phi = 0 \quad (6)$$

This in fact says, that total derivative of  $\phi$  is equal to zero. Equation (6) can be reformulated into form of Hamilton-Jacobi equation, which can be solved using positive explicit scheme. Drawback of level set method is that is not conservative, when assumption of divergence free velocity is used. Therefore, one has to use some re-initialization technique to recover sign distance property of level set function. This can be found for example in (Osher & Fedkiw 2003). The initial results are shown in Fig. 3, where squared domain is transported through the mesh, due to prescribed velocity, by convective effects.



## 5. Conclusions

To conclude, satisfying agreement with both T1P1 and Q1P0 elements has been obtained. Reasons for differences with T2P1 element is to be further analyzed, but partially can be explained by better approximation properties of T2P1 and by the fact that analysis with T2P1 elements was done with number of DOFs almost doubled. In problems with interface-tracking, initial results are promising, however deformations of transported domain can be observed. This can attributed to poor approximation of T1P0 and to the coarse mesh used.

## Acknowledgement

This work was supported by the Grant Agency of the Czech Technical University in Prague, grant „Advanced algorithms for numerical analysis and modeling“, 2011.

## References

- Donea J., Huerta A. (2003) Finite element method in flow problems. 1.st edition, John Wiley & Sons, Ltd. 362p. ISBN 0471496669.
- Marchi C. H., Suero R., Araki L. K. (2009) The lid-driven square cavity flow: numerical solution with a 1024 x 1024 grid. J. Braz. Soc. Mech. Sci. & Eng. [online]. 2009, vol.31, n.3, pp. 186-198. ISSN 1678-5878.
- Osher S., Fedkiw R. P. (2001) Level Set Methods: An Overview and Some Recent Results. Journal of Computational Physics, Volume 169, Issue 2, 20 May 2001, Pages 463-502.
- Osher S., Fedkiw R. P. (2003) Level Set Methods and Dynamic Implicit Surfaces, 1. St edition, Springer, 396 p., ISBN-10: 0387954821.
- Patzák B., Bittnar Z. (2009) Modeling of fresh concrete. Computers & Structures, Volume 87, Issues 15-16, August 2009, Pages 962-969.
- Tezduyar T. E., Osawa Y. (2000) Finite element stabilization parameters computed from element matrices and vectors, Computer Methods in Applied Mechanics and Engineering, Volume 190, Issues 3-4, 27 October 2000, Pages 411-430.
- Tezduyar T. E. (2006) Interface-tracking and interface-capturing techniques for finite element computation of moving boundaries and interfaces, Computer Methods in Applied Mechanics and Engineering, Volume 195, Issues 23-24, 15 April 2006, Pages 2983-3000.

## EXPERIMENTAL STUDY OF THE FLOW FIELD IN T-JUNCTION MODEL USING PIV METHOD

M. Kotek<sup>\*</sup>, D. Jašíková<sup>\*</sup>, V. Kopecký<sup>\*</sup>

**Abstract:** Reported here is the experimental study in the pipe line element T-junction. The velocity fields were measured by PIV method with 3-camera alignment. This alignment makes accessible T-junction areas covered by image distortions and refraction irregularities in drilled glass block. Four basic connection regimes are studied with flow ratios into inlet branches in turn. Flow field is described with a numerical vector maps and presented as scalar maps with streamlines. Velocity profiles in the inlet and outlet branches are generated. Visualizations of the flow with streamlines and vector fields provide the basic characteristic of flows mixing, separations, vorticities etc. Analyzed datasets are used for evaluation and verification of numerical models.

**Keywords:** T-junction, PIV, measurement, calibration.

### 1. Introduction

In these days every industrial application includes the complex system of conducting pipes. The pipe systems are used for water delivery in agriculture, combustion chambers, cooling and heating systems, and chemical reactors, as well as for household application. Every system is divided into many branches. The pipeline nets consist of pipes, shaped pieces: T-junctions, elbows, contracting and expanding elements, pumps, valves, taps, etc. Each splitting and T-junction brings unsteady structures to the flow field and generates disturbances and energy losses.

The aim of the research in this area is to design pipe system that enables to keep required parameters at the exit of the system with minimum consumed energy and without any systems destruction.

The suitable way for the system behavior prediction is a numerical simulation of the whole complex system or its most exposed parts. The mathematical models have to deal with the pressure variables as the system is unsteady, the energy balance and many boundary conditions.

The applicable mathematical model has to be confirmed by the dataset measured on the real model. The previous experimental studies approached the model with the square pipe profiles (Hirota et al., 2008; Louda et al., 2010). This simplification enables comfortable optical access, but brings incomparable dataset to the real situation.

This study was realized on the real glass model of the T-junction with circular profile, the numerical model of this geometry type was designed and described in (Stigler, 2006; 2006a, 2007). The PIV measurement of the circular profile meets many procedural problems such as image distortions, border refraction changes and the image shift in the tube intersection. The solving of these basic problems is described in this paper.

The 3-camera PIV system was applied for the experimental study of the unsteady turbulent flow. This paper is focused on designing the calibration sequence method. The functionality of this method is proved and demonstrated on the real model instance measurement.

---

<sup>\*</sup> Ing. Michal Kotek, Ing. Darina Jašíková, prof. Ing. Václav Kopecký, CSc.: Fakulty of mechatronics, informatics and interdisciplinary studies, Technical University of Liberec, Studentská 2, 461 17, Liberec, e-mails: [michal.kotek@tul.cz](mailto:michal.kotek@tul.cz), [darina.jasikova@tul.cz](mailto:darina.jasikova@tul.cz), [vaclav.kopecky@tul.cz](mailto:vaclav.kopecky@tul.cz)

## 2. Experimental setup

The experimental study of the T-junction real model with circular profile meets many procedural problems such as image distortions, border refractive index changes and the image shift in the tube intersection. These problems emphasize during the image analyzing and flow velocity processing. The 3-camera alignment is used to avoid further complications. This new alignment brings enough information for the calibration sequence method application and image rectification.

The Fig. 1 shows the laser and the 3-camera alignment to the model position. The real glass model was connected to the open pipe system with the pump and the header tank. The T-junction is drilled and polished into the monolithic glass block. The inner diameter of the circular profiled branch is  $\varnothing 50$  mm and it is branched under  $90^\circ$ . The whole system was filled with test fluid - water at  $20^\circ\text{C}$ .

The investigated area was illuminated by Nd:YAG 532 nm green pulse laser horizontally set to the model. The first camera was fixed above the model to observe the T-junction area. The next two cameras were put together and fixed in angle  $45^\circ$  with laser plane.

The inflow rate was constantly kept on 5.5 l/s. The flow field was measured in several states: a) branch A opened, branch B closed, b) branch B opened, branch A closed, c) branch A and branch B opened with the flow dividing in the ratios 20% - 80%, 40% - 60%, 60% - 40%, 80% - 20%.

The test fluid was seeded with Rhodamine B coated  $10\ \mu\text{m}$  particles and the cameras were set with orange 570 nm filter to reduce the glass wall reflections.

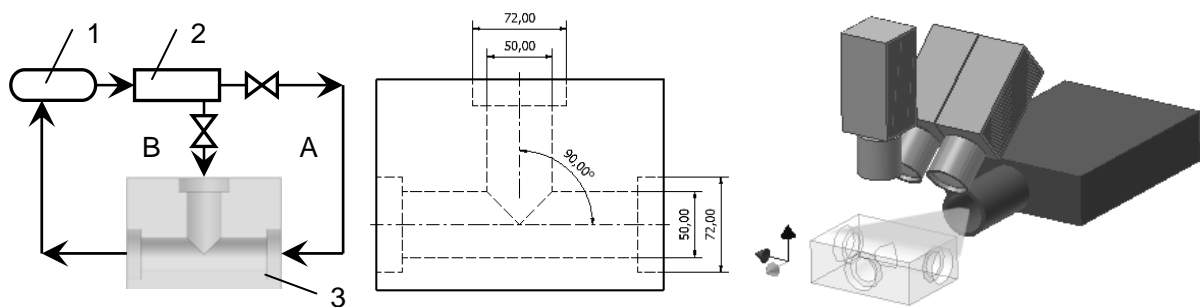


Fig. 1: Measurement circuit (1) header tank, (2) pump, (3) glass model, (A) and (B) inlet branches; T-junction model proportion; Experimental setup and measurement system alignment.

## 3. Calibration methods

Experimental data were recorded according to the setup mentioned in Chapter 2. Three cameras captured the laser lighted plane under different angle and with non-equal magnitude. Image analyzing algorithms were designed to assemble these camera's images. The calibration procedure was split into four steps:

1. calibration images recording and pre-processing,
2. camera image dewarping,
3. dewarped image rotation and the change of magnitude,
4. images assembling.

The special calibration target was manufactured for the purpose of calibration. The target filled whole area of the T-junction model. Plane of the target covered with dot matrix was aligned into the laser light sheet in the central line of T-junction. Calibration records of this target were used to calculate the image distortion model.

The distortion of the image was caused by the camera recording parallax (see the experimental setup in Fig. 1) and the curvature of drilled glass wall. Calibration images were preprocessed to identify the maximal amount of dots in the target matrix, original captured image was not well lighted and did not offer sufficient contrast between matrix dots and background. Partial thresholding algorithm and



mathematical morphology functions solved this drawback. All camera images were calibrated and dewarped separately with appropriate calibration model.

The optical axes of cameras were not parallel, so the images should be rotated before assembling. Dot matrix was used again to define the rotation angle of each camera image. Distance between the laser sheet and the camera chip differs a little, so the magnitude of each camera image was adjusted. The methods of subpixel interpolation were used for the ratio recalculation to keep the maximal accuracy.

In the final step the rebuilt images from three cameras were put together. The area with the examined volume was selected, so the masking procedures were not necessary. The result of images rebuilding and assembling is seen in Fig. 2.

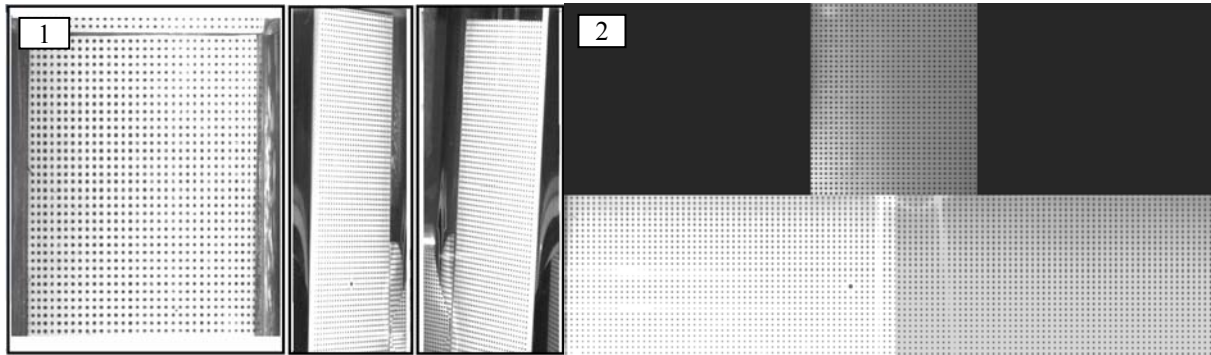


Fig. 2: Image distortion (1) before and (2) after calibration process and camera images assembling.

#### 4. Results and discussion

In this chapter there are presented only some typical results of the flow field in one specific regime. Datasets of all regimes and all ratios will be used for the evaluation and verification of numerical model. The flow incomes to the straight branch A and the sideward branch B. On the vector map in Fig. 3 the flow field of ratio 40% - 60% is captured. Vectors in the area close to the outlet demonstrate 3-dimensional character of the flow.

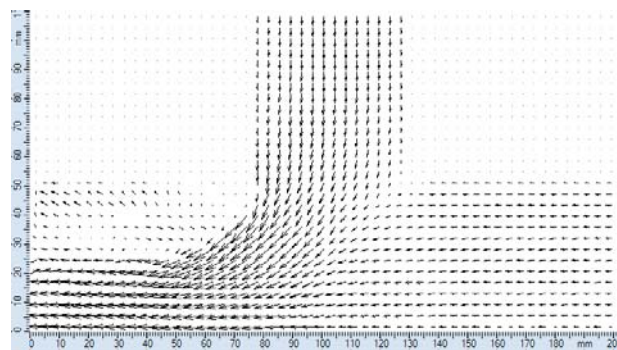


Fig. 3: Flow field of the ratio 40% - 60%.

Mixing of the flow, snap to zone and the flow separation changes are displayed and compared on the scalar maps with stream lines of the ratios 40% - 60% and 80% - 20%.

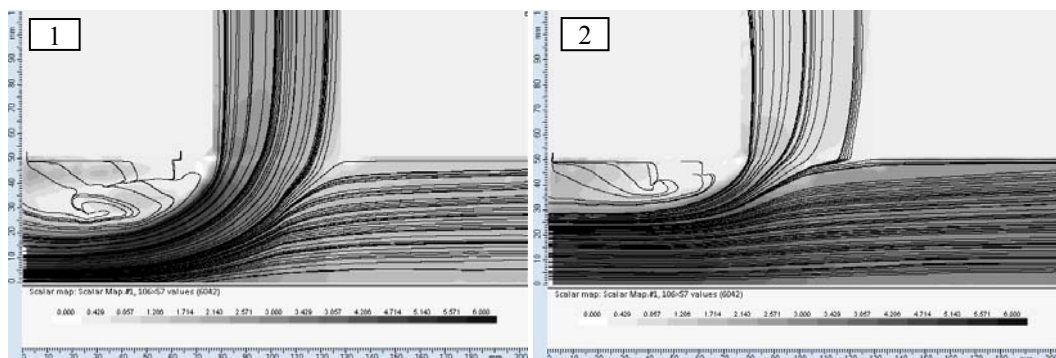


Fig. 4: Comparison of the flow in the ratios (1) 40% - 60% and (2) 80% - 20%.

Velocity profiles in all three branches are presented in the Fig. 5. Profiles are plotted in the distance of 1.5 diameters from the T-junction axes intersection. As it is seen in Fig. 5 the velocities are not calculated close to the wall. PIV results are influenced by laser light reflections on the glass surface and also by considerable velocity gradient in the interrogation area in which velocity vector is determined. This effect is significant in the boundary layer of the flow. The dimensions of interrogation area correspond to  $1.8 \times 1.8$  mm. Half of this area closer to the wall is masked and not exploited for velocity calculation to suppress these systematic errors.

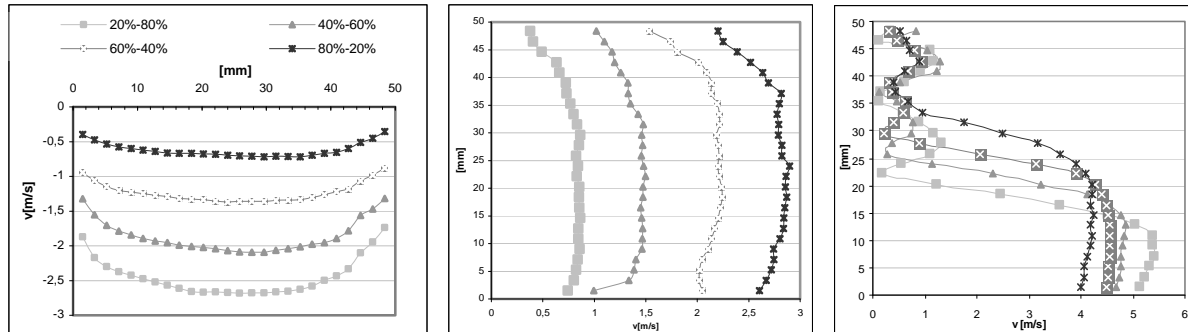


Fig. 5: Velocity profiles, 1.5 diameters from the axes intersection; left-branch B, center – branch A, right – outlet branch.

It is an obvious influence of the flow inlet in the sideward branch B. Velocities closer to the (right) wall are decreased by the flow blending (ratios 20% - 80%, 40% - 60%, 60% - 40%).

## 5. Conclusion

Experimental study of the flow in real T-junction model with circular profile has been made. Flow field was observed with a 3-camera PIV alignment. Unique image analyzing and calibration methods were designed. The T-junction flow characteristics were studied in four regimes of connection and various input flow ratios. Fluctuations, flow separations characteristics and 3-dimensional character of the flow were identified.

It confirmed the suitability of the designed 3-camera alignment and calibration methods on the experiment, where the image distortion occurs and direct optical access is unavailable.

## Acknowledgement

This work has been supported by the GACR – project num. GA101/09/1539 and GA102/08/H081.

## References

- Hirota, M., Nakayama, H., Koide, S., Takeuchi, I. (2008) Experimental Study on Turbulent Flow and Mixing in Counter-Flow Type T-Junction, in: Journal of Thermal Science and Technology, 3, 1, pp. 147-158.
- Louda, P., Kozel, K., Příhoda, J., Beneš, L., Kopáček T. (2010) Numerical solution of incompressible flow through branched channels, Comput. Fluids, doi:10.1016/j.compfluid.2010.12.003.
- Stigler, J. (2006) Tee junction as a pipeline net element Part 1. A new mathematical model, in: Journal of Mechanical Engineering 57, 5, pp. 249-262.
- Stigler, J. (2006) Tee junction as a pipeline net element Part 2. Coefficients determination, in: Journal of Mechanical Engineering 57, 5, pp. 263-270.
- Stigler, J. (2007) Mathematical model of the unsteady fluid flow through tee-junction, in: 2<sup>nd</sup> IAHR Int. Meeting of the Workgroup on Cavitation and Dynamic Problems in Hydraulic Machinery and Systems, Timisoara, Romania, pp. 83-92.

## VARIABILITY OF BEARING RESISTANCE PROPERTIES OF SOILS

P. Koudelka<sup>\*</sup>

**Abstract:** *The Institute of Theoretical and Applied Mechanics gathers long time (from 1997) identification data and shear resistance data of soils into a database. The database make it possible to register up to 145 data on any sample (39 identification data, 5 weight property data and 101 data of shearing resistance). The database has been completed from 1997 every year and temporarily it covers data of 258 samples, hereof 5 gravel, 71 sandy and 182 fine grained ones. The Paper presents results of statistical evaluation of the last contemporary state of the database of year 2010. Implications for soil mechanics are mentioned.*

**Keywords:** *Soil properties, shear strength, unit weight, identification data, statistical analysis.*

### 1. Introduction

Behaviour of soil and granular materials differs from other structural materials (e.g. concrete, steel, masonry, timber). In opposite to other structural materials the soil and granular masses are constructed from innumerable quantity of natural or artificial grains. Due to this fact, a basic attribute of soils is their variability and of course, also variability of their physical properties. Moreover, matter of all granular materials is diphasic or three-phasic (grain, water, air) and their behaviour is complex and non-linear.

It is logically resulting from upper mentioned facts that knowledge of both materials and their location is not perfect but, on the contrary often very low. The strong material variability occurs not only between different layers and their location but also usually due to the variability characterizes material into a layer. This fact is well-known but it causes fundamental difficulties both for design theories and practice. The greatest difficulty appears for the *geotechnical* Limit State Design (LSD) where an application of derived *design material* properties (instead most probable properties - probably B. Hansen 1953) has led due to non-linearity of geotechnical tasks to a fatal theoretical error.

Nevertheless, the soil and rock variability is a constitutive characteristics of geotechnical materials and it is important to know utmost on it. This knowledge is very important and useful for practice design but also necessary for a regular and solid calibration of both the LSD theory and of course, designs according to EC 7-1. The most important input data for the Ultimate Limit State Design (ULSD) are data of shear strength and unit weight. The upper mentioned reasons led to the establishment of a database of physical properties of soils in solid and reliable laboratories tested and concentrating on shear strength and unit weight.

### 2. Database

The database, according to its purposes, is specialized in demands of ULSD, shear strength and unit weight data (not deformation data). The shear strength database system is compounded from an identification block (39 data fields) and a block of physical properties (98 data fields). The database is divided according to soils up three parts: fine-grained and sandy soils and gravels regarding to the Czech standard ČSN 73 1001 "Subsoil under shallow foundations". The standard distinguishes five gravel groups (G), five sandy groups (S) and eight fine-grained groups (F). Denotation of soil kinds keeps the Czech standard ČSN 73 1001 and international usances as they follow:

---

<sup>\*</sup> Ing. Petr Koudelka, DrSc.: Institute of Theoretical and Applied Mechanics of the Czech Academy of Sciences, Prosecká 76; 190 00, Prague, CZ, e-mail: koudelka@itam.cas.cz

Fine grained soils:

F1 = MG (not applied),	F2 = CG (1 sample),
F3 = MS (32 samples),	F4 = CS (35 samples),
F5 = ML-MI (21 samples),	F6 = CL-CI (50 samples),
F7 = MH-MV-ME (10 samples),	F8 = CH-CV-CE (15 samples).

Sandy soils:

S1 = SW (not applied),	S2 = SP (17 samples),
S3 = S-F (13 samples),	S4 = SM (29 samples),
S5 = SC (11 samples).	

Gravel soils:

G1 = GW (not applied),	G2 = GP (3 samples),
G3 = G-F (1 sample)	G4 = GM (not applied),
G5 = GC (1 sample).	

The database to date has data of 164 fine grained samples of groups F2 – F8, 70 sandy samples of groups S2 – S5 and 5 gravel samples of groups G2 – G3, altogether data of 239 samples of Bohemian soils.

## 2.1. Identification data

The identification part involves all usual constitutive data about samples, i.e. soil description, year of performance of the tests, sample place in the soil mass, underground water level, sample location, testing person, stratigraphy and all basic characteristics of the sample soil: granularity, water volume, density.

Identification data are chosen so that it would be possible to make an exact comparison of data samples with other soils; a number of fields is of 39.

## 2.2. Weight properties

Data of volume weigh belong to fundamental physical properties which can be measured relatively easy and accurately. These data are placed in the database in 5 fields: natural unit weight, maximal and minimal ones, dry weight, material density.

From point of view of the ULS design the most applied property of this section is unit weight but others values can be useful for another tasks and for practice.

## 2.3. Shearing resistance properties

Values defining shear resistance are in the second section of the physical property part. The database is specialised in shearing resistance in terms of effective stress and both in top and residual values. However, not all tests are performed according to ČSN 73 1030 (Tests of shear strength) also for residual shear strength because the last movements do not satisfy prescribed values. For these cases, the residual values are derived from the accordant tests of top shear strength.

The database presents resulting values of shearing resistance in terms of effective stress both top and residual in 101 fields, i.e. top values of shearing resistance angle  $\phi_{ef}$  and cohesion  $c_{ef}$  and residual values of shearing resistance angle  $\phi_r$  and residual cohesion  $c_r$ , but also detailed results of box shear tests. Total shear strength value can be registered if it is tested but it is not needed or preferred.

## 2.4. Similarity parameters

The database monitors also two similarity soil parameters of ultimate design which are calculated using unit weight and shear strength properties. These parameters are denoted *Hamilton's* and *Janbu's* similarity heights  $h_\pi$  and  $h_\lambda$  resp. of quantity [m]. The parameters are defined as follows:

$$h_\pi = c_{ef} / \gamma \quad (1)$$

$$h_\lambda = c_{ef} / (\gamma * \tan \phi_{ef}) \quad (2)$$

Both parameters can be found together with vertical parameters of soil or rock structures (e.g. height, depth) in ultimate design and then those are denoted as *Hamilton's* and *Janbu's similarity coefficients*:

$$\pi = c_{ef} / (\gamma * h) \quad (3)$$

$$\lambda = c_{ef} / (\gamma * h * \tan \phi_{ef}) \quad (4)$$

where  $c_{ef}$  and  $\phi_{ef}$  are values shearing resistance (shear strength),  $\gamma$  is unit weight and  $h$  is vertical parameter.

The first similarity parameter (Hamilton's) according to equation (3) influences ultimate designs directly, the second one (Janbu's) according to equation (4) influences ultimate designs indirectly inducing locations of critical shear surfaces.

### 3. Statistical analysis

The presented statistical analysis has been carried out on the base of altogether 258 samples. Total sizes of single sets of soils are obvious in the description of the database in the Chapter 2.

Tab. 1: Statistical parameters of sandy and fine grained soils according to the database 2010.

TABLE OF STATISTICAL QUANTITIES OF SOIL DATABASE										
Mark	Samples	Average values			Medium deviations			Variability coefficients		
	n	$\square_m$	$f_m$	$c_m$	$S_\square$	$S_f$	$S_c$	$V_\square$	$V_f$	$V_c$
-	1	kgm <sup>3</sup>	°	kPa	kgm <sup>3</sup>	°	kPa	1	1	1
SANDY SOILS										
S1	0	-	-	-	-	-	-	-	-	-
S2	17	1810	39.1	7.3	112.96	5.01	4.57	0.062	0.128	0.627
S3	13	1880	36.7	13.8	171.17	5.91	10.99	0.091	0.161	0.794
S4	29	1927	33.8	19.9	150.35	6.59	17.11	0.078	0.195	0.860
S5	11	2115	24.5	18.0	91.24	2.57	19.97	0.044	0.096	0.678
SS	70	1912	30.7	12.9	138.61	5.53	14.54	0.072	0.180	1.123
FINE GRAINED SOILS										
F1	0	-	-	-	-	-	-	-	-	-
F2	1	2197	29.9	27	-	-	-	-	-	-
F3	32	1955	27.64	33.89	99.583	4.029	20.00	0.0509	0.1458	0.590
F4	35	2003	23.95	44.89	133.65	3.831	28.74	0.0667	0.160	0.640
F5	21	1993	22.42	38.00	99.81	3.035	22.27	0.050	0.1354	0.586
F6	50	2021	22.36	41.70	92.94	3.107	20.47	0.046	0.139	0.491
F7	10	1982	19.54	74.60	137.14	2.95	53.93	0.069	0.1511	0.723
F8	11	1953	16.76	47.80	137.29	1.894	17.03	0.070	0.113	0.356
SF	160	1993	23.18	43.16	91.42	3.394	26.00	0.046	0.146	0.602

Denotation of statistical quantities in the table is presented and the others are:  $n$  – number of samples,  $\gamma$  – unit weight,  $\phi_m$  – average value of shearing resistance angle,  $c_m$  – average value of cohesion,  $s_x$  – medium deviations of relevant quantities in subscripts denoted,  $v_x$  – variability coefficients of the relevant quantity  $x$ . The groups S2 and F8 comprehend also properties of fills of soils belonging in the groups (5 samples and 4 samples resp.).

The Tab. 1 is a result of statistical analysis and it makes it possible to compare differences between quantities the single soil groups and their variability. Statistical weight of the results is given by size of the statistical sample set but all analysed sets are statistically sufficient and reliable. Statistical average parameters of the categories accord to well-known values very well.

#### **4. Conclusion**

The database and its statistical analyses can be very useful both for geotechnical research and practice. It has to be mentioned that statistical parameters of single soil groups have been derived from the whole sample sets of a number of sites and due to this fact statistical parameters of other sites can be distinct. However, they should lie into or near range of the group/category according to the database.

The derived similarity parameters of soils, i.e. Hamilton's and Janbu's similarity heights, can be used to calculations of Hamilton's and Janbu's similarity coefficients if some geotechnical tasks are analyzed. A similarity approach appears very useful and effective.

#### **5. Presentation of the database**

The database has been developed through a number of years deriving benefit from a number of grant projects of the Grant Agency of the Czech Academy of Sciences and the Grant Agency of the Czech Republic. The database will be available at Internet address of ITAM

[www.itam.cas.cz/](http://www.itam.cas.cz/)

on the path (lidé/koudelka). The presented database is composed of four files: "Report" (in Czech), "Gravels", "Sands" and "Fine grained soils" in format pdf.

#### **Acknowledgement**

The Grant Agency of the Czech Republic and the Grant Agency of the Czech Academy of Sciences provided financial support of the connected research (GP Nos.103/2002/0956, 103/2005/2130, 103/07/0557, 103/08/1617 and No. A2071302 resp.). The author would like to thank them all for support.

#### **References**

- ČSN 73 0031 Structural and subsoil reliability - Basic requirements for design (1989). Prague: ÚNM, p. 22. (in Czech).
- ČSN 73 0037 Earth pressure acting on structures. (1992), Prague: Vydavatelství norem, p. 52. (in Czech).
- ČSN 73 1001 Foundation of structures - Subsoil under shallow foundations (1987), p. 75. Prague: ÚNM.
- EN 1997-1 - Eurocode 7, Geotechnical design – Part 1: General rules (Final draft), (11/2004). Brussels, CEN/TC 250/SC7-WG1, p. 168.
- Koudelka, P. (1997): Podobnost zrnitých materiálů se smykovou pevností (Similarity of Granular Materials with Shear Strength). Proc.NC IF TMM (International Federation for the Theory of Machines and Mechanisms) Engineering Mechanics 97-Svratka, Vol. 1, 123-128.



## DETERMINISTIC AND PROBABILITY ANALYSIS OF THE STEEL CHIMNEY UNDER WIND LOADS

J. Králik<sup>\*</sup>, J. Králik jr.<sup>\*\*</sup>

**Abstract:** *This paper describes the static and dynamic analyses used for welded steel chimneys expertise according to European standard EN 1991 and EN 1993. More details are concerned with wind loading determination and its using for static analysis and lateral resonance analysis. On the base of the VEAB chimney model with and without the pendulum mass damper the wind load effect is presented. The deterministic and probability analysis were performed. The simple spring and damper model and the FEA model under system ANSYS using shell elements are presented. The effect of the wind cycle loading to the fatigue evaluation of the chimney is discussed.*

**Keywords:** *Chimney, wind, dynamic, pendulum mass damper, probability, FEM, ANSYS.*

### 1. Introduction

The frameless welded steel chimneys are modern and economic solution for the transmittion of the smoke gas from the plants. The steel chimneys are constructed in dependency on the plant powers with diameter more than 5 m and 150 m of the height. The steel chimney consist two pipes – the structural pipe and the inner pipe. Furthermore there is the thermal insulation. The structural pipe can be constructed from one or more segments connected by the flanges and bolts. The chimney is anchored in the concrete block. The design of the chimney can be optimized by static and dynamic analysis considered various load effects. The critical load of the chimneys is the wind impact. For slender structures subjected to wind loading there are three main actions to consider, gust wind, vortex shedding and ring oscillation ovalling. Assessment of the design chimney due to wind effect is defined in standard ENV 1991-2-4. The previous standard was STN 730035 in Slovakia. Pirner, M., Fischer, O. (2003) and Szabo, G. Gyorgyi, J. (2010) prezent the new methodology to design of the chimneys. In the case of the design of the chimneys the german standard DIN 4133 is recommended.



*Fig. 1: VEAB steel chimney.*

In this paper the VEAB steel chimney (Travnik, 2002) of the height 90 m is considered. The behavior of the steel chimney was investigated in the real plant. The experimental and numerical analyses were published in report of the Sweden Company (Travnik, 2002).

### 2. Deterministic contra probability reliability analysis

Most problems concerning the reliability of building structures (Králik, 2009) are defined today as a comparison of two stochastic values, loading effects  $E$  and the resistance  $R$ , depending on the variable

<sup>\*</sup> prof. Ing. Juraj Králik, CSc.: Faculty of Civil Engineering, STU in Bratislava; Radlinského 11; 813 68 Bratislava; e-mail: juraj.kralik@stuba.sk

<sup>\*\*</sup> Ing. Juraj Králik, PhD.: Faculty of Architecture, STU in Bratislava; 812 45 Bratislava; Námestie Slobody 19; e-mail: juraj.kralik@stuba.sk

material and geometric characteristics of the structural element. In the case of a deterministic approach to a design, the deterministic (nominal) attributes of those parameters  $R_d$  and  $E_d$  are compared.

The deterministic definition of the reliability condition has the form

$$R_d \geq E_d \quad (1)$$

And in the case of the probabilistic approach, it has the form

$$RF = R - E \geq 0 \quad (2)$$

The probability of failure can be defined by the simple expression

$$P_f = P[R < E] = P[(R - E) < 0] \quad (3)$$

### 3. Uncertainties of input data

The uncertainties of the input data – action effect and resistance are for the case of the probabilistic calculation of the structure reliability defined in JCSS and Eurocode 1990.

Tab. 1: Probabilistic model of input parameters.

Name	Quantity	Charact. value	Variable paramet.	Histogram	Mean	Stand. deviation	Min. value	Max. value
Material	Young's modulus	$E_k$	$e_{var}$	Normal	1	0,120	0,645	1,293
Load	Dead	$G_k$	$g_{var}$	Normal	1	0,010	0,755	1,282
	Live	$Q_k$	$q_{var}$	Gumbel	0,60	0,200	0	1
	Earthquake	$A_{E,k}$	$a_{var}$	Gama(T.II)	0,67	0,142	0,419	1,032
	Wind extrem	$A_{W,k}$	$w_{var}$	Gumbel	0,30	0,150	0,500	1,032
Resistance	Steel strength $f_{sk}$	$F_k$	$f_{var}$	Lognormal	1	0,100	0,726	1,325
Model	Action uncertaint	$\theta_E$	$Te_{var}$	Normal	1	0,100	0,875	1,135
	Resistance uncert.	$\theta_R$	$Tr_{var}$	Normal	1	0,100	0,875	1,135

The stiffness of the structure is determined with the characteristic value of Young's modulus  $E_k$  and variable factor  $e_{var}$ . A load is taken with characteristic values  $G_k$ ,  $Q_k$ ,  $A_{E,k}$ ,  $A_{W,k}$  and variable factors  $g_{var}$ ,  $q_{var}$ ,  $a_{var}$  and  $w_{var}$ . The resistance of the steel is delimited by the characteristic values of the strength  $f_{sk}$  and the variable factor  $f_{var}$ . The uncertainties of the calculation model are considered by variable model factor  $\theta_R$  and variable load factor  $\theta_E$  for Gauss's normal distribution.

### 4. Static and dynamic calculation of the chimney

The most importance parameters for the static design of the steel chimneys by EN 1991-1-4 are the mean wind velocity  $v_m$ . The mean wind velocity depends of the roughness factor  $c_r(z)$  and the orography factor  $c_o(z)$ ,  $v_m = c_r(z) \cdot c_o \cdot v_b$ , where  $v_b$  is the basic wind velocity. The dynamic analysis of the steel chimneys must be realized in accordance of the ENV considering the across resonance vibration due to buffering effects, galloping, divergence and fluttering. The base of the dynamic analysis is the calculation of the first mode of the chimney. The critical wind velocity and pressure at vortex shedding is calculated as

$$v_{cr} = \frac{f \cdot d}{St}, \quad p_{cr} = 0.5 \cdot \rho \cdot v_{cr}^2 \quad (4)$$

where  $f$  is the natural frequency of the chimney,  $d$  is the diameter,  $St$  is the Strouhal number ( $= 0.2$ ) at ordinary vortex,  $\rho$  is assumed equal to  $1.25 \text{ kg/m}^3$

Tab. 2: Critical wind velocity.

	Critical wind velocity $v_{cr}$ [m/s]		
	first mode	second mode	third mode
At chimney shell $d = 2.3 \text{ m}$	3.24	16.6	44.4
At damper shell $d = 2.8 \text{ m}$	3.95	20.2	54.0

The equivalent load during vortex shedding may be calculated as

$$w_{eq} = \mu_{tr} \cdot p_{cr} \cdot d \left( \frac{\pi}{\delta_m} \right), \quad (5)$$

where  $\mu_{tr}$  is the shape factor,  $p_{cr}$  is the wind velocity pressure,  $d$  is the diameter,  $\delta_m$  is the logarithmic decrement ( $= 0.7$ ).

## 5. Computational model of the steel chimney with damper

The tuned pendulum damper is one from the effective damper. This damper was tested on the VEAB chimney (Travnik, P. Alpsten, G., 2002). The damper consists of a pendulum mass ring hinged in three chains, located in 120 degrees direction, connected to the damper house roof. The damping is achieved by friction between the friction mass and the damper house floor. The manufacturer calculated the generalized mass to  $M_{gen} = 12460$  kg. The pendulum mass was defined as 10% of the generalized mass.

The generalized mass is defined as

$$M_{gen} = \int_0^H m(x) \cdot \left( \frac{u(x)}{u_{top}} \right)^2 dx, \quad (6)$$

where  $m(x)$  is the mass per length at height  $x$ ,  $u(x)$  is the deflection at height  $(x)$ ,  $u_{top}$  is the top deflection and  $H$  is the chimney height. The horizontal force necessary to accelerate the friction masses into motion by an inclination of the pendulum damper is

$$F_H = \mu \cdot m_f \cdot g, \quad (7)$$

where  $\mu$  is the friction coefficient ( $= 0.15 - 0.30$ ),  $m_f$  is the friction mass.

The calculation model of the chimney with damper can be defined as the system of the springs and damping elements (Fig. 2). The following differential equations describes this model

$$M_{gen} \frac{d^2 u_1}{dt^2} + k_1 u_1 + k_2 (u_1 - u_2) + c_1 \frac{du_1}{dt} + c_2 \left( \frac{du_1}{dt} - \frac{du_2}{dt} \right) = F \cdot \sin(\omega t), \quad (8)$$

$$m \frac{d^2 u_2}{dt^2} + k_2 (u_2 - u_1) + c_2 \left( \frac{du_2}{dt} - \frac{du_1}{dt} \right) = 0,$$

where  $F$  is the amplitude for vortex shedding force determined from the condition of the equivalent deflection of the chimney as from the distributed vortex load along the chimney corp. The top deflection of the chimney with and without damper was calculated from the equations (8) in dependency of the frequency (Fig. 3).

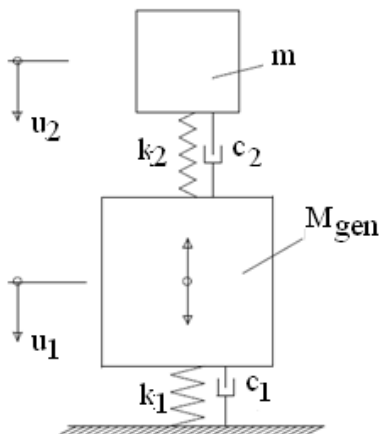


Fig. 2: Model of the chimney damper.

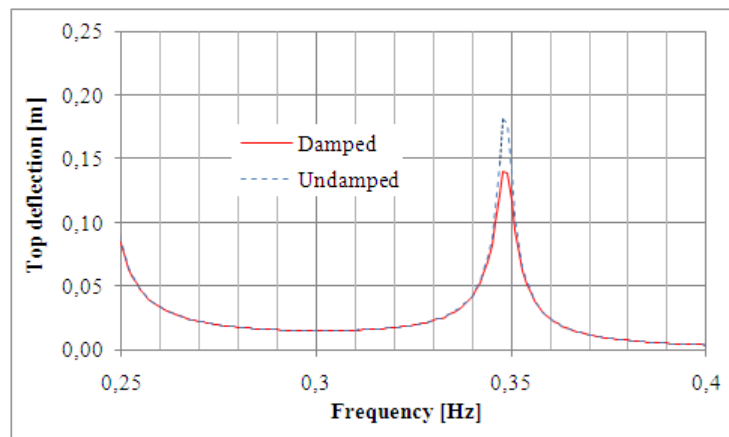


Fig. 3: Top deflection with and without damper.

The probability analysis of the chimney with damper was considered in 200 simulations of the LHS method in system ANSYS. The simulated top deflections of the chimney are presented in the Fig. 4. The sensitivity analysis of the influence of the variable input parameters to the reliability of the structures depends on the statistical independency between input and output parameters. The variability of the wind load, the stiffness and masses of the chimney has the most significant influence on the top deflection (Fig. 5).

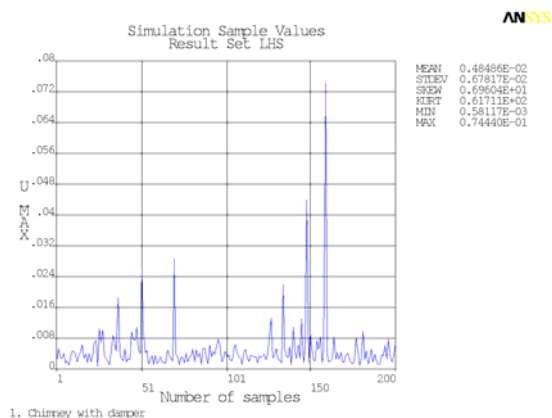


Fig. 4: The simulated top deflection.

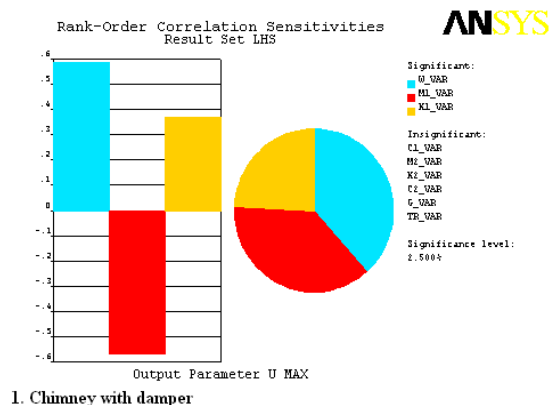


Fig. 5: The sensitivity analysis of the deflection.

The sensitivity analysis gives the valuable information about the influence of uncertainties of input variables (load, material, model and other) to engineer for optimal design of the structures.

## 6. Conclusions

This paper presents that a detailed analysis of top deflection of the chimney with and without the damper. The damper consists of a pendulum mass ring hinged in three chains, located in 120 degrees direction, connected to the damper house roof. The damping is achieved by friction between the friction mass and the damper house floor. The affectivity of the tuned pendulum damper depends on the frequency of the vortex load and the eigenvalue of the chimney. The stochastic methods give us the possibility of the complex analysis of the influence of uncertainties of input variables (load, material, model and other) to engineer for optimal design of the structures.

## Acknowledgement

The project was realized with the financial support of the Grant Agency of the Slovak Republic (VEGA). The project registration number is VEGA 1/0849/08.

## References

- EN 1991-1-4 Eurocode 1 (2005) Actions on structures-Part 1-4: General actions-Wind actions.
- JCSS-OSTL/DIA/VROU (2000), Probabilistic Model Code, Part 1 Basis of Design, Working material, <http://www.jcss.ethz.ch/>, 2001.
- Králik, J. Králik, J. jr. (2009) Deterministic and Probabilistic Analysis of Nonsymmetrical Wind Effects to Symmetrical High Rise Buildings. In proc. *European Safety and Reliability Conference, ESREL 2009, Reliability, Risk and Safety, Theory and Applications*, CRC Press/A.Balkema Book, Prague, CR, 7-10 September, Vol.2, p.1393-1396, Full in CD.
- Králik, J. (2009) *Reliability Analysis of Structures Using Stochastic Finite Element Method*, Published by STU Bratislava, 2009, 143pp. ISBN 978-80-227-3130-0.
- Pirner, M., Fischer, O. (2003) *Zatížení staveb větrem*. ČKAIT, Praha, 256 strán, ISBN 80-86769-10-0.
- Szabo, G. Gyorgyi, J. (2010) Application of the ANSYS Software to Fluid-Structure Interaction Analysis, In proc. of the *Seventh International Conference on Engineering Computational Technology*, Civil-Comp Press, Stirlingshire, Scotland. 19pp, in CD.
- Travnik, P. Alpsten, G. (2002) *Dynamic Behaviour under Wind Loading of a 90 m Steel Chimney*, Alstom Power Sweden AB, Report S-01041.

## **NANOINDENTATION BASED EVALUATION OF EFFECTIVE ELASTIC PROPERTIES OF METAL FOAM**

**V. Králík<sup>\*</sup>, J. Němeček<sup>\*</sup>**

**Abstract:** *The paper aims to evaluate effective properties of a solid phase of metal foam on the level of a few microns. Basic principles of micromechanics are applied to the experimental results gained from nanoindentation. The paper describes microstructure and micromechanical properties of this highly porous material system. Results of elastic moduli were monitored in two distant locations on the metal foam pore walls. Elastic parameters were obtained on a statistical set of nanoindentation results from which one dominant and one minor mechanical phase were separated by the deconvolution algorithm. Effective elastic properties of a cell wall were evaluated by the Mori-Tanaka elastic homogenization.*

**Keywords:** *Metal foam, porous system, nanoindentation, micromechanical properties, deconvolution.*

### **1. Introduction**

Metal foams belong to the up-to-date structural materials with high potential to many engineering applications. This highly porous material with a cellular structure is known for its attractive mechanical and physical characteristics such as high stiffness in conjunction with very low weight, high strength, excellent impact energy absorption, high damping capacity and good sound absorption capability. The usual source material for the production of metal foams is aluminium and aluminium alloys because of low specific density ( $\sim 2700 \text{ kg/m}^3$ ), low melting point ( $\sim 660^\circ\text{C}$ ), nonflammability, possibility of recycling and excellent corrosion resistivity, (see e.g. the review by Banhart, 2001).

In general, mechanical properties of metal foams are governed by two major factors: (i) cell morphology (shape, size and distribution of cells) and (ii) material properties of the cell walls (Hasan et al., 2008). However, measurement of mechanical properties of the cell walls is a difficult problem that cannot be solved with conventional methods due to their small dimensions, low local bearing capacity and local yielding and bending of the cell walls. These problems can be overcome using micromechanical methods in which the load–displacement curve is obtained in the sub-micrometer range.

In this study, nanoindentation was applied to access elastic properties of the distinct phases within the cell walls. Based on these results, overall effective elastic properties of the solid phase were evaluated by micromechanical homogenization.

### **2. Materials and methods**

#### **2.1. Tested material**

Commercial aluminium foam ‘Alporas’ (Shinko Wire Co., Ltd) was tested in this study. The manufacturing process of the Alporas is a batch casting process (Miyoshi et al., 1998). A typical resulting internal structure of the aluminium foam is shown in Fig. 1a.

Small Alporas block  $18 \times 18 \times 14 \text{ mm}$  was firstly embedded into cylindrical mould which was filled with a low viscosity epoxy resin (Struers<sup>®</sup>). Then,  $\sim 5 \text{ mm}$  slice was cut by diamond saw and polished with fine SiC papers. Resulting surface roughness was checked with in-situ imaging (surface scanning was performed with the same tip as for nanoindentation). As a rule of thumb, the surface roughness should

---

<sup>\*</sup> Ing. Vlastimil Králík and assoc. prof. Ing. Jiří Němeček, Ph.D.: Czech Technical University in Prague, Faculty of Civil Engineering, Department of Mechanics, Thákurova 2077/7; 166 29, Prague; CZ, e-mails: vlastimil.kralik@fsv.cvut.cz, jiri.nemecek@fsv.cvut.cz

be kept within 10% of the expected maximum depths used in nanoindentation. In our case, quadratic deviation from the mean plane (root-mean-square) was found to be  $R_q \approx 9$  nm (according to ISO 4287:1997) which was acceptable compared to the maximum indentation depths 100 - 300 nm.

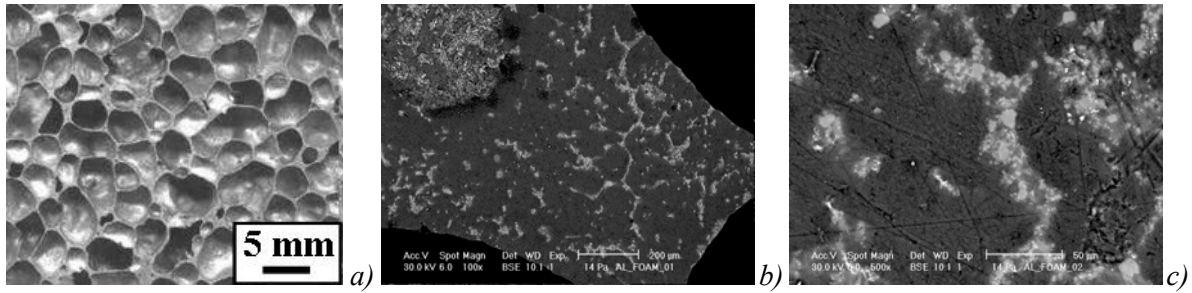


Fig. 1: a) Overall view on a typical structure of aluminium foam. b) ESEM image of a cell wall. c) Detailed ESEM image of a cell wall showing Ca/Ti-rich area (light zones).

The microstructure of the foam was studied in electron microscope (ESEM). Two distinct phases, visible as differently colored areas in ESEM images were distinguished (Fig. 1b, c). The chemical composition of the two phases was checked with EDX element analysis in ESEM. As expected, the majority of the volume (dark zone) was composed of aluminum and aluminium oxide  $\text{Al}_2\text{O}_3$  (further denoted as Al-rich area). Lighter zones contained significant amount of calcium and titanium (further denoted as Ca/Ti-rich area). The non-uniform distribution of these zones shows on inhomogeneous mixing of the admixtures that are added during the production process.

## 2.2. Nanoindentation

The nanoindentation testing was performed using a Hysitron Tribolab system<sup>®</sup> at the CTU in Prague. Two distant locations were chosen on the sample to capture its heterogeneity. Both locations were covered by a series of ~220 indents which was considered to give sufficiently large statistical set of data. Standard load controlled test of an individual loading diagram consisting of three segments: loading, holding at the peak and unloading was used. Loading and unloading of this trapezoidal loading function lasted for 5 seconds, the holding part lasted for 10 seconds. Maximum applied load was 1500  $\mu\text{N}$ .

Elastic modulus was evaluated for individual indents using standard methodology (Oliver and Pharr, 1992) which accounts for elasto-plastic contact of a conical indenter with an isotropic half-space as:

$$E_r = \frac{1}{2\beta} \frac{\sqrt{\pi}}{\sqrt{A}} \frac{dP}{dh} \quad (1)$$

in which  $E_r$  is the reduced modulus measured in an experiment,  $A$  is the projected contact area of the indenter at the peak load,  $\beta$  is geometrical constant ( $\beta = 1.034$  for the used Berkovich tip) and  $\frac{dP}{dh}$  is a slope of the unloading branch evaluated at the peak. Elastic modulus  $E$  of the measured media can be found using contact mechanics which accounts for the effect of non-rigid indenter as:

$$\frac{1}{E_r} = \frac{(1-\nu^2)}{E} - \frac{(1-\nu_i^2)}{E_i} \quad (2)$$

in which  $\nu$  is the Poisson's ratio of the tested material,  $E_i$  a  $\nu_i$  are known elastic modulus and Poisson's ratio of the indenter. In our case,  $\nu = 0.35$  was taken as an estimate for all indents.

## 3. Results and discussion

### 3.1. Statistical and deconvolution results from nanoindentation

An example of a typical loading diagram gained from nanoindentation at Al-rich area (dark zone in Fig. 1b, c) is shown in Fig. 2a. Average contact depth is around 220 nm and maximum depth reaches values around 234 nm. Variety of results from different positions is shown on an example in Fig. 2b in which a pair of curves belongs to Al-rich and a pair to Ca/Ti-rich zones, respectively.



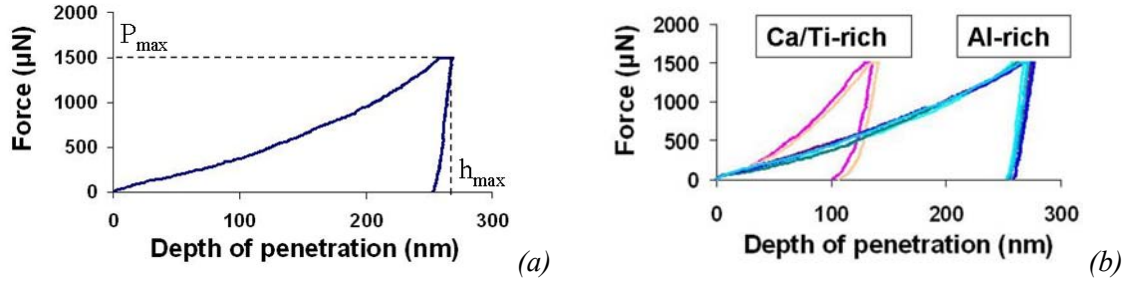


Fig. 2: (a) Typical loading diagram for Al-rich zone, (b) example of variation in loading diagrams for Al- and Ca/Ti-rich zones.

Elastic moduli were evaluated for each individual indent. Overall results are depicted in Fig. 3a in which histogram of all elastic moduli from two different positions and results merged from both positions are shown. No significant differences between the positions were found. Therefore, merged results were further used for the deconvolution of elastic properties. It can be seen in Fig. 3a that a significant peak appears around 60 GPa. This value can be considered as a dominant characteristic of a solid phase (Al-rich). The scatter in the results is affected mainly by the position in different zones (Al-rich, Ca/Ti-rich) and related hardnesses of its constituents in the sample.

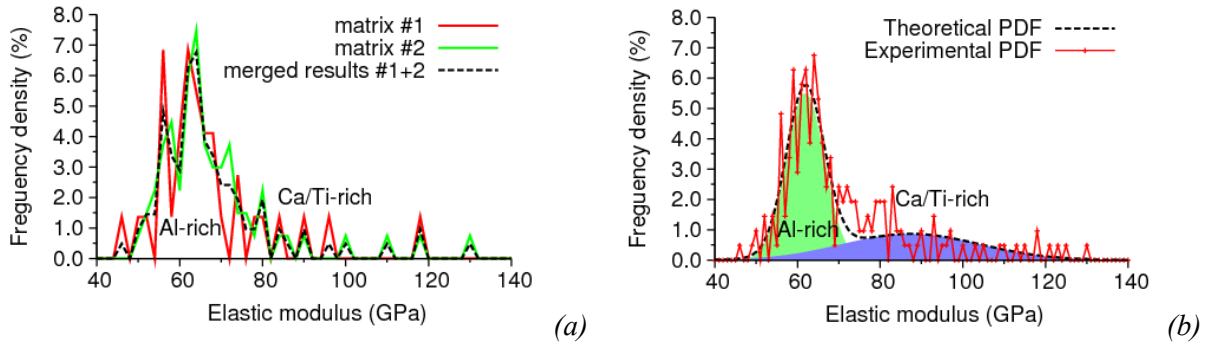


Fig. 3: (a) Probability density functions of elastic moduli from two measured positions and merged results. (b) Deconvolution of elastic moduli in two phases (Al-rich and Ca/Ti-rich).

Statistical results of elastic moduli (Fig. 3a) have been further analyzed with a deconvolution technique (Constantinides et al., 1998; Němeček et al., 2010; Němeček et al., 2011) which seeks for parameters of individual phases included in overall results. The deconvolution algorithm searches for n-Gauss distributions in an experimental probability density function - PDF (Fig. 3b). Random seed and minimizing criteria of the differences between the experimental and theoretical overall PDFs are computed in the algorithm to find the best fit. Two-phase system (one dominant Al-rich phase and one minor Ca/Ti-rich phase) was assumed in the deconvolution. Tab. 1 contains numerical results from the deconvolution with the estimated volume fractions of the phases.

Tab. 1: Elastic moduli and volume fractions from deconvolution.

Phase	Mean (GPa)	St. dev. (GPa)	Volume fraction (-)
1 (Al-rich zone)	61.883	4.618	0.638
2 (Ca/Ti-rich zone)	87.395	16.684	0.362

### 3.2. Effective material properties

Continuum micromechanics provides a framework, in which elastic properties of heterogeneous microscale phases are homogenized to give overall effective properties on the macroscale (Zaoui, 2002). In this context, representative volume element (RVE) is introduced in order to separate the scales. The RVE must be substantially smaller than the macroscale body, which allows imposing homogeneous boundary conditions over the RVE. This leads to constant stress/strain field in individual microscale components of ellipsoidal shapes. Effective elastic properties are then obtained through averaging over the local contributions. Considering isotropic spherical inclusions in a matrix leads to estimation of effective bulk modulus using so called Mori-Tanaka method as:

$$k_{\text{hom}} = \frac{\sum_r f_r k_r (1 + \alpha_0 (\frac{k_r}{k_0} - 1))^{-1}}{\sum_r f_r (1 + \alpha_0 (\frac{k_r}{k_0} - 1))^{-1}} \quad (3)$$

where  $f_r$  is the volume fraction of the  $r^{\text{th}}$  phase,  $k_r$  its bulk modulus and the coefficient  $\alpha_0$  describes bulk and shear properties of the  $0^{\text{th}}$  phase, i.e. the reference medium (Zaoui, 2002).

The homogenized elastic properties for the two considered microscale phases were found to be  $E_{\text{hom}} = 70.083$  GPa,  $\nu_{\text{hom}} = 0.35$ .

#### 4. Conclusions

Performed microstructural observations and results from nanoindentation revealed that the heterogeneity included in the aluminium foam at the production process has consequences in its micromechanical behavior. Large scatter of elastic parameters have been obtained. Harder and softer areas measured with nanoindentation can be linked with ESEM analyses and denoted as Al- and Ca/Ti-rich areas. Statistical deconvolution was applied to find average elastic modulus of a dominant Al-rich phase (61.883 GPa) and minor Ca/Ti-rich phase (87.395 GPa). These microscale parameters together with their volume fractions were used in micromechanical up-scaling (Mori-Tanaka method) in which overall elastic properties for the homogenized medium (the whole metal foam wall) were found ( $E_{\text{hom}} = 70.083$  GPa). It is planned to use the homogenized properties for further analysis of the macroscale behavior of the whole metal foam system including air pores.

#### Acknowledgement

Supports of the Czech Science Foundation (GAČR 103/09/1748) and Agency of the Czech Technical University in Prague, grant No. SGS10/135/OHK1/2T/11 are gratefully acknowledged.

#### References

- Banhart J. (2001) Manufacture, characterisation and application of cellular metals and metal foams. *Progress in Materials Science*, 46, 6, pp.559-632.
- Constantinides G., Chandran K.R., Ulm F.-J. & Vliet K.V. (2006) Grid indentation analysis of composite microstructure and mechanics: Principles of validation, *Mat. Sci. and Eng.*, 430, 1-2, pp.189-202.
- Hasan M.A., Kim A. & Lee H.-J. (2008) Measuring the cell wall mechanical properties of Al-alloy foams using the nanoindentation method, *Composite Structures*, 83, 2, pp.180-188.
- ISO 4287:1997, "Geometrical Product Specifications (GPS) - Surface texture: Profile method".
- Miyoshi T., Itoh M., Akiyama S. & Kitahara A. (1998) Aluminium foam, "ALPORAS": The production process, properties and application, *Mat. Res. Soc. Symp. Proc.*, 521, pp.133-137.
- Němeček J. & Lukeš J. (2010) On the evaluation of elastic properties from nanoindentation of heterogeneous systems, *Chemické Listy*, 104, pp.279-282.
- Němeček J., Šmilauer V. & Kopecký L. (2011) Nanoindentation characteristics of alkali-activated aluminosilicate materials, *Cement and Concrete Composites*, 33, 2, pp.163-170.
- Oliver W. & Pharr G. (1992) An improved technique for determining hardness and elastic modulus using load and displacement sensing indentation experiments, *Journal of Material Research*, 7, 6, pp.1564-1583.
- Zaoui A. (2002) Continuum Micromechanics: Survey, *Journal of Engineering Mechanics*, 128, 8, pp.808-816.

## **PROBLEM OF IDENTIFICATION OF DETERMINISTIC CHAOS IN THE INTERACTIVE DRIVE SYSTEMS**

**C. Kratochvíl<sup>\*</sup>, P. Švéda<sup>\*\*</sup>, M. Houfek<sup>\*</sup>, L. Houfek<sup>\*</sup>**

**Abstract:** *Chaos and chaos theory is a field of study in mathematics, computer sciences, electronics, physics and also engineering too. In our article will be explored chaotic behaviour and numerical solutions of the models of drive systems with electric DC motors. These solutions are also bounded like equilibrium, periodic and quasiperiodic solution. There is no precise definition for a chaotic solution because it cannot be represented through standard mathematical functions. However, a chaotic solution is aperiodic solution, which is endowed with some special identifiable characteristics, for example attractors, bifurcations or one-and two dimensional maps.*

**Keywords:** *Chaos theory, attractor, assessment, phase portrait, power spectral density.*

### **1. Introduction**

Chaotic behaviour of deterministic system usually means that behaviour is an appearance of absolute random without causing any inherent laws. We can characterize the behaviour of real systems in engineering practice by their trajectories, which remain bounded in the phase space. These time-ordered set of states of a dynamical system are critically dependent on even small changes in initial conditions. That is why the chaotic behaviour of systems is long-term unpredictable. Despite the common belief that chaotic states occurs at a very low frequency, the chaotic behaviour can we mainly observe by the controlled systems. As well as the existence of nonlinearities, the fundamental attributes of everyday reality.

We can describe the behaviour of real systems in engineering practice as a deterministic chaos. Especially, in case of complex interactive systems, those arise in systems of coherent structures. We can observe random elements during system development even though the system as a whole may seem deterministic. It appears that under certain conditions we can see extreme amplification of certain disorders. That is because the systems act as filters, suppressing or amplifying certain disorders.

These partial processes can be initially linear. But they can lead after a certain time to the massive application of pervasive non-linearity (Moon, 1992). Especially in cases, if there is failure to gain over a certain limit, shifting the entire system into a chaotic state. This is a general property of nonlinear dynamical systems described by mathematical equations; sensitivity to small changes in initial conditions, excitation or change some parameters vary depending on the conditions and nature of these disorders. We can observe states of disorder – at first appears extreme increasing vulnerability to certain disorders, then there is a loss of stability of the system changing the quality of its behaviour. The chaotic behaviour of the system increases its complexity (the number of degrees of freedom grows). There is a simple reason why the study of the chaotic states has no research attention so long. It is because the researchers were not able to use linear mathematical models.

---

<sup>\*</sup> prof. Ing. Ctirad Kratochvíl, DrSc. FEng., Ing. Martin Houfek and Ing. Lubomír Houfek, Ph.D.: Centre of Mechatronics – Institute of Thermomechanics AS CR and Institute of Solid Mechanics, Mechatronics and Biomechanics, Department of Mechatronics, Faculty of Mechanical Engineering, Brno University of Technology, Technická 2, 616 69 Brno; CZ, e-mails: kratochvil@fme.vutbr.cz, houfek.m@fme.vutbr.cz, houfek@fme.vutbr.cz

<sup>\*\*</sup> Mgr. Petr Švéda: Institute of Solid Mechanics, Mechatronics and Biomechanics, Department of Mechatronics, Faculty of Mechanical Engineering, Brno University of Technology, Technická 2896/2, 616 69 Brno; CZ, e-mail: y120953@stud.fme.vutbr.cz

In recent years much attention has been devoted to the study the phenomena of chaos. It is shown that chaos control can be extremely effective and often the only possible solution to many difficult problems. But chaos identification is not simple or straightforward especially in case of complex sets of systems. We are able to identify chaos rapidly in case of simple dynamical systems with typical grading procedures – e.g. Lyapunov exponents, Poincaré maps, conditional and unconditional methods for identification of coherent structures, bifurcation diagrams, etc. All these approaches are often ambiguous and considered as rarely applicable for complex technical systems. Therefore they are unacceptable in engineering practice at the present state of knowledge. For this reason, we assumed alternative approaches and this paper presents some interesting results.

## 2. Identification of chaotic states of complex dynamical systems

At first, we must remember, that there is no standard definition of chaos in science and technology yet. However, we can specify a range of attributes of chaos. And we use ones which can characterize the notion of chaos and identify states of disorder. There is an important way to evaluate the chaotic states – the assessment of genesis and structure of chaotic attractors.

Some attractors, e.g. point attractor, represent the final state of a system in equilibrium. Others, e.g. cycle attractor, describe the final state of periodically repetitive variation between two or more different states. Chaotic attractor, also known as strange attractor, characterizes the system that never reaches the final state of equilibrium or repeating cycle. We are able to observe the second and third ones, cycle or strange attractors, in phase space – even in response to changes in any critical parameter. Attractors are more than a mathematical abstraction. They represent a very important type, so called in-form. The system state is close to the attractor more probably and therefore more developed, than other possible states. If the trajectory of the dynamical system in the attractor would be in line with the image of the desired future state, the history contains this attractor will be strengthened and increases the likelihood of its implementation. On the contrary, inconsistency of both images will lead to suppression of unwanted history (Kratochvíl & Heriban, 2010).

Very interesting is also the relation between the phase diagrams before and during stabilization of chaotic attractors, and some statistical characteristics of the signals.

And also these changes can predict achieving closeness or reaching chaotic states. This is not about any breakthrough – it is only the ability to correctly interpret the results easily reachable and resulting from realistic simulation experiments.

## 3. Dynamical system analysis example

We demonstrate the methodology outlined to identify chaotic states of drive system on a model (see Fig. 1).

The drive system model is controlled and the control scheme is as shown in Figure 2. Consider only the basic structure, including the effects of excitation, as shown in Figure 1. We can describe this mathematical model (discretized time-invariant system) in the form of matrix equation (Sprott, 2003)

$$\dot{x} = A(t).x, \quad x(t) \in R^n \quad (1)$$

where  $x(t)$  is the vector of state variables and  $A(t)$  the matrix system. Eq. (1) represents an approximate linearization of the system  $\dot{x} = f(x)$ ,  $x(t) \in X \subset R^n$  along a reference trajectory. Due to linearity, we can assume that equation (1) is known and any initial conditions are given by

$$x(t) = \Phi(t, t_0), \quad \forall(t, t_0) \in R^1 \quad (2)$$

which is called the fundamental matrix of linearized system. Lyapunov coefficients, which indicate the range of sensitivity to initial conditions, are then given by the equation

$$\lambda_i = \lim_{t \rightarrow \infty} \frac{\|\Phi(t, t_0)\|}{t - t_0} \quad (3)$$

Matrix  $A(t)$  obtained by linearization along the trajectory in phase portraits of non-linear system of order  $n$  generates  $n$  Lyapunov coefficients, which are always real. However, numerical calculations of

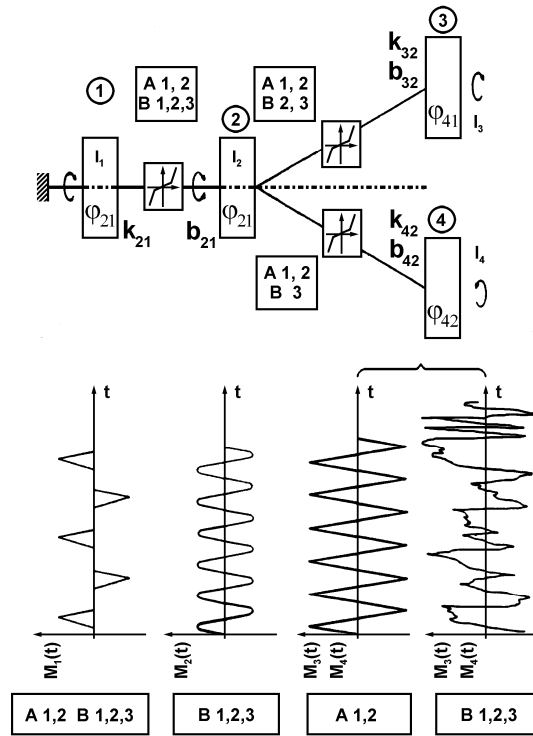


Fig. 1: Drive system model.

their values require different approximations and averaging are often problematic (Moon, 1992). In described case it is doubly true, the solution is given by the extra control method as indicated in Fig. 2.

The analysis of state trajectories but also allows the identification of chaos (Kratochvíl & Heriban, 2010), as we discussed in previous paragraph. In our case, we choose following combinations of tightness in linkage: will assume 0.010 [rad] in the linkage (1-2), and one after another 0.015, 0.030 and 0.050 [rad] in the linkage (2-3). The top row of Fig. 3 shows the phase portraits for third combination and the bottom row second combinations of tightness in second linkage. We will begin with the chaotic state, as shown in the left column, and see how the behaviour of the growing tightness in the linkage (2-3) is gradually changing the system in order to stabilize it. The process is also obvious in the progression of standard stochastic characteristics – the power spectral densities (PSD), see Fig. 4. Left part of Fig. 4 shows a progression of PSD for third linear case without tightness. Middle part of Figure 4 shows results for a combination of tightness 0.010 and 0.015 [rad]. Right part of Figure 4 shows results for a combination of tightness 0.010 and 0.030 [rad]. We can clearly identify differences of linear and nonlinear model of drive. Also, we can describe the suppression of spurious interprocedural cycles for gradual stabilization of the system. At the same time, we demonstrate a correlation between the statistical characteristics of phase portraits in the phase plane.

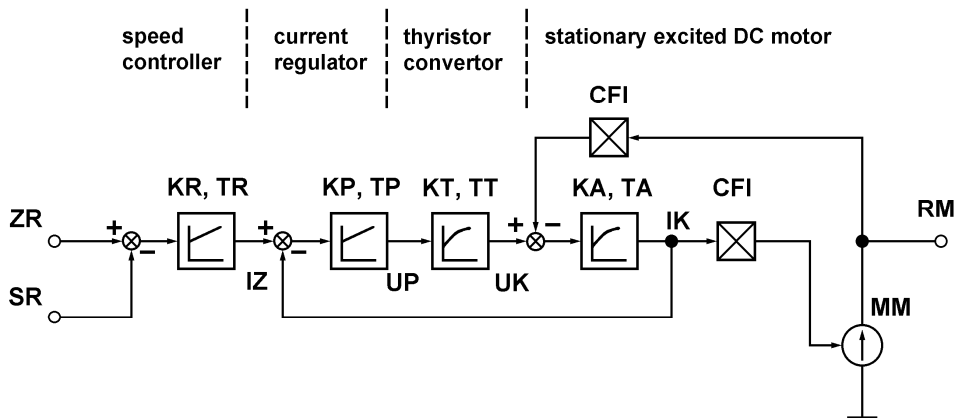
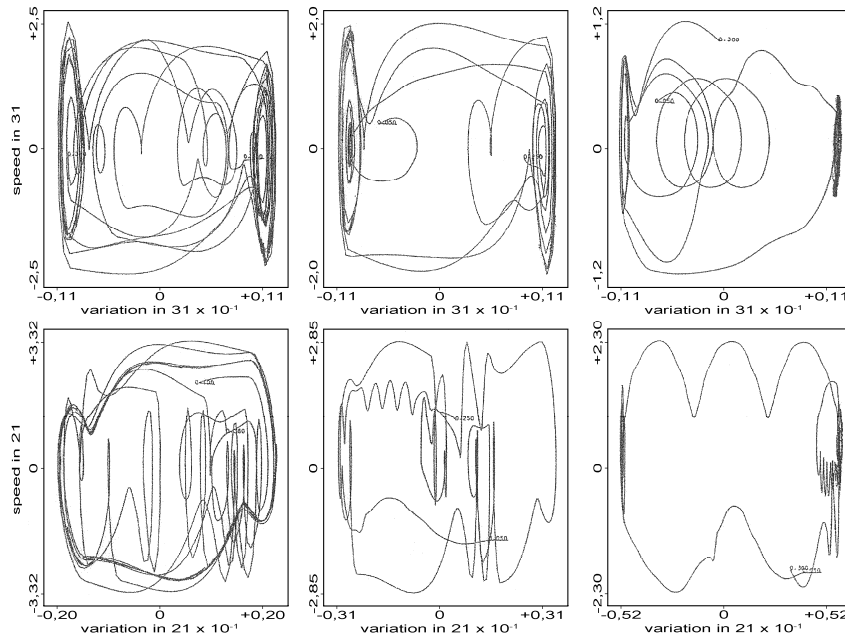
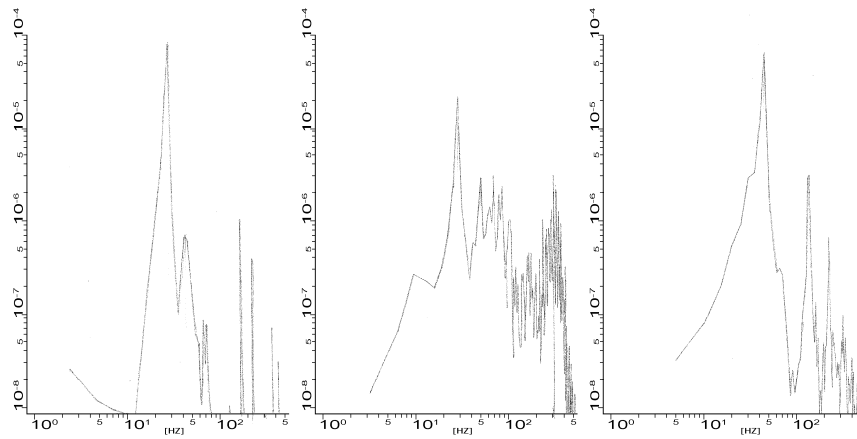


Fig. 2: Control scheme.



*Fig. 3: Phase portraits.*



*Fig. 4: Power spectral density (PSD).*

#### 4. Conclusions

In recent days we analyze different combinations of parameters and models of dynamical systems. And we compare the entire spectrum of the primary statistical characteristics and its correlation. We are able to observe clear links between these waveforms and waveform characteristics of phase portraits in the phase planes. We detect characteristic changes that appear just before the systems reaches chaos states and after the transitions. Also we hope that we will be able to generalize. These results would lead to a significant simplification of the computational analysis of complex dynamical systems.

#### Acknowledgement

Institute of Termomechanics, Academy of Sciences of the Czech Republic is gratefully acknowledged to support this work under research plan no. AV0Z20760514.

#### References

- Kratochvíl, C. & Heriban, P. (2010) Dynamical systems and chaos. BUT Brno, Brno.
- Moon, F.C. (1992) Chaotic and Fractal Dynamic: An Introduction for Applied Scientists and Engineers. J. Wiley & Sons, Inc., New York.
- Sprott, J.C. (2003) Chaos and Time-Series Analysis. Oxford University Press, New York.



## ANALYSIS OF SLENDER BRIDGE STRUCTURE

O. Kratochvíl<sup>\*</sup>, J. Křížan<sup>\*</sup>

**Abstract:** *The following article presents the results of analysis of slender bridge structure to dynamic loads induced by movement of people. Further is emphasized the importance of modal analysis of structures thus the calculation of eigenfrequencies and modes of vibrations such as prediction of behaviour under dynamic load. In considering of large ratio between the weight of structure and pedestrians will not be discussed the type of loading causing adverse response of the structure in terms of first and second limit state. In this case the decisive criteria are on the part of pedestrians. Detailed examination and comparison with the criteria of comfort specified in the standards is not carried out in this paper. Attention is focused on the design of the computational model and method of application load representing the movement of people. Computational model of footbridge is designed to allow for variable load application in space and time. The same procedure can simulate the movement of small group of pedestrians that move in sync walking. The program system ANSYS was used for the analysis.*

**Keywords:** *Footbridge, eigenfrequencies, vibrations modes, moving dynamic loads.*

### 1. Introduction

The paper deals with the analysis of the dynamic response of slender footbridges under human-induced dynamic loads. These loads are a frequently occurring and often dominant load for footbridges. Due to the development of new materials and advanced engineering technology slender footbridges are increasingly becoming popular to satisfy the modern transportation needs and the aesthetical requirements of the society. However these structures are always lively with low stiffness, low mass, low damping and low eigenfrequencies. As a consequence they are predisposed to vibration induced by human activities and can suffer weighty vibration and problems of serviceability particularly in the lateral direction. Weighty vibration and problems of serviceability can arise particularly in the lateral direction as pedestrians are more sensitive to the low-frequency lateral vibration than the vertical one.

This is a problem that has a lot of uncertain input factors. The effect of the influence of parameters on the mass and stiffness can be studied by methods of sensitivity analysis Kala (2009). Advanced is a method of global sensitivity analysis that allows us to analyze the higher order interaction effects Kala (2010).

### 2. Human-induced dynamic loads

The force transmitted by the foot on the pad was thoroughly examined and then expressed analytically. Treading force has a nonzero component in three orthogonal directions: longitudinal, lateral and vertical. The vertical component of stepping force is the most important. The course of stepping force in time is approximately periodic. The frequency of normal walking is in the range from 1.3 to 2.4 Hz. Two types of load's models depending on the time can found in the literature: deterministic and probabilistic. The first type is given by the force representing the weight of pedestrians. Value of force varies according to the periodic time-dependent functions. For one frequency of walking is one formulation of the load created. The second type is given by the randomization of input values such as weight and speed of pedestrian. The average weight of a person takes 70 kg. This force is transmitted by the foot on the pad in the value of changing the amplitude of the dynamic components of stepping force which is 18 kg.

---

<sup>\*</sup> Ing. Ondřej Kratochvíl and Ing. Jiří Křížan: Institute of Structural Mechanics, Brno University of Technology, Faculty of Civil Engineering, Veveří 95; 602 00, Brno; CZ, e-mails: [ondrej.kratochvil@seznam.cz](mailto:ondrej.kratochvil@seznam.cz), [krizan.j@fce.vutbr.cz](mailto:krizan.j@fce.vutbr.cz)

Three harmonic frequencies are defined in the paper Block & Schlaich (2002):  $f(1) = 2$  Hz,  $f(2) = 4$  Hz,  $f(3) = 6$  Hz. Simple expression of dynamic force  $F(t)$  is:

$$F(t) = \alpha \cdot m_p \cdot g \cdot \cos \omega(t) \quad (1)$$

where:  $\alpha$  is a correction factor reflecting the difficulty of determining the vertical load and its diversity and its value is linearly dependent on the number of steps per second;  $m_p \cdot g$  weight of pedestrian [N];  $\omega = 2\pi f_p$ ;  $f_p$  step frequency described in the paper Block & Schlaich (2002).

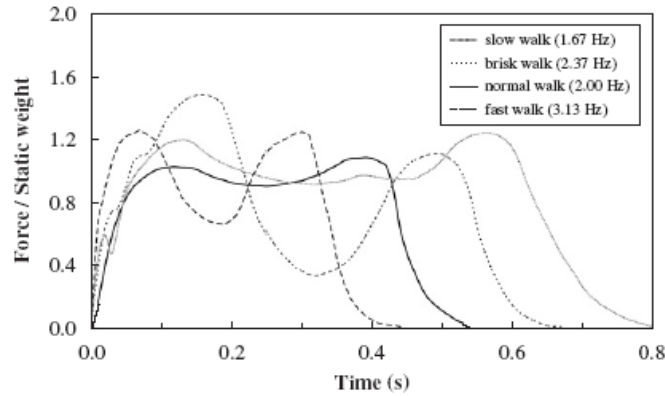


Fig. 1: Vertical force produced by one person taking one step.

Dynamic load is recommended for all types of footbridges by one pedestrian described in the paper Block & Schlaich (2002).

$$F(t) = 700 \cdot 0.257 \cdot \sin(2\pi f_0 t) \quad (2)$$

where 700 [N] is the weight of one pedestrian; 0.257 dynamic coefficient;  $f_0$  step frequency complying with the frequency of the footbridge.

Analysis of footbridge, described in this paper, is carried out by load of pedestrians expressed by the equations (3) and (4). Equations express two perpendicular components of stepping force. The dominant component of stepping force is given by equation (3) and smaller component perpendicular to the direction of walking is given by equation (4).

$$F(t) = 700 + 180 \cdot \sin(2\pi f t) \quad (3)$$

$$F(t) = 45 \cdot \sin(2\pi f t) \quad (4)$$

### 3. Description of the bridge structure

Construction of footbridge is designed as a suspended. Total length of the footbridge is 84 m and height of pylons is 16 m. The slack of the main supporting cable is 13 m. The roadway is 3 m width and is composed of runners 200 mm high which strengthen plate of roadway 8 mm thick. Surface coarse is made of poured resin with fill of thickness of 12 mm.

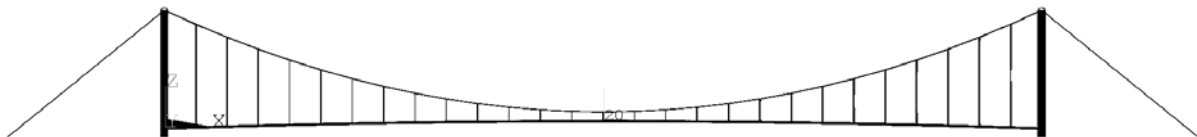


Fig. 2: One span suspended footbridge with 84 m long deck.

#### 4. Eigenfrequencies and mode vibrations

Eigenfrequency and corresponding eigenvector are important dynamic properties. They describe the behaviour of structure under dynamic load. Three basic eigenvector are: bending, torsional and longitudinal. There are also combinations of shapes such as torsion-bending wave shape. Eigenfrequencies found in the frequency range of human walking are in the case of load by moving people for the structure dangerous. It means occurrence of vibrations of structure by movement certain number of people in sync walking.

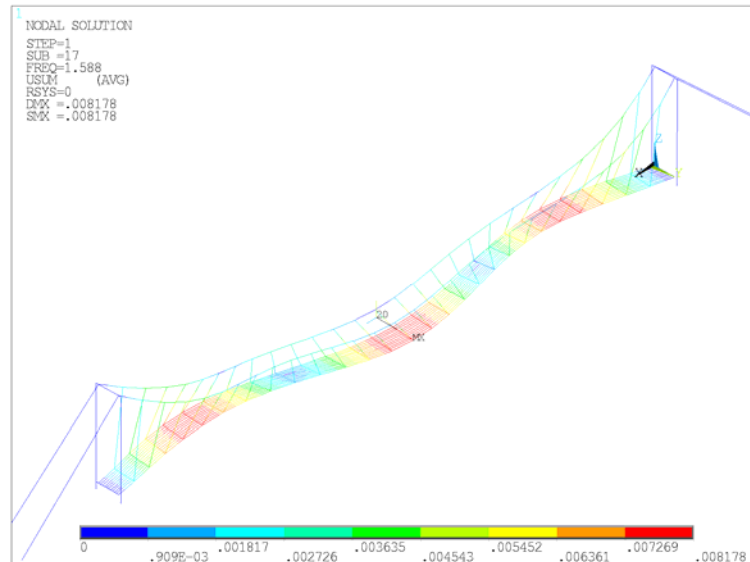


Fig. 3: Eigenvector according to  $f = 1.588$  Hz.

#### 5. Dynamic response of the bridge structures on single pedestrian load

The frequency step was chosen according to the bending frequency of the structure. The force representing pedestrian was moved by 10 cm and by 5 cm. Densification of finite elements was performed on runners which are distant 60 cm from the midline of the roadway on both sides. The load corresponding to the intensity of stepping force in the time is applied to the nodes on these runners. The frequency was selected to the higher bending eigenfrequency of the structure. Evaluation of the response of the structure is performed in chosen nodes for the time of the load. This means the time required to pass the footbridge. Evaluated sites are in the mid-range and in the quarter of span of the roadway. The graphs Fig. 4 and Fig. 5 present the response of the structure in a selected point on the load of a pedestrian as defined in equation (3). Load is allocated to individual points along the roadway in the selected time step and corresponds to walking speed. The graphs on the left side of Fig. 4 and Fig. 5 describe the displacement of the point in time and the graphs on the right side of Fig. 4 and Fig. 5 acceleration of the point in time. The difference between Fig. 4 and Fig. 5 is given by the density of roadway finite element mesh. Fig. 5 presents finer mesh.

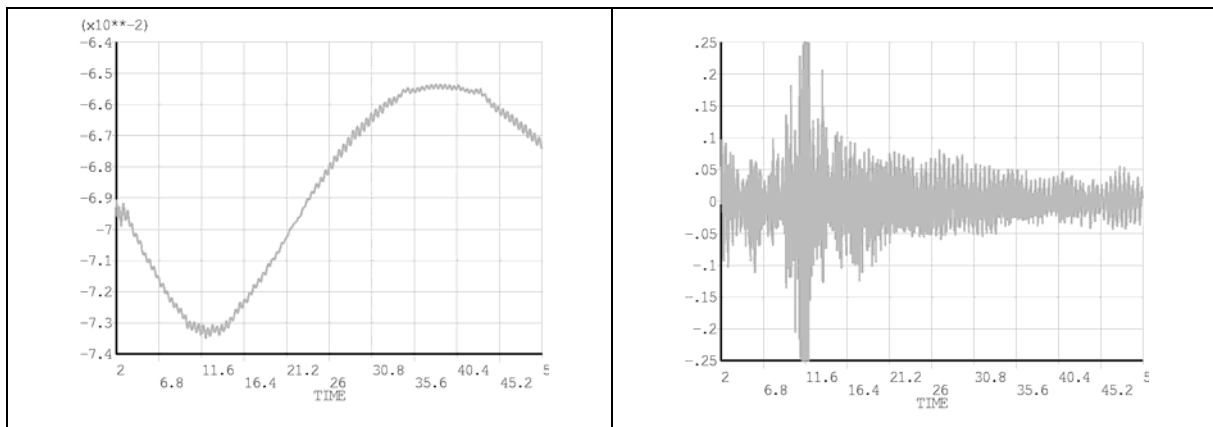


Fig. 4: Vertical displacements  $U_z$ , vertical acceleration, near  $L/4$ .

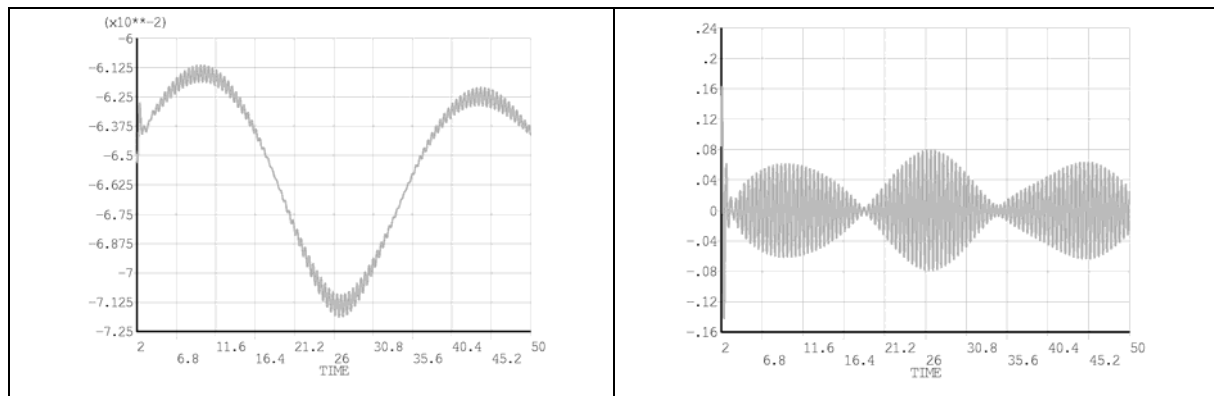


Fig. 5: Vertical displacements  $U_z$ , vertical acceleration, mid span.

## 6. Conclusions

The response of the footbridge on the movement of pedestrians was solved for the motion simulation by 1 and 2 pedestrians. Stepping force was expressed in two variants. In the first variant the stepping force is represented only by its dominant vertical component. In the second variant is added also lateral component of stepping force. Walking speed was chosen according to the eigenfrequency of 2.1 Hz which corresponds to the bending shape with three vertical antinode loops along the roadway. The results show that the structure vibrated under load of pedestrians in sync walking. The selected point achieves the maximum acceleration  $0.45 \text{ ms}^{-2}$  and threshold, defining the acceptable comfort for such a structure, is according to Eurocode  $0.7 \text{ ms}^{-2}$ . Thus there is some distortion of walking comfort but not fatal.

The second aim of this paper was to present the influence of discretization of the computational model on the results analysis of dynamic load. It is recommended to use a finer division in compiling the computational model and its subsequent discretization namely approximately to the maximum element length 50 mm.

## Acknowledgement

The article was elaborated within the framework of research project GACR 103/09/1258 and GACR 104/11/0703.

## References

- Bachmann, H. (2002) "Lively" footbridges – a real challenge. Proceedings of the International Conference on the Design and Dynamic Behaviour of Footbridges, Paris, 18p.
- Block, C. & Schlaich, M. (2002) Dynamic behaviour of a multi-span stress-ribbon bridge. International conference IABSE, Paris, 15 p.
- Kala, J., Hradil, P., Salajka, V. & Jutner, V. (2010) Dynamic response of cable stayed steel bridge with tuned mass damper installed - numerical and experimental approach, In proc. 10th Int. conf. Modern building materials, Structures and techniques, Selected papers, Vilnius, Lithuania, pp. 658-667,
- Kala, J., Hradil, P. & Salajka, V. (2010) Comfort criteria for suspension footbridge response on single pedestrian induced vibration analysis, In proc. ESREL 2010 - Reliability, Risk and Safety, Rhodes, Greece, pp. 1535-1540, ISBN 978-0-415-60427-7.
- Kala, Z. (2009) Sensitivity assessment of steel members under compression. Engineering Structures, 31, 6, pp.1344-1348.
- Kala, Z. (2010) Sensitivity analysis of stability problems of steel plane frames. Thin-Walled Structures, (in print) doi:10.1016/j.tws.2010.09.006.
- Ming, H. J. (2006) Dynamic Characteristics of Slender Suspension Footbridges. Queensland University of Technology, 13p.
- Stoyanoff, S., Hunter, M. & Byuers, D. (2002) Human – induced vibrations on footbridges. Proceedings of the International Conference on the Design and Dynamic Behaviour of Footbridges, Paris, France.
- Živanovic, S., Pavic, A. & Reynolds, P. (2005) Vibration serviceability of footbridges under human-induced excitation: a literature review. Journal of Sound and Vibration, 76 p.

## MOBILE ROBOT MOTION PLANNER VIA NEURAL NETWORK

J. Krejsa<sup>\*</sup>, S. Věchet<sup>\*\*</sup>

**Abstract:** *Motion planning is essential for mobile robot successful navigation. There are many algorithms for motion planning under various constraints. However, in some cases the human can still do a better job, therefore it would be advantageous to create a planner based on data gathered from the robot simulation when humans do the planning. The paper presents the method of using the neural network to transfer the previously gained knowledge into the machine learning based planner. In particular the neural network task is to mimic the planner based on finite state machine. The tests proved that neural network can successfully learn to navigate in constrained environment.*

**Keywords:** *Mobile robot, motion planning, neural networks.*

### 1. Introduction

Navigation of mobile robots usually incorporates several modules among which the path planning and position estimation are the most important ones. There is a vast number of approaches for path planning in both constrained and unconstrained environment. Most of the planning algorithms do not take into account dynamic obstacles or when they do, low number of obstacles is expected. The usual solution is to detect the dynamic obstacle and predict its motion thus creating another constrain in the configuration space.

In our application the safe path planner controls the robot in indoor environment with dynamic obstacles. There is high number of obstacles and their motion is hard to predict. This excludes most of the planning algorithms that calculate the whole track to the goal as unpredictable movement can create constraint that suppress validity of the path proposed. Further issues to consider in the application are: the optimality of the path is not required, available computational power is limited. Therefore some kind of semireactive navigation must be used, that is fast enough but does not ignore the goal position. That lead to idea to use complex controller, gather the data and use machine learning to mimic (approximate) such controller in a fast manner. Neural networks (NN) are a natural choice of machine learning engine for such a case. In (Yang, 2003, Janglová, 2004, Sirotenko, 2006) the NN is used for mobile robot navigation based on proximity sensors values. Our proposed method also uses the proximity sensors values, but additionally incorporates the past values of planner output as NN inputs. Such approach enables NN to learn the internal state of the planner and solve the navigation problem when the nonholonomic constraints require the robot to backup.

The paper describes proposed method on the case, when motion planner based on finite state machine (FSM) with internal state was used to generate the data for feedforward neural network. The network is then trained and further used as the motion planner.

### 2. Methods

In order to use neural network based planner, the data must be gathered first for NN training. While our ultimate goal is to use observations of human controlling the robot, in the first attempts we used the planner currently used in our robot that is based on finite state machine with internal state. The scheme of the simulation data flow is shown in Fig. 1.

---

<sup>\*</sup> Ing. Jiří Krejsa, PhD.: Institute of Thermomechanics AS CR, v.v.i., Brno branch, Technická 2, 616 69, Brno, CZ, email: krejsa@fme.vutbr.cz

<sup>\*\*</sup> Ing. Stanislav Věchet, PhD.: Faculty of Mechanical Engineering, Brno University of Technology, Technická 2, 616 69, Brno, CZ, , e-mail: vechet.s@fme.vutbr.cz

The planner receives the array of ultrasound sensors proximity measurements, the estimate of the robot position ( $x$  and  $y$  coordinates and heading angle in global coordinate system) and the position of the goal. The estimate of robot position is obtained from the estimator that implements extended Kalman filter. The output from the planner consists of generalized velocities (translation and rotation) that are fed into robot simulation module in the case of simulation or to the action converter in the case of real robot, where the velocities are recalculated into main drive velocity and front wheels steering angle. Those actions are then fed into the actuator controllers. The estimator receives the action (velocities) and measurement of static beacons placed in known positions. Extended Kalman filter produces the estimate of the robot position, further used in the planner.

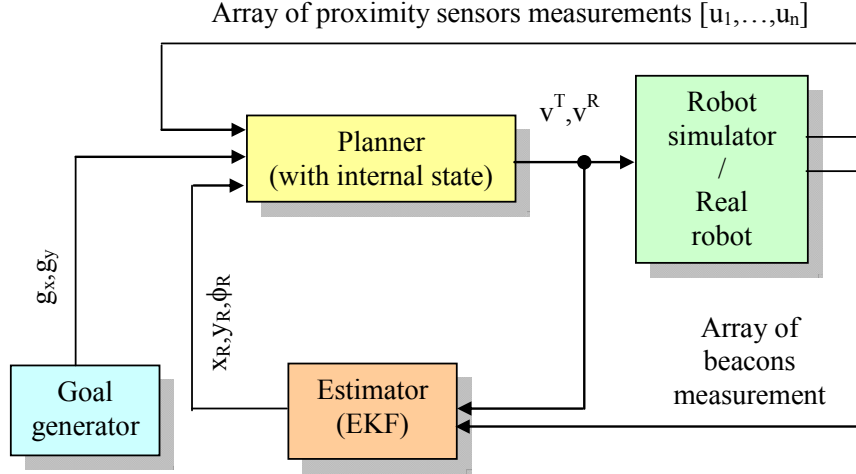


Fig. 1: Gathering data for NN training.

Neural network based planner uses feed forward NN to approximate the planner to be learned. The feed forward NN does not contain the feedback connections, however, the feedback is required as the original planner contains the internal state. Therefore the delayed outputs (generalized velocities) are used as additional inputs to the network. Furthermore the recalculation of the angle towards the goal position is also performed before the data are fed into the network. To summarize the inputs to the NN, it consists of following variables;

$$NN_{inp} = [u_1, \dots, u_n, \Delta\varphi_g, v_{k-1}^T, v_{k-1}^R, \dots, v_{k-m}^T, v_{k-m}^R]^T \quad (1)$$

where  $n$  is number of proximity sensors,  $u_i$  is  $i$ -th proximity sensor measurement,  $\Delta\varphi_g$  is the angle towards the goal,  $v_{k-1}^T, v_{k-1}^R$  are the translational and rotational velocities delayed for a single step delay and  $m$  is maximum number of delays used.

The angle towards the goal is calculated from the estimated position, the proximity measurement is in simulation disturbed with the Gaussian noise with experimentally found characteristics. Once the data are gathered and NN is trained to sufficient level of precision, it can be incorporated into the robot navigation structure. The overall scheme is shown in Fig. 2.

### 3. Numerical experiments details

The robot used for experiments is test wheeled robot with driven back wheels and Ackerman steering. Robot motion is modeled in discrete time steps. The motion model incorporates the noise on front wheels IRC sensors used to calculate the estimate of odometry readings. The localization of the robot is obtained via extended Kalman filter that uses the actions given by the planner, motion model and readings of beacon receiver that gives the relative angle to beacons placed in fixed known positions. Details about the position estimator can be found e.g. in (Krejsa, 2010).

The data used for training were obtained from a single experiment where the robot was driven by FSM based planner to the goals sequentially regenerated once the robot approached to the given distance to the current goal. The goals were generated randomly in a simulated room of H shape with overall size of 20x20 meters. The training run included dynamic obstacles of various sizes moving in various, but



constant velocities. The translation velocity of the robot was limited to 0.6m/s and data were calculated in time step of 0.5 sec. Total of 2351 sets of data were gathered and preprocessed for the training.

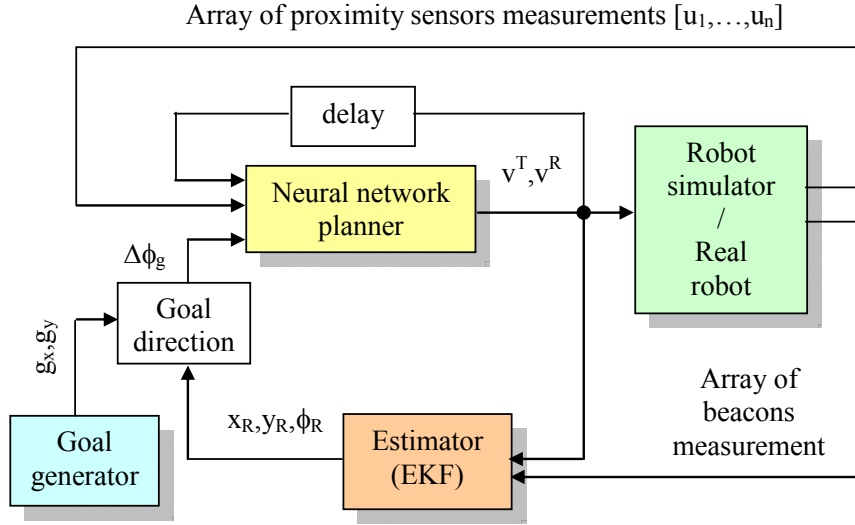


Fig. 2: NN used as motion planner.

Neural network was trained off-line with traditional Levenberg-Marquardt algorithm implemented in Matlab Neural Network Toolbox. Initially the number of past actions fed back as the input to the network (parameter  $m$  from (1)) was set to 1. The learning MSE stayed at about  $1.26e^{-3}$  and when NN was used in navigation process it exhibited occasional unstable behavior. Therefore  $m$  was increased to 2, which proved to be sufficient. The learning MSE quickly dropped to  $2.31e^{-4}$ . The first impression of the quality of the training was obtained by testing the network on previously unseen set of test data gathered by the same process as the training data. The comparison of network output and known outputs are shown in Fig. 3.

For further testing the learned network was used in simulation of the whole navigation process. As the dynamic obstacles move in random directions, NN planner can not be directly compared with its predecessor. In order to determine successfulness of the planner the number of simulations were run and results were expressed in two simple parameters: number of steps required to reach the goal and number hits to the obstacles (both static and dynamic). Regarding both parameters the methods are directly comparable, see Tab. 1.

Tab. 1: FSM and NN planners comparison.

<i>Planner</i>	<i>hits / 1000 steps</i>	<i>average path length</i>
FSM based	0.272	95.4 [m]
NN based	0.261	98.2 [m]

#### 4. Conclusions

Simulation results proved that neural network based planner is capable of learning required behavior. The main advantage of using the NN planner is the speed and low computational requirements. The drawback might be in inability to guarantee safe planning in all times, therefore certain safety measure module must be incorporated that will stop the robot when proximity sensors detect distances below safety threshold. Such system is already implemented and used in real robot.

NN planner with the feedback of previously generated actions used as additional inputs enables the planner to consider the state of the robot, enabling the use of such planner under nonholonomic constraints when backing up is necessary to meet the goal.

Regarding future work, the next step is in gathering the data from simulator when human will be used to control the robot based on the robot sensor information available. Whether the NN planner trained

on such data is capable of planning in hard to solve situation (typically overcrowded space) is the question we would like to answer.

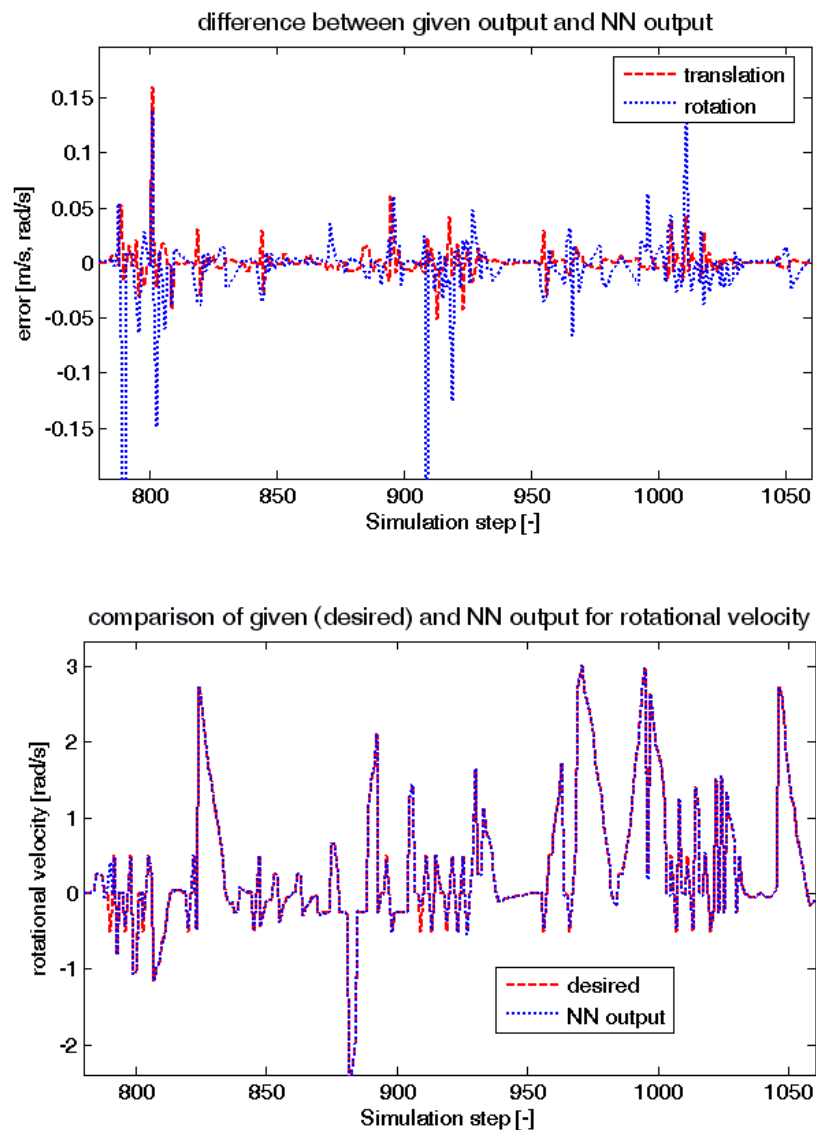


*Fig. 3: Test run results.*

### Acknowledgement

Published results were acquired with the support of the Academy of Sciences of the Czech Republic under the research plan AV0Z20760514 and with the support of the Operational Programme Education for Competitiveness, project number CZ.1.07/2.3.00/09.0162.

### References

- Janglová, D. (2004) Neural Networks in Mobile Robot Motion, International Journal of Advanced Robotic Systems, vol. 1 (1), pp. 15-22.
- Krejsa J., Věchet S. (2010) Odometry-free mobile robot localization using bearing only beacons, in Proceedigns of EPE-PEMC 2010 conference, Republic of Macedonia, pp. T5/40-T5/45.
- Sirotenko M.Y. (2006) Applications of Convolutional Neural Networks in Mobile Robots Motion Trajectory Planning. Mobile Robots and Mechatronic Systems: Proceedings of Scientific Conference and Workshop, Moscow, pp. 174-181.
- Yang S.X., Meng M.H. (2003) Real-time collision-free motion planning of a mobile robot using a Neural Dynamics-based approach, IEEE Transaction of neural networks, 2003; vol. 14 (6), pp 1541-1552.

## PARALLELIZATION OF THE DELAUNAY TRIANGULATION

D. Krybus<sup>\*</sup>, B. Patzák<sup>\*</sup>

**Abstract:** *This paper deals with the parallelization of Delaunay triangulation. Meshing algorithms are relatively time and memory consuming for large problems. In connection with the spread of multi-core CPUs even among personal computers, the parallelization of the meshing process permits optimal utilization of available computational resources. The triangulation is used for the mesh generation in the context of numerical modeling of fluid flow via Lagrangian finite element method. The possibility of the reuse of the previously developed sequential code in terms of parallelization is discussed and other possible approaches are outlined.*

**Keywords:** *Delaunay triangulation, mesh generation, parallelization, shared memory, distributed memory.*

### 1. Introduction

Typical approach in modeling fluid flow consists in the use of Eulerian description of motion. The computational mesh is fixed and the material points move with the respect to the grid. In Lagrangian description, each node of the computational mesh is associated with the material particle during the motion. Arbitrary Lagrangian – Eulerian (ALE) formulation combines these two classical approaches mentioned in order to gain their best features and avoid their disadvantages (Donea & Huerta, 2004).

The fact that the movement of a domain occurs separately from moving a finite element mesh, is common for both ALE and Eulerian approaches. The relationship between them introduces convective terms of movement in momentum equations. Their treatment is not the only numerical difficulty coming with ALE and Eulerian approaches. Also the proper treatment of the incompressibility condition, tracking of a free surface, correct interaction on a phases contact or description of large movements need to be secured.

The use of Lagrangian description has several advantages and some of the mentioned difficulties are not involved. Usually, it is widely applied for modeling large deformations in structural mechanics. Perhaps the main drawback of this approach consists in the frequent demands for re-meshing in order to avoid numerical instability due to large distortions of computational mesh. On the other hand, tracking of free surfaces and material interfaces is possible in a natural way. The Lagrangian formulation of the problem is set by a collection of so-called particles which represents a certain part of continuum. To integrate governing equations in each solution step, a mesh built from particles is needed. The mesh is generated by connecting particles together, actual positions of which are given by initial conditions or are determined by solution procedure. In this work, a triangulation of set of particles is used, as triangular elements are simple to formulate and numerically efficient. The algorithm based on Delaunay triangulation has been chosen.

The requirements for the parallelization of the meshing process are hard mainly due to relatively high time and memory demands of these algorithms. The parallelization allows obtaining results in reasonable time by utilization of potential of modern multi-core processing units. Nowadays, almost every personal computer or laptop comes with a multi-core CPU. It is natural and reasonable to use these available resources.

---

<sup>\*</sup> Ing. David Krybus and prof. Dr. Ing. Bořek Patzák: Department of Mechanics, Faculty of Civil Engineering, Czech Technical University in Prague; Thákurova 7; 166 29 Prague; CZ, e-mails: david.krybus@fsv.cvut.cz, borek.patzak@fsv.cvut.cz

## 2. Delaunay triangulation

Many algorithms for mesh generation are based on Delaunay triangulation. It consists in such triangulation of a general set of points that no point lies inside circumscribed circle of any triangle except three points forming triangle, that actually lie on circle. Delaunay triangulation maximizes the minimum angle in triangles and it leads to a quite numerically stable mesh. This definition can be simply extended to a three-dimensional space, where the triangulation results in set of tetrahedrons with empty circumscribed spheres.

There are a lot of algorithms constructing the Delaunay triangulation. Incremental algorithms build a large group. In each step, a new point is added to the current triangulation, and then the mesh is rebuilt in order to satisfy the Delaunay condition. Flipping algorithms consist in changing, so called “flipping” non-Delaunay triangle edges. At the beginning, a general mesh is constructed. In the next step, it is optimized with the flipping to satisfy the Delaunay property. Other methods are based on the “divide and conquer” or the projection algorithms. The different approaches are discussed and compared in the Shewchuk’s paper (1996).

Delaunay triangulation using Bowyer/Watson incremental algorithm was implemented by authors and results were presented in the past (Krybus & Patzák, 2010). The meshing code is fully integrated into the OOFEM package (Patzak & Bittnar, 2001). It uses an octree data sorting in order to speed-up the search for non-Delaunay triangles during the mesh build-up phase.

## 3. Parallelization strategies

In general, several approaches to parallelization of Delaunay triangulation can be found in the literature. A very common way is the divide-and-conquer strategy, first proposed by Guibas & Stolfi (1985). It is based on recursive partitioning of the point sets and local triangulation of the subsets. The global triangulation results from merging in the final phase. Regarding these facts, this algorithm represents a naturally parallelizable approach. The points can be partitioned into certain regions upon their position in space. Next, each partition is assigned to a processor which builds the local triangulation. On the other hand, the merging phase is neither natural nor easy and in fact, it is the bottleneck of the method. In addition, the merging phase must be done only by one processing element with a considerable influence on the overall performance.

Other approaches are based on the concept of incremental insertion. To avoid multiple access to same data structure, the whole set of points is first partitioned into sub-regions. A load balancing technique must be employed in order to obtain reasonable speed up for general data (Chrischoides & Sukup, 1996). The Delaunay triangulation can be constructed incrementally by starting with the first triangle and building-up the triangulation in direction given by the outer normal vector of every edge. The “closest” point giving the “smallest” circumcircle with the edge is searched during the step (Cignoni et al. 1993), see Fig. 1. Finally, the parallelization of incremental approaches can be done without assigning regions to single processors. Kohout and Kolingerova (2003) developed an algorithm working with a shared global list of points, which is accessed by particular CPUs.

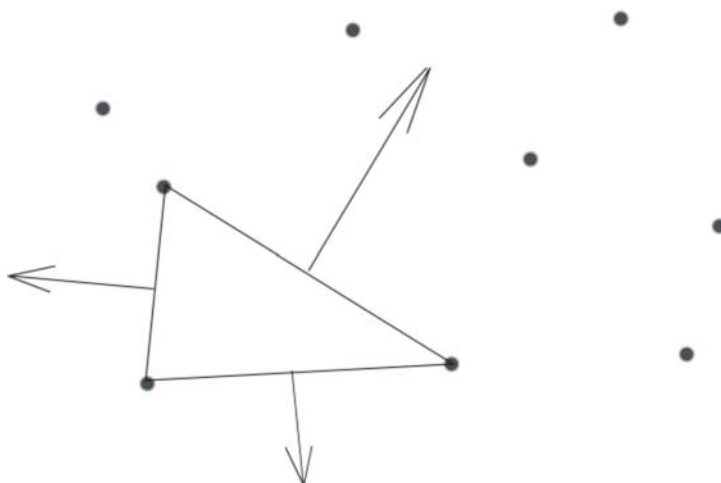


*Fig. 1: Incremental construction.*

### 3.1. Shared memory systems

Regarding the spread of multiple core personal computers, the first idea was to reuse the existing code and to improve it in order to allow its parallelization. The incremental algorithm is based on the insertion of the points one by one into the current triangulation. In one step, all triangles violating the Delaunay empty circle property are erased and the cavity is re-triangulated.

Considering shared memory parallel computer, the triangulation itself and its data structure is typically managed in the shared memory. When individual points are concurrently inserted, overlapping of the different cavities must be avoided in order to secure uniqueness of the triangulation or even crash of the triangulating execution. For example, consider the dark grey filled triangle in Fig. 2, the Delaunay property of which is affected by both inserted points, potentially leading to data access collision that must be resolved. Moreover, sophisticated data structures, i.e., spatial containers are usually used to allow fast search for non-Delaunay triangles. The point is that one must optimally ensure concurrent data access without excessive data locking, which is otherwise needed to obtain correct triangulation. Consequently, the scalability of the parallel code is affected in a negative way by these aspects.

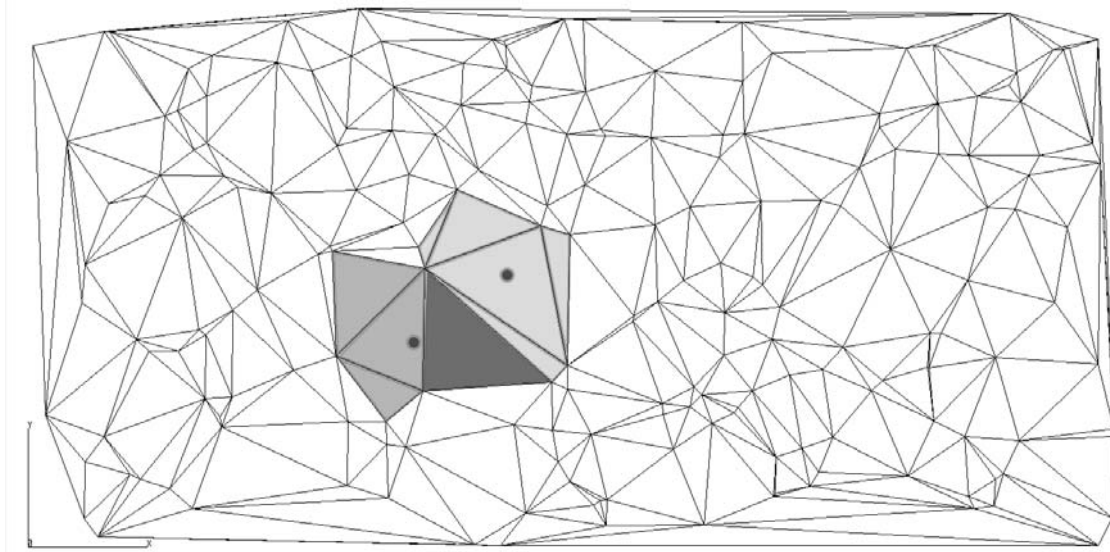


*Fig. 2: Triangulation of overlapping cavities.*

### 3.2. Systems with distributed memory

The original Bowyer/Watson algorithm is not very suitable for parallelization on distributed systems. In this case, each computational node manages the data stored in the own memory and any remote data has to be obtained by an explicit communication, contrary to shared memory systems, where data are globally accessible. However, the problem can be decomposed into sub-domains, meshed by single CPUs. This allows performing triangulation in parallel, but there is a significant data transfer between neighbouring domains to secure proper triangulation of the region borders. Every additional communication leads to a lower parallel efficiency of the resulting code.

A smart solution was proposed by Cignoni et al. (1993). Referring to the general classification, it is an incremental constructive algorithm. Contrary to the refining the triangulation by inserting points in Bowyer's /Watson's approach, it starts with one triangle which is final taking into account the resulting triangulation. The other triangles grow from the very first one, until all points are connected. This approach is reused in parallel context, where the idea consists in triangulating the region borders by the constructive algorithm first, so no more synchronization between processors is needed and until merging individual processors can work independently. Every processing unit responsible for triangulation of a certain area obtains a list of points contained and a "boundary" formed by appropriate edges of truly Delaunay triangles on the border. This is illustrated on Fig. 3, showing sub-domain boundary triangulation of rectangular domain, when four CPUs are considered. This step is performed sequentially. Then all processors receive corresponding part of boundary triangulation, list of particles inside each sub-region and start triangulation, which can be performed by any algorithm.

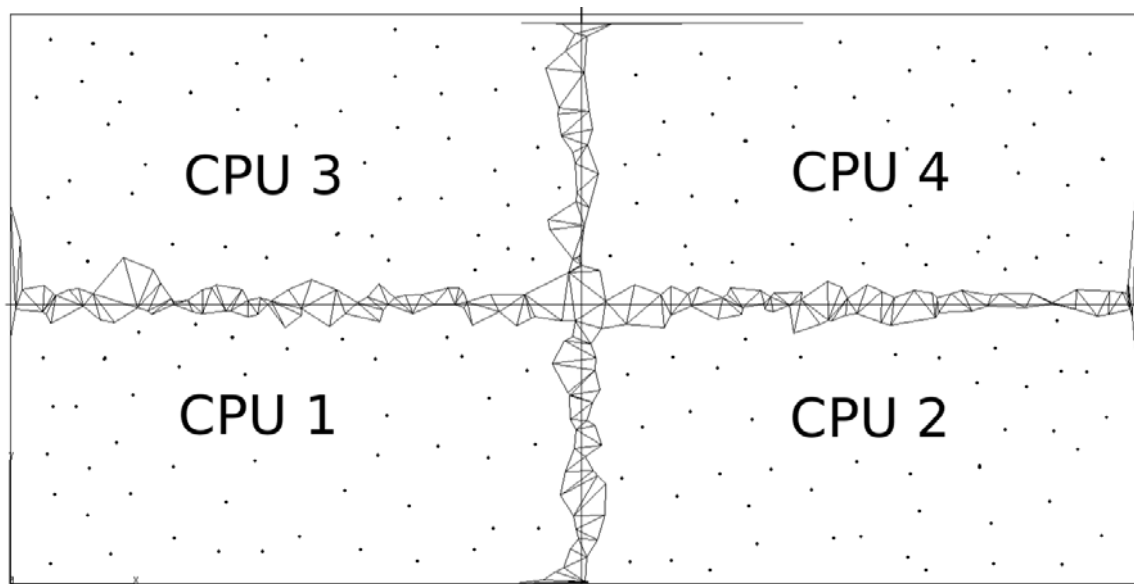


*Fig. 3: Triangulation of regions' borders.*

#### 4. Conclusions

In this work, Delaunay triangulation is used to construct a finite element mesh from particles representing a Lagrangian formulated fluid problem. Two different approaches to parallelization of Delaunay triangulation were described. The difficulties resulting from parallelization of the basic sequential algorithm were discussed. An approach based on the incremental construction algorithm suitable for the use on systems with distributed memory is proposed. Implementation of parallel algorithms, both the original Bowyer/Watson algorithm as well as the incremental construction, is the objective of present research. The task is not just the scalability of the algorithms but also their overall efficiency in comparison to existing codes. Future work will be focused on examination of practical application of meshing algorithm on fluid problems to answer the question whether a creating of a completely new mesh from scratch is faster than improvement of the distorted one.

#### Acknowledgement

Financial support of Grant agency of Czech Republic under the project No. 103/09/H078 is gratefully acknowledged.

#### References

- Chrisochoides, N. & Sukup, F. (1996) Task parallel implementation of the Bowyer-Watson algorithm, in: Proceedings of the Fifth International Conference on Numerical Grid Generation in Computational Fluid Dynamic and Related Fields: 773—782.
- Cignoni, P., Montani, C., Perego, R. & Scopigno, R. (1993) Parallel 3D Delaunay triangulation, Computer Graphics Forum 12(3): 129-142.
- Donea, J. & Huerta, A. (2004) Finite element methods for flow problems, J.Wiley, England.
- Guibas, L.J. & Stolfi, J. (1985) Primitives for the manipulation of general subdivisions and the computation of Voronoi diagrams, ACM Transactions on Graphics, Vol.4 (2): 74-123.
- Kohout, J. & Kolingerová, I. (2003). Parallel Delaunay triangulation based on circum-circle criterion. In Proceedings of the 19th Spring Conference on Computer Graphics: 73-81.
- Krybus, D. & Patzák, B. (2010). On the efficient triangulation of random point sets. Computer and Experimental Analysis of Civil Engineering Materials and their Multilayered Systems. CTU in Prague.
- Patzák, B. & Bittnar, Z. (2001) Design of object oriented finite element code. Advances in Engineering Software 32(10-11): 759-767.
- Shewchuck, J.R. (1996) Triangle: Engineering a 2D quality mesh generator and Delaunay triangulator. Applied Computational Geometry: 203-222.



## **DESIGN AND RELIABILITY ASSESSMENT OF ROOF STRUCTURAL ELEMENTS USING THE NEW DIGITAL GROUND SNOW LOAD MAP OF THE CZECH REPUBLIC**

**V. Křivý<sup>\*</sup>, R. Čajka<sup>\*</sup>**

**Abstract:** *The paper deals with the problems of design and reliability assessment of roof structural elements exposed to the effects of snow load. A new digital ground snow load map of the Czech Republic is introduced in this paper. This digital map provides to structural designers detailed information about the characteristics of snow load on the ground for arbitrary selected locality in the Czech Republic. The digital map covers the area of the Czech Republic by the net 100 x 100 m. The following data are given to every square 100 x 100 m: (a) characteristic value of snow load on the ground according to European standards; (b) statistical characteristics of annual maximum ground snow load (mean value  $\mu$ , standard deviation  $\sigma$ , variation coefficient  $V$  and skewness  $a$ ); (c) sorted ground snow load history - so called load duration curves. Possibilities of utilizing the data from digital map are demonstrated in this paper using an example of steel purlin design. The Partial Factors Method as well as Simulation-Based Reliability Method are used for design and assessment in this example.*

**Keywords:** *Snow load, probabilistic, reliability assessment, SBRA, steel structures.*

### **1. Introduction**

Transition from national to European standards for reliability assessment of structures (so called Eurocodes) is connected with many problems in the Czech Republic. One of them is an expressive increase in design values of climatic actions, mainly of snow and wind loads. Higher design values of snow loads may affect the economics of roof structural elements design. Lightweight steel and timber roofs are mostly influenced. The assessment of existing structures designed in agreement with national standards could be also complicated due to higher design values of snow loads according to Eurocodes.

Non-negligible economic savings could be achieved by applying some improvements to the reliability assessment procedures proposed in the European standards. The first possibility is improvement (refinement) of European ground snow load maps given in EN 1991-1-3, the second one is the application of more appropriate probabilistic-based design methods if compared to the traditional partial factors method proposed in Eurocodes.

### **2. Digital ground snow load map**

#### **2.1. Conception of the digital map**

The new digital ground snow load map covers the area of the Czech Republic by the net 100 x 100 m. Needed snow characteristics were calculated for every square of the net using the Multiple Weighted Linear Regression method, see (Křivý & Stříž, 2010).

The map conception is such as to be user friendly. Snow characteristic of the selected location are obtained either by clicking on a virtual map or directly by entering the GPS coordinates - see [www.snehovamapa.cz](http://www.snehovamapa.cz). The map is applicable not only for the traditional analysis using partial factor method but also for the direct probabilistic assessment of structures. The following data are given to every square 100 x 100 m:

---

<sup>\*</sup> Ing. Vít Křivý, Ph.D. and prof. Ing. Radim Čajka, CSc.: Faculty of Civil Engineering, VŠB-Technical University of Ostrava, L. Poděštil 1875; 708 33, Ostrava - Poruba; CZ, e-mails: [vit.krivy@vsb.cz](mailto:vit.krivy@vsb.cz), [radim.cajka@vsb.cz](mailto:radim.cajka@vsb.cz)

- a) The first data is the characteristic value of snow load on the ground ( $s_k$ ). The characteristic value is based upon the probability of 0.02 of its time-varying part being exceeded for a reference period of one year, see EN 1990. This is equivalent to a mean return period of 50 years for the time-varying part. The characteristic value ( $s_k$ ) is applicable for common analysis using partial factor method given in Eurocodes.
- b) Statistical characteristics of annual maximum ground snow load (mean value  $\mu$ , standard deviation  $\sigma$ , variation coefficient  $V$  and skewness  $\alpha$ ) constitute the second group of data provided by the digital map. Arbitrary fractile can be derived from these statistical characteristics (including the characteristic value ( $s_k$ ) defined in point (a)). The statistical characteristics can be used also for the direct probabilistic analysis according to EN 1990 and JCSS documents (2001). The suitable probabilistic distributions are the three-parametric lognormal distribution or Gumbel distribution.
- c) The sorted ground snow load history, so called Load Duration Curves (Marek et al., 1996), is the next characteristic that is given to each section 100 x 100 m. The load duration curves are derived from data being measured during the whole year, *i.e.* including periods when the snow does not occur. The load duration curve is obtained by the ascending sort of the measured data. The most lasting value of ground snow load is  $s = 0$ . Distribution function and corresponding histogram is very easy to derive from the load duration curve – the distribution function is an inverse function to the load duration curve.

## 2.2. Characteristic values comparison of snow load on the ground ( $s_k$ ) for selected localities

The characteristic values of ground snow load ( $s_k$ ) are mostly applicable in practical design based on partial factor method. Tab. 1 compares the characteristic values ( $s_k$ ) taken from the current ground snow load map of the Czech Republic given in ČSN EN 1991-1-3 and the characteristic values calculated for new digital map. The comparison is carried out for 28 selected locations in the area of the Czech Republic. GPS coordinates of the localities are given in (Křivý & Stříž, 2010).

Tab. 1: Snow load on the ground according to the ČSN EN 1991-1-3 and new digital map.

Locality	ČSN EN 1991-1-3 $s_k$ (kN/m <sup>2</sup> )	digital map $s_k$ (kN/m <sup>2</sup> )	difference (%)	difference (kN/m <sup>2</sup> )
Praha (Prosek)	0.70	0.54	-22.9	-0.16
Pardubice (Pardubičky)	0.70	0.52	-25.7	-0.18
Brno (Žabovřesky)	1.00	0.73	-27.0	-0.27
Ostrava (Hrabůvka)	1.00	0.91	-9.0	-0.09
Havířov (Šumbark)	1.50	0.99	-34.0	-0.51
Valašské Meziříčí	1.50	1.44	-4.0	-0.06
Jeseník	2.00	1.62	-19.0	-0.38
Frýdlant N/O (north)	2.00	1.32	-34.0	-0.68
Frýdlant N/O (south)	2.50	1.42	-43.2	-1.08
Frenštát p/R (Trojanovice)	2.50	2.52	+0.8	+0.02
Vrbno p/P (west)	3.00	2.01	-33.0	-0.99
Moravský Beroun	3.00	2.31	-23.0	-0.69
Hanušovice	4.00	2.36	-41.0	-1.64
Mosty u Jablunkova	4.00	2.45	-38.8	-1.55

Tab. 1 shows significant differences between the characteristic values. Lower values taken from the digital map are more numerous. The comparison results shows that mainly the localities with higher snow load are often classed to higher snow region than necessary. The reasons leading to such differences between the both characteristic values are following:

- The new digital snow map does not work with eight discrete snow regions as defined in the current ground snow load map of the Czech Republic given in ČSN EN 1991-1-3. The net with basic size 100 x 100 m covers the area of the Czech Republic so closely, that we can speak about continuous distribution of the ground snow load. The term “snow region” is irrelevant. The largest differences are at the localities lying closely behind the boundary of snow regions defined

in the map given in ČSN EN 1991-1-3.

- It is important to keep in mind that every snow region covers specific range of values, e.g. the third snow region covers the range 100 till 150 kg/m<sup>2</sup>.
- The local ground characteristics (valleys, solitary hills etc.) are not often taken into account in the printed map in ČSN EN 1991-1-3 because of its resolution limits.
- More sophisticated model for calculating snow characteristics was applied to the digital map by comparing it with the map given in ČSN EN 1991-1-3. The influence of slope gradient, orientation and convexity were not considered when processing the map of snow regions for ČSN EN 1991-1-3. Suitable climatological stations for regression analysis were selected only upon their horizontal distance from investigated grid point.
- Statistical data from the period 1962 – 2009 were used for the new digital map, data from the period 1962 – 2006 were used for the map in ČSN EN 1991-1-3.

### 3. Design of a roof element

This chapter contains a study dealing with design of steel purlin according to six following procedures:

- (a) Partial factors design according to national Czech standards (are not in force anymore) ČSN 73 0035 a ČSN 73 1401.
- (b) Partial factors design according to Eurocodes; characteristic values ( $s_k$ ) taken from the current ground snow load map of the Czech Republic given in ČSN EN 1991-1-3;  $\gamma_Q = 1.50$ .
- (c) Partial factors design according to Eurocodes; characteristic values ( $s_k$ ) taken from the new digital ground snow load map of the Czech Republic;  $\gamma_Q = 1.50$ .
- (d) Partial factors design according to Eurocodes; characteristic values ( $s_k$ ) taken from the new digital ground snow load map of the Czech Republic; design value of snow load ( $s_d$ ) derived according to EN 1990 - Annex C.
- (e) Direct probabilistic design according to Eurocodes and JCSS documents; permanent action represented by normal distribution  $N(\mu = g_k, V = 0.02)$ ; snow load on the ground represented by 50-year maxima distribution (Gumbel distribution);  $P_d = 7.2 \cdot 10^{-5}$  for safety assessment and  $P_d = 6.7 \cdot 10^{-2}$  for serviceability assessment; in accordance with JCSS documents  $\theta_R$  is considered as lognormal distribution  $LN0(\mu = 1, V = 0.05)$  and  $\theta_R$  as lognormal distribution  $LN0(\mu = 1, V = 0.1)$ ; yield strength of steel S235 is according to (Marek et al., 2006) represented by normal distribution  $N(\mu = 292 \text{ MPa}, V = 0.055)$ ; the probabilistic analysis is carried out using Monte-Carlo method.
- (f) Direct probabilistic design according to the SBRA method (Křivý & Marek, 2007); permanent action represented by normal distribution  $N(\mu = g_k, V = 0.02)$ ; snow load on the ground represented by corresponding load duration curves;  $P_d = 7.2 \cdot 10^{-5}$  for safety assessment and  $P_d = 6.7 \cdot 10^{-2}$  for serviceability assessment (the values of target probability  $P_d$  are given for probabilistic analysis based on EN 1990;  $P_d$  for analysis based on load duration curves are not available yet); in accordance with JCSS documents  $\theta_R$  is considered as lognormal distribution  $LN0(\mu = 1, V = 0.05)$  and  $\theta_R$  as lognormal distribution  $LN0(\mu = 1, V = 0.1)$ ; yield strength of steel S235 is according to (Marek et al., 2006) represented by normal distribution  $N(\mu = 292 \text{ MPa}, V = 0.055)$ ; the probabilistic analysis is carried out using Monte-Carlo method.

The purlin from steel S235 is a part of a flat roof structure. The purlin is designed as a simple supported beam with the length of 5 m. Spacing of purlins is 2.5 m. The purlin is secured against lateral-torsional buckling by roof cladding. Normal topography according to EN 1991-1-3 is considered. Limit vertical deflections are  $\delta_{\max} = L/200$  a  $\delta_2 = L/250$ . Only the combination of permanent and snow load is considered in this study. The design is carried out for three selected localities from Tab. 1:

- 1) Prague (permanent action from roof cladding and self-weight of purlin:  $g_k = 35 \text{ kg/m}$ );
- 2) Havířov (permanent action from roof cladding and self-weight of purlin:  $g_k = 45 \text{ kg/m}$ );
- 3) Hanušovice (permanent action from roof cladding and self-weight of purlin:  $g_k = 110 \text{ kg/m}$ ).

Results of the study are summarized in Tab. 2. Table contains minimal required section modulus of the purlin  $W_{\min}$  (safety assessment) and minimal required moment of inertia  $I_{\min}$  (serviceability assessment).

Tab. 2: Minimal required cross-sectional characteristics.

procedure according to point	$W_{\min}$ (mm <sup>3</sup> · 10 <sup>3</sup> )	$I_{\min}$ (mm <sup>4</sup> · 10 <sup>6</sup> )	$W_{\min}$ (mm <sup>3</sup> · 10 <sup>3</sup> )	$I_{\min}$ (mm <sup>4</sup> · 10 <sup>6</sup> )	$W_{\min}$ (mm <sup>3</sup> · 10 <sup>3</sup> )	$I_{\min}$ (mm <sup>4</sup> · 10 <sup>6</sup> )
	Prague		Havířov		Hanušovice	
(a)	38.54	2.91	53.22	4.07	110.11	8.72
(b)	34.18	2.71	67.92	5.81	179.32	15.50
(c)	29.13	2.32	48.07	3.89	110.51	8.82
(d)	37.53	2.32	62.53	3.89	142.02	8.82
(e)	46.41	3.63	78.60	6.34	179.01	14.31
(f)	21.63	0.70	37.04	1.20	84.20	3.55

#### 4. Conclusions

The values given in Tab. 2 show considerable differences between the results obtained using the six different procedures. It is interesting to compare the results obtained according to the European standards, *i.e.* the results corresponding to points (b) till (e) in Tab. 2. The direct probabilistic design in line with EN 1990 is most conservative. On the contrary, the procedure according to point (c) leads to the lowest required values of cross-sectional characteristics.

Considerably lower values of cross-sectional characteristics are required when applying the direct probabilistic design using SBRA method – see point (f) in Tab. 2. This disproportion is caused by unsuitable selection of target probabilities  $P_d$  that are not calibrated for probabilistic analysis with the load duration curves ( $P_d$  calibrated for probabilistic analysis applying 50-year maximum distributions according to EN 1990 were used in this study).

The procedure according to point (c) is most suitable for the practical designing of roof structural elements – *i.e.* characteristic value of snow load on the ground is determined from new digital map and partial factor  $\gamma_Q = 1.50$  is considered. The procedure according to point (b) is significantly influenced by conservative values taken from the current ground snow load map of the Czech Republic given in ČSN EN 1991-1-3 (see the comparison of characteristic values given in Tab. 1). The procedures according to points (d) and (e) are influenced by the fact that the snow load is derived from the theoretical 50-year maximum distributions. The general problem of both direct probabilistic approaches (e) and (f) is a suitable choice of target probability  $P_d$  (mainly the relationship between the definition of random variable quantities and  $P_d$ ). The study shows that the procedure according to point (e) may lead to unreasonably conservative results. On the contrary, an introducing of target probabilities  $P_d$  from EN 1990 to the probabilistic analysis based on load duration curves, see point (f), leads to unreasonably low values of cross-sectional characteristics.

#### Acknowledgement

Support for this project has been provided by MŠMT, project 1M0579 – research centre CIDEAS.

#### References

- Křivý, V. & Marek, P. (2007) Zur probabilistischen Bemessung von Stahlrahmen. Stahlbau, 76. Jahrgang, Heft 1, pp. 12 – 20, ISSN 0038-9145.
- Křivý, V. & Stříž, M. (2010) Reliability-Based Design of Roof Structural Elements Exposed to Snow Load, in: Proc. 5<sup>th</sup> International conference ASRANet 2010, ASRANet Ltd., Edinburgh, ISBN 978-0-9553550-6-6.
- Marek, P. et al. (1996) Simulation-Based Reliability Assessment for Structural Engineers. CCR Press, Boca-Raton, USA, ISBN 0-8493-8286-6.
- Marek, P. et al. (2006) Probabilistic Assessment of Structures using Monte Carlo Method. Basics, Exercises, Software (2nd ed.), ITAM CAS CR, Prague, ISBN 80-86246-19-1.
- The JCSS Probabilistic Model Code [on-line]. (2001) JCSS, 2001, available from WWW: <http://www.jcss.ethz.ch/>, ISBN 978-3-909386-79-6.

## DUCTILE FRACTURE CRITERIA IN PREDICTION OF CHEVRON CRACKS

P. Kubík<sup>\*</sup>, J. Petruška<sup>\*</sup>, J. Hůlka<sup>\*</sup>

**Abstract:** Seven ductile fracture criteria are applied to simulation of cold forward extrusion and their performance in prediction of chevron cracks is presented. The criteria are implemented as user material subroutine (VUMAT) into ABAQUS/Explicit code and their calibration is based on tensile testing of several types of tensile specimens. Ability of the criteria to predict material damage in forward extrusion is tested under various combinations of process parameters.

**Keywords:** Fracture criteria, calibration, forward extrusion, chevron cracks.

### 1. Introduction

During forward extrusion of long products, their cross-section is reduced by extensive plastic deformation. Chevron cracks which originate on the symmetry axis represent a typical extrusion-related damage, which is not too frequent, but dangerous due its invisibility on the product surface. Process parameters such as die cone angle, area reduction ratio and friction have significant effect on the stress triaxiality  $\eta$  and equivalent plastic strain which are the main factors influencing damage. Definition of the frequently used criteria like Rice-Tracey, Xue-Wierzbicki (Rice & Tracey, 1969; Wierzbicki & Xue, 2006) and others are based on these quantities. This paper contains a qualitative analysis of the ability of selected fracture criteria to describe the influence of process parameters on the damage cumulation.

All the analyzed criteria were implemented into ABAQUS/Explicit by user subroutine, their parameters calibrated from independent tensile tests and applied to extrusion simulation. In case of reaching critical value of damage, crack initiation is simulated by deleting appropriate finite elements.

### 2. Implementation and calibration of seven fracture criteria

There are two basic mechanisms of ductile failure of metals. Shear mechanism is prevailing for triaxiality close to zero, whereas growth and coalescence of voids is typical for tensile loading with large positive values of triaxiality. Chevron cracks are caused by the second mechanism, generated at the symmetry axis in the process zone of extruded material.

To describe the damage evolution under different stress-strain history represented by different stress triaxiality, four different tensile test specimen geometry of steel no. 41 2050.3 were used for fracture criteria calibration. Besides a standard smooth tensile specimen, three others with notch radii 5 mm, 2.5 mm and 1.2 mm were used. Multilinear model of stress-strain curve was used in all the simulations. To identify the flow curve, a trial-and-error strategy with the MLR correction as described in (Borkovec, 2008) and (Mirone, 2006) was used. Experimental results of tensile tests and their computational simulations with identified flow curve are compared in Fig. 1 for two of the specimens.

Analysis of mesh sensitivity of the flow curve identification showed that element size less than 0.15 mm is necessary to reach negligible effect on the force response. The difference between computed and experimental curves in all the simulated tests is less than 10%. This was accepted as a

---

<sup>\*</sup> Ing. Petr Kubík, prof. Ing. Jindřich Petruška, CSc. and Ing. Jiří Hůlka: Institute of Solid Mechanics, Mechatronics and Biomechanics, Brno University of Technology; Technická 2896/2; 616 69, Brno; CZ, e-mails: ykubik05@stud.fme.vutbr.cz, petruska@fme.vutbr.cz, hulka@c-box.cz

reasonable correspondence if we take into account the variability of geometry and material properties among various specimens.

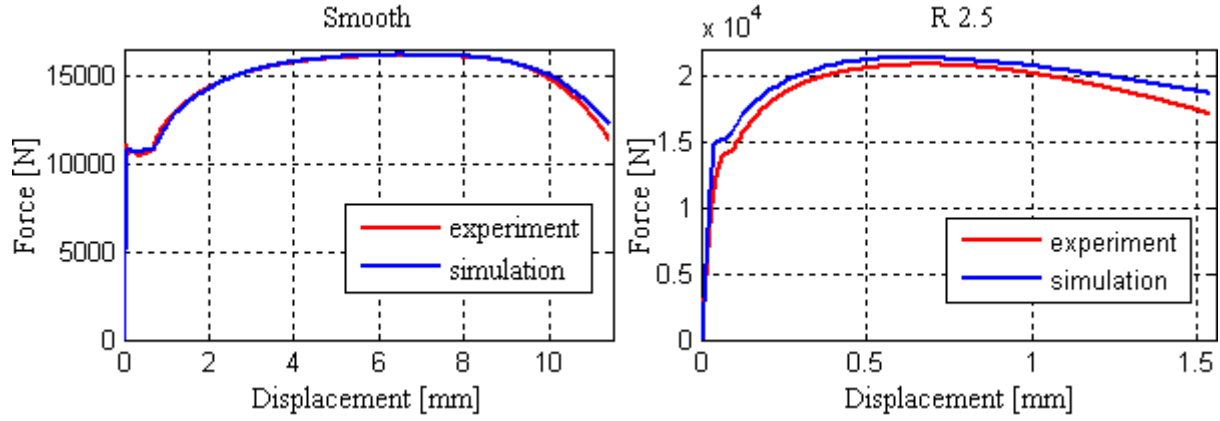


Fig. 1: Tensile test results – standard (left) and notched (right) specimen with radius 2.5 mm.

The data from four independent tensile tests are used in calibration of selected fracture models according to Tab 1. Unknown fracture criteria parameters are found in MATLAB by least-squares minimization in the following form:

$$\min_x \sum_{i=1}^4 f_i^2(C), \quad (1)$$

where, for example, in case of the Cockcroft-Latham fracture criterion the calibration constant  $C = C_{CLO}$  and minimized function is given by equation:

$$f_i(C) = C_{CLO} - \int_0^{\bar{\epsilon}_i^f} \frac{\langle \sigma_{1i} \rangle}{\bar{\sigma}_i} d\bar{\epsilon}_i^p. \quad (2)$$

Calibrated parameters of each fracture model are listed in Table 1. Due to aim of this study, only the parameters relevant for tensile loading damage were identified in case of complex fracture models like CrashFEM and EWK.

Tab. 1: The parameters for the different criteria calibrated to fit the tensile tests.

Criterion	Formula	Parameters
Rice - Tracey (Rice & Tracey, 1969)	$C_{RT} = \frac{1}{1.65} \int_0^{\bar{\epsilon}^f} \exp\left(\frac{3}{2}\eta\right) d\bar{\epsilon}^p$	$C_{RT} = 1.36$
Cockcroft - Latham (Cockcroft & Latham, 1968)	$C_{CL} = \int_0^{\bar{\epsilon}^f} \langle \sigma_1 \rangle d\bar{\epsilon}^p$	$C_{CL} = 802$
Cockcroft - Latham - Oh (Oh et al., 1979)	$C_{CLO} = \int_0^{\bar{\epsilon}^f} \frac{\langle \sigma_1 \rangle}{\bar{\sigma}} d\bar{\epsilon}^p$	$C_{CLO} = 0.976$
Johnson - Cook (Johnson & Cook, 1985)	$\bar{\epsilon}^f = [D_1 + D_2 \exp(D_3 \eta)] [1 + D_4 \ln \dot{\epsilon}^*] [1 + D_5 T^*]$	$D_1 = 0.182, D_2 = 4.23$ $D_3 = 2.75, D_4 = 0, D_5 = 0$
EWK (Wilkins, 1981)	$D_C = \int_0^{\bar{\epsilon}^f} \frac{1}{\left(1 - \frac{\sigma_m}{P_{lim}}\right)^\alpha} \left[1 - \sup\left(\frac{S_2}{S_3}, \frac{S_2}{S_1}\right)\right]^\beta d\bar{\epsilon}^p$	$D_C = 5.7, P_{lim} = 1820 [MPa]$ $\alpha = 4.19, \beta = 0$

<i>Xue – Wierzbicki</i> (Wierzbicki & Xue, 2006)	$\bar{\varepsilon}^f = k - [k - C_3 \exp(-C_4 \eta)] [1 -  \xi ^n]^{\frac{1}{n}}$ Where $k = C_1 \exp(-C_2 \eta)$	$C_1 = 3.07, C_2 = 1.86$ for axisymmetric case $\xi = 1$
<i>CrashFEM</i> (Borkovec, 2008)	$\bar{\varepsilon}_d^f = d_0 \exp(-3c\eta) + d_1 \exp(3c\eta)$ tensile loading only	$d_0 = 2.56, c = 0.42,$ $d_1 = -0.07$

### 3. Influence of process parameters on extruded material damage

By repeated simulation of the extrusion process with different reduction and die cone angle, their influence on material damage can be quantified by different fracture criteria as shown in Fig. 2. The contours in Fig. 2 show damage values actually reached from appropriate criterion equations given in Tab. 1. Typical pattern can be found in all fracture models with a single exception of slightly different results of Johnson-Cook criterion.

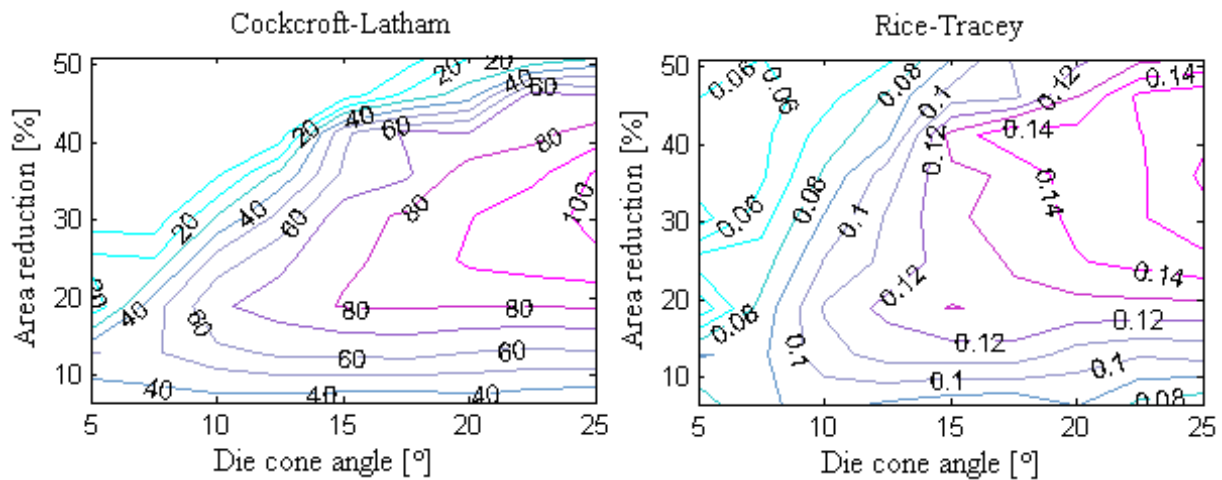


Fig. 2: Influence of process parameters on damage obtained from selected criteria.

The results show maximum values of damage for increasing die cone angles and medium reductions – about 30-40%. Similar results were obtained in (Saanouni, 2004; McVeigh, 2005). On the other hand the Johnson-Cook criterion shows that maximum values of damage compared to other criteria are located in the area of smaller die cone angles and smaller reductions. In terms of security and forming forces it is then preferable to use small angle of reduction. Repeated analysis also shows that it is more dangerous to reach final reduction of the product in several successive small reductions than doing it all in one extrusion run.

### 4. Simulation of chevron crack development

Initiation and growth of ductile fracture is described by deletion of elements, where the level of damage surpasses critical fracture parameters, specified in Table 1. Element size is the same as it was for calibration to eliminate mesh sensitivity. Results obtained with the Cockcroft-Latham-Oh criterion are given in Fig. 3, other criteria produced very similar results. We can see that the simulation is corresponding to real chevron crack discontinuous character and arrow-like shape oriented in the direction of material flow. Because of relatively large ductility of material, first cracks are developed at area reduction reaching 61%. We can also see that cracks are generated only if the total reduction 61% is obtained in four consecutive partial reductions. If the same reduction is reached in only three larger reduction steps, material remains intact. This is in correspondence with literature and practical industrial experience – most dangerous are the last, although small finishing reductions.



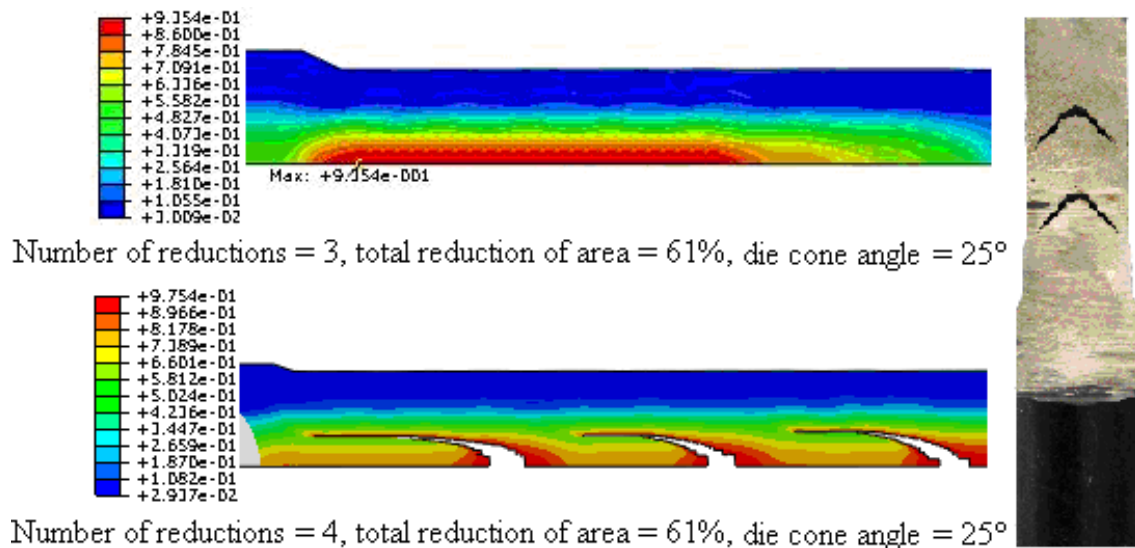


Fig. 3: Shape of chevron crack by using the model Cockcroft-Latham-Oh.

## 5. Conclusions

Complex problem of calibration and application of several fracture criteria to simulation of cold forward extrusion of long products was presented. Obtained results show good correspondence between simulated and real position, distribution and shape of chevron cracks. Computational analysis thus presents appropriate tool to predict potential problems with forward extrusion processes and can be helpful to prevent them already in the process design stage. Nevertheless, following research steps should be directed at least towards precise prediction of cracks shape and frequency, influence of friction and element-size dependence of the FE results.

## Acknowledgement

Financial help of the grant projects GA101/09/1630 and FSI-S-10-12 is gratefully acknowledged.

## References

- Borkovec, J. (2008) Computational simulation of separation process. PhD Thesis, Brno University of Technology.
- Cockcroft, M. G., Latham, D. J. (1968) Ductility and the workability of metals. *International Journal of the Institute of Metals*, vol. 96, pp. 33-39.
- Johnson, G. R., Cook, W. H. (1985) Fracture characteristics of three metals subjected to various strains, strain rates, temperatures and pressures. *Engineering Fracture Mechanics*, vol. 21, pp. 31-48.
- McVeigh, C., Liu, W. K. (2005) Prediction of central bursting during axisymmetric cold extrusion of a metal alloy containing particles. *International Journal of Solids and Structures*, vol. 43, pp. 3087-3105.
- Mirone, G. (2006) Role of stress triaxiality in elastoplastic characterization and ductile failure prediction. *Engineering Fracture Mechanics*, vol. 74, pp. 1203-1221.
- Oh, S., Chen, C. C., Kobayashi, S. (1979) Ductile failure in axisymmetric extrusion and drawing. *Journal of Engineering for Industry*, vol. 101, pp. 36-44.
- Rice, J. R., Tracey, D.M. (1969) On the ductile enlargement of voids in triaxial stress fields. *Journal of the Mechanics and Physics of Solids*, vol. 17, pp. 201-217.
- Saanouni, K., Mariage, J.F., Cherouat, A., Lestriez, P. (2004) Numerical prediction of discontinuous central bursting in axisymmetric forward extrusion by continuum damage mechanics. *Computers and Structures*, vol. 82, pp. 2309-2332.
- Wierzbicki, T., Xue, L. (2006) On the effect of the third invariant of the stress deviator on ductile fracture. *International Journal of Fracture*, vol. 47, pp. 719-743.
- Wilkins, M. L. (1981) Calculation of elastic-plastic flow. Lawrence Livermore National Laboratory, Report no. UCLR-7322.

## INFLUENCE OF ECCENTRICITY ON THE AXIAL FLOW IN LEAKAGE JOINTS

A. Kubis<sup>\*</sup>, P. Navrátil<sup>\*\*</sup>

**Abstract:** This article is concerned with comparison of velocity field size depending on size of the eccentricity in leakage joints of centrifugal pumps. Eccentricity is created by gravitation and radial force from impeller. This report describes approach for calculating the straight seal without rotation. An eccentricity dependence of the axial velocity field in the article is numerically verified by using FLUENT software.

**Keywords:** Leakage joint, seal, velocity field, centrifugal pumps, eccentricity.

### 1. Introduction

It is very important, that centrifugal pumps works at high efficiency. Efficiency can be modified by minimization of hydraulic, mechanical and volume losses in the pump. Volume losses are generated by fluid flow through sealing rings back to suction, they are dependent on shape of sealing rings, whereas cannot be equal to zero. It could happen to seize of sealing rings, that's why there always must be precisely defined gap  $\delta$  between sealing rings (tenths of mm). Flow  $q$  is circulating through the leakage joint, volume efficiency is defined by (1), (Fig. 1). (Nechleba & Hušek, 1966)

$$\eta_v = \frac{Q}{Q+q} \quad (1)$$

### 2. Theory and principle of sealing ring modeling

In this case are leakage joints (Karassik & Carter, 1966) straight without labyrinths and cells. They are replaced by cylinder annular area for simplification. In real leakage joint happens due to radial and gravitation forces from impeller to eccentricity and displacement of inner leakage joint cylinder axis (displacement of whole shaft in bearings) (Fig. 1). In the flow simulation is modelled eccentricity by axial displacement of the inner cylinder, whereas angle displacement is neglected.

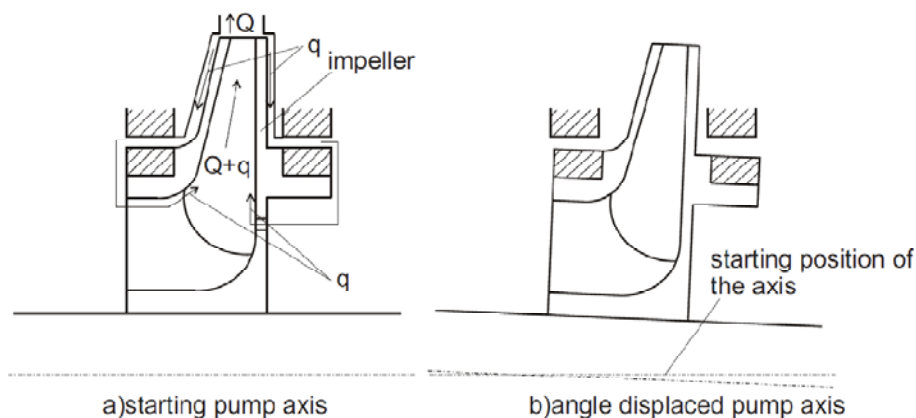


Fig. 1: Narrow and displaced pump axis.

<sup>\*</sup> Ing. Aleš Kubis.: Institute of Fluid Mechanics Viktora Kaplana, Faculty of Mechanical Engineering, Technická 2896/2; 616 69, Brno; CZ, e-mail: ykubis03@stud.fme.vutbr.cz

<sup>\*\*</sup> Ing. Petr Navrátil.: Institute of Solid Mechanics, Mechatronics and Biomechanics, Faculty of Mechanical Engineering; Technická 2896/2; 616 69, Brno; CZ, e-mail: ynavra26@stud.fme.vutbr.cz

Fig. 2 describes cylindrical annular area even with axes schematics, these schematics are important to derive formulas which describe rising flow processes in sealing joint. Kinetic equation is needed to describe processes inside leakage joint for direction  $r$ ,  $\phi$ ,  $z$  (Navier – Stokes equation) and continuity equation (2), (3) (Brdlička & Sopko & Samek, 2005).

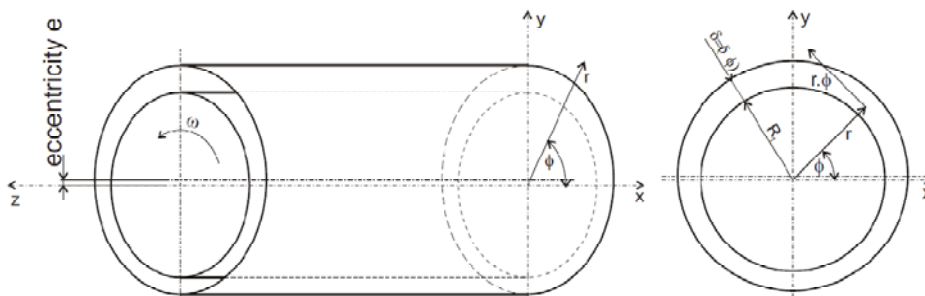


Fig. 2: Cylindrical annular area geometry.

$$r: \rho \left( \frac{\partial c_r}{\partial t} + \frac{\partial c_r}{\partial r} c_r + \frac{1}{r} \frac{\partial c_r}{\partial \phi} c_\phi + \frac{\partial c_r}{\partial z} c_z - \frac{c_\phi^2}{r} \right) + \frac{\partial p}{\partial r} - \mu \left[ \frac{1}{r} \frac{\partial}{\partial r} \left( r \frac{\partial c_r}{\partial r} \right) + \frac{1}{r^2} \frac{\partial^2 c_r}{\partial \phi^2} + \frac{\partial^2 c_r}{\partial z^2} - \frac{c_r}{r^2} - \frac{2}{r^2} \frac{\partial c_\phi}{\partial \phi} \right] = \rho \cdot g_r \quad (2)$$

$$\phi: \rho \left( \frac{\partial c_\phi}{\partial t} + \frac{\partial c_\phi}{\partial r} c_r + \frac{1}{r} \frac{\partial c_\phi}{\partial \phi} c_\phi + \frac{\partial c_\phi}{\partial z} c_z - \frac{c_r c_\phi}{r} \right) + \frac{1}{r} \frac{\partial p}{\partial \phi} - \mu \left[ \frac{1}{r} \frac{\partial}{\partial r} \left( r \frac{\partial c_\phi}{\partial r} \right) + \frac{1}{r^2} \frac{\partial^2 c_\phi}{\partial \phi^2} + \frac{\partial^2 c_\phi}{\partial z^2} - \frac{c_\phi}{r^2} + \frac{2}{r^2} \frac{\partial c_r}{\partial \phi} \right] = \rho \cdot g_\phi$$

$$z: \rho \left( \frac{\partial c_z}{\partial t} + \frac{\partial c_z}{\partial r} c_r + \frac{1}{r} \frac{\partial c_z}{\partial \phi} c_\phi + \frac{\partial c_z}{\partial z} c_z \right) + \frac{\partial p}{\partial z} - \mu \left[ \frac{1}{r} \frac{\partial}{\partial r} \left( r \frac{\partial c_z}{\partial r} \right) + \frac{1}{r^2} \frac{\partial^2 c_z}{\partial \phi^2} + \frac{\partial^2 c_z}{\partial z^2} \right] = \rho \cdot g_z$$

$$\text{continuity:} \quad \frac{\partial \rho}{\partial t} + \frac{\partial(\rho \cdot c_r)}{\partial r} + \frac{1}{r} \frac{\partial(\rho \cdot c_\phi)}{\partial \phi} + \frac{\partial(\rho \cdot c_z)}{\partial z} = 0 \quad (3)$$

These equations describe complex flow in straight seal, inside of seal happens to superposition of two processes, to flow through the leakage joint in  $z$  direction (axial flow) and to instabilities which are generated inside of leakage joint due to rotation of inner cylinder by angle speed  $\omega$  - dependence of these instabilities are Taylor vortexes. Starting, ending and size of Taylor vortexes are given by Taylor number (Reynolds number function).

### 3. Simulation and numerical verification of axial flow in dependence of eccentricity size

In this chapter is described dependence of eccentricity size on axial flow in leakage joint, solving separately flow in  $z$  axis (with neglecting rotation of inner cylinder). Numerical calculation will be done with help of Fluent software, which can be compared with analytically calculated values. Formulas which is needed for calculation is modified Navier – Stokes equation for  $z$  axis (4) (for  $e = 0$ ). Values added to formula (4) are displayed on Fig. 3.

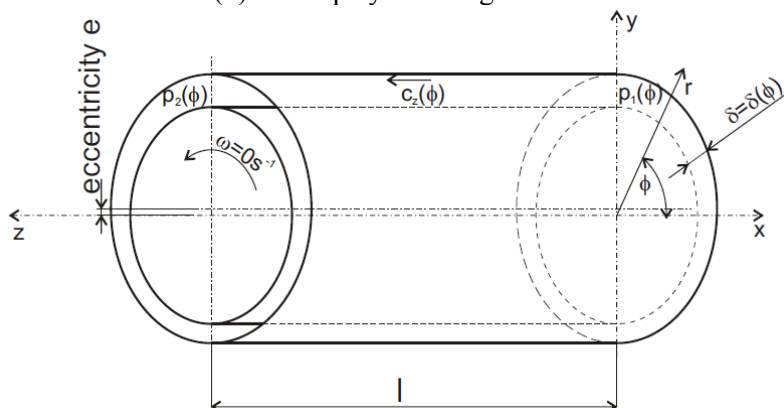


Fig. 3: Input values in axial flow calculation.

$$\bar{c}_z = \frac{1}{\sqrt{\lambda \cdot \frac{l}{2 \cdot \delta} + \xi_{vytok} + \xi_{vtok}}} \cdot \sqrt{\frac{2 \cdot (p_1 - p_2)}{\rho}} \quad (4)$$

Fig. 3 displays varying width of leakage joint on angle  $\phi$ , pressures  $p_1(\phi)$  and  $p_2(\phi)$  are generally considered as constant by  $\phi$ , because leakage joint flow is generated with pressure difference and difference in flow is compensated by decreasing axial speed. Elements ( $\xi_{vtok} = 0.5$ ) and ( $\xi_{vytok} = 1$ ) in formula (4) mean inlet and outlet dissipation.

### 3.1. Numeric calculation

Mesh was made in Gambit software before beginning the calculation. The task in Fluent is axisymmetric by y axis, Fig. 2. Due to calculation simplification is sufficient to do only half of geometry. In formula (4) figure components  $\xi_{vytok} + \xi_{vtok}$ , they are modelled on large input and output area, Fig. 4. In the figure, there are also displayed boundary conditions used with solving, for all models. Tab. 1 contains eccentricity values, for which the calculation was solved and pressure boundary conditions, which are similar for all geometries. Geometry contains 1 200 000 3D elements, most of them (605 000) contains the part of leakage joint. Before calculation it must be also estimated, which type of flow will be inside of leakage joint. Reynolds number  $Re$  will be suitable for this purpose, for its calculation we need to know fluid speed inside of leakage joint, formula (5), surface roughness factor is equal to  $\lambda = 0.04$ . Basic estimation is that speed will not change with eccentricity variation.  $Re$  is calculated only once, eccentricity  $e = 0$  (area is constant by  $\phi$  coordinate and speed is steady), formula (6), (Paciga, 1967).

$$\bar{c}_z = \frac{1}{\sqrt{1,5 + \frac{0,04 \cdot 0,015}{2,0,0004}}} \cdot \sqrt{\frac{2 \cdot (500000 - 200000)}{1000}} = 16.33 \text{ m/s} \quad (5)$$

$$Re = \frac{c_z \cdot 2 \cdot \delta}{\nu} = \frac{16,33 \cdot 2,0,0004}{0,000001} = 13064 \quad (6)$$

Turbulence model is set for calculation in Fluent. For calculation has been used realizable k- $\epsilon$  model.

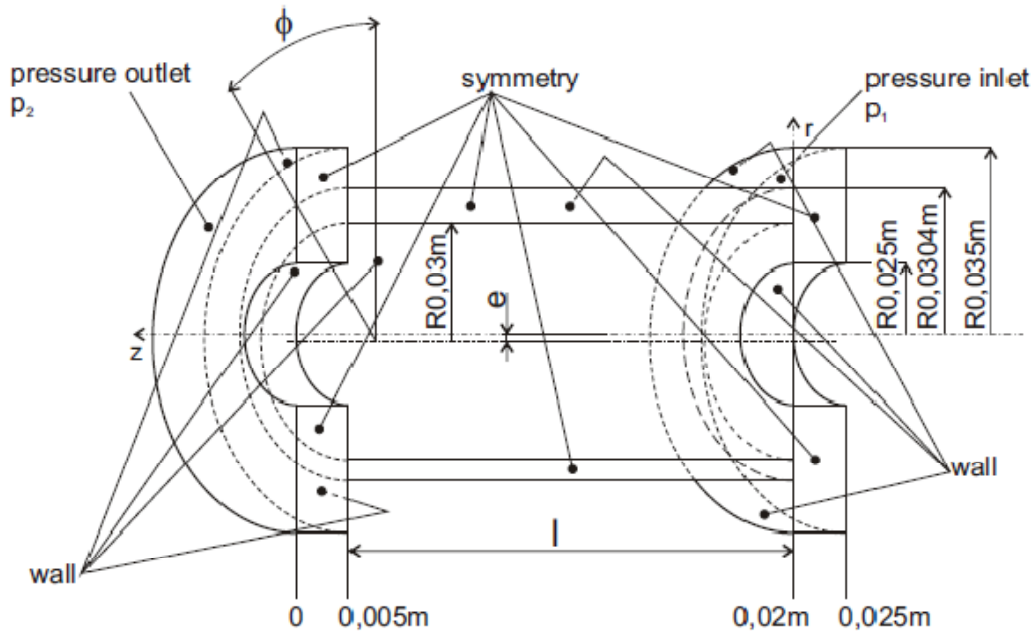


Fig. 4: Calculation geometry with boundary conditions.

Tab. 1: Size of eccentricity, pressure boundary conditions and flow through the leakage joint.

eccentricity $e[\text{mm}]$	pressure b.c. $p_1[\text{Pa}]$	pressure b.c. $p_2[\text{Pa}]$	flow through the leakage joint $[\text{m}^3/\text{s}]$
0	500000	200000	$1.168 \times 10^{-3}$
0.075			$1.164 \times 10^{-3}$
0.15			$1.167 \times 10^{-3}$
0.225			$1.164 \times 10^{-3}$
0.3			$1.166 \times 10^{-3}$

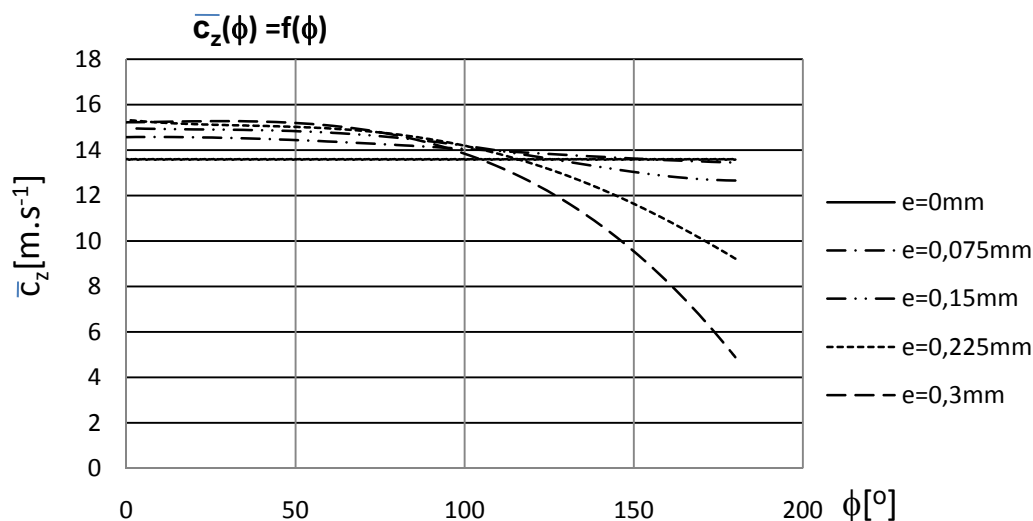


Fig. 5: Graph of axial speed dependence on  $\phi$  coordinate for different eccentricity values.

Fig. 5 describes behavior of average axial speed by  $\phi$  angle for different eccentricity sizes. These speeds are derived from Fluent by numerical integration in each area by trapeze rule. In the end is checked numerical calculation validity. Average speed  $c_z$  is calculated for case of zero eccentricity. Equation (4) is used and values  $p_1$ ,  $p_2$  are determined by Fluent). These pressures generally needn't be the same with boundary conditions on boundaries of calculation area. From numerically calculated data - pressures on input and output are  $p_1 = 200\,000\text{ Pa}$  and  $p_2 = 415\,000\text{ Pa}$ . Theoretical flow speed in straight seal (4) is nearly the same as calculated one from numerical simulation (7). Numerical calculation can be considered as correct.

$$\overline{c_{z_{analytical}}} = \frac{1}{\sqrt{1,5 + \frac{0,04 \cdot 0,015}{2 \cdot 0,0004}}} \cdot \sqrt{\frac{2 \cdot (415000 - 200000)}{1000}} = 13.82\text{ m/s} \quad (7)$$

#### 4. Conclusions

The objective of this article was to numerically describe progress of axial speed with variable eccentricity. Results are in graph on Fig. 5, where are each speeds displayed by  $\phi$  coordinate, see Fig. 5. Variable size of axial speed is very important, because it corresponds with stiffness of fluid layer. It has been verified that, axial flow doesn't correspond on eccentricity size (see Tab. 1 - flow through the leakage joints - calculated from Fluent software). Objective of next articles will be to describe instabilities, that are generated in leakage joint by rotation and description of fluid layers stiffness.

#### References

- Brdička, M., Sopko, B. & Samek, L. (2005) Continuum mechanics, Academia, pp.426-610.
- Nechleba, M. & Hušek, J. (1966) Hydraulic machines, Prague, pp. 81-86.
- Karassik, I. & Carter, R. (1960) Centrifugal pumps, Mc Graw-Hill book company, pp. 42-44.
- Paciga, A. (1967) Projektovanie zariadení čerpacej techniky, Slovenské vydavateľstvo technickej literatúry, pp. 40-47.

## USE OF RESONANCE IN WATERJET TECHNOLOGY

M. Kušnerová\*, R. Čep\*\*, J. Valíček\*, M. Harničárová\*\*\*, M. Zeleňák\*, P. Hlaváček\*,  
W. Kaplonek\*\*\*\*, P. Židlík\*\*\*\*\*, B. Haluzíková\*

**Abstract:** *Abstract: The paper deals with increasing the efficiency of material disintegration process by the action of – non abrasive waterjet. The greater efficiency of this process can be achieved through the resonance of water flow in a hydrodynamic system. It concerns the generation of flow pulses and flow modulation through an acoustic circuit. Currently known patented and unpatented modulation methods are mentioned in this paper.*

**Keywords:** *Hydrodynamic system, resonance, disintegration of surface.*

### 1. Introduction

A conventional use of the waterjet technology includes many areas such as surface disintegration, cutting of wide range of materials and removal of surface layers during surface cleaning. The effectiveness of the continuous flow action can be significantly raised by its modulation, mainly by pulses. Currently there are known laboratory and technical positive expertises in generating a flow modulation in various ways: an unpatented way by a throttle rotation segment, or a patented way by an oscillating tip and acoustic actuator. In current practice it is used a self-resonating nozzle (unpatented) with an integral mechanical modulator of the flow in the form of a spline rotor that is placed before the nozzle exit area. The flow resistance is cyclically changing by rotation and thus modulates the velocity of the water flow exiting the nozzle. A disadvantage is a high wear rate of the moving parts in the nozzle and a need to maintain the rotor drive. A built-in acoustic transformer connected to a magnetostrictive or piezoelectric converter is placed near the outlet end of a patented ultrasound nozzle. In principle the oscillating tip generates in front of the outlet nozzle end a high - intensive ultrasound field, i.e. the field that modulates the high speed water flow at the nozzle exit. (Vijay, 1992).

Pressure pulsations are primarily generated in the acoustic chamber filled with a pressure liquid by the acoustic actuator and secondarily amplified by the acoustic concentrator (Foldyna, 2005). The author together with a team has filed a patent application (Kušnerová, 2008), which concerns the possibility of using the flow resonance in the hydrodynamic system (Fig. 1). The pulsation is primarily implemented by friction and secondarily amplified by the resonant chamber.

### 2. Theoretical solution

The hydrodynamic system generates modulated oscillations of a resonant frequency which depend on the input parameters, i.e. on the geometric dimensions of system elements and also on the fluid

---

\* RNDr. Milena Kušnerová, Ph.D., assoc. prof. Ing. Jan Valíček, Ph.D., Ing. Michal Zeleňák, Ing. Petr Hlaváček, and Ing. Barbora Haluzíková: Institute of Physics, Faculty of Mining and Geology, VSB - Technical University of Ostrava, 17. listopadu, 708 33 Ostrava-Poruba, Czech Republic

\*\* Ing. Robert Čep, Ph.D.: Department of Working and Assembly, Faculty of Mechanical Engineering, VSB-Technical University of Ostrava, 17. listopadu, 708 33 Ostrava-Poruba, Czech Republic

\*\*\* Ing. Marta Harničárová: Faculty of manufacturing Technologies of Technical University of Košice with a seat in Prešov, Bayerova 1, 080 01 Prešov, Slovak Republic

\*\*\*\* Ing. W. Kaplonek, Ph.D.: Division of Electrochemistry and Surface Technology, Koszalin University of Technology, Raclawicka 15-17, PL 75-620 Koszalin, Poland

\*\*\*\*\* Ing. Pavel Židlík: Laboratory of structural integrity and surface dezintegrity, Centre for Advanced Technology and Innovation, Ostrava-Poruba, Czech Republic

pressure settings. The fundamental frequencies of fluid oscillation represent the output parameters.

1. Method of solution is based on the equation of motion, which generally describes the phenomenon of proper oscillations of the system. We compile and solve linear ordinary differential equation with constant coefficients without the right hand side of the equation (1), where  $y$  is the variable of the oscillation deflection,  $\omega_0$  is the fundamental angular frequency and  $f_0$  is the fundamental simple frequency.

$$m_a \frac{d^2 y}{dt^2} + r_a \frac{dy}{dt} + \frac{1}{c_a} y = 0 \Rightarrow \omega_0^2 = \frac{1}{m_a c_a} \Rightarrow f_0 = \frac{1}{2\pi} \sqrt{\frac{1}{m_a c_a}}. \quad (1)$$

The equation (1) is not solved with the right hand side, because the surround resistance effects  $r_a$  are solved by using a material - quality conversion coefficient for acoustic mass that is experimentally determined.

2. Method of solution is based on the evaluation of the acoustic impedance  $Z_a$  of the oscillating system at resonance. The acoustic impedance as a complex acoustic resistance shall receive minimum values by analogy to the Thomson relation if the reactance of acoustic mass  $X_{ma}$  equals to the acoustic compliance  $X_{ca}$ . The solution (2) displays the same expression of the fundamental fluid oscillation frequency as the equation (1).

$$\vec{Z}_a = r_a + i X_a = r_a + i \left( \omega_0 m_a - \frac{1}{\omega_0 c_a} \right); X_{ma} = X_{ca} \Rightarrow f_0 = \frac{1}{2\pi} \sqrt{\frac{1}{m_a c_a}}. \quad (2)$$

The total impedance equals to the sum of the individual impedances in the electromagnetic oscillation circuit. By analogy, even in the hydrodynamic oscillation system as well as in the acoustic circuit, the total acoustic mass  $m_a$  corresponds to the sum of partial acoustic mass and a reciprocal value of the total acoustic compliance  $c_a$  equals to the sum of reciprocal values of the individual acoustic compliance. In our particular case it concerns these elements: three tubes (supply tube, connecting tube and output nozzle,  $i = 3$ ) and two chambers (inlet chamber and resonance chamber,  $j = 2$ )

$$m_a = \sum_{i=1}^3 m_{ai}; \quad \frac{1}{c_a} = \sum_{j=1}^2 \frac{1}{c_{aj}}. \quad (3)$$

The analytical derivation of the acoustic mass and acoustic compliance corresponding to the relevant elements must respect diversity in a carrier environment, i.e. liquid and gas (Kušnerová, 2008). The fundamental frequency of fluid oscillations was predicted by both methods and was verified by measuring.

### 3. Experimental solution

The laboratory measurements of force effects of the modulated jet were carried out at the Institute of Geonics AS CR, v. v. i. in Ostrava (with the oscillating chamber without any friction element). An amplitude dependence of the applied forces on the resonant frequencies was expressed after the fast Fourier transformation (Fig. 2). The fluid pressure was adjusted into a set of discrete values of 5 MPa, 10 MPa, 15 MPa, 20 MPa and 25 MPa. The high-speed liquid jet was generated by a high-pressure plunger pump with a water flow rate of  $43 \text{ l} \cdot \text{min}^{-1}$  and a working pressure of 120 MPa. A piezoresistive pressure sensor was placed at the outlet section of the pump, which was used to adjust the working pressure. The force effects of the jet were measured by the apparatus for the measurement of stagnation force of the jet (Sitek, 1994), (Vala, 1994), consisting of piezoelectric force sensor Kistler 9301A. The signal obtained from that sensor was amplified in a charge amplifier KISTLER 5007. We conducted a total of 186 direct measurements of the frequency when setting of the input parameters with different values, i.e. liquid pressure and geometric dimensions of the system. The presented demonstration of the experiment corresponds to the fluid pressure of 15 MPa and the fundamental resonant frequency of 8.3 kHz. The amplitude of force reaches about 5.6 % of the static force component.



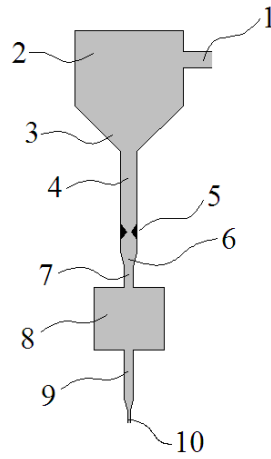


*Fig. 1: Scheme of the hydrodynamic oscillating system. 1 supply tube; 2 upper part of the inlet chamber; 3 bottom part of the inlet chamber with a conical taper working as the mechanical amplifier; 4 connecting tube; 5 pulse generator; 6 connecting tube with a conical taper working as the mechanical amplifier; 7 inlet tube of the resonance chamber; 8 resonance chamber; 9 connecting tube; 10 nozzle at the exit from the system.*

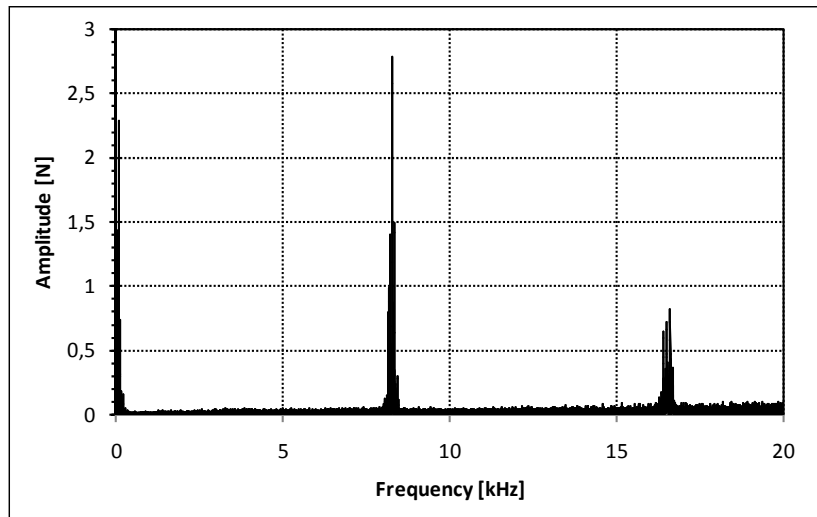


*Fig. 2: Frequency record of the force amplitude measurement.*

#### 4. Comparison of theoretical and experimental results

A source of data used for the development and verification of the fundamental oscillation frequency of the hydrodynamic system was as follows: the direct measurement of the tunable geometric dimensions of elements, the adjustment of the fluid pressure, the indirect flow rate and velocity of acoustic oscillation measurement, the direct measurement of the fundamental oscillation frequency and other different indirect measurements using the tabulated values and regression calculations in Excel.

A comparison of the results of calculations and measurements (Tab. 1) is done by evaluating of the relative differences between the fundamental frequencies  $f_{ZM}$  and predicted fundamental frequencies of oscillations  $f_0$ .

$$\rho_{\Delta f} = \frac{|f_0 - f_{ZM}|}{f_{ZM}} 100 \% . \quad (4)$$

The arithmetical mean of the partial relative differences  $\overline{\rho_{\Delta f}}$  for given discrete values of pressure  $p$  reaches the required compliance of less than 5 %.

Tab. 1: Comparison of the theoretical  $f_0$  and measured  $f_{ZM}$  fundamental frequencies.

$P$ [MPa]	$f_0$ [kHz]	$f_{ZM}$ [kHz]	$\rho_{\Delta f}$ [%]
5	4.697	4.986	5.8
10	6.617	6.363	4.0
15	8.071	8.259	2.3
20	9.281	8.914	4.1
25	10.987	10.269	0.7
$\overline{\rho_{\Delta f}}$			3.4

## 5. Conclusions

The paper gives brief information on current possibilities of using the waterjet technology with emphasis on the importance of using resonance in this technology. The measurements show that the water jet has the variable axial velocity component due to pulse generation. At a certain distance from the nozzle, the initial continuous flow breaks up into a series of water clusters and the jet begins to behave as the pulsating jet. Its cutting ability can be greatly increased. The impact pressure generated by the impact of water clusters on the disintegrated material is considerably higher than the stagnation pressure generated by the impact of the continuous jet of comparable parameters (Foldyna, 2004), (Vijay, 1992, 1994). The pilot testing of disintegration by the action of pulsating waterjet showed at least twice high performance of the material disintegration compared with the performance when using the continuous waterjet of the same parameters (Foldyna, 2004). This analysis and experiments also show that the level of pressure pulsations generated only by modulation of the acoustic circuit, i.e. by the hydrodynamic oscillating system is not high enough. The resonance chamber may be similarly used as the secondary acoustic source (amplifier) in acoustic.

## Acknowledgement

The work has been supported by projects GA ČR No. 101/09/0650, MŠMT No. MSM6198910016, RMTVC No. CZ.1.05/2.1.00/01.0040 and MEB051021. Thanks are also of the Moravian-Silesian Region for finance support.

## References

- Foldyna, J. (2005) Method of generating pressure pulsation and equipment for making the same. ÚPV ČR, CZ 2005-168 A3.
- Foldyna, J., Sitek, L., Švehla, B., Švehla, Š. (2004) Utilization of ultrasound to enhance high-speed water jet effects. Ultrasonics Sonochemistry 11, p. 131-137.
- Kušnerová, M., Valíček, J., Hloch, S. et al. (2008) Derivation and Measurement of the Velocity Parameters of Hydrodynamics Oscillating System, STROJARSTVO, Vol. 50, Issue 6, pp. 375-379.
- Kušnerová, M., Valíček, J., Hloch, S., Hlaváček, P. (2008) Modulation method of generating a liquid flow friction element and the resonant chamber and apparatus for its implementation. CTT VŠB-TUO.
- Sitek, L., Vala, M., Vašek, J. (1994) Investigation of high pressure water jet behaviour using jet/target interaction. Proc. of the 12th Int. Conf. On Jet Cutting Technology, Mech. Eng. Public. Ltd., London, p. 59-66.
- Vala, M. (1994) The measurement of the non-setting parameters of the high pressure water jets. Geomechanics 93, Rakowski (ed.), Balkema, Rotterdam, 1994.
- Vijay M. M., Foldyna J. (1994): Ultrasonically Modulated Pulsed Jets: Basic Study. In: 12th International Conference on Jet Cutting Technology, N.G. Allen, Editor, BHR Group Conference Series, Publication No.13, Mechanical Engineering Publications Limited, London, 1994, p.15-35.
- Vijay, M. M. (1992) Ultrasonically generated cavitating or interrupted jet. U.S. Patent No. 5,154,347.

## EXPERIMENTAL DETERMINATION OF RELATIVE SLIPPING DURING FRETTING FATIGUE TESTS

J. Kuželka \*, M. Nesládek \*, J. Růžička \*, J. Jurenka \*, M. Španiel \*

**Abstract:** *This paper briefly summarizes basic facts about fretting fatigue phenomena. It discusses the method of fretting fatigue measurement and partial slip estimation. It further it describes the set-up of the experiment in detail, the optimal configuration of the optical system and the technique of postprocessing the acquired image data. The results of the carried out experiment are shown and discussed.*

**Keywords:** *Fretting, experiment, relative slips, digital image correlation.*

### 1. Introduction

At present, most construction failures are caused by fatigue. Fatigue can be seen as a continuous and irreversible degradation of material which occurs at microscopic level. From the macroscopic point of view it has quite a random character. The use of physical models for fatigue damage prediction that involve its nature is difficult and almost impossible in practice. Phenomenological models involving only observed relations among the important factors for fatigue are commonly used.

A fatigue life of a construction can be divided into three basic stages: crack initiation, crack growth and ultimate failure. The first two mentioned stages represent practically the whole fatigue life and can take a very different portion of it depending on the particular case.

The location where fatigue crack initiation takes place can be generally considered as a notch. The stress and strain concentration (the increase of gradient) is a typical characteristic. The contact interface between bodies can also be treated as a notch from this point of view. In the case of pure geometrical notch the stress field in its vicinity is determined only by its shape (beside boundary conditions and material behaviour) contrary to the “contact notch”. The fatigue of the contacting bodies is determined not only by their geometry but also by the tribological conditions of the contact interface and by the magnitudes of the relative slips of the contacting surfaces.

#### 1.1. Factors influencing fretting fatigue

The fretting fatigue usually takes place in the vicinity of the contact interface of two bodies with no relative movements. The slips between contact surfaces appear only in the small regions near the border of the contact interface. Flanges, dovetails, hub-shaft connections, cable stands interface, leaf spring washers, leaf and wound springs are typical construction joints that are exposed to fretting conditions.

This type of fatigue is influenced by numerous factors thus it is necessary to be restricted to the most influencing ones. There are three major factors of fretting fatigue. The first and the basic one is the field of strains and stresses in the vicinity of the contact interface. The second one is the amplitude of the partial slips between the contact surfaces. Regarding this factor the contact conditions can be divided into three ranges: the stick range with the slip magnitudes up to 3  $\mu\text{m}$ , the partial slip range with the slip magnitudes between 5 – 50  $\mu\text{m}$  and the gross sliding range with the slip magnitudes greater than 100  $\mu\text{m}$  as can be found in Madge et al. (2007) or in Vingsbo et al. (1988). The dependence of the fatigue life on the magnitude of the relative slips is not monotonic but it deeply

---

\*Ing. Jiří Kuželka, Ing. Martin Nesládek, Ing. Jan Růžička, Ing. Josef Jurenka and assoc. prof. Ing. Miroslav Španiel, CSc.: Department of Mechanics, Biomechanics and Mechatronics, Faculty of Mechanical Engineering, Czech Technical University in Prague, Technická 6; 166 07, Prague; CZ, e-mails: Jiri.Kuzelka@fs.cvut.cz, Martin.Nesladek@fs.cvut.cz, Jan.Ruzicka@fs.cvut.cz, Josef.Jurenka@fs.cvut.cz, Miroslav.Spaniel@fs.cvut.cz

decreases in the range of the partial slips. The third crucial factor is the friction or, generally, tribological conditions between the contact areas. All the three essential factors influence each other and can change during the construction life.

## 1.2. Fretting fatigue damage estimations

Both crack initiation and growth stages are usually considered in the models used for fatigue life estimations. The crack initiation may not be the fatigue limit state so the short sometimes long crack growth stage is governing.

The multiaxial fatigue criteria in connection with the critical distance theory described in Araujo et al. (2007) and also in Bhattacharya et al. (1998) are usually used for computations of a number of cycles to crack initiation. It assumes that the physical processes leading to crack initiation take place in small material volume characterised by the length which is considered to be a material property. The summary of these criteria can be found e.g. in Navarro et al. (2008). There are also criteria based on the energy balance concept described in Vidner et al. (2007) requiring a relatively huge experimental base. In connection with the mentioned concepts it is necessary in particular cases to consider also the wear of the material. More about this topic can be found in Madge et al. (2007) and also in McColl et al. (2004).

All computational models, both analytical and commonly used numerical, must be based on relevant experimental data. The parameters of a numerical model are fitted to experimental data with regard to amplitudes of partial slips and the tribological behaviour of the contact surfaces especially.

## 2. The experiment

In order to develop a reliable numerical model of fretting damage, the first set of experiments was designed and carried out. The goal of these experiments is an estimation of the partial slips between the contact surfaces. The amplitudes of the partial slips can be expected in order of  $\mu\text{m}$  and there is a need to probe them along the contact area (in order of mm) with a sufficiently small spatial step. The above requirements can hardly be met using conventional experimental methods, thus optical measuring system using the digital image correlation method was employed.

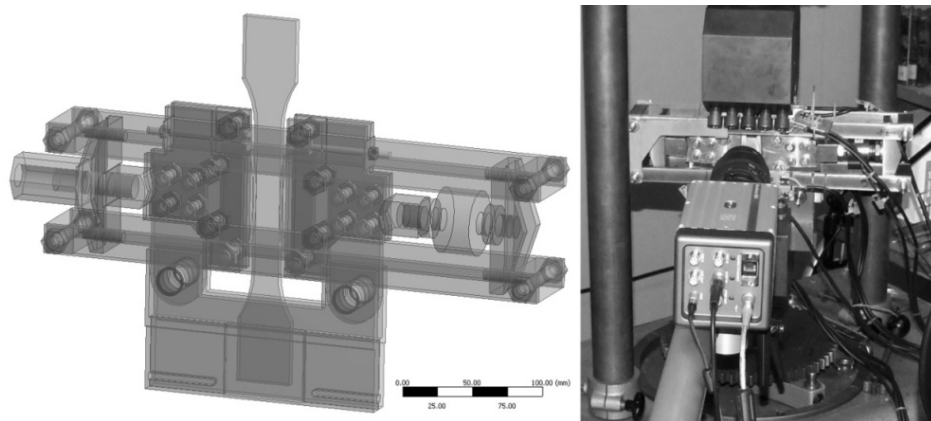


*Fig. 1: Design of the fretting fatigue device (left) and experimental set-up (right).*

### 2.1 Set-up of the experiment

The fretting fatigue experiment was carried out on a classical dog-bone specimen (with a cross-section of 15 mm width and 6 mm thickness) mounted in a special device with cylindrical pressure pads with the radius of 200 mm. The design of this device and the whole experimental set-up can be seen in Fig. 1. The whole device with the specimen was fixed in jaws of an electromagnetic Amsler loading machine. The specimen was loaded by static pressure force  $P$  (with magnitudes 5, 10 and 15 kN) and by sine cyclic force  $F$  (with the mean 10 kN and amplitude 9 kN) with the frequency 100 Hz caused by the Amsler machine. The data were acquired during a relatively short period of about 50 cycles after every 200 thousand cycles. The data related to the sequence of images of the contact interface, traction force transmitted by pads and pressure force  $P$  were gathered.

The Dantec Dynamics Q-450 optical system was used for relative displacements measurements. Since displacements in order of  $\mu\text{m}$  had been measured at high frame rate, the demands on pattern quality and lighting were quite high. Regarding 1Mpix resolution of CCD chip the objective and extension tubes were used to achieve spatial resolution of approximately  $8\ \mu\text{m}/\text{pix}$  with the field of view of about  $5 \times 8\ \text{mm}$ . The viewed surfaces were clothed in a very fine contrast stochastic speckle pattern created with airbrush considering the recommendations in Sutton et al. (2009). Two special high frequency lamps with 1 kW power each were used for sufficient lighting. The images of the vicinity of the contact interface between the specimen and pad were recorded by a high speed NanoSense Mk III camera with the frequency of 2 kHz (corresponds to 20 images per loading cycle).

## 2.2. Evaluation and results

The acquired sets of image sequences were processed in the commercial image correlation software Istra 4-D. The images were divided into two rectangular regions corresponding to the specimen and pad. In each area the displacements were evaluated in a  $0.1\ \text{mm}$  (12 pix) equally spaced grid. Each grid point corresponds to a subset  $0.2 \times 0.2\ \text{mm}$  ( $25 \times 25\ \text{pix}$ ). The obtained results were exported into hdf5 file format for further postprocessing in Matlab.

With regard to the noise corruption of the displacement data, the appropriate filtering should be done in order to obtain the relevant data. The uncertainty and confidence margins of displacements were consequently estimated. The results in the regions of interest were gathered and eventually plotted. Parametric scripts using Matlab were created to accomplish the mentioned postprocessing operations.

At first the region where the contact takes place was estimated. The point with maximal contact pressure (and thus the centre of contact area) was estimated on the basis of displacement field in case of pure pressure loading of magnitude 10 kN as shown in Fig. 2. At this point, a coordinate system for relative slip evaluation was introduced. The Hertz contact theory was used for the estimation of the contact area width.

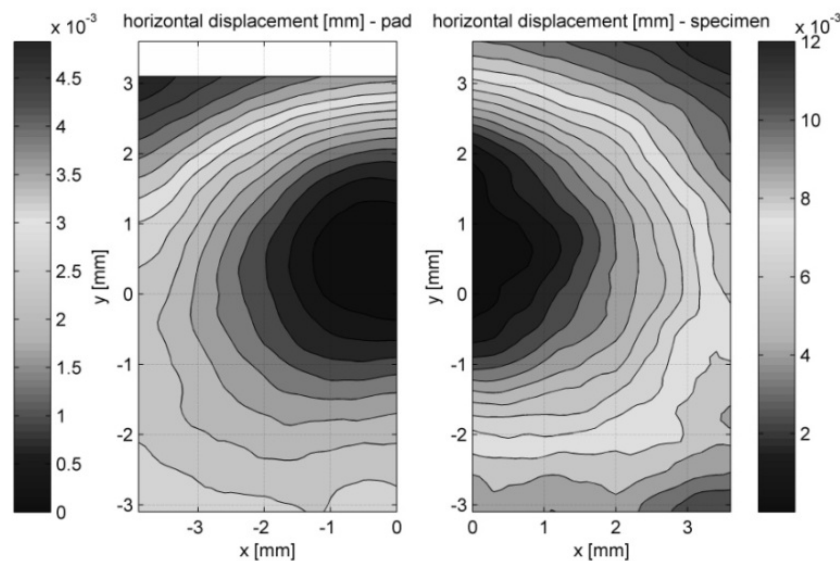


*Fig. 2: Horizontal displacement distribution on the surface of the pad (left) and specimen (right) in case of pure pressure loading 10 kN.*

The relative slips were computed as a difference between displacements along a line near the contact edge on the pad and specimen. The state corresponding to mean force  $F$  was taken as a reference. The relative slips were evaluated for states of maximal and minimal cyclic force  $F$  in one period. It corresponds to peaks in tension and compression in relation to the reference state. The displacements were previously smoothed by the disc filter with radius 12, thus they differ from the measured ones. The sum of squares residuals between the measured and smoothed data was used for displacement standard deviation estimation. The standard deviations estimations are taken on a 95 % confidence level. The measured relative slips for the three magnitudes of pressure force (5, 10 and 15kN) are shown in Fig. 3. The confidence margins corresponding to standard deviation are marked. So these margins represent bounds for approximately 68 % of the relative slips.

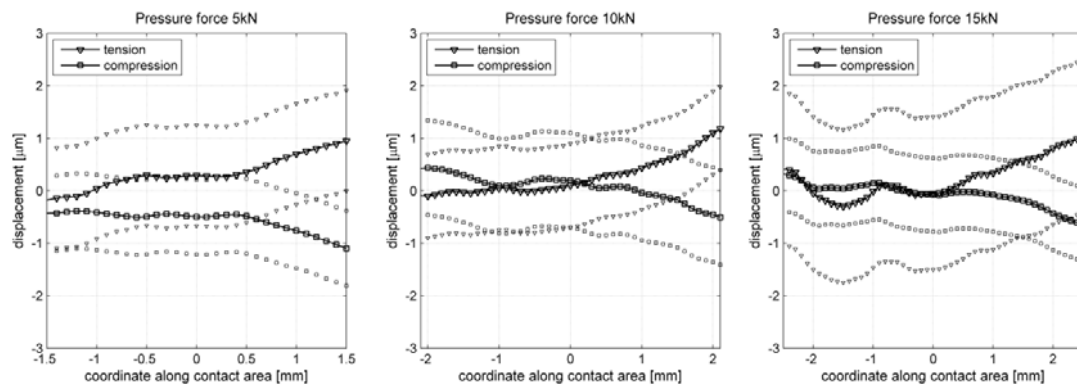


Fig. 3: Relative displacement in contact regions for different pressure forces.

### 3. Conclusions

Fretting fatigue tests were carried out in order to obtain relevant data for numerical model fitting and verification and in order to estimate amplitudes of relative slip in the contact interface. The displacement field in the contact region (8 x 5 mm) was measured and evaluated by the Q-450 Dantec Dynamics optical system and consequently processed in Matlab. The data related to pressure force and traction force transmitted through the contact interface were acquired. The methods for contact area location, partial slips evaluation and their confidence margins estimation were created and used on the measured data set.

Several conclusions based on the experimental results can be drawn. Firstly it must be mentioned that the confidence margins of the relative slips are quite wide and thus the slip amplitudes should be seen from the statistical point of view. Nevertheless, the tendency of the partial slip to decrease with increasing pressure force is quite obvious, especially between 5 and 10 (15) kN. Secondly there probably was pure slip regime for 5 kN case contrary to the other two. For 10 and 15 kN cases slight asymmetry between the slips in tension and compression can be observed. It could be caused by the fact that the pressure force does not intersect the axis of the cylindrical pad. The amplitudes of partial slips seem to be insufficient and the whole contact could be considered as sticking. This disadvantage of the current configuration could be probably suppressed by an increase of the cylindrical pad radius.

### Acknowledgement

This work was supported by the GACR No. 101/09/1709 grant.

### References

- Araujo J. A., Susmel L., Taylor D., Ferro J. C. T., Mamiya E. N. (2007) On the use of the Theory of Critical Distances and the Modified Wohler Curve Method to estimate fretting fatigue strength of cylindrical contacts. *International Journal of Fatigue* 29, 95–107.
- Bhattacharya B., Ellingwood B. (1998) Continuum damage mechanics analysis of fatigue crack initiation. *International Journal of Fatigue* Vol. 20, No. 9, pp. 631–639.
- Madge J. J., Leen S. B., McColl I.R., Shipway P.H. (2007) Contact-evolution based prediction of fretting fatigue life: Effect of slip amplitude. *Wear* 262, 1159–1170.
- Madge J. J., Leen S. B., Shipway P. H. (2007) The critical role of fretting wear in the analysis of fretting fatigue, *Wear* 263, 542–551.
- McColl I. R., Ding K., Leen S. B. (2004) Finite element simulation and experimental validation of fretting wear, *Wear* 256 (11-12) 1114-1.
- Navarro C., Munoz S., Domínguez J. (2008) On the use of multiaxial fatigue criteria for fretting fatigue life assessment, *International Journal of Fatigue* 30, 32–44.
- Vidner J., Leidich E. (2007) Enhanced Ruitz criterion for the evaluation of crack initiation in contact subjected to fretting fatigue, *International Journal of Fatigue* 29, 2040-2049.
- Vingsbo O., Soderberg S. (1988) On fretting wears, *Wear* 126, 131-147.
- Sutton A. M., Orteu J., Schreier W. H. (2009) *Image Correlation for Shape, Motion and Deformation Measurements*, Springer, New York.

## **ASSESSMENT OF C/PPS COMPOSITES DEGRADATION INDICATORS USING ACOUSTIC MEASUREMENT**

**D. Kytýř<sup>\*</sup>, J. Valach<sup>\*</sup>, T. Doktor<sup>\*</sup>, O. Jiroušek<sup>\*\*</sup>**

**Abstract:** *Changes of mechanical properties, namely of modulus of elasticity, often play a role of damage accumulation indicators in the framework of fatigue behaviour of composite materials. In order to improve the reliability of these indicators for identification of material degradation process it is necessary to eliminate the influence of external loading and volume forces associated with thermal expansion of heterogeneous material at various temperatures. Therefore the paper deals with description of experimental assessment of relation between external load and material stiffness and also studies the dependency of material stiffness on temperature. For the monitoring of degradation process ultrasonic measurement was used. Obtained results are discussed with respect to fatigue testing of material and also interpreted from the micromechanical point of view.*

**Keywords:** *Material degradation, acoustic measurement.*

### **1. Introduction**

This paper describes a simple acoustic measurement technique for determination of material's degradation in cyclic loading. Motivation is not only to develop a simple, yet reliable method to examine alternations in mechanical properties of material during fatigue test, but also to measure material's properties at elevated temperatures. Importance of the second point becomes especially urgent when the temperatures, the material can withstand, far exceeds conditions in which electronic devices can operate. Therefore a need for a method capable to work in extreme environments is clearly recognizable. To meet this objective, a simple experimental technique based on specimen's free vibration analysis was developed.

### **2. Studied material**

Studied material is extensively used in aerospace industry and in other hi-tech applications. Its stiffness to density and strength to density ratios allows this material to compete with established alloys. Internal structure of the material can be described as carbon fibres in polyphenylene sulfide (C/PPS) thermoplastics matrix composite. C/PPS is quasi-isotropic, it consist of 8-ply of carbon fabric bonded by thermoplastics matrix. Detailed list of properties of the C/PPS composite can be found in manufacturer's material datasheet (Aims, 2007).

The statistical sample – the whole set of specimens undergoing fatigue testing are prepared in the 'dog bone' shape of identical size as computer controlled water cutting machine is used. Having specimens of identical size and material properties simplifies greatly the task of comparison as a tool for investigation of material degradation not only under fatigue loading, but also impact loading and in wide range of operational conditions.

---

<sup>\*</sup> Ing. Daniel Kytýř, Ing. Jaroslav Valach, Ph.D. and Bc. Tomáš Doktor: CTU in Prague, Faculty of Transportation Science, Department of Mechanics and Materials, Na Florenci 25, 110 00 Prague 1, CZ, e-mails: xkytyr@fd.cvut.cz, valach@fd.cvut.cz, xdoktor@fd.cvut.cz

<sup>\*\*</sup> assoc. prof. Ing. Ondřej Jiroušek, Ph.D.: Academy of Sciences of the Czech Republic, Institute of Theoretical and Applied Mechanics, v. v. i, Departament of Biomechanics, Prosecká 809/76, 190 00 Prague 9, CZ, e-mail: jirousek@itam.cas.cz



### 3. Comparison of methods

Degradation of material subjected to fatigue loading can be related to the concepts of residual strength or remaining service life (van Paepegem, Degrieck 2002, Degrieck, Paepegem 2001). The degradation summarizes accumulated damage in the form of key indicator that is preferably easily measurable. Some material's property, decisive for its mechanical performance is selected or a property related to measurement technique itself is chosen. Among these parameters longitudinal wave velocity or modulus of elasticity ought to be mentioned.

These phenomenological approaches have to be related to micromechanical explanation of the nature of damage (Vasiliev, Morozov 2001). Long fibre composites resist fatigue damage because load bearing component, carbon fibres, carry the majority of loads while remaining fully elastic. The fact that fibres are not affected during fatigue process implies that the degradation takes part mainly in the thermoplastics matrix. The same conclusion can be drawn from nanoindentation measurement enabling to separate contributions of individual components in the performance of the whole material. Nanoindentation clearly demonstrates that material degradation can be related to the decrease in stiffness of the matrix (Minster 2010). It means that parameters reflecting state of the matrix can be used as sensitive descriptors of degradation process. On the other hand, parameters sensitive to fibre content of composite cannot elucidate processes in the material, are in this sense insensitive.

*Tab. 1: Comparison of sensitivity of discussed experimental methods to material's degradation expressed as the ratio of intact and fatigue state's values.*

<i>measurement technique</i>	<i>parameter</i>	<i>decrement [%]</i>
<i>matrix nanoindentation</i>	<i>Young's modulus</i>	<i>37.65</i>
<i>ultrasonic wave propagation</i>	<i>attenuation</i>	<i>17.91</i>
<i>3 point bending</i>	<i>Young's modulus</i>	<i>11.60</i>
<i>modal analysis</i>	<i>frequency</i>	<i>1.03</i>
<i>ultrasonic wave propagation</i>	<i>velocity</i>	<i>0.48</i>

In the course of work several investigation methods were deployed for estimation of material's degradation. These experimental methods are listed in Tab. 1. The table also shows influence of cyclic loading on studied parameter when compared to the intact state. This change indicates sensitivity of the given method: if matrix weakening is considered a primary cause, as indicated by nanoindentation, other methods perform differently.

Increasing difference between modulus of elasticity as determined by 3PB and ultrasonically indicates undergoing degradation process (see Fig. 1). As pointed out in (Nagy 1998), formation of discontinuities, voids and microcracks manifests in different response of material on compression and tension. While in compressive loading, microdefects tend to close and inhibit their influence on measured mechanical properties. Such a configuration occurs during ultrasonic measurement, which tests materials via longitudinal pressure waves (Rojek et al. 2007). On contrary, these defects are fully active in the tension and therefore decreasing the overall stiffness of material as happens in 3PB. Shift in free vibration frequencies of the specimen sensitively reflects internal degradation processes as modal shape formation involves simultaneous tension and compression stresses similar to that in 3PB. The great advantage of the applied modal analysis to 3PB is simplicity and almost no instrumentation requirements opening up possibility to examine materials' properties far from laboratory conditions.

In ultrasonic method, attenuation can be deduced from the first amplitude of the train of waves detected by transducer. This amplitude, provided acoustic impedance of contact between transducer/receiver and specimen is maintained for every measurement in a reproducible way, depends on measured length and material's internal damping. Identical dimensions of all specimens excludes the difference in the length as a source of attenuation and the only possible cause – internal flaws of material have to be taken under consideration.

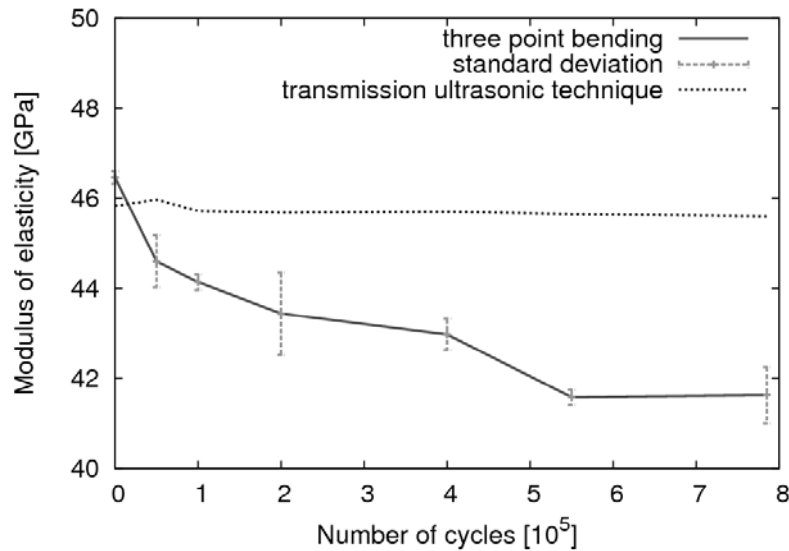


*Fig. 1: When two different indirect methods are used for determination of elastic modulus – as in this case ultrasonic and 3PB - results can be dissimilar. The cause of dissimilarity is in different mechanisms involved in the property determination; which can be also used for identification of undergoing degradation process.*

However the analysis of free vibration of specimen recorded only 1% difference between fatigued and intact state, it is inherently very precise as it deals with time measurement. The method utilizes only a simple frame for hanging specimen and mechanical rig for exciting vibrations – enabling it to be used at elevated temperatures as the only one among all discussed techniques. Fig. 2 depicts typical frequencies and spectral density peaks, reflecting excitation of modes for specimen vibrations.

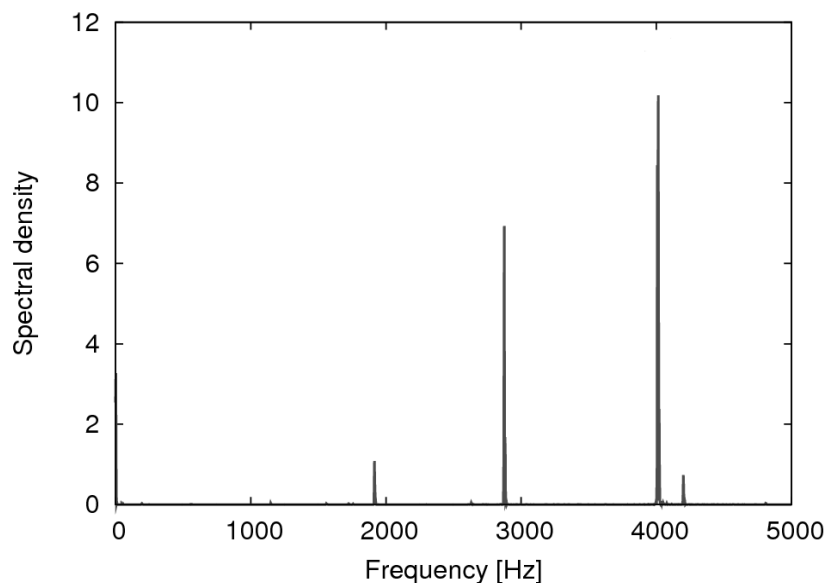


*Fig. 2: Acoustically determined natural modes of vibration and their frequencies. Due to precise manufacturing the specimens seem to be nearly identical in their mechanical properties. Any shift in eigenfrequencies can be ascribed to material degradation.*

Tab. 2 documents shift in specimen's eigenfrequencies due to material degradation. This decrease occurs for every frequency and can be measured with a high accuracy. Significance of the frequency change is supported by the fact that value of measurements' standard deviation is only a fraction of frequency decrease.

*Tab. 2: Documentation of specimen's eigenfrequency decrease as an indicator of advanced degradation of fatigued material. Specimens in upper part of the table are intact while the specimen #2 underwent circa 1 million of loading cycles.*

<i>specimen</i>	<i>spectral density peak frequencies</i>			
	<i>1<sup>st</sup></i>	<i>2<sup>nd</sup></i>	<i>3<sup>rd</sup></i>	<i>4<sup>th</sup></i>
<i>14</i>	<i>1170</i>	<i>1938</i>	<i>2913</i>	<i>4064</i>
<i>13</i>	<i>1164</i>	<i>1939</i>	<i>2909</i>	<i>4047</i>
<i>7</i>	<i>1159</i>	<i>1927</i>	<i>2893</i>	<i>4032</i>
<i>4</i>	<i>1153</i>	<i>1922</i>	<i>2876</i>	<i>4011</i>
<i>Mean</i>	<i>1161</i>	<i>1931</i>	<i>2898</i>	<i>4038</i>
<i>Std</i>	<i>5.53</i>	<i>8.92</i>	<i>16.63</i>	<i>18.20</i>
<i>2</i>	<i>1133</i>	<i>1883.25</i>	<i>2811</i>	<i>3915</i>
<i>freq. dec. [Hz]</i>	<i>28.25</i>	<i>48.24</i>	<i>86.69</i>	<i>123.14</i>
<i>freq. dec. [%]</i>	<i>1.02</i>	<i>1.03</i>	<i>1.03</i>	<i>1.03</i>

#### 4. Conclusions

Experimental technique based on free vibration of specimen was developed and utilized for investigation of material's degradation. This technique proved effective for detection of material's degradation, because it enhances matrix-dominant properties. Advantage of this technique is its sensitivity and ability to be used at elevated temperatures.

#### Acknowledgement

The research has been supported by Grant Agency of the Czech Technical University in Prague (grant No. SGS10/218/OHK2/2T/16), research plan of the Academy of Sciences of the Czech Republic AV0Z20710524 and by research plan of the Ministry of Education, Youth and Sports MSM6840770043.

#### References

- AIMS - Airbus Material Specification, Airbus S.A.S (2007).
- Degrieck, J. & van Paepegem, W. (2001) Fatigue damage modeling of fibre-reinforced composite materials: review, *Applied Mechanics Reviews*, 54, 4, pp. 279-301.
- Minster, J., Blahova, O., Lukes, J., & Nemecek, J. (2010) Time-dependent mechanical characteristics measured through the use of a microindentation technique, *Mechanics of Time-Dependent Materials*, 14, pp. 243-251.
- Nagy, P.B. (1998) Fatigue damage assessment by nonlinear ultrasonic materials characterization, *Ultrasonics*, 36, pp. 375-381.
- Rojek, M., Stabik, J. & Sokół, S. (2007) Fatigue and ultrasonic testing of epoxy-glass composites, *Journal of Achievements in Materials and Manufacturing Engineering*, 20, 1, pp. 183-186.
- van Paepegem, W. & Degrieck, J. (2002). A New Coupled Approach of Residual Stiffness and Strength for Fatigue of Fibre-reinforced Composites. *International Journal of Fatigue*, 24, 7, pp. 747-762.
- Vasiliev V.V. & Morozov, E.V. (2001) *Mechanics and analysis of composite material*, Elsevier.

## CHANGE OF MODAL PROPERTIES DUE TO DAMAGE IN BEAM BUCKLING PROBLEM

D. Lehký\*, P. Frantík\*

**Abstract:** *The paper is focused on analysis of changes of eigenfrequencies due to local damage in beam buckling problem. The aim is determination of suitable initial parameters for consequent inverse analysis. Relative changes of the first five eigenfrequencies when local damage in individual parts of the beam occurs were studied together with influence of axial force size to those changes. Even with the knowledge of significant simplification, such a task can serve as a prefiguration for damage identification of pre-stressed structures.*

**Keywords:** *Eigenfrequencies, damage, beam buckling problem.*

### 1. Introduction

In the field of damage identification using structural health monitoring data (SHM, ambient vibration monitoring) the analysis of change of modal properties due to damage is important (Wenzel & Pichler, 2005; Lehký & Novák, 2009). The task of damage identification using vibration data is based on the premise that damaged structure has smaller stiffness in some parts – and this difference will affect vibration (modal properties). The comparison of vibration of virgin (undamaged) structure and damaged structure can be then used for the detection of damaged parts (localization of damage). Integral part of research in this field is the study of modal properties and analysis of its applicability for damage identification, see e.g. Frantík et al. (2007) for numerical analyses and Lehký & Novák (2009) for experimental analysis.

In the paper, beam buckling problem from the damage point of view is studied. Such a task can serve as a prefiguration for pre-stressed bridges. Limiting factor for damage identification using changes of modal properties are their relatively small values compared to the size of the damage. The aim of the study is to find out if changes in vibration are bigger with higher pre-stressing of a structure and if there is a change in dominance of eigenfrequencies changes in individual damaged parts.

### 2. Computational model

Computational model was created using physical discretization method implemented in application FyDiK (Frantík, 2009). The beam is divided into a specific number of elements with the same length. Every element has an inner normal spring. The elements are connected together by hinges with rotational springs, see Fig. 1. Both types of springs are considered to be linear, but large deflections are taken into account in the mathematical representation. For the sake of simplicity the mass of the beam is concentrated in hinges. Model is then formulated as a nonlinear dynamical system.

In our study the model of a wooden beam with 20 elements is used. The beam has length  $l = 80$  cm, mass  $m = 84$  g, normal stiffness  $EA = 1.26 \cdot 10^6$  N, bending stiffness  $EI = 2.625$  Nm<sup>2</sup>. According to analytical solution (Brepta a kol., 1994):

$$f_j = \frac{\lambda_j^2}{2\pi} \sqrt{\frac{EI}{ml^3}}, \quad \lambda_j = j\pi, \quad j = 1, 2, 3, \dots, \quad (1)$$

---

\* Ing. David Lehký, Ph.D. and Ing. Petr Frantík, Ph.D.: Institute of Structural Mechanics, Faculty of Civil Engineering, Brno University of Technology, Veveří 95; 602 00, Brno; CZ, e-mails: lehky.d@fce.vutbr.cz, kitnarf@centrum.cz

the unloaded beam should have following bending eigenfrequencies  $f_1 = 12.27$  Hz,  $f_2 = 49.09$  Hz,  $f_3 = 110.45$  Hz,  $f_4 = 196.35$  Hz,  $f_5 = 306.80$  Hz. For the comparison, model (with 20 elements) gives  $f_1 = 12.25$  Hz,  $f_2 = 48.69$  Hz,  $f_3 = 108.41$  Hz,  $f_4 = 189.97$  Hz,  $f_5 = 291.35$  Hz.

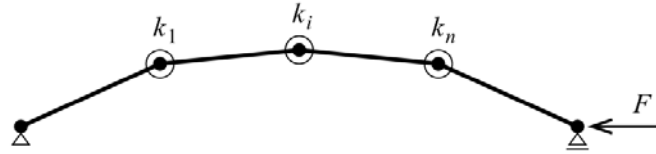


Fig. 1: Discrete model of a beam with rotational springs.

### 3. Parametric study

Changes of modal properties were studied on simply supported beam without imperfection and pre-loaded by axial force. The aim of this study was to find out which eigenfrequencies are affected by change of stiffness in individual location on the beam. This kind of information is important for damage identification using SHM data. Let's mention that evaluation of eigenfrequencies (especially the higher ones) from experiment is not an easy task. For study purposes, first five eigenfrequencies were taken into account. Ratio between the first one and the fifth one is approximately 1:25. As mentioned in chapter 2, bending of the beam is realized by 19 rotational springs with stiffness  $k_1, k_2, \dots, k_{19}$  corresponding to bending stiffness  $EI_1$  to  $EI_{19}$ . A damage of beam in individual location is modeled by decrease of bending stiffness down to one tenth of its nominal value. Such damages were applied step by step for all parts (only one part was damaged at each time).

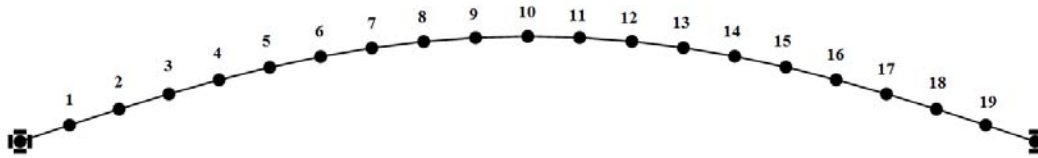


Fig. 2: Scheme of computational model of simply supported beam.

#### 3.1. Unloaded beam

First study was performed on a beam without axial force. Figure 3a shows the relative changes of the first eigenfrequency  $f_1$  as a function of the level of damage and position of damage. It can be seen that changes of eigenfrequency correspond in some sense to the first mode shape of the beam – position of extreme value corresponds to position of amplitude of mode shape. The same results were also obtained for higher eigenfrequencies. A distinctive change of eigenfrequencies (more than 5 %) can be detected only for higher levels of damage (more than 50 % of nominal stiffness). The damage in nodes of mode shape will not influence corresponding eigenfrequency. It is obvious that for efficient damage identification a higher number of eigenfrequencies must be taken into account because the absence of frequency change in certain part of the structure (node of mode shape) is then compensated by the change of another frequency. That can be seen in Fig.3b which shows which eigenfrequency has changed the most due to damage in certain part of the beam. In the middle part of the beam (parts 7-13) the first eigenfrequency is dominant. But in outer parts its influence decreases and higher eigenfrequencies become more important.

#### 3.2. Pre-loaded beam

The main aim of the study is to analyze an influence of axial (pre-stressing) force on eigenfrequency change of the beam due to damage. With increasing axial force, eigenfrequencies are decreasing for undamaged as well as damaged beam. Fig.4a shows such decrease for one particular case where middle part of the beam was damage to one half of the nominal stiffness. Critical force of that case is 36.65 N, for undamaged beam it is 40.40 N. In case of damaged beam, decrease of all eigenfrequencies is faster compared to undamaged beam (dashed line vs. solid line in Fig.4a). In the figure, there are no lines of the second and the fourth eigenfrequencies of damaged beam. The reason is that damage is located in the node of both corresponding mode shapes and therefore those eigenfrequencies are not affected by damage.

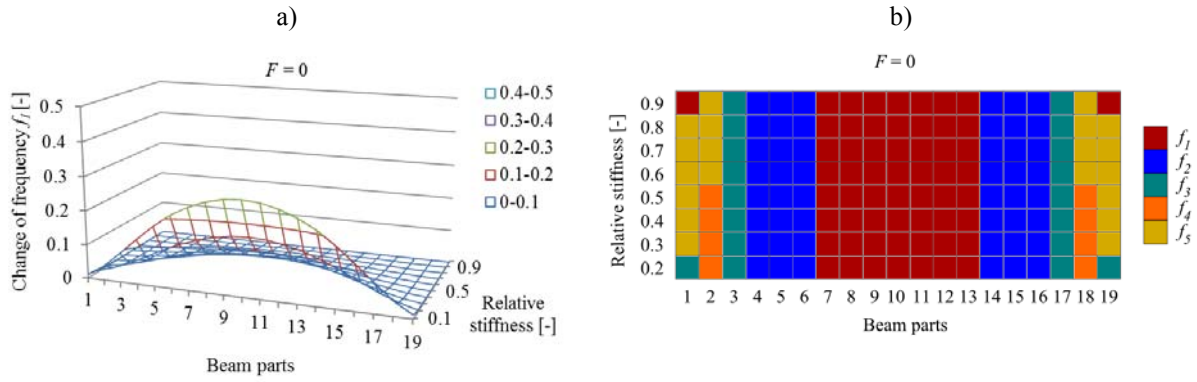


Fig. 3: a) Relative changes of the first eigenfrequency for different levels of stiffness in individual damaged parts of unloaded beam; b) division of unloaded beam to regions with maximum relative changes of each eigenfrequency.

Fig. 4b shows relationship between axial force and relative changes of eigenfrequencies. It is obvious that with increasing force (pre-stressing) a relative changes of eigenfrequencies are being increased too. Especially change of the first eigenfrequency is very strong. Higher eigenfrequencies are less affected. Again, the second and the fourth eigenfrequencies are not depicted in the figure since their values are not influenced by damage of the middle part of the beam. More detailed picture of dependence of axial force on eigenfrequencies changes caused by damage of individual parts of the beam to 50% of its nominal value gives Fig. 5. Fig. 5a shows relative changes of the first eigenfrequency which increases hand by hand with axial force. Fig. 5b shows relative changes of the second eigenfrequency. Changes increase again together with axial force but not so quickly as for the first eigenfrequency. One can also see zero change of the second eigenfrequency if the middle part (No. 10) of the beam is damaged – that for any size of axial force.

In Fig. 6a there are relative changes of the first eigenfrequency for different levels of damage and axial force  $F = 30$  N. Increase of eigenfrequency changes is distinctive compared to unloaded beam (see Fig. 3a). It is valid for lower levels of damage too. In the figure, one can see that critical forces for cases where damage of parts close to middle of the beam is relatively large (stiffness is reduced to 20% of its nominal size) is lower than axial force  $F = 30$  N. Fig. 6b shows regions of beam loaded by axial force  $F = 20$  N where each eigenfrequency is dominant (relative change of that eigenfrequency outweigh the others). In comparison with unloaded beam a region where the first eigenfrequency is dominant is wider for pre-loaded beam.

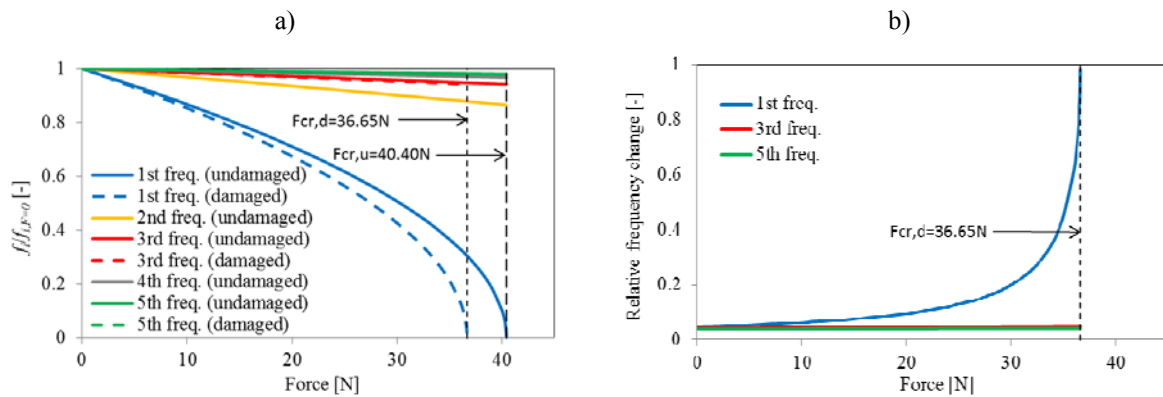


Fig. 4: a) Changes of eigenfrequencies with increase of axial force for undamaged and damaged beam; b) relative changes of eigenfrequencies due to damage (in both graphs the damage is represented by decrease of stiffness of middle part No. 10 to 50% of nominal stiffness).

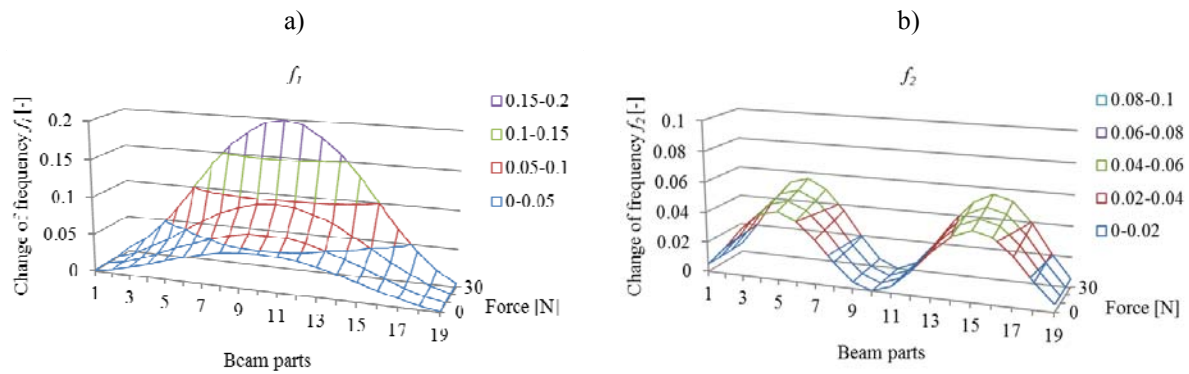


Fig. 5: Relative changes of (a) first and (b) second eigenfrequency caused by damage to 50% of nominal stiffness of individual damaged parts and their dependence on increase of axial force.

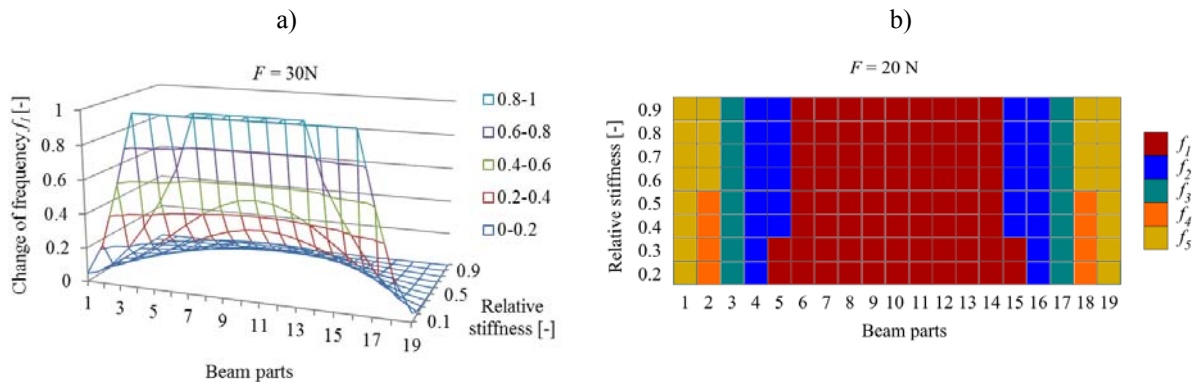


Fig. 6 a) Relative changes of the first eigenfrequency for different levels of stiffness in individual damaged parts of beam pre-loaded by axial force 30 N; b) division of pre-loaded beam (20 N) to regions with maximum relative changes of each eigenfrequency.

#### 4. Conclusions

A dominance of changes of particular eigenfrequencies when damage in individual parts of the buckled beam occurs was studied together with an influence of axial force size to those changes. Even with the knowledge of significant simplification, such a task can serve as a prefiguration for damage identification of pre-stressed structures. Results show that thanks to pre-stressing there are more significant changes of modal properties due to damage. It will be positive for damage identification using SHM data. Spreading region of dominance of the first eigenfrequency due to increasing axial force is also positive since the relative changes of frequency are bigger in comparison with higher ones.

#### Acknowledgement

This outcome has been achieved with the financial support of the Ministry of Education, Youth and Sports of the Czech Republic, project No. 1M0579 (CIDEAS research centre). Theoretical results gained in the project GACR COMOCOS No. P105/10/1156, were partially exploited.

#### References

- Brepta, R., Půst, L., Turek, F. (1994) Mechanické kmitání (Mechanical vibration). Technický průvodce 71, Sobotáles, Prague, Czech Republic (in Czech).
- Frantík, P. (2009) Diskrétní model FyDiK2D (Discrete model FyDiK2D). CD Proc. of Int. Conf. Modeling in Mechanics 2009, VŠB-TU Ostrava, Czech Republic, 10 pages (in Czech).
- Frantík, P., Lehký, D. & Novák, D. (2007) Modal properties study for damage identification of dynamically loaded structures. 3rd Int. Conf. on Struct. Eng., Mech. and Comp., Cape Town, South Africa, pp. 703-704.
- Lehký, D. & Novák, D. (2009) Neural network based damage detection of dynamically loaded structures. 11th Int. Conf. on Engineering Applications of Neural Networks (EANN 2009), London, Great Britain, pp. 17-27.
- Wenzel, H. & Pichler, D. (2005) Ambient vibration monitoring. John Wiley & Sons Ltd, West Sussex.



## CONTRIBUTION TO THE PROBABILISTIC APPROACH OF THE IMPACT STRENGTH OF WOOD

A. Lokaj\*, K. Vavrušová\*

**Abstract:** *The content of this paper relates to the impact bending strength determination of selected types of coniferous and broadleaved wood boards by means of destructive testing on the Charpy hammer, creating of histograms with obtained values and determination of impact bending strength statistical quantities for various sampling sets.*

**Keywords:** *Impact bending strength, Charpy hammer.*

### 1. Introduction

Wood is a natural renewable resource which is abundant in most European countries; therefore, it is often used in civil construction. Besides its common usage in structures, wood is traditionally used in highway construction, for construction of footbridges and wooden bridges, and, currently and most recently, for the manufacture of wooden-steel crash barriers. The latter started to be produced, for example, in Switzerland for roads with lower speed limits and in areas of tourist concentration, where higher requirements for crash barrier appearance are imposed. It is supposed that their usage will spread into other European countries.

All these elements (crash barriers, railings of bridges and footbridges) must meet the specified level of restraint which is related to the wood impact strength.

### 2. Impact bending strength

The impact strength is the ability of wood to absorb work done by an impact bend and it characterizes the ability of material to withstand impact loads. The impact strength is expressed by the consumed energy for breaking of wood with defined dimensions.

A measure of the energy absorbed by a timber can be obtained from a simple experiment involving observation of the initial and final velocities of a mass which impacts the timber. A mass  $m$  travelling at velocity  $v_0$  will slow to velocity  $v_1$  after impact. The energy or work absorbed by the timber is the difference in kinetic energy of the mass before and after impact (Bodig & Jayne, 1993):

$$W = -(U_{K0} - U_{K1}) \quad (1)$$

$U_{K0}$  ... is kinetic energy of the mass before impact;

$U_{K1}$  ... kinetic energy of the mass after impact;

Instituted to well-known equation:

$$U_K = \frac{1}{2}mv^2 \quad (2)$$

The equation of work is following:

---

\* assoc. prof. Ing. Antonín Lokaj, Ph.D. and Ing. Kristýna Vavrušová: Faculty of Civil Engineering, VSB – Technical University of Ostrava, Ludvika Poděště 1 875; 708 33, Ostrava - Poruba; CZ, e-mails: antonin.lokaj@vsb.cz, kristyna.vavrusova@vsb.cz

$$W = -\left(\frac{1}{2}mv_0^2 - \frac{1}{2}mv_1^2\right) = -\frac{1}{2}m(v_0^2 - v_1^2) \quad (3)$$

where:  $m$  ... is the mass;

$v_0$  ... velocity before impact;

$v_1$  ... velocity after impact;

### 3. Laboratory testing

Sets of more than 40 samples of spruce, beech and oak boards were created for impact bending strength tests. The Charpy hammer PSd 50H by WPM Leipzig Machines was used for impact bending strength of the selected sets.

The Charpy hammer PSd50H (Figs. 1, 2) by WPM Leipzig Testing Machines with the following parameters was used for impact bending strength of the selected sets.

- working capacity of the hammer 50 J;
- fall angle 160°,
- hammer impact velocity 3.8 m.s<sup>-1</sup>,
- pendulum impact testing machine weight 6.917 ± 0.035 kg,
- hammer face radius of curvature 15 mm,
- pendulum length 380 mm,
- resolution 0.01 J.



*Figs. 1, 2: The Charpy hammer PSd 50H.*

Test specimens had the shape of right-angle prisms with a base of 20 × 20 mm and a length in the direction of the grain of 300 mm. One side of the test specimen was in the radial plane, whereas the other one was in the tangential plane.

The test specimen was symmetrically laid on supports and disturbed by one hammer impact on the radial surface (tangential bend). The work absorbed by the test specimen was measured with the accuracy of 0.01 J.

#### 4. Laboratory testing results

Impact bending strength  $A_w$  with humidity at the moment of testing was determined from the formula according to ČSN 49 0117:

$$A_w = \frac{Q}{b \cdot h} \quad (4)$$

where:  $Q$  ... is work exercised for sample disturbance;

$b, h$  ... dimensions of test specimen in the radial and tangential directions.

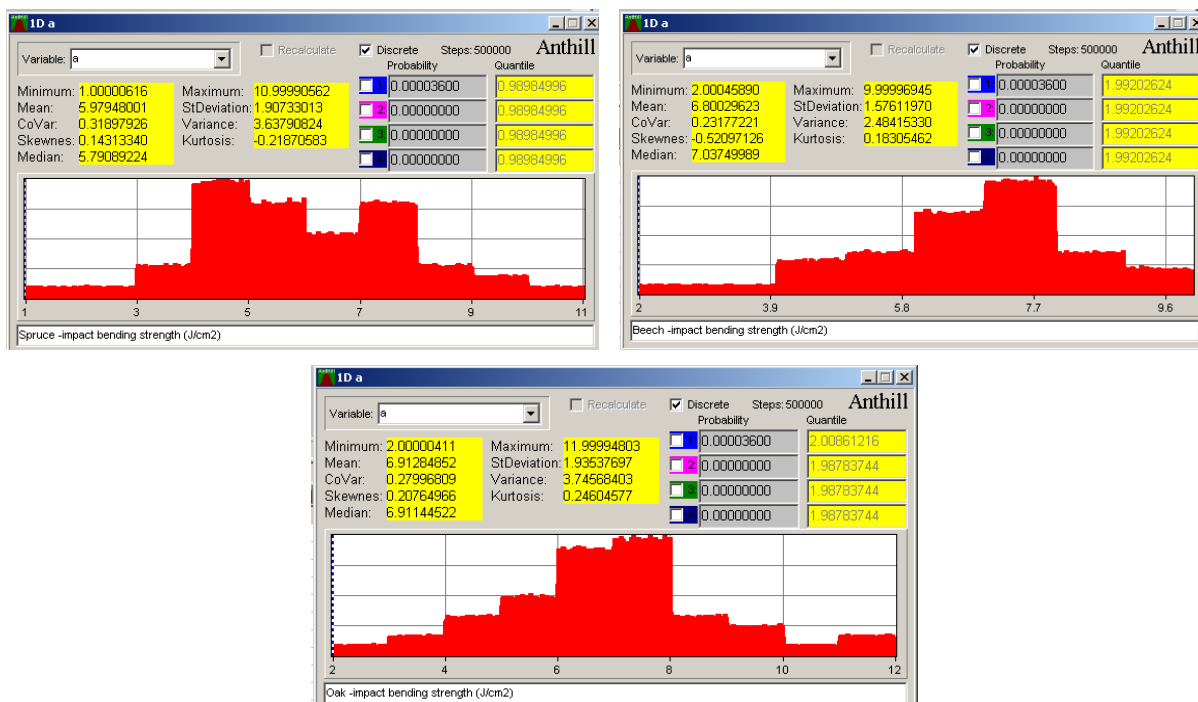
According to ČSN 49 0117 the impact bending strength was calculated for 12% humidity according to the formula:

$$A_{12} = A_w (1 + \alpha (W - 12)) \quad (5)$$

$\alpha$  ... is a correction factor for humidity which is 0.02 for all wood species;

$W$  ... wood humidity at the moment of testing.

The values of statistical quantities (average value, standard deviation and 5% quantile) were set and arranged by means of the calculation programs PASW Statistics 18 and Anthill.



Figs. 3, 4, 5: Histogram of measured values and Gaussian distribution approximation for the impact bending strength of spruce beech and oak.

The typical disturbance of spruce samples during impact bending strength testing was the splitting of the samples along the grain (along its whole length) and creation of splintering in growth rings (Fig. 6).

Splitting without splintering along the grain (Fig. 7) is typical of beech and oak. Sometimes even clear “cutting” occurred (Fig. 8).



*Figs. 6, 7, 8: Typical disturbance of spruce, beech and oak samples.*

Tab. 1 shows brief summary of the values gained during the impact bending test by means of the Charpy hammer.

*Tab. 1: Table with the resultant values of sample sets of individual board samples ( $\bar{\sigma}$  – average quantity value,  $\sigma$  - standard deviation,  $A_{05}$  - 5% quantile).*

	Impact bending strength [ $\text{J.cm}^{-2}$ ]		
	$\bar{\sigma}$	$\sigma$	$A_{05}$
Spruce	6.04	1.784	3.09
Oak	6.85	1.893	3.74
Beech	6.94	1.65	4.23

## 5. Conclusions

It is evident from table (1) that the highest impact bending strength is shown with beech (average value  $6.94 \text{ J.cm}^{-2}$ ); whereas the lowest impact bending strength is shown with coniferous – spruce (average value  $6.00 \text{ J.cm}^{-2}$ ). At 5% quantiles, the difference is much higher.

Impact bending strength was tested at an average humidity of 8% in the sample sets. As wood characteristics are dependent on humidity, it would be convenient to test wood strength for various humidity levels and to check humidity influence on wood strength because the elements of crash barriers and footbridge railings are exposed to various climatic conditions.

## Acknowledgement

This outcome has been achieved with the financial support of the Ministry of Education, Youth and Sports of the Czech Republic, project No. 1M0579, within activities of the CIDEAS research centre.

## References

- ČSN 49 0117 – WOOD – impact bending strength, Prague. (iIn Czech): ČSN 49 0117 – DREVO – rázová hůževnatost' v ohybe, ČNI, Praha.
- Křivý, V. & Marek, P. (2007) Zur probabilistischen Bemessung von Stahlrahmen. Stahlbau, 76. Jahrgang, Heft 1, pp. 12 - 20, ISSN 0038-9145.
- Bodig, J., Jayne, B. A., (1993) Mechanics of Wood and Wood Composites, pp. 230 – 233.
- Anthill, computational program for PC.
- PASW Statistics 18, computational program for PC.

## OPTIMIZATION OF BLADED DISK PASSIVE DAMPING ELEMENT

P. Lošák<sup>\*</sup>, E. Malenovský<sup>\*</sup>

**Abstract:** *This paper is aimed at reducing vibrations of bladed disk in particular operating state. The damping element used in this contribution is realized by a strap with isosceles trapezoidal cross-section area which is placed in hoop dovetail groove in the blade shrouding. The friction effect between the damping element and the groove side walls is included. Sliding between the contact surfaces leads to the dissipation of energy which causes decreasing of undesirable vibrations. The frictional force is influenced by centrifugal force acting on the damping element. The centrifugal force depends on disk angular speed, mass of the damping element and also on the size of contact area. It is shown that the axial vibrations of bladed disk in particular operating state is influenced by dimensions of the damping element cross-section. Dimensional optimization is used to find the optimal dimensions. The process of finding optimal dimensions is described in this paper. The finite element model of bladed disk involving passive damping element is created and the critical operating state is selected. The selection of design variables is discussed. The objective function is defined and optimization is performed.*

**Keywords:** *Bladed disk vibrations, vibrations damping, transient analysis, optimization.*

### 1. Introduction

The steam turbines are high loaded equipments. There are many possible resonant states which may result in high cycle fatigue failure. Sometimes the operating state can be close to the resonance state, which causes undesirable vibrations of bladed disk. One way of decreasing the excessive vibrations is employing a frictional effect of the suitable damping element. The damping element can be realized by a strap having isosceles trapezoidal cross-section area and can be placed in hoop dovetail groove in the blade shrouding. This type of the damping element is suitable especially for damping of the vibrations in the axial direction along with the mode shape with the nodal diameters. The damping effect is reached by sliding between the contact surfaces. The modal properties of the bladed disk are influenced by the sliding distance. Since the friction force depends on centrifugal force acting on the damping element and on angle of the side walls of groove and strap, the sliding distance can be influenced by dimensions of damping element. Optimal dimensions for considered operating state can be found.

The strategy of finding optimal dimensions can be following. Afterward the finite element model is created the modal analysis is performed since the knowledge of the modal properties (natural frequencies and mode shapes) is important for determination of the critical resonance states. The critical speed and corresponding excitation frequency are determined based on the selected resonance state. Since resonance frequency is influenced by the damping, it is difficult to determine corresponding critical excitation frequency exactly. Thus the transient analysis is performed, and excitation frequency is swept in this simulation. The assumed critical excitation frequency is between initial and end value of excitation frequency. This condition ensures that disk pass through the resonance state.

The objective function quantifies the vibration in axial direction. The definition is based on displacement of nodes on the disk circumference.

---

<sup>\*</sup> Ing. Petr Lošák and prof. Ing. Eduard Malenovský, DrSc.: Institute of Solid Mechanics, Mechatronics and Biomechanics, University of Technology, Technická 2896/2; 616 69 Brno; CZ, e-mails: ylosak00@stud.fme.vutbr.cz, malenovsky@fme.vutbr.cz

## 2. Model of Bladed Disk

The ANSYS v11.0 is used to create the finite element model. The geometry is shown in the Fig.1a). The bladed disk has 54 blades, which are coupled in 18 packets by segmental shrouding. The damping element (highlighted by red color in Fig. 1) is placed in the dovetail groove, created in the shrouding. The mesh is generated by 8-nodes structural elements SOLID 45. The contact respecting Coulomb's Law of friction is modeled between the side walls of the groove and the damping element. The surface-to-surface contact elements are used for the contact definition. Element type CONTA173 is used on the side walls of the damping element, and element type TARGE170 is used on the side walls of the groove. Static coefficient of friction is set to 0.7, kinetic coefficient is set to 0.6.

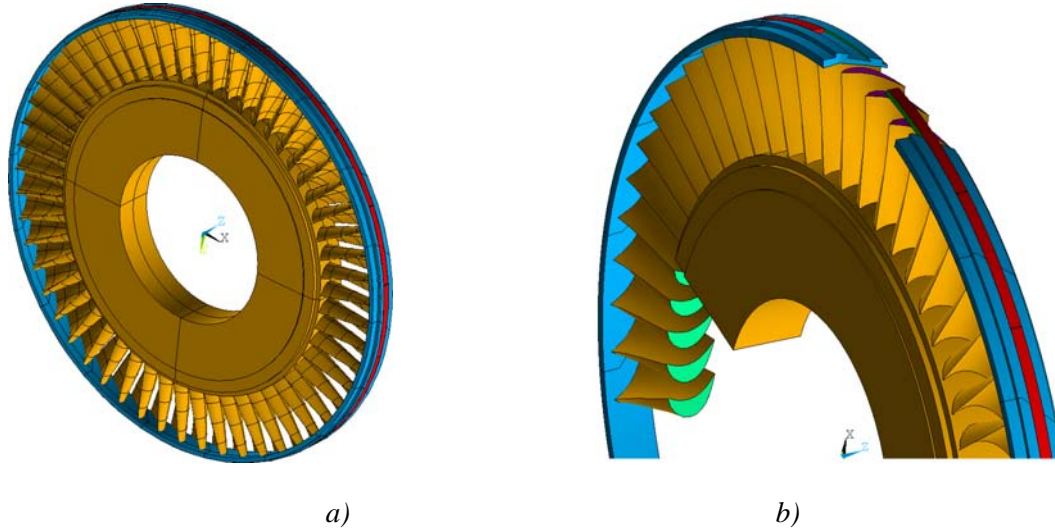


Fig. 1: Model of Bladed Disk.

## 3. Critical Operating State

Critical operating state is selected based on the results of the modal analysis. Since including of the contact-type nonlinearities is not allowed in the modal analysis, two linear models are considered for performing modal analysis. In the first case the contact algorithm for contact elements between damping element and groove. Thus the strap and shrouding are stick together. The modal analysis results are labeled as "Case A" in the Fig. 2. In the second case the damping element is removed and contacts are deleted. Results are labeled as "Case B" in the Fig.2. Resonance frequencies of model including friction are considered between frequencies of Case A and Case B, or in close surroundings eventually. The operating state (resonance frequency and number of nodal diameters) that dimensions of damping element are optimized for is selected based on previous work (Lošák, Malenovský 2007). This operating state is marked by red color in Fig. 2.

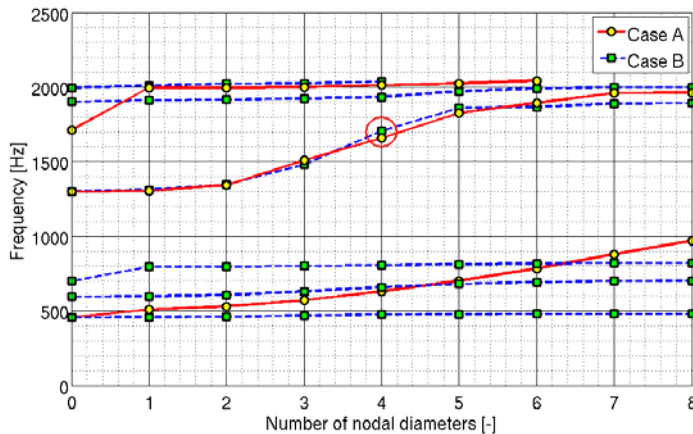


Fig. 2: Natural Frequency vs. Number of nodal Diameters Plot.

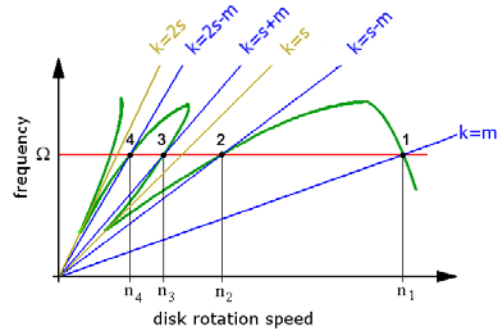


Fig. 3: Campbell Diagram.



#### 4. Boundary and Initial Conditions

The bladed disk is rigidly fixed on the inside diameter in the disk bore. The bladed disk is excited due to nonuniform pressure distribution behind stator grid. This pressure fluctuation is represented by axial and tangential harmonic force, acting on the end of each blade. The force on each following blade is shifted against the previous of the phase angle, which is calculated as:

$$\beta = \frac{z}{r} 2\pi \quad (1)$$

where:  $\beta$  is phase angle,  $z$  is number of the stator blades, and  $r$  is number of the rotor blades.

The frequency of the excitation force depends on selected operating state. The operating state assumed in this paper is marked by the red circle in Fig. 2. Determination of the corresponding critical rotation speeds is shown in the Fig. 3. The critical rotation speed is defined as cross point of the disk natural frequency with  $k$ -multiple of the natural frequency (Campbell, 1924). Calculation of  $k$  is also shown in the Fig. 3,  $m$  is number of the nodal diameters and  $s$  is number of the cyclic sectors,  $n_1$  through  $n_4$  are critical disk rotation speeds. As stated in Section 3 the excitation frequency is swept to ensure that the disk passes the resonance state. Thus it is necessary to calculate the excitation frequencies for both limiting states and define angular acceleration of excitation frequency. The angular velocity and corresponding frequency of excitation force can be determined as:

$$\alpha = \frac{\omega_e - \omega_i}{t} \quad (2)$$

$$F(t) = F_0 \sin\left(\left(\omega_i t + \frac{1}{2} \alpha t^2\right) + \beta(l_r - 1)\right) \quad (3)$$

where  $\alpha$  is angular acceleration of excitation force,  $\omega_i$ , and  $\omega_e$  is excitation angular frequency corresponding to initial resp. end rotation speed,  $t$  is time of simulation.  $F(t)$  is time-depended force (axial or tangential)  $F_0$  is force amplitude (axial or tangential),  $\beta$  is phase angle (see Equation 1),  $l_r$  is sequential number of rotor blade (1 through 54).

#### 5. Optimization

Since the damping element cross-section dimensions is optimized, the design variables are characteristics dimensions of the cross section area - height of damping element, cross section middle width and side wall slope angle. The damping element cross section along with visualization of design variables limits are shown in Fig. 4.

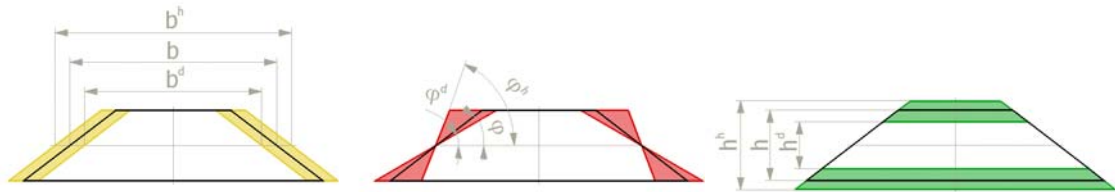


Fig. 4: Optimization Variables and Dimension Limits Visualization.

The objective function has to quantify the vibrations of the bladed disk. Since some nodes on the disk circumference can lie on the nodal diameters, the displacement in all nodes of the disk circumference is evaluated. This approach ensures that objective function quantify the axial vibration all around the disk. The objective function is shown in Equation 4. It is a sum of displacement absolute value of every node integrated over time.

$$\psi(\mathbf{x}) = \sum_{i=1}^n \left( \int_{T_1}^{T_2} |q_i(\mathbf{x}, t)| dt \right) \quad (4)$$



where:  $\psi(x)$  is objective function, which depends on design variables  $x$ ,  $T_1$  and  $T_2$  are initial and end point of evaluated time interval. Variable  $q_i$  is axial displacement of particular node,  $n$  is number of nodes on the disk circumference.

The Subproblem Approximation Method is used to find the minimum of the objective function. The number of nodal diameters vs. simulation time and magnitude is shown in Fig. 5a for starting values of optimization variables and in Fig. 5b for final values. Figures show that optimization of the passive damping element dimensions leads to decreasing of vibration. It can be seen that level of vibration is lower for mode shape with four nodal diameters as well as for mode shape with eight nodal diameters as. It seems that vibrations associated with eight nodal diameters mode shape are damped even more intense than those associated with four nodal diameters mode shape.

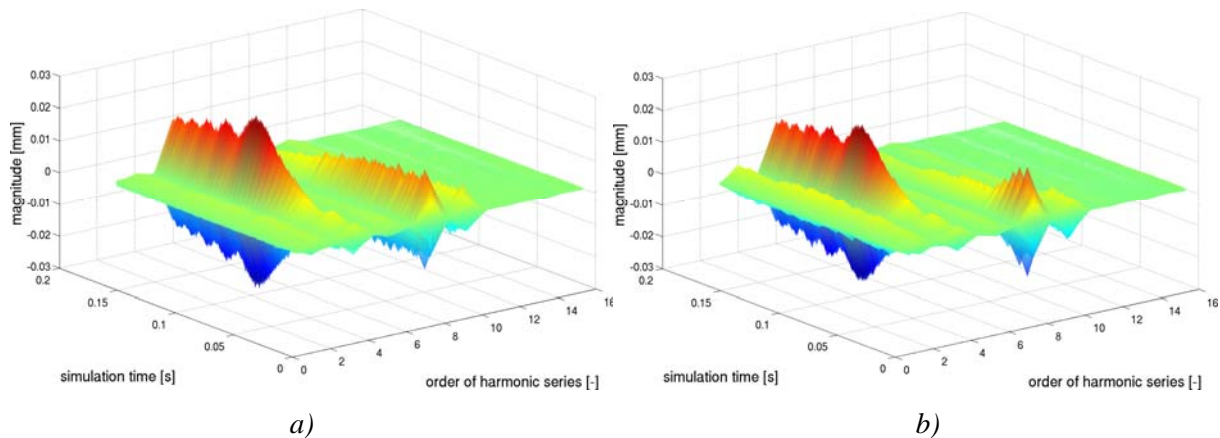


Fig. 5: Representation of nodal diameters and amplitudes during simulation for a) not optimized and b) optimized dimension of damping element.

## 6. Conclusions

The strategy of optimization of the passive damping element cross section dimensions is shown in this paper. The dimensions are optimized for selected operating state with particular number of nodal diameters. The objective function composition is discussed and optimization is performed. The optimal dimensions are found. It is shown, that optimization leads to decreasing vibration generally, not only those associated with selected operating states and corresponding number of nodal diameters. It turns out that it is possible to use this process to optimize passive damping element geometry to decrease undesirable oscillations of bladed disk

## Acknowledgement

This paper was written with the support of grant CZ.1.07/2.4.00/12.0030.

## References

- Campbell, W., (1924) The Protection of Steam-Turbines Disk Wheels From Axial Vibration, ASME Transaction, Vol. 46.
- Lošák, P., Malenovský, E. (2007) Contribution to the dynamic behaviour of bladed disk, Applied and Computational Mechanics, roč. 1, č. 2, s. 531-540. ISSN: 1802- 680X.
- Lošák, P., Malenovský, E. (2008) Optimization of the Damping Element Dimensions, Computational Mechanics, pp.1-2, ISBN 978-80-7043-712-4.
- Malenovský, E.; Lošák, P. (2007) Dynamické vlastnosti olopatkovaných turbínových kol, Parní turbíny a jiné stroje, pp.1-10, ISBN 3-200-00689-7 (in Czech).

## INFLUENCE OF THE SPHEROID PROLONGATION ON THE DRAG FORCE

N. Lukerchenko<sup>\*</sup>, I. Keita<sup>\*</sup>, Y. Kvurt<sup>\*\*</sup>, J. Miles<sup>\*</sup>

**Abstract:** *The drag force acting on a spheroid moving perpendicularly to its axis of rotation in water was studied experimentally. Along the spheroid axis, which is normal to its axis of rotation, a round narrow hole was bored. The spheroid moved along a thin vertical thread stretched in water. A video system recorded the spheroid motion and the spheroid velocity was determined from the record. The drag force coefficient was calculated from the balance of forces acting on the spheroid. Two oblate, two prolate spheroids and one sphere with ratio of the axes 0.67; 0.81; 1.33; 2 and 1 (sphere), respectively, with approximately the same volumes, were used. The friction coefficient between the thread and spheroid was determined from the comparison of the experimental and calculated motions of the sphere, for which the drag force coefficient is known. The dependence of the drag force coefficient of the spheroid on the ratio of its semi-axes was obtained.*

**Keywords:** *Spheroid, drag force coefficient.*

### 1. Introduction

Spherical particle is usually used for modelling of solid particle movement in fluid (e.g., Nino & Garcia, 1994; Kholpanov & Ibyatov, 2005; Lukerchenko et al., 2006, 2009a,b). However, the influence of the particle shape on its motion in fluid can be significant. For example, in the case of particle saltation in a channel with rough bed, the elongated shape of the particles leads to a significant increase of the angular velocity (Nino & Garcia, 1998), which strongly affect numerical models. A spheroid is the simplest shape, which can be compared with a sphere, and it is suitable to study the influence of the particle elongation.

Let the semi-axis of a spheroid that corresponds to the axis of rotation (axis of symmetry) is  $a_0$  and the semi-axis that is normal to the axis of rotation, i.e. the equatorial radius, is  $b_0$  (Fig. 1). If the spheroid moves slowly in fluid without rotation (i.e. for Stokes conditions,  $Re \ll 1$ ), its drag force can be calculated using the drag force components parallel to the axis of rotation  $F_{\parallel}$  and perpendicularly to this axis  $F_{\perp}$  (Happel, 1973). The correlations for the drag force coefficients  $C_{\parallel}$  and  $C_{\perp}$  that are dimensionless analogues of the drag force components  $F_{\parallel}$  and  $F_{\perp}$  were derived for Stokes flow theoretically (e.g., Happel, 1973; Clift et al., 2005). Unfortunately, there are not available relationship for the drag force coefficients  $C_{\parallel}$  and  $C_{\perp}$  for different ratios of the spheroid semi-axes  $E = a_0 / b_0$  when Reynolds number  $Re \gg 1$ . Experimental results for axisymmetric motion ( $F_{\perp} = 0$ ) outside the Stokes range appear to be limited to oblate spheroids ( $E < 1$ ) for which is the preferred orientation (Clift et al., 2005). List et al. (1973) studied experimentally the drag force acting on the oblate spheroids with axis ratios  $0.5 < E < 0.79$  over a range of Reynolds numbers from 40 000 to 400 000 at various inclination angles of the fluid flow.

The present paper deals with an experimental evaluation of the drag force coefficient  $C_{\perp}$  for the semi-axes ratio  $E$  ranging from 0.67 to 2 (Tab. 1) and  $Re \sim 10\,000$ .

---

<sup>\*</sup> Nikolay Lukerchenko, PhD., Ibrahima Keita, PhD. and Ing. Jiri Miles: Institute of Hydrodynamics of Academy of Sciences of the Czech Republic, v.v.i.; Pod Patankou 30/5, 166 12, Prague 6; CZ, e-mails: lukerchenko@ih.cas.cz, keita@ih.cas.cz, miles@ih.cas.cz

<sup>\*\*</sup> Dr. Yury Kvurt, CSc.: Institute of Problems of Chemical Physics of Russian Academy of Sciences; Chernogolovka, Moscow reg., 142432 Russia, e-kvurt@icp.ac.ru

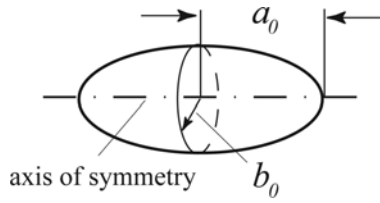


Fig. 1: Test spheroid.

Tab. 1: Parameters of spheroids.

No.	$a_0$ , mm	$b_0$ , mm	$E=a_0/b_0$	
1	12.6	18.9	0.67	Oblate spheroids
2	14.6	18.0	0.81	
3	16.4	16.4	1.0	Sphere
4	20.0	15.0	1.33	Prolate spheroids
5	26.2	13.1	2.0	

## 2. Experimental procedure

The experiments were carried out in a rectangular glass vessel 0.780 m long, 0.580 m wide, and 0.980 m high. The water depth was about 0.900 m.

The spheroid masses were measured using the electronic balance SARTORIUS BA2100S; the maximum absolute error was  $10^{-5}$  kg.

The five Plexiglas models of spheroid were used. Along one of the equatorial diameters, i.e. normally to the axis of rotation, a round narrow hole of diameter 1 mm was bored. The spheroid moved along a thin thread of diameter 0.1 mm that was passed through the hole and was stretched in water vertically.

The measurement of spheroids sedimentation start just under the water surface in order to avoid air entrainment and the effect of the water surface on its motion.

The spheroid movement in water was recorded using the digital video camera NanoSenze MKIII+ with frequency up to 1000 frames per second. The spheroid terminal fall velocity was determined by evaluation of the video record. The drag force coefficient was calculated using the balance of forces acting on the spheroid.

## 3. Mathematical model

The following forces act on the spheroid of mass  $m$  moving steady in water along the vertical thread: gravity force  $F_g = mg = \rho_s \Omega g$ , Archimedean force  $F_A = \rho \Omega g$ , friction force  $F_f = k_f l$  and drag force  $F_d = C_{\perp} S \rho V^2 / 2$ , where  $\rho_s$  is the spheroid density,  $\rho$  is the water density,  $g$  is the gravitational acceleration.  $\Omega = 4/3 \pi a_0 b_0^2$  is the spheroid volume,  $k_f$  is the friction coefficient,  $l = 2b_0$  is the length of the hole in spheroid,  $V$  is the fall velocity, and  $S = \pi a_0 b_0$  is the spheroid cross-section area perpendicular to direction of movement. The force  $F_f$  due to the mutual friction between the spheroid and the thread is supposed to be proportional to the length of the hole  $l$ .

The balance of the forces gives:

$$m g = \rho \Omega g + 2k_f b_0 + C_{\perp} \pi a_0 b_0 \rho V^2 / 2. \quad (1)$$

For the each spheroid, Eq. (1) includes two unknowns: the friction coefficient  $k_f$  and the drag force coefficient  $C_{\perp}$ . However, for the sphere, the drag force coefficient is known and the Eq. (1) can be used for the definition of the friction coefficient  $k_f$ .

## 4. Results

The spheroid volume can be specified in two ways: (I) using the formula for the spheroid volume  $\Omega_0 = 4/3 \pi a_0 b_0^2$  and, (II) using the values of the Archimedean force  $\Omega_A = F_A / \rho g$ . The Archimedean force was measured the following way. A beaker filled with water was put on the balance, which was zeroed. The spheroid was submerged into the water in the beaker without touching the beaker wall and bed. The balance shows the Archimedean force. For the used balance the accuracy of the volume measurement for this method is  $10^{-8} \text{ m}^3$ . The calculated and measured data in Tab. 2 shows that the spheroid production error (shape inaccuracy) was less than 5%.

For the drag force coefficient of the sphere the following correlation was used (Nino&Garcia, 1994):

$$C_{\perp} = \frac{24}{Re} \left( 1 + 0.15(Re)^{\frac{1}{2}} + 0.017Re \right) - \frac{0.208}{1 + 10^4 Re^{-0.5}}, \quad (2)$$

where  $Re = 2rV/\nu$  is the Reynolds number,  $r=a_0=b_0$  is the sphere radius,  $\nu$  is the water kinematical viscosity. The value of the drag force coefficient for the sphere of measured size is  $C_{\perp} = C_{d0} = 0.445$ . The fall velocity is 0.35 m/s. The value of the friction coefficient from the Eq. (1) is  $k_f = 0.353$  N/m.

Tab. 2: The spheroid production accuracy.

No.	$E=a_0/b_0$	$\Omega_0 \cdot 10^{-5}$ m <sup>3</sup>	$\Omega_A \cdot 10^{-5}$ m <sup>3</sup>	$(\Omega_0 - \Omega_A)/\Omega_A$ %
1	0.67	1.885	1.889	0.2
2	0.81	1.970	1.883	4.6
3	1.0	1.831	1.831	0.0
4	1.33	1.885	1.850	1.9
5	2.0	1.883	1.871	0.6

The values of the drag force coefficient  $C_{\perp}$  for the oblate and prolate spheroids were calculated using Eq. (1) and they are presented in Tab. 3. The equivalent Reynolds number is  $Re_e = 2r_e V/\nu$ , where the equivalent radius  $r_e = (a_0 b_0)^{0.5}$  is the radius of the sphere with the same midlength section area.

Tab. 3: The drag force coefficients of the spheroids.

No.	$E=a_0/b_0$	$V$ , m/s	$Re_e$	$C_{\perp}$
1	0.67	0.42	13 000	0.34
2	0.81	0.38	12 400	0.39
3	1.0	0.35	11 400	0.45
4	1.33	0.31	10 600	0.55
5	2.0	0.26	9 800	0.72

The dependence of the drag force coefficient  $C_{\perp}$  on the ratio of the spheroid semi-axes  $E = a_0/b_0$  is depicted in Fig. 2. This dependence matches well with the correlation:

$$C_{\perp} = C_{d0} E^{0.7}, \quad (3)$$

where  $C_{d0} = 0.445$  is the drag force coefficient of the sphere in turbulent regime.

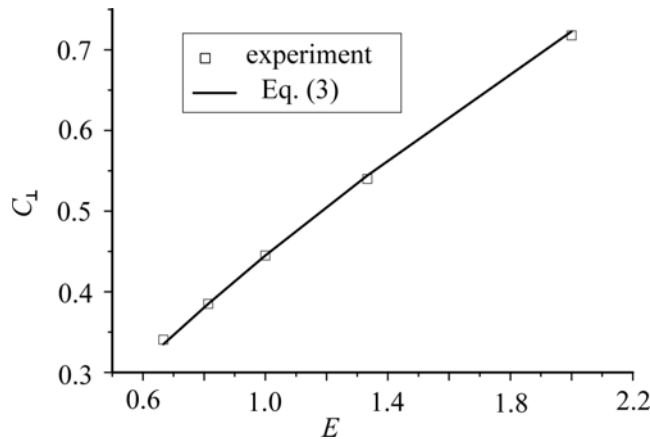


Fig. 2: The dependence of the spheroid drag force coefficient  $C_{\perp}$  on the ratio of the spheroid semi-axes  $E$ .

## 5. Conclusions

The dependence of the drag force coefficient of the spheroids moving perpendicularly to the axis of rotation on the spheroid semi-axes ratio were determined for the spheroid semi-axes ratio ranging from 0.67 to 2. The values of the Reynolds number are in the range from 9 800 to 13 000. The dependence corresponds well with the experimental data and it can be used in the numerical models of the particle movement in fluid. The experimental method can be used for investigation of the drag force coefficients of spheroids as well as the bodies with more complex shape.

## Acknowledgement

This work was supported under the project No. 103/09/1718 of the Grant Agency of the Czech Republic and the Institutional Research Plan AV0Z20600510 of Academy of Sciences of the Czech Republic.

## References

- Clift R., Grace J.R. & Weber M.E. (2005) Bubbles, Drops, and Particles, Dover, New York.
- Happel J. (1973) Low Reynolds number hydrodynamics, Noordhoff International Publishing, the Netherlands
- Kholpanov L.P. & Ibyatov R.I. (2005) Mathematical modelling of the dispersed phase dynamics, Theor. Found. Chem. Eng., Vol. 39, No. 2, pp. 190–199.
- List R., Rentsch U. W., Byram A.C., & Lozowski E.P. (1973) On the Aerodynamics of Spheroidal Hailstone Models, J. Atmos. Sci., 30, 653- 661.
- Lukerchenko N., Chára Z., & Vlasák P. (2006) 2D numerical model particle-bed collision in fluid-particle flows over bed, J. Hydraul. Res., Vol. 44, No. 1, pp. 70–78.
- Lukerchenko N., Piatsevich S., Chára Z., & Vlasák P. (2009a) 3D numerical model of the spherical particle saltation in a channel with a rough fixed bed, J. Hydrol. Hydromech., Vol. 57, No. 2, pp. 100-112.
- Lukerchenko N., Piatsevich S., Chára Z., & Vlasák P. (2009b). “Numerical model of the spherical particle saltation in channel with transversely tilted rough bed”. J. Hydrol. Hydromech., 57(3): 182-190.
- Nino Y. & Garcia M. (1994) Gravel saltation. 2. Modeling, Water Resour. Res., Vol. 30, No. 6, pp. 1915–1924.
- Nino, Y. & Garcia, M. (1998) Experiments on saltation of sand in water. J. Hydraul. Eng., ASCE 124, pp. 1014-1025.

## EFFECT OF VIBRO-INSULATION ON RESTRICTION OF VIBRATION TRANSFER FROM SUBSOIL INTO THE BUILDING

D. Makovička<sup>\*</sup>, D. Makovička<sup>\*\*</sup>

**Abstract:** *The solution of vibration transfer from the subsoil to the structure is demonstrated using the example of a multi-storey reinforced concrete building, founded on a dual foundation plate. An anti-vibration layer of rubber has been designed between the two plates. Two 3-D numerical models of the building take into account the individual storeys, firstly together with the lay-out of the rubber distribution in the foundation part and secondly without this rubber part. For response analysis, the measured time histories in the construction area were selected and then the typical response was used as an input for a dynamic analysis of the structure.*

**Keywords:** *Technical seismicity, insulation, building, dynamic analysis, response prognosis.*

### 1. Introduction

Trains running through underground tunnels produce vibrations which, together with the vibrations from a wide range of constituents of the underground railway, such as ventilation fans and escalator drives, propagate from the source to more distant structures. As a rule, these vibrations propagate into building foundations at the foundations/subsoil interface. Vibrations produced by subsurface traffic usually do not threaten the safety of structures. Nevertheless, they may be significant because of their undesirable impacts on people living or working in the residential or office parts of the building, especially due to their tuning. The applied springing is, consequently, a very efficient instrument for reducing the vibration propagation (Jacquet, 2002).

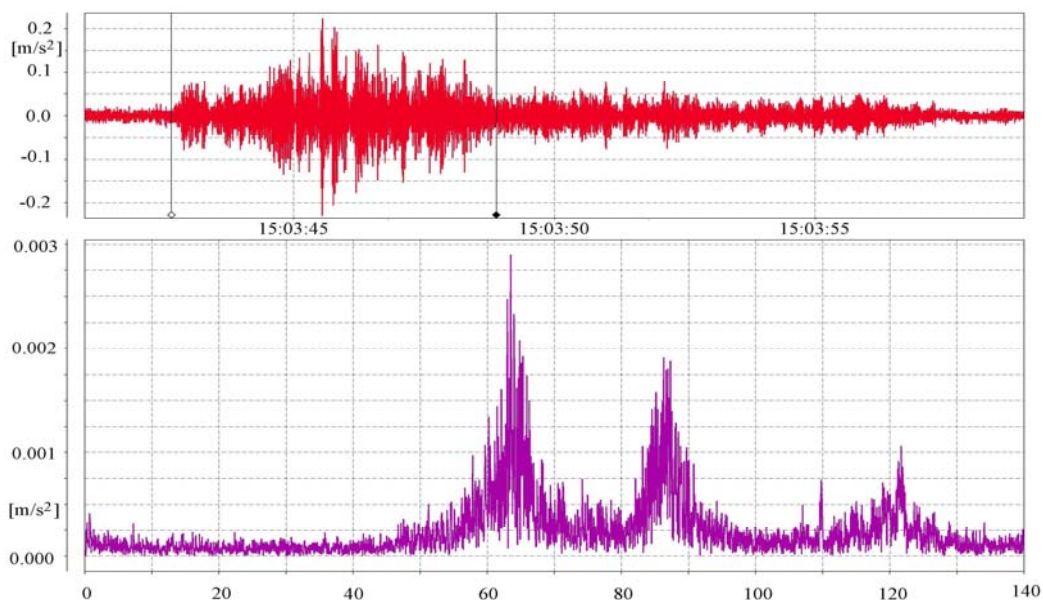


*Fig. 1: Measured vertical of the underground station excited by a train pass  
 (the whole course, FFT spectrum).*

<sup>\*</sup> assoc. prof. Ing. Daniel Makovička, DrSc.: Klokner Institute, Czech Technical University, Šolínova 7; 166 08, Prague 6; CZ, e-mail: daniel.makovicka@klok.cvut.cz

<sup>\*\*</sup> Ing. Daniel Makovička jr.: Static and Dynamic Consulting, Šultysova 170; 284 01 Kutná Hora; CZ, e-mail: d.makovicka@makovicka.cz



## 2. Technical seismicity effect

The character of vibrations depends on their parameters at their source, i.e. the character of the train motion, the structure and occupancy of the rolling stock, the geometry and characteristics of the permanent way (above all, the fastening of the rails, etc.), the structure of the tunnel or station, the parameters of the equipment of the tunnel or station, etc. The magnitude of the vibrations is influenced not only by the vibration parameters at the source, but also by the composition of the geological environment in the proximity of the underground railway, i.e. the route from the source to the threatened structure. Last but not least, the magnitude of these vibrations may be increased or damped by the actual execution of the structure loaded by them (Makovička, 2005). The measured real characteristics of the vibrations may show considerable mutual differences, because the magnitude of the vibrations and their frequency structure depend not only on the general parameters of source (train characteristics, way, underground structure, etc.) but also on the local parameters on the site (particularly the composition of the geological environment, foundation design, etc.) These measurements produce typical histories of vibrations affecting selected parts of the structure (Fig. 1), which can be considered as the dynamic load of the future or existing structure at its foundation level. This vibration load has a non-stationary character.

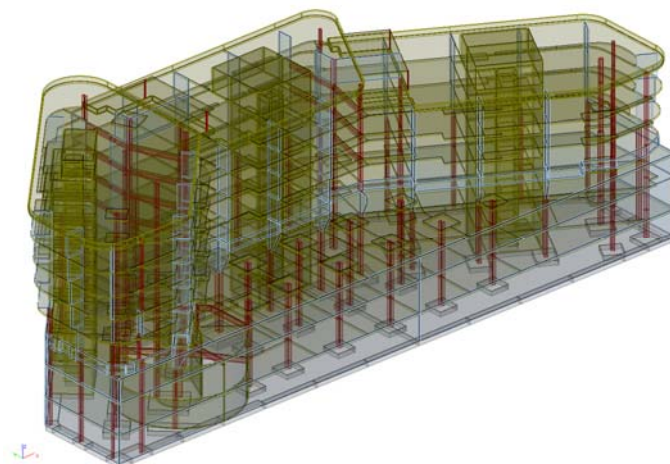


*Fig. 2: Calculation model North-West view.*

## 3. Structure analysis

The multistorey reinforced concrete building (Fig. 2) is founded on the base plate. On top of this plate an antivibration layer of rubber has been designed. Above the rubber there is an upper foundation plate in which the cast-in-place skeleton building structure is constrained. The rubber 500×500×30 mm (slabs) are butt-jointed (not interlocked) in a single layer with 3 – 5 mm joints enabling the rubber to buckle, thus assuring identical conditions of deformability and, consequently, stiffness corresponding to the conditions at the foundation base. The principle involves consistent separation of the upper part of the structure from the foundation structure by an elastic layer (Makovička, 2009). The advantage of rubber layers is that they provide sufficient damping to reduce the resonance peaks of the vibrations of the elastic supported structure.

The calculation model takes into account the individual storeys, broken down into the floor, foundation and roof slabs, columns, load-bearing walls and peripheral and interior girders. The layer of rubber was considered as the elastic subsoil of the Winkler-Pasternak model below the whole area of the upper part of the foundation plate. The mass of the floor and the foundation plates includes the masses of the non-load-bearing components (thin partitions, floorings, etc.) as well as the equivalent of the live loads of floors, roof and terraces (Makovička, 2005).

The dynamic load, i.e., the vibrations (Fig. 1), was introduced into the model as a normalized load and with the identical phase all over the foundation plate. The vibrations of the building produced by underground traffic were predicted by the response analysis of the whole system. The time histories for selected points on all the floors located on the chosen vertical line on the margin of the left highest structure part on its rear side are shown in Fig. 3. The most intensive vibrations can be observed in the proximity of columns, balconies, terraces and structural parts situated on the underground side. With



increasing height, this excitation mode will manifest itself by vibrations of the building in one of the natural frequencies of the structure. More significant influence of vibration is in most cases limited to the lowest two or three storeys. In the higher storeys, the time characteristic of the vibrations is divided into lower frequencies.

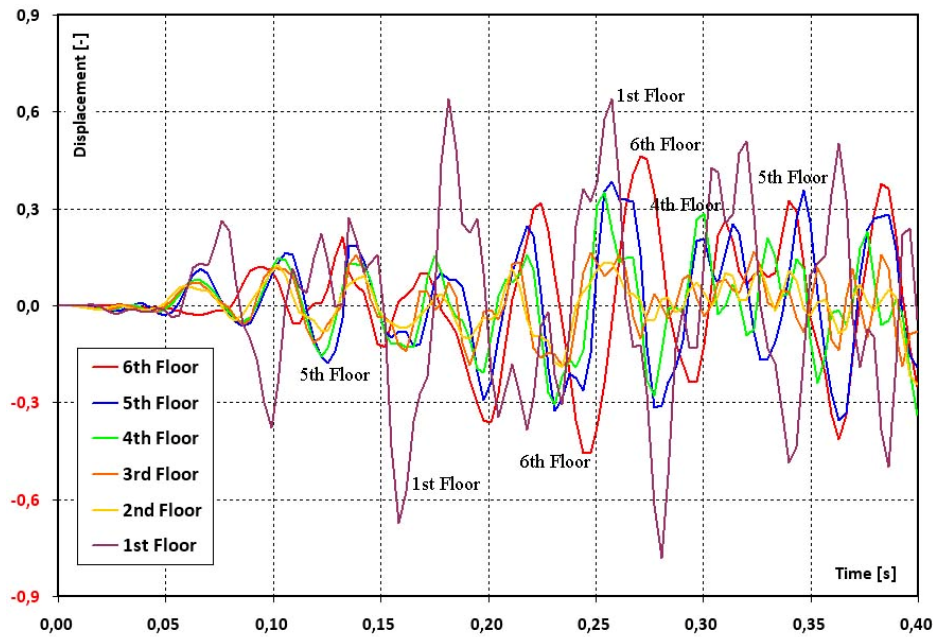


Fig. 3: Time histories of relative displacements on line B for vertical excitation.

Tab. 1: Extremes of relative floor displacements under vertical and horizontal excitation.

Floor level	Insulated structure				Noninsulated structure			
	Vertical		Horizontal		Vertical		Horizontal	
	$u_z$		$u_y$		$u_z$		$u_y$	
	Max	Min	Max	Min	Max	Min	Max	Min
-3 <sup>rd</sup> Floor	1.00	-0.76	1.00	-0.83	1.00	-1.00	1.00	-1.00
-2 <sup>nd</sup> Floor	1.22	-1.29	0.96	-1.07	1.43	-1.00	1.28	-1.89
-1 <sup>st</sup> Floor	1.24	-0.97	0.89	-0.89	1.00	-1.00	1.12	-1.23
+1 <sup>st</sup> Floor	0.87	-0.92	0.70	-0.59	0.85	-0.82	1.18	-1.49
+2 <sup>nd</sup> Floor	0.74	-0.64	1.00	-1.02	0.70	-0.53	0.85	-0.91
+3 <sup>rd</sup> Floor	0.70	-0.69	0.85	-0.76	0.54	-0.72	0.91	-0.95
+4 <sup>th</sup> Floor	0.73	-0.72	1.08	-1.13	0.63	-0.51	0.81	-1.04
+5 <sup>th</sup> Floor	0.66	-0.66	1.08	-0.93	0.63	-0.56	0.81	-1.19
+6 <sup>th</sup> Floor	0.69	-0.71	0.85	-1.04	0.52	-0.47	1.09	-1.32

#### 4. An assessment of the effectiveness of springing

An assessment of the effectiveness of the sprung system can be based on a comparison between the measured vibrations (Fig. 1) and the vibration level of the individual storeys in the sprung building (Fig. 3) and vibration of insulated and noninsulated structure (Tab. 1). The measured dominant excitation frequencies of underground train traffic are 63 Hz and 87 Hz on the frequency peaks. The measured dominant excitation frequencies of underground train traffic are 63 Hz and 87 Hz on the frequency peaks. The springing of the building will shift its dominant vibrations into the range of the lowest natural frequencies (from 1.7 Hz to about 20 Hz, see Fig. 3) of the sliding or flexural vibrations of the building as a whole. For frequencies of up to 20 Hz, this maximum response acceleration value corresponds approximately to the effective acceleration  $a_{\text{RMS}}$  according to Tab. 2.

Tab. 2: Prognosis of maximum floor vibration

Excitation $a_{RMS}$ [mm/s <sup>2</sup> ]	Vertical excitation		Horizontal excitation	
	Middle part of floors	Balconies	Middle part of floors	Balconies
	Response $a_{RMS}$ [mm/s <sup>2</sup> ]			
0.80-0.84	0.736-0.773	1.152-1.210		
0.22-0.24			0.238-0.259	0.235-0.257

The above results show that the influence of springing will manifest itself by redistribution of the dominant vibrations into the low frequency range of the springing and by the practically negligible amplitude range of the vibration level in comparison with the initially dominant excitation frequencies (Fig. 1).

## 5. Conclusion

This paper deals with the application of an elastic antivibration layer at foundation base level in order to eliminate excessive vibrations propagating to the assessed building through the geological environment from an underground railway structure. When the train is in motion, the dominant vibrations are transferred to the environs in the form of non-stationary vibrations produced by the pass of the train and of the tunnel station structure vibration (in our case).

The histories of the measured vibrations were used as loads applied to a modelled building structure at the foundation base of which, as an alternative, a separating elastic rubber layer had been designed. The response of the vibroinsulated structure is compared with the non-isolated structure. The computed vibration histories reveal that the vibrations of the sprung structure are decreased in almost all the above-ground storeys. The effectiveness of the springing is determined by the frequency tuning of the sprung structure. The lower the tuning of the structure based on springs (the lower the dominant natural frequencies), the greater the decrease in the higher vibration frequencies and acoustic frequency effects propagating into the structure from its geological environment.

More significant influence of vibration is in most cases limited to the lowest two or three storeys. The predicted vibrations in the individual storeys were shown for a model with and without insulation, and were compared with the level of excitation vibrations at the foundation base. In the case of hard inelastic placing of the building on subsoil without springing, the vibrations would propagate from the subsoil in the whole frequency interval directly into the building structure, practically without decreasing. The applied springing is, consequently, a very efficient instrument for reducing the transfer of vibration from the soil to the interior parts of the building.

## Acknowledgement

This research was supported as a part of the research projects in GAČR P105/11/1580 "Transient response of structure under short-term dynamic or impact load due to seismic effects and explosions", for which the authors would like to thank the Agency.

## References

- Makovička, D. & Makovička, D., Jr. (2009) Response analysis and vibroinsulation of buildings subject to technical seismicity, in: Earthquake Resistant Engineering Structures VII, WIT Press, Southampton, UK, pp. 197-205.
- Makovička, D. & Makovička, D., Jr. (2005) Structure insulation exposed to excessive vibration of underground traffic (in Czech), Stavební obzor, 14, 1.
- Jacquet, T. & Heiland, D. (2002) Tieffrequente Bauwerken-Kopplungen als Schutz gegen Erschütterungen, Gerb Berlin.

## CREATION OF COMPUTATIONAL MODELS OF CANCELLOUS BONE

P. Marcián<sup>\*</sup>, L. Borák<sup>\*</sup>, J. Valášek<sup>\*</sup>, D. Krpalek<sup>\*</sup>, K. Řehák<sup>\*</sup>, P. Navrátil<sup>\*</sup>

**Abstract:** *The paper deals with a creation of computational model of cancellous bone. Cancellous bone is inner porous part of bones and it is of a very complex geometry. It is composed of special trabecular architecture and the trabeculae can be less than 1 mm in diameter. In most cases, cancellous bone is modeled as a “non-trabecular” solid body with an apparent Young’s modulus. The creation of a “trabecular” model of cancellous bone (which, in our opinion, is more appropriate) is quite difficult. MicroCT images are indispensable for this case as well as the software for their processing. Authors of this paper developed for this purpose a specialized software called STL Model Creator which works in Matlab platform. The software uses image processing methods in segmentation of cancellous bone images (thresholding). The paper introduces a method of creating of computational model and initial stress-strain analysis utilizing this model is presented as well.*

**Keywords:** *Micro CT, bone, finite element method, stress strain analysis, image processing.*

### 1. Introduction

The most common problems addressing the biomechanics of the musculo-skeletal system include determining the material properties of bone tissue. There are two types of bone: Hard outer cortical bone and porous inner cancellous bone. In general, bones are inhomogeneous anisotropic biomaterials which are changing their properties and shape during the whole life. This work is focused on creating a computational model of cancellous bone which includes trabeculae and which quantity, distribution and orientation within the bone is strongly individual. A number of these trabeculae determines the density of cancellous bone. In most cases, a “non-trabecular” solid body with an apparent Young’s modulus and an apparent density is used as the model of cancellous bone. A higher level of this material, specifically an inhomogeneous isotropic model of cancellous bone, can be created by using computer tomography (CT) image processing (Valášek, 2010). Nevertheless, this model is the “non-trabecular” as well. Since no trabecular architecture is included, the adequacy of these two models used for the analyses of interactions between dental implants and the bone tissue is disputable. We believe that the effect of the trabecular architecture on the mechanical interaction between the mentioned parts especially in the mandible is rather significant and it should be included in the models of cancellous bone. This is easy to do in case of 2D modeling-level as we can get the architecture from images of histological sections. The creation of the “trabecular” model of cancellous bone in 3D is much more difficult. One way how to obtain the images for 3D reconstruction of the bone is to cut thin layers of the bone embedded in dyed epoxy resin. Much more appropriate and faster is using a microCT device which directly stores series of images. By using the image processing the final 3D trabecular model can be then reconstructed. For this particular purpose, authors have developed specialized software called STL Model Creator (Konečný, 2010) which is implemented into Matlab.

### 2. Methods

By using the method explained below, cancellous bone specimen was modeled and stress-strain analysis was performed. The most popular numerical method – finite element method (FEM) – was used; specifically, commercial product based on this method - ANSYS 11.0 (Ansys Inc., Canonsburg,

---

<sup>\*</sup> Ing. Petr Marcián, Ing. Libor Borák, Ing. Jiří Valášek, Ing. David Krpalek, Ing. Kamil Řehák and Ing. Petr Navrátil: Institute of Solid Mechanics, Mechatronics and Biomechanics, Faculty of Mechanical Engineering, Technická 2896/2; 616 69, Brno; CZ, e-mails: ymarci00@stud.fme.vutbr.cz, liborborak@seznam.cz, yvalas05@stud.fme.vutbr.cz, ykrpal00@stud.fme.vutbr.cz, yrehak04@stud.fme.vutbr.cz, ynavra26@stud.fme.vutbr.cz

PA, USA). In general, computational model consists of four submodels: model of geometry, model of material, model of loads and model of boundary conditions. Model of geometry of cancellous bone specimen was obtained from microCT images series which are available for downloading online from Biomed Town database ([www.biomedtown.org](http://www.biomedtown.org)). Images of the bone tissue were obtained from the bone biopsy of 61-old man's femur neck by Baruffaldi and Perilli by using Skyscan microCT (see Fig. 1). Detailed description of the creation of the geometry model is given in Section 2.1.

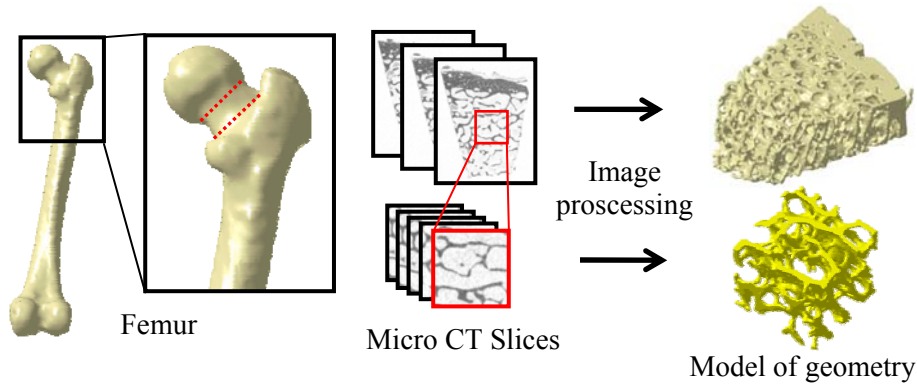


*Fig. 1: MicroCT imaging procedure and the final model of geometry.*

## 2.1. Model of geometry and FE model

The above mentioned database contains a series of microCT images of slices through the whole bone specimen and also through a specific site of the specimen. Log files containing detailed information about microCT settings are in the database available as well. In terms of geometry-modeling, the information on the number and size of pixels or voxels are the most important. In the specific case investigated in this paper, the voxel size is of 0.019479 mm, 0.019479 mm, 0.019479 mm (x, y, z). In total, 195 images with a resolution of 200x200 pixels were used. After segmentation and obtaining of a cloud of points in STL Model Creator software, a trabecular architecture specimen of approx. 4 x 4 x 4 mm in size was created (STL polygonal mesh - see Fig. 2).

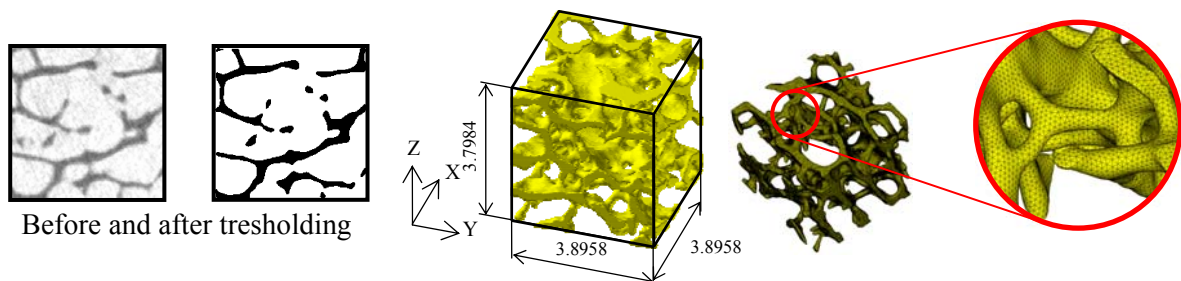


*Fig. 2: Illustration of thresholding, the specimen size and the final FE mesh.*

Trabecular architecture was discretized in ANSYS by using tetrahedral structural SOLID185 element (see Fig. 3). Since trabecular structures are of a very complex shape, a considerable attention should be paid to meshing of their models. A sensitivity study was performed to obtain the optimal element size. The study revealed that more than 300 000 nodes are needed for the specimen so as the results could be accurate enough.

## 2.2. Model of material

At micro-level, cancellous bone is of the same mechanical properties as cortical bone (Rho, 1998). The material used in the computational model is homogenous, isotropic and linearly elastic – which is defined by two independent characteristics: Young's modulus  $E = 13\,700\text{ MPa}$  (Bratu, 2003) and Poisson's number  $\mu = 0.3$  (Bratu, 2003).

## 2.3. Model of loads and boundary conditions

The specimen was loaded in Z-axis by means of pre-defined displacements of all nodes at one side of the specimen in XY-plane. The specimen was fixed on the opposite side. The specimen was loaded in

tension as well as in compression so as the proportional elongation of the specimen would be 0.25%, 0.5%, 1%, 2% and 3%.

### 3. Results

Several testing models based on different numbers of microCT images were created in STL Model Creator software. The purpose was to assess an effect of the number of the microCT images on the quality of the model, i.e. if omitting the microCT images in the 3D reconstruction can affect the quality of the model. Therefore, computational models based on omitting one, two, three and four microCT images were created. Each image which was omitted has the voxel height of 0.097395 mm. The specimen was firstly loaded by the displacement causing the proportional elongation of 1% (in tension only). Maximum 1st and 3rd principal stresses, stress intensity and von Mises stress as well as maximum 1st and 3rd principal strains and strain intensity were plotted in the graphs below (see Fig. 4). The results show significant differences between the model based on all microCT images and the model where 4 images were omitted. The most significant differences occurred in 1st principal stress and in strain intensity which were 27.9% and 15.8%, respectively.

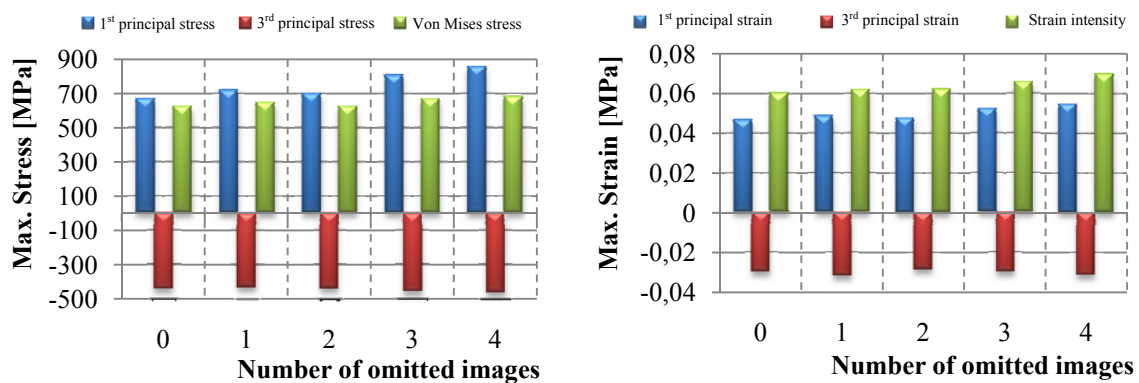


Fig. 4: Maximum stresses and strains for various models (loaded by the 1% elongation).

Omitting one and two images caused no significant difference in the monitored quantities. Omitting more images caused increase in differences. For the next analysis, model with no omitted image was used. This model was loaded again in tension and now also in compression. The representative distributions of the 1st and 3rd principal stresses are plotted in Fig. 5. The representative distributions of the 1st and 3rd principal strains are plotted in Fig. 6

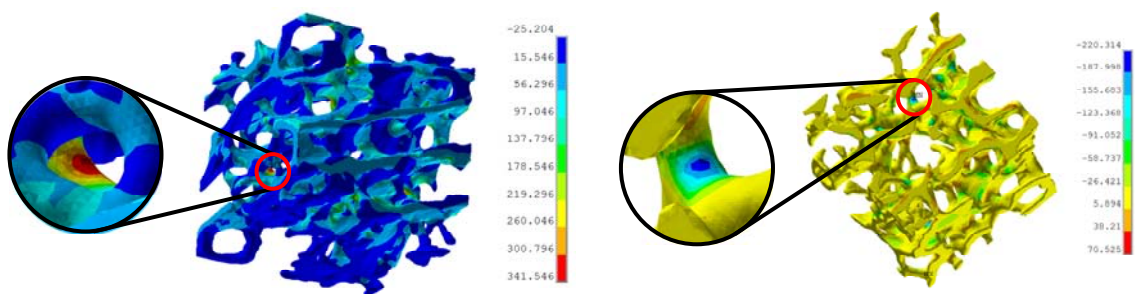


Fig. 5: 1<sup>st</sup> and 3<sup>rd</sup> principal stresses [MPa] (0.5% elongation).

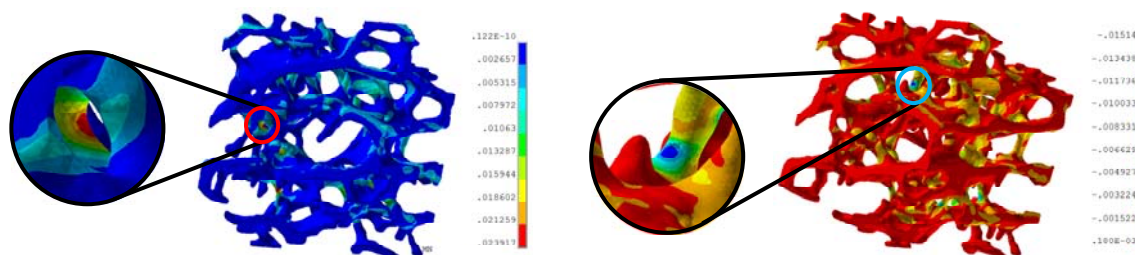


Fig. 6: 1<sup>st</sup> and 3<sup>rd</sup> principal strains [-] (0.5% elongation).



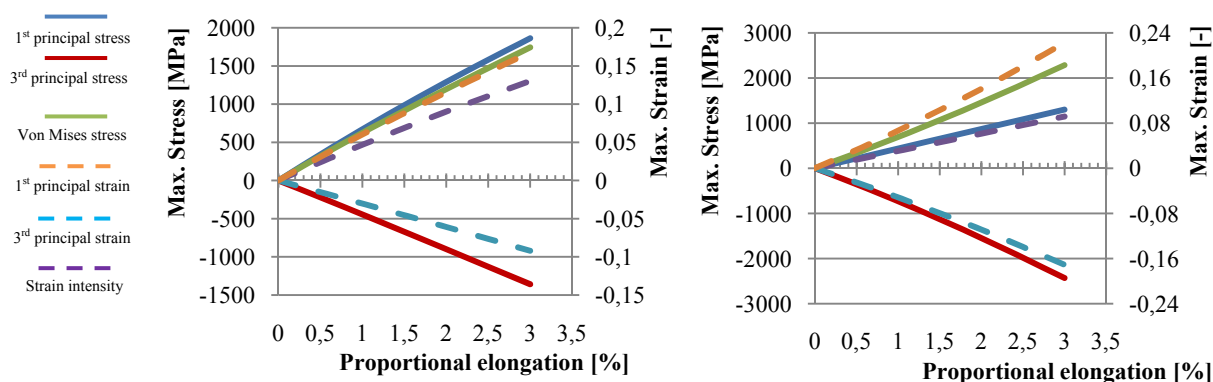


Fig. 7: Results (tension of the left, compression on the right).

When loaded by displacement causing proportional elongation of 3.5%, the monitored quantities reached extremely high values (von Mises stress = 1800 MPa, strain intensity = 0.17). The dependence of the mechanical quantities on the loading (elongation/contraction) is of a linear character (see Fig. 7). Only the inclination of the graphs changes with the changing load - significantly in case of principal stresses/strains, insignificantly in case of von Mises stress.

#### 4. Conclusions

The aim of this paper was to create a computational model of cancellous bone specimen reflecting the trabecular architecture. For this purpose, microCT images of the real bone were processed and afterwards 3D model was reconstructed on their basis. STL Model Creator software developed by the authors was used for the reconstruction. The computational model created this way belongs to models at the highest modeling-level used up-to-date. Series of models created from lesser number of available microCT images (i.e. with omitting some images) was created and used. Stress-strain analysis revealed that sufficiently fine microCT imaging of the trabecular structures is needed, i.e. images should be at a close offset. When images are obtained from the structure embedded in a dyed epoxy resin, the specimen should be milled in thin layers of less than 0.05 mm. The results obtained from the calculation of the specimen in tension/compression revealed linear character of stresses and strains.

#### Acknowledgement

This work was supported by grant project FRVS No. 2829/2011 and specific research FSI-J-11-3.

#### References

- Bratu, E., Steigmann, M. (2003) Analyse der strukturalen Spannungen zwischen Implantat und Knochen. *Implantologie J*, vol. 7, pp. 47–49.
  - Konečný, O., Marcián, P. et al. (2010), software, STL Model Creator, biomechanika.fme.vutbr.cz
  - Rho, J. Y., Tsui, T. Y., Pharr, G. M. (1998) Elastic properties of osteon and trabecular bone measured by nano-indentation, *Journal of Biomechanics*, vol.31, pp 21.
  - Valášek, J., Marcián, P., et. al. (2010) Material Properties of Bone Tissue Obtained from CT for Biomechanics Purposes, In MENDEL 2010. Mendel Journal series. pp. 483-490.
- www.biomedtown.org

## ANALYSIS OF LONG-TERM BEHAVIOR OF AN INSULATION BLOCK FROM RECYCLED HDPE BY COMRESS LOADING

L. Matějka \*, J. Pěňčík \*

**Abstract:** Use of waste materials is an actual topic that corresponds to current trends associated with the decreasing of power exigency and sustainable development. The possibility to reduce depletion of natural resources and decrease the produced waste lies in an efficient and possibly repeated use of resources. An important subgroup of waste is formed by materials from petroleum derivatives - polymers (PP, PE, HDPE etc.). Polymers and their composite materials can be used as a base material for most products including products used in civil engineering. One of these products is an insulation block for elimination of thermal bridges in wall footing. During design of this product the MAP method (modelling-analysis-prediction) has been used together with experimental testing. This paper deals with description of long term behaviour of an insulation block made of recycled polymers using full scale testing. Experimental data are compared to different rheological models.

**Keywords:** Waste materials, recycling, polymer, experimental testing, rheological models.

### 1. Introduction

Use of waste materials is an actual topic, which corresponds to current trends of decreasing of power exigency and sustainable development. Current capacity of natural resources is limited. The possibility to reduce depletion of natural resources lies in an efficient and possibly repeated use of resources – resource recycling. The advantage of recycling is the minimization of waste as well as decrease of power consumption and CO<sub>2</sub> production.

An important subgroup of waste is formed by petroleum derivatives – polymers. There exists a huge quantity of waste polymers: PP, PE, HDPE, PET, PVC, PUR etc. (Fig. 1). These materials belong to the group of thermoplastic materials and they can be easily recycled thanks to their basic property – thermal plasticity. Another advantage of using recycled polymers is the possibility to improve their resistance against atmospheric ageing, fire resistance and thermal-technical and mechanical properties (Fig. 2).

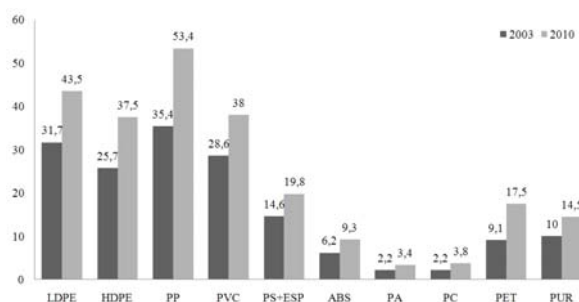


Fig. 1: Global production of polymers in mil. tons in year 2003 and 2010 (OECD 2008).

Properties	HDPE	modified HDPE
Volume mass	952,81 kg/m <sup>3</sup>	1206,43 kg/m <sup>3</sup>
Thermal conductivity (ČSN 64 0526)	0,418 Wm <sup>-1</sup> K <sup>-1</sup>	0,339 Wm <sup>-1</sup> K <sup>-1</sup>
Notch impact resistance (ČSN EN ISO 179-1)	as HDPE	4,8 kJm <sup>-2</sup>
Flexural elasticity modulus (ČSN EN ISO 178)	904 MPa	1001 MPa
Yield stress	23,1 MPa	18,7 MPa

Fig. 2: Example of improvement of mechanical and thermal-technical properties of HDPE.

\* Ing. Libor Matějka, CSc., Ph.D., MBA and Ing. Jan Pěňčík, Ph.D.: Institute of Civil Engineering, Brno University of Technology, Faculty of Civil Engineering, Veveří 95; 602 00, Brno; CZ, e-mails: matejka.l@fce.vutbr.cz, pencik.j@fce.vutbr.cz



## 2. Solution of wall footing detail using an insulation block

The detail of wall footing i.e. place between the foundation and the masonry and inner floor brings problems (Fig. 3a). In this place thermal bridges originate due to decrease of heat resistance of the structure, if this problem is not solved.

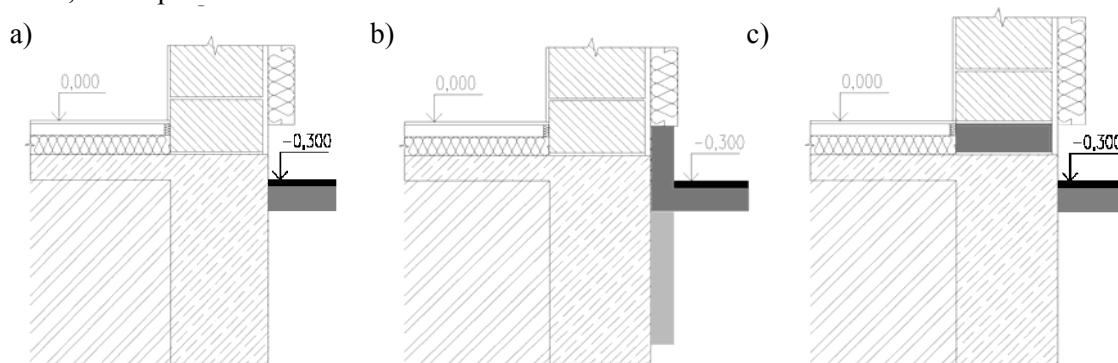


*Fig. 3: Wall footing detail - interruption of thermal bridge, methods of solution.*

Two methods can be used for elimination of thermal bridge – direct and indirect. Both of them interrupt the thermal flow. The indirect method of solution (see Fig. 3b) inserts a thermal insulation under adjusted terrain to the necessary depth or in case of impossibility to insert thermal insulation under the terrain it is possible to lay the thermal insulation horizontally on the terrain to the required distance from the walling (Fig. 3b). The direct method of solution (see Fig. 3c) inserts a thermal insulation directly to the place of thermal bridge. This solution solves directly and efficiently the described issues of the detail.

A new product for the direct solution is designed – an insulation block (Fig. 4) which can be made from recycled polymer such as recycled HDPE, PP or as a recycled polymer composite (Fig. 5). The design of the insulation block is carried out using FEA analysis by the help of ANSYS system depending on designed material. By mathematical modelling it is assessed in terms of statics and thermal mechanics. The FEA analysis is supplemented by experimental testing.

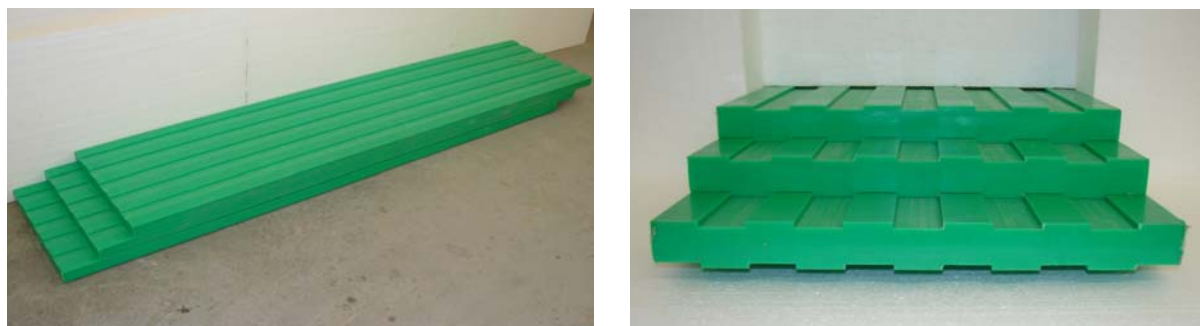


*Fig. 4: Insulation block made from recycled HDPE.*



*Fig. 5: Recycled polymer composite.*

### 3. Experimental testing

The simulation of a long-term state of stress and a verification of a long-term behaviour of the insulation block is done using a stressing frame (Fig. 6) is scale 1:1 i.e. testing in a real cut of masonry. The width of the insulation block boards is 440 mm, the height is 120 mm ( $3 \times 40$  mm) and length is 2000 mm. The insulation blocks and masonry is loaded by a contact pressure of intensity 1.2 MPa by means of controlled system of high pressure pneumatic bellows. Vertical and horizontal deformation of the insulation block caused by the load is measured continuously on long-term basis in selected sections using mechanical sensors measuring the track (Fig. 6).



Fig. 6: Stressing frame and detail of mechanical sensors.

The goal of the experimental testing is to ascertain the long term compression of the insulation block in order to enable verification of numerically calculated data with experimental data and to obtain creep curve by means of measuring in 1:1 scale. The experimental data is also used to compare general rheological models for viscoelastic materials (Maxwell model, Kelvin model, Maxwell-Kelvin model and Standard solid model) and for selection of the most appropriate rheological model for modelling of a long term behaviour of recycled polymers, here of recycled HDPE.

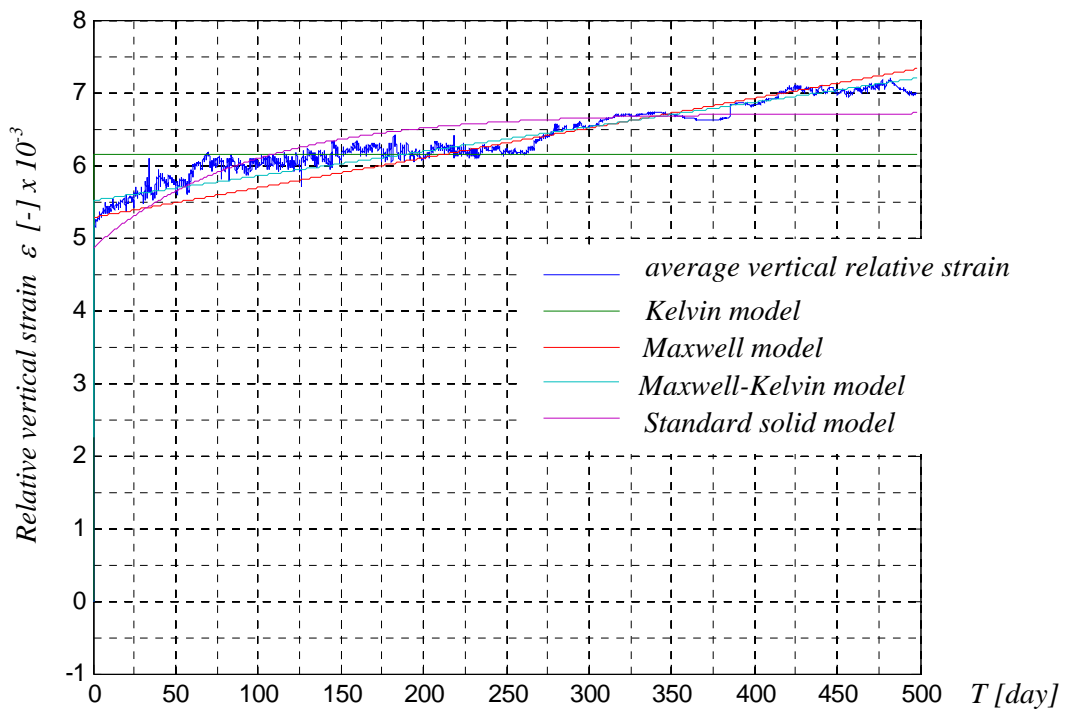


Fig. 7: Long time measuring.

Long time measurement is shown in graph in Fig. 7 where average vertical relative strain from all measuring sensors is drawn together with compensation of temperature influence (blue line) and results obtained using general rheological models for viscoelastic materials mentioned in Barbero (2008). The graph represents a time interval of 500 days. Using measured data the ratio of strain to applied stress, which is a compliance  $D(t) = \varepsilon(t)/\sigma_0$ , is found.

Maxwell model:

$$D(t) = 1/E_0 + 1/\tau E_0 \quad (1)$$

$$E_0 = 227.135; \tau = 1284.492$$

Kelvin model:

$$D(t) = 1/E_0[1 - \exp(-t/\tau)] \quad (2)$$

$$E_0 = 194.533; \tau = 0.025$$

Maxwell-Kelvin model:

$$D(t) = 1/E_0 + 1/\tau_1 E_0 + (1/E_2)[1 - \exp(-t/\tau_2)] \quad (3)$$

$$E_0 = 534.012; E_2 = 366.676; \tau_1 = 664.565; \tau_2 = 0.036$$

Standard solid model:

$$D(t) = 1/E_0 + (1/E_2)[1 - \exp(-t/\tau_2)] \quad (4)$$

$$E_0 = 247.215; E_2 = 639.075; \tau_2 = 92.166$$

#### 4. Conclusions

Waste polymers in general may play an important role in selection of building materials in the future. Resistance against atmospheric ageing, fire resistance, and thermal-technical and mechanical properties can be improved.

The mentioned materials can be used for example for elimination of thermal bridges in wall footing detail in a form of an insulation block. Because of the nature of polymers it is necessary to test, verify and predict their long term behaviour. This can be achieved through experimental testing and modelling based on general rheological models for viscoelastic materials.

By comparing results for recycled HDPE insulation block (Fig. 7) for different rheological models for viscoelastic materials can be concluded that Maxwell-Kelvin rheological model represents the most accurate approximation of behaviour of the insulation block under long term constant pressure. The suitability of this model is confirmed by comparing the results of the evaluation criteria, which was the smallest sum of squares.

#### Acknowledgement

The article was created within the solutions of survey intentions of MSM 0021630511.

#### References

- Barbero, E. J. (2008) Finite Element Analysis of Composite Materials. CRC Press, Boca Raton.  
 OECD (2008) Organisation for Economic Co-operation and Development. Online at <http://www.oecd.org>

## COMPARISON OF NUMERICAL AND EXPERIMENTAL METHODS OF SOLUTION OF THE FLOW FIELD OF HUMP

M. Matějka<sup>\*</sup>, T. Hyhlík<sup>\*</sup>, P. Pick<sup>\*</sup>

**Abstract:** *The paper is focused on comparison of numerical solution and experimental work of the flow field near model of hump. The hump is located in closed measurement area of Eiffel type wind tunnel. Commercial code Fluent was used to perform numerical solution. Experimental measurement was done by using hot wire anemometry traversing probe.*

**Keywords:** *Numerical solution, 3D, experimental measurement, hot wire anemometry.*

### 1. Introduction

Vortex structures have significant impact to the flow field. Studying of character of vortex structure is important to understand possibilities how to influence them, namely how to reduce their negative effect to the flow field.

Focusing on comparison of numerical simulation and experimental data of the flow field is important part of research. Main reason of this work is to visualize and identify vortex structures (Kolar, 2007; Berdahl et al., 1989; Zhou et al., 1999), in the flow field and to verify numerical model. Use of numerical simulation is very important, because describing and visualizing of vortex structure in three-dimensional space from experimental data is very difficult.

### 2. Numerical simulation

Numerical simulation of the flow field near model of hump was done by using commercial code Fluent. Mesh consists of about 6 million cells, see Tab. 1 and Fig. 1 and 2. Numerical simulation is based on pressure correction SIMPLE method. Convective terms are discretized using second order upwind. For the turbulent modeling RANS approach with SST  $k - \omega$  model is used. Values of dimensionless distance of center of the first cell from wall  $y^+$  are shown in Tab. 2.

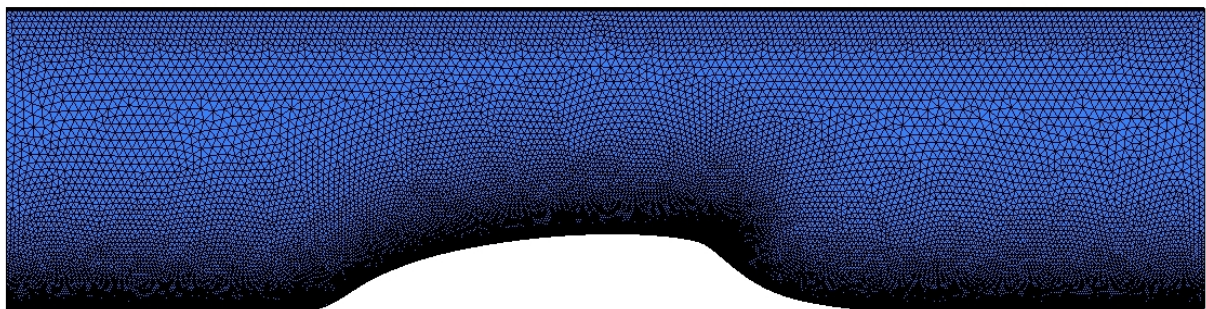


*Fig. 1: Mesh of calculated area.*

---

<sup>\*</sup> Ing. Milan Matějka, PhD., Ing. Tomáš Hyhlík, PhD. and Ing. Petr Pick: Institute of Fluid Mechanics and Power Engineering, Faculty of Mechanical Engineering, Czech Technical University in Prague, Technická 4; 16607, Prague; CZ, e-mails: milan.matejka@fs.cvut.cz, tomas.hyhlik@fs.cvut.cz, petr.pick@fs.cvut.cz



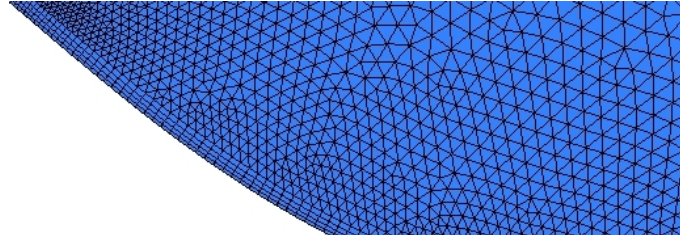


Fig. 2: Mesh of calculated area – detail.

Tab. 1: Basic mesh characteristic.

cells	number		
Prismatic	5 702 214	Skewness	0.414
Hexa	580 880	Size Change max.	3.77
Total	6 283 094	Aspect Ratio max.	32

Tab. 2: Values of dimensionless distance of center of the first cell from wall  $y^+$

velocity	average	max
$2.5 \text{ m.s}^{-1}$	1.46	5.47
$8 \text{ m.s}^{-1}$	4.47	10.5
$16 \text{ m.s}^{-1}$	8.25	16.04

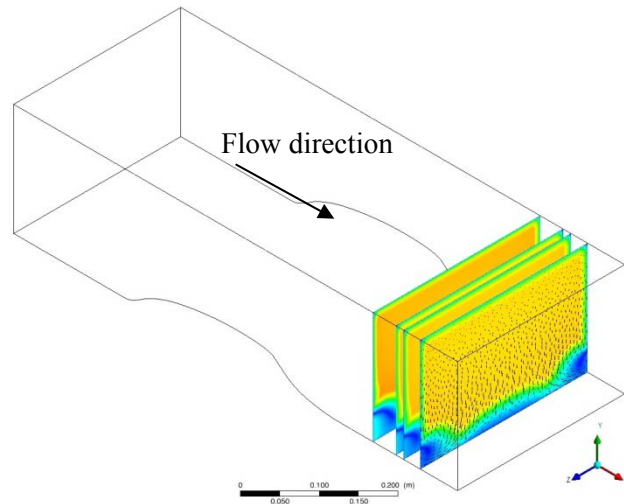


Fig. 3: Main parallel plains for comparison of numerical solution and experimental data. Distance of plains is 445, 486, 500 and 530 mm from starting point of hump. Dimension of plain  $200 \times 300 \text{ mm}$ .

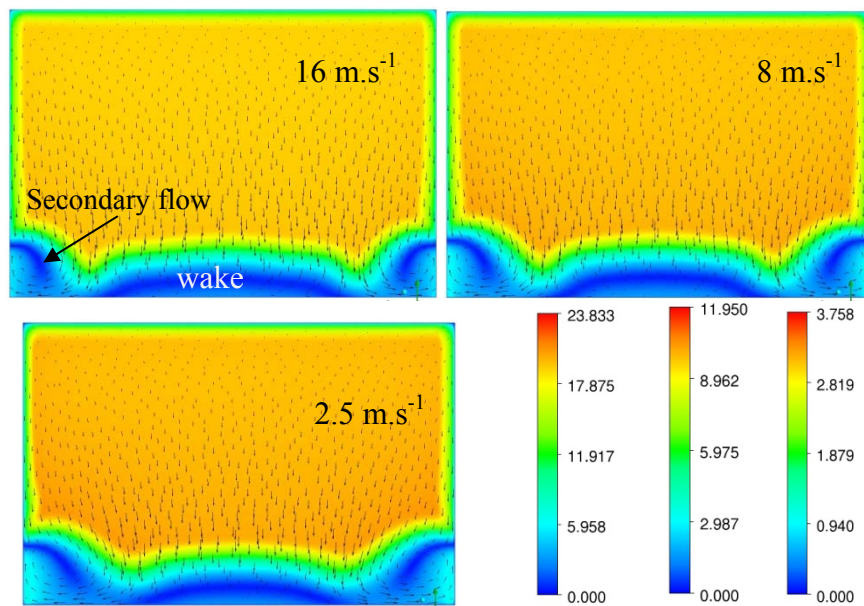


Fig. 4: Velocity distribution - parallel plains in position 445 mm for input velocity  $16, 8$  and  $2.5 \text{ m.s}^{-1}$ . Main flow direction is towards to the reader. On the figure are shown projection of velocity vectors.

In Fig. 3 the position of parallel plain with respect to hump location is marked. Velocity distribution of parallel plain in position 445 mm for different input velocity 2.5, 8 and 16 m.s<sup>-1</sup> is shown in Fig. 4. Changing size of wake is obvious. On next two figures the change of vortex structures with respect to input velocity is evident, see Figures 5 and 6. For lower velocity the vortex structures reach more closely to the centre of the domain, where in that case interact strongly with separation zone. In the case of higher velocity the vortex structures are closer to the side walls. Colors in Figs. 5 and 6 represent values of swirling x-velocity. Blue one corresponds to a clockwise direction and red one to the counter clockwise.

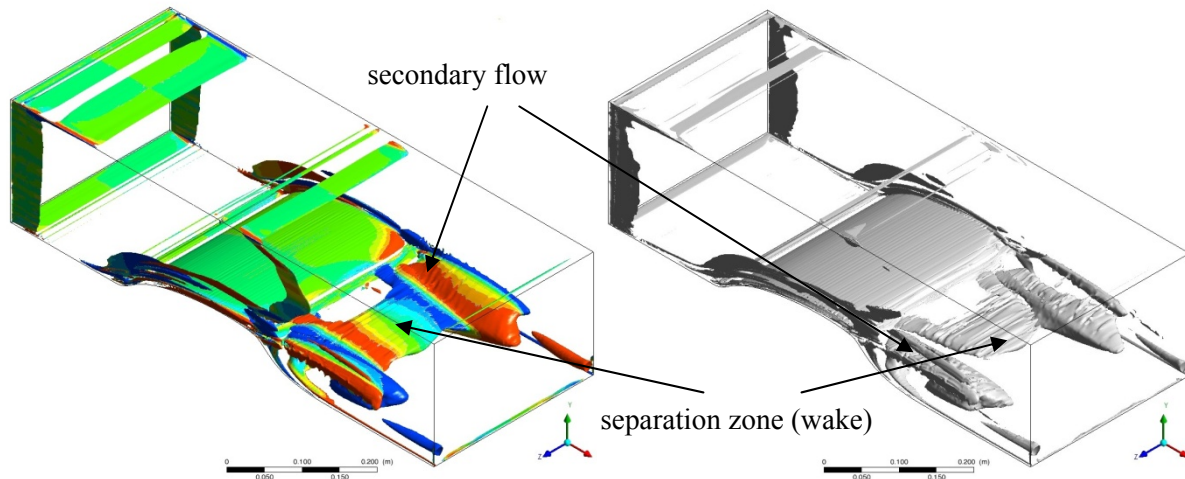


Fig. 5: Swirling strength and  $\lambda_2$  criterion (Kolar, 2007) for velocity 2.5 m.s<sup>-1</sup>.

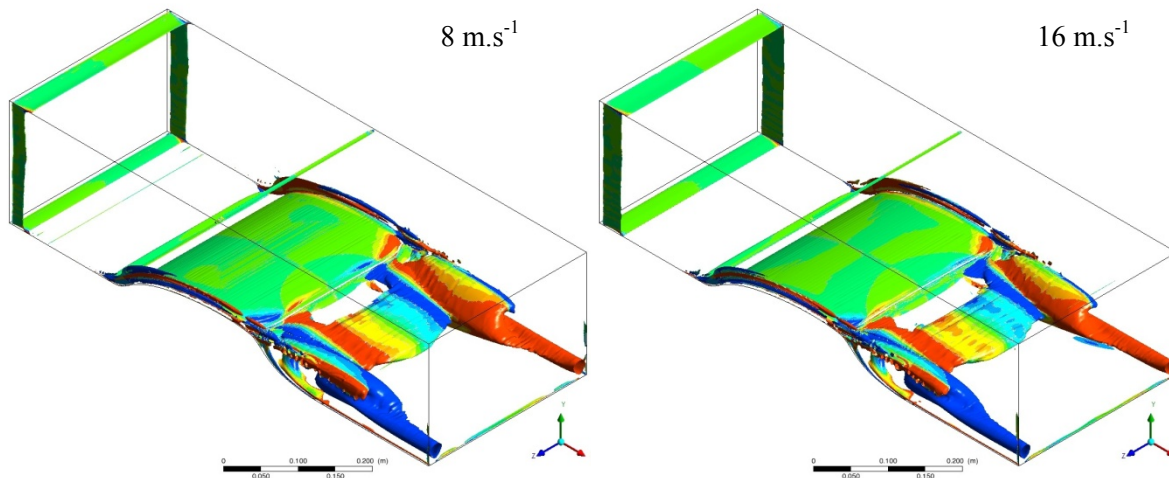


Fig. 6: Swirling strength (Kolar, 2007) for velocity 8 and 16 m.s<sup>-1</sup>.

### 3. Experimental data

Experimental data (see Fig. 7) were obtained by using traversing hot wire probe in position 445 mm from starting point of hump. Input velocity was set up to the value 2.6, 8 and 15 m.s<sup>-1</sup>. Intensity of turbulence in the input part of measurement area was from 0.4 to 0.8 with respect to the velocity. Sizes of measured areas are smaller due to limits of measuring techniques – about 240 x 182 mm. From comparison of measured and simulated velocity of the flow field the appreciable difference for lowest velocity 2.5 m.s<sup>-1</sup> is clearly visible, see Fig. 4 and 7. Other two alternatives of the characters of the flow field for 8 and 16 m.s<sup>-1</sup> obtained from experimental measurements are close to numerical solution; see bottom part of Figs. 4 and 7.

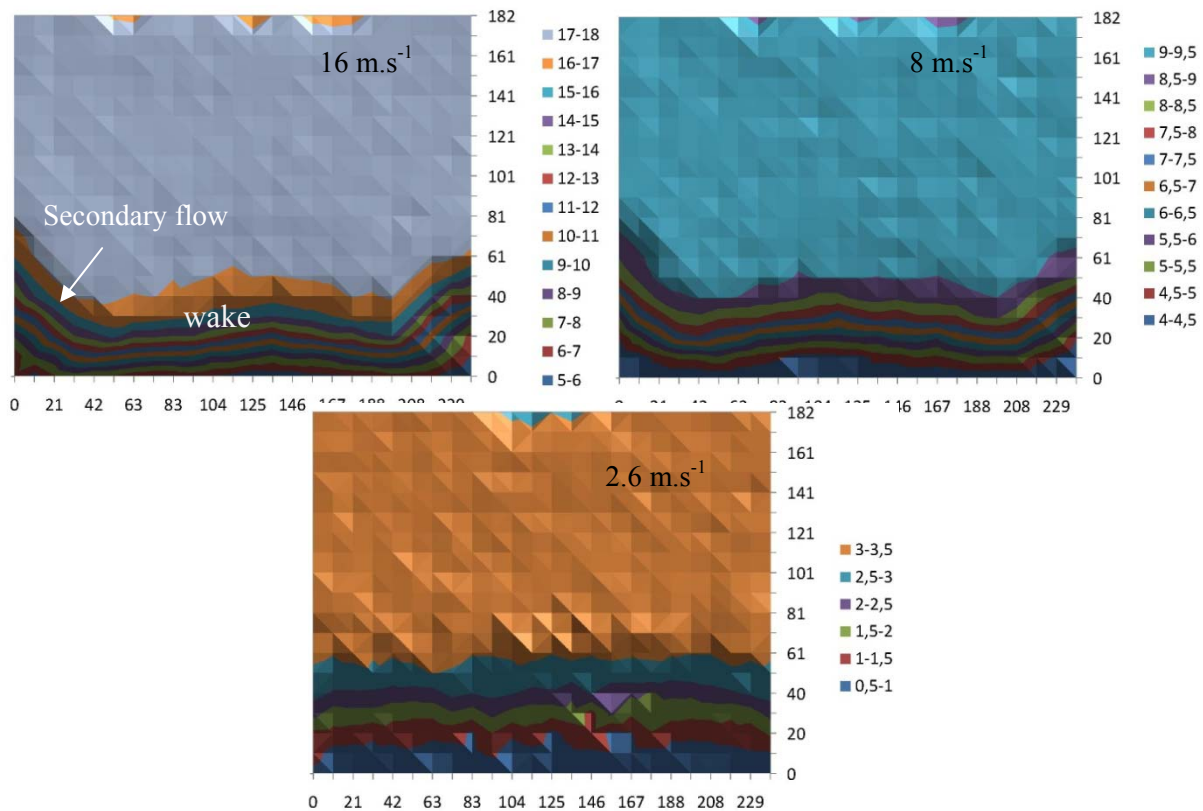


Fig. 7: Velocity flow field in parallel plain in position 445 mm for input velocity 16, 8 and 2.5  $\text{m.s}^{-1}$ , experimental data. Dimension of measured plane 182 x 240 mm.

#### 4. Conclusions

Data from numerical solution (Figs. 4, 5 and 6) and experiment (Fig. 7) were obtained. From comparison of numerical solution and experimental data is obvious difference for lowest velocity  $2.6 \text{ m.s}^{-1}$ . There are probably two reasons. First is that in the case of experimental model, there are small differences in the design of measurement area, like attachment of the model and some other details, comparing to numerical model. And second reason is caused by setting inaccurate boundary conditions for velocity inlet. Namely the thickness of the boundary layer must be measured precisely.

#### Acknowledgement

The work has been supported by Ministry of Education, Youth and Sports of the Czech Republic within project No. 1M06059. Support by the Czech Science Foundation under grants No. GA 101/08/1112.

#### References

- Kolar, V. (2007) Vortex identification: New requirements and limitations, in: International Journal Heat and Fluid Flow 28, pp.638-652.
- C. H. Berdahl and D. S. Thompson (1989) Eduction of Swirling Structure Using the Velocity Gradient Tensor, in: AIAA JOURNAL, Vol. 31, No. 1, January 1993, pp. 97-105.
- Zhou, J., Adrian, R.J., Balachandar, S., Kendall, T.M., (1999) Mechanisms for generating coherent packets of hairpin vortices in channel flow. J. Fluid Mech. 387, 353-396.



## **ANALYSIS OF INFLUENCE OF VOCAL FOLD –VOCAL TRACT MODELS CONNECTION BY USING FEM**

**M. Matug<sup>\*</sup>, M. Vašek<sup>\*</sup>, V. Mišun<sup>\*</sup>, P. Navrátil<sup>\*</sup>, A. Cívín<sup>\*</sup>, K. Řehák<sup>\*</sup>**

**Abstract:** *The Source-filter theory does not take into account many important circumstances for generating of vowels, e.g. the effects of source on filter. One of these effects is investigated in this paper, specifically changing of the glottal gap. Modal analyses were performed using 2-D models comprising a part of trachea, the glottal gap and straightened simplified vocal tracts for various vowels. Based on the modal analyses, classification of each cavity mode (vocal tract/trachea modes) for various glottal gaps was recognized. The glottal gap size ranged between 0 to 10 mm. The results show that some of the first ten natural frequencies of the model are significantly dependent on the glottal gap and the other natural frequencies are almost independent. From the glottal gap size of 5 mm towards lower values, an abrupt change in acoustic pressure occurs in the glottal gap zone. At higher pressure this change is not apparent at all.*

**Keywords:** *Artificial vocal chords, vocal tract, trachea, modal analysis, vowel production.*

### **1. Introduction**

The paper deals with an investigation of the glottal gap effect on modal characteristics of respiratory and vocal tracts air cavities. The respiratory tract is represented by a 2-D model of the trachea. The vocal tract is represented by a 2-D model based on simplified models of vocal tracts for each vowel (Arai et al., 2009).

Universally accepted and respected Source-Filter theory (Fant, 1970; Mišun, 2010) in its simple form, i.e. linearity and independence of the sources on the filter and vice versa, does not take into account many important circumstances which occur during generation of vowels (Rothenberg 1980). Besides the other omitted circumstances, it is also the effect of the source on the filter when glottal gap changes (g). This effect is investigated in this paper. Characteristics of artificial source-voices are investigated in (Mišun et al., 2010). First ten natural frequencies of models with various glottal gap settings are evaluated. Vocal tract and trachea are divided by the laryngeal part represented in the model by a gap of a certain size. Extreme cases of this size can either divide the model into two separate cavities ( $g = 0$ ) or the models are linked together into single cavity without any obstruction ( $g = g_{\max}$ ).

### **2. Material and Methods**

For computational modeling, finite element method (FEM) – which is commonly used in similar biomechanical problems – was chosen. In our case, models linking together the vocal tract, vocal cords and trachea were modeled in 2-D by using ANSYS 12.0. The geometry was discretized using 2-D elements FLUID29 which allow modal analysis. As for material properties, typical characteristics of the air at temperature of 20 °C and at atmospheric pressure of 101.325 kPa were used; i.e. density =  $1.2041 \text{ kg} \cdot \text{m}^{-3}$ , sonic velocity =  $343 \text{ m} \cdot \text{s}^{-1}$ . UNSYM method was used for eigenvalue and eigenvector extraction. This method allows using unsymmetrical mass matrix as well as stiffness matrix.

For the following analyses, only inside space of the airways consisting of air without structural tissues was considered. In APDL programming language, parametric models representing the trachea,

---

<sup>\*</sup> Ing. Michal Matug, Ing. Martin Vašek, doc. Ing. Vojtěch Mišun, CSc., Ing. Petr Navrátil, Ing. Adam Cívín and Ing. Kamil Řehák: Faculty of Mechanical Engineering, Brno University of Technology, Technická 2896/2; 616 69, Brno; CZ, e-mails: ymatug01@stud.fme.vutbr.cz, yvasek00@stud.fme.vutbr.cz, misun@fme.vutbr.cz, ynavra26@stud.fme.vutbr.cz, ycivin01@stud.fme.vutbr.cz, yrehak04@stud.fme.vutbr.cz

artificial vocal cords and vocal tracts for each vowel were created. Trachea was of a constant size in all analyzed cases. Dimensions of straightened simplified vocal tract were taken from (Arai et al., 2009), dimensions and shape of the trachea were obtained from the respiratory tract anatomy literature. Distances between the vocal cords at their closest points in various cases ranged from 0 to 10 mm.

The significant boundary conditions in the investigated cases were impermeable wall around the flowing media (i.e. the condition of zero displacements) and also balancing of internal pressure with the outer one at the outflow of the vocal tract as well as at the trachea-lung junction (i.e. the condition of zero acoustic pressure).

The series of calculations for the investigated vowel follows. The glottal gap is changed gradually ( $g = [0 \ 0.25 \ 0.50 \ 0.75 \ 1.00 \ 1.25 \ 1.50 \ 1.75 \ 2.00 \ 2.25 \ 2.50 \ 2.75 \ 3.00 \ 5.00 \ 7.00 \ 10.00]$  mm). All models are analyzed and the first 10 natural frequencies  $F_1 - F_{10}$  of each model are stored.

### 3. Results

Results presented in this paper come from the model representing the Czech vowel A (i.e. [a:] according to International Phonetic Alphabet). The dependence of natural frequencies on the size of the glottal gap is shown in Fig. 1. It is evident that some natural frequencies are dependent significantly. On the other hand, the significance of other natural frequencies is barely noticeable. Specifically for the Czech vowel A, the second, the fourth and the eighth natural frequency is dependent very significantly. Frequency shift is the largest at the second natural frequency (336 Hz).

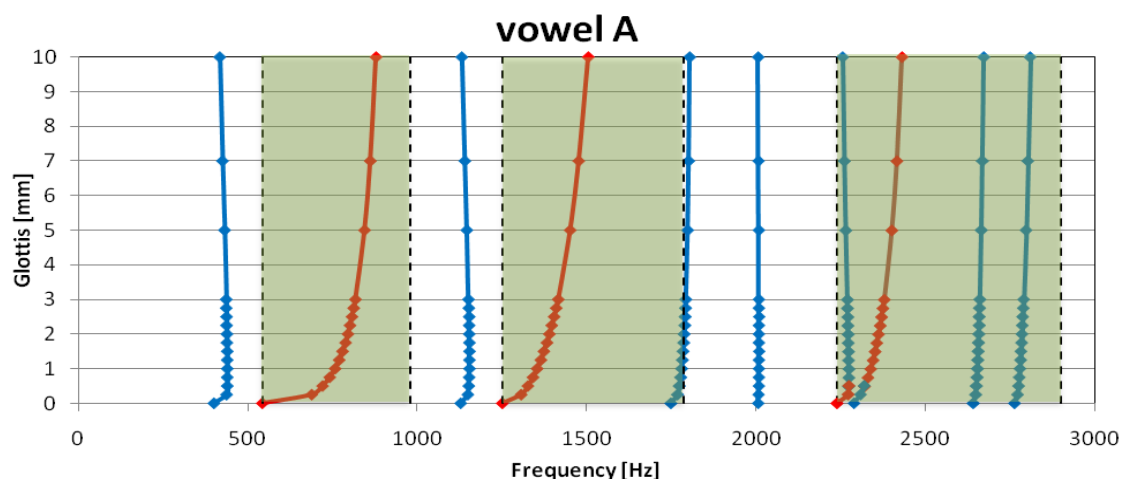


Fig. 1: The dependence of natural frequencies on the size of the glottal gap for Czech vowel A.

For the case the glottal gap is closed ( $g = 0$ ) the model is divided into two separate cavities. From the analysis, one can decide which of the evaluated natural frequencies belongs to vocal tracts and which one belongs to the trachea. This differentiation is graphically illustrated in Fig. 1. Natural frequencies  $F_2$ ,  $F_4$  and  $F_7$  (in some cases also  $F_8$ ) denoted in red belong to the vocal tract. The other frequencies denoted in blue belong to natural frequencies of trachea. The green zone in Fig. 1 represents boundary between the two cases:

1. only the vocal tract without the trachea is analyzed;
2. the vocal tract is linked together with the trachea without any obstruction for the first three natural frequencies of the vocal tract.

The Fig. 1 also shows that some frequency values are independent of their size of the gap (almost vertical lines) and that some frequencies significantly decrease with closing the glottal gap. Uncertainty in the classification of frequencies  $F_7$  and  $F_8$  is because for the small gap these two frequencies approach each other to the minimum (approx. 30 Hz).

Fig. 2 shows the first 7 modal shapes of the model representing modes of the vocal tract and the trachea (for  $g = 0.25$  mm). For this size of glottal gap, frequencies  $F_2$ ,  $F_4$  and  $F_7$  belong to the vocal tract modes. The other frequencies belong to the trachea.

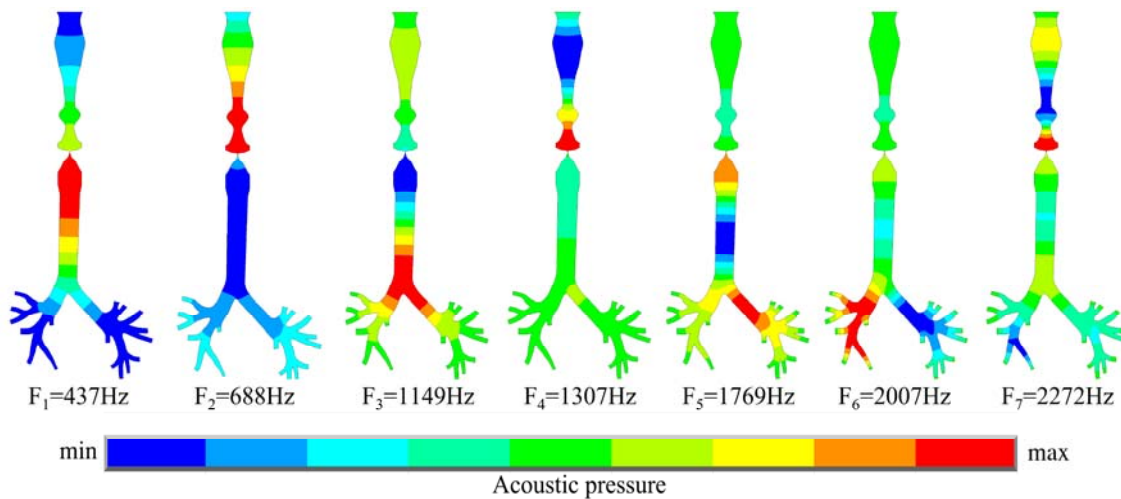


Fig. 2: Modal shapes of the first seven modes of model for Czech vowel A.

The lowest values of natural frequencies occur in the model which is divided by the vocal cord ( $g = 0$ ) into two separate cavities. On the contrary, the highest values of natural frequencies occur in the model with the largest glottal gap ( $g = 10$  mm). One can expect that even higher value of the natural frequency of the vocal tract can be obtained when the vocal tract is opened at both ends (the boundary condition  $p = 0$ ). This case is plotted in Fig. 1 as the upper border in the colored zones.

Fig. 3a shows the abrupt change in acoustic pressure for the Czech vowel A ( $g = 0.25$ ). This change occurs in the narrowest point of the model (glottal gap) – see yellow zone. The red zone corresponds to the vocal tract from the outflow of the vocal tract towards the vocal cords. The blue zone corresponds to the trachea from the vocal cords to its bifurcation. Fig. 3b shows the same situation for the 10 mm gap. It is seen that the whole system behaves as one continuous unit and that the change in acoustic pressure is not even noticeable. This pressure change starts from the glottal gap size of 5 mm towards lower values.

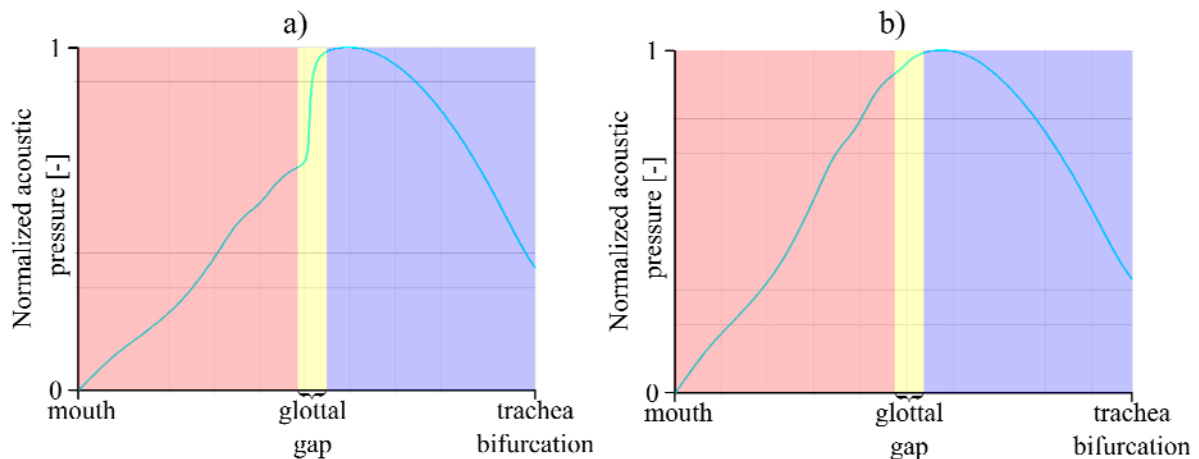


Fig. 3: The acoustic pressure distribution along the path (from mouth to trachea bifurcation) for Czech vowel A: a) glottal gap 0.25 mm b) glottal gap 10 mm.

The calculated values of the first three natural frequencies of the vocal tract (formants) for each vowel are compared in Tab. 1. The distribution of the formants associated with the ability to distinguish between various vowels from the calculated values corresponds with the values presented in (Mišun et al., 2010).

*Tab. 1: The comparison of the first 3 natural frequencies, computed for glottal gap 0.25 mm.*

<i>Czech vowel</i>	<i>F1</i>	<i>F2</i>	<i>F3</i>
<i>A [a:]</i>	688	1307	2272
<i>E [ɛ:]</i>	582	1536	2245
<i>I [i:]</i>	378	1518	2385
<i>O [o:]</i>	652	1275	2221

#### 4. Conclusions

Similarly to removing the tonsils (Laukkanen et al., 2007), the size of the glottal gap has a significant effect on some natural frequencies of the vocal tract / trachea connection, especially on the natural frequencies of the vocal tract. Mainly these frequencies (formants), especially the first three of them, affect the quality and clarity of voiced vowels. It is quite difficult to determine exactly what boundary conditions must be prescribed for the correct modeling of whisper.

The changing glottal gap  $g$  has a significant effect on the modal properties of the vocal tract. The simplest approach of the generally accepted theory of generation of vowels, the Source-filter theory, does not take this into account. Although only the modal analysis of the interconnected models of the vocal tract and the trachea was performed in this paper, one can expect that this effect will be also taken into account when similar models are investigated in the time domain.

Further investigation should follow and the question why the natural frequencies are differently sensitive to the change of the glottal gap  $g$  should be answered.

#### Acknowledgement

This work was supported by grant project FRVS No. 2829/2011 and specific research FSI-J-11-3 and FSI-S-11-12.

#### References

- Arai, T. (2009) Simple Physical Models of the Vocal Tract for Education in Speech Science. Interspeech 2009, Brighton, pp. 780-783, ISBN 978-1-61567-692-7.
- Fant, G., (1970) Acoustic Theory of Speech Production. 2nd ed. The Hague, Netherlands: Mouton.
- Laukkanen, A.M., Horáček, J., Švancara, P., Lehtinen, E. (2007) Effects of FE Modelled Consequences of Tonsillectomy on Perceptual Evaluation of Voice. Interspeech 2007, Antwerp, pp. 1489-1492, ISBN 978-1-60560-316-2.
- Mišun, V. (2010) Tajemství lidského hlasu, VUTIUM, ISBN 978-80-214-3499-8.
- Mišun, V., Švancara, P., Vašek, M. (2010) Experimental Analysis of the Characteristics of Artificial Vocal Folds, Journal of Voice, doi:10.1016/j.jvoice.2009.12.002.
- Rothenberg, M. (1980) Acoustic interaction between the glottal source and the vocal tract. Vocal fold physiology, U. of Tokyo, pp. 305-328.

## OPTIMIZATION OF THE PRESS FRAME LKDS 800

J. Mrkos<sup>\*</sup>, J. Omes<sup>\*</sup>

**Abstract:** *This paper deals with the elasticity analysis of the design of the frame of the LKDS 800 blanking crank press. Mentioned thereafter is a description of the optimization procedure executed by the Technical Calculation Department in cooperation with the Designing department. The aim of designing of the press frame (and also of the whole press) is the most effective design of the structure.*

**Keywords:** *Elasticity analysis, blank crank press.*

### 1. Introduction

The paper includes the description of the optimization procedure of the frame of the LKDS 800 blanking crank press based on the elasticity and strength analysis (this analysis is performed at Žďas for all designs of new structures and equipment in cooperation between the Technical Calculation Department and Forming Machines Designing Department).

The model of the press is created by the Designing Department using software Unigraphics NX3, then exported to the computing software MSC-Mentat, where the model will be created for the computing system or the solver Marc. From the results we obtain the deformation and stress state of the given frame of the press; these values are used for elasticity and strength evaluation. In case of elasticity evaluation, the design is being changed until the calculated deformations conform to those required.

If the elasticity analysis is finished, then the execution of the strength analysis (it is not presented herein) can be started using software SKALA. The design is changed again to conform to the limit states of sudden fracture, ductile fracture and fatigue fracture and crack propagation.

### 2. Model description

The LKDS 800 blanking double point crank press (see Fig. 1) is intended for production of blanks for the transfer press, version 4000.

As this is an extensive task for which there is no place in this paper, so only one component of the press structure has been chosen for analysis. In this paper, the frame is the subject to be analyzed. The aim is to make the most effective design of the press frame (even the whole press) to meet the required values of side and longitudinal rigidity and also strength.

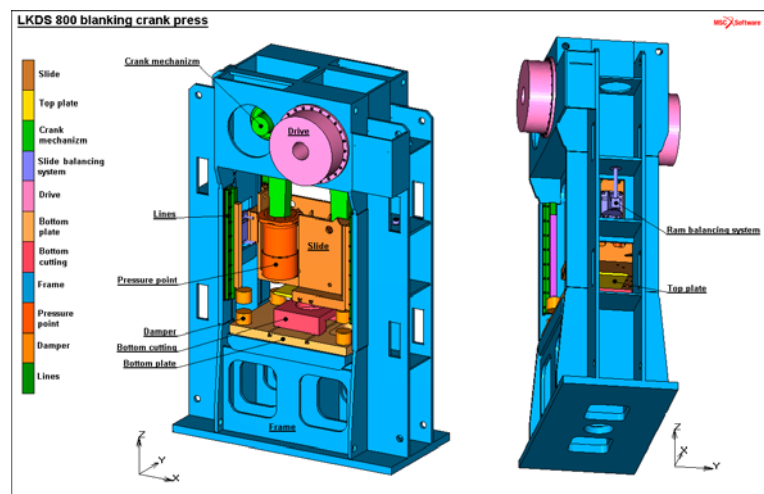


Fig. 1: LKDS 800.

For correct determination of the frame rigidity and strength, the design model of the press must consist of the following: frame, slide, slide balancing system, crank mechanism, pressure point, holder (holder

<sup>\*</sup> Ing. Josef Mrkos and Ing. Jiří Omes, Ph.D.: ŽĎAS, a.s., Strojírenská 6, 591 71 Žďár nad Sázavou; CZ, e-mails: josef.mrkos@zdas.cz, jiri.omes@zdas.cz

load), blanking stroke dampers and drive. The correct arrangement of these components will have an influence on the flow of forces in the whole equipment. The components have an essential effect on the press and frame rigidity.

### 3. Elasticity calculation

The computing system MSC.Marc 2008 – elastic field has been applied with the utilization of spatial elements. The optimization is performed using direct method (calculation repetition).

The whole press assembly is solved taking into account a contact between the individual parts of the welded structure, which are in interaction – Z1 load. Design model, load and boundary conditions are illustrated in Fig. 2.

The operating load spectrum is not specified by the structure, so the above mentioned stationary load (Fig. 2) is only taken into account. The press performs cutting with a frequency of 28 cuts/min. It is, therefore, necessary to consider the permanent life of all critical parts.

To get satisfactory results from the task, the following preconditions for the design have to be met: The load is considered to be static. It is a linear calculation (permanent force of Hooke's law). Geometrical non-linearities have been applied (contact task). The dead weight of equipment is taken into account in the calculation.

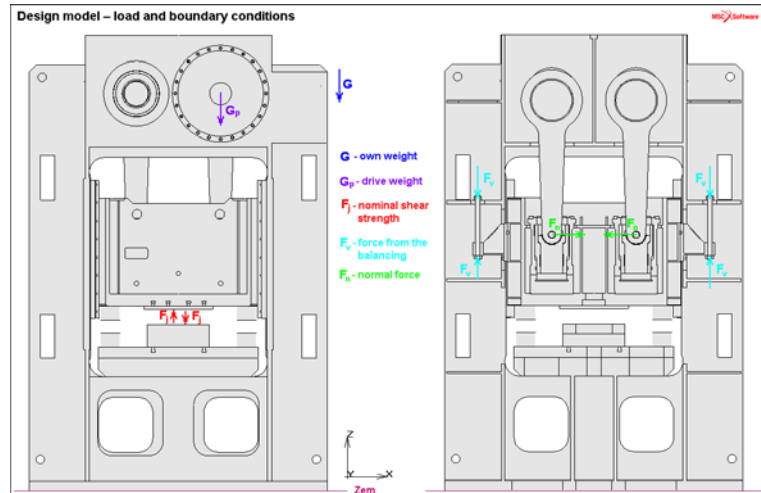


Fig. 2: Design model – load and boundary conditions.

### 4. Elasticity calculation results

The frame is checked that the deformations in the direction of the global Z-axis of the bearing hub and frame plate do not exceed the limit values of deformation. The bearing hub was designed in three versions – see Figs. 3 - 5. After the calculations are finished, the calculation considered to be the best variant has been chosen by comparison of deformations and production labour consumption.

The frame plate was designed so that it conforms immediately to the required deformation value (higher deformation would be undesirable), see Fig. 6.

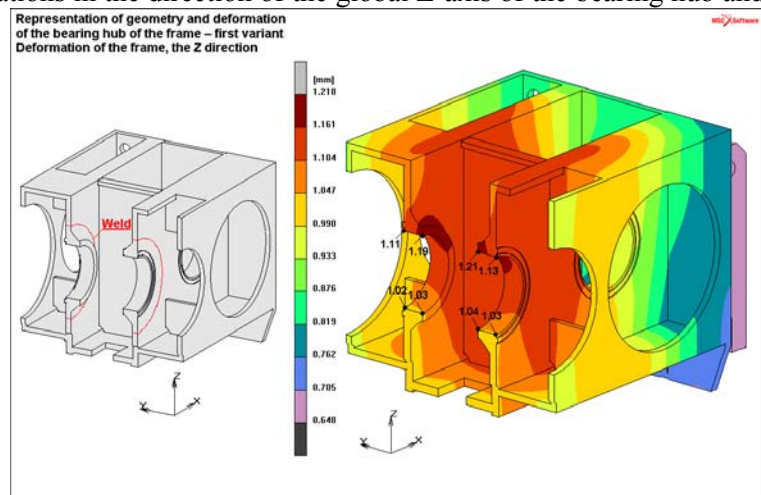


Fig. 3: Geometry and deformation of the first variant.

The stress is checked in the whole structure of the frame and subsequently the critical points are chosen for strength evaluation, Fig. 7.

Graphic outputs of individual variants of the bearing hub and bolster plate (deformation in the direction of the global Z-axis, main stress  $\sigma_1$ , design (reduced) stress  $\sigma_{HMH}$  (acc. to HMH) - all values in mm, MPa]), see Figs. 3 - 7.



The first variant (Fig. 3) is most intricate as regards the shape of the bearing hub design. This hub is inserted in the wall panel and then through-welded using the weld K.

The second variant (Fig. 4) is not intricate in light of manufacture. The rim hub is placed on the panel of the wall and welded all round from the inside and outside using the weld 1/2 V; for this design variant, the weld is not through-welded.

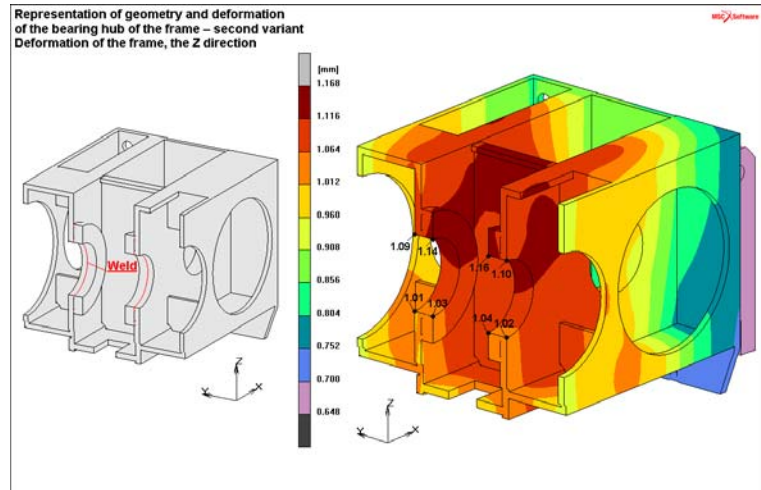


Fig. 4: Geometry and deformation of the second variant.

The third variant (Fig. 5) is not also intricate as regards the production. The tubular hub is inserted into the plate and then through-welded using K-weld.

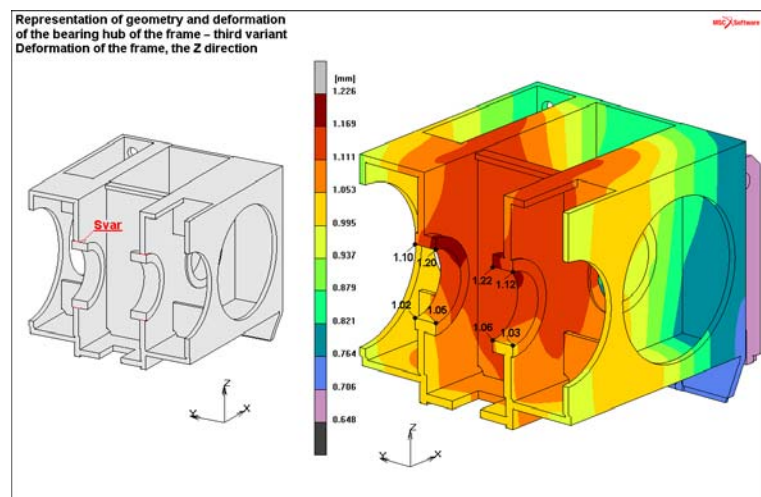


Fig. 5: Geometry and deformation of the third variant.

The design of the frame plate can be seen in Fig. 6. Frame plate rigidity is influenced by holes for removal of blanks and waste.

By the difference in deformations of the bearing hub at the front and rear parts we will get a review of possible displacement of the crank mechanism (Tab. 1). From the designers' experience, the difference should not reach the value 0.1 mm, so it results in the avoidance of edge contact between the slide bearing and the eccentric shaft. If the difference reaches the above value, it is necessary to optimize the design.

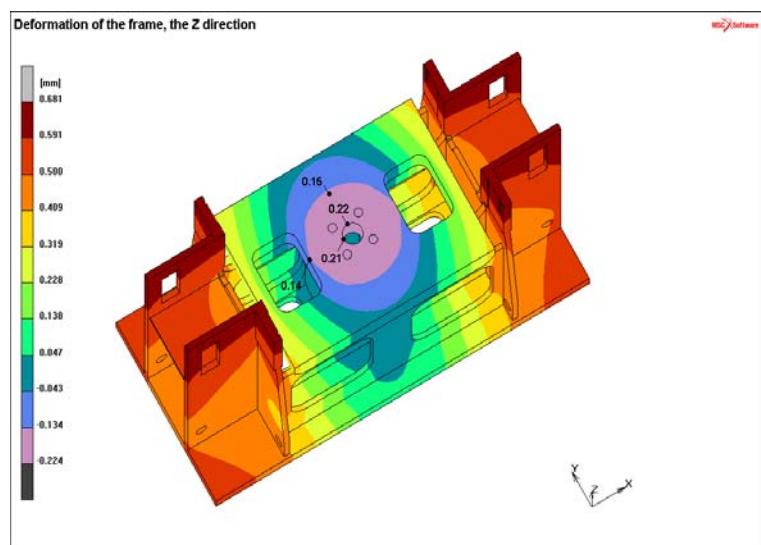


Fig. 6: Frame plate deformation.

Tab. 1: Bearing hub deformation.

Bearing hub	part 1 [mm]		Deformation difference	part 2 [mm]		Deformation difference
	front	rear		front	rear	
First var.	1.11	1.19	0.08	1.21	1.13	0.08
Second v.	1.09	1.14	0.05	1.16	1.10	0.06
Third var.	1.10	1.20	0.10	1.22	1.12	0.10
The limit value is 0.10 mm						

Tab. 1 shows that the third variant is not satisfactory. So we can choose only the first variant or the second variant. The designers have chosen the first one.

By the difference in deformation of the frame plate on the inside and outside we will obtain the plate deflection value that cannot exceed 0.1 mm (derived again based on the experience. Then it is also necessary to optimize the frame.

Tab. 2: Frame plate deformation.

Table plate	part 1 [mm]		Deformation difference	part 2 [mm]		Deformation difference
	inside	outside		inside	outside	
First var.	-0.21	-0.14	0.07	-0.22	-0.15	0.07
The limit value is 0.10 mm						

For this node of the frame, we succeeded in achieving satisfactory results just after performing the first calculation. It was not, therefore, necessary to make further design changes and calculations accordingly.

The above Fig. 7 - principal and reduced stress - shows that in the structure there is no local increase of tension values (this has been tested by the subsequent strength evaluation which is not, however, presented herein in view of the extensive task).

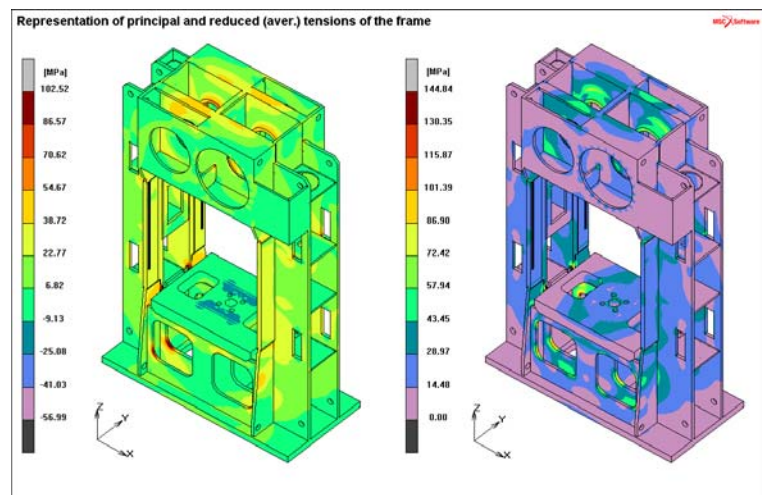


Fig. 7: Principal and reduced tensions of the frame.

## 5. Conclusion

This paper includes the description of the optimization procedure carried out in designing of new structures at ŽDAS, a.s. The model has been created using the computing system MSC. Mentat and it serves for sequential designing of equipment and its nodes. This procedure enables the designer to check the elasticity and strength possibilities of the structure. Based on the results he decides how to modify the structure next. At present (when this paper is being drawn up) the whole structure is still in the phase of development, but there will not be made any changes in the shape of the chosen bearing and table parts.

## References

- C. Kratochvíl, J. Slavík (1997), Solid mechanics, Brno (in Czech).  
 MSC.Marc Version 2008 (2008), U.S.A., www.mssoftware.com.

## COMPARISON OF SPACE-FILLING DESIGN STRATEGIES

E. Myšáková\*, M. Lepš\*

**Abstract:** *Space-Filling Design Strategies create an essential part of a surrogate modeling. Two main objectives are usually placed on the resulting designs - orthogonality and space-filling properties. The last decade has witnessed the development of several methods for the latter objective. These methods are based on very different ideas and are characterized by distant complexities. Since the computing time can be the limiting constraint, we inspect the computing demands against the space-filling performances. In detail, our contribution presents and compares several different techniques of quazi-random numbers generators utilizing Latine Hypercube Sampling (LHS) methods as well as Delaunay triangulations.*

**Keywords:** *Design of experiments, space-filling, Latin Hypercube Sampling, Delaunay triangulation, maximin.*

### 1. Introduction

The design of experiments (DoE) is an essential part of the development of any meta-model (surrogate) (Simpson et al., 2001, Jin, 2005). The aim is to gain maximum knowledge from a given system with a minimum number of designs. Since we assume that the final meta-model is a priori unknown, the design should be spread over the domain as uniformly as possible. The effectiveness of such DoE can be measured by several metrics aiming mainly at orthogonality or space-filling properties. See references (Cioppa and Lucas, 2007, Hofwing and Sternberg, 2010) for orthogonal and sources (Toropov et al., 2007, Crombecq et al., 2009) for space-filling metrics, respectively. We have selected the *maximin* metric (Mm) for its simplicity and easiness in visualization. The Mm is the minimal distance out of all distances between any two design points and is to be maximized. Using this metric, we would like to compare several methods that have been proposed in recent years to create good DoEs.

### 2. Space-Filling Methods

#### 2.1. Latin Hypercube Sampling (L)

The LHS is one of the most popular space-filling algorithms, although its resulting space-filling properties can be very low. In the LHS, each variable is divided into  $n$  levels. Each level is selected randomly once, independently for each variable. This leads to a regular DoE, see Fig. 1. Note that the design can be placed in the middle of the level as well as everywhere (randomly) within the level.

The worst case LHS design is such that all points lie on a diagonal. To solve this deficiency, the simplest solution is to create a brand new LHS design, i.e. this is actually an application of a brute force method. Such an approach is used for example in MATLAB environment within the `lhs_design` routine. Hereafter, we denote this method as regular.

#### 2.2. Optimized Latin Hypercube Sampling by Random Moves (HC)

A bad LHS design can be also improved by changing the positions of individual levels, see e.g. references (Novák and Lehký, 2006, Kučerová, 2007) for more details. At each iteration, in comparison to the above mentioned references where the Simulated Annealing algorithm is used, we accept only an improvement step here, and, therefore, this method is denoted as the random Hill Climbing algorithm.

---

\* Eva Myšáková, Ing. Matěj Lepš, Ph.D., Faculty of Civil Engineering, Czech Technical University in Prague, Thákurova 7, 166 29 Prague 6, CZ, e-mail: leps@cml.fsv.cvut.cz

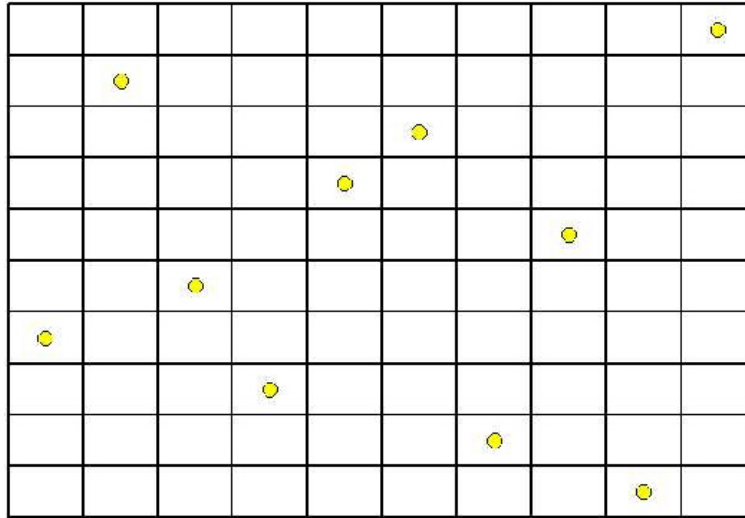


Fig. 1: Example of LHS design for two variables and ten levels with points selected in middle of levels.

### 2.3. Optimized Latin Hypercube Sampling by Heuristic Moves (H)

Since we know, which pair of points creates the worst value within the Mm metric, we have applied heuristic procedure, where we try to change only the position of levels of those two bad designs. The algorithm is changing the inappropriate level position with one randomly chosen position until an improvement occurs (and then follows with the next bad position).

### 2.4. Removing Points from LHS Design (R)

The last method, based again on the LHS design, is utilizing the speed of the LHS design. The creation of the LHS design with more points does not waste too much time. Therefore, we construct a design with more points than needed, and then, we are repeatedly removing the point that creates the worst Mm distance until the original number of points is attained.

### 2.5. Delaunay Triangulation Based methods (DC, DT)

The last sort of methods is based on the triangulation of an admissible domain by simplexes (Crombecq et al., 2009). Because it is relatively simple to compute a volume of a simplex, we have a rough estimation, where is the biggest unsampled region. We are starting from a basic LHS design with a few points. Then, our procedure iteratively adds a centroid of the biggest simplex into the designs. There are two variants that differ in whether (after each step) a whole triangulation is repeated or not. The first possibility computes better estimates of an unsampled space, but is more time consuming; the second possibility is unprecise but faster.

## 3. Results and Conclusions

It is evident from Fig. 2 that the regular LHS and the LHS with random moves cannot compete with others. It is also clear that Delaunay-based methods cannot compete with the heuristic method. Moreover, with the growing number of dimensions Delaunay-based methods are more time consuming than LHS-based methods. Our experience shows that at four dimensions the heuristic method attains, at the same time, four times bigger maximin values.

Finally, our contribution has shown results for rectangular domains. Our next research will inspect the abilities of presented methods for designs within irregular domains. From the first view, the LHS-based methods seem unsuitable in comparison to those based on Delaunay triangulation. One can describe almost any shape by a triangulation, and therefore, the application of triangulation-based methods seems reasonable.



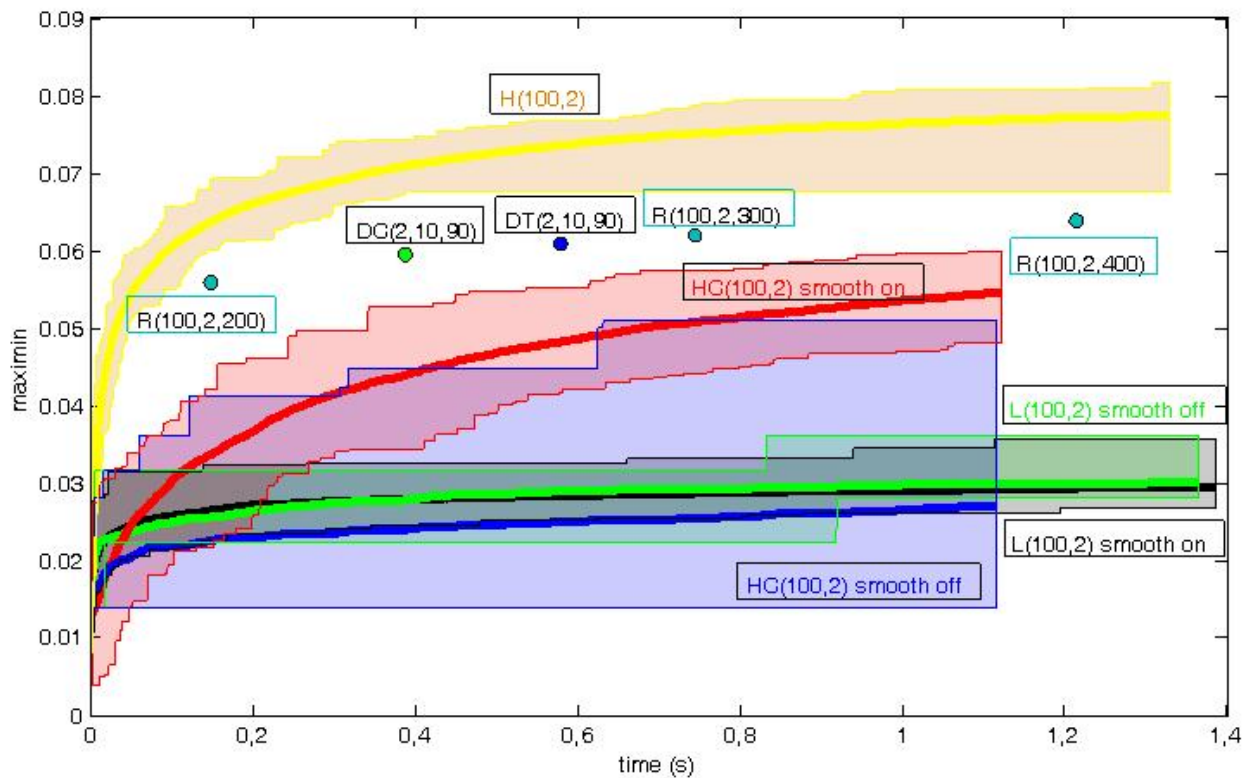


Fig. 2: Comparison of speed (time) vs. quality (maximin - higher is better) of spacefilling algorithms. Key: Yellow lines/H = Heuristic method, Cyan dots/R = Removing points, Green dot/DC = Delaunay triangulation without re-meshing, Blue dot/DT = Multiple Delaunay triangulations, Red and Blue lines/HC = random Hill Climbing algorithm, Green and Black lines/L = repeatedly created regular LHS design; smooth on generates random points within LHS level, smooth off in the middle; -(100, 2) stems for 100 points in two dimensions, (2,10, 90) means 2 dimensions, 10 random starting points and 90 points added by triangulation and (100, 2, x) equals to 100 points in two dimensions remaining from x original points; color boundary lines stem for obtained maximum and minimum values, bold line is for averages.

## Acknowledgement

The authors gratefully acknowledge the financial support from the Ministry of Education, Youth and Sports MSM 6840770003 (Algorithms for computer simulation and application in engineering).

## References

- Cioppa, T. M. & Lucas, T. (2007) Efficient nearly orthogonal and space-filling latin hypercubes. *Technometrics*, 49(1):45-55.
- Crombecq, K., Couckuyt, I., Gorissen, D., & Dhaene, T. (2009) Space-filling sequential design strategies for adaptive surrogate modelling. in: *Proceedings of the First International Conference on Soft Computing Technology in Civil, Structural and Environmental Engineering* (Topping, B. H. V. & Tsompanakis, Y., eds), Civil-Comp Press, Stirlingshire, UK.
- Hofwing, M. & Strmberg, N. (2010) D-optimality of non-regular design spaces by using a Bayesian modification and a hybrid method. *Structural and Multidisciplinary Optimization*, 42:73-88.
- Jin, Y. (2005) A comprehensive survey of fitness approximation in evolutionary computation. *Soft Computing*, 9:3-12.
- Kučerová, A. (2007) *Identification of nonlinear mechanical model parameters based on softcomputing methods*. PhD thesis, Ecole Normale Supérieure de Cachan, Laboratoire de Mécanique et Technologie.
- Novák, D. & Lehký, D. (2006) ANN inverse analysis based on stochastic small-sample training set simulation. *Engineering Applications of Artificial Intelligence*, 19(7):731-740.
- Simpson, T. W., Peplinski, J. D., Koch, P. N., & Allen, J. K. (2001) Metamodels for computer-based engineering design: Survey and recommendations. *Engineering with Computers*, 17:129-150.

Toropov, V. V., Bates, S. J., & Querin, O. M. (2007) Generation of extended uniform latin hypercube designs of experiments. In Topping, B. H. V., editor, Proceedings of the Ninth International Conference on the Application of Artificial Intelligence to Civil, Structural and Environmental Engineering. Civil-Comp Press, Stirlingshire, UK.



## **DYNAMICS OF A VIBRATION DAMPERWORKING ON A PRINCIPLE OF A HEAVY BALL ROLLING INSIDE A SPHERICAL DISH**

**J. Náprstek<sup>\*</sup>, C. Fischer<sup>\*</sup>, M. Pirner<sup>\*</sup>**

**Abstract:** *Wind excited vibrations of slender structures such as towers, masts or certain types of bridges can be reduced using passive or active vibration absorbers. If there is available only a limited vertical space to install such a device, a ball type of absorber can be recommended. In general, it is a semi-spherical horizontal dish in which a ball of a smaller diameter is rolling. Ratio of both diameters, mass of the rolling ball, quality of contact surfaces and other parameters should correspond with characteristics of the structure. The ball absorber is modeled as a holonomous system. Using Lagrange equations of the second type, governing non-linear differential system is carried out. The solution procedure combines analytical and numerical processes. As the main tool for dynamic stability investigation the 2nd Lyapunov method is used. The function and effectiveness of the absorber identical with those installed at the existing TV towers was examined in the laboratory. The response spectrum demonstrates a strongly non-linear character of the absorber.*

**Keywords:** *Vibration ball absorber, dynamic stability, non-linear vibration.*

### **1. Introduction**

Passive vibration absorbers of various types are very widely used in civil engineering, especially when wind induced vibration should be suppressed. TV towers, masts and other slender structures exposed to wind excitation are usually equipped by such devices. Conventional passive absorbers are of the pendulum type. Although they are very effective and reliable, they have several disadvantages limiting their application. First of all, they have certain requirements to space, particularly in a vertical direction. These requirements cannot be satisfied any time when an absorber should be installed as supplementary equipment. Also horizontal construction, like foot bridges, cannot accept any absorber of the pendulum type. Another disadvantage represents a need of a regular maintenance.

Both above shortcomings can be avoided using the absorber of ball type. The basic principle comes out of a rolling movement of a metallic ball of a radius  $r$  inside of a metallic rubber coated dish of a radius  $R > r$ . This system is closed in an airtight case. Such a device is practically maintenance free. Its vertical dimension is relatively very small and can be used also in such cases where a pendulum absorber is inapplicable due to lack of vertical space or difficult maintenance. First papers dealing with the theory and practical aspects of ball absorbers have been published during the last two decades, see Pirner (1994) and Pirner and Fischer (2000). The first paper dealing with the problem on the basis of the rational dynamics has been published some years ago, see Náprstek and Pirner (2002).

Dynamics of the ball absorber is more complicated in comparison with the pendulum one. Its movement can be hardly described in a linear state although for the first view its behavior is similar to the pendulum absorber type. A number of problems are still open being related with movement stability, bifurcations, auto-parametric resonances and at least but not last with the spherical dish and ball surface imperfections. This paper should be the first attempt to present basic mathematical model in 2D together with its numerical evaluation and practical application as far as to the state of the realization including some results of long-term measurements.

---

<sup>\*</sup> Ing. Jiří Náprstek, DrSc., RNDr. Cyril Fischer, PhD. and prof. Ing. Miroš, Pirner, DrSc. Institute of Theoretical and Applied Mechanics ASCR, v.v.i.; Prosecká 76, 190 00 Praha 9, CZ, e-mails: naprstek@itam.cas.cz, fischer@itam.cas.cz, pirner@itam.cas.cz

## 2. Mathematical model

The dish is fixed to a vibrating structure. Their dynamic character is represented by a linear SDOF system represented by a mass  $M$ . Inside of a dish an internal ball  $m$  in a vertical plane is moving, i.e. 2DOF system should be investigated, as it is outlined in the Fig. 1. It follows from geometric relations:

$$R \cdot \varphi = r(\psi + \varphi) \Rightarrow r\psi = \varphi r, \quad \text{where } \varphi = R - r \quad (1)$$

It holds for both components of a displacement and velocity of the internal sphere center:

$$\left. \begin{array}{l} \text{horizontal: } u + \varphi \cdot \sin \varphi \Rightarrow \dot{u} + \varphi \dot{\varphi} \cos \varphi \\ \text{vertical: } \quad \varphi \cdot \cos \varphi \Rightarrow -\varphi \dot{\varphi} \sin \varphi \end{array} \right\} \quad (2)$$

Kinetic energy of a moving system of dish and ball  $m, M$  can be written in a form:

$$T = \frac{1}{2} m [(\dot{u} + \varphi \dot{\varphi} \cos \varphi)^2 + \varphi^2 \dot{\varphi}^2 \sin^2 \varphi] + \frac{1}{2} J \dot{\psi}^2 + \frac{1}{2} M \dot{u}^2 = \frac{1}{2} (m + M) \dot{u}^2 + m \varphi \dot{u} \dot{\varphi} \cos \varphi + \frac{m}{2\kappa} \varphi^2 \dot{\varphi}^2 \quad (3)$$

$$\frac{m}{\kappa} = m + \frac{J}{r^2} \Rightarrow \kappa = \frac{5}{7}$$

while the potential energy is given by an expression:

$$V = mg\varphi(1 - \cos \varphi) + \frac{1}{2} Cu^2 \quad (4)$$

The damping should be introduced in a form of a simple Rayleigh function:

$$B = \frac{1}{2} (M \cdot b_u \dot{u}^2 + m \cdot b_\varphi \varphi^2 \dot{\varphi}^2) \quad (5)$$

$m$  – mass of the ball  $m$ ;

$J$  – inertia moment of the ball  $m$ ;

$b_u, b_\varphi$  – damping coefficients (logarithmic decrements);

Expressions (3), (4), (5) should be put into the Lagrange equations of the second type, see any of the basic monographs, e.g. Hamel (1978):

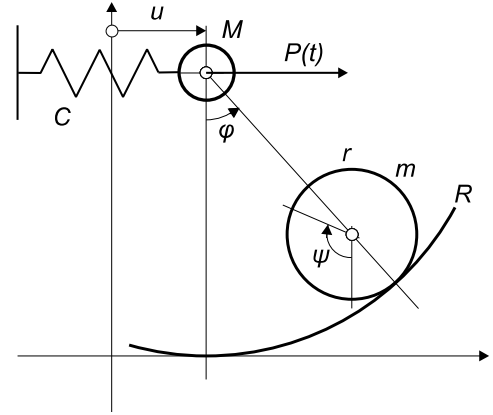


Fig. 1: Basic scheme of a system.

$$\sum_{r=1}^n \left\{ \frac{d}{dt} \left( \frac{\partial T}{\partial \dot{q}_r} \right) - \frac{\partial T}{\partial q_r} + \frac{\partial V}{\partial q_r} + \frac{\partial B}{\partial \dot{q}_r} \right\} \delta q_r = P_r(t) \quad (6)$$

$$q_1 = u = \zeta \cdot \varphi; \quad q_2 = \varphi; \quad P_u(t) = p(t) \cdot M\varphi; \quad P_\varphi(t) = 0$$

which give the governing equations of the system:

$$\left. \begin{array}{l} \ddot{\varphi} + \kappa b_\varphi \dot{\varphi} + \kappa \omega_m^2 \sin \varphi + \kappa \ddot{\zeta} \cos \varphi = 0 \quad (a) \\ \mu \ddot{\varphi} \cos \varphi - \mu \dot{\varphi}^2 \sin \varphi + (1 + \mu) \ddot{\zeta} + b_u \dot{\zeta} + \omega_M^2 \zeta = p(t) \quad (b) \\ \mu = \frac{m}{M}; \quad \omega_M^2 = \frac{C}{M}; \quad \omega_m^2 = \frac{g}{\varphi} \quad (c) \end{array} \right\} \quad (7)$$

Eq. (7) describes 2D movement of a ball absorber under excitation by the force  $P(t)$  at any arbitrary deviation amplitudes including incidental transition through a limit cycle towards an open regime.

## 3. Basic properties of the absorber

Theoretical efficiency of the absorber will be assessed using its frequency characteristics for excitation of the mass  $M$  by harmonic force  $P(t) = p_0 \sin \omega t$  simulating influence of external loading or kinematic excitation of the same mass  $M$ . In the later case the movement of the ball  $m$  rolling inside of the dish is fully described by Eq. (7a). Should we solve the deviation  $\varphi(t)$ , Eq. (7b) can serve us subsequently for an evaluation of the force  $P(t)$ , which is necessary when the deviation  $u(t) = \varphi \cdot \zeta(t)$  should be achieved.

To obtain frequency characteristics the harmonic excitation  $\zeta(t) = \zeta_0 \cos(\omega t)$  should be introduced into Eq. (7), which yields:

$$\left. \begin{array}{l} \ddot{\varphi} + \kappa b_\varphi \dot{\varphi} + \kappa \omega_m^2 \sin \varphi - \kappa \omega^2 \cos \varphi \cdot \zeta_0 \cos \omega t = 0 \quad (a) \\ \mu \ddot{\varphi} \cos \varphi - \mu \dot{\varphi}^2 \sin \varphi + (-(1 + \mu) \omega^2 + \omega_M^2) \zeta_0 \cos \omega t - b_u \omega \cdot \zeta_0 \sin \omega t = p(t) \quad (b) \end{array} \right\} \quad (8)$$

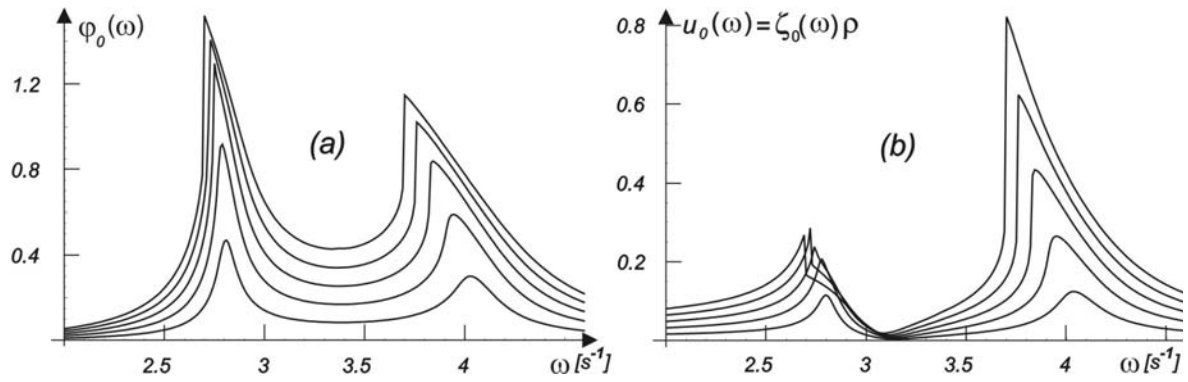


Fig. 2: Frequency characteristics of a ball absorber.

Eq. (8a) corresponds to the equation of a mathematical pendulum excited in a point of suspension. Its effective mass is increased due to a moment of inertia of the ball  $m$  by the factor  $1/\kappa = 7/5$ . Even in practice the movement amplitudes of this ball doesn't admit to linearize the Eq. (8a). At least a simple Duffing non-linear form should be retained:

$$\ddot{\varphi} + \kappa b_{\varphi} \dot{\varphi} + \kappa \omega_m^2 \left( \varphi - \frac{1}{6} \varphi^3 \right) - \kappa \omega^2 \left( 1 - \frac{1}{2} \varphi^2 \right) \cdot \zeta_0 \cos \omega t = 0 \quad (9)$$

Nevertheless the aim of this study is a basic engineering approach demonstrating the problem as a whole from the theoretical background until realization in practice. For this reason a strong analytical investigation working with the simplified Eq. (9) is postponed to a next paper which will be oriented predominantly to mathematical aspects of the problem. This time numerical analysis has been preferred as it leads the most quickly to a basic overview about dynamic properties of a ball absorber. For numerical analysis the original form of Eq. (8) is more suitable for further investigation. Indeed, it does not introduce any limitations of the response amplitudes without any complication in the analysis itself. Excitation by harmonic force  $P(t) = p_0 \sin \omega t$  has been applied and response in a form of  $u(t)$ ,  $\varphi(t)$  computed.

With respect to actual experiences, following reference input data have been introduced:

$$M = 10.0; m = 2.0; \Rightarrow \mu = 0.2 \quad \varrho = 0.71; b_{\varphi} = 0.1; b_u = 0.2; p_0 = 1 \div 5$$

A wide parametric analysis has been done. Sample results obtained have been summarized and plotted in Fig. 2. It is obvious for the first view the non-linear character manifesting oneself by a dependence of a position of extreme points on an amplitude of excitation force. This effect is visible predominantly in a neighborhood of a conventional "linear" natural frequency of the absorber although also the second natural frequency related with the original first natural frequency of the structure is affected. The resonance curves are typical for a system with "softening" non-linearities. It turns out that the non-linear element represented by a ball absorber can be more effective when broad band random response should be reduced. Even better results can be expected in case of non-stationary excitation when amplitude spectrum is significantly variable in time. In such a case no doubt non-linear absorber should be preferred, while the linear one works better in cases of strong narrow band excitation mostly of deterministic character.

The effective damping should not drop below a certain limit, as the stability loss of the ball movement inside the dish can occur. Then the damper can exhibit negative influence as long as the stable régime is regained. However, it is of interest to note that the increase of instable chaotic response domains under random excitation can act for the sake of the structure, as the effective response amplitudes are decreasing under these circumstances due to the rapid increase of the entropy of the response probability density. Nevertheless the sub-critical regime of the system is highly recommended.

On the other hand it is necessary to remain realistic. During testing in laboratory many effects corresponding to various critical and post-critical effects have been observed which are not yet described and quantified theoretically. As regards the damping, the use of the logarithmic decrement as the measure of damping does not correspond very well to the non-linear nature of the phenomenon. However, a comparison of the behavior of different physical models which were examined is very useful. Fig. 3 shows the value of the logarithmic decrement  $b_{\varphi}$  of the model plotted against the absorber - mass ratio  $\mu$ , see Eq. (7c). The model was put into vibration by initial deflection from its

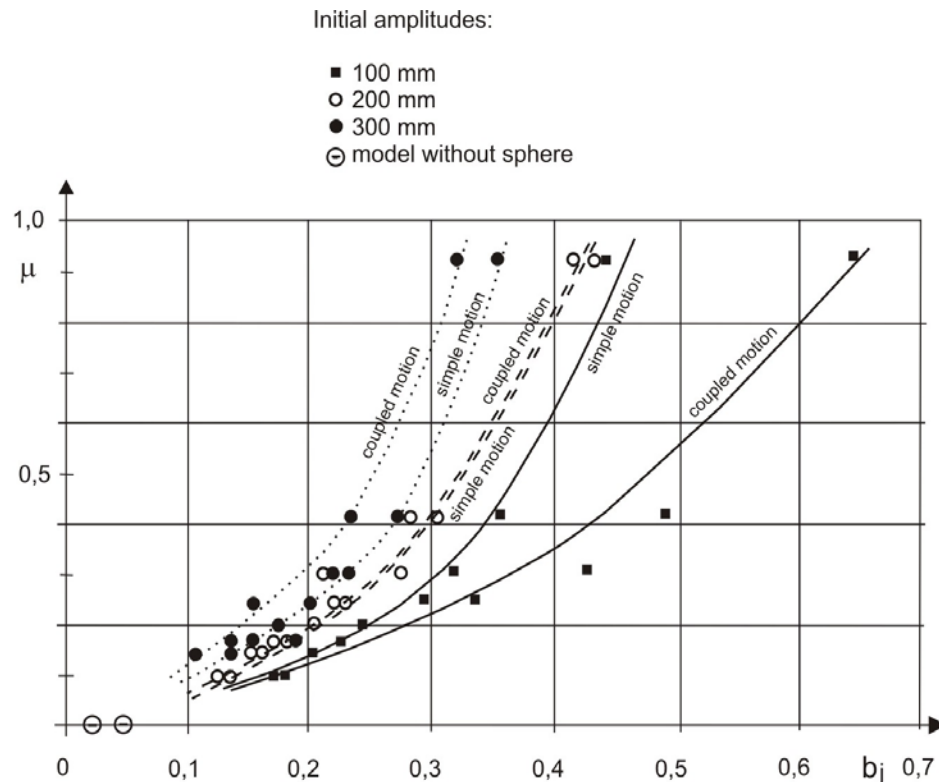


Fig. 3: Logarithmic decrement  $b_\varphi$  plotted against the mass-ratio  $\mu$  for different initial amplitudes.

equilibrium position. In this figure diagrams for several values of initial displacement have been plotted. It can be seen that the model without ball ( $\mu = 0$ ) has the damping nearly 0.02 (the point on the horizontal axis  $\mu = 0$ ), while adding the ball absorber the damping reaches 0.17 - 0.25, i.e. nearly 8 times more. Similar effect appears also using conventional pendulum absorbers, see Pirner (1994).

#### 4. Conclusions

The mathematical model of the ball type vibration absorber has been outlined. The basic Lagrangian analytical theory of non-linear behavior has been done. Very wide numerical investigation reveals that the non-linear character of this device is an important factor influencing significantly its dynamic properties and practical efficiency. It turns out, that the non-linear character making the form of resonance curves dependent on the excitation amplitude leads to better efficiency in comparison with linear mechanism. Laboratory tests of the vibration ball absorber with the dish without and with rubber coating have demonstrated several aspects of real operation of the damper. With respect to laboratory tests and long-term in situ measurements can be concluded that the vibration ball absorber is a simple nearly maintenance free low cost device with very small vertical dimensions. For these properties it is very convenient for application especially in cases when broad band excitation of random character prevails and when very limited vertical space is available.

#### Acknowledgement

The kind support of the Czech Science Foundation project No. 103/09/0094, G.A. ASCR (projects No. IAA200710902, No. IAA200710805) and of the research plan AV0Z720710524 are acknowledged.

#### References

- Hamel, G. (1978) Theoretische Mechanik, Springer, Berlin.
- Náprstek, J., Pirner, M. (2002) Non-linear behaviour and dynamic stability of a vibration spherical absorber. In: Proc. 15th ASCE Engineering Mechanics Division Conference (A. Smyth et al. eds). Columbia Univ., New York, CD ROM, paper #150, 10 pp.
- Pirner, M. (1994) Dissipation of kinetic energy of large-span bridges. Acta Technica, CSAV, Vol 39, pp. 407-418.
- Pirner, M. and Fischer, O. (2000) The development of a ball vibration absorber for the use on towers. Jour.Int.Assoc.for Shell and Spatial Structures, Vol. 41, No.2, pp 91-99.

## IMPACT BEHAVIOUR OF A NEWLY DESIGNED RAILROAD WHEEL

P. Navrátil\*, P. Janíček\*, L. Brabenec\*, P. Marcián\*, M. Matug\*, A. Cívín\*

**Abstract:** *The FEM study presented in this paper deals with a continuum mechanics approach to determination of the stress-strain behaviour in a newly designed shape of railroad wheel for different ways of ride. The reliability of the railroad wheel is related to achieved failures of material. This paper emphasises on the failures of material that are related to the first plastic deformation of the wheel material. This study focuses on designing the new shape of disc with a usage of special algorithm written for the ANSYS software and to determine an influence of stress waves in the material of the railroad wheel. This analysis gives answer to a rail-railroad wheel interaction on impact behaviour of a railroad wheel and a newly designed disc shape in different ways of ride. It shows the weak spots of the designed wheel.*

**Keywords:** *Railroad wheel, stress-waves, finite element method, transient analysis.*

### 1. Introduction

Computational simulations of stress waves belong to the most often solved problems in the applied mechanics. These transient simulations are very difficult to solve, because they need a very fine mesh which means that the time of transient simulation is very long. Our task was to solve a newly designed railroad wheel (further referred to as: RW) in terms of stress-strain states. The design and the shape of the RW (Navrátil et al, 2009) based on mechanical compliance analysis. For this case new algorithm was written for usage in the APDL. For simulation of stress waves we can use 2D or full 3D geometry. Using 2D geometry is very inaccurate; therefore, to get the right results it is necessary to use full 3D geometry of the RW. The cross-section shaped RW is irregular for usage of 2D simulation; thus, it is not suitable to use 2D simulation for the real wheel. The stress results obtained from the analysis are compared with the possible value of yield strength (Dozela et. al, 2010) and the critical spot on the wheel will be discussed further.

### 2. Methods

The finite element method was used for the computational simulation as it is the most common numeric method used. For the analysis we used the ANSYS 11.0 software (Ansys Inc., Canonsburg, PA, USA). The model is compared from different points of view: the model of geometry, model of materials, model of boundary conditions and loads.

#### 2.1. Model of geometry

The model of the wagon RW was gained from the shape optimization routine by using the FEM simulations. We assumed that the value of the mechanical compliance in normal direction would be high and the value of mechanical compliance in axial direction would be low. Both presumptions come out from the last analysis (Navrátil et. al, 2009). For obtaining the new shape the cosine function and displacement analyses were used. A large set of displacement analyses give values to axial and normal mechanical compliance. From these results the maximum ratio of axial to normal mechanical compliance was obtained. We can observe the final shape of wheel and mesh in Fig. 1. The rail was assumed to have 1:40 cant.

---

\* Ing. Petr Navrátil, Prof. Ing. Přemysl Janíček, DrSc., Bc. Ladislav Brabenec, Ing. Petr Marcián, Ing. Michal Matug and Ing. Adam Cívín: Institute of Solid Mechanics, Mechatronics and Biomechanics, Faculty of Mechanical Engineering, Technická 2896/2; 616 69, Brno; Czech Republic, e-mails: ynavra26@stud.fme.vutbr.cz, janicek@fme.vutbr.cz, ybrabe04@stud.fme.vutbr.cz, ymarci00@stud.fme.vutbr.cz, ymatug01@stud.fme.vutbr.cz, ycivin01@stud.fme.vutbr.cz

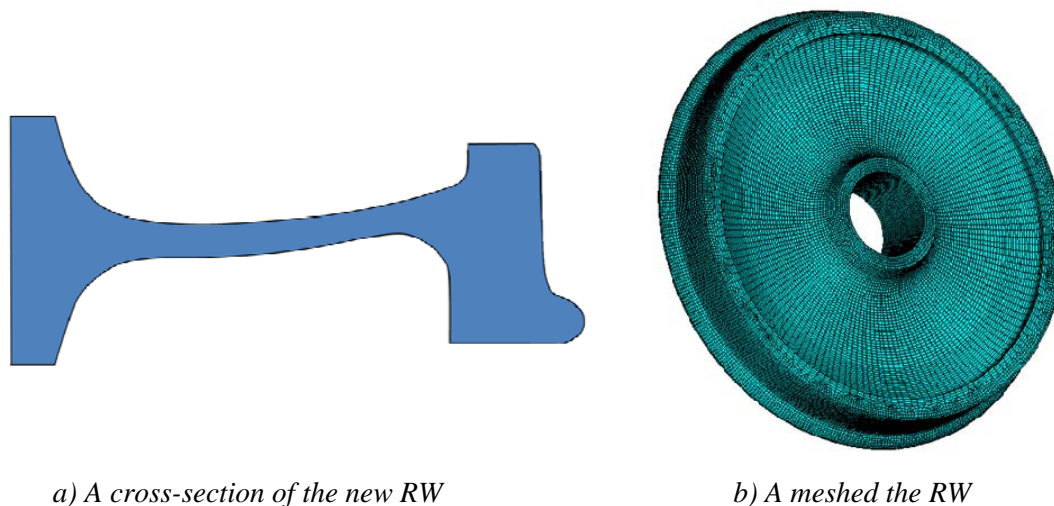


*Fig. 1: A geometry and mesh of the RW.*

## 2.2. Model of material

The material of the wheel was assumed to be homogeneous isotropic and linear elastic. We used a material characteristics Young's modulus  $E = 210\,000\text{ MPa}$  Poisson's ratio  $\nu = 0.3$  and yield strength  $Re = 420\text{ MPa}$  corresponding with R7T steel (Dozela et. al, 2010).

## 2.3. Model of boundary conditions and loads

In case of a stress waves, the load was realized as you can see in Fig. 2 – see below. The RW was loaded in a two ways. For the case of straight ride we assumed 10 tons load to one railroad wheel, i.e.  $10^5\text{ N}$  value of normal force loading. In case of a ride in an arc the normal load is the same as it is in the case of the normal ride. The second load in the case of the ride in the arc is loaded in axial direction of RW, with force value  $1.2 \cdot 10^5\text{ N}$ . The boundary conditions were set only in the RW hub and all domains of freedom were set to zero value.

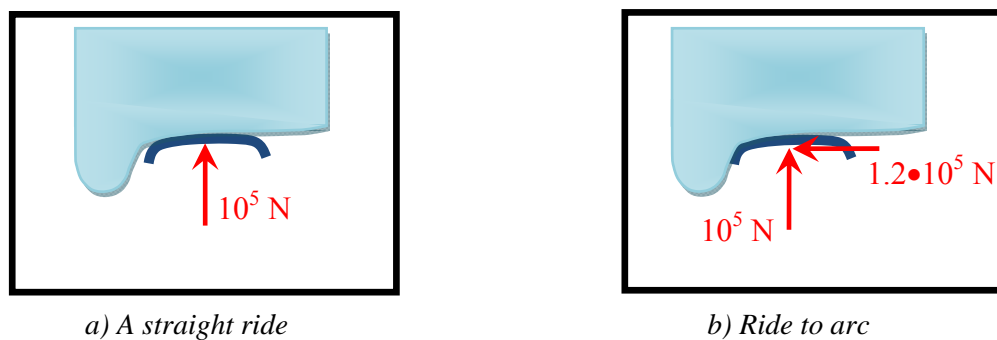


*Fig. 2: A load modes of the RW.*

## 3. Results

Analyses in FEM simulation program ANSYS were created. The first step of simulations was to design the new RW. The ratios of mechanical compliances were compared. You can observe the best results in figure 1a), which has a ratio of mechanical compliances of 57.944 (the maximum ratio) in normal and axial direction. Secondly, we used computational simulation for solving stress waves of the RW. In the first step the case of straight ride was solved. An achieved Von Mises results can be seen in Fig. 3, which shows one of the critical state.



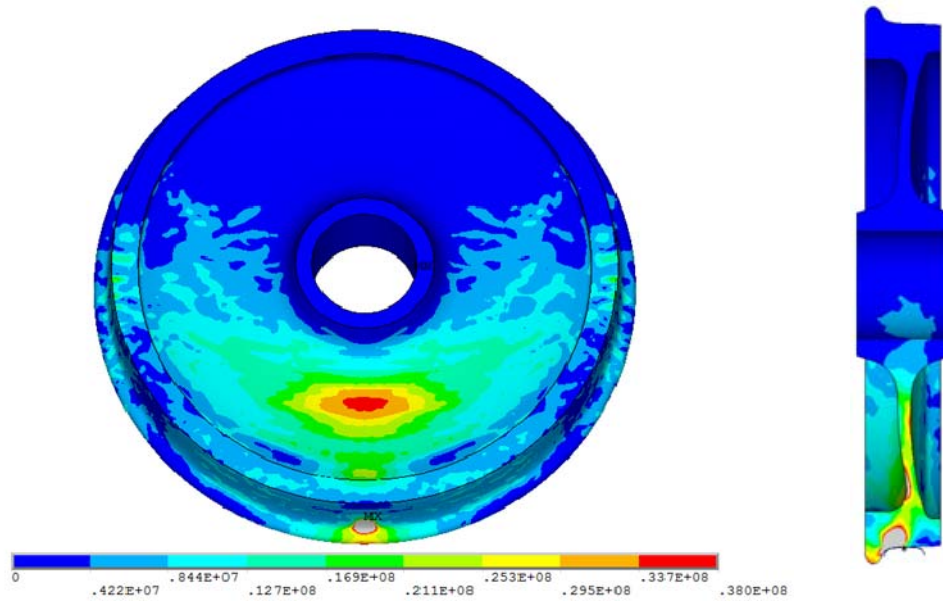


*Fig. 3: The stress waves for the case of straight ride – Von Mises.*

For this operating state can be said that it you should not overstep the value of yield strength of 420 MPa, because maximum value is 47.5 MPa. That means, in this case the plastic deformation will not occur. The second case was the ride in the arc. As we can see in Fig. 4, the Von Mises results were plotted, as in the previous case.

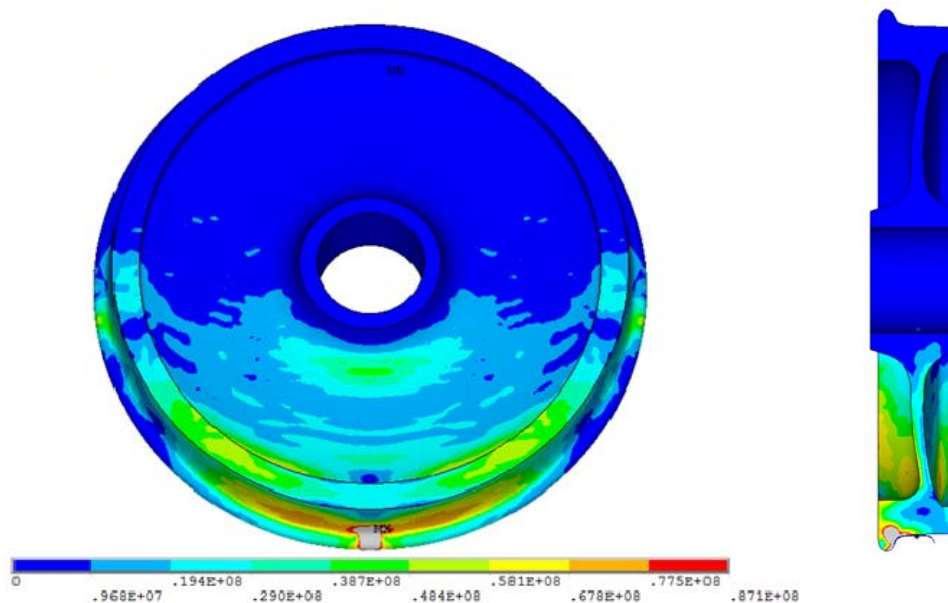


*Fig. 4: The stress waves for the case of ride to arc – Von Mises.*

In case of the ride in the arc a value of yield strength of 420 MPa for steel R7T cannot be overstepped, because the maximum value is 87 MPa. That means, in this case the plastic deformation will not occur. The stress wave analysis proved that the RW has some critical spots. The first critical spot is between the wheel disc and the wheel rim. Other critical spot is in the middle of the wheel disc. We can see both spots in Figs. 3 and 4. All figures are assessed in terms of stress-waves in the part of the wheel disc. The wheel hub doesn't contact load in the wheel rim. From the analyses ensue that stress in the wheel-rail contact spot exceed the value of yield strength. The average of the equivalent stress value in wheel-rail contact spot is near 880 MPa but in term of these analyses it is not essential.

#### **4. Conclusions**

The new shape of the railroad wheel is shown in this paper. The aim of this paper was to determine impact behaviour of the new shaped RW for different ways of the ride. The transient analyses of stress waves for two different cases of the ride were done. From these analyses the stress distributions were obtained. We can say that the stress fields stemmed by stress waves causes less value of stress than the value of the yield strength of R7T steel; however, as the analysis proved, the stress distribution on contact surface oversteps value that causes permanent plastic strain on rail-wheel contact spot. In conclusion, we can say that stress waves in the new designed type of the RW do not exceed a value of yield strength of R7T steel and maximum values of stress are much smaller than yield strength.

#### **Acknowledgement**

The authors are thankful for great support by the specific research FSI-S-11-11/1190 and specific research FSI-J-11-18.

#### **References**

- Donzella, G., Faccoli, M., Mazzù, A., Perogalli, C., Roberti, R. (2010) Progressive damage assessment in the near-surface layer of railway wheel-rail couple under cyclic contact, *Wear*, 9 pages, in press.
- Navrátil, P., Janíček, P., Brabenec, L., Matug, M., Marcián, P. (2009) A design influence of mechanical compliance railroad wheel to fracture behaviour, *Proceed. of conference Computational Mechanics*, Pilsen, 2 p.

## INFLUENCE OF MOISTURE TO MECHANICAL PROPERTIES OF MATERIALS

H. Němcová\*, T. Plachý\*, R. Ťoupek\*, P. Tesárek\*, M. Polák\*

**Abstract:** *This paper deals with the influence of moisture in determining the mechanical properties (dynamic modulus of elasticity) of porous building materials using nondestructive impulse excitation method. The gypsum specimens of dimensions 40×40×160 mm were dried and during their drying the basic natural frequencies of longitudinal vibration were measured in different time instants. Based on these frequencies, the dynamic moduli of elasticity were determined and their dependence on the moisture content of the gypsum specimens was evaluated.*

**Keywords:** *Dynamic modulus, impulse excitation method.*

### 1. Introduction

The process of solid structure evolution relates with hardening of gypsum paste. As basic mechanical properties for characterization of gypsum properties are usually used compressive and bending strength, other mechanical gypsum properties, as modulus of elasticity, are tested less often. The strength characteristics correspond mainly with physical properties of hardened gypsum as total open porosity, arrangement of gypsum crystals, and type of used gypsum binder. On the other hand, properties of gypsum depend on conditions where the hardened gypsum is placed (Kuechler, 2002). Temperature and moisture (relative humidity but especially a liquid water content) prejudice mechanical properties of gypsum (Hájková, 2010).

The main aim of this research is to determine dependence of hardened gypsum mechanical properties on moisture content of tested specimens, respectively the effect of drying out of free water after hardening of gypsum pastes, which are placed at laboratory conditions with constant temperature 25 °C and relative humidity 50 %.

For the determination of dynamic modulus of elasticity, non-destructive method was used currently for a short preparation time and mainly for the matter of fact that it is possible to test one sample several times.

### 2. Materials and specimens

Tested specimens were prepared according to the Czech standard ČSN 72 23 01 Gypsum binders. Specimens with dimensions 40×40×160 mm were made from the “Grey calcined gypsum” which is produced by company Gypstrend. This gypsum binder is  $\beta$ -gypsum ( $\beta$ -calcium sulphate hemihydrate) and is calcined from two different calcium sulphate dihydrates (naturally gypsum and gypsum from a chemistry industry, ratio is 1:1). According to the ČSN 72 23 01 (1978), the Grey gypsum is classified as G2 BIII. Mark G2 means that compressive strength after two hours is at least 2 MPa, the gypsum is with normal-setting (B) determined using the Vicat device and partially corresponds to testing of cement materials. The last criterion is the fineness of grinding, where the tested gypsum is medium ground and the fineness of grinding is marked II in our case.

The tested specimens were prepared from a gypsum binder with a mass of 1.0 kg and water, where amount of water corresponded with the water/gypsum ratio 0.71. Gypsum was poured inside a beaker with water for 20 seconds. While it was poured and for 60 seconds after the whole amount of gypsum

---

\* Ing. Hana Němcová, DiS., Ing. Tomáš Plachý, Ph.D., Bc. Richard Ťoupek, Ing. Pavel Tesárek, Ph.D., assoc. prof. Ing. Michal Polák, CSc.: Czech Technical University in Prague, Faculty of Civil Engineering, Department of Mechanics; Thákurova 7, 166 29 Prague 6 - Dejvice, Czech Republic, e-mails: hana.nemcova@fsv.cvut.cz, plachy@fsv.cvut.cz, richard.toupek@fsv.cvut.cz, tesarek@fsv.cvut.cz, polak@fsv.cvut.cz

had been poured, the mixture was intensively stirred with a manual stirrer until a uniform paste was obtained. Then, the paste was poured inside the mould so that all three sections would be simultaneously filled. To remove air from a gypsum paste, the mould was shook 5 times after filling using a standard shake (the mould is lifted at its face side to a height of 10 mm and dropped). As soon as the paste started to set, its surface was cut off in the direction perpendicular to the bar surface. After 15 minutes, i.e. after the finish of setting, the mould was removed and the samples were marked and placed in the test room at an average temperature of 25 °C and a relative humidity of 50 %.

### 3. Impulse excitation method

The test procedure was performed in accordance with ASTM C215 (2008). At first, the dimensions of all specimens were measured and the mass were weighed. Then the basic natural frequency of longitudinal vibration of the tested specimens was measured using impulse excitation method.

Test specimen was supported in the middle of its longest dimension - the nodal line of the first longitudinal shape of natural vibration. Vibration has been energized by striking shock hammer on one side of the sample and the response was measured using acceleration transducer Bruel&Kjaer of Type 4519-003 on the opposite side (Fig. 1). The measured excitation force and the response, in our case acceleration, were transformed from time domain to the frequency domain using Fast Fourier Transform (FFT) (Tůma, 1997). The fundamental natural frequency of longitudinal vibration  $f_L$  [Hz] was determined as the basic resonant frequency of the Frequency Response Function (FRF). The dynamic modulus of elasticity  $E_d$  can be determined using the relation:

$$E_d = \frac{4lmf_L^2}{bt} \quad (1)$$

where  $l$  [m] is the length of the specimen,  $m$  [kg] is the mass of the specimen,  $f_L$  [Hz] is the fundamental natural frequency of the longitudinal vibration of the specimen,  $b$  [m] is the width of the specimen and  $t$  [m] is the thickness of the specimen.

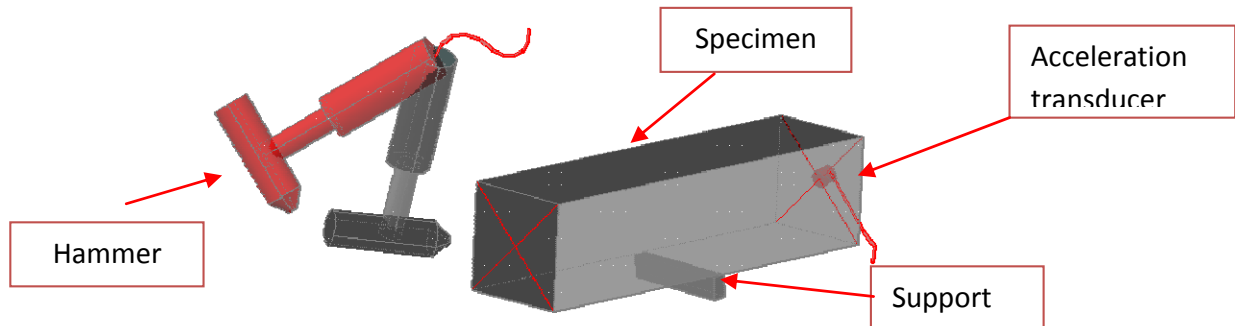


Fig. 1: Measurement of the natural frequency of longitudinal vibration.

### 4. Measurement results

The investigation was focused on two types of moisture content in the gypsum specimens: uniformly and non-uniformly distributed moisture.

In the first part of the experiment, the 70 days old specimens were put to the water bath for 10 days. After water saturation of the specimens, they were removed and put to the laboratory conditions (temperature 25 °C and relative humidity 50 %). During their drying, they were tested using impulse excitation method in different time instants with different moisture content. The Fig. 2 shows the dependence of the basic natural frequency of the tested specimens on their weight, respectively on their moisture content. The Fig. 3 shows the dependence of the dynamic modulus of elasticity of the tested specimens on their weight, respectively on their moisture content.

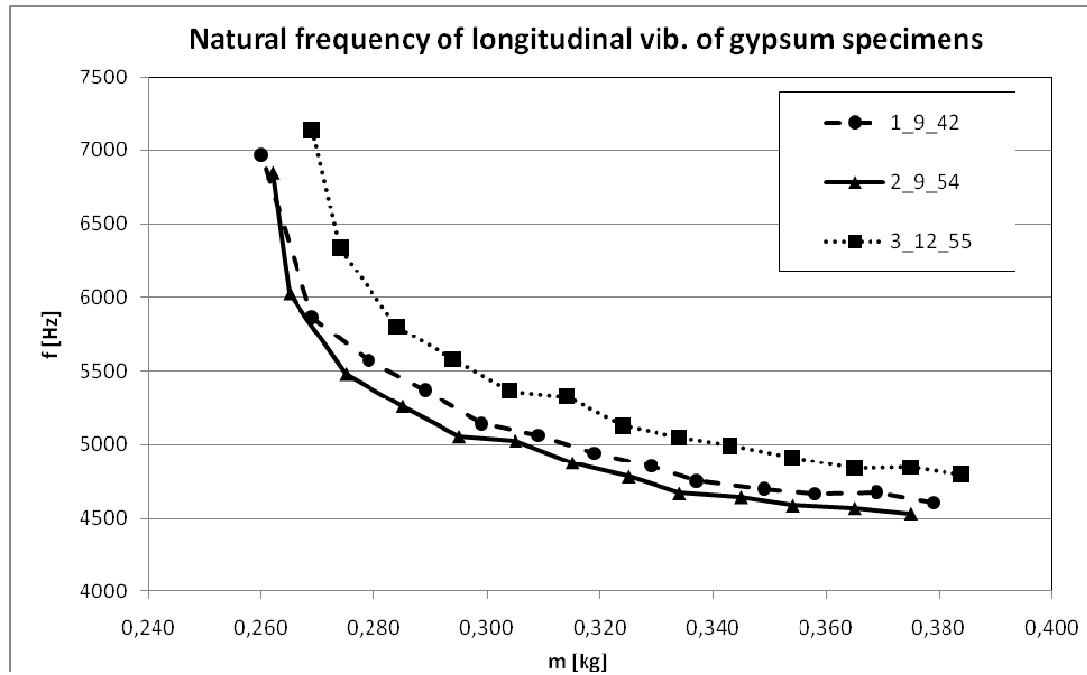


Fig. 2: Dependence of the 1<sup>st</sup> natural frequency of the tested specimens on their moisture content.

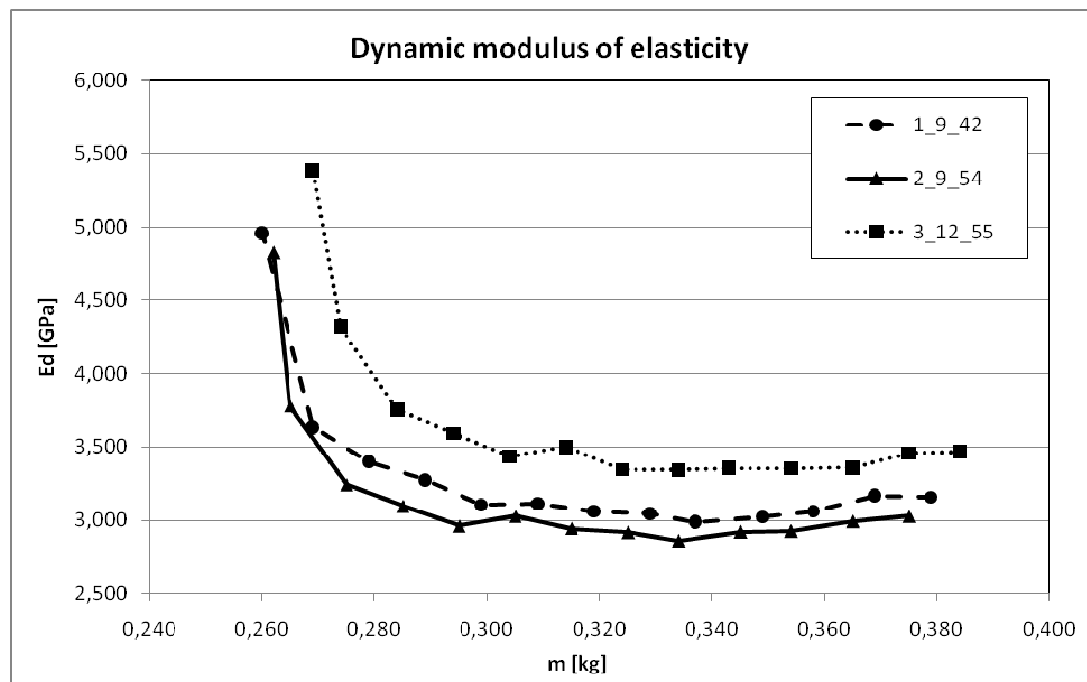


Fig. 3: Dependence of the dynamic modulus of elasticity of the specimens on their moisture content.

In the second part of the experiment, the dried specimens were rolled around its longest axis in the water bath to be the moisture non-uniformly distributed in the specimen. The whole process of dipping lasted approximately 10 s. The central part of the specimen was dry and edges were wet. The specimens were tested twice, in dried state and in the wet state. The comparison of these two states is done in the Fig. 4.

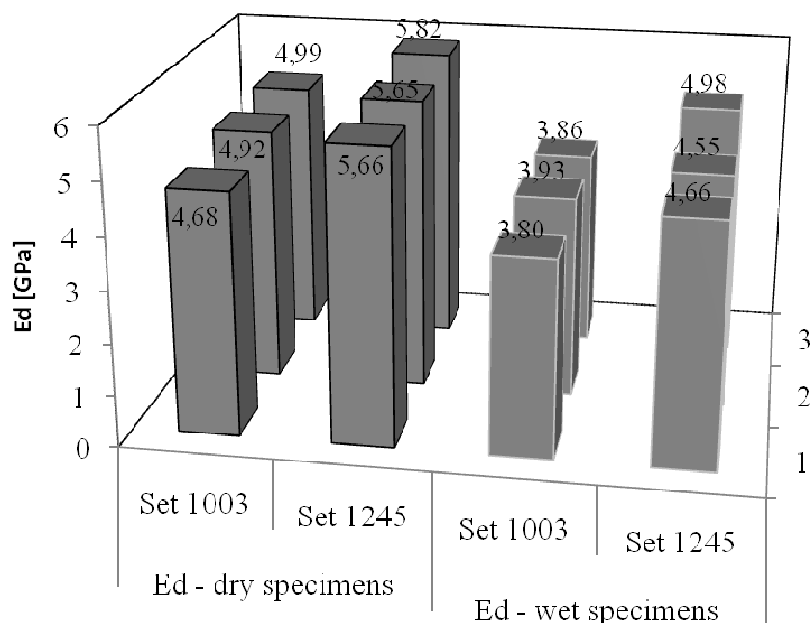


Fig. 4: The influence of the non-uniformly distributed moisture to the dynamic modulus of elasticity.

## 5. Conclusions

The paper presents the dependence of the dynamic modulus of elasticity on the moisture content of the gypsum specimens. From the measured data it is visible that dynamic modulus of elasticity increases especially at the end of the drying of the gypsum specimens (Fig. 3). There can be also seen that specimens made with same technology, with same materials and with the same water/gypsum ratio have different moduli of elasticity (Fig. 3, Fig. 4). Also the small amount of non-uniformly distributed water in the specimens has big influence to the values of dynamic modulus of elasticity, for the set 1003 the decrease is approximately 17% and for the set 1245 it is about 20%.

## Acknowledgement

This project was supported by Czech Technical University as the project Advanced experimental methods SGS10/136/OHK1/2T/11.

## References

- ČSN 72 2301 (1978) Sádrová pojiva. Klasifikace. Všeobecné technické požadavky. Zkušební metody. Prague: Czechoslovak standardization institutions, pp. 17.
- Hájková, A. (2010) Energosádra a možnosti její recyklace s ohledem na mechanické vlastnosti, Prague, Thesis, Czech Technical University in Prague, pp. 93.
- Tůma, J. (1997) Zpracování signálů získaných z mechanických systémů užitím FFT, Sdělovací technika s.r.o, Praha, ISBN: 80-901936-1-7, pp. 174.
- Wirshing, F. (1983) Calcium Sulfate, In: Ullmanns Encyclopedia of Industrial Chemistry, Volume 6, Weinheim, Wiley-VCH Verlag, pp. 90 – 94.
- Vranken, K. C., Laethem, B. (2000) Recycling Options for Gypsum from Construction and Demolition Waste, Waste Management Series, Volume 1, Waste Materials in Construction Wascon 2000 - Proceedings of the International Conference on the Science and Engineering of Recycling for Environmental Protection, Harrogate, England 31 May, pp. 325 – 331.
- Ahmed, A., Ugai, K. (2010) Environmental Effects on Durability of Soil Stabilized with Recycled Gypsum, Cold Regions Science and Technology, doi:10.1016/j.coldregions.2010.12.004.
- Kuechler R., Noack K. & Zorn T. (2002): Investigation of gypsum dissolution under saturated and unsaturated water conditions, Ecological Modelling, Volume 176, Issues 1-2, pp. 1-14.
- ASTM C215 (2008) Standard Test Method for Fundamental Transverse, Longitudinal, and Torsional Frequencies of Concrete Specimens, DOI: 10.1520/C0215-08, pp.



## DYNAMIC ANALYSIS OF COLLAPSE OF A HIGH BUILDING

I. Němec<sup>\*</sup>, M. Juránová<sup>\*</sup>, P. Frantík<sup>\*</sup>, I. Ševčík<sup>\*\*</sup>

**Abstract:** The differential equation of collapse of a high building is derived taking into account many influences. Computer simulation of the collapse of the WTC building is presented using two independent programs for some variations of parameters. The results of both, differential equation and computer simulation, are compared.

**Keywords:** Dynamics, structural mechanics, collapse.

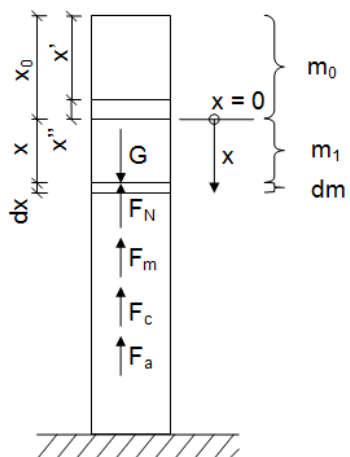
### 1. Introduction

This article deals with collapse of a high building. Its aim is not to investigate a cause of the collapse but to examine the falling process itself. The article studies theory of collapse of a high building. Process of the falling is investigated from the point of view of basic laws of mechanics. Differential equation of a high building collapse is derived and all major influences of the falling process are included. Several parameters which influence the falling process are introduced. The conditions which are to be considered to let the building collapse completely are set and the falling speed is examined.

### 2. Derivation of a differential equation of collapse of a high building

Let's assume that columns in the location between the coordinates  $x'$  and  $x_0$  lose stability and a top part of the building above  $x'$  starts to fall and hits the still undamaged lower part of the building under the location  $x_0$  with velocity  $v_0$ .

We will introduce equation of dynamical equilibrium for the location  $x$ :



$$G - F_N - F_m - F_c - F_a = 0 \quad (1)$$

Where  $G$  is weight of a part of the building above the location  $x$ , for which equilibrium equation is formulated

$F_N$  is resistance put up by the columns against the collapse

$F_m$  is resistance originated by hitting of a falling part of the building into a motionless mass

$F_c$  is a viscous damping

$F_a$  is an inertial force of a falling mass

Fig. 1: Scheme of a high building with acting forces.

#### Derivation of individual parts of the equilibrium equation (1)

a) The weight of the building above the location  $x$ :

$$G = mg\beta, \quad (2)$$

<sup>\*</sup> assoc. prof. Ing. Ivan Němec, CSc., Ing. Martina Juránová and Ing. Petr Frantík, PhD.: Institute of Structural Mechanics, Brno University of Technology, Veveří 95; 602 00, Brno; CZ, e-mail: nemec@fem.cz, martina.juranova@seznam.cz, kitnarf@centrum.cz

<sup>\*\*</sup> Ing. Ivan Ševčík, PhD: FEM consulting Veveří 95; 602 00, Brno; CZ, e-mail sevcik@fem.cz

where  $m$  is the mass of the building above the location  $x$ ,  $g$  is acceleration of gravity,  $\beta$  is portion of the total mass above the location  $x$  which pushes to a lower part of the building. The mass which falls outside of the building is subtracted.

b) The columns resistance:

$$F_N = mgs\kappa \quad (3)$$

where  $s$  is a rate of the ultimate force of columns to the current force in columns in the moment of the collapse,  $\kappa$  is the factor of the ultimate force of columns which represents average column resistance during its deformation related to an ultimate force.

The assessment of the column pressing was done using the method of controlled deformation in order to obtain this factor and receive its operational chart (see picture below). Factor  $\kappa$  is then the rate of the ultimate force to its median value.

c) The resistance of a motionless mass:

It is inertial force of a still mass  $dm$  accelerated in a time  $dt$  to the speed  $v$  ( $a = dv / dt$ ). We can use the term  $a = v / dt$  for acceleration in the equation due to acceleration starting from zero up to the speed  $v$ .

The force  $F_m$  can be then expressed in this way:

$$F_m = dm \cdot a = dm \cdot \frac{v}{dt} \quad (4)$$

When considering that  $v = dx / dt$ , the equation (4) can be rewritten as follows:

$$F_m = dm \cdot \frac{v^2}{dx} = \mu v^2, \quad (5)$$

where  $\mu = dm / dx$  is a line density of the building.

d) The viscous damping:

$$F_c = C \cdot v = m\alpha v, \quad (6)$$

where  $C$  is a factor of the viscous damping. We are considering Rayleigh damping here which is depending on mass quantity  $C = m\alpha$  only.

e) The inertial force of a falling mass:

$$F_a = \beta m \cdot a = \beta m \frac{dv}{dt} = \beta m v \frac{dv}{dx} \quad (7)$$

Again, only the inertial force of a mass which does not fall outside of the building is considered here.

### 3. Differential equation of the building collapse

By substituting relations which we derived above into the equation (1) we get:

$$mg\beta - mgs\kappa - \mu v^2 - m\alpha v - \beta m v \frac{dv}{dx} = 0 \quad (8)$$

We will divide the equation with speed  $v$  and mass  $m$  and adjust:

$$\frac{b}{v} - \frac{v}{x + x_0} - \alpha - \frac{\beta dv}{dx} = 0, \quad (9)$$

where  $b = g(\beta - s\kappa)$ . We used relation  $\mu(x + x_0) = m$  when adjusting the equation.

Analytical solution of the differential equation was found only when influence of damping was omitted:

$$v(x) = \sqrt{\frac{2b(x+x_0)}{2+\beta} + (x+x_0)^{\frac{-2}{\beta}} \cdot C_1} \quad (10)$$

To specify the constant  $C_1$  the magnitude of the speed  $v_0$  is needed. This is the speed of the mass  $m_0$  above  $x_0$  falling into the undamaged part of the building. We will start from the same differential equation where we will modify factor  $b$  into  $b_0 = (\beta - s_0 \kappa) g$ , whereas  $s_0 < 1$ :

$$\frac{b_0}{v(x)} - \frac{v(x)}{x+x'} - \frac{\beta dv(x)}{dx} = 0 \quad (11)$$

The solution will thus have a similar form. We will use boundary conditions  $v(0) = 0$  for finding the magnitude of the integration constant. Then we are looking for  $v(x') = v_0(x)$ . After that we can return to searching the integration constant  $C_1$ :

$$v_0(x) = \sqrt{\frac{2b_0(x+x_0)}{2+\beta} + (x+x_0)^{\frac{-2}{\beta}} \cdot C_1} \quad (12)$$

$$C_1 = \frac{v_0^2(x)(2+\beta) - 2b_0(x+x_0)}{(x+x_0)^{\frac{-2}{\beta}}(2+\beta)} \quad (13)$$

We will establish  $C_1$  in (10):

$$v(x) = \sqrt{\frac{2b(x+x_0)}{2+\beta} + (x+x_0)^{\frac{-2}{\beta}} \cdot \frac{v_0^2(x)(2+\beta) - 2b_0(x+x_0)}{(x+x_0)^{\frac{-2}{\beta}}(2+\beta)}} \quad (14)$$

We have now the solution of the equation (14). Therefore we can find out when the collapse of the building will stop so that the speed will be zero  $v(x) = 0$ . There was not found any solution of this equation in the closed form so we are going to return to treat the equation (9) with numerical method. The Euler implicit method of solving a differential equation was found to be the most suitable method. Its principle is:

$$v_{i+1} = v_i + h \cdot f(x_i, v(x_i)) \quad (15)$$

We will get this in our equation:

$$v(x_{i+1}) = v(x_i) + \frac{h}{\beta} \left( \frac{b}{v(x_{i+1})} - \frac{v(x_{i+1})}{x_{i+1} + x_0} - \alpha \right) \quad (16)$$

After deduction of the speed  $v(x_{i+1})$  we get this relation:

$$v(x_{i+1}) = \frac{1}{2(h + \beta x_{i+1} + \beta x_0)} * \left\{ -\alpha h x_{i+1} + \beta v(x_i) x_{i+1} - \alpha h x_0 + \beta v(x_i) x_0 + \sqrt{-4(h + \beta x_{i+1} + \beta x_0)(-b h x_{i+1} - b h x_0) + (\alpha h x_{i+1} - \beta v(x_i) x_{i+1} + \alpha h x_0 - \beta v(x_i) x_0)^2} \right\} \quad (17)$$

We will compute the speed  $v(0)$  in a similar way.

### Discussion of the magnitude of damping, the safety factor $s$ and the ultimate force ratio $\kappa$

Before we start solving equation in the numerical way we are going to clarify the magnitude of the damping  $\alpha$ .

$$\alpha = \frac{C}{m} = \frac{2m\omega_n \xi}{m} = 2\omega_n \xi \quad (18)$$

For the ratio of damping, we will consider the value 10-30% and the limiting value 0 that yields the damping ratios  $\alpha = 0, 147, \alpha = 3, 18, \alpha = 0$ . We will consider value 0 in order to solve the collapse without the effect of damping.

Much less uncertainty is about the value of the parameter  $s$ . We are assuming it to be around 2.5 – 3. e. The coefficient of the ultimate strength in columns  $\kappa$  was computed from simulation of pressing of the columns by the method of controlled deformation.

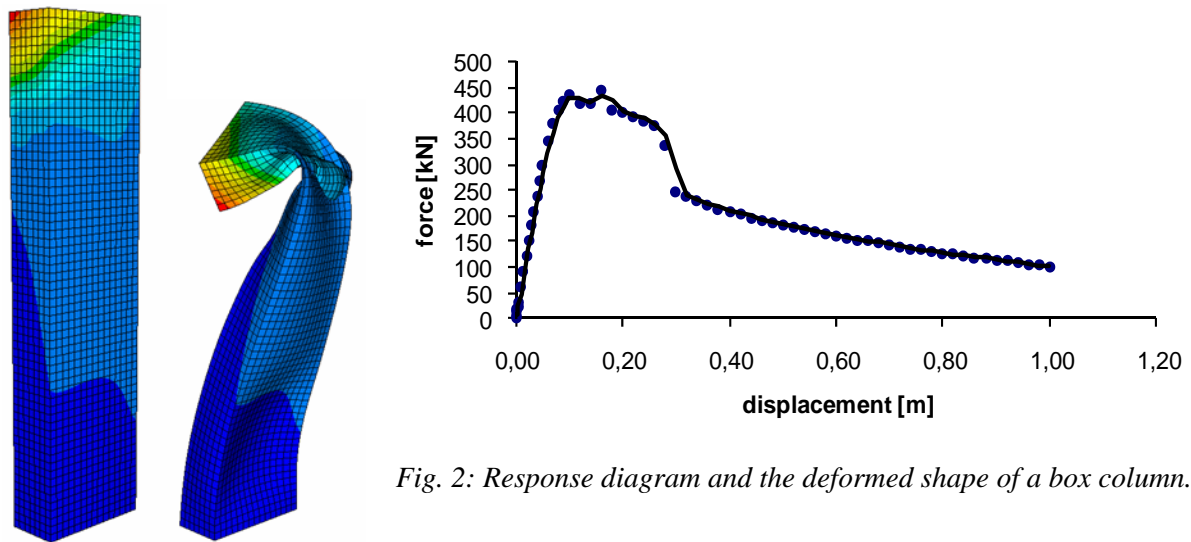


Fig. 2: Response diagram and the deformed shape of a box column.

It is clear from the graph that the value of the  $\kappa$  coefficient will be around 0.25.

#### Results – times and extends of the fall for various parameters

s[-]	alpha	The theory without falling away of a mass x[m]	The theory with falling away of a mass x[m]	RFEM x[m]	FyDiK x[m]	The theory without falling away of a mass t[s]	The theory with falling away of a mass t[s]	RFEM t[s]	FyDiK t[s]
2.0	0.147	330	330	331.0	278.7	15.2	25.8	15.7	19.0
2.0	3.18	330	330	18.2	63.2	83.1	357.1	7.4	31.5
3.0	0	330	330	259.8	287.1	20.5	36.1	17.9	20.4
3.0	0.147	330	330	324.5	304.2	24.2	103.0	28.6	33.1
3.0	0.5	330	330	79.6	72.3	36.5	330.5	12.1	28.1
3.0	1.06	330	330	64.6	66.5	60.2	707.3	15.9	37.4

#### 4. Conclusions

It was possible to solve a differential equation of the building collapse in closed form only when the damping was omitted. Real damping is indispensable considering massive destruction of all components of a building construction. Therefore this solution represents limit of a speed and an extent of the collapse. General form of the differential equation was solved only in the numerical way. Two independent computer programs were used for the simulation, named RFEM (Němec et al., 2010) and FyDiK. Despite the difference in the approaches both computer programs gave comparatively similar solutions. The difference between the solution of the differential equation and that of the computer simulation is greater. The computer simulation gives more reliable solution as there is no need to keep continuity of all values used in differential equation.

#### Reference

Němec, I. at al. (2010) Finite Elements Analysis of Structures. Aachen: Shaker Verlag.

## A THEORETICALLY CORRECT ALGORITHM FOR NONLINEAR CONSTITUTIVE MATRIX OF A SHELL

I. Němec<sup>\*</sup>, L. Weis<sup>\*</sup>

**Abstract:** *A theoretically correct algorithm for nonlinear constitutive matrix of shell is introduced. The derivation starts with general formulas defining the constitutive matrices and it is applied to a specific problem of a shell respective to material nonlinearity.*

**Keywords:** *Shell, constitutive matrix, material nonlinearity.*

### 1. Introduction

The paper starts from the basic relation defining a tensor of tangent material stiffness (e.g. Belytschko, Liu & Moran, 2000). From this definition a theoretically correct algorithm of the tangent constitutive matrix of a shell is derived.

### 2. Basic relations

Let us start from the relation for the tangent material stiffness (1), which can be applied for a wide scale of materials, where the material modulus  $\mathbf{C}$  is the fourth order tensor,  $\mathbf{S}$  is the second Piola-Kirchhoff stress tensor and  $\mathbf{E}$  is the Green-Lagrange strain tensor.

$$\mathbf{C}(\mathbf{E}) = \frac{\partial \mathbf{S}}{\partial \mathbf{E}} \quad (2)$$

When proceeding to the Voigt notation, we introduce the material stiffness matrix  $\bar{\mathbf{C}}$ , the matrix of the second Piola-Kirchhoff stress  $\bar{\mathbf{S}}$  and the matrix of the Green-Lagrange strain  $\bar{\mathbf{E}}$ . Then the equation (3) can be rewritten as follows:

$$\bar{\mathbf{C}}(\bar{\mathbf{E}}) = \frac{\partial \bar{\mathbf{S}}}{\partial \bar{\mathbf{E}}} \quad (4)$$

When a load increment is small enough then the constitutive relation (5) can be linearized.

$$\delta \bar{\mathbf{S}} = \bar{\mathbf{C}} \cdot \delta \bar{\mathbf{E}} \quad (6)$$

Then we can write the following relation for particular members of the constitutive matrix  $\bar{\mathbf{C}}$ :

$$\bar{C}_{ij} = \frac{\partial \bar{S}_i}{\partial \bar{E}_j} \quad (7)$$

With regard to linearity of the relations (8) and (9), for determination of members of the constitutive matrix we can choose an arbitrary value of  $\delta \bar{E}_j$ , then also  $\delta \bar{E}_j = 1$ . Then we can easily determine members of the constitutive matrix  $\bar{\mathbf{C}}$  as pertinent components of the stress vector  $\bar{\mathbf{S}}$  for the unit magnitude of the strain vector  $\bar{\mathbf{E}}$ .

---

<sup>\*</sup> assoc. prof. Ing. Ivan Němec, CSc. and Ing. Lukáš Weis: Institute of Structural Mechanics, University of Technology, Faculty of Civil Engineering, Veveří 331/95; 602 00, Brno; CZ, e-mails: nemec@fem.cz, weis@fem.cz

$$\bar{C}_{ij} = \delta \bar{S}_i \left( \delta \bar{E}_j = 1 \right) \quad (10)$$

The similar way can be used for obtaining members of the constitutive matrix of a shell. Let us define the vector of internal forces of a shell (11), where particular internal forces are defined in a usual way as integral factors of stress components (7).

$$\mathbf{S}^{(s)} = \begin{bmatrix} m_x & m_y & m_{xy} & v_x & v_y & n_x & n_y & n_{xy} \end{bmatrix}^T \quad (12)$$

$$\begin{aligned} m_x &= \int_h \sigma_x z \, dz & m_y &= \int_h \sigma_y z \, dz & m_{xy} &= \int_h \tau_{xy} z \, dz \\ v_x &= \int_h \tau_{xz} \, dz & v_y &= \int_h \tau_{yz} \, dz \\ n_x &= \int_h \sigma_x \, dz & n_y &= \int_h \sigma_y \, dz & n_{xy} &= \int_h \tau_{xy} \, dz \end{aligned} \quad (13)$$

Let us define the strain vector of a shell in a usual way.

$$\mathbf{E}^{(s)} = \begin{bmatrix} \kappa_x & \kappa_y & \kappa_{xy} & \gamma_{xz} & \gamma_{yz} & \varepsilon_x & \varepsilon_y & \gamma_{xy} \end{bmatrix}^T \quad (14)$$

$$\begin{aligned} \kappa_x &= \frac{\partial \varphi_y}{\partial x} & \kappa_y &= -\frac{\partial \varphi_x}{\partial y} & \kappa_{xy} &= \frac{\partial \varphi_y}{\partial y} - \frac{\partial \varphi_x}{\partial x} \\ \gamma_{xz} &= \frac{\partial u_z}{\partial x} + \varphi_y & \gamma_{yz} &= \frac{\partial u_z}{\partial y} - \varphi_x \\ \varepsilon_x &= \frac{\partial u_x}{\partial x} & \varepsilon_y &= \frac{\partial u_y}{\partial y} & \gamma_{xy} &= \frac{\partial u_x}{\partial y} + \frac{\partial u_y}{\partial x} \end{aligned}$$

Similar relation as the equation (15) can be written also for the constitutive matrix of a shell:

$$\mathbf{C}^{(s)} = \frac{\partial \mathbf{S}^{(s)}}{\partial \mathbf{E}^{(s)}} \quad (16)$$

To obtain particular members of the constitutive matrix of a shell, similar relation as in the equation (17) can be written:

$$C_{ij}^{(s)} = \frac{\delta S_i^{(s)}}{\delta E_j^{(s)}} \quad (18)$$

With regard to linearity of the constitutive matrix in each iteration step, particular members of the constitutive matrix can be again determined as the pertinent components of the vector  $\delta S_i^{(s)}$  for unit value of the strain component  $\delta E_j^{(s)}$ .

### 3. Algorithm of the calculation of the constitutive matrix of a shell

#### 3.1. Layered shell element

Inasmuch as the internal forces  $\delta S_i^{(s)}$  corresponding to the strain  $\delta \bar{E}_j$  must be obtained by numerical integration (Šolín, Segeth & Doležel 2004), the shell must be divided along its thickness  $h$  into layers. A layer  $i$  is determined by its thickness  $h_{lr,i}$  and by the location of its central surface  $z_{lr,i}$ . The pertinent integrals can be evaluated by Gauss quadrature formula which defines the location of



Gaussian points  $z_{gp,j}$ . This quadrature formula gives exact results for polynomials of the  $(2n-1)$ -th and lower order, where  $n$  is the number of Gaussian points in each layer.

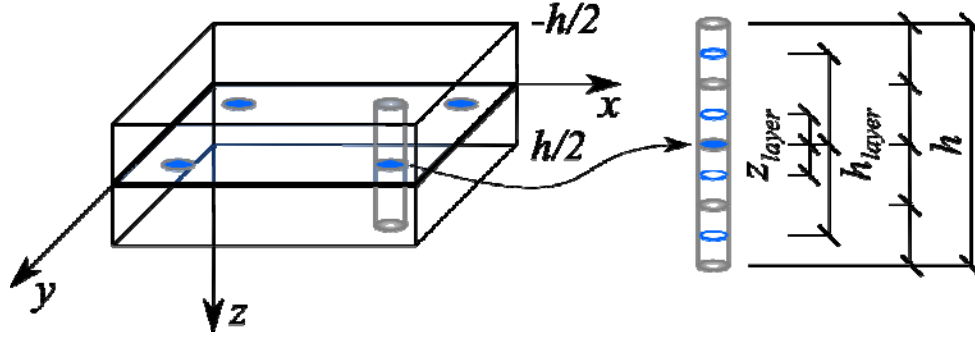


Fig. 1: Division of element along its thickness  $h$  into 4 layers with one Gaussian point in each layer

$$z_{lr,i} = z_{gp,j}.$$

### 3.2. Bending and membrane members of the constitutive matrix

A bending and membrane members of the constitutive matrix of a shell  $\mathbf{C}^{(s)}$  are calculated from the constitutive matrices of layers  $\mathbf{c}_{lr,i}$  (11) transformed into such coordinate system in which the shell constitutive matrix  $\mathbf{C}^{(s)}$  should be assembled.

$$\mathbf{c}_{lr,i} = (\mathbf{T}_c^{-1})^T \mathbf{c}_{lr,i}^{local} \mathbf{T}_c^{-1} = \begin{bmatrix} c_{lr,i,xxxx} & c_{lr,i,xxxy} & c_{lr,i,xxxxy} \\ c_{lr,i,yyxx} & c_{lr,i,yyxy} & c_{lr,i,yyyxy} \\ c_{lr,i,xyxx} & c_{lr,i,xyxy} & c_{lr,i,xyxy} \end{bmatrix} \quad (19)$$

For assemblage of the constitutive matrix  $\mathbf{C}^{(s)}$  the equation (12) shall be used. When choosing the first member  $\kappa_x$  of the deformation vector  $\mathbf{E}^{(s)}$  equal to one, and the remaining members of this vector are zero, then the vector of internal forces  $\mathbf{S}^{(s)}$  is equal to the first column of the constitutive matrix  $\mathbf{C}^{(s)}$ .

$$\mathbf{S}^{(s)} = \mathbf{C}^{(s)} \mathbf{E}^{(s)} \quad (20)$$

$$\begin{bmatrix} m_x \\ m_y \\ m_{xy} \\ v_x \\ v_y \\ n_x \\ n_y \\ n_{xy} \end{bmatrix} = \begin{bmatrix} C_{11} & 0 & 0 & 0 & 0 & 0 & 0 & 0 \\ C_{21} & 0 & 0 & 0 & 0 & 0 & 0 & 0 \\ C_{31} & 0 & 0 & 0 & 0 & 0 & 0 & 0 \\ C_{41} & 0 & 0 & 0 & 0 & 0 & 0 & 0 \\ C_{51} & 0 & 0 & 0 & 0 & 0 & 0 & 0 \\ C_{61} & 0 & 0 & 0 & 0 & 0 & 0 & 0 \\ C_{71} & 0 & 0 & 0 & 0 & 0 & 0 & 0 \\ C_{81} & 0 & 0 & 0 & 0 & 0 & 0 & 0 \end{bmatrix} \cdot \begin{bmatrix} \kappa_x = 1 \\ 0 \\ 0 \\ 0 \\ 0 \\ 0 \\ 0 \\ 0 \end{bmatrix} \Rightarrow \begin{matrix} C_{11} = m_x \\ C_{21} = m_y \\ C_{31} = m_{xy} \\ C_{41} = v_x \\ C_{51} = v_y \\ C_{61} = n_x \\ C_{71} = n_y \\ C_{81} = n_{xy} \end{matrix}$$

This algorithm will be used for evaluating the first three and the last three columns of the constitutive matrix  $\mathbf{C}^{(s)}$ . The chosen vector of deformation  $\mathbf{E}^{(s)}$  containing only one nonzero member i.e. curvature  $\kappa_x = 1$  will yield the strain in the layers as follows.

$$\varepsilon_{lr,i,x} = \varepsilon_x + \kappa_x z_{lr,i} \quad \varepsilon_{lr,i,y} = \varepsilon_y + \kappa_y z_{lr,i} \quad \gamma_{lr,i,xy} = \gamma_{xy} + \kappa_{xy} z_{lr,i} \quad (21)$$

A constitutive matrix of a layer  $\mathbf{c}_{lr,i}$  obtained from a nonlinear calculation will be multiplied by the strain vector  $\boldsymbol{\varepsilon}_{lr,i}$  to obtain the pertinent stress vector.

$$\boldsymbol{\sigma}_{lr,i} = \mathbf{c}_{lr,i} \boldsymbol{\varepsilon}_{lr,i} \quad (22)$$

Then the stress  $\sigma_{vr,i}$  in each layer will be integrated related to the central surface of the shell by the relation (7). The resulting vector of the internal forces  $\mathbf{S}^{(s)}$  will be substituted into the first column of the constitutive matrix  $\mathbf{C}^{(s)}$ . This procedure will be repeated also for the remaining columns of the constitutive matrix except the fourth a fifth one, which will be evaluated by a different procedure.

### 3.3. Shear members of the shell constitutive matrix

To complete all the members of the constitutive matrix  $\mathbf{C}^{(s)}$  it remains to determine the shear stiffnesses  $C_{44}$  in the  $x$  direction and  $C_{55}$  in the direction. The  $C_{44}$  and  $C_{55}$  stiffnesses will be calculated by the relations (23) that were derived from the demand of the equivalence of the virtual work of the 3D and the 2D models.

$$C_{44} = \frac{1}{\int_h \frac{1}{G_{lr,i,x}} \left[ \frac{\int_h E_{lr,i,x} \bar{z}_{lr,i} d\bar{z}}{\int_h E_{lr,i,x} \bar{z}_{lr,i}^2 d\bar{z}} \right]^2 dz} \quad C_{55} = \frac{1}{\int_h \frac{1}{G_{lr,i,y}} \left[ \frac{\int_h E_{lr,i,y} \bar{z}_{lr,i} d\bar{z}}{\int_h E_{lr,i,y} \bar{z}_{lr,i}^2 d\bar{z}} \right]^2 dz} \quad (24)$$

$E_{lr,i,x}$ ,  $E_{lr,i,y}$ ,  $G_{lr,i,x}$  and  $G_{lr,i,y}$  are the Young and shear modules of each layer.

## 4. Conclusions

The paper has shown a theoretically correct and practically useful algorithm for calculation of tangent constitutive matrix of a shell. This algorithm is applied in the RFEM program for finite element analysis of structures (Němec et al., 2010).

## References

- Belytschko, T., Liu, W. K., Moran B. (2000) Nonlinear Finite Elements for Continua and Structures, New York: John Wiley & sons. ISBN 0-471-98773-5.
- Němec, I. et al. (2010) Finite Elements Analysis of Structures. Aachen: Shaker Verlag. ISBN 978-3-85-322-9314-7.
- Šolín P., Segeth K., Doležel I. (2004) Higher-Order Finite Element Methods, Chapman & Hall/CRC, Boca Raton, London, New York, Washington, D.C., pp.244-247.

## HYDROSTATIC SYSTEMS OF WIND MILLS

L. Němec<sup>\*</sup>

**Abstract:** *Renewable energy sources - theirs using and ratio; wind mills – using in Europe, used hydrostatic systems and gears; wind mills with adjustable planetary gears ratio + conclusion.*

**Keywords:** *Alternative sources, hydrostatic systems, wind mills, planetary gears.*

### 1. Renewable Energy Sources

The requirement of maximum use of alternative sources is one of the key points of the world economy. According to the surveys' results, the most developed countries of the world see the increasing share of using the alternative sources of energy as one of the priorities. The current tendency in the energy commodity balance promotes a balanced “energy mix” of respective types of the sources. Their role is directly depending on the assessment from the point of view of the sustainable development and from the point of view of the economic indicators. Apart from the primary sources (fossil fuels, i.e. classical power plants, uranium), this holds true also for the so-called **alternative sources**, more often called the renewable sources. Using the existence of the mankind and its needs as a scale, the inexhaustible forms of energy come from the Sun and the Earth. The Fig. 1 shows share of world energy consumption in relations to alternative sources.

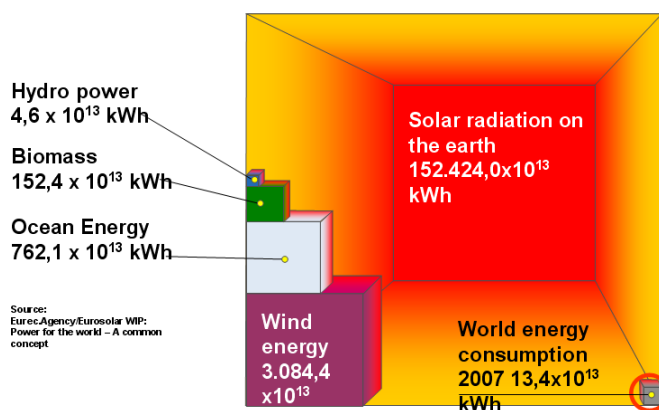


Fig. 1: Share of world energy consumption and the size of alternative energy sources.

### 2. Wind Mills

The industry of wind power generation has been witnessing a fast development in Europe and has been gaining a strong position on the global market. Number of wind mills in Europe 2008 is shown in figure 2. For instance, this industry employs more than 45,000 people in Germany. Significant is technological progress towards larger and larger wind generators and reduction of investment costs. While in 1992, 200kW units with the rotor diameter of 35 m were used, in 2000, 900kW units (rotor – 80m) were used. Currently, wind mills of 5 MW output and rotor of up to 129 m in diameter are being tested. The rotors are optimized in order to minimize sound emissions. Adjustable rotor blades are used to regulate the rotation speed. Nacelle of the wind mills are designed with a gear and asynchronous generators mounted by the majority of manufacturers (current share of approximately 59% of applications), or multi-pole generators right behind the rotor and efficient electronic rectifiers.

<sup>\*</sup> Ing. Luděk Němec: Bosch Rexroth spol. s r.o., Těžební 2, 627 00 Brno; CZ, e-mail: ludek.nemec@boschrexroth.cz



Fig. 2: Capacity of wind mills in Europe by the end of 2008.

Company Bosch Rexroth has been manufacturing drives and related technology for approximately 100 years. Since the beginning of the 90s, company REXROTH has been delivering gears for 3.2 MW equipment. Thus, the company was at the development of the wind mills right from the beginning. The cooperation with leading universities and dialogue with the global manufacturers of bearings help to increase the state-of-the-art level of these drives. Company Bosch Rexroth focuses its know-how and technical expertise on a wide spectre of products for applications of renewable sources' use. The specialized development centre is able to address both the issues of hydraulic/electric drives and hydraulic/control circuits and also specific features of these technologies. Thus, company Bosch Rexroth enhances its role on the market as a partner of choice for global manufacturers of wind mills. Description of wind mill is in the Fig. 3.

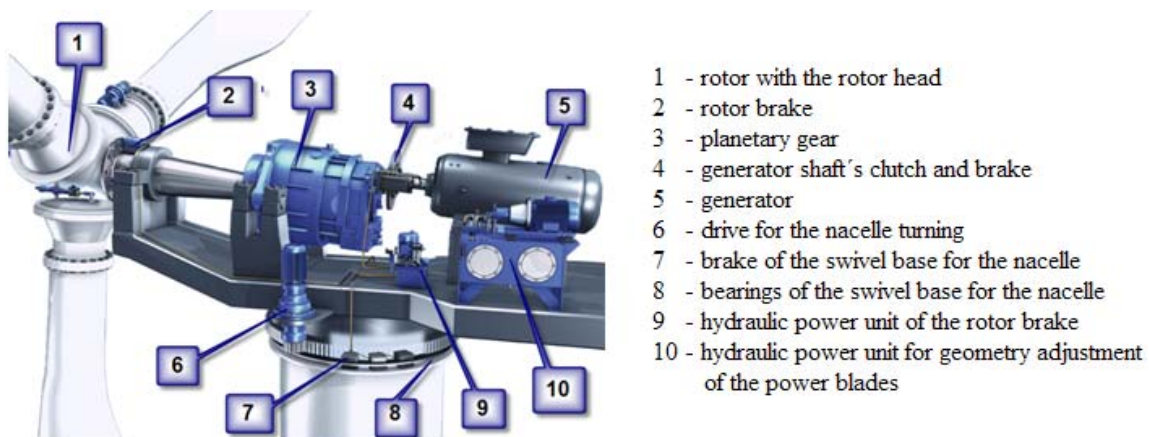
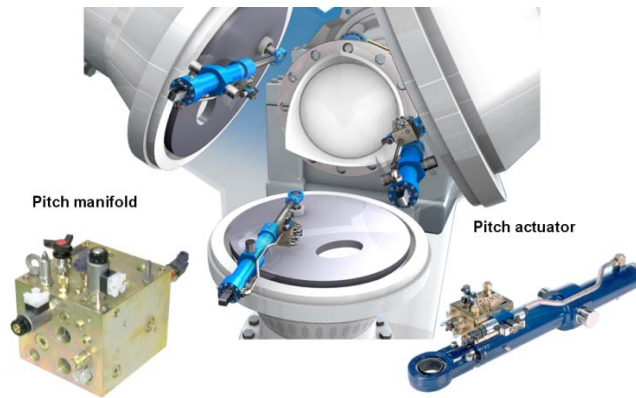


Fig. 3: Description of a wind mill.

### 3. Hydrostatic Systems of Wind Mills

The drive for hydraulic setting of the blades' geometry (Fig. 4) complies with all the requirements: accurate regulation for the position, compact design, high dynamics, long service life and excellent reliability. All these drives are tested on the test stand and, simultaneously, all the electrical quantities are mutually harmonized. This mutual approval of signals and harmonization of electrical characteristics allows a very fast setting up of the drives for operation right after their assembly on the site. Security against failure is provided by the logical interconnection of the respective components. Their functions are based on solely mechanical principle and thus secure high reliability. Should a failure state occur, blades of the turbine are adjusted for the safe end position with accumulator without any need of an external device.



*Fig. 4: Systems for the adjustment of rotor blades geometry.*

#### **4. Planetary Gears of Wind Mills**

Most wind mills use gears with a constant gear ratio which changes the rotation speed and torque between the rotor and the generator. The speed of the rotor is very slow and moves between 6 – 20 rev/min with high torque. The speed of the generator is between 900 – 2000 rev/min with low torque to achieve high efficiency and adjustment of the network frequency to 50 or 60 Hz.

Bosch Rexroth manufactures and delivers two-stage planetary gears for wind mills with the constant gear ratio from 70 to 150. Gears for the wind mills are a combination of planetary and spur gearings. The special technology of grinding of the teeth's surface secures a smooth running. The gears are also equipped with sensors for the oil pressure of the internal lubricating system and sensors for the oil heat. The gears may be custom-delivered including the sensors for monitoring the bearings vibrations with remote indication. The gear designed for generators of up to 2000 kW, with 50 – 120 gear ratio is showed on the figure 5. The gear is a combination of a planetary stage with two spur gear stages. The gears for generators of up to 5000 kW (see Fig. 6) are manufactured with 70 – 150 gear ratios. These gears are a combination of two planetary gear stages, one differential and two spur gear stages.



*Fig. 5: Design of gears for generators up to 2000 kW.*



*Fig. 6: Design of gears for generators up to 5000 kW.*

#### **5. Systems of wind mills with adjustable gear ratio of planetary gears and a synchronous generator**

The principle of regulation of a wind mill using the gear with adjustable gear ratio and a synchronous generator with constant rotation speed was successfully verified in a wind mill with output of 3 MW in 1987, for the first time.

A hydrostatic transmission on the second stage of the planetary gear allows smooth regulation of the gear ratio depending on the wind strength and speed of the wind mill rotor. The hydrostatic closed

## 6. Conclusion



## Resources

Hydraulic Power Units for Systems of Wind Turbines, Bosch Rexroth 02/2011



## FEM ANALYSES FOR DESIGN VERIFICATION OF AIRCRAFT ENGINE PARTS

M. Nesládek\*, M. Španiel\*

**Abstract:** *The presented paper documents the concept and some major results of the heat transfer and stress analyses performed on a cylinder and a cylinder head of an aircraft piston engine. Both stress and temperature fields were computed by the FEM software Abaqus/CAE. The stresses in the assembly were calculated as a consequence of major mechanical loads together with the influence of the steady state temperature field on deformation. Several modifications of geometry were considered in the sense of their influence on cooling performance and strength. It should be noted that these analyses are preliminary and were performed for the purpose of supporting the engine design optimization. In the future prospects, it is assumed that all these models will be calibrated by data measured on the engine prototype in order to get more relevant results for the planned engine series.*

**Keywords:** *FEM analysis, aircraft piston engine, cylinder, cylinder head.*

### 1. Introduction

The analyses presented here were a part of the project based on the cooperation between ADW, s.r.o. and Josef Božek Research Centre of Engine and Automotive Engineering. The aim of this project is to design a new small four-cylinder aircraft engine. The proposed conception is diesel with supercharging and common rail fuel injection system and it is supposed to be air-cooled.

The given task was mainly to analyze stresses in the structure with geometry shown in Fig. 1, resulting from service and assembly loads. The stress analysis was also focused on the problematic contact of the cylinder liner and the inner surface of the cylinder. Problems can arise here since the temperature expansion of cast iron, which the cylinder liner is made of, is about half of the value of the aluminum alloy. Especially in places with high temperature load, this difference can cause large contact gaps having unfavourable effect on the heat transfer from the combustion chamber. However, it was not possible to design the cylinder to be made exclusively of the aluminum alloy because of its poor tribological properties.

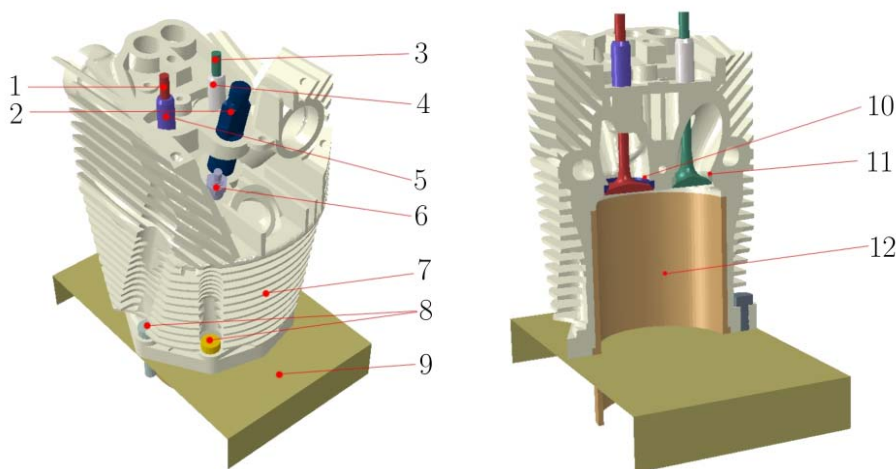


Fig. 1: CAD model of the assembly used for FEM model creation.

---

\* Ing. Martin Nesládek and assoc. prof. Ing. Miroslav Španiel, CSc.: Faculty of Mechanical Engineering CTU Prague, Technická 4; 166 07, Prague 6; CZ, e-mails: martin.nesladek@fs.cvut.cz, miroslav.spaniel@fs.cvut.cz

*Tab. 1: The list of parts included in the FEM model.*

<i>Link</i>	<i>Part name</i>		<i>Link</i>
<i>1</i>	<i>intake valve</i>	<i>cylinder and head body</i>	<i>7</i>
<i>2</i>	<i>injector</i>	<i>bolts</i>	<i>8</i>
<i>3</i>	<i>exhaust valve</i>	<i>engine block replacement</i>	<i>9</i>
<i>4</i>	<i>exhaust-valve guide</i>	<i>intake seat</i>	<i>10</i>
<i>5</i>	<i>intake-valve guide</i>	<i>exhaust seat</i>	<i>11</i>
<i>6</i>	<i>heating plug</i>	<i>cylinder liner</i>	<i>12</i>

## **2. Conception of the analyses**

The stress analysis of the cylinder and the cylinder head was conceived as an uncoupled problem of thermo-elasticity. This means that the first step was an evaluation of the steady-state temperature field from known boundary conditions consisting of film coefficient and temperature of gas contacting certain surface. Further, a static mechanical analysis followed where the previously calculated temperature field was applied together with mechanical loads in order to establish displacement and stress fields. The local temperature difference computed from the initial value and previously evaluated temperature field then caused additional displacements and stresses.

The above problem was solved using the Finite Element Method (FEM) implemented in the commercial code Abaqus. The preparation of numerical models was performed in the Abaqus/CAE GUI using the geometry imported from Pro/Engineer. The Python script was applied to simulate the finishing of seats and guides surfaces that are in contact with the valves. This eliminates their radial deformations after assembling them by pressing into the cylinder head.

### **2.1. FEM model description**

Some modifications of the original geometry were performed to avoid mesh generation problems and to keep the number of nodes reasonable. This is especially related to technological radiuses and chamfers making meshing algorithm to produce either poor or high-density mesh locally.

Mostly 3D continuum elements with linear interpolation of displacements were used for the model discretization. A different mathematical formulation was chosen only in the case of the cylinder liner which was meshed by continuum-shell elements allowing again keeping the number of nodes reasonably low.

It is convenient to create an identical mesh for both stress and heat transfer analyses to avoid problems with the correct upload of temperature to the mechanical model. Nevertheless, this was not possible in this case because of the complexity of the model and the fact that it had to be rebuilt several times for different reasons. For these situations, interpolation of nodal temperatures between dissimilar meshes is needed. The algorithm is also a part of the Abaqus code and gave satisfactory results for this purpose.

The stress analysis consisted of several computation steps respecting assembling and loading sequence. In a simplistic form (skipping the initiation steps added to the model for better convergence) these steps are as follows:

1. Assembling the valve guides and seats and the cylinder liner by pressing them into the cylinder and the cylinder head.
2. Contact constraint creation among valves and the appropriate seats and guides, activation of the traction force simulating the effect of valve springs.
3. Loading by bolt pretension simulating the connection between the cylinder and the engine block (the engine block was substituted by analytically rigid surface in this model).
4. Pressure loading of the combustion chamber.
5. Temperature loading of the completely assembled and mechanically-loaded model.

Due to the nature of the structure, the plastic state can be achieved only locally, e.g. in the valve guides or seats, and is marginal problem. Thus the mechanical behaviour of the material was assumed to be linear-elastic with variation of properties with temperature. In general, this is a problematic approach since obtaining temperature-dependent material data is nowadays still a rather difficult and expensive task. That is the reason why proper data were only obtained from different sources for the aluminum alloy and cast iron.

Number of constraints was defined between contacting pairs of parts. Mostly they were based on the Abaqus contact algorithm using surface-to-surface discretization and finite-sliding tracking approach (the simpler one, small-sliding gave biased results of contact quantities in the case of temperature-loading analysis step). For the friction model, the coefficient of friction equal to 0.15 was assumed and was enforced by the penalty method.

To support convergence, kinematical constraint was applied to the valve stems that prevented rotation around the longitudinal axes. The heating plug and injector were connected to the cylinder head by the tie constraint that keeps zero gradients of the displacement at the interfaces.

The boundary conditions of the inner cylinder and cylinder-head surfaces were calculated by the GT-POWER software package. The cooling effect of airflow in the cooling ribs was supplied by the temperature of air and film coefficients. They were estimated by analytical relations based on an analogy with airflow through straight and curved channels (Doleček et al., 2010).

A more detailed description of the model conception together with boundary conditions and material data can be found in Nesládek & Španiel (2011).

## 2.2. Design modifications compared by the analyses

The influence of some design modifications on the strength and cooling performance of the structure was studied. These modifications are summarized in the following list:

1. Influence of the oil gallery on cooling of the cylinder bottom and the exhaust duct
2. Adjustment of the cylinder-liner wall thickness (from 2.2 to 3.4 mm).
3. Outer geometry modifications, i.e. decreased thickness and increased number of the cooling ribs in the exhaust duct area. Together with these changes, the shape of the oil gallery was modified in compliance with technological recommendations.
4. Change in the cylinder-liner pressing overlap from 0.093 to 0.073 mm per diameter.

As a result of this comparison, the optimal geometry was chosen for further design process.

## 3. Results

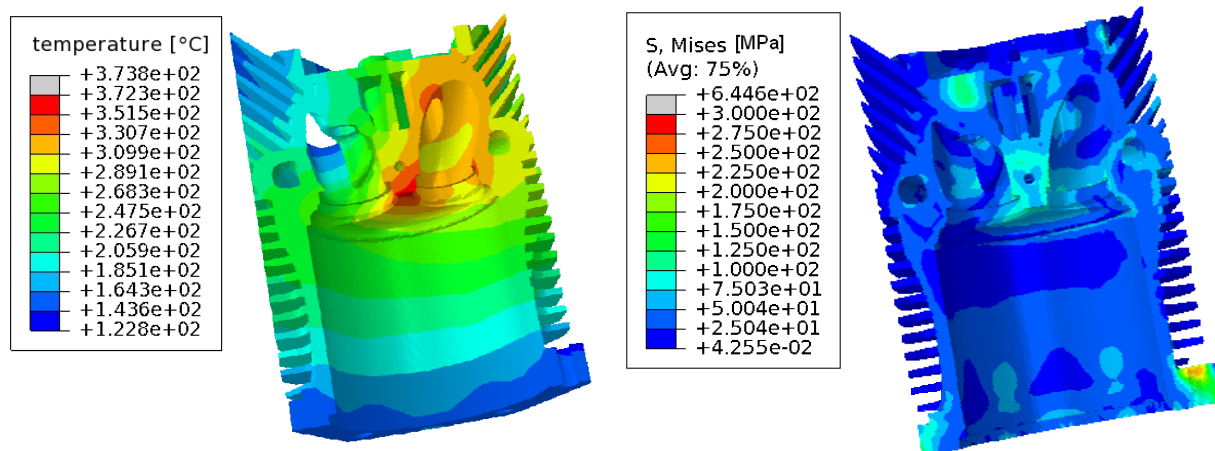
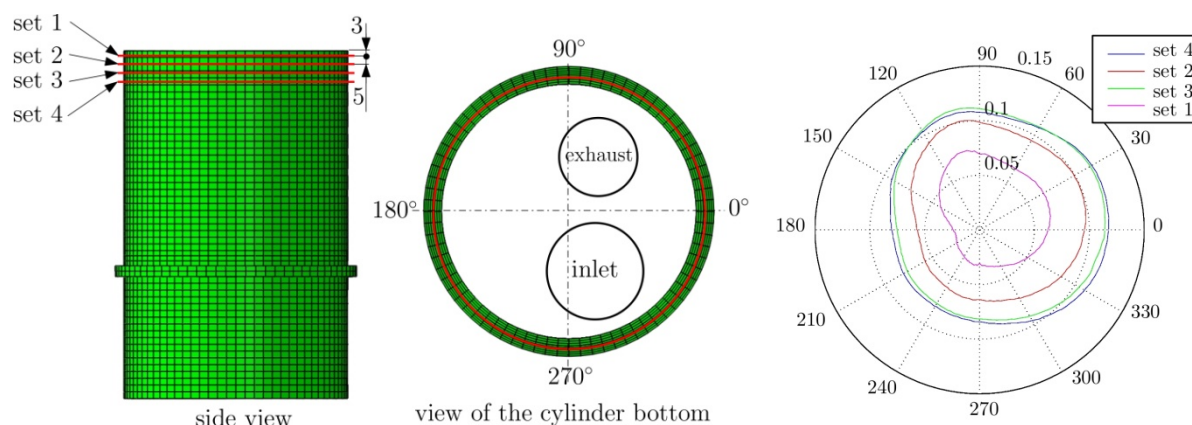


Fig. 2: An example of results – temperature field (left) and von Mises stress after all mechanical and temperature loads were applied to the structure (right).



*Fig. 3: A plot example of contact gaps between the cylinder and the cylinder liner (right); radial coordinate represents the contact gaps in mm, while tangential direction stands for circumferential position on the contacting surfaces; geometrical meaning is clarified by the two pictures on the left.*

Sample results of the main monitored quantities (i.e. temperature, stress and contact gaps between the cylinder and the cylinder liner) are shown in Fig. 2 and 3. As can be seen from the polar plot, relatively high contact gaps are predicted by the model. They were plotted for several data sets measured near the cylinder end where the gaps are at the maximum.

The maximum stresses in the cylinder liner were close to the strength limit when all the assumed loading was applied. At this point, high tensile stress components prevailed which could be severely damaging to cast iron. Raising the wall thickness to 3.4 mm has overcome this problem but with two side effects observed. The first one results in slightly larger contact gaps and a consequence of the second one is the increased temperature of the structure which is about 5 °C higher in the monitored hot spots. This is due to significantly lower heat conductivity of the cast iron compared with the aluminum alloy.

If the oil gallery is present in the structure, the temperature of the measured hot spots is about 25 °C lower. Thus it significantly contributes to lowering the stress response.

The modification of the outer design which was focused on the heat transferring surface enlargement leads to improved cooling performance, as expected. The obtained results show that it can eliminate problems with the increased cylinder liner thickness mentioned above.

#### 4. Conclusions

The previously described computation methodology and numerical model have the capability to predict response of the designed structure to different types of loading. Possible problems with strength and contact gaps were revealed in connection with the cylinder liner. Based on the computed values and their comparison the best-performing modifications were selected. They are mainly represented by the reinforced cylinder liner, presence of the oil gallery and enlarged outer surfaces for better cooling performance.

#### Acknowledgement

The authors would like to acknowledge the support of the subsidy programme Research and Development for Innovations of the Ministry of Industry and Trade of the Czech Republic.

#### References

- Doleček, V., Tichánek, R. & Macek, J. (2010) Crankshaft modal analysis, valve-operating mechanism optimization and boundary conditions for heat transfer analysis of a small diesel aircraft engine. Technical report no. Z10-15 (in Czech), Josef Božek Research Centre of Engine and Automotive Engineering.
- Nesládek, M. & Španiel, M. (2011) FEM analyses for design verification of an aircraft engine cylinder and a head of cylinder. Technical report no. 12105/10/28 (in Czech). Faculty of Mechanical Engineering CTU in Prague, Department of Mechanics, Biomechanics and Mechatronics.

## SELECTED APPROACHES TO MATHEMATIC MODELING OF RAIN-WIND INDUCED VIBRATIONS

A. Nevařil<sup>\*</sup>, P. Hradil<sup>\*</sup>, M. Mrózek<sup>\*</sup>

**Abstract:** *Large amplitude vibrations of cylindrical structural elements are observed when under the simultaneous action of wind and rain. Due to the action of wind and rain a translating water rivulet forms on the skew cable surface changing significantly the aerodynamic properties of the cable. General mathematic description of the problem is in the form of nonlinear equations, thus this problem is frequently simplified to 1 or 2 degree of freedom system. Another possibility of avoiding complex mathematic description is numerical simulation of the problem using CFD computer program. The paper describes the fundamental principles of modeling rain-wind flow interacting with an obstacle.*

**Keywords:** *Computational fluid dynamics, fluid-solid interaction, multiphase flow, rain-wind induced vibrations.*

### 1. Introduction

There are many real-world situations where engineering solutions use in advance mathematical modeling of multiphase flow, e.g. mixers and vessels analysis, spraying of fluid in fire mitigation or in agriculture. Wind-rain conditions also appear to be crucial in analysis of many everyday requirements.

There have been observed large amplitude vibrations of cables in some of the constructed cable suspended bridges in the last decades. These vibrations occur at simultaneous wind and rain conditions (RWIV) and were for the first time described on a French bridge (Wianecki, 1979). A detailed investigation of this phenomenon was performed in Japan where vibrations neither of vortex shedding nor galloping type were observed on cable-stayed bridge Meikonishi (Hikami & Shiraishi, 1988).

### 2. Types of Water Rivulet Vibration

Under the conditions of rain accompanied by low velocity wind, a water rivulet forms on the inclined cable. This rivulet dominantly changes aerodynamic properties of the cable. Its movement on the cable surface is influenced by wind action, inertia action of the cable and gravity force. Generally the formation and movement of the rivulet(s) can be divided into three types: two rivulets (one on the upper side, the other on the lower side of the cable) symmetrically vibrating (in phase vibration); two rivulets (one on the upper side, the other on the lower side of the cable) anti-symmetrically vibrating (anti-phase vibration); one rivulet (on the lower side of the cable), vibrating dominantly in the wake.

The opinions on the formation and principle of vibration differ. In (Matsumoto et al., 1992) is stated that the vibration is determined by the formation of the upper rivulet and the subsequent flow change in the cylinder wake (deviation of the resultant force out of the cylinder's gravity center axis). On the contrary, (Bosdogianni & Oliver, 1996) declare that predominantly, the position of the rivulet is of essence, not its vibrating movement. (Ruscheweyh, 1999) completely disagrees with this opinion and asserts that it is exactly the cyclic movement of the water rivulet which is crucial for the development of the phenomenon.

---

<sup>\*</sup> Ing. Aleš Nevařil, Ph.D., Ing. Petr Hradil, Ph.D., Ing. Michal Mrózek: Department of Structural Mechanics, Brno University of Technology, Veveří 331/95; 602 00, Brno; CZ, e-mails: nevaril.a@fce.vutbr.cz, hradil.p@fce.vutbr.cz, mrozek.m@fce.vutbr.cz

### 3. Models of rain-wind induced vibration

A cylindrical body is symmetric (with respect to the flow) and thus no galloping type vibration arises under common conditions. This fact significantly changes if a small body is attached to the cylindrical surface, altering the surrounding flow to non-symmetry. Similar conditions can be obtained by placing a simulated solid rivulet that is used in experimental analysis of RWIV. The mechanism of loosing stability under this type of vibration is known and can be understood using quasi-stationary models and analyses. An important role is played here by the so called den Hartog criterion, expressing the non-stability condition as

$$c_D + \frac{dc_L}{d\alpha} + 2\beta / K < 0, \quad (1)$$

where  $2\beta = c/m\omega$  and  $K = \rho d L_R U / 2m\omega$ . Detailed information can be obtained for example in (Van der Burgh & Hartono, 2004).

General mathematic description of cylinder vibration with attached moving water rivulet leads to nonlinear equations (Van der Burgh & Hartono, 2004). This problem is therefore often simplified to one degree of freedom (Ruscheweyh, 1999 and Wang & Xu, 2003) or two degrees of freedom problem (Yamaguchi, 1990). Another possibility how to avoid complex mathematic description is numerical simulation of the problem using computation fluid dynamics code, for example ANSYS CFX or Fluent (ANSYS Revision 12.0, 2009).

#### 3.1. Computational fluid dynamics model

Due to complexity of the wind, rain and cylinder interaction problem, it is usually necessary to apply many simplifications. Often, reduction of the dimension into 2D problem is utilized. Many input data (e.g. upper rivulet position, water mass vibrating together with the cylinder, aerodynamic properties of the system, etc.) must be obtained from scientific literature, or by wind tunnel experiments.

Mathematic theory of fluid flow in rain-wind-obstacle interaction problem is based on the behavior of incompressible Newtonian fluid. The governing equations of the fluid motion are Navier-Stokes equations

$$\rho \left( \frac{\partial \mathbf{v}}{\partial t} + \mathbf{v} \cdot \nabla \mathbf{v} \right) = -\nabla p + \mu \nabla^2 \mathbf{v} + \mathbf{S}, \quad (2)$$

where  $\rho$  is the fluid density,  $\mathbf{v}$  is the velocity vector,  $p$  is the pressure,  $\mu$  is the kinematic viscosity and  $\mathbf{S}$  if the body forces vector.

Aerodynamic properties of cylindrical body are changed by the formation of water film on the cylinder's surface. In this case for Eulerian-Eulerian inter-fluid transfer is used the homogeneous model. The free surface then uses the full buoyancy model described as

$$\frac{dp}{dz} = -(\rho - \rho_{ref})g, \quad (3)$$

where  $\rho_{ref}$  is the reference density,  $g$  is the gravity acceleration vector and  $z$  is the coordinate in the direction of the gravity vector.

Interaction of the fluids on their contact can be described, for example, according to Brackbill, where normal force (dependent upon curvature effect) and tangent force (dependent on variation in the surface tension coefficient) appear.

An illustrative example of the water film formation on the cylinder of  $D = 0.154$  m with uniformly distributed water source  $m = 1.389 \cdot 10^{-3} \text{ kg} \cdot \text{m}^{-2} \cdot \text{s}^{-1}$  around the surface of the cylinder is depicted in Fig. 1. Wind velocity with constant value of  $U = 9.5 \text{ m} \cdot \text{s}^{-1}$  and SAS SST (Scale Adaptive Simulation Shear Stress Transport) turbulent model were used in the simulation. Turbulence intensity in the inlet was 1 %; the outlet was defined using the relative pressure value of 0 Pa averaged over the whole outlet. Wall contact angle of the water was expected to be approx.  $70^\circ$ . In the discretization process authors use high resolution advection scheme and second order Euler backward scheme for time discretization.



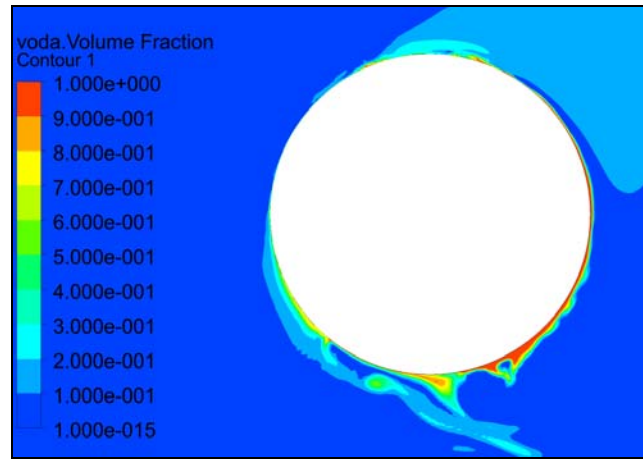


Fig. 1: Formation of lower rivulet in a cylinder wake (CFD analysis at  $Re = 2.5 \cdot 10^5$ ).

### 3.2. One and two degree of freedom models

One degree of freedom models usually presume that the rivulet vibrates with the same frequency as the cylinder, their amplitude ratio is constant and depends only on wind speed, and rivulet's mass can be neglected. Although the obtained equation of motion (4) can be easily solved, it is a problem to evaluate the actuating force  $F$ , see formula (5), as described in (Wilde & Witkowski, 2003).

$$\ddot{y} + 2\xi_S \omega \dot{y} + \omega^2 y = -\frac{F}{m} \quad (4)$$

$$F = \frac{\rho U_{rel}^2 d}{2} [c_L(\phi_e) \cos(\phi^*) + c_D(\phi_e) \sin(\phi^*)] \quad (5)$$

where  $\phi_e = \phi^* - \theta - \theta_i$ . The meaning of the individual quantities is identical with the following engineering model. Relative wind velocity  $U_{rel}$  and angle of rivulet position  $\theta$  are depicted in Fig. 2.

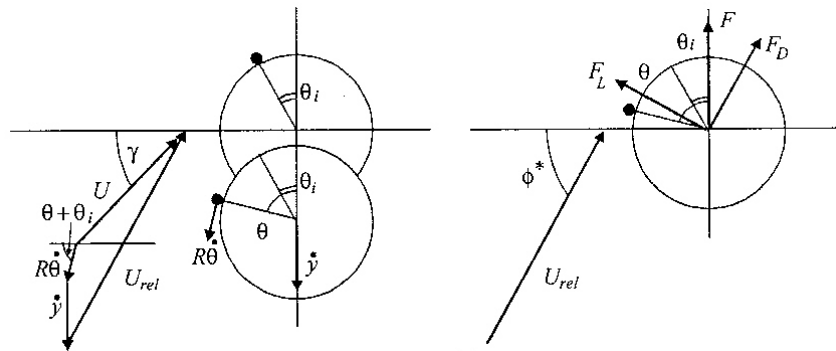


Fig. 2: Action of quasi-static wind force on cylinder (Wilde & Witkowski, 2003).

### 3.3. Engineering models

A simple mathematic model suitable for engineering application was derived by (Ruscheweyh, 1999). Forces action upon the cylinder are qualified by the following relations

$$\Delta F_x = \Delta c_D \frac{\rho}{2} \bar{V}^2 d L_R \sin(\omega_0 t + \phi_x), \quad (6)$$

$$\Delta F_y = \Delta c_L \frac{\rho}{2} \bar{V}^2 d L_R \sin(\omega_0 t + \phi_y) \quad (7)$$

where  $\rho$  is air density,  $d$  is cylinder diameter,  $L_R$  is rivulet length,  $\omega_0$  is natural frequency of cylinder vibrations,  $\bar{V}$  is wind mean velocity,  $\Delta c_D$  and  $\Delta c_L$  are first harmonic components of coefficient of drag and lift and  $\phi_x$ ,  $\phi_y$  are phase shifts between translations and forces acting upon the cylinder. Quantities  $\Delta c_D$ ,  $\Delta c_L$ ,  $\phi_x$  and  $\phi_y$  can be obtained from model test in wind tunnel or using the computational fluid dynamics.

An example of velocity field around a plane stationary cylinder model with diameter  $D = 0.154$  m and an attached virtual stationary rivulet at position  $\alpha = -30^\circ$  calculated by authors of the paper is presented in Fig. 3. Corresponding values of  $\Delta c_D$ ,  $\Delta c_L$  can be calculated from simulations carried out with different wind angle of attack.

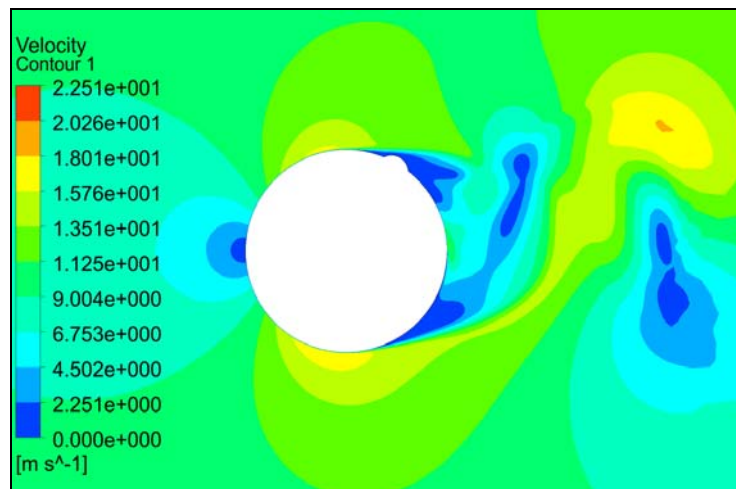


Fig. 3: Flow over a cylinder with permanently attached rivulet in the wake.

#### 4. Conclusions

The paper provides an introduction into the area of vibration of cylinder-like structural elements under the conditions of simultaneous wind and rain. Fundamental characteristics and types of RWIV are presented. There is introduced an overview of mathematic models of RWIV, from simple one or two degree of freedom systems to nonlinear model. The question of advantageous use of numerical CFD simulation for acquiring input data into simple models is discussed.

#### Acknowledgement

This outcome has been achieved with financial support of Czech Science Foundation, within the solution of research project MSM0021630519 “Progressive reliable and durable structures“ and also with financial support of the grant fund GRAFO BUT, Faculty of Civil Engineering.

#### References

- ANSYS Revision 12.0 (2009) *Documentation Manual*, SAS IP, Inc., www.ansys.com.
- Bosdogianni, A. & Oliver, D. (1996) Wind and rain induced oscillations of cables of stayed bridges. *J. Wind Eng. Ind. Aerodyn.* 64, pp. 171–185.
- Hikami, Y. & Shiraishi, N. (1988) Rain-wind-induced vibrations of cables in cable-stayed bridges. *J. Wind. Eng. Ind. Aerodyn.* 29, pp. 409–418.
- Matsumoto, M. & Shirashi, N. & Shirato, H. (1992) Rain-wind induced vibration of cables of cable-stayed bridges. *J. Wind Eng. Ind. Aerodyn.* 41–44, pp. 2011–2022.
- Ruscheweyh, H. P. (1999) The mechanism of rain-wind induced vibration, In: *Proc. 10th Int. Conf. Wind Eng.*, vol. 2, Denmark, Balkema, Rotterdam, pp. 1041–1047.
- Van der Burgh, A. H. P. & Hartono, J. (2004) Rain-wind-induced vibrations of a simple oscillator. *Int. J. Non-Linear Mech.* 39, pp. 93–100.
- Wang, L. & Xu, Y. L. (2003) Wind-rain-induced vibration of cable: an analytical model (1). *Int. J. Solids Struct.* 40, pp. 1265–1280.
- Wianecki, J. (1979) Cables wind excited vibrations of cable-stayed bridge. In: *Proc. of the 5th Int. Conf. of Wind Eng.*, Colorado, Oxford – New York, Pergamon Press, pp. 1381–1393.
- Wilde, K. & Witkowski, W. (2003) Simple model of rain-wind-induced vibrations of stayed cables. *J. Wind. Eng. Ind. Aerodyn.* 91, pp. 873–891.
- Yamaguchi, H. (1990) Analytical study on growth mechanism of rain vibration of cables. *J. Wind. Eng. Ind. Aerodyn.* 33, pp. 73–80.

## SIMULATION OF VIBROIMPACT ROTOR-SEALING RING SYSTEM

A. Nikiforov<sup>\*</sup>

**Abstract:** *Mathematical model describing the vibratory impact motion of rotor and floating sealing ring is suggested. Hertz's theory is used. The model allows studying the stationary and nonstationary oscillations of rotor and ring.*

**Keywords:** *Rotor, shaft, floating seal, impact.*

### 1. Introduction

In the new liquid-propellant rocket engines a fuel feed is fulfilled by turbine pumps of the latest generation (Patent of Russian Federation). Main working part of these machines is a rotor with floating seals which is the rings with comparatively high stiffness and established with small radial clearance (0.05...0.1 mm) (Childs, 1993). A short-term drift of rotor vibration above acceptable limits often causes the inflammation of turbine pumps due to the contacts between rotor and seals (Gurov & Shestakov, 2000). Vibration problem becomes more sharply in case of the flexible rotor. Lateral (bending) oscillations of rotor rotating with angular velocity close to the natural frequency are attended by considerable amplitudes. Obviously, the breakdown risk may be come to zero by means of theoretical research for vibratory impact regimes in the rotor-sealing ring system on the basis of correct mathematical model.

Choice of the impact model for solving of assigned task is made in agreement with the following. Local deformations occur in the rotor-sealing ring system at the impacts because an impact velocity and a hardness of system bodies correspond to the low-velocity impact not causing the bodies interpenetration. It is possible to neglect an effect of elastic oscillations and to consider a character of contact interactions at the impact same as in a static condition because a period of the slowest natural oscillations for the colliding bodies or a time of elastic waves passing in the bodies is much less than a impact duration. Such assumptions underlie static impact theory from which Hertz and other authors proceeded (Babitsky & Krupenin, 2001; Hunt & Grossley, 1975). The discrete models of impact describing deformations partially are its foundation. In these models it is supposed that bodies motion during impact is described by the differential equations of motion of a solid (by the equations «force - acceleration»  $P_y = m\ddot{x}$ ) which rather easily are solved by the known methods. Forces  $P_y$  acting during contacting take into account the viscid and elastic properties of real bodies and are modeled by a set of springs and dampers.

### 2. Mathematical model of rotor-sealing ring system

Considering constructive and dynamic features, the motion equations of researched mechanical system (Fig.1) should be written down taking into account the mass and inertia moment of rotor  $m$  and  $J$ , torsion torque  $M_0$ , rotor imbalance  $a = O_1G$ , equivalent stiffness of the shaft and supports  $k = k_{on}k_b/(k_{on} + k_b)$ , hydrodynamic and impact forces as components  $P_n$  and  $P_r$  initiated by the floating sealing ring  $m_k$  which is pressed to the frame  $\Pi_k$  of turbine pump by the pressure difference  $\Delta p = p_1 - p_2$ .

Due to small length of ring (in comparison with length of rotor) along the axis  $z$ , it is possible to suppose the rotor motion in the ring is flat. Thus let  $x, y$  are coordinates for an axis of rotor  $O_1, x_k, y_k$

---

<sup>\*</sup> Senior staff scientist Andrey Nikiforov, Ph.D.: Mechanical Engineering Research Institute of Russian Academy of Sciences; M.Khritonjevsky Lane, 4; 101990, Moscow; Russia, e-mail: n.andre@mail.ru

are coordinates for an axis of ring  $O_2$ ,  $x_G, y_G$  are coordinates for the line penetrating through the centre of rotor gravity  $G$ ,  $\theta$  is polar angle of centers line (angle between relative displacement  $e=O_1O_2$  and axis  $x$ ).

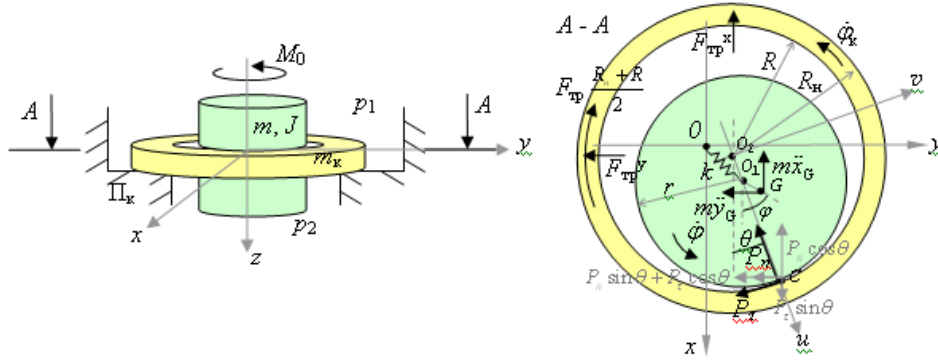


Fig. 1: Dynamical model for rotor with floating sealing ring.

Considering the model, it is possible to notice that the point  $O_1$  doesn't have a mass but has the inertia moment  $J$ , the forces  $P_n \sin \theta, P_n \cos \theta, m\ddot{x}_G$  and  $kx$  act in the direction  $x$ , the forces  $P_n \sin \theta, P_n \cos \theta, m\ddot{y}_G$  and  $ky$  act in the direction  $y$ . Besides around the point  $O_1$  the moments  $M_0, m\ddot{x}_G \cdot a \sin \varphi, m\ddot{y}_G \cdot a \cos \varphi$  and  $P_\tau r$  operate. Thus, the motion equations for a rotor are:

$$\begin{cases} 0 = -m\ddot{x}_G - kx - P_n \cos \theta + P_\tau \sin \theta \\ 0 = -m\ddot{y}_G - ky - P_n \sin \theta - P_\tau \cos \theta \\ J\ddot{\varphi} = M_0 + ma(\ddot{x}_G \sin \varphi - \ddot{y}_G \cos \varphi) - P_\tau r \end{cases}, \quad (1)$$

where  $\varphi$  is an angular displacement of rotor gravity center or a rotation angle of the rotor. Coordinates  $x, y$  are connected to coordinates  $x_G, y_G$  by the expressions  $x_G = x + a \cos \varphi$  and  $y_G = y + a \sin \varphi$  so:  $\ddot{x}_G = \ddot{x} - a\dot{\varphi}^2 \cos \varphi - a\ddot{\varphi} \sin \varphi$  and  $\ddot{y}_G = \ddot{y} - a\dot{\varphi}^2 \sin \varphi + a\ddot{\varphi} \cos \varphi$ . Substituting these expressions in (1), it is easy to transform the received motion equations to homogeneous and standard form for the oscillations theory:

$$\begin{cases} m\ddot{x} + b\dot{x} + kx = ma(\dot{\varphi}^2 \cos \varphi + \ddot{\varphi} \sin \varphi) - P_n \cos \theta + P_\tau \sin \theta \\ m\ddot{y} + b\dot{y} + ky = ma(\dot{\varphi}^2 \sin \varphi - \ddot{\varphi} \cos \varphi) - P_n \sin \theta - P_\tau \cos \theta \\ (J + ma^2)\ddot{\varphi} + ma(\ddot{y} \cos \varphi - \ddot{x} \sin \varphi) = M_0 - P_\tau r \end{cases} \quad (2)$$

The inevitable friction obstructing real rotor motion as a linear viscous force with proportionality coefficient  $b$  is brought here too.

In turbo-pumps the torque moment  $M_0$  depends on pressure of gases in front of the turbine and angular velocity  $\dot{\varphi}$ . This dependence is usually set as the joint characteristic of the turbine (the driving torque  $M_1$ ) and the pump (the resisting moment  $M_2$  induced by working load) (Grobov, 1959):

$$M_0 = M_1 - M_2 = M_n (2 - \dot{\varphi} / \omega_n) - M_n (\dot{\varphi} / \omega_n)^2 \quad (3)$$

where  $M_n$  and  $\omega_n$  is nominal torque moment and nominal angular speed accordingly.

Definitions for external forces in the equations system (2) are:

$$P_n = \begin{cases} k_n e, & \text{при } e < \delta \\ k_n e + P_y, & \text{при } e > \delta \end{cases}, \quad P_\tau = \begin{cases} (\dot{\theta} - 0.5\dot{\varphi})d_h e, & \text{при } e < \delta \\ (\dot{\theta} - 0.5\dot{\varphi})d_h e + fP_y, & \text{при } e > \delta \end{cases} \quad (4)$$

where  $\delta = R - r$  is value of radial clearance,  $k_n e$  is hydrodynamic normal force,  $(\dot{\theta} - 0.5\dot{\varphi})d_h e$  is hydrodynamic tangential force,  $P_y$  is impact force between rotor and ring,  $f$  is coefficient of sliding friction.

Here the model of "short seal» (Simonovsky, 1986) is used, that is allowable proceeding from the real sizes of floating sealing rings. Accordingly the hydrodynamic stiffness and damping of ring are:

$$k_h = \frac{\pi LR\eta}{2\delta(1+\eta)^2} \Delta p, \quad d_h = \frac{\pi\mu_c k_z L^3 R}{12\delta^3} \quad (5)$$

where  $\eta = 75\delta/L$ ,  $L$  is length of sealing surface of ring,  $\mu_c$  is fluid viscosity,  $k_z = 0.005\text{Re}$  is turbulence coefficient dependent on the Reynolds' number.

It is important to note also that in the turbo-pumps a pressure difference at the seals of rotor wheels depends on a pressure of turbine stage which is proportional to a square of angular velocity of rotor  $\Delta p = \Delta p_n \omega^2 / \omega_n^2$ , where  $\Delta p_n$  is the pressure difference appropriate to nominal angular velocity  $\omega_n$ . In this connection, hydrodynamic stiffness of sealing rings changes on dependences of kind  $k_h = k_h^n \omega^2 / \omega_n^2$ , where  $k_h^n$  is value for  $\omega_n$ . The hydrodynamic damping of sealing rings is proportional to number  $\text{Re} = 2\rho\delta w / \mu_c$ , where  $\rho$  is fluid density,  $w = \sqrt{2\Delta p\eta/\rho}$  is fluid velocity in the rings clearance. From here, hydrodynamic damping is proportional to rotor velocity  $d_h = d_h^n \omega / \omega_n$ .

Known Hertz's formula is used for definition of the impact force:

$$P_y = K e_{\max}^{3/2} = K^{2/5} \left( \frac{5}{4} M V^2 \right)^{3/5} \quad (6)$$

where  $K = 4/(3\eta)\sqrt{Rr(R-r)^{-1}}$  is coefficient dependent on materials  $\eta = (1-\mu_p^2)E_p^{-1} + (1-\mu_k^2)E_k^{-1}$  and curvature of rotor and ring surfaces at the contact point,  $\mu_p$ ,  $E_p$ ,  $\mu_k$  and  $E_k$  are Poisson's ratio and elastic modules for materials of rotor and ring,  $e_{\max}$  is the maximal approach of their centers,  $M = mm_k/(m+m_k)$  is equivalent mass,  $V=\dot{e}$  is approach velocity for the centers of rotor and ring before impact.

The motion equations of ring as a solid also can be written down proceeding from d'Alembert principle and taking into account that to the ring are applied same external forces  $P_n$  and  $P_\tau$  but other sign. Then (see Fig.1) the point  $O_2$  has mass  $m_k$  and inertia moment  $J_k$ , the forces  $P_n \cos\theta$ ,  $P_\tau \sin\theta$  and  $F_{\text{tp}}^x$  act in the direction  $x$ , the forces  $P_n \sin\theta$ ,  $P_\tau \cos\theta$  and  $F_{\text{tp}}^y$  act in the direction  $y$ . Besides around ring axis the moments  $P_\tau R$  and  $F_{\text{tp}}(R_n+R)/2$  operate. Thus, the required motion equations of sealing ring are:

$$\begin{cases} m_k \ddot{x}_k = P_n \cos\theta - P_\tau \sin\theta - F_{\text{tp}}^x \\ m_k \ddot{y}_k = P_n \sin\theta + P_\tau \cos\theta - F_{\text{tp}}^y \\ J_k \ddot{\varphi}_k = P_\tau R - F_{\text{tp}}(R_n + R)/2 \end{cases} \quad (7)$$

where  $F_{\text{tp}}^x = F_{\text{tp}} \dot{x}_k / \sqrt{\dot{x}_k^2 + \dot{y}_k^2}$ ,  $F_{\text{tp}}^y = F_{\text{tp}} \dot{y}_k / \sqrt{\dot{x}_k^2 + \dot{y}_k^2}$ ,  $F_{\text{tp}} = fN$ ,  $N = F_{\text{np}} + \Delta p S_{\text{tp}} + m_k g$ ,  $S_{\text{tp}} = \pi(R_n^2 - R^2)$  is friction surface of ring about the turbo-pump frame,  $g$  is gravitational acceleration,  $F_{\text{np}}$  is force of an axial spring (it is widely used in turbine pumps of the latest generation).

Hydrodynamic and impact forces connect the rotor and ring in closed system. For bunch of equations (2) and (7) it is necessary to express relative displacement  $e$  and polar angle  $\theta$  through coordinates of the rotor centre  $x$ ,  $y$  and coordinates of the ring centre  $x_k$ ,  $y_k$ .

Returning to Fig. 1, it is possible to find  $x - x_k = e \cos\theta$  and  $y - y_k = e \sin\theta$  consequently:

$$e = \sqrt{(x - x_k)^2 + (y - y_k)^2}, \quad \cos\theta = \frac{x - x_k}{e}, \quad \sin\theta = \frac{y - y_k}{e} \quad (8)$$

Using the appropriate derivative expressions  $\dot{x} - \dot{x}_k = \dot{e} \cos\theta - e\dot{\theta} \sin\theta$  and  $\dot{y} - \dot{y}_k = \dot{e} \sin\theta + e\dot{\theta} \cos\theta$ , it is possible to obtain from first of them:

$$\dot{e} = \frac{\dot{x} - \dot{x}_k + e\dot{\theta} \sin\theta}{\cos\theta}, \quad \dot{\theta} = \frac{\dot{e} \cos\theta - (\dot{x} - \dot{x}_k)}{e \sin\theta}.$$

Further substituting the expression for  $\dot{e}$  initially and then for  $\dot{\theta}$  in second of them and also taking into account (8), it is possible to obtain to required dependences:

$$\dot{e} = \frac{(x - x_k)(\dot{x} - \dot{x}_k) + (y - y_k)(\dot{y} - \dot{y}_k)}{e}, \quad \dot{\theta} = \frac{(\dot{y} - \dot{y}_k)(x - x_k) - (\dot{x} - \dot{x}_k)(y - y_k)}{e^2} \quad (9)$$

The received set of equations (2) and (7) together with conditions (4) and dependences (3), (5), (6), (8), (9) is mathematical model and describes the impact dynamics of considered system.

### 3. Conclusions

Integration of these equations is possible by the only numerical methods. Calculation of transient impact oscillations of rotor-sealing ring system is made by the Runge-Kutta method. Results are presented in the Fig. 2.

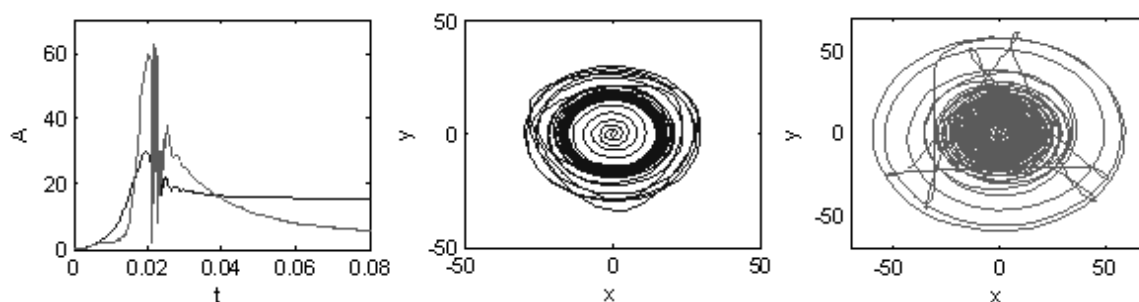


Fig. 2: Amplitudes ( $A = \sqrt{x^2 + y^2}$ ) and trajectories ( $x, y$ ) of transient impact oscillations of flexible rotor and floating sealing ring.

It is start up of rotor (from 0 to  $\omega_n$ ). In the beginning the motion is non-impact. But further there are eight impacts occurring at the passage of critical speed. It is visible from characteristic two jumps and six loops in the ring trajectory. Impact regime in system after the resonance is replaced by the non-impact regime again.

The developed model allows studying the stationary and nonstationary oscillations of rotor and ring at the impacts between them for specified parameters (Banakh & Nikiforov, 2007, 2008).

### Acknowledgement

The financial support provided by the Russian Foundation for Basic Research and RFBR Grant No 10-08-00500-a award scheme is gratefully acknowledged.

### References

- Device patent of Russian Federation RU 2083881. Turbo-pump.
- Childs D. (1993) Turbomachinery Rotordynamics. Canada: John Wiley and Sons. 476 p.
- Gurov V.I., Shestakov K.N. (2000) Engineering of Cryogenic Turbo-pumps. Moscow: Informkonversia. 132 p. (In Russian).
- Babitsky V.I., Krupenin V.L. (2001) Vibration of Strongly Nonlinear Discontinuous Systems. Springer, 330 p.
- Hunt K.H., Grossley F.R.E. (1975) Coefficient of Restitution Interpreted as Damping in Vibroimpact. // ASME Journal of Applied Mechanics. - No 6. - Vol. 42, Series E. Pp. 440-445.
- Grobov V.A. (1959) Non-stationary Rotor Vibration in Turbo-machines at Passing of Critical Speeds. Riga: RVIAVU. 120 p. (In Russian).
- Simonovsky V.I. (1986) Dynamical Stability and Non-linear Rotor Vibration of Centrifugal Machines. Khar'kov: Vishcha shkola. 128 c. (In Russian).
- Banakh L., Nikiforov A. (2007) Vibroimpact regimes and stability of system "Rotor—Sealing Ring", Journal of Sound and Vibration, Vol. 308, pp. 785–793, online at <http://www.sciencedirect.com>
- Banakh L., Nikiforov A., Panovko G. (2008) Vibroimpact Motion of Rotor taking into account Friction at the Contact. Proceedings of 6<sup>th</sup> EUROMECH Nonlinear Dynamics Conference «ENOC 2008», Saint-Petersburg. URL: <http://lib.physcon.ru/?item=1605>



## NUMERICAL SIMULATIONS OF RECOVERY HEAT EXCHANGERS

P. Novotný<sup>\*</sup>, T. Vít<sup>\*\*</sup>, P. Dančová<sup>\*\*\*</sup>

**Abstract:** *This paper is focused on evaluation and comparison of air-air heat exchangers of plate type used for retrieving the heat from the waste air. The first part of this paper shows how it is possible to evaluate and compare each exchanger with another one. Process and procedure of numerical simulation is described in the main part. The procedure involves selecting an appropriate geometry of the exchanger, computational mesh generating, defining boundary conditions and the choice of a viscous flow model. Three geometrical types of heat transfer surface were compared in this work. Results of numerical simulations were compared with experimental measurement.*

**Keywords:** *Recovery heat exchangers, heat recovery, numerical simulations, Fluent.*

### 1. Introduction

Saving every kind of energy is an important requirement. Thermal energy is the most important in environmental technology. For that reason equipment for heat recovery from waste air is supplied to system of power ventilation. This part of ventilation unit can take back heat (or cold in summertime) from a waste outlet air and transfer it to a fresh inlet air. This work deals with recovery heat exchangers which have air flows separated by a solid wall. Specially shaped aluminum foil is used for a parallel heat transfer surface. Heat exchangers have a cross-contra flow set of air flow. Heat transfer plates are implanted to the body of exchanger.

Production of a stamping tool is the most expensive operation when designing and optimizing the heat transfer surface. For this reason author of this paper tried to solve this problem by numerical simulation of the flow between heat transfer plates.

### 2. A way of evaluation of a recuperative heat exchanger for heat recovery

#### 2.1. Experiment

Results of measurements must be comparable with results of numerical simulations. The experiment respected some principles of European norm ČSN EN 308. Mass flow rates of inlet and outlet side were the same. Each exchanger was measured at five different volume flows from 100 up to  $500 \text{ m}^3 \cdot \text{hod}^{-1}$ . Waste air stayed at  $25^\circ\text{C}$  and its air humidity stayed above the condensation level of heat transfer surface (wet bulb temperature c.  $14^\circ\text{C}$ ), so it could meet cold fresh air with  $5^\circ\text{C}$ . In this case, dry air was taken as flow medium in numerical simulation.

#### 2.2.1. Pressure loss of a recovery heat exchanger

Pressure loss  $\Delta p_{rek}$  of a recovery heat exchanger is a very important parameter in determining the quality of exchanger. The loss increases a total pressure loss in air distribution. In our case the loss only depends on air mass flow. Intensive heat transfer on surface by convection is desired as well as lowering the pressure loss. High pressure loss will increase operational costs for electric gear of radial ventilator.

---

<sup>\*</sup> Ing. Petr Novotný: Technical University in Liberec; Studentská 2; 461 17, Liberec; CZ, e-mail: novotnypck@seznam.cz

<sup>\*\*</sup> assoc. prof. Ing. Tomáš Vít, Ph.D.: Toptec - Institute of Plasma Physics AS CR, v.v.i.; Skálava 89; 511 01, Turnov; CZ, e-mail: vit@ipp.cas.cz

<sup>\*\*\*</sup> Ing. Petra Dančová: Institute of Thermomechanics AS CR, v.v.i.; Dolejškova 1402/5; 182 00, Prague 8; CZ, e-mail: petra.dancova@tul.cz

### 2.2.2. Recuperation efficiency of recovery heat exchangers

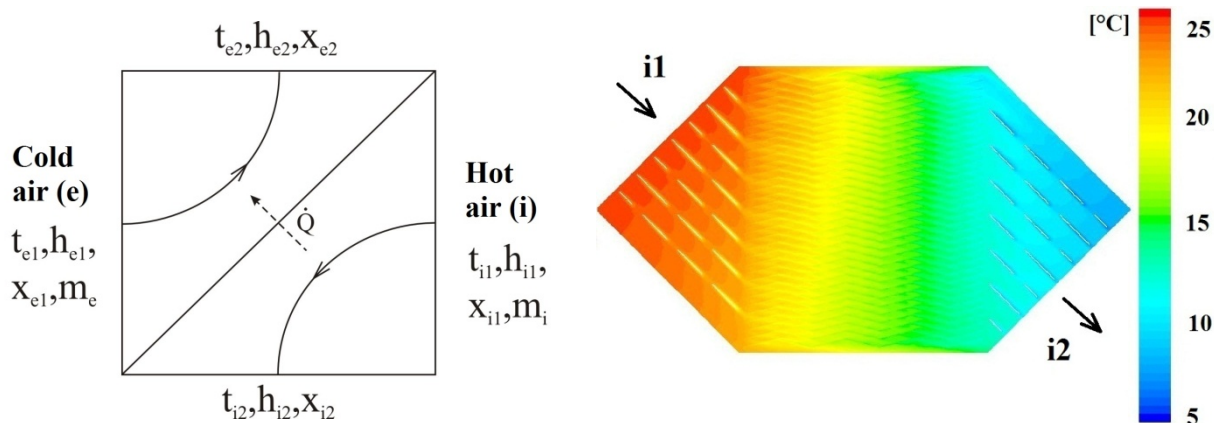


Fig. 1: Scheme of recuperative heat exchangers and a sample of the heat transfer surface (temperature field).

Heat fluxes that vent through a plate are equal in a heat insulated system. One of the main characteristics is heat recuperate efficiency  $\eta_{ZZT}$ . It is defined as:

$$\eta_{ZZT} = \frac{\dot{m}_i \cdot (h_{i1} - h_{i2})}{\dot{m}_i \cdot h_{i1} - \dot{m}_e \cdot h_{e1}} = \frac{\dot{m}_e \cdot (h_{e2} - h_{e1})}{\dot{m}_i \cdot h_{i1} - \dot{m}_e \cdot h_{e1}} \quad (1)$$

where  $\dot{m}$  is mass flow rate and  $h$  is specific enthalpy of air. If condensation doesn't come and mass flow rates are the same, the relation is:

$$\eta_0 = \frac{t_{e2} - t_{e1}}{t_{i1} - t_{e1}} \quad (2)$$

This means ratio of warmed-up air temperature increment and difference between air inlet temperatures. Recuperation efficiency depends on many parameters, but in our case it only depends on volume flow rate of fresh air.

### 2.3. Numerical simulation

First of all geometry of a model must be defined. Because an exchanger is large (c. 500 x 300 x 200 mm), a model was chosen as only a small part of the whole exchanger. A model consists of one layer between plates, which represents a warm outlet air. A layer was between half layers of a cold inlet air as a sandwich (Fig. 2). All models are 3D and consist of hexahedrons mainly. Numerical mesh was made in MSC Marc Mentat software and boundary conditions were supplied in Gambit 6.3.26. Numbers of elements in a model were from 1.2 up to 2 million. Creating a computation model consumes most of the time. Spacing between plates in exchangers was 2.0, 2.2 and 2.6 mm. Thickness of a plate was 0.1 mm, but it was neglected in a model. It was published in the diploma work Recovery heat exchangers by Petr Novotný (2010).

Important part of producing the computation model is setting of suitable boundary conditions (Fig. 2). Boundary condition of upper parallel surfaces was set as *periodic*, heat transfer surface was set as *wall* with a possibility of heat flux. Every contact surface was set as *interface* (cross and contra-flow parts were made separately).

Computations of simulation were done in Fluent 6.3.26 software by Ansys Fluent Inc., where *pressure inlet* boundary conditions (temperature and pressure) on inlets of air surface were defined. Heat transfer surfaces created small gaps between each other, which allowed us to approximately calculate Reynolds number. In this case maximum Reynolds number was 1500 which is under critical value (without considering next shanking). Viscous models of turbulence  $k-\epsilon$ ,  $k-\omega$  and viscous *laminar* model were tested by author. Results from numerical simulations show their applicability for this type of problems.

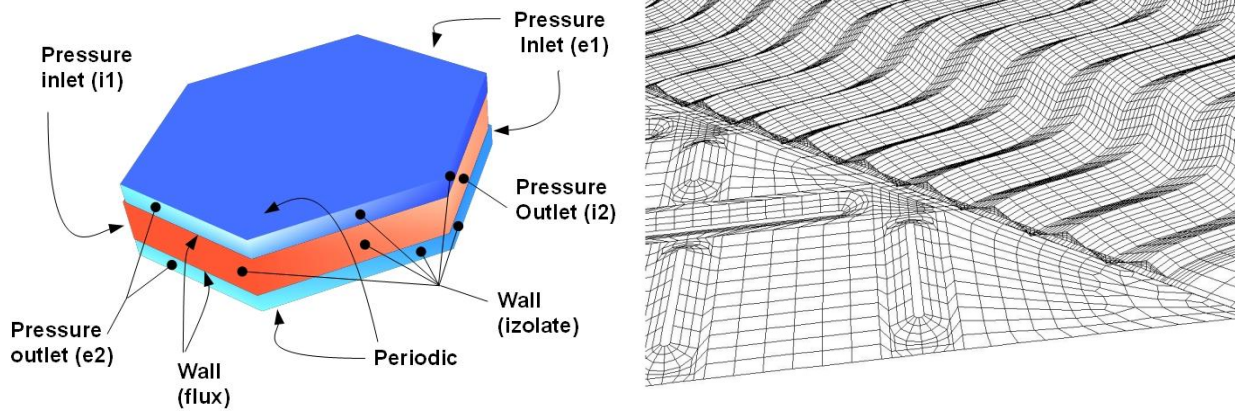


Fig. 2: Boundary conditions and a sample of computational mesh.

Air was considered an ideal gas in numerical simulations during a steady mode. Useful values were detected in important sections and surfaces. The most important values are average outlet temperatures, pressure loss between inlet and outlet of exchangers and heat flow through the heat transfer surface.

#### 2.4. Comparison of experiment and numerical simulation

Values of boundary conditions were set on the basis of measurement results for objective comparing simulation and experiment. All characteristics depend on fresh air volume flow. Efficiency of heat recuperator  $\eta_0$  can be determined by equation No. 2.

Heat recuperate efficiency and pressure loss with viscous turbulence model  $k-\varepsilon$  were preferable than in experiment. A viscous turbulence model  $k-\varepsilon$  is more suitable for developed turbulent flow (in this case Re number was from 500 up to 1500 in inlet of exchanger's gap). For this reason  $k-\varepsilon$  model isn't suitable for numerical simulations of plate exchangers.

A model  $k-\omega$  respects areas near wall during turbulence flow better. In this case values of thermal efficiency and pressure loss were closer to experiment results. This viscous model is more suitable for flow between parallel formed plates.

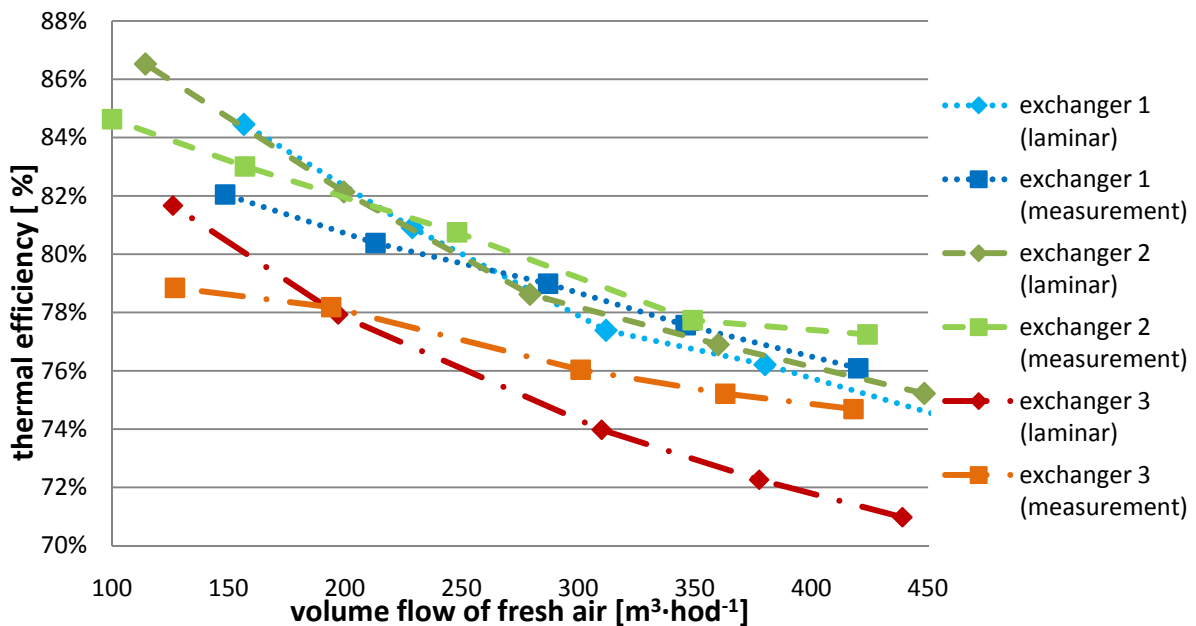


Fig. 3: Comparison of thermal efficiency from measurement and simulation with viscous laminar model.

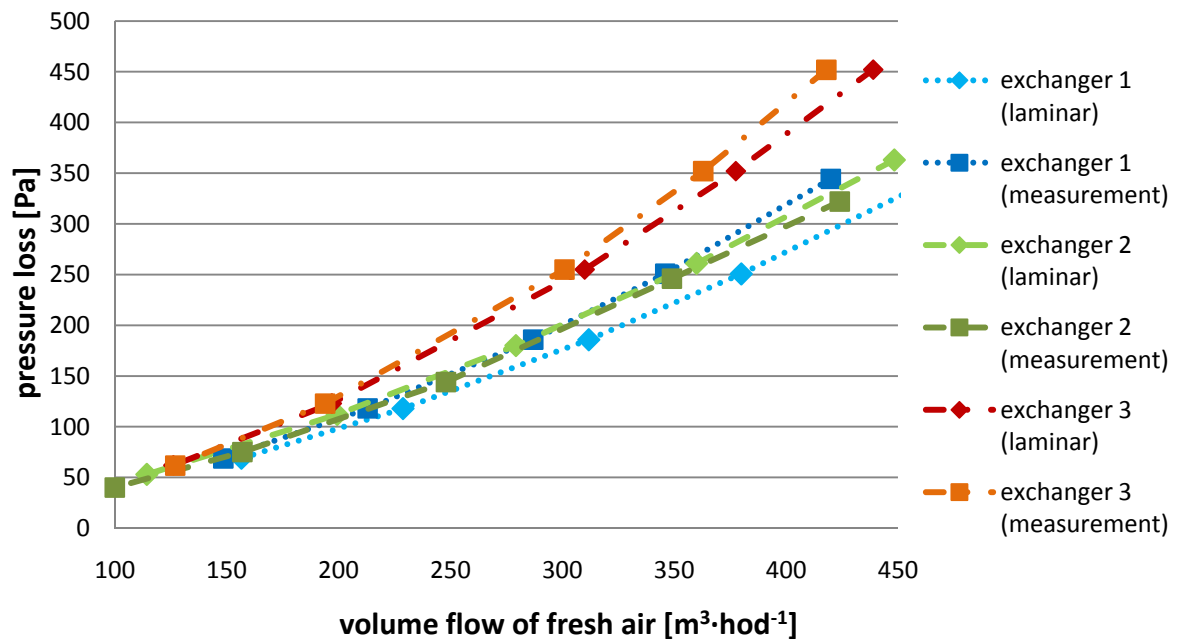


Fig. 4: Comparison of pressure loss from measurement and simulation with laminar model.

In the last part of this work the *laminar* viscous model of flow was set at Fluent. A laminar model results respected measurement much more. We can see comparison of thermal efficiency (Fig. 3) and pressure loss (Fig. 4). Bigger difference of results is expected at greater volume flows, because there might develop a turbulence of the flow. *Laminar* viscous model should be the most suitable one for a development of recuperative heat exchangers with parallel heat transfer surface.

### 3. Conclusions

We could look into some interesting areas in an unsteady flow simulation in the next step of the research. Considering a condensation of air humidity on the heat transfer surface in numerical simulations would be beneficial. Another aim is to develop a heat transfer surface that can transport air humidity (without phase change).

### Acknowledgement

We gratefully acknowledge the support of the Technological Agency of the Czech Republic, project number TA01020313.

### References

- Novotný, P. (2010) Recovery heat exchangers, diploma work, Liberec: Technical University in Liberec.
- Lienhard, J. H. (2005) A Heat Transfer Textbook, Phlogiston Press, MIT.
- Shaw, C.T. (1992) Using Computational Fluid Dynamics, Prentice Hall.
- Ansys Fluent: FLUENT 6.3 User's Guide.
- ČSN EN 308 (1998) Heat Exchangem.
- Székyová, M., Ferst, K., Nový, R. (2006) Větrání a klimatizace, Bratislava: Jaga.

## VERIFICATION OF THE DESIGN RELIABILITY OF STEEL STRUCTURES

A. Omishore\*

**Abstract:** *The verification of the design reliability of a steel element according to the concepts of standards EUROCODE 3 and EN1990 is presented in the article. Reliability analysis is used for the determination of the probability of failure, which is evaluated using the Monte Carlo methodology. Reliability analysis presents a valuable tool for the verification of reliability indices of the fore mentioned standards, generalization of evaluated results and further development of design methodology of structures according to the limit state theories. The article presents an overview of random input imperfections of steel structures whose histograms and statistical characteristics have been monitored and measured over a long time period. The completeness of statistical information on input data for the purpose of utilization in probabilistic studies is discussed. The quantification of uncertainty of the statistical characteristics of difficult to measure imperfections utilizing the theory of fuzzy set is illustrated on a numerical example. The analysis of the influence of fuzzy uncertainty of random input variables on the fuzzy uncertainty of failure probability is presented. Uncertainty of computational models is discussed and modern instruments utilizable in the analysis of these uncertainties are listed. The analysis of the load carrying capacity of a steel plane frame with compression members is presented.*

**Keywords:** *Design reliability, failure probability, random, Monte Carlo, limit state, fuzzy, uncertainty.*

### 1. Introduction

At present, the best method in practice for the verification of structural reliability of standards is according to the limit state methods. In standard procedures characteristic and design values, which guarantee design reliability, are used. Design values are obtained with the aid of partial safety factors, which present the basic indicators of the reliability of structural design. Reliability analysis may be performed using a number of methods, see e.g. (Kala, 2008; Gottvald, 2010). Probabilistic methods are also frequently used, see e.g. (Li et al., 1995; Kala et al., 2010). A prerequisite for the utilization of probabilistic methods is that ample statistical information is available from experimental research; see e.g. (Melcher et al., 2004; Strauss et al., 2006; Karmazínová et al., 2009). This article focuses on the analysis of the influence of partial safety factors of standards EUROCODE 3 and EN 1990 on the resulting structure reliability. The probabilistic analysis is supplemented with fuzzy analysis enabling the analysis of the effects of epistemic uncertainties (Kala, 2007; Kala, 2008). The fuzzy inputs were considered as model uncertainties in determining the load action and load-carrying capacity effects. The fuzzy analysis of output failure probabilities was evaluated according to the general extension principle (Zadeh, 1965; Möller & Reuter, 2007).

### 2. Verification of design procedures of structural stability

A simplified example of a compression member under the load effects of permanent load action  $G$  in combination with single variable load action  $Q$  is considered for the elaboration of a parametric study. The reliability design condition according to EC3 and EN1990 may be expressed as:

$$\gamma_G \cdot G_k + \gamma_Q \cdot Q_k \leq R_{A\chi} \cdot f_{yk} / \gamma_M \quad (1)$$

where  $R_{A\chi} = \chi A$  is the product of buckling coefficient  $\chi$  and nominal cross-sectional area  $A$ ,  $\gamma_M$  is the material partial safety factor, and  $G_k$ ,  $Q_k$ ,  $f_{yk}$  are characteristic values of load actions and yield strength

---

\* Ing. Abayomi Omishore, Ph.D.: Institute of Structural Mechanics, Brno University of Technology, Faculty of Civil Engineering, Veveří Street 95; 602 00, Brno; CZ, e-mail: omishore.a@fce.vutbr.cz

respectively. Reliability of design is ensured by partial safety factors  $\gamma$ . The condition of design reliability (1) can be rewritten as the inequality of design load action  $F_d$  and design load-carrying capacity  $R_d$ . It was assumed in the reliability study that the design load action is equal to the design load-carrying capacity,

$$F_d = R_d \quad (2)$$

i.e., the structure is designed economically with maximum load carrying capacity. Characteristic values  $G_k, Q_k$  are expressed using the ratio  $\delta$  of load action  $Q_k$  to the total load action  $G_k + Q_k$ :

$$\delta = \frac{Q_k}{G_k + Q_k} \quad (3)$$

Characteristic values  $G_k$  and  $Q_k$  are evaluated from the relation:

$$1.35 \cdot G_k + 1.5 \cdot Q_k = 382.3 \text{ kN} \quad (4)$$

Equation (4) is derived from (1) for partial safety factors  $\gamma_G = 1.35$ ;  $\gamma_Q = 1.5$  (EN1990) and  $\gamma_M = 1.0$  (EC3). The value  $R_d = 382.3 \text{ kN}$  on the right-hand side of the equation is the design load carrying capacity of strut profile IPE 200 of length 2.1m and non-dimensional slenderness  $\bar{\lambda} = 1.0$  calculated acc. to EC3:

$$R_d = \frac{\chi_b \cdot f_y \cdot A_n}{\gamma_{M1}} = \frac{0.597 \cdot 235 \text{ MPa} \cdot 2.7248 \cdot 10^{-3} \text{ m}^2}{1.0} = 382.3 \text{ kN} \quad (5)$$

where  $\chi_b$  is the buckling coefficient for the buckling strength curve  $b$ ,  $A_n$  is the nominal cross-sectional area evaluated from the nominal values of the cross section comprised of rectangular segments, and  $f_{yk}$  is the characteristic value of yield strength.

## 2.1. Probabilistic verification of design procedures of structural stability

The random characteristics of load action effects  $G$  and  $Q$  are obtained from the characteristic values listed in (Kala, 2007). It was assumed for the dead load that the characteristic value  $G_k$  is also the mean value of the normal distribution. Furthermore a variation coefficient of 0.1 was assumed according to (Kala, 2007). Gumbel distribution with mean value  $m_Q = 0.6 Q_k$  and standard deviation  $S_Q = 0.21 Q_k$  was considered for the variable load in accordance with (Kala, 2007). According to EUROCODE 3, the failure probability of a strut occurs when the reliability condition (6), in which  $R$  is the random load-carrying capacity, and  $G, Q$  are random load action effects, is not satisfied.

$$G + Q < R \quad (6)$$

The variable quantifying reliability or unreliability is the probability that condition (6) isn't fulfilled during the life span of the structure with regard to structural, aesthetical, service, energetic, economic and ecological aspects. Attainment of the limit state or generally occurrence of failure cannot be absolutely eliminated due to technical and economical reasons and hence we try to design the structure so that the probability  $P_f$  that failure occurs is very small.

The failure probability  $P_f$  is the most important and objective indicator of reliability and is commonly related to a certain reference time (usually 50 to 100 years). Within this time interval the given degree of reliability should be maintained. The load carrying capacity  $R$  in (6) may be obtained from the response function described in (Kala, 2009):

$$R = - \frac{\sqrt{A^2 \cdot Q^2 + 2 \cdot A \cdot F_{cr} \cdot W_z \cdot (|e_0| \cdot F_{cr} - f_y \cdot W_z) + F_{cr}^2 \cdot W_z^2} - A \cdot Q - F_{cr} \cdot W_z}{2 \cdot W_z} \quad (7)$$

where  $e_0$  is the amplitude of initial strut curvature formatively identical to a half-wave of the sine function,  $A$  is cross-sectional area,  $F_{cr}$  is Euler's critical force of a bilaterally hinged steel strut,  $W_z$  is the sectional modulus to axis  $Z$  (axis perpendicular to the flange around which the section bends during buckling), and  $f_y$  is the yield strength.



## 2.2. Input random quantities

Statistical characteristics  $h$ ,  $b$ ,  $t_1$ ,  $t_2$ ,  $f_y$  were considered as histograms of experimentally obtained results (Melcher et al., 2004; Kala et al., 2009). Young's modulus was considered as a Gaussian probability distribution with statistical characteristics given acc. to (Fukumoto et al., 1976). According to results of experimental research (Fukumoto et al., 1976), the dominant shape of initial curvature is given as a half-wave of the sine function. A Hermite four-parametric probability distribution, which makes provision for skewness and kurtosis, was considered for the amplitude of initial imperfection  $e_0$ , see Fig. 1. We know with certainty that the mean value and skewness of symmetrical elements comprising of IPE profiles is equal to zero. Standard deviation of the Hermite density function is designated on the assumption that 95 % of the realizations of the amplitude of initial imperfection  $e_0$  are found within the tolerance limits  $\langle -3.15; 3.15 \rangle$  mm of the standard EN 10034. Kurtosis is given as a symmetric fuzzy number, see Figure 1. The support of the membership function is  $\langle 1.816; 4.184 \rangle$  and the kernel = 3.

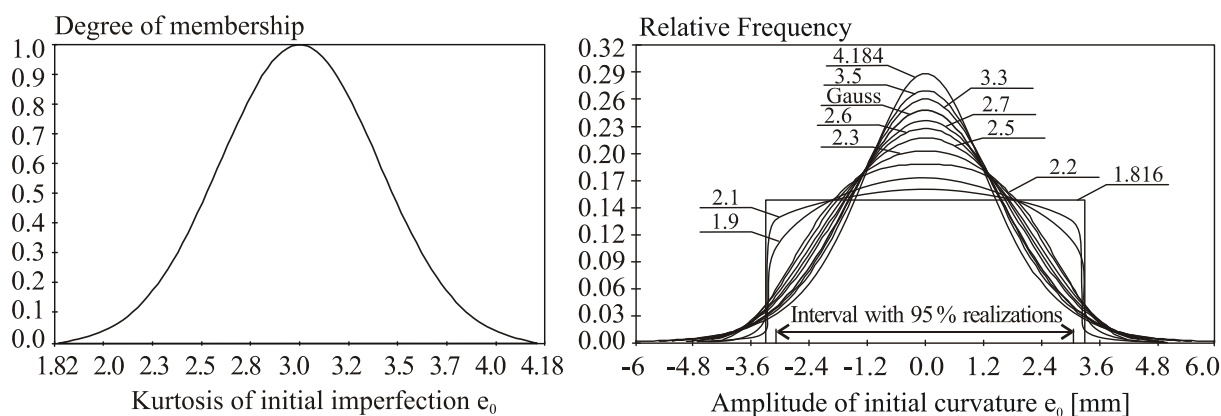


Fig. 1: Hermite density distribution function and fuzzy number of kurtosis.

The parameters of the four-parametric Hermite density function include: mean value, standard deviation, skewness and kurtosis. The limit case arises for kurtosis of 1.816 corresponding to a rectangular density function. The kurtosis of the Gaussian density function has a value of 3.0. The maximum kurtosis was considered as 4.184, (i.e.  $3.0 + 3.0 - 1.816$ ) leading to symmetrical minimal and maximal support values around the kernel. The left side of Fig. 1 illustrates an example of a set of density functions. The functions vary in kurtosis values, which is listed for each function. The standard deviation of the amplitude of initial imperfection  $e_0$  is also a fuzzy number. Twenty cuts of the  $\alpha$ -cut method were utilized (Möller & Reuter, 2007). The standard deviation of the Gaussian density function is given by the kernel value of 1.607. The fuzzy number of standard deviation  $e_0$  was evaluated using the general extension principle (Zadeh, 1965). The support and kernel of the failure probability distribution is depicted in Figure 4. The main output of the study is represented by the dashed curve, which was obtained utilizing the COG (centre of gravity) defuzzification method.

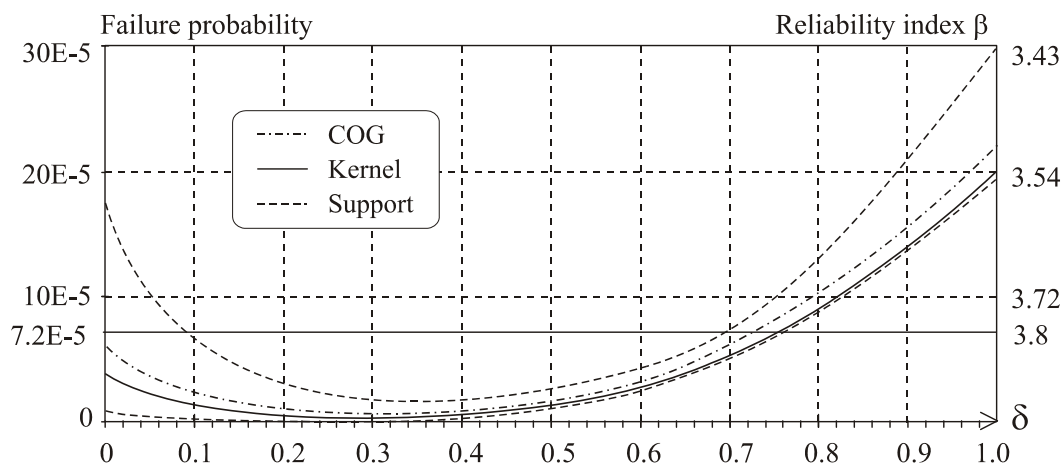


Fig. 2: Fuzzy random analysis of misalignment of failure probability.

### 3. Conclusions

The presented study illustrates fuzzy uncertainty of failure probability emanating from the vague (fuzzy) uncertainty of the kurtosis of the random amplitude of initial member curvature  $e_0$ . Discrepancies between obtained results are considerable and point to the necessity of fuzzy analysis whenever input random variables are assigned subjectively. It is apparent that the defuzzified values (centroids) represented graphically by the dashed curves are higher than the values evaluated by means of purely stochastic analysis (kernels) represented by the full curves in all cases. Results of the application of probabilistic analysis point out the significant discrepancies of design reliability of steel structures acc. to the EUROCODE concept. Dominant input variables which have the greatest influence on the design reliability can be identified using sensitivity analysis methods (Kala, 2005; Melcher et al., 2009; Kala, 2011a; Kala, 2011b). In the future it is necessary to continue in the verification and calibration of the reliability indicators based on results of experimental research.

### Acknowledgement

The article was elaborated within the framework of projects of AVČR IAA201720901, CIDEAS No. 1M0579 and project GAČR 105/10/1156.

### References

- Fukumoto, Y., Kajita, N. & Aoki, T. (1976) Evaluation of column curves based on probabilistic concept, in: Proc. Int. Conf. on Stability, Prelim. Rep., publ. by Gakujutsu Bunken Fukyu - Kai, Tokyo, pp.1-37.
- Gottvald, J. (2010) The calculation and measurement of the natural frequencies of the bucket wheel excavator SchRs 1320/4x30. Transport, 25, 3, pp.269-277.
- Kala, Z. (2005) Sensitivity analysis of the stability problems of thin-walled structures. Journal of Constructional Steel Research, 61, 3, pp.415-422.
- Kala, Z. (2007) Stability problems of steel structures in the presence of stochastic and fuzzy uncertainty. Thin-Walled Structures, 45, 10-11, pp. 861-865.
- Kala, Z. (2008) Fuzzy probability analysis of the fatigue resistance of steel structural members under bending. Journal of Civil Engineering and Management, 14, 1, pp.67-72.
- Kala, Z. (2009) Sensitivity assessment of steel members under compression. Engineering Structures, 31, 6, pp.1344-1348.
- Kala, Z., Melcher, J. & Puklický, L. (2009) Material and geometrical characteristics of structural steels based on statistical analysis of metallurgical products. Journal of Civil Engineering and Management, 15, 3, pp.299-307.
- Kala, Z., Puklický, L., Omishore, A., Karmazínová, M. & Melcher, J. (2010) Stability problems of steel-concrete members composed of high strength materials. Journal of Civil Engineering and Management, 16, 3, pp.352-362.
- Kala, Z. (2011a) Sensitivity analysis of stability problems of steel plane frames. Thin-Walled Structures, 49, 5, pp.645-651. doi:10.1016/j.tws.2010.09.006.
- Kala, Z. (2011b) Sensitivity analysis of steel plane frames with initial imperfections. Engineering Structures, (in print). ISSN: 0141-0296. doi:10.1016/j.engstruct.2011.04.007.
- Karmazínová, M., Melcher, J. & Kala, Z. (2009) Design of expansion anchors to concrete based on results of experimental verification. Advanced Steel Construction, 5, 4, pp.390-405.
- Li, YW., Elishakoff, I., Starnes JH. & Shinozuka M. (1995) Nonlinear buckling of a structure with random imperfection and random axial compression by a conditional simulation technique. Computers & Structures, 56, 1, pp.59-64.
- Melcher, J., Kala, Z., Holický, M., Fajkus, M. & Rozlívka, L. (2004) Design characteristics of structural steels based on statistical analysis of metallurgical products. Journal of Constructional Steel Research, 60, 3-5, pp.795-808.
- Melcher, J., Škaloud, M., Kala, Z. & Karmazínová, M. (2009) Sensitivity and statistical analysis within the elaboration of steel plated girder resistance. Advanced Steel Construction, 5, 2, pp.120-126.
- Möller, B. & Reuter, U. (2007) Uncertainty Forecasting in Engineering. Springer Press, p.202. ISBN 978-3-540-37173-1.
- Strauss, A., Kala, Z., Bergmeister, K., Hoffmann, S. & Novák, D. (2006) Technologische eigenschaften von stählen im europäischen vergleich. Stahlbau, 75, Heft 1.
- Zadeh, L.H. (1965) Fuzzy sets. Information and Control, 8, 3, pp.338-353.

## HIGH TEMPERATURE AND ITS INFLUENCE ON THE CREEP OF CEMENT PASTE FROM CEM II

P. Padevět\*, P. Bittnar\*

**Abstract:** *Material properties provide the basic inputs for mathematic modeling of material. Creep of cement paste is possible to be assigned to the basic properties. In the paper, there are presented results of experimental testing of creep of cement paste. Cement pastes were prepared from Portland cement CEM II. Selected w/c ratios 0.3; 0.4 and 0.5 were used for preparation. Tested specimens were heated by temperature of 300 °C before start of testing. The shape of specimens was a cylinder with diameter 10 mm and length 70 mm, and specimens were tested in special lever mechanism designed for creep test of small-grained materials. The results of testing are divided into the creep of specimens and shrinkage of specimens. In the first chapter, there is described the preparation of specimens. The second one includes the results of material tests, i.e., compression strength and modulus of elasticity. Results of creep tests, especially graphs from creep tests are described in the next chapter, and finally, results are summarized. In the results of creep tests, there are presented graphs of water dried and saturated specimens and results are discussed.*

**Keywords:** *Cement paste, creep, shrinkage, compression strength, computational model.*

### 1. Introduction

The creep is considered to be among primary properties of concrete. Size of creep is very important for design concrete structures. Concrete is a composite material (Neville, 1997) which consists of ingredients: cement, water, aggregates, additives and special admixtures. However, the basic part of concrete is mixture (Rixom, Mailvaganam, 1999) of cement and water (De Larrard, 1999). The mixture of cement and water is named cement paste. The properties of cement paste are basic properties for knowledge about performance of concrete.

Cement paste usually achieves the high values of strength (Takada, 1999). If area of loading is large, then applying high load is necessary for achieving correct level of loading. It is reason for reduction of specimen's loading area. The same type of specimens is used for the creep and compression tests. Cylindrical specimens are made into the plastic moulds. Lengths of made out specimens are between 90 and 100 mm. Sufficient length of specimens is 70 mm for testing the cement paste creep. Small kind of gauges is necessary to use for measurement of deformation. Optoelectronic probes are a suitable alternative to the LVDT gauges. By the optoelectronic probe, it is possible to achieve good results of measuring the creep. Their sensitivity is at 0.2 µmm.

Specimen length 100 mm is reduced to 70 mm, length which is suitable for creep tests. Diameter of all specimens in the moulds is 10 mm. Area of specimen for application of load is 78 mm<sup>2</sup>. Specimens were prepared for this set of tests from Portland cement CEM II 32.5R, it is cement with addition of slag and a little bit of fly ash, calcium sulfate and calcite. Properties of cement characterize a lower heat of hydration and higher resistance for aggressive influence of environment.

Specimens were made with water-cement ratio 0.3, 0.4 and 0.5. Water cement ratio (w/c) is the weight proportion of water and cement. The second series of specimens was made from Portland cement CEM II with w/c = 0.4, see Fig 1. The third series was made from Portland cement and water too, but with w/c ratio 0.3. Cement mixture was sufficiently liquid (w/c = 0.5) and it was possible pour to the moulds. Better properties were achieved by using the plasticizer during the production, namely for w/c ratio 0.3 and 0.4. Content of plasticizer was 1.3 % of weight of cement. Cement paste with water-

---

\* Ing. Pavel Padevět, Ph.D and Ing. Petr Bittnar: Department of Mechanics, CTU in Prague, Faculty of Civil Engineering, Thákurova 7; 166 29, Prague 6; CZ, e-mails: pavel.padevet@fsv.cvut.cz, petr.bittnar@fsv.cvut.cz

cement ratio 0.3 was prepared by using the plasticizer too, namely Spolstan with quantity of 3 % from cement weight.

All specimens were before testing heated in the temperature cube. Temperature was applied to the specimens by below described procedure. Specimens were heated to 300 °C during 1 hour. After then specimens were heated at 300 °C during 2.5 hours. The specimens were then 20 hours cooled at temperature 20 °.

Lever mechanism (Fig. 2) is the equipment for creep measuring and shrinkage of cement paste and it was developed as a special equipment for creep tests of homogenous materials. Stationary load is applied to the specimen. The size of the applied load depends on the weight of plumb and location of plumb at the lever. The measurement of deformation is realized by using three optoelectronic probes. The length of deformation is the whole length of specimen which is placed into the lever mechanism. Axial deformations are measured by the three optoelectronic gauges. The average deformation is calculated after termination of measuring.

In executed experiments, there were used specimens with diameter 10 mm. The applied loads were approximately between 740 and 760 N. For the measuring of the specimens shrinkage was applied load 76 N. Applied loads on specimens were invariable for whole measuring period. Specimens were firstly placed into the lever mechanism and after then systems were loaded by plumb. Measuring the deformation was started after specimen placing into the lever mechanism. Period of measuring was from 27 to 30 days. The plumbs were taken off before finishing of measuring. After then, all specimens were taken out of lever mechanisms and prepared for compression testing.

Parameters of material properties were measured during the testing continuously. The modulus of elasticity and compression strength was computed from data of measured data (Kala, 2010). Young's modulus of elasticity was calculated like a secant, linking the start and value at stress-strain curve which correspond to 1/3 of the strength. An extensometer with measurement length 25 mm was used for measuring of strain. The extensometer was placed in axial direction at the middle part of the specimen (Van Mier, J.).

## 2. Results of creep tests

Results of creep and shrinkage were achieved from tests in lever mechanism. The 6 specimens were tested in the whole series. Specimens tested in creep tests were loaded by load 740 N. Creep tests were executed in two conditions. The first condition was represented by water saturated specimens. The second one was represented by drying of water from specimens. The first set of specimens was placed back into the water basin for 24 hours after their temperature loading. The specimens were placed into the lever mechanisms after their water saturation.

Two specimens were tested in the water saturated condition. Next two specimens were tested in water dried conditions (after temperature heating). The shrinkage was tested in saturated and dried condition, too. Only one specimen saturated and one specimen dried was tested for shrinkage. The cement paste prepared with w/c ratio 0.4 was tested on shrinkage in wet condition only.

Specimens were covered by plastic wrap before the creep and shrinkage tests. Before covering, some specimens were placed into the water basin. All specimens were 1 year old.

*Tab. 1: Deformation of specimens from creep and shrinkage tests.*

Specimen	w/c 0.3	w/c 0.4	w/c 0.5
1	70 *	30.66	137.7
2	49.56	-0.16	251.8
3	-44.3 *	-30.13	-21.9 **
4	-93.63	-36.3	-73.7 ***
5	39.2	-24	0.2
6	64.83	-29.46	14.4

\* Test finished 13<sup>th</sup> day, \*\* Test finished 4<sup>th</sup> day, \*\*\* Test finished 24<sup>th</sup> day.

In the next figures Fig. 1, there are presented typical graphs of creep test. In last graphs, it is possible to see comparison of experimental results of basic creep and simulation in OOFEM (Patzák).

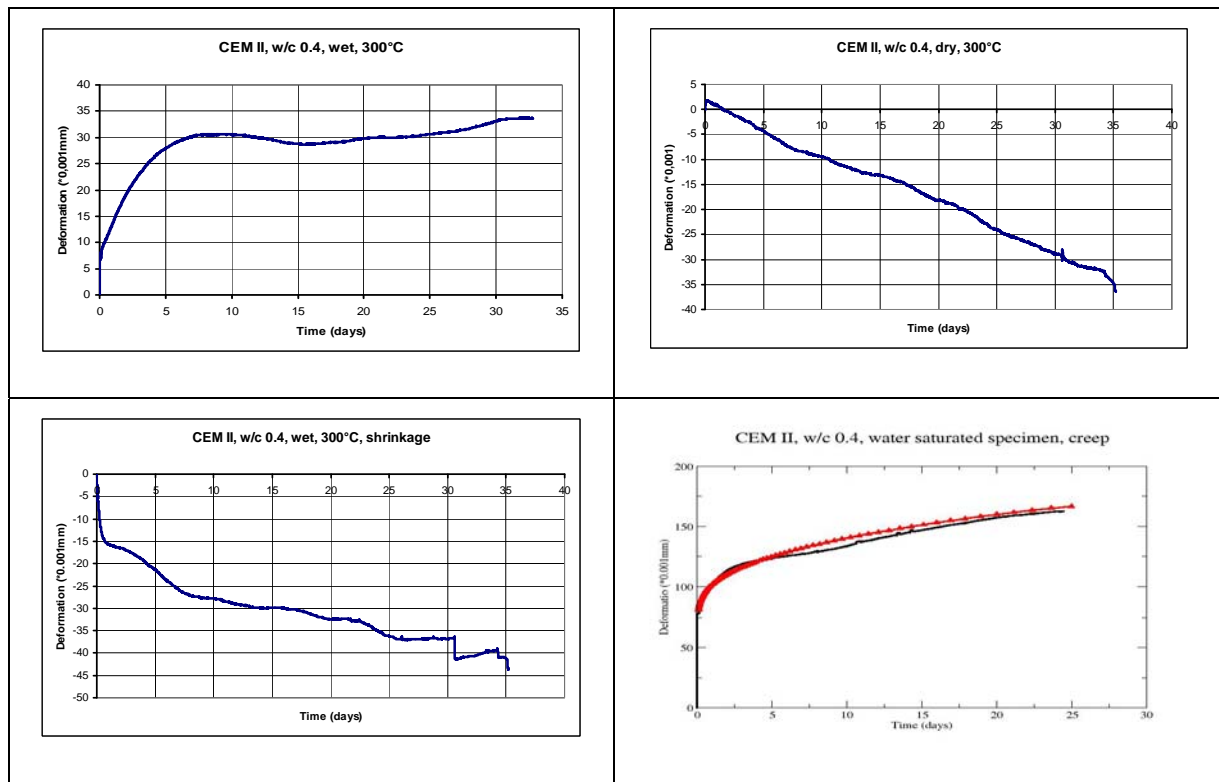


Fig. 1: Creep and shrinkage of cement paste prepared with w/c 0.4.

### 3. Results of compression tests

Values of compressive strength were obtained from stress- strain diagrams of specimens. Measuring was executed after finishing creep tests. Weights of the specimens were checked before start of compression tests. Average weight of the specimen prepared by w/c 0.3 was 10.308 g, with standard deviation 0.267. Cement paste prepared with w/c 0.4 had average weight 10,725 g, and standard deviation was 0.287. Specimens had average weight 8.897 grams with standard deviation 0.269 in the third series (w/c 0.5).

In Tab. 2, there are displayed results of compression tests of the specimens. 5 specimens were tested in the first series (w/c 0.3). In the next two series, 6 and 5 specimens were tested. Specimens in w/c 0.3 series had values of strength from 74.5 MPa to 150.3 MPa. The lowest values of compression strength were achieved for specimens tested in shrinkage test and water dried specimens tested in creep test. The second series (w/c ratio 0.4) had closer values; from 70.4 MPa to 129.4 MPa. Specimens No. 4 and 6 had extreme values of strength to the average value of strength 101.3 MPa

Tab. 2: Deformation of specimens from creep and shrinkage tests.

Specimen	w/c 0.3	w/c 0.4	w/c 0.5
1	140.0	100.9	80.5
2	153.3	106.8	78.7
3	77.1	105.9	-
4	74.5	94.6	53.8
5	136.5	70.4	60.2
6	-	129.4	78.3

Five tested specimens in third series had the average value of strength 70.3 MPa. The lowest value of strength was stated for specimen No. 4, it was the dried specimen tested in shrinkage test, before. Cement paste prepared by w/c ratio 0.5 had lower strength than cement pastes including lesser content of water (Fig. 6). Average strength was 143.26 MPa, 102.05 MPa and 74.42 MPa for specimens prepared by content of water in the mixture 0.3; 0.4 and 0.5. Standard deviations for results of compressive strength were 9.531, 5.603, and 8.863 (w/c ratio 0.3, 0.4 and 0.5).

#### 4. Conclusions

The values of compression strength were determined in experimental part of work. Curves of creep and shrinkage were determined for three types of cement pastes, too. The first series (average strength was 143.2 MPa) was the strongest in the compression tests, and it was prepared by w/c ratio 0.3. The third series (w/c = 0.5) achieved only half value (74.4 MPa) of average strength of the first series. Content of water in cement paste mixture influences the strength of hardened cement paste. The values of compression strength depend on the type of cement, too.

If the content of water in cement gel is increasing, deformation of the water saturated specimens is increasing, too. Shrinkage of the all types of water saturated cement pastes was between 22 and 44  $\mu\text{m}$ . Shrinkage of water in dried cement paste specimens was 93.6  $\mu\text{m}$ , and 73.7  $\mu\text{m}$  for cement paste prepared with w/c 0.3 and 0.5. The size of shrinkage influences both the rate and size of creep

Conformity between simulation and experiment illustrate that the model B3 (Patzák, 2000) is suitable for analysis of the creep of cement paste.

#### Acknowledgement

This work was supported by project GACR under No. P105/11/2285.

#### References

- De Larrard, F. (1999) Concrete Mixture Proportioning, a Scientific Approach, E & F.N. Spon Ltd. 1999, ISBN 0-419-23500-0.
- Kala, Z. (2010) Sensitivity Analysis of Stability Problems of Steel Plane Frames, Thin-Walled Structures, 2010, (in print) doi:10.1016/j.tws.2010.09.006.
- Neville, A., M., (1997) Properties of Concrete, John Wiley & Sons, Inc, 1997.
- Padevĕt, P., Bittnar, P. (2010) Measuring of Creep Cement Paste CEM II, Conference Information: 48th International Scientific Conference on Experimentalni Analýza Napeti Experimental Stress Analysis, May 31-Jun 03, 2010 Velke Losiny, CZECH Republic, Proceedings of the 48<sup>th</sup> International Scientific Conference on Experimentální Analýza Napětí 2010 Experimental Stress Analysis, Pages: 293-299.
- Patzák, B. (2000) OOFEM project home page, <http://www.oofem.org>, 2000.
- Rixom, R, Mailvaganam, N. (1999) Chemical Admixtures for Concrete, E & F.N. Spon Ltd, 1999, ISBN 0-419-22520-X.
- Takada, K. (1999) Influence of Admixtures and Mixing Efficiency on the Properties of Self Compacting Concrete, DOP Science, ISBN 90-407-2501-2.
- Van Mier, J., G., M. (1997) Fracture Processes of Concrete, CRC Press, Inc, 1997.



## A NEW QUANTITATIVE DESCRIPTION OF INTRACELLULAR $\text{Ca}^{2+}$ DYNAMICS IN THE MODEL OF RAT VENTRICULAR MYOCYTE

M. Pásek\*, J. Šimurda\*\*

**Abstract:** *In this paper, a new description of intracellular  $\text{Ca}^{2+}$  dynamics in the model of rat ventricular cardiomyocyte is presented. The principal modifications based on the recently published data comprise: formulation of the function of peripheral dyads, incorporation of peripheral and tubular intracellular subspaces, reformulation of inactivation properties of surface of tubular  $I_{\text{Ca}}$  and description of the function of exogenous  $\text{Ca}^{2+}$  buffer in intracellular space. The modified model will be used to explore the activity induced ion-concentration changes in rat transverse-axial tubular system in a more detail and to investigate their effects on excitation – contraction coupling in ventricular cardiomyocytes.*

**Keywords:** *Cardiac cell, intracellular  $\text{Ca}^{2+}$  dynamics, quantitative modelling.*

### 1. Introduction

In our previous work we developed a mathematical model of rat ventricular cell electrical activity (Pásek et al., 2006) that firstly included a quantitative description of membrane transverse-axial tubular system (TATS). The model was used to explore the extent of activity induced ion concentration changes in rat TATS and their role in electromechanical activity of rat ventricular myocytes. The experimental data that have been published in the recent years show, however, that some cellular events related to intracellular  $\text{Ca}^{2+}$  dynamics are more complex than formulated in the model. In this work, we describe a modified model of rat ventricular cardiomyocyte that includes a novel description of intracellular  $\text{Ca}^{2+}$  handling respecting the recent findings. The principal modifications of the model include: (i) partition of originally single dyadic space into two compartments, one adjacent to surface membrane and another one adjacent to tubular membrane; (ii) incorporation of peripheral and tubular intracellular subspaces; (iii) reformulation of calcium current ( $I_{\text{Ca}}$ ) inactivation including its differentiation between surface and tubular membrane; (iv) incorporation of quantitative description of the function of exogenous  $\text{Ca}^{2+}$  buffers in intracellular space.

### 2. Modification of the model

#### 2.1. Model structure

The structure of the modified model is based on the previous model (Pásek et al., 2006) and is illustrated in Fig. 1. The presence of peripheral dyads (Brette et al., 2004) and ion gradients under the membrane (Shannon et al., 2004) is taken into account by incorporation of the following new compartments: dyadic space adjacent to surface membrane (surface dyadic space); junctional compartment of sarcoplasmic reticulum adjacent to surface dyadic space ( $\text{JSR}_s$ ); subsarcolemmal spaces adjacent to surface and tubular membranes (surface subsarcolemmal space and tubular subsarcolemmal space). The volumes of all intracellular compartments are specified in Tab. 1.

Readjustment of parameters related to cellular membrane was performed according to the results published in Pásek et al., 2008; the fractional area of tubular membrane was lowered to 49% and the specific capacitances of tubular and surface membrane were set to  $1.275 \mu\text{F}/\text{cm}^2$  and to  $0.714 \mu\text{F}/\text{cm}^2$ ,

---

\* assoc. prof. Ing. Michal Pásek, Ph.D.: Institute of Thermomechanics, CAS - branch Brno; Technická 2; 616 69 Brno & Department of Physiology, Medical Faculty of Masaryk University, Kamenice 5; 62500 Brno; CZ e-mail: pasek.avcr@centrum.cz

\*\* assoc. prof. RNDr. Ing. Jiří Šimurda, CSc.: Department of Physiology, Medical Faculty of Masaryk University, Kamenice 5; 62500; Brno; Czech Republic; e-mail: simurda@med.muni.cz

respectively. This adjustment is consistent with commonly used value of total membrane specific capacitance of  $1 \mu\text{F}/\text{cm}^2$ .

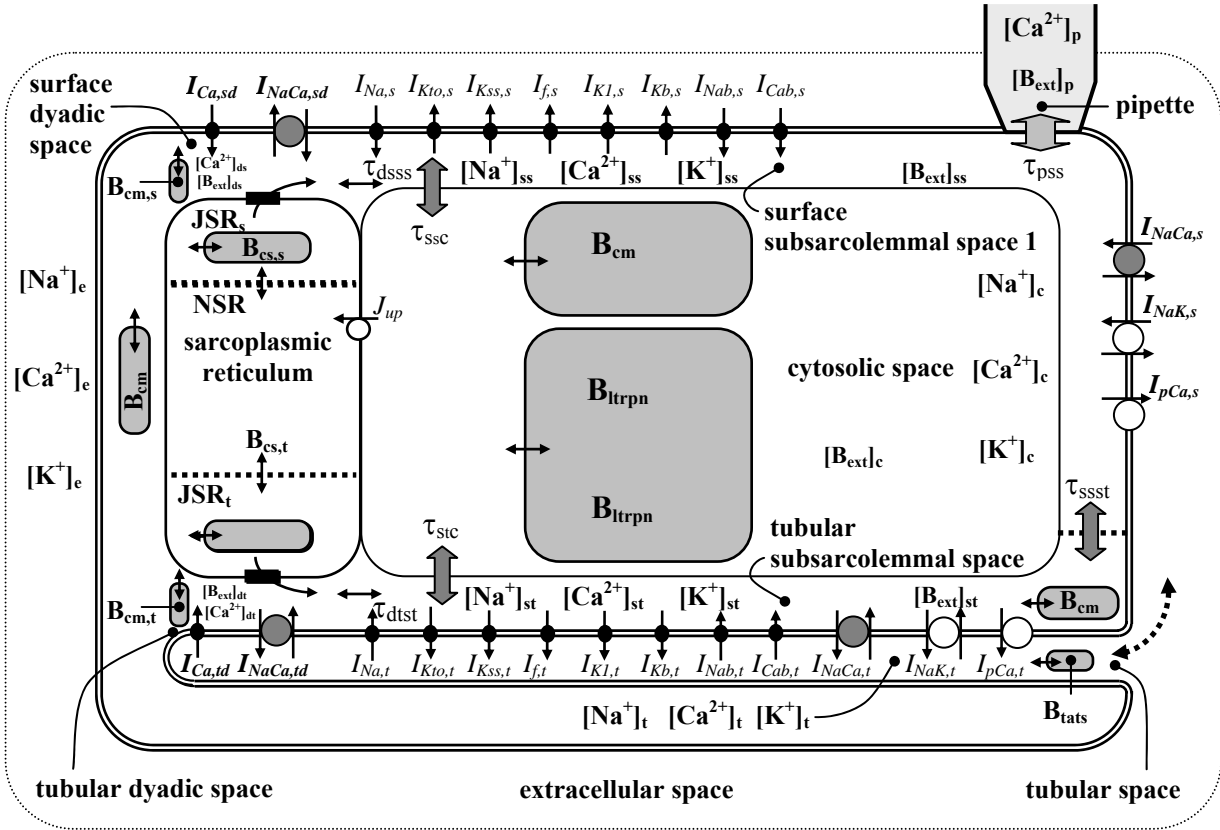


Fig. 1: Schematic diagram of the modified rat ventricular cell model. The description of electrical activity of surface (*s*, *sd*) and tubular (*t*, *td*) membrane comprises formulations of the following ion currents: fast sodium current ( $I_{Na}$ ), calcium currents through L-type channels ( $I_{Ca}$ ), transient outward potassium current ( $I_{to}$ ), steady-state outward potassium current ( $I_{Kss}$ ), hyperpolarization-activated potassium current ( $I_p$ ); inward rectifying potassium current ( $I_{K1}$ ), background currents ( $I_{Kb}$ ,  $I_{Nab}$ ,  $I_{Cab}$ ), sodium-calcium exchange current ( $I_{NaCa}$ ), sodium-potassium pump current ( $I_{NaK}$ ) and calcium pump current ( $I_{pCa}$ ). The intracellular space contains the cytosolic space, surface and tubular subsarcolemmal subspaces, surface and tubular dyadic spaces, the network and junctional compartments of sarcoplasmic reticulum (NSR, JSR<sub>s</sub>, JSR<sub>t</sub>), the endogenous  $\text{Ca}^{2+}$  buffers (calmodulin ( $B_{cm}$ ), troponin ( $B_{ltrpn}$ ,  $B_{ltrpn}$ ), calsequestrin ( $B_{cs}$ )) and the exogenous  $\text{Ca}^{2+}$  buffer (e.g. BAPTA or EGTA ( $B_{ext}$ )).  $B_{tats}$  denotes the non-specific  $\text{Ca}^{2+}$  buffer associated with luminal part of tubular membrane. The small filled rectangles in JSR membrane represent ryanodine receptors. The small bi-directional arrows denote  $\text{Ca}^{2+}$  diffusion. Ionic diffusion between the tubular and the extracellular space is represented by the dashed arrow.

Tab. 1: Volumes of intracellular compartments.

symbol	specification	value [pl]
$V_c$	cytosolic space	11.137
$V_{ss}$	surface subsarcolemmal subspace	0.1440
$V_{st}$	tubular subsarcolemmal subspace	0.0775
$V_{ds}$	surface dyadic space	0.0001671
$V_{dt}$	tubular dyadic space	0.0006682
$V_{JSRs}$	surface junctional compartment of sarcoplasmic reticulum	0.0078
$V_{JSRt}$	tubular junctional compartment of sarcoplasmic reticulum	0.0312
$V_{NSR}$	network compartment of sarcoplasmic reticulum	0.3508

## 2.2. Membrane transport system

Voltage dependent inactivation (VDI) and  $\text{Ca}^{2+}$  dependent inactivation (CDI) of  $I_{Ca}$  was newly formulated on the basis of experimental results of Brette et al. (2004). All parameters of CDI are regarded as dependent on the level of calmodulin saturation with  $\text{Ca}^{2+}$  ( $B_{cm,Casat}$ , Shannon et al., 2004). The steady state levels and time constants of VDI ( $ss_{VDI}$ ,  $\tau_{VDI}$ ) and CDI ( $ss_{CDI}$ ,  $\tau_{CDI,s}$ ,  $\tau_{CDI,t}$ ) are described by the following equations:

$$ss_{VDI,x} = 1 / (1 + \exp((V_{m,x} + 26.7) / 5.4)),$$

$$\tau_{VDI,x} = 1.15 \cdot (0.041 \cdot \exp(-(V_{m,x} + 47) / 12)^2 + 0.08 / (1 + \exp(-(V_{m,x} + 55) / 5)) + 0.015 / (1 + \exp((V_{m,x} + 75) / 25))),$$

$$ss_{CDI,x} = 1 / (1 + 0.244 \cdot (B_{cm,Casat,x}^4 + 0.318^4) / B_{cm,Casat,x}^4),$$

$$\tau_{CDI,s} = 1 / (43.827 \cdot B_{cm,Casat,s}^4 / (B_{cm,Casat,s}^4 + 0.976^4) + 25.006),$$

$$\tau_{CDI,t} = 1 / (1160 \cdot B_{cm,Casat,t}^8 / (B_{cm,Casat,t}^8 + 1.14^8) + 16.66).$$

While the formulations of  $ss_{VDI}$ ,  $\tau_{VDI}$  and  $ss_{CDI}$  in the description of  $I_{Ca,s}$  and  $I_{Ca,t}$  are identical (the suffix x in the equations stands for s (surface) or t (tubular)), the  $\tau_{CDI}$  of these two currents is formulated differently (see  $\tau_{CDI,s}$  and  $\tau_{CDI,t}$ ). This takes into account the observed different modulation of surface and tubular  $I_{Ca}$  by  $\text{Ca}^{2+}$  released from SR (Brette et al., 2004).

The conductivity of  $I_{to}$  was increased by 20% for action potentials of the model to exhibit physiological duration.

The fractions of membrane currents in the tubular membrane were set to meet the results published in Pásek et al. (2008) except for the values of  $f_{I_{Ca,t}}$  and  $f_{I_{pCa,t}}$  that were set to 80% (Brette et al., 2004) and 95% (Chase & Orchard, 2011), respectively.

## 2.3. Intracellular $\text{Ca}^{2+}$ - handling

The formulation of the function of ryanodine receptors in JSR (RyR) was adopted from Shannon et al. (2004). The constants  $k_s$  and  $k_{oCa}$  were increased from  $25 \text{ ms}^{-1}$  to  $250 \text{ ms}^{-1}$  and from  $10 \text{ mM}^{-2} \text{ ms}^{-1}$  to  $50 \text{ mM}^{-2} \text{ ms}^{-1}$ , respectively, for  $\text{Ca}^{2+}$  transients in the dyadic space to reach magnitude close to  $100 \mu\text{M}$  at the level of free  $[\text{Ca}^{2+}]$  in NSR of  $0.5 \text{ mM}$  (Shannon et al., 2004). Description of SR  $\text{Ca}^{2+}$  pump ( $J_{up}$ ) was modified to be consistent with data of Shannon and Bers (1997). The constants used are:  $V_{max} = 286 \mu\text{M/s}$ ,  $K_{mf} = 168 \text{ nM}$ ,  $K_{mr} = 1.176 \text{ mM}$ ,  $h_f = 1.2$  and  $h_r = 1.287$ . The dissociation constant ( $K_d$ ) of calsequestrin in JSR was decreased from original value  $0.8 \mu\text{M}$  to  $0.65 \mu\text{M}$  (Shannon et al., 2004).  $\text{Ca}^{2+}$  buffering by calmodulin was described by differential equations with  $k_{on} = 100000 \text{ mM}^{-1} \text{ s}^{-1}$  and  $k_{off} = 238 \text{ s}^{-1}$ .

The model was supplemented by the description of exogenous  $\text{Ca}^{2+}$  buffer diffusion (BAPTA or EGTA) among the pipette, subsarcolemmal spaces, dyadic spaces and cytosol. All time constants controlling the rate of exogenous  $\text{Ca}^{2+}$  buffer and  $\text{Ca}^{2+}$  diffusion between individual cellular compartments are specified in Tab. 2 (the time constants of intracellular  $\text{Na}^+$  and  $\text{K}^+$  diffusion were set to the same values as in the case of  $\text{Ca}^{2+}$  diffusion).

## 2.4. Ion diffusion between tubular and extracellular space

The time constants of ion exchange between the TATS lumen and the extracellular solution ( $\tau_{Ca,TATS}$ ,  $\tau_{K,TATS}$ ,  $\tau_{Na,TATS}$ ) were readjusted for the model to better reproduce the changes in  $I_{Ca}$  and resting voltage following rapid decrease or increase of external ion concentrations at  $37^\circ \text{C}$  (Yao et al., 1997). To reconstruct the biphasic time course of  $I_{Ca}$ -decrease after rapid exposure of myocytes to  $\text{Ca}^{2+}$ -free external solution, the model was supplemented by a formulation of  $\text{Ca}^{2+}$  buffer in TATS ( $B_{tats}$ ). Using the same pulse and solution change protocols the reconstructions led to the following values of buffer parameters and time constants:  $k_{on} = 2.2 \text{ s}^{-1} \text{ mM}^{-1}$ ,  $k_{off} = 2.398 \text{ s}^{-1}$ ,  $B_{tats} = 2.6 \text{ mM}$ ,  $\tau_{Ca,TATS} = 155 \text{ ms}$  and  $\tau_{Na,TATS} = \tau_{K,TATS} = 150 \text{ ms}$ . Finally, the time constants were corrected for the lower temperature of the model cell ( $22^\circ \text{C}$ ,  $Q_{10} = 1.3$ ) and their final values were:  $\tau_{Ca,TATS} = \tau_{Na,TATS} = \tau_{K,TATS} = 220 \text{ ms}$ .

Tab. 2: Time constants related to intracellular transport of  $Ca^{2+}$  and  $Ca^{2+}$ -buffers.

symbol	specification	value [s]
$\tau_{pss,buffer-free}$	controls buffer diffusion from the pipette into the surface subspace	1.36
$\tau_{pss,buffer-Ca}$	controls buffer- $Ca^{2+}$ diffusion from the pipette into the cytosolic space	1.36
$\tau_{pss,Ca}$	controls $Ca^{2+}$ diffusion from the pipette into the cytosolic space	1.36
$\tau_{dss,buffer-free}$	controls buffer diffusion from the surface dyadic space into surface subspace	$0.34E^{-3}$
$\tau_{dss,buffer-Ca}$	controls buffer- $Ca^{2+}$ diffusion from surface dyadic space into surface subspace	$0.34E^{-3}$
$\tau_{dss,Ca}$	controls $Ca^{2+}$ diffusion from the surface dyadic space into the surface subspace	$0.34E^{-3}$
$\tau_{dst,buffer-free}$	controls buffer diffusion from the tubular dyadic space into tubular subspace	$0.34E^{-3}$
$\tau_{dst,buffer-Ca}$	controls buffer- $Ca^{2+}$ diffusion from the tubular dyadic space into tubular subspace	$0.34E^{-3}$
$\tau_{dst,Ca}$	controls $Ca^{2+}$ diffusion from the tubular dyadic space into tubular subspace	$0.34E^{-3}$
$\tau_{ssc,buffer-free}$	controls buffer diffusion from the surface subspace into cytosolic space	0.004
$\tau_{ssc,buffer-Ca}$	controls buffer- $Ca^{2+}$ diffusion from the surface subspace into cytosolic space	0.004
$\tau_{ssc,Ca}$	controls $Ca^{2+}$ diffusion from the surface subspace into cytosolic space	0.004
$\tau_{stc,buffer-free}$	controls buffer diffusion from the tubular subspace into cytosolic space	0.001
$\tau_{stc,buffer-Ca}$	controls buffer- $Ca^{2+}$ diffusion from the tubular subspace into cytosolic space	0.001
$\tau_{stc,Ca}$	controls $Ca^{2+}$ diffusion from the tubular subspace into cytosolic space	0.001
$\tau_{sst,buffer-free}$	controls buffer diffusion from the surface subspace into tubular subspace	0.1
$\tau_{sst,buffer-Ca}$	controls buffer- $Ca^{2+}$ diffusion from the surface subspace into tubular subspace	0.1
$\tau_{sst,Ca}$	controls $Ca^{2+}$ diffusion from the surface subspace into tubular subspace	0.1

### 3. Conclusions

The present novel description of intracellular  $Ca^{2+}$  dynamics in the model of rat ventricular myocytes is an important step toward understanding of specific details of excitation-contraction coupling in cardiac ventricular myocytes. The principal modifications based on the recently published data comprise: formulation of the function of peripheral dyads, incorporation of peripheral and tubular intracellular subspaces, reformulation of inactivation properties of surface of tubular  $I_{Ca}$  and description of the function of exogenous  $Ca^{2+}$  buffer in the intracellular space. The modified model will be used to further investigate the effects of activity induced ion-concentration changes in TATS on electrical and mechanical activity of ventricular cardiomyocytes.

### Acknowledgement

This study was supported by the project AV0Z 20760514 from the Institute of Thermomechanics of Czech Academy of Sciences and by the project MSM 0021622402 from the Ministry of Education, Youth and Sports of the Czech Republic.

### References

- Pásek, M. et al. (2006) The functional role of cardiac T-tubules explored in a model of rat ventricular myocytes. Philosophical Transactions of the Royal Society A, 364, pp. 1187-1206.
- Brette, F. et al. (2004) Differential modulation of L-type  $Ca^{2+}$  current by SR  $Ca^{2+}$  release at the t-tubules and surface membrane of rat ventricular myocytes. Circulation Research, 95, pp. e1-e7.
- Shannon, T.R. et al. (2004) A mathematical treatment of integrated Ca dynamics within the ventricular myocytes. Biophysical Journal, 87, pp. 3351-3371.
- Pásek, M. et al. (2008) Quantification of t-tubule area and protein distribution in rat cardiac ventricular myocytes. Progress in Biophysics and Molecular Biology, 96, pp. 244-257.
- Chase, A. & Orchard, C.H. (2011) Ca efflux via the sarcolemmal Ca ATPase occurs only in the t-tubules of rat ventricular myocytes. Journal of Molecular and Cellular Cardiology, 50, pp.187-193.
- Shannon, T.R. & Bers D.M. (1997) Assessment of intra-SR free [Ca] and buffering in rat heart. Biophysical Journal, 73, pp. 1524-1531.
- Yao, A. et al. (1997) The restriction of diffusion of cations at the external surface of cardiac myocytes varies between species. Cell Calcium, 22, pp. 431-438.

## **VIBRATORY STIMULATION OF FLUID FLOWS IN POROUS MEDIUM OF COAL SEAM**

**M. V. Pavlenko<sup>\*</sup>**

**Abstract:** *The present article describes the results of research related to vibration wave impact on the coal array and the coal seam in particular, which is used to increase the methane recovery in the seam. The known methods of vibrating wave impact on coal array do not always successfully ensure the necessary methane recovery. For experimental research, the effects obtained in laboratory conditions through vibratory simulations of fluid flows in porous medium of coal seam are also considered. A highly recommended method of well treatment is the method of low-frequency effects on the coal seam through wells drilled from the surface. A vibration facility developed with direct participation of the author of this article allows a near-well zone to work in several hydrodynamic regimes without changing the wellhead. Complex research of vibrating wave impact based on a wide range of seam thickness, methane content, pressure and temperature is also needed to account for the impact on the dynamic features of the array. This research allows us to select optimal working parameters of technological facilities using the vibrating wave impact and thereby reduce energy costs and increase the duration of their effectiveness.*

**Keywords:** *Vibrating wave impact, fluid flow, porous medium, coal seam, coal array, well treatment, seam face zone, near-the-well zone.*

### **1. Introduction**

Vibrating wave effects on coal array have recently become a promising subject for research of porous medium of the coal seam. One of the most effective methods of vibrating wave – the impact on coal seam - is used to increase the methane recovery from the seam. This article reviews the relevant studies on changes in hydrodynamics in the coal seam associated with the changing nature of fluid absorption. The studies describe experimental research of vibrating wave effects under the conditions of saturation of the coal seam with fluid. The known methods of vibrating wave effects on coal array do not always successfully ensure the necessary methane recovery. For experimental research, the effects obtained in laboratory conditions are also considered; even the obtained in vitro data that allow in natural conditions to reproduce quite accurately the effects of sufficiently high accuracy.

One of the main ways of increasing the efficiency of methane recovery is to improve the technology of integrated effects when preparing the exploitation of coal deposits.

### **2. Methods and materials**

A choice of method to impact the coal seam is mainly carried out empirically, since the experimental studies are always associated with high costs; therefore it is not always possible to choose effective hydrodynamic modes of processing (Nozhkin N.V., 1971).

Among many methods of well treatment, a highly recommended method is the method of low-frequency effects on the coal seam through wells drilled from the surface (Nicholaevski V.1989).

A vibration facility developed with direct participation of the author of this article allows a seam face well zone to work in several hydrodynamic regimes without changing the wellhead. Subjects of gas recovery intensification in the minefield were represented by low-permeability coals. Their porosity was 3-5%, the type of coal was crack - porous, and deposit depth of 600 - 650 m. Duration of vibrating wave impact on the well averaged from 0.1 to 0.5 hours. As a result of the above intensification by the

---

<sup>\*</sup> prof. Michail V. Pavlenko: Moscow State Mining University, Street Leninski. 6. 119991 Moscow; Russia, e-mail: mihail\_mggy@mail.ru

method of vibrating wave impact (VVI) in a coal array, absorption has increased by 4-5 times. Technology of vibrating wave impact solves the tasks of how to increase permeability of seams and enhance the recovery of methane and is considered as a set of measures of how to employ the vibrating wave impact of the wells drilled from the surface on the coal seam. A low coefficient of gas recovery and reduced methane recovery from coal seams is a consequence of various physical processes taking place in both the seam face zone and in the seam zones remote from the well. The effectiveness of any impact will depend on how these physical processes generated by this impact are able to neutralize those processes that are responsible for reduction of gas recovery.

If, in the process of hydro-division of the seam due to sliming and blockage of near-the-well zone of the seam, permeability of seam face zone has decreased, degassing of the seam should be started after the measures have been taken to restore its permeability.

The technology of vibrating wave impact is based on a comprehensive approach to how to solve the problems of increasing gas recovery, as well as to how to treat the seam face zone of the well with the aim to increase the gas recovery from the seam including the analysis and calculation of those processes on the basis of which the facility is designed and manufactured, and the impact parameters are selected.

### 3. Results

Hydraulic fracturing of the seam is widely used to increase the permeability of the seam zone. This, however, does not always yield positive results. In particular, the results of hydraulic fracturing of the seam are often unpredictable; out of a series of operations carried out, at least 5-10% are terminated prematurely due to breakthrough of seam water to nearby mining drifts. In addition, an improper choice as for fluid filters, can, by contrast, lead to blockage of seam face zones.

Technology of vibrating wave impact (VVI) has established itself exclusively in the positive terms. Its application at the stage of development enables us to start the well operation through the change of collecting properties of the coal seam. It is noteworthy that during the vibrating wave impact the well fluid starts to be absorbed by the seam within a few hours after the impact. This effect is achieved by the initiation of periodic elastic vibrations in both the seam face zone and the whole coal seam (Fig. 1).

Long-term results of research give reasons to consider the effects of elastic vibrations on the filtration processes in saturated porous media as an established fact (Pavlenko M.V., 2001).

Following the impact on the well, the fracture of zone with low seam permeability was often observed due to formation of high crack areas. The treated seams exerted the changes in the area of crack formation spread over more than 70-120 meters.

This phenomenon can be explained by the fact that these effects were due to the resonance phenomena in the productive seams (Kurlenya M.V., Serdyukov S.V., 1999).

The impact excites fluid oscillations in the coal seam saturated with fluid; these oscillations are accompanied by significant alternating loads contributing to the increase in the seam permeability and subsequently to the enhanced recovery of methane due to the following main effects:

- Increase in volumes of seam filtration in the existing pore radius and the pressure gradient due to the "piston effect", which leads to the increase in the number of cracks.
- Increase or restoration of seam permeability and its face zone is achieved due to cleaning the porous and perforated flues of slack coal, as well as the increase in effective cross-section of cracks, involving in the process of filtering the remote zones of coal seam after its hydraulic fracturing.
- Involvement in the process of filtering of the fixed volume of fluid injected within the previous hydro-division of the seam, as well as under the current radius of the developed cracks and the pressure gradient, which leads to the increase of the coefficient of gas recovery.
- Weakening of the link between the fluid and the cracks surface  $s$  in the coal increases the phase permeability of methane, which contributes to the increase in methane recovery.
- Manifestation of seismic effect contributes to the displacement of stationary fluid layers fixed at the surface; therefore their involvement in the filtering process increases the permeability of the coal seam and of the coefficient of gas recovery from the coal.



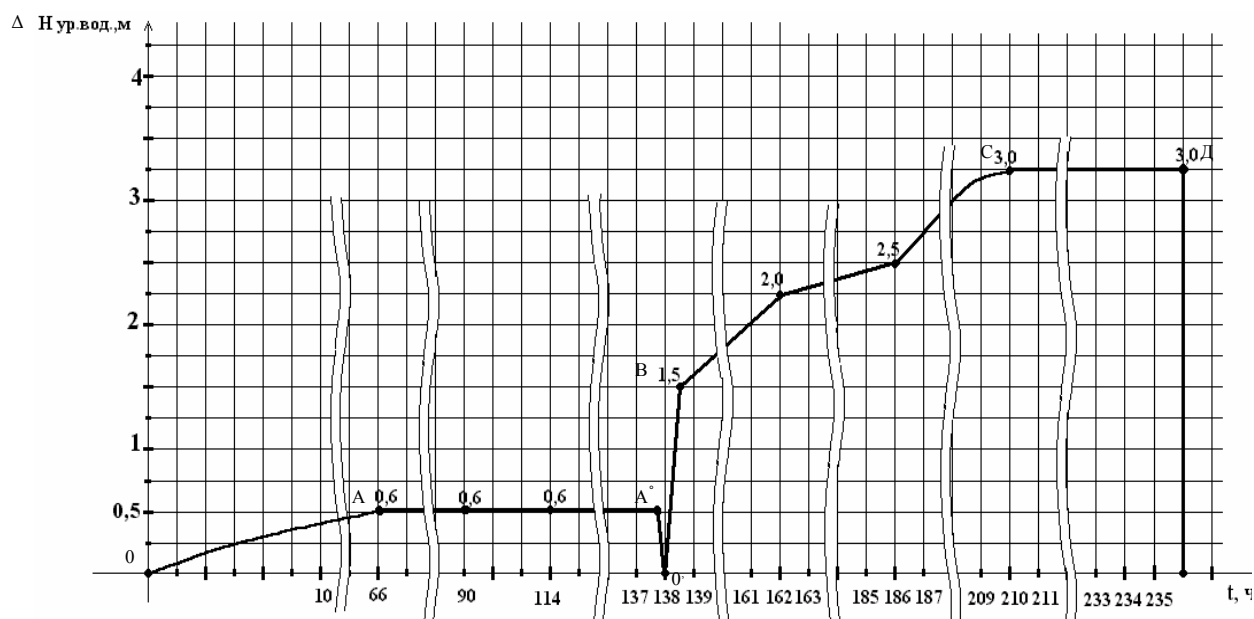


Fig. 1: Hydrodynamics of seam during the period of vibration impact after hydro-division through the well number 4447 on the coal seam of "Komsomolskaya" Vorkutaugol.

$\Delta H$ -lowering of water level in the well relative to its filling, m;

OA-lowering of level under hydrostatic column;

AO'-water topping to the well;

O'B-period of vibration impact;

BC- lowering of level due to imposition of oscillations;

DM-level stabilization.

A controllable source of elastic waves in the well used to impact the coal seam must, on the one hand, have a sufficient power to start the stagnant water moving. This can be offered by vibrating wave impact. The application of wave vibration impact, necessary for the initiation of considerable formation and growth of cracks in the coal array, facilitates the formation of steady flow of methane from the coal fractured structure, regardless of coal permeability and hydrostatic pressure of the surrounding array.

The process of wave formation in the array from the source of oscillations is accompanied by an elastic impact of the frequency of 30-40 Hz and the amplitude of 3-5 mm, and the pressure of more than 10 - 40 MPa.

Wave vibration impact exhibits alternating loads on the seam face zone of the seam and the seam as a whole. As a result of multiple cycles "compression – expansion", alternating hydraulic pressure waves propagate along the seam skeleton and through its porous medium, and improve the capacity and filtration properties of rocks in the near-well zone. Pressure pulses reveal the natural cracks and contribute to the formation of new cracks.

An important factor is that the coal seam itself has its own resonant frequency and this should be considered through the wave impacts.

On the other hand, a rigorous theory based on broad frequency ranges of vibrating wave impact avoids an overcomplexity of mathematic modeling of the process which is characterized by the following parameters: pressure of methane in the seam, temperature of rocks, methane absorption, limiting volume of coal array.

#### **4. Conclusions**

Complex research of vibrating wave impact based on a wide range of seam thickness, methane content, pressure and temperature is also needed to account for the impact on the dynamic features of the array. This research allows us to select optimal working parameters of technological facilities using the vibrating wave impact and thereby to reduce energy costs and increase the duration of their effectiveness (Pavlenko M.V., 2001).

The solution of the tasks mentioned in connection with the spread of vibrating wave impact technology is becoming increasingly important for the study of porous-crack coals and requires an integrated approach based on modern research methods and new theoretical approaches to describe them.

#### **References**

- Nicholaevski V. (1989) The mechanism of vibration exposure on the recovery of oil deposits and the dominant frequency, Dokl. USSR .- 1989 .- T. 307, № 3, S. 570-575.
- Kurlenya M.V., Serdyukov S.V. (1999) Low-frequency resonances of seismic luminescence of rocks in the field of low energy vibroseis. Journal of Mining Science, № .1, - p. 3 - 7.
- Pavlenko M.V., et al. (2001) Vibration exposure through the hole at the ground surface in order to increase the permeability of the coal array. GIABA. M.: Moscow State Mining University. - 2001 .- № 1.-p.40-43.
- Nozhkin N.V. (1971) Preliminary decontamination with directional hydraulic dissection bed. - M.: MGI.

## **APPLICATION OF THE SIMULATION BASED RELIABILITY ANALYSIS ON THE ASSESSMENT OF THE CRITICAL THROUGH WALL CRACK STABILITY**

**L. Pečínka<sup>\*</sup>, M. Švrček<sup>\*</sup>**

**Abstract:** *Specific feature of the nuclear power plants is in comparison with coal fired plants the break postulation of each high energy piping. Fluid system is considered as high-energy piping if the maximum operating temperature exceeds 100°C and the maximum operating pressure exceeds 2MPa. Based on the progress of the linear fracture mechanics US NRC approved deterministic „leak before break“ methodology. If the defined requirements are met, the break postulation may be canceled. The first step is the assessment of the through wall critical length  $l_{crit}$ . Using the Simulation Based Reliability Analysis approach all uncertainties in the input data of  $l_{crit}$  are in the paper analyzed and the related probability of pipe failure is predicted.*

**Keywords:** *Leak-before-break, probabilistic calculations, crack.*

### **1. Historical Background**

Break postulation of the primary piping of PWR type reactors has been established in 1959 as the part of the US NPP Shipping port design. In 1975 US Nuclear Regulatory Commission (NRC) explained their position on the determination of break locations and dynamic effects associated with the postulated rupture of piping in the Standard Review Plan 3.6.2 (SRP 3.6.2). The basis for postulating pipe breaks inside containment were at that time expressed in the Regulatory Guide 1.46 while the rules for postulating pipe breaks outside containment were summarized in the SRP 3.6.2, part Mechanical Engineering Branch 3-1. This version of S.R.P. was updated in 1981 (US NRC, 1981). One of the major modifications was the extension of the MEB 3-1 from break locations outside containment to break location inside and outside containment.

In 1987 MEB 3-1 again went through some substantial changes. The US NRC recognized that the need for two intermediate breaks in a pipe line, that respects the imposed stress criteria, is no longer required. And in parallel with the changes in the ASME Code, they also updated the stress criterion in accordance with these changes (US NRC, 1987).

Based on the advanced fracture mechanics technology Westinghouse submitted in 1982 to the NRC staff topical reports “Mechanistic Fracture Evaluation of Reactor Coolant Pipe Containing a Postulated Circumferential Through Wall Crack” (WCAP 9558, Rev. 2) and “Tensile and Toughness Properties of Primary Piping Weld Metal for Use in Mechanistic Fracture Evaluation” (WCAP 9787). The NRC staff concluded that large margins against unstable crack extension exist postulated to have large flaws and subject to the safe shutdown earthquake (SSE) in combination with the loads associated with normal plant conditions. This approach has been called “leak-before-break” and US NRC issued in October 1986 the S.R.P. 3.6.3 “Leak-Before-Break Procedures” where explained their position to elimination of pipe ruptures and also elimination of pipe whipping dynamic effects (US NRC, 1986).

### **2. Deterministic LBB approach**

The potential users of the LBB approach shall submit to NRC staff the following calculations

- length of the circumferential through wall crack with leak rate 38 l/min.,

---

<sup>\*</sup> Ing. Ladislav Pečínka, CSc. and Ing. Miroslav Švrček: Nuclear Research Institute Rez, Husinec-Rez, čp. 130, 250 68 Rez, CZ, e-mails: pel@ujv.cz, smi@ujv.cz

- length of the critical through wall crack,
- to demonstrate that there is a margin of at least 2 between the leakage size flaw and the critical size crack to account for the uncertainties inherent in the analyses and leak detection capability,
- determine margin in terms of applied loads by a crack stability analysis. Demonstrate that the unstable crack growth of leakage cracks will not occur. Or demonstrate that crack growth is stable and the final crack size is limited such that a double-ended pipe break will not occur.

### 3. Probabilistic LBB

Probabilistic LBB is essential to highlight effects of uncertainties around the deterministic criteria of LBB. All of them have a key request-good understanding of the different degradation mechanism. The level of integration in the decision process of probabilistic considerations on structural integrity of piping as passive component

- is different by country (from decision based on risk level in some countries to no consideration in few other countries),
- need a large investment from all partners (Utilities, Safety Authorities and Technical Support Organizations) to obtain conclusion acceptance,
- can be completed by “economic” considerations.

In NRI the probabilistic approach is based on the Simulation Base Reliability Analysis (SBRA) (Marek, 2003). The key elements are as follows

- the probability of pipe failure is calculated based on the theory of limit states,
- all random input quantities as loadings, mechanical and geometrical properties etc. are transformed on the output quantities which express effects of loadings and resistances,
- using Monte-Carlo simulation the empirical distribution of this output quantities is obtained,
- the reliability function of solved problem is developed and the region of interest is divided on the reliable and the failure parts,
- finally the probability of pipe break as a needed parameter of reliability is calculated.

All this calculations are based on the computer code Anthill (Guštar). In the next chapter the application on the critical circumferential through wall crack length  $l_{crit}$  is demonstrated.

### 4. Application of the SBRA methodology to the $l_{crit}$ calculations

According (ČSKAE, 1991; Pečínka, 2010) the master equation for calculation of the critical through wall crack (TWC) takes the form

$$\frac{2\sigma_f}{\pi}(2\sin\beta - \sin\theta) + M(\sigma_{red})_m = M[(\sigma_{red})_m + (\sigma_{red})_b + (\sigma_{red})_c]Z \quad (1)$$

where

- $\theta$  half angle of the postulated TWC
- $(\sigma_{red})_m$  effective primary stress induced by internal pressure, sustained loads and safe shutdown earthquake (SSG)
- $M$  prescribed safety coefficient (Pečínka, 2010)
- $\sigma_f$  flow stress of the pipe material
- $\beta = 0,5[(\pi - \theta) - \pi(\sigma_{red})_m / \sigma_f]$
- $(\sigma_{red})_b$  effective bending stresses at normal operational mode

$(\sigma_{red})_c$  thermal expansion stresses at normal operational mode

$Z$  Z factor according ASME Code Section XI

It is possible to use equation (1) for the definition of the reliability function  $RF$ , but more advantageous seems to apply modification according (ČSKAE, 1991) where is defined that the allowable values of  $\theta = l_{crit} / 2R$  shall met the conditions (Pečínka, 2010).

$$S = \frac{2\sigma_f}{\pi} \left\{ \cos \frac{l_{crit}}{4R} \times \cos \frac{\pi}{2} \frac{(\sigma_{red})_m}{\sigma_f} - \sin \frac{l_{crit}}{4R} \sin \frac{\pi}{2} \frac{(\sigma_{red})_m}{\sigma_f} - \sin \frac{l_{crit}}{4R} \right\} > 0 \quad (2)$$

or

$$S = \frac{2\sigma_f}{\pi} \sin \left[ -\pi \frac{(\sigma_{red})_m}{\sigma_f} \right] > 0 \quad (3)$$

where  $R$  denote mean radius of the pipe.

For the application of the SBRA the reliability function shall met the condition  $RF = S > 0$  and we shall search the cases at which  $RF > 0$ . As the independent coordinates will be chosen  $l_{crit}/2R$  and  $\pi(\sigma_{red})_m / 2\sigma_f$ , and using computer code Anthill we will search regions where condition  $RF > 0$  will be met together with related probability.

## 5. Numerical example

Numerical example will be demonstrated on the primary circuit of Armenia NPP primary circuit, see Fig. 1. The critical cross section is marked as O.

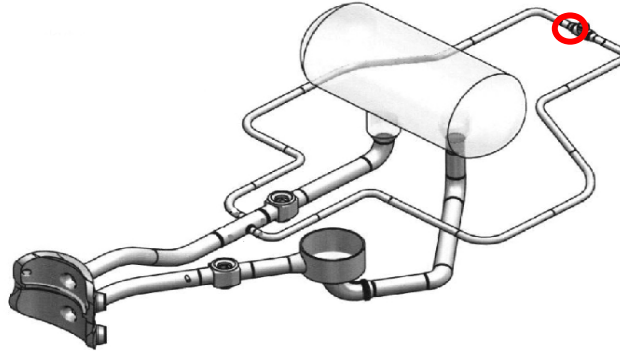


Fig. 1: Primary circuit of the Armenia NPP Metsamor.

Results of the deterministic calculations are as follows:  $l_{leak} = 156.7 \text{ mm}$ ,  $l_{crit} = 450 \text{ mm}$ ,  $l_{crit}/l_{leak} = 2.9$ ,  $M_{nom} = 3\,037 \text{ Nm}$ ,  $F_{nom} = 433\,130 \text{ N}$ ,  $M_{SSE} = 44\,850 \text{ Nm}$ ,  $F_{SSE} = 10\,084 \text{ N}$ . As the variable input quantities are chosen: diameter  $D$  and wall thickness  $t$  of the pipe, loadings ( $M_{nom}$ ,  $F_{nom}$ ,  $M_{SSE}$ ,  $F_{SSE}$ ) and material properties ( $R_{p0.2}$ ,  $R_m$  and relater  $\sigma_f$ ). Histograms are illustrated in the Figs. 2 - 4.

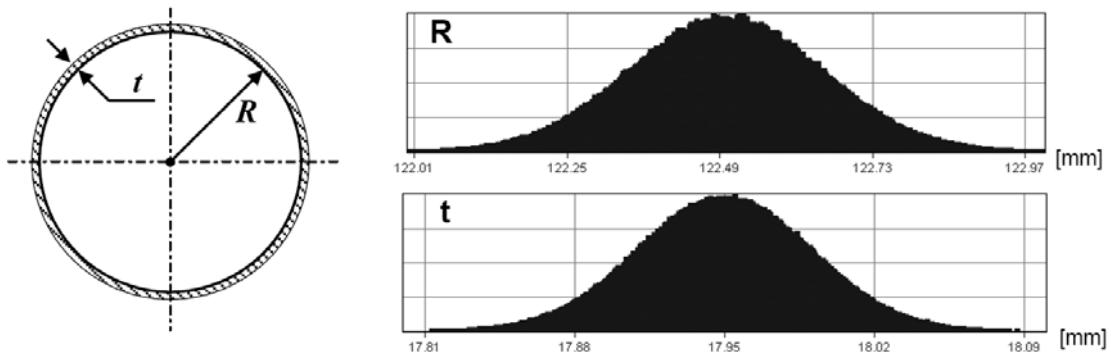


Fig. 2: Histograms of pipe parameters.

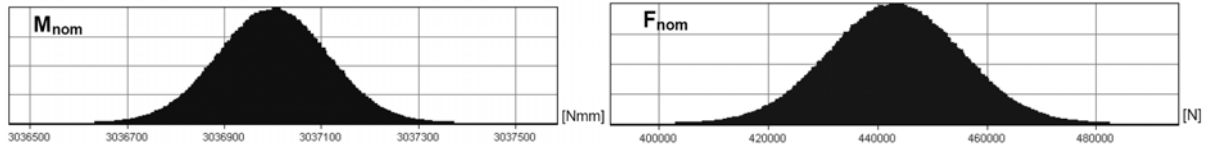


Fig. 3: Histograms of  $M_{nom}$  and  $F_{nom}$ .

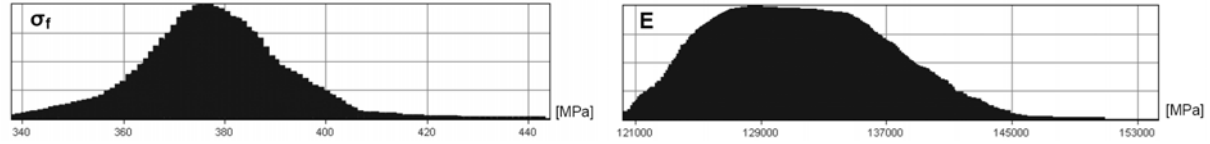


Fig. 4: Histograms of material parameters.

We will suppose in the next the random variability of the crack length  $l_{leak}$ . The normal distribution function and the variability  $\pm 10\%$  are supposed. The numerical calculations are performed for  $l_{leak} = (311 \pm 10\%, 370 \pm 10\%, 405 \pm 10\% \text{ and } 415 \pm 10\%,)mm$ . Using Anthill computer code the result are illustrated in the form of pseudo-2D diagrams  $l_{crit}/2R$  and  $\pi(\sigma_{red})_m / 2\sigma_f$ , see Fig. 5. Each point of the diagram represents one step of the simulation. Red color represents the region with most density of probability. Orange color represents those steps of simulation, where reliability function do not met the requirement  $RF > 0$ .

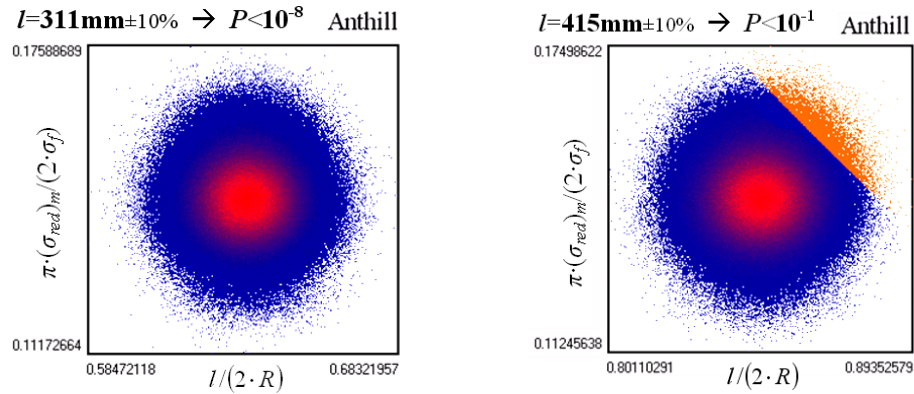


Fig. 5: 2D diagrams representing results of all simulation steps.

## 6. Conclusions

As mentioned in chapter 3 the probabilistic LBB is essential to highlight the effects of uncertainties around the deterministic criteria of LBB. The most important deterministic criterion takes the form  $l_{crit}/l_{lead} \geq 2$ . The probabilistic approach proved that the corresponding probability of pipe rupture is lesser than  $10^{-8}$ . If the probability  $10^{-7}$  would be accepted then the ratio  $l_{crit}/l_{lead}$  should be lesser than 2.

## References

- US NRC: Standard Review Plan for the Review of Safety Analysis Reports for Nuclear Power Plants, Chapter 3.6.2, NUREG 0800, 1981.
- US NRC: Relaxation in Arbitrary Intermediate Pipe Rupture Requirements, Generic Letter 87-11, 1987.
- US NRC: Leak-Before-Break, Standard Review Plan for the Review of Safety Analysis Reports for Nuclear Power Plants, Chapter 3.6.3, NUREG 0800, 1986.
- Marek, P. et al., (2003) Probabilistic Assessment of Structures Using Monte Carlo Simulation, TeReCo, 2<sup>nd</sup> Edition, Prague.
- Guštar, M., Marek, P.: Windows help file of program Anthill™ 2.5.0.1 Professional.
- ČSKAE: Požadavky pro sestavení a obsah bezpečnostních zpráv a jejich dodatků: Postup pro stanovení průřezu únik před roztržením, № 1, 1991.
- Pečínka, L., Švrček, M. (2010) Application of the Simulation Based Reliability Assessment Method on the Assessment of the Critical Circumferential Through Wall Crack Length, Report NRI, № DITI 2300/21.



## DYNAMIC MODULUS OF ELASTICITY OF DENTAL GYPSUM

T. Plachý\*, H. Němcová\*, P. Tesárek\*, M. Polák\*

**Abstract:** The paper describes the influence of water/gypsum ratio to the dynamic modulus of elasticity of dental gypsum. Commercially available dental gypsum Interdent® (with compressive strength 250 MPa after 24 hours) was used in our study. It was assumed that water to gypsum (w/g) ratio would have influence on its mechanical properties. Therefore, five different types of specimens with w/g=0.18, 0.19, 0.20, 0.21 and 0.22, further denoted as G0, G1, G2, G3 and G4, were prepared. These samples were tested using nondestructive method. The dynamic modulus of elasticity was determined based on measured basic resonant frequency of longitudinal vibration of the specimens. At the end, the comparison of obtained values in dependence on water/gypsum ratio was done.

**Keywords:** Water/gypsum ratio, dental gypsum, dynamic modulus of elasticity, resonant method, natural frequency.

### 1. Introduction

The commercially available dental gypsum was used in our tests. The dental gypsum a little bit differs from the classic gypsum used in building industry. The main difference is in strength of the dental gypsum which should be much higher. Tab. 1 shows types of dental gypsum. Every type is described from a point of view on strength (compressive) of hardened gypsum and expression during hardening. The table concludes expansion rates during hardening and usual value of water/gypsum ratio.

Tab. 1: Types of dental gypsum.

Type of gypsum	Description	Expansion rate [%]	Water/gypsum ratio
Type I	Expression plaster	0.15	0.50
Type II	Model plaster	0.30	0.50
Type III	Hard stone	0.20	0.30
Type IV	Super hard stone (low expansion)	0.10	0.22
Type V	Super hard stone (high expansion)	0.30	0.22

A common gypsum binder on a dental application was used for testing of the determination of dependence between water/gypsum ratio and mechanical properties of gypsum samples. This gypsum binder is an extra hard material for precision techniques during the construction of porcelain crown sand and bridges. The dental gypsum binder is a material with high resistance to compression (resistance after 24 hours is 250 N/mm<sup>2</sup> for a water/gypsum ratio 0.2) with high surface density, resistance to abrasion and low setting expansion (0.1 %).

### 2. Preparation of specimens

The commercially available dental gypsum Interdent® (with compressive strength 250 MPa after 24 hours) was used in our study. It was assumed that water to gypsum (w/g) ratio would have influence

---

\* Ing. Tomáš Plachý, Ph.D., Ing. Hana Němcová, Ing. Pavel Tesárek, Ph.D. and assoc. prof. Ing. Michal Polák, CSc.: Czech Technical University in Prague, Faculty of Civil Engineering, Department of Mechanics; Thákurova 7, 166 29 Prague 6 - Dejvice, Czech Republic, e-mails: plachy@fsv.cvut.cz, hana.nemcova@fsv.cvut.cz, tesarek@fsv.cvut.cz, polak@fsv.cvut.cz

on its mechanical properties. Therefore, five different types of specimens with  $w/g=0.18, 0.19, 0.20, 0.21$  and  $0.22$ , further denoted as G0, G1, G2, G3 and G4, were prepared.

During preparing gypsum specimens, amount of the gypsum binder and amount of water which corresponded with used water/gypsum ratio (in our case five different values) were weighted at first. Then the gypsum was slowly added into the water and vigorously hand mixed with a spade approximately 1 minute until the mass was smooth. The mass was cast into a shape and 30 second vibrated on the vibration table. The specimens were removed from the mould twenty four hours after mixing.

The five specimens of dimensions  $40 \times 40 \times 160$  mm with different water to gypsum ratios were prepared and tested (Fig. 1).

### 3. Impulse excitation method

The impulse excitation method was used for dynamic Young's modulus determination of the gypsum specimens. It is based on measuring the fundamental resonant frequencies. The test arrangement was done for longitudinal vibration (Fig. 1).

The specimen was supported in the middle of its span (Fig. 1), the fundamental longitudinal nodal position. The acceleration transducer Bruel&Kjaer of Type 4519-003 was placed at the centre of one of the end faces of the gypsum specimen (Fig. 1- the right end face). The end face of the gypsum specimen opposite to the face, where the transducer was located, was struck by the impact hammer Bruel&Kjaer of Type 8206. Both signals, the excitation force and the acceleration, were recorded and transformed using Fast Fourier Transform (FFT) to the frequency domain, and the Frequency Response Function (FRF) was evaluated from these signals using the vibration control station Bruel&Kjaer Front-end 3560-B-120 and program PULSE 10.5 (Fig. 2). The test was repeated five times for each gypsum specimen and resultant readings were averaged. From an averaged FRF, the fundamental longitudinal resonant frequency was determined for each specimen. Based on the equation for longitudinal vibration of the beam with continuously distributed mass with free-free boundary condition, the dynamic modulus of elasticity  $E_d$  can be determined using the relation

$$E_d = \frac{4lmf^2}{bt} \quad (1)$$

where  $l$  is the length of the specimen,  $m$  is the mass of the specimen,  $f$  is the fundamental longitudinal resonant frequency of the specimen,  $b$  is the width of the specimen and  $t$  is the thickness of the specimen.



*Fig. 1: Measurement of the natural frequency of longitudinal vibration.*



Fig. 2: Measurement line for the Impulse Excitation Method.

#### 4. Results

At first all three dimensions and weight of the gypsum blocks were measured and weighed (Tab. 2). Based on these properties and the fundamental longitudinal natural frequencies evaluated from FRFs of these gypsum specimens, dynamic modulus of elasticity was evaluated (Tab. 2) using equation (1). The dependence of the 1<sup>st</sup> natural longitudinal frequency of the gypsum specimens on the water/gypsum ratio is shown in Fig. 1 and the dependence of the dynamic modulus of elasticity of the gypsum specimens on the water/gypsum ratio is shown in Fig. 2.

Tab. 2: The measured characteristics of the dental gypsum specimens.

Specimen:	water/gypsum ratio	Weight [g]	Dimensions [mm]			f [Hz]	E <sub>d</sub> [GPa]
			t	b	L		
G0	0.18	452	34.8	40	160	11680	28.37
G1	0.19	465	35.6	40	160	11648	28.18
G2	0.20	481	37.3	40	160	11488	27.27
G3	0.21	462	36.5	40	160	11530	26.80
G4	0.22	458	36.6	40	160	11380	25.77

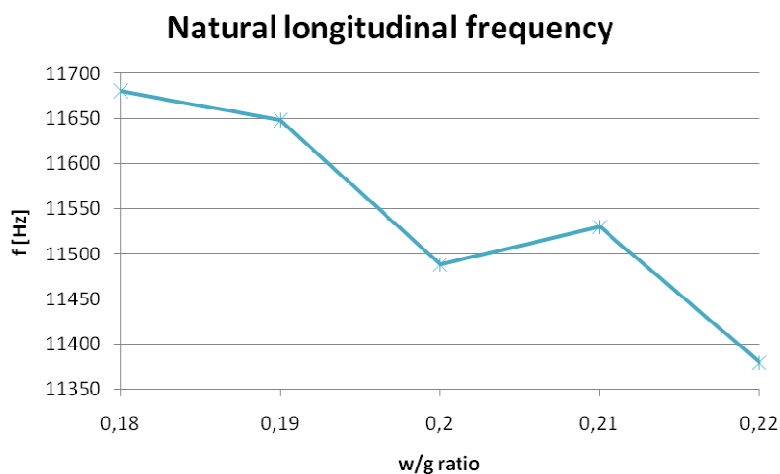
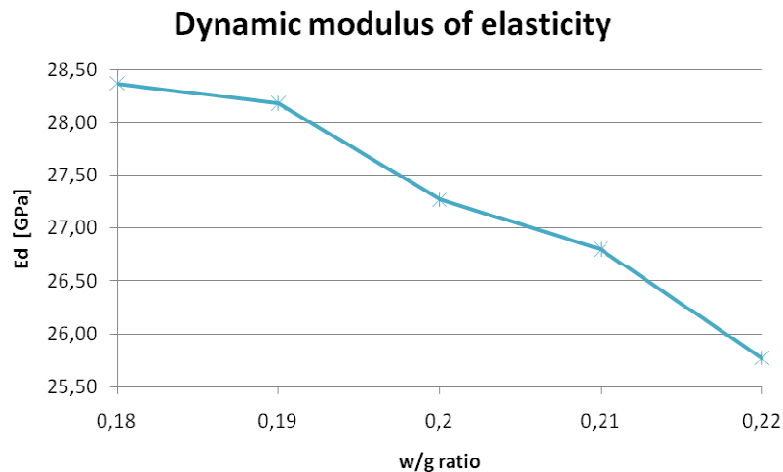


Fig. 3: Dependence of the 1<sup>st</sup> natural longitudinal frequency of the gypsum specimens on the water/gypsum ratio.



*Fig. 4: Dependence of the dynamic modulus of elasticity of the gypsum specimens on the water/gypsum ratio.*

## 5. Conclusions

The paper describes the influence of water/gypsum ratio on the dynamic modulus of elasticity of dental gypsum. The dynamic modulus of elasticity was measured using nondestructive impulse excitation method. From the obtained results (Fig. 2, Tab. 2), it can be seen that the dynamic modulus of elasticity decreases in dependence on increase of the used water/gypsum ratio of the dental gypsum specimens. The total difference between the dynamic moduli of elasticity of the specimens G0 and G4 is about 10 %. Even if we take into account that the accuracy of this method in this case is about 3.5 % of the value  $E_d$ , we can say that the water/gypsum ratio influences the value  $E_d$  of the dental gypsum specimens.

## Acknowledgement

This work has been supported by Czech Technical University under the project No. SGS10/136/OHK1/2T/11 “Advanced experimental methods”.

## References

- ASTM C215 (1991), Standard Test Method for Fundamental Transverse, Longitudinal, and Torsional Resonant Frequencies of Concrete Specimens, Annual Book of ASTM Standards, American Society for Testing and Materials.
- ASTM E1876-01 (2006), Standard Test Method for Dynamic Young's Modulus, Shear Modulus, and Poisson's Ratio by Impulse Excitation of Vibration, Annual Book of ASTM Standards, American Society for Testing and Materials.
- Hájková, A. (2010) Energo-gypsum and its Recycling Options with Regard to Mechanical Properties, (in Czech) Prague, Thesis, Czech Technical University in Prague, pp. 93.
- Jianquan Li, Guozhong Li, & Yanzhen Yu (2005): The influences of gypsum water-proofing additive on gypsum crystal growth, Material Letters, Volume 61, Issue 3, pp. 872-876.
- Malaikah A., Al-Saif K., Al-Zaid R. (2004), Prediction of The Dynamic Modulus of Elasticity of Concrete under Different Loading Conditions, Proceedings of The 8th International Conference on Concrete Engineering and Technology, Kuala Lumpur, University Malaya, Malaysia, pp. 1-7.
- Pickett G. (1945), Equation for Computing Elastic Constants from Flexural and Torsional Resonant Frequencies of Vibration of Prisms and Cylinders, Proceedings ASTEA, American Society for Testing and Materials, Vol. 45, pp. 846-863.
- Radovic M., Lara-Curzio E., Riester L. (2004), Comparison of Different Techniques for Determination of Elastic Properties of Solids, Materials Science and Engineering, Vol. 368, No. 1, pp. 56-70.

## THE DOMAIN DECOMPOSITION WITH THE CONTACT PROBLEM

J. Podešva<sup>\*</sup>

**Abstract:** *The modeling of the mechanical structures with large number of degrees of freedom (DOF) was in the past the problem of the machine time and disk space. On the today's hardware it is possible to solve 106 equations without big problem. But if the algorithm requires the iteration approach (non-linearities) or solving the dynamic problem via direct numerical integration this could take long time and large disk space. In this case the domain decomposition could give the advantage. The paper describes the solution of the large mechanical structure of the bearing with rather high number of contact pairs using so called "super-elements".*

**Keywords:** *Domain decomposition, substructures, super-elements, contact.*

### 1. Introduction

The domain decomposition is the special approach to solving the large number of equations. It belongs to the group of elimination methods of strong decreasing the number of degrees of freedom (DOF). It consist in selecting the small number of DOF and solving this small system of equations. This takes short time and needs small disk space. The solution is then expanded to the original set of DOF.

The subject of modeling in this paper is the roller bearing with two rings and large number of rolling elements (balls or cylinders). Every touch line between the ring and the roller element represents the contact pair.

The model has four attributes :

- large number of DOF (fine model with large number of small finite elements),
- is naturally divided into substructures (rings and roller elements),
- the single substructures touch the others in the cramped area,
- the touch area between rings and roller elements is a typical contact pair.

Both static and dynamic analysis of the mechanical behavior of such a roller bearing brings the necessity of solution of the large system of equations with non-linear problem - contact.

For such problems the special solvers were developed (Daněk, 2003, Dobiáš, 2010).

### 2. The Domain Decomposition

The domain decomposition technique allows to strongly decrease the number of DOF. The methods of reduction can be split into two groups.

The elimination methods consist in eliminating (neglecting) the large number of DOF. The typical representative is the static condensation method.

The transformation methods consist in defining the totally new set of unknown coordinates (usually of no physical meaning) using transformation matrix. The typical representative is the modal transformation method.

The domain decomposition method belongs to the first group.

---

<sup>\*</sup> assoc. prof.. Ing. Jiří Podešva, Ph.D.: VŠB - Technical University of Ostrava, 17. listopadu 15; 708 33, Ostrava; CZ, e-mail: jiri.podesva@vsb.cz

Consider the classic task of the linear static, written in matrix form.

$$\mathbf{K} \cdot \mathbf{q} = \mathbf{f} \quad (1)$$

where  $\mathbf{K}$  is the stiffness matrix,  $\mathbf{q}$  is the vector of unknown translations and  $\mathbf{f}$  is the vector of loading forces. Let us split the original set of DOF  $\mathbf{q}$  into the sub-set  $\mathbf{q}_m$  of so called “master” DOF, which will be retained after reduction, and the sub-set  $\mathbf{q}_s$  of so called “slave” DOF, which will be eliminated. The mathematical record will then be :

$$\begin{bmatrix} \mathbf{K}_{mm} & \mathbf{K}_{ms} \\ \mathbf{K}_{sm} & \mathbf{K}_{ss} \end{bmatrix} \cdot \begin{Bmatrix} \mathbf{q}_m \\ \mathbf{q}_s \end{Bmatrix} = \begin{Bmatrix} \mathbf{f}_m \\ \mathbf{f}_s \end{Bmatrix} \quad (2)$$

or

$$\begin{aligned} \mathbf{K}_{mm} \cdot \mathbf{q}_m + \mathbf{K}_{ms} \cdot \mathbf{q}_s &= \mathbf{f}_m \\ \mathbf{K}_{sm} \cdot \mathbf{q}_m + \mathbf{K}_{ss} \cdot \mathbf{q}_s &= \mathbf{f}_s \end{aligned} \quad (3)$$

If we will derive from the second group of equations:

$$\mathbf{q}_s = \mathbf{K}_{ss}^{-1} \cdot (\mathbf{f}_s - \mathbf{K}_{sm} \cdot \mathbf{q}_m) \quad (4)$$

or

$$\mathbf{q}_s = \mathbf{K}_{ss}^{-1} \cdot \mathbf{f}_s - \mathbf{K}_{ss}^{-1} \cdot \mathbf{K}_{sm} \cdot \mathbf{q}_m \quad (5)$$

putting into the first group of equations we obtain the system of equations for the master DOF.

$$(\mathbf{K}_{mm} - \mathbf{K}_{ms} \cdot \mathbf{K}_{ss}^{-1} \cdot \mathbf{K}_{sm}) \cdot \mathbf{q}_m = \mathbf{f}_m - \mathbf{K}_{ms} \cdot \mathbf{K}_{ss}^{-1} \cdot \mathbf{f}_s \quad (6)$$

After substitution:

$$\begin{aligned} \tilde{\mathbf{K}} &= \mathbf{K}_{mm} - \mathbf{K}_{ms} \cdot \mathbf{K}_{ss}^{-1} \cdot \mathbf{K}_{sm} \\ \tilde{\mathbf{f}} &= \mathbf{f}_m - \mathbf{K}_{ms} \cdot \mathbf{K}_{ss}^{-1} \cdot \mathbf{f}_s \end{aligned} \quad (7)$$

the equations have the same form as the original equations.

$$\tilde{\mathbf{K}} \cdot \mathbf{q}_m = \tilde{\mathbf{f}} \quad (8)$$

Here  $\tilde{\mathbf{K}}$  is the reduced stiffness matrix, and  $\tilde{\mathbf{f}}$  is the reduced force vector. The solution can be extended by the reduced mass matrix  $\tilde{\mathbf{M}}$  and reduced damping matrix  $\tilde{\mathbf{B}}$  into the area of linear dynamics.

To the above written we must note that while the original stiffness matrix  $\mathbf{K}$  is narrow strip and sparse, the reduced stiffness matrix  $\tilde{\mathbf{K}}$  is full. That is why the set of master DOF must be as small as possible.

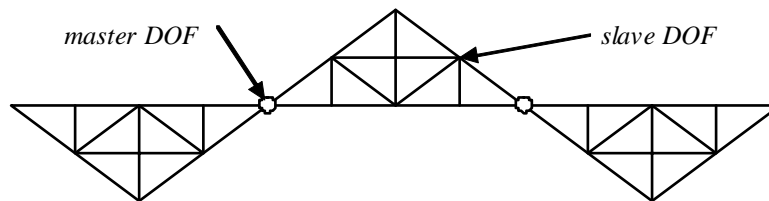


Fig. 1: The main structure divided into three sub-structures.

If the mechanical structure (see Fig. 1) can be naturally dividing into a few sub-structures, these will be the sub-domains. The sub-structures are joined together in the narrow boundaries of the very small number of DOF. These interface DOF will be retained as masters, the interior DOF will be hidden as slaves.



The reduced stiffness matrix  $\tilde{\mathbf{K}}$  of such structure represents the stiffness matrix of the structure in which the single sub-structure seems to be the single finite element. However because in real they are rather large-scale systems they are called “super-elements”.

The sub-domains (super-elements) must be internally linear. If the super-elements are used to build the “macro model”, this can contain also elements of other types, including contact elements, and other non-linearities.

### 3. The Contact Problem

The two bodies, contacting one the other, represents the contact problem. It is usually solved by two sets of surface elements, covering the bodies. In the Ansys program they are called “contact elements” and “target elements” (see Fig. 2). One body is covered by contact elements, the other by target elements. The penetration of the contact surface nodes into the target surface is checked during the solution. There are two main methods, the Lagrange method and the penalty method, and the number of auxiliary tools for this.

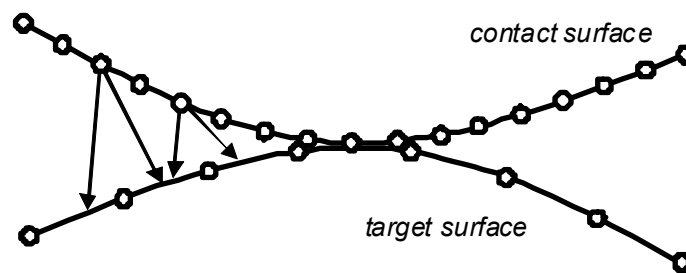


Fig. 2: The contact and the target surface.

The basic principals of mathematical description and solution methods are described in (Crisfield, 2000) and (Zhi Hua Zhong, 1993)

### 4. The Bearing Model

The modeling of the two row roller bearing (see Fig 3) is described in the paper. The objective is to determine the contact pressure on the rollers. The standard finite element model was built using the eight-nodes 3D elements (bricks). On the touching surfaces of the inner ring, two outer rings and rollers the contact pair elements were generated. The bearing consists of the inner ring, two outer rings and 70 rollers (in two series, 35 rollers both).

Each roller has the contact with inner and outer ring, it means 140 contact surfaces in total. For such a number of contact pairs it was not possible to use the “contact wizard” in the Ansys program. To generate the 140 meshes of contact elements the macro was written. This macro contains the cycle of 35 loops. In every loop the nodes on the rings and the rollers were selected on the ring circumference by 360/35 degrees and then on the lower and upper ring. On selected nodes the contact (the roller) and target (the ring) elements were generated.

### 5. The Super-element Model

The bearing is the typical structure, mentioned in the chapter 2. The natural sub-domains are the inner ring, the two outer rings and the 70 rollers (see Fig. 3). To define the single super-elements (the rings) the Ansys tools were used. The 70 super-elements (the rollers) were defined in the cycle of 35 loops (one lower and one upper roller in each loop). To do this the macro was written.

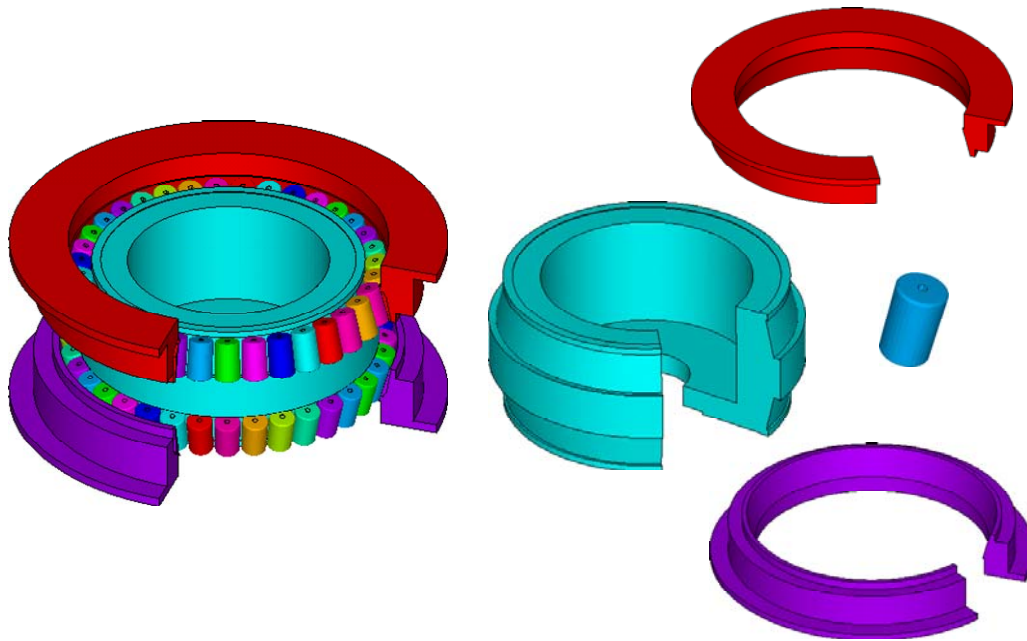


*Fig. 3: The bearing and the super-elements.*

To define the mesh of contact and target elements the 3D mesh of brick elements must exist. This gives the topology on which the mesh of surface elements is generated automatically. But the super-element model does not contain the brick elements and the topology for the surface mesh does not exist. To build the contact pairs the mesh of surface elements (both contact and target) on the standard model was exported into the special file and then imported into the super-element model. Of course it was strongly necessary to conserve the node numbering.

The final model of super-elements and contact elements was completed by boundary condition (the support) and force loading (the same as on the standard model) and then ready for analysis.

## 6. Conclusion

While the standard model of brick elements consists of 2 272 617 DOF, the super-element model consists of 65 940 DOF. This means the strong reduction of the model scale. The prize is rather complicated procedure to build the super-element model with contacts. The question is the efficiency of this approach. For single analysis it is much more effective to use the standard model. The super-element model will be effective to perform a number of analyses with iterations.

## Acknowledgement

The work was done under support of the MSM 6198910027 project.

## References

- Crisfield, M.A. (2000) Non-linear Finite Element Analysis of Solids and Structures. John Wiley & sons, Chichester, 2000. ISBN 0 471 92956 5
- Zhi Hua Zhong. (1993) Finite Element Procedures For Contact - Impact Problems. Oxford University Press, Oxford, 1993, ISBN 0 19 856383 3
- Daněk, J. (2003) Domain decomposition method for contact problems with small range contact. Mathematics and Computers in Simulation. 2003. ISSN 0378-4754
- Dobiáš, J., Pták, S., Dostál, Z., Vondrák, V., Kozubek, T. (2010) Non-linear scalable TFETI domain decomposition based contact algorithm. IOP Conference Series: Materials Science and Engineering. Vol. 10, N. 1. 2010.

## **ADDED MASS AND DAMPING OF INCOMPRESSIBLE VISCOUS FLUID**

**L. Pohanka<sup>\*</sup>, E. Malenovský<sup>\*</sup>**

**Abstract:** Approach for determination of the dynamic behavior of an elastic body submerged in fluid is presented in this contribution. Method is based on independent solution of the fluid and structure. Commercial computational fluid dynamic software (ANSYS CFX) is used for determination of added effects of the fluid. These added effects are included into finite element model of the body in form of MATRIX27 finite element.

**Keywords:** Fluid structure interaction, FEM, added mass, added damping, ANSYS.

### **1. Introduction**

An incompressible fluid which surrounds an elastic body has significant influence on his dynamic behaviors. If the body is displaced, surrounding fluid is also displaced to accommodate its moving. This move generates pressure change and forces acting on this solid body. This effect has significant influence on eigenfrequencies and damping value. Computation of these values is important for effective construction of a hydraulic machine, vessels and so on.

Researches have been interested in this problem for long time and lots of various approaches have been used for its solution. An added mass which replace the inertia effects of the fluid can be solved. Another possible approach is direct solution of eigenfrequencies of the fluid-structure system. Simulation in time domain and subsequent evaluation of the response can also be used.

Finite element method (FEM) is widespread use because it allows solution of body which has general shape. Pressure field in the compressible fluid as solution of the wave equation has been presented by Zienkiewicz. FEM is used for determination of the displacement of the structure and also pressure in the fluid. This description gives one system of linear equations. Solution of the eigenvalue problem of the nonsymmetrical matrices gives eigen values and eigen vectors. Similar approach has been described in Schroeder (1975). Laplace equation for description of the incompressible fluid is used for example by Altinisik (1981) and transformation of the matrices to a symmetric form was presented by Everstine (1981).

More advanced than previous approach is using of potential flow. FEM also determines displacement of the structure and flow in the fluid. This method can be used for determination of the eigenfrequencies an eigenmodes for the structures in flowing fluid. Nitikitpaiboon (1993) introduce ALE (Arbitrary Lagrangian-Eulerian) description for this approach.

Solution in time domain is most universal. Monolithic approach has been used by Zhang (2003). The structure deformation and fluid flow is solved in one system of the equation. Main advantage of the partitioned approach is that widespread commercial computer programs can be used. On the other hand, solution in time domain can be complicated because ALE which is used for representation of the displacement of the fluid boundary is not suitable for problems with small deformations. Combination of the Lagrangian desription for the structure and Arbitrary Lagrengiane Eulerien desription for the fluid flow on the moving grid my cause problems with numerical stabilyty. Transpiration method tries to remove this disadvantage. This method solves the problem on fixed grid and special transpiration

---

<sup>\*</sup> Ing. Lukáš Pohanka and prof. Ing. Eduard Malenovský, DrSc.: Institute of Solid Mechanics, Mechatronics and Biomechanics, Brno University of Technology, Technická 2896/2; 616 69, Brno; CZ, e-mails: ypohan00@stud.fme.vutbr.cz, malenovsky@fme.vutbr.cz

boundary condition is used. de Morais (2007) compared results of this method with results which was obtained by using ALE.

## 2. Methods

Inclusion of the influence of fluid on the elastic body in the form of added effects (added mass, added damping, added stiffness) is simplest and most effective. In the case of viscous fluid, this approach is not exact. Exact solution of the influence of viscous fluid on the body is very difficult and may not be feasible. If the fluid is incompressible viscous and has no mean flow can be body motion expressed in simplified form:

$$(\mathbf{m}_{add} + \mathbf{m})\ddot{\mathbf{x}} + (\mathbf{b}_{add} + \mathbf{b})\dot{\mathbf{x}} + \mathbf{k}\mathbf{x} = \mathbf{F}_{ext} \quad (1)$$

Where:  $\mathbf{m}_{add}$  - added mass matrix,  $\mathbf{m}$  - mass matrix,  $\ddot{\mathbf{x}}$  - acceleration vector,  $\mathbf{b}_{add}$  - added damping matrix,  $\mathbf{b}$  - damping matrix,  $\dot{\mathbf{x}}$  - velocity vector,  $\mathbf{k}$  - stiffness matrix,  $\mathbf{F}_{ext}$  - external forces matrix.

Some simplifying assumptions must be accepted to obtain additional effects. Neglect of convective term of the Navier-Stokes equation or irrotational flow may not be suitable for this task. Determination of the fluid force act on the body can be difficult in this case. Determination of damping value by linearized model has been valid only for extremely small displacement, but displacement has been much greater in practice.

Approach which is presented is based on independent solution of deformation of the elastic body and flow in the fluid (Pochylý, 2008). The solution assumes that solid body vibrates harmonically and modal shape of the isolated body is the same as modal shape of the body which is surrounded by fluid. This approach is significantly modified. The neglect of the convective term of the N-S equation and Laplace transformation are not used for solution. The motion of the elastic body is described by equation (1). The flow in the fluid is expressed by simplified Navier-Stokes equation in form (2) and continuity (3). This system of equations is linear.

$$\frac{\partial \mathbf{c}}{\partial t} = -\frac{1}{\rho} \frac{\partial p}{\partial \mathbf{x}} \quad (2)$$

$$\frac{\partial \mathbf{c}}{\partial \mathbf{x}} = 0 \quad (3)$$

Where:  $\mathbf{c}$  – velocity vector,  $t$  – time,  $p$  – pressure,  $\mathbf{x}$  – coordinate,  $\mathbf{w}$  – modal shape,  $\mathbf{n}$  – normal vector. Boundary condition on the interface is:

$$\mathbf{c} = \ddot{\mathbf{x}}_s \mathbf{w} \quad (4)$$

Added mass is obtained as force which fluid acts on the body, which is moved by unit acceleration (5). Assumption is that displacements of the body are small given the size of the body and fluid velocity is also small.

$$\mathbf{m}_{add} \ddot{\mathbf{x}}_s \mathbf{w} = \int_S p \mathbf{n} dS \quad (5)$$

Commercial computational programs ANSYS and CFX are used for solution. Solution must be provided in time domain so that fluid velocity on the interface is increased during time steps. Resulting velocity on the end of the solution must be small. Full Navier-Stokes equations are used in CFX, but above described procedure cause that are significant only terms playing in equation (2-4). Calculated added mass is crucial for the eigenfrequency value.

Added damping is similarly obtained from force which fluid acts on the body if this is moved by constant velocity. Small displacement of the body is assumed. The flow in the fluid is expressed by Navier-Stokes equations (6) and continuity (7). Navier-Stokes equation has some term neglected and ALE description is used. This system of equations is not linear, but we will treat it as a linear.

$$(\mathbf{c} - \dot{\mathbf{v}}) \frac{\partial \mathbf{c}}{\partial \mathbf{x}} = -\frac{1}{\rho} \frac{\partial p}{\partial \mathbf{x}} + \frac{\mu}{\rho} \frac{\partial^2 \mathbf{c}}{\partial \mathbf{x}^2} \quad (6)$$

$$\frac{\partial \mathbf{c}}{\partial \mathbf{x}} = 0 \quad (7)$$

Boundary condition on the interface is:

$$\dot{\mathbf{v}} = \dot{x}_s \mathbf{w} \quad (8)$$

Procedure of solution of the added damping in CFX is similar as in the previous case.

$$\mathbf{b}_{add} \dot{x}_s \mathbf{w} = \int_S p \mathbf{n} dS + \mu \int_S \frac{\partial c}{\partial x} ds \quad (9)$$

Where:  $\dot{\mathbf{v}}$  – mesh velocity,  $\mu$  – dynamic viscosity,  $\dot{x}_s$  – selected velocity,  $\ddot{x}_s$  – selected acceleration.

Solved added damping then will be correct only for corresponding frequency and amplitude of the vibration.

Thus, obtained value of the added mass and added damping can be used for solution of the dynamic behavior of the body in ANSYS.

### 3. Numerical example

The procedure is used for determination of the first eigenfrequency of turbine runner. Modal shape of the isolated runner is obtained by using ANSYS. This shape is used for determination of the added mass by using CFX. Fig. 1 shows pressure field on the face of the runner which is moved by unit acceleration. Fluid force act on the individual nodes of the computational grid gives added mass appropriate of this node. Added mass is inserted into node in form of MATRIX27 finite element. New finite element model with added mass determine eigenfrequency appropriate of this shape. This eigenfrequency can be used for approximate calculation of the damping for selected amplitude.

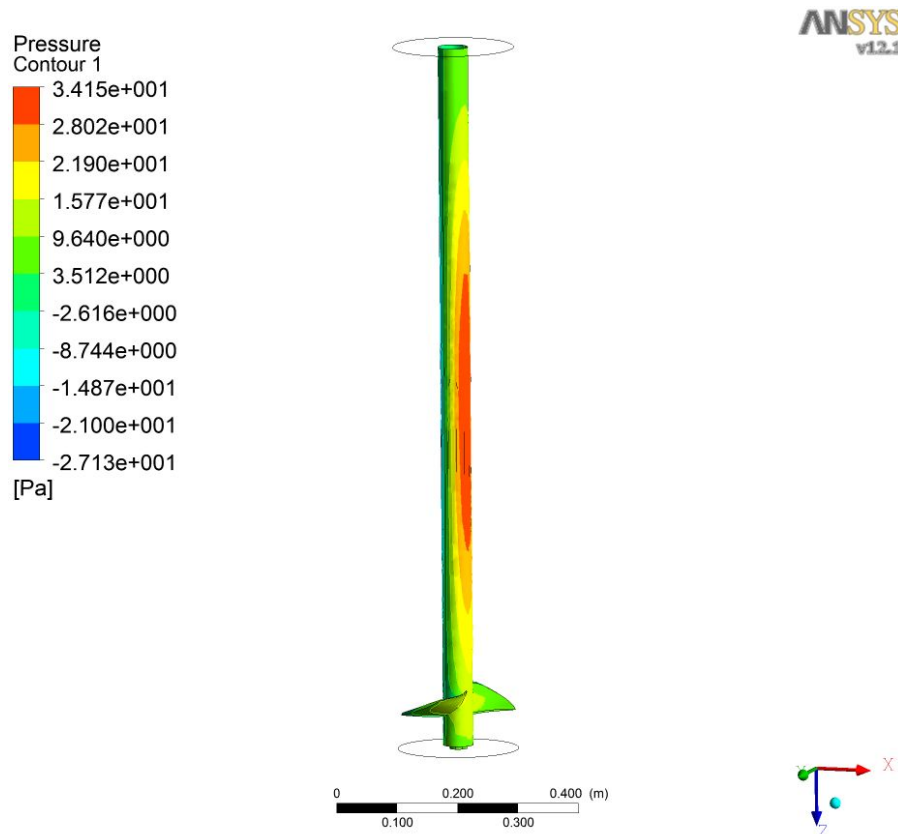


Fig. 1: Pressure field on the face of the runner.

Effective velocity  $\dot{x}_s$  is calculated from the eigenfrequency and selected value of amplitude. Added damping is obtained for this velocity and is also inserted into FEM model in form of MATRIX27 finite element. This new model is useable only for transient simulations.

Resulting lowest eigenfrequency obtained by this method is 75.82 Hz. This value is in good agreement with experiment. Experimentally measured value is 74.1 Hz (Malenovský et al., 2010).

#### 4. Conclusion

Above described solution is not exact and is usable only in case of stagnant fluid. Obtaining of the exact solution of the dynamic behavior is very difficult in this case. Real modal shape of the body surrounded by fluid may be different from modal shape of the isolated body. Computed value of the damping must be compared with experiment because real action of the fluid on the body is more complicated than this model assume. On the other hand, this approach seems to be suitable replacement of the complicated solutions in time domain.

#### References

- Altinisik, D., Karadeniz, H. & Severn, R.T. (1981) Theoretical and experimental studies on dynamic structure-fluid coupling. *Proc Instn Civ Eng 2 Res Theor*, 71, , pp. 675-704.
- Everstine, G.C (1981) Symmetric Potential Formulation for Fluid-Structure Interaction. *J.Sound and Vibration*, 79, 1, pp. 157-160.
- Fritz, R.J. (1972) Effect of Liquids on the Dynamic Motions of Immersed Solids. *Journal of Engineering for Industry, Trans.* ,pp.167-173.
- Malenovský E., et al. (2010) New approach to the numerical analysis of the swirl water turbine and experimental verification. *Proc. of the 8<sup>th</sup> IFToMM international conference on rotor dynamic*, Soul, pp. 502-208.
- de Morais, M.V.G., et al. (2007) Numerical inertia and damping coefficients determination of a tube-bundle in incompressible viscous laminar fluid. *Latin American Journal of Solids and Structures*, 4, 3, pp. 179-202.
- Nikitpaiboon, C. & Bathe, K.J. (1993) An Arbitrary Lagrangian-Eulerian Velocity Potential Formulation for Fluid-Structure Interaction. *Computers and Structures*, 47, 4/5, pp. 871-891.
- Pochylý, F. & Malenovský, E. (2008) New Mathematical and Computational Model of Fluid-Structure Interaction using FEM. In *proceedings of the 9th International Conference on Flow Inducted Vibration*, Prague.
- Schroeder, E.A. & Marcus, M.S. (1975) Finite Element Solution of Fluid-Structure Interaction Problems. In *46th. Shock and Vibration Symposium*, San Diego.
- Zhang, H., et al. (2003) Recent development of fluid-structure interaction capabilities in the ADINA system. *Computers and Structures*, 81, pp. 1071-1085.



## INVESTIGATION OF VERTICAL DYNAMICS OF A HYDROGEN FUEL BUS

P. Polach<sup>\*</sup>, M. Hajžman<sup>\*\*</sup>

**Abstract:** *The paper deals with two approaches to the creation of hydrogen fuel bus multibody models intended for the investigation of the bus dynamic response. The basic dynamic model for vertical dynamics was derived in the form of an ordinary differential equation system and was implemented in the MATLAB system. In order to study more complex behaviour the bus multibody model was also created using the alaska simulation tool based on a relative coordinate multibody formalism. Both models were used for the studying of the bus vertical dynamics. A very important issue of missing or inaccurate model data caused by the lack of a design documentation is discussed in the paper.*

**Keywords:** *Multibody dynamics, suspension, vertical dynamics, air spring, shock absorber.*

### 1. Introduction

As new and progressive fuel systems are designed for the means of public transport, dynamic properties of these new vehicles should be tested and verified. The paper deals with the approaches to the creation of TriHyBus multibody models intended for the investigation of the bus dynamic response.



*Fig. 1: Front view of TriHyBus and a fuel cell in the back of TriHyBus.*

The TriHyBus project, which has been coordinated by Nuclear Research Institute Rez plc (the Czech Republic) for several years, comprises R&D, implementation and a test operation of a 12 m city bus (see figure 1) with a hybrid electric propulsion using hydrogen fuel cells. The bus was manufactured by ŠKODA ELECTRIC Inc. using the chassis of the Irisbus Citelis 12M bus (produced by Iveco Czech Republic, Inc.) and operates in the city of Neratovice, where the first Czech Hydrogen filling station was built in the Veolia Transport bus park. The 48 kW Proton Motor Membrane fuel cell is used as a main power-source for the 120 kW electric traction motor. Additional 28 kWh traction accumulators and ultra-capacitors are used when the bus accelerates or ascends, working together the fuel cell, allowing the energy recuperation while decelerating. The bus equipped with a hybrid power unit has a higher efficiency of the propulsion system.

<sup>\*</sup> Dr. Ing. Pavel Polach: Section of Materials and Mechanical Engineering Research, ŠKODA VÝZKUM Ltd., Tylova 1/57; 316 00, Plzeň; CZ, e-mail: pavel.polach@skodavyzkum.cz

<sup>\*\*</sup> Ing. Michal Hajžman, Ph.D.: Department of Computer-Aided Modeling, ŠKODA VÝZKUM Ltd., Tylova 1/57; 316 00, Plzeň; CZ, e-mail: michal.hajzman@skodavyzkum.cz

The vehicle driveability is comparable with the characteristics of standard buses. However, the distribution and total bus mass are rather different. It is the reason of the verification of the bus skeleton strength (connected with vertical dynamics) and of investigating the bus stability. The approaches to the creation of a TriHyBus dynamic model in the MATLAB system and two types of TriHyBus multibody models are introduced in this paper.

## 2. Basic dynamic model of the bus

The basic dynamic model of the TriHyBus was prepared in order to simulate the bus vertical dynamic response with a relatively simple model, which is suitably parameterized. The simulation with the model is very fast (Zhu & Ishitobi, 2004) and the model can be used for the fast sensitivity analysis and optimization. It is characterized by four rigid bodies (see figure 2). The bus sprung body is represented by one rigid body with three degrees of freedom (two rotations  $\varphi$  and  $\theta$ , one translation  $z$ ). The divided front axle (two half-axes) is simplified and represented by two rigid bodies (each one with one degree of freedom, translations  $z_1, z_2$ ). The rear axle is supposed to be rigid and is modelled using one rigid body with two degrees of freedom (one rotation  $\varphi_3$  and one translation  $z_3$ ). Air-springs, hydraulic shock absorbers and tires are represented by nonlinear spring-damper elements. The model was derived by the free body method in Hajžman & Polach (2004) and can be written in the form

$$\mathbf{M}\ddot{\mathbf{q}} = \mathbf{f}(\dot{\mathbf{q}}, \mathbf{q}, t), \quad (1)$$

where  $\mathbf{M}$  is the diagonal mass matrix,  $\mathbf{q}$  is the vector of the model generalized coordinates and the right hand side function represents all linear and nonlinear forces in suspension and gravity forces in bodies' centers of mass.

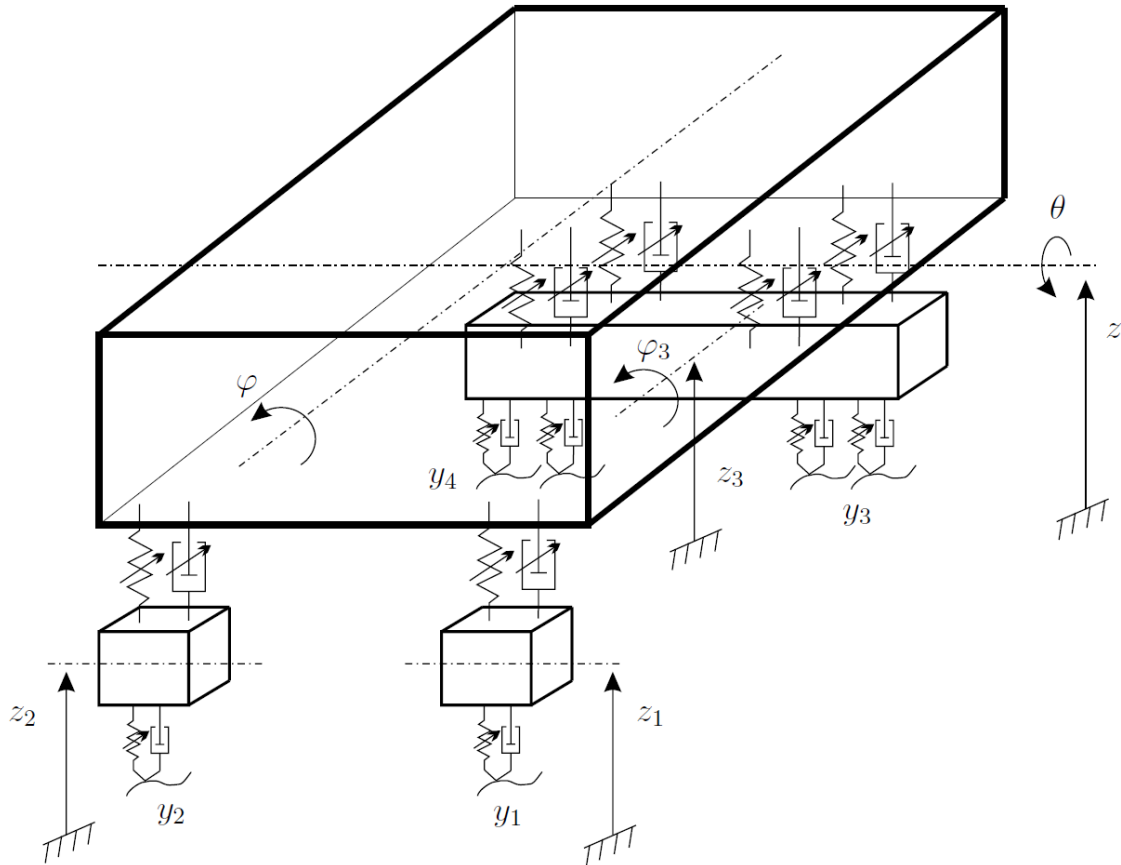


Fig. 2: Scheme of a basic dynamic model.

The model was implemented in the MATLAB system by means of real TriHyBus parameters (see the next chapter for more detail). The excitation of the bus is defined by functions  $y_1(t)$  to  $y_4(t)$  for each tire. The most direct way for the investigation of vertical dynamics problems is the numerical solution of the equations of motion (1).

### 3. Multibody models of the bus

In order to obtain a more comprehensive tool for dynamic analysis (e.g. Hegazy et al., 2000), multibody models of an empty and a fully loaded hydrogen bus were created. For the buses of the two weights a basic multibody model and a multibody model with more precise kinematics of axles' suspension were created in the **alaska 2.3** simulation tool (Maißer et al., 1998). A creation of relatively simple multibody models (in this case of the basic multibody model) and an effort to improve them are important due to the significant shortening of the computational time.

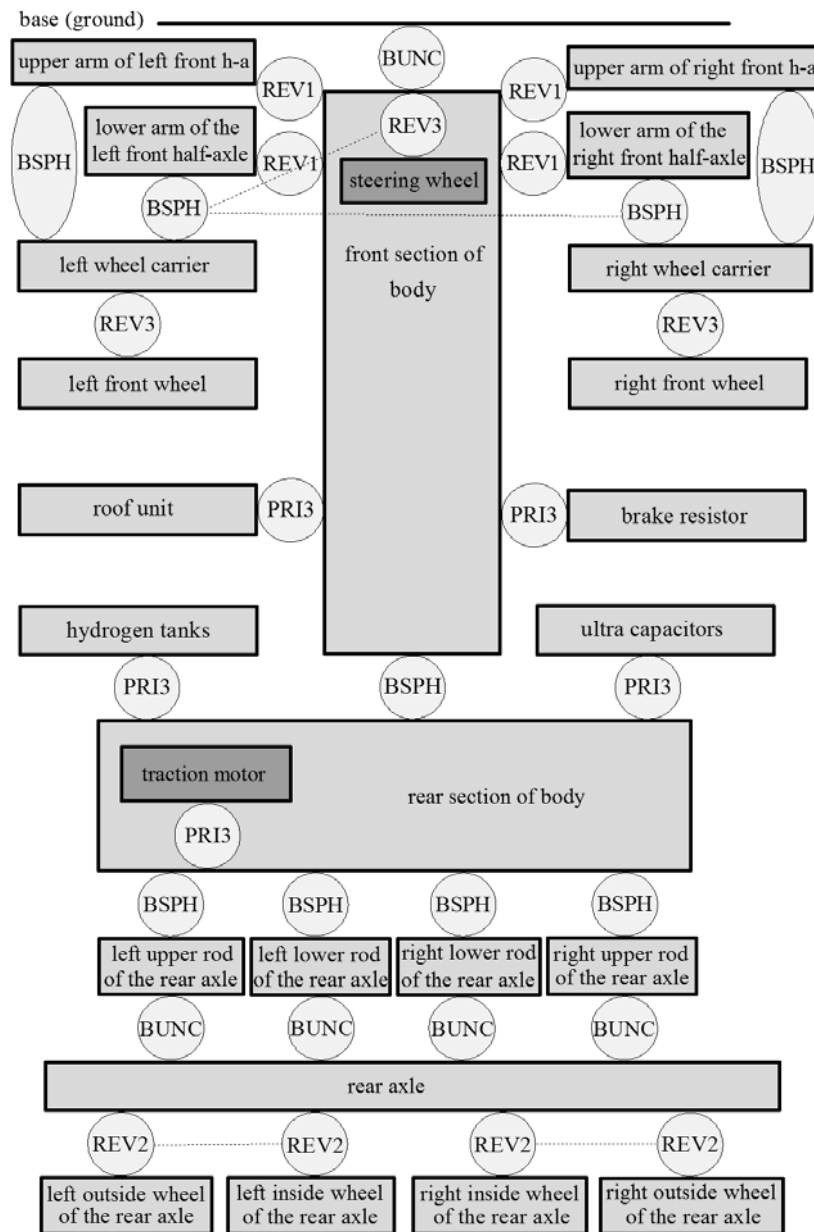


Fig. 3: Kinematic scheme of the multibody model with more precise kinematics of axles' suspension.

The basic multibody model of the hydrogen bus is formed by 21 rigid bodies mutually coupled by 24 kinematic joints. The number of degrees of freedom of multibody models in kinematic joints is 39. A kinematic scheme of the TriHyBus multibody model with more precise kinematics of the axles suspension is in figure 3. Rectangles designate the rigid bodies, circles (or ellipses) designate the kinematic joints (BUNC – unconstrained, BSPH – spherical, PRI3 – prismatic in vertical axis, REV1 – revolute around longitudinal axis, REV2 – revolute around lateral axis, REV3 – revolute around vertical axis). Dashed lines connect mutually dependent kinematic joints. The multibody model with more precise kinematics of the axles suspension (figure 3) is formed by 24 rigid bodies mutually coupled by 30 kinematic joints, the number of degrees of freedom of multibody models in kinematic joints is 73. The rigid bodies correspond to the bus individual structural parts and are defined by mass,

centre of gravity coordinates and mass moments of inertia. Air springs and hydraulic shock absorbers in axles' suspension and bushings in the places of mounting certain bus structural parts are modelled by connecting the corresponding bodies by nonlinear spring-damper elements. When simulating driving on an uneven road surface the contact point model of tires is used in the multibody models; radial stiffness and radial damping properties of tires are modelled by linear spring-damper elements considering the possibility of a bounce of the tire from the road surface.

The basic dynamic model and both multibody models of the hydrogen bus are created especially on the basis of data (numerical data and technical documentation) provided by ŠKODA ELECTRIC Inc. Certain input data were derived or taken from the data used in the multibody models of the ŠKODA 21 Ab low-floor bus (Polach, 1997) and the SOR C 12 intercity bus (Polach & Hajžman, 2005). Characteristics of axles' air springs are determined on the basis of static loadings of axles derived from the data provided by Iveco Czech Republic, Inc. Characteristics of shock absorbers in axles' suspension were derived from the shock absorbers characteristics of the SOR C 12 intercity bus. Stiffness data of bushings in assembly eyes for connecting radius rods to axles and chassis frame are taken from the documentation of the Lemförder Metallwaren and the Autófelszerelési Vállalat Sopron companies. Radial stiffness and radial damping characteristics of the public transport vehicle tires were experimentally measured in the Dynamic Testing Laboratory ŠKODA VÝZKUM Ltd. (Hajžman & Polach, 2006).

All multibody models can be used for the solution of the bus vertical dynamics with various types of excitation by uneven road surface as well as for the solution of horizontal dynamics problems (i.e. for handling and stability analyses).

#### 4. Conclusions

Due to the need of studying the hydrogen fuel bus vertical dynamics several types of bus mathematical models were created. The basic dynamic model for vertical dynamics was derived in the form of an ordinary differential equation system and was implemented in the MATLAB system. In order to study a more complex behaviour two types of bus multibody models were created using the alaska simulation tool based on a relative coordinate multibody formalism. The described basic dynamic and multibody models can be used for the studying of the bus vertical dynamics. While the basic dynamic model is more suitable for fast analyses and optimization tasks the multibody models are efficient for a more accurate analysis of vertical and horizontal motion. The results from the vertical dynamics calculations are important inputs for the analysis of the strength and fatigue of the bus structure.

#### Acknowledgement

This work was supported by the research project FR-TI2/442 of the Ministry of Industry and Trade of the Czech Republic.

#### References

- Hajžman, M. & Polach, P. (2004) Jednoduchý nelineární model trolejbusu pro úlohy vertikální dynamiky vozidel, in: Proc. 20th Conf. Computational Mechanics 2004 (J. Vimmr ed.), UWB in Plzeň, Hrad Nečtiny, Vol. I, pp. 123-130.
- Hajžman, M. & Polach, P. (2006) Identifikace radiální tuhostní a tlumicí charakteristiky pneumatiky trolejbusu, in: Proc. Int. Conf. Dynamics of Rigid and Deformable Bodies 2006 (B. Skočilasová ed.), University of J. E. Purkyně in Ústí nad Labem, Ústí nad Labem, pp. 55-62.
- Hegazy, S., Rahnejat, H. & Hussain, K. (2000) Multi-Body Dynamics in Full-Vehicle Handling Analysis under Transient Manoeuvre. *Vehicle System Dynamics*, 34, pp. 1-24.
- Maißer, P. et al. (1998) *alaska*, User Manual, Version 2.3. Institute of Mechatronics, Chemnitz.
- Polach, P. (1997) MBS – Model of the ŠKODA Bus II. COPERNICUS Project No. 94-0520, Deliverable D51/2, ŠKODA RESEARCH, Pilsen.
- Polach, P. & Hajžman, M. (2005) Přístupy k tvorbě multibody modelů meziměstského autobusu SOR, in: Proc. 21st Conf. Computational Mechanics 2005 (J. Vimmr ed.), UWB in Plzeň, Hrad Nečtiny, Vol. II, pp. 477-484.
- Zhu, Q. & Ishitobi, M. (2004) Chaos and bifurcation in a nonlinear vehicle model. *Journal of Sound and Vibration*, 275, pp. 1136-1146.

## REALIZATION OF GEOMETRIC NONLINEARITIES IN THE DETERMINATION OF EIGEN FREQUENCIES AND SHAPES BY FINITE ELEMENT METHOD

**Z. Poruba<sup>\*</sup>, J. Szweda<sup>\*</sup>, R. Sikora<sup>\*</sup>**

**Abstract:** *The presented paper describes the process of determination of eigen shapes and eigen frequencies of the structure with non-linear joint. The presented method uses three different configurations of applied boundary conditions for describing the non-linear behaviour of the structure using linear tools of FE software.*

**Keywords:** *FEM, non-linear joint, eigen frequency, eigen shape.*

### 1. Introduction

The subject is the test lifting platform used in theatre applications. The device consists of fixed horizontal frame, two vertical pillars and two tables. The lifting of the tables is realized by two devices – so called spiralift and erective chain. The longitudinal and lateral guiding of the tables is ensured by U-profiles fixed with pillars and by combined bearings connected with tables.

The aim of the work is to determine the modal properties – eigen shapes and eigen frequencies of the introduced platform. Since the connection of both tables and guiding profiles does not transfer the tension forces in longitudinal direction the joint has to be considered as non-linear. With respect to this fact the appropriate solution has to be proposed. Its description is described in following articles. The modal analysis is performed by the computational modelling method in the software ANSYS – Mechanical APDL v12.0 (Ferrecki et al., 2007). The device is depicted in Fig. 1.

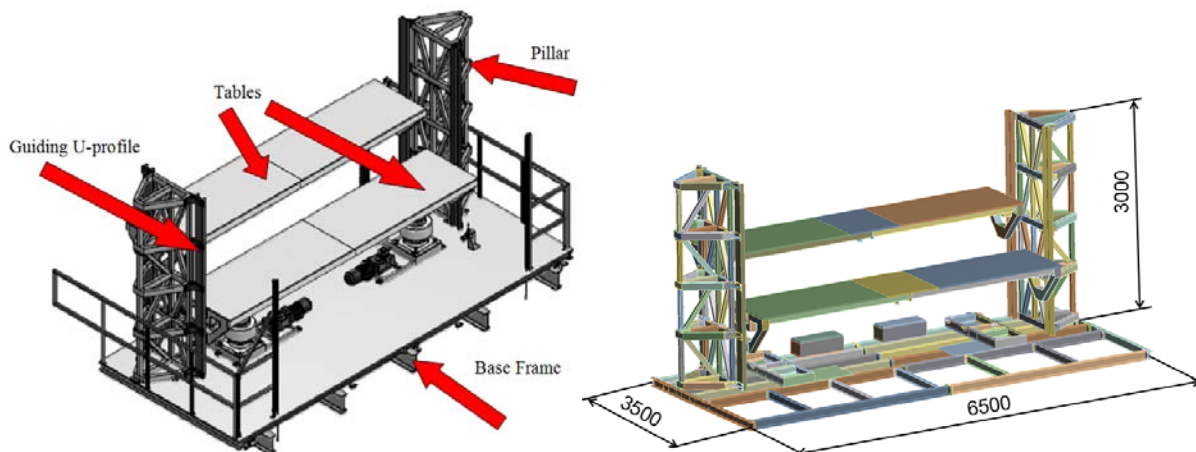


*Fig. 1: Geometry of Lifting Platform.*

### 2. Computation

Before the model properties were identified the mechanism was simplified in order to reduce the hardware and time demands (Poruba et al., 2010). The stiffness of lifting devices was determined via

---

<sup>\*</sup> Ing. Zdenek Poruba, Ph.D., Ing. Jan Szweda, Ph.D. and Ing. Roman Sikora, Ph.D.: Department of Mechanics, Technical University of Ostrava, 17. listopadu 15; 708 00, Ostrava; CZ, e-mails: zdenek.poruba@vsb.cz, jan.szweda@vsb.cz, roman.sikora@vsb.cz

FEM (Finite Element Method) and consequently compared with stiffness of other components (tables, pillars). Since the stiffness of both lifting devices is of higher order, their modelling can be realized by appropriate boundary condition – by removing of degrees of freedom in vertical direction in the location of connection of lifting devices and tables – see Fig. 2. The base frame firmly coupled with the ground was substituted by appropriate boundary condition as well. Its influence on the modal properties can be neglected. Regarding to this fact all degrees of freedom of the pillars were removed in the location of their connection with the base frame – see Fig. 3.

The beam elements BEAM188 (pillars) (Saeed et al., 2009) and shell elements (tables, reinforcements) were used in the finite element model. The device was loaded by the MASS21 element located in the middle of both tables – symmetrical loading of 1000 kg was assumed. The model contained 12726 finite elements and 33662 nodes.

The two types of materials were assumed in the model – construction steel  $E = 210000 \text{ MPa}$ ,  $\mu = 0.3$ ,  $\rho = 7850 \text{ kg.m}^{-3}$  and wood  $E = 10000 \text{ MPa}$ ,  $\mu = 0.2$ ,  $\rho = 600 \text{ kg.m}^{-3}$  which is located in the form of wooden board on the top sides of both tables.

The important chapter is the realization of non-linear joint between the tables and guiding U-profiles. Placing of the table in guiding profile is obvious from Fig. 1 and Fig. 4. The tables are on both sides provided by two rollers (see Fig. 4) guided in U-profile so the longitudinal and lateral guidance is ensured. Regarding to the shape of the cross-section area of U-profile, the possible lateral vibration is hindered in both directions. In case of longitudinal vibration only the compression force is transferred because the contact between the roller and guiding profile occurs only at one its side. This fact has to be considered in the FE model.

The transfer of the forces between roller and guiding profile was realized by coupling of degrees of freedom belonging to both parts. The rise of compression force in lateral direction is ensured in all cases (at one or other parallel side of U-profile). As already mentioned above, the force transfer in longitudinal direction can occur only if the transferred force has compression character. In the case when coupling is applied at both sides of the tables (at one side the transfer of tension force occurs) the calculated eigen frequencies and eigen shapes do not need to correspond with those of real structure. The further calculations were carried out in following steps:

- Coupling in longitudinal direction was applied at both sides of both tables. The eigen frequencies and corresponding eigen shapes were calculated – see Tab. 1, column “Coupling everywhere”,
- Coupling in longitudinal direction was applied only at one side of table. In case of the other table the coupling was applied at the opposite side. The eigen frequencies and corresponding eigen shapes were calculated – see Tab. 1, column “Coupling opposite”,
- Coupling in longitudinal direction was applied only at one side of table. In case of the other table the coupling was applied at the same side as at neighbouring table. The eigen frequencies and corresponding eigen shapes were calculated – see Tab. 1, column “Coupling same”.

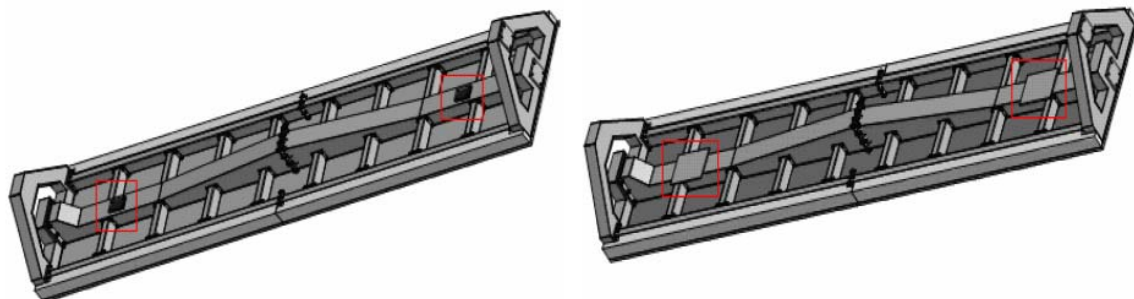


*Fig. 2: Location of Boundary Condition Substituting Erective Chain and Spiralift.*



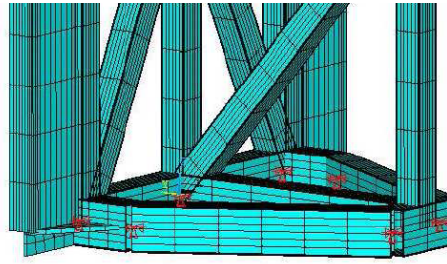


*Fig. 3: Location of Boundary Condition Substituting Influence of Base Frame.*

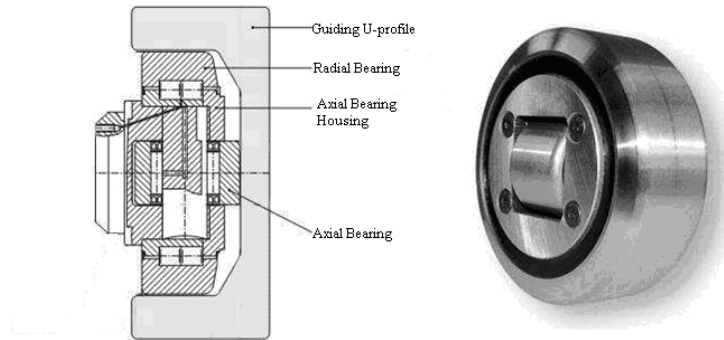


*Fig. 4: Scheme of Roller Used for Table Guiding.*

### 3. Results

The realization of described steps produces the eigen frequencies and eigen shapes of investigated structure – both real and unreal ones for all possible configurations of applied coupling in longitudinal direction. The results are summarized in Tab. 1. Only such results can be considered as real where the tension force in longitudinal direction between roller and guiding U-profile is not transferred. This fact was found out on the base of visualization of particular eigen shapes. The example is depicted in Fig. 5 which presents the first eigen shape for the coupling configuration “Coupling everywhere”. The mutual position of tables and pillars requires the presence of tension forces, hence the eigen shape is considered as unreal. The first real eigen shape was then evaluated from the column “Coupling opposite” with frequency  $6.5 \text{ Hz}$ . The eigen shapes and eigen frequencies for all described configurations of boundary conditions could be divided into two groups – real and unreal. The calculated real values of eigen shapes and eigen frequencies were consequently sorted in increasing order (marked in Tab. 1 by number of eigen frequency in brackets) and could be used for the description of dynamical behaviour of lifting platform.

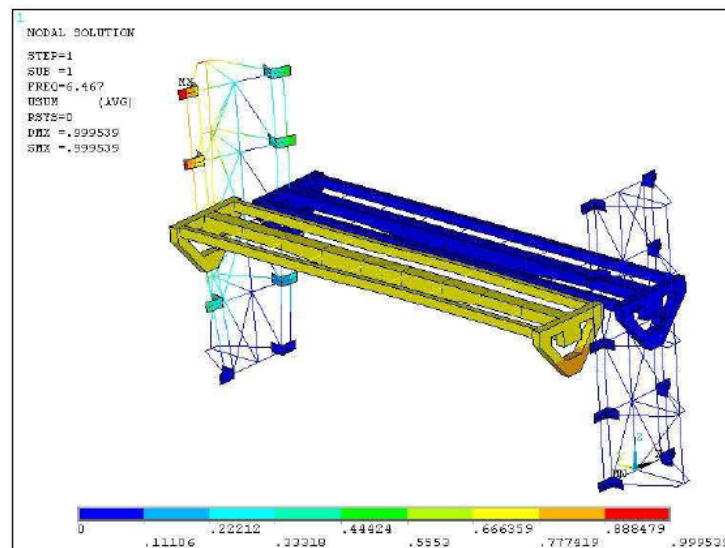


*Fig. 5: Visualization of First Eigen shape.*

#### 4. Conclusion

The article describes the determination of eigen shapes and eigen frequencies of the lifting platform containing the non-linear joint between table and guiding U-profile. The non-linear joint transfers only the compression forces in longitudinal direction. This fact was respected in the FE analysis by appropriate setting of boundary conditions so that both real and unreal vibration shape was captured. From the obtained results those eigen shapes and eigen frequencies were identified as real which transferred only compression forces between tables and guiding U-profiles.

*Tab. 1: Calculated Eigen shapes and Eigen Frequencies with Marked Real Values of Eigen frequencies.*

Eigen shape Nr.	Coupling everywhere		Coupling opposite		Coupling same	
	Frequency [Hz]	Description	Frequency [Hz]	Description	Frequency [Hz]	Description
1.	7.232	In-phase pillar torsion	<b>6.467 (1)</b>	Pillar torsion (left side)	5.407	Pillar torsion (right side)
2.	<b>7.684 (2)</b>	In-phase table torsion	<b>6.495 (1)</b>	Pillar torsion (left side)	<b>7.684 (2)</b>	In-phase table torsion
3.	<b>8.842 (3)</b>	Anti-phase table torsion	<b>7.685 (2)</b>	In-phase table torsion	<b>8.840 (3)</b>	Anti-phase table torsion
4.	<b>10.715 (5)</b>	Table bending (err. Chain)	<b>8.842 (3)</b>	Anti-phase table torsion	<b>8.969 (4)</b>	Pillar bending (right side)
5.	11.732	In-phase pillar bending	<b>10.713 (5)</b>	Table bending (err. chain)	<b>10.715 (5)</b>	Table bending (err. chain)
6.	<b>12.349 (6)</b>	Table bending (spiralift)	<b>12.348 (6)</b>	Table bending (spiralift)	<b>12.348 (6)</b>	Table bending (spiralift)
7.	<b>26.72 (7)</b>	Pillar bending (right side)	22.001	Pillar torsion (right side)	17.389	Pillar torsion (left side)
8.	28.538	Pillar bending (left side)	22.245	Pillar torsion (left side)	25.169	Pillar torsion (right side)
9.	34.381	Anti-phase pillar torsion	27.216	Pillar bending&torsion (r.s.)	<b>26.720 (7)</b>	Pillar bending&torsion (r.s.)
10.	34.787	Anti-phase pillar torsion	29.240	Pillar bending (left side)	29.552	Pillar bending&torsion (l.s.)
11.	39.064	Anti-phase pillar torsion	<b>35.804 (8)</b>	Pillar torsion (right side)	<b>35.730 (8)</b>	Pillar torsion (right side)
12.	43.665	Anti-phase pillar bending	36.379	Pillar torsion (left side)	<b>36.320 (9)</b>	Pillar bending (right side)

#### Acknowledgement

The work has been supported by the research project MSM6198910027 of the Ministry of Education, Youth and Sports of the Czech Republic and by the research project TA01010705 of the Technology Agency of the Czech Republic what is highly appreciated.

#### References

- Ferfecki, P., Ondrouch, J. & Sikora, R. (2007) Comparison of Numerically Computed and Experimentally Measured Response of a Rotor System Rotor KIT 4 with a Schaft Weakened by a Notch Excited by a Centrifugal Force, in: Proc. Conf. on Dynamics of Machines, Ind. of Thermomechanics AS CR, Prague, pp. 63-70.
- Poruba, Z. & Szveda, J. (2010) Simulation and optimization of the electromotor cooling. Metalurgija, 49, 2, pp. 474-478.
- Saeed, R.A. & Galybin, A.N. (2009) Simplified model of the turbine runner blade. Engineering Failure Analysis, 16, 7, pp. 2473-2484.

## MULTIPURPOSE EXPERIMENTAL RIG FOR AEROELASTIC TESTS ON BRIDGE GIRDERS AND SLENDER BEAMS

S. Pospíšil\*, R. Král\*, J. Náprstek\*

**Abstract:** *The bridges, footbridges and broadcast towers create an important subset of infrastructure subjected to dynamic loading of various origins. Especially, exposed to wind, they are susceptible to vibrations under certain circumstances due to pure load action or aero-elastic effects. This means that once an element or a structure starts to vibrate, a complex interaction between the moving boundary and the airflow takes place. Because of the complexity, the research has been in progress for several decades in both theoretical and experimental way. The article describes an original and multi-purpose experimental frame for the analysis of complex linear and non-linear aspects of aero-elastic behavior of the slender beams. The apparatus meets the rigorous theoretical assumptions and allows very precise and quick adjustment of the stiffness and mass of the structure, which is not always possible with a traditional "parallel spring-supported bridge" approach used by many researchers. The principal advantages are described together with key construction details.*

**Keywords:** *Bridge aero-elasticity, wind tunnel, experimental set-up, non-linear response.*

### 1. Introduction

The bridges and footbridges create an important subset of the infrastructure. The spans have lengthened to a great extent over the last hundred years with limits being established constantly by civil engineers and architects. These structures typically have low natural frequencies of oscillation and low damping, which makes them sensitive to wind loading. Once such a structure starts to vibrate, a complex interaction (self-excited) between the moving boundary and the airflow may take place, which either effectively attenuate or reinforce the driving force of the wind.

The investigations showed that some of the violent oscillations couldn't be predicted by static or quasi-static analyses. Indeed, the interaction of oscillating flexible structures and the fluid flow around them can give rise to a number of different responses. For the last few decades' extensive studies were carried (Scruton, 1963; Novak & Davenport, 1970; Ricciardelli, 2003). They revealed a relatively considerable diversity of results, with subsequent understanding that the discrepancies can be caused by hidden or obvious linear treatment. Because many experimental works create their own experimental conditions in accordance with emphasis on own parameters, the results are often incompatible (O'Neil, 1996). It is uncertain which parameters are at the origin of instability and which are only for the particular technical branch.

In the context of above-mentioned references, the authors want to propagate a generalized experimental approach, which would include the analysis of non-linear post- and pre-critical system behavior in both smooth and turbulent airflow. Therefore an original and multi-purpose experimental set-up has been designed. It allows observing both the linear and non-linear aero-elastic behavior of slender beams. The apparatus meets the rigorous theoretical assumptions together with practical very precise and quick adjustment of the stiffness and mass of the structure, which is not always possible with a traditional "parallel spring supported bridge" or its modifications being used by many researchers (Hjorth Hansen, 1992). Examples of the large amplitude non-linear response are presented, to illustrate the capacity and usefulness of the stand.

The current trends of aero-elasticity are focused on the description of full three-dimensional behavior of a body, taking into account the along-body distribution of the load. In many cases, this type of

---

\* Ing. Stanislav Pospíšil, Ph.D., Ing. Radomil Král and Ing. Jiří Náprstek, DrSc.: Institute of Theoretical and Applied Mechanics, Prosecká 76; 190 00, Prague; CZ, e-mail: pospisil@itam.cas.cz, kral@itam.cas.cz, naprstek@itam.cas.cz

investigation is, however, an ultimate goal with regard to the experimental time and economic requirements. Two-dimensional models are therefore prevailing in both theory and experiments and used for initial analysis starting for example with the model in Fig. 1.

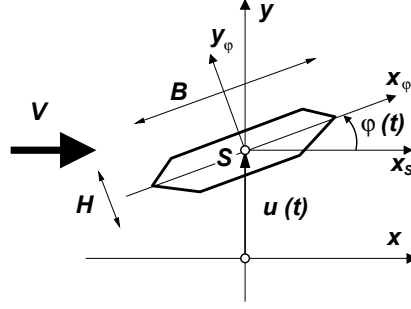


Fig. 1: Double degree of freedom model of the bridge girder. It can move only in the direction of principal response components  $u$  and  $\varphi$  or simultaneously.

Mathematical model for such double-degree-of-freedom (DDOF) system can be described, for instance, by a couple of differential equations related to the Fig. 1:

$$\begin{aligned} m_0 \ddot{u} + b_{u0} \dot{u} + k_{u0} u &= F(\ddot{u}, \dot{u}, u, \ddot{\varphi}, \dot{\varphi}, \varphi, t) \\ I_0 \ddot{\varphi} + b_{\varphi0} \dot{\varphi} + k_{\varphi0} \varphi &= M(\ddot{u}, \dot{u}, u, \ddot{\varphi}, \dot{\varphi}, \varphi, t) \end{aligned} \quad (1)$$

Here,  $F = q_s B C_L$  is the lift force, while  $M = q_s B^2 C_M$  is the moment around point  $S$ . These forces, or rather the lift and moment coefficients  $C_L$  and  $C_M$  are functions of explicit time and the response components  $u(t)$  and  $\varphi(t)$  stemming from the aerodynamic load. The coefficients  $m_0$  and  $I_0$  represent mass and mass moment of inertia of the cross-section with unit length. They are referred to the still air, respectively, while the effective parameters consist of these basic values and aeroelastic influences. Similarly,  $b_{u0}, b_{\varphi0}$  are the damping coefficients in the still air. Finally,  $k_{u0}, k_{\varphi0}$  stand for stiffness for  $u$  and  $\varphi$  in the still air. Variable  $q_s$  is the stagnation pressure in the bridge height given by the Bernoulli formula  $q_s = \rho/2V^2$  using a free stream wind velocity  $V$ .

The most fundamental task of experimental aero-elasticity lies in the formulation of the self-excited forces  $F$  and  $M$  (the wind load caused by the movement of the structure interaction) and in the determination of the critical state (Jain et al., 1996).

## 2. Novel experimental approach

Despite some disadvantages, structures are most commonly analyzed experimentally using section models. The model is mounted on a set of springs, which are tuned to produce an appropriate relation of the modal stiffness. The flow of the wind along such model results in the model movement with possible two components; in a vertical ( $u$ ) and pitch ( $\varphi$ ) directions. Such approach with the set of springs of stiffness  $k_i$  is depicted in Fig. 2 left. Aerodynamic properties of the cross section can be determined by either pressure measurements along the perimeter or by a force balance on the whole model. The behavior of a static, harmonically forced or freely vibrating deck can thus be studied.

Although the method is used predominantly these days, it is rather slow and costs much experimental time, because every change of the parameters is related to the change of the springs or other important parts, which makes it inefficient. With usage of the proposed experimental rig, this aspect is negligible. It is constructed to allow very quick manipulation before measurement itself. The second important issue stems from the theoretical aspect and actual trend, i.e. the need of the measurement of both linear and non-linear aero-elastic complex behavior.

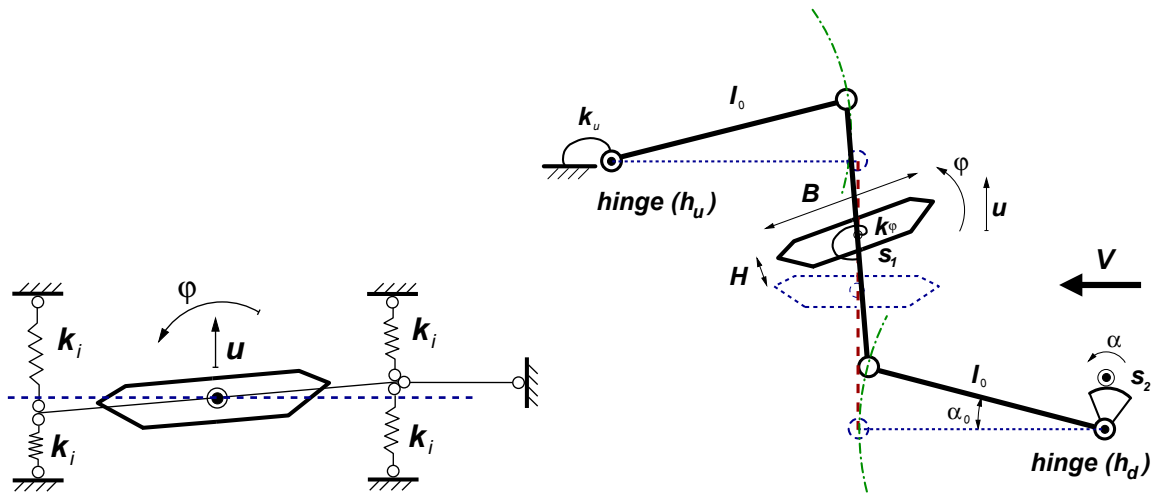


Fig. 2: The common concept of mounting of the section models using spring-supported body (left); Working principles of original multi-purpose stand (right).

In Fig. 2 right, the principal idea of the new type of model attachment is illustrated. The framework of moveable parts was designed to be as light as possible. It is made of fiber composite bars linked to each other with joints. Special gadgets are able to simulate the elastic properties inherent to the structure. Two levers with the length  $l_0$  are supported by hinges  $h_u$  and  $h_d$ . The stiffness  $k_u$  can be adjusted by means of gadget depicted in Fig. 3 left, while the stiffness  $k_\phi$  uses the system from the Fig. 3 right.

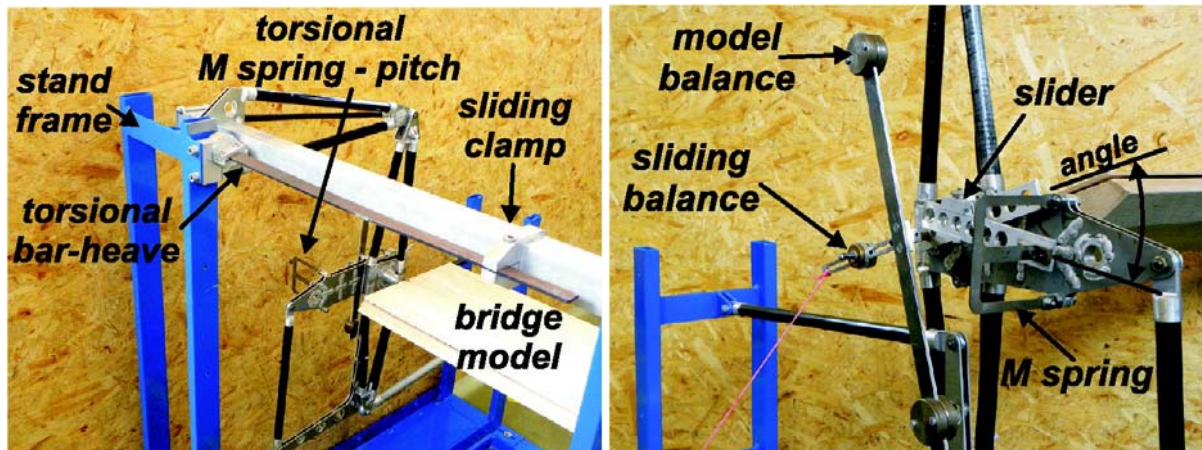


Fig. 3: The overall view at the stand with important mechanical details. System for the change of heave (left) and torsional (right) stiffness.

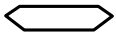
The centroid of the girder moves along the dotted horizontal (red) line independently of the pitch. The oscillations in both degrees of freedom (response components) can have large amplitudes. Due to movable fixation, the frequency tuning is fast and precise. The mechanical damping of the model at the stand itself is very low, the logarithmic decrement around  $\delta = 0.05$ . The two sides of the frame can be adjusted to fit the model size as well as the wind tunnel cross dimension.

### 3. Example of model response

The responses of several cross-sections with the span of  $L = 60 \text{ cm}$  were measured in a wind tunnel. One example is given here. Special attention has been devoted to the response of the girder at and after the critical state. The deck is of a bridge-like shape with a height-to-width ratio  $H/B = 0.2$ . The deck motion measurement was ensured by means of rotary magnetic transducers and accelerometers. Tab. 1 gives basic information about the characteristics and the frequency tuning range of the selected model.



Tab. 1: Aerodynamic characteristics of experimentally analyzed girders.

section	$H$ (m)	$B$ (m)	$m$ (kg)	$I$ (kgm <sup>2</sup> )	$f_{\varphi}$ (Hz)	$f_u$ (Hz)
	0.05	0.03	3.74	0.016	2-6	2.5-7

The wind speed has been increasing continuously during the wind tunnel experiments. Excessive responses occurred when the flow speed in the wind tunnel was near, or identical to the critical velocity and afterwards. Periodic limit cycle oscillations occurred in the coupled mode shape consisting of both heave and torsional components. Amplitudes of torsional motion of the deck were small until it reached the critical, in mathematical parlance, bifurcation point. The sudden growth of the experimental vibration amplitudes of bridge-like girder is depicted in Fig. 4. This time history shows also large amplitudes of vibration, especially in the torsion branch.

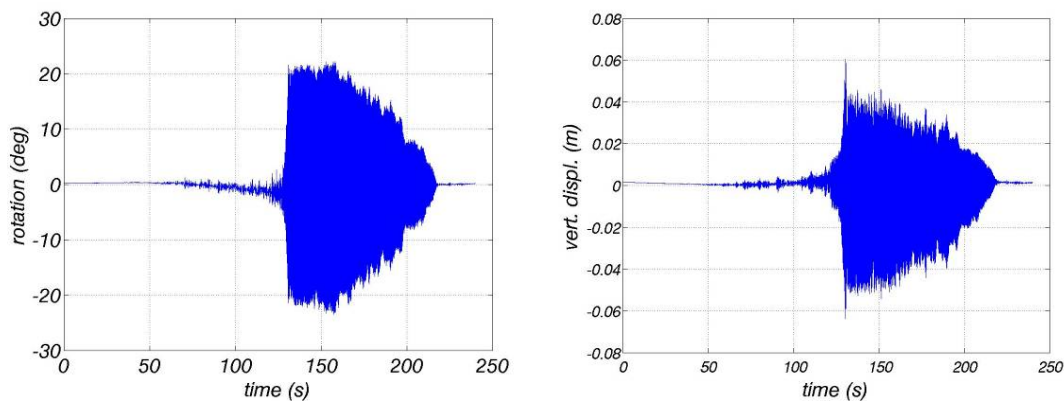


Fig. 4: Time histories of pitch (left) and heave (right) motion of bridge-like girder during continuous increase and decrease of wind speed in the wind tunnel.

#### 4. Conclusions

The article describes an original and multi-purpose experimental set-up for the analyzing of linear and also non-linear aspects of aero-elastic behavior of the slender beams. The apparatus meets the rigorous theoretical assumptions and allows very precise and quick adjustment of the stiffness and mass of the structure, which is not always possible with a traditional "parallel spring-supported bridge" approach used by many researchers. It has been used in practical applications for the real bridge measurements (Rhine Bridge near Wessel in Germany, Sava River in Belgrade, River Vltava pedestrian bridge in Prague). The principal advantages are described together with key construction details.

#### Acknowledgement

The support of the Czech Scientific Foundation No. 103/09/0094, Grant Agency ASCR A200710902 and AVOZ 20710524 research plan is acknowledged.

#### References

- Hjorth-Hansen, E. (1992) Section model test, Proc. Aerodynamics of Large Bridges, Balkema, Rotterdam, pp. 95-113.
- Jain, A., Jones, N.P. & Scanlan, R.H. (1996) Coupled aero-elastic and aerodynamic response analysis of long-span bridge, Journal of Wind Engineering and Industrial Aerodynamics, 70, pp. 69-80.
- Novák, M. & Davenport, A.G. (1970) Aero-elastic Instability of Prism in Turbulent Flow, Journal of Engineering Mechanics Division ASCE, 96, pp. 17-39.
- O'Neil, T. (1996) Non-linear aero-elastic response - Analyses and experiments, AIAA Meeting, 96-0014.
- Ricciardelli F. (2003) On the wind loading mechanism of long-span bridge deck box sections, Journal of Wind Engineering and Industrial Aerodynamics, 91, pp. 1411-1430.
- Scruton, C. (1963) On the wind excited oscillation of stacks, towers and masts,, Proc. Int. Conf. on Wind Effects on Buildings and Structures, London, UK, pp. 798-836.

## **NON-STATIONARY HEATING OF SHELL MOULDS IN THE PROCESS OF MANUFACTURE OF ARTIFICIAL LEATHERS**

**A. Potěšil\***

**Abstract:** *Efficient manufacture of artificial leathers of extensive and complicated shapes in the company Magna Exteriors & Interiors (Bohemia), s.r.o., used for example in sandwich switchboards in cars, is a very complex engineering problem. To achieve satisfactory precision and stability of a production process of artificial leathers, it is necessary to apply special methods and procedures. Considering heating is realized by means of a large number of infra-red emitters, both the heating of the moulds and finally their abrupt cooling are very dynamic thermal processes. The paper deals with a possible prediction of non-stationary thermal processes in the shell moulds by means of finite element method. The discussed problems are part of innovation activities realized within the project MPO TIP 2009 registered under the registration number FR-TII/266.*

**Keywords:** *Non-stationary thermal process, artificial leather, finite element method.*

### **1. Introduction**

It is well known, that innovations in a technology of production of new products demand a complex approach and participation of a number of specialists. The main aim of the processes during development or innovation, respectively, of the technology in question is to increase its efficiency and decrease the product price. This approach was chosen by the company Magna Interiors & Interiors Bohemia, s.r.o. (hereafter Magna), which uses so called “slush technology” to produce artificial leathers in one of its plants in the Czech Republic (plant in Libáň). These are then used for fabrication of softened interior elements in vehicles. One representative of such a product is, for example, a switchboard, which is a complicated product from the point of view of design, complexity of design shapes, dimensions and energy exigency of its fabrication.

### **2. Methods**

The procedure of artificial leather production is as follows: a powder of thermoplastic polymer based on PU or PVC is applied on a hot metal mould face. The powder melts and sinters into a thin compact layer. Having cooled the mould, the finished product is stripped from the mould. The mould imprints appropriate desirable shape on the artificial leather and at the same time a precise mark of the mould surface, which is usually a fine embossed design. With the view of productivity it is desirable that the heating and cooling of the mould were as fast as possible. The procedure of high-quality sintering of artificial leathers, however, necessitates keeping rather a narrow interval of sintering temperature – approximately 20°C.

As early as during the determination of the concept of evidently non-stationary heating of the shell moulds it turned out that technical preparation of the mould heating and its realisation demand application of virtual prediction of heating. This was intensified by the fact that from the efficiency viewpoint, heating by infra-radiators had been chosen. At present, dozens of infra-radiators are used for the mould heating, depending on the external dimensions and shape complexity of a mould. The largest number of infra-radiators applied in the procedure of mould heating was less than two hundred. Infra-radiators of various types and performances are applied.

It is evident from the above-stated description that the basis of technical preparation of heating

---

\* assoc. prof. Ing. Antonín Potěšil, CSc.: LENAM, s.r.o., Klostermannova 690/15; 460 01, Liberec; CZ, e-mail: antonin.potesil@lenam.cz



technology is spacing of a large number of infra-radiators over the back side surface of the shell mould. First attempts of infra-radiators spacing into special holders on a frame of a so called “heating back” using an ad-hoc method did not lead to a satisfactory result. That is why experts of the company LENAM, s.r.o. developed methodology of infra-radiators spacing using environment of software tools of simulation systems CAD (computer aided design) and FEM (finite element method) in a suitable combination (Potěšil et al., 2010).

In order that utilization of the above-mentioned method was users-friendly and accessible for the staff of technical preparation of heating, it was decided to realise the method of radiator positioning in several steps with possible optimisation loops, see Fig. 1.

At the same time it was decided to replace originally used licensed software product CAD (ProE) by a completely new tool, more friendly to technicians, which would have simultaneously more special functions necessary for preparation and satisfactory optimisation of the mould heating. The development of this tool with a working name IREview is one of the main activities of the solved project MPO TIP 2009, registration number FR-TI1/266.

## 2.1. IREview Function

On the basis of the executed analyses, acquired theoretical and practical experience with the “Slush” technology in the company Magna and creative visions of development experts of the company LENAM, s.r.o., a conception of a SW toll has been designed, which, having been completed, will perform the following functions:

- Imports of objects and data structures into the complete configuration of the mould heating (moulds, infra-radiators including their performance characteristics, relevant subsidiary constructions...)
- Control of visualisation and/or suppression of objects, definition of their identifications
- Manipulation with objects (displacements, rotation, transformation, suppression or visualisation of objects, ...)
- Check-up of intersections and collisions of objects
- Acquisition of geometrical information on objects in required systems of coordinates
- Creation and modification of meshes of moulds for radiation calculations
- Computational procedures for radiation of moulds
- Further and other functions (statistics, lists of materials, values of mould radiation, deviations from criterion values, ...)
- Data export for further sophisticated applications (physical spacing of radiators and thermocouples by a robot, initial conditions for non-stationary thermal structural FEM simulations, ...)

The realized study of feasibility for the software IREview (Živný, 2009) development realised in the first stages of solution within the above-mentioned MPO project, directed the researches of this part of the project towards utilisation of the open source graphical environment Blender. It appeared, among others, that for the considered purposes, a number of sophisticated graphical options of the development environment Blender can be exploited immediately.

## 2.2. Figures

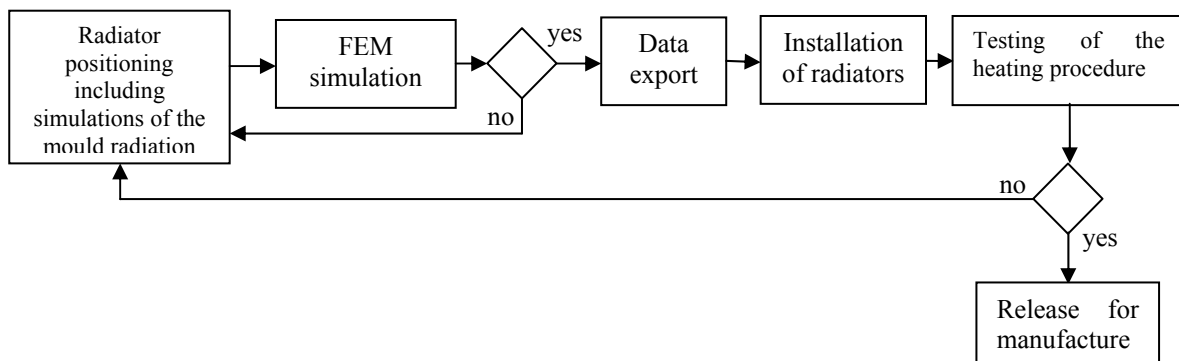


Fig. 1: Scheme of procedure of virtual non-stationary mould heating design.

The following illustrations present the up-to-date stage of development of the IREview software according to the activities planned in the project

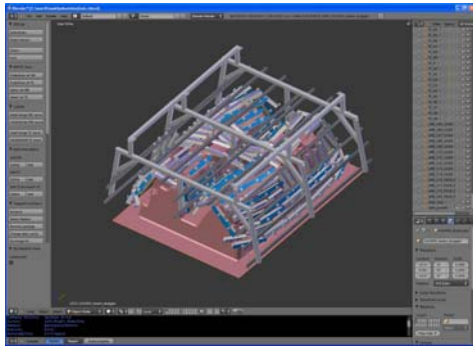


Fig. 2: Import and visualization of objects.

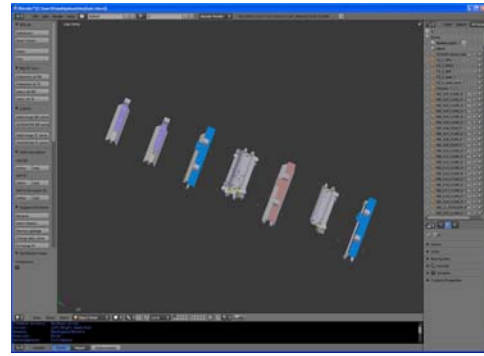


Fig. 3: Database of radiators with their characteristics.

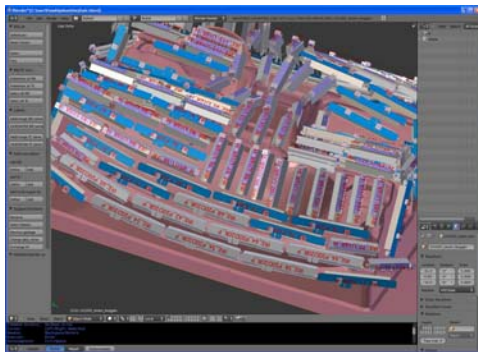


Fig. 4: Identification of radiators.

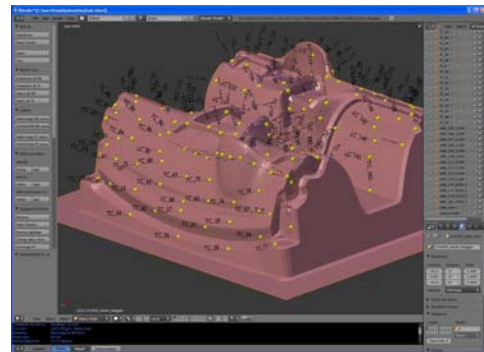


Fig. 5: Identification of thermocouples.

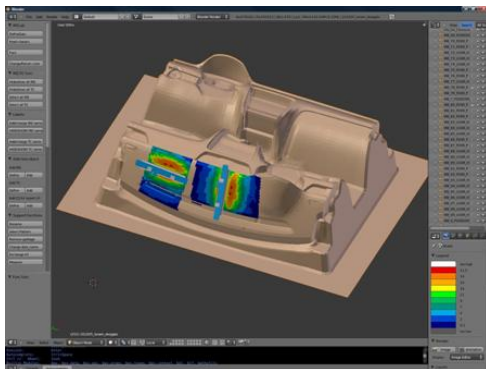


Fig. 6: Simulation of the mould radiation intensity.

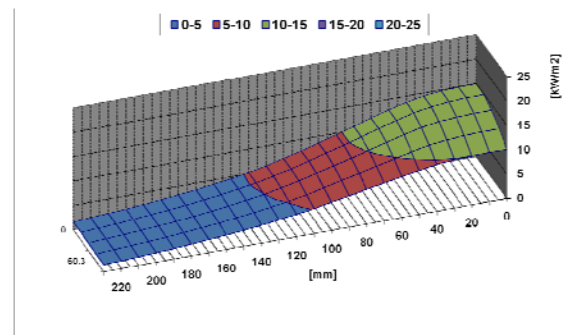


Fig. 7: Measured characteristics of the radiator.

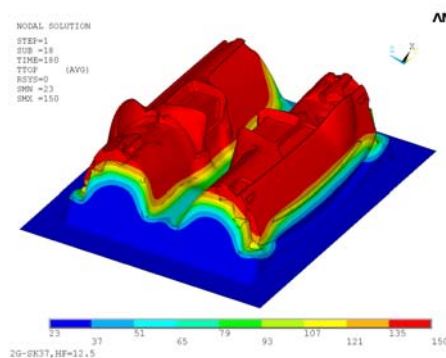


Fig. 8: Simulation of the mould temperature distribution.

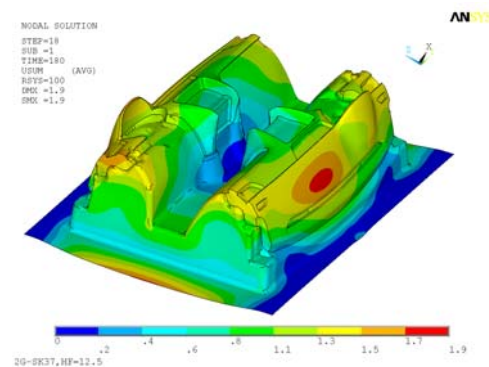


Fig. 9: Simulation of the mould deformation.

### 3. Conclusions

The paper introduces the reader into the problems of design of non-stationary heating of thin-walled shell moulds by means of a large number of infra-radiators used in fabrication of artificial leathers. They are applied in technologies of production of softened interior parts, mainly in personal vehicles.

The chosen conception of efficient mould heating induced a necessity of design and realisation of new sophisticated procedures so that they facilitated the process of technical preparation of the mould heating. Application of virtual information and simulation technologies proved to be correct and efficient.

The designed methodology of the mould heating combines several innovation approaches. The first one is solved by development of an in-house software tool IREview by means of which 3-dimensional spacing of the infra-radiators over a complicated and spacious metal mould is realized, with a possibility of a controlled visualisation of the mould radiation intensity including the export of the result into some FEM environment for further simulation of the non-stationary temperature field. Following an acceptable numerical optimisation of the mould heating, relevant data are exported from the environment of IREview that are used for conducting a robotic hand during physical positioning of the radiators in the production facilities.

As a conclusion it is to be mentioned that the developed virtual technology for optimal spacing of infra-radiators required designing and realisation of an experimental workplace that serves to measure directional radiation performance characteristics of used infra-radiators and their special types of construction. Without these real physical measurements the above described virtual procedures and software tools could not be successfully used.

The whole project aim can be found at <http://www.lenam.cz/?action=projekty>. Selected details of the project solving shall be presented to the participants of the Conference EM 2011

### Acknowledgement

It is a pleasant duty of the author of the paper, who is a guarantee of the MPO TIP 2009 project, reg. number FR-TI1/266 on behalf of the company LENAM, s.r.o., to thank his team colleagues of the company LENAM, s.r.o., namely to Mr. Martin Živný, Tomáš Vít, Martin Hušek and Zbyněk Hlava for their important contribution to the project solutions, further to Mr. Jiří Hnídek from the Technical University of Liberec for consultancy support of programming in the graphical environment Blender and last but not least to Mr. Jaroslav Kozák from the company Magna for precious information related to the technology of manufacture of artificial leathers and for successful collaboration of partner companies Magna and LENAM.

Acknowledgements belong also to further unnamed colleagues from the partner Technical University of Liberec, faculty of Mechatronics, who work on further related topics within the project, oriented to non-stationary temperature fields of moulds and regulation algorithms controlling the radiation processes of heating.

### References

- Potěšil, A., Vít, T., Živný, M. (2010) Metoda rozmístění infrazářičů pro ohřev formy pro výrobu umělých kůží, Interní zpráva projektu FR-TI1/266, Liberec.
- Živný, M. (2009): Studie proveditelnosti sw aplikace IREview, Interní zpráva projektu FR-TI1/266, Liberec.

## THE ANALYSIS OF THE CRACK INITIATED FROM THE ORTHOTROPIC BI-MATERIAL SHARP NOTCH

T. Profant<sup>\*</sup>, J. Klusák<sup>\*\*</sup>, M. Kotoul<sup>\*</sup>

**Abstract:** Under the consideration of the bi-material notch composed of two orthotropic materials the potential direction of the crack initiated from the notch tip is determined from the maximum mean value of the tangential stresses and local minimum of the mean value of the generalized strain energy density factor in both materials. Following the assumption of the same mechanism of the rupture in the case of the crack and the notch, an expression for the critical values of the generalized stress intensity factor can be obtained. The radial and tangential stresses and strain energy density are expressed using the Lekhnitskii-Eshelby-Stroh (LES) formalism for the plane elasticity. The stress singular exponents and corresponding eigenvectors are the solution of the eigenvalue problem leading from the prescribed notch boundary and compatibility conditions. In generally, there is more than one solution of this eigenvalue problem and consequently the generalized stress intensity factors.

**Keywords:** Orthotropic, bi-material, sharp notch, LES formalism,  $\Psi$ -integral, MTS theory.

### 1. Stress distribution

In the contribution the orthotropic bi-material notch is analyzed from the perspective of generalized linear elastic fracture mechanics, i.e. the validity of small-scale yielding conditions is assumed. It is further assumed ideal adhesion at the bi-material interface and the notch radius  $r \rightarrow 0$  (the sharp bi-material notch tip), see Fig. 1. The necessary step for the crack initiation assessment is detailed knowledge of the stress distribution. Within plane elasticity of anisotropic media the Lekhnitskii-Eshelby-Stroh (LES) formalism based on Lekhnitskii (1963) can be used. The relations for displacements and stresses can be found in Klusák et al. (2010) and Profant et al. (2010). In the case of the studied notch, the potentials  $f_j(z_j)$  appearing in the LES formalism have the following form  $\mathbf{f} = H \langle z_*^\delta \rangle \mathbf{v}$ , where  $H$  is the generalized stress intensity factor,  $\mathbf{v}_i = v_i' + i v_i''$  is an eigenvector corresponding to the eigenvalue  $\delta = \delta' + i \delta''$  representing the exponent of the stress singularity at the notch tip  $p$  via the relation  $p = \delta - 1$ . The expression  $\langle z_*^\delta \rangle$  represents the diagonal matrix with

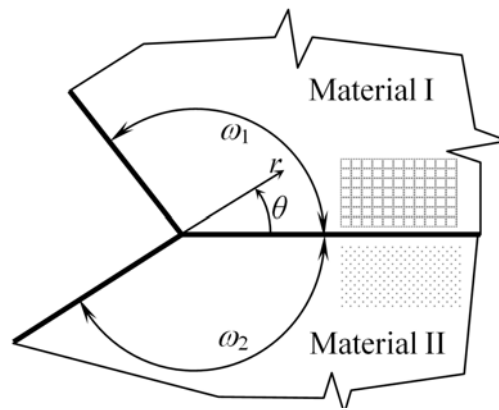


Fig. 1: Bi-material orthotropic notch with corresponding polar coordinate system.

<sup>\*</sup> Ing. Tomáš Profant, Ph.D. and prof. RNDr. Michal Kotoul, DrSc.: Brno University of Technology, Technická 2, 616 69, Brno, Czech Republic, e-mails: profant@fme.vutbr.cz, kotoul@fme.vutbr.cz

<sup>\*\*</sup> Ing. Jan Klusák, Ph.D.: Institute of Physics of Materials, Academy of Sciences of the Czech Republic, Žitkova 22, 616 62, Brno, Czech Republic, e-mail: klusak@ipm.cz

diagonal elements  $z_i = x + \mu_i y$ , where  $i = 1, 2$  and  $\mu_i$  is an eigenvalue of the material, Lekhnitskii (1963), Klusák et al. (2010) and Profant et al. (2010). Eigenvector  $v_i$  and eigenvalue  $\delta$  are the solution of the eigenvalue problem leading from the prescribed notch boundary and compatibility conditions.

## 2. GSIFs, crack initiation direction and stability criterion

**Generalized stress intensity factors determination:** The GSIFs can be determined using the so-called  $\Psi$  - integral, Klusák et al. (2010) and Profant et al. (2010). This method is an implication of Betti's reciprocity theorem which in the absence of body forces states that the following integral is path-independent

$$\Psi(\mathbf{u}, \hat{\mathbf{u}}) = \int_{\Gamma} (\sigma_{ij}(\mathbf{u}) n_i \hat{u}_j - \sigma_{ij}(\hat{\mathbf{u}}) n_i u_j) ds \quad (i, j = 1, 2). \quad (1)$$

The contour  $\Gamma$  surrounds the notch tip and the displacements  $u_j$  are considered as the regular and  $\hat{u}_j$  as the auxiliary solutions of the eigenvalue problem of the notch.

**Mean value of the tangential stress:** For mixed mode fields a crack may grow along the interface or at a certain angle  $\theta_0$  with the interface into the material I or II. The criterion of the MTS theory, Erdogan & Sih (1963), states that the crack is initiated in the direction  $\theta_0$  where the circumferential stress  $\sigma_{\theta\theta}$  at some distance from the crack tip has its maximum and reaches a critical tensile value. In order to suppress the influence of the distance  $r$ , the mean value of the tangential stress is evaluated over a certain distance  $d$  and the potential direction of the crack initiation is determined from the maximum of this mean value of tangential stress in both materials. Hence the following realations have to be satisfied

$$\left( \frac{\partial \bar{\sigma}_{m\theta\theta}}{\partial \theta} \right)_{\theta=\theta_0} = 0, \quad \left( \frac{\partial^2 \bar{\sigma}_{m\theta\theta}}{\partial \theta^2} \right)_{\theta=\theta_0} < 0, \quad \bar{\sigma}_{\theta\theta}(\theta) = H_1 F_{\theta\theta 1m}(\theta, d) + H_2 F_{\theta\theta 2m}(\theta, d), \quad (2)$$

where  $H_i$  are generalized stress intensity faktors and functions  $F_{\theta\theta m}(\theta, d)$  can be found in Profant et al. (2010).

**Strain energy density factor:** Similarly, the crack initiation direction can be derived via the generalization of the mean value of the strain energy density factor  $\bar{\Sigma}_m(\theta, d)$  defined in Profant et al. (2010). To find the minimum of  $\bar{\Sigma}_m(\theta, d)$  and consequently the crack initiation direction in materials I or II, following conditions have to be determined

$$\left( \frac{\partial \bar{\Sigma}_m}{\partial \theta} \right)_{\theta=\theta_0} = 0, \quad \left( \frac{\partial^2 \bar{\Sigma}_m}{\partial \theta^2} \right)_{\theta=\theta_0} > 0, \quad (3)$$

$$\bar{\Sigma}_m(\theta, d) = \frac{1}{4\pi d} \int_0^d (r^{2\delta_1'-1} H_1^2 U_{1m} + r^{2\delta_2'-1} H_2^2 U_{2m} + 2r^{\delta_1'+\delta_2'-1} H_1 H_2 U_{12m}) dr. \quad (4)$$

The function  $U_{ijm}(\theta)$  as well as the functions  $F_{\theta\theta m}(\theta, d)$  hold an complicated form and can be found in Profant et al. (2010).

**Stability criterion.** The stability criterion of the orthotropic bimaterial notches defines the loading conditions above that a crack is initiated in the tip of the singular stress concentrator. Consider the fact that for the GSIFs and their critical values the folowing condition holds,  $\Gamma_{21} = H_2 / H_1 = H_{2C} / H_{1C}$ , and that the boundary conditions does not depend on the absolute value of the applied stress  $\sigma_{appl}$ .

The assumption of the same mechanism of a rupture of the crack and the notch leads to the expression of the critical value of  $H_1$ , Klusák et al. (2010) and Profant et al. (2010),

$$H_{1C} = \frac{2K_{IC}}{\sqrt{2\pi d} (F_{\theta\theta 1m}(\theta_0) + \Gamma_{21} F_{\theta\theta 2m}(\theta_0))}, \quad (5)$$

where  $K_{IC}$  is the fracture toughness of the material  $m$ .

**Stability of the notch - Matched asymptotic procedure:** Matched asymptotic procedure is used to derive the change of potential energy for the debonding crack and the crack initiated in the direction derived via the mean value of the tangential stress or the mean value of the strain energy density factor. Asymptotic expansion for the notch before the perturbation inception takes place reads

$$U^0(x) = H_1 r^{\delta_1} u_1(\theta) + H_2 r^{\delta_2} u_2(\theta) + \dots \quad (6)$$

where only singular terms are considered and  $r$  is the distance from the notch tip. The outer  $U^\varepsilon$  and inner expansion  $V^\varepsilon$  for the perturbed domain  $\Omega^\varepsilon$  is

$$U^\varepsilon(x) = U^0(x) + k_1(\varepsilon) K_{1d(p)} r^{-\delta_1} u_{-1}(\theta) + k_2(\varepsilon) K_{2d(p)} r^{-\delta_2} u_{-2}(\theta) + \dots, \quad (7)$$

$$V^\varepsilon(y) = F_1(\varepsilon) [\rho^{\delta_1} u_1(\theta) + K_{1d(p)} \rho^{-\delta_1} u_{-1}(\theta) + K_{2d(p)} \rho^{-\delta_2} u_{-2}(\theta) + \dots] + \\ + F_2(\varepsilon) [\rho^{\delta_2} u_2(\theta) + K'_{1d(p)} \rho^{-\delta_1} u_{-1}(\theta) + K'_{2d(p)} \rho^{-\delta_2} u_{-2}(\theta) + \dots] + \dots \quad (8)$$

The terms in the brackets on the right-hand side of (8) are basis functions of inner expansion and their first terms describe their behavior for  $\rho = r/\varepsilon \rightarrow \infty$ , where  $\varepsilon$  is the small perturbation parameter. The  $u_{-1}(\theta)$  and  $u_{-2}(\theta)$ , are dual (auxiliary) solutions to  $u_1(\theta)$  and  $u_2(\theta)$ . The  $K_{1d(p)}$ ,  $K_{2d(p)}$  are calculated using the  $\Psi$ -integral in the inner domain whose remote boundary  $\partial\Omega^{in}$  is subjected to the boundary condition  $U|_{\partial\Omega^{in}} = \rho^{\delta_1} u_1(\theta)$

$$K_{1d(p)} = \frac{\Psi(V_1^h, \rho^{\delta_1} u_1)}{\Psi(\rho^{-\delta_1} u_{-1}, \rho^{\delta_1} u_1)}, \quad K_{2d(p)} = \frac{\Psi(V_1^h, \rho^{\delta_2} u_2)}{\Psi(\rho^{-\delta_2} u_{-2}, \rho^{\delta_2} u_2)}, \quad (9)$$

where  $V_1^h$  is the finite element approximation to the first basis function of (8). Similarly, the coefficients  $K'_{1d(p)}$ ,  $K'_{2d(p)}$  are calculated in the inner domain whose remote boundary  $\partial\Omega^{in}$  is subjected to the boundary condition  $U|_{\partial\Omega^{in}} = \rho^{\delta_2} u_2(\theta)$

$$K'_{1d(p)} = \frac{\Psi(V_2^h, \rho^{\delta_1} u_1)}{\Psi(\rho^{-\delta_1} u_{-1}, \rho^{\delta_1} u_1)}, \quad K'_{2d(p)} = \frac{\Psi(V_2^h, \rho^{\delta_2} u_2)}{\Psi(\rho^{-\delta_2} u_{-2}, \rho^{\delta_2} u_2)}, \quad (10)$$

where  $V_2^h$  is the finite element approximation to the second basis function of (8). The ratio of the debonding to the penetrating (propagating into material I or II) ERR is following

$$\frac{G_d}{G_p} = \frac{K_{1d} \Psi_1 + (K'_{1d} \Psi_1 + K_{2d} \Psi_2) \eta_d + K'_{2d} \Psi_2 \eta_d^2 \frac{a_d^{2\delta_1-1}}{a_p^{2\delta_1-1}}}{K_{1p} \Psi_1 + (K'_{1p} \Psi_1 + K_{2p} \Psi_2) \eta_p + K'_{2p} \Psi_2 \eta_p^2 \frac{a_d^{2\delta_1-1}}{a_p^{2\delta_1-1}}}, \quad \eta_{d,p} = \frac{H_2}{H_1} \frac{a_{d,p}^{\delta_2-\delta_1}}{L^{\delta_2-\delta_1}}, \quad (11)$$

$$\Psi_{1,2} \equiv \Psi(\rho^{-\delta_{1,2}} u_{-1,-2}, \rho^{\delta_{1,2}} u_{1,2}), \quad (12)$$

where  $a_{d,p}$  is the length of the debonding or propagating crack,  $L$  is the characteristic length of the perturbed domain, Profant et al. (2011). The debonding occurs if the condition  $G_d/G_p > G_c^I/G_c^{I,II}$  is satisfied, where  $G_c^I$  is the interface toughness,  $G_c^{I,II}$  toughness of the material I, II.

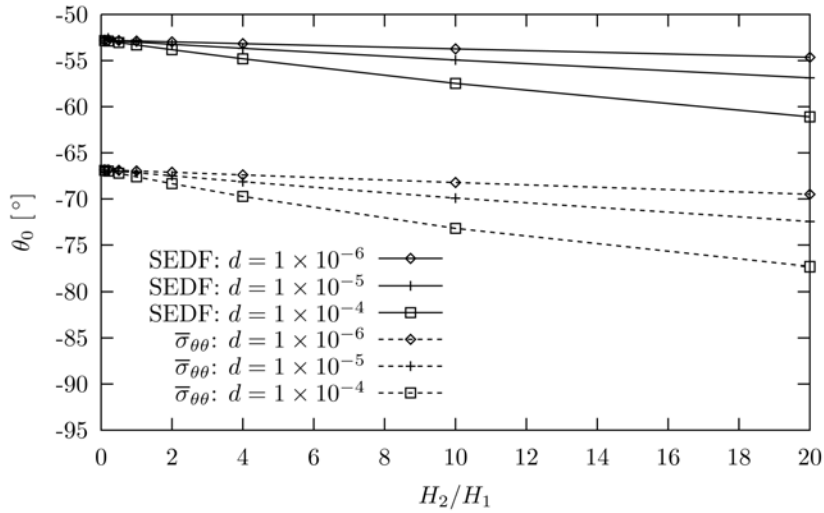


Fig. 2: Crack initiation angles for varying loading conditions (expressed by  $H_2/H_1$ ) and for selected distances  $d$ .

### 3. Numerical results

The parametric study of the crack initiation directions is determined for specific geometry. The rectangular bi-material orthotropic notch characterized by angles  $\omega_1 = 90^\circ$  and  $\omega_2 = 180^\circ$  and materials with the Young's modulus  $(E_x)_I = 100$ ,  $(E_y)_I = 50$ ,  $(E_x)_{II} = 400$ ,  $(E_y)_{II} = 50$  [MPa] is considered. The corresponding stress singularity exponents have values  $\delta_1 = 0.573$  and  $\delta_2 = 0.941$ . There are received GSIFs  $H_1 = 6.43 [MPa^{1-\delta_1}]$  and  $H_1 = 39.99 [MPa^{1-\delta_2}]$  under the remote loading  $\sigma_{xx}^{appl} = 100$  [MPa] of the bi-material notch. The direction of the applied stress need not be specified directly, but it can be expressed by varying ratios  $\Gamma_{21} = H_2 / H_1$ . The angles  $\theta_0$  are determined on the basis of finding the maximum of the mean value of the tangential stress and the minimum of the strain energy density factor. For the considered material the results of the crack initiation direction are shown in Fig. 2. The averaging distance  $d$  was taken as  $1e-4$ ,  $1e-5$  and  $1e-6$ . It is shown that the direction  $\theta_0$  depends on  $d$  especially for larger differences between  $H_1$  and  $H_2$ .

### 4. Conclusions

It was developed the procedure for evaluation of the GSIFs of the bi-material notch using the  $\Psi$ -integral method and consequently it was developed the stability criterion of the notch. The matched asymptotic expansion method was introduced as the other stability criterion of the notch. Finally, the numerical study of the crack growth potential direction was shown.

### Acknowledgements

The authors are grateful for financial support through the Research projects of the Czech Science Foundation (P108/10/2049).

### References

- Lekhnitskii, S. G. (1963) Theory of Elasticity of an Anisotropic body, Holden-Day, San Francisco.
- Klusák, J., Profant T. & Kotoul, M. (2010) Study of the stress distribution around an orthotropic bi-material notch tip, *Key Engineering Materials*, 417-418, pp. 385-38.
- Profant, T., Klusák, J. & Ktoul, M. (2010) A study of the stability of sharp notches in the orthotropic heterogeneous media. The Ninth International Conference on Multiaxial Fatigue & Fracture (ICMFF9), pp. 733 – 740.
- Erdogan, F. & Sih, G.C. (1963) On the crack extension in plates under plane loading and transverse shear. Transactions of the ASME, *Journal of Basic Engineering*, 85D, pp. 519-527.
- Profant, T., Klusák, J. & Kotoul, M. (2011). Case Criterion of Crack Onset in Orthotropic Bi-Material Notches. *Key Engineering Materials*, 465, pp. 157–160.



## MODELLING OF SUPERCRITICAL TURBULENT FLOW OVER AN INCLINED BACKWARD-FACING STEP IN A OPEN CHANNEL

J. Příhoda<sup>\*</sup>, P. Zubík<sup>\*\*</sup>, J. Šulc<sup>\*\*</sup>, M. Sedlár<sup>\*\*\*</sup>

**Abstract:** *The contribution deals with the experimental and numerical modelling of supercritical turbulent flow in an open channel with an inclined backward-facing step on its bottom. The step with the height  $h = 100$  mm and the inclination angle  $\alpha = 20^\circ$  was placed in the water channel of the cross-section  $200 \times 200$  mm. Experiments were carried out by means of the PIV and LDA measuring techniques. Numerical simulations were executed by the commercial software ANSYS CFX 12.0. Numerical results obtained by the two-equation SST model and the EARSM model completed by transport equations for turbulent energy and specific dissipation rate were compared with experimental data. The modelling was concentrated particularly on the flow pattern near the step including the possible flow separation and the corresponding changes of free surface. The agreement of numerical results obtained by means of the EARSM model with experimental data is quite good.*

**Keywords:** *Backward-facing inclined step, free-surface supercritical flow.*

### 1. Introduction

An inclined backward-facing step occurs in many practical applications of aerodynamics and hydrodynamics. While the flow pattern behind the step in closed channels is given mainly by the extent of the separation, the flow over an inclined step in open channels is much more complicated. For flows in open channels with an inclined step, the flow character is quite different for sub- and supercritical flow due to the gravitational forces. The subcritical flow is characterized by a relatively massive separation but only small changes of free surface. On the contrary, the supercritical flow is practically without separation with changes of free surface corresponding to the form of the inclined step. Results of the investigation of turbulent flow over an inclined step in the closed channel and in the open channel with sub- and supercritical flow are summarized by Zubík et al. (2010). The subcritical flow over the inclined step was described by Příhoda et al. (2010). The presented contribution deals with modelling of supercritical flow characterised by the Froude number  $Fr = 2.14$ .

### 2. Experimental arrangement

Experiments were carried out in a straight channel of constant cross-section  $0.2 \times 0.2$  m with the length 4.475 m and with the slope of the bottom 2.025 deg corresponding to the chosen supercritical regime. The open channel was linked to the water tank with a pump driven by a motor equipped with a frequency converter. The pump with the maximum flow rate of  $Q = 7.2$  m<sup>3</sup>/min. enabled the maximum speed in the channel of 3 m/s. To stabilize the inflow rate, a wire mesh screens and a honeycomb were installed at the entry of the straight inflow part. The particle image velocimetry method (PIV) was used for measurements of the velocity field in selected channel sections and the laser Doppler anemometry (LDA) for measurements of one and/or two velocity components in selected points of the flow field. The extended uncertainty guess of flow velocity determination at reliability level of 95% was less than 5% for LDA and 15% for PIV techniques.

---

<sup>\*</sup> prof. Ing. Jaromír Příhoda, CSc., Institute of Thermomechanics AS CR, v.v.i., Dolejškova 5, 182 00 Praha 8, CZ, e-mail: prihoda@it.cas.cz

<sup>\*\*</sup> Ing. Pavel Zubík, PhD. and prof. Ing. Jan Šulc, CSc., Institute of Hydraulic Structures, Faculty of Civil Engineering, Brno University of Technology, Veveří 331/95, 602 00 Brno; CZ, e-mail: Zubik.P@fce.vutbr.cz, Sulc.J@fce.vutbr.cz

<sup>\*\*\*</sup> RNDr. Milan Sedlár, CSc., SIGMA – Research and Development Institute, Jana Sigmunda 79, 783 50 Lutín, CZ, e-mail: milan.sedlar@sigma-vvu.cz

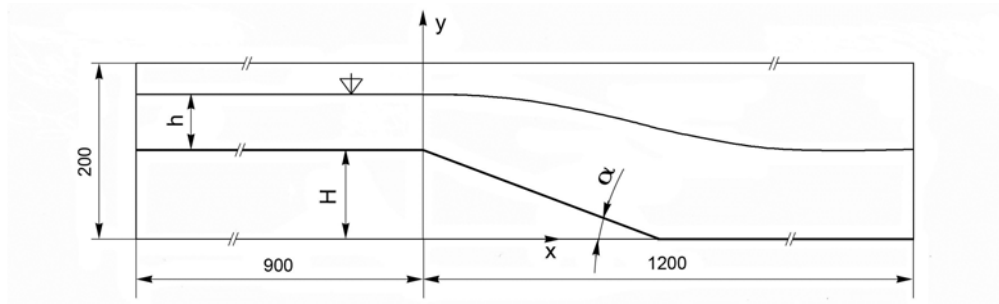


Fig. 1: Sketch of the geometrical arrangement.

The sketch of the geometrical arrangement of the channel with an inclined backward-facing step is given in Fig. 1. The height of the inclined step is  $H = 0.1$  m. The PIV measurements were taken at vertical and horizontal planes parallel with the channel axis. For comparison, profiles of mean and fluctuation longitudinal velocities were measured by the LDA method in the mean vertical plane at selected sections  $x = \text{const}$ . The measurement of the supercritical free-surface flow was carried out for the mean bulk velocity  $U_m = 1.92$  m/s and for the initial height of the water level  $h = 0.086$  m, i.e. for the Reynolds number  $Re_b = U_m H / \nu = 200100$  and the Froude number  $Fr = U_m / (gh)^{1/2} = 2.14$ . At the chosen mean bulk velocity, the turbulence level in the stream core was about 2 %.

### 3. Mathematical model

The numerical simulation of the turbulent flow over the inclined step in an open channel was carried out by means of the commercial software ANSYS CFX version 12.0 solving Reynolds-averaged Navier-Stokes equations including the gravity effect. A second-order scheme was used for calculations. The numerical solution of free-surface flow was carried out by means of the Volume-of-Fluid (VOF) method monitoring of the volume fraction of both fluids in the each computational cell. The “non-homogeneous” model where the governing equations for the both fluids are solved separately was chosen for the calculation. The EARSIM (Explicit Algebraic Reynolds Stress) model based on transport equations for turbulent energy  $k$  and specific dissipation rate  $\omega$  was used for the supercritical flow. Besides, the SST  $k-\omega$  model proposed by Menter (1994) was used for comparison.

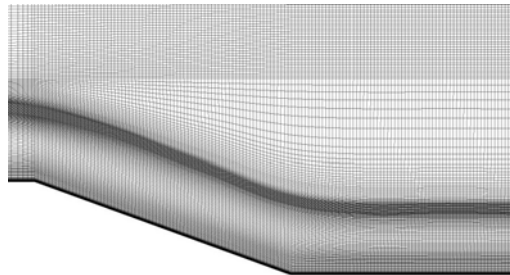


Fig. 2: Detail of the computational grid.

The computational domain corresponding to the experimental arrangement starts in the cross-section  $x = -0.6$  mm before the edge of the inclined step and finishes at the distance  $x = 1.2$  m. The computational domain consists of one half of the channel width with the symmetric boundary condition in the symmetry plane ( $z = 0$ ). The computational grid in the channel with the inclined step is shown in Fig.2. A structured mono-block type grid refined near walls and near the free-surface was used for calculations. The grid refinement was adapted to the shape of free surface obtained by preliminary calculations. The grid consists of  $367 \times 169 \times 51$  grid points, i.e. approx.  $3.1 \times 10^6$  points. The distribution of mean velocity, turbulent energy, and dissipation rate was prescribed as inflow boundary conditions according to experimental data. The mean value of static pressure was prescribed as the outflow boundary condition and the open-boundary condition was applied at the upper boundary.

The EARSIM model is based on a nonlinear relation between the Reynolds stresses and the mean strain rate and vorticity tensors. The used version corresponds to the models proposed by Wallin and Johansson (2000). The constitutive relation for the turbulent viscosity is replaced by the introduction of the anisotropy tensor  $a_{ij}$  by the relation

$$a_{ij} = \frac{\overline{u_i u_j}}{k} - \frac{2}{3} \delta_{ij} \quad (1)$$

The anisotropy tensor  $a_{ij}$  is given by the equation

$$\begin{aligned} a_{ij} = & \beta_1 S_{ij} + \beta_3 \left( \Omega_{ik} \Omega_{kj} - \frac{1}{3} \delta_{ij} II_{\Omega} \right) + \beta_4 (S_{ik} \Omega_{kj} - \Omega_{ik} S_{kj}) \\ & + \beta_6 \left( S_{ik} \Omega_{kl} \Omega_{lj} + \Omega_{ik} \Omega_{kl} S_{lj} - \frac{2}{3} \delta_{ij} IV \right) + \beta_9 (\Omega_{ik} S_{kl} \Omega_{lm} \Omega_{mj} - \Omega_{ik} \Omega_{kl} S_{lm} \Omega_{mj}) \end{aligned} \quad (2)$$

where  $S_{ij}$  and  $\Omega_{ij}$  are non-dimensional strain rate and vorticity tensors, and  $II_S$ ,  $II_{\Omega}$  and  $IV$  are their invariants. The coefficients  $\beta_i$  are functions of the ratio  $P_k/\varepsilon$  and invariants of the strain-rate and vorticity tensors. The model is closed by the transport equations for turbulent scales. The SST model is formed by transport equations

$$\frac{Dk}{Dt} = P_k - c_{\mu} \omega k + \frac{\partial}{\partial x_j} \left[ \left( \nu + \frac{\nu_t}{\sigma_k} \right) \frac{\partial k}{\partial x_j} \right] \quad (3)$$

$$\frac{D\omega}{Dt} = \alpha \frac{\omega}{k} P_k - \beta \omega^2 + \frac{\partial}{\partial x_j} \left[ \left( \nu + \frac{\nu_t}{\sigma_{\omega}} \right) \frac{\partial \omega}{\partial x_j} \right] + (1 - F_1) \frac{2}{\sigma_{\omega 2}} \frac{1}{\omega} \frac{\partial k}{\partial x_j} \frac{\partial \omega}{\partial x_j} \quad (4)$$

with turbulent viscosity given by the relation

$$\nu_t = \frac{a_1 k}{\min(a_1 \omega; F_2 S)} \quad (5)$$

where  $F_1$  and  $F_2$  are blending function for the switching from the  $k$ - $\varepsilon$  mode to the  $k$ - $\omega$  mode and  $S$  is a scalar invariant of the strain rate tensor. The function  $F_2$  is equal to zero everywhere for the standard  $k$ - $\omega$  model.

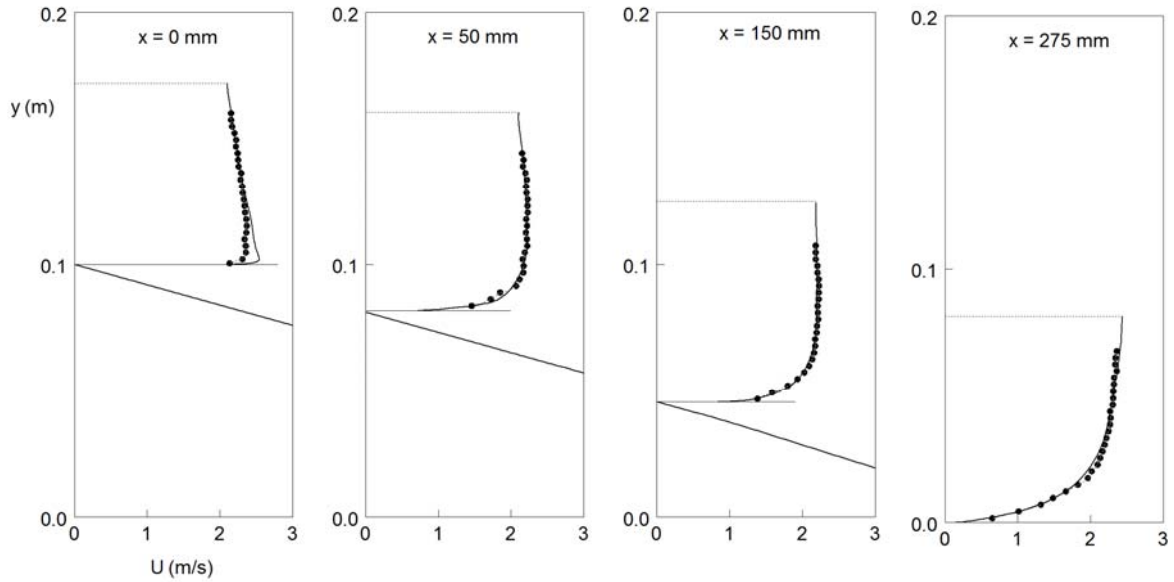


Fig. 3: Mean velocity profiles in the channel with the inclined step.

#### 4. Results

The analysis of experimental and numerical results was concentrated mainly on the region behind the inclined step and on the corresponding changes of free surface. Further, the development of secondary flow near side walls of the channel behind the inclined step was investigated. Fig. 3 shows mean longitudinal velocity profiles in the symmetry plane over the step and in the outlet channel. Velocity profiles obtained by the EARS model are compared with experimental data from PIV measurement.

A surprisingly satisfactory agreement with experimental data was obtained for the EARS model. The SST model gives nearly same velocity profiles unlike the subcritical flow with a large separation region, where the differences between various turbulence models were distinct.

The form of free surface in the middle plane  $z = 0$  and in the plane  $z = -85$  mm near the side wall are compared in Fig. 4 with experimental data. The supercritical flow over the inclined step is practically without any separation. The form of free surface imitates the bottom of the channel. The free surface is slightly waving behind the root of the step. Besides transversal waves, two distinct oblique waves arise at side walls. The form of free surface predicted by the EARS model corresponds very well with experiment, even though the response of the numerical model on any change is rather slower than in reality.

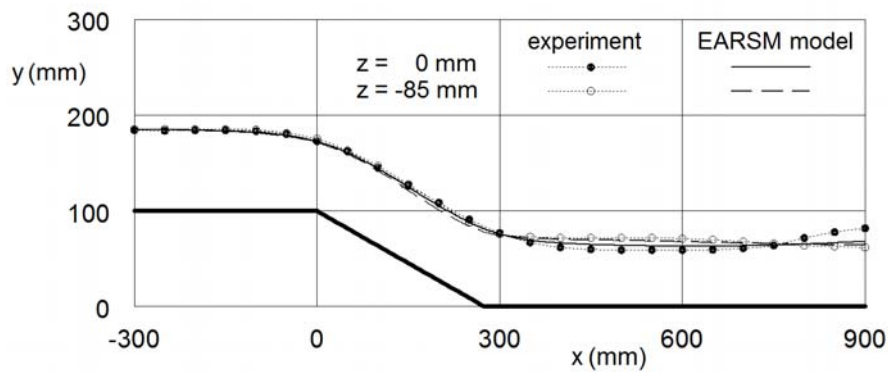


Fig. 4: The form of the free surface in planes  $z = 0$  and  $-85$  mm.

## 5. Conclusions

The supercritical free-surface flow over a backward-facing inclined step in a rather narrow channel was experimentally and numerically investigated. The flow over the inclined step is practically without any separation and free surface imitates the bottom of the channel. A very satisfactory agreement with experimental data was obtained for the EARS model. Unlike the subcritical flow, the free surface of the supercritical flow is slightly waving behind the root of the step. Besides transversal waves, two distinct oblique waves arise at side walls. The predicted free surface corresponds very well with experiment, even though the response of the numerical model on any change is rather slower than in reality.

## Acknowledgement

The work was supported by the grant project No.103/09/0977 of the Czech Science Foundation and by the Research Plan AV0Z20760514.

## References

- Přihoda J., Zubík P., Šulc J., Sedlář M. (2010) Modelling of subcritical free-surface flow over an inclined backward-facing step in a water channel, In: Proc. Int. Conf. Experimental Fluid Mechanics 2010, Liberec, 555-560.
- Zubík P., Šulc J., Přihoda J., Sedlář M. (2010) Experimental and numerical modelling of fluid flow with separation, In: Proc. 9th Conference Power System Engineering, Thermodynamics and Fluid Flow, CD-ROM, 8p., Plzeň (in Czech).
- Menter F.R. (1994) Two-equation eddy-viscosity turbulence models for engineering applications, AIAA Jour., 32, 1598-1605.
- Wallin S., Johansson A. (2000) A complete explicit algebraic Reynolds stress model for incompressible and compressible flows, Jour. Fluid Mechanics, 403, 89-132.

## PROBABILISTIC ANALYSIS FOR DESIGN ASSESSMENT OF COMPOSITE STEEL-AND-CONCRETE COMPRESSION MEMBERS

L. Puklický\*

**Abstract:** *Steel-concrete composite columns are extensively used in modern buildings. Steel being of high tensile strength presents a high quality building material, concrete on the other hand carries the compressive stresses and protects the steel from high temperatures and corrosion. The theoretical analysis of the actual behaviour of modern concrete-steel structures is more frequently performed during design, realization and utilization of such structures. The main goal of the presented paper is the non-linear analysis of the load-carrying capacity of concrete encased steel columns. Ample information, obtained from experimental research, on the material characteristics of steel was available and was considered during analysis as random input variables. Statistical information on the input variables has an influence on the reliability of results obtained from statistical analysis of the ultimate limit state. Stresses in both concrete and steel sections were evaluated using principles of elasticity and plasticity. Numerical LHS simulation methods were applied. These methods take into account the variability influences of input imperfections. Obtained output is the random load-carrying capacity, which quantifies the uncertainty due to the random character of material and geometrical characteristics. The important output of the statistical analysis is the design load-carrying capacity, which was evaluated according to EN1990 as 0.1 percentile.*

**Keywords:** *Steel, concrete, stability, strut, stochastic.*

### 1. Introduction

Generally, two types of composite columns are commonly used in the building industry, i.e., those with steel section in-filled with concrete and those with steel section encased in concrete. Basic examples of composite column cross-sections are illustrated in Fig. 1.

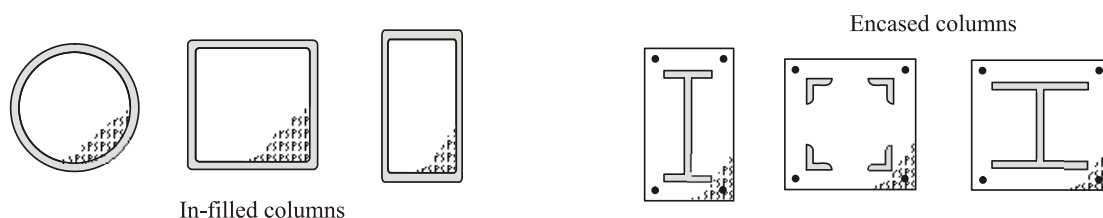


Fig. 1: Types of composite columns.

Concrete-encased steel composite columns have become more popular for many resistant structures. Under severe flexural overload, the concrete encasement cracks which results in the reduction of stiffness, however, the steel core provides the shear capacity and the ductile resistance to subsequent cycles of overload.

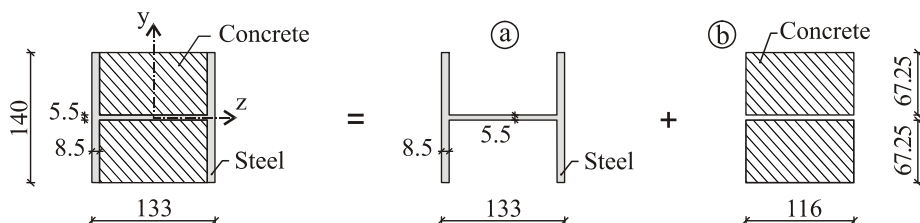


Fig. 2: Theoretical decomposition and nominal values of steel-concrete cross section.

\* Ing. Libor Puklický: Institute of Structural Mechanics, Brno University of Technology, Faculty of Civil Engineering, Veveří Street 95; 602 00, Brno; CZ, e-mail: l.puklicky@fce.vutbr.cz

## 2. Theoretical model

The subject of analysis is the ultimate limit state of a steel-concrete column of system length equal to its critical length,  $L = L_{cr} = 3$  m, in compression. The column consists of steel profile HEA140 encased in high strength concrete, see Fig. 1. The load  $F$  acting on the column consists of load  $F_S$ , which is carried by the steel section, and of load  $F_C$ , which is carried by the concrete section, i.e.,  $F = F_S + F_C$ . Let us assume that the strut is produced in the shape affine to eventual buckling, with deflection at mid length denoted as  $e_0$ . The maximum deflection mid-span of the strut  $e$  which is loaded by axial force  $F$  in its elastic state may be determined according to (Timoshenko, 1961) as:

$$e = e_0 / (1 - F / F_{cr}) \quad (1)$$

where  $F$  is the load acting on the column, and  $F_{cr}$  is Euler's critical force  $F_{cr} = \pi^2 EI / L_{cr}^2$ . In accordance with article 6.7.3.1 (3) of standard EN 1994-1-1: 2006, the effective elastic flexural rigidity  $EI$  of the steel-concrete column which is given according to the formula listed below may be used for short term loading:

$$EI = E_S \cdot I_S + K_E \cdot E_C \cdot I_C \quad (2)$$

where  $I_S$  and  $I_C$  are the second moments of area in the plane of bending of structural steel and concrete (without consideration of cracking),  $E_S$  is the modulus of the steel elasticity,  $E_C$  is the tangent modulus of the elasticity of concrete,  $K_E \cdot E_C \cdot I_C$  is the effective flexural rigidity of the concrete section,  $E_S \cdot I_S$  is the effective flexural rigidity of the steel section.

Values of forces  $F_S$ ,  $F_C$  and parameter  $K_E$  can be obtained from the following deformation conditions:

- (i) Bending around the z-axis: Deflection mid-span of the strut in the direction of y-axis  $e$  is given as the deflection of the steel section  $e_S$  which is equal to the deflection of the concrete section  $e_C$ ; i.e.  $e = e_S = e_C$ .
- (ii) Compression in direction of x-axis: The compression of the steel section by  $F_S$  equals the compression of the concrete section by  $F_C$ . The load carried by the steel section  $F_S = F \cdot E_S I_S / (EI)$  and the load carried by the concrete section  $F_C = F \cdot K_E \cdot E_C I_C / (EI)$  with parameter  $K_E = I_S \cdot A_C / (I_C \cdot A_S)$  can be determined from the above listed mathematical dependencies (where  $A_C$  is the area of concrete and  $A_S$  is the area of steel cross section).

The elastic load-carrying capacity of the steel-concrete column is given as the minimum of the elastic load-carrying capacities of the steel and concrete sections, which are determined as follows:

- (i) The elastic load-carrying capacity of the steel member is given by the yield strength attained in the most stressed section.
- (ii) The elastic load-carrying capacity of the concrete section is given as the cubic strength in the most compressed section or as 10 % of the cubic strength in the most tensed part of the section. Detailed description of the calculation of both elastic and ultimate load-carrying capacities is described in the paper (Kala et al., 2010).

## 3. Input random variables

Generally, all input variables are of random character. Results obtained from a long-term experimental research were used for the input random characteristics (Melcher et al., 2004; Kala et al., 2009). Input random material characteristics of steel S420 were published in (Kala et al., 2010). The mean value of cubic strength  $f_{cc}$  of the concrete section in Fig. 2b was considered according to the results obtained from experimental research (Kala et al., 2010). The modulus of elasticity  $E_C$  of concrete was evaluated in compliance with standard Eurocode 2 according to the formula:

$$E_C = 22 \cdot \left( \frac{5 \cdot f_{cc}}{6 \cdot 10} \right)^{0.3} \cdot \Theta_{E_C} \quad (3)$$

Statistical characteristics of parameter  $\Theta_{E_C}$  were identified so that maximum agreement between the theoretical analysis and experiment has been attained. The statistical characteristics of all input random variables were published in (Kala et al., 2010). All input random variables were considered with Gauss density distribution function.



#### 4. Statistical analysis and discussion

The curves of “load action - deformation” determined under the presumption that all variables are considered as random ones are depicted in the left part of Fig. 3. The numerical simulation method LHS (McKey et al., 1979; Iman and Conover, 1980), which is a method of type Monte Carlo, was applied. Obtained curves of “load action - deformation” are one of the main outputs describing the random characteristics of the ultimate limit state of the examined strut.

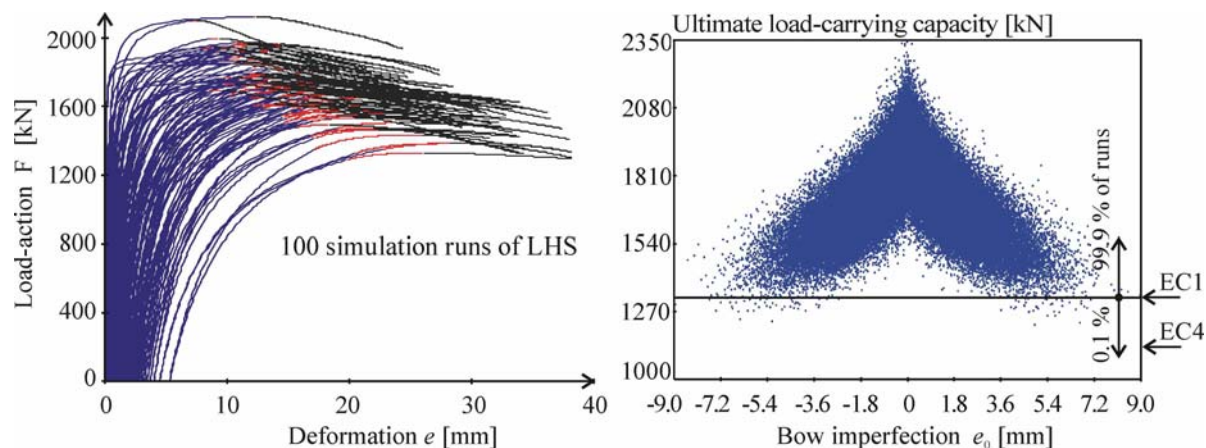


Fig. 3: Theoretical decomposition of steel-concrete cross section.

The maximum possible load which the column is able to carry is defined as the ultimate load-carrying capacity; see Fig. 3. The dependence between random initial bar crookedness  $e_0$  (bow imperfection) and 100 000 runs of load-carrying capacities is very interesting; see Fig. 3. Let us note that the ultimate load-carrying capacity is approximately 3% higher than the elastic load-carrying capacity. This is relatively insignificant. The theoretical model described in chapters 2 and in (Kala et al., 2010) is sufficiently accurate. This was verified using the geometrical and material nonlinear solution with SHELL 181 elements of the ANSYS software, see the stress state in Fig. 4.

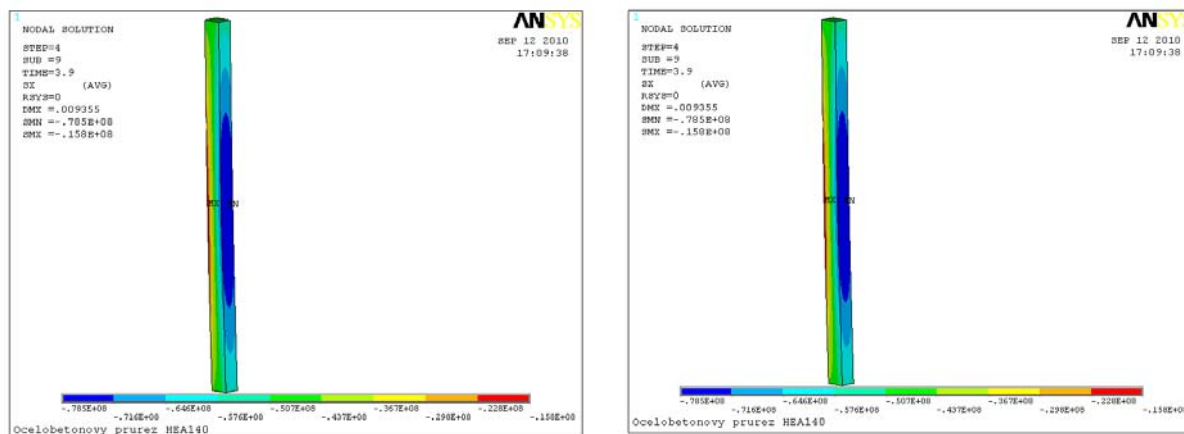


Fig. 4: Theoretical decomposition of steel-concrete cross section.

From Fig. 3, large variance of the load - deformation curves is evident; it will manifest itself on the dispersion of ultimate load-carrying capacity and on its design value. In future, it will be necessary to get concentrated on the study of the ultimate load-carrying capacity on behalf of specialized sensitivity analysis methods. The local sensitivity measures determine the influence of parameters by varying one parameter at the time and keeping the other parameters constant (Kala, 2005; Melcher et al., 2009). The global sensitivity analysis identifies the influence of individual imperfections, and of their mutual interactions (Kala, 2011a; Kala, 2011b). In sophisticated systems, the application of advanced methods of the reliability analysis including the sensitivity analysis methods is indispensable, see, e.g., (Karmazinová et al., 2009; Gottvald et al., 2010). Let us note that, when creating a computation model, it is necessary to distinguish between epistemic uncertainty a stochastic uncertainty, see, e.g., (Kala, 2007; Kala, 2008). The generally given problematic leads to the applications of „soft computing“ method, which form an appropriate unifying framework.

## 5. Conclusions

The output of the probability analysis is the set of random realizations of the load-carrying capacity mapping the influence of random uncertainties of geometrical and material characteristics on the load-carrying capacity. The output of the standards solutions is the design value of load-carrying capacity. The design load-carrying capacity was calculated, according to EN1990, as 0.1 percentile. The difference between standard design load-carrying capacities evaluated according to EN1990 and EUROCODE 4 solution is alarming. The basic probabilistic background of Eurocode is in EN 1990. If the design probability of failure is  $7.2\text{E-}5$  ( $\beta_d = 3.8$ ), then the design load-carrying capacity evaluated according to EN 1990 should be approximately equal to 0.1 percentile; however, it is not fulfilled. The quantification of these differences would require a more detailed study with application of global sensitivity analysis. The results of sensitivity analyses in (Kala, 2009) have shown that the influence of higher order interaction effects is low for the steel member. This knowledge will have to be verified also for the steel-concrete composite column solved here.

## Acknowledgement

The article was elaborated within the framework of project AVČR IAA201720901 and GAČR 103/09/0597.

## References

- Gottvald, J. (2010) The calculation and measurement of the natural frequencies of the bucket wheel excavator SchRs 1320/4x30. *Transport*, 25, 3, pp.269-277.
- Iman, RC. & Conover, WJ. (1980) Small sample sensitivity analysis techniques for computer models with an application to risk assessment. *Communications in Statistics – Theory and Methods*, 9, 17, pp.1749–1842.
- Kala, Z. (2005) Sensitivity analysis of the stability problems of thin-walled structures. *Journal of Constructional Steel Research*, 61, 3, pp.415-422.
- Kala, Z. (2007) Stability problems of steel structures in the presence of stochastic and fuzzy uncertainty. *Thin-Walled Structures*, 45, 10-11, pp. 861-865.
- Kala, Z. (2008) Fuzzy probability analysis of the fatigue resistance of steel structural members under bending. *Journal of Civil Engineering and Management*, 14, 1, pp.67-72.
- Kala, Z. (2009) Sensitivity assessment of steel members under compression. *Engineering Structures*, 31, 6, pp.1344-1348.
- Kala, Z., Melcher, J. & Puklický, L. (2009) Material and geometrical characteristics of structural steels based on statistical analysis of metallurgical products. *Journal of Civil Engineering and Management*, 15, 3, pp.299-307.
- Kala, Z., Puklický, L., Omishore, A., Karmazínová, M. & Melcher, J. (2010) Stability problems of steel-concrete members composed of high strength materials. *Journal of Civil Engineering and Management*, 16, 3, pp.352-362.
- Kala, Z. (2011a) Sensitivity analysis of stability problems of steel plane frames. *Thin-Walled Structures*, 49, 5, pp.645-651.
- Kala, Z. (2011b) Sensitivity analysis of steel plane frames with initial imperfections. *Engineering Structures*, (in print). ISSN: 0141-0296. doi:10.1016/j.engstruct.2011.04.007.
- Karmazínová, M., Melcher, J. & Kala, Z. (2009) Design of expansion anchors to concrete based on results of experimental verification. *Advanced Steel Construction*, 5, 4, pp.390-405.
- McKey, MD, Conover, WJ, Beckman, & RJ. (1979) A comparison of the three methods of selecting values of input variables in the analysis of output from a computer code. *Technometrics*, 1, 2, pp.239-245.
- Melcher, J., Kala, Z., Holický, M., Fajkus, M. & Rozlívka, L. (2004) Design characteristics of structural steels based on statistical analysis of metallurgical products. *Journal of Constructional Steel Research*, 60, 3-5, pp.795-808.
- Melcher, J., Škaloud, M., Kala, Z. & Karmazínová, M. (2009) Sensitivity and statistical analysis within the elaboration of steel plated girder resistance. *Advanced Steel Construction*, 5, 2, pp.120-126.
- Timoshenko, S. & Gere, J. (1961) *Theory of Elastic Stability*. McGraw-Hill, New York.

## EXCITATION OF ROTATING DISK BY STATIONARY PERMANENT MAGNETS

L. Půst\*, L. Pešek\*

**Abstract:** *Flexural vibrations of rotating disk contain forward and backward traveling waves can be excited at certain speed of rotating disk also by a standing constant single point force or by multiple points standing forces, realized e.g. by permanent magnets fixed in non-rotating space. Presented paper is contribution to the theoretical background of a new experimental excitation technique elaborated in Institute of Thermomechanics for investigation of a bladed turbine disk model with imperfection by addition several damping heads on ends of blades. Mathematical model of imperfect rotating disk was derived by using data gained experimentally and by FE computed for three lowest split modes of vibrations. It was shown how either the whole spectrum of modes of vibrations can be recorded or some resonance of selected mode can be suppressed or emphasized by means of appropriate number and positions of permanent magnets.*

**Keywords:** *Rotating disk, traveling backwards waves, constant force excitation, resonance suppression, resonance isolation.*

### 1. Introduction

The need of more exact design of machinery particularly from the dynamic properties increases with higher demand on power and reliability. Among general engineering structures, the rotating machines have a specific place and the knowledge of rotordynamics and vibrations of disk with blades have a important role. Since the beginning of last century a great attention has been given to the theoretical and experimental investigations of bladed disk vibrations at rotation (Lalanne & Ferraris, 1990; Malenovský & Lošák, 2007; Rao, 1991; Tobias & Arnold, 1957; Tondl, 1965).

In order to test a disk for dynamic investigation, it is usually excited by an external force. When the real structure or its model does not rotate, various methods of excitation – as electro-dynamic shaker, instrumental hammer, mechanic exciter in single point or multi-point excitation technique - are applied. Excitation of rotating structure is more difficult. Two methods of rotating disk excitation have been developed in the Institute of Thermomechanics ASCR, v.v.i. These methods are based on influence of magnetic forces of the electromagnetic or permanent magnets vibrator in space fixed on rotating disk (Půst & Pešek, 2009, 2010). Electromagnetic vibrator with suitable frequency of feeding current is more general apparatus as it can excite various forms of rotating disk vibrations – fixed vibrations with nodal diameters standing on the disk, backward and forward traveling waves. The excitation apparatus using permanent magnets is considerable simple, but it can excite only backward traveling waves. In spite of this limitation it is valuable method for laboratory experiments, because it enables to determine dynamic parameters, separate modes of vibration, etc.

Presented paper is a contribution to the theoretical background for analysis of results of measurement on the experimental model of bladed mistuned disk in dynamic laboratory IT ASCR.

### 2. Motion equations of rotating disk

Experimental model of bladed disk consist of a steel disk with 60 blades of rectangle cross-section. Two bunches of five blades lying on opposite ends of one diameter are provided by damping heads. Such bladed disk losses its perfect central symmetry and the double eigenfrequencies split owing to

---

\* Ing. Ladislav Půst, DrSc and Ing. Luděk Pešek, CSc.: Institute of Thermomechanics AS CR, v.v.i., Dolejškova 5, 182 00 Praha 8 CZ, e-mails: pust@it.cas.cz, pesek@it.cas.cz

disk imperfection. Modes of split eigenfrequencies are orthogonal with imperfections either on one of the nodal diameters (mode b) or in the place of anti-node position (mode a). The split eigenfrequencies of three lowest modes with 1, 2 and 3 diameters and no nodal circle ascertained on experimental bladed disk IT ASCR are:  $\Omega_{1a} = 287.8$ ,  $\Omega_{1b} = 370.8$ ,  $\Omega_{2a} = 456.8$ ,  $\Omega_{2b} = 490.0$ ,  $\Omega_{3a} = 673.5$ ,  $\Omega_{3b} = 759.9$  rad/s.

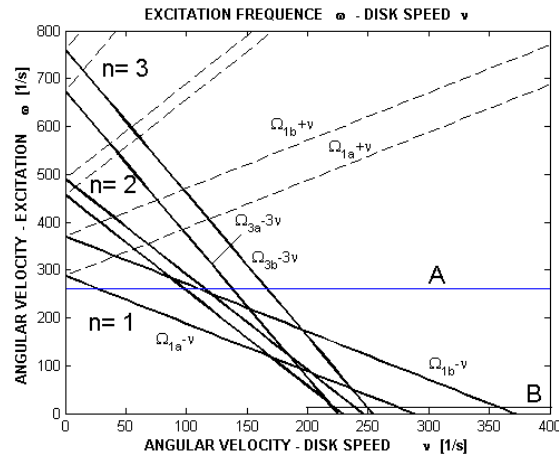


Fig. 1: Frequency – Speed diagram.

Two opposite traveling waves forms stationary vibration of a circular disk. If the disk rotates, these waves are recorded by a standing observer as forward and backward waves in relation to the disk rotation. Graphical representation of angular velocities of traveling waves for various speeds of disk rotation  $v$  is in Fig. 1. Motion of imperfect disk rotating at angular velocity  $v$  and forced by a harmonic force  $F_0 \cos \omega t$  standing in position given by angle  $\lambda$  can excite all vibrations modes (Pešek et al. 2008; Půst & Pešek, 2009). The intersection points of horizontal line A with the oblique lines ascertain the resonance frequencies at variable disk speed  $v \in (0, 400)$  rad/s and at excitation frequency  $\omega = 260$  rad/s. Decreasing this line to horizontal axis  $v$ , we get the resonance positions at  $\omega = 0$ , i.e. at excitation by constant force  $F_0 = \text{const}$ . Flat area B is in increased form drawn in Fig. 2.

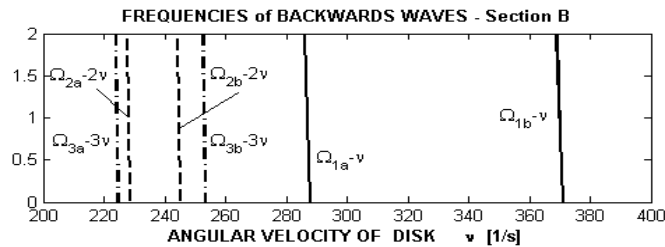


Fig. 2: Velocities of backwards traveling waves.

Using adapted expressions derived for similar case in (Malenovský et al. 2007) after substituting  $\omega = 0$  we get for excitation by  $l = 1, 2, \dots$  magnets with constant forces  $F_l$  differential equations in general coordinates

$$\begin{aligned} m_{redan} \ddot{q}_{nal} + (b_{redan} + 2\Delta b) \dot{q}_{nal} + c_{redan} q_{nal} &= q_0(r) \sin n\varphi F_l \sin n(\lambda_e + vt) \\ (m_{redn} + 2\Delta m) \ddot{q}_{nbl} + b_{redbn} \dot{q}_{nbl} + (c_{redn} + 2\Delta c) q_{nbl} &= q_0(r) \cos n\varphi F_l \cos n(\lambda_l + vt). \end{aligned} \quad (1)$$

$$l = 1, 2, \dots \quad n = 1, 2, 3$$

Here  $n$  is number of nodal diameters,  $\lambda_l$ ,  $l = 1, 2, 3$  are angles of magnets positions, where one of this locations can be chosen  $\lambda_l = 0$ .

### 3. Example

Intersections of axis  $\omega = 0$  with lines of angular velocities of traveling waves determine the resonance speeds of rotating disk excited by constant force of magnets. These resonances occur at speeds  $\Omega_{1a}$ ,  $\Omega_{1b}$ ,  $\Omega_{2a}/2$ ,  $\Omega_{2b}/2$ ,  $\Omega_{3a}/3$ ,  $\Omega_{3b}/3$ . By means of appropriate distribution and orientation of magnets,

selected modes can be emphasized or suppressed. Excitation of all six resonances by means of one magnet ( $l = 1, \lambda_1 = 0$ ) for  $q(r_0)F_1/m_{red} = 1$  is shown as response curve in Fig. 3.

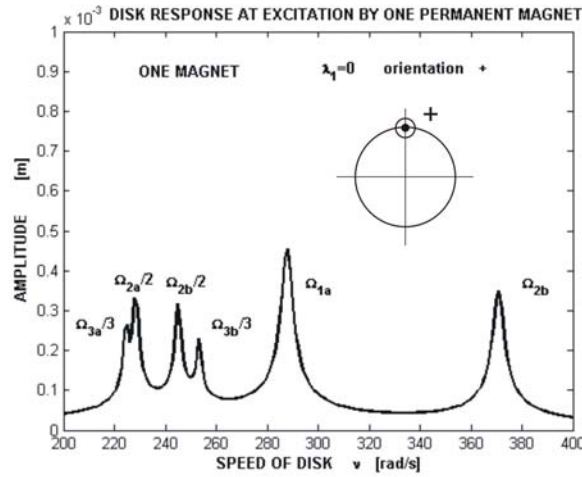


Fig. 3: Response curve excited by 1 magnet.

Adding second magnet ( $l = 1, 2$ ) into opposite position ( $\lambda_1 = 0, \lambda_2 = \pi$ ) suppresses modes with add number of nodal diameters ( $n = 1, 3$ ) and emphasizes mode with even nodal diameter ( $n = 2$ ) as shown in Fig. 4.

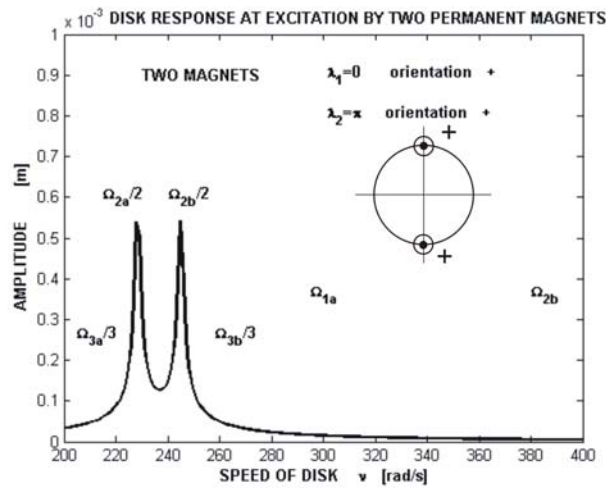


Fig. 4: Response curve excited by 2 magnets.

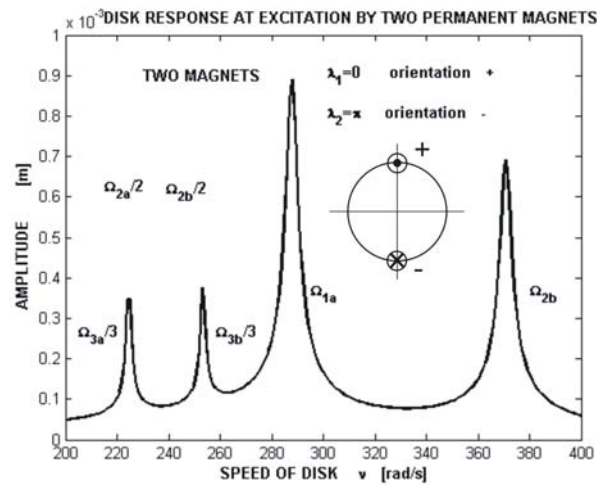


Fig. 5: Response curve excited by 2 opposite acting magnets.

If we change the orientation of attraction force of the second magnet, the even nodal diameters mode is suppressed and on the contrary the odd nodal diameters modes ( $n = 1, 3$ ) are emphasized as seen in Fig. 5.

Similar method can be applied also for suppressing or amplifying and isolating other selected modes of vibrations by using higher number of permanent magnets.

#### 4. Conclusions

Possibility of application of a simple excitation method for investigation of dynamic properties of rotating disk is studied. Analytical and experimental research of rotating imperfect disk shows the existence of backward and forward traveling waves. Presented study is focused on the excitation of backward traveling waves of modes with 1, 2 and 3 nodal diameters.

Theoretical background of this method is based on equations describing vibrations of rotating imperfect disk excited by an external harmonic transversal force after setting excitation frequency equal zero. On selected examples it is shown that by using appropriate number and positions of permanent magnets, this excitation method enables to measure response curves with resonance corresponding to the split eigenfrequencies of imperfect disk and it enables also suppressing or amplifying some resonance peaks.

#### Acknowledgement

This work has been elaborated in a frame of the grant project GA CR 101/09/1166 “Research of dynamic behavior and optimization of complex rotating system with non-linear couplings and high damping materials”.

#### References

- Lalanne, M. & Ferraris, G. (1990) Rotordynamics Prediction in Engineering, John Wiley & Sons, Toronto
- Malenovský, E. & Lošák, P. (2007) Dynamické vlastnosti olopatkovaných turbinových kol, *Parní turbíny a jiné turbostroje 2007*, Plzeň.
- Pešek, L. et al. (2008) Dynamics of Rotating Blade Disk Identical by Magneto-Kinematic Measuring System, in: *Proc. ISMA 2008*, (Sas, P., Bergen, B., eds), Katholieke Univ. Leuven, pp. 1097-1111.
- Půst, L. & Pešek, L. (2009) Traveling Waves in Rotational Machines, in: *Proc. Engineering Mechanics 2009*, (Náprstek J., Fischer C., eds.) ITAM, ASCR, Prague, CD ROM, pp.1065-1078.
- Půst, L. & Pešek, L. (2009) Traveling Waves in Circular Disk with Imperfections, *10th. Conf. on Dynamical Systems – Theory and Applications*, DESTA 2009, Lodž, Vol. 1, pp.345-352.
- Půst, L. & Pešek, L. (2009) Vibration of Imperfect Rotating Disk. Computational Mechanics, in: Book of Extended Abstracts, Pilsen, University of West Bohemia, 2p.
- Půst, L. & Pešek, L. (2010) Combined Vibration of Imperfect Rotating Bladed Disk, Computational Mechanics 2010 in: Book of Extended Abstracts, Pilsen, University of West Bohemia, 2p.
- Půst, L. & Pešek, L. (2010) Nonlinear Damping in Rotating Disk, in: *Proc. Dynamics of Machines 2010*, ed. Pešek L., IT ASCR Prague, pp. 63-72.
- Rao J.S. (1991) Turbomachine Blade Vibration, Wiley Eastern Limited, New Delhi.
- Tobias, S.A. & Arnold, R.N. (1957) The Influence of Dynamical Imperfection on the Vibration of Rotating Disks, *Proc. Inst. Mech. Engrs.*, 171, Edinburgh, pp. 669-690.
- Tondl, A. (1965) Some problems of Rotor Dynamics, Chapman and Hall, London.



## NUMERICAL SIMULATION OF ACOUSTIC CHARACTERISTICS OF PROFESSIONAL VOICE BASED ON MRI AND ACOUSTIC MEASUREMENTS

V. Radolf<sup>\*</sup>, A. M. Laukkanen<sup>\*\*</sup>, R. Havlík<sup>\*\*\*</sup>, J. Horáček<sup>\*</sup>

**Abstract:** *Inverse method was used for numerical simulation of acoustic characteristics of a professional musical actor before and after vocal exercises. The geometrical data for a 1D model of the acoustic cavities of the vocal tract were evaluated from magnetic resonance images (MRI) registered during sustained phonation of vowel [a:] before and after a vocal warm-up. The numerically simulated voice signals are compared with the acoustic recordings and warm-up related changes in the vocal tract are discussed.*

**Keywords:** *Biomechanics of voice, singer's and speaker's formant cluster, acoustic effects of vocal exercises.*

### 1. Introduction

In operatic singing, singers make use of a special voice quality in order to be heard over the orchestra without a microphone. The important acoustic component which determines the operatic quality of the voice, especially in male singers, is the so-called “singer’s formant” (Sundberg, 2003; Titze, 2000). Similarly the voice quality of speakers, especially actors, is improved by the so-called “speaker’s formant” (Leino et al., 2011). The epilarynx tube located just above the vocal folds is theoretically considered as a dominant source of clustering of formant frequencies especially when the cross-sectional area of this tube is approximately six times less than the area of the lower pharynx (Story, 2003). However, the physiological adjustment used in singers or in actors has not been known in sufficient details. The rationale of the present paper is to estimate the anatomical/geometrical adjustments and to model the acoustic changes that occur in the voice of a male professional musical actor after vocal warming up by vocal exercises.

### 2. Methods

#### 2.1. MRI experiment

A Czech male musical actor (60 years, baritone) served as a subject in the magnetic resonance imaging investigation. Lying supine in the MRI machine he first produced the vowel [a:] in a naive technique and after ca 5 minute vocal exercising again in a professional “musical actors” manner, aiming at the best voice quality. Each sample was produced for at least 20 s to enable the MRI scanning. The samples were produced on a comfortable pitch, at approximately the same fundamental frequency. Being vocally trained, the subject was able to keep the articulation and phonation constant through a sustained vowel phonation. The subject’s head position was stabilized with a support. Before starting the MRI measurement the subject phonated each sample with normal auditory feedback (i.e. without the MRI device on) and sustained the same phonation setting during MRI scanning. Due to noise and magnetic field no acoustic recording was possible during the MR imaging. For acoustic measurements the subject’s voice was recorded during the same tasks afterwards in a

---

<sup>\*</sup> Ing. Vojtěch Radolf, Ph.D. and Ing. Jaromír Horáček, DrSc.: Institute of Thermomechanics, Academy of Sciences of the Czech Republic; Dolejškova 1402/5; 182 00, Prague; CZ, e-mails: radolf@it.cas.cz and e-mail: jaromirh@it.cas.cz

<sup>\*\*</sup> prof. Anne-Maria Laukkanen, Ph.D.: Speech and Voice Research Laboratory, School of Education, University of Tampere; FIN-33014, Tampere; Finland, e-mail: Anne-Maria.Laukkanen@uta.fi

<sup>\*\*\*</sup> MUDr. Radan Havlík, Ph.D.: AUDIO – Fon Centr. s.r.o.; Obilní trh 4; 602 00, Brno; CZ, e-mail: radan.ha@seznam.cz

sound-treated studio. The sampling frequency of 44.1 kHz was used. MRI scanning was performed at the Dept. of Medical Imaging, St. Anne's Faculty Hospital in Brno, using a 1.5 Tesla MRI device (Symphony Magnetom, Siemens).

The imaging parameters were as follows: Field of view  $236 \times 270 \text{ mm}^2$ , slice thickness 1.5 mm, acquisition time 20.07 s, number of averages 1, repetition time 5.49 s, echo time 2.88 s, number of sagittal images 44, resolution  $512 \times 448$  pixels. For viewing the MR images and for measuring the changes of the vocal tract a Syngo FastView software (Siemens AG) and image software (ImageJ 1.42q Wayne Rasband, National Institutes of Health, USA and ITK-Snap, version 2.0) were used.

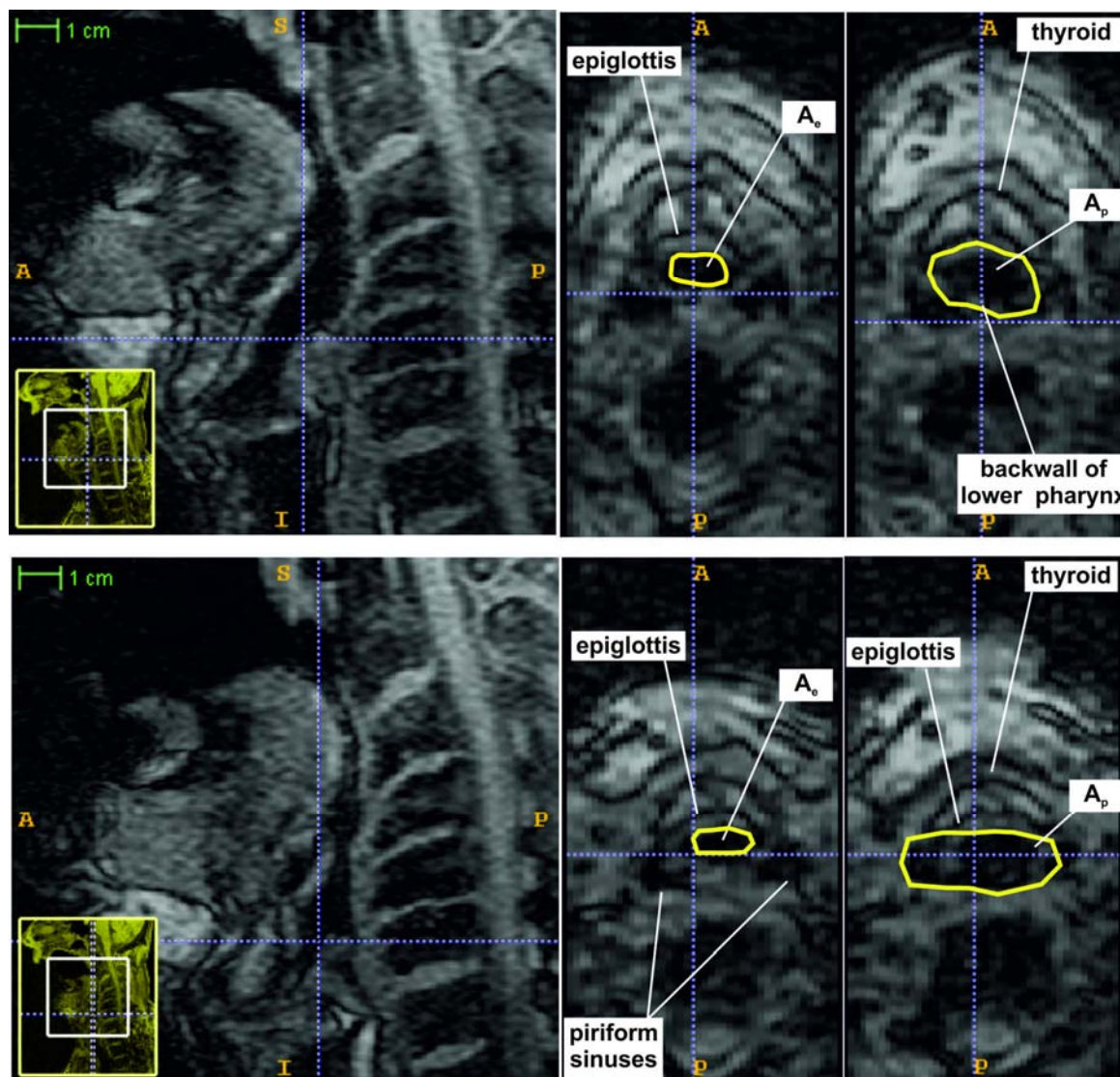


*Fig. 1: MR images for the vowel [a:] before (upper panel) and after (lower panel) the vocal exercising and measurement of the transversal areas. Left: Midsagittal views of the corresponding locations. In the middle: Area  $A_e$  of the epilaryngeal outlet. Right: Area  $A_p$  of the pharyngeal inlet (just above the plane where the epilaryngeal cavity merges with the pharyngeal cavity).*

Especially the areas of the outlet of the epilarynx and the inlet of the low pharynx were studied from transversal slices, see Figure 1. The area of the inlet to the pharynx was studied just above the collar of epiglottis, while the area of the outlet of the epilarynx was studied just below the collar of epiglottis, at the point where the epilaryngeal tube and the sinus piriformes are separated. The ratio of the inlet to the pharynx over the outlet of the epilarynx was calculated from the areas.

## 2.2. Analyses

The MR images revealed lowering of the larynx (about 19 mm), raising of the soft palate, prolongation of the vocal tract (ca 17 mm) and of the epilaryngeal tube (ca 4.5 mm) and narrowing of the epilaryngeal region and/or widening of the pharyngeal region in phonation after the vocal exercising.

The acoustic analyses showed that a cluster of two or three formants was formed in the range of  $F_3$ - $F_5$  after exercising (see Fig. 2 and Tab. 1) that leads to a stronger speaker's/singer's formant. A weak resonance between  $F_2$  and  $F_3$  can be caused by a slight nasality.

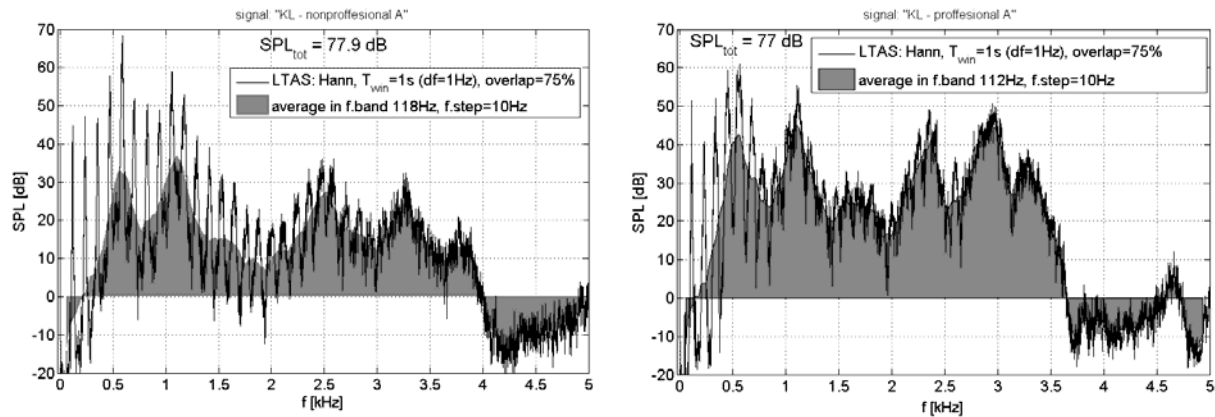


Fig. 2: Spectra (LTAS) of the acoustic signals before (left) and after (right) the vocal exercise.

Tab. 1: Fundamental frequency ( $F_0$ ) and the five lowest formant ( $F_1$  -  $F_5$ ) frequencies evaluated from the acoustic recordings and obtained from the modeling.

[Hz]	$F_0$	$F_1$	$F_2$	$F_3$	$F_4$	$F_5$
Acoustic signal – before exercising	118	560	1100	2510	3260	3780
Model – before exercising		560	1099	2507	3254	3787
Acoustic signal - after exercising	112	560	1100	2370	2940	3260
Model - after exercising		560	1099	2367	2935	3268

### 2.3. Modeling approach

The possible vocal tract changes resulting in the formation of a speaker's (or singer's) formant cluster were studied using a 1D mathematical model of voice production. The 1D vocal tract model was developed from the 3D volume model obtained from the MR images (Vampola et al., 2008). The formant frequencies measured from the vowel [a:] recorded from the subject of the present study before and after exercising were prescribed to the model and by a tuning procedure (changing the vocal tract shape, i.e. the size of area cross-sections) the best fitting vocal tract configurations were obtained.

Length of the real vocal tract of the subject was measured using MRI data. The values  $L_{\text{BEF}} = 182.5$  mm and  $L_{\text{AFT}} = 199.5$  mm were used for total length of the vocal tract model before and after vocal exercising. Vocal tract channel was modeled as a system of conical elements of 4 mm in length except for the last element which was 2.5 mm long in the case “before” and the first and the last element in the case “after” which were 1 mm and 2.5 mm long respectively.

The mathematical model used is based on an analytical solution of 1D wave equation for conical acoustical elements in frequency domain. Radiation impedance at lips as well as viscous losses in the model are considered. Tuning procedure uses sensitivity functions as described in Leino et al. (2011). The iteration stops when the root of the sum of the squared differences between desired and instantaneous eigenfrequencies is less than a desired tolerance value. This value was set to 10 Hz in both cases. The speed of sound, the density, and the dynamic viscosity of the air were considered as follows:  $c_o = 353$  ms<sup>-1</sup>;  $\rho_o = 1.2$  kgm<sup>-3</sup>,  $\mu = 1.8 \cdot 10^{-5}$  kgm<sup>-1</sup>s<sup>-1</sup>. Number of iteration steps was 56 (for the case before) and 193 (for after). The results of the modeling are summarized in Fig. 3 and Tab. 1.

### 3. Conclusions

The area ratio of the lower pharynx over the epilaryngeal tube increased after the exercises. Results from modeling were  $A_p/A_e = 260\text{mm}^2/85\text{mm}^2 = 2.59$  for phonation before (coordinates 16-28 mm) and

$220\text{mm}^2/46\text{mm}^2 = 4.78$  for after (coordinates 0 - 20 mm). This is in agreement with the measured areas from the MRI where  $A_p/A_e = 3.32$  for before increased to 5.61 for after. The change in the areas is in agreement with the results found for operatic singers by Story (2003) as well as the changes in the formant frequencies measured in the present study. After the vocal exercising the formants  $F_1$  and  $F_2$  of [a:] remained nearly unchanged while the formants  $F_3 - F_5$  were clustering, thereby considerably increasing the SPL level (ca 15 dB) in the frequency band of 2-4 kHz. The distance between  $F_3$  and  $F_5$  in the acoustic measurement decreased from 1270 Hz down to 890 Hz, and in the modeling the distance between these formants decreased from 1280 Hz to 901 Hz (see Tab. 1). Fig. 3 shows increased volume of the pharyngeal part, the changes in the oral cavity that can be realized by changes of the tongue position, while the lips opening remained the same as before the vocal exercising.

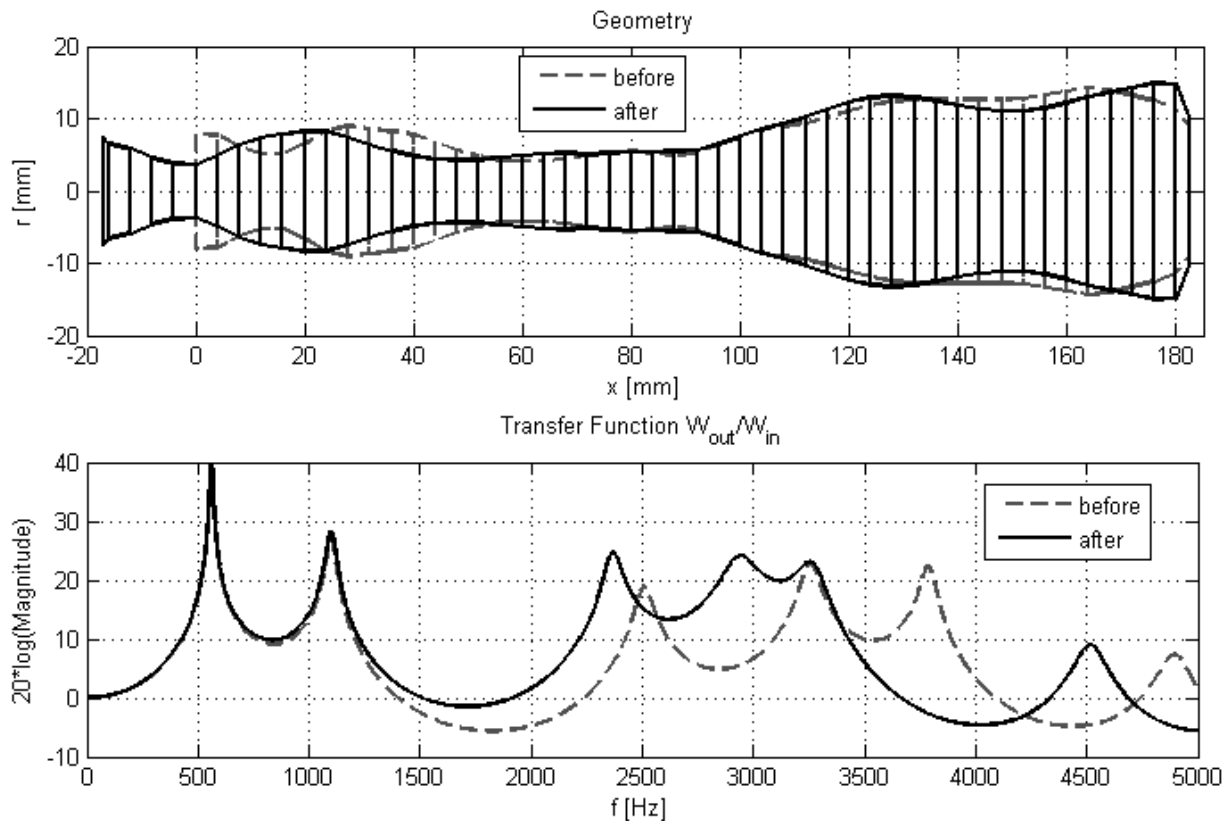


Fig. 3: Vocal tract geometry (top) and transfer function (below) between acoustic airflow rate at the vocal folds and the airflow rate at the lips – results of modeling.

## Acknowledgement

The research was supported by the research plan AV0Z20760514 of the Institute of Thermomechanics and by the project GAČR 101/08/1155. The authors are also very grateful to Doc. MUDr. Petr Krupa from the Hospital U Svaté Anny in Brno for enabling the MRI measurements.

## References

- Leino, T., Laukkanen, A. M. & Radolf, V. (2011) Formation of the Actor's/Speaker's Formant: A Study Applying Spectrum Analysis and Computer Modeling. *Journal of Voice*, 25(2), pp. 150-158.
- Story, B. H. (2003) Using imaging and modeling techniques to understand the relation between vocal tract shape to acoustic characteristics, in: *Proc. of the Stockholm Music Acoustics Conf.*, Aug. 6-9, 2003 (SMAC 03), Stockholm, Sweden, pp. 435-438.
- Sundberg, J. (2003) Research on the singing voice in retrospect. *Speech, Music and Hearing*, KTH Stockholm, TMH-QPSR Vol. 45, pp. 11-22.
- Titze, I. R. (2000) *Principles of voice production*. Iowa City, IA: National Center for Voice and Speech.
- Vampola, T., Horáček, J. & Švec, J. G. (2008) FE modeling of human vocal tract acoustic. Part I: Production of Czech vowels. *Acta Acoustica united with Acoustica*, 94, pp. 433-447.

## ANALYSIS OF THE EFFECT OF HYDRODYNAMIC BEARINGS AND DAMPING ON ROTOR STABILITY

Z. Rendlová\*, V. Zeman\*

**Abstract:** *The paper deals with the modeling and evaluation of stability conditions of the balanced rotating system with rigid discs supported on two anisotropic hydrodynamic bearings. The model respects internal and external damping of the shaft considered as one-dimensional continuum. The evaluation of stability is based on eigenvalues in dependence on system rotating speed. Real and imaginary parts of computed eigenvalues are displayed by means of Campbell diagram.*

**Keywords:** *Stability, internal damping, external damping, eigenvalues, rotating system.*

### 1. Introduction

The most of real mechanical systems are continuous and non-homogenous elastic systems. Therefore an approximation, which helps to simplify the description of a real system behavior with enough accuracy, is used. For that reason, it is necessary to specify material and geometric properties of a real system and the impact of each characteristic on its behavior. The damping effects are these properties which are necessary to include into a mathematical model. In case of rotating systems there are two kinds of damping effects. It is so-called external damping effect that is dependent on surroundings of the system and the internal damping effect caused by material properties of the system. Both these damping impacts cause the change of model parameters and the system stability.

The aim of this paper is to present the impact of external and internal damping on the stability of a rotating flexible shaft with rigid discs supported on hydrodynamic bearings.

### 2. Mathematical model of a rotor

We suppose the rotor which rotates with constant angular velocity  $\omega_0$ . It is composed of a circular cross-section shaft with continuously distributed mass. The rigid discs are attached to the shaft in given positions. The shaft with discs is supported by two identical hydrodynamic bearings. The layout of test rotor is shown in Fig. 1.

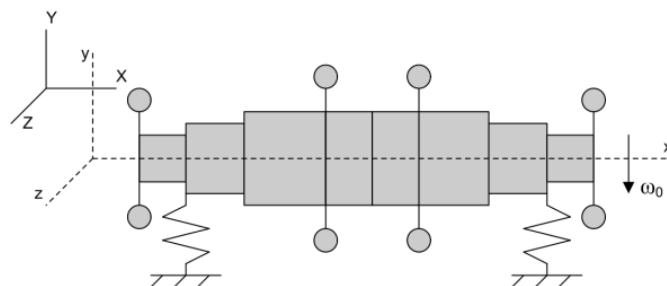


Fig. 1: Scheme of the rotor supported on hydrodynamics bearings.

The mathematical model of the rotor bending vibration is created by the finite element method (FEM), which is based on a shaft division into finite elements (shaft elements). The shaft element  $e$  of length  $l$  is defined by two end nodes  $i$  and  $i+1$ . The non-deformable cross-section area of each shaft element is considered and it is still perpendicular to the deformed shaft axis after deformation. Therefore the

---

\* Ing. Zdeňka Rendlová and prof. Ing. Vladimír Zeman, DrSc.: Department of Mechanics, University of West Bohemia, Univerzitní 22; 306 14, Plzeň; CZ, e-mails: zrendlov@kme.zcu.cz, zemanv@kme.zcu.cz

motion of the shaft is described by two displacements  $v, w$  in  $Y, Z$  direction and two angular displacements  $\mathcal{Q}, \psi$  around  $Y, Z$  axis. For each shaft finite element, the coordinates are arranged in the vector  $\tilde{\mathbf{q}}^{(e)} = [v_i \ \psi_i \ v_{i+1} \ \psi_{i+1} \ w_i \ \mathcal{Q}_i \ w_{i+1} \ \mathcal{Q}_{i+1}]^T$ . The mass, gyroscopic and stiffness finite element matrices  $\mathbf{M}^{(e)}, \mathbf{G}^{(e)}, \mathbf{K}^{(e)}$  are derived by Lagrange's equations using an expression for kinetic and potential energy of the shaft element in fixed configuration space  $XYZ$ . The rigid disc placed in  $i^{th}$  node is described by the mass and gyroscopic matrices  $\mathbf{M}^{(d)}, \mathbf{G}^{(d)}$ . All these matrices describing shaft elements and discs are derived according to Slavik et al. (1998).

The anisotropic support located in  $i^{th}$  node of the shaft represents the fluid film bearing. Considering the linear relation between forces generated in fluid film, each support can be characterized by the stiffness and damping matrices  $\mathbf{K}_{B_i}(\omega_0), \mathbf{B}_{B_i}(\omega_0)$ . Their coefficients depend on angular velocity  $\omega_0$  according to Muszynska (2005).

## 2.1. Damping effects

Considering the isotropic external damping the forces are perpendicular to the finite element surface. If the bending vibration is supposed then the external damping impact results from the Rayleigh dissipation function. The external damping in fixed coordinates  $XYZ$  is expressed by means of external damping matrix

$$\mathbf{B}_E^{(e)} = b_E \begin{bmatrix} \mathbf{S}_1^{-T} \mathbf{I}_\Phi \mathbf{S}_1^{-1} & \mathbf{0} \\ \mathbf{0} & \mathbf{S}_2^{-T} \mathbf{I}_\Phi \mathbf{S}_2^{-1} \end{bmatrix}, \quad (1)$$

where  $b_E [\text{kgm}^{-1}\text{s}^{-1}]$  is external isotropic damping coefficient per unit length.

In case of internal isotropic damping we assume that internal damping forces are induced by shaft deformation and are of viscous character. Therefore the internal damping forces effect could be expressed in the rotating coordinates  $xyz$  by means of the internal damping matrix

$$\mathbf{B}_I^{(e)} = b_I E J \begin{bmatrix} \mathbf{S}_1^{-T} \mathbf{I}_{\Phi^*} \mathbf{S}_1^{-1} & \mathbf{0} \\ \mathbf{0} & \mathbf{S}_2^{-T} \mathbf{I}_{\Phi^*} \mathbf{S}_2^{-1} \end{bmatrix}, \quad (2)$$

where  $b_I [\text{s}]$  is coefficient of viscous internal damping,  $E [\text{Pa}]$  is Young's modulus of elasticity and  $J [\text{m}^4]$  is cross-section area polar moment. Note that  $\mathbf{S}_1, \mathbf{S}_2, \mathbf{I}_\Phi$  and  $\mathbf{I}_{\Phi^*}$  are constant coefficient matrices of order four derived in Byrtus et al. (2011). But the matrix (3) must be transformed from rotating frame  $xyz$  to the fixed frame  $XYZ$  by using a transformation matrix  $\mathbf{R}(t)$

$$\mathbf{R}(t) = \begin{bmatrix} \cos(\omega_0 t) \cdot \mathbf{E} & \sin(\omega_0 t) \cdot \mathbf{D} \\ -\sin(\omega_0 t) \cdot \mathbf{D} & \cos(\omega_0 t) \cdot \mathbf{E} \end{bmatrix}, \quad (3)$$

where  $\mathbf{D} = \text{diag}(-1 \ 1 \ -1 \ 1)$ ,  $\mathbf{E} = \text{diag}(1 \ 1 \ 1 \ 1)$ . Then the relation between a vector of generalized coordinates  $\hat{\mathbf{q}}^{(e)}(t)$  in rotating frame  $xyz$  and vector of generalized coordinates  $\mathbf{q}^{(e)}(t)$  in fixed frame  $XYZ$  is  $\hat{\mathbf{q}}^{(e)}(t) = \mathbf{R}^T(t) \mathbf{q}^{(e)}(t)$ , the internal damping forces in fixed frame could be expressed as

$$\mathbf{R}(t) \mathbf{B}_I^{(e)} \dot{\hat{\mathbf{q}}}^{(e)}(t) = \mathbf{R}(t) \mathbf{B}_I^{(e)} \mathbf{R}^T(t) \dot{\mathbf{q}}^{(e)}(t) + \mathbf{R}(t) \mathbf{B}_I^{(e)} \dot{\mathbf{R}}^T(t) \mathbf{q}^{(e)}(t), \quad (4)$$

where  $\mathbf{R}(t) \mathbf{B}_I^{(e)} \mathbf{R}^T(t) = \mathbf{B}_I^{(e)}(t)$  is so-called dissipation matrix and  $\mathbf{R}(t) \mathbf{B}_I^{(e)} \dot{\mathbf{R}}^T(t) = \mathbf{K}_I^{(e)}(t)$  is so-called circulatory matrix. It was demonstrated that for the isotropic shaft element these two matrices are constant in time.

Therefore the mathematical model of the shaft element respecting damping effect in fixed frame  $XYZ$  could be expressed as

$$\mathbf{M}^{(e)} \ddot{\tilde{\mathbf{q}}}^{(e)}(t) + (\mathbf{B}_E^{(e)} + \mathbf{B}_I^{(e)} + \omega_0 \mathbf{G}^{(e)}) \dot{\tilde{\mathbf{q}}}^{(e)}(t) + (\mathbf{K}^{(e)} + \mathbf{K}_I^{(e)}) \tilde{\mathbf{q}}^{(e)}(t) = \mathbf{0}. \quad (5)$$



## 2.2. Mathematical model of a whole rotating system

Mathematical model of the whole rotating system with bearing supports is derived in the space with the configuration  $\mathbf{q}_i = [\dots \ v_i \ w_i \ \mathcal{G}_i \ \psi_i \ \dots]^T$ , therefore matrices describing the shaft element must be transformed from the configuration space defined by vector  $\tilde{\mathbf{q}}^{(e)}$  to the new configuration space. Then the equation of the motion could be expressed as

$$\mathbf{M}\ddot{\mathbf{q}}(t) + (\mathbf{B}_E + \mathbf{B}_I + \mathbf{B}_B(\omega_0) + \omega_0 \mathbf{G})\dot{\mathbf{q}}(t) + (\mathbf{K} + \mathbf{K}_I + \mathbf{K}_B(\omega_0))\mathbf{q}(t) = \mathbf{0}, \quad (6)$$

where each matrix is composed of transformed block matrices and  $\omega_0$  is an angular velocity of the rotation. Matrices  $\mathbf{B}_B(\omega_0)$  and  $\mathbf{K}_B(\omega_0)$  are global damping and stiffness matrices of the hydrodynamic bearings.

## 3. Application

The model respecting damping effect was tested using the rotor supported on two hydrodynamics bearings. The shaft is derived into eight shaft elements and equipped with four discs (see Fig. 1). The shaft elements are described by length  $l$  [m], material density  $\rho = 7850 \text{ kgm}^{-3}$ , Young's modulus of elasticity  $E = 2.10^{11} \text{ Pa}$ , outer diameter  $D$  [m] and inner diameter  $d$  [m]. The rigid discs are characterized by mass  $m$  [kg], moment of inertia with respect to lateral axis  $I_0$  [kgm<sup>2</sup>] and moment of inertia with respect to axis of symmetry  $I$  [kgm<sup>2</sup>]. These parameters are written in Tab. 1.

Tab. 1: Parameters of the shaft elements (on the left) and discs (on the right).

element	$D$ [m]	$d$ [m]	$l$ [m]
1	0.43	0	0.9
2	0.53	0	1.12
3	0.735	0	0.52
4	0.735	0	0.995
5	0.735	0	0.925
6	0.735	0	0.52
7	0.53	0	1.12
8	0.43	0	0.75

node	$m$ [kg]	$I_0$ [kgm <sup>2</sup> ]	$I$ [kgm <sup>2</sup> ]
1	670	78.88	39.44
4	549	1035	517.5
6	549	1035	517.5
9	670	78.88	39.44

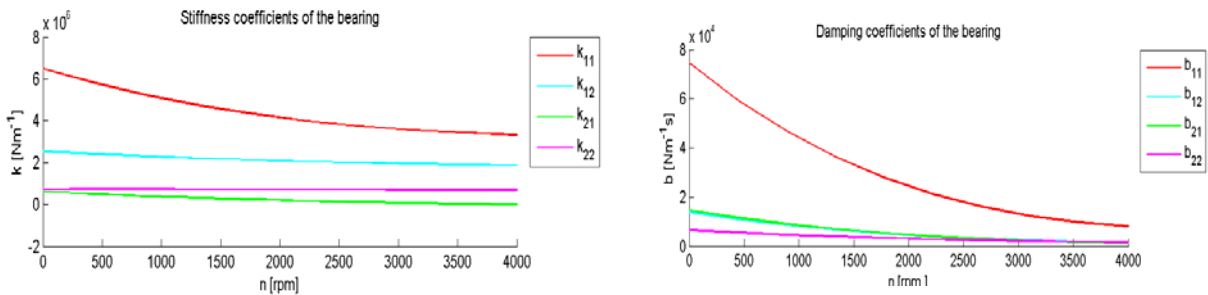


Fig. 2: Stiffness and damping coefficients of hydrodynamic bearings dependent on rotating speeds  $n$ .

The bearing stiffness and damping coefficients are approximated by cubic polynomials in dependence of rotating speed  $n \in \langle 0, 4000 \rangle$  rpm. see Fig. 2.

According to Gasch & Pfützner (1980) the internal damping coefficient is set  $b_I = 0.01 \text{ s}$  and the external damping coefficient is set as  $b_E = 0.1 \text{ kgm}^{-1}\text{s}^{-1}$ .

The eigenvalues are obtained by solving the eigenvalue problem and the Campbell diagrams expressing the dependence of eigenvalue imaginary parts on the rotor speed  $n$  for both systems are shown in Fig. 3. The eight eigenvalues with the smallest positive imaginary parts are written in Tab. 2.



Tab. 2: The eigenvalues with eight smallest imaginary parts corresponding with the system without damping effect and system considering damping effect for  $n=2000$  rpm.

eigenvalue	$b_I = 0$ s. $b_E = 0$ $\text{kgm}^{-1}\text{s}^{-1}$	$b_I = 0.01$ s. $b_E = 0.1$ $\text{kgm}^{-1}\text{s}^{-1}$
$\lambda_1$	$-2.19+3.27i$	$-2.20+3.27i$
$\lambda_2$	$-0.03+8.02i$	$-0.03+8.02i$
$\lambda_3$	$-1.32+20.13i$	$-1.32+20.14i$
$\lambda_4$	$-0.17+71.29i$	$-0.17+71.29i$
$\lambda_5$	$-0.57+335.77i$	$-2.92+335.76i$
$\lambda_6$	$-0.44+395.30i$	$-3.70+395.29i$
$\lambda_7$	$-0.06+627.60i$	$-11.97+627.51i$
$\lambda_8$	$-0.03+739.28i$	$-14.18+739.20i$

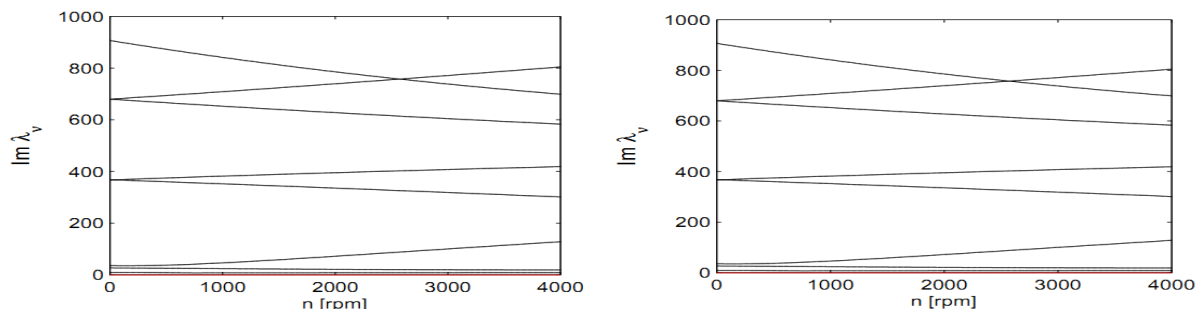


Fig. 3: Campbell diagrams for system without damping effect (on the left) and system with damping effect (on the right).

#### 4. Conclusions

This paper presents the basic dynamic model of the rotating system supported on two hydrodynamic bearings respecting damping effects. The finite element approach was used and the shaft was modeled by means of eight shaft elements and four rigid discs are attached to the shaft in chosen nodes. The hydrodynamic bearings are modeled as supports with stiffness and damping coefficients depending on the rotating speed  $n$ .

The analysis of the damping effects was performed for rotating speed  $n \in \langle 0, 4000 \rangle$  rpm. whereas the operating rotating speed is  $n = 2000$  rpm. Based on eigenvalues corresponding to both cases of model see Tab. 2. it is obvious that the real parts of eigenvalues of the system with damping are smaller than real parts of eigenvalues of the system without damping. It was shown that external damping causes a stabilizing effect in the analyzed rotating speed range. On the other hand, the internal damping affects the eigenvalues of the system minimally. The conclusions shown in this paper are valid in case of rotor systems supported on hydrodynamic bearings with relatively large values of damping coefficients.

#### Acknowledgement

This work was supported by the research project MSM 4977751303 of the Ministry of Education, Youth and Sports of the Czech Republic and SGS-2010-046.

#### References

- Byrtus, M., Hajžman, M. & Zeman, V. (2011) Dynamics of Rotating Systems. UWB, Pilsen. (in Czech).
- Muszynska, A. (2005) Rotordynamics. CRC Press, Boca Raton.
- Gasch, R & Pfützner, H. (1980) Rotordynamics. SNTL, Prague. (in Czech).
- Slavík, J., Stejskal, J. & Zeman, V. (1998) Elements of dynamics of machines. CTU Publishing House 1997. Prague. (in Czech).

## **DESIGN OF THE FRAME FOR AUTONOMOUS MOBILE ROBOT WITH ACKERMAN PLATFORM**

**T. Ripel<sup>\*</sup>, J. Hrbáček<sup>\*</sup>, J. Krejsa<sup>\*</sup>**

**Abstract:** *This paper describes the design of the frame and power system of autonomous mobile robot intended to operate as an information portal, or an electronic hostess for indoor environment. The main goal is the construction of rigid and stable chassis considering sufficient proportions and low weight, considering other demands, such as low power consumption, robust safety precautions, construction ergonomics and sufficient space for all necessary equipment. On the contrary to commonly used differential chassis for indoor robots, the Ackerman type of chassis was chosen with additional swinging rear axle feature added, resulting in ability to overcome common indoor obstacles while keeping the stability and low power consumption.*

**Keywords:** *Mobile robot, Ackerman steering.*

### **1. Introduction**

When designing mobile robot, there are several concepts of chassis available (Campion, 1996; Iagnemma, 2000; Furukawa). Each approach has specific features that make it preferable for certain operating conditions and expected performance of the designed vehicle under these conditions. In indoor environment the majority of the robots use differential steering chassis due to its maneuverability (Caracciolo, 1999). However when prolonged operational time is required, the energy efficiency demands favor Ackerman steering even with the cost of limited maneuverability resulting in more complex motion planners due to nonholonomic constraints.

This paper describes the design of the chassis for autonomous mobile robot Advée, developed by Bender Robotics s.r.o in cooperation with Faculty of Mechanical Engineering, Brno University of Technology. Advée is the device that purveys information in many ways from audiovisual form to printed documents. It operates as a mobile information portal which is able to orient in space, detect obstacles and avoid physical contact with persons filling the space around it. The platform is intended to operate indoor, while capable of overcoming minor obstacles common in such an environment. When using Ackerman steering, the suspension system is required to keep all the wheels on ground, lowering the rigidity in vertical direction. Such behavior is unacceptable for presentation robots. To overcome this problem, the suspension system is replaced by rear swinging axle, allowing to overcome minor obstacles while keeping the robot rigid in vertical direction.

### **2. Platform description**

Advée is 80 kg heavy four-wheeled robot with overall dimensions of 1100 x 660 x 1600 mm. The platform consists of three parts where the front part represents the main body, in the rear part the actuator with control unit is embedded and the upper part positions electronic equipment into proper location important for its function as the touch screen and the printer output are. Fig. 1 shows the configuration of chassis.

---

<sup>\*</sup> Ing. Tomáš Ripel, Bc. Jan Hrbáček and Ing. Jiří Krejsa, Ph.D.: Institute of Solid Mechanics, Mechatronics and Biomechanics, Brno University of technology, Technická 2896/2; 616 69, Brno; CZ, e-mails: tripel@centrum.cz, jan@hrbacek.info, krejsa@fme.vutbr.cz

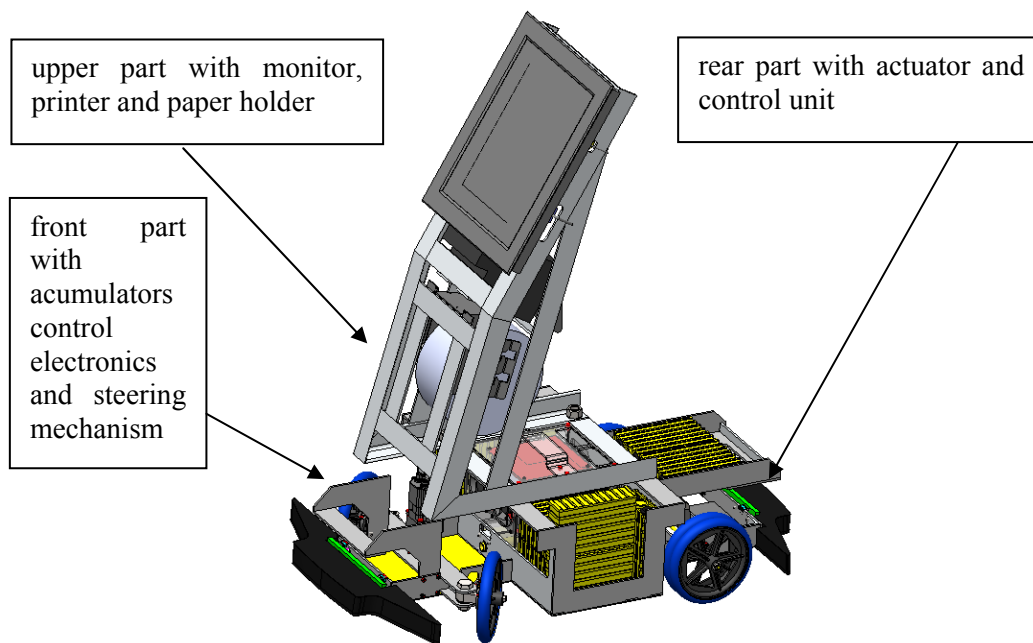


*Fig. 1: Advée concept.*

Mechanical concept of Advée takes into consideration the weight and position of all equipment of the robot. The loading on each axle is divided approximately in 1:1 ratio, which positively influences the riding qualities. To ensure continuous contact of rear wheels with the floor even while crossing the obstacles the rear swinging axle is utilized. Rear part is rotary embedded in the front part to avoid the slippage of the actuated wheel. This solution increases the load on the front wheels, but keeps the upper part of the robot rigid.

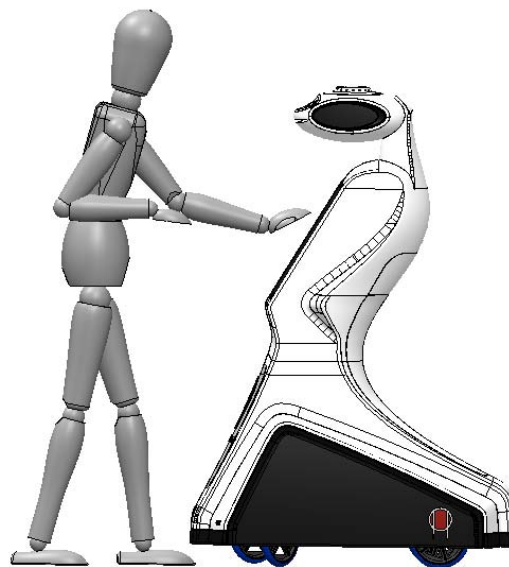


*Fig. 2: Study of touch screen position.*

The height of the platform results from optimal position of touch screen for comfortable manipulation. The proper angle and height of the monitor was determined on the 1:1 simplified model. Fig. 2 gives an impression of relative position of average height adult human and the monitor placed on the frame.

Wheel gauge of the platform is a compromise between the stability of the robot and its trafficability. The value of wheel gauge was initially proposed based on static stability calculations, allowing up to 15 degrees deflection from vertical axis. The dynamic stability of the chassis was tested on the physical model (Bender II platform with additional upper frame simulating the mass of the Advée equipment (Hrbáček, 2010)).

### 3. Frame construction description

The frame represents the base of the mobile robot construction. The main task while designing the proper frame concept is the weight, proportion and rigidity optimization, which can be achieved by appropriate material selection and mechanical design.

Material significantly affects weight and rigidity of the construction. Aluminum is evaluated for its durability combined with small density. These properties make it the optimal material for mobile robots where the robustness and low weight are most demanded attributes.

Considering large proportions of the robot the manufacture of the frame from monolith intermediate would be expensive and complicated. Therefore the welded assembly of aluminum profile is used. Although the connection by welds is undetectable and imprecise, there are lesser demands to geometric complexity of components and total weight is decreased by absence of connecting parts. The geometry of the chassis follows the dimensions and shape of the equipment, that is predefined (accumulators, touch screen, printer).

Fig. 3 shows all three parts of the frame. Utilization of rear differential makes the rear part of the robot difficult to assemble and there are also higher demands to accuracy, therefore as the only one is assembled by screw connection.

The stress and strain analysis of the frame was performed using FEM, leading to modifications in upper part of the frame, where even low displacement can cause damage of the outer shell. Modified frame (Fig. 3d) exhibits maximum displacement of 0.13mm, after full static load of the equipment.

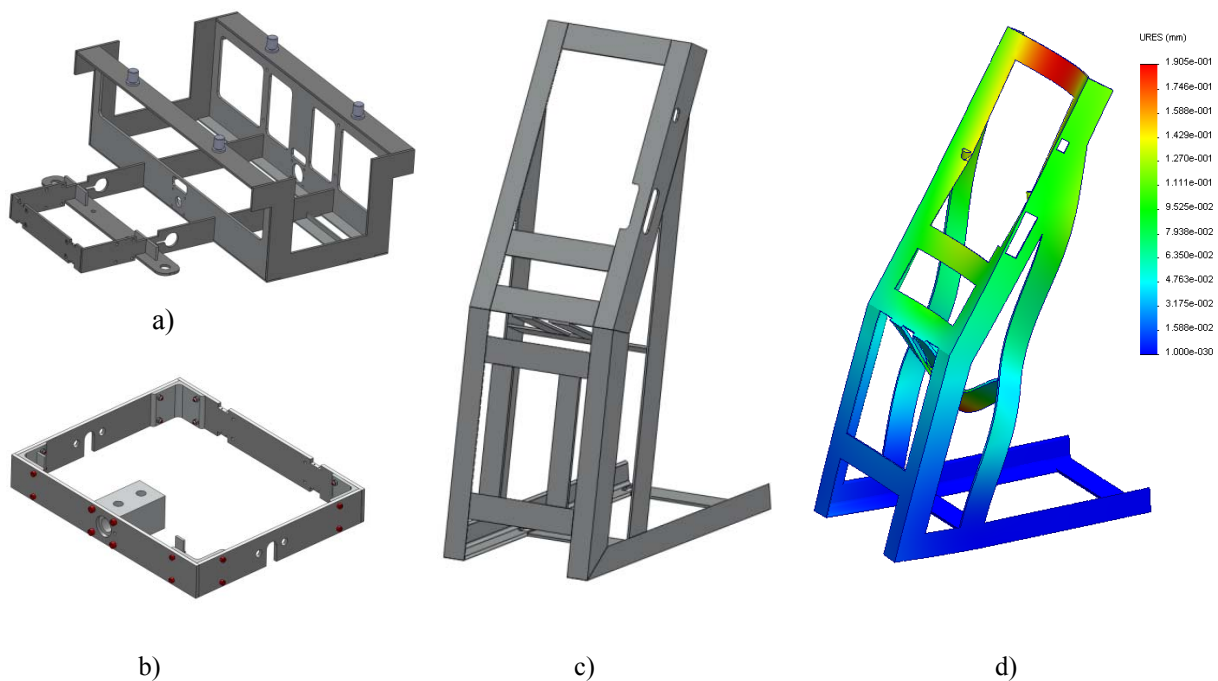


Fig. 3: a) Front part, b) Rear part, c) Upper part, d) Deformation analysis of the upper part.

Mobile robots have to carry numerous amounts of electronics which is connected by cables. Since the first study of mechanical design of the frame the path of the cables must be considered. The chassis of Advée allows connecting passage among all three parts. Between the front and rear part there is enough space designed, as those two parts move towards each other.

Rear swinging axle is realized by separation of the rear part from the rest of the frame. The rear part contains the drive unit, while the front part represents the main construction, to which all others components are assembled. Front and rear parts are connected by torsional shaft allowing them to swing around each other in the maximum relative angle of about 10°. This way the constant contact between rear wheel and surface is ensured even while the platform has to deal with heavy load. Disadvantage of this concept is decrease of stiffness which exhibits by oscillating while passing an obstacle. This problem is solved by torsion spring embedded between moving parts.

#### 4. Actuators design

The selection of the proper actuator reflects in energy consumption and riding qualities of the robot. While designing the power system many conditions must be considered (as for example the weight, maximum speed, type of wheels and the maximum ascent). Based on the calculation comprising all the physical influences the actuator Maxon RE 50 with 24V/200W DC motor, planetary gear (26:1) and incremental sensor been chosen.

The determination of sufficient power of the steering mechanism is difficult task, as the calculation would depend on very precise acquaintance with mechanical model simulation and used friction model, that can vary for different types of surfaces the robot is intended to move on. Therefore the required power was determined on the base of the measurement of forces actions in the testing platform Bender II steering mechanism, adjusted to the wheel load of Advée, resulting in Berger Lahr actuator with planetary gear (40:1). The measurement scheme is shown on Fig. 4. and the torque required on different surfaces is shown at Tab. 1.

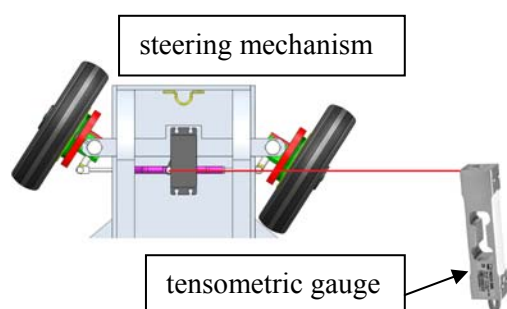


Fig. 4: Scheme of measurement..

Tab. 1: Steering power measurements.

Surface	Force	Torque
Bituminous road	35 N	2.1Nm
Sheet pavement	28 N	1.68Nm
Linoleum	26 N	1.56Nm
Carpet (long pile)	60 N	3.6Nm

#### 5. Conclusions

This paper describes the design of chassis of autonomous mobile robot Advée. Used solution provides energetically efficient and robust robotic platform. The 1600 mm high and 80 kg four wheeled robot offers excellent stability and riding qualities. The concept of Ackerman steering with swinging axle proved superior behavior in indoor environment. Single motor and differential proved to be sufficient while keeping the cost of motion module at reasonable level. Although the use of automotive chassis brings intricacy caused by nature of its motion control in space, the energetic efficiency exceeds all the other concepts utilized in mobile robotics. Thanks to motion efficiency Advée can offer over 8 hours of autonomous service for a single battery charge.

The platform was tested in range of environments. The prototype is currently commercially used and after over 100 hours of operation the mechanical chassis does not exhibit any flaws.

#### Acknowledgement

Published results were acquired with the support of the Ministry of Education, Youth and Sports of the Czech Republic, research plan MSM 0021630518 “Simulation modeling of mechatronic systems”.

#### References

- Iagnemma, R., A. Rzepniewski, S. Dubowsky, P. Pirjaniab, T. Huntsberger, P. Schenker (2000) Mobile robot kinematic reconfigurability for rough-terrain, Proc. SPIE, Vol. 4196, 413.
- Furukawa, T., MTRN9224 Robot Design, School of Mechanical and Manufacturing Engineering, University of New South Walesinternet, technical report.
- Campion G., G. Bastin, B. dAndrea-Novet, (1996) Structural properties and classification of kinematic and dynamic models of wheeled mobile robots, IEEE Trans. Robot. Autom. 12, pp.47-62.
- Caracciolo L., A. De Luca, and S. Iannitti, (1999) Trajectory tracking control of a four-wheel differentially driven mobile robot”, In Proceedings of the International Conference on Robotics and Automation, pp. 2632–2638, Detroit, MI.
- Hrbáček, J., Ripel, T., Krejsa, J. (2010) Ackermann mobile robot chassis with independent rear wheel drives. In Proceedings of EPE- PEMC 2010, Skopje, Republic of Macedonia: s. T5- 46 (T5-51 s.) ISBN: 978-1-4244-7854- 5.



## CHANGING THE BEHAVIOR OF MR FLUIDS DURING LONG TERM OPERATION

J. Roupec<sup>\*</sup>, I. Mazůrek<sup>\*</sup>, Z. Strecker<sup>\*</sup>

**Abstract:** The article describes results of durability test of a magnetorheological fluid (MRF) which was carried out in a custom design rheometer. The rheometer design allows measurement of the rheological properties of MR fluid and its exposure to a long-term loading simultaneously, without any manipulation of the measured sample. Owing to this, changes of the two most important parameters describing the behavior of MR fluids - dynamic viscosity and yield stress - could be followed during the durability test. The dependence of yield stress and dynamic viscosity on temperature and magnetization current was evaluated. The results show a significant change of the yield strength (500%) during the durability test. Independence of the yield stress on the temperature was conclusively proven. The viscosity decreased by 35% from its initial value after dissipation of 9000kJ out of total 119000kJ and then remained the same until the end of the durability test. Viscosity dependence on temperature was evaluated.

**Keywords:** Magnetorheological fluid, MRF, durability test, yield stress, dynamic viscosity, shear rate.

### 1. Introduction

Current magnetorheological (MR) fluids are suspensions formed by a carrying fluid and ferromagnetic particles, most commonly powdered iron. Upon the application of an external magnetic field (Fig.1) the MR fluids can change their state from fluid to a semi-solid or plastic state, and back, in several milliseconds.

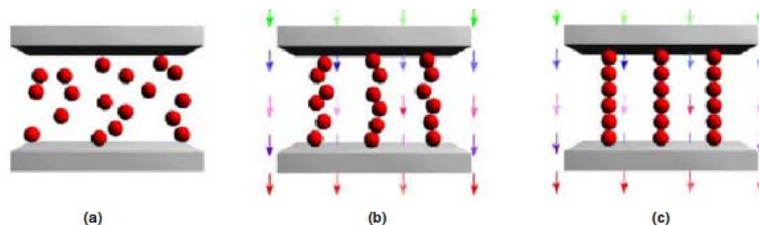


Fig. 1: MR fluid behavior (a) without application of a magnetic field; (b) with application of a magnetic field; (c) with full activation of a magnetic field (Lord Corporation, 2008).

These properties can be appropriately utilized for regulation of linear and rotary motion. The widest commercial application of these fluids is in mechatronic damping elements – MR dampers. MR dampers are frequently used in car suspension systems, suspension of driver seats in goods vehicles, vibration damping during seismic activity or damping of cable bridge vibrations caused by wind and rain. For rotary or linear MR devices the resultant effects of the magnetic field can be described simply by the Bingham model which is represented by the following equation:

$$\tau = \tau_y(H) + \eta \cdot \dot{\gamma}, \quad (1)$$

where  $\tau_y$  is a yield stress component which depends on the intensity of the magnetic field and acts in the direction of fluid flow,  $\eta$  is the dynamic viscosity of MR fluid in off-state and  $\dot{\gamma}$  is the shear rate. Most of the research teams concerned with production of MR fluids and their testing use commercial rheometers to measure rheological properties (yield stress, dynamic viscosity, storage modulus  $G'$ , loss modulus  $G''$ , etc.). The measuring ranges of such devices are up to the shear rates of about  $10^3 \text{ s}^{-1}$  (the

<sup>\*</sup> Ing. Jakub Roupec, assoc. prof. Ing. Ivan Mazůrek, CSc. and Ing. Zbyněk Strecker: Institute of machine and industrial design, Brno University of Technology, Technická 2896/2; 602 00, Brno; CZ, e-mails: jroupec@hotmail.com, mazurek@fme.vutbr.cz, streckerz@gmail.com

most commonly used one is Anton Paar Physica MCR). For linear MR devices the maximal shear rate typically ranges from  $10^4$  to  $10^5 \text{ s}^{-1}$  which is far beyond the measuring range of commercial rheometers. Most of the new MR fluid samples have never been subjected to durability tests (Cheng, 2008; Fang et al., 2009; Bombard et al., 2009; etc.) because the commercial rheometers do not allow sufficient mechanical loading. In addition, the long-term operation could destroy this expensive equipment. The knowledge of MR fluids behavior in real life devices and of the fluid lifetime represents one of the basic parameters considered by designers when designing a machine set. The research team around Carlson and Ahmadian developed their own design of a piston slit rheometer which can measure the shear rates up to  $10^5 \text{ s}^{-1}$  (Goncalves, 2005). However, it is unsuitable for the long-term loading required for durability tests of MR fluids. For these reasons, our research team designed and constructed such a slit-flow rheometer (Fig. 2) which can measure yield stress and dynamic viscosity dependence on accurately measured temperature in the active zone of MR valve during durability test. Furthermore, it is possible to ensure stable thermal conditions due to the regulated water cooling.

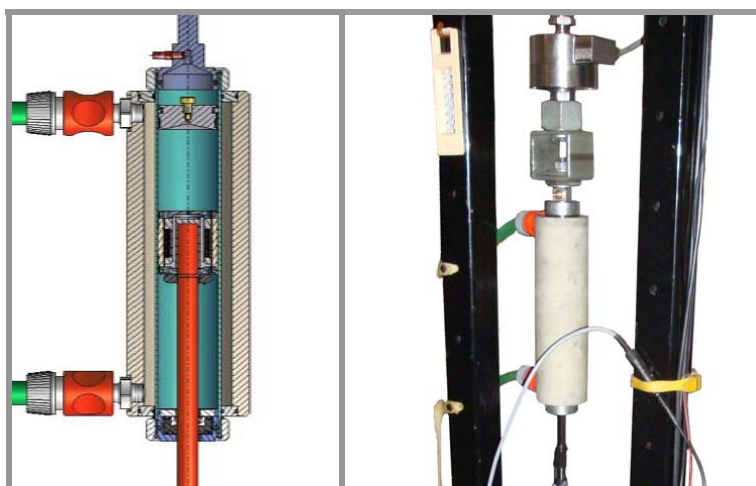


Fig. 2: The new design of slit-flow rheometer.

## 2. Methods

### 2.1. Operating parameters of the rheometer

Rheometric unit is designed to be mounted in a mechanical, hydraulic or pneumatic pulsator. The maximum piston speed of  $7.8 \text{ m.s}^{-1}$  corresponds to the maximum shear rate of  $8.7 \cdot 10^5 \text{ s}^{-1}$  inside the throttle slit. Maximum operating magnetizing current is 2 A. This current flowing through the coil creates the magnetic field of 160mT in the air gap of the rheometer throttle slit. The exact description of the magnetic and hydraulic conditions can be found in (Mazûrek et al., 2009).

### 2.2. Properties of tested MR fluid

Properties of the tested MR fluid are given in Tab. 1. It is the liquid with the highest ratio of Fe particles to the carrier fluid from the range offered by LORD Corp. company.

Tab. 1: Properties of the MR fluid used.

<i>fluid type</i>	<i>140-CG</i>
<i>density</i>	<i><math>3.69 \text{ kg/dm}^3</math></i>
<i>mass percentage of Fe particles</i>	<i>86.4%</i>
<i>volume percentage of Fe particles</i>	<i>40.5%</i>
<i>mean size of Fe particles</i>	<i><math>1.89 \mu\text{m}</math></i>
<i>viscosity at <math>20^\circ\text{C}</math> and <math>\dot{\gamma} = 800 \text{ s}^{-1}</math></i>	<i><math>0.880 \text{ Pa.s}</math></i>
<i>indicated Lifetime Dissipated Energy (LDE)</i>	<i><math>10^7 \text{ J.cm}^{-3}</math></i>



### 2.3. Experiment progress

Rheometer was filled with 100 ml of the MR fluid. Before the start of the durability test current and temperature characteristics were measured for temperatures between 20 and 80 °C and for currents 0 A, 0.5 A, 1 A, 1.5 A and 2 A. The temperature inside the throttle slit was obtained from the temperature dependence on the magnetization coil winding resistance. Thus, at least a minimum current had to pass through the circuit in order for the temperature to be measurable. In fact, the measurement for 0 A was carried out with the actual current of 50 mA. In order to increase the mechanical load during the loading cycle the magnetizing current was set to the maximum operating level of 2 A and the maximum operating speed of the mechanical pulsator in which the rheometric units was installed was set to the constant level of 126 rpm. This rate of rotation corresponds to the maximum piston velocity of 0.33 m/s which results in the shear rate of  $3.7 \cdot 10^4 \text{ s}^{-1}$  for given hydraulic conditions of the MR valve active zone. During the durability test the temperature was maintained within the range of 45-56°C by water cooling. After each load cycle the mechanical pulsator was stopped and the operating parameters (system pressure, lubrication of pulsator, flow rate of cooling, fixture of rheometer, etc.) were checked. Series of measurements of rheological properties of the MR fluid was then carried out followed immediately by the next loading cycle. Changes of properties of the MR fluid during the long-term operation were evaluated in inactivated state, thus with the current of 0 A. The dynamic viscosity and yield stress of the MR fluid were determined from the flow curves using the methodology described in (Mazurek et al., 2009). Dissipated energy of the rheometric unit was described by a parameter named *Lifetime dissipated energy* (LDE) (Carlson, 2003), which can be defined as:

$$LDE = \frac{I}{V} \cdot \int_0^{life} P \cdot dt \quad (2)$$

where V is a working volume of MR fluid and P is a dissipated performance of MR device.

### 3. Conclusions

Fig. 3 shows the values of dynamic viscosity measured during the durability test. Pink points indicate the visco-temperature characteristics of MR fluid at the beginning of the durability test. Between 1500 and 9000 kJ of dissipated energy, the dynamic viscosity decreased on average by 36% (yellow points). The dynamic viscosity and yield strength were not measured in a wider temperature range after further load cycles but the measured viscosity was compared with the viscosity curve of new MR fluids and the curve after the first loading cycle. As Fig. 3 shows, the values of dynamic viscosity in consequent load cycles (green, red, blue and black points) lie very close to the viscosity curve after the first loading cycle. Equation coefficients from the exponential regression curves of the new MR fluid and fluid after the first loading cycle are almost identical (Fig. 3). This means that the percentage change of the dynamic viscosity in the given range of the temperatures is the same for both curves. Therefore, it was possible to convert the measured values of dynamic viscosity from the entire durability test into one reference temperature. The temperature of 45 °C which lies at the center of the measured interval was selected as the reference temperature (Tab. 2). The results show that after the first load cycle the dynamic viscosity did not change significantly.

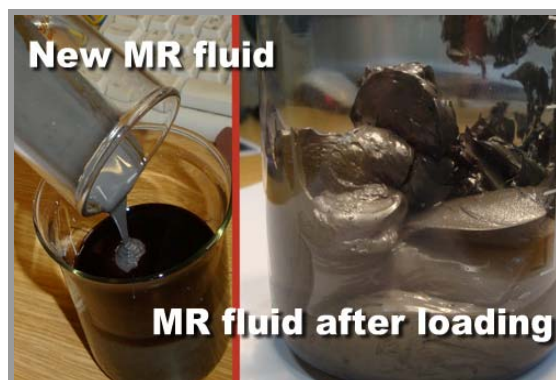
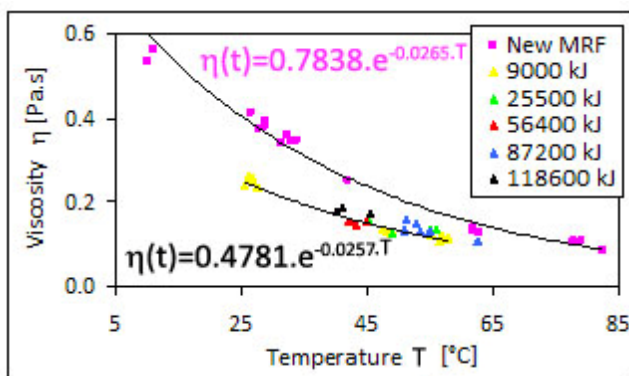


Fig. 3: Viscosity measurements during the durability test.

Fig. 4: New MR fluid and after loading.

Tab. 2: Dynamic viscosity during the durability test at the reference temperature.

	<i>new MRF</i> (regression)	<i>9.000 kJ</i> (regression)	<i>25.500 kJ</i>	<i>56.400 kJ</i>	<i>87.200 kJ</i>	<i>118.600 kJ</i>
$\eta(45^{\circ}\text{C}) \text{ Pa.s}$	0.238	0.150	0.164	0.146	0.167	0.169

Yield stress was another monitored parameter describing the behavior of the MR fluid. First, the hypothesis that the yield strength is independent of the temperature (Fig. 5a) was confirmed and then evolution of the yield stress during the durability test was analyzed. It was found that the yield stress increased up to five times with respect to the original value (Fig. 5b). The yield stress is the parameter which, similarly to the consistency of the MR fluid, changed significantly during the loading (Fig. 4). Therefore, it can be concluded that the increase in yield strength has a direct influence on the consistency of the fluid but not on its dynamic viscosity which is in contrast to what has been presented in many publications to date.

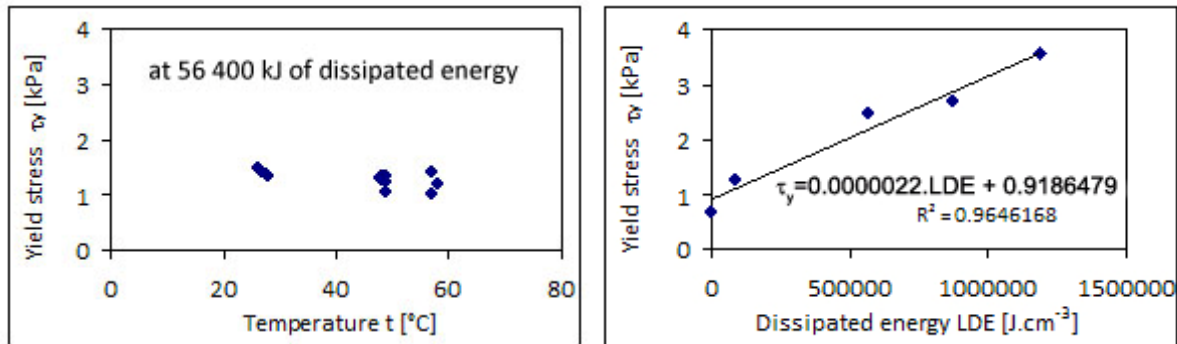


Fig. 5: a) Yield stress dependence on temperature; b) yield stress during the durability test.

These findings have serious consequences in particular for control in the off-state and for lifetime considerations in an MR node design. It is important to note that a fivefold increase in yield stress leads to a fivefold increase in force (torque) required for initial motion of MR device. For an MR damper this means that up to a certain force it will not absorb and, from the mechatronic point of view, it will behave rather like a spring. This implies, e.g. for MR clutch, an increase in torque in the switched-off mode. The LORD Company declares the MR fluid LDE of up to  $10^7 \text{ J.cm}^{-3}$ . However, at  $1.2 \cdot 10^6 \text{ J.cm}^{-3}$  already the MR fluid is not a liquid anymore.

## Acknowledgement

This work was developed with the support of the research plan MSM 0021 630 518, and grant BD 130 02003.

## References

- Specialty Adhesives & Coatings - Environmentally Friendly Adhesives, Water Based, Aqueous Rubber [online]. c2008 [cit. 2010-05-10]. URL: <<http://www.lord.com>>.
- Cheng, H.B. (2008) Stability and anti-oxidization of aqueous MR fluids improved by modifying iron particle surface with organic molecule. *Acta Physico-Chimica Sinica*, 24, 10, pp.1869-1874.
- Fang, F.F., Byung, I.Ch. & Choi, H.J. (2009) Magnetorheological characteristics of carbon nanotube wrapped carbonyl iron particles. *Journal of Physics: Conference series*, 149, 1.
- Bombard, A.J.F., Antunes, L.S., Balestrassi, P.P. & Anderson, A.P. (2009) Magneto-rheological fluids redispersibility - a factorial design study of phosphate shell on carbonyl iron powder with dispersing additives. *Journal of Physics: Conference series*, 149, 1.
- Goncalves, F.D. (2005) Characterizing the behavior of magnetorheological fluids at high velocities and high shear rates. Dissertation on Faculty of the Virginia Polytechnic Inst. Dissertation advisor Mehdi Ahamadian.
- Mazurek, I., Roupec, J. & Klapka, M. (2009) Identification of MR Fluids properties in Mechatronic Damping Elements, in: *Recent Advances in Mechatronics 2008 – 2009*, Berlin, pp.115-120.
- Carlson, J.D. (2003) Critical factors for MR fluids in vehicle systems. *International Journal of Vehicle Design*. 33, 1-3, pp.207-217.

## STRESS ANALYSIS OF BURCH-SCHNEIDER CAGE

K. Řehák<sup>\*</sup>, Z. Florian<sup>\*</sup>, P. Marcián<sup>\*</sup>, J. Valášek<sup>\*</sup>, D. Krpalek<sup>\*</sup>, M. Matug<sup>\*</sup>

**Abstract:** *This article deals with the stress analysis of the Burch-Schneider (BS) cage as applied to a hip joint. Due to the complex geometry of the solved problem, material properties and complex boundary condition, the finite element method was chosen. The solved system consists of the pelvic bone, a part of the os sacrum, a polyethylene cup and ceramic heads. In this work a poor-quality cancellous bone was given by the value of the modulus of elasticity is modelled. Furthermore, two model types are considered in this study – a model with degraded mechanical properties of the cancellous bone, which does not worsen due to stress, whereas the other model shows a case of bone necrosis due to stress. Load was applied to the ceramic head in the direction of the resultant butt force, which had been determined by the resultant forces. The analysis of the results indicates that in the model variant with the necrotic bone tissue of such an extent that was considered, damage may occur due to the cyclical loading. However, in the variant with degraded mechanical properties, which are not deteriorating due to stress anymore, the limit state does not occur.*

**Keywords:** *Burch-Schneider cage, hip joint, Finite element method, stress-strain analysis.*

### 1. Introduction

In the 1960s Charnley and Mc Kee paved the way to the modern hip joint implant. With the increasing quantity of total joint replacements for younger patients it was gradually necessary to perform reimplantations due to loosening or wear of some of their components. The problem with reimplantation occurs in cases where there is a loss of the bone tissue for example because of inappropriate loading leading to the atrophy of the bone tissue, usually near the region of the acetabulum. As the number of patients with this problem has been increasing, a variety of solutions have been proposed. These methods may include the resection arthroplasty (Jasty et al., 1990), reconstruction of the bone defect using a large amount of acrylic cement (Salvati et al., 1975), the use of bipolar prostheses, massive bulk allografts or cementless acetabular components. The anti-protrusion cage belongs into the group of cementless acetabular components can solve the problem of the bone loss in the acetabulum area. It was designed in 1974 to treat a patient with an unhealed acetabular fracture. A year later, this cage was adjusted by Dr. Schneider to use the screw fixation in the distal area (Berry et al., 1992). This adjustment was made to use the cage for bridging defects. The cages are made from titanium alloys because of the biocompatibility and good mechanical properties. The implant is attached to the os ilium by screws, the attachment to the os ischium is performed in two ways, either by embedding it into the bone with a subsequent fixation with screws or by fixing it to the bone surface by screws. At every step the hip joint is loaded and subsequently unloaded. In the case of the Burch-Schneider (BS) cage implantation cyclical stress occurs, which may cause damage. The system with the established BS cage can be assessed by using the stress-strain analysis. Determination of the strain and stress of the BS cage is highly problematic as a consequence of the complex system elements geometry, material and load. An effective solution can be computational modelling.

### 2. Methods

To solve the above-mentioned problems effectively by using computational modelling, numerical methods can be applied, including the finite element method, which is widely used in biomechanics. In

---

<sup>\*</sup> Ing. Kamil Řehák, Ing. Zdeněk Florian, CSc., Ing. Petr Marcián, Ing. Jiří Valášek, Ing. David Krpalek and Ing. Michal Matug: Institute of Solid Mechanics, Mechatronics and Biomechanics, Faculty of Mechanical Engineering, Technická 2896/2; 616 69, Brno; CZ, e-mails: yrehak04@stud.fme.vutbr.cz, florian@fme.vutbr.cz, ymarci00@stud.fme.vutbr.cz, yvalas05@stud.fme.vutbr.cz, ykrpal00@stud.fme.vutbr.cz, ymatug01@stud.fme.vutbr.cz

our case, the ANSYS 12.0 programming environment was used. Solving this problem can be divided into the sub-problems of the geometry model, material, boundary conditions and loads.

## **2.1. Model of geometry**

The BS cage model of geometry was created using the data obtained by the ATOS photometric sensing system, which were subsequently adjusted using the Rhinoceros programme and SolidWorks. The bone tissue model of geometry was created from the input data obtained from CT scans from St. Anna's Hospital in Brno using the STL Model Creator software (Konečný et al., 2010). The model of polyethylene cup was developed with regard to the perfectly corresponding shape with the BS cage using SolidWorks. All the mentioned parts were used in order to create a system to solve the problem. The system created this way was imported into the ANSYS Workbench environment, where the last element of the required system – the ceramic head - was created. The discretization of the cancellous bone tissue in the pelvic area, a part of the polyethylene cup and the ceramic head was performed using SOLID 186 element (hexahedrons). The os sacrum, the BS cage and the second part of the polyethylene cup were discretized using the SOLID 187 element (tetrahedrons). The cortical bone was created using the SHELL 181 element at 1mm of defined thickness. The TARGE 170 and CONTA 174 elements were used to define the mutual contact. Maximum attention was paid to the meshing, so there were 330,000 elements.

## **2.2. Model of material**

It is not difficult to determine the characteristics of technical materials. Living bone tissue changes throughout its life and so do its properties. The quality assessment of the bone tissue can be done based on its CT images, which can further serve for the determination of the material characteristics (Valášek et al., 2010). The BS cage was used in clinical problem where bone quality is quite poor and therefore the cancellous bone tissue has poor mechanical properties too. For this reason lower modulus of elasticity was used. The used values were  $E = 100 - 800$  MPa, the Poisson's ratio  $\mu = 0.3$  (Fütterling et al., 1998). Cortical bone is defined as an isotropic material of linear elasticity with  $E = 14\,000$  MPa and  $\mu = 0.3$  (Fütterling et al., 1998). The polyethylene cup model material  $E = 800$  MPa,  $\mu = 0.4$ ; BS cage  $E = 113\,800$  MPa,  $\mu = 0.3$  and ceramic head  $E = 380\,000$  MPa,  $\mu = 0.24$  were all chosen based on the material data.

## **2.3. Model of loads and constraints**

The calculation is realized for the load acting on the joint when standing on one leg, which occurs at some point during slow walking. The calculation was performed using the resultant butt force on a man weighing 80kg. Taking into account the symmetry of a human skeleton, symmetry restraints are defined in the area of the os sacrum and the symphysis pubica. With the implant fixation the variant of embedding into the os ischium was assumed, as well as, subsequently, a trouble-free reception of the implant, which was simulated by the bonded contact. The space between the BS cage and the polyethylene cup is, in clinical practice, filled with cement therefore this relationship is defined as bonded. The movement of the hip joint with the applied total joint replacement with the BS cage occurs between the ceramic head and the polyethylene cup, for this reason it was necessary to define the contact pair with friction.

## **3. Results**

In scientific literature, cases of implant ruptures may be encountered (Gallo et al., 2005; Pieringer et al., 2006). These are fractures in the area of the spinous or flat protrusion, especially around the screw holes. When the hip joint of the operated leg is loaded, the load is transferred from the ceramic head through the polyethylene cup to the BS cage and then to the bone tissue. When the cage works correctly, the polyethylene cup determines the life of the whole total endoprosthesis. It is beneficial to evaluate the contact pressure which is directly proportional to its wear. The value of the contact pressure depends increasingly on the angle of the resultant contact force over the final quality of the cancellous bone, see Fig. 1. The values of the contact pressure are higher in the variant with the necrotic bone tissue.



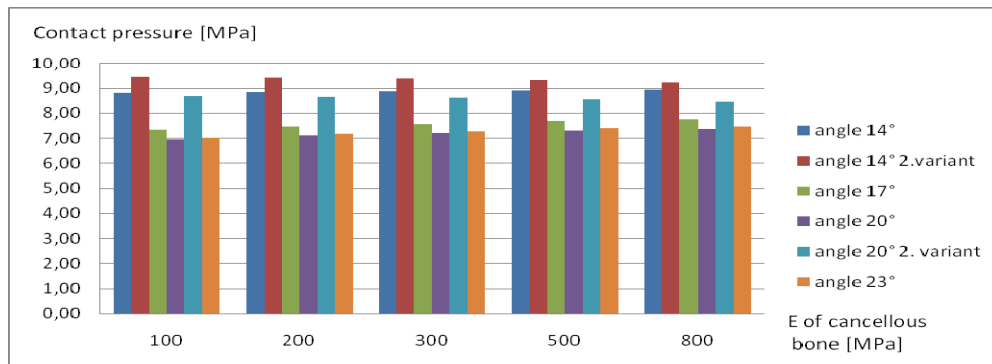


Fig. 1: Contact pressure between polyethylene cup and ceramic head.

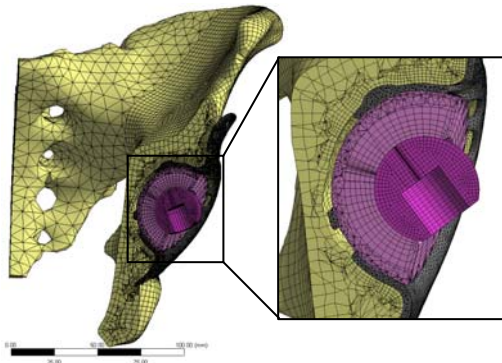


Fig. 2: Variant 1, detail of the acetabulum.

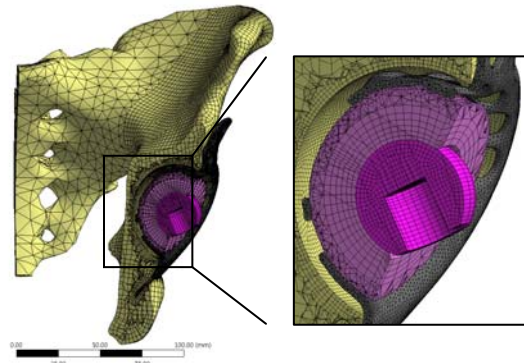


Fig. 3: Variant 2, detail of the necrosis bone.

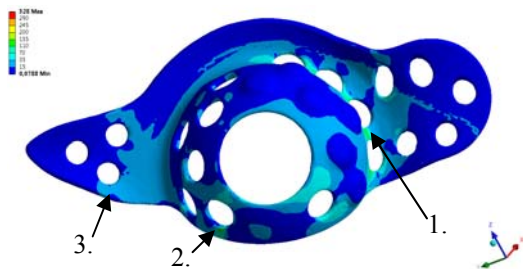


Fig. 4: Critical location for variant 1.

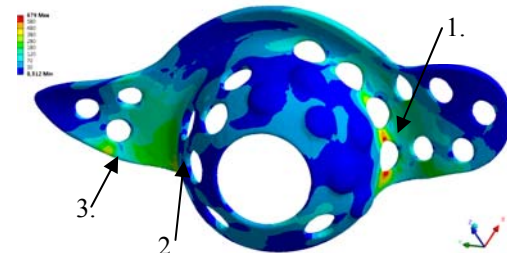


Fig. 5: Critical location for variant 2.

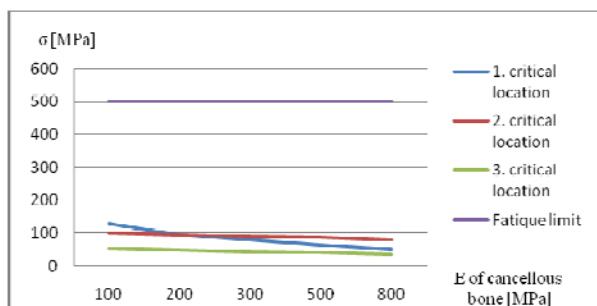


Fig. 6: Equivalent stress in critical location for variant 1.

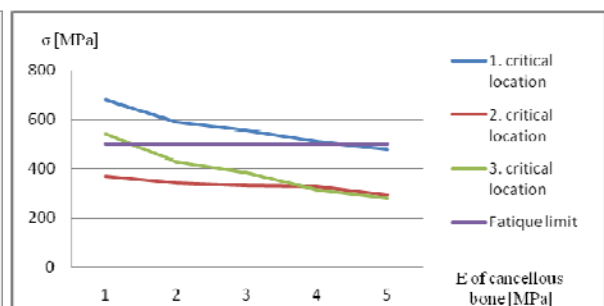


Fig. 7: Equivalent stress in critical location for variant 2.

The analysis of results of the stress distribution in the BS cage is very different for each model. These models can be seen in Fig. 2 and Fig. 3. The corresponding stress values in critical location are shown in Fig. 4 for variant 1 and in Fig. 5 for variant 2. These values are reflected in Fig. 6 and Fig. 7. These figures show that the value of stress in critical location goes down with increasing quality of bone tissue. In the case of variant 2 the stresses exceeded the fatigue limit which can cause a damage of the BS cage under which the necrotic bone tissue is located.

#### 4. Conclusion

The presented biomechanical study aims to assess the stress states of the BS cage at the hip joint total endoprosthesis with applied armature. For calculations, two models of geometry were created. Five material models were subsequently added. Implant shifting and maximum stress in critical locations were evaluated and the values transferred to a graph. From the results analysis the following conclusions may be drawn:

In the variant with the worsened bone tissue mechanical properties, which do not deteriorate due to the load in the case where the fixation is embedded into the os ischii, the limit state is not reached. The comparison between the fatigue limit and the maximum stress at critical locations is shown in Fig. 6.

In the case of the necrotic bone tissue under the BS cage, to the extent modelled in this study, the stress reaches unacceptable values. These occur mainly in two critical points – firstly in the transition area between the cup and the rim around the stress concentrators (holes), see Fig. 8, and the second critical point is located on the spinous protrusion in the area of the stress concentrator, see Fig. 8. In Fig. 9 we can see the damaged BS cage in the same critical point as shown in Fig. 8.

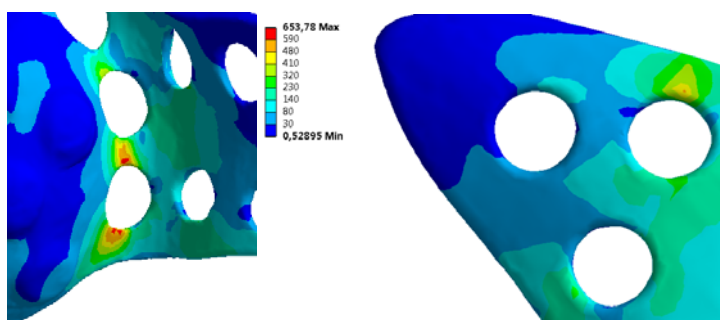


Fig. 8: Critical location for variant 2.



Fig. 9: Damaged BS cage.

These conclusions were based on the biomechanical study. The analysis of the fracture causes of the BS cage is a complex and difficult problem. It is necessary to take the clinical, chemical and biological disciplines into account in way to be able to solve it.

#### Acknowledgement

This work was supported by the FRVS grant project No. 2829/2011 and the FSI-J-11-3 specific research.

#### References

- Berry, J. D., Müller, M. E. (1992) Revision arthroplasty using an anti-protrusion cage for massive acetabular bone deficiency, *Journal of Bone Joint Surgery*, pp. 711-715.
- Fütterling, S., Klein, R., Strasser, W., Weber, H. (1998) Automated finite element modeling of a human mandible with dental implants, WSCG.
- Gallo, J., Florschütz, V. A. (2005) Burch-Schneider cage fracture: A case report, *Biomed Pap Med Fac Univ Palacky Olomouc Czech Repub.* pp. 281-284.
- Jasty, M., Harris, W. H. (1990) Salvage total hip reconstruction in patients with major acetabular bone deficiency using structural femoral head allografts, *Journal of Bone and Joint Surgery*, pp. 63-67.
- Konečný, O., Marcián P. et al. (2010), software, STL Model Creator, biomechanika.fme.vutbr.cz.
- Pieringer, H., Auerperg, V., Böhler, N. (2006) Reconstruction of Severe Acetabular Bone - deficiency, *Journal of Arthroplasty*, pp. 489-496.
- Salvati, E. A., Bullough, P., Wilson P. D. Jr. (1975) Intrapelvic protrusion of the acetabular component following total hip replacement. *Clin Orthop*, pp. 212-217.
- Valášek, J., Marcián, P., Krpálek, D., Borák, L., Florian, Z., Konečný, O. (2010) Material Properties of Bone Tissue Obtained from CT for Biomechanics Purposes, In *MENDEL 2010*, Mendel Journal series, Brno: BUT FME Brno, ISBN: 978-80-214-4120-0, ISSN: 1803-3814, pp. 483-490.

## CAN THE FOAM MODEL SIMULATE THE BONE BEHAVIOUR?

Z. Sant<sup>\*</sup>, A. Casha<sup>\*\*</sup>, J. Cilia<sup>\*\*\*</sup>

**Abstract:** *Dehiscence of median sternotomy wounds due to excessive forces caused by high pressure within the chest during coughing can lead to breaking closures sternotomy. This remains a clinical problem leading to significant risks of mortality and morbidity. The evaluation of the suture and the sternotomy biomechanical feedback is tested usually on the human cadaveric sternum or in some cases using suitable animal sternum. The foam sternal model was proposed as the alternative source that provides cheap, easily accessible sternum, without mentioning other advantages. The computational approach combined with experiment can provide more information about the foam behaviour and confirm the statement: “the foam model sternum behaves as a real bone” as advertised by supplier. The foam model sternum was scanned, and digitized geometry data was used to create the virtual computational model used to simulate the laboratory experiment by means of Finite Element Method. The data collected from the two experiments, the laboratory test and computational simulation, are compared and verified against the outcome of the experiment with the sternum from cadaver.*

**Keywords:** *Sternum, finite element analysis, foam model.*

### 1. Introduction

The sternotomy incision is preferred path to access the heart and other vascular tissues in spite of the rising popularity of minimal invasive techniques. Dehiscence of the sternotomy closure represents a serious complication in the early post-operative period prior to start of significant bone healing. It is usually caused by sternal instability, disruption of the bone or the wire, and associated with wound infection. The rate of median sternotomy dehiscence falls between 0.5 to 2.5% with mortality ranging from 10 to 45%, which demands better understanding of the problem followed by improvement of the closure technique. To carry out the proper analysis of the situation after the surgery there is a need to conduct number of tests with application of different closure techniques. The number of suitable sternal plates from cadaver is limited therefore the alternative way or source has to be identified to be able to provide reliable results. The animal bone or artificial model made of polyurethane foam is offered as the alternative material to test techniques sternotomy. It is rather difficult to obtain an animal sternum that would have significant similarity to human sternum (Magovern, 1999). The model artificial sternum offers more or less uniform material properties, and shape thus seems to be the most suitable for the comparison studies. The first comparison between sternum cadaver and the artificial bone was carried by D. R. Trumble (2002). Even though the result supported the idea of similar behaviour between the foam model and human sternum the question mark related to biomechanical feedback and stress-strain response remained. The similarity of biomechanical response between sternum cadaver and the model from polyurethane foam has to be proved prior to further tests.

### 2. Methods

The similarity of biomechanical response between sternum cadaver, and the foam model can be proved via laboratory experiments or virtual simulation. In this paper we are going to discuss the virtual simulation of the sternum behaviour. Before we start the simulation of sternotomy closure, our

---

<sup>\*</sup> Dr. Ing. Zdenka Sant: Mechanical Engineering Department, University of Malta, Tal Qroqq; Msida MSD 2080; Malta, e-mail: zdenka.sant@um.edu.mt

<sup>\*\*</sup> Aaron Casha, MD: Departments of Cardiothoracic Surgery, Mater Dei Hospital, Msida, MSD 2080; Malta, e-mail: casha@waldonet.net.mt

<sup>\*\*\*</sup> Jeffrey Cilia: Mechanical Engineering Department, University of Malta, Tal Qroqq; Msida MSD 2080; Malta, e-mail: jeffrey\_cilia@hotmail.com



task is to verify the identity or similarity of the behaviour of the sternum and the polyurethane model of sternum. The determination of the boundary conditions for computational model was subordinated to this goal thus the forces are applied at the points where the holder of the foam model will be clamped into the jaws of the tensile machine. Thus even though the loading conditions do not correspond to the reality we can conduct the comparative study under the same load condition for the foam model, computational model, and human cadaver.

## 2.1. Sternum

The sternum is a long flat bone that forms the anterior wall of the thorax whilst creating an anchor for the ribs meeting centrally along the midline of the body. The main function sternum that is anchored anteriorly to the rib cage and posteriorly in the vertebrae, is to protect vital organs against physical trauma. It is composed of three parts, which are the manubrium, the sternum, and the small irregular xiphoid process. The adjacent parts articulate via secondary cartilaginous joints that allow more movement between the bones than the fibrous joint.

## 2.2. Computational model

The model consisting of the manubrium, sternum, and short cartilages attached to the sternum is moulded as one solid piece. The first goal was to create the geometry model therefore the data of the shape were obtained in form of a cloud point, using laser scan. The virtual model sternum made of solid polyurethane foam was created in drawing software Rhinoceros. The material properties of the foam were obtained from manufacturer with certification of the compliance with testing standards ASTM D-1621, D-1623, D-273. The type of foam with density 20pcf (pound per cubic foot) was proposed by medical person as the equivalent substitute they use for testing of the suture sternotomy.



*Fig. 1: Artificial Model Sternum.*

## 2.3. Load during the cough

The mathematical model created for computation of the force load during the cough is based on the similarity between the shape of the chest and the pressure vessel. In both cases the internal pressure creates the load on the wall that encloses the pressurized space. This approach, proposed by Mr. Casha (1999, 2001) takes into account the pressure developed inside the chest during the cough without contribution from other structures such as intercostal or abdominal muscles. This simplified model of the chest is well accepted within the medical society even these days.

Thus the total force acting on the chest wall is modelled as uniformly distributed pressure over the projected chest area that is considered to form a cylinder

$$F = p \cdot D \cdot L \quad (1)$$

Considering the pressure  $p$  that can reach values 13 kPa to 40 kPa during the cough, and the average dimension of the human chest given as thickness  $D = 150$  mm and length  $L = 300$  mm measured in sagittal plane, based on the anthropometrics data available. The total force of 1350 N that was computed for given geometry and pressure of 30 kPa, is transferred through the adjacent structures to the sternum. This result is in agreement with an independent research that has been carried out by Losanoff (2004) by means of the experiment with cadavers.

## 2.4. Materials and simulation

Due to considerable difference between values of Young's modulus in relation to the density we computed the density of our model that we have available, and together with the graph of Young's modulus, plotted from the data provided by the manufacturer, we evaluated correct Young's modulus. The value of density for the polyurethane foam was  $0.414 \text{ g/cm}^3$ , which corresponds to 25.9 pcf and the extrapolated Young's modulus reached 460MPa in tension, and 348 MPa in compression. The results of the computational simulation are going to serve as a benchmark for our future work utilising the foam model.

To identify the biomechanical differences in the response of the polyurethane foam model and the human sternum we need to simulate the material properties corresponding to the cortical and cancellous bone. The thickness of the sternum was measured at the valley, the position of the cartilage attachment, and at the ridge to be  $9.5 \pm 1.5$  mm, and  $13.15 \pm 1.6$  mm respectively while the thickness of the cortical bone at the valleys is around 1 mm, and at the ridges exceeds 2 mm. The effect of the cortical and cancellous bone on the magnitude and distribution of stress is investigated virtually, utilizing the geometry of the foam model that is coated with uniform layer of cortical bone 1mm, and 2 mm thick enclosing the cancellous bone of very low density. The given values of Young's modulus 5000 MPa and 50 MPa associated with cortical and cancellous bone respectively are based on the CT scans of six human cadaveric sternums. The data analysis was carried out at the Anatomy Department of University of Malta by evaluation of the average radio-density 1500 HU and 300 HU (Hounsfield Units) for cortical and cancellous bone respectively followed by the estimation of Young's modulus that corresponds to the radio-density related to the colour intensity of the CT scan image.

### 3. Results

The results of the three models were summarized in the following graphs recording the variation of stress and strain along the path as marked on the sternum in Fig. 2. The stress distribution for intact sternum indicates the areas that would be exposed to large force during the cough. Thus these would represent the potential sites of the sternotomy failure. Except of the stresses and strains investigated at the region of sternotomy the overall stress distribution was evaluated based on the Von Mises stress and strain.

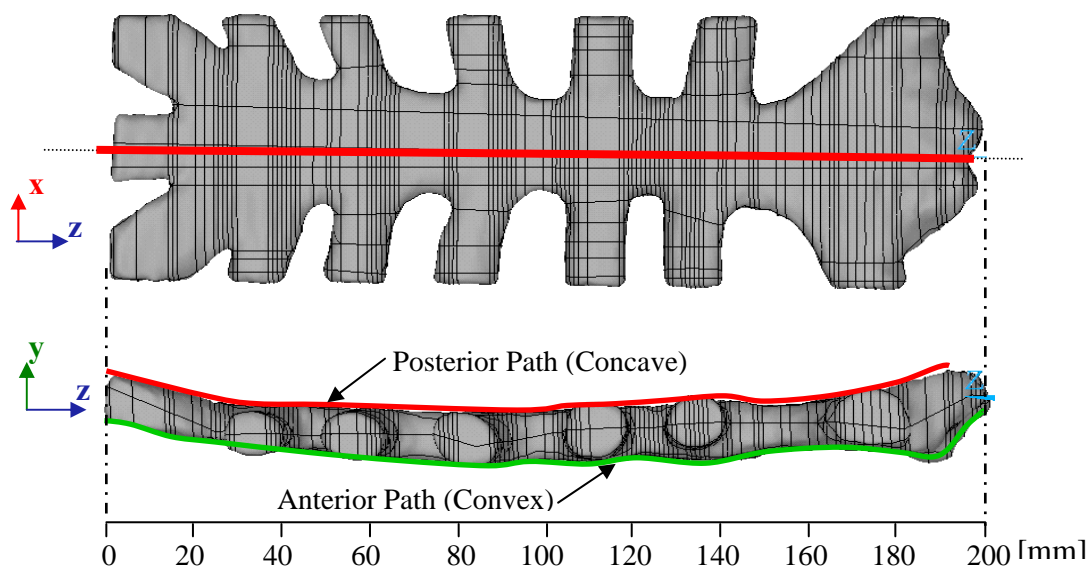


Fig. 2: The paths created along the sternum Finite Element Model to analyse the stress distribution within the sternum median plane.

Tab. 1: Summary of maximum equivalent stress and strain.

	Maximum Von Mises Stress ( $\times 10^6$ Pa)	Maximum Von Mises Strain $\times 10^{-3}$
<b>Foam Model</b>	5.279	11.5
<b>Bone 1 mm Cortical</b>	18.867	4.16
<b>Bone 2 mm Cortical</b>	12.616	2.52
<b>Bone 1 mm Cancellous</b>	0.320	6.41
<b>Bone 2 mm Cancellous</b>	0.110	2.19

The maximum stress was developed at the region of the rib attachment near the xiphoid in case of the foam model. In other two cases simulating the human bone the maximum stress developed was at the region of attachment of 3<sup>rd</sup> and 4<sup>th</sup> rib. As indicated in Tab. 1 above the stress within the cortical bone increased its value compared to the result from foam model. The highest stresses encountered in case

of 1 mm cortical shell model were reduced by approximately one third in case of 2 mm shell model that depicts more closely the real thickness of the cortical bone that supports better redistribution of the load within both types of bone that is confirmed by the resulting lower stress within the cancellous bone.

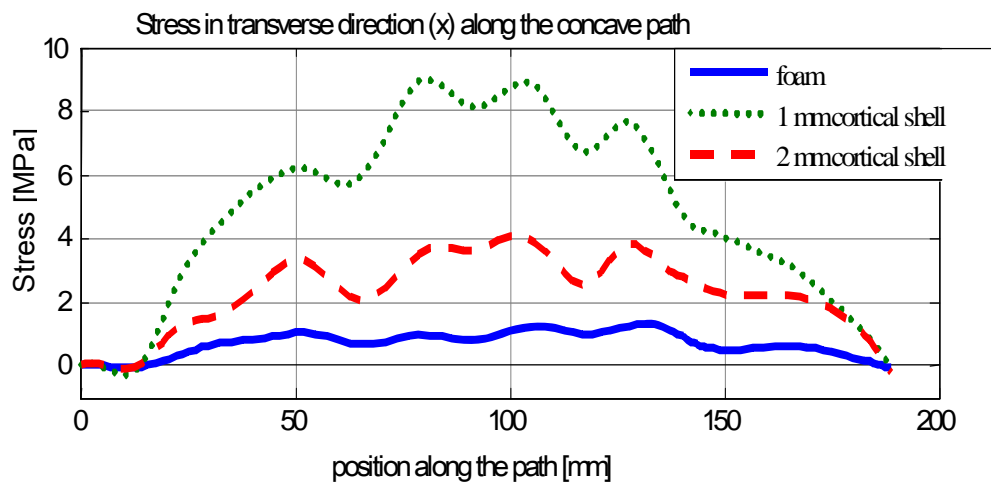


Fig. 3: Comparison of stress developed along the median path in coronal plane.

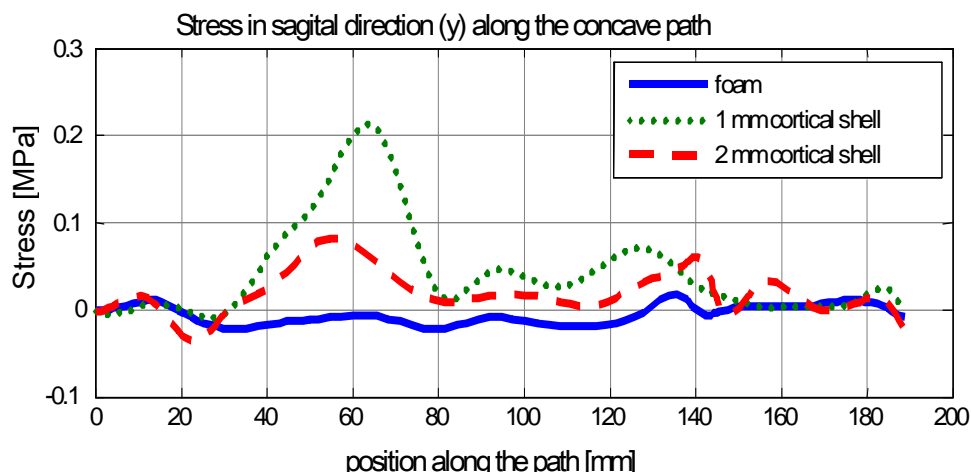


Fig. 4: Comparison of stress developed along the median path in sagittal plane.

#### 4. Conclusions

Our task was to answer the first question that crop out in our discussion about future tests of different closure techniques using the foam model of sternum. Based on the results from our simulation it can be concluded that there are considerable differences in the material response. The laboratory tests that are going to be carried in our laboratory in a very near future should verify our results and throw more light on the foam behaviour.

#### References

- Casha, A. R., Gauci, M., Yang, L., Saleh, M., Kay, P. H., Cooper, G. J. (2001) Calculating stress magnitude between sternotomy closure and sternum, *European Journal of Cardio-Thoracic Surgery*, 2001, June, 20, pp.1072-3.
- Dennis R. Trumble, Walter E. McGregor, James A. Magovern (2002) Validation of a Bone Analog Model for Studies of Sternal Closure, *The Annals of Thoracic Surgery*, 2002,74,pp. 739-744.
- J. E. Losanoff, A. D. Collier, C. C. Wagner-Mann, B. W. Richman, H. Huff, Fu-hung Hsieh, A. Diaz-Arias, J. W. Jones (2004) Biomechanical comparison of median sternotomy closure, *The Annals of Thoracic Surgery*, 77, 1, pp. 203-209.
- Magovern, J. A. (1999) Measurement of chest wall forces on coughing with the use of human cadavers, *The Journal of Thoracic and Cardiovascular Surgery*, 1999, Dec, 118, pp.1157-8.

## ERROR OF FATIGUE LIFE DETERMINATED ACCORDING TO THE FITNET METHOD

J. Sempruch\*, P. Strzelecki\*

**Abstract:** Procedures FITNET were developed by the European Fitness-for-service Thematic Network. One of the modules of this procedure is module fatigue of materials and construction. In this paper, the authors focused on the path 2b of this module, which refer to determination of fatigue life of components made of homogeneous material for which we can accept the linear-elastic characteristics (estimated of unlimited and limited fatigue life). Because this procedure is dedicated to engineers, there is the question how credible this method is. Aim of this study is to verify the accuracy of the presented above procedure for estimation of limited fatigue life. The verification was based on experimental data of structural materials which are widely used in practice.

**Keywords:** *Fatigue design, S-N curve, high-cycle fatigue, FITNET method.*

### 1. Problem formulation

Determination of S-N characteristic for components or materials according to the recommendations of relevant standards such as PN-H-04325:1976 lead to a very precise result (which is an advantage of this approach), but unfortunately due to the time of research generates significant costs (which is a disadvantage method). In standard PN-H-04325:1976 it is recommended to testing for at least 5 levels of loads with min. 3 samples at a frequency of changes in load 5 to 100 Hz. Should also be noted that the obtained result is very conservative in terms of its relationship with the conditions of the laboratory tests.

This situation has led to the existence a lot of proposals in the literature of analytical methods and analytical assisted simple experiment to determined approximate (also faster) the S-N characteristics. These methods are primarily dedicated to engineering applications and the authors of this paper taken interested of their accuracy and recommendations of range of application.

### 2. Presentation of FITNET method

Presented FITNET method allows to determine the fatigue characteristics of high-cycle fatigue. One of reason choice this algorithm is allowed to designate S-N curve after a simple experiment (tensile test). Moreover, this method is easy to use by engineer. Precision of this approach was not estimated in the scientific literature.

This approach written in the path 2b FITNET procedures (before Neimitz A. et al., 2008) assume the designation of fatigue limit by multiplying the tensile strength by the appropriate factor (formula 1 and 2).

$$\sigma_w = f_{w,\sigma} \times R_m, \quad (1)$$

$$\sigma_\tau = f_{w,\tau} \times \sigma_w, \quad (2)$$

where:  $R_m$  – tensile strength,

$\sigma_w, \tau_w$  – fatigue limit adequate for normal and shear stress,

$f_{w,\sigma}, f_{w,\tau}$  – factor depend on the type of material.

---

\* prof. Ing. Janusz Sempruch, M.Sc. and Ing. Przemysław Strzelecki, Ph. D. student: Institute of Mechanical Engineering, University of Technology and Life Sciences, 85-789, Bydgoszcz, Poland; Poland, e-mails: semjan@utp.edu.pl, przemstrzel@poczta.onet.pl

We put a point with coordinates  $10^6$  cycles and the fatigue limit values. To the right of this point a line is determine parallel to the abscissa for steel (except austenitic stainless steel) and the cast. For other materials (including austenitic steel) is defined by a line with a coefficient of  $m_D$ , until reached  $10^8$  cycles, and from that point a line is determine parallel to the abscissa. For the life of less than  $10^6$  cycles to create a line with coefficient  $m$ , which is 5 for normal stress and 8 for shear stress. Schematic procedure described above is shown in Fig. 1.

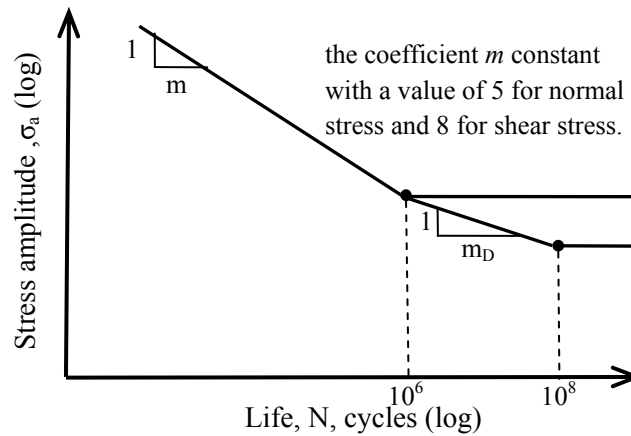


Fig. 1: S-N curve according FITNET (Neimitz A. et al., 2008).

### 3. Method of verification

In order to conduct a quantitative verification was determined the load, which corresponds to the fatigue life equal to  $10^5$  cycles for the experimentally determined curve (point A in Fig. 2). For this established the load was estimated a number of cycles to be damage according to the method FITNET (point B in Fig. 2). Calculated the number of cycles were compared to the initial number of cycles ( $10^5$  cycles), that is to say the estimation error was calculated from the difference in  $N_A - N_B$ .

Tab. 1: Specification of material used to verification and sources of dates.

Material	State	Source	Value of coefficient $m$
S235JR	Raw state steel	Niezgodziński M.E. & Niezgodziński T., 1973	11.5
S355J0	Raw state steel	Szala G. & Ligaj B., 2010	12.3
E355	Raw state steel	Dyląg Z. & Orłoś Z., 1962	18.8
C40	Normalised steel	American Society for Metals, 2003	12.8
C45	Normalised steel	Kocańda S. & Szala J., 1997 ; Kocańda D., 2000	11.1; 10.1
15Cr2	Quenched and tempered steel	Niezgodziński M.E. & Niezgodziński T., 1973	20
14CrMoV69	Quenched and tempered steel	American Society for Metals, 2003	16.1
30CrNiMo8	Quenched and tempered steel	Romanowicz P., 2009	11.7; 19.3
34CrMo4	Normalised steel	American Society for Metals, 2003	8.4
42CrMo4	After plastic forming	American Society for Metals, 2003	23.2
42CrMoS4	Quenched and tempered steel	Pyttel B., Schwerdt D. & Berger Ch., 2010	14
SAE 8630	Quenched and tempered steel	American Society for Metals, 2003	11.8
D38MSV5S	Normalised steel	Marines-García et al., 2007; Xue H.Q. et al., 2008	19.5; 10.9

In order to conduct a quantitative verification was determined the load, which corresponds to the fatigue life equal to  $10^5$  cycles for the experimentally determined curve (point A in Fig. 2). For this established the load was estimated a number of cycles to be damage according to the method FITNET (point B in Fig. 2). Calculated the number of cycles were compared to the initial number of cycles ( $10^5$  cycles), that is to say the estimation error was calculated from the difference in  $N_A - N_B$ .

In order to carry out a qualitative review was applied to the fatigue curve obtained from experimental data and the method presented on one diagram. The described verification was conducted for the materials presented in Tab. 1.

#### 4. Results of verification

Results of quantitative verification are presented in Tab. 2. The absolute values of fatigue life estimation was presented in penultimate column. Relative error was showed in last column.

For the purposes of this publication has been presented above, only one comparative figure of the experimental curve and is obtained by the method FITNET.

Tab. 2: Comparison between estimated fatigue life according FITNET and experimental date.

<i>Material</i>	<i>Value of coefficient m according to</i>	<i>Value of coefficient m according to FITNET</i>	<i>Number cycle to failure</i>	<i>Different between assumption <math>10^5</math> cycle and calculate cycles</i>	<i>Error of estimated fatigue life [%]</i>
<i>Normal stress</i>					
<i>S235JR</i>	<i>11.5</i>	<i>5</i>	$1.4 \times 10^5$	$-4.3 \times 10^4$	-43
<i>S355J0</i>	<i>12.3</i>	<i>5</i>	$6.7 \times 10^5$	$-5.7 \times 10^5$	-573
<i>E355</i>	<i>18.8</i>	<i>5</i>	$6.2 \times 10^5$	$-5.2 \times 10^5$	-518
<i>C40</i>	<i>12.8</i>	<i>5</i>	$4.0 \times 10^5$	$-3.0 \times 10^5$	-301
<i>C45</i>	<i>11.1</i>	<i>5</i>	$4.0 \times 10^5$	$-3.0 \times 10^5$	-308
<i>15Cr2</i>	<i>20</i>	<i>5</i>	$2.1 \times 10^5$	$-1.1 \times 10^5$	-109
<i>14CrMoV69</i>	<i>16.1</i>	<i>5</i>	$1.1 \times 10^5$	$-1.4 \times 10^4$	-15
<i>30CrNiMo8</i>	<i>11.7</i>	<i>5</i>	$5.7 \times 10^5$	$-4.7 \times 10^5$	-467
<i>34CrMo4</i>	<i>8.4</i>	<i>5</i>	$2.6 \times 10^5$	$-1.6 \times 10^5$	-157
<i>42CrMo4</i>	<i>23.2</i>	<i>5</i>	$1.9 \times 10^5$	$-8.5 \times 10^4$	-85
<i>42CrMoS4</i>	<i>14</i>	<i>5</i>	$2.4 \times 10^5$	$-1.4 \times 10^5$	-137
<i>SAE 8630</i>	<i>11.8</i>	<i>5</i>	$5.5 \times 10^5$	$-4.5 \times 10^5$	-451
<i>D38MSV5S</i>	<i>19.5</i>	<i>5</i>	$5.2 \times 10^5$	$-4.2 \times 10^5$	-422
<i>Shear stress</i>					
<i>C45</i>	<i>10.1</i>	<i>8</i>	$2.7 \times 10^5$	$-1.7 \times 10^5$	-169
<i>30CrNiMo8</i>	<i>19.3</i>	<i>8</i>	$8.6 \times 10^4$	$1.4 \times 10^4$	14
<i>D38MSV5S</i>	<i>10.9</i>	<i>8</i>	$7.5 \times 10^4$	$2.5 \times 10^4$	25

#### 5. Summary

Based on the received the verification results can be permit the following conclusions:

- error estimation of fatigue life (by FITNET) on a limited life may be significant (from 14% to 573%),
- in most cases, the estimated value obtained number of cycles to destruction of the element were overestimated,
- after comparing values of coefficient of fatigue curve in table 2 between second and third column it can be ascertain that variation in this factor for the material is too large to be reasonably ignored,
- it should be considered to the proposed rate dependence of fatigue on the inclination of the curve wider to defined test conditions (shape of the sample, the method of load, a group of materials).

It should be emphasized that the reported statement of the data, analyze it and present proposals are for a limited number of sample material data. This review points to certain trends and on the desirability of presenting such an analysis for broader groups of materials.

Proposed modification of the method FITNET, allowing significantly reduce the value of the error will be signaled during the conference.

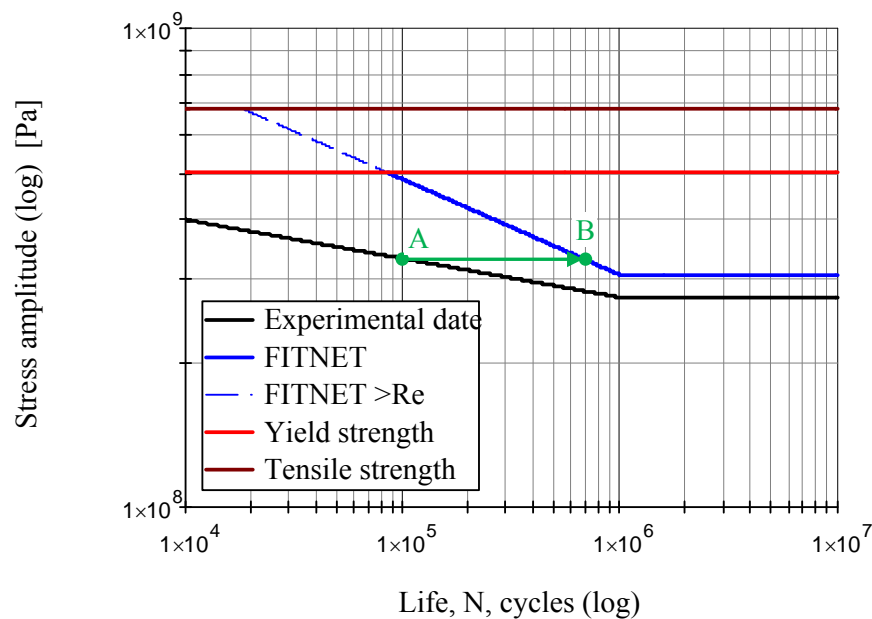


Fig. 2: Example S-N curve for experimental data and estimated curve according to FITNET of S355J0 steel (Szala & Ligaj, 2010).

## References

- American Society for Metals (2003) Atlas of fatigue curves. Edited by Boyer H.E. American Society for Metals.
- Dyląg Z. & Orłoś Z. (1962), Fatigue Strength of Materials, WNT, Warszawa.
- Kocańda D. (2000) Research of short fatigue cracks. Experimental methods in fatigue of materials and structures. Basic research, Monograph edited by Szali J., ATR Bydgoszcz.
- Kocańda S. & Szala J. (1997) Basis for the calculation of fatigue, PWN, Warszawa.
- Marines-García I., Galván-Montiel D. & Bathias C. (2007) Fatigue Life Assessment Of High-Strength Low Alloy Steel At High frequency. The Arabian Journal for Science and Engineering, Volume 33, Number 1B.
- Neimitz A., Dzioba I., Graba M. & Okrajni J. (2008) Evaluation of strength, life and safety of structural components contain defects, Politechnika Świętokrzyska, Kielce.
- Niezgodziński M.E. & Niezgodziński T. (1973) Calculations of fatigue strength for machine elements, PWN Warszawa.
- PN-H-04325:1976, Test of metal fatigue - Basic terms and general guidelines for preparing of samples and carry out tests.
- Pyttel B., Schwerdt D. & Berger Ch. (2010) Fatigue strength and failure mechanisms in the VHCF-region for quenched and tempered steel 42CrMoS4 and consequences to fatigue design. Procedia Engineering 2.
- Romanowicz P. (2009) Fatigue Analysis of selected machine elements operating under rolling contact. PhD thesis, Kraków.
- Szala G. & Ligaj B. (2010) Experimental study of the impact of a load cycle asymmetry on fatigue life of steel S355J0, XXIII Sympozjum Zmęczenie i Mechanika Pękania, UTP.
- Xue H.Q., Bayraktar E., Marines-Garcia I. & Bathias C. (2008) Torsional fatigue behaviour in gigacycle regime and damage mechanism of the perlite steel. Journal of Achievements in Materials and Manufacturing Engineering, Volume 31 issue 2 December.



## INFLUENCE OF PERTURBATION ON OILWHIRL PHENOMENON GENESIS

**R. Sikora<sup>\*</sup>, Z. Poruba<sup>\*</sup>, J. Szweda<sup>\*</sup>**

**Abstract:** *In this paper is surveyed the influence of the perturbation using model RK4. The perturbation was induced by centrifugal force. The measurement was made to evaluate influences of the single factors for future including to the mathematical model. There were used various combination of shaft speed and perturbation speed and the vibration spectra were recorded. It was found that the perturbation caused by even a small amplitude of centrifugal force could cause the very dangerous "oilwhirl vibration" even if the amplitude of vibration developed by perturbation itself is low. The simplified mathematical model suggested by Muszynska does not response the situation. This model was not in agreement with measured data. Another mathematical model should be used.*

**Keywords:** *Oilwhirl, perturbation, threshold, spectra.*

### 1. Introduction

The oilwhirl phenomenon can occur under some circumstances in hydrodynamic bearing. This phenomenon could be very dangerous as the amplitude of vibrations is very high. It is a nonlinear phenomenon. The speed threshold of this phenomenon depends on many factors. The most important of them are the rotational speed, diameter of the journal, bearing gap, pressure of oil and its, viscosity etc. The amplitude of this vibration is very high and this phenomenon could cause severe damages.

### 2. Methods

The vibrations were measured on model RK4 rotor kit. The configuration can be seen in the picture. The shaft was loaded by two discs per 800 g located 60 mm from the bearing. There was a perturbation disc, which can rotate with the range 250 to 10 000 rpm as well as the shaft. The shaft diameter was 10 mm. The pressure in bearing is ensured by pump. The arranging is displayed in the Fig. 1.



*Fig. 1: Rotor kit.*

---

<sup>\*</sup> Mgr. Ing. Roman Sikora, Ph.D., Ing. Zdeněk Poruba, Ph.D. and Ing. Jan Szweda Ph.D.: Department of mechanics, VŠB-Technical University of Ostrava, Street 17.listopadu 15; 708 33, Ostrava; CZ, e-mails: roman.sikora@vsb.cz, zdenek.poruba@vsb.cz, jan.szweda@vsb.cz



The excitation was induced by rotating weight mounted in perturbation disc. The press in the bearing was 10000 Pa ( $\approx 1,45$  p.s.i). The journal-bearing diameter was 25 mm and the bearing gap was 0,25 mm. The signal was taken by eddy current sensors and using the datacollector MICROLOG CMVA 10 in was processed to proximity values in  $\mu\text{m}$ . (peak-peak) and the spectra were calculated by FFT (fast Fourier transformation). The signal from horizontal and vertical sensors was approximately the same, so the horizontal was chosen for processing. The bearing is displayed in the Fig. 2.

Fig. 2: The bearing and perturbation disc.

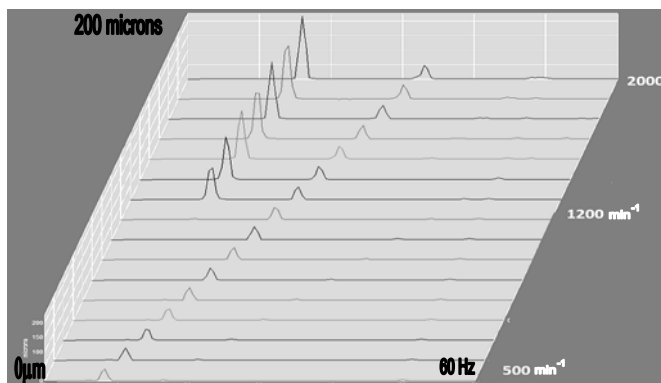


Fig. 3: Oilwhirl waterfall spectrum.

### 3. Measured data

First, the spectra were taken without any excitation by perturbation and waterfall of them can be seen in Fig. 3. The oilwhirl vibration arises at once at about 1300 revolution per minute. The amplitude of this vibration reaches 200  $\mu\text{m}$  (almost the completely bearing gap). This amplitude comparing to the amplitude caused of imbalance, which was maximally 40  $\mu\text{m}$ , was at least five times higher.

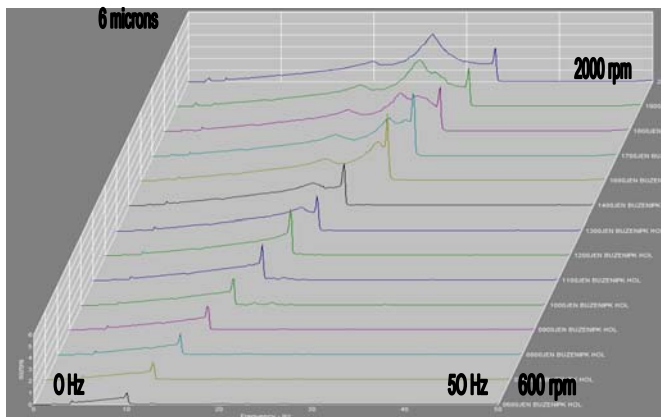


Fig. 4: Perturbation waterfall spectrum.

#### 3.1. Perturbation

The speed of perturbation were run up and down slowly (acceleration 1000 revolution  $\cdot \text{min}^{-2}$ ) from 450 rpm to set value from 600 to 2000 rpm. The maximum amplitude was recorded on every frequency. When only the perturbation disc rotated and the shaft was stopped the highest amplitude of the vibration was only about 4  $\mu\text{m}$  at most. The waterfall of series spectra caused only by ramping up perturbation could be seen in Fig. 4.

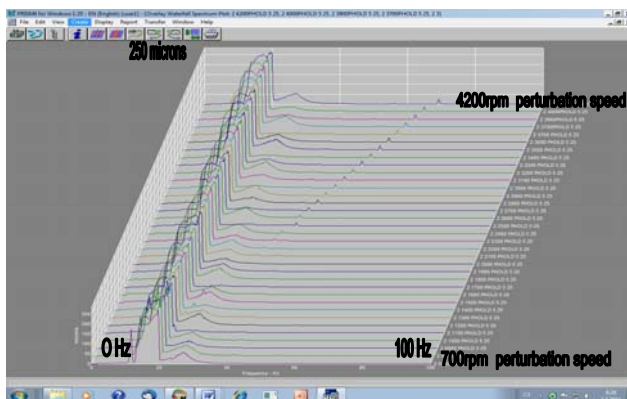


Fig. 5: Perturbation waterfall spectrum.

#### 3.2. Perturbation with various shaft speeds

When the perturbation speed was set on, certain value and the shaft speed varied from 500 to 2000 rpm and only the pick values were hold on preset value. It is seen in the picture that perturbation has no significant effect when the oilwhirl phenomenon had already arisen no regardless its speed and amplitudes. From previous experiences, it is possible to suppress the phenomenon only when the perturbation amplitude is comparable with the amplitude of oilwhirl.

### 3.3. Combination of shaft speed with perturbation varied speed

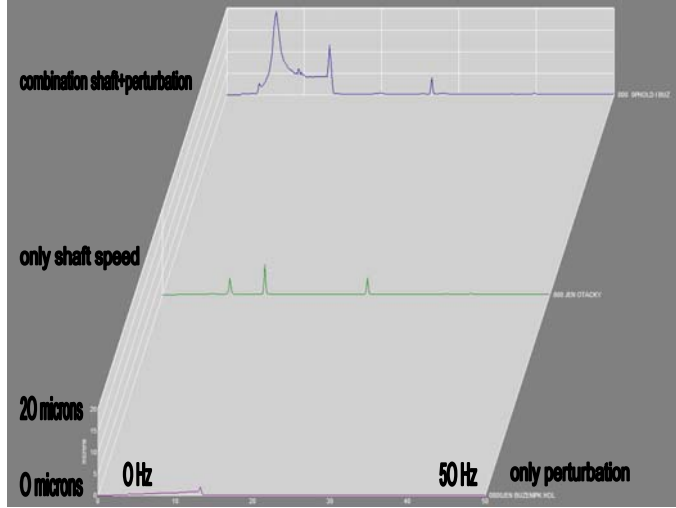


Fig. 6: Oilwhirl shaft speed 800 rpm.

The next measurements were done for given speed of shaft and varied speed of perturbation from 500 rpm of running shaft speed. The amplitude of perturbation was relatively very low. The shaft vibration without any excitation was also relatively low. The combination of perturbation and the shaft rotation led to uprising the vibration caused by oilwhirl phenomenon. This vibration occurs especially when the speed frequency of perturbation was approximately 0.48 multiply of the shaft running speed frequency. It even starts for much lower shaft speed.

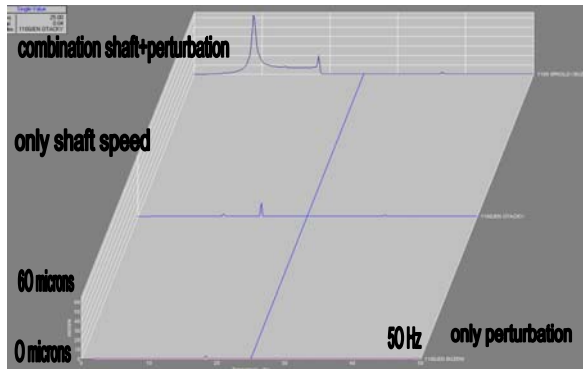


Fig. 7: Oilwhirl shaft speed 1100 rpm.

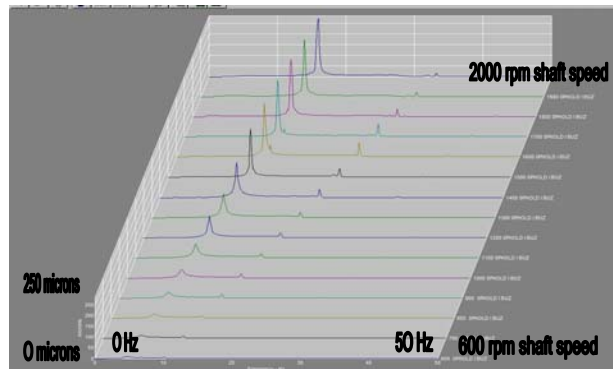


Fig. 8: Perturbation waterfall spectrum.

The waterfall spectrum, which could be seen in Fig. 8, shows the gradual genesis of the oilwhirl phenomenon, when the excitation using the perturbation is used.

### 4. Mathematical models

As the very first approximation was tested the equation of motion by Muszynska (2005):

$$-Kr + \left( D1 \cdot \frac{dr}{dt} + i \cdot \lambda \cdot D2 \cdot \omega s \cdot r \right) + ms \cdot rs \cdot \omega s^2 \cdot e^{i(\omega s t + \delta)} + mp \cdot rp \cdot \omega p^2 \cdot e^{i(\omega p t + \varepsilon)} = M \cdot \frac{d^2 r}{dt^2} \quad (1)$$

Where: **K** is the spring stiffness coefficient (complex)  
**D1, D2** are coefficients of damping (complex)  
**ms**, is imbalance rotating mass with eccentricity **rs**  
**ωs** is angular speed of shaft  
**mp**, is rotating mass on perturbation disc with eccentricity **rp**  
**ωp** is angular speed of perturbation disc  
**λ** is fluid circumferential average ratio (usually about 0.48)  
**r** position of journal centre (complex)

The amplitude of **r** was assumed to be consist of to harmonic signals one with frequency of shaft speed and second with frequency of **λ** times shaft speed frequency. The determination of coefficients, which could be in good agreement with measured data, was impossible. So the different mathematical model should be used.

## 5. Conclusions

Oilwhirl is a phenomenon when oil film excites the vibration, when the relative eccentricity of shaft and the angle of shaft centre "push" the shaft circumferentially in bearing. The destabilization force in rotation direction causes the whirl. Oilwhirl is an unstable phenomenon as the centrifugal forces increase oilwhirl vibration, which again increase the centrifugal forces. This phenomenon can cause the destruction of machine.

The influence of various combination shaft speed and perturbation speed were tested and their influence on the oilwhirl phenomenon generation. It was found that when the frequency of perturbation is close to this of oilwhirl (approximately 0.48 times of shaft speed frequency) the vibration peak on this frequency occurs even for much lower shaft speed. This should be taken in account when there are other machines close the machine with hydrodynamic bearing which operate with speed close to the oilwhirl.

To understand the phenomenon it is necessary to suggest mathematical model, which could be in good agreement with measurement. The first suggested mathematical model was not convenient to describe the phenomenon.

## Acknowledgement

The work has been supported by the research project MSM6198910027 of the Ministry of Education, Youth and Sports of the Czech Republic and by the research project TA01010705 of the Technology Agency of the Czech Republic what is highly appreciated.

## References

- Muszynska, A.; Rotordynamic, (2005) Boca Raton Florida, ISBN 10-8247-2399-6.
- Glenn D. White, (1997) Machine Vibration, DLI Engineering Corp., page 200. Bearing maintenance, Copyright SKF 1991, 332 pages.
- Pochylý, F., Malenovský, F., Hlavoň, P. (1999) Hydrodynamic damper. National conference with international participation Engineering mechanics 99", Svratka 1999, pages. 199-202, (in Czech).
- Malenovský, E. (1999) Computational modeling of dynamic features for nonlinear rotor systems. Engineering mechanics, volume 6, pages. 411 – 426, (in Czech).

## HDL MODEL OF MACHINE TOOL SLIDEWAY

A. Skarolek<sup>\*</sup>, M. Pustka<sup>\*</sup>, N. Pomp<sup>\*</sup>

**Abstract:** *The paper describes a modelling technique of tool rest of modern machining centre with focus at damping of dovetail groove slideway. Damping of tool rest structure strongly affects the stability of machining process, which must be maintained at wide range of machining condition, thus the adequate model of such damping should respect its physical origin to enable realistic estimation of boundaries between stable regions and self-excited vibrations at design stage of a new machine. Presented model of tool rest comprises damping characteristics obtained by HDL analysis of oil film of dovetail groove.*

**Keywords:** *Hydrodynamic Lubrication, Dovetail Groove, Damping, Tool Rest.*

### 1. Introduction

Stability of machining is a critical parameter of development process of new machine tool. Potential instability in form of self-excited vibrations of system: tool—workpiece is an inadmissible event, which profoundly degrades geometric precision and surface finish of work surface, accelerates tool wear and creates excessive noise. This phenomenon, caused by nonlinearity of the system of tool—workpiece—machine, restricts applicable cutting conditions in given case of machining process. It is understandable that the ability to predict regions of stable cutting conditions of future products is one of machine tool manufacturers' key initiatives, assisting analysis lead development (Altintas et al., 2005). Damping of the machine structures affects instability thresholds and plays important role in preventing self-excited vibrations. Major source of damping of tool rest structure has its origin in slideways, where the oil film present between the slide and the saddle acts as a squeeze film damper. See fig.1 for the tool rest geometry. This paper deals with hydrodynamic lubrication (HDL) analysis of the oil film. Results of the HDL analysis are used for calculation of damping coefficients that were used in the model of tool rest built by Craig-Bampton substructuring technique; such linear model can be treated in frequency domain, which is convenient for incorporating it into complex models of machine tool, built in order to analyse stability of cutting process (Turkes et al., 2010). More complex models respecting interaction between the slide and the saddle via squeeze film and mechanical contacts are strongly nonlinear, what leaves the option of time domain analysis only.

### 2. Model of the oil film

Clearances between dovetail groove surfaces of the slide and the saddle are adjustable and maintained at order of magnitude of 0.01 mm. With respect to the other two spatial dimensions of overlapped portion of groove surfaces, which are both at least thousand times the order of magnitude, the oil flow inside gaps can be expected laminar with negligible inertial volume forces. Such situation is ensured provided that Reynolds squeeze number is significantly smaller than one (Bilkay & Anlagan, 2004):

$$Re_s = \frac{\rho \omega d^2}{\mu}, \quad (1)$$

where symbols  $\mu$ ,  $\rho$ ,  $\omega$  and  $d$  mean oil viscosity, oil density, angular frequency of vibration and clearance respectively. On such condition, the pressure within the oil film satisfies Reynolds equation.

---

<sup>\*</sup> Ing. Antonín Skarolek, Ing. Martin Pustka, Ph.D. and Ing. Norbert Pomp, Ph.D.: VUTS, a.s., U Jezu 525/4; 460 01, Liberec; CZ, e-mails: antonin.skarolek@vuts.cz, martin.pustka@vuts.cz, norbert.pomp@vuts.cz



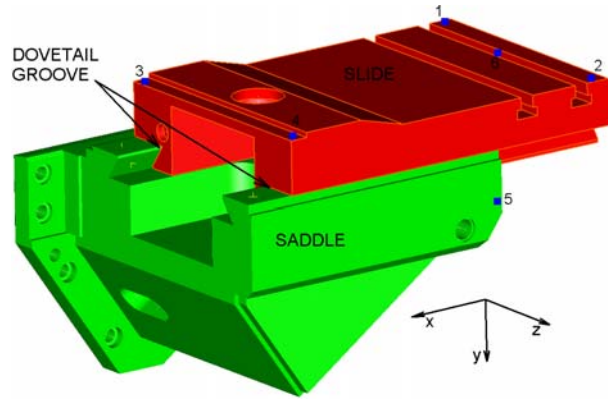


Fig. 1: Geometry of the tool rest.

Considering incompressibility of the oil, the Reynolds equation can be put into dimensionless form:

$$\frac{\partial}{\partial \xi} \left( H^3 \frac{\partial P}{\partial \xi} \right) + \frac{\partial}{\partial \eta} \left( H^3 \frac{\partial P}{\partial \eta} \right) = 120 \mu_R \frac{\partial H}{\partial \tau}, \quad (2)$$

using following quantities:

$$\xi = \frac{x}{1 \cdot \text{mm}}, \quad \eta = \frac{y}{1 \cdot \text{mm}}, \quad H = \frac{h}{1 \cdot \mu\text{m}}, \quad P = \frac{p}{1 \cdot 10^5 \text{ Pa}}, \quad \mu_R = \frac{\mu}{1 \cdot \text{Pa s}}, \quad \tau = \frac{t}{1 \cdot \text{s}}, \quad (3)$$

where  $x, y$  are coordinates on the groove surface,  $p$  is the oil film pressure,  $h$  means oil film thickness and  $t$  is time. The equation (2) permits the oil pressure to become negative, i.e. lower than ambient pressure, when the relative motion of slide and saddle causes growth of the oil film thickness. In reality, the oil contains dissolved air, which cavitates when pressure drops slightly below atmospheric pressure. The air can also enter the volume of the oil film from the boundaries, also causing fluid film rupture. The simplest way to account for cavitation and air entrance is to restrict the oil film pressure to positive values with respect to the atmospheric pressure.

### 3. Numerical analysis of the oil film

The Reynolds equation (2) was solved by means of finite elements method. The mesh of the single surface of the dovetail groove was created using quadrilateral isoparametric elements; see fig. 2. The elements displayed in red belong to the oil feed groove. This groove is very deep ( $\sim 1$  mm) compared to the film thickness of the rest of the surface plotted in blue. The volume of the oil feed groove serves as the lubricant reservoir delivering the oil to the entire surface. With regards to the big volume of the oil feed groove, the boundary conditions prescribing ambient pressure to all feed groove nodes as well as to the surface boundary nodes were applied. The oil supplied to the tool rest is delivered periodically in small amounts of oil compared to the total volume of the feed grooves and oil ducts inside tool rest bodies.

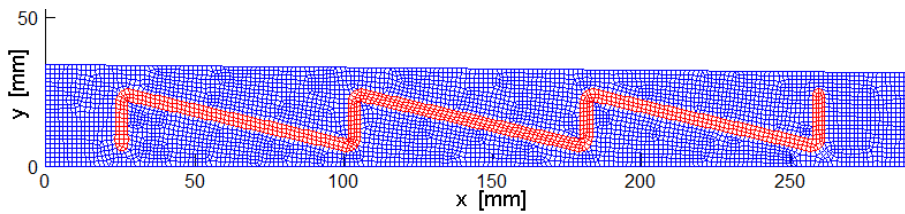


Fig. 2: Mesh of the single surface of the dovetail groove geometry.

Weak solution of the pressure is obtained by solving set of linear equations  $\mathbf{K} \cdot \mathbf{P} = \mathbf{F}$ , where matrix  $\mathbf{K}$  and right-hand side vector  $\mathbf{F}$  are composed of elemental *stiffness* matrix and elemental forcing vector calculated as

$$K_{ij}^{\{e\}} = - \int_{\Omega} H^3 \left( \frac{\partial e_i}{\partial \xi} \frac{\partial e_j}{\partial \xi} + \frac{\partial e_i}{\partial \eta} \frac{\partial e_j}{\partial \eta} \right) d\Omega, \quad F_j^{\{e\}} = 120 \mu_R \int_{\Omega} \frac{\partial H}{\partial \tau} e_j d\Omega. \quad (4)$$



Example of calculated weak solution of the pressure profile is depicted in Fig. 3.

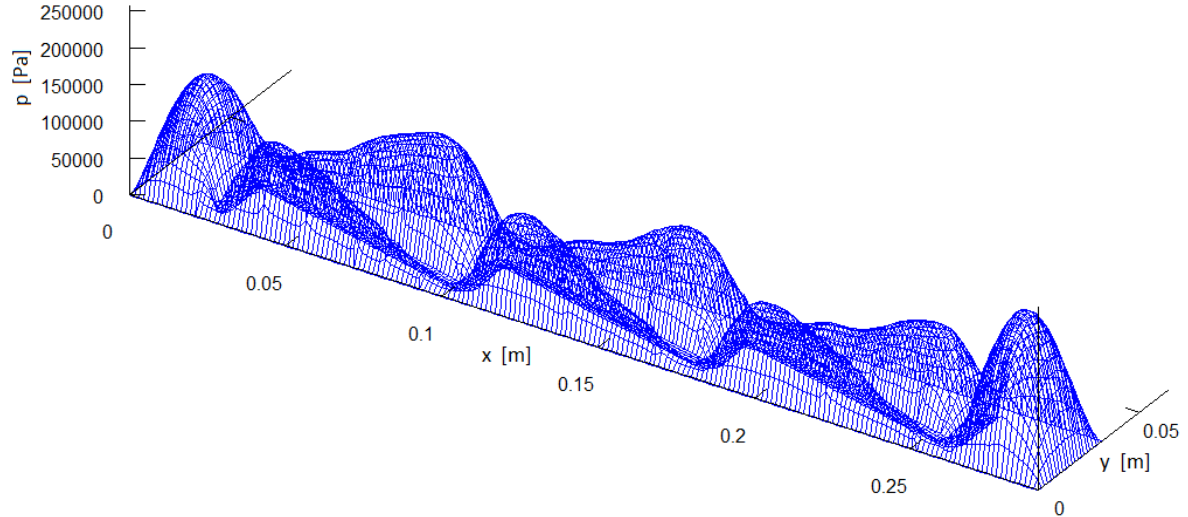


Fig. 3: Example of the weak solution of pressure profile of dovetail groove surface.

Integral of the pressure distribution over groove surface provides resultant of the hydrodynamic force, by which the slide and the saddle interact during defined relative motion. The equation (2) is linear, so the force interaction can be described by means of linear damping coefficients dependant on clearance and lubricant viscosity, provided that the amplitudes of relative motion are small with respect to the actual clearance. Damping coefficients evaluated from series of analyses are plotted in the Fig. 4.

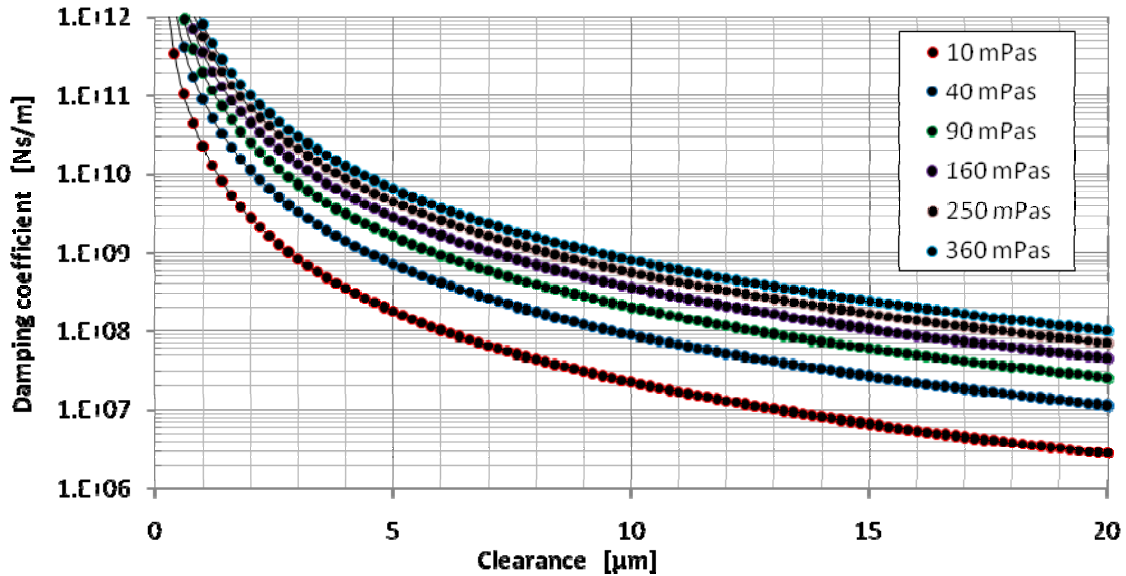


Fig. 4: Damping coefficients of single surface of dovetail groove.

#### 4. Model of the tool rest

Model of the tool rest was built by means of Craig-Bampton substructuring technique. Normal modes along with boundary nodes were calculated from finite elements models of those parts. Boundary nodes had been chosen, such that each functional surface of dovetail groove contained 6 of them evenly distributed along the length ( $x$ ) of the surface. Adjacent nodes of both bodies have been linked via linear dampers, whose damping coefficients have been selected according to results of HDL analysis (one twelfth of the values in the Fig. 4; Due to gaseous cavitation of the lubricant, the oil film damper works only when the oil film is being squeezed). Frequency response functions (FRF) were calculated from results of transient analysis of the model being excited by sine sweep signal at location 6 in direction  $y$  (Fig. 1).

## 5. Comparison to experimental data

FRF were also obtained experimentally on tool rest hardware in configuration corresponding to the analyzed case. Sine sweep, random signal and impact hammer signal were used. Some of the calculated and experimental frequency response functions are depicted in Fig. 5.

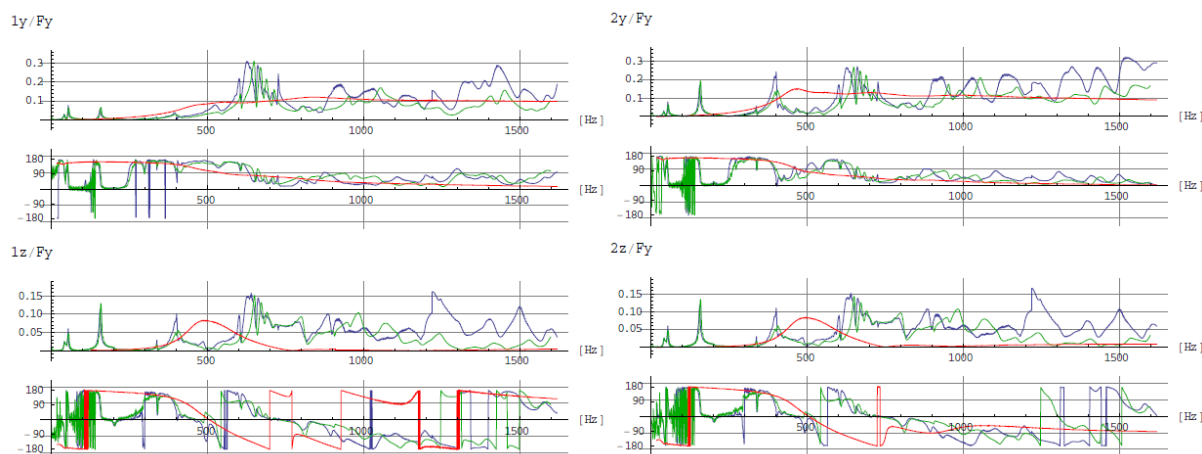


*Fig. 5: Frequency response functions: Amplitudes [ $\text{ms}^{-2}/\text{N}$ ] and phases [deg] of inertance; Red: Numerical results (linear model), Blue: Experimental results (harmonic sweep), Green: Experimental results (impact hammer).*

The measured peaks in amplitude of inertance lower than 250 Hz have been proven to have origin in finite stiffness of saddle clamping to heavy cast iron block. In the numerical model, the saddle was clamped by rigid restraints. Amplitude peaks that occur at higher frequencies are influenced by nonlinearity of the system and its polyharmonic response to a harmonic excitation. Agreement of the experimental and calculated data is better for direction y at locations 1 and 2 than in the lateral direction z. In the former direction, the nonlinear system of tool rest is reasonably approximated by linear model. Potential cause of greater discrepancies in the latter case is the asymmetry of tested hardware, especially the presence of wedge at one side of saddle, by which the groove clearances are set up.

## 6. Conclusions

Analysed tool rest exhibited significant nonlinear behaviour confirmed by experiments. Presented linear model provides estimation of frequency characteristics for models of machining process for investigation of its stability formulated in the frequency domain; however the agreement of numerical and experimental results varies upon different locations and directions of the sensor. The outcomes foreshow that further improvement of the tool rest model should be made by taking into account nonlinear forces, originating in fluid film and mechanical contacts. Such complex models would not be accessible in frequency domain.

## Acknowledgements

Authors would like to thank the company Tajmac-ZPS, a.s. for permission to publish this part of joint project. Project 2A-2TP1/038 “Nové metody a postupy při využití mechatronických prvků v konstrukci a stavbě obráběcích strojů” was generously supported by Ministry of Industry and Trade of the Czech Republic.

## References

- Altintas, Y., Brecher, C., Weck, M. & Witt, S. (2005) Virtual Machine Tool. CIRP Annals - Manufacturing Technology, 54, 2, pp. 115-138, ISSN 0007-8506.
- Bilkay, O. & Anlagan, O. (2004) Computer simulation of stick-slip motion in machine tool slideways. Tribology International, 37, 4, pp. 347-351, ISSN 0301-679X.
- Turkes, E., Orak, S., Neseli, S. & Yaldiz, S. (2011) Linear analysis of chatter vibration and stability for orthogonal cutting in turning. International Journal of Refractory Metals and Hard Materials, 29, 2, pp. 163-169, ISSN 0263-4368.

## THE SORPTION OF HYDROCARBONS IN THE CONDITIONS OF COAL MOISTENING

O. V. Skopintseva \*

**Abstract:** *Here it has been presented a method of efficiency improvement of preliminary coal massive moistening. This method is that thermal chemical treatment of coal massive used to decrease dust formation at the process of coal extraction, coal seam degasification as well as to reduce coal hardness. It has been carried out a chromatographic analysis of both dry coal samples (seam E<sub>5</sub>, coal rank F, Kuzbass) and coal from the same after thermal treatment, using chemical agents. Optimal concentration of penetrating agent has been estimated. The developed method is recommended at coal mines having highly gas-containing seams, which are dangerous because of coal dust explosions.*

**Keywords:** *Methane, sorption, desorption, coal moistening, chromatographic analysis.*

### 1. Introduction

In the problem of dust control in coal mines hydro-dust removal occupies a leading position, forming the basis of anti-dust complex. In this set of actions moistening of a massive plays an important role. It prevents the ingress of dust into the air by reducing the dust-raising capacity of coal. Pre-moistening of coal seams was first used in coal mines in 1980 as a means to prevent dust explosion. Later this method was replaced by rock dusting, and only in the mid 1930-s it was again used in Ruhr (Germany), and then in other basins all over the world. In Russia, the first experiments on the moistening of layers were carried out 1935.

The choice of measures for dust suppression is determined on the basis of mining and geological conditions, depending on the specific dust emission during the destruction of a rock massive. According to the Rules of Safety in coal mines in order to reduce dust emission while conducting clearing and preparation works, preliminary moistening should be carried out in a coal massive if the specific dust emission is more than 50 g/t.

### 2. Methods

Studying the experience of pre-moistening of coal revealed that the main reasons for the low efficiency of the method is the low wettability of the coal surface, as well as uneven distribution of injected moisture in the seam. One of the ways to improve its efficiency is thermal treatment of a coal massive, using chemical agents (TVHO) (Kudryashov, 1991; Skopintseva, 2006). It increases the moisture content and evenness of coal massive moistening; physical and chemical effects reduce dust formation when extracting coal; coal hardness decreases as well as coal degasation. This is achieved by capillary absorption of liquid into narrow cracks and pores in the movement of moisture in the direction of temperature gradient and concentration gradient of a penetrating agent.

In the process of pre-moistening of coal seams a balance in a coal-methane system is upset. Under the pressure of liquid, free gas is forced out of large cracks and pores into smaller ones, where gas is in absorbed and free state. When coal is moistened with surface active substances, absorbed gas can be forced out.

The results of moistening of gas-saturated coal with water has been studied for more than 70 years. A lot of scientists have studied the behavior of gas-saturated coals when their moisture content has been

---

\* prof. Olga V. Skopintseva: Moscow State Mining University, Street Leninski. 6. 119991 Moscow; Russia, e-mail: skopintseva54@mail.ru

changed. The results of these experiments differ from each other both in quality and quantity. So far there hasn't been developed a unified theory of moistening of gas-saturated coal.

Some scientists have recorded a decrease of gas emission out of wet coal, admitting that methane is blocked by water in pores and crevices, others have seen increasing gassing after coal moistening, assuming that moisture assists in the desorption of methane.

The analysis of vast and contradictory experimental data has shown that moistening of gas-saturated coal cannot be simply taken as a single elementary action – methane replacing and its blocking. As a result of generalization of numerous experimental data and research works carried out by Vasyuchkov (1986), it has been stated a provision about a three staged process of interactions in the system methane-carbon while treating it with water. The first stage – water filtering through macropores and crevices, filling them with water and free methane displacement; the second stage – capillary soaking, poros moistening and reducing of gas emission from coal; the third – water molecules diffusion coal and methane desorption.

In the real conditions the process of liquid sorption on the free gas-saturated coal and the absence of methane desorption based on the principle of substitution, is the most probable.

Under the sorption of dropping liquid, adhesion heat and heat of sorption are released. This heat helps the desorption of methane by increasing the temperature in the coal-gas system. This conclusion has been confirmed by research works carried out in Moscow State Mining University. It was found that within 1-2 days the increase of coal temperature after moistening is 1.8 °C, while after hydrochloric solution up to 3 °C (Kirin, 1983).

Thus, from the standpoint of thermodynamics, water helps the desorption of methane, but it cannot be a powerful means of gas extracting from the sorption volume, as it desorbes methane, mainly on the thermal basis. Introducing additives of surface-active substances into the working fluid, one can increase the rate of soaking, and therefore may reduce the time of seam degassing by increasing the rate of gas displacement from the sorption volume of coal.

To study the interactions in the "coal-liquid-gas" system we have carried out a chromatographic analysis of dry coal samples from the seam E5 (rank F, the coal seam Kolchuginsky series of Permian age, Kuzbass) and samples of the same coal seam after thermal treatment, using chemical agents.

For the experiments coal samples weighing 10 g seam E5 with fraction size from 0.5 to 1.0 mm. have been chosen. The samples were moistened with solution of surfactants "Neolas" in the following concentrations (%): 0, 0.15; 0.5; 0.75 1.0. There were prepared 10 samples: five of them were moistened with a solution at 25 °C, the other five - solution at 60 °C. The time of moistening was 24 hours. After that these coal samples were investigated by M-3700 chromatograph with a flame ionization detector. Liquid penetrating agent "Neolas" is an aqueous solution of a balanced mixture of anionic and nonionic surfactants as well as mineral supplements. "Neolas" is a colorless and odorless liquid. The mass fraction for this surfactant is  $20 \pm 1\%$  of active parts.

Fig. 1 shows the diagrams of the desorption of hydrocarbon gases (methane, ethane, propane), depending on the concentration of penetrating agent "Neolas" at 25 °C. The diagrams have the form of a parabola with a pronounced optimum concentration of moistening solution, equal to 0.5%, at which the residual gas content for all three investigated gases is minimal, compared with pure water and the concentration of penetrating agent 1 %. Consequently, for pure water and 1 % concentration of penetrating agent, blocking of methane by working fluid was observed. As a result, residual gas content of coal has risen relative to the untreated coal. From the figure it also follows that of the presented adsorbed gases, content of propane is the largest (more than 3 times higher than that of methane and ethane).

Fig. 2 shows the diagrams of the desorption of the same hydrocarbon gases (methane, ethane, propane) depending on the same concentration of the solution "Neolas", but at a different temperature of 60 °C. From the diagram a clear dependence between the residual gas content of coal and the concentration of penetrating agent can't be seen, i.e, at all studied concentrations of a penetrating agent, the residual gas content remained almost the same, except pure water. In this case, for methane and propane the value of the residual gas content decreased from 1.5 to 3 times. We can say that clean water degasses the best.

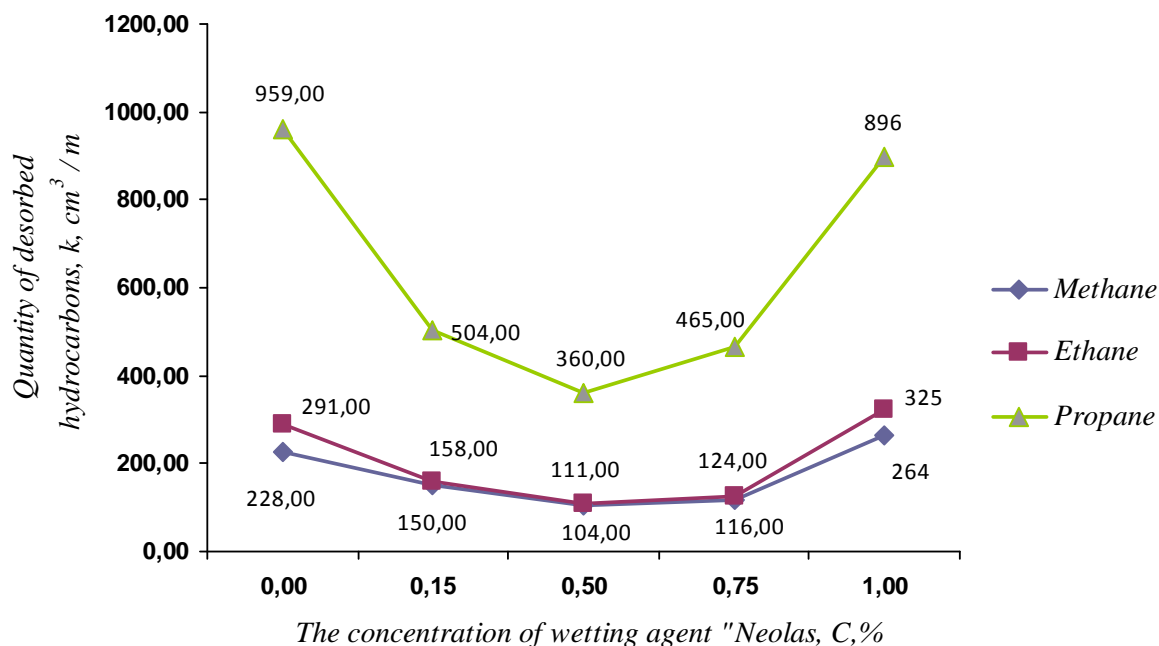


Fig. 1: The dependence of the desorption of hydrocarbons from coal, the concentration of wetting agent at a temperature of 25 °C.

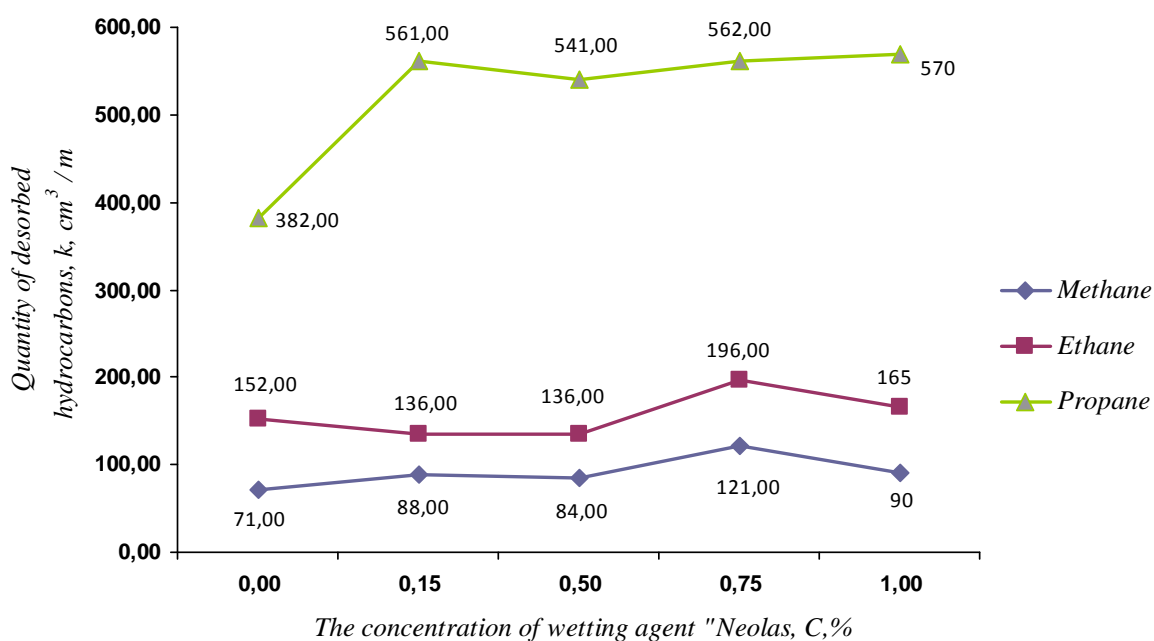


Fig. 2: The dependence of the desorption of hydrocarbons from coal, the concentration of wetting agent at a temperature of 60 °C.

### 3. Conclusions

One of the ways to improve the effectiveness of pre-moistening of a coal massive is its thermal treatment using chemical agents (TVHO), which aims to increase the humidity of the coal massive and the moistening more even. Chromatographic analysis of dry coal samples (seam E5) and coal samples of the same seam, treated with thermal method shows that the lowest residual gas content of coal has been determined at the concentration of penetrating agent 0.5% at 25 °C. At a temperature of 60 °C wetting clean water degasses the best.

The developed method of thermal treatment of a coal massive using chemical agents can be recommended at coal mines having highly gas-containing seams, which are dangerous because of coal dust explosions. The concentration of penetrating agent of 0.3-0.5% is optimal, in terms of reducing dust-raising capacity of coal and seam degassing .

## **References**

- Kirin B. F., Zhuravlev V. P., Ryzhih L. I. (1983) Measures of dust suppression in coal mines. - M: Nedra.
- Kudryashov V. V., Umantsev R. F., Shurinova M. K. (1991) Thermal dust-reducing treatment of a permafrost destroyed coal massive -M.: USSR Academy of Sciences.
- Skopintseva O.V., Prokopovich A.J., Gashenko A.O., Savinsky P.A. (2006) Scientific bases of thermal dedusting process in coal and solid rock. Mining information and analytical bulletin. - Moscow: Moscow State Mining University. - 2006. - Topics, etc. "Aerology.
- Vasyuchkov Y.F. (1986) Physico-chemical methods of coal seams degassing. -M.: Nedra.



## IMPELLER BLADE DESIGN BASED ON THE DIFFERENTIAL GEOMETRY

Z. Sloupenský\*, F. Pochylý\*

**Abstract:** A new method of blade design based on the previously determined meridional velocity field is introduced in this contribution. The aim of calculation is the spatial shape of the blade, based on the field of  $\beta$  angles across the blade. This field, obtained through the system of equations, originates from differential geometry principles. The blade angles prescribed on the leading and the trailing edges serve as the boundary conditions.

**Keywords:** Impeller blade, meridional section, curvilinear coordinate system, differential geometry.

### 1. Introduction

The commonly used way of pump designing consists of more or less interconnected steps. The results of calculations come from various numerical methods and are interpolated with simple or weighted polynomials or splines. Generally, sophisticated flow simulation program is not used until the basic design is finished. The centrifugal pumps are widely used in various applications and there are also intentions to enter new features (Choi et al., 2006). Large efforts were also made to streamline the process of pump design and to maximize the pump efficiency using CFD (Anagnostopoulos, 2009). Another field of improvements was defining the appropriate designing methods for the different ranges of pump usage (Kyparissis et al., 2009) or seeking for the designs with the best characteristics (Zhou et al., 2003).

The improved design approach, part of which is presented below, is based on the differential geometry in the curvilinear coordinate system. Its main aim is the interconnection of pump components based on the assumptions of flow in the early stages of the design. It would allow prevention of errors made in the initial stages of design, which consequently means time savings. Below presented paper deals with one part of the pump design, the blade design. The blade shape is closely connected with previously performed meridional cut design associated with determination of the meridional velocity.

### 2. Meridional velocity

The cornerstone of successful blade design is properly designed meridional section. The applied method uses meridional section defined as Bezier surface. Data computed in the intersections of the Bezier surface curves serve for the characterization of flow.

Consider curvilinear coordinate system  $u, v \in \langle 0, 1 \rangle$ ;  $w = \varphi \in \langle 0, 2\pi \rangle$  (Brdička et al., 2005).  $\mathbf{g}_i$  denotes the vector tangent to the appropriate coordinate curve, see Fig. 1. The coordinate curves are not generally orthogonal. The calculations presented below require mutually orthogonal vectors  $\mathbf{g}_i$ . Such orthogonalization can be performed by following equation, (Sloupenský, 2010):

$$\mathbf{c}(t) = \left( \mathbf{g}_1 - \frac{\mathbf{g}_1 \cdot \mathbf{g}_2}{\mathbf{g}_2 \cdot \mathbf{g}_2} \mathbf{g}_2 \right) \frac{du}{dt} \quad (1)$$

---

\* Ing. Zdeněk Sloupenský and prof. Ing. František Pochylý, CSc: Victor Kaplan Department of Fluid Engineering, Brno University of Technology, Technická 2896/2; 602 00, Brno; CZ, e-mails: ysloup00@stud.fme.vutbr.cz, pochyl@fme.vutbr.cz

Initial assumption and boundary conditions:

$$\mathbf{c} \cdot \mathbf{g}_2 = 0 \quad (2)$$

$$v = v_0; u = 0 \quad (3)$$

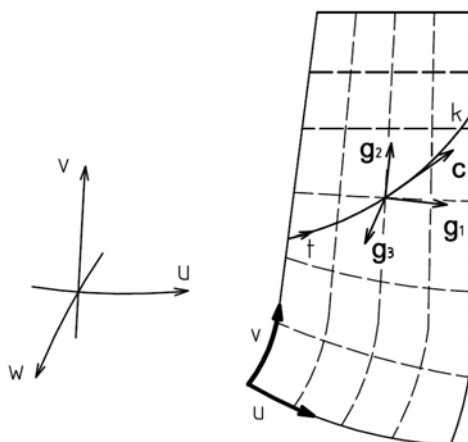


Fig. 1: Curvilinear coordinate system.

The interior of the meridional section is determined by iterative method of progressive selection according to required flow in the specific area of the impeller. It is possible to obtain required values of meridional velocity in different parts of the impeller through this procedure. The flow assumptions of rotational, quasi-potential and potential flow and adjustment of the flow within the curvilinear coordinate system are described in (Sloupenský & Pochylý, 2010). Equations which determine the system of coordinate curves for potential, rotational and quasi-potential flow are presented in this reference.

### 3. Spatial form of the blade

The blade proper performance is ensured by its spatial shape. This is based on the  $\beta$  angles of the velocity triangles in each of the points of the blade. It is necessary to know some initial conditions to define those angles. The  $\beta$  angles entered in six points on the blade serve for this purpose. Three of them are specified on the leading edge and three of them on the trailing edge, see Fig. 2.

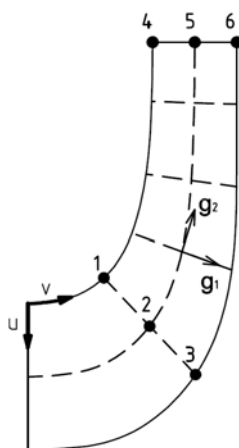


Fig. 2: Location of the entered points.

To calculate angles across the blade the polynomial (4) is used. Changes in the longitudinal direction  $v$  are linear and in the traverse  $u$  quadratic. Experiments were also carried out with quadratic definition in the longitudinal direction. However, the results were poor.

$$\beta(u, v) = A_1 + A_2u + A_3v + A_4uv + A_5u^2 + A_6u^2v \quad (4)$$

There are six unknown variables in the previous equation. The prescribed values of  $\beta$  angles shall serve as the boundary conditions. It is recommended to take into account the total length of the blade during the procedure. Excessive length could cause substantial friction losses.

$$\begin{bmatrix} 1 & u_1 & \cdots & u_1^2 v_1 \\ 1 & u_2 & \cdots & u_2^2 v_2 \\ \vdots & \vdots & \ddots & \vdots \\ 1 & u_6 & \cdots & u_6^2 v_6 \end{bmatrix} \begin{bmatrix} A_1 \\ A_2 \\ \vdots \\ A_6 \end{bmatrix} = \begin{bmatrix} \beta_1 \\ \beta_2 \\ \vdots \\ \beta_6 \end{bmatrix} \quad (5)$$

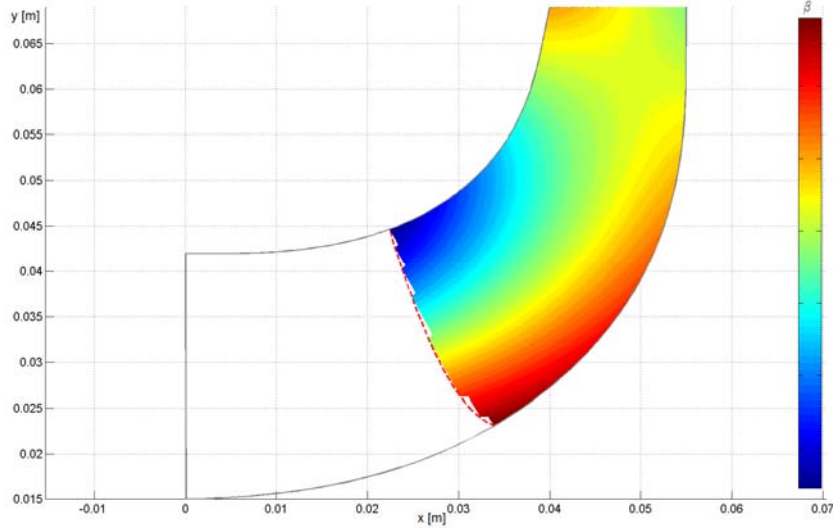


Fig. 3: Example of calculated values.

Lets say, surface  $u = \text{const.}$  It is possible to design the blade shape based on this assumption and with known  $\beta(u, v = \text{const.}) = \beta(v)$ , see Fig. 3.

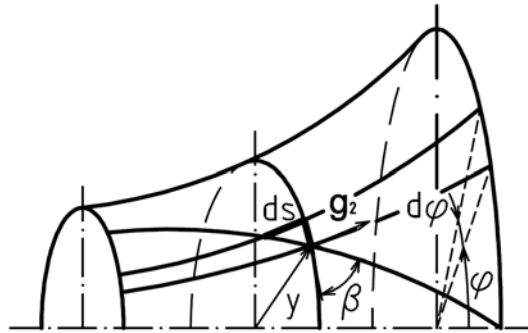


Fig. 4: Calculation of the blade from the trailing edge.

$$\tan \beta = \frac{ds}{y d\phi} = - \frac{|\mathbf{g}_2| du}{y d\phi} \quad (6)$$

$$\frac{d\phi}{du} = - \frac{|\mathbf{g}_2|}{y} \cot \beta \quad (7)$$

Boundary conditions:

$$u = u_i \quad (8)$$

$$\phi = f(\zeta) \quad (9)$$

$$y = r_2 \quad (10)$$

Where  $\zeta$  is prescribed trailing edge angle.

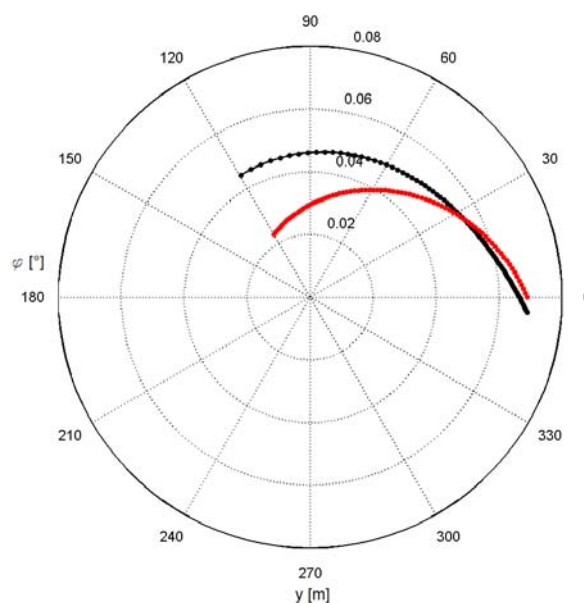


Fig. 5: Example of the blade curvature on the shroud (black line) and on the hub (red line).

#### 4. Conclusions

The computational procedure introduced in this paper offers the possibility to control the blade spatial shape. The blade spatial shape is controlled by the values of the blade angles prescribed on the leading and the trailing edges and by the trailing edge angle. The blade shape is also interconnected with previously designed meridional section. The initial values mostly serve only for the preliminary blade rendering. The following procedure is the step by step adjustment of the prescribed values until the desired shape is obtained. It is possible to transfer the final blade shape into one of the flow simulation programs.

#### Acknowledgement

Support of following grant projects is gratefully acknowledged:

FR-TI1/418 Research of impeller pumps

The specific research for the year 2011 supported by Faculty of Mechanical Engineering, Brno University of Technology.

#### References

- Anagnostopoulos, J. S. (2009) A fast numerical method of flow analysis and blade design in centrifugal pump impellers. *Computer & Fluids*, vol. 38, pp 284 – 289.
- Brdička, M., Samek, L. & Sopko, B. (2005) *Continuum Mechanics*. Academia, ISBN 80-200-1344-X, (in Czech).
- Choi, Y., Kurokawa, J. & Matsui, J. (2006) Performance and Internal Flow Characteristics of a Very Low Specific Speed Centrifugal Pump. *Journal of Fluids Engineering*, vol. 128, pp. 341 – 349.
- Kyparissis, S. D., Margaritis, D. P., Panagiotopoulos, E. E. & Filios, A. E. (2009) CFD Analysis on the Effects of the Blade Design Method to the Centrifugal Pump Performance. *International Review of Mechanical Engineering (I.R.E.M.E.)*, Vol. 3, N. 5, pp. 553 – 561.
- Sloupenský, Z. & Pochylý, F. (2010) The meridian velocity flow field within the impeller. in: *Proc. 13<sup>th</sup> Int. Conf. on Mechanical Engineering 2010*, Bratislava, ISBN 978-80-227-3304-5, pp. S40-60 – 67.
- Sloupenský, Z. (2010) Design of centrifugal pump using methods of differential geometry. Essay of Ph.D. thesis, FME BUT, Brno, ID 87790, (in Czech).
- Zhou, W., Zhao, Z., Lee, T. S., Winoto, S. H. (2003) Investigation of Flow Through Centrifugal Pump Impellers Using Computational Fluid Dynamics. *International Journal of Rotating Machinery*, 9(1), pp. 49 – 61.

## ON APPLICATIONS OF GENERALIZED FUNCTIONS TO CALCULATION OF THIN CYLINDRICAL SHELLS

J. Sobotka<sup>\*</sup>

**Abstract:** *The mathematical model of a thin cylindrical shell according to Timoshenko and Love bending theory contains derivatives of generalized internal forces and deformation components. However these derivatives are not defined at such points between ends of the shell where a concentrated loading or an internal support or coupling is located. In order that the mathematical model of a thin cylindrical shell subjected to axisymmetric loading may hold true at the points of discontinuity mentioned, which are common in calculating experience, we have used the distributional derivative for the unknown quantities, and developed a generalized mathematical model in the form of a system of ordinary differential equations (SODE). We have found the general solution to the SODE by using the Laplace transform method and symbolic programming approach. The solution found is a generalization of Krylov functions method.*

**Keywords:** *Thin cylindrical shell, discontinuities, Dirac singular distribution, Heaviside step function.*

### 1. Introduction

Solving analytically a thin cylindrical shell subjected to an axisymmetric bending with discontinuous loading, support or geometry, we at first divide it into segments without discontinuities. Then, we find continuous solutions with integration constants for each shell segment separately. Finally, we determine integration constants using boundary conditions and continuity conditions among shell segments.

Applying distributional derivative (Schwartz, 1966) for the transverse shear force per unit length, the axial bending moment per unit length, and for the angle of rotation of a middle-surface normal in a meridian plane, we can derive a generalized mathematical model of the thin-walled cylindrical shell with discontinuities in loading, support and geometry that may be solved like only one differential problem without dividing shells into cylindrical segments, and without using continuity conditions.

### 2. The classical mathematical model of an axisymmetric bending of the thin cylindrical shell

According to the Love-Timoshenko shell bending theory (Love, 1944; Timoshenko, 1959), a system of differential equations describing axisymmetric bending of thin cylindrical shells may be composed of four ordinary differential equations of the first order (Höschl, 1971; Markuš, 1982; Němec et al., 1989) as follows

$$\frac{d}{dx} T(x) = p_n(x) - \frac{N_t(x)}{r}, \quad (1)$$

$$\frac{d}{dx} M_a(x) = T(x), \quad (2)$$

$$\frac{d}{dx} \phi(x) = \frac{M_a(x)}{D}, \quad (3)$$

$$\frac{d}{dx} w(x) = \phi(x), \quad (4)$$

---

<sup>\*</sup> Ing. Jiří Sobotka, ČEZ, a.s., 67550 Dukovany, tel. +420 561 10 5234, e-mail: jiri.sobotka@cez.cz

for

$$\left(\frac{d}{dx} w(x)\right)^2 \ll 1, \quad \frac{w(x)}{r^2} \approx 0, \quad (5)$$

where

$T(x)$	transverse shear force per unit length,
$M_a(x)$	axial bending moment per unit length,
$\phi(x)$	angle of rotation of a middle-surface normal in a meridian plane,
$w(x)$	radial displacement component,
$p_n(x)$	surface loading in normal direction to the middle surface,
$N_t(x)$	membrane normal force per unit length in the circumferential direction,
$r$	radius of the middle surface of the shell,
$D$	shell wall bending stiffness,
$x$	axial coordinate.

Equations (1), (2) are equilibrium conditions of a shell element cut out in the undeformed shape. The equation (3) expresses relationship between the axial bending moment per unit length and a middle-surface curvature change supposing (5). Membrane normal force per unit length acting in the circumferential direction may be expressed as follows

$$N_t(x) = \frac{E w(x) h}{r} + \mu N_a, \quad (6)$$

where

$E$	Young's modulus,
$\mu$	Poisson's ratio,
$h$	thickness of the shell wall,
$N_a$	axial membrane normal force per unit length.

### 3. The generalized mathematical model of axisymmetric bending of the thin cylindrical shell

Concentrated radial circumferential-line force loadings per unit length and concentrated supports along circumferential lines situated between ends of the shell may cause jump discontinuities of the transverse shear force per unit length. Concentrated circumferential-line moment loadings placed between ends of the shell may cause jump discontinuities of the bending moments per unit length. Circumferential hinges connecting cylindrical shell segments may cause jump discontinuities of the angle of rotation of the middle-surface normal in a meridian plane.

Classical derivatives (1) to (3) do not hold true at points of the jump discontinuities mentioned because quantities  $T(x)$ ,  $M_a(x)$  and  $\phi(x)$  were supposed to be continuous. In order to remove this inconsistency, we have used the distributional derivative (Kanwal, 2004; Štěpánek, 2001) for discontinuous unknown quantities  $T(x)$ ,  $M_a(x)$ ,  $\phi(x)$ , and regarding (6), we have derived the following generalized mathematical model

$$\frac{d}{dx} T(x) = p_n(x) - \frac{\mu N_a}{r} - \frac{E w(x) h}{r^2} + \left( \sum_{i=1}^{n_1} F_i \text{Dirac}(x - a_i) \right) - \left( \sum_{i=1}^{n_2} R_i \text{Dirac}(x - b_i) \right), \quad (7)$$

$$\frac{d}{dx} M_a(x) = T(x) + \left( \sum_{i=1}^{n_3} C_i \text{Dirac}(x - g_i) \right), \quad (8)$$



$$\frac{d}{dx} \phi(x) = \frac{M_a(x)}{D} + \left( \sum_{i=1}^{n_4} \Phi_i \text{Dirac}(x - k_i) \right), \quad (9)$$

$$\frac{d}{dx} w(x) = \phi(x), \quad (10)$$

where

$F_i$	i-th concentrated radial circumferential-line force loading per unit length,
$R_i$	i-th concentrated radial circumferential-line reaction force per unit length,
$C_i$	i-th concentrated circumferential-line moment loading per unit length,
$\Phi_i$	magnitude of a jump discontinuity of $\phi(x)$ at i-th circumferential hinge connection of shell segments,
$n_1$	number of concentrated radial circumferential-line force loadings,
$n_2$	number of concentrated radial circumferential-line reaction forces,
$n_3$	number of concentrated circumferential-line moment loadings,
$n_4$	number of circumferential hinge connections of cylindrical shell segments,
$\text{Dirac}(x-x_0)$	Dirac singular distribution moved to $x = x_0, x_0 > 0$ .

#### 4. The general solution to the generalized system of differential equations (7) to (10)

First, we introduce an auxiliary constant as follows

$$\Omega^4 = \frac{E h}{4 r^2 D}, \quad (11)$$

where the shell wall bending stiffness is

$$D = \frac{E h^3}{12 (1 - \mu^2)}. \quad (12)$$

Applying the Laplace transformation to equation (7) to (10) with respect to  $x$ , we obtain an algebraic system from which we can find the Laplace transforms of all four unknown quantities. Regarding the short extent of this paper, we have presented here only the Laplace transform of the radial displacement component as follows

$$\begin{aligned} \text{laplace}(w(x), x, p) = & \frac{p^3 w(0)}{(2 \Omega^2 - 2 \Omega p + p^2) (2 \Omega^2 + 2 \Omega p + p^2)} + \frac{p^2 \phi(0)}{(2 \Omega^2 - 2 \Omega p + p^2) (2 \Omega^2 + 2 \Omega p + p^2)} \\ & + \frac{p M_a(0)}{(2 \Omega^2 - 2 \Omega p + p^2) (2 \Omega^2 + 2 \Omega p + p^2) D} + \frac{T(0)}{(2 \Omega^2 - 2 \Omega p + p^2) (2 \Omega^2 + 2 \Omega p + p^2) D} \\ & + \frac{\sum_{i=1}^{n_1} e^{(-p a_i)} F_i}{(2 \Omega^2 - 2 \Omega p + p^2) (2 \Omega^2 + 2 \Omega p + p^2) D} - \frac{\sum_{i=1}^{n_2} e^{(-p b_i)} R_i}{(2 \Omega^2 - 2 \Omega p + p^2) (2 \Omega^2 + 2 \Omega p + p^2) D} \\ & + \frac{p \left( \sum_{i=1}^{n_3} e^{(-p g_i)} C_i \right)}{(2 \Omega^2 - 2 \Omega p + p^2) (2 \Omega^2 + 2 \Omega p + p^2) D} + \frac{p^2 \left( \sum_{i=1}^{n_4} e^{(-p k_i)} \Phi_i \right)}{(2 \Omega^2 - 2 \Omega p + p^2) (2 \Omega^2 + 2 \Omega p + p^2)} \\ & - \frac{\mu N_a}{(2 \Omega^2 - 2 \Omega p + p^2) (2 \Omega^2 + 2 \Omega p + p^2) D r p} + \frac{\text{laplace}(p_n(x), x, p)}{(2 \Omega^2 - 2 \Omega p + p^2) (2 \Omega^2 + 2 \Omega p + p^2) D} \end{aligned} \quad (13)$$

where  $p$  is a complex variable. Converting the right side of (13) into partial fractions and applying the inverse Laplace transformation, we can express the radial displacement component as follows

$$\begin{aligned}
w(x) = & \cosh(\Omega x) \cos(\Omega x) w(0) + \frac{(\sinh(\Omega x) \cos(\Omega x) + \cosh(\Omega x) \sin(\Omega x)) \phi(0)}{2 \Omega} \\
& + \frac{1}{2} \frac{\sin(\Omega x) \sinh(\Omega x) M_a(0)}{\Omega^2 D} + \frac{1}{8} \frac{(2 \cosh(\Omega x) \sin(\Omega x) - 2 \sinh(\Omega x) \cos(\Omega x)) T(0)}{\Omega^3 D} \\
& + \frac{\sum_{i=1}^{n_1} \text{Heaviside}(x - a_i) (\cosh(\Omega (x - a_i)) \sin(\Omega (x - a_i)) - \sinh(\Omega (x - a_i)) \cos(\Omega (x - a_i))) F_i}{4 \Omega^3 D} \\
& + \frac{\sum_{i=1}^{n_2} (-\cosh(\Omega (x - b_i)) \sin(\Omega (x - b_i)) + \sinh(\Omega (x - b_i)) \cos(\Omega (x - b_i))) \text{Heaviside}(x - b_i) R_i}{4 \Omega^3 D} \\
& + \frac{\sum_{i=1}^{n_3} \sinh(\Omega (x - g_i)) \sin(\Omega (x - g_i)) \text{Heaviside}(x - g_i) C_i}{2 \Omega^2 D} \\
& + \frac{\sum_{i=1}^{n_4} \text{Heaviside}(x - k_i) \Phi_i (\sinh(\Omega (x - k_i)) \cos(\Omega (x - k_i)) + \cosh(\Omega (x - k_i)) \sin(\Omega (x - k_i)))}{2 \Omega} \\
& + \frac{1}{4} \frac{\mu (-1 + \cosh(\Omega x) \cos(\Omega x)) N_a}{\Omega^4 D r} \\
& + \int_0^x \frac{1}{4} \frac{p_n(\xi) (\cosh(\Omega (x - \xi)) \sin(\Omega (x - \xi)) - \sinh(\Omega (x - \xi)) \cos(\Omega (x - \xi)))}{\Omega^3 D} d\xi
\end{aligned} \tag{14}$$

## 5. Conclusions

The contribution of this paper is that the generalized mathematical model of a thin cylindrical shell (7) to (10) holds true also for discontinuous graphs of the transverse shear force per unit length, the axial bending moment per unit length, and the angle of rotation of the middle-surface normal in a meridian plane caused by concentrated radial circumferential-line force loadings, concentrated supports along circumferential lines, concentrated circumferential-line moment loadings situated between ends of the shell, and circumferential hinges connecting cylindrical shell segments. The jump discontinuities of the unknown quantities have been expressed using Dirac singular distribution at the right side of Eq. (7) to (9). In order to determine magnitudes of the unknown jump discontinuities owing to the supports or hinges between ends of the shell, we have to use deformation conditions at points of these discontinuities. The general solution to the Eq. (7) to (10) has been computed using the Laplace transform method and symbolic programming approach, and has been partly presented in (14). The integration constants have got the form of initial parameters, and may be determined using boundary conditions. The jump discontinuities of the axisymmetric radial surface loading  $p_n(x)$  may be expressed using Heaviside step function.

## References

- Höschl, C. (1971) Mechanics of solids in mechanical engineering (in Czech). SNTL, Praha.
- Kanwal, R. P. (2004) Generalized Functions. Birkhäuser, Boston.
- Love, A. E. H. (1944) A treatise on the mathematical theory of elasticity. Dover Publ., N.Y.
- Markuš, Š. (1982) Mechanics of vibrations of cylindrical shells (in Slovak). VEDA, Bratislava.
- Němec, J., Dvořák, J. & Höschl, C. (1989) Mechanics of solids in mechanical engineering (in Czech). SNTL, Praha.
- Schwartz, L., (1966) Theory of distributions (in French). Hermann, Paris.
- Štěpánek, J. (2001) Distributions and differential equations (in Czech). Karolinum, Praha.
- Timoshenko, S. (1959) Theory of plates and shells. McGraw-Hill, N.Y.

## LOADING TO STRUCTURES BY REMOTE EXPLOSION

**E. Sochorová\*, M. Foglar\*, V. Křístek\*, A. Kohoutková\***

**Abstract:** *There are many events which are not solved as extreme design situations in present standards used for bridge design, maintenance and refurbishment - the safety of the users must be a priority of the bridge design. Explosions which endanger bridges can be caused by two cases – an explosion due to terrorist attack and the explosion due to an accident. It is necessary to study both of these cases. The blast loading of a structure can cause fatalities due to the blast wave and possible consequent progressive collapse. The paper summarizes numerical methods used for evaluation of fast dynamic phenomena and methods for determination of substitute loading of an explosion adjacent to a structure.*

**Keywords:** *Design situation, bridges, remote explosion, blast wave, computational tool.*

### 1. Methods for determination of substitute loading of an explosion

In a case of a remote explosion it is not necessary to perform sophisticated numerical simulations; the results can be obtained easily by the methods for determination of substitute loadings of an explosion. These allow us to specify loadings on structures according to position of the detonation epicentre and its strength. The damage of a structure can be then specified from the effect of this loading (Karasová et al., 2010).

#### 1.1. The procedure of solution

Moving solid is affected by inertial, damping and elastic forces. These forces are in equilibrium with external loading. The equation of motion (Eq. 1) is strongly time dependent.

$$M \cdot u''(t) + C \cdot u'(t) + K \cdot u(t) = p(t) \quad (1)$$

The solution of motion equation can be carried out easily by direct numerical integration. It is necessary to perform time discretization for the solution. The solution can be carried out by method of implicit or explicit time integration.

The effects of impulse waves can be evaluated by empirical methods. These methods are based on reduced and dimensionless characteristics. The basis for the solution of the impulse wave parameters became “cube root law” Eq. (2), by Hopkinson (1915). If two charges of same material and geometry, but different weight detonate, they produce similar impulse waves in the same reduced distances. A reduced distance  $Z$  is approximated by formula

$$Z = \frac{R}{W^{1/3}} \quad (2)$$

where  $R$  is the epicenter distance,  $W$  explosive weight (TNT equivalent)

Many formulae by different authors exist for overpressure in the front of impulse wave. One of the most widely used formulae is based on equations developed by Russian authors and given by

$$p_+ = \frac{0,1}{Z} + \frac{0,43}{Z^2} + \frac{1,4}{Z^3} \quad (3)$$

where  $Z$  is the reduced distance Eq. (2),  $p_+$  is overpressure in the front of impulse wave.

---

\* Ing. Eva Sochorová, Ing. Marek Foglar, Ph.D., prof. Ing. Vladimír Křístek, DrSc. and prof. Ing. Alena Kohoutková, CSc.: Faculty of Civil Engineering, CTU Prague, Thákurova 7/2077; 166 29, Prague; CZ, e-mails: eva.sochorova@fsv.cvut.cz, marek.foglar@fsv.cvut.cz, kristek@fsv.cvut.cz, akohout@fsv.cvut.cz

The reflected wave - overpressure  $p_{ref}$  is created by normal impact of impulse wave on a barrier. The reflected wave loads the structure on the front side. The overpressure in reflected wave multiplies the overpressure in reflected wave 2 to 8 times for a given distance  $Z$ .

$$p_{ref} = 2p_+ + \frac{6p_+^2}{p_+ + 0,72} \quad (4)$$

### 1.2. The effect of instantaneous pulse

The univariant system can be represented by material, which is fixed to an immaterial post. By stretching (compressing) of the post, the force increases linearly, as long as the deflection obtains to the value of full elastic deflection  $v_e$ . The post is stretched by a constant force  $R_0$  as long as the post breaks. We expect that the system, which is impacted with an instantaneous pulse  $S$ , is at rest. The pulse gives the system an initial velocity  $v(0) = S/m$ . The material  $m$  has a kinetic energy of

$$K = \frac{1}{2}mv^2(0) = \frac{1}{2} \frac{S^2}{m} \quad (5)$$

and the work necessary for stretching the post to a deflection  $v_m$  is

$$L = \frac{1}{2}R_0v_e + R_0(v_m - v_e) \quad (6)$$

Equating  $K = L$ , the pulse can be formulated as

$$S_0 = \sqrt{mv_e R_0 (2k_m - 1)}; k_m = \frac{v_m}{v_e} \quad (7)$$

An overshoot to negative direction by  $v_m \geq 2v_e$  does not arise. The material should make undamped oscillation with an amplitude  $v_e$  around the new neutral position moved by  $v_t = v_m - v_e$ . Due to the influence of damping, the vibration amplitude is smaller. The vibration stops and the material stays at rest, deflected in constant deformation  $v_t$  from the starting position.

### 1.3. Determination of the dynamic coefficient

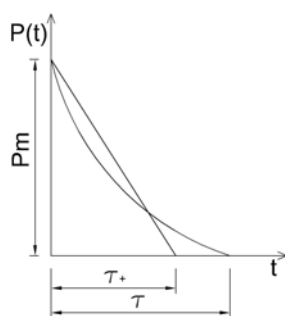


Fig. 1: A substitute of real impulse wave progress by a triangle.

If the impulse wave overpressure time  $t_+$  is big in comparison to the period of natural vibration  $T$  of the structural element, the maximal deflection arises in a fraction of total overpressure time  $t_+$ . Only small part of the curve  $P(t)$  reflects structural loading.

The solution for triangle force

$$P(t) = P\left(1 - \frac{t}{\tau_+}\right) \quad (8)$$

N. M. Newmark formulated following empirical formula for the dynamic coefficient:

$$\frac{1}{\delta} = \frac{T}{\pi \cdot \tau_+} \sqrt{2k_m - 1} + \frac{1 - \frac{1}{2k_m}}{1 + 0.7 \frac{T}{\tau}} \quad (9)$$

where  $T=2\pi/\omega$  – a period of natural vibration,  $\omega$  – radial frequency of natural vibration,  $\tau_+$  – an alternate pressure time,  $k_m = v_m / v_e$  – a modulus of ability of deformation,  $d = R_0 / P$  – a dynamic coefficient (a ratio of system resistance  $R_0$  and a maximal force  $P$ ).

## 2. Loading caused by remote explosion

A computational tool for assessing the effect of remote explosion was developed. It combines the described methods and produces comprehensive results. Several case studies for most important bridges in Prague were performed using this tool REMEX - <http://concrete.fsv.cvut.cz/~foglar/>.

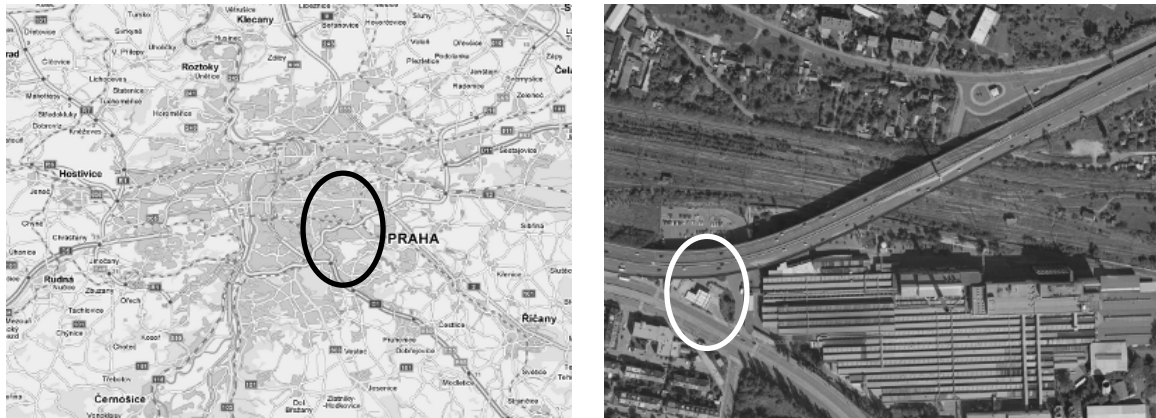
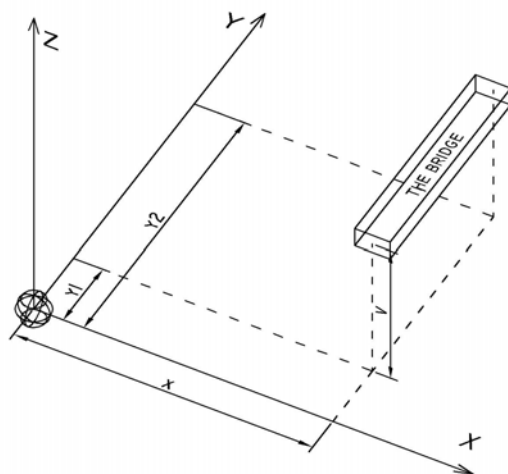


Fig. 2: Petrol station near the cable-stayed bridge in Prague (source: [www.mapy.cz](http://www.mapy.cz)).



### THE BRIDGE LOADING

#### THE CHARGE PARAMETERS

weight of the charge	W	50	kg
kind of the charge	Semtex	5	
the equivalent TNT charge weight	Cw	118.57	kg
the vertical distance to bridge axis	coordinate x	50	m

#### THE BRIDGE PARAMETERS

the lenght of the bridge		100	m
the bridge start	coordinate y <sub>1</sub>	-50	m
the bridge end	coordinate y <sub>2</sub>	50	m
the bridge elevation	coordinate z	8.5	m

Fig. 3: The input data for solution.

The rates of distant detonation (due to fire and consequent detonation of a petrol station) were analysed as well. The scheme (Fig. 3) shows determination of charge parameters and 3-D relations between epicentre and endangered structure (Sochorová E. & al. 2011).

Fig. 4 shows overpressure (underpressure) in front of impulse wave and loading of the bridge. These values are adequate for 50 kg of Semtex explosive placed 50 m far from the centre of a 100 m long bridge structure.

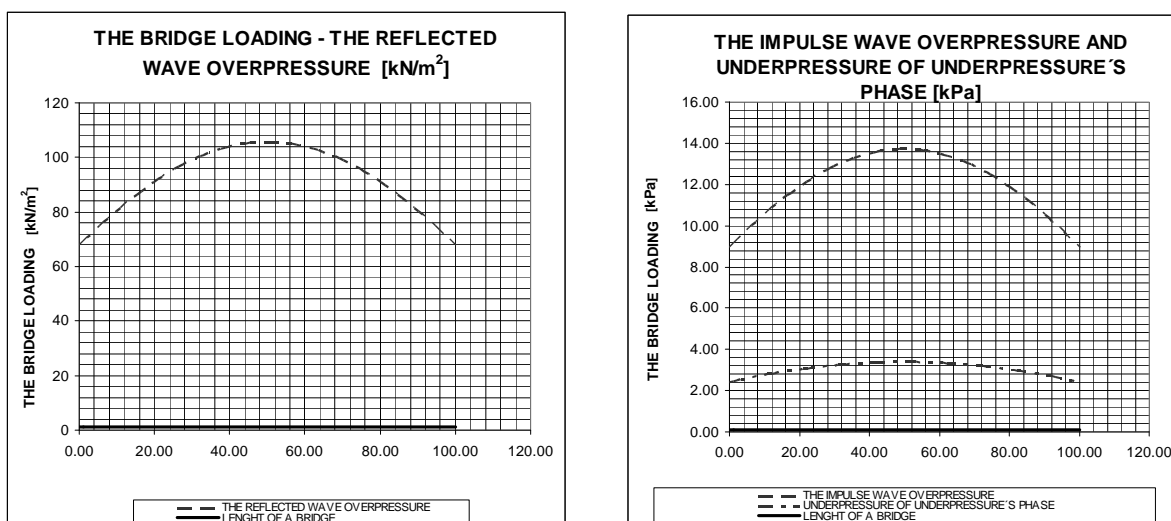


Fig. 4: Overpressure (underpressure) at the front of an impulse wave, loading of a bridge.

Another possible outcome of the explosion of the petrol station is the infringement of the foundation soil. One of the basic boundary conditions for using this tool is that the foundations of the bridge are not damaged by the explosion.

The values of overpressure and behaviour of the impulse wave were produced by the described computational tool. The caused loading can be used as extreme loading from the point of view of bridge design.

### 3. Conclusions

The paper summarized numerical methods used for evaluation of fast dynamic phenomena and methods for determination of substitute loading of an explosion adjacent to a structure.

### Acknowledgement

This outcome has been achieved with the financial support of the Ministry of Education, Youth and Sports, project Sustainable development No. VZ 04 CEZ MSM 6840770005. The support of the Grant Agency of the Czech Republic Grant Projects No. 103/09/2071 and the support of the CTU Prague research project No. SGS10/137/OHK1/2T/11 is also gratefully acknowledged.

### References

- Sochorová E. & al. (2011) Sensitivity of various structural systems of bridges to the pressure wave loading induced by remote explosion (czech), Natural hazards (optimalisation of protection, interaction with structures), CTU Press, Prague, pp. 129-134.
- Sochorová E. & al. (2011) The method of supplementary loading for evaluation of the effect of blast loading on bridges (czech), Natural hazards (optimalisation of protection, interaction with structures), CTU Press, Prague, pp. 129-134.
- Karasová E. & al. (2010) The Method of Supplementary Loading for evaluation of the effect of blast loading on bridges (czech), Bridges 2010, Sekurkon, Prague, pp. 266-270.
- Karasová E. & al. (2011) The effect of blast in bridge design, Reliability, Risk and Safety. Back to the Future, Taylor & Francis, London, pp. 1-8.



## TURBULENCE MODELS FOR SIMULATION OF FLOW OVER WEIRS

M. Spano<sup>\*</sup>, V. Stara<sup>\*</sup>

**Abstract:** *Weirs belong to one of most common water structures. Various shapes of weirs are used at various conditions (e.g. emergency spillway, river weir, volumetric weir, etc.). For estimation of the weir capacity and determination of discharge coefficient the physical modelling is usually performed. Recently, numerical simulations take place here too. The main advantages of numerical simulation compared to hydraulic research are the volume of information gained, relatively lower price, and no scale effects. However, results from simulations are strongly affected by the computation setup. The choice of turbulence model belongs to most important options. Within this study the flow over weir was simulated with seven flow models. Those were inviscid, laminar and seven turbulence models. The aim was to find the most suitable one. All simulations were compared with results from hydraulic research.*

**Keywords:** *Flow over weir, turbulence models, numerical simulations.*

### 1. Introduction

Simulations of flow were performed for a given 0.4 m height and 0.1 m thick weir. The problem was solved with commercial CFD software ANSYS-Fluent which uses a finite volume method (FVM). All achieved results were further compared with results from hydraulic research. Simulations were made for a flow rate of  $0.029 \text{ m}^3 \cdot \text{s}^{-1}$  because the water head (above the weir crest) of 0.1 m was measured at this flow rate. Thus, the weir thickness and water head ratio is equal to 1.0. Compared were water and total heads above the weir crest measured 0.5 m upstream of the weir and pressures along the weir crest. Shape and dimensions of the weir are shown in Fig. 1.

Hydraulic research was performed in a 0.4 m wide channel. A model of the weir was made from plexiglass. Water levels upstream of the weir were measured with a point gauge. Pressures along the weir surface were measured using piezometric holes. Various sets of measurements were performed within the hydraulic research. Detailed description of the hydraulic research is summarized in Koutková & Stara (2003).

### 2. Models of flow, boundary conditions and basic domain

Nine 2D models of incompressible open channel flow were used for simulation of flow over the weir. Short overview of used modes is summarized in Tab. 1. Detailed description of each model can be found in user guide Fluent Inc. (2006). Water levels were reconstructed with the volume of fluid (VOF) method. Water was considered viscous (except of inviscid flow) with a constant density of  $\rho_w = 998.2 \text{ kg} \cdot \text{m}^{-3}$  and viscosity  $\mu_w = 1.003 \cdot 10^{-3} \text{ Pa} \cdot \text{s}$ . The density and viscosity of air were also considered as constant.

Boundary conditions (BC) were set as a wall at the bottom, pressure outlet with zero gauge pressure at the outflow and at the top boundary. Velocity inlet BC was set up at the inflow as known velocity profile. In this case a uniform velocity of  $0.184 \text{ m} \cdot \text{s}^{-1}$  was used at lower 0.4 m of the boundary and  $0.0 \text{ m} \cdot \text{s}^{-1}$  at the rest part of the boundary. A detailed description of the boundary types and its application can be found in user guide Fluent Inc. (2006). The initial condition was set up such that a volume of fluid with a head  $h = 0.100 \text{ m}$  was located at the crest of the weir. Fig. 1 shows a general layout of the problem.

---

<sup>\*</sup> Ing. Miroslav Spano, Ph.D. and assoc. prof. Ing. Vlastimil Stara, CSc.: Water structures Institute, Faculty of Civil Engineering, Brno University of Technology, Veverí 95; 602 00, Brno; CZ, e-mails: spano.m@fce.vutbr.cz, stara.v@fce.vutbr.cz

Tab. 1: Overview of turbulence models used for simulation.

No	Mark	Description
1	inv	Inviscid flow
2	lam	Laminar flow
3	sa	Spalart-Allmaras model
4	ske	Standard $k-\epsilon$ model
5	rngke	RNG $k-\epsilon$ model
6	rke	Realizable $k-\epsilon$ model
7	skw	Standard $k-\omega$ model
8	lowrsm	Reynolds stress model with low Re stress- $\omega$ model
9	quadrsm	Reynolds stress model with quadratic pressure-strain model

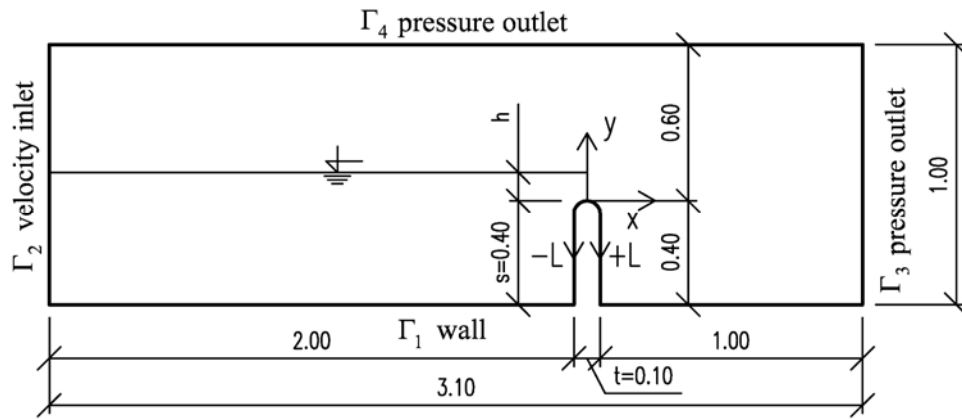


Fig. 1: A general layout of the problem and boundary conditions.

Triangle cells were used for discretisation of the domain. The grid size varied from 2 mm near the weir (at rounded section and downstream face) to 10 mm near the top boundary and in the basin upstream of the weir. The grid consist from 79 459 cells with 40 165 nodes.

A proper time step which provides converged results is a function of grid size. Time step value of  $\Delta t = 1.10^{-4}$  s was chosen. According to the results in (Abdolmaleki et al., 2004 or Bhajantri et al., 2006), the value of the Courant number  $C = 0.9$  or  $0.7$ , respectively, should ensure a stable solution. The maximum Courant number across the domain here reached up to  $C = 0.4$ . A pressure based solver with the parameter setup recommended for this purpose was used, see Fluent Inc. (2006).

### 3. Results and discussion

Results of simulations describing the flow field around the weir are shown in Fig. 2.

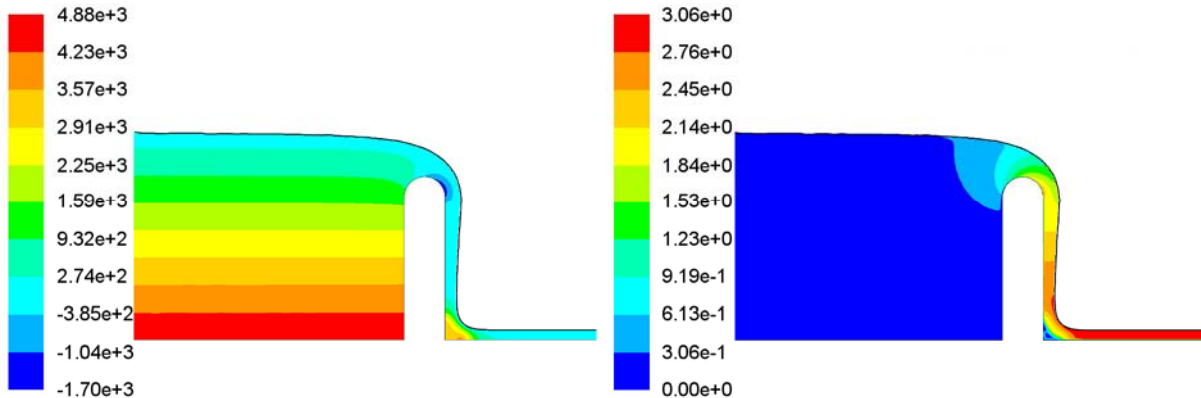


Fig. 2: Flow field around the weir - from left pressure [Pa], velocity [ $m.s^{-1}$ ].

### 3.1. Total head

The total head was computed from equation (1):

$$h_0 = h + \frac{\alpha}{2g} \left[ \frac{Q}{B \cdot (h + s)} \right]^2 \quad [\text{m}] \quad (1)$$

where  $Q$  is discharge  $Q = 0.029 \text{ m}^3 \cdot \text{s}^{-1}$ ,  $g$  – gravity acceleration  $g = 9.81 \text{ m} \cdot \text{s}^{-2}$ ,  $h$  and  $h_0$  – water and total head, respectively, above the weir crest [m],  $\alpha$  – energy coefficient [-],  $B$  – channel width upstream of the weir  $B = 0.40 \text{ m}$ ,  $s$  – height of the weir  $s = 0.40 \text{ m}$ .

The energy coefficient depends on the velocity profile and therefore slightly differs for each model. An analysis has shown that the value of energy coefficient is up to  $\alpha = 1.08$  (1.05 for most models). A comparison of measured and computed total heads is summarized in Tab. 2.

Tab. 2: Summary of measured and computed total heads.

Variable		Measured	inv	lam	sa	ske	rngke	rke	skw	lowrersm	quadrsm
$h$	$\text{m}$	0.100	0.099	0.098	0.098	0.095	0.096	0.098	0.097	0.096	0.109
$h_0$	$\text{m}$	0.101	0.100	0.100	0.099	0.096	0.097	0.099	0.098	0.097	0.110
$v_{\text{mean}}$	$\text{m} \cdot \text{s}^{-1}$	0.147	0.148	0.146	0.146	0.149	0.148	0.146	0.147	0.146	0.139
$Re$	-	$84 \cdot 10^3$	$84 \cdot 10^3$	$83 \cdot 10^3$	$83 \cdot 10^3$	$84 \cdot 10^3$	$84 \cdot 10^3$	$83 \cdot 10^3$	$83 \cdot 10^3$	$83 \cdot 10^3$	$79 \cdot 10^3$
$\alpha$	-	1.05*	1.01	1.05	1.05	1.06	1.05	1.05	1.08	1.05	1.04

\* estimated value

The results have shown a quite good agreement between the measurements and simulations. Most of models compute lower total head in order of millimetres in comparison with measurements. This is probably due to the assumption of a perfectly smooth wall (see Ho et al., 2003). In reality (on a physical model), some additional energy losses can occur. Also, the effect of the turbulent boundary layer and the wall function should be further investigated.

### 3.2. Pressure along weir surface

A comparison of pressures along the spillway surface is shown in Fig. 3. The pressures computed fit well with the data measured. However, some models (skw, ske, quadrsm) tend to underestimate the peak value of negative gauge pressure. Also, some deviation can be seen in the pressure values on the downstream face of the weir regardless the model used.

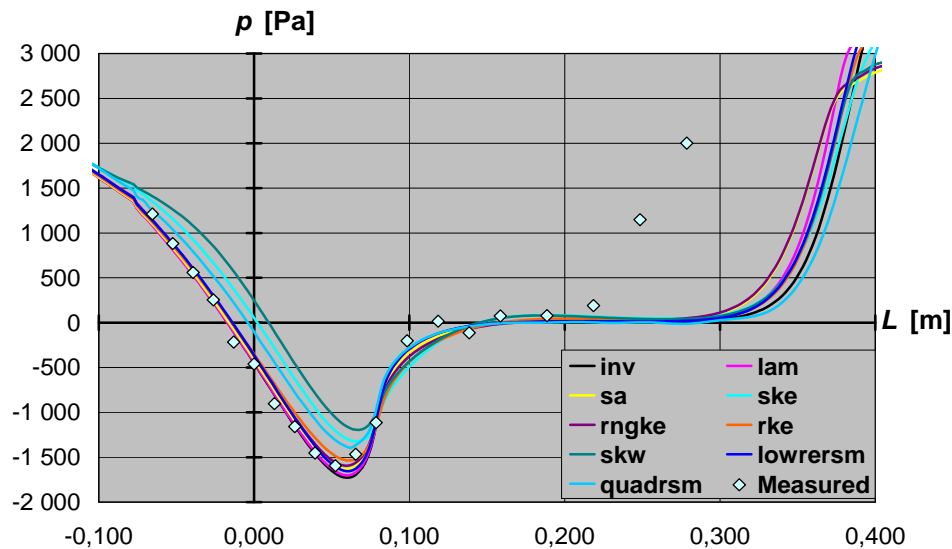


Fig. 3: A comparison of pressure distribution along the spillway surface;  $L$  – distance along weir surface [m],  $p$  – pressure (relative to atmospheric pressure) [Pa];  $L = 0$  at the weir crest.

### 3.3. Comparison

Water heads were compared upon relative error related to measured value according to equation (2). Pressure was compared by Pearson correlation coefficient computed from measured and simulated pressure values. Here the pressure values within interval  $-0.1 < L < 0.2$  m were taken into account only. Results of comparison are summarized in Tab. 3.

$$r_h = 1 - \frac{|h_s - h_m|}{h_m} [-] \quad (2)$$

where  $r_h$  is comparison coefficient for water head [-],  $h_s$  and  $h_m$  – simulated and measured water head, respectively [m].

Tab. 3: Comparison of turbulence models.

<i>comparison coefficient for water head <math>r_h</math></i>	<i>measured</i>	<i>inv</i>	<i>lam</i>	<i>sa</i>	<i>rke</i>	<i>skw</i>	<i>rngke</i>	<i>lowrersm</i>	<i>ske</i>	<i>quadrsm</i>
	1.000	0.982	0.982	0.979	0.973	0.964	0.958	0.957	0.946	0.917
<i>Pearson correlation coeff. for pressure</i>	<i>measured</i>	<i>lam</i>	<i>inv</i>	<i>sa</i>	<i>lowrersm</i>	<i>rngke</i>	<i>rke</i>	<i>quadrsm</i>	<i>ske</i>	<i>skw</i>
	1.000	0.995	0.994	0.994	0.992	0.991	0.987	0.973	0.940	0.910

Comparison coefficients in Tab. 3 are sorted decreasingly. They shows that most accurate results of simulations related to measurements are given by Inviscid flow, Laminar flow, and Spallart-Almaras model.

### 4. Conclusion

Upon the above-mentioned results it can be concluded that most of the models used are suitable for prediction of the spillway capacity (and the discharge coefficient) of presented round-shaped weir.

Generally, the Inviscid and Laminar flow models provide very accurate information about the weir capacity, discharge coefficient values, and pressure along the weir surface. Probable reason is that the flow upstream is very slow (Reynolds number approx.  $84 \cdot 10^3$ ) and the effect of turbulence is small here. On the other hand, the flow downstream of the weir is very fast (Reynolds number here is approx.  $220 \cdot 10^3$ ) and the use of turbulence model for simulation is appropriate. Among turbulence models the most suitable for this case are Spalart-Allmaras model, Realizable k- $\epsilon$  model and RNG k- $\epsilon$  model.

### Acknowledgement

This work has been carried out with a financial support of the Ministry of Education, Youth, and Sports of the Czech Republic, Project No. 1M0579, and the Czech Science Foundation, Project No. GA103/08/P538, and the internal foundation agency of Brno University of Technology, Project No. FAST-S-10-54.

### References

- Koutková, H. & Stara, V. (2003) Součinitel přepadu přelivu s kruhově zaoblenou korunou z fyzikálních experimentů [Coefficients of discharge for round-shaped weirs obtained from physical experiments], in *3. Vodohospodářská konference 2003 s mezinárodní účastí 2003*, Conference Proceedings, Brno University of Technology, Brno, 2003, pp. 379-387.
- Fluent Inc. (2006) *FLUENT 6.3 User guide*, Fluent Inc., Centerra Resource Park, 10 Cavendish Court, Lebanon, NH 03766, 2006.
- Abdolmaleki, K., Thiagarajan, K. P. & Morris-Thomas, M. T. (2004) Simulation of the dam break problem and impact flows using a Navier-Stokes solver, in *15th Australian Fluid Mechanics Conference-2004*, Conference Proceedings, The University of Sydney, Sydney, Australia, 2004.
- Bhajantri, M. R., Eldho, T. I. & Deolalikar, P. B. (2006) Hydrodynamic modelling of flow over a spillway using a two-dimensional finite volume-based numerical model, *Sadhana-Academy Proceedings in Engineering Sciences*, Vol. 31, Part 6, pp. 743-754, 2006.
- Ho, D., Boyes, K., Donohoo, S. & Cooper, B. (2003) Numerical flow analysis for spillways, in *43rd ANCOLD Conference 2003*, Conference Proceedings, ANCOLD, Hobart, Tasmania, 2003.

## APPLICATION OF MESHLESS MLPG METHOD FOR TRANSIENT ANALYSIS OF AXISYMMETRIC CIRCULAR PLATE BENDING PROBLEM

P. Staňák\*, J. Sládek\*, V. Sládek\*

**Abstract:** Axisymmetric circular plates subjected to stationary and transient dynamic loads are analyzed in the presented paper. Effect of viscous damping is also considered. Dynamic loading with impact and stepped time history is taken into account. The governing equation for the bending of plate represented by partial differential equation (PDE) of the fourth order is decomposed into two coupled PDEs of the second order. Clamped plate edge as a boundary condition is assumed. Axisymmetric assumptions reduce the problem to one dimensional. Each node is a center of 1-D interval subdomain. The weak-form on these small subdomains is applied to derive local integral equations with a unit step function as the test function. Moving least-squares (MLS) approximation technique is applied to obtain system of ordinary differential equations (ODE). Houbolt finite difference scheme is finally applied to solve this system of ODE for certain nodal unknowns.

**Keywords:** Local integral equations, meshless approximation, Kirchhoff plate theory, Houbolt finite-difference scheme.

### 1. Introduction

Analysis of circular plates is basic problem in structural mechanics, as long as many structures, like containers or reservoirs, have circular basement. Another reason why to deal with circular plates is the availability of exact solution that is convenient for assessment of new numerical techniques.

The MLPG (Meshless Local Petrov-Galerkin) method (Atluri, 2004) is one of the most rapidly developing meshless method. The MLPG method was applied to static and dynamic loading of thin circular and square plates (Sladek et al., 2003), also to dynamic loading of thick Reissner-Mindlin plates (Sladek et al., 2007). Recently, MLPG method was applied also to laminated composite plates (Sladek et al., 2010a) and piezoelectric plates (Sladek et al., 2010b).

Presented approach reduces the problem of bending of circular plate to 1-D with the assumption of axisymmetric conditions. The governing equation for plate bending problem is decomposed to reduce the order of differentiation. Application of MLS approximation to derive local integral equations leads to the system of ordinary differential equations that is solved by the Houbolt method.

### 2. Local integral equations for an axisymmetric circular plate

Let us consider a homogeneous axisymmetric clamped circular plate with the radius  $r$  and thickness  $h$  occupying the domain  $\Omega$ . The plate is subjected to the transverse dynamic load  $q(\mathbf{x}, t)$ . According to the classical (Kirchhoff) plate theory the differential equation for the plate deflection  $w(\mathbf{x}, t)$  can be written in the form

$$D\nabla^2\nabla^2 w(\mathbf{x}, t) + \rho h \ddot{w}(\mathbf{x}, t) + g \dot{w}(\mathbf{x}, t) = q(\mathbf{x}, t) \quad (1)$$

---

\* Ing. Peter Staňák, prof. Ing. Ján Sládek, DrSc. and prof. RNDr. Vladimír Sládek, DrSc.: Institute of Construction and Architecture, Slovak Academy of Sciences, Dúbravská cesta 9; 845 03, Bratislava; Slovakia, e-mails: peter.stanak@savba.sk, jan.sladek@savba.sk, vladimir.sladek@savba.sk

where  $\rho$  is the mass density,  $g$  is the viscous damping coefficient and  $D = Eh^3 / 12(1 - \nu^2)$  is the plate stiffness, with  $E$  as Young's modulus and  $\nu$  denoting Poisson's ratio. The dots over the quantity represent differentiation with respect to time  $t$ .

It is possible to decrease the order of differentiation in eq. (1) by its decomposition into two PDEs of the second order (Sladek et al., 2003) as

$$-D\nabla^2 w(\mathbf{x}, t) = m(\mathbf{x}, t) \quad (2)$$

$$\nabla^2 m(\mathbf{x}, t) - \rho h \ddot{w}(\mathbf{x}, t) - g \dot{w}(\mathbf{x}, t) = -q(\mathbf{x}, t) \quad (3)$$

where the quantity  $m(\mathbf{x}, t)$  is proportional to the spur of the bending moment tensor as  $m = M_{ii} / (1 + \nu)$  (Balas et al., 1989). On a clamped edge of the plate, however,  $m(\mathbf{x}, t)$  is equal to the bending moment  $M(\mathbf{x}, t)$ . For a simply supported edge this is only valid if the edge is straight (Sladek et al., 2003). For a circular plate with curved edges the quantity  $m(\mathbf{x}, t)$  has no physical interpretation and the definition of boundary conditions is impossible. This is the main reason why only clamped circular plates will be analyzed. Note that Eqs. (2), (3) are coupled and that is why they must be solved simultaneously. If we restrict ourselves to symmetric material properties, loading and boundary conditions throughout the plate, the problem can be simplified to axisymmetric case in polar coordinates. Under axisymmetric conditions all the variables in Eqs. (2) and (3) will be function of the radial coordinate  $r$  only.

The MLPG method is based on the local weak form of the governing equations. The local weak form for Eqs. (2), (3) is then written over a small local subdomain  $\Omega_s$  (Atluri, 2004) as

$$\int_{\Omega_s} [D\nabla^2 w(r, t) + m(r, t)] h^*(r) d\Omega = 0 \quad (4)$$

$$\int_{\Omega_s} [\nabla^2 m(r, t) - \rho h \ddot{w}(r, t) - g \dot{w}(r, t) + q(r, t)] h^*(r) d\Omega = 0 \quad (5)$$

where  $h^*(r)$  is the weight or test function. In the present analysis unit step function is used, as defined by Sladek et al. (2010a). Let  $w$  and  $m$ , hereafter called the trial functions, be an approximate solution to the problem. Integrating Eqs. (4), (5) by parts with assumptions of Laplace operator  $\nabla^2$  in polar coordinates, considering the integration element  $d\Omega = r dr$  for the axisymmetric circular plate and making use of the unit step weight function defined over  $\Omega_s$  is leading to local integral equations for the presented problem. This process can be also observed in papers by Sladek et al. (2003, 2010a).

The MLS (Moving least-squares) approximation (Lancaster & Salkaustas, 1981; Atluri, 2004) can be used for the approximation of unknown quantities in terms of the nodal values as

$$\mathbf{w}^h(r, \tau) = \sum_{a=1}^n \phi^a(r) \hat{\mathbf{w}}^a(\tau) \quad , \quad \mathbf{w}_{,r}^h(r, \tau) = \sum_{a=1}^n \phi_{,r}^a(r) \hat{\mathbf{w}}^a(\tau) \quad (6)$$

where  $\phi^a(r)$ ,  $\phi_{,r}^a(r)$  are called MLS shape functions for unknown quantity and its derivative. Applying Eq. (6) for approximation of trial functions  $w(r, t)$ ,  $m(r, t)$  and their derivatives with subsequent introduction into local integral equations gives the discretized local integral equations

$$\sum_{i=1}^n \left[ D (r \phi_{,r}^i(r)) \Big|_a^b \right] \hat{w}^i(t) + \sum_{i=1}^n \left[ \int_{\Omega_s} r \phi^i(r) dr \right] \hat{m}^i(t) = 0 \quad (7)$$

$$\sum_{i=1}^n \left[ (r \phi_{,r}^i(r)) \Big|_a^b \right] \hat{m}^i(t) - \sum_{i=1}^n \left[ \rho h \int_{\Omega_s} r \phi^i(r) dr \right] \hat{\ddot{w}}^i(t) - \sum_{i=1}^n \left[ g \int_{\Omega_s} r \phi^i(r) dr \right] \hat{\dot{w}}^i(t) = - \int_{\Omega_s} q r dr \quad (8)$$

To impose boundary conditions, method of Lagrange multipliers or penalty method can be used in most of the numerical solution methods. MLPG, however, allows us to use also collocation approach to impose boundary conditions directly, using interpolation approximations (6) as  $\sum_{i=1}^n \phi^i(r^j) \hat{w}^i(\tau) = \tilde{w}^i(r^j, \tau)$  where  $\tilde{w}^i(r, \tau)$  is the prescribed value of the deflection on the boundary.

Similar approach can be adopted for the quantity  $m(r, t)$ . Collecting the discretized local boundary-domain integral equations together with the discretized boundary conditions for the generalized displacements, one obtains a complete system of ordinary differential equations (ODE) which can be rearranged in such a way that all known quantities are on the r.h.s. Thus, in the matrix form the system becomes

$$\mathbf{A}\ddot{\mathbf{x}} + \mathbf{B}\dot{\mathbf{x}} + \mathbf{C}\mathbf{x} = \mathbf{Y} \quad (9)$$

This system of ODE (9) can be conveniently solved by the Houbolt finite-difference scheme (Houbolt, 1950; Sladek et al., 2010a). This method is strongly dependent on the size of the time step. The value of the time step must be appropriately selected with respect to material parameters and time dependence of boundary conditions.

### 3. Numerical examples

Let us consider a circular plate with the radius  $r_0 = 0.5$  m and the thickness  $h = 0.002$  m. Material properties are as follows: Young's modulus  $E = 2 \times 10^{11}$  Nm<sup>-2</sup>, Poisson's ratio  $\nu = 0.3$  and mass density  $\rho = 7850$  kg.m<sup>-3</sup>. Two load cases are considered, a uniform static loading with  $q = 10$  Pa and dynamic loading with the Heaviside time variation with amplitude  $q = 10$  Pa. 21 equally-spaced nodes are used for the discretization of plate geometry. For the clamped axisymmetric circular plate under uniform static loading the exact solution is given as

$$w(r) = \frac{qr_0^4}{64D} \left[ 1 - \left( \frac{r}{r_0} \right)^2 \right]^2 \quad (10)$$

Assuming  $r = r_0$  in Eq. (10) and inserting all quantities, the exact deflection of the plate center is obtained as  $w(r = r_0) = 0.667e^{-4}$  m. The variation of the deflection with the radial coordinate is presented in Fig. 1. The results are in excellent agreement.

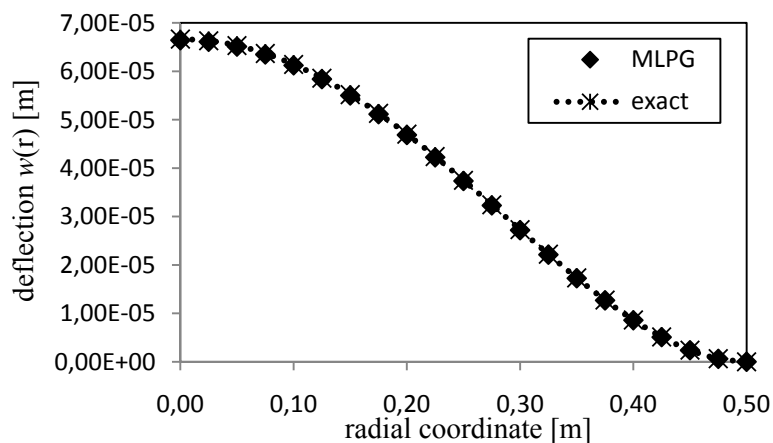
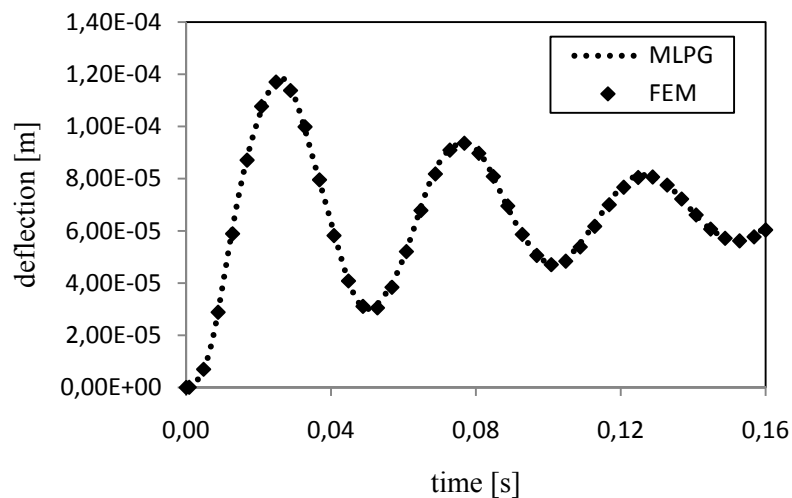


Fig. 1: Variation of the deflection with radial coordinate for clamped axisymmetric circular plate.

Next dynamic loading is considered with the Heaviside time variation. Again 21 equally distributed nodes are used with radius of support domain with size of 10 times nodal distance of two neighboring nodes. Numerical calculations were carried out for a time step  $\Delta t = 0.8e^{-3}$  s with 200 time increments. Viscous damping is also considered. It is defined through the damping parameter  $\xi = g/g_c = 0.1$ , where the critical damping is  $g_c = 2\omega_1\rho h$ , with  $\omega_1 = 125$  rad/s being the first natural frequency. Variation of the center point deflection with time is presented in Fig. 2. Results from MLPG analysis



are compared to transient FEM analysis with the same geometry and mesh as in the previous static case. A quarter of the plate is modeled due to symmetry in FEM/ANSYS code with fine mesh. Again, excellent match of the result is observed.



*Fig. 2: Variation of deflection at center of the considered plate with respect to time.*

#### 4. Conclusion

The MLPG method is presented for solving bending problems of thin axisymmetric circular plates. Both static and dynamic loads are considered. The analysed domain is divided into small overlapping subdomains. A unit step function is used as the test function in the local weak form. The MLS approximation scheme is adopted for approximation of unknown physical quantities. The proposed method is a truly meshless method as it requires no background mesh in neither interpolation, nor integration. It can be considered as an alternative to many existing computational methods.

#### Acknowledgement

The support of the grant VEGA-2/0039/09 by Slovak Grant Agency is gratefully acknowledged.

#### References

- Atluri, S. N. (2004) The meshless method (MLPG) for domain & BIE discretizations. Tech Science Press, Forsyth, USA.
- Balas, J., Sladek, J. & Sladek, V. (1989) Stress analysis by boundary element methods. Elsevier, Amsterdam.
- Houbolt, J. C. (1950) A recurrence matrix solution for the dynamic response of elastic aircraft. Journal of Aeronautical Sciences, 17, pp. 371-376.
- Lancaster, P., Salkauskas, T. (1981) Surfaces generated by moving least square methods. Math. Comput., 37, pp. 141-158.
- Sladek, J., Sladek, V., Krivacek, J., Wen, P. & Zhang, Ch. (2007) Meshless Local Petrov-Galerkin (MLPG) method for Reissner-Mindlin plates under dynamic load. Computer Meth Appl Mech Engn, 196, pp. 2681-2691.
- Sladek, J., Sladek, V. & Mang, H. A. (2003) Meshless LBIE formulations for simply supported and clamped plates under dynamic load. Computers and Structures, 81, pp. 1643-1651.
- Sladek, J., Sladek, V., Stanak, P., Zhang, Ch. (2010a) Meshless Local Petrov-Galerkin (MLPG) Method for Laminate Plates under Dynamic Loading. CMC- Computers, Materials & Continua, 15, pp. 1-26.
- Sladek, J., Sladek, V., Stanak, P., Pan, E. (2010b) The MLPG for bending of electroelastic plates. CMES- Computer Modeling in Engineering & Sciences, 64, pp. 267-298.

## A CLAMPED-CLAMPED BEAM STATIC SAG LIMITS UNDER PERPENDICULAR MAGNETIC FORCE

G. J. Stein<sup>\*</sup>, R. Darula<sup>\*\*</sup>, R. Chmúrny<sup>\*</sup>

**Abstract:** *There are mechatronic applications, where a slender beam or plate is subjected to static magnetic force generated by an electromagnetic actuator consisting of a solenoid on a ferromagnetic core and a yoke, fixed to the beam. The static magnetic force, acting perpendicularly onto the beam, causes sag (downwards bending) of the beam. If the magnitude of the magnetic force surpasses some threshold value the beam is buckled. For small deflections the mathematical expression of the magnetic force can be approximated by a polynomial dependence on the distance to the magnet. It is important to analyse the nature of the sag and to determine the limits of the linear approximation, as well as the limits leading to the buckled state. The mathematical generalisation of the sag is valid for electrostatic force between planar electrodes, too.*

**Keywords:** *Clamped beam sag, electromagnetic actuator threshold current, sag approximation.*

### 1. Introduction

There are mechatronic applications, where a slender beam or plate of length  $L$  is subjected to static magnetic force  $F_M$ , generated by an electromagnetic actuator. The actuator consists of a solenoid wound on a pot-form ferromagnetic core and an armature (of length  $L_m \ll L$ ), fixed to the beam at its midpoint (Fig. 1). The magnetic force  $F_M$  is acting in the middle of the beam at distance  $L/2$  from rigid fixtures on both ends and induces a sag (downwards deflection)  $z_{max}$ . If the intensity of the magnetic force  $F_M$  exceeds certain threshold, the beam is permanently attracted to the end-stops (Bishop, 2002).

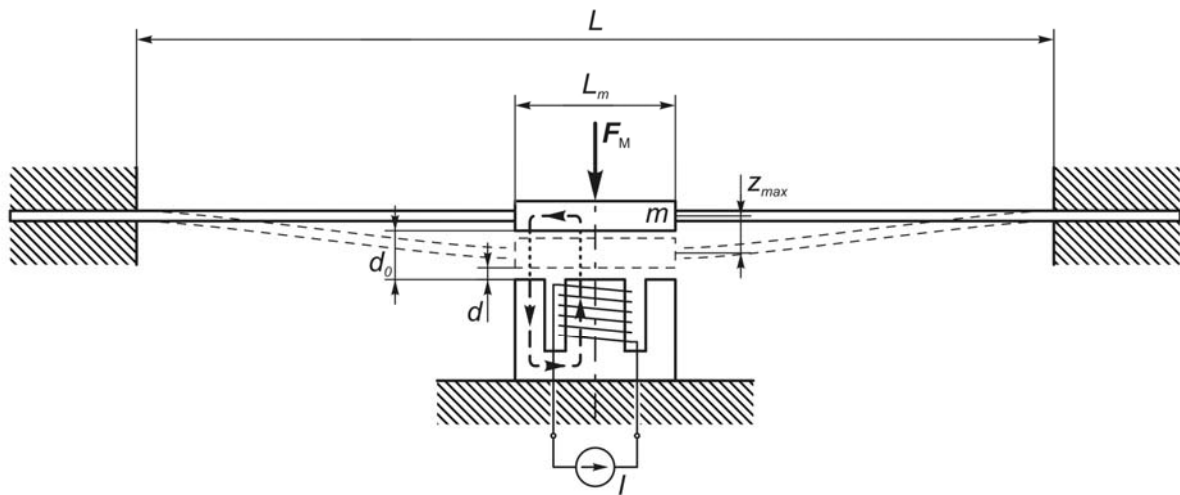


Fig. 1: Schematics of the clamped-clamped beam with electromagnet (flux line is denoted dashed).

### 2. Mathematical model of the equilibrium state

The sag,  $z_{max}$ , at the beam midpoint due to the magnetic force  $F_M$  is, according to (Rao, 2004) is:

<sup>\*</sup> Ing. George Juraj Stein, PhD. and Ing. Rudolf Chmúrny, PhD.: Institute of Materials and Machine Mechanics of the Slovak Academy of Sciences, Račianska 75, 831 02 Bratislava, SK, e-mail: stein@savba.sk; ummschmu@savba.sk

<sup>\*\*</sup> Radoslav Darula MSc. (Eng.): Department of Mechanical and Manufacturing Engineering, Aalborg University, Pontoppidanstræde 101, DK- 9220 Aalborg East, DK, e-mail: dra@m-tech.aau.dk

$$z_{\max}(F_M) = \frac{F_M}{192} \cdot \frac{L^3}{E_b I_b}, \quad (1)$$

where  $E_b$  is the modulus of elasticity (Young's module) of the beam material and  $I_b$  is the second moment of inertia of the beam. This can be expressed as  $F_M = z_{\max} \cdot k_{\text{ef}}$ , too. The theoretical value of the effective (lumped) stiffness  $k_{\text{ef}}$  of the clamped-clamped slender beam loaded at the midpoint is given as  $k_{\text{ef}} = 192 \cdot (E_b I_b) / L^3$  (e.g. (Rao, 2004)).

Energizing the electromagnet with a steady state (DC) current  $I$  the magnitude of magnetic force  $F_M$  is described by a scalar equation (Giurgiutiu & Lyschewski, 2009; Mayer & Ulrych, 2009):

$$F_M(d, I) = \frac{\mu_0 S N^2 I^2}{(2d + l_\phi / \mu_r)^2}. \quad (2)$$

The magnetic flux line is crossing twice the air gap, as shown in Fig. 1;  $\mu_0$  is the permeability of air and  $l_\phi$  is the flux line length in the ferromagnetic material of relative permeability  $\mu_r$ . All parameters are known from vendor's data, were measured or calculated from set-up geometry (Darula, 2008).

The static equilibrium of the magnetic force  $F_M(d, I)$  and the elastic force due to the beam deflection  $z_{\max} \cdot k_{\text{ef}}$  is described by Eq. (3). From the geometry follows:  $z_{\max} = d_0 - d$ , where  $d_0$  is the initial distance between electromagnet and the beam in de-energised state:

$$(d_0 - d) k_{\text{ef}} = F_M(d, I). \quad (3)$$

Let's introduce a non-dimensional air gap width  $\alpha$ :  $\alpha = (d_0 - d) / d_0$ . (4)

From physical point of view, the quantity  $\alpha$  is non-negative and cannot be larger than one. If  $\alpha = 1$ , beam is fully attracted by the electromagnet and would adhere to its poles.

Further the middle magnetic flux line path of length  $l_\phi$  will be considered. A more thorough magnetic field analysis by FEM approach would be beyond the scope of this contribution. The flux line length  $l_\phi$  can be transformed into an equivalent half flux line length in air  $d_{\text{Fe}}$ , assuming *linear properties* of the core magnetic material:  $d_{\text{Fe}} = \frac{1}{2} l_\phi / \mu_r$ . This is also a simplifying assumption, because for common magnetic materials B-H relation is non-linear (Giurgiutiu & Lyschewski, 2009; Mayer & Ulrych, 2009). However, up to the saturation point, the concept of linear permeability can be used.

Introducing  $\alpha$  into Eq. (3) and using Eq. (2), the equilibrium equation is:

$$\alpha \cdot k_{\text{ef}} = \frac{F_M}{d_0} = \left( \frac{\mu_0 S N^2}{4d_0} \right) \cdot \frac{I^2}{[(d_0 - \alpha d_0 + d_{\text{Fe}})]^2} = \left( \frac{\mu_0 S N^2}{4d_0} \right) \cdot \frac{I^2}{d_0^2 [(1 + \delta_M) - \alpha]^2}. \quad (5)$$

A relative measure  $\delta_M = d_{\text{Fe}} / d_0$  can be introduced, while  $\delta_M < 1$ , because  $\mu_r > 1$ . Eq. (5) can be, after some algebraic manipulation, re-written as follows:

$$\frac{\alpha(I)}{(1 + \delta_M)} \cdot k_{\text{ef}} = \left( \frac{\mu_0 S N^2}{4d_0^3} \right) \cdot \frac{I^2}{(1 + \delta_M)^3 \left[ 1 - \frac{\alpha(I)}{(1 + \delta_M)} \right]^2}, \quad (6a)$$

which calls for introduction of a normalised parameter  $\beta$ :  $\beta = \alpha / (1 + \delta_M)$ . Parameter  $\beta$  relates the *air gap width change* ( $d - d_0$ ) to the properties of the magnetic circuit  $\delta_M$ , which are constant for the initial distance  $d_0$ . Obviously  $\beta < 1$ . The physically feasible limit is  $\beta \leq 1 / (1 + \delta_M)$ . Then Eq.(6a) is modified:

$$\beta(I) \cdot k_{\text{ef}} = \left[ \frac{\mu_0 S N^2}{4(d_0 + d_{\text{Fe}})^3} \right] \cdot \frac{I^2}{[1 - \beta(I)]^2} = K_M \frac{I^2}{[1 - \beta(I)]^2}. \quad (6b)$$

### 3. Solution of the equilibrium equation

The Eq. (6b) can be solved for variable  $\beta(I)$  by an approximate approach using linear approximation, or in the exact way, applying analytical or numerical tools.

The denominator of the right hand side of Eq. (6b) can be approximated by a McLaurin's series:

$$\beta k_{ef} = K_M I^2 \cdot \{1 + 2\beta + 3\beta^2 + \dots\}. \quad (7)$$

Just the first two terms of the expansion are considered, i.e. the linear approximation is used. After some algebra the formula for approximate calculation of  $\beta'$  emerges:

$$\beta' = \frac{K_M I^2}{k_{ef} - 2K_M I^2}. \quad (8)$$

The exact solution stems from the cubic equation obtained by rewriting Eq. (6b):

$$\beta \cdot [1 - \beta]^2 = (K_M / k_{ef}) I^2, \text{ i.e.: } \beta^3 - 2\beta^2 + \beta - (K_M / k_{ef}) I^2 = 0. \quad (9a, b)$$

The solution of Eq. (9b) calls for the use of Cardano's formulas for evaluation of cubic equations or rely on numerical solvers of algebraic equations, embedded in simulation programming environment, e.g. MATLAB<sup>®</sup>. The numerical solution leads, according to (Frank et al., 1973), to three different complex roots. In analogy to the quadratic equation there is a cubic discriminator  $D_3$ , furnishing for  $D_3 > 0$  three real roots. This is the case here. By further analysis, two pairs of special real solutions of this cubic equation were found:

- a pair for  $\beta = 0$  and  $\beta = 1$ , which is a result for  $I = 0$ ;
- a pair for  $\beta = 1/3$  and  $\beta = 4/3$ , which results if  $I$  attains a specific threshold value  $I_{crit}$ :

$$I_{crit}^2 = \frac{4}{27} \left( \frac{k_{ef}}{K_M} \right). \quad (10)$$

The threshold current  $I_{crit}$  is determined by the beam stiffness  $k_{ef}$  and the magnetic circuit properties  $K_M$ . The value  $\beta = 4/3$  corresponds to the *triple real root* at  $D_3 = 0$ . For  $I > I_{crit}$  (when  $D_3 < 0$ ) there is only a single real root and two complex conjugate roots.

Let us introduce a generalized variable  $q_N$ , which is physically the current  $I$  normalized by the value of threshold current,  $q_N = I/I_{crit} \leq 1$ . Then Eqs. (8) and (9b) can be re-formulated and simplified:

$$\beta' = \frac{1}{\left( \frac{27}{4} \right) \frac{1}{q_N^2} - 2}, \quad (11a)$$

$$\beta^3 - 2\beta^2 + \beta - (4/27) q_N^2 = 0. \quad (11b)$$

For calculation of the exact solutions of  $\beta$  the MATLAB<sup>®</sup> function 'roots' was used, returning a complex three element vector for each  $q_N$  value. Then the roots are ordered in ascending order and plotted in the form of line graphs (Fig. 2 – medium lines). Note, that this is not a plot of a function, because for any positive value of  $q_N < 1$  three different values are possible. The course of the approximate solution  $\beta'$  (Eq. (11a)) is plotted as a thin line.

Physically feasible values of numerical solution of the cubic Eq. (11b) are bound to the interval  $[0, \beta \leq 1/(1+\delta_M)]$  (white area in Fig. 2); hence the solutions above the bold limit (in the grey area) have no physical meaning (the beam would have to move within the electromagnetic core!). The dashed course is not physically realistic either, because this would assume that the elastic beam was buckled prior to energising the field. The physically plausible course is the lowest curve, starting at zero and reaching for  $q_N = 1$  the value of  $\beta = 1/3$ . However, for the value  $q_N = 1$  two different solutions do exist:  $\beta = 1/3$  and  $\beta = 4/3$ . This can be interpreted as the limit of stability: **at the threshold current the beam buckles** from the value of  $\beta = 1/3$  to  $\beta = 1/(1+\delta_M)$ , as denoted by the red vertical line.

If the current would revert from a value of  $I > I_{crit}$  the beam would follow the same trajectory, i.e. as soon as the value of  $q_N$  drops below unity the beam, firstly adhering to the magnet core, would attain (after extinction of the transient phenomenon) a position corresponding to the  $\beta = 1/3$ .



## MODELING OF DYNAMIC FRAGMENTATION: ONE-DIMENSIONAL CASE

J. Stránský\*, M. Jirásek\*

**Abstract:** *Dynamic fragmentation (disintegration of continuous body into smaller pieces under dynamic loading) is a physical phenomenon observed in many fields of engineering and science. The crack initiation and propagation combined with stress release waves makes the whole situation nontrivial and difficult to describe by analytical means. In this contribution, continuum damage mechanics and finite element method are used for numerical simulation of a ring (or cylindrical shell) subjected to radial loading at a high strain rate (e.g. explosive). The solution is simplified to the one-dimensional case and the results (average fragment size, fragment size distribution and energy dissipation) are compared for different finite element discretizations and for different perturbations of material properties. A comparison is also made between numerical results and analytical models including newly proposed ones.*

**Keywords:** *Dynamic fragmentation, finite element method, mesh size dependency, average fragment size, convergence of dissipated energy.*

### 1. Introduction

A continuous body under rapid dynamic loading is, in contrast to the static case, usually split into many smaller pieces. Numerous studies of this phenomenon (dynamic fragmentation) have been focused on the case of an expanding ring (see Fig. 1), because it is simple to analyze both experimentally and numerically. In this contribution, we present two new analytical models for prediction of average fragment size, and also finite element simulations which are in certain aspects superior to other methods reported in literature.

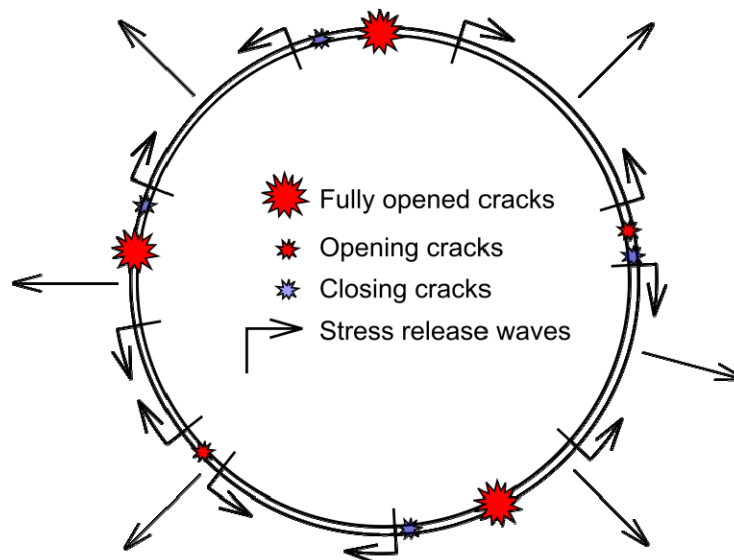


Fig. 1: Schematic representation of an expanding ring according to (Molinari et al., 2007).

---

\* Ing. Jan Stránský and prof. Ing. Milan Jirásek, DrSc.: Czech Technical University in Prague, Faculty of Civil Engineering, Department of Mechanics, Thákurova 7; 166 29, Prague; Czech Republic, e-mails: Jan.Stransky.1@fsv.cvut.cz, Milan.Jirasek@fsv.cvut.cz

## 2. Analytical prediction of average fragment size

There exist several simple analytical models for predicting the average fragment size  $l_{avg}$  as a function of the strain rate  $\dot{\epsilon}$  and material parameters (e.g. Young's modulus  $E$ , bulk density  $\rho$ , fracture energy  $G_f$ , tensile strength  $\sigma_0$ ). One of the most cited approaches is Grady's model (Grady & Olsen, 2003), which assumes that the fragment size is minimizes the sum of kinetic energy density  $k = \frac{1}{24}\rho\dot{\epsilon}l^2$  (Miller et al., 1999; Zhou et al., 2005) and surface energy “volume density” (energy consumed for the fragment creation divided by the fragment volume)  $\bar{\gamma} = \frac{G_f}{l}$ . This condition yields the estimate

$$l_{avg} = \sqrt[3]{12} \left( \frac{G_f}{\rho\dot{\epsilon}^2} \right)^{\frac{1}{3}}. \quad (1)$$

The Glenn–Chudnovsky (1986) model (GC) balances the kinetic, surface and strain energy density  $w_e = \frac{1}{2}\frac{\sigma_0^2}{E}$  (considered at the moment of fragment creation, therefore computed for tensile strength  $\sigma_0$ ) and leads to

$$l_{avg} = 2\sqrt{\frac{\alpha}{3}} \sinh\left(\frac{\phi}{3}\right), \quad \text{where} \quad \phi = \sinh^{-1}\left[\beta\left(\frac{3}{\alpha}\right)^{\frac{3}{2}}\right], \quad \alpha = \frac{12\sigma_0^2}{\rho E \dot{\epsilon}^2}, \quad \beta = \frac{12G_f}{\rho \dot{\epsilon}^2}. \quad (2)$$

We propose two new analytical models. The first one is derived from a model presented by Yew & Taylor (1994) and therefore named “modified Yew–Taylor model” (modYT). It assumes, that the time when the peak stress is reached is negligible compared to the time of the whole fragmentation process  $t_c = \frac{l}{2c}$ , which is equal to half of the fragment length divided by the value of elastic wave speed  $c = \sqrt{\frac{E}{\rho}}$ . Minimizing the sum of kinetic, surface and strain energy density  $w_e = \frac{1}{2}E\epsilon = \frac{1}{2}E\dot{\epsilon}t_c = \frac{1}{8}\rho\dot{\epsilon}^2l^2$  results into

$$l_{avg} = \sqrt[3]{3} \left( \frac{G_f}{\rho\dot{\epsilon}^2} \right)^{\frac{1}{3}}. \quad (3)$$

The second model is a combination of modYT and GC model, and therefore named YTGC. The assumptions are: the time of fragment creation is again  $t_c = \frac{l}{2c}$ , but it is small such that the stress distribution along the fragment is not affected and is equal to  $\sigma_0$ . Balancing of strain energy density increment  $\Delta w_e = \sigma_0\dot{\epsilon}t_c = \sigma_0\dot{\epsilon}\frac{1}{2c}l$  and surface energy density (as well as minimization of their sum) results into

$$l_{avg} = \sqrt{\frac{2G_fc}{\sigma_0\dot{\epsilon}}}. \quad (4)$$

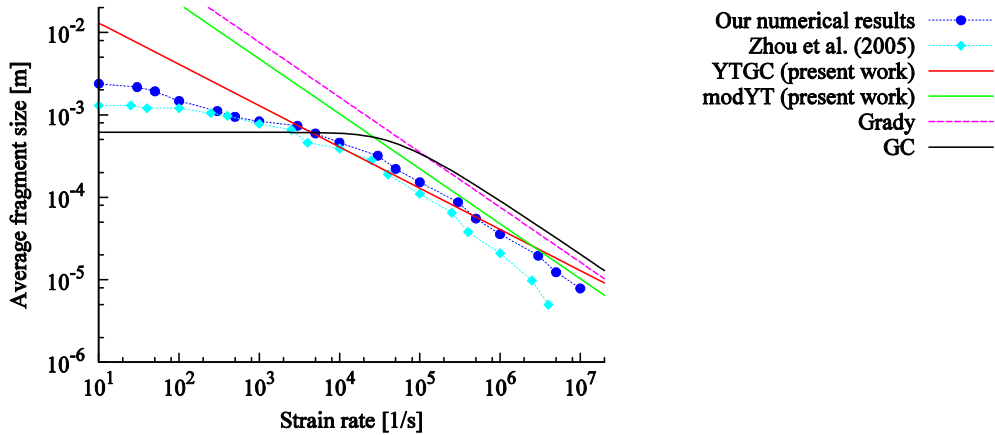


Fig. 2: Comparison of different analytical models and numerical results.

For comparison of analytical models, the following material properties are considered:  $E = 275$  GPa,  $\rho = 2750$  kg/m<sup>3</sup>,  $G_f = 100$  J/m<sup>2</sup>,  $\sigma_0 = 300$  MPa. The results are summarized in Fig. 2. Clearly, for the present set of material parameters the newly proposed models modYT and YTGC predict the average fragment size better than previously existing models (Grady and Glenn–Chudnovsky)



### 3. Numerical solution

The expanding ring is simulated as a one-dimensional bar (approximately representing a certain small part of the ring). The numerical solution is based on the finite element method (FEM) with linear approximation of the displacement field. Cracking is modeled in the smeared manner using 1D damage mechanics with linear softening. The initial condition prescribes a constant strain rate (and therefore linear velocity along the bar length). To “macroscopically retain” the constant strain rate, the velocity of boundary nodes is prescribed by a constant value for the whole simulation, see Fig. 3.

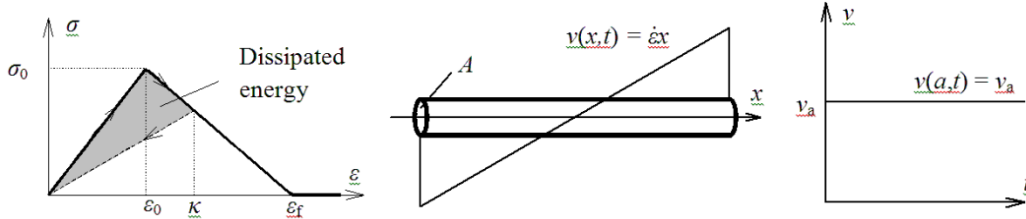


Fig. 3: Considered material model and initial and boundary conditions.

For an ideal rod with all material parameters constant along its length, a uniform solution exists but is instable (similar to the static case). To eliminate such solution, it is sufficient to slightly perturb the material parameters. The simplest approach is to define the material parameter value independently in each element (to consider the parameter values as uncorrelated). Physically more realistic is to assume a certain spatial correlation of material parameters. We assume a simple exponential covariance function  $C(x_1, x_2) = \sigma^2 e^{-|x_1 - x_2|/r}$ , where  $\sigma$  is the standard deviation and  $r$  is the correlation length.

### 4. Results

Convergence of the results with increasing number of elements for different uncorrelated perturbations is shown in Fig. 4. Curves marked by  $A$  correspond to 1% perturbation of the cross-section area, curves marked by  $\sigma_0$  to 1% perturbation of the tensile strength and curves marked by  $l_e$  to 40% perturbation of element length. Results from an ideal rod exhibit non-monotonic convergence (given by the instability of results, which is triggered by round-off error in if the number of elements is sufficiently high). Fig. 5 shows the convergence for different strain rates. Finally, convergence results considering spatial correlation are shown in Fig. 6. Dissipated energy is higher for a higher correlation length.

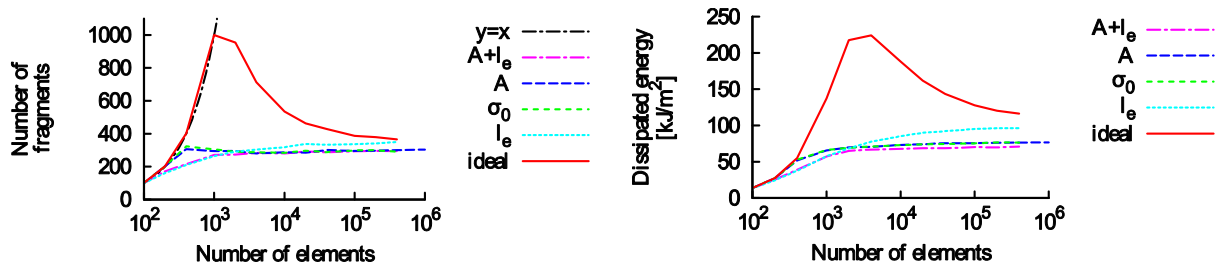


Fig. 4: Number of fragments (left) and dissipated energy (right) for  $\dot{\epsilon} = 10^5 \text{ s}^{-1}$  and for various uncorrelated perturbations.

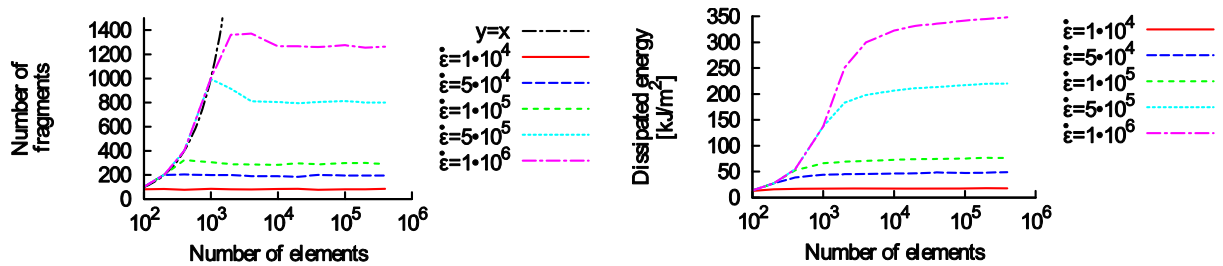


Fig. 5: Number of fragments (left) and dissipated energy (right) for uncorrelated 1% perturbation of tensile strength  $\sigma_0$  and for various strain rates  $\dot{\epsilon}$ .

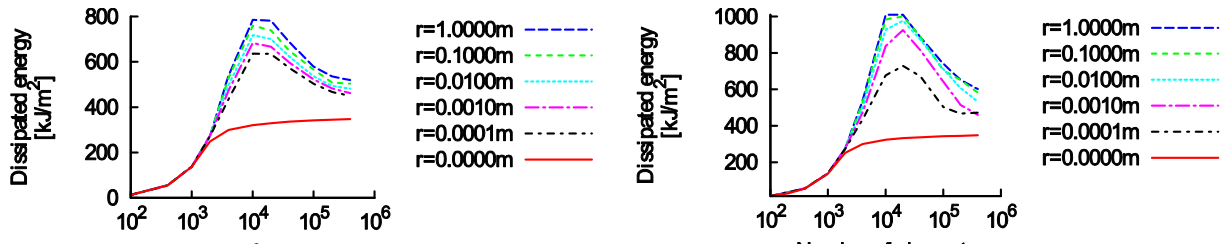


Fig. 6: Dissipated energy for  $\dot{\epsilon} = 10^6 \text{ s}^{-1}$ , various correlation length and 1% perturbation of cross-section area  $A$  (left) and tensile strength  $\sigma_0$  (right).

## 5. Conclusions

The present article deals with dynamic fragmentation of materials under high strain rates, with focus on the case of an expanding ring. The main results can be summarized as follows:

- New analytical models for prediction of average fragment size are proposed. In comparison with existing models from the literature they agree better with numerical results.
- Combination of the finite element method and damage mechanics leads to monotonic convergence of dissipated energy. This is in contrast to the method of characteristics combined with cohesive elements using 1% perturbation of strength presented by Molinari et al. (2007), which gives non-monotonic convergence of dissipated energy.
- For a bar with a spatial correlation of material properties corresponding to a finite correlation length, the results are almost always between two extremes – the ideal bar (equivalent to an infinite correlation length) and uncorrelated parameters (equivalent to zero correlation length).

Future work on this topic will address in more detail the influence of spatial correlation (including a larger standard deviation), validation of newly proposed analytical models for different material parameters, extension of the analysis to more dimensions, etc.

## Acknowledgement

The financial support of project SGS 10/020/OHK1/1T/11 is gratefully acknowledged.

## References

- Glenn, L. A. & Chudnovsky, A. (1986) Strain-energy effects in on dynamic fragmentation. *Journal of Applied Physics*, 59, pp. 1379-1380.
- Grady, D. E. & Olsen, M. L. (2003) A statistics and energy based theory of dynamic fragmentation. *International Journal of Impact Mechanics*, 29, pp. 293-306.
- Miller, O., Freund, L. B. & Needleman, A. (1999) Modeling and simulation of dynamic fragmentation. *International Journal of Fracture*, 96, pp. 101-125.
- Molinari, J. F., Gazonas, G., Raghupathy, R., Rusinek, A. & Zhou, F. (2007) The cohesive element approach to dynamic fragmentation: The question of energy convergence. *International Journal for Numerical Methods in Engineering*, 69, pp. 484-503.
- Yew, C. H. & Taylor, P. A. (1994) A thermodynamic theory of dynamic fragmentation. *International Journal of Impact Engineering*, 15, pp. 385-394.
- Zhou, F., Molinari, J. F. & Ramesh, K. T. (2005) A cohesive model based fragmentation analysis: effect of strain rate and initial defects distribution. *International Journal of Solids and Structures*, 42, pp. 5181-5207.

## MECHANICS OF FLAT TEXTILE FABRICS – THEORY

B. Striz<sup>\*</sup>, M. Vysanska<sup>\*</sup>

**Abstract:** *The presented work is focused, from wide textile problems, on research of mechanical properties of flat textile fabrics, the geometrically and also physically non-linear directionally oriented formations. The method of continuum mechanics is used, where textile flat fabric is substitute by continuous medium with the same mechanical properties.*

**Keywords:** *Continuum mechanics, conjugated pair, biaxial loading of fabric.*

### 1. Introduction

Identification of mechanical properties of uniaxially or biaxially loaded flat textiles is physical problem, which leads in general case to seven unknowns' task.

Fabric is so unique formation, that it is necessary to describe its mechanical properties (contrary to solids) for each concrete state of stress and transformation. Constitutive dependence in plane composition is possible to express by three equations.

Substitution of fabric with expressive structure by plain continuum with the same mechanical properties allows to use continuum mechanics equations and to define basic mechanical properties of textile fabric. Dependence between Euler and Lagrange coordinates of points (previously described by Chandrasekharaiah & Lokenath Debnath, 1994; Okrouhlik, 1995; Striz, 2003) is possible to determine from measured movements of observed points on the flat textile (Fig. 1):

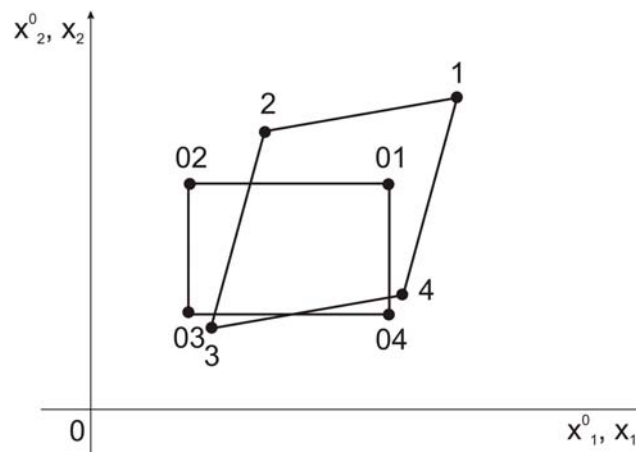


Fig. 1: Show of original and deformed sample and way of its coordinates reading.

$$x_i^p = x_i^{0p} + w_i^p, \quad i = 1, 2, \quad (1)$$

where  $p$  is a number of point, circle indicates Lagrange coordinates. If we replace derivations in equation (1) by differences of ending points of diagonals of selected generally irregular element (Fig. 1), we can define material deformational rate  $F$  by solution of equation systems:

---

<sup>\*</sup> prof. RNDr. Bohuslav Stríž, DrSc. and Ing. Monika Vyšanská, Ph.D.: Department of Textile Technologies, Faculty of Textile Engineering, Technical University of Liberec, Studentska 2, Liberec 1, 461 17, Czech Republic, e-mails: bohuslav.striz@tul.cz, monika.vysanska@tul.cz

$$\Delta x_{ir} = \Delta x_{ir}^0 + w_{i,j} \Delta x_{jr}^0, \quad i, j, r = 1, 2, \quad (2)$$

where  $\Delta x_{i1} = x_i^1 - x_i^3$ ,  $\Delta x_{i2} = x_i^2 - x_i^4$ ,  $\Delta x_{i1}^0 = x_i^{01} - x_i^{03}$ ,  $\Delta x_{i2}^0 = x_i^{02} - x_i^{04}$ .

Differential of movement  $w_{i,j}$ ,  $i, j = 1, 2$  in a plain of element is set like a constant and labeling  $(:)$ , i.e. derivation according to Lagrange coordinate, is not used and  $w_{i,j} = v_{ij}$  is implemented. From difference equation (2) the algebraic equation system is obtained:

$$\begin{aligned} (1+v)(x_1^{01} - x_1^{03}) + v_{12}(x_2^{01} - x_2^{03}) &= x_1^1 - x_1^3, \\ (1+v)(x_1^{02} - x_1^{04}) + v_{12}(x_2^{02} - x_2^{04}) &= x_1^2 - x_1^4, \\ v_{21}(x_1^{01} - x_1^{03}) + (1+v_{22})(x_2^{01} - x_2^{03}) &= x_2^1 - x_2^3, \\ v_{21}(x_1^{02} - x_1^{04}) + (1+v_{22})(x_2^{02} - x_2^{04}) &= x_2^2 - x_2^4. \end{aligned} \quad (3)$$

Material deformational rate  $F = \frac{\Delta x_i^r}{\Delta x_j^{0r}}$  is given by equation system (3) solution. The result is:

$$F = \begin{pmatrix} 1+v_{11} & v_{12} \\ v_{21} & 1+v_{22} \end{pmatrix}, \quad F^T = \begin{pmatrix} 1+v_{11} & v_{21} \\ v_{12} & 1+v_{22} \end{pmatrix}.$$

Let's extend tensor  $F$  with non-dimensional movement  $w_{3,3} = v_{33}$ . The result is

$$F = \begin{pmatrix} 1+v_{11} & v_{12} & 0 \\ v_{21} & 1+v_{22} & 0 \\ 0 & 0 & 1+v_{33} \end{pmatrix} \quad (4)$$

and jacobian

$$J = (1+v_{33})J_0 = (1+v_{33})[(1+v_{11})(1+v_{22}) - v_{12}v_{21}] \quad (5)$$

Quantity  $v_{33}$  is determined by fabric thickness change:

$$h = h_0(1+v_{33}), \quad (6)$$

where  $h_0$  is original measured thickness of fabric. Elongation tensor  $U$  and tensor of rotation  $R$  is defined by material deformational rate  $F$ . It is valid:

$$U^2 = F^T F, \quad F = RU. \quad (7)$$

Elongation tensor  $U$  is possible to define e.g. by projector method defined e.g. by Striz (2001). Let's label tensors  $U, R$  with components:

$$U = \begin{pmatrix} u_{11} & u_{12} & 0 \\ u_{12} & u_{22} & 0 \\ 0 & 0 & 1+v_{33} \end{pmatrix}, \quad R = \begin{pmatrix} r_{11} & r_{12} & 0 \\ -r_{12} & r_{11} & 0 \\ 0 & 0 & 1 \end{pmatrix}. \quad (8), (9)$$

The clamping of measured fabric sample has to allow movements in both directions of loading. In case of angular rotation of main axes of fabric sample anisotropy the clamping has to allow sample's slope.

On a basement of these assumptions the values of  $v_{ij}$  defined on an element of sample is possible to spread on a whole sample. Coordinates of peaks, lengths of deformed sides and goniometric functions of bevel angle are defined from sample shape. Tensor of real specific forces  $\Sigma$  [N/m] is determined with help of forces  $Q_1, Q_2$  (operate in axes of loading) from equations of mechanics. Let's mark

$$\Sigma = \begin{pmatrix} \sigma_{11} & \sigma_{12} & 0 \\ \sigma_{12} & \sigma_{22} & 0 \\ 0 & 0 & 0 \end{pmatrix}. \quad (10)$$

## 2. Conjugated Pairs

The continuum mechanics introduces so-called conjugated pairs, i.e. connection among different types of definitions of stress tensor and strain tensor. Their scalar product on chosen interval of loading has to satisfy condition of equability of mechanical work or power. Just perfect sample loading and its homogenous shape can fulfill this.

Conjugated pairs differ in parameter „ $n$ “. The best known are conjugated pairs with parameters 2, 1, 0, -1, -2. The big number of them can exist, but special importance has Biott's pair ( $n = 1$ ), which very often gives on so-called “conventional” tension, related to original size of the sample.

Biott's tension and deformation can be expressed like:

$$S(1) = \frac{J_0}{2h_0} [F^{-1} \Sigma R + R^T \Sigma F^{-1T}], \quad (11)$$

$$\varepsilon_{ij}(1) = U - I, \quad (12)$$

where  $I$  is unit tensor. Other stress tensors (except Cauchy's) can be expressed like:

$$S(n) = \frac{1}{2} [S(1)U^{1-n} + U^{1-n} S(1)] \quad (13)$$

and for strain tensors is valid

$$\varepsilon_{ij}(n) = \frac{1}{n} (U^n - I). \quad (14)$$

All conjugated pairs have to fulfill condition of mechanical work (power) equality. The following equation is for textile fabric plane state of stress

$$I(n) = \int_0^{x_{\max}} \left[ \sigma_{11} \frac{d\varepsilon_{11}}{dx} + \sigma_{22} \frac{d\varepsilon_{22}}{dx} + 2\sigma_{12} \frac{d\varepsilon_{12}}{dx} \right] dx, \quad (15)$$

where  $x = \frac{Q_1(x)}{Q_1 \max}$ . Permanency of equation (15), for given load and for all conjugated pairs depends

on accuracy of reading of fabric sample peaks' coordinates (fig. 1) and on determination of material deformational gradient  $F$  (4).

## 3. Nonlinear Task

Six mechanical modules determine monoclinic anisotropy and can be expressed by this tensor:

$$\bar{E}_{ij} = \begin{pmatrix} \bar{E}_{11} & \bar{E}_{12} & \bar{E}_{14} \\ \bar{E}_{12} & \bar{E}_{22} & \bar{E}_{24} \\ \bar{E}_{14} & \bar{E}_{24} & \bar{E}_4 \end{pmatrix}. \quad (16)$$

Strip over the modules indicates plane state of stress according to  $\bar{E}_{ij} = \frac{E_{ij}}{(1 - \nu_{ij}^2)}$ , where  $E_{ij}$  is modulus of triaxial state of stress,  $\nu_{ij}$  is Poisson's ratio.

Equation system for modules determination  $\bar{E}_{ij}$ :

$$\begin{aligned}
\bar{E}_{11} \varepsilon_{11} + \bar{E}_{12} \varepsilon_{22} + 2 \bar{E}_{14} \varepsilon_{12} - J_0 \sigma_{11} &= 0, \\
\bar{E}_{12} \varepsilon_{11} + \bar{E}_{22} \varepsilon_{22} + 2 \bar{E}_{24} \varepsilon_{12} - J_0 \sigma_{22} &= 0, \\
\bar{E}_{14} \varepsilon_{11} + \bar{E}_{24} \varepsilon_{22} + 2 \bar{E}_4 \varepsilon_{12} - J_0 \sigma_{12} &= 0, \\
\tan 2\omega (\bar{E}_{11} - \bar{E}_{22}) - 2(\bar{E}_{14} + \bar{E}_{24}) &= 0, \\
\tan 4\omega (\bar{E}_{11} + \bar{E}_{22} - 2 \bar{E}_{12} - 4 \bar{E}_4) - 4(\bar{E}_{14} - \bar{E}_{24}) &= 0, \\
(\bar{E}_{11} \bar{E}_{22} - \bar{E}_{12}^2)(\varepsilon_{11} - \varepsilon_{22})^2 - [\bar{E}_4 ((\varepsilon_{11} - \varepsilon_{22})^2 + 4 \varepsilon_{12}^2) - \\
- 2 J_0 \sigma_{12} \varepsilon_{12}] (\bar{E}_{11} + \bar{E}_{22} + 2 \bar{E}_{12}) &= 0,
\end{aligned} \tag{17}$$

where  $\tan 2\omega = \frac{2\sigma_{12}}{\sigma_{11} - \sigma_{22}}$ . Angle  $\omega$  is between main anisotropy axis and load axis.

Shear stress is zero on the main axis. This enables to define angle  $\omega$ . The  $\bar{E}'_{14}$  and  $\bar{E}'_{24}$  are on this axes zero. Then it is valid  $\bar{E}'_{14} + \bar{E}'_{24} = 0$ ,  $\bar{E}'_{14} - \bar{E}'_{24} = 0$  and from these conditions fourth and fifth equation follows (17). The following equation is used for isotropic materials:

$$G = \frac{\tau_i}{\gamma_i}, \tag{18}$$

Where the intensity of shear stress of plane state of stress  $\tau_i = \frac{1}{\sqrt{6}} \sqrt{(\sigma_{11} - \sigma_{22})^2 + \sigma_{11}^2 + \sigma_{22}^2 + 6\sigma_{12}^2}$

and the slope intensity  $\gamma_i = \sqrt{\frac{2}{3}} \sqrt{(\varepsilon_{11} - \varepsilon_{22})^2 + (\varepsilon_{22} - \varepsilon_{33})^2 + (\varepsilon_{33} - \varepsilon_{11})^2 + 6\varepsilon_{12}^2}$  are invariant.

$G = \frac{E}{2(1+\nu)}$  is shear modules. Let's change modulus  $G$  for  $\bar{K}_4$  in equation (18) and we get equation

$$\bar{K}_4 = \frac{1}{2} \left[ \frac{1}{4} (\bar{E}_{11} + \bar{E}_{22} - 2 \bar{E}_{12}) + \bar{E}_4 \right] = \frac{J_0 \tau_i}{\gamma_i}, \tag{19}$$

where just  $\varepsilon_{33}$  is unknown. Deformation  $\varepsilon_{33}$  is possible to express in dependence on conjugated pair

$$n \varepsilon_{33} = (1 + \nu_{33})^n - 1. \tag{20}$$

Transverse proportion of fabric  $h = h_0 (1 + \nu_{33})$  is in equation (20) dependent on choice of conjugated pair. If the method of fabric attenuation measurement (under defined loading) will be realized, then exponent „ $n$ “ and choice of conjugated pair can be done.

#### 4. Conclusion

Determination of explicit conjugated pair depends on perfect biaxial loading apparatus, equipped with stepper, with possibility of fabric free welts movement during loading increment. This equipment is prepared. Development of methodic for fabric attenuation measurement (for given loading) is further condition. Only measurement of real change of fabric transverse proportion allows choosing suitable conjugated pair. These are conditions for fabric mechanical properties determination.

#### Acknowledgements

This work was done under the support of the Czech Grant GACR 1311.

#### References

- Chandrasekharaiah, D. S., Lokenath Debnath (1994) Continuum Mechanics, Academic Press.  
Okrouhlik, M. (1995) Fundamentals of Continuum Mechanics, Prague.  
Striz, B. (2001) Mechanics of Textiles, Part 1: Basis of Continuum Mechanics, TU Liberec, (in Czech).

## NEW APPROACH FOR EVALUATING THE SURFACE TOPOGRAPHY OF ROLLED SHEETS

V. Szarková<sup>\*</sup>, J. Valíček<sup>\*\*</sup>, M. Řepka<sup>\*</sup>, M. Harničárová<sup>\*\*\*</sup>, M. Spurný<sup>\*\*\*\*</sup>, P.  
Kawulok<sup>\*\*\*\*\*</sup>, K. Rokosz<sup>\*\*\*\*\*</sup>, V. Kuběna<sup>\*\*</sup>

**Abstract:** *The paper deals with the evaluation and surface quality improvement of sheets produced by longitudinal cold rolling. In this paper we analyze relations between the arithmetic mean deviation of the assessed profile  $R_a$  and technological parameters of the laboratory rolling mill such as rolling force, rolling speed, rolling reduction etc.*

**Keywords:** *Surface topography, cold rolling.*

### 1. Introduction

A knowledge of surface quality is very important both for manufacturers and customers. Having knowledge of the surface quality would help to affect the technological process of cold rolling in any manufacturing company. This goal can not be achieved without a high level of automatization, monitoring and controlling throughout the whole manufacturing process with minimal manual intervention. Continuous cold rolling is an important process within the steel industry. Its performance directly affects the quality of the finished product. Any correctly designed system renovation can bring many financial gains for a company, mainly in performance and quality improvement as well as in overall business competitiveness (Alsman et al., 2004; Kenmochi et al., 1997; Mišičko et al., 2009; Othmani et al., 1998; Valíček et al., 2009; Valiev et al., 2006; Zrník et al., 2008).

### 2. Experimental set up

The experimental part is primarily focused on examining the relationship between the mean arithmetic deviation  $R_a$  and technological parameters of the rolling mill such as rolling force  $F_{roll}$  [kN], rolling reduction  $\Delta h$  [mm], rolling speed  $v_{roll}$  [m.s<sup>-1</sup>] and revolutions of the rolls  $n_{roll}$  [s<sup>-1</sup>], which affect the process of rolling.

An initial material was a low carbon structural sheet steel PN EN 10263-2:2004. The steel stripes with dimensions of 72 x 33 x 1.6 mm were cold rolled at the Technical University of Košice by the laboratory rolling mill DUO 210 Sva. The chemical compositions of the used sheet steel is given in Tab. 1.

---

<sup>\*</sup> Ing. Veronika Szarková and Ing. Michal Řepka, Ph.D.: Institute of Economics and Control Systems, Faculty of Mining and Geology, VSB-Technical University of Ostrava, 17. listopadu, 708 33 Ostrava - Poruba, CZ, e-mails: veronika.szarkova@vsb.cz, michal.repka@vsb.cz

<sup>\*\*</sup> Assoc. prof. Ing. Jan Valíček, Ph.D. and Ing. Vlastimil Kuběna: Institute of Physics, Faculty of Mining and Geology, VSB-Technical University of Ostrava, 17. listopadu, 708 33, Ostrava - Poruba, CZ, e-mails: jan.valicek@vsb.cz, vlastimil.kubena@vsb.cz

<sup>\*\*\*</sup> Ing. Marta Harničárová, Faculty of manufacturing Technologies of Technical University of Košice with a seat in Prešov, Bayerova 1, 080 01 Prešov, SK, e-mail: marta.harnicarova@tuke.sk

<sup>\*\*\*\*</sup> Ing. Miloslav Spurný, Department of Control Systems and Instrumentation, Faculty of Mechanical Engineering, VSB - Technical University of Ostrava, 17. listopadu, 708 33 Ostrava-Poruba, CZ, e-mail: miloslav.spurny@vsb.cz

<sup>\*\*\*\*\*</sup> Ing. Petr Kawulok, Department of Material Forming, Faculty of Metallurgy and Materials Engineering, VSB - Technical University of Ostrava, 17. listopadu, 708 33 Ostrava-Poruba, CZ, e-mail: petr.kawulok@vsb.cz

<sup>\*\*\*\*\*</sup> Ing. Krzysztof Rokosz, Ph.D.: Division of Electrochemistry and Surface Technology, Koszalin University of Technology, RACŁAWICKA 15-17, PL 75-620 Koszalin, PL, e-mail: rokosz@tu.koszalin.pl








Tab. 1: Chemical composition of low carbon steel (%).

C	Mn	Si	P	S	Cr
0.0228	0.1928	0.0117	0.0081	0.0053	0.0209
V	Cu	Al	Co	B	As
0.0014	0.0275	0.0562	0.0075	0.0004	0.0047

Chemical analysis was performed by a glow discharge optical emission spectrometer LECO GDS 750.

This device allows to perform quantitative chemical analysis of metals and alloys, which is based on the measurement and subsequent evaluation of the intensities of selected spectral lines of the given elements. It is a device for the simultaneous determination of all elements. The device is equipped with channels for the determination of 28 elements. These are: Mg, Al, Cu, B, Mo, Cd, Ni, Fe, Mn, Na, C, S, P, As, Si, Zn, Ti, Co, Ta, V, Cr, Pb, Sb, Bi, Sn, Nb, Zr and W. The analysis by means of this device depends on calibration using reference materials with a known advanced content of elements. Through plastic deformation that occurs during cold rolling, there were made four rolled pieces with different rolling reductions which are listed in Tab. 2.

Tab. 2: Technological parameters of created steel strips.

<i>Steel strips marking</i>	$h_0$ [mm]	$h_1$ [mm]	$\Delta h$ [mm]	<i>Picture</i>
a	1.6	1.6	-	
b	1.6	1.2	0.4	
c	1.6	1.1	0.5	
d	1.6	1.0	0.6	
e	1.6	0.8	0.8	

The steel strips *b*, *c*, *d*, *e* were several times rerolled at the rolling force  $F_{roll}$  from 65.55 to 90.07 kN and at the rolling speed of  $v_{roll} = 0.7 \text{ m.s}^{-1}$ . The original sample *a* did not pass through the rolling mill by reason of a mutual comparison of surface roughness on the rolled pieces.

### 3. Results and discussion

The surface topography of the sheet steel strips was measured in three regions due to different deformation of material. The region I represents the entrance zone of the steel strip and its surface topography within this region. The region II represents the middle zone and the region III represents the bottom zone of the steel strip. The surface topography was measured by an optical profilometer MicroProf FRT. The steel strips were placed on the scanning table and these three regions with dimensions of 5 x 5 mm were scanned by a stationary sensor with a step of 3  $\mu\text{m}$  and frequency of 1 kHz. In this manner, the surface topography data were obtained.

The collected data were analyzed using Gwyddion. The surface roughness data were obtained from all measured regions using this program. The surface roughness information in explicit form for each of the selected parameters (the rolling reduction  $\Delta h$ , the mean arithmetic deviation of the assessed surface profile  $Ra$ , the root mean square deviation from the assessed profile  $Rq$  and the maximum height of profile  $Rz$ ) are given in Tab. 3.

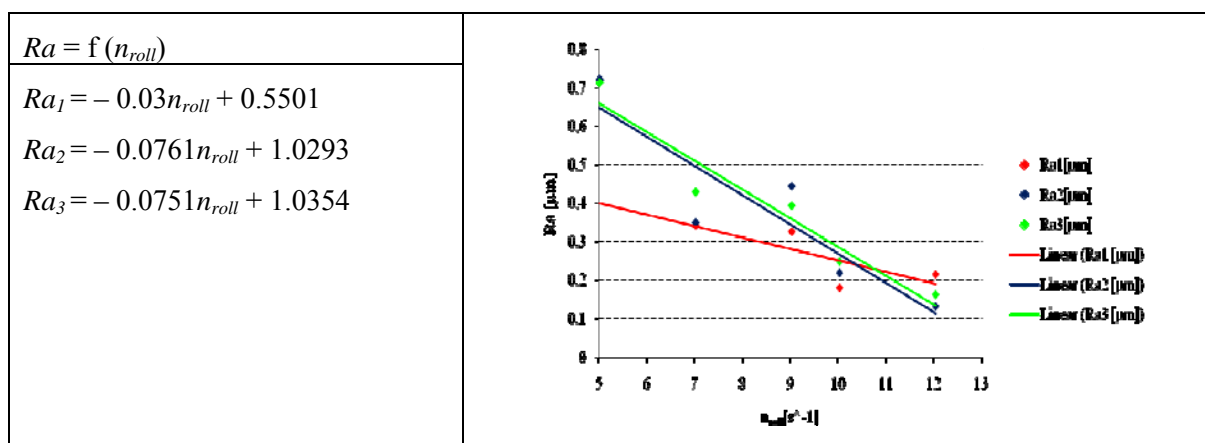
Tab. 3: Assessment parameters of the surface roughness obtained from each sample and region.

	Region I			Region II			Region III		
Steel strips marking	Ra[μm]	Rq[μm]	Rz[μm]	Ra[μm]	Rq[μm]	Rz[μm]	Ra[μm]	Rq[μm]	Rz[μm]
a	-	-	-	0.722	0.967	6.860	0.712	0.955	7.053
b	0.341	0.479	3.011	0.349	0.485	3.293	0.428	0.593	3.946
c	0.325	0.425	2.545	0.444	0.583	3.714	0.392	0.569	5.277
d	0.179	0.235	1.448	0.218	0.293	2.097	0.247	0.340	2.519
e	0.214	0.284	2.244	0.131	0.185	1.769	0.161	0.229	2.136

The surface roughness is expressed in implicit form as follows:  $Ra = f(F_{roll}, \Delta h, v_{roll}, n_{roll})$ . It is necessary to search for the relations between the technology, material and final surface quality. The charts (Tab. 4) were created on the basis of the obtained data.

Tab. 4: Dependence of the Ra on the technological parameters of rolling mill.

Regression equation	Dependence of the Ra on the technological parameters
$Ra = f(F_{roll})$ $Ra_1 = -0.0065F_{roll} + 0.7721$ $Ra_2 = -0.0108F_{roll} + 1.1291$ $Ra_3 = -0.0114F_{roll} + 1.1964$	
$Ra = f(\Delta h)$ $Ra_1 = -0.3591\Delta h + 0.4713$ $Ra_2 = -0.7392\Delta h + 0.7129$ $Ra_3 = -0.7051\Delta h + 0.7124$	
$Ra = f(v_{roll})$ $Ra_1 = -0.3004v_{roll} + 0.5501$ $Ra_2 = -0.7633v_{roll} + 1.0293$ $Ra_3 = -0.7527v_{roll} + 1.0354$	



The best correspondence between experimentally determined data and correlation equations is obtained in the third region, where the correlation coefficient ranges from 93 to 98.3%. It appears from this, that the analyzed region III the best corresponds to our assumption.

#### 4. Conclusions

The paper describes the methodology of surface topography evaluation of sheet strips from low carbon structural steel PN 10263-2:2004, which is based on the comparison of the mean arithmetic deviation with the technological parameters of the rolling mill DUO 210 SVa. The benefit is the relation between the surface topography that is in our case represented by the mean arithmetic deviation  $Ra$  and technological parameters. The presented results from this rolling mill confirm the correctness of the assumption, that with an increase in rolling force  $F_{roll}$ , rolling reduction  $\Delta h$ , rolling speed  $v_{roll}$ , and revolutions of the rolls  $n_{roll}$ , the quality of the rolled surface can be improved. It is obvious that the surface quality is very important for manufacturing companies, because the requirements on the quality during cold rolling are steadily increasing.

#### Acknowledgements

The work has been supported by projects SGS No. SP2011/76, GA ČR No. 101/09/0650, MŠMT No. MSM6198910016, RMTVC No. CZ.1.05/2.1.00/01.0040 and MEB051021. Thanks are also of the Moravian-Silesian Region 01737/2010/RRC for finance support.

#### References

- Alsamhan, A., Pillinger, I., Hartely, P. (2004) The development of real time re-meshing technique for simulating cold-roll-forming using FE methods. *Journal of Materials Processing Technology*. 147, pp 1-9.
- Kenmochi, K., Yarita, I., Abe, H., Fukuhara, A., Komatu, T., Kaito, H. (1997) Effect of micro-defects on the surface brightness of cold-rolled stainless-steel strip. *Journal of Materials Processing Technology*. 69, pp. 106-111.
- Mišičko, R., Kvačkaj, T., Vlado, M., Gulová, L., Lupták, M., Bidulská, J. (2009) Defects simulation of rolling strip. *Materials Engineering*, vol. 16, no. 3, pp. 7-12.
- Othmani, A., Kaminsky, C. (1998) Three dimensional fractal analysis of sheet metal surfaces. *Wear*, 214. pp. 147-150.
- Valíček, J., Hloch, S., Kozak, D. (2009) Study of Surface Topography Created by Abrasive Waterjet Cutting. *Slovanski Brod, Strojarski fakultet u Slovanskem Brodu*.
- Valiev, R. Z., Estrin, Y., Horita, Z. et al. (2006) Producing bulk ultrafine grained materials by severe plastic deformation. *Journal of the Minerals, Metals and Materials Society*, vol. 58, no. 4, pp. 33-39.
- Zrník, J., Dobatkin, S. V., Mamuzič, I. (2008) Processing of metals by severe plastic deformation (SPD) – structure and mechanical properties respond. *Metalurgija*, vol 47, no 3, pp. 211.

## APPROACH FOR DYNAMIC PROPERTIES ADJUSTMENT OF STEEL STRUCTURE FEM MODELS

J. Szweda<sup>\*</sup>, Z. Poruba<sup>\*</sup>, R. Sikora<sup>\*</sup>

**Abstract:** *The presented paper deals with an analysis of steel structure dynamic properties. The construction, which consists of stationary and movable parts, is expected to be under a significant dynamic loading caused by a change of motion state during run up and run down. The following three ways of the analysis are presented – the finite element method for two types of 3-D models, both the beam-shell and the volume model, and an experimental verification of modal properties relating to a selected type of eigenshapes.*

**Keywords:** *Lifting platform, simplification, eigenshape, eigenfrequency, FEM.*

### 1. Introduction

Numerous engineering projects are inseparably linked with a design and an analysis of steel structure properties although the construction itself represents an insignificant part of a given project. It is essential to verify its dynamic behaviour and possibly carry out necessary adjustments, especially if the construction is kept in motion or submitted to different loading ranges.

The assignment described below is the analysis of the construction dynamic properties. The device consists of stationary and movable components. It is expected a significant portion of the dynamic loading caused by motion state during run up and run down. The analysed construction serves as a stand for testing, a development and a drive control adjustment of movable platforms. The tested stand itself, and in particular the moving platforms, is nearly identical with the real operating devices. On that account, the realized testing simulations are an accurate “mirror” of the complete system operating in the real service conditions.

The aim of the implemented analyses is to identify the dynamic properties of the movable components, i.e. to determine the eigenfrequencies of the platforms bedded in the stationary part. Taking into consideration the reliability of the results, the dynamic properties analysis is made numerically with an application of the two models. Additionally, the verification of the identified results is achieved experimentally by EMA (experimental modal analysis) method.

This article presents the reached agreement of the numerical simulation results with experimentally obtained outcomes. Furthermore, it demonstrates positive and negative features of the particular solution methods. The purpose of the task is to verify the construction dynamic properties in regard to the expected significant operational dynamic loading.

The construction consists of two movable platforms, two guide pillars, base frame and driving unit. General data: overall dimensions:  $6.5 \times 3.7 \times 3.0$  m (w  $\times$  d  $\times$  h); movable platforms – weight approx. 750 kg + considered load of 1000 kg; construction – total weight approx. 6 200 kg. Fully equipped construction 3D drawing represents Fig. 1.

---

<sup>\*</sup> Ing. Jan Szweda, Ph.D., Ing. Zdeněk Poruba, Ph.D. and Ing. Roman Sikora, Ph.D.: Department of Mechanics, Technical University of Ostrava, 17. listopadu 15; 708 00, Ostrava; CZ, e-mails: jan.szweda@vsb.cz, zdenek.poruba@vsb.cz, roman.sikora@vsb.cz

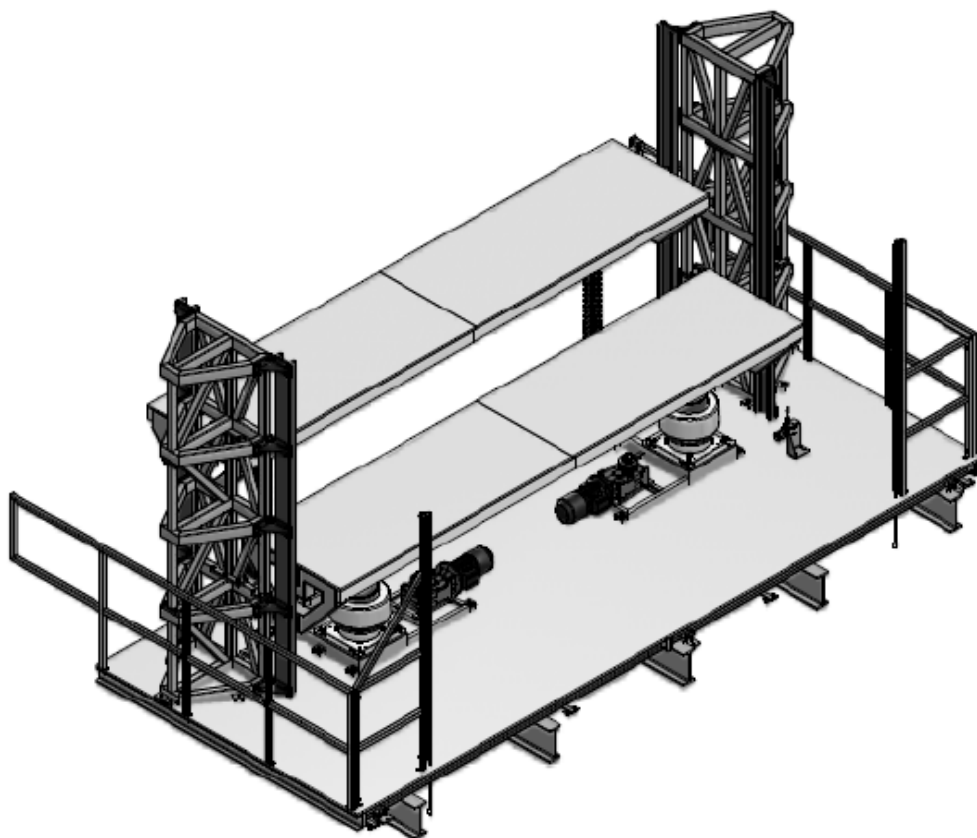


*Fig. 1: 3D Model of Lifting Platform.*

## **2. Determination and verification of the dynamic properties**

The computational modelling method and simulation of the steel structure dynamic properties by the finite element method (FEM) is used for the solution of the given problem. The method is realized with the finite element software ANSYS Workbench 11 and 12. Consequently, the adjustment and verification of the mathematical model is performed; the respective experimental measurements of the eigenfrequencies and eigenshapes are carried out by the experimental modal analysis method realized by the measuring system PULSE by Bruel&Kjaer according paper (Ferfecki et al., 2007). The veracity and reliability of the dynamic analyses results strongly depend on a discretization quality, i.e. on a type and size selection of finite elements and the rate of geometry simplification as compared with the real system; in most cases the simplification is necessary according paper (Saeed et al., 2009). Since the performed analyses, both the modal and the platform fetch-up response analysis, are highly time-consuming (Laxalde et al., 2010), the aim is to develop the possible simplest numerical model to reduce the computation time without losing the accuracy of the results according paper (Poruba et al., 2010).

Within the solution the two computational models are applied:

**Model A** – after the adjustment, this model is used for the further numerical simulations of system behaviour. The model consists of the beam and shell elements, which are from the computing requirements point of view less demanding than the solid elements used in Model B. On the other hand, to describe the real properties correctly, the mentioned model is more settings-demanding due to a higher degree of simplification. This model is created on the basis of the received technical drawings.

**Model B** – the model is created on the basis of CAD volume model of the lifting platform. Even in this model, certain simplifications in the form of removed screws, nuts or washers are carried out. The rest of the geometry is kept identical. The details of the model are depicted in the Fig. 2. The modal analysis is applied to this model for three different platform positions. Model A is adjusted according to the calculated results, so that the eigenfrequencies and eigenshapes reach the values of the same ones obtained from the reality closer Model B.

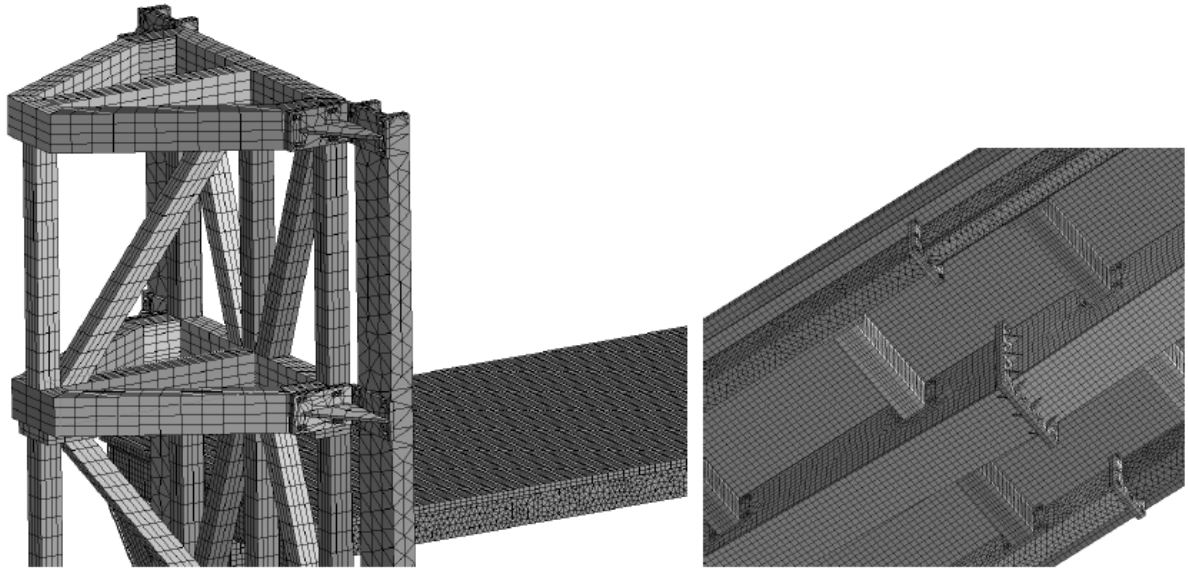


*Fig. 2: Geometry and Mesh of Model B.*

The next source of data for the best possible adjustment of Model A is the measurement performed by the experimental modal analysis method. The eigenfrequencies and eigenshapes are obtained from vibrations in the vertical direction on the both platforms (not the pillars). Thus, the eigenfrequencies and eigenshapes describing the vibration in other directions are not captured by this measurement. Since this is only the supporting tool for the adjustment of the mathematical model, this simplification is acceptable. The mentioned facts imply the properties of the adjusted mathematical model (Model A) are the intersection of the results obtained from the computational modal analysis of Model B and the experimentally detected values. The reached agreement is presented in Tab. 1. It can be stated the successive adjustment of Model A has reached the appropriate congruence level between results from Model B and the experimental modal analysis. Thus, Model A can be considered as the standard and be used e.g. for numerical simulations of the steel structure dynamic phenomena.

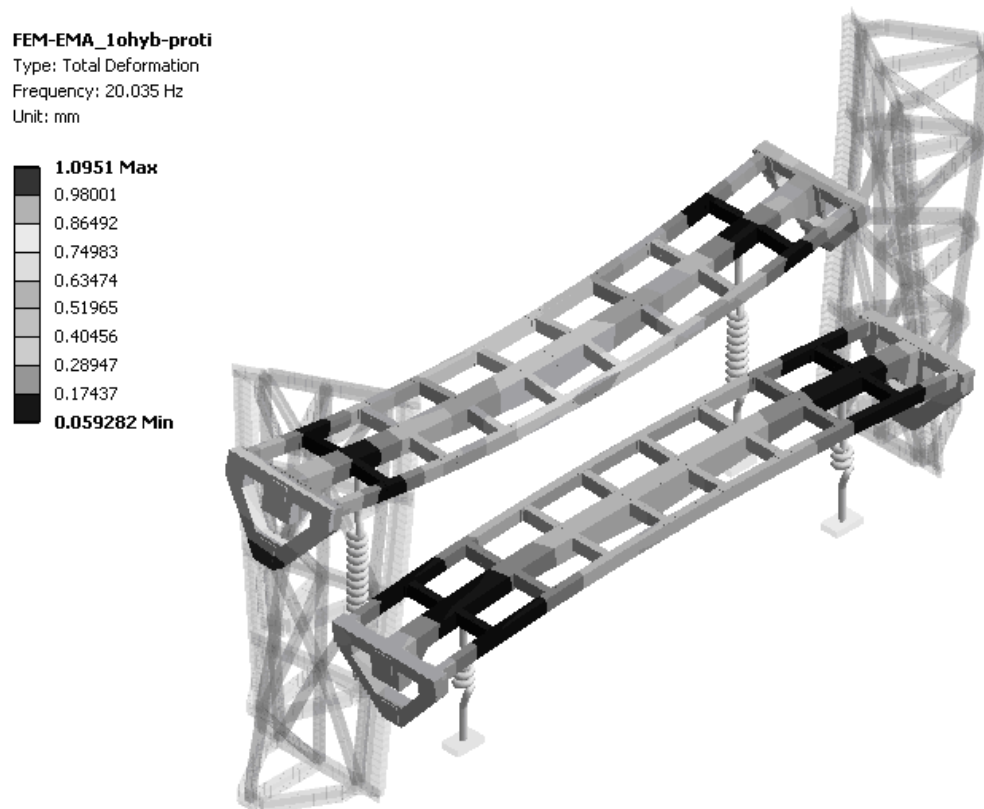


*Fig. 3: First Bending Eigenshape – 20.4 Hz (platforms move against each other).*

Tab. 1: Eigenfrequencies during the numerical model adjustment.

<i>Eigenshape</i>	<i>Model A [Hz]</i>	<i>Model B [Hz]</i>	<i>Measurement [Hz]</i>
Platform bending (motion against each other)	20.0	20.5	N/A
Bending with wave	24.1	22.6	28.5
Platform bending (motion in phase)	25.7	21.0	28.8

### 3. Conclusions

The accomplished computer simulations and analyses in the conjunction with the experimental measurements allow claiming that the computational model developed on the basis of the adjustment and the experiment is able to describe the dynamic behaviour of the steel structure accurately. Next, the consumed computational time of both the modal numerical analysis and possible following analyses of transition phenomena is acceptable.

Aberrations of the eigenfrequencies in comparison with the computational model A and the measurements are less than 4 Hz, the measured first and the second eigenfrequencies are approximately 28 Hz and 30 Hz. Thus adjusted model determines the eigenfrequencies and eigenshapes in the range of  $\langle 0, 40 \rangle$  Hz for various load of the lifting platform (unloaded, symmetric load, asymmetric load).

The eigenshapes with the dominant vertical component of the vibration is experimentally identified within the models adjustment. The analysis of the eigenfrequencies and eigenshapes establishes that the vertical platforms arrangement does not have a significant influence on the values of the eigenfrequencies and eigenshapes whereas the first eigenfrequency of the first bending eigenshape takes approx. 10 Hz.

### Acknowledgement

The work has been supported by the research project MSM6198910027 of the Ministry of Education, Youth and Sports of the Czech Republic and by the research project TA01010705 of the Technology Agency of the Czech Republic what is highly appreciated.

### References

- Ferfecki, P., Ondrouch, J. & Sikora, R. (2007) Porovnání numericky vypočítané a experimentálně změřené odezvy na buzení odstředivou silou u rotorové soustavy Rotor KIT 4 s hřídelem zeslabeným trh vrubem, in: Proc. Conf. on Dynamics of Machines, Ind. of Thermomechanics AS CR, Prague, pp. 63-70.
- Laxalde, D; Legrand, M. (2010) Nonlinear modal analysis of mechanical systems with frictionless contact interfaces. Computational Mechanics [online]. pp. 1-10. <<http://dx.doi.org/10.1007/s00466-010-0556-3>>.
- Poruba, Z. & Szveda, J. (2010) Simulation and optimization of the electromotor cooling. Metalurgija, 49, 2, pp. 474-478.
- Saeed, R.A. & Galybin, A.N. (2009) Simplified model of the turbine runner blade. Engineering Failure Analysis, 16, 7, pp. 2473-2484.



## **MODAL ANALYSIS OF THE IMPERFECT BLADED DISK WITH FRICTION ELEMENTS**

**J. Šašek<sup>\*</sup>, V. Zeman<sup>\*</sup>, J. Kellner<sup>\*</sup>**

**Abstract:** *This paper is concerned with mathematical modeling of the imperfect bladed disk with friction elements, which are used to suppress blade vibration. These kinds of systems are mainly used in steam turbines where our interests are aimed. The friction elements are placed between shrouds of selected central symmetrical mounted blades (imperfection). A slipping is considered on the both contact surfaces. The model of the bladed disk is based on decomposition into a disk subsystem and a blading subsystem. The finite element method is used for modeling of the both subsystems. All influences of steady-state rotation are respected as centrifugal forces, gyroscopic effects, centrifugal stiffening of blades and dynamic softening. The model is used for a modal analysis of non-rotating and rotating imperfect bladed disk. Selected natural modes of non-rotating system will be shown. Dependency of eigenfrequencies on the angular velocity is presented in Campbell diagram. The methodology of simulation and post-processing are implemented in an in-house software.*

**Keywords:** *Bladed disk, modal analysis, FEM, friction element.*

### **1. Introduction**

Requirements on higher efficiency and wide operation range of steam turbines lead to thinner blade profile, which has better properties in term of computation of fluid dynamics (CFD) but dynamic properties get worse. The purpose of friction elements is to decrease potential high amplitudes of blade vibration, which may occur due to resonances or high applied forces of steam flow fluctuation. The aim of this paper is to present methodology for bladed disk vibration analysis of damped blades applicable for test imperfect bladed disk used in Institute of Thermomechanics AS CR.

The presented method is based on discretization of 3D disk (Šašek & Hajžman, 2006) and 1D blades (Kellner & Zeman, 2006) by FEM. A harmonic balance method will be further used for modeling of bladed disk vibration with friction elements, which are placed between blade shrouds (see Fig. 1 and Fig. 2). The comparison between flexible and rigid shroud is performed in Zeman et al. (2009) entitles the shroud modeled as a rigid body fixed with blade in the end of blade's profile.

### **2. Model of imperfect bladed disk**

The imperfect bladed disk is consists of a disk, which is fixed on inner radius to rigid shaft, and two kinds of blades. Blades of the first type are mounted to disk with rigid joint. A rigid shroud is placed in the end of the second type of blades. Friction elements are placed between shrouds (see Fig. 2). Each type of blades is separated into two sets (2x25 blades of the first type, 2x5 blades of the second type), which create bladed disk with two perpendicular axis of symmetry. There are 2x4 friction elements in the both sets of the second type of blade.

The stiffness coupling matrix between friction elements and blade shrouds is derived from deformation of adjacent shroud contact areas caused by relative movements of blades and friction elements and by centrifugal forces acting on friction elements.

---

<sup>\*</sup> Ing. Jakub Šašek, Ph.D., prof. Ing. Vladimír Zeman, DrSc. and Ing. Josef Kellner, Ph.D.: Faculty of Applied Sciences, University of West Bohemia in Pilsen, Univerzitní 22; 306 14, Plzeň; CZ, e-mails: jsasek@kme.zcu.cz, zemanv@kme.zcu.cz, kennyk@kme.zcu.cz

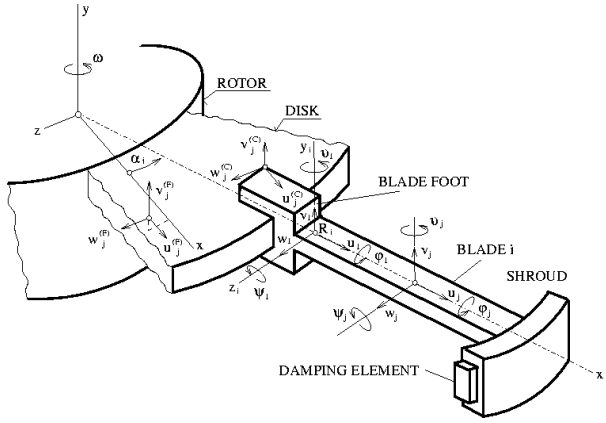


Fig. 1: The second type of blades with friction elements.

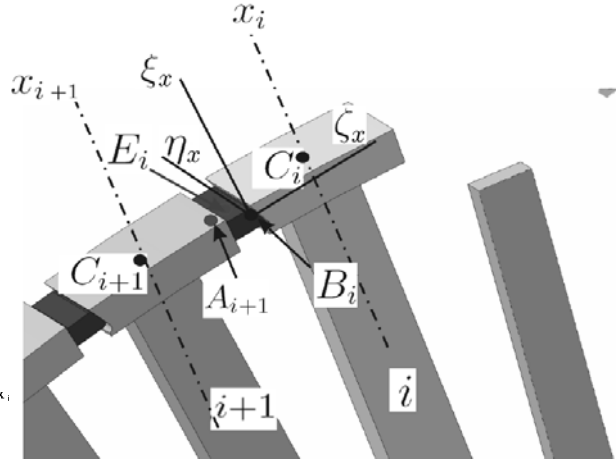


Fig. 2: Detail of shrouds with friction elements.

This model respects contact stiffnesses between blades and damping elements  $E_i$  on both contact areas, defined by contact stiffness matrices

$$\mathbf{K}_C^{(X)} = \text{diag} \begin{pmatrix} 0 & 0 & k_{\zeta_x} & k_{\xi_x \eta_x} & k_{\eta_x \eta_x} & 0 \end{pmatrix}, \quad X = A_{i+1}, B_i, \quad (1)$$

The matrices express the constraint between the circumferential displacement and two rotations by means of contact stiffness  $k_{\zeta}$  in normal direction to concrete contact area  $\xi_x \eta_x$  and two flexural stiffnesses  $k_{\xi_x \xi_x}$ ,  $k_{\eta_x \eta_x}$ , whereas  $\mathbf{K}_C^{(B_i)} = \mathbf{K}_C^{(B)}$ ,  $\mathbf{K}_C^{(A_{i+1})} = \mathbf{K}_C^{(A)}$ .

These matrices are expressed in local coordinate systems  $\xi_x, \eta_x, \zeta_x$  placed in central contact point  $B_i$  of the radial contact area of blade shroud  $i$ , respective in central contact point  $A_{i+1}$  of the blade shroud  $i+1$  on the slope area. The point  $E_i$  is the center of gravity of the friction element. The coupling (deformation) energy between two adjacent blades  $i$  and  $i+1$  is expressed as

$$E_C^{i,i+1} = \frac{1}{2} (\mathbf{q}_{B,i} - \mathbf{T}_{B,E} \mathbf{q}_{E,i})^T \mathbf{K}_C^{(B)} (\mathbf{q}_{B,i} - \mathbf{T}_{B,E} \mathbf{q}_{E,i}) + \frac{1}{2} (\mathbf{T}_{A,E} \mathbf{q}_{E,i} - \mathbf{q}_{A,i+1})^T \mathbf{K}_C^{(A)} (\mathbf{T}_{A,E} \mathbf{q}_{E,i} - \mathbf{q}_{A,i+1}), \quad (2)$$

where  $\mathbf{q}_{B,i}, \mathbf{q}_{A,i+1}$  are vectors of blade shroud displacements of points  $B_i, A_{i+1}$  and  $\mathbf{q}_{E,i}$  is vector of gravity center  $E_i$  displacements of friction elements, where  $i$  is blade index. The transformation between vectors  $\mathbf{q}_{B,i}, \mathbf{q}_{A,i+1}$  in local coordinate systems  $\xi_x \eta_x \zeta_x$ ,  $x = B_i, A_{i+1}$  and vectors  $\mathbf{q}_{C,i}, \mathbf{q}_{C,i+1}$  of global coordinates of end nodal points of the adjacent blades is

$$\mathbf{q}_{B,i} = \mathbf{T}_B \mathbf{q}_{C,i}, \quad \mathbf{q}_{A,i+1} = \mathbf{T}_A \mathbf{q}_{C,i+1}. \quad (3)$$

Matrices  $\mathbf{T}_{B,E}$  and  $\mathbf{T}_{A,E}$  transform vector  $\mathbf{q}_{E,i}$  into displacements of contact points  $B_i$  and  $A_{i+1}$  in the local coordinate systems  $\xi_x \eta_x \zeta_x$ ,  $x = B_i, A_{i+1}$ .

The disk is modeled analogously as in paper (Šašek & Hajžman, 2006) by means of 3D continuum FE discretization. The mathematical model of the bladed disk rotating with angular velocity  $\omega$  ad interim with smooth friction elements was derived in configuration space  $\mathbf{q} = [\mathbf{q}_D^T \quad \mathbf{q}_R^T]^T$ , where  $\mathbf{q}_D$  is vector of generalized coordinates of the disk and  $\mathbf{q}_R$  is vector of generalized coordinates of all blades and friction elements. The connection of the blades and the disk is realized by rigid joint which is described in Kellner, J. & Zeman, V. (2010).

The conservative mathematical model of the centrally clamped bladed disk rotating with constant angular velocity  $\omega$  around  $y$  axis has the form

$$\mathbf{M}\ddot{\mathbf{q}} + \omega\mathbf{G}\dot{\mathbf{q}} + (\mathbf{K}_s + \mathbf{K}_C + \omega^2\mathbf{K}_\omega - \omega^2\mathbf{K}_d)\mathbf{q} = \omega^2\mathbf{f}_2, \quad (4)$$

where  $\mathbf{M}$  is mass matrix,  $\omega\mathbf{G}$  is skew-symmetric matrix of gyroscopic effects,  $\mathbf{K}_s$  is static stiffness matrix,  $\mathbf{K}_\omega$  is matrix of blade centrifugal stiffening and  $\mathbf{K}_d$  is matrix of dynamic softening of 1D and 3D continuum in centrifugal field. The contact stiffness matrix  $\mathbf{K}_C$  between friction elements and shroud contact areas are calculated from identity  $\frac{\partial E_C}{\partial \mathbf{q}} = \mathbf{K}_C\mathbf{q}$ , where  $E_C = \sum_i E_C^{i,i+1}$ .

### 3. Modal analysis of bladed disk

Correctness of the modeling methodology of the imperfect bladed disk is advised by modal analysis of the test bladed disk (Půst & Pešek, 2009). First eight natural modes of non-rotating bladed disk are rigid ( $f_{1,2...8} = 0$  Hz). These natural modes are characterized by oscillation of the friction elements in  $y$  direction because of smoothness of the friction elements. The next four mode shapes are shown on Fig. 3 to Fig. 6. We can separate the modes into 2 pairs. The first pair, where blades oscillate in the opposite way, is consists of the 9th and 11th natural mode. The 10th and 12th natural mode, where blades oscillate in the same direction, create second pair. All pairs are characterized by 1 nodal diameter (ND), where the disk and the blades don't oscillate. The nodal diameters are perpendicular in corresponding mode shapes of one pair. Different values of pair eigenfrequencies are given by imperfect blades.

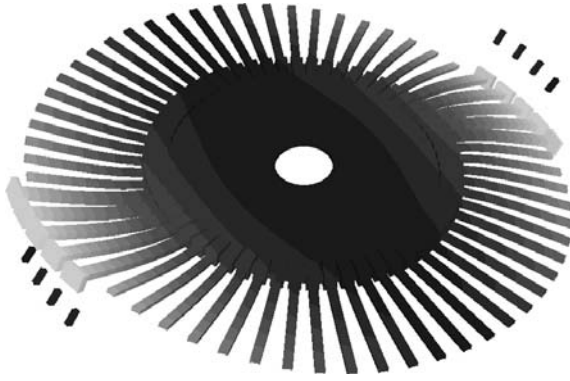


Fig. 3: The 9th natural mode ( $f_9 = 89.23$  Hz, 1 ND).

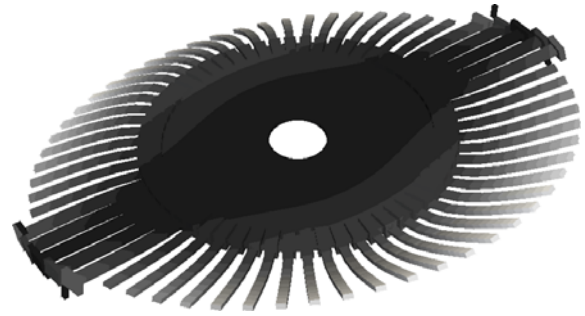


Fig. 4: The 11th natural mode ( $f_{11} = 110.41$  Hz, 1 ND).

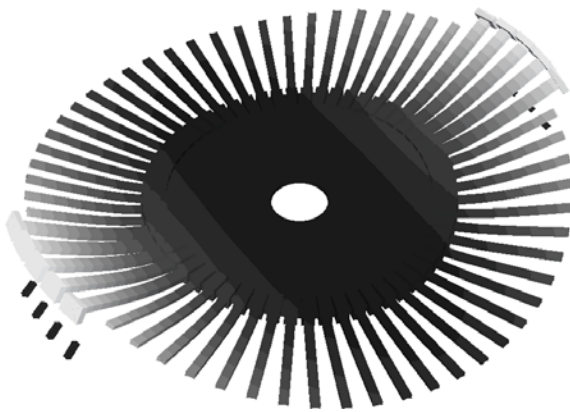


Fig. 5: The 10th natural mode ( $f_{10} = 93.73$  Hz, 1 ND).

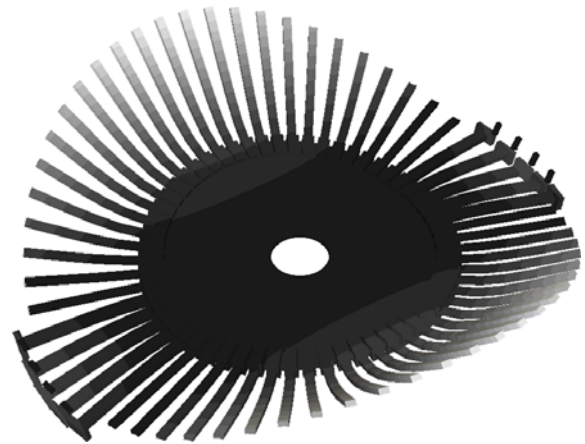


Fig. 6: The 12th natural mode ( $f_{12} = 120.38$  Hz, 1 ND).

The dependency of eigenfrequencies is shown in the Campbell diagram (see Fig. 7) diagram for 9th to 16th eigenfrequencies and for angular velocity  $\omega = \langle 0, 3000 \rangle$  RPM. The blade centrifugal stiffening effect represented by matrix  $\mathbf{K}_\omega$  influences the eigenfrequencies mostly. The other effects of rotation affects less the eigenfrequencies.

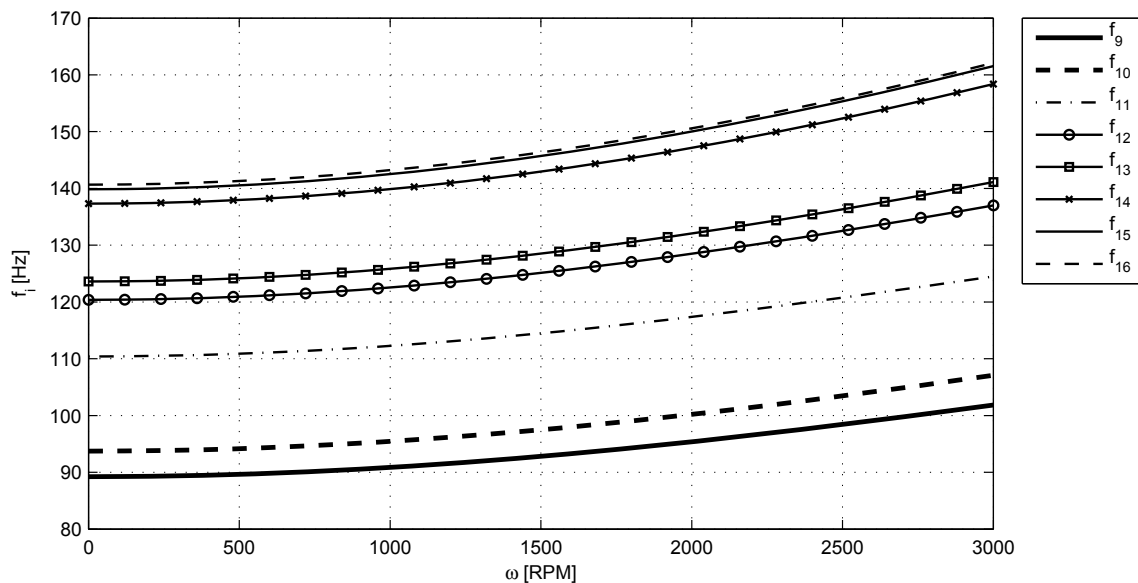


Fig. 7: Campbell diagram for 9th to 16th eigenfrequencies and for angular velocity  $\omega = \langle 0, 3000 \rangle$  RPM.

#### 4. Conclusions

The presented model of the imperfect bladed disk with the smooth friction elements is the first step for bladed disk vibration analysis of damped blades. The correctness of the methodology is checked on the modal analysis of non-rotating and rotating testing bladed disk, where all influences of steady-state rotation are considered.

The developed methodology and mathematical model of the imperfect bladed disk will be further used for modeling of the test bladed disk vibration respecting friction forces in contact surfaces between blade shrouds and friction elements using harmonic (balance) linearization method.

#### Acknowledgement

This work was supported by GA CR in the project No. 101/09/1166 “Research of the dynamic behaviour and optimization of complex rotating system with non-linear couplings and high damping materials”.

#### References

- Šašek, J. & Hajžman, M. (2006) Modal properties of rotating disk, in: Proc. of the 22nd Computational Mechanics, UWB in Pilsen, Hrad Nečtiny, pp. 593-600.
- Kellner, J. & Zeman, V. (2006) Influences of dynamic stiffness, centrifugal forces and blade's elastic seating on blade modal properties, in: Proc. of the 8th International Conference Applied Mechanics, UWB in Pilsen, Srní, pp. 47-48.
- Zeman, V., Šašek, J. & Byrtus, M. (2009) Modelling of rotating disk vibration with fixed blades, Modelling and optimization of physical systéme 8, Gliwice, 125-130.
- Kellner, J. & Zeman, V. (2010) Modelling of the bladed disk vibration with damping elements in blade shroud, Applied and Computational Mechanics, 4, 1, pp. 37-48.
- Půst, L. & Pešek, L. (2009) Vibration of imperfect rotating disk, in: Computational Mechanics 2009 – Book of Extended Abstracts, UWB in Pilsen, pp. 1-2.

## FE-MODELING OF STIFFNESS EQUIVALENT RIVETED JOINTS

J. Šedek<sup>\*</sup>

**Abstract:** *This paper deals with the FE-modeling of the riveted joints usable on the structures with a large number of rivets. The quick built capacity and the load-carrying characteristic close to reality are preferred. The 1D connecting element is used and determination of the stiffness characteristic is presented.*

**Keywords:** *Rivet, riveted joint, FEM, stiffness equivalent joint.*

### 1. Introduction

The sheet stiffening of the structure is one of basic parameters determining the stress and strain state in the vicinity of a crack in the stiffened structure. Stiffening is important when connecting sheets to the structural parts like beams, stringers and ribs and it can affect the fatigue crack growth rates. The influence of the structure stiffening has to be included in the analysis of the fatigue crack characteristics in order to determine the life prediction in accordance with the damage tolerance philosophy.

Current airframes are mostly riveted and bolted. The structural joint fatigue life depends on many factors such as a type of joint, characteristics of the local stress state, stiffening, loading, quality of material and assembly, etc. The stiffness of joint elements affects the load transfer between the sheet and stiffeners. The joint is the critical point of the structure with respect to the fatigue and a crack is initialized right here.

The most of the finite element models of the aircraft structures are built by means of the 1D and 2D elements. However, principal structure elements with complicated geometry should be analysed by 3D elements to ensure the correct local stress state representation. So there is an effort to get a suitable model of riveted joints to ensure the quick built capacity and the load-carrying characteristic close to reality.

### 2. Riveted joint stiffness determination

The riveted joints stiffness influence to the assembly stiffness may be significant. There are applied complete adjustments in order not to neglect the stiffness variations.

Basic analyses of the riveted joint applicable to the large assemblies deal with the model of equivalent cross-sections of the rivet and the modeled part of the substitutive structure scheme and with the model of the stiffness equivalent joint. Comparison of both approaches in Běhal (1985) shows the ability of the second model to give better representation of the real properties of the joint.

Characteristics of the joint stiffness and the joint deformation are available from experimental measurements on geometrically, mechanically and technologically analogical specimens of the real joint or from the FEM analysis. Analytical equations to specify the joint stiffness characteristics were determined by the experimental measurements by Swift (1974) and Vogt (1947) and by the derivation on the basis of differential equations of the deflection curve by Barrois (1978).

Analytical models formulated generally by the term (1) enable analysis of the aircraft structure joints with a wide thickness range. There are different abilities regarding the usage of the joint material

---

<sup>\*</sup>Ing. Jakub Šedek: Strength of Structures Dpt., Aeronautical Research and Test Institute (VZLÚ, a.s.), Beranových 130; 199 05, Prague; CZ, e-mail: sedek@vzlu.cz

(Young's modulus  $E_s$ ), jointed materials (Young's modulus  $E_1$  and  $E_2$ ) and the joint geometry (rivet diameter  $d$  and thicknesses  $t_1$  and  $t_2$ ).

$$\delta_R = \delta_R(F, d, t_1, t_2, E_1, E_2, E_s) \quad (1)$$

Models were verified by the experimental stiffness measurements of the specimens representing the typical riveted joint in the aircraft structure (Doubrava & Beránková, 1998). The experimental data comparing to the analytical models of Swift and Barrois shows the adequate specimen stiffness at the unloaded area (see Fig. 1). The riveted joint stiffness depends on the loading history, therefore the nonlinear behaviour should be taken into account.

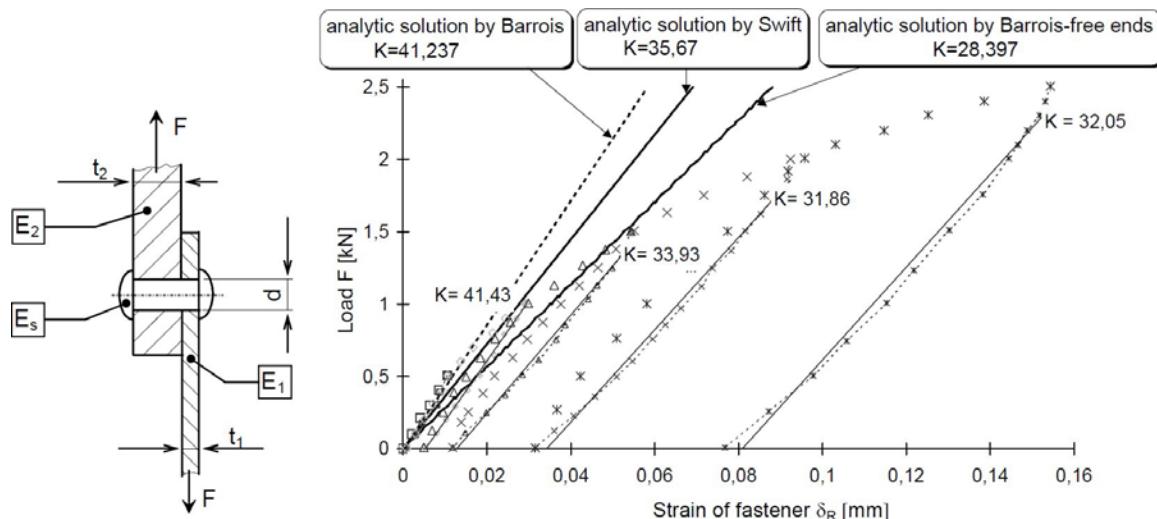


Fig. 1: Experimental data comparison to analytical solutions (lines) – single-shear rivet joint (Doubrava, 1998).

The finite element method (FEM) is possible approach to obtain the stiffness characteristics of joints. The detailed nonlinear 3D analysis including the simulation of the riveting process can be carried out. A sufficient correlation between the experimental data and data from the simulation was reached using elastic-plastic behavior derived from a simple uniaxial experiment (Kaniowski, 2009). However, there was found a high dependency on the friction between jointed materials (Fárek, 2010).

### 3. Simple rivet replacement for more complex FE-analyses

In practice, it is impossible to perform the FE-analyses of the above mentioned solid model on the structure with a large number of rivets. Models are usually built from the shell elements, also the usage of the 1D elements with a tuned stiffness characteristic in order to simulate the joint stiffness adequately is applicable.

#### 3.1. FE-model of the joint

FE-models of the tested specimens were created to study the joint model properties. The ABAQUS 6.10–2 software was used. The 1D element connects 3D part mesh with 2D sheet mesh through single nodes (see Fig. 2).

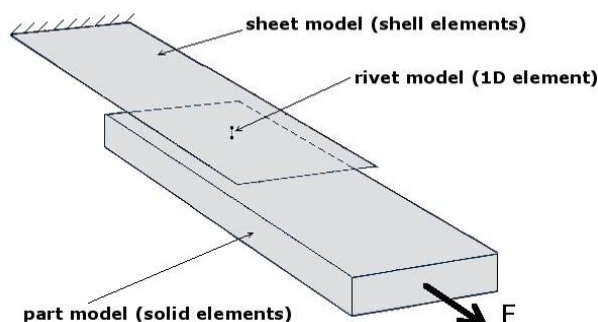


Fig. 2: Schematic model of the specimen.



Firstly, the study of the mesh influence was made using the 3D part with an aluminum material. The analysis was focused on the deformation change in the cylindrical mesh section (see Fig. 3). The mesh around the virtual rivet axis consists of 2<sup>nd</sup> order hexahedral elements round distribution and 2<sup>nd</sup> order wedge elements (collapsed hexahedrons) in the centre. The rest of the part is meshed with hexahedral or tetrahedral elements with the size of about 2 mm. The element density increases at the cylindrical section boundary. The number of elements in the direction of the radius varies from 2 to 10. The unit load representing the rivet shear loading is applied to the single outer node on the virtual rivet axis.

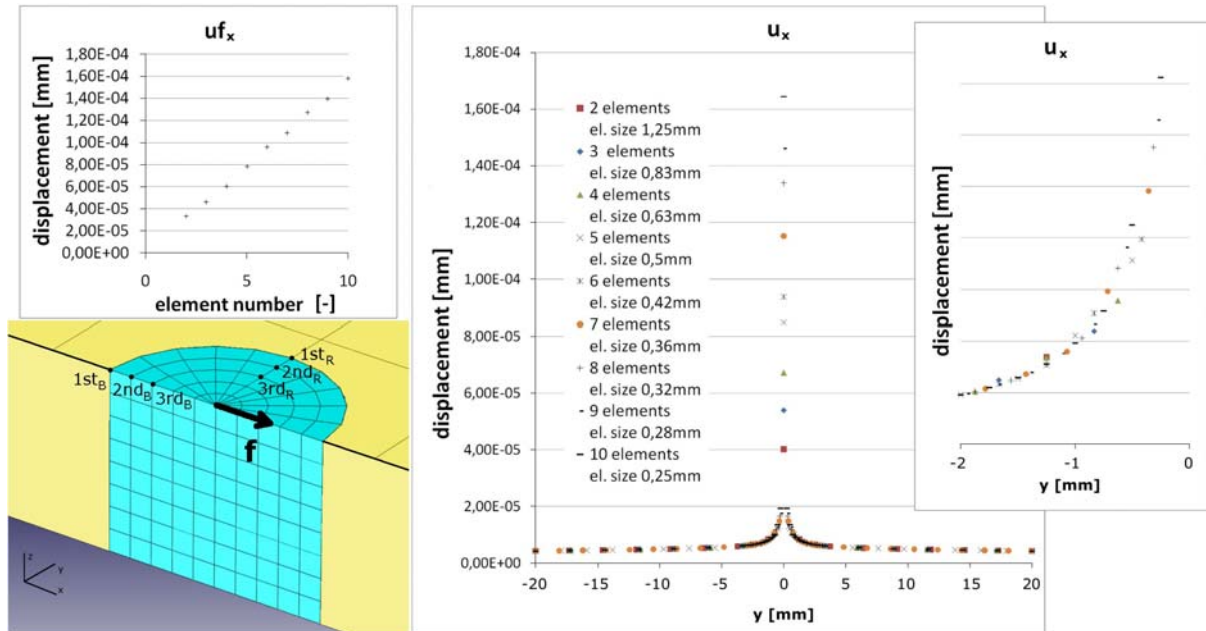


Fig. 3: Mesh type and nodal displacements on the line perpendicular to the load direction in the direction of diameter.

Nodal displacements in the section perpendicular to the load direction rapidly increase about 3 mm around the center (see Fig. 3). The displacement of the loaded outer center node linearly increases in the range of 10 elements along the radius and it is not possible to obtain the higher stiffness by refining the mesh. Reducing the element size doesn't affect the displacement accuracy out of the 1mm radius zone significantly (see the detail in Fig. 3).

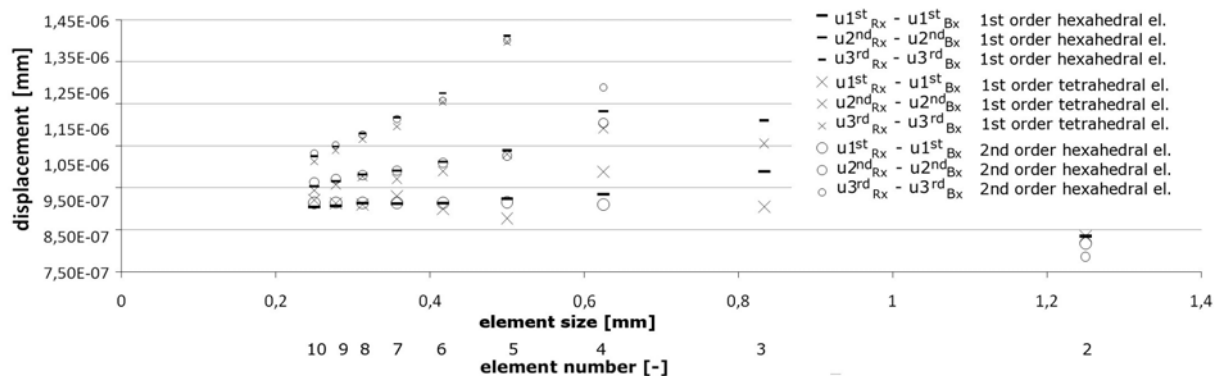


Fig. 4: Displacement differences of 1<sup>st</sup>, 2<sup>nd</sup> and 3<sup>rd</sup> surface nodes in the x-axis direction (signed by Fig.3).

The most of the fatigue crack analyses using the FEM need 1<sup>st</sup> order elements. The out-of-cylinder mesh quality takes more effect to the inner nodal displacements using the 1<sup>st</sup> order elements than the 2<sup>nd</sup> order elements. The bias of the out-of-cylinder mesh decreases with the distance from the cylinder edge. In Fig. 4 there are shown the x-axis displacement differences of signed surface nodes. The 3<sup>rd</sup> node displacement seems not to alternate a lot anymore and could be suitable for the stiffness determination. The similar analysis was made on the sheet represented by the shell elements as well.



### 3.2. Methodology for modeling

Since the FE-assembly stiffness must be higher than the experimental in order to keep the ability to tune the connector stiffness, it is necessary to expand the center elements and to include the finer elements around them to reduce the out-of-cylinder mesh bias. The evaluation of the proposed procedure was made by using the experimental test results. The stiffness characteristic of the connecting BUSH type element was set by the part and sheet computed stiffnesses and the experimental stiffness in several steps in order to respect the nonlinearity of the experimental deformation curve. The procedure of the joint stiffness FE-model determination is following:

- Joint geometry determination from the assembly model;
- Joint stiffness determination on the experimental, analytical or numerical basis;
- Joint area mesh design and the FEM stiffness computation of the jointed parts;
- Stiffness characteristic setting of the 1D connecting element.

The formation and application of the stiffness equivalent riveted joints are shown in Fig. 5.

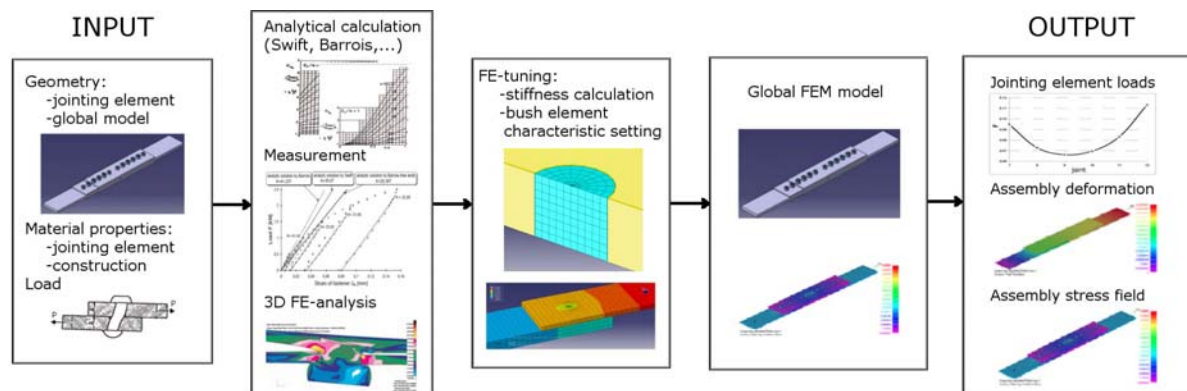


Fig. 5: Formation and application diagram of the stiffness equivalent riveted joints.

### 4. Conclusions

Crack analyses are affected by the stiffening of the structure due to the connected parts. It is necessary to use simple method to reflect real loading characteristics of the joints in FE-analyses of structures with a large number of rivets. Usage of the 1D element connected to single nodes enables easy preprocessing and gives the possibility to choose the element type and the properties. On the other side it requires the more detailed analysis of the mesh stiffness influence.

### References

- Barrois, W. (1978) Stress and Displacement Due to Load Transfer by Fasteners in Structural Assemblies. Engineering Fracture Mechanics, Vol. 10, Pergamon Press
- Běhal, J. (1985) Model of Stiffness Equivalent Riveted Joint (Model nýtového spoje ekvivalentní tuhosti). VZLÚ, a.s, Prague, V-1563/86.
- Doubrava, R. (1998) Stiffness Characteristics for FE-Modeling of Stiffness Equivalent Riveted Joints. (Tuhostní charakteristiky pro modelování nýtových spojů ekvivalentní tuhosti pomocí MKP). VZLÚ, a.s., Prague, R-2936/98.
- Doubrava, R. & Beránková, I. (1998) Stiffness Characteristics of Specimens of Jointed Skin and Flange models (Tuhostní charakteristiky těles modelů připojení potahu k pásnici křídla). VZLÚ, a.s., Prague, Z-3671/98.
- Fárek, J. (2010) FE-Modelling Methodology of Riveted Joints. Czech Aerospace Proceedings, No. 2/2010, Prague, pp. 12-16. ISSN 1211 - 877X.
- Kaniowski, J., Wronicz, W., Jachimowicz, J. & Szymczyk, E. (2009) Methods for FEM Analysis of Riveted Joints of Thin-Walled Aircraft Structures within the IMPERJA Project. ICAF 2009, Bridging the Gap between Theory and Operational Practice, Part 6, pp. 939-967, DOI: 10.1007/978-90-481-2746-7\_52.
- Swift, T. (1974) Development of the Fail-safe Design Features of the DC- 10, ASTM STP 486, pp. 164-214.
- Vogt, F. (1947) The Load Distribution in Bolted or Riveted Joints in Light-Alloy Structures. U.S. NACA TM. No 1135.

## **CORRECTION OF FATIGUE PARAMETER VALUES OF CONCRETE USING APPROXIMATION OF MECHANICAL-FRACTURE PARAMETER VALUES IN TIME**

**H. Šimonová<sup>\*</sup>, Z. Keršner<sup>\*</sup>, S. Seitzl<sup>\*\*</sup>**

**Abstract:** *Selected approximation curves of mechanical-fracture parameter values – modulus of elasticity, effective fracture toughness, specific fracture energy, compressive cube strength, splitting tensile strength, maximum load force – in time are used to determine the most accurate fatigue parameter values corresponding to the age of specimens when dynamic tests were performed.*

**Keywords:** *Fatigue, concrete, fracture test, approximation.*

### **1. Introduction**

Concrete is one of the most widely used materials in civil engineering structures. For concrete structures under cyclic loading – bridges, tunnels, concrete sleepers etc. – fatigue is a serious problem: a process of progressive and permanent internal damage in materials subjected to repeated loading. This is attributed to the propagation of internal micro-cracks that may result in the propagation of macro-cracks and unpredictable failure.

Fatigue phenomena related to the behaviour of reinforced/concrete structures under cyclic loading has been studied for only a few decades (see Lee & Barr, 2004, for a review; Seitzl et al., 2010a,b; Pryl et al., 2010). Concrete is a highly heterogeneous material and the processes occurring in its structure and leading to its degradation under cyclic loading are more complicated in comparison to those affecting metals. The fatigue mechanism may be attributed to progressive bond degradation between coarse aggregates and the cement paste or by the development of cracks existing in the cement paste. Similarly as with metals, the process leading to fatigue failure caused by macro-crack propagation consists of three parts. The first of these is connected with crack initiation and typically takes place in the vicinity of stress concentrators in the weaker part(s) of the microstructure. The second phase is characterized by the stable growth of the initiated crack up to its critical length. The final part is associated with unstable growth of the macro-crack and leads to the final fracture (usually of the brittle type) of the structure. With regard to the service life of the structure, the most important is the second part, which represents up to 80% of the total life cycle. Quantification of the crack behaviour in this phase is of paramount importance.

An extensive laboratory experiment was conducted on a set of specimens of plain class C30/37 concrete. The specimens were used for determining the values of fundamental fracture characteristics and related fatigue parameters using static fracture and dynamic experiments. The problem seems to be the gradually increasing age of the concrete samples during the dynamic tests. The aim of this paper is to present results from fatigue experiments and – mainly – correction of the values of fatigue parameters using approximation curves obtained from mechanical-fracture parameter values in time (modulus of elasticity, effective fracture toughness, specific fracture energy, compressive cube strength, splitting tensile strength, maximum load force).

---

<sup>\*</sup> Ing. Hana Šimonová and assoc. prof. Ing. Zbyněk Keršner, CSc.: Brno University of Technology, Faculty of Civil Engineering, Institute of Structural Mechanics; Veveří 331/95; 602 00, Brno; CZ, e-mails: simonova.h@fce.vutbr.cz, kersner.z@fce.vutbr.cz

<sup>\*\*</sup> Ing. Stanislav Seitzl, Ph.D.: Academy of Sciences of the Czech republic, v. v. i., Institute of Physics of Materials; Žitkova 22; 616 62, Brno; CZ, e-mail: seitzl@ipm.cz

## 2. Simple approximation of the values of basic parameters of concrete

Approximation curves of the above-mentioned parameters in time were determined in the following way. In the first instance the relative values of individual parameters for all examined ages of specimens were obtained: the values of parameters obtained from measurement were divided by the appropriate mean average value for specimens at the age of 28 days. In the next step adaptation data for individual parameters were plotted in charts depending on the age of specimens. The analytical expressions for simple approximation (regression) curves were determined. Power, logarithmic and polynomial functions were used (EXCEL software). The index of dispersion ( $R^2$ ) was obtained for each type of regression curve. For illustration, approximation curves for relative maximum load force obtained from static three point bending fracture tests are depicted in Fig. 1. In the equations  $x$  indicates time in days and  $y$  indicates the dimensionless relative values of the appropriate parameter. The same is valid for Tab. 1.

Analytical expressions for simple approximation curves of all mentioned mechanical-fracture parameter values are introduced in Tab. 1, including the dimensionless index of dispersion. It stands to reason that the best approximation was obtained for the following parameters: compressive cube strength and maximum load force obtained from dynamic tests (1 cycle).

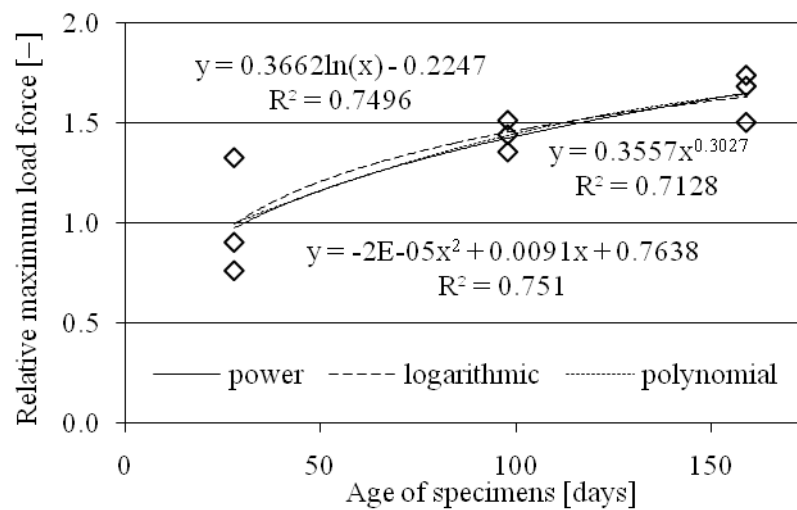


Fig. 1: Approximation curves for relative maximum load force.

Tab. 1: Coefficients of analytical expressions for simple approximation curves.

Regression curve	Power $y = a \times x^b$			Logarithmic $y = a \times \ln(x) + b$			Polynomial $y = ax^2 + bx + c$			
	$a$	$b$	$R^2$	$a$	$b$	$R^2$	$a$	$b$	$c$	$R^2$
Compressive cube strength	0.6367	0.1377	0.9396	0.1542	0.4939	0.9404	$-2 \cdot 10^{-5}$	0.0060	0.8494	0.9706
Compressive strength – fractions	0.6631	0.1233	0.9227	0.1359	0.5478	0.9345	$-1 \cdot 10^{-5}$	0.0040	0.8974	0.9352
Tensile splitting strength – fractions	0.7373	0.0927	0.8263	0.1001	0.6713	0.8231	$-2 \cdot 10^{-5}$	0.0048	0.8812	0.8877
Modulus of elasticity	0.6673	0.1113	0.2676	0.1185	0.5786	0.2906	$1 \cdot 10^{-5}$	-0.0010	1.0160	0.4004
Fracture toughness	0.4909	0.2007	0.5347	0.2380	0.1664	0.5255	$-5 \cdot 10^{-5}$	-0.0058	1.1224	0.7849
Fracture energy	0.2877	0.3639	0.7960	0.4882	-0.6576	0.7889	$2 \cdot 10^{-5}$	0.0040	0.8758	0.8428
Maximum load force – static fracture tests	0.3557	0.3027	0.7128	0.3662	-0.2247	0.7496	$-2 \cdot 10^{-5}$	0.0091	0.7638	0.7510
Maximum load force – dynamic tests (1 cycle)	0.6157	0.1440	0.9742	0.1596	0.4622	0.9774	$-2 \cdot 10^{-5}$	0.0058	0.8447	0.9964

### 3. Fatigue experiments

Fatigue properties were obtained from three point bending tests of beam specimens with a central edge notch. The nominal dimensions of the beams were  $100 \times 100 \times 400$  mm, span length 300 mm. The initial notch was made by a diamond blade saw. Note the depth of the notches was 10 mm.

The experimental test program was carried out at the Laboratory of the Institute of Metal and Timber Structures, Faculty of Civil Engineering, Brno University of Technology. The controlled values for temperature and relative humidity were  $22 \pm 2$  °C and 50%. The fatigue experiments (Wöhler curves) were carried out in a computer-controlled servo hydraulic testing machine (INOVA-U2).

Fatigue testing was conducted under load control. The stress ratio  $R = P_{min}/P_{max} = 0.1$ , where  $P_{min}$  and  $P_{max}$  refer to the minimum and maximum load of a sinusoidal wave in each cycle. The load frequency used for all repeated-load tests was approximately 10 Hz. The fatigue failure numbers of cycles were recorded.

Concrete specimens were loaded in the range of high-cycle fatigue; therefore, the upper limit to the number of cycles to be applied was selected as 2 million cycles. The test finished when the failure of the specimen occurred or the upper limit of loading cycles was reached, whichever occurred first.

### 4. Results of the fatigue tests

The results of the fatigue tests under a varying maximum bending stress level are summarized in Fig. 2, where the maximum bending stress ( $S$ ) obtained from the fatigue experiments is plotted against the logarithm of the number of cycles to failure ( $N$ ). Along with data points, the analytical expressions for the curves were obtained in the following form:

$$S = a \times N^b \quad (1)$$

In an ideal case, all specimens would fail in the same cycle group and after the same number of cycles. However, the fatigue behaviour of a heterogeneous material like concrete is far from being ideal and the results are usually highly scattered; therefore, it is necessary to determine not only the analytical expression but also the index of dispersion.

The power function and the index of dispersion for the tested material are as follows:

$$S = 3.7739 \times N^{0.026} \text{ and } R^2 = 0.4613 \quad (2)$$

The index of dispersion is relatively low; therefore, the measured data were corrected using approximation curves obtained from the values of mechanical-fracture parameters in time. The measured data were divided by a coefficient corresponding to the age of the specimens when dynamic tests were conducted. Coefficients were determined from regression curves of all observed parameters. Data obtained in this manner are standardized to a specimen age of 28 days.

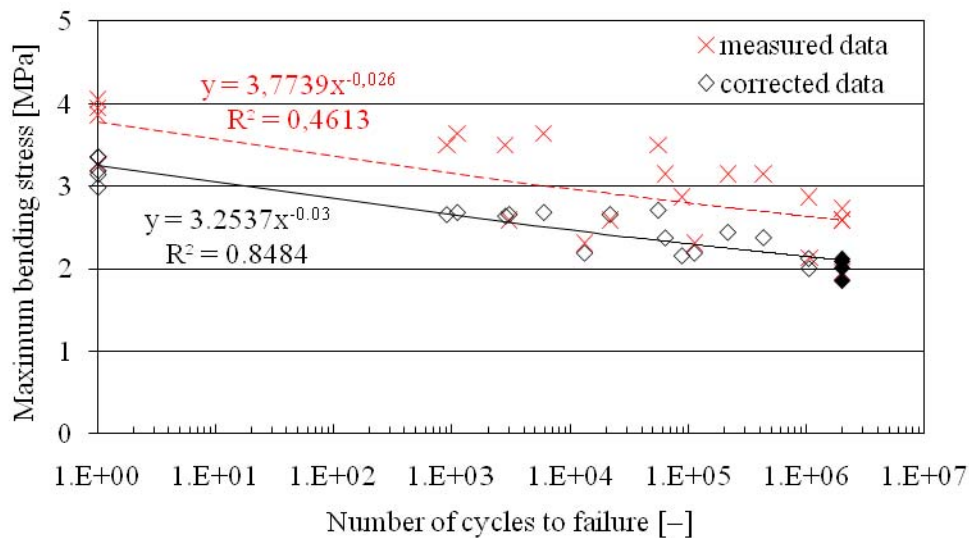


Fig. 2:  $S$ - $N$  diagrams for the tested concrete.  
(white symbol: broken specimen; black symbol: unbroken specimen).

In the next step, fatigue parameter adaptation data were plotted in the same way as the measured data. Fig. 2 introduces an example of a corrected  $S-N$  curve (using a logarithmic approximation curve for relative effective fracture toughness obtained from static three point bending fracture tests, see Tab. 1). The coefficients of analytical expressions (1) for  $S-N$  curves corrected by approximation curves and index of dispersion are summarized in Tab. 2.

Tab. 2: Coefficients of  $S-N$  curves and index of dispersion.

Regression curve Relative parameter	$S = a \times N^b$								
	Power			Logarithmic			Polynomial		
	$a$	$b$	$R^2$	$a$	$b$	$R^2$	$a$	$b$	$R^2$
Compressive cube strength	3.3126	-0.029	0.7750	3.3096	-0.029	0.7698	3.2561	-0.029	0.8232
Compressive strength – fractions	3.3803	-0.028	0.7475	3.3757	-0.028	0.7436	3.3246	-0.029	0.7982
Tensile splitting strength – fractions	3.4597	-0.028	0.6807	3.4560	-0.028	0.6783	3.4505	-0.028	0.6833
Modulus of elasticity	3.5337	-0.028	0.7224	3.5071	-0.028	0.7197	3.6758	-0.027	0.5683
Fracture toughness	3.2923	-0.030	0.8497	<b>3.2537</b>	<b>-0.030</b>	<b>0.8484</b>	3.4282	-0.027	0.6706
Fracture energy	2.8189	-0.033	0.7043	2.7722	-0.033	0.7145	2.7738	-0.032	0.6116
Maximum load force – static fracture tests	2.9528	-0.032	0.7966	2.9102	-0.032	0.8171	2.8723	-0.032	0.7836
Maximum load force – dynamic tests (1 cycle)	3.3356	-0.029	0.7860	3.3368	-0.029	0.7801	3.3155	-0.029	0.8083

## 5. Conclusions

In this paper results from fatigue tests carried out on plain class C30/37 concrete specimens were presented. The fatigue experiments lasted for a long time, which is problematic from the point of view of the ageing of specimen material. Because of this, data obtained from the fatigue tests were standardized to a specimen age of 28 days. Selected approximation curves obtained from mechanical-fracture parameter values in time were used for this purpose. The success of this procedure shows a substantial reduction in the values' index of dispersion from 0.46 to 0.85 [–].

## Acknowledgement

This outcome has been achieved with the financial support of the Ministry of Education, Youth and Sports, project No. 1M0579, within the activities of the CIDEAS research centre. In this undertaking, results gained in the Czech Scientific Foundation project No. P104/11/0833 were exploited.

## References

- Lee, M.K. & Barr, B.I.G. (2004) An overview of the fatigue behaviour of plain and fibre reinforced concrete. *Cement & Concrete Composites*, Vol. 26, pp. 299–305.
- Seitl, S., Keršner, Z., Bílek, V. & Knésl, Z. (2010a) Fatigue parameters of cement-based composites with various types of fibres. *Key Engineering Materials*, Vols. 417–418, pp. 129–132.
- Seitl, S., Bílek, V., Keršner, Z. & Veselý, J. (2010b) Cement based composites for thin building elements: Fracture and fatigue parameters. *Procedia Engineering*, Vol. 2, pp. 911–916.
- Pryl, D., Červenka, J. & Pukl, R. (2010) Material model for finite element modelling of fatigue crack growth in concrete. *Procedia Engineering*, Vol. 2, pp. 203–212.

## TOTAL FLUID MANAGEMENT FOR HYDRAULIC LIQUIDS

P. Štěrba \*

**Abstract:** *Increases of lifetime and reliability of hydraulic systems by regular attendance of hydraulic liquids. VacuClean – Filtration and separating of water, gases and oxidants by vacuuming of operational liquid.*

**Keywords:** *Hydraulic liquids, contamination, filtration, VacuClean, lifetime, vacuum chamber.*

### 1. Introduction

Our company Bosch Rexroth cooperate invariably and intensively with their customers on enhancement of life time and reliability of hydraulic systems. Reliability of lifetime of hydraulic systems depends mainly on quality and purity of hydraulic liquids. There are some main issues regarding hydraulic liquids (Schaefer, 2010). These are defined as follows:

#### 1.1. Mechanical contamination

It causes to abrasion or collapse of hydraulic components. It effects shorter lifetime, breakdown of hydraulic systems and failure of production.

Prevention: effective filtration hydraulic liquid.

#### 1.2. Contamination mainly by free and fixed water

It causes corrosion, abrasion; lowering of viscosity and worse lubrication ability(see Fig. 5); chemical reaction with working fluid; aging of working fluid; (diesel effect, oxidation of oil); lower ability to filtrate; shorter lifetime and in the end failure of production

Prevention: use of air filter AS (aquasorb); oil filter AS (separates only free water) and Vacuum Chamber.

#### 1.3. Air and gases

It causes corrosion, abrasion; inaccurate function of valves; lower power efficiency; shorter life of pumps (cavitation); foam in hydraulic liquid; chemical reaction with operating fluid – lifetime of hydraulic liquid; oxidation – aging; diesel effect.

Prevention: air venting of hydraulic liquid... reseal of pumps and using of Vacuum Chamber.

### 2. Effects of water with the presence of metallic particles

Water creates serious harm to hydraulic systems (Trahan, 2009) especially when high amounts of metallic particles are present. In addition, water changes properties of hydraulic liquids by chemical reactions such as hydrolysis and cracking. As a consequence, quality and lifetime of hydraulic fluid can be significantly reduced. Lifetime of hydraulic components can be reduced by water presence in hydraulic liquid. Increase of water content in hydraulic liquid from 100 ppm to 500 ppm reduces the lifetime of the hydraulic components by 50%. On the other hand, lowering of water content below 100 ppm in hydraulic liquid usually doubles the lifetime of hydraulic components (see Fig. 1).

---

\* Ing. Pavel Štěrba: Bosch Rexroth, spol. s r.o., Těžební 2, 627 00 Brno, e-mail: pavel.sterba@boschrexroth.cz

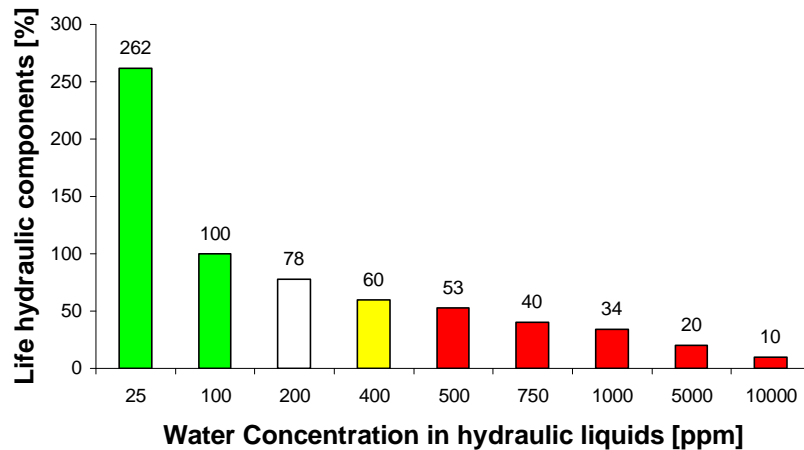


Fig. 1: Lifetime of the hydraulic components (Trahan, 2009).

### 3. Separation of water, air and oil oxidation products using VacuClean®

Due to high vacuum in the VacuClean® (vacuum chamber) (Trahan, 2009) it is possible to separate not only water, but also oxidants with low boiling point from the hydraulic liquid. Because of design of the vacuum chamber, building of foam of hydraulic liquid is reduced. Dissolved air and other gases are nearly completely separated. As a consequence, hydraulic liquid oxidation is reduced dramatically and usage of the hydraulic liquid is enhanced.

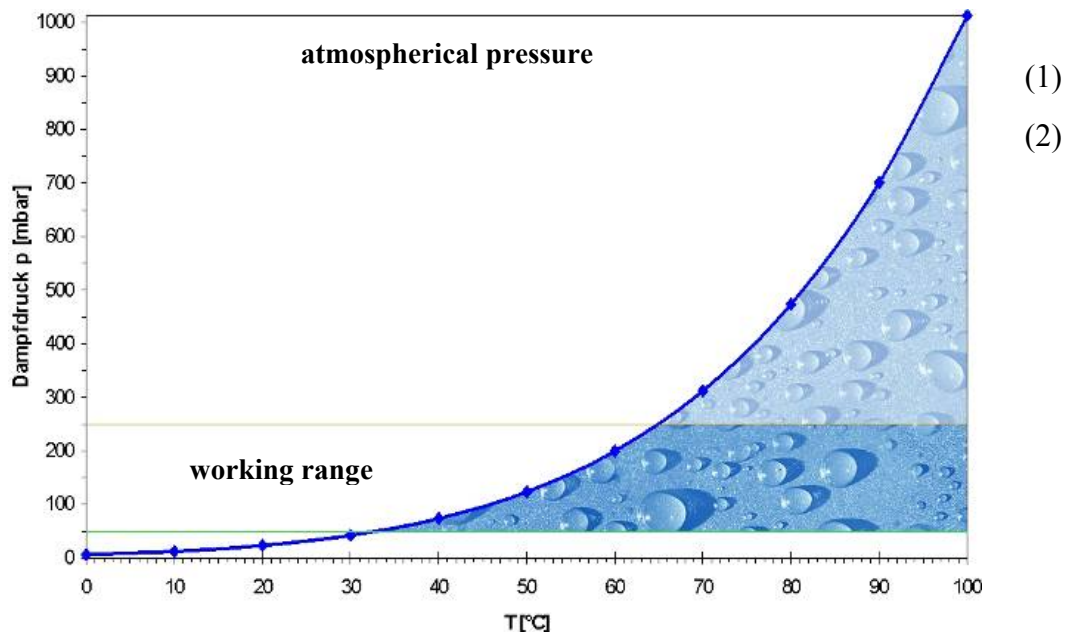


Fig. 2: Performance data VacuClean (Trahan, 2009).

The process of decontamination with help of VacuClean (see Fig. 3) is also very careful to working fluid, due to working temperature. The advantage of VacuClean is that there is no high temperature exposure to working fluid because of working temperature range from 32 to 65 degrees Celsius (see Fig. 2).





Fig. 3: VacuClean VCM 20 (Boecher, 2010).

#### 4. Basics about water in oil

To specify water content in hydraulic liquid, ppm units (parts per million) are used:

1 ppm of water .... 1mililiter of water per 1000 liter of oil

Hydraulic liquid (oil) contains blocked and free water (after reaching of a saturation point) (Schaefer, 2010). Free water causes emulsion. Saturation point (indicated in ppm of water content) depends on temperature and chemical condition of hydraulic liquid. Saturation point is indicated with aw coefficient (for example  $a_w = 0.4$  means 40 % of contamination and 60% to saturation point). Saturated oil has  $a_w = 1$  (100% water).

Hydraulic liquid's ability to block water depends on its temperature and chemical condition. Due to the change of temperature in our example from 70 to 30 °C, saturation point falls to 3000 ppm. Ability to block water falls down to 1000 ppm (see "Difference" in Fig. 4).

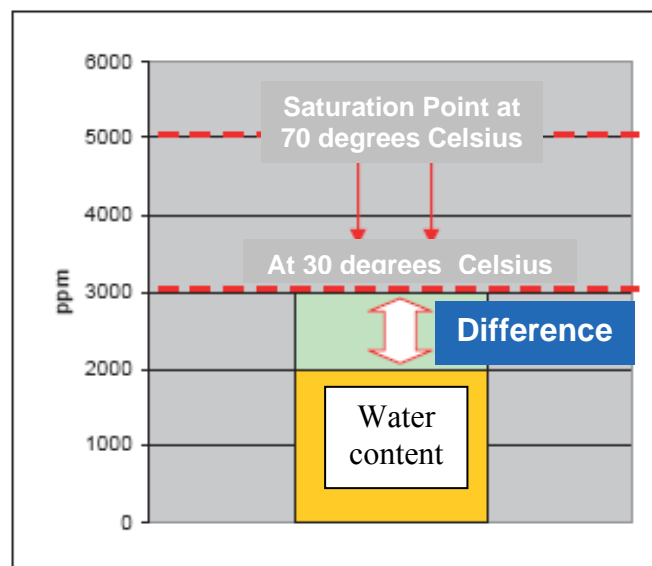
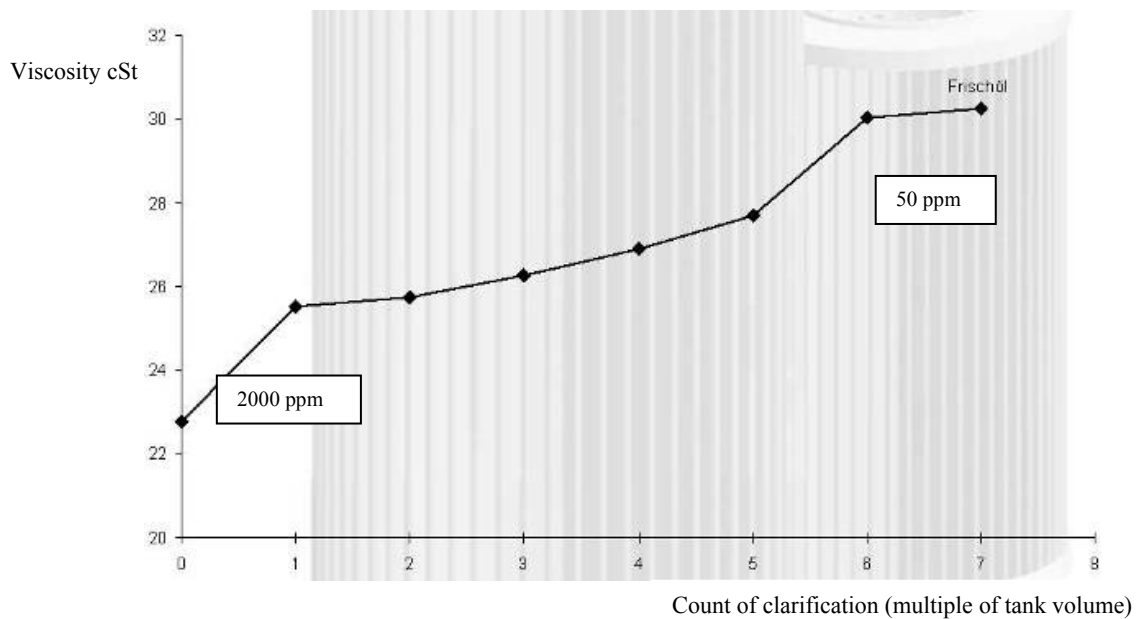


Fig. 4: Saturation point - dependence on temperature (Bosch Rexroth, 2002-10).



*Fig. 5: Step by step regeneration of viscosity during VacuClean using (Schaefer, 2010). (Oil VG 46 at temperature 50 °C, Tank content 2000 l, VacuClean VCM 50).*

## 5. Conclusion

By continuous operation of VacuClean equipment on hydraulic system, it is likely to extend lifetime of the hydraulic liquid by 3 – 7 times (practical experiences of Bosch Rexroth). In addition, lifetime of the hydraulic systems is extended and production issues minimized. As a result, customers benefit from lowering production costs which are clearly visible within 2 – 5 years after the start of machine operation.

## References

- Boecher C. (2010) Product programm of Bosch Rexroth Filtration Systems.
- Schaefer T. (2010) Basic of Filtration / Presentation materials of Bosch Rexroth Filtration Systems.
- Trahan C. (2009) Basic of Filtration / Presentation materials of Bosch Rexroth Filtration Systems.
- Bosch Rexroth data sheets and project materials (published 2002-2010).

## PRELIMINARY DESIGN OF BASIC PARAMETERS OF THE AERATOR

J. Štigler<sup>\*</sup>, M. Haluza<sup>\*</sup>, M. Bílek<sup>\*</sup>

**Abstract:** *The method of preliminary design of the basic runner parameters of the hydrodynamics submersible aerator is presented in this very brief paper. The problem of these parameters design is in the fact that flow rate (discharge) of the liquid (water) flowing through the aerator is unknown. The discharge is crucial parameter for a runner design. Therefore some basic ideas and basic expressions which can help with a preliminary design of the runner are outlined in this paper. After setting of the basic parameters of the aerator runner, this problem can continue with using some CFD code.*

**Keywords:** *Submersible aerator, design of a runner, angle of a blades.*

### 1. Introduction

Aerators are used in waste water treatment plants, for adding the air to the lakes, in chemical industry and so on. The devices for the oxygen adding into the water, aerators, are based on different principles. Some of these different principles of aerators are described in papers (Baylar, A. 2003), (Pandit, A. B., et al. 1991), (Muller, G., Sell, G.1984), (Vandermeulen, H. 1992), (Zhu, J., et al.2007) and so on. Each of these aerators has some advantages and also disadvantages. One of aerator categories are submersible aerators. The aerator, which preliminary design will be presented in this paper, belongs to this category. This kind of aerator is designed as a centrifugal radial pump. The air is added to the water on the ejector principle behind of the runner. Similar aerator type is described in (Pandit, A. B., et al. 1991). The runner is designed as a double sided runner. The blades on one side are designed for the water and the blades on the other side are designed for the air inflow. Advantages of this aerator type are as follows:

- It is a very simple device.
- There is low level of noise because the aerator is submerged.
- Its installation is very simple. It is also easy removable.
- It can also work as a mixer after closing the inflow air pipe.
- There is no need any other device outside of tank (air pump).

Heart of this aerator is the runner. The Design of this runner is rather complicated because the aerator discharge is unknown. It is not also possible to measure it, because it is impossible to place there a flow-meter. Therefore it is a problem to design the runner blades. Now it is a question how to find basic parameters as the radius of the runner, inlet and outlet blade angles, the intake and outlet widths of the runner.

### 2. Design procedure

The basic idea of this design procedure is that flow rate (discharge) is unknown. Therefore the power transferred into the water is assumed instead of it. Then the basic parameters are designed in such a way to reach the maximal flow rate through the aerator. The power transferred into the water by aerator can be expressed this way

---

<sup>\*</sup> assoc. prof. Ing. Jaroslav Štigler, Ph.D., assoc. prof. Ing. Miloslav Haluza, CSc. and Ing. Martin Bílek: Victor Kaplan's Department of Fluid Engineering, Institute of Energy, Brno University of Technology, Faculty of Mechanical Engineering, Technická 2896/2; 616 69, Brno; CZ, e-mails: stigler@fme.vutbr.cz, haluza.m@fme.vutbr.cz, ybilek14@stud.fme.vutbr.cz

$$P_h = \rho \cdot Q \cdot \Delta Y_{Run} \quad (1)$$

Where  $P_h$  is a power transferred to the water by the aerator,  $\rho$  is a density of water,  $Q$  is a flow rate (in our case it is an unknown value),  $\Delta Y_{Run}$  is a unit energy added to water by a runner.

The unit energy added to the water by the aerator in case of axial inflow can be expressed this way

$$\Delta Y_{Run} = v_{u2} \cdot u_2 \quad (2)$$

The subscript 2 represents the parameters on the runner outlet. The velocity  $v_{u2}$  is a component of the absolute outlet velocity in the direction of the circumferential velocity  $u_2$  on the runner outlet. All these velocities are outlined in the Fig. 1. These parameters can be expressed this way

$$u_2 = \pi \cdot n \cdot D_2 \quad (3)$$

$$v_{u2} = u_2 - \frac{v_{m2}}{\tan \beta_2} \quad (4)$$

$$v_{m2} = \frac{Q}{\pi \cdot D_2 \cdot b_2} \quad (5)$$

where  $\pi = 3.14$ ,  $n$  is a speed of the runner [rev.s<sup>-1</sup>],  $D_2$  is the outlet runner diameter,  $v_{m2}$  is the meridional velocity on the runner outlet,  $\beta_2$  is the blade angle on the runner outlet and  $b_2$  is the width of the runner on the outlet.

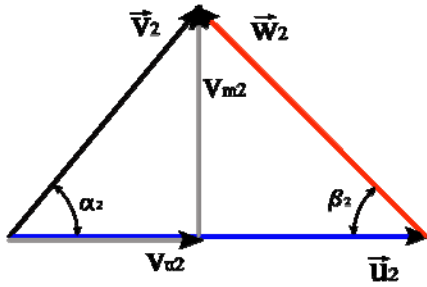


Fig. 1: The Outlet velocity triangle.

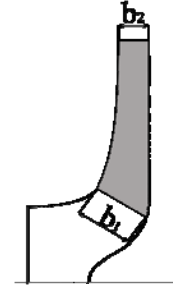


Fig. 2: Meridional cross-section of runner.

The unit energy can be then expressed

$$\Delta Y_{Run} = \left( 1 - \frac{v_{m2}}{u_2 \tan \beta_2} \right) u_2^2 \quad (6)$$

The expressions (5) and (6) can be applied into equation (1). The equation (1) can be then modified to receive a quadratic equation for the flow rate  $Q$ .

$$\frac{\rho \cdot Q^2 \cdot n}{b_2 \cdot \tan \beta_2} - \rho \cdot Q \cdot (\pi \cdot n \cdot D_2)^2 + P_h = 0 \quad (7)$$

Previous quadratic equation can be rewritten in this way

$$A \cdot Q^2 - B \cdot Q + C = 0 \quad (8)$$

The solution can be found in a form

$$Q_{1,2} = \frac{-B \pm \sqrt{B^2 - 4 \cdot A \cdot C}}{2 \cdot A} \quad (9)$$

Two solutions of the previous quadratic equation are available

$$Q_1 = \frac{1}{2}(\pi.D_2)^2 .n.b_2.tg\beta_2 + \sqrt{\frac{1}{4}n^2 .(\pi.D_2)^4 .(b_2.tg\beta_2)^2 - \frac{b_2.tg\beta_2.P_h}{\rho.n}} \quad (10)$$

$$Q_2 = \frac{1}{2}(\pi.D_2)^2 .n.b_2.tg\beta_2 - \sqrt{\frac{1}{4}n^2 .(\pi.D_2)^4 .(b_2.tg\beta_2)^2 - \frac{b_2.tg\beta_2.P_h}{\rho.n}} \quad (11)$$

The second solution is the right one, from the physical point of view, because when the power  $P_h$  is zero the flow rate is also zero. This is not true in case of first solution. So the solution for a flow rate is this

$$Q = \frac{1}{2}(\pi.D_2)^2 .n.b_2.tg\beta_2 - \sqrt{\frac{1}{4}n^2 .(\pi.D_2)^4 .(b_2.tg\beta_2)^2 - \frac{b_2.tg\beta_2.P_h}{\rho.n}} \quad (12)$$

If the maximum flow rate is demanded then the argument under the radical has to be zero. It means that

$$b_2.tg\beta_2 = \frac{4.P_h}{\rho.n^3 .(\pi.D_2)^4} \quad (13)$$

The maximal flow rate is given by the expression

$$Q_{\max} = \frac{1}{2}(\pi.D_2)^2 .n.b_2.tg\beta_2 \quad (14)$$

The expressions (12), (13), (14) are derived for a case of an infinite number of the blades. There is possible introduce correction for finite number of blades into previous solution. The correction has to be introduced in expression (6) in this way

$$\Delta Y_{Run} = \left( \kappa - \frac{\frac{v_{m2}}{u_2}}{tg\beta_2} \right) u_2^2 \quad (15)$$

Correction factor  $\kappa$  can be expressed in a form taken from (Waisser, Z. 1976)

$$\kappa = 1,103 - \frac{0,523 + 0,582.\sin \beta_2}{\sqrt{z}} \quad (16)$$

Where  $z$  is a number of blades (3-16) and  $\beta_2$  is an outlet blade angle. With the applying of this correction the expressions (12), (13), (14) are modified in the next way.

$$\frac{\rho.n.Q^2}{b_2.tg\beta_2} - \kappa .(\pi.n.D_2)^2 .\rho.Q + P_h = 0 \quad (17)$$

$$Q = \frac{1}{2}(\pi.D_2)^2 .\kappa.n.b_2.tg\beta_2 - \sqrt{\frac{1}{4}n^2 .\kappa^2 .(\pi.D_2)^4 .(b_2.tg\beta_2)^2 - \frac{b_2.tg\beta_2.P_h}{\rho.n}} \quad (18)$$

The maximal flow rate will be in the case that the expression under the radical, in (18), will be zero. The only width of runner outlet can be expressed from this condition because correction factor  $\kappa$  also depends on the outlet blade angle  $\beta_2$ .

$$b_2 = \frac{4.P_h}{\rho.n^3 .\kappa^2 .(\pi.D_2)^4 .tg\beta_2} \quad (19)$$

Then the maximal available flow rate then is

$$Q_{\max} = \frac{1}{2}(\pi.D_2)^2 \cdot \kappa \cdot n \cdot b_2 \cdot \tan \beta_2 \quad (20)$$

The expressions (18), (19), (20) are derived for a finite number of blades. There is introduced correction factor  $\kappa$  which is expressed in (16).

### 3. Conclusion

The equations (16), (18), (19), (20) can be used for a preliminary design of the basic runner parameters of the aerator in the case that the flow rate (discharge) through the aerator is unknown. The power which is transferred into the liquid is taken into consideration instead of it. Some parameters, as a outlet diameter of the runner, runner speed, number of blades, outlet blade angle, has to be chosen first and then the other, as the width of the runner outlet, flow rate, can be evaluated from the above equations. Next important parameters, as the inlet blade angle and inlet width of the runner and so on, can be then evaluated. The CFD computation of the flow inside of the runner or even the aerator has to come after this preliminary design to finish the hydraulic design of the aerator.

### Acknowledgement

The authors are grateful to the Ministry of Education Youth and Sports of Czech Republic for funding this research under project with title "Simulation modelling of mechatronics systems". Registration number of this project is MSM0021630518.

### References

- Baylar, A. (2003) An Investigation on the Use of Venturi Weirs as an Aerator., Water Quality Research Journal of Canada, 38, 4, 753-767.
- Pandit, A. B., et al. (1991) PUMP-STIRRED AERATOR. Chemical Engineering Science, 46, pp. 2293-2301.
- Muller, G., Sell, G.(1984) Radial Flow Aerator - a High-Performance Aerator for Biological Wastewater-Treatment Plant, Chemie Ingenieur Technik, 56, 5, pp. 399-401.
- Vandermeulen, H. (1992) Design and Testing of a Propeller Aerator for Reservoirs, Water Research, 26, 6, 857-861.
- Waisser, Z. (1976) Vliv změny geometrických tvarů průtočné části odstředivých čepadel na jejich parametry. ACADEMIA, Praha, pp 138.
- Zhu, J., et al.(2007) Aerator module development using venturi air injectors to improve aeration efficiency. Applied Engineering in Agriculture, 23, pp. 661-667.

## **A MATHEMATICAL MODEL OF THE FLUID FLOW IN THE TEE-JUNCTION. THE COMPARISON OF THE CFD COMPUTATION AND THE MEASUREMENTS.**

**J. Štigler<sup>\*</sup>, O. Šperka<sup>\*</sup>, R. Klas<sup>\*</sup>**

**Abstract:** *This paper deals with a mathematical model of fluid flow in Tee-junction with the 90° angle of adjacent branch and with the same diameter of all branches. There is only a brief theory for some term explanation at beginning of the paper. Some measurements were done for determining of the Tee-junction coefficients. These coefficients are function of a ratio of flow rates in given branches, see Fig 02. These results were compared with CFD calculations.*

**Keywords:** *T-junction, fluid flow in pipeline net, steady flow, unsteady flow, mixing.*

### **1. Introduction**

The mathematical model of the fluid flow in the Tee-junction with the 90° angle (MMFFTJ90) of the adjacent branch and with the same diameter of all branches is presented in this paper. This kind of Tee-junction is one of the adapting pieces and it is used very often. It is used for the division or the combination of flow in pipeline Fig. 2. Sometimes it is also used as a mixing device of two different liquids or phases. It is necessary to have a mathematical model of this Tee-junction because of solving of the flow parameters in the pipeline. The simplest and very often used model is based on an assumption that the pressure is constant at the ends of all branches connected to the T-junction. It is obvious that this model is not precise and that this assumption is not true (Štigler 2006, Part1). Therefore a new mathematical model of Tee-Junction was derived (Štigler 2006, Part1). This new MMFFTJ90 is also possible to use for both steady and unsteady flow (Štigler 2007), it takes into account position of the Tee-junction in respect of gravity acceleration and it is also possible to use it for a mixture flow. This model introduces coefficients of the Tee-Junction which have a correct physical meaning. This model has been also extended for an arbitrary angle of the adjacent branch (Štigler 2010). The Tee-junction coefficients are dependent on the ratio of flow rates in two branches. These coefficients were expressed by using of CFD computations (Štigler 2006, Part2). There is presented a comparison of these CFD computations with experiment in this paper, now. There were made some experiments for example by (Oka K & Ito H. 2005). New experiments have to be made because there was not enough information in papers where the previous measurements were presented.

### **2. Brief Theory**

The details of the theoretical backgrounds of the MMFFTJ are outlined in (Štigler, 2010). The mathematical model of the Tee-junction consists of three equations. Power equation, which represents the energy conservation law, Momentum equation, which represents of the momentum conservation law and the last equation is the continuity equation which represents the mass conservation law. The tests presented in this paper were done under next assumptions: steady flow, plain of T-junction was horizontal, incompressible liquid (water), the angle of adjacent branch was 90° and diameters of all branches were the same (50 mm).

---

<sup>\*</sup> assoc. prof. Ing. Jaroslav Štigler, Ph.D., Ing. Oldřich Šperka and Ing. Roman Klas, Ph.D.: Victor Kaplan's Department of Fluid Engineering, Institute of Energy, Brno University of Technology, Faculty of Mechanical Engineering, Technická 2896/2; 616 69, Brno; CZ, e-mails: stigler@fme.vutbr.cz, ysperk01@stud.fme.vutbr.cz, klas@fme.vutbr.cz



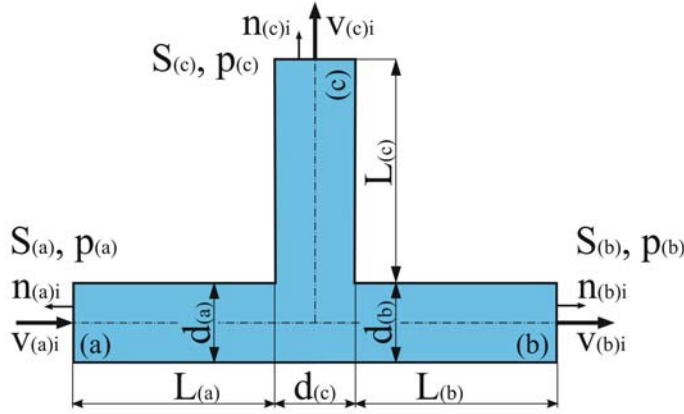


Fig. 1: T-Junction and variables.

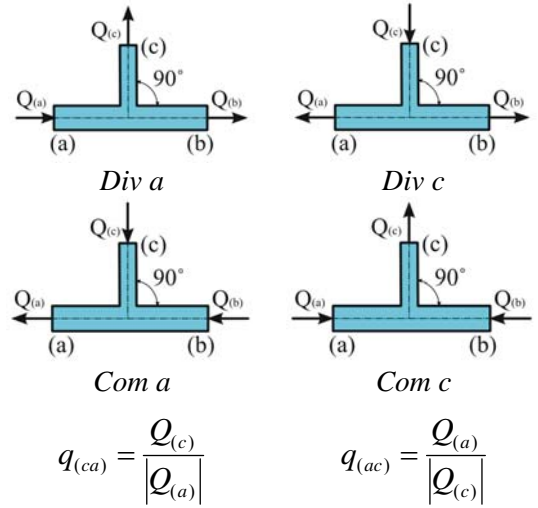


Fig. 2: Flow adjustments and variable ratio of flow rate.

MMFFTJ has this form under these assumptions

Power equation

$$\begin{aligned} & \left( \frac{1}{2} \alpha_{(Ca)} \cdot \frac{Q_{(ma)}^2}{\rho^2 \cdot S^2} + \frac{p_{(a)}}{\rho} \right) \cdot Q_{(ma)} + \left( \frac{1}{2} \alpha_{(Cb)} \cdot \frac{Q_{(mb)}^2}{\rho^2 \cdot S^2} + \frac{p_{(b)}}{\rho} \right) \cdot Q_{(mb)} + \\ & + \left( \frac{1}{2} \alpha_{(Cc)} \cdot \frac{Q_{(mc)}^2}{\rho^2 \cdot S^2} + \frac{p_{(c)}}{\rho} \right) \cdot Q_{(mc)} + \frac{1}{2} \xi_{(P)} \cdot \frac{Q_{(mC)}^2}{\rho^2 \cdot S^2} \cdot |Q_{(mC)}| = 0 \end{aligned} \quad (1)$$

Momentum equation

$$\begin{aligned} & \left( \frac{Q_{(ma)}^2}{\alpha_{(Ba)} \cdot \rho \cdot S} + p_{(a)} \cdot S \right) \cdot n_{(a)i} + \left( \frac{Q_{(mb)}^2}{\alpha_{(Bb)} \cdot \rho \cdot S} + p_{(b)} \cdot S \right) \cdot n_{(b)i} + \left( \frac{Q_{(mc)}^2}{\alpha_{(Bc)} \cdot \rho \cdot S} + p_{(c)} \cdot S \right) \cdot n_{(c)i} + \\ & + \xi_{(M)i} \cdot \frac{Q_{(mC)}^2}{\rho \cdot S} = F_{(g)i} \end{aligned} \quad (2)$$

Continuity equation

$$Q_{(ma)} + Q_{(mb)} + Q_{(mc)} = 0 \quad (3)$$

Where  $Q_{(mx)}$  is the mass flow rate in the particular branch  $\alpha_{(Cx)}$  is a kinetic energy correction factor on the particular cross-section,  $\alpha_{(Bx)}$  is a Bousinesque number on the particular cross-section,  $n_{(x)i}$  is an outward unit normal vector of the particular cross-section,  $p_{(x)}$  is an average pressure on the particular cross-section. The letter x should be replaced with the letter a, b, c. This letters determine the branch to which the given quantity is related. Next quantities are  $\rho$  – density,  $S$  – area of the branch cross-section.  $Q_{(mC)}$  is a total mass flow rate. The letter C should be replaced with the letter mark of the branch where the total flow rate is in it.

There are introduced the two coefficients of the T-junction in the above equations. First, the power coefficient  $\xi_{(P)}$  which represents the energy losses in the T-Junction, second, the momentum coefficient  $\xi_{(M)i}$  which represents a vector which is proportional to the force which the flow affects the T-Junction. The proportionality is given through a momentum magnitude in the branch with total flow rate. Each of these coefficients can be divided into two parts

$$\xi_{(P)} = \xi_{(PF)} + \xi_{(PG)} \quad (4)$$

$$\xi_{(M)i} = \xi_{(MF)i} + \xi_{(MG)i} \quad (5)$$

The first parts  $\xi_{(PF)}$  and  $\xi_{(MF)i}$  represent influence of friction in the Tee-junction. These coefficients can be determined from pressure drop in straight pipes. The second parts  $\xi_{(PG)}$  and  $\xi_{(MG)i}$  represent the influence of T-Junction shape or geometry. The goal of the experiments and CFD computations is to find these geometry coefficients.

### 3. Solution

#### 3.1. The testing circuit description and measuring procedure

The testing circuit has been built in a heavy laboratory of V. Kaplan's Department of Fluid Engineering of Brno University of Technology, Faculty of Mechanical Engineering. The testing circuit was designed as an open loop. The scheme of testing circuit is in the Fig. 4. The model of the Tee-junction together with straight pipes was fixed to the special construction which allowed the horizontal adapting of the supports to ensure horizontal position of the plane of Tee-junction. The Tee-junction was made of the special optical glass, because the PIV measuring has been also planned. The pipes connected with the T-junction were made from transparent PVC. The measured quantities are as follows: average absolute pressure at branch marked *a* see Fig. 4, the pressure differences ( $p_{(b)} - p_{(a)}$ ) and ( $p_{(c)} - p_{(a)}$ ), flow rates in each branch  $Q_{(a)}$ ,  $Q_{(b)}$ ,  $Q_{(c)}$  and the temperature of water. Absolute pressure has been measured with manometer, pressure differences were measured with two different methods, first using the membrane differential manometers, second using the U-tube manometers. Each branch was equipped with the magnetic flow-meter. The total fluid flow was driven by the pump equipped with the frequency variator.

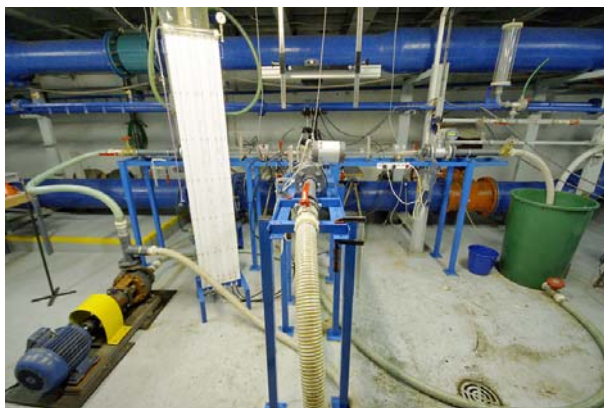


Fig. 3: Photo of the testing circuit.

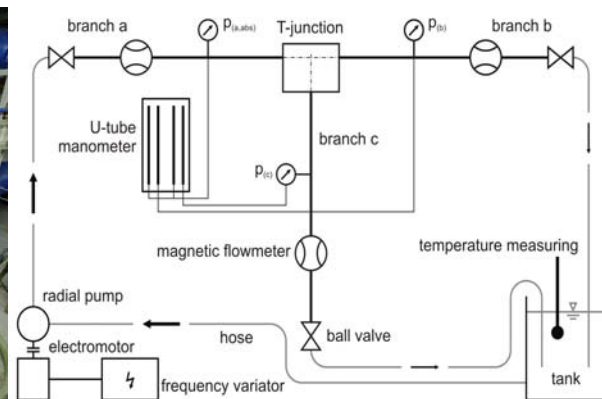


Fig. 4: Scheme of the testing circuit.

The goal of these measurements was to find the coefficients of Tee-junction which can be applied in a MMFFT90. These coefficients are the function of the ratio  $q$  of the given flow rates with respect to particular flow order. The ratio value of flow rates  $q$  varies from 0 to 1. The measurements were made for all flow adjustments Fig. 2. The eleven different ratios of flow rates were measured for each flow adjustment. The measurement was repeated.

#### 3.2. CFD Computation

The coefficients of Tee-junction were also determined by using CFD calculations. The geometrical model of the Tee-junction was created in the preprocessor GAMBIT 2.2.30. The computational mesh contained approximately the 2.3 million hexahedral cells with the worst skewness equal to 0.51. The straight pipes were extended in the length of 25 diameters from the T-junction. The computational mesh set in this way was consequently used for the analysis of pressure field in software Fluent 12.1. The setting of solver was chosen according to the dominant flow i.e. unsteady calculation with  $k-\epsilon$  realizable turbulence model and non-equilibrium wall functions. The velocity inlet or outflow boundary conditions were used on cross-sections  $S_{(a)}$ ,  $S_{(b)}$  and  $S_{(c)}$ . Twenty different values of ratios  $q$  of flow rates were calculated for each flow adjustment.

#### 3.3. Comparison of results and discussion

The comparison of the geometrical coefficients  $\xi_{(MG)I}$ ,  $\xi_{(PG)}$  gained from the experiment and

coefficients gained from the CFD computation are in the Figs. 5 - 8. These coefficients are evaluated for all kind of flow adjustments. There is a very good agreement in case of the flow combination. In case of flow division there are slight differences in case Div a for low ratios of flow rates  $q_{(ca)}$ . The worst agreement is in case of Div c. The flow was very unsteady in this case. This is probably the reason for the disagreement.

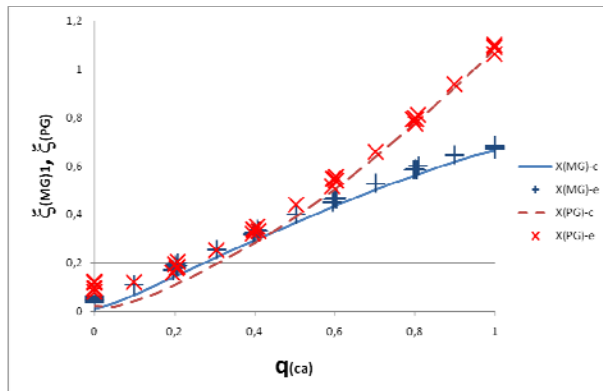


Fig. 5: Geometry coefficients for Div a.

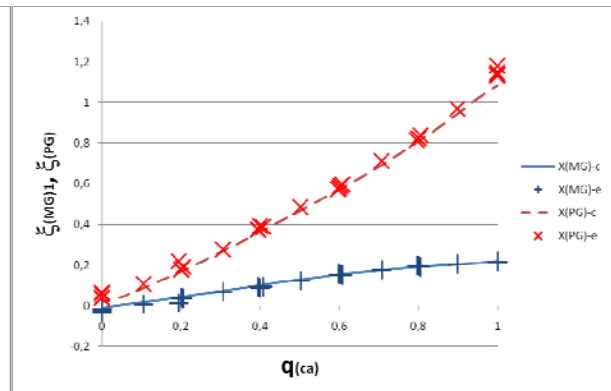


Fig. 6: Geometry coefficients for Com a.

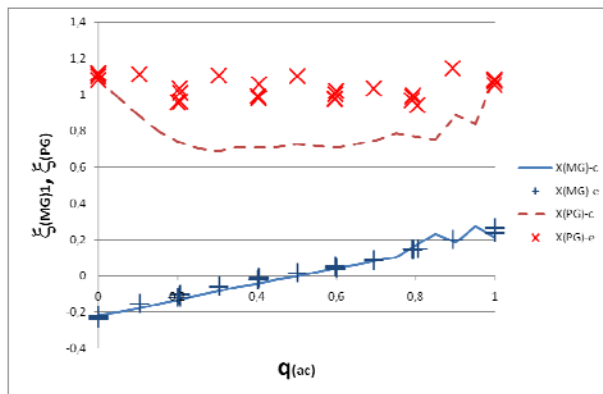


Fig. 7: Geometry coefficients for Div c.

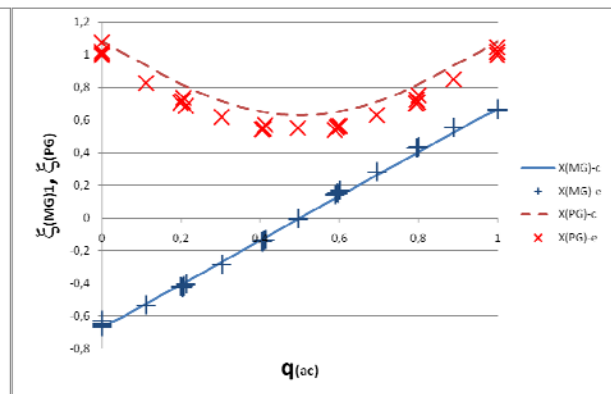


Fig. 8: Geometry coefficients for Com c.

#### 4. Conclusions

The agreement between the measurements and CFD calculations is very good. The determining of friction coefficients in experiment plays very important role.

#### Acknowledgement

The author is grateful to the Grant Agency of Czech Republic for funding this research under project "Mathematical and Numerical Modeling of Flow in Pipe Junction and its Comparison with Experiment". Registration number of this project is 101/09/1539.

#### References

- Oka K, Ito H. (2005) Energy losses at tees with large area ratios. Journal of Fluids Engineering-Transactions of the ASME. 127, pp.110-6.
- Štigler J. (2010) T-part as an Element of the Pipe-line System. The introduction of the Mathematical Model of the Fluid Flow in T-part for the Arbitrary Angle of the Adjacent Branch. IOP Conf. Ser.: Earth Environ. Sci. 12 012102 (10pp).12,1, pp 1-10.
- Štigler, J. (2007) Mathematical Model of the Unsteady Fluid Flow Through Tee-Junction. Proc. of 2nd IAHR Scientific Buletin of the "Politehnica" University of Timisoara, Romania Transactions on Mechanics. 52, 6, pp. 83-92.
- Štigler, J. (2006) Tee junction as a pipeline net element. Part 1. A new mathematical model. Journal of Mechanical Engineering, 57, 5, pp. 249-262.
- Štigler, J. (2006) Tee junction as a pipeline net element. Part 2. Coefficients Determination. Journal of Mechanical Engineering, 57, 5, pp. 263-270.

## SHEAR LAG EFFECT IN RESPONSE OF BOX BRIDGES

A. Tesár\*

**Abstract:** *The paper describes the application of technical theory of thin-walled box structures for the assessment of shear lag effects in thin-walled box bridges subjected to dynamic loads. The approach takes into account multiple functions in assessment of slender box bridges constructed of thin-walled members. Theoretical and numerical assessments of the problem are presented.*

**Keywords:** *Bridges, dynamic loads, Fourier integral transformation, shear lag, technical theory of thin-walled structures.*

### 1. Introduction

Due to economy and weight restrictions slender thin-walled box members are often utilized in advanced bridge engineering. Even for structures that behave in linear fashion under service loads the safety considerations require that an analysis is to be carried out for the nonlinear range of behavior in order to determine the reliability with respect to collapse or possible damage due to overloading.

### 2. Methods adopted

The stress distribution in thin-walled members of box bridges is given by combination of sectorial influences stated in scope of technical torsion-bending theory and additional sectorial influences due to distortion and shear. The decrease of rigidity in thin-walled box members is specified by the shear lag appearing in additional degrees of freedom in mechanics of cross-sectional distortion. In order to take into account the decrease of normal rigidity, there are introduced additional sectorial functions  $w_s$  due to distortional kinematics of thin-walled box cross-section studied (Bornscheuer, F.W., 1952 and Sedlacek, G., 1967). Such functions are dependent on additional cross-sectional deformations  $v_s$  given by

$$|w| = |w_t, w_s|^T = |x, y, \omega; w_1, w_2, \dots|^T, \quad (1)$$

and

$$|v| = |v_t, v_s|^T = |\xi, \eta, v; v_1, v_2, \dots|^T, \quad (2)$$

The warping  $u$  is given by

$$u = -w^T \cdot v', \quad (3)$$

with strain

$$\varepsilon = -w^T \cdot v'', \quad (4)$$

and with normal and shear stresses given by

$$\sigma = E \cdot \varepsilon = -E \cdot w^T \cdot v'' \quad (5)$$

and

$$\tau = -G \cdot w_s \cdot v_s'. \quad (6)$$

The choice of additional sectorial functions  $w_s$  appearing as linear functions of shear stress  $\tau$  along the cross-section is made in accordance with rules of technical theory of thin-walled beams. Used are the

---

\* Alexander Tesár, Civ. Eng., PhD, DrSc, visiting prof.: Institute of Construction and Architecture, Slovak Academy of Sciences, Dúbravská cesta 9, 845 03 Bratislava 45, Slovak Republic, e-mail: usarate@savba.sk

functions  $S_s \approx S_x, S_y, S_\omega = \int x dA, \int y dA, \int \omega dA$ , respectively, (A is the cross-sectional area) together with additional unit sectorial function  $w_s = \int S_s ds$  along the centre-line  $s$ .

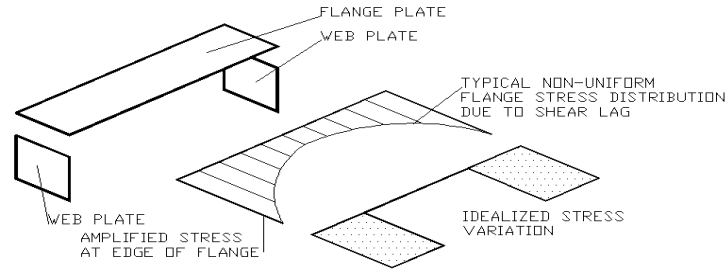


Fig. 1: Shear lag effect.

The equilibrium state of thin-walled box system is given by

$$\delta\pi = \int_0^l \left\{ \int_A (\sigma \cdot \delta\varepsilon + \tau \cdot \delta\gamma) dA - p \cdot r \cdot \delta v - \int_s n_s \cdot w_s \cdot \delta v' \right\} dz = 0, \quad (7)$$

with shear strain  $\gamma$  and with first terms representing the virtual work of internal forces and further terms specifying the virtual work of external forces on displacements  $\delta v$ .

If in above equation the stress  $\sigma$  is replaced by corresponding functions of displacements  $v_s$  the modified Eq. (7) is given by

$$\delta\pi_s = \int_0^1 [\delta v_s'' \cdot E \cdot J_s \cdot v_s'' + \delta v_s' \cdot G \cdot K_s \cdot v_s' - \delta v_s' \cdot p - \delta v_s' \cdot n \cdot w_s'] dz = 0, \quad (8)$$

with  $E \cdot J_s$  and  $G \cdot K_s$  as sectorial and shear rigidities of the cross-section studied and with corresponding load components  $p$  and  $n$ . The double integration of Eq. (8) gives

$$\int_0^1 \{ \delta v_s [ E \cdot J_s \cdot v_s^{IV} - G \cdot K_s \cdot v_s^{II} - p - n' \cdot w_s ] \} dz = 0, \quad (9)$$

and submits for each  $\delta v_s \neq 0$  the system of simultaneous differential equations

$$E \cdot J_s \cdot v_s^{IV} - G \cdot K_s \cdot v_s^{II} = p + n' \cdot w_s, \quad (10)$$

for numerical treatment of the problem.

Matrix equation (10) with unknown components of cross-sectional shear deformations  $v_s$  is modified into diagonal shape of  $s$  differential equations given by

$$E \cdot J_{s,ii} \cdot v_{s,i}^{IV} - G \cdot K_{s,ii} \cdot v_{s,i}^{II} = p_{s,i} + n_{s,i}' \cdot w_{s,i}. \quad (11)$$

Resulting displacements are given by strain components of non-deformable thin-walled cross-section, combined with components of unit shear deformations.

Differential equations (10) and (11) are formally identical with differential equation of the girder with flexural rigidity  $E \cdot J_s$  subjected to axial force  $G \cdot K_s$ . The solution is known with the analogy of components

$$-E \cdot J_{s,ii} \cdot v_{s,i}'' = M_{s,i}, \quad (12)$$

$$-E \cdot J_{s,ii} \cdot v_{s,i}''' = M'_{s,i} = T_{s,i}, \quad (13)$$

with flexural moment  $M$  and lateral force  $T$ . Corresponding normal and shear stresses are given by

$$\sigma_{s,i} = \frac{M_{s,i}}{J_{s,ii}} \cdot w_{s,i} \quad (14)$$

and

$$\tau_{s,i} = -G \cdot w_{s,i} \cdot v'_{s,i}. \quad (15)$$

With implementation of the Fourier integral transformation into the Transfer Matrix Method (Tesar, A., 1977, 1988, 2005, 2006 and 2010) is studied the influence of the shear lag in the response of thin-walled box bridges subjected to periodic, non-periodic and moving dynamic loads.

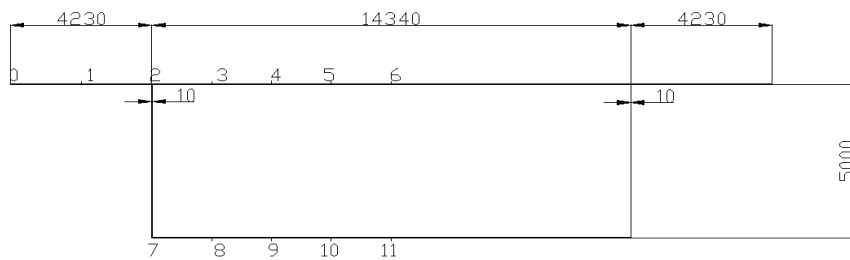


Fig. 2: Thin-walled box bridge with nodal points for assessment of torsion.

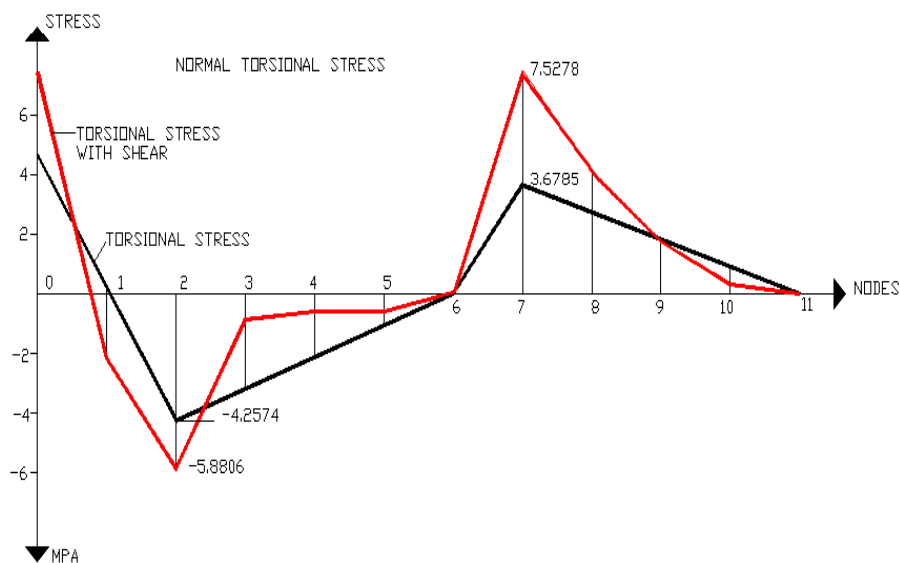


Fig. 3: Comparison of normal torsion stress without and with of shear lag.

### 3. Application

Cross-sectional geometry of the single span bridge studied is plotted in Fig. 2. The span of the bridge is  $L = 70$  m. Concentrated load  $P$  acts in location  $L/2 = 35$  m. Torsion is initiated by two mid-span loads  $P/2$  acting in vertical direction up and down in the flanges of thin-walled cross-section studied. Calculated are the stresses in flexure and torsion due to shear lag. Maximal shear stress and resulting normal stresses in torsion without and with consideration of the shear lag are summed up in Fig. 3. For real situations all stresses obtained are to be multiplied by actual value of the load  $P$ .

Such results are to be taken into account in the assessment of ultimate behavior of thin-walled members of slender box bridges.

#### **4. Conclusions**

The approach for assessment of the shear lag effect in thin-walled box bridges is suggested. Technical torsion-bending theory of thin-walled structures is adopted for theoretical and numerical treatment of the problem. Such assessment is a part of the bridge design and monitoring in order to specify the safety with respect to collapse and damage due to overloading.

#### **Acknowledgement**

Author is indebted to Slovak scientific agencies VEGA and APVV for supporting the research reported.

#### **References**

- Bornscheuer, F.W. (1952) Systematische Darstellung des Biege- und Verdrehvorganges unter besonderer Berücksichtigung der Wölbkrafttorsion. *Der Stahlbau* 21, pp. 342-346.
- Sedlacek, G. (1967) Systematische Darstellung des Biege- und Verdrehvorganges für prismatische Stäbe unter Berücksichtigung der Profilverformung. Diss. TU Berlin.
- Tesár, A. (1977) Vibration of Thinwalled Box Structures. *Proceedings of Czechoslovak Academy of Sciences, ACADEMIA*, Prague, 87, 1.
- Tesar, A. (1988) *Transfer Matrix Method*. KLUWER Academic Publishers, Dordrecht/Boston/London.
- Tesar, A. (2005) Load-bearing control of slender bridges. *International Journal for Numerical Methods in Engineering*, 62, pp. 924-936.
- Tesar, A. (2006) Bionics and fractal configurations in structural engineering. *International Journal for Numerical Methods in Engineering*, 68, pp. 790-807.
- Tesár, A. (2010) Testing of the Old Bridge Crossing Danube in Bratislava. Technical Report, TESAR@PARTNER.



## **EFFECT OF A WATER-GYPSUM RATIO ON MECHANICAL PROPERTIES OF GYPSUM**

**P. Tesárek<sup>\*</sup>, A. Hájková<sup>\*</sup>, T. Plachý<sup>\*</sup>**

**Abstract:** *Water-gypsum ratio is one factor of material parameters, which has a significant influence on the behavior of materials at the macro level. The article presents the dependence of selected mechanical properties on the water-gypsum ratio for several materials based on gypsum, which are modified using different types of additives as plasticizers, water proof agents and PP fibers.*

**Keywords:** *Flue gas desulphurization gypsum, water-gypsum ratio, mechanical properties, gypsum.*

### **1. Introduction**

The process changing gypsum – hemihydrates – into hardened gypsum – dehydrate – is hydration; it is typical effect for hydraulic binders. During this process, a solid material structure is formed, and the accompanying phenomenon is the generation of hydration heat and a volume increase – expansion. Hydration is set off after mixing water with gypsum. The process of gypsum hydration and setting relies on multiple factors: the temperature during preparing of the gypsum paste, the water-gypsum ratio, the method of gypsum mixing, the mixing intensity and time, the fineness of grinding, purity of gypsum binder, composition of gypsum binder – ratio of individual components, its mean anhydrite in different forms, hemihydrates and dehydrate of calcium sulfate etc. (Wirsching, 1983).

One of the important factors, as it has already been said, is the water-gypsum ratio. It is the ratio of the mass of water and gypsum. The water-gypsum ratio has a fundamental influence on the basic characteristics of hardened gypsum, such as its volume density, total open porosity and other related characteristics like its moisture, mechanical, thermal and sound insulation material properties. The theoretical water-gypsum ratio necessary for the hydration of calcium sulphate hemihydrates into calcium sulfate dehydrate is 0.187. Additional water, in a so-called over stoichiometric quantity, is necessary for the processing of the hardening gypsum paste.

Proper modification is a possibility how to eliminate gypsum negative properties and how to contribute to a wider utilization of gypsum even in exterior applications. The second effect of modifications lies in improving of hardened gypsum properties (e.g. mechanical properties, lower volume density and thermal properties). Depending on the type of modification, two basic groups may be distinguished. The first option is to modify the input raw material during its production, while the second choice is to modify the final product. In the modification of input raw materials, substances are added to input raw materials with the aim of changing, or affecting the properties of the basic raw materials. Additives may be classified by their effect on the gypsum binder into the following basic groups: plasticizers, hydrophobic agents, setting regulators, foaming. Sometimes, the effect of modifiers can be double-edged:

- Using of plasticizer yields reduction of gypsum/water ratio and reduction of total open porosity and improvement of mechanical and hygric properties. On the other hand, it can worsen thermal properties,
- Hydrophobic agents cause improvement of hygric properties (transport of liquid water) but can deteriorate mechanical properties and other parameters.
- Foaming agents increase the total open porosity and cause improvement of thermal properties. However, they deteriorate mechanical and hygric properties (transport of liquid water), etc.

---

<sup>\*</sup> Ing. Pavel Tesárek, Ph.D., Ing. Andrea Hájková and Ing. Tomáš Plachý, Ph.D.: Czech Technical University in Prague, Faculty of Civil Engineering, Department of Mechanics; Thákurova 7, 166 29 Prague 6 - Dejvice, Czech Republic, e-mails: tesarek@fsv.cvut.cz, andrea.hajkova@fsv.cvut.cz, plachy@fsv.cvut.cz

## 2. Test samples and additives

Flue gas desulphurization (FGD) gypsum from Počerady (ČEZ) was used for testing, this one is investigated according ČSN 72 2301 classified as G-13 BIII (binder = finely ground, normal setting-up with a compressive strength 13 MPa after 2 hours). This gypsum mixture was made by five different materials. The four of them were added to one or more ingredients (Table 1). The sample labeled S0 is free of additives, thus the reference. Selected ingredients were the plasticizer *Peramin SMF 20*, the hydrophobic agent *Imesta IBS 47* and *Zonyl 301*. For one set of samples, there was used as a filler of polypropylene fibers: *Fibrecrete*.

Tab. 1: Composition of tested gypsum samples.

Material	Kind of additives	Name of additives	Quantity [%]	Water-gypsum ratio
S0	-	-	-	0.627
S1	plasticizer	Peramin SMF 20	0.5 % wt.	0.500
S3	hydrophob. ingred.	Imesta IBS 47	0.5 % wt.	0.627
S5	hydrophob. ingred.	Zonyl 301	5 % of solution	0.627
S6	plasticizer hydrophob. ingred.	Peramin SMF 20 Imesta IBS 47	1 % wt. 1 % wt.	0.500
S7	plasticizer hydrophob. ingred. PP fibres	Peramin SMF 20 Imesta IBS 47 Fibrecrete	1 % wt. 1 % wt. 1 % wt.	0.500

Each set of samples in the form figures a 40×40×160 mm were manufactured using two different water-gypsum ratios: 0.627 and 0.500 in accordance with the standard ČSN 72 2301 (ČSN 72 2301, 1978). Samples were made and kept in constant laboratory conditions of 23 °C ± 1 °C and relative humidity of 30 ± 2 % for four weeks. At a specific time intervals the samples were tested.

## 3. Experimental results

Before the evaluation of strength tests, it was necessary to determine for each set: bulk density, density of matrix and total open porosity (Tab. 2). These characteristics have great influence on the final compressive strength and bending strength, and corresponded with the values presented in Tab. 1.

Tab. 2: Bulk density, density of matrix and total open porosity of the tested gypsum samples

Material	Kind of additives	Density [kg/m <sup>3</sup> ]	Density matrix [kg/m <sup>3</sup> ]	Total open porosity [%]
S0	-	1170	1900	38
S1	plasticizer	1270	1950	35
S3	hydrophobic ingredients	1100	1900	42
S5	hydrophobic ingredients	1120	1900	41
S6	plasticizer, hydrophobic ingredients	1280	1900	33
S7	plasticizer, hydrophobic ingredients, PP fibres	1265	1880	33

Tab. 2 shows that the influence of additives and polypropylene fiber on bulk density and the density of matrix are almost negligible, as well, as the impact of different water-gypsum ratio. In contrast, the strength values (Figs. 1 and 2) are different. Fig. 1 shows the values for compressive strengths and Fig. 2 for bending strengths. Both figures are done in time intervals of 2 hours, 3, 7 and 28 days after mixing the gypsum with water.

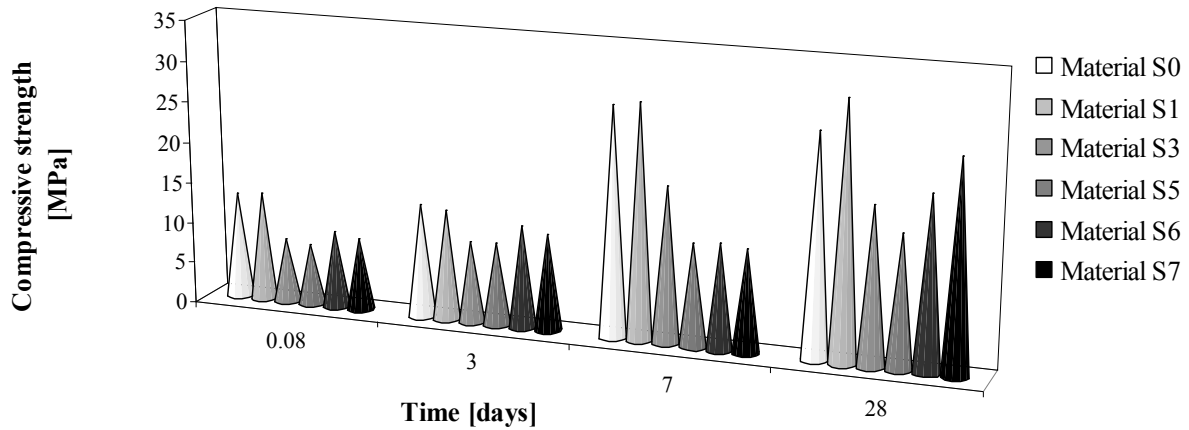


Fig. 1: The compressive strengths at various time intervals.

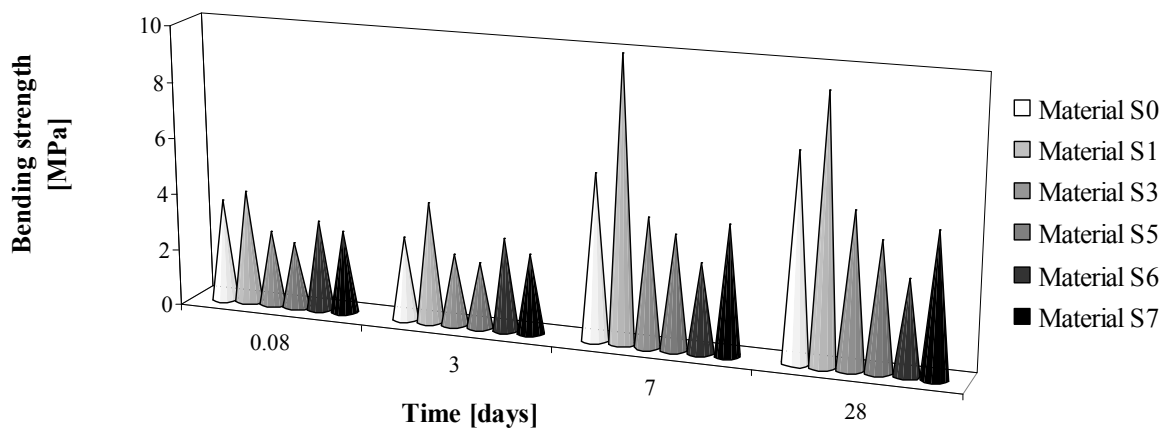


Fig. 2: The bending strengths at various time intervals.

#### 4. Conclusions

The presented results show that for most materials are 2 hours, 1 and 3 days strengths nearly identical, then there is a significant increase in strengths. For the materials S0 and S1, the value of compressive strengths is doubled. The materials S6 and S7 behave somewhat different, which can be obtained according to previously observed values of the time dependence of compressive strength, which is an increasing trend in the reporting period. For the material with the addition of plasticizer (S1), compressive strength positively increased in comparison with untreated FGD gypsum – S0 material. The strength of this material is about 5 MPa higher (Shater et al, 1983) in comparison with the material after 28 days. For other materials, we can observe a reduction in compression strength values compared with the reference material. This effect was most pronounced for samples S3 and S5 produced with the addition of hydrophobic additives but with the same water-gypsum ratio. The least negative effect was achieved with material S3, but even here the 28-day strength decreased by 8 MPa. For S5 material, this value is lower by 10 and 11 MPa. The combination of plasticizer, hydrophobic additives, and lower water-gypsum ratio (0.500) for materials S6 and S7, which also includes the PP fibers, have led to improved compressive strength. Strength after 28 days is lower, only about 6.0 or 1.5 MPa compared with the reference material S0.

Similarly in Fig. 2 comparison of bending strength of materials, depending on time was investigated. The time intervals are the same as in the previous figure. From these results we can see that the reduction of water-gypsum ratio for material S1 resulted in an increase in bending strength in comparison with the reference material S0. Trend of increasing the bending strength was similar to that for compressive strength. For the first three measurement periods the measured values for each material was almost identical. Then the increase follows, which was between 3 and 7 day, it was the

highest for the material S1. The plasticizer, which was used on material S1 compared with S0 material, seems to be preferable because its bending strength increased by 2 MPa after 28 days. Hydrophobic additives led to reduction in strength in comparison with the reference material. It had the least negative impact on material hydrophobization S3, where the strength decreased by 2 MPa, S5 fell by nearly 3 MPa with the same water-gypsum ratio as the reference sample S0. The strength of material S6 still decline about 4 MPa. The combination of plasticizer, hydrophobic additives and lower water-gypsum ratio had such a positive influence on compressive strength (Jianquan et al, 2005). Some improvement was achieved in the S7 material, in comparison with the material S6 which also includes PP fibers. Here, the measured bending strength is 2.2 MPa lower than for the reference material S0.

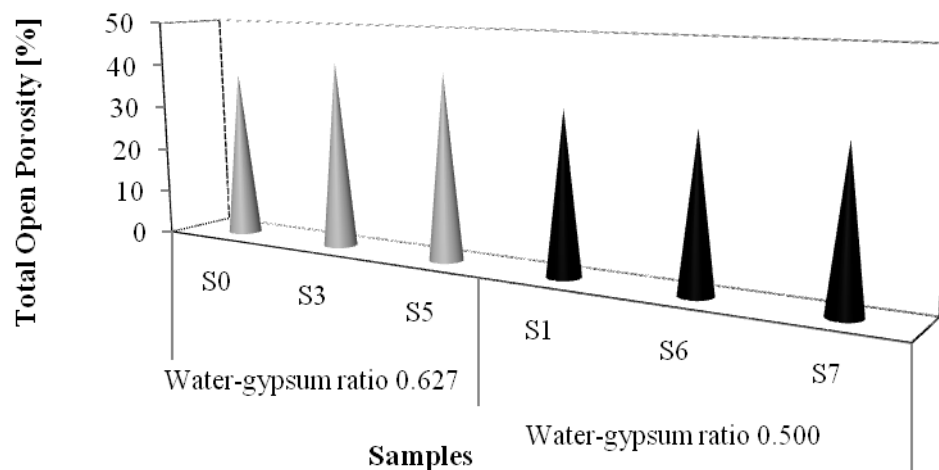


Fig. 3: Relationship between the total open porosity and water-gypsum ratio.

In the Fig. 3, there are clearly visible the differences in the values of total open porosity depending on the water-gypsum ratio. The difference of total open porosity for gypsum samples with the water-gypsum ratio 0.627 and 0.500 is more than 17 %. Taking into account that the value of 0.627 water-gypsum ratio is about 20 % higher than the value 0.500 then we can consider almost direct proportionality between water-gypsum ratio and total open porosity (Kuechler et al, 2002). Very interesting is the total open porosity shown in spite of added ingredients and PP fibers for the material S7.

### Acknowledgement

This research has been supported by the Ministry of Education of the Czech - project MSM 6840770003.

### References

- ČSN 72 2301 (1978) Sádrová pojiva. Klasifikace. Všeobecné technické požadavky. Zkušební metody. Prague: Czechoslovak standardization institutions, pp. 17.
- Wirshing, F. (1983) Calcium Sulfate, In: Ullmanns Encyclopedia of Industrial Chemistry, Volume 6, Weinheim, Wiley-VCH Verlag, pp. 90 – 94.
- Shater, M. A. & Mosalamy F. H., El-Sheikh R. & El-Didamony H. (1983) Mechanism of the hydration of tricalcium aluminate and gypsum of 1:3 mole ratio at low water/solid ratio and in suspension, *Thermochimica Acta*, Volume 69, Issue 3, pp. 379-388.
- Jianquan Li, Guozhong Li, & Yanzhen Yu (2005) The influences of gypsum water-proofing additive on gypsum crystal growth, *Material Letters*, Volume 61, Issue 3, pp. 872-876.
- Kuechler R., Noack K. & Zorn T. (2002) Investigation of gypsum dissolution under saturated and unsaturated water conditions, *Ecological Modelling*, Volume 176, Issues 1-2, pp. 1-14.

## HYBRID-SYNTHETIC IMPINGING JETS

V. Tesař\*

**Abstract:** *Impinging jets can achieve the highest convective heat or mass transfer rate. An increase beyond present limits is possible by pulsation of the flow. The extreme case of the synthetic jets could be particularly effective – were there not the re-ingestion of the fluid. A solution brings the new concept of non-zero time mean hybrid synthetic jet.*

**Keywords:** *Synthetic jet, impinging jet, heat transfer, mass transfer.*

### 1. Introduction

Effectiveness of cooling, heating, and drying by a fluid is limited by a layer of the fluid, usually very thin (typically of the order 0.1 mm or less) held on the transfer surface by viscous forces. The transport crosses this layer by the much less effective conduction mechanism. The highest transfer rates are achieved by the fluid impinging on the surface as an accelerated jet, penetrating so as to leave the shortest remaining conduction distance. Nevertheless, the limiting effect of the stagnant layer is still there (Fig. 1).

### 2. Destroying the layer by pulsation

The idea of eliminating the conduction layer or at least decreasing its influence by pulsation of the flow has been there for at least half a century. It is supported by numerical solutions (e.g., Xu et al.,

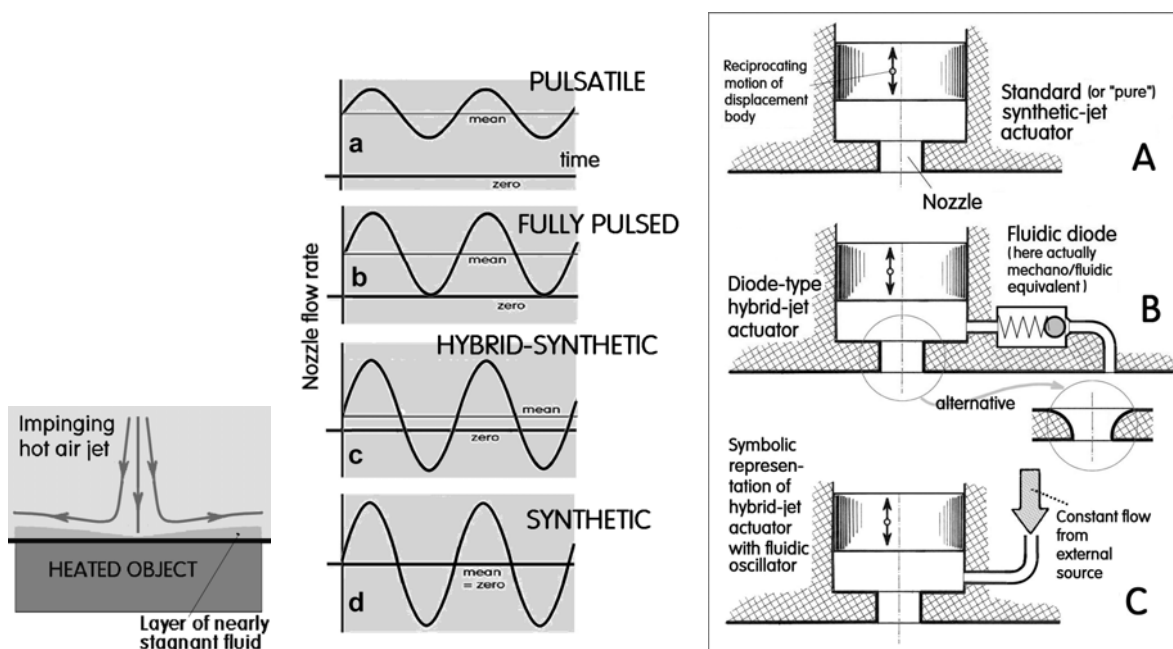


Fig. 1: (Left) The limit to convective transfer rate is imposed by the layer held on the surface by viscosity.

Fig. 2: (Middle) Pulsations of the jet can destroy the conduction layer.

Fig. 3: (Right) Synthetic jets: A – pure zero time-mean flow B – hybrid-synthetic jet with enhancement by pumping C – Action of fluidic oscillator symbolically represented by the superimposed steady flow.

\* prof. Ing. Václav Tesař CSc.: Institute of Thermomechanics v.v.i., Academy of Sciences of the Czech Republic, Dolejšková 5, 182 00 Praha 8, Czech Republic, e-mail: tesar@it.cas.cz

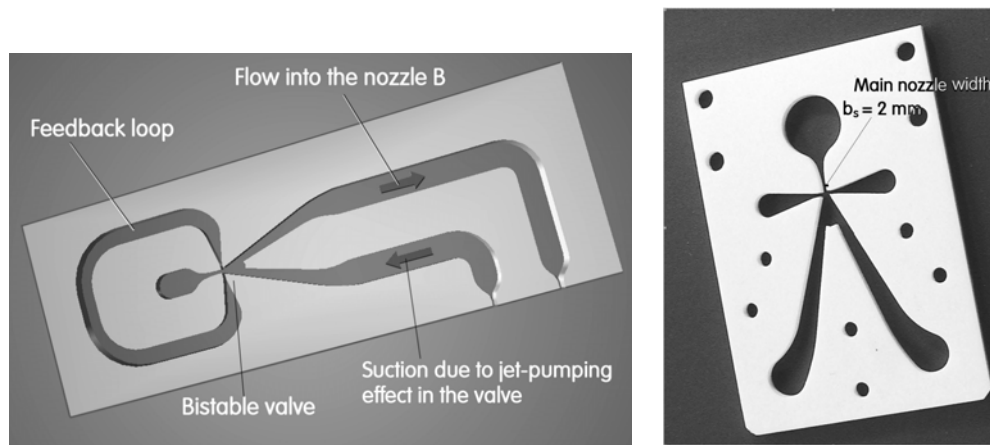


Fig. 4: (Left) A typical fluidic oscillator (here with the Spyropoulos-type feedback loop, Tesař V., et al. (2007a).

Fig. 5 (Right) Photograph of the bistable diverter valve, laser-cut in 5mm thick Teflon, used in the tests described in Tesař, 2009).

2010) but experimental verification has been so far inconclusive – some researchers have, in fact, found the pulsation actually decreasing the heat transfer effectiveness. Other factors that has led to non-acceptance of the idea in practice were: (a) complexity and cost of the mechanical pulsators compared with the simple nozzle for steady flow, and (b) the power required to generate the pulsation. New impetus came recently from two directions. The first was the development in synthetic jets – the extreme in pulsation intensity (case d in Fig. 2) which should act on the layer most effectively (Pavlova & Amitay 2006), The other was development of fluidics – no moving-part flow control. Fluidic oscillators based on hydrodynamic instabilities (usually bolstered up by a feedback) are inexpensive and consume very low power. The problem with synthetic jets e.g. in cooling is their gradual loss of effectiveness due to re-ingestion of the fluid already heated in previous cycles.

### 3. The solution

The answer was found in the **hybrid-synthetic** jet - with superimposed small steady flow component, case (c) in Fig. 2. The idea was first introduced by Trávníček in 2005. There are two alternatives. In the first one, following the original scheme of Trávníček, Tesař, & Wang (2005), cf. also Trávníček, Vít, & Tesař (2006), schematically represented as case B in Fig. 3, the necessary fresh outside fluid replacing the already heated one flows into the displacement-type actuator during the suction part of the period. Its escape in the next part of the period is prevented in this illustration by the non-return valve, in actual operational actuators replaced by a no-moving-part fluidic diode (Tesař, 2008).

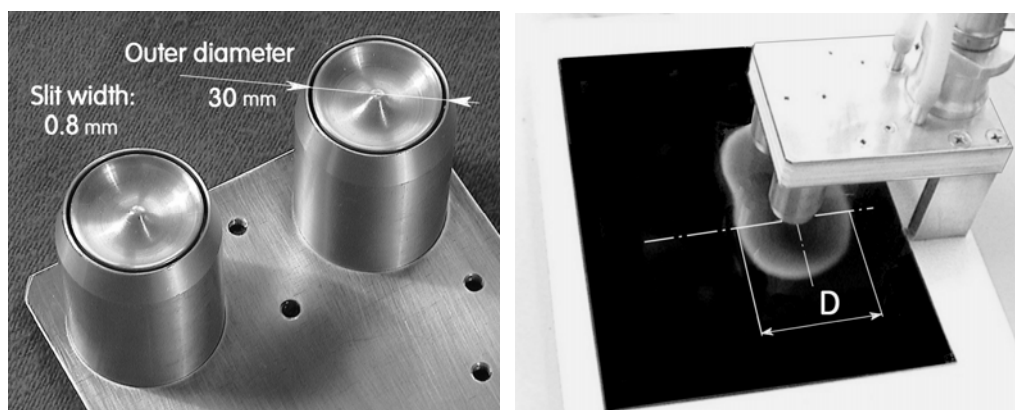


Fig. 6: (Left) The pair of annular nozzles used in the laboratory model. Each nozzle was connected to one of the two outlets of the fluidic valve.

Fig. 7: (Right) Definition of the characteristic distance  $D$  measured on the impingement distance covered with thermochromic liquid crystals.

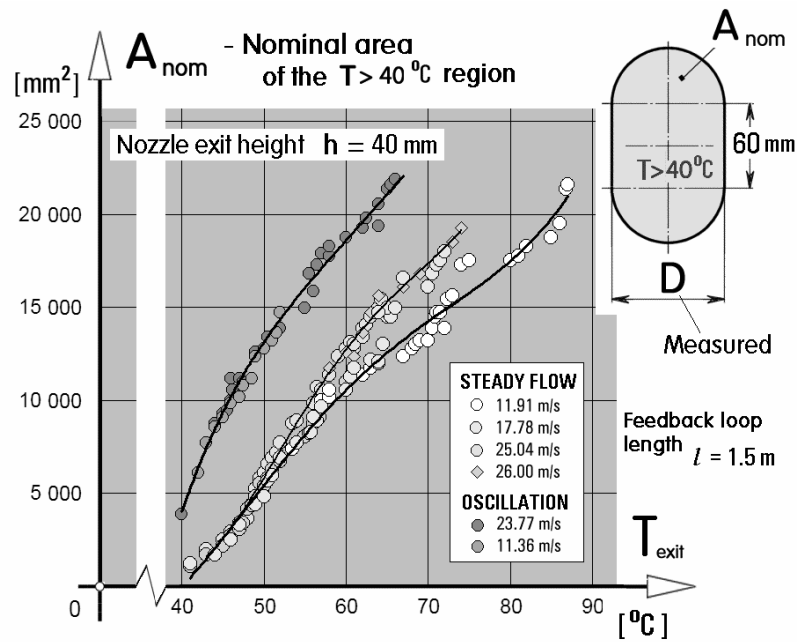


Fig. 8: The extent of the nominal (simplified) hot spot area  $A$  evaluated from the measured distance  $D$  in heating by steady flow and by hybrid-synthetic jets. The advantage of the latter case is here convincingly demonstrated.

In the other version, Tesař, Hung, & Zimmerman (2006), the actuator is supplied with the fluid from an external source. The oscillation is generated in the oscillator consisting of a diverter valve (Fig. 5) with a feedback loop (e.g. as shown in Fig. 4). This way, it is possible to eliminate all moving components – such as the piston schematically represented in the case C, Fig. 3. The return flow into the nozzle during the suction phase is generated by the jet-pumping effect of the flow through the main nozzle in the valve.

Successful tests that demonstrated convincingly the increase in heat transfer made possible by synthetic jets, are described in Tesař (2007a). The nozzles, shown in Fig. 6, were with annular exits due to the reasons discussed in Trávníček & Tesař (2003). Each nozzle was connected to one of the two the outputs of the valve shown in Fig. 5, cut in 5 mm thick Teflon plates. There were 2 plates stacked on top of one another, both with 2 mm wide main nozzle – so that the impinging nozzle exit area was 3.7-times larger than that of the main nozzle in the oscillator. Oscillation frequency was in the tests shown in Figs. 7 and 8 adjusted to either 10 Hz or 14 Hz, with negligible difference in the heating effect. This rather low frequency levels required feedback loop length 1.5 m - obviously much longer than in Fig. 4, so that it could not be laser-cut in the plate and had a form of a Teflon tubing. Air supplied into the oscillator was heated using the heater from a commercial hot-air gun. Typical heating-nozzle exit velocities were  $\sim 17$  m/s, at which the power dissipated by hydraulic losses in the oscillator, nozzles and electric heater upstream from the oscillator, was mere 5 W, a value practically negligible compared with the supplied heating power input  $\sim 1$  kW.

The effectiveness of the heating was evaluated by means of thermochromic liquid-crystals, a foil containing them covering the impingement surface. This particular crystals reacted by initial colour change when the temperature reached  $40^\circ\text{C}$ , and the location of this change could be quite accurately measured as shown in Fig. 7. The next Fig. 8 shows that under the impinging hot air, the area of the region with temperatures higher than  $40^\circ\text{C}$  was significantly larger with the hybrid-synthetic jet than with steady hot-air jet.

#### 4. Conclusions

A model of an impingement heating device with two nozzles operated in opposite phases of a hybrid-synthetic jet, generated by a no-moving-part fluidic oscillator, was built and tested using the temperature field visualisation by means of thermochromic liquid crystals. It was demonstrated that the operation in the hybrid-synthetic annular jet regime exhibits a substantially higher total heat transfer rate



than steady jets. Depending on the regime, the increase is to 300% and even more, though values 180% – 200% may be more typical.

## Acknowledgments

Gratefully acknowledged is financial support by the research plan AV0Z20760514 and by grants 101/07/1499 as well as 101/11/J019 donated by GAČR - Grant Agency of the Czech Republic.

## References

- Pavlova A., Amitay M. (2006) Electronic Cooling Using Synthetic jet Impingement, *Journ. of Heat Transfer*, Vol. 128, p. 897.
- Tesař V., Zhong S. (2003) Efficiency of Synthetic Jet Generation, *Zhongguo Hangkong Taikong Xuehui Hui-kan*, Vol. 35, p. 45, Taiwan .
- Trávníček Z., Tesař V. (2003) Annular Synthetic Jet Used for Impinging Flow Mass Transfer", *International Journal of Heat and Mass Transfer*, Vol. 46, p. 3291.
- Tesař V., Trávníček Z. (2005a) Increasing Heat and/or Mass Transfer Rates in Impinging Jets, *Journal of Visualization*, Vol. 8, p. 91.
- Tesař V., Trávníček Z. (2005b) Pulsating and Synthetic Impinging Jets, *Journal of Visualization*, Vol. 8, No. 3, p. 201.
- Trávníček Z., Tesař V., Wang A.-B. (2005) Enhancement of Synthetic Jets by Means of an Integrated Valve-Less Pump, Part II: Numerical and Experimental Studies, *Sensors and Actuators A*, Vol. 125, p. 50, 2005.
- Tesař V., Hung C.-H., Zimmerman W. (2006) No-Moving-Part Hybrid-Synthetic Jet Actuator“ *Sensors and Actuators A*, Vol. 125, p. 159.
- Trávníček Z., Vít T., Tesař V. (2006) Hybrid Synthetic Jets as the Nonzero-Net-Mass-Flux Synthetic Jets, *Physics of Fluids*, Vol. 18, p. 081701-1.
- Tesař V., et al. (2007a) Experimental Investigation of a Fluidic Actuator Generating Hybrid-Synthetic Jets, *Sensors and Actuators A*, Vol. 138, p. 213.
- Tesař V. (2007b) Configurations of Fluidic Actuators for Generating Hybrid-Synthetic Jets, *Sensors and Actuators A*, Vol. 138, p. 394.
- Trávníček Z. et al. (2007) Bifurcated and Helical Impinging Jet Controlled by Azimuthally Arranged Synthetic Jets, *Proc. of HEFAT 2007*, Paper TZ1; Sun City, South Africa, p.35 July 2007.
- Trávníček Z., Tesař V., Kordík J. (2007) Double-acting Hybrid Synthetic Jets with Hexagonally Arranged Nozzles, *Proc. of FLUCOME 2007*, Paper 12, Tallahassee, U.S.A., Sept. 2007.
- Trávníček Z., Tesař V., Kordík, J. (2008) Performance of Synthetic Jet Actuators Based on Hybrid and Double-Acting Principle, *Journal of Visualization*, Vol.11, p. 221.
- Tesař V. (2008) Valve-less rectification pumps, in “*Encyclopedia of Microfluidics and Nanofluidics*“, Ed.: Dongqing Li, publ. by Springer Science+Business Media, p. 2132.
- Trávníček Z., Tesař V. (2008) Synthetic Jets used to Control Spreading of an Annular Impinging Jet, *Proc. of ISFV13 and FLUVISU12*, Nice, France, July 2008.
- Tesař V. (2009) Enhancing Impinging-Jet Heat or Mass Transfer by Fluidically Generated Flow Pulsation, *Chem.Eng. Research and Design*, Vol.: 87, p. 181.
- Tesař V., Něnička V. (2009a) Phase-Synchronised Investigations of Triggered Vortices in Impinging Jets, *Proc of “ENGINEERING MECHANICS 2009”*, p. 1321, Svratka, May 2009.
- Tesař V., Něnička V. (2009b) Study of Vortical Structures in Impinging Jets - New Methods and Approaches *Proc. of ExHFT-7*, Krakow, Poland, June-July 2009.
- Tesař V., Něnička V. (2009c) Instability Structures in Impinging-Jet Flows, *Proc. of EMT 2009*, p. 335, Liberec, November 2009.
- Xu et al., (2010) Turbulent impinging jet heat transfer enhancement due to intermittent pulsation, *Journ. of Thermal Sciences*, Vol. 49, p. 1247.

## HYDRAULIC SYSTEMS FOR THE FUTURE

**J. Tlustoš\***

**Abstract:** *Survey of conventional hydraulic systems development and the last progressive trends in hydraulic systems architecture. Aspects of advanced control concepts implementation. Potential of high efficiency systems performance. The foreshadowing of future visions of the “Green hydraulics”.*

**Keywords:** *Hydraulics, control systems, system dynamics, artificial intelligence, fuzzy logic.*

### 1. Introduction

In the last years, a fast development of electronics and mechatronics has caused the replacement of hydraulic and pneumatic systems by these new progressive technologies. Anyway, there is a warranted wide area of applications for fluid systems, especially for hydraulic systems in the age of electronics too. We can also see great progress in the field of hydraulic systems, especially by means of implementation of electronics, cybernetics, mechatronics and new design and development approaches and concepts. The last century development of hydraulic components including pumps, valves and actuators reaches its limits. There is still way ahead, but the focus of up to date activities has to be concentrated on the system architecture. New complex and comprehensive approach to the system design enables to implement general dynamic systems theories and means of the artificial intelligence.

### 2. Hydraulic Systems Performance

Hydraulic systems cannot be replaced by any means of automation for the extremely exposed applications with high forces, torques and velocities. They are produced in different designs related to goal application. In some industrial applications the hydraulic systems are spread on the whole mechanical equipment, only power source with fluid conditioning is mostly centralized. On the other hand, for the installation of hydraulic systems in mobile machines the system has to be adapted and it has to enable effective and optimal usage of the available space. We can name such examples as aircrafts and space shuttles.

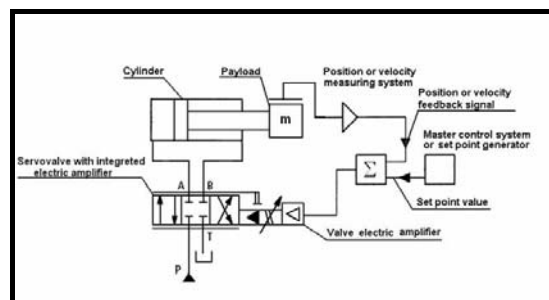


*Fig. 1: Hydraulic Axis fundamental diagram.*

Straight-line motions can be easily executed by means of hydraulics with high efficiency. Closed loop systems enable to control position, velocity and force with high precision (see Fig. 1). These subsystems are called “hydraulic axis”. From the point of view of control system architecture, we are dealing with autonomous decentralized control units with self-diagnostics. They are able to communicate in duplex mode with other units on the same control level and also with higher-level automation system via standardized communication interfaces.

\* Ing. Bc. Jiří Tlustoš: Hydraulic Systems Department, ŽDAS Company, Strojírenská 6; 591 71, Žďár nad Sázavou; CZ, e-mail: jiri.tlustos@zdas.cz

### 3. Potential for Improvement

During the last century hydraulic systems have gone through a long process of development, from the primitive hydraulic units with basic functionality, reduced applicability and manual control of the process, through advanced systems with better performance and implementation of basic autonomous control units up to nowadays modern fluid systems with extensive integration of electronics.

#### 3.1. Efficiency of Components and System

There are several possibilities how to reach higher efficiency of the system there. The overall efficiency of the system is given as the product of individual efficiencies (see Eq. (1)). The basic hydraulic circuit can be represented by the linear chain of individual efficiencies. It is illustrated in Fig. 2. It is obvious that the first possibility of higher system efficiency achievement is to increase the efficiency of elementary parts of the system.

$$\eta_T = \prod_{i=1}^n \eta_i \quad [ - ] \quad (1)$$

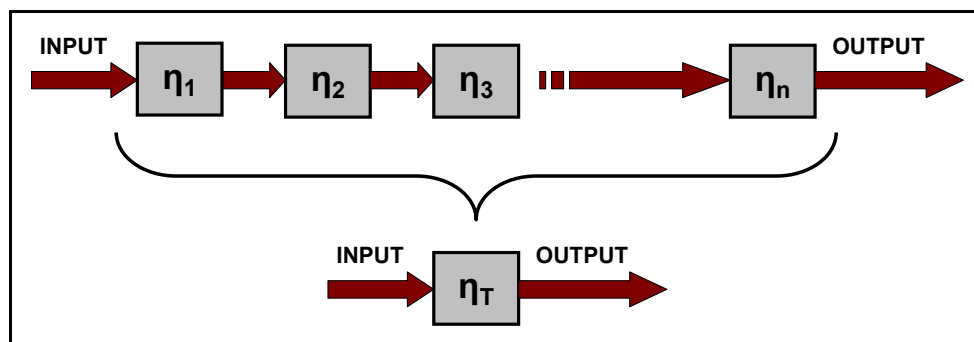


Fig. 2: Linear Chain Diagram of Individual Efficiencies.

The efficiency of the power sources and actuators is given by efficiency of energy transformation. The mechanical energy is transformed into pressure energy of the working fluid in pumps (hydraulic generators). In case of the actuators there is the inverse transformation executed. These basic principles are illustrated in Fig. 3 with examples of the real representation of individual blocks.

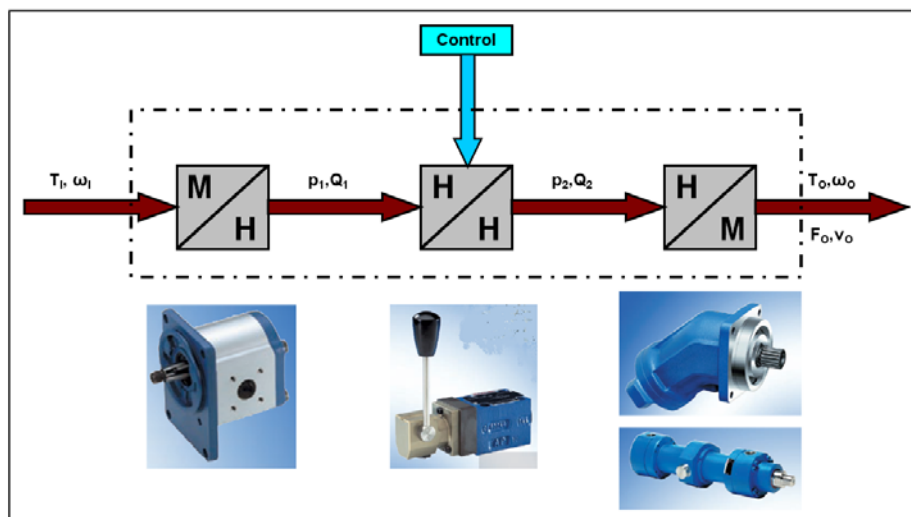


Fig. 3: Block Diagram of Basic Hydraulic System.

High quality materials and high quality of production processes are used during the production of the hydraulic components. New approaches of the quality management are implemented in the production of hydraulic components. Better performance parameters of the components can be achieved and the lifetime is also longer. The conclusion is that there is no significant possibility for improvement in the optimization of the hydraulic components, e.g. valves, pumps, hydraulic cylinders and motors.

### 3.2. Design of the Hydraulic System

The designing of the hydraulic system is a key activity, which has to be done based upon all system requirements and options with respect to control system implementation. The system architecture, which means how the system is composed and designed, is a very important factor. Hydraulic systems enable wide flexibility and there can be a lot of possibilities how to design system for the specific application. We have to observe many criteria of the system performance. Economical criteria are operating cost, maintenance cost and cost of the equipment. Technical criteria are especially the precision of the system performance, safety operation, and also reliability of the system. We can design several options of the specific circuit, they can accomplish the initial requirements but the solution can be totally different. Fast development of information technologies and their implementation into engineering processes enables to increase productivity, quality and effectiveness of the design. CAE tools are widely used in the design of hydraulic components and manifolds. There are also a lot of CAD tools for design of circuit diagrams and system function simulations. The example of the software which supports both functions is in the Fig. 4. Nevertheless the circuit design is still the matter of creativity, knowledge and intuition (Rao, 2000).

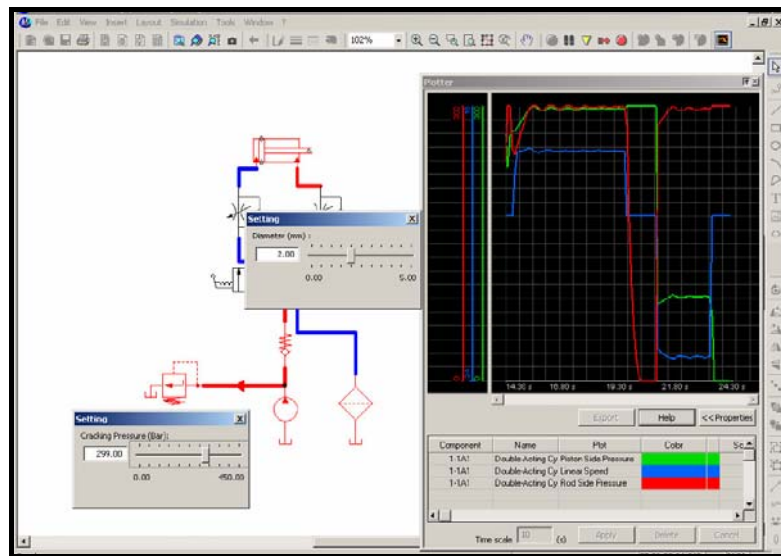


Fig. 4: Hydraulic Circuit Design and Simulation.

Energy efficiency of the system is defined by the selected components and especially by the circuit and system architecture. The effective usage of energy plays the fundamental role in nowadays technology. Design of new machines and equipment requires high degree of automation and low energy consumption. The main reasons are economical aspects, which mean reducing of operational costs, and in wider perspective also environmental aspects. The energy efficient and environment friendly hydraulic systems are sometimes called the “Green Hydraulics”

### 3.3. Control System Design

When we see the Fig. 3 the transformation block which converts hydraulic energy to the hydraulic energy with different parameters, is controlled by some kind of the control unit. In this case the control action is done manually via a hand lever. The advanced concept of control system is illustrated in Fig. 1. In the most cases hydraulic systems are more forked and complex. The principal Drive & Control pyramidal diagram is visible in the Fig. 5. We can see that design of the hydraulic system has to be done with respect of the electrical control system.

## 4. New System Approach

The new mechatronics approach applied during component designing is not sufficient for the design of vast spread systems. Hydraulics is not only connected via appropriate interfaces with control electronics but it is an integral part of whole control system as far as new automation systems are concerned (Kalman, 1960). In this case we have to apply the cybernetic principles and dynamic systems theories (Forrester, 1968).

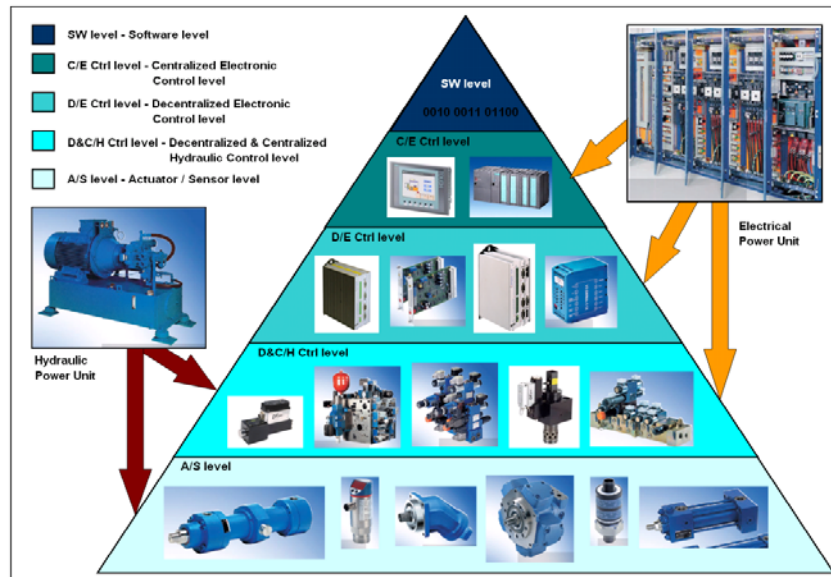


Fig. 5: Hydraulic & Electronic Drive & Control System Architecture.

## 5. Implementation of Artificial Intelligence

Hydraulic systems are multiple-parametrical and the optimal operating point is hardly accessible with conventional control algorithms. Very good results can be obtained using the means of artificial intelligence (AI), especially using self-tuning control system with fuzzy logic and neural networks. Knowledge-based system can be implemented in the diagnostic or the failure prediction (Muto, 2003).

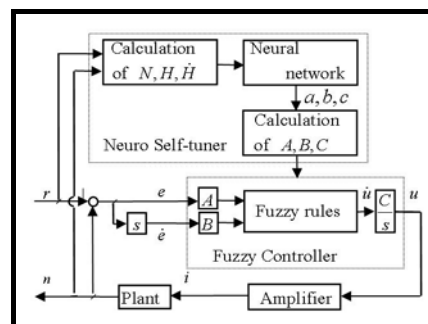


Fig. 6: Control Algorithm using means of AI.

## 6. Conclusions

It is obvious from all the mentioned facts, that there is still a significant potential for future progress in hydraulic systems, especially for the advanced system architecture and for new control concepts implementation. The synergic action of the heterogenous parts benefits integration will lead to the system performance excellence and will help us to create safer and energy efficient world.

## Acknowledgement

The survey and research of future potential of hydraulic systems is fully supported by the management of the ŽDAS Company and it has an impact on various grants and technical development projects solved by the Company. This support is gratefully acknowledged.

## References

- Forrester, Jay W. (1968) Principles of Systems, (2nd. ed.). Waltham, MA: Pegasus Communications, 391 pp.
- Kalman, R. E. (1960) On the General Theory of Control Systems. In: Proceedings of the First Triennial World Congress of IFAC, Moscow.
- Muto, Takayoshi. (2003) Self-tuning Fuzzy Control of Electro-hydraulic System, Journal of Fluid Power, Japan
- Rao A.K.& Subash B.A. (2000) Industrial Dynamics to Systems Thinking, Indian Institute of Technology, Bombay, 33 pp.



## RELATIONS BETWEEN FRACTAL DIMENSION AND VOLUME OF TRABECULAR BONE AND ITS BEHAVIOUR UNDER LOADING

T. Topoliński\*, A. Cichański\*, A. Mazurkiewicz\*, K. Nowicki\*, S. Jung\*\*

**Abstract:** Two parameters of bone microarchitecture: volume of bone layer and fractal dimension were used. 42 human bone samples were cut to cylindrical testing samples of 8.5 mm thickness and 10 mm diameter. We obtained 230 images (microCT) which, using binarisation technique, were transformed into pixels and voxels. We created geometrical mesh of layers of bone mass. This allowed the calculation of each layers volume and fractal dimension. Fractal dimension for each single layer has been calculated applying set of voxels using Sarkar's and Chaudhuri's box-counting algorithm. When comparing scatter for layers' volume and scatter for layers' fractal dimension we can see that scatter is clearly higher for volume. This might mean that relative scatter for fractal dimension is narrower, thus in diagnostic procedure fewer measurement data of fractal dimension than of volume are sufficient to conclude about bone structure.

**Keywords:** MicroCT, bone structure, bone volume, fractal dimension.

### 1. Introduction

The fact that life expectancy is constantly increasing imposes new challenges for medicine with the aim of providing not only longer life, but also good physical and mental health. One of the factors that contributes to the quality of life is physical fitness, which involves bone strength adequate for one's lifestyle. It is a natural phenomenon that bone density decreases with time, and this process starts at the age of 25-28, at first slowly and then at an accelerating rate (Seeman E., 2008).

These changes occur along with the decreasing activity of a person. The problem begins when the decrease of 'bone in bone' – usually osteoporosis related – definitely exceeds the norm, it can lead to fracture of the bone and fracture of femoral neck, distal radius or vertebral body are most common.

We ascertained that the process of destruction of the loaded bone is localized only at certain parts of the sample. Using microCT we obtained layers of 36 micrometers thickness. This allowed to determine the volume and fractal dimension for each sample. Analysis of variability of these bone structure indicators may show more effective one in the analysis of bone strength.

### 2. Materials and methods

#### 2.1. Specimen

We tested trabecular bone samples. Samples were collected from 42 femoral heads (21 osteoporotic and 21 arthritic), the mean age of the patients with osteoporosis was 77 yrs (range 63 - 91) and the mean age of the patients with osteoarthritis was 70 yrs (range 50-79). These specimens were obtained during hip arthroplasty. First, slices were cut out from the base of the head 8.5 mm thickness, perpendicular to the axis of the neck of the bone. Next, from the central region of the slices, samples were cut out in the shape of a cylinder, about 10 mm diameter and 8.5 mm height. The method of obtaining samples is shown in Fig. 1.

---

\* prof. Ing. Tomasz Topoliński, Ing. Artur Cichański Ph.D., Ing. Adam Mazurkiewicz Ph.D. and Ing. Krzysztof Nowicki Ph.D.: Faculty of Mechanical Engineering, University of Technology and Life Sciences, Kaliskiego 7 Street; 85-789, Bydgoszcz; PL, e-mails: tomasz.topolinski@utp.edu.pl, artur.cichanski@utp.edu.pl, adam.mazurkiewicz@utp.edu.pl, krzysztof.nowicki@utp.edu.pl

\*\* Stanisław Jung: South Tyneside Hospital, South Shields, UK

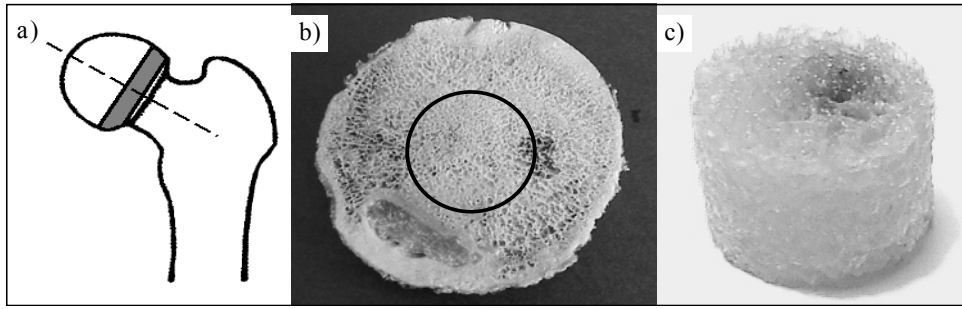


Fig. 1: Method of obtaining sample: a) cutting of slice; b) cutting of sample; c) final shape.

## 2.2. Micro CT technique

MicroCT investigations of cylindrical samples were done on  $\mu$ CT 80 machine (SCANCO Medical AG, Bruettisellen, Switzerland) with resolutions of 36  $\mu$ m and with basic parameters: 70 kV, 114  $\mu$ A, 500 projections/180°, 300 ms integration time. Thus we obtained around 230 scans for each sample. In this algorithm, single layers of a model were created by comparing images of two neighboring scans.

## 2.3. Volume calculation

On the basis of obtained images, bone volume was calculated for every layer and for sample: minimum volume  $V_{\min}$ , maximum volume  $V_{\max}$ , mean volume  $V_m$ , and standard deviation  $SD_v$ . Then we related  $SD_v$  to mean volume and we obtained relative standard deviation ( $RSD_v$ ). Bone volume for layer was performed by calculating number of bone voxels of known dimensions. The resulting volume indicators for individual samples are shown in Fig. 2 (the numbering of the samples in Fig. 2 is used to determine the clinical case and has no connection with the calculated values of volumes).

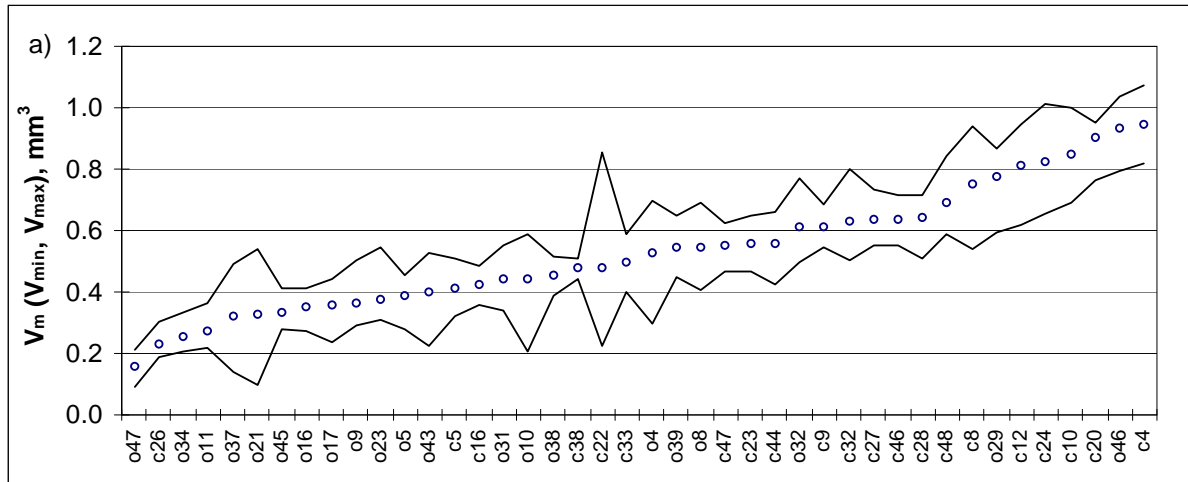


Fig. 2: Values of layer volume  $V$ .

## 2.4. Fractal dimension

To calculate fractal dimensions we applied box - counting method (Chen S.S., Keller J.M., Crownover R.M., 1993) using Sarkar's and Chaudhuri's algorithm (Sarkar N., Chaudhuri B.B., 1994). For each single layer, the fractal dimension  $D_f$  was calculated and then the mean ( $D_{f_m}$ ), minimum ( $D_{f_{\min}}$ ), maximum ( $D_{f_{\max}}$ ) and standard deviation  $SD_{D_f}$  values of those dimensions for each sample was determined. The relative standard deviation as standard deviation of fractal dimension to mean fractal dimension was calculated ( $RSD_{D_f}$ ). The resulting fractal dimension indicators for individual samples are shown in Figure 3 (the numbering of the samples in Figure 3 is used to determine the clinical case and has no connection with the calculated values of fractal dimensions).



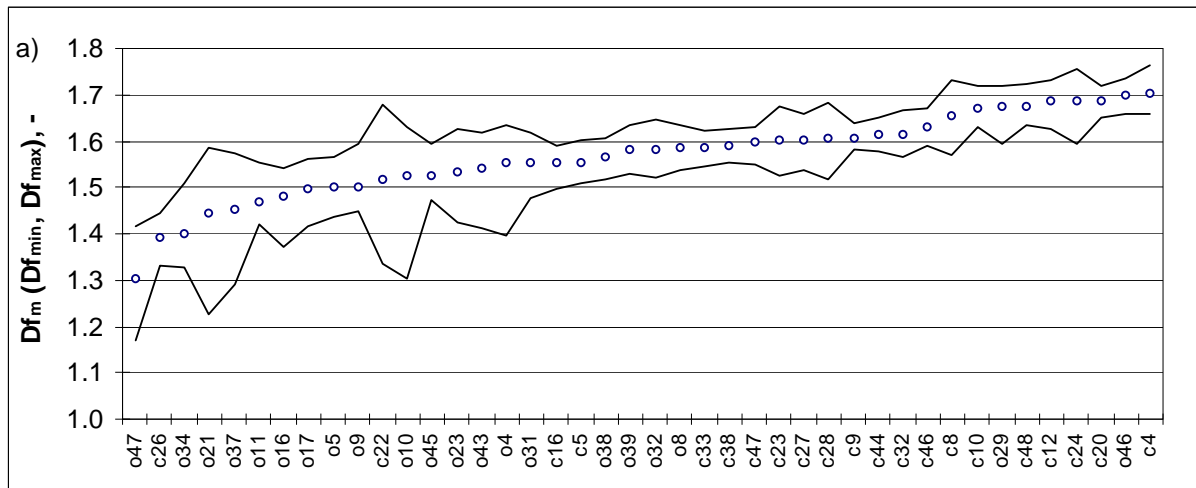


Fig. 3: Values of fractal dimension of layer *Df*.

### 3. Results

In both Figs. 2 and 3 the arthritic samples were marked as *c* while the osteoporotic – as *o*, although we did not assessed these samples according to etiology.

The range of variability of mean bone volume of the layers is between 0.18 and 0.94 mm<sup>3</sup>, mean 0.54 mm<sup>3</sup> (Fig. 2). This variability is within the range from 42.6% and 174.8% of the mean value of the volume. Variability of the values of the volume of the layers is significant, 21 of 42 samples had relative standard deviation  $RSD_v$  below 10%, 15 of 42 samples –between 10 and 20% (closer to 10%), the remaining samples i.e. six are above 20% (in two cases above 30%).

The range of variability of mean fractal dimension (Fig. 3) is within 1.3 to 1.7 with mean value of 1.56. This variability is within the range between 83.1% and 108.7% of the mean value of the fractal dimension. The variability of the fractal dimension of the layers of the samples described by relative standard deviation  $RSD_{Df}$  is smaller than for relative standard deviation for volume. It is no more than 2% for 26 of 42 samples and between 4 to 6.5 % - for 4 samples. The remaining twelve samples are within 2 to 4 % of  $RSD_{Df}$ .

### 4. Discussion

Analyzing the process of volume variability (Fig. 2), it can be seen that the differences between the maximum and minimum values are similar in the whole range of mean volume variability. However the relative standard deviation slightly decreases with growth of mean volume of sample's layer. It proves that the uniformity of distribution of the bone tissue in the volume of the samples grows together with growth in mean volume.

Analyzing the process of variability in fractal dimension for the layers of the samples (Fig. 3), it can be seen that the difference between the minimum and maximum values is clearly bigger for samples of lower mean values of this dimension, i.e. for samples of less dense trabecular structures. These big differences between minimal and maximal values of *Df* may be in keeping with Bousson et al (2006) who found that for low BMD values local-microscopic variables contribute more to bone strength than macroscopic variables. Values of relative standard deviation of fractal dimension slightly decrease with increase of mean fractal dimension.

When comparing  $RSD$  for layers' volume and for layers' fractal dimension we can see that  $RSD$  is clearly higher for volume. This might mean that relative scatter for fractal dimension is narrower, thus in diagnostic procedure fewer measurement data of fractal dimension than of volume are sufficient to conclude about bone structure.

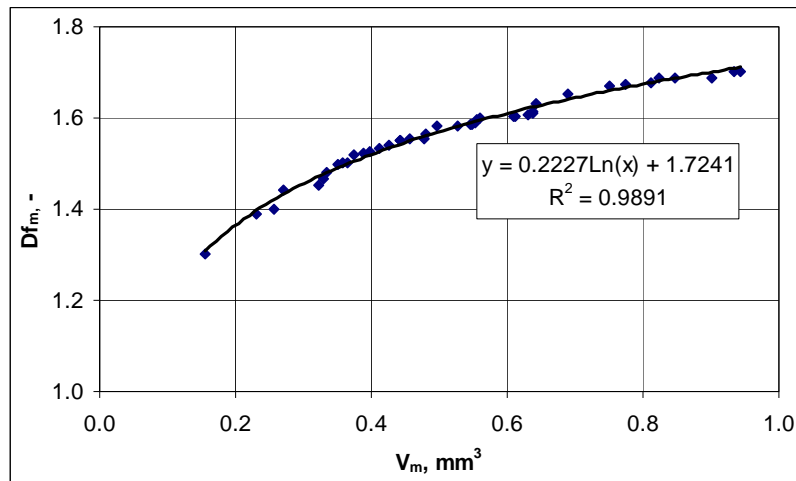


*Fig. 4: Variability of mean fractal dimension in relation to mean volume.*

There is a correlation between evaluated mean volume and mean fractal dimension (Fig. 4) (described by logarithmic function) and it is very strong as determination coefficient is nearly 1.

### Acknowledgement

This work was supported by the State Committee for Scientific Research under grant No. N N501 308934.

### References

- Seeman E. (2008) Structural basis of growth-related gain and age-related loss of bone strength. *Rheumatology* 2008; 47: 2-8.
- Chen S.S., Keller J.M., Crownover R.M. (1993) On the calculation of fractal features from images. *IEEE Trans. on Pattern Analysis and Machine Intelligence*, vol. PAMI-I 5 1993, 10: 1087-1090.
- Sarkar N., Chaudhuri B.B. (1994) An efficient differential box-counting approach to compute fractal dimension of image. *IEEE Trans. on Systems, Man, and Cybernetics* 1994; 24 (1): 115-120.
- Bousson V, La Bras A, Roqueplan F, Kang Y, Mitton D, Kolta S, Bergot C, Skalli W, Vicaud E, Kalender W, Engelke K, Laredo J-D. (2006) Volumetric quantitative computed tomography of the proximal femur: relationship linking geometric and densitometric variables to bone strength. Role for compact bone. *Osteoporosis Int* 2006; 17: 855-64.

## INDEPENDENT MODES IN A BOUNDARY LAYER SEPARATION REGION

V. Uruba<sup>\*</sup>

**Abstract:** *The method for evaluation of temporal and spatial independent modes of a dynamical system is suggested. The dynamical system is represented by time dependent vector field representing experimental data from separation of a boundary layer.*

**Keywords:** *Boundary layer separation, independent component analysis.*

### 1. Introduction

Recently we have at our disposal time evolutions of vector fields obtained using time-resolved PIV method representing turbulent flow-field as extended dynamical system. Analysis of this data requires adequate methods. Proper Orthogonal Decomposition (POD) working on energetic principle became classical method used for this purpose. The POD provides set of orthogonal spatial modes, number of which could be easily truncated to obtain reduced model of the system optimal from the point of view energetic content. However physical interpretation of the modes is very unclear and confusing. This is price for nonphysical condition of the modes orthogonality, howsoever this is very convenient and practical for treatment. A different model is needed for study the dynamical system dynamical behavior.

Individual sources of perturbations in turbulent field could be assigned to independent time signals detected within the flow-field. Although the POD modes are orthogonal and thus uncorrelated they are not necessarily independent. To decompose the turbulent signals into independent components some other method should be used. We suggest application of Independent Component Analysis (ICA) method. The ICA has been introduced in 80's to treat some neurophysiological problems (muscle contraction), while from 90's it is applied in numerous fields of mathematics and physics. ICA is a statistical method, its goal is decomposition of a given multivariate data into a sum of statistically independent components. The method works with little prior information.

### 2. Independent Component Analysis

The ICA finds the independent components (aka factors, latent variables or sources) by maximizing the statistical independence of the estimated components. We may choose one of many ways to define independence, and this choice governs the form of the ICA algorithms. The two broadest definitions of independence for ICA are minimization of mutual information and maximization of non-Gaussianity.

The Non-Gaussianity family of ICA algorithms, motivated by the central limit theorem, uses kurtosis and negentropy. The Minimization of Mutual Information family of ICA algorithms uses measures like Kullback-Leibler Divergence and Maximum-Entropy.

Let us define the statistical latent variables model first. We observe  $n$  linear mixtures  $x_1, \dots, x_n$  of  $m$  signals  $s_1, \dots, s_m$ :

$$x_j = a_{j1}s_1 + a_{j2}s_2 + \dots + a_{jm}s_m, \quad j = 1, \dots, n \quad (1)$$

---

<sup>\*</sup> assoc. prof. Ing. Václav Uruba, CSc.: Institute of Thermomechanics, AS CR, v.v.i., Dolejškova 5, 182 00 Praha 8; CZ, e-mail: uruba@it.cas.cz

Note, that number of signals and mixtures could be different in general, there are no restrictions even for their relation, i.e. the  $n$  could be equal, larger or even smaller than  $m$ . All mixtures and independent components are random variables

The starting point for ICA is the very simple assumption that the components  $s_i$  are statistically independent. In addition we also assume that the independent components must have Non-Gaussian distributions, however we do not assume these distributions known. Then, after estimating the matrix  $\mathbf{A}$ , we can compute its inverse and obtain the independent components. In tensor notation we have vectors  $\mathbf{x}$ ,  $\mathbf{s}$  and matrix  $\mathbf{A}$ :

$$\mathbf{x} = \mathbf{A} \cdot \mathbf{s}, \quad \mathbf{s} = \mathbf{A}^{-1} \cdot \mathbf{x} \quad (2)$$

ICA is very closely related to the method called Blind Source Separation or Blind Signal Separation (BSS). “Blind” means that we know very little, if anything, on the mixing matrix, and make little assumptions on the source signals. ICA is one of the methods, perhaps the most widely used, for performing blind source separation.

Typical algorithms for ICA use centering, whitening (usually with the eigenvalue decomposition), and dimensionality reduction as preprocessing steps in order to simplify and reduce the complexity of the problem for the actual iterative algorithm. Whitening and dimension reduction can be achieved with POD or similar method. Whitening ensures that all dimensions are treated equally a priori before the algorithm is run.

However there are some ambiguities connected with the ICA method. In general, ICA cannot identify the actual number of source signals, a uniquely correct ordering of the source signals, nor the proper scaling (including sign) of the source signals. It could not indicate the components variances as well, because it introduces components normalization.

### 3. Experiment

Experiments on a boundary layer separation in adverse pressure gradient have been carried out in the IT AS CR using the time-resolved PIV technique. We acquired 5000 doublesnaps in frequency 1518 Hz corresponding to 3.2 s of record. Fields of  $18 \times 79$  2-component vectors result in dynamical system with 2844 degrees of freedom and the phase space same size. The setup of this experiment and results were published in Uruba (2008, 2009).

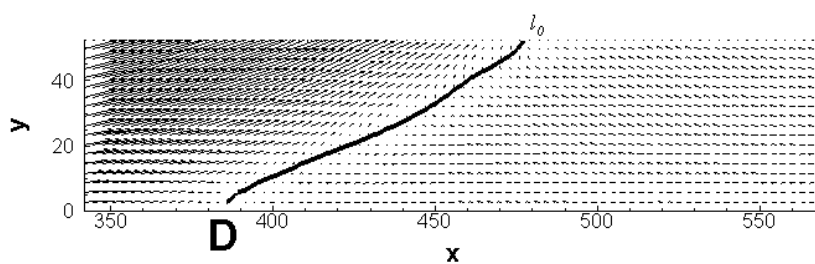
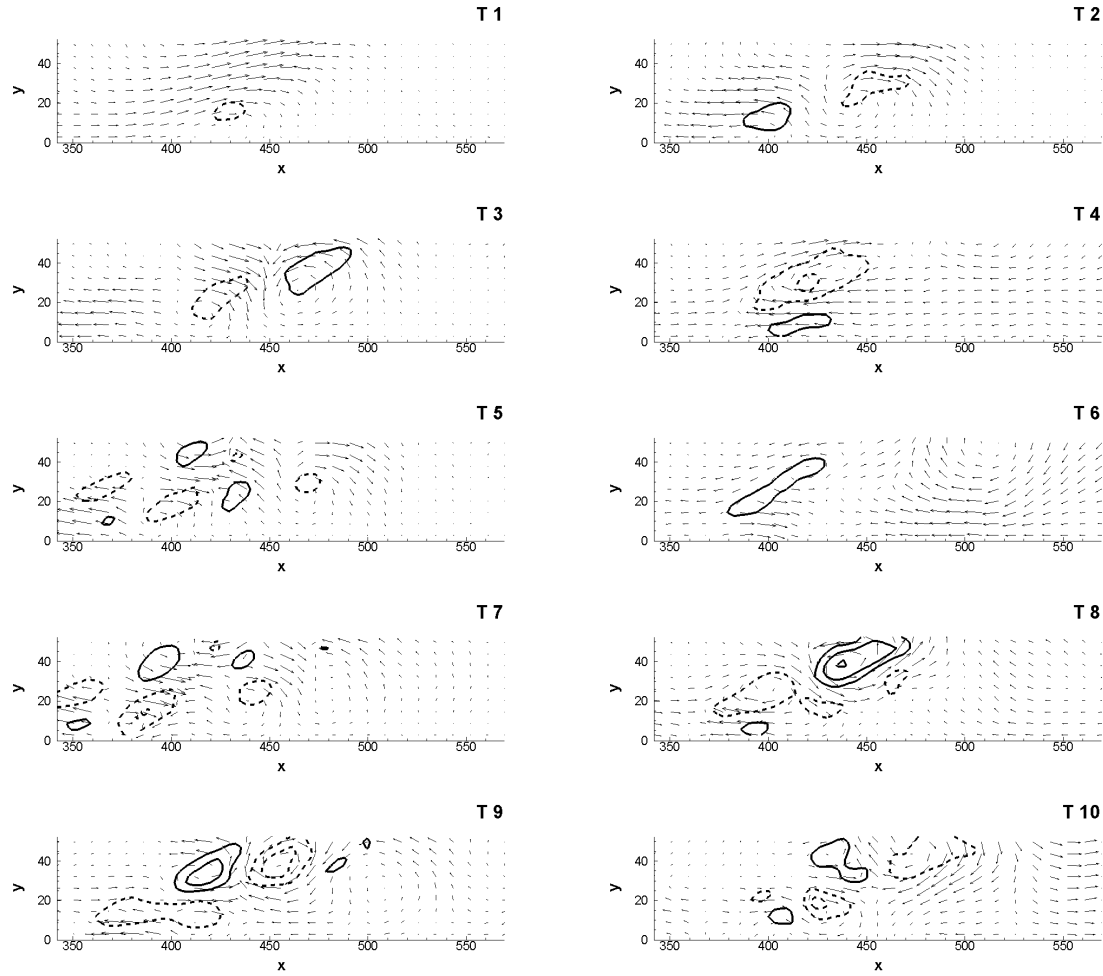


Fig. 1: Mean velocity vectors distribution.

The boundary layer shows highly dynamical behavior with many vortical structures arising within the free shear layer. However the mean vector field in Fig. 1 is very regular and smooth. The line  $l_0$  represents positions with zero streamwise velocity component. Extrapolation of this line on the wall ( $y = 0$ ) denoted  $D$  is the detachment point after classical definition ( $x = 382 \text{ mm}$ ).

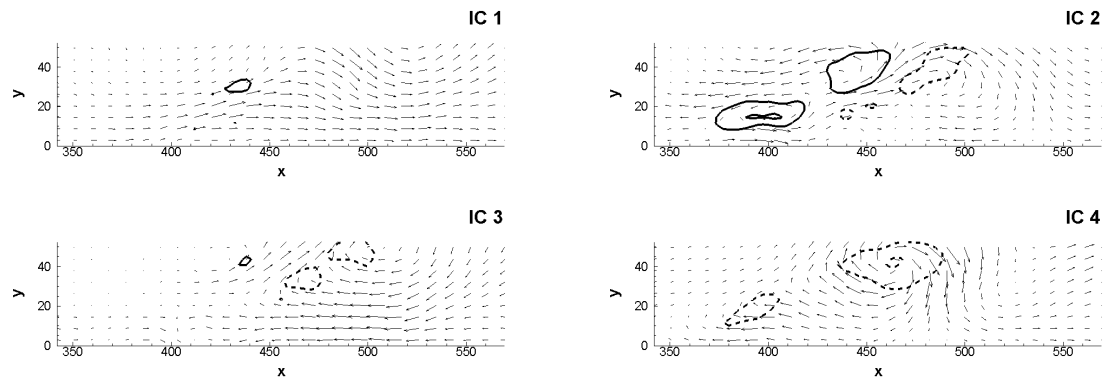
### 4. Results

The POD modes have been evaluated both in spatial (topoi) and temporal (chronoses) domains. In the analysis we will consider the 10 most energetic modes covering 65 % of total fluctuating energy. Thus we treat the flow-field as a dynamical system with 10 degrees of freedom. The first 10 topoi are depicted in Fig. 2 as vector fields with vorticity isolines (negative vorticity is dashed line).



*Fig. 2: The first 10 toposes.*

We could observe the systems of vortical structures in proximity of the  $l_0$  line. Than the ICA has been applied on the 10 chronoses, the implementation using matrix pencil method has been chosen. This method consists in two steps. In first step the time series is filtered by a selected FIR filter and the matrix pencil is formed. Than the general eigenvector of the matrix pencil is calculated. The details of the method are described in Chang et al. (2000). Thus the 10 ICA temporal modes have been constructed as recombination of the original POD modes. Unlike the POD modes, the ICA modes are really statistically independent. Then the corresponding topological ICA modes were evaluated – see Fig. 2.



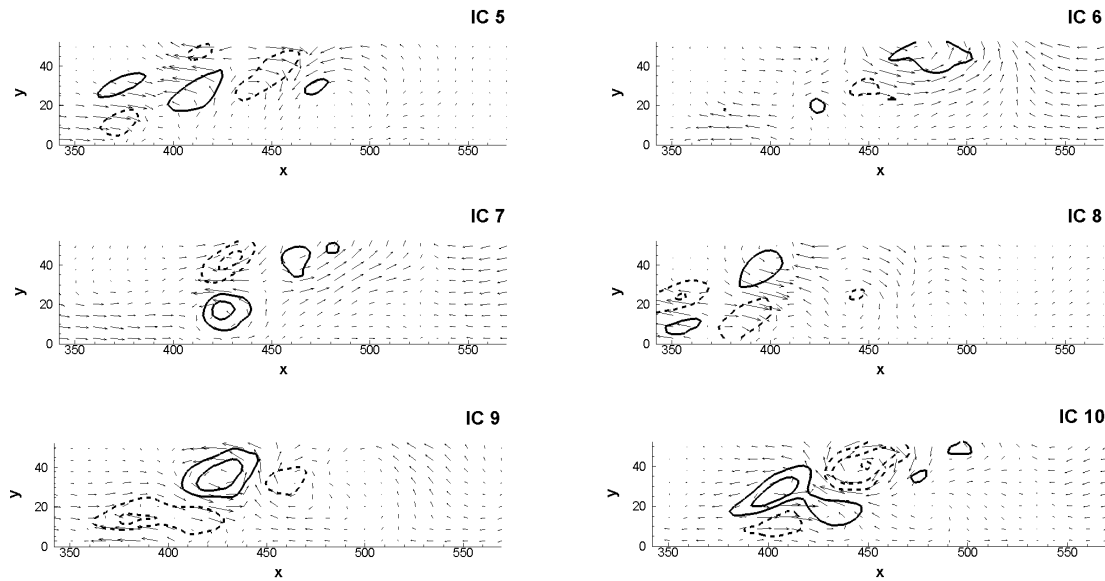


*Fig. 3: The first 10 independent modes.*

Comparing the Figs. 2 and 3 it is clear that the ICA modes are of a different structure than the POD modes however they consist of vortical structures close to  $l_0$  as well. The ICA modes better represent the dynamical behavior of the underlying dynamical system. However the 10 ICA modes cover only 40 % of the total fluctuating energy (the 10 POD modes cover 65 %).

## 5. Conclusions

Both temporal and topological independent modes of the dynamical system represented by time dependent vector fields were evaluated by consecutive application of the POD and ICA methods. The evaluated modes could be used for detailed study of the dynamical system properties as they have clear physical meaning and interpretation.

## Acknowledgement

This work has been supported by the Grant Agency of the Czech Republic, projects Nos. 101/08/1112 and P101/10/1230.

## References

- Chang, C., Ding, Z., Yau, S.F. & Chan, F.H.Y. (2000) A Matrix-Pencil Approach to Blind Source Separation of Colored Nonstationary Signals, IEEE Transaction on Signal Processing, vol. 48, No. 3, pp. 900-907.
- Hyvarinen, A. & Oja, E. (2000) Independent Component Analysis: Algorithms and Applications, Neural Networks, vol. 13, No. 4-5, pp. 411-430.
- Hyvarinen, A., Karhunen, J. & Oja, E. (2001) Independent Component Analysis, John Wiley & Sons.
- Uruba, V. (2008) Boundary Layer Separation Dynamics, In: Conference Topical Problems of Fluid Mechanics 2008, Praha, ÚT AV ČR, v.v.i., (J.Příhoda, K.Kozel eds.), pp. 125-128.
- Uruba, V. (2009) Dynamics of a Boundary Layer Separation. In: 14th CMFF 09, University of Technology and Economics, Budapest, (Ed.:Vad, J.), pp. 268-275.
- Uruba, V. (2010) Independent Component Analysis for Identification of Coherent Structures, In: 24<sup>th</sup> Symposium on Anemometry (Z.Chára & L.Klaboch eds.), pp. 1-6.

## STRESS-STRAIN ANALYSIS OF RESTORED FIRST MOLAR WITH CAVITY OF CLASS I.

J. Valášek\*, P. Marcián\*, D. Krpalek\*, K. Řehák\*, F. Manek\*, Z. Florian\*

**Abstract:** *The presented paper is focused on the stress – strain analysis of the restored tooth. From the reason of general geometry, complex material properties and boundary conditions a computational modeling was chosen. For this problem finite element method (FEM) was used. Solved system is focused on the first lower molar where dental caries is modeled and on its subsequent treatment with restoration. The tooth, which is modeled from the dentin and enamel, is established in the segment of the mandible. The tooth with cavity class I. (according to Black) is modeled in this work. The size of dental cavity is considered in three sizes, depending on the range of dental caries. For restoration of tooth, filling materials were used. These materials are commonly used in dental practice. Force was prescribed at the occlusal surface of tooth. The model of physiological tooth was created for comparison of stress - strain states on the restored tooth. The analysis of the results shows that amalgam is the best material for tooth restoration in molar segment.*

**Keywords:** *Save tooth, molar tooth, finite element method, amalgam, composite resin.*

### 1. Introduction

Currently there are only few people who can boast with healthy teeth without any intervention by a physician. Teeth are an integral part of the oral cavity and each person uses them several times a day for receiving and processing food. Important role of the teeth is their irreplaceable place in the overall appearance of person. In the case of the extensive damage or even loss of the tooth is appropriate to insert a dental implant (Borák, L., et al, Marcián, P., et al, 2010). For these reasons it is very important to take care of teeth and mouth and keep them in good condition. Although the teeth consist of the most resistant and hardest material in the human body, the tooth can be damaged by the mechanical, chemical and biological processes. The most common damage of the dental tissues is dental caries (Fontana, M., et al., 2010). The area of treatment of the dental caries is concerned with restorative dentistry. Tooth decay is removed by dental instruments and a new vacant place is ready for the application of the filling material. This procedure is called tooth restoration. Well executed restoration of the tooth helps to prevent further spread of dental decay and it maintains the basic function of teeth like separating and crushing food. In this activity the teeth are significantly mechanically loaded. Restoration of the teeth significantly changes coherence and mechanical properties of impaired dental tissue, which also affects the deformation and stress of loaded tooth. For saved tooth there is a sudden change in stiffness resulting in stress concentrations and it may cause undesirable break of the loaded tooth. Determination of stress and strain at the physiological and saved tooth is a problem due to the complex geometry, material properties, location, and last but not least, the boundary condition of the tooth. This problem can be effectively solved by computational modeling.

### 2. Material and methods

The finite element method (FEM) was chosen for solving of this problem. It is the most frequently used numerical method. It is possible to create a computational model on a high level using the advanced computing systems. For the solved system the FEM program ANSYS was used. To obtain

---

\* Ing. Jiří Valášek, Ing. Petr Marcián, Ing. David Krpalek, Ing. Kamil Řehák, Ing. Filip Manek and Ing. Zdeněk Florian, CSc.: Institute of Solid Mechanics, Mechatronics and Biomechanics, Faculty of Mechanical Engineering, Technická 2896/2; 616 69, Brno; CZ, e-mails: yvalas05@stud.fme.vutbr.cz, ymarci00@stud.fme.vutbr.cz, ykrpal00@stud.fme.vutbr.cz, yrehak04@stud.fme.vutbr.cz, ymanek00@stud.fme.vutbr.cz, florian@fme.vutbr.cz



the computational model it is necessary to create sub-models. These are a model of geometry, materials, loads and model of boundary condition.

The models of geometry which occur in biomechanics have generally complex shapes (Fig. 1). The creation of these models at a high level is difficult for software and hardware. To obtain the high quality models of geometry there are two possible approaches. One approach is based on technologies and methods of rapid prototyping. It means that a solved system is scanned by 3D scanner. The second method to obtain a high level model of geometry is use of modern imaging techniques like Magnetic resonance (MRI) and Computer tomography (CT) where the model of geometry is based on CT images (Valášek, J., et al, 2010). The first approach was used for this work. The tooth is composed of several layers and each of them has different mechanical and material properties. Due to the interaction between tooth and dental filling, the tooth was divided into two layers on the enamel and dentin. It was necessary to create the model of geometry of tooth cavity. The model of dental cavity was made in three sizes, which represents the different ranges of dental caries. For completeness of the solved problem the models of geometry for cortical and cancellous bone were created.

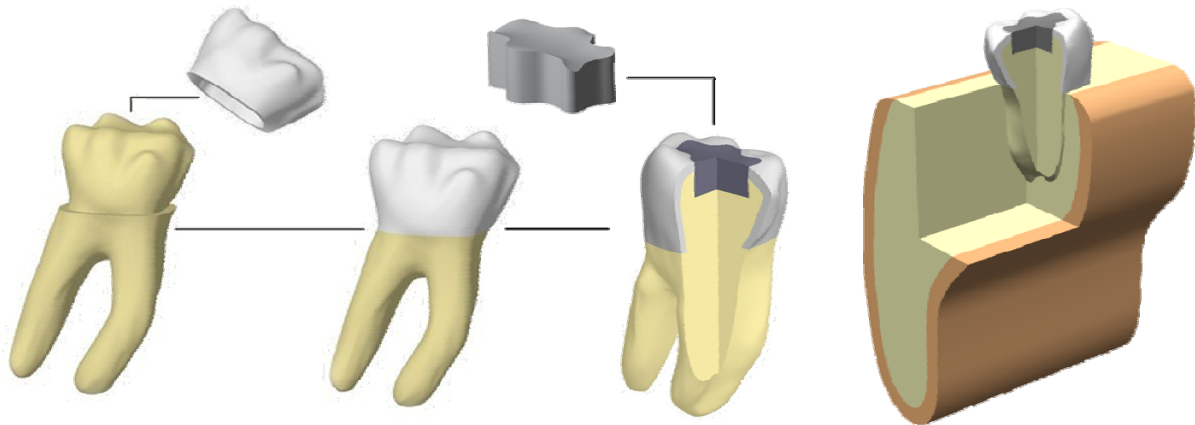


*Fig. 1: Parts of solved system.*

In the solved systems which occur in biomechanics, there is interaction between living tissues (bone, muscle, dental tissue) and technical materials (titanium implants or fixation, dental filling material). The material properties of technical materials are well known but obtaining the material properties of real objects occurring in biomechanics is a difficult problem. In terms of the level of the solved problem, the appropriate and validated model of mechanical properties is a homogenous, isotropic and linear elastic model, which is explicitly described by two material characteristics: Young's modulus  $E$  [MPa] and Poisson's ratio  $\mu$  [-]. Model of material was created for each part of the solved system. Used material characteristics are shown in Tab. 1.

During mastication, the tooth is loaded in a general direction and force directed into the occlusal plane. After a decomposition of the general loading to the coronapical (CP), buccolingual (BL) and mesiodistal (ML) directions, the dominant component is in the coronapical direction. It is direct to the occlusal surface of the tooth. The study is considering a dominant load of 200 N, which is usually reached in the molar section. The load of the solved system was obtained from the study (Curtis, D.A., et al., (1999).

The computational model is necessary to clearly defined in a space. For the solved system boundary conditions were prescribed for the cortical and cancellous bone. On the edge of the cortical and cancellous bone were prescribed prohibitions displacements in all directions. The connection between organic tissues (enamel, dentin, cortical and cancellous bone) were modeled like solid connections (elements have shared nodes). The boundary conditions between the dental tissue and the dental filling were modeled with contact pair where friction was prescribed. The discretization was created hexahedral and tetrahedral elements with quadratic approximation (SOLID 186) and a pair of contact elements (TARGE 170 and CONTA 174). Maximum attention was paid to the meshing and the number of elements was within 200 thousand.

Tab. 1: Material properties for solved system.

Model of material	$E$ [MPa]	$\mu$ [-]	Literature
Enamel	80 000	0.3	(Gei, M., et al., 2002)
Dentin	20 000	0.3	(Gei, M., et al., 2002)
Cortical bone	13 700	0.3	(Carter, D., et al., 1987)
Cancelous bone	1 370	0.3	(Bratu, E., et al., 2003)
Amalgam	15 870	0.3	(Beatty, M.W., 1993)
Composite resin	6 260	0.3	(Beatty, M.W., 1993)
Glassionomer cement	3 000	0.3	(Beatty, M.W., 1993)

### 3. Results

To assess the mechanical interaction between filling material and tooth tissue, especially enamel, 9 variants of computational model were created. Individual variants differed in modeled size of dental caries and various filling materials used for restoration of the tooth. Distribution of stress and strain in restored tooth were compared with these distribution in healthy tooth. On closer study of distributions of stress and strain for individual dental tissues it was found that enamel is the most affected tissue by restoration. For this reason an analysis will be focused to the enamel. The first analysis was done for parameter of the effect of size of the dental decay. The first picture from left is a model of the healthy tooth. Towards the right the results for different sizes of tooth cavity are plotted. The equivalent stress reached value  $\sigma_{\text{HMH}} = 9.5$  MPa for the healthy tooth on the occlusal surface. The maximum value  $\sigma_{\text{HMH}} = 15.5$  MPa is reached on transition between enamel and dentin. Fig. 2 shows that if the contour of cavity reaches a place between the dental bumps, the concentration of stress may occur. The maximum value  $\sigma_{\text{HMH}}^{(3)} = 43$  MPa is achieved at cavity size 3 on the mesial wall. In the case of cavity sizes 1 and 2 the equivalent stress reached the values  $\sigma_{\text{HMH}}^{(1)} = 20.9$  MPa and  $\sigma_{\text{HMH}}^{(2)} = 23.8$  MPa on the contour of cavity in distal direction. The maximum value of equivalent stress is  $\sigma_{\text{HMH}}^{(2)} = 53$  MPa and it is reached on transition between enamel and dentin. This value is caused by influence of geometry of solved system especially crossing between dentin and enamel.

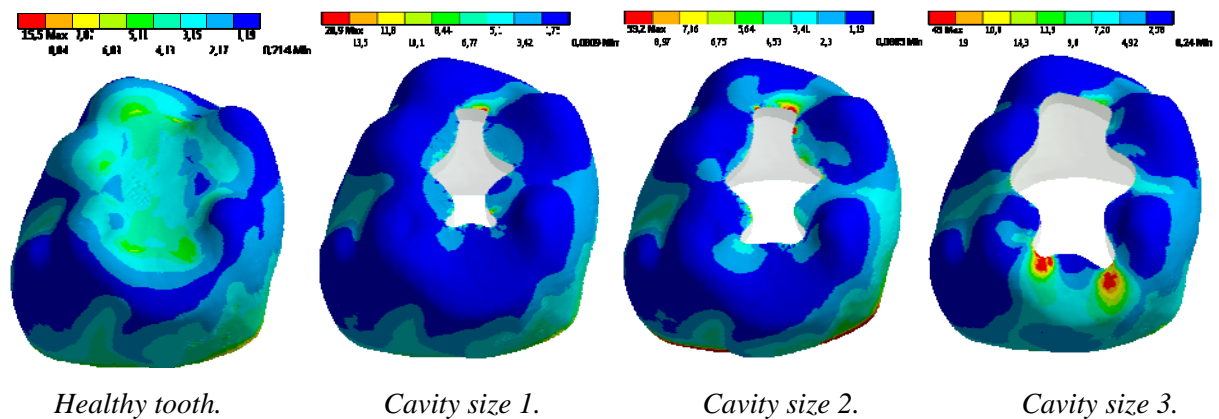


Fig. 2: Equivalent stress for enamel with amalgam filling.

The next analysis was focused on the influence of dental filling materials onto the distribution of stress and strain in the dental tissue. For every filling material the equivalent stress was observed for the enamel and dentin. The values of equivalent stress were plotted in Fig. 3. The graph shows that an amalgam was used as a filling material for the specific cavity class, the values of equivalent stress are the lowest. For other filling materials the values of equivalent stress rise.

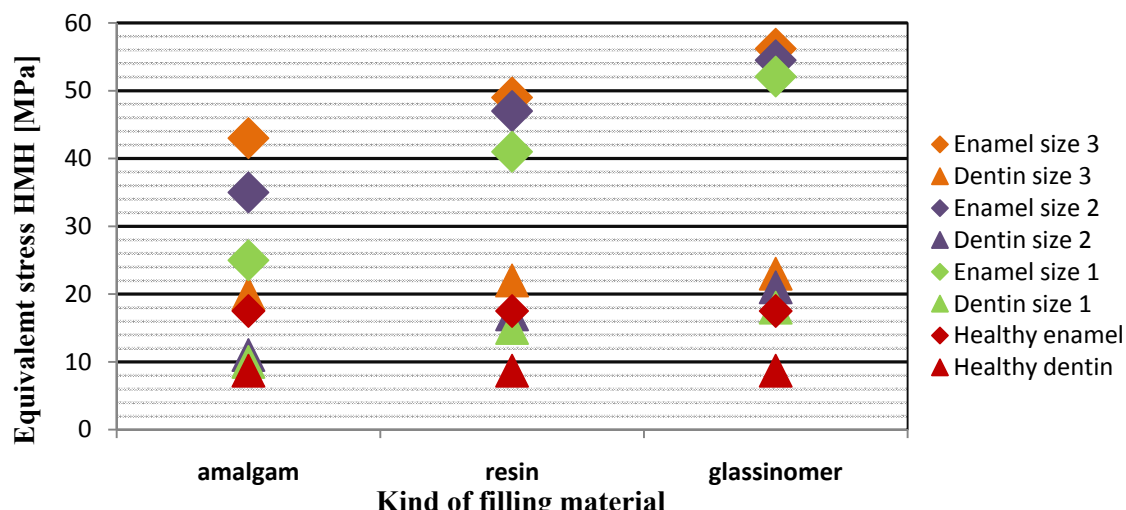


Fig. 3: Equivalent stress in enamel and dentin for different cavity size.

#### 4. Conclusion

The presented biomechanical study was focused on stress-strain analysis of the restored first molar tooth with three sizes of dental caries. Three different types of filling materials were used for restoration. The values of equivalent stress were evaluated for solved problem. The analysis of the influence of the different tooth cavity sizes shows that if a tooth decay is large and newly created cavity reached the places between the dental bumps, there is a place where the stress concentrations may occur. These places are dangerous with considering of the high values of equivalent stress for beginning of the crack. This behavior is reflected in clinical practice, which confirmed the results of this study. The next influence that was analyzed was the influence of filling material. The analysis shows that due to the large masticatory forces for restored tooth in a molar section amalgam should be used as a filling material.

#### Acknowledgement

This work was supported by grant project FRVS No. 2829/2011 and specific research FSI-J-11-3.

#### References

- Marcián, P., et al. (2010) Biomechanical Study of Disk Implants Part II. Engineering Mechanics, vol. 17, no. 2, ISSN: 1802- 1484, pp. 111-121.
- Valášek, J., et al. (2010) Material Properties of Bone Tissue Obtained from CT for Biomechanics Purposes, In MENDEL 2010, Mendel Journal series, Brno: BUT FME Brno, ISBN: 978-80-214-4120- 0, ISSN: 1803-3814, pp. 483-490.
- Borák, L., et al. (2010) Biomechanical Study of Disk Implants Part I, Engineering Mechanics, vol. 17, no. 2, ISSN: 1802- 1484, pp. 49-60.
- Gei, M., et al. (2002) An inter-face model for the periodontal ligament, Journal of Biomechanical Engineering, Vol. 124, No. 5, pp. 538-546.
- Carter, D., et al. (1987) Mechanical properties and composition of cortical bone, Clinical Orthopaedics and Related Research, vol.135, pp. 733-741
- Bratu, E., et al. (2003) Analyse der strukturalen Spannungen zwischen Implantat und Knochen, Implantologie, vol. 7, pp. 47-49.
- Curtis, D.A., et al. (1999) Modeling of jaw biomechanics in the reconstructed mandibulectomy patient, The Journal of Prosthetic Dentistry, vol. 81, issue 2, pp. 167-173.
- Fontana, M., et al. (2010) Defining Dental Caries for 2010 and Beyond, Dental Clinics of North America, vol. 4, issue 3, pp. 423 - 440
- Beatty, M.W. (1993) Elastic and fracture properties of dental direct filling materials, Biomaterials, vol. 14, issue 13, pp. 999 - 1002

## TUNING OF SHOCK ABSORBERS ON VEHICLE

R. Valášek\*

**Abstract:** *The article deals with the tuning of shock absorbers for trucks on a vehicle, and with data collection for later laboratory testing. The used measuring technology is described, too.*

**Keywords:** *Shock absorber, tuning, testing, devetron.*

### 1. Introduction

Stability of a moving vehicle on the road is influenced by many factors. Weight distribution, speed, road situation and wind are the factors determining the behaviour of a vehicle on the road. Some of these variables can be controlled or changed, determining the way of a vehicle behaviour. If we need to keep control over vehicle stability and its comfort, the undercarriage, suspension springs and especially shock absorbers must be tuned in a way to keep the wheels in a continuous contact with the road, maintaining the vehicle crew's comfort and favourable conditions for the truck load transport.

Shock absorbers tuning is a complex issue and requires extensive experience and good knowledge of the hydraulic shock absorbers functioning principles. Moreover, such tuning is time consuming and financially demanding process, regarding the need to drive a great number of test kilometers, measuring device installation and, last but not least, a multiplied assembly and disassembly of the absorbers and their re-setting. The danger of displacement sensors and accelerometers present a great risk, not speaking about the damaging of the measuring central and accessories in the proper testing. These components are very expensive.

The testing I participated and described in this article was carried out in October 2010 at company Paccar in Leyland, England. Undercarriage tuning for the new version DAF LF class 3 (N3) was in question.

### 2. Setting of shock absorbers

Comfort and safety are judged according to the proper vehicle oscillation frequency. A subjectively comfortable, periodically repeated motion of a person (rocking, swinging, oscillating,...) is a motion with its frequency close to human heart frequency or to that of a comfortable human walk. This is the frequency  $f_0 = 60 \text{ min}^{-1} = 1 \text{ Hz}$ . The proper vehicle suspension frequency  $\omega_0$  corresponds to the following equation

$$\omega_0 = 2\pi \cdot f_0 = \sqrt{k/m} = 2\pi \text{ (s}^{-1}\text{)} \quad (1)$$

where  $m$  is the vehicle weight component over the suspension unit and  $k$  is the suspension unit rigidity. Mechanical springs mostly have fixed rigidity and linear characteristics. Pneumatic springs have variable rigidity, growing with the increased load according to a non-linear (hyperbolic) characteristics. A higher proper frequency corresponds to a higher suspension rigidity, resulting in a more aggressive driver's behaviour and contributing to a sport-like character of the driving (bends can be negotiated at a higher speed), being inconsiderate to the transported load.

Soft suspension with a lower proper frequency makes the driver sleep, creating the feeling of higher comfort for the co-travelers and being considerate to the transported load. Shock absorbers have to be in line with the suspension.

---

\* Ing. Radek Valášek: Jan Perner Transport Faculty, University of Pardubice, Studentská 95; 532 10, Pardubice 2; CZ, e-mail: radek.valasek@gmail.com

Providing that a shock absorber is tuned softly, that is with a small resistance against the motion, the whole system would oscillate, adhesion between the tire and road surface would get lost and the vehicle would be difficult to maneuver and control. On contrary, if a shock absorber is tuned hard, that is with a high resistance to the motion, the drive is not comfortable for the crew, and the load is in danger. Last but not least, the vehicle can be damaged, e.g. in running over a road pothole.

Attenuation forces setup is carried out by the change in the assembly of valve (Fig. 1, positions 3 and 6), or using disc springs (Fig. 2, position 9), which is more suitable for large trucks. The setup is performed on a shock absorber piston for the making of extension attenuation forces or on a suction valve (Fig. 3, position 6) for the making of compressive attenuation forces. Another factor affecting the attenuation forces is the size of used supports (Fig. 1, positions 2 and 7) at the power plotting boards on the shock absorber piston. For the proper function of a shock absorber it is important that the attenuation at the extension is about 10 times higher than that of compression.



*Fig. 1: Piston assembly.*

1) piston rod, 2) stay, 3) over piston foil, 4) piston, 5) permanent flow foil, 6) under piston foils, 7) assembly of stay, 8) nut, 9) piston ring.

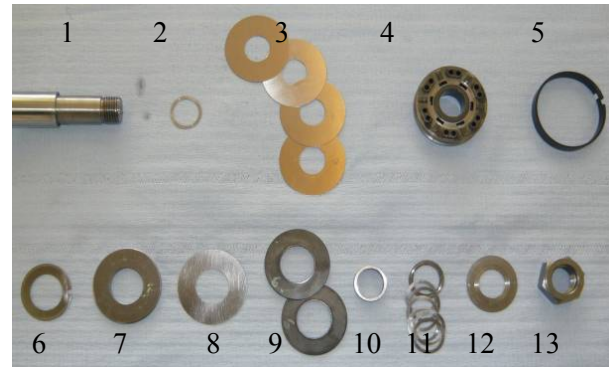


*Fig. 2: Assembly of a disc springs piston.*

1) piston rod, 2) stay, 3) over piston foil, 4) piston, 5) piston ring, 6) permanent flow foil, 7) board, 8) sliding bearing, 9) disc springs, 10) cervix, 11) distance stay, 12) stay, 13) nut.

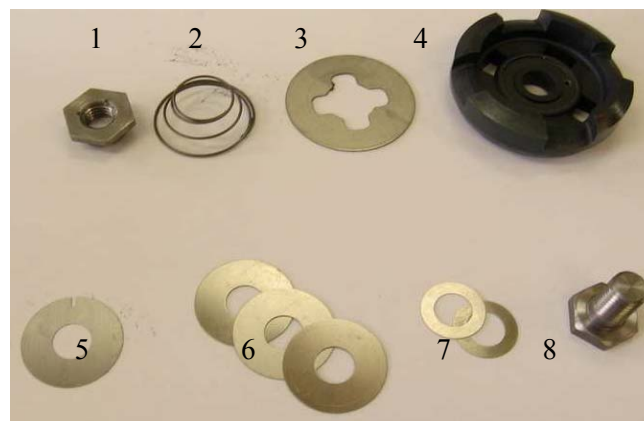


*Fig. 3: Base valve assembly.*

1) nut, 2) spring of reverse valve, 3) reverse valve, 4) base valve, 5) permanent flow foil, 6) assembly of foil of base valve, 7) assembly of stay, 8) screw.

### 3. Shock absorbers setting and testing on a vehicle

Telescopic shock absorbers were tuned for truck DAF LF class 3 (N3). The main reason was the setting of attenuation forces for a new front absorbers concept for the vehicle. The truck was equipped with a measuring centre by Devetron, model 501 with an external touch-screen (Fig. 4) and DEWESoft 7.0.1 RC3 software. In parallel with the telescopic shock absorber a displacement sensor was installed on the front axle, with a measuring range of 500 mm (Fig. 5) and on the rear axle with the range of



300 mm. The vehicle was further equipped with four electric meters, one at each side for unsuspended material (Fig. 6) and one for suspended material was located at the vehicle frame over the axle.



*Fig. 4: Measuring equipment.*



*Fig. 5: Displacement sensor.*

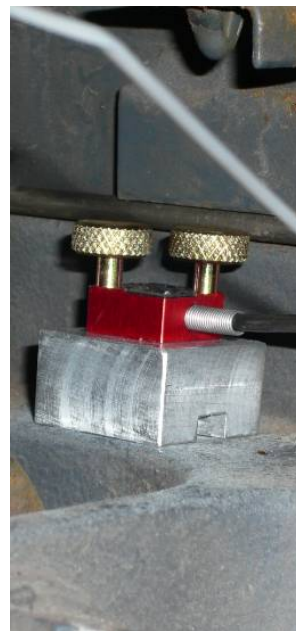


*Fig. 6: Accelerometer.*

The vehicle ran through the pre-determined route of roughly 30 miles (about 48 km), while recording the data from individual sensors. The testing route was divided into several sections: an urban section with a low-quality surface (potholes, wavy road) and a speed section where the vehicle kept reaching a maximum construction speeds. After driving through the indicated section, the current shock absorbers setting data collected by the test driver and his feelings of the vehicle behaviour were recorded. Data was saved in digital format without breakeven as d7d file, which is special file of Dewetron company. Consequently, the data collected were compared with the measured data (Fig. 7).

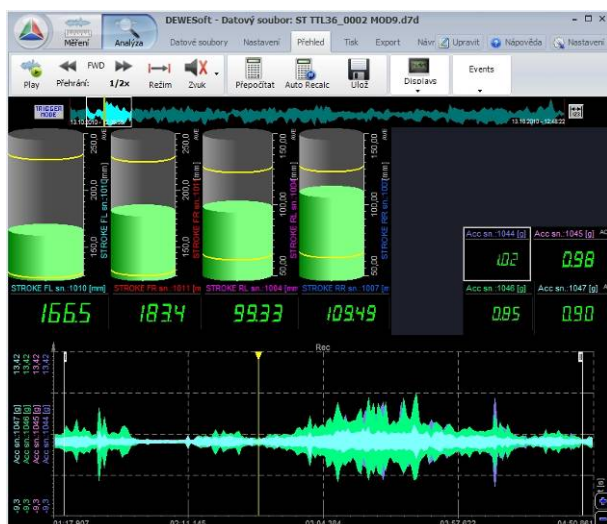


Fig. 7: Measured values in Devesoft.

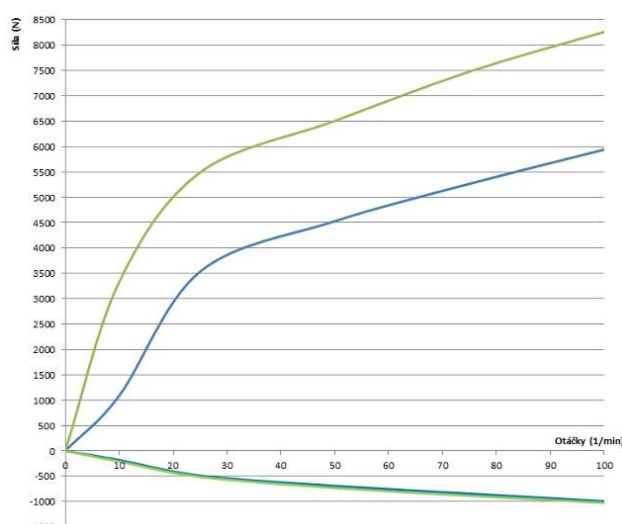


Fig. 8: Setting limits of shock absorbers.

Minimum and maximum attenuation values were calculated before the proper testing and then verified by the test drives (Fig. 8). After each test drive and the measured data analysis, the shock absorbers were removed from the vehicle, disassembled, re-tuned and re-installed for the next testing.

This procedure was repeated until the required tuning and the best compromise between the driving properties of an empty and fully loaded vehicle were achieved. In this event, the shock absorbers have been disassembled, re-tuned and re-installed about forty times.

All the data collected from all the measuring outcomes were thoroughly filed by reason of laboratory measuring and for working-life testing of a shock absorber.

#### 4. Conclusions

The above indicated shock absorber testing and tuning presents only a rough description of the problem. Despite shock absorbers seem to be a simple topic at first sight, in fact it is a complex issue requiring extensive theoretical and practical experience and expensive background with different testing situations, prototype workshop and other facilities.

At present, the new trends in the field encounter the controlled type of shock absorbers even at trucks and trailers. Company BRANO a.s. proceeds this way, concentrating on several different systems of telescopic shock absorbers control systems.

#### Acknowledgement

I would like to express my gratitude to my employer, company BRANO a.s. for their effort in enabling me to participate in the testing and tuning of shock absorbers.



## INFLUENCE OF SURFACE DENTS ON ELASTOHYDRODYNAMIC AND MIXED LUBRICATION

M. Vaverka<sup>\*</sup>, L. Zapletal<sup>\*</sup>, O. Šamánek<sup>\*</sup> M. Vrbka<sup>\*</sup>

**Abstract:** Machine parts with non-conformal contact surfaces frequently operate in elastohydrodynamic or mixed regime of lubrication. In surroundings of asperities significant changes in lubricant film thickness and also contact pressure occur, which can lead to failure. The article deals with the influence of surface dents on film thickness, contact pressure and rolling contact fatigue. These quantities are important for machine design in terms of failure (pitting and scuffing). Lubricant film thickness is measured by thin film colorimetric interferometry (TCFI) and contact pressure is calculated using inverse elasticity theory enhanced by convolution algorithms. Rolling contact fatigue tests show that it is possible to design surface textures of suitable layout of microdents which can have positive effect on lubrication and rolling contact fatigue life.

**Keywords:** Elastohydrodynamic lubrication, EHL, surfaces, roughness, contact pressure, asperities, dents, contact fatigue.

### 1. Introduction

Many machine parts with non-conformal friction surfaces operate in elastohydrodynamic or mixed lubrication regime. Asperities on real friction surfaces cause changes of lubricant film thickness and contact pressure distribution in the vicinity (Kaneta et al., 1980; Luo et al., 2001; Choo et al., 2003; Cann et al., 2005). These changes can lead to failure like lubrication film rupture, pitting or scuffing. Surface asperities can be created unwillingly from technological process or from particles of wear, from foreign particles in oil etc. On the other hand, asperities can be created purposely by mechanical way (shot peening, indentation) or by laser surface texturing (LST) in order to improve tribological performances. Dents within surface texture can act like reservoir of lubricant (Hartl et al., 2004) in starvation phase of lubrication. These dents can also modify friction between surfaces and it is believed that they can have positive effect on rolling contact fatigue. The behavior of surface asperities in lubricated contact, their positive or negative influences and suitable arrangement of dents in surface texture is still discussed (Guangteng et al., 2000; Vrbka et al., 2010). The change of real asperities in contact is based on roughness attenuation (Venner et al., 2005; Šperka et al., 2009).

### 2. Objective

The aim is to study the influence of dents on lubrication film, contact pressure distribution, and rolling contact fatigue (RCF). The knowledge of the influence of dents on tribological quantities will be important for design of suitable surface texture which can prolong contact fatigue life.

### 3. Methods

The experimental study of real rough surface attenuation requires the evaluation of both the undeformed surface roughness and lubrication film thickness. Lubrication film thickness that carries the information about in-contact deformation is measured using an optical test rig. Thin film colorimetric interferometry (TCFI) was used for film thickness measurement. This technique (Hartl, 2004) is based upon colorimetric analysis of chromatic interferograms (Fig. 1) using appropriate

---

<sup>\*</sup> Ing. Michal Vaverka, Ph.D., Ing. Lukáš Zapletal, Ing. Otakar Šamánek, Ph.D. and Ing. Michal Vrbka, Ph.D.: Institute of Machine and Industrial Design, FME Brno University of Technology, Technická 2896/2; 616 69, Brno; CZ, e-mails: vaverka@fme.vutbr.cz, lukaszapletal@atlas.cz, ysaman02@stud.fme.vutbr.cz, vrbka.m@fme.vutbr.cz

colour matching algorithm and colour-film thickness calibration. Based on previously obtained results it is believed that the film thickness resolution is approximately 1 nm. Operating conditons are described in Tab. 1. The contact is realized between steel ball and glass disc.

Contact pressure is in relation with deformation of friction surfaces, which can be derived from experimentally evaluated film thickness. Determination of contact pressure from surface deformations is an inverse problem based on the elasticity theory (Vaverka et al., 2008). The force balance condition must be included into the system of equations.

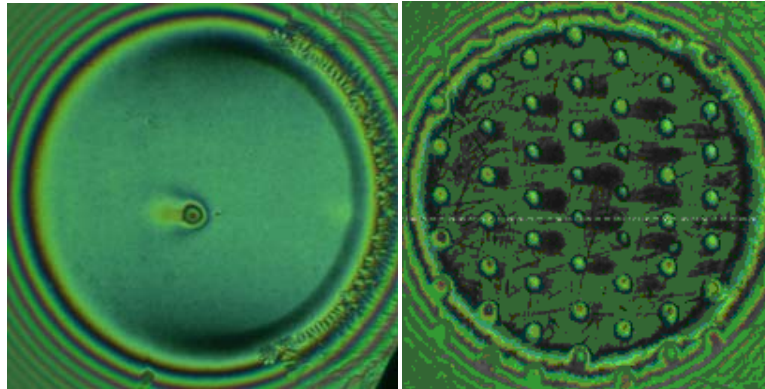


Fig. 1: Interferogram of surface with single dent (on the left), surface texture (on the right).

A mechanical Rockwell C type indenter has been used for indentation of specimen surface. Indentation process is fully controlled by PC, so it allows us to create accurately desired surface textures. The design of selected surface textures is in Tab. 2. Two types of arrangements of dents are depicted in Fig. 2. The aim was to find suitable surface texture, which prolong RCF life of a test specimen. Rolling contact fatigue tests was conducted on R-mat device. Cylindrical specimen is in contact with steel disc. Rolling-sliding conditions were applied during experiments (rolling-sliding ratio is 0.05). These vibrations had been monitored during experiments. When failure was observed, measurement was automatically stopped.

Tab. 1: Basic data decribing operating conditions.

Load $F$	29 N
Pressure viscosity coefficient $a$	23 GPa <sup>-1</sup>
Dynamic viscosity $\eta$	0.421 Pa·s
Radius of the ball $R$	12.7 mm
Reduced modulus of elasticity $E_r$	313.7 GPa

Tab. 2: Layout of dents in surface textures.

Texture designation	Arrangement of dents	Distance in the direction of rolling	Distance perpendicular to the direction of rolling	Depth of dents
<b>T0</b>	Smooth surface without dents (RMS =0.04 after polishing)			
<b>T1</b>	Triangular	150 $\mu$ m	75 $\mu$ m	0.6 mm
<b>T2</b>	Triangular	150 $\mu$ m	75 $\mu$ m	1.45 mm
<b>T3</b>	Triangular	75 $\mu$ m	75 $\mu$ m	0.6 mm
<b>T4</b>	Square	75 $\mu$ m	75 $\mu$ m	0.6 mm

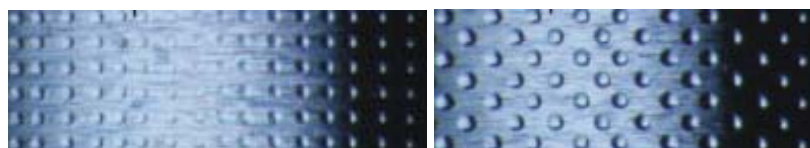


Fig. 2: Layout of surface textures with square (on the left) and triangular arrangement (on the right).

#### 4. Results

Chromatic interferograms (Fig. 1) were obtained from experiment using optical test rig. Contact pressure was calculated using the inverse elasticity theory. This calculation is very time consuming, hence it is enhanced by convolution algorithm. Fig. 3 shows changes in lubricant film thickness and contact pressure distribution on the area with single dent (depth of dent is 360 nm, slide to roll ratio is 0.45). It is evident that lubricant deforms the surface in the vicinity of dent.

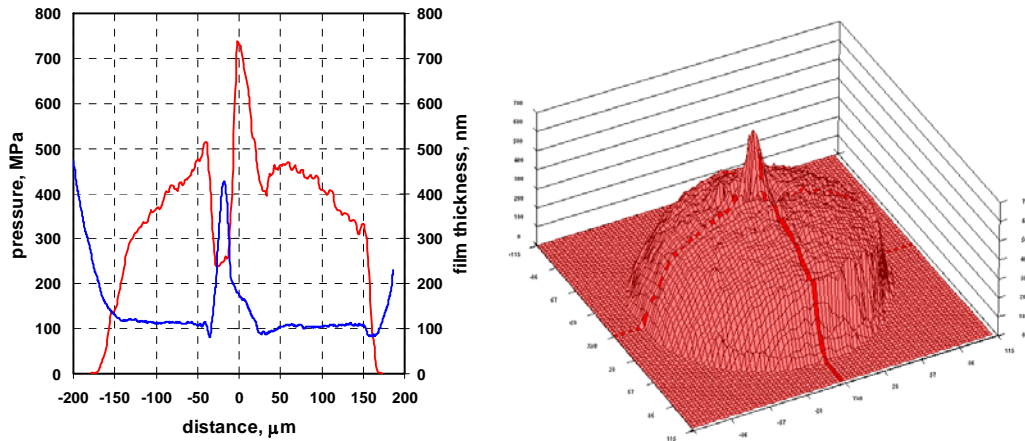


Fig. 3: Influence of dent on lubricant film thickness (blue) and contact pressure (red).

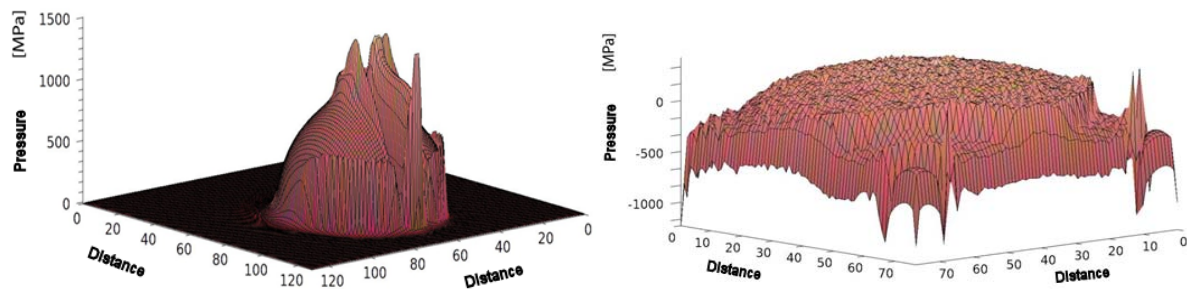


Fig. 4: Contact pressure distribution with single dent (on the left) and with real asperities including cavitation (on the right).

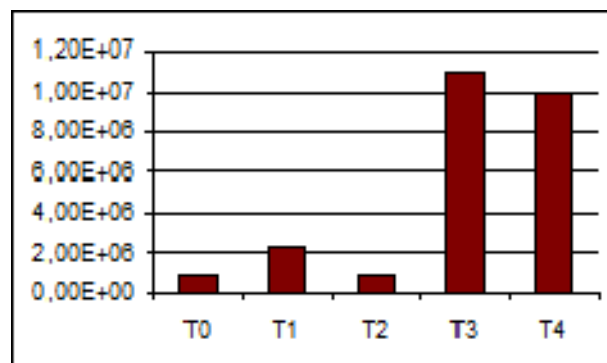


Fig. 5: Interferogram of surface texture (on the left), fatigue life of individual surface textures in cycles to failure (on the right).

The contact pressure distribution on the domain with single dent (depth is 700 nm) is in Fig. 4 on the left. The algorithm for calculation of contact pressure is very sensitive on the purity of input data, cavitation in the outlet cause contamination of input values of lubricant film thickness (Fig. 4 on the right). Fig. 5 shows the contact fatigue life in cycles obtained from RCF test of individual surface textures T1, T2, T3, and T4 in comparison with specimen having smooth surface (T0). The influence of dents arrangement on RCF was not observed. Depth and density of dents can have positive influence on fatigue life (textures T3 and T4). Example of failure is in Fig. 6.



*Fig. 6: Example of failure.*

## 5. Conclusions

The results show that shallow dents can have positive effect on lubrication and rolling contact fatigue, nevertheless it is suitable to make further experiments and calculations with big amount of samples under variety of operating conditions. It is assumed that local increases of mixed lubrication film thickness have positive influence on contact fatigue life. Presence of a texture on a friction surface can also lead to local hardening of the surface. In the future we would like to use method of pressure attenuation (Hooke, 2006) to study contact pressure distribution in more detail.

## Acknowledgement

This article and research was supported by Czech Science Foundation, grant no. GP 101/09/P427.

## References

- Cann, P. M., Spikes, H.A. (2005) Measurement of Pressure Distribution in EHL-Development of Method and Application to Dry Static Contacts. *Tribology Trans.* 48, 2005, pp 474-483.
- Kaneta, M. Cameron, A. (1980) Effects of Asperities in Elastohydrodynamic Lubrication, *ASME J. Lubr. Tech.*, 102, 3, pp 374-379.
- Choo, J.W., Glovnea, R.P., Olver, A.V. and Spikes, H. A. (2003) The Effects of Threedimensional Model Surface Roughness Features on Lubricant Film Thickness in EHL Contacts, *Journal of Tribology, Trans. of the ASME*, 125, 3, pp 533-542.
- Guangteng, G., Cann, P.M., Olver, A.V. Spikes, H.A. (2000), Lubricant Film Thickness in Rough Surface, Mixed Elastohydrodynamic Contact, *ASME J. Tribol.*, 122, 1, pp 65-76.
- Hartl, M., Křupka, I., Liška, M., Fuis, V. (2004) Experimental Study of Lubricant Film Thickness Behavior in the Vicinity of Real Asperities Passing through Lubricated Contact, *Tribology Transactions*, 47, 2004, pp. 376-385.
- Hooke C.J. (2006) Roughness Attenuation And Pressure Rippling in EHL Contacts, R.W. Snidle and H.P. Evans (eds), *IUTAM Symposium on Elastohydrodynamics and Microelastohydrodynamics, IUTAM Symposium on Elastohydrodynamics and Micro-elastohydrodynamics Solid Mechanics and Its Applications*, Springer 2006, Vol. 134, Part 10, 411-422.
- Šperka, P., Křupka, I., Hartl, M. (2009) Experimental study of real roughness attenuation in concentrated contacts. *Tribology International*, doi:10.1016/j.triboint.2009.11.003.
- Vaverka, M.; Vrbka, M.; Poliščuk, R.; Křupka, I.; Hartl, M. (2008) Numerical Evaluation of Pressure from Experimentally Measured Film Thickness in EHL Point Contact, *Lubrication Science*, Vol.20, No.1, ISSN 0954-0075, John Wiley & Sons, Ltd. pp. 47-59.
- Vrbka, M., Šamánek O., Šperka, P., Návrát, T. Křupka I. Hartl M. (2010) Effect of surface texturing on rolling contact fatigue within mixed lubricated non-conformal rolling/sliding contacts. *Tribology International* Vol. 43, Issue 8, August 2010, pp. 1457-1465.
- Venner CH, Lubrecht AA.(2005) An engineering tool for the quantitative prediction of general roughness deformation in EHL contacts based on harmonic waviness attenuation. *Proc Instn Mech Eng Part J J Eng Tribol* 2005;219: 303–312.

## CONCURRENT MAPPING AND LOCALIZATION BASED ON POTENTIAL FIELDS

S. Věchet<sup>\*</sup>, J. Krejsa<sup>\*\*</sup>

**Abstract:** *Presented paper deals with Concurrent Mapping and Localization as a method to build the local map for the autonomous mobile robot. Building accurate local map is necessary for the successful navigation through the crowded environment densely populated with dynamic obstacles. The occupancy grid mapping algorithm was used due to the high uncertainty in the measurements of dynamic obstacles. As the occupancy grid algorithm is of probabilistic nature the implementation is straightforward and is also capable to generate the results in real-time.*

**Keywords:** *Occupancy grid mapping, binary Bayes filter.*

### 1. Introduction

Concurrent Mapping and Localization (CML), also known as Simultaneous Localization and Mapping (SLAM) problem belongs to the most complicated tasks in mobile robotics. In some simple cases the autonomous robot could solve only the mapping or localization problem separately. The mapping problem is addressed to the robots for which the location is known and the robots goal is to create a map of its environment (Thrun et al., 2005). On the other hand, the localization problem is usually solved via robot with known map and its goal is to find the path through environment (Lazanas & Latombe, 1995).

When the map and initial position of the robot are unknown, the online CML problem needs to be solved to accomplish the navigation task. The robot has to create online map from sensor readings and simultaneously localize itself in such a map (Deans, 2005).

Presented paper briefly describes CML algorithm based on occupancy grid method, which belongs to the group of probabilistic mapping techniques. The method is used to create a real-time local map of nearby environment of autonomous mobile robot during its movement in crowded space full of dynamic obstacles - moving people. Online generated local map is used to navigate the robot through the environment.

The paper is organized as follows: Chapter 2 describes binary Bayes filter with static state which is the basic principle in Occupancy grid mapping method. The Occupancy grid mapping method is described in chapter 3 and the final results obtained from experiments on mobile robot Advee are shown in chapter 5.

### 2. Binary Bayes filter with static state

Binary Bayes filter with static state is a special case of discrete Bayes filter (Thrun et al., 2005) and is usually presented in log odds form. The static state means that the state does not change in time (in other words: during sensing). In practice, this is the case when the robot is faced to detect some gap in its path. So the robot has to decide based on repetitive sensor readings if the gap is presented or not (binary static state – the presence of the gap does not depends on time).

The algorithm of binary Bayes filter with static state is shown in Tab. 1.

---

<sup>\*</sup> Ing. Stanislav Věchet, Ph.D.: Institute of thermomechanics AS CR, v.v.i., Brno branch, Technická 2, Brno; CZ, e-mail: vechet.s@fme.vutbr.cz

<sup>\*\*</sup> Ing. Jiří Krejsa, Ph.D.: Faculty of Mechanical Engineering, Brno University of Technology, Technická 2, 616 69, Brno, CZ, e-mail: krejsa@fme.vutbr.cz

Tab. 1: Binary Bayes filter algorithm.

Step	Description
1.	<b>BinaryBayesFilter</b> ( $l_{t-1}, x, z_t$ )
2.	<b>return</b> $l_t = l_{t-1} + \log \frac{p(x   z_t)}{1 - p(x   z_t)} - \log \frac{p(x)}{1 - p(x)}$

where:

- $l_t$  is a posterior belief over a binary state
- $x$  is a static state; it does not change in time
- $z_t$  is an actual measurement
- $p(x | z_t)$  is an inverse measurement model; It is a distribution over the binary state variable  $x$  as a function of measurement  $z_t$
- $p(x)$  is the prior probability of the state  $x$

The part of the equation  $\log \frac{p(x)}{1 - p(x)}$  can be written in short form as  $l(x)$ . Usually it is a constant variable  $l_0$  as it represents the prior information about the process.

### 3. Occupancy grid mapping

Occupancy grid mapping technique is a probabilistic method based on binary Bayes filter with static state. The map of environment is represented as a discrete grid  $m = \{m_i\}$

Each cell  $m_i$  in the grid represents the binary state occupied/free, practically there is occupancy information only (0-free; 1-occupied).

The algorithm of occupancy grid mapping is a version of binary Bayes filter as it is shown in Tab. 2. The inverse sensor model on step 3 represents the probability that the given cell in the map  $x$  is occupied when sensor performs the measurement  $z_t$ . The algorithm of inverse sensor model is shown in Tab. 3.

Tab. 2: Occupancy grid algorithm.

Step	Description
1.	<b>OccupancyGridMapping</b> ( $\{l_{t-1,i}\}, x, z_t$ )
2.	<b>for</b> $m_i$ <b>in</b> $m$
3.	$l_{t,i} = l_{t-1,i} + \text{InverseSensorModel}(m_i, x_t, z_t) - l_0$
4.	<b>return</b> $\{l_{t,i}\}$

### 4. Inverse sensor model

The inverse sensor model represents the probability  $p(m_i | x_t, z_t)$  in log odds form. A few cases are shown on figure 1. There are results from sensor model based on different sensor readings.



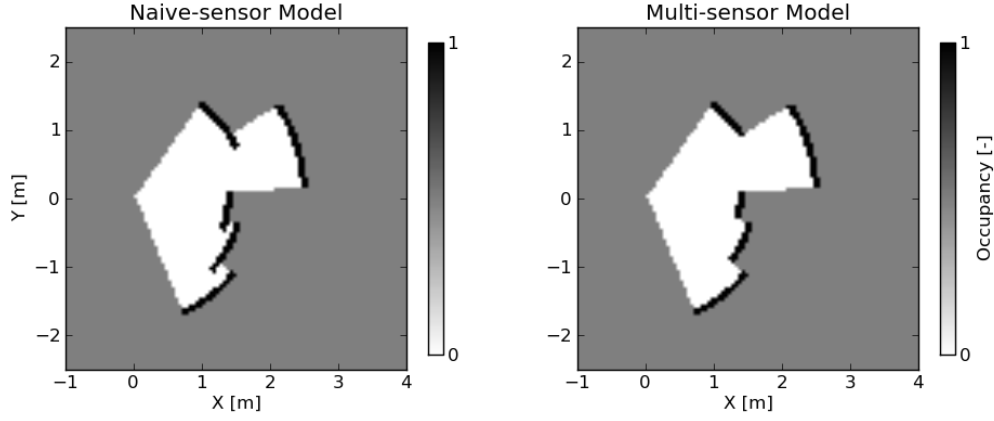


Fig. 1: Inverse sensor models.

This sensor model can be implemented in various ways. The simplest implementation is shown on figure 1-left which describes so called single sensor model. This sensor model considers each sensor beam independent on each other (naive sensor model). This consideration can be an issue if the robot deals with some kind of range finders (ultrasonic or laser) that returns an array of range measurements for a set of angles. There are some errors on borders of sensor beams.

This problem can be solved with multi-sensor model. This kind of model includes the cross-correlation of nearest sensor beams. This approach returns more realistic results (see Fig. 1 - right).

Tab. 3: Inverse sensor model algorithm.

Step	Description
1.	<b><i>InverseSensorModel</i></b> ( $m_i, x_t, z_t$ )
2.	$r_z, \varphi_z = f(x_t, z_t); r_m, \varphi_m = f(x_t, m_i)$
3.	<b>if</b> $\varphi_m < \varphi_z + \beta$ <b>and</b> $\varphi_m > \varphi_z - \beta$
4.	<b>if</b> $r_m < r_z + 1$ <b>and</b> $r_m > r_z - 1$ <b>return</b> $l_{occupied}$
5.	<b>elif</b> $r_m \leq r_z - 1$ <b>return</b> $l_{free}$
6.	<b>else return</b> $l_0$

Where  $r_z, \varphi_z$  are radius and angle of sensor beam end point,  $r_m, \varphi_m$  are radius and angle of given cell in the map, both relative to the actual position of the robot  $x_t$ ,  $\beta$  is the width of sensor beam, the log odds values describes the walls or free space as follows:  $l_{occupied} = 1$ ,  $l_{free} = 0$ ,  $l_0 = 0.5$ .

## 5. Building a local map

Practical experiments were performed on autonomous mobile robot Advee. Advee is equipped with sixteen ultrasonic sensors SRFS08, that are used for collision detection and obstacle avoidance. Sensors are located around the robot in the planar configuration, therefore the task in hand can be considered 2D. Each ultrasonic sensor is capable to detect an obstacle up to 3 meters and the sonic beam is 50 degrees wide. The usage of this kind of sensors is motivated with the nature of obstacles (usually the moving people).



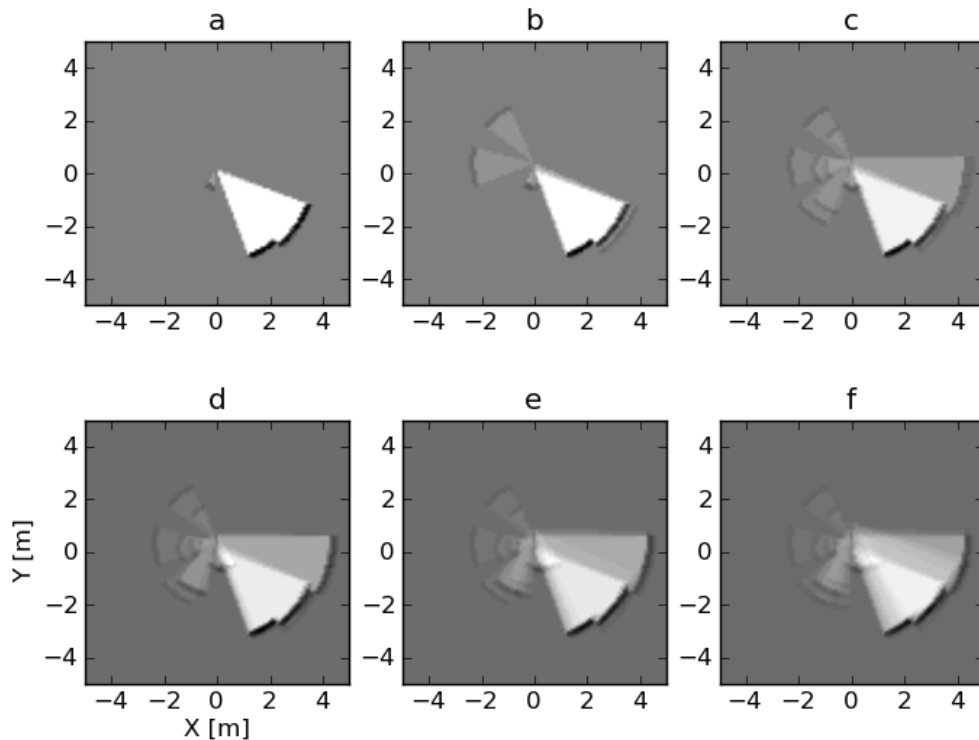


*Fig. 2: Building a local map from sensor scans.*

The local map generated via occupancy grid method uses several complete sensor scans. An example is shown in Fig. 2. On that figure one can observe subsequent building of the local map from the sensor readings. The process begins in Fig. 2a and ends in Fig. 2f. In each figure the local map is updated based on the sensor readings. In Fig. 2a only two readings are registered (other readings are invalid or obstacle undetected), in Fig. 2b there are four readings, etc. Resulting local map is used for local path planning and obstacle avoidance.

## 6. Conclusions

We have presented a method called occupancy grid mapping as an approach to build a local map for navigation of an autonomous robot through unknown environment. Presented method was integrated into the navigation system of autonomous mobile robot Advée that has to move in crowded environment densely occupied with dynamic obstacles. The tests in real world environment proved that the method can successfully build local map of the close surrounding of the robot. Such information is further utilized in the motion planner of the robot.

## Acknowledgement

Published results were acquired with the support of the Academy of Sciences of the Czech Republic under the research plan AV0Z20760514 "Complex dynamical systems in thermodynamics, fluid and solid mechanics" and with the support of the Operational Programme Education for Competitiveness, project number CZ.1.07/2.3.00/09.0162 „Knowledge and Skills in Mechatronics – Innovations Transfer to Practice“.

## References

- Sebastian Thrun, Wolfram Burgard, and Dieter Fox. (2005) Probabilistic robotics, Intelligent robotics and autonomous agents. MIT Press, September 2005., 218, 5, pp.123-132.
- A. Lazanas and J.C. Latombe. (1995) Motion planning with uncertainty: a landmark approach. Artificial Intelligence, 76, pp 287-317, 1995.
- Deans M.C. (2005) Bearings-only Localization and Mapping, PhD Thesis, Carnegie Mellon University, Pittsburg PA, USA.

## APPLICATION OF ADVANCED TECHNOLOGIES IN REHABILITATION PROCESS

M. Veseliny\*, K. Židek\*, O. Líška\*

**Abstract:** Analyses show great progress in developing non-conventional actuators. Artificial muscles have properties suitable for use in the rehabilitation area. The combination of artificial muscle with artificial intelligence gives space to the creation of modern rehabilitation equipment. This article presents a simple rehabilitation device and its control. Emphasis is placed on the usability and implementation of artificial intelligence in this type of devices. There are used neural networks and their application to prediction load during rehabilitation.

**Keywords:** Rehabilitation, pneumatic artificial muscle, artificial intelligence, neural networks.

### 1. Introduction

An article is aimed to implementation of modern technologies in rehabilitation process. It is concerned with combination of artificial muscle and elements of artificial intelligence in rehabilitation process. Rehabilitation process is time and personal very difficult. There are problems mainly in absence of modern autonomous rehabilitations equipments. Many of equipments used in rehabilitation are just simply modified fitness equipments. This is main reason for development of equipments to simplify individual rehabilitation process. The autonomous device can shorten the rehabilitation period and must be universal so that it can implement a variety of rehabilitation activities. Pneumatic artificial muscles are with their attributes in many cases like human muscles. It is combination of strengthen fibers arranged to system and closed to elastic rubber tube. Both of ends are connected by terminal to mechanical load. Principle of function artificial muscle is simple. There is change of volume by moving of muscle (muscle is increasing) and there is consequently perform power to load. From engineering aspect artificial muscle is relatively simply and has low productions costs. There is a problem with high precision control system based on pneumatic artificial muscles, because there is high non-linearity. Important preference is exact and slow movement between extreme positions of muscle what avoids jerky operation (stick-slip effect) in the start of movement. Next advantages of pneumatic artificial muscles are high reliability and minimal maintenance. Mc. Kibbens Pneumatic Artificial Muscle has power to weight around 400:1 (incomparable with pneumatic piston or DC motor). The disadvantages of pneumatic artificial muscle are: rotational movement needs pair of muscles and big stroke needs long artificial muscles. The pneumatic artificial muscle is meantime underused because there is need of more robust control. Conventional methods for control non-linearity are less applicable, better results are possible to achieved e. g. by using elements of artificial intelligence. (Pitel' et al., 2007), (Havran et al., 2010), (Pitel' et al., 2006).

### 2. Proposal of rehabilitation device based on artificial muscles

Modern rehabilitation systems must meet all terms setting to this type of equipment. A major condition is the safety of a patient who comes into contact with the device.

The design of rehabilitation device consists of several steps, which essentially copied the design of automated equipment procedures:

- analysis of rehabilitation process,

---

\*Ing. Marián Veseliny, Ing. Kamil Židek, Ph.D. and assoc. prof. Ing. Ondrej Líška, CSc.: Technická Univerzita v Košiciach, Strojnícka Fakulta, Katedra biomedicínskeho inžinierstva automatizácie a merania. Kontakt: Letná 9, 042 00 Košice, e-mails: marian.veseliny@tuke.sk, kamil.zidek@tuke.sk, ondrej.liska@tuke.sk

- estimation of security criterions and safety circuit definition,
- design of construction,
- selection of suitable actuator,
- design of control system and communication interface.

Simple diagram of device is displayed in Fig. 1, which illustrates rehabilitation device and description of several circuits.

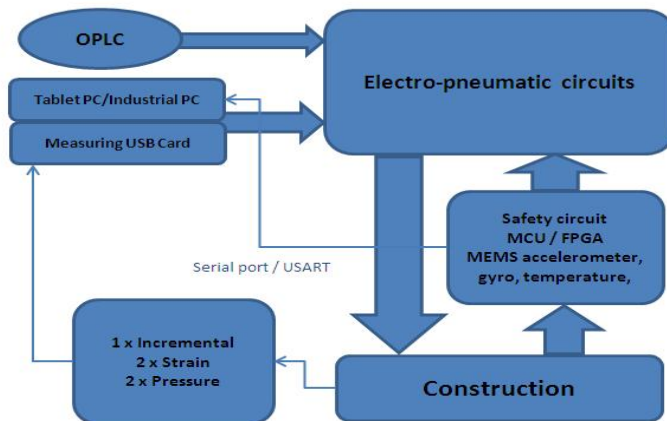


Fig. 1: Diagram of Rehabilitation Device.

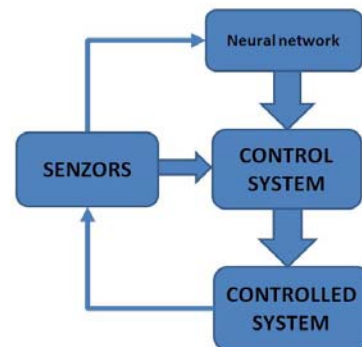


Fig. 2: Sequence of operation.

### 3. Proposal of control rehabilitation system with using elements of artificial intelligence

Utilization of artificial intelligence is widely applied in control non-linear system. There are experiments with various algorithms, methods and their combination e. g.: neural networks, theory of learning machines (machine learning), fuzzy logic, genetic algorithms, experts systems etc. How it was mentioned before pneumatic artificial muscle is unused because of complicated control. Block scheme of neural network implementation for control is visible in the Fig. 2. Rehabilitation device is represented by controlled system. Sensors are transmitting information to control system and neural network. Control system basis on information acquired by sensors and output from neural network regulates load in for rehabilitation process. Application of artificial intelligence in rehabilitation device consists of control of pneumatic muscle and control of rehabilitation movement. Initial testing was realized in Matlab which is suitable for control circuit simulation. There is possible to use combine neural network with another AI element for example Genetics algorithms or Fuzzy-relational network. There is possibility to dynamic change input in neural network and new regulations during learning process. Suitable combination of different sensing element and artificial intelligence is possible to obtain device which will be able to learn and eventually improve. Before rehabilitation start patient must be identified as userXY. After the exercise quit all data will be stored with progresses that it obtain during rehabilitation. With improvement of user fitness, the device alone will increase the load and conversely, if the device recorded the reduction in force it immediately reacts by reducing load (resistance). Such a device is particularly suitable for users who are now after the surgery. Patients will start with minimal of load (resistance) and device will increase load not only according to program but also according to actual patient condition. There are described suitable sensing elements and their combination with artificial intelligence (Sinčák, Andrejková, 1996).

### 4. Application of AI for control of load

Utilization of AI for control load in rehabilitation exercise movement is thought change of pressure in pneumatic artificial muscle. Increasing or decreasing of pressure is changing load which patient has to overcome. This device need for AI control define input and adequate output to NN. Output to NN could get 3 stages: maintain constant load, increase load, load reduction. A value of output depends on several factors that must be ahead known. One of factors can be for example current physical condition of patient, program of rehabilitation etc. Rehabilitation program is in advance known factor which artificial intelligence non-affect. What we need to know to use the AI in this rehabilitation process, we learn from the NN simulation. This NN was developed for management of load of rehabilitation device.

## 5. Definition of inputs and outputs

Input step for Neural network (NN) is definition of inputs and outputs. Outputs have already been described in previous chapter. Values of inputs depend on problem which NN has to solve. If we wish to obtain patient improvements it is necessary to define sense parameters. One of the main inputs parameters is speed. Based on the value of speed captured from device we are able to define current condition. If speed of movement raise without unchanged load from NN it means improvement of condition and it is necessary to increase load. And reversal reduction of speed reacts by decreasing of load. Load changes must be adequate to avoid step changes. In case of a big load increase patient respond by reduction of speed so NN respond by decreasing of load. To avoid described situation serves process of learning. Additional very interesting parameter is direction of movement. Direction of movement is recognized in 2 variants from 180° to 45° grades and from 45° to 180° grades. Direction of movement is important for next upgrading of intelligent rehabilitation device. It is about automatic identification of safety risk. It is situation when patient feels pain during exercise. Primary reaction in this situation is automatic change of direction of movement. NN is able to identify and evaluate safety risk and respond by decreasing load to anticipate potential injury. To recognize this situation it is necessary to know direction in time  $t$  and in time  $t-1$ . Layout of inputs and outputs is displayed in Tab. 1.

Tab. 1: NN inputs and outputs.

Inputs	Outputs
Speed of movement	Load
Direction of movement	
Direction of movement in time $t$	
Direction of movement in time $t-1$	

## 6. Simulation of neural network

After the definition of inputs and outputs there is possibility to realize simulation of NN. This Simulation has been made in program Java NNS. Simulation of NN runs in these steps:

- assigning concrete values to single inputs/outputs,
- developing trained set of data,
- creating and defining of NN,
- developing tested set of data,
- testing and interpretation of NN.

Assigning values to single inputs/outputs is important for correct function of NN. There are assignments of numeric values to status that inputs and outputs could get. The assignment is visible in Tab. 2.

Tab. 2: The Assignment of values.

Inputs	Assigned value		
INPUT 1 – speed	constant	going down	going up
	0.5	0	1
INPUT 2 – direction	180° - 45°	45° - 180°	-
	0	1	-
INPUT 3 – direction $t$	180°	...	45°
	1.8	...	0.45
INPUT 4 – direction $t-1$	180°	...	45°
	1.8	...	0.45
<b>Output</b>			
OUTPUT – load	constant	go down	go up
	0.5	1	0

Next step is application of assigned values in trained set of data. Application is realized in program Java NNA and created NN is visible in Fig. 3 with described layers.

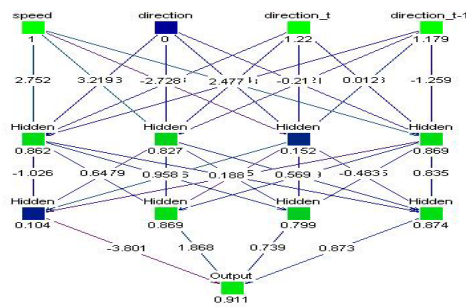


Fig. 3: Suggested NN.

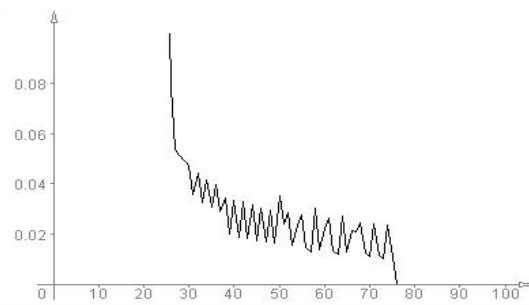


Fig. 4: Error graph proposed NN.

The Learning of NN is working with help of Error graph, with which it is possible to evaluate the learning error. The program offers a selection of several learning functions. It is possible to set up various important parameters during learning of NN, for example number of steps, activation function and similarly. In Fig. 4 is visible Error graph created for neural network. Proposed NN has been able to learn with acceptably mistake of learning in less than 80 cycles. After leaning NN there is time to create set of test data. After creating a set of test data is time for running testing of NN and interpretation of testing NN. Interpretation is running on basis of comparison serious and expected results of classification. It is defined some of coefficients of estimate precision of classification. Coefficient PCC express percentage correct classified vectors from set of test data to all vectors from set of test data. PS is numbers of correct classified vectors and PV is number of all vectors. In this case value of coefficient PSS is equal to 100%. All vectors were classified correct (Fischer et al., 2005).

$$PCC = \frac{P_s}{P_v} \cdot 100 \quad (1)$$

## 7. Conclusions

With development of unconventional actuators and advanced systems of control it was just matter of time when their application penetrates also into the rehabilitation area. Their integration into a specific rehabilitation device based on advanced control and pneumatic artificial muscles is very perspective. Control system of pneumatic muscle has to regulate non-linearity, and there is possible to use AI. Rehabilitation equipment with elements of artificial intelligence can work half or fully autonomous. It is reduces necessary attendance of therapeutics. Simulation of a specific NS pointed to the possibility of using AI in the rehabilitation process. As suitable solution appears to be the neuro-fuzzy systems that combine fuzzy logic and neural networks.

## Acknowledgement



The research work is supported by the Project of the Structural Funds of the EU, Operational Program Research and Development, Measure 2.2 Transfer of knowledge and technology from research and development into practice: Title of the project: Research and development of the intelligent non-conventional actuators based on artificial muscles ITMS code: 26220220103.

**We are support research activities in Slovakia / Project is cofounded from sources of ES.**

## References

- Piteľ J., Balara M., Boržiková J. (2007) Control of the actuator with pneumatic artificial muscles in antagonistic connection. Sborník vědeckých prací Vysoké školy báňské, TU Ostrava. Vol. 53, no. 2
- Havran M., Balara, M. (2010) Smerovanie vývoja manipulačných zariadení na báze nekonvenčných aktuátorov, Available on the Internet: <http://www.strojartstvo.sk>
- Piteľ J., Balara M. (2006) Model aktuátora s pneumatickými umelými svalmi. Process control 2006. Pardubice Univerzita Pardubice.
- Sinčák P., Andrejková G. (1996) Neural networks. Fakulta elektrotechniky a informatiky. Katedra kybernetiky a umelej inteligencie Košice : Elfa, 1996.
- Fischer I., Hennecke F., Bannes Ch., Zell A., (2005) Java Neural Network Simulator - Manual, 1.1, Available on the Internet: <http://www.ra.cs.uni-tuebingen.de/software/JavaNNS/manual/JavaNNS-manual.html>.

## OPTIMIZATION OF THE HOLE DRILLING METHOD FOR THE STRESS STATE IDENTIFICATION

K. Vítek\*

**Abstract:** *The idea of the presented numerical simulation technique corresponds to the E 837 standard concepts but is more universal. It transforms the strains, arising during the hole drilling experiment, in a way similar to that of the E 837 standard but, unlike the E 837 standard, it executes the transformation completely. This theory enlargement enables the drilling method to be applied for a wider spectrum of further measuring appliances. Moreover, the hole drilling process do not have to be extremely precise, which the whole procedure simplifies, since the new method principle includes an objective stress state identification, when evaluating drilling experiments, with respect to the drilled hole eccentricity.*

**Keywords:** *Stress state identification, hole drilling method, sensitivity gain.*

### 1. Introduction

The hole-drilling experimental method for stress state identification results in a small cylindrical hole drilled into an examined component surface. The hole drilling method for the stress state identification is based on the assumption that the free surface is one of the principal planes. The stress state in the surface layer thus can be only a uniaxial or a plane one. As such, it should be identifiable by measuring strains relieved on the free surface of the pre-strained structure during the drilling of a hole perpendicular to the surface. The semi-destructive hole drilling principle is based on impairing of the inner force equilibrium of a strained structure by drilling a relatively small circular hole perpendicularly to the surface. A drilled hole induces a change of the strain state in its close vicinity. These changes can be adjusted to define the strains arisen by drilling and thus used later for an identification of the original strain state after the strains relieved by the drilled hole are measured.

$$\left\{ \begin{array}{l} \sigma'_r = \frac{\sigma_x}{2} (1 + \cos 2\alpha) \\ \sigma'_\theta = \frac{\sigma_x}{2} (1 - \cos 2\alpha) \\ \tau'_{r\theta} = \frac{\sigma_x}{2} \sin 2\alpha \end{array} \right\} \quad (1)$$

$$\left\{ \begin{array}{l} \sigma''_r = \frac{\sigma_x}{2} \left(1 - \frac{1}{r^2}\right) + \frac{\sigma_x}{2} \left(1 + \frac{3}{r^4} - \frac{4}{r^2}\right) \cos 2\alpha \\ \sigma''_\theta = \frac{\sigma_x}{2} \left(1 + \frac{1}{r^2}\right) - \frac{\sigma_x}{2} \left(1 + \frac{3}{r^4}\right) \cos 2\alpha \\ \tau''_{r\theta} = \frac{\sigma_x}{2} \left(1 - \frac{3}{r^4} + \frac{2}{r^2}\right) \sin 2\alpha \end{array} \right\} \quad (2)$$

If the hole of the radius  $R_0$  has not been drilled yet, the thin plate depicted in Fig. 1, which is loaded uni-axially by principal stress  $\sigma_x$ , is loaded by stresses  $\sigma'_r$ ,  $\sigma'_\theta$ ,  $\tau'_{r\theta}$  in planes defined by  $r$  and  $\alpha$  polar coordinates and marked by indices of their normal lines  $r$ ,  $\theta$ , which are determined in Eq. 1. The theory of the hole drilling principle is based on the analytical Kirsch's stress-state solution of a plate with a hole drilled through perpendicularly and loaded on its x-borders by principal stress  $\sigma_x$  (Timoshenko, 1934). The Kirsch's equations (Eq. 2) describe the state of plane strain in the vicinity of the hole of radius  $R_0$  (Fig. 1). In comparison with Eq. (1), Eq. (2) include terms dependent on the drilled hole, which are left in Eq. (3) that are otherwise of a character similar to Eq. (1) and (2). If  $E$  stands for Young's modulus and  $\nu$  for Poisson's ratio, the changes of plane stresses  $\sigma_r$ ,  $\sigma_\theta$ ,  $\tau_{r\theta}$  can be used for any isotropic material for a calculation of changes related to strains  $\varepsilon_r$ ,  $\varepsilon_\theta$ ,  $\gamma_{r\theta}$  and  $\varepsilon_z$  (see Fig. 1) in a point on the plate using Hooke's law.

---

\* Dr. Ing. Karel Vítek: Department of Mechanics, Biomechanics and Mechatronics, Faculty of Mechanical Engineering, CTU in Prague, Technická 4, 16607 Prague 6, Czech Republic, karel.vitek@fs.cvut.cz





Strain gauge rosette sizes are comparable with those of the drilled hole diameters  $2R_0$  or middle radii  $R$ , at which the strain gauges of the rosettes are placed. The measuring properties of the rosettes during the hole drilling according to E 837 standard are considerably dependent on the accuracy of compliance with standardized conditions of the experiment. If the hole is drilled eccentrically, then the hole drilling experiment, as formulated by E 837 standard, cannot be used for any more complex determination of the strain state in the vicinity of the drilled hole, which would be necessary for any eventual improving corrections. This simple standard drilled theory is not probably reliable for imperfections occurring in drilled holes.

## 2. Optimization principles applied to the Hole drilling method

In (Vítek, 2008, Vítek, 2008a), we describe the principle used for an objective experimental evaluation of surface strains. There we do not have to use the completely rosette strain gages around the drilling hole but only short winding segments of this strain gages. We expect that the stress state components in the surroundings of the blind drilled hole, as written in Eq. (6), are analogous to those by Eq. (3) used for a straight-through hole. Let us also modify all the seven polytropic terms of the complete Kirsch's theory by constants  $c_k(r, z)$ , which are dependent on the distance from the center of the drilled hole, to be used for the blind hole. The distance is described by the relative radius  $r$  and the depth  $z$  of the drilled hole. By the way, a similar approach is also used by E 837 standard for strain - gage strains. These complete components of the stress state change, induced by drilling the hole, can

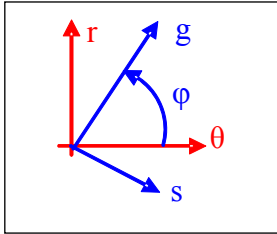


Fig. 2: Winding angle.

be transformed to the strain components. A strain state on planes perpendicular to the surface can be set by an angular transformation, where the use of the first three components (see Fig. 1)  $\varepsilon_r$ ,  $\varepsilon_\theta$ ,  $\gamma_{r\theta}$  in Eq. (7) is sufficient, because the principal strain  $\varepsilon_z$  does not have any effect on it. Fig. 2 defines the position of  $g$  axis towards  $\Theta$  axis for an acute angle  $\varphi$ . The strain in the  $g$  direction is derived from  $\varepsilon_r$ ,  $\varepsilon_\theta$ ,  $\gamma_{r\theta}$  strains according to the Mohr's transformation Eq. (5) by the use of goniometric functions of a double angle  $2\varphi$ .

$$\varepsilon_g = \frac{\varepsilon_\theta + \varepsilon_r}{2} + \frac{\varepsilon_\theta - \varepsilon_r}{2} \cos 2\varphi + \frac{\gamma_{\theta,r}}{2} \sin 2\varphi \quad (5)$$

$$\left\{ \begin{aligned} \sigma_r'' - \sigma_r' &= \frac{\sigma_x}{2} \left( -\frac{1 \cdot c_1(r, z)}{r^2} \right) + \frac{\sigma_x}{2} \left( \frac{3 \cdot c_2(r, z)}{r^4} - \frac{4 \cdot c_3(r, z)}{r^2} \right) \cos 2\alpha \\ \sigma_\theta'' - \sigma_\theta' &= \frac{\sigma_x}{2} \left( \frac{1 \cdot c_4(r, z)}{r^2} \right) - \frac{\sigma_x}{2} \left( \frac{3 \cdot c_5(r, z)}{r^4} \right) \cos 2\alpha \\ \tau_{r\theta}'' - \tau_{r\theta}' &= \frac{\sigma_x}{2} \left( -\frac{3 \cdot c_6(r, z)}{r^4} + \frac{2 \cdot c_7(r, z)}{r^2} \right) \sin 2\alpha \end{aligned} \right\} \quad (6)$$

$$\begin{bmatrix} \varepsilon_r \\ \varepsilon_\theta \\ \gamma_{r\theta} \\ \varepsilon_z \end{bmatrix} = \frac{1}{E} \begin{bmatrix} 1 & -\nu & 0 \\ -\nu & 1 & 0 \\ 0 & 0 & 2(1+\nu) \\ -\nu & -\nu & 0 \end{bmatrix} \cdot \begin{bmatrix} \sigma_r'' - \sigma_r' \\ \sigma_\theta'' - \sigma_\theta' \\ \tau_{r\theta}'' - \tau_{r\theta}' \end{bmatrix} = \frac{\sigma_x}{2E} \begin{bmatrix} \left\{ \left[ -\frac{c_1}{r^2} - \frac{c_4}{r^2} \nu \right] + \left[ \frac{c_2}{r^4} 3 + \frac{c_5}{r^4} 3\nu - \frac{c_3}{r^2} 4 \right] \cdot \cos 2\alpha \right\} \\ \left\{ \left[ \frac{c_4}{r^2} + \frac{c_1}{r^2} \nu \right] - \left[ \frac{c_5}{r^4} 3 + \frac{c_2}{r^4} 3\nu - \frac{c_3}{r^2} 4\nu \right] \cdot \cos 2\alpha \right\} \\ \left\{ \left[ -\frac{c_6}{r^4} 3 + \frac{c_7}{r^2} 2 - \frac{c_6}{r^4} 3\nu + \frac{c_7}{r^2} 2\nu \right] \cdot 2 \cdot \sin 2\alpha \right\} \\ \left\{ \left[ \frac{c_1}{r^2} \nu - \frac{c_4}{r^2} \nu \right] + \left[ -\frac{c_2}{r^4} 3\nu + \frac{c_5}{r^4} 3\nu + \frac{c_3}{r^2} 4\nu \right] \cdot \cos 2\alpha \right\} \end{bmatrix} \quad (7)$$

In (Vítek, 2010), we describe the principle used for increasing the drilling hole method sensitivity. The measurement sensitivity during the hole drilling thus can be increased by putting the strain gauges closer to the hole edge or by relative augmenting of the drill diameter to the diameter, at which the strain gauges are placed in the rosette. The experiment also can be run repeatedly with a gradual increase of the drilled hole diameter. If a minor drill diameter is chosen in the experiment first phase and the rosette strain gauges are installed in a relative distance  $r = 2 \div 4$ , the measurement of relaxed strain depletes about 40% of its potential, approximately. The potential of relaxed strains thus can be

better exploited by increasing the drill diameter, which results in a relative shift of the strain gauges to the edge of the hole, or by the second measurement using the same drilling rosette and the drill of a bigger diameter. The stress state calibration around the hole is realized by applying seven constants  $c_{11}, c_{12}, \dots, c_{17}$ , in Eq. (6) and Eq. (7), that modify the polytrope terms analogous to constants  $c_1, \dots, c_7$ .

These seven constants are dependent on relative distance from the drilled hole and on relation between the two drilled holes depths.

In (Vítek, 2010a), we describe the theory for the stress state identification in the surface at the place of already drilled holes with a complete drilling rosette equipment already installed either centrically or even eccentrically. The method thus allows a further reusing of already installed measuring items, which were originally placed there for the residual stress state identification, for measurements of the stress states induced by any following external loading as if the hole had not been drilled at all. Nevertheless, the individual components reported in Eq. (2) have to be modified by multiplication by twelve different constants  $c_{21}, c_{22}, \dots, c_{32}$  according to Eq. (2), analogously to the Eq. (6) and Eq. (7). The multipliers rectify the stress state for the real conditions of the bottom hole with a perpendicular direction to the free surface. In the case of the bottom hole, the  $c_{21}, c_{22}, \dots, c_{32}$  constants depend first on the distance from the hole center described by the  $r$  radius and, second, on the  $h$  depth of the hole.

### 3. Conclusions

We expect the direction of the principal stress  $\sigma_x$  given by the angular parameter  $\alpha$  and the second principal stress  $\sigma_y$  (see Fig. 1). The bonded strain gauge reads the strain field of the contact surface and we suppose that the strains in points and direction of the conductive winding, correspond to the strain values measured by the strain gauge. The strains  $\varepsilon_r, \varepsilon_\theta, \gamma_{r\theta}$  are standardized by a unit load vector introduced in the direction of principal stress and transformed by Eq. 5 to the winding direction of the strain gages. An analogy to Eq. (4) allows assembling a system of three independent equations for three unknown - principal stresses  $\sigma_x, \sigma_y$  and the angle of their position  $\alpha$ , where strain gauges signals are simultaneously experimentally examined.

### Acknowledgement

This research was supported by the grant of the Czech Science Foundation, N: 101/09/1492: "The experimental method for the stress state identification".

### References

- Timoshenko, S. (1934) Theory of Elasticity. 1st ed. New York and London : McGraw-Hill Book Company, Inc., 1934. pp. 52-81.
- Vishay Micro-Measurements: Measurement of Residual Stresses by the Hole-Drilling Strain Gage Method. Tech Note TN-503. USA, 2007, Revision 09, pp. 19-33.
- ASTM International, Standard Test Method for Determining Residual Stresses by the Hole-Drilling Strain Gage Method. Designation: E 837-01. USA, updated in January 2002, pp. 1-10.
- Vítek, K.(2008) Stress State Identification By Numerical Simulation of the Hole Drilling Principle – Part A, in Proceedings of 46th International Scientific Conference Experimental Stress Analysis 2008, TU Ostrava, Horní Bečva 2008, pp. 271 – 274.
- Vítek, K. (2008) Stress State Identification By Numerical Simulation of the Hole Drilling Principle – Part B, in Proceedings of 46th International Scientific Conference Experimental Stress Analysis 2008, TU Ostrava, Horní Bečva 2008, pp. 275 – 278.
- Vítek, K. (2010) Sensitivity Gain of the Hole Drilling Method for Stress State Identification, in Proceedings of 48th International Scientific Conference Experimental Stress Analysis 2010, Palacky University, Olomouc, 2010, pp. 517 – 525.
- Vítek, K.(2010) Theory of Stress State Identification After Hole-Drilling Method Application, in Proceedings of 48th International Scientific Conference Experimental Stress Analysis 2010, Palacky University, Olomouc, 2010, pp. 511 – 516.

## COARSE-PARTICLES CONVEYING IN PIPES

P. Vlasák\*, B. Kysela\*, Z. Chára\*

**Abstract:** *Flow behavior of coarse-grained slurry depends generally on particle size, shape, density and concentration. The present paper describes the results of experimental investigation of the model coarse-grained slurries on the pipe loop of inner diameter 36 mm with smooth pipes. Graded pebble gravel and glass balls conveyed in water were studied. Research was focused on evaluation of the effect of slurry velocity and concentration on hydraulic gradient versus slurry velocity relationship and the slurry flow behavior. Particle distribution in the pipe vertical cross section and motion of particles along the pipe bottom were studied in a transparent pipe section.*

**Keywords:** *Coarse-grained slurry, gravel-water mixture, pressure drops, flow structure.*

### 1. Introduction

Many materials of commercial and industrial interest are handled and transported in the form of slurries in pipes that requires advance knowledge of their flow behavior in pipes, which is important for the safe and economical design of the transport technology.

The internal friction in the conveyed slurry and the friction between the pipe and the slurry produce pressure drops, which determine the power consumption and the technology of pumping. The pressure drops depend on the flow velocity, solids concentration, density, shape, and size distribution of the conveyed solid material, the size and roughness of the pipe, and also the mutual particle-liquid, particle-particle, and particle-pipe interactions. Power consumption represents a substantial portion of the pipeline transport operational costs. For that reason great attention was paid to the reduction of hydraulic losses. One possibility of the power requirement reduction, besides the use of macromolecular or micellar additives, is based on the use of optimal particle size distribution or on addition of a small percentage of fine particles (Vlasak & Chara, 2010; Vlasak et al., 2004).

The present paper describes experimental investigation of two different coarse-grained slurries on pipe loop with smooth pipes. The slurry flow behavior was experimentally investigated with respect to the effect of solid concentration and focused on the hydraulic gradient versus the slurry average velocity relationship. The studied slurries are model slurries for a pipeline transport and handling of poly-metallic nodules (PMK) mined from the sea bottom at a depth of several km (Sobota et al., 2009)

### 2. Experimental equipment and material

The slurry flow parameters were measured on an experimental re-circulation pipe loop with a test section of smooth stainless steel pipes with inner diameter  $D = 36$  mm (Vlasak & Chara, 2010). The slurry was forced by a booster pump WARMAN 3/2 C – AH from an open storage tank, a variable speed drive was used to control slurry flow rates. The measurement section was equipped with three Hottinger-Baldvin PD-1 differential pressure transducers monitored by a computer. The slurry flow rate and concentration were measured by a KROHNE-CORIMASS-800 G+ mass flow-meter. The temperature of the slurry was maintained at about 12 °C by the heat exchanger. A two meter long transparent section was used for a visual observation of flow pattern of particle movement, which was recorded using the digital camera NanoSenze MKIII+ with a frequency up to 2 000 frames per second.

The effects of the two different solid materials, flow velocity  $V_s$ , and volumetric concentration  $c_v$  on pressure drops, slurry flow behavior and pattern were studied experimentally. Graded washed pebble

---

\* prof. Ing. Pavel Vlasák, DrSc., Ing. Bohus Kysela, Ph.D. and Ing. Zdenek Chara, CSc.: Institute of Hydrodynamics AS CR, v. v. i., Pod Patankou 30/5, 166 12 Prague 6; CZ, e-mails: vlasak@ih.cas.cz, kysela@ih.cas.cz, chara@ih.cas.cz

gravel and glass balls were used as solids. The measured suspensions consisted of bulk materials of different particle shape, but of the same mean diameter,  $d_{50} = 6$  mm. The glass balls were of uniform size (particle diameter  $d = 6$  mm, density  $\rho_p = 2540$  kg/m<sup>3</sup>), the graded pebble gravel has a narrow particle size distribution ( $d$  ranged from 4 to 8 mm,  $\rho_p = 2650$  kg/m<sup>3</sup>). Water was used as the carrier liquid. The volumetric concentration of the studied slurries reached relatively low values ( $c_v$  ranged from 2.6 to 13.4%), which reflects the supposed concentration in nodules transport.

### 3. Results and Discussion

Heterogeneous slurries may be defined as the flow with asymmetrical concentration and velocity distribution and a Coulombic friction contribution to the friction losses (Coulombic friction is slightly velocity-dependent). The threshold (deposition critical) velocity is a very important parameter for heterogeneous slurries; it is of the same importance as friction losses for design and operation.

For heterogeneous slurries many empirical correlations exist, which can be successfully used after calibration (Vlasak, P. & Chara, Z., 2009). The empirical model developed by Durand (1951) for the horizontal flow and monodisperse particle size distribution was constructed by the using of dimensional analysis. Based on the experimental results the following relationship was proposed for the slurry hydraulic gradient

$$\phi = (i_s - i_o) / i_o \cdot c_v = K \left[ Fr / \sqrt{Fr_w (\rho_p / \rho_o - 1)} \right]^\alpha = \beta \cdot Fr^{-\alpha} \quad (1)$$

where  $i_o$  and  $i_s$  are the carrier liquid and slurry hydraulic gradient, respectively,  $c_v$  is the slurry concentration,  $Fr = V_s^2 / gD$  and  $Fr_w = w_{50}^2 / gD$  are the slurry and mean particle Froude numbers,  $D$  is the pipe diameter,  $\rho_o$  and  $\rho_p$  are water and the particle density, respectively,  $w_{50}$  is the fall velocity of a medium particle. The Durand model can be used to scale up the frictional pressure drops of the sand and gravel slurries at medium velocities, supposing the material parameters are determined experimentally (Vlasak & Chara, 2011). Its disadvantage is that it does not reflect different slurry flow patterns, especially fully stratified and fully suspended flow patterns.

For this reason the so-called two-layer model, which applies the conservation equations to a large control volume of slurry, was developed. In the chosen volume (e.g. a pipe cross sectional area of a unit length with approximately uniform concentration of solids) the conservation equations are formulated using averaged quantities over the control volume. Wilson (1976) considered a fully stratified flow in which all particles are concentrated in the lower portion of the pipe (concentration in the layer near the bottom approaches the loose-packed value) and the Coulombic contribution to particle-wall friction is dominant. The RSC two-layer model (Shook & Roco, 1991, Saskatchewan Research Council, Canada) is based upon force balance for the horizontal layers:

$$\text{upper layer} \quad -dP/dz = (\tau_1 S_1 + \tau_{12} S_{12}) / A_1 \quad (2)$$

$$\text{lower layer} \quad -dP/dz = (\tau_2 S_2 + \tau_{12} S_{12} + F_2) / A_2 \quad (3)$$

where  $\tau_1$ ,  $\tau_2$  and  $\tau_{12}$  are kinematical stresses,  $S_i$  is responsible partial perimeter and  $A_i$  is responsible cross-sectional area,  $F_2$  is Coulombic force. The model satisfied the material balance constraints on total flow and solids transport rate for  $V_i$  as bulk velocity in the respective layer or total in situ solids concentration  $C_i$  is related to the partial concentrations by

$$AV = A_1 V_1 + A_2 V_2 \text{ and } C_v AV = C_1 A_1 V_1 + C_2 A_2 V_2 \text{ or } C_v A = C_1 A_1 + C_2 A_2 \quad (4)$$

All above mentioned quantities, including Reynolds number, friction factor, and Coulombic friction are defined for each layer as well as the interfacial friction factor  $f_{12}$  and the flow parameters could be determined. The model may be used for description of the stratified flow and prediction of the deposition-limit velocity, pressure drop due to friction, thickness and translational velocity of the sliding-bed, and also the value of the mean slip between the solid and liquid phases (Matousek, 1997; Matousek, 2007).

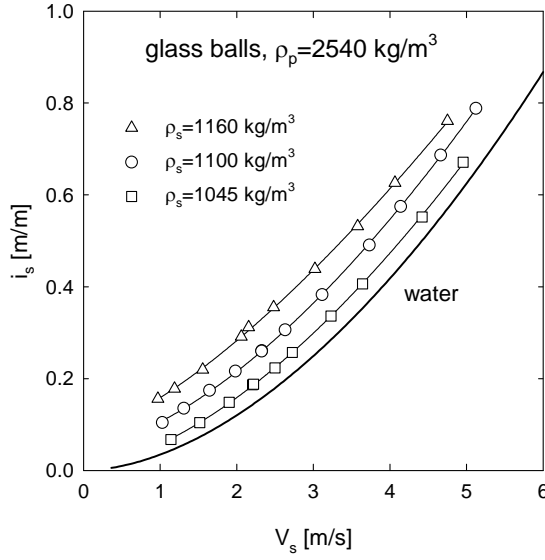


Fig. 1: Hydraulic gradient  $i_s$  vs. average slurry velocity  $V_s$  for glass slurries.

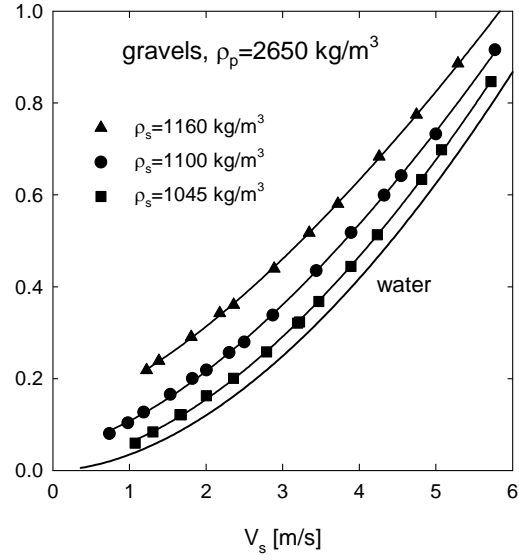


Fig. 2: Hydraulic gradient  $i_s$  vs. average slurry velocity  $V_s$  for gravel slurries.

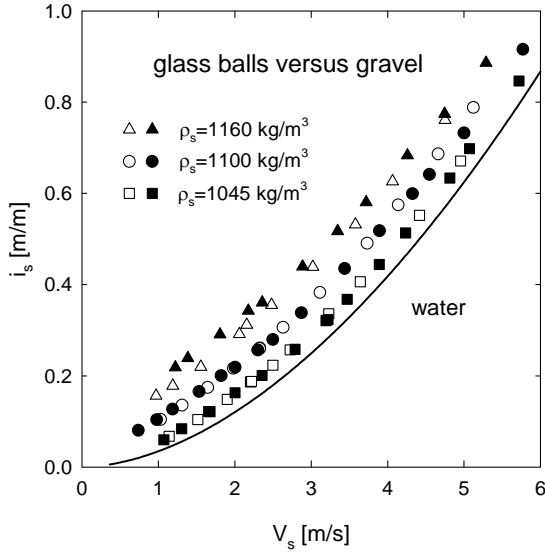


Fig. 3: Comparison of  $i_s/V_s$  relationship for glass balls and gravel slurries.

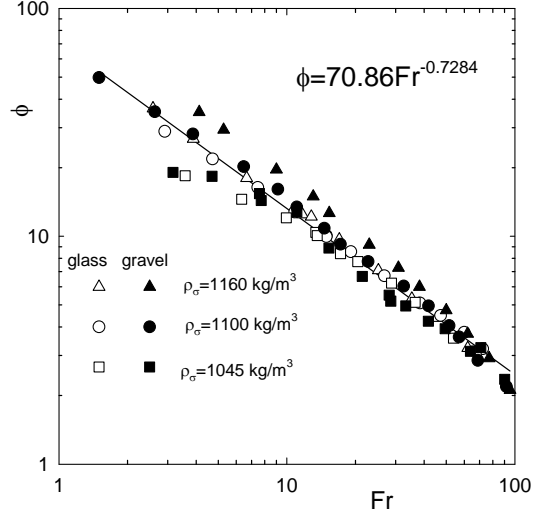


Fig. 4: Plot of Durand function  $\phi$  versus slurry Froude number  $Fr$ .

The effect of solids concentration and slurry average velocity on the hydraulic gradient ratio  $i_s$  vs. the slurry velocity  $V_s$  relationship of glass balls and pebble gravel slurries is illustrated in Figs. 1 and 2. The effect of particle concentration depends on the slurry velocity, i.e. it slightly increases with increasing velocity. This behavior can be described by a model of equivalent liquid

$$i_s = i_o + B (\rho_s / \rho_o - 1), \quad (5)$$

where  $B$  is a coefficient, which gives the proportion of suspended solids that contribute to the viscous shear stress at the pipe wall. Because density of both solid materials slightly differs the densities were used for comparison of the slurries instead of volumetric concentration, which is for gravel slurries with the same density as glass balls slurry slightly lower.

It follows from Fig. 3, that the effect of particle shape is negligible, pressure drops for measured slurries of densities  $\rho_s = 1045$  and  $\rho_s = 1100$  kg/m<sup>3</sup> are practically the same. A slight difference was found out for the higher slurry density  $\rho_s = 1160$  kg/m<sup>3</sup>, the difference increases with decreasing slurry average velocity. For lower slurry velocities can play a role that gravel particles are slightly different size and the bigger particles slide along the pipe bottom as against the glass balls, which move in rolling patterns even for low flow velocities.

Interesting is that even for the studied very coarse particles (compared with pipe) the Durand model describes well the hydraulic gradient for slurries of density  $\rho_s > 1\,100\text{ kg/m}^3$  (i.e. concentration  $c_v > 5\%$ ). For lower concentrations it is valid when  $Fr > 8$  (i.e.  $V_s > 1.7\text{ m/s}$ ). It can be explained by the visually confirmed fact that glass particles similarly as gravel particles do not move in a continuous layer along the pipe bottom. Probably with regard to their size they originated significant eddies in the bottom layer of pipe, mainly for higher flow velocities. They influence motion of individual particles, help them to reach a saltation pattern or in some case even to move fully suspended in the carrier liquid.

#### 4. Conclusions

The Durand model or two-layer model approximated well the flow behavior of coarse-grained slurries in the turbulent region. Accuracy of the models is influenced by the model parameters, which should be verified or determined experimentally.

The Durand model can be used for prediction of the frictional pressure drops, better for higher velocities. For fully stratified heterogeneous slurries, the two-layer model provided a good approximation. The glass balls slurry reaches nearly the same hydraulic gradient as the narrow-sized pebble gravel slurry of the same size of particle mean diameter, the difference decreases with decreasing concentration.

The study revealed that coarse particles moved in the pipe in a layer close to the pipe bottom, however for higher flow velocities and concentration saltation of particles was observed and particles moved also in the central area of the pipe.

#### Acknowledgement

The support under the project P105/10/1574 of the Grant Agency of the Czech Republic and the Institutional Research Plan No. AV0Z20600510 of Academy of Sciences of the Czech Republic is gratefully acknowledged.

#### References

- Durand, R. (1951) Transport hydraulique de graviers et galets en conduite. La Houille Blanche, No. Special B (1951), pp. 609-619.
- Matousek, V. (1997) Flow Mechanism of Sand-Water Mixtures in Pipelines, Delft University Press, Delft (The Netherlands).
- Matousek, V. (2007) Distribution of medium-sand particles in flow above erodible bed, J. Hydrol. Hydrodyn., 55, 4, pp.274-281.
- Shook, C.A. & Roco M.C. (1991) Slurry flow: principles and practice, Butterworth-Heinemann.
- Sobota, J., Kolarcik, W., Marek, P. & Vlasak, P. (2009) Conception of Nodules Feeder to Vertical Transport Pipeline, in: Proc. ISOPE Ocean Mining Symposium, ISOPE, Chennai (India), pp. 213-215.
- Vlasak, P. & Chara, Z. (2004) Laminar and Turbulent Transition of Fine-Grained Slurries. Particulate Sciences and Technology, 22, pp.189-200.
- Vlasak, P. & Chara, Z. (2009) Conveying of Solid Particles in Newtonian and Non-Newtonian Carriers, Particulate Sciences and Technology, 22, pp.428-443.
- Vlasak, P. & Chara, Z. (2011) Effect of Particle size distribution and concentration on flow behaviour of dense slurries. Particulate Science and Technology, 22, pp.53-65.
- Vlasak, P., Chara, Z. & Stern, P. (2010) Drag reduction of dense slurries. J. Hydrol. Hydrodyn., 58, 4, pp. 261-270.
- Wilson, K.C. (1976) A unified physically based analysis of solid-liquid pipeline flow. In: Proc. Hydrotransport 4, BHRA, U.K., Paper A1, 1-16.

## THE EFFECT OF TURBULENCE ANISOTROPY ON PARTICLE DEPOSITION IN PARTICLE-LADEN CHANNEL FLOW

J. Volavý\*, M. Forman\*, M. Jícha\*

**Abstract:** *This work contains the study of turbulent particle-laden channel flow, in which the particles experience a drag force. The method used for simulation of the liquid phase was Large Eddy Simulation using approximate deconvolution method as a subgrid model. For tracking the dispersed phase were used Lagrangian equations of motion. The effect of turbulence anisotropy on motion of particles is obtained by adding the stochastic term into particle equation of motion. This term is proportional to the turbulent kinetic energy of each velocity component. The simulations were performed for various sizes of particles. The results are compared with the previous studies of LES particle-laden flows and DNS simulation. The anisotropic model proposed in this work shows improvement in prediction of turbulent statistics of particles and concentration of particles close to the wall.*

**Keywords:** *Large Eddy Simulation, channel flow, particles, turbulence anisotropy.*

### 1. Introduction

In many technical applications we encounter with processes in which the dispersed phase (particles) is transported by the carrier phase (gas or liquid). In recent years the Large Eddy Simulation method has been improved so far that this method became fully applicable in most engineering applications concerning one-phase flow. So it is convenient to use this method for simulations of the carrier phase in two-phase flows.

Proper representation of turbulence in the near-wall region is very important in the Large Eddy Simulation of the two-phase flow. In this region, particle deposition occurs not only due to the impact of particles and gravity, but also due to turbulent diffusion. For this reason, it should be used an accurate subgrid model capable resolving near-wall region with sufficient accuracy. Another important issue is simulation of interaction of particles with fluid turbulence. The most used model for simulation of fluid-particle interaction is Eddy interaction Model (Gosman a Ioannides, 1981). However, this model shows overprediction of particles deposition in the near-wall region in combination with standard subgrid models, especially for particles with small relaxation time (Matida, 2000). This is caused by isotropic decomposition of turbulence kinetic energy. Wittig (1999) proposed three function for decomposition of turbulent kinetic energy to different direction in the near-wall region. Wang and Squires (1996) developed model, which solves additional transport equation in order to determine the velocity fluctuation close to the wall.

In this work is introduced new approach for including turbulence anisotropy and its impact on motion of particles. For the simulation of system fluid-particles was used Euler-Lagrange method. In the following sections are briefly described methods for solution of liquid and solid phase. Then is described test case used for validation of proposed model and introduced results obtained by this model.

### 2. Liquid phase

For the simulation of the liquid (carrier) phase was used Large Eddy Simulation method. The main idea of Large Eddy Simulation is to separate large scales (grid-scales) from small scales (subgrid-

---

\* Ing. Jaroslav Volavý, Ing. Matej Forman, Ph.D. and prof. Ing. Miroslav Jícha, CSc.: Energy Institute, Brno University of Technology, Technická 2896/2; 616 69, Brno; CZ, e-mails: yvolav00@stud.fme.vutbr.cz, forman@fme.vutbr.cz, jicha@fme.vutbr.cz



scales) in order to lower computational cost. The subgrid scales are modeled using subgrid model. The scale separation is done by applying filter operator on Navier-Stokes equation. If we apply the filter operator on Navier-Stokes equations we obtain filtered Navier-Stokes equations:

$$\frac{\partial \bar{u}_i}{\partial t} + \frac{\partial \bar{u}_j \bar{u}_i}{\partial x_j} + \frac{\partial \bar{p}}{\partial x_i} - \frac{1}{Re} \frac{\partial^2 \bar{u}_i}{\partial x_k \partial x_k} = \frac{\partial \bar{u}_j \bar{u}_i}{\partial x_j} - \overline{\frac{\partial u_j u_i}{\partial x_j}}, \quad (1)$$

where  $\bar{u}_i$  are filtered velocity components,  $\bar{p}$  is filtered pressure and  $Re$  is Reynolds number of the flow. For the evaluation of the subgrid stress tensor (rand hand side of equation 1) is used here approximate deconvolution model proposed by Stolz (2001). The basis of approximate deconvolution model is replacement of the unfiltered velocity in subgrid stress tensor by an approximate defiltering of the filtered velocity:

$$\frac{\partial \bar{u}_j \bar{u}_i}{\partial x_j} - \overline{\frac{\partial u_j u_i}{\partial x_j}} \approx \frac{\partial \bar{u}_j \bar{u}_i}{\partial x_j} - \overline{\frac{\partial u_j^* u_i^*}{\partial x_j}}$$

The approximate doconvolution of  $u_i^*$  is given by applying the approximate deconvolution operator to  $\bar{u}_i$ :

$$u_i^* = Q_N * \bar{u}_i,$$

where

$$Q_N = \sum_{v=0}^N (I - G)^v \approx G^{-1}$$

and  $G$  is the filter operator and  $I$  is identity operator. In our simulation we used  $N = 5$ .

### 3. Solid phase

The motion of particles is described by Lagrangian equations of motion for each particle. The only force considered here is drag force. Because of low concentration of particles we do not consider the influence of particles on the fluid. So it is used so called one-way coupling. The equation of motion for particle is:

$$\frac{d\mathbf{v}_j}{dt} = \frac{\mathbf{u}(\mathbf{x}_j, t) - \mathbf{v}_j}{\tau_p} (1 + 0.15 Re_p^{0.687}), \quad (2)$$

where  $\mathbf{v}_j$  is velocity of j-th particle,  $\mathbf{u}(\mathbf{x}_j, t)$  is velocity of fluid on particle position  $\mathbf{x}_j$ ,  $\tau_p = \rho_p d_p^2 / (18 \rho_f \nu)$  is particle relaxation time. The standard drag correlation for particles with particle Reynolds number  $Re_p$  is not small compared to 1 is applied.

In order to include the effect of turbulence anisotropy we proposed following model. The velocity on the particle position is evaluated as:

$$u_i = \bar{u}_i + X \sqrt{u_i^{*2} - \bar{u}_i^2}, \quad i = x, y, z \quad (3)$$

where the root square on the right hand side represents the estimation of subgrid kinetic energy of i-th velocity component and  $X$  is the normal Gaussian random variable.

### 4. Results and discussion

The effect turbulence anisotropy on particles proposed in this work was studied on case of particle-laden channel flow. This study is based on work (Kuerten, 2006). It was used the same geometry and flow conditions. More information can be found in this work. Simulation are performed for Reynolds number  $Re_\tau = 150$ . The channel has dimensions  $4\pi \times 2 \times 2\pi$  (length x height x width). The computational grid consists of 33 Chebyshev collocation modes in wall-normal direction, 32 Fourier modes in streamwise direction and 64 in the spanwise direction. The simulations were done in in-house developed code.

The simulations were carried out for three different particles with different Stokes number (defined as  $St = \tau_p^+ = \tau_p u_\tau^2 / \nu$ ) of 1, 5 and 25. The results are compared with results of LES and DNS simulations presented in (Kuerten, 2006). Full line represents DNS data, triangles refer to the LES simulation without anisotropic model. Here proposed anisotropic model is referred in the following paragraphs and graphs as LES anisotropic model.

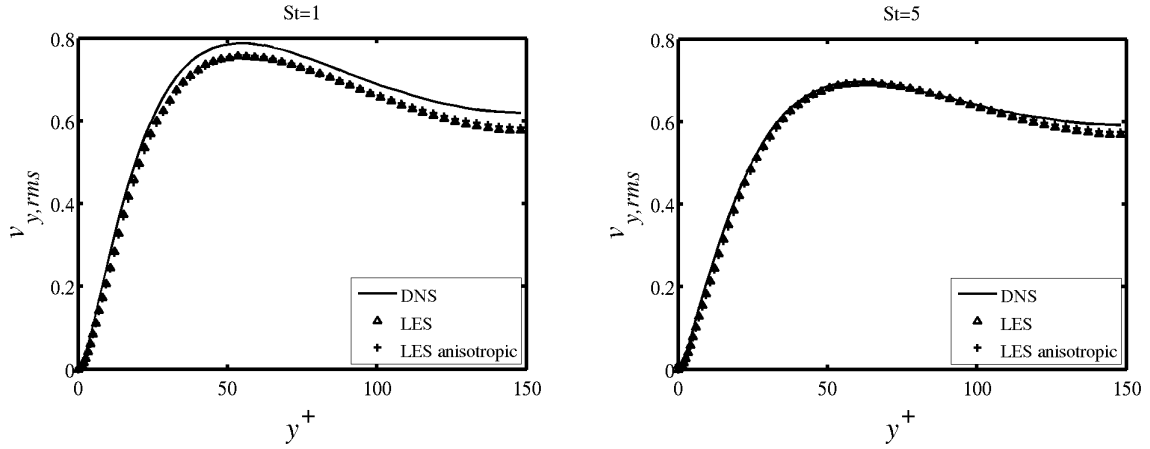


Fig. 1: Wall-normal component of particle velocity fluctuation of particles with Stokes number  $St = 1$  and  $St = 5$ .

The wall-normal velocity fluctuations of particles are depicted on Fig. 1. The accurate prediction of this quantity is very important, because the particle deposition is directly influenced by this variable. The figure illustrates well-known fact, that the particle velocity fluctuation decrease with increasing Stokes number (the motion of heavier particles is more “smooth”). From the figure is evident, that the inclusion of the turbulence anisotropy has favorable effect. The error of prediction of this quantity is smaller with anisotropic model than with model neglecting the anisotropy of turbulence.

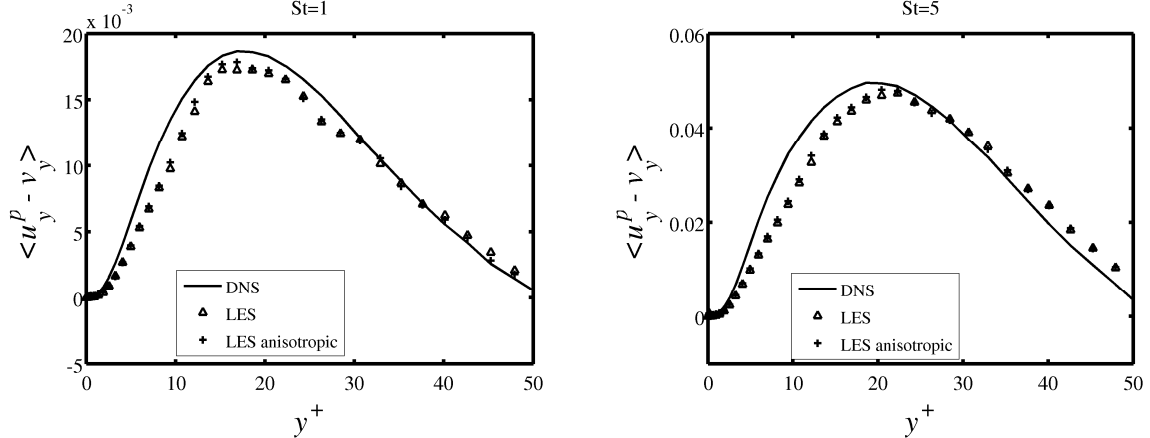


Fig. 2: Mean relative velocity of particles with Stokes number  $St = 1$  and  $St = 5$ .

In Fig. 2 are y-components (wall-normal) of mean relative velocities of particles across the channel. The anisotropic model shows better agreement with DNS results than model without anisotropic decomposition. The difference between models is very small.

The nonzero mean wall-normal particle velocity fluctuation leads to accumulation of particles near to the walls of the channel. Fig. 3 shows the development of concentration of the particles near the wall in time. For this propose the computational domain was divided in 40 equidistant strips parallel to the wall and particles in the strips closest to the wall are counted. For Stokes number 1 both models overpredict the concentration. For Stokes number 5 and time  $t^+ < 1 \cdot 10^4$  the concentration predicted by LES with and without including turbulence anisotropy model are almost identical, but for time  $t^+ > 1.2 \cdot 10^4$  there is good agreement of LES anisotropic model with DNS.

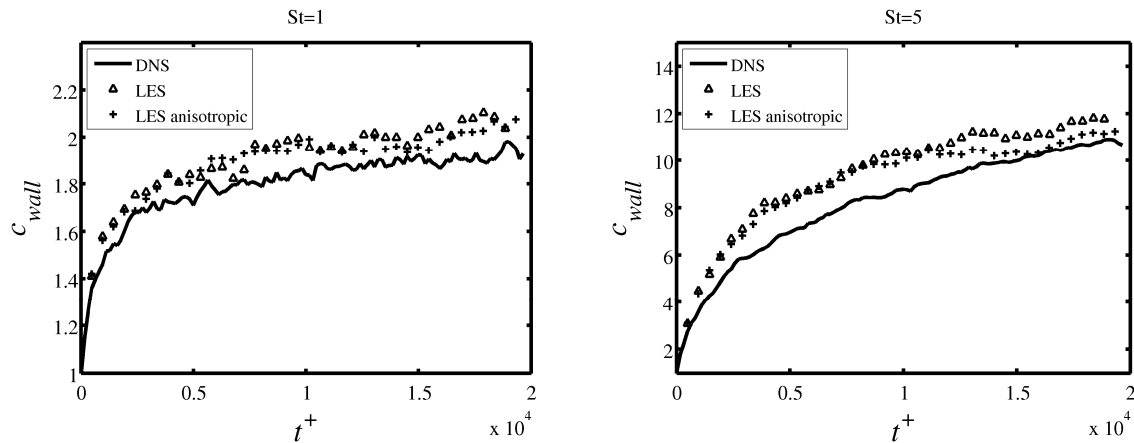


Fig. 3: Concentration of particles close to the wall

## 5. Conclusions

The modified model for particle motion in two phase flows (fluid + particles) was introduced in this work. This model includes the effect of turbulence anisotropy. Turbulence anisotropy becomes significant in the near-wall region. This effect was obtained by adding special term into particle equation of motion. This term is proportional to subgrid kinetic energy of corresponding velocity component. Here proposed model was tested on case of turbulent particle-laden channel flow. Model shows good results in combination with Large Eddy Simulation for solution of carrier phase and approximate deconvolution model for representation of subgrid scales. It was achieved improvement in prediction of turbulence statistics of particles, especially wall-normal component of velocity fluctuation. Better prediction of this quantity consequently leads to the more accurate estimation of particle concentration close to the walls. So the model is applicable for wall-bounded particle-laden flows.

## Acknowledgement

The support of grants GA CR 101/08/0096 as well as the project FSI-J-10-7 and BD13001007 is gratefully acknowledged.

## References

- Gosman, A.D. & Ioannides, E. (1981) Aspects of computer simulation of liquid fueled combustors, Paper AIAA-81-0323, 19th Aerospace Science Meeting, St. Louis, MO.
- Kuerten, J.G.M. (2006) Subgrid modeling in particle-laden channel flow, Phys. Fluids 18.
- Matida, E.A. & Nishino, K. & Torii, K., (2000) Statistical simulation of particle deposition on the wall from turbulent dispersed flow, Int. J. Heat and Fluid Flow, vol. 21, pp. 389-402.
- Shotorban, B. & Mashayek, F. (2006) A stochastic model for particle motion in large-eddy simulation, J. Turbulence, 7, N18.
- Stolz, S. & Adams, N. A. & Kleiser, L. (2001) An approximate deconvolution model for large-eddy simulation with application to incompressible wall-bounded flows, Phys. Fluids 13, 997.
- Wittig, S. & Wang, Y. & James, P.W. (1999) On the effect of anisotropy on the turbulence dispersion and deposition of small particles, Int. J. Multiphase Flow, vol. 25, pp. 551-558.

## VIRTUAL TESTING OF CONCRETE

**J. Vorel<sup>\*</sup>, A. Kučerová<sup>\*</sup>, V. Šmilauer<sup>\*</sup>, Z. Bittnar<sup>\*</sup>**

**Abstract:** *The concrete is one of the oldest materials used in the building industry for ages. The models of this material are often designed to capture the behaviour of real constructions. To use these kinds of models the loading curves and basic experimental tests are needed. Since these experiments are expensive and often time consuming there is a new trend of replacing them by virtual numerical tests. This paper concentrates on one particular step towards developing such virtual laboratory – construction of a suitable representative volume element (RVE). Preliminary results addressing the influence of grain size distribution and their discretization inside RVE on finite element simulations of compressive damage of concrete sample are discussed.*

**Keywords:** *Concrete, finite element method, virtual testing, isotropic damage.*

### 1. Introduction

In civil engineering, computational modeling is widely used in the design process at the structural level. Powerful commercial packages based on the theory of beams, plates and shells and on the finite element method (FEM) have been developed for structural analysis and are nowadays considered as one of the fundamental design tools. In contrast to that, an automated support for a selection or design of construction materials is currently not available. Specification of material properties and model parameters needed for structural analysis is not an easy task, yet it has a strong influence on the accuracy of the results. This is especially important if the influence of the mix composition, processing steps and environmental conditions during the construction stage on the long-term durability of the structure needs to be evaluated. Values of model parameters could be determined by experiments, but this is a time-consuming, tedious process that can considerably slow down the design process. Therefore, a virtual testing tool, i.e. integrated set of models, algorithms and procedures for the prediction of mechanical properties of materials, seems to be an attractive alternative.

Today, the most important construction material is concrete, which is a complex composite material over a wide range of length scales from nanometer to meter. The main objective of our work is to develop the virtual testing tool for concrete which will provide the material parameters for existing numerical models. Hence this paper serves as a preliminary study and is focused on the mesoscopic level of concrete where shapes of grains (aggregates) and their distribution play an important role. To assess their influence on numerical predictions of damage processes taking place in a concrete sample under compressive loading is the main objective of this contribution.

The paper is organized as follows. In Section 2 the preprocessing of numerical simulations is outlined. The comparison of numerical results of compression cube tests, for which the isotropic damage model is used, is demonstrated in Section 3. The concluding remarks and future extensions are presented in Section 4.

### 2. Preprocessing of numerical simulations

It has been demonstrated that creating a numerical model presents a crucial step influencing reliability and accuracy of numerical predictions, see e.g. (Zeman & Šejnoha, 2001; Zeman & Šejnoha, 2007). Here, preparation of a concrete sample at a mesoscopic level suitable for three-dimensional numerical

---

<sup>\*</sup> Ing. Jan Vorel, Ph.D., Ing. Anna Kučerová, Ph.D., assoc. prof. Ing. Vít Šmilauer, Ph.D. and prof. Ing. Zdeněk Bittnar, Ph.D. D.Sc.: Czech Technical University in Prague, Faculty of Civil Engineering, Thákurova 7; 166 29, Prague; CZ, e-mails: jan.vorel@fsv.cvut.cz, anicka@cml.fsv.cvut.cz, vit.smilauer@fsv.cvut.cz, bittnar@fsv.cvut.cz

simulations is described next with emphases on two essential steps: geometry preparation and generation of finite element mesh.

## 2.1. Geometry preparation

Generation of a numerical model in a realistic way follows a “take and place” method to place aggregates with a specific orientation one by one at the right position. The generation mechanism is designed here to fulfill the following requirements:

- The size distribution function of aggregates (grading curve) in real concrete should be matched.
- Shapes of grains should be approximated in a realistic way. Note that only convex shapes of aggregates and the shape factor (Eq. 1) are assumed.
- The minimum distance and volume control should be implemented.
- The periodicity of the grains crossing the model boundaries should be taken into account.

The generation procedure basically follows the steps mentioned above. First, the set of aggregates is created in accordance with a grading curve. The shape and size of grains is defined in this step. The grain shape can be seen as sphere, ellipsoid or polytope (polyhedron for 3D) and the breadth of the particle has to pass through a given upper sieve size and cannot be smaller than the lower sieve size, see Fig. 1 and (Mora et al., 1998) for more details. The length of the particle is given by the shape factor

$$\alpha = \frac{\text{length of particle}}{\text{breadth of particle}} \quad (1)$$

Dimensions of all shapes are generated purely randomly with the only constrain to fit the prescribed interval of the specific part of the grading curve. Moreover, for the polytope shapes the number of vertexes is also randomly generated in the appropriate limits. Whereas our interest is to obtain reasonably good agreement of the response of virtual testing sample with the true laboratory measurements, we still have to bear in mind the computational cost of such a simulation. Therefore, it is inevitable to implement into the generation procedures some control mechanisms which reduce the unsuitable small facets and angles in the particle.

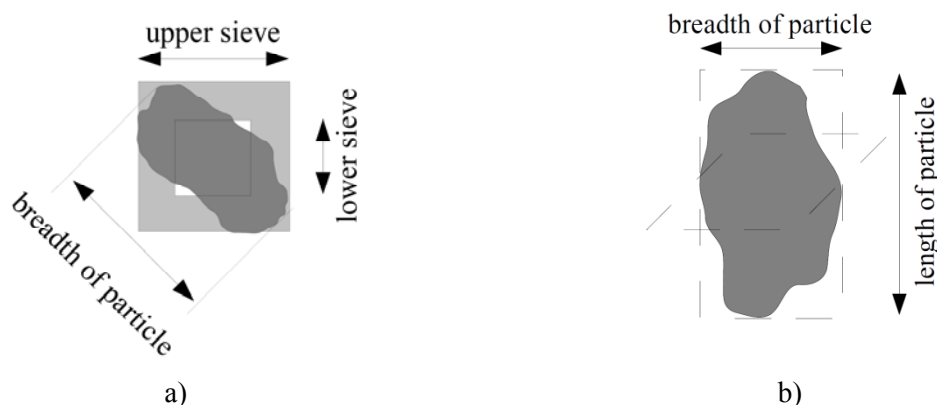


Fig. 1: Definition of grain: a) Breadth, b) length.

When all aggregates are produced, they are taken out one by one from the aggregate base and randomly assigned positions and orientations and placed in the packing region. The larger aggregates are placed first to reduce overlapping and computational time. However, even if doing so the packed aggregates inevitably overlap each other, so that overlapping judgment is necessary for a successful 3D numerical modeling. If some minimal distance between grains is required each particle is first slightly enlarged before placing and after a successful positioning it is brought back to its original shape.

The last control mechanism is employed only when the grain exceeds the model boundaries and the periodicity condition has to be fulfilled. In such a case the aggregate is divided into the required number of parts placed at relevant positions. In addition, to provide conforming meshes a checking

procedure is invoked to ensure that the fractions of a given particle are not under some specified limits. The whole procedure described herein was implemented into the MATLAB high-level language and interactive environment (MathWorks, 2010). The multi-parametric toolbox for MATLAB (Kvasnica, 2009) is used to perform all operations with volumes including copying, merging, splitting, intersecting, etc.

## 2.2. Mesh generation

This technique implies the use of conforming finite element meshes easily enabling the implementation of periodic boundary conditions if needed. This might seem daunting in that it requires not only incorporation of an arbitrary number of aggregates, but also a complicated structure of cement paste around. In the present study these obstacles are overcome by employing the volumetric modeling capacities of the ANSYS package (ANSYS, 2005).

## 3. Numerical simulations

To address the influence of shapes of aggregates on the prediction of compressive damage, three different approximations (polytopes, ellipsoids and spheres) are considered for simulations, see Fig. 2. To that end, five different cube samples (50 x 50 x 50 mm) of each shape are constructed and used in the numerical analysis performed in the OOFEM finite element code with object oriented architecture for solving mechanical, transport and fluid mechanics problems (Patzák & Bittnar, 2001). Note that the volume of stones for all samples is considered equal to 15% of the total volume (4 – 8 mm = 30%, 8 – 16 mm = 70%) and the shape factor is set equal to 1.5.

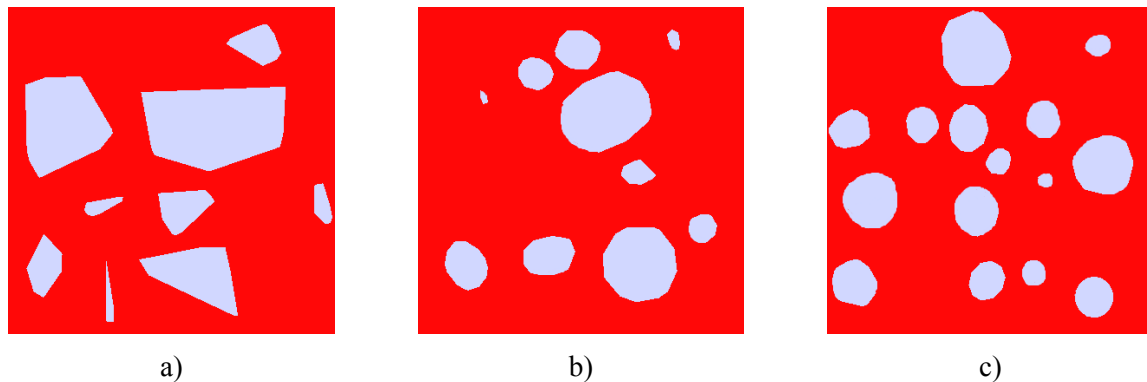


Fig. 2: 2D cuts through 3D samples: a) Polytopes, b) ellipsoids, c) spheres.

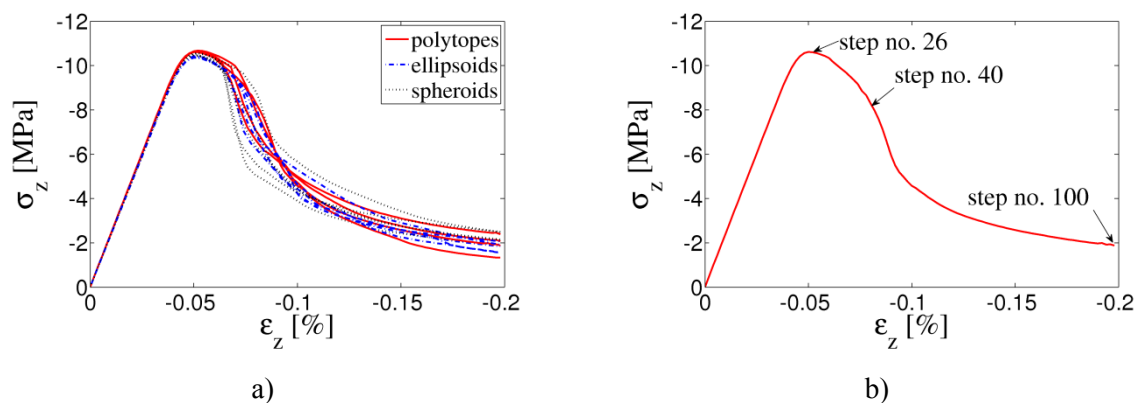


Fig. 3: Average stress-strain diagrams: a) Comparison, b) sample with the polyhedron grains.

The isotropic damage material model with the exponential softening is assumed for both the stones and cement paste. The required parameters are taken from (Wittmann, 2002). The obtained average stress-strain diagrams are compared in Fig. 3a. Fig. 3b then presents one selected loading diagram for the grains substituted by polyhedrons. The evolution of damage parameter in reference steps for the 2D cut depicted in Fig. 3a is shown in Fig. 4.

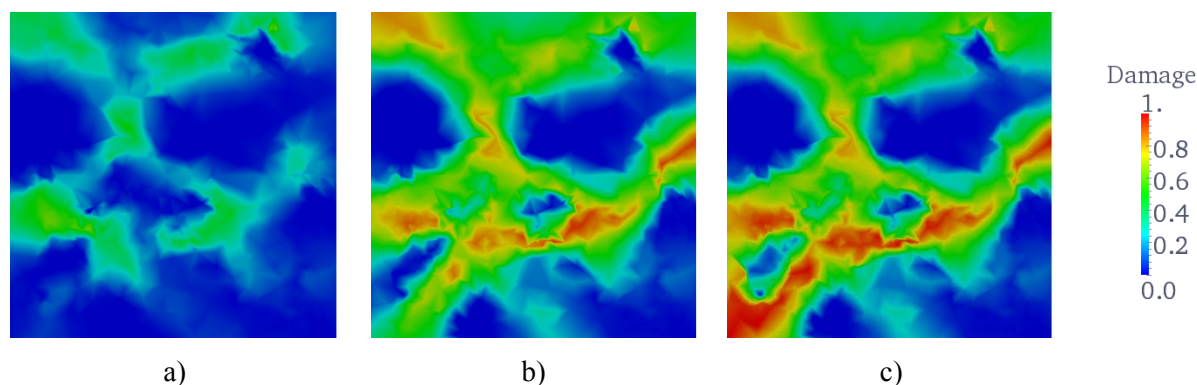


Fig. 4: Evolution of damage parameter for the sample with aggregates approximated as polytopes (Fig. 3a): a) Step no. 26, b) step no. 40, c) step no. 100.

#### 4. Conclusions

The comparison of the compression cube tests was presented in this paper. As can be seen from Fig. 3a no significant difference appeared between the simulations for various shapes of grains. This information should be verified for miscellaneous types of loading and material models as well. It is noteworthy that the approximation with polyhedrons required lower number of elements substantially influencing the computational time. Bear in mind that no interface elements have been used so far. This task we will be addressed in a forthcoming study. The following work will also focus on the possibility of introducing smaller fractions of stones into the calculations by means of some homogenization procedures (Vorel & Šejnoha, 2009; Sýkora et al., 2009).

#### Acknowledgement

The financial support provided by the GAČR grants No. 105/10/2400 and partially also by the research project CEZ MSM 6840770003 is gratefully acknowledged.

#### References

- ANSYS (2009) Documentation for ANSYS. ANSYS, Inc. Home page: <http://www.ansys.com>.
- Kvasnica, M. (2009) Real-Time Model Predictive Control via Multi-Parametric Programming: Theory and Tools. VDM Verlag Dr. Müller, Saarbrücken.
- MathWorks (2010) Documentation for MATLAB. MathWorks. Home page: <http://www.mathworks.com>.
- Mora, C.F., Kwan, A.K.H. & Chan, H.C. (1998) Particle size distribution analysis of coarse aggregate using digital image processing. *Cement and Concrete Research*, 28, 6, pp. 921-932.
- Patzák, B. & Bittnar, Z. (2001) Design of object oriented finite element code. *Advances in Engineering Software*, 32, 10-11, pp. 759-767.
- Sýkora, J., Vorel, J., Krejčí, T., Šejnoha, M. & Šejnoha, J. (2009) Analysis of coupled heat and moisture transfer in masonry structures. *Materials and Structures*, 42, 8, pp. 1153-1167.
- Vorel, J. & Šejnoha, M. (2009) Evaluation of homogenized thermal conductivities of imperfect carbon-carbon textile composites using the Mori-Tanaka method. *Structural Engineering and Mechanics*, 33, 4, pp. 429-446.
- Wittmann, F. (2002) Crack formation and fracture energy of normal and high strength concrete. *Sadhana*, 27, 4, pp. 413-423.
- Zeman, J. & Šejnoha, M. (2007) From random microstructures to representative volume elements. *Modelling and Simulation in Materials Science and Engineering*, 15, 4, pp. 325-335.
- Zeman, J. & Šejnoha, M. (2001) Numerical evaluation of effective properties of graphite fiber tow impregnated by polymer matrix. *Journal of the Mechanics and Physics of Solids*, 49, 1, pp. 69-90.



## EFFECT OF EQUALIZING GAPS ON THE FLOW IN THE TURBINE STAGES

K. Yun <sup>\*</sup>, Z. Jůza <sup>\*\*</sup>, M. Hoznedl <sup>\*\*</sup>, L. Bednář <sup>\*\*</sup>, L. Tajč <sup>\*\*</sup>

**Abstract:** A stage with impulse blading on a drum rotor is considered. Steam leakage through the shroud and shaft sealing has been determined by means of a numerical simulation. The effect of equalizing gaps on the stage efficiency, flow coefficient and axial force on the rotor has been proved.

**Keywords:** Steam turbine, efficiency, drum rotor, numerical simulation.

### 1. Introduction

Using a drum rotor system represents a way of improving efficiency of the turbine stages. Blades are longer and slimmer in this design. So as not to change the number of stages, the turbine runs at a higher velocity. This method requires using a gearbox between the turbine and the generator. Ventilation loss also increases. Equalizing holes for taking steam from the shaft seal cannot be used in this conception. Equalizing holes are replaced with equalizing gaps which are made on each stator blade. Numerical simulation determining the flow coefficient in the gaps and the assessment of the flow through all sections of the turbine stage was performed. The number of gaps and the influence of the number of gaps and the shape of the gaps on the axial force were assessed. The configuration of an experimental 1 MW steam turbine in the ŠKODA POWER laboratory served as a model for the calculation study.

### 2. CFD analysis

The calculation study considers four basic models:

Model 1 - A basic configuration of the turbine stage incorporating only the blading section of the stator and the rotor.

Model 2 - As per model 1, but with an added shroud sealing.

Model 3 - The blade section of the stage including a shroud sealing and a shaft sealing is considered.

Model 4 - Complete configuration of the stage together with seals and equalizing gaps.

*Tab. 1: Stage characteristic.*

<i>Parameter</i>	<i>Stator disc</i>	<i>Rotor disc</i>
Chord, b [mm]	27	20
Aspect ratio l/b [-]	0.57	0.87
Number of blades z [-]	170	258
Pitch to chord ratio t/b [-]	0.7	0.623

The numerical simulation was performed with the FLUENT program. In the calculation, a single-equation Spalart-Allmaras turbulent model was set up. A mesh interface together with a reference

<sup>\*</sup> Ing. Kukchol Yun.: ČVUT Praha, Fakulta strojní; Zikova 1905/4; 16636, Praha, e-mail: kukchol.yun@skoda.cz

<sup>\*\*</sup> Ing. Zdeněk Jůza, Ph.D., Ing. Michal Hoznedl, Ph.D., Ing. Lukáš Bednář and Ing. Ladislav Tajč, CSc.: ŠKODA POWER s.r.o.; Tylova 1/57, 30128, Plzeň, CZ, e-mails: ladislav.tajc@doosanskoda.com, zdenek.juza@doosanskoda.com, michal.hoznedl@doosanskoda.com, lukas.bednar@doosanskoda.com

frame model was used for the stator-rotor transition. Boundary conditions were analogous to the experimental configuration of the turbine. They are shown in Tab. 2. A combination of two blades for the stator and three blades for the rotor was considered.

Tab. 2: Boundary conditions.

Position	Parameters			
	Total pressure [Pa]	Static pressure [Pa]	Total temperature [K]	Turbulence intensity [%]
Input	58383	-	388	3
Output	-	36904	-	3

The numerical simulation was focused on an optimum velocity ratio  $u/c$ . From the previous experiments (Ščeglajev, 1983; Škopek et al., 1988) it is known that the flow coefficient depends on the rotational speed as well as the Reynolds number. These affects were not tested in the calculation study.

### 3. Calculation results

The main conclusions from the calculations are described in the report (Yun et al., 2009). This article explains the impact of the factual configuration of the stage on its efficiency.

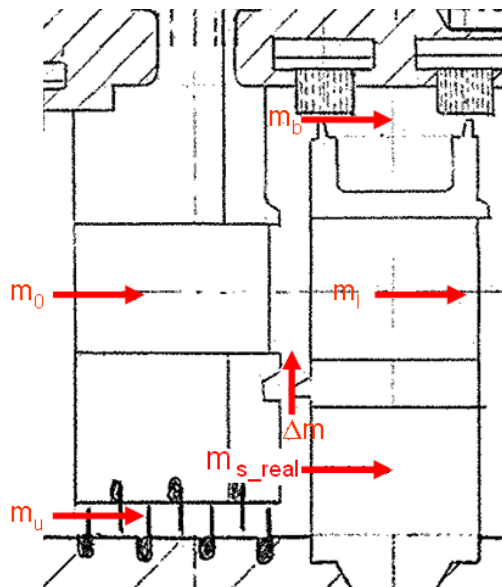


Fig. 1: Mass flows through the stages.

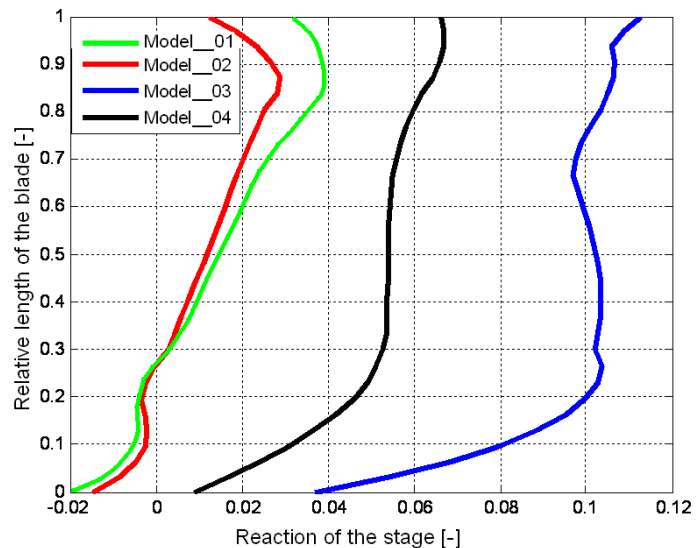


Fig. 2: Reaction curves along the blade.

The calculations allow determination of mass flows in front of individual sections of the stage. Marking of the flows is illustrated in Fig. 1. The main conclusions from the calculations for the respective models are shown in Tab. 3.

Tab. 3: Calculated flows.

Model	$m_0$ [kg/s]	$m_1$ [kg/s]	$m_u \cdot 10^2$ [kg/s]	$m_{s\_real} \cdot 10^2$ [kg/s]	$\Delta m \cdot 10^2$ [kg/s]	$m_b \cdot 10^2$ [kg/s]	$\mu$ [-]	$\eta_{td}$ [-]
1	0.9456	0.9456	-	-	-	-	-	0.8277
2	0.9731	0.9528	-	-	-	2.0255	-	0.7848
3	0.936	0.9568	5.6332	-	5.6332	3.5474	-	0.6732
4	0.9422	0.9381	6.4069	3.9715	2.4354	2.8493	0.0899	0.7026

The flow coefficient of equalizing hole determined from CFD is defined as follows :

$$\mu = m_{s\_real} / m_{s\_teor} \quad (1)$$

It regards the ratio of the factual and theoretical amount of the working medium that flows through the gap.

The thermodynamic efficiency has been calculated as follows:

$$\eta_{td} = \frac{a_u}{l_0} \cdot \frac{m_l - m_u}{m_c} \quad (2)$$

Here:

$a_u$  – mechanical work,

$l_0$  – available energy,

$m_c$  – total amount of operational medium,

$m_u$  – amount of leaked operational medium without performing work.

Tab. 3 shows that even a slight slackness of the shroud sealing ( $s = 0.7$  mm) significantly affects the efficiency. Leakage of steam through the shaft sealing should not be underestimated either. The overall decrease of efficiency is 12 %. Steam coming through the shaft sealing could not be taken away through the gaps. This is the fact that aggravates the efficiency. The flow through the shroud sealing and the shaft sealing also affects distribution of pressure heads on the rotor blade. The change of the reaction is illustrated in Fig. 2. The 01 and 02 options have a negative reaction at the root. This means that there is an increase in pressure in the rotor blade. If a shroud sealing is considered (option 2), there is a drop of pressure before the rotor blade in the tip. The shaft sealing affects the flow in the entire stage (option 3). In this case, pressure grows before the rotor blade. The equalizing gaps help reduce the overpressure on the rotor - model 04. The question is, whether it is necessary to make the gaps on each blade. For seeing of gap shape, see Fig. 3. Calculation where two gaps were considered out of three and a calculation with only one gap were made. The results are in Fig. 4 to Fig. 7.

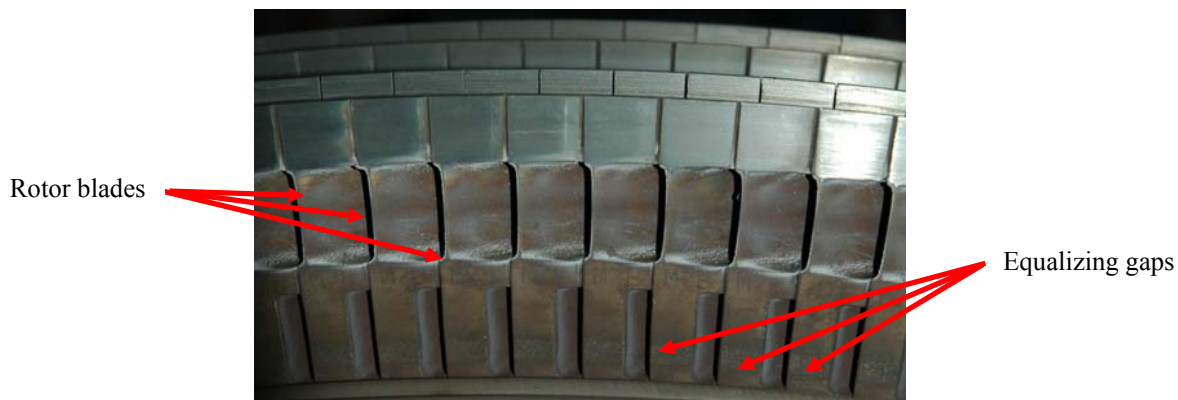


Fig. 3: Rotor blades with equalizing gaps.

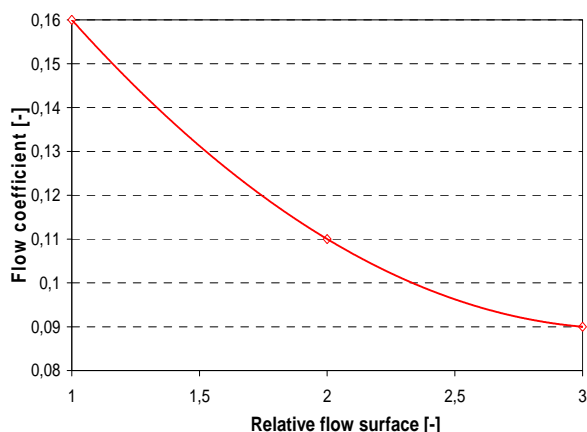


Fig. 4: The flow coefficient.

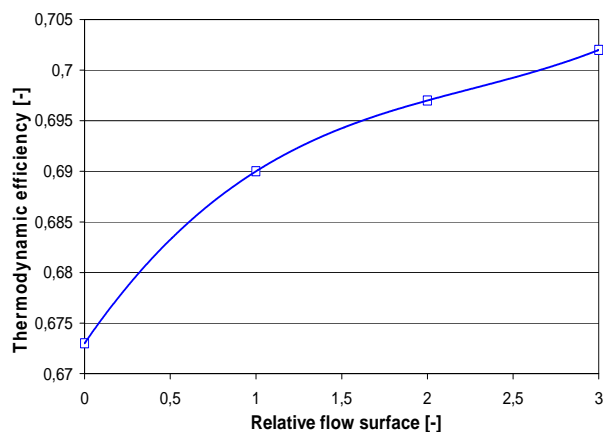


Fig. 5: Effect of gaps on the efficiency.

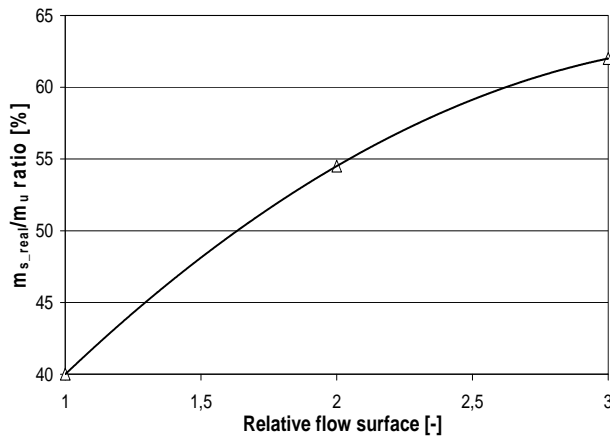


Fig. 6: Flow of the steam through the gap.

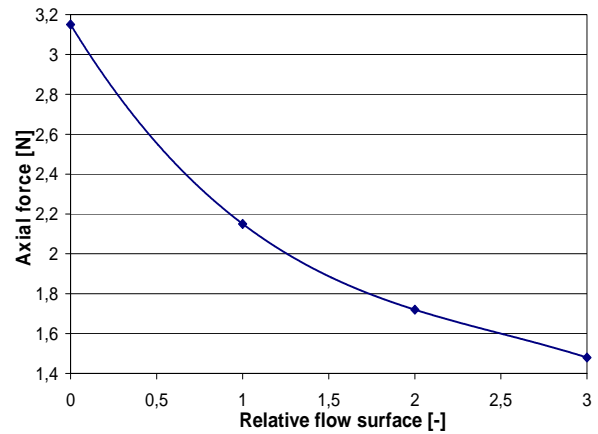


Fig. 7: Axial force on the rotor.

Value 0 on x axis in fig above means that no equalizing gap is present at this alternative. Value 1 means that one gap out of three is considered, value 2 means that two gaps out of three are considered and finally value 3 on x axis correspond to Model 4 in Tab. 3.

Clogging of the flow-surface leads to increased pressure before the rotor blade and, consequently, to an increase of the  $\mu$  coefficient. The respective change is illustrated in Fig. 4. Clogging of the gaps, however, significantly affects the thermodynamic efficiency of the stage despite the growth of the flow coefficient. This is illustrated in Fig. 5. This corresponds with a lower flow of steam through the gaps, which is illustrated in Fig. 6 and the growth of the axial force on the rotor – Fig. 7. It is clear that the complete area of the gaps is insufficient. Enlargement of the area, however, is limited. The solution lies in searching for an optimum shape of the gaps so that their flow coefficient increases and in a transition to a slightly over-pressured stage. However, an increase of axial force on the rotor must be considered. There are reserves in minimizing leakage of steam through the shaft sealing, as well.

#### 4. Conclusions

Leakage of steam through the shroud sealing and the shaft sealing affects distribution of pressure on the relatively short blades in the blade section of the stage. The shroud sealing before the rotor blade reduces the pressure; conversely, the shaft sealing increases it.

The flow coefficient has the value  $\mu \cong 0.09$ , which is a small value. All the steam leaking through the shaft sealing cannot just be taken away through the equalizing gaps.

The more steam gets to the rotor from the sealing, the worse the thermodynamic efficiency of the stage becomes. Clogging of the gap surfaces leads to an increase of the flow coefficient, drop of efficiency and increase of axial force on the rotor.

The solution lies in modification of the shape of the equalizing gaps, in designing over-pressurized blading and minimizing leakage of steam through the shaft sealing.

#### Acknowledgement

The authors of this paper wish to thank the Ministry of Industry and Commerce of the Czech Republic for the financial support of Grant No. FT-TI3/432.

#### References

- Ščeglajev, A. V. (1983) Steam turbines, SNTL Prague.
- Škopek, J., Šťastný, M., Biskup, P. (1988) Research into the Flow Coefficient in Equalizing Holes, in: Research report VŠSE, Pilsen.
- Yun, K., Jůza, Z. & Tajč L. (2009) Effect of Compensating Gaps in a Drum Rotor with Impulse Blading on Flows in a Turbine Stage, in: Research report SKODA, Pilsen.

## **ALGORITHM FOR CALCULATION OF HEAT TRANSFER COEFFICIENT OF CYLINDRICAL BAR BLOWN BY HOT AIR**

**R. Zahradník\*, J. Kvapil\***

**Abstract:** *This paper is focused on creation of an algorithm for calculating an envelope boundary condition obtained from experimental measurements performed for calculation of surface heat transfer coefficient of a cylindrical bar installed in a rectangular air channel blown by hot air.*

**Keywords:** *Heat transfer coefficient, experiment, hot air, ANSYS, boundary condition.*

### **1. Introduction**

Goal of this paper is describing the developing of an algorithm needed for an evaluation of results obtained from the experimental measurements of surface temperatures of a cylindrical bar placed inside an air channel. The measurements were done in order to obtain the data for a determination of heat transfer coefficient between hot air and steel bar.

The heat transfer coefficient will be determined from the following parameters: calculated heat flux, actual temperature of blowing air and surface temperature. The heat flux is computed by a transient analysis using ANSYS. Other values are measured directly. For the most accurate results an envelope boundary condition is required using the ANSYS model including a layout of surface temperatures measured during the experiments.

### **2. Experimental measuring**

The entry point of this task is an experimental measuring. The bar is blown over by hot air in a rectangular channel. The bar is attached to a pivot to keep its position during the measurement performed. The temperature of the bar is measured by 5 thermocouples in five positions on the surface. These 5 thermocouples are on same radial plane. The temperature of blowing air is captured together with each bar measured by the thermocouple placed inside the outlet of the channel. The data from the thermocouples are recorded in a data logger, inside its onboard memory they are downloaded by USB connection into PC after each measurement completed for an upcoming data-processing.

#### **2.1. Description of experimental apparatus**

The bar is placed in air channel which is about 0.3 meter long; the outlet holes are installed into the rectangular air channel in a periodical distance of 0.03 meter at the bottom. The sketch of the configuration is shown in Fig. 1. Each channel outlet has the same inlet velocity and air pressure during one experiment. Due to this configuration, an interesting temperature distribution is only in an area between 0 mm to 15 mm from the nozzle outlet. Other temperature distributions are identical (in ideal case) and they are periodically repeated along the total length of the bar. One experiment contains three measurements. The radial plane with installed thermocouples is placed in the distances of 0 mm, 7.5 mm and 15 mm from the hole outlet. This system produces three data sets which are coupled during post processing. The variables of experiments are: air pressure and a distance of bar's axis from the bottom of air channel.

---

\* Ing. Radek Zahradník and Ing. Jiří Kvapil: Heat Transfer and Fluid Flow Laboratory, Faculty of Mechanical Engineering, Brno University of Technology, Technická 2896/2; 616 69, Brno; CZ, e-mails: rzahradnik@lptap.fme.vutbr.cz, kvapil@lptap.fme.vutbr.cz

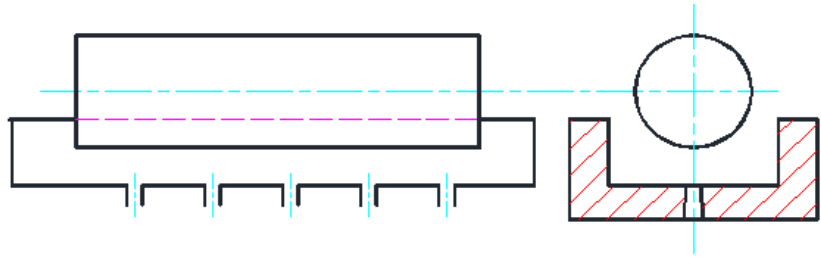


Fig. 1: Sketch of the experimental set-up.

### 3. Data processing

The measured data are in a raw unfiltered text form, which is needed to be processed for creation of the envelope boundary condition. This process contains filtering, data minding, interpolation, coupling and output formatting. At the beginning of the process there are 3 sets of the measured (pink planes in Fig. 2) surface temperatures in our area of interest (gray cylinder in Fig. 2) and at the end there should be a smooth temperature layout on the cylinder surface in every time step.

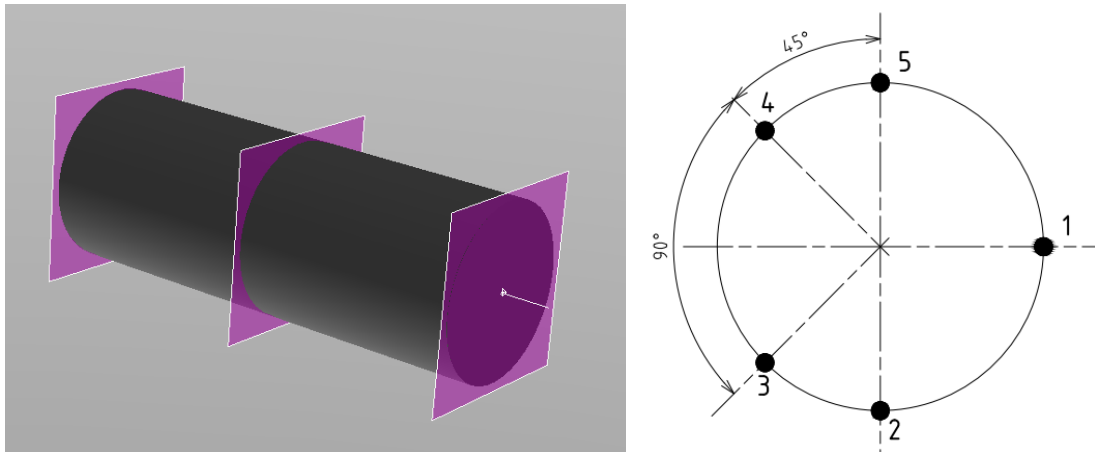


Fig. 2: Illustrations of planes where the surface temperatures were taken (on the left side) and position of thermocouples (on the right side).

#### 3.1. Data filtering

The raw data which is downloaded into PC needs to be filtered to reduce noise which is naturally created in the experiment apparatus. The Gauss filter with a convolute mask was chosen as filtering method. Filtration was performed with the help of the software developed at the Heat Transfer and Fluid Flow Laboratory. Each data set was filtered by the same filtration method. The next operation is data coupling. Due to the fact that each set is actually different measurement, each data set has different lengths and time when the bar starts to heat its self. The different time starting point is solved manually during filtration. The length of data is solved in a MATLAB's script.

#### 3.2. Developing envelope boundary condition

Merit of case is how to handle a 5D matrix (position of point in 3D space, time and its temperature) in a way that is easy to program and that is natural for human mind. ANSYS supports 5D arrays (tables) but in this particular case this is not the way how to do it. Author decided to use the cylindrical coordinate system ( $\rho$ ,  $\phi$ ,  $Z$ ) together with the 3D table together in ANSYS to apply boundary condition. This boundary condition will be placed on the cylindrical area, thus one coordinate ( $\rho$  axis) will be constant and there is no need to consider it. 3D table in ANSYS has possible 3 variables ( $X$ ,  $Y$ ,  $Z$ ) which can be override by global ANSYS variables, in this case  $X$  by  $TIME$ ,  $Y$  by  $\phi$ .  $Z$  coordinate in the 3D table has the same meaning like the global variable  $Z$  axis. The temperature of the point in an exact location and time is stored in a cell; and each point is fully described in 3D space and time with its own temperature.



The other thing is a filling of table for the boundary condition. The internal ANSYS algorithm for degrees of freedom value assignment (nodal temperatures in this case) requires having all temperatures across time and position for whole model in one table. Filling such a large table is possible only by an automatic internal file input algorithm. The ANSYS will allocate enough memory space for a required table but allocating the memory for the data is a separated task from reading data. ANSYS reads the data from input file and fills the cells of the table until it finds the end of a file marker or it has space for storing data. By the time when ANSYS allocates its memory for the table, it needs to know the table dimensions. Because of that there must be a link between data size and ANSYS table before reading the data from the text file and all data must be in one text file, written sequentially plane by plane.

### 3.3. Developing envelope boundary condition

MATLAB was selected for developing specific algorithm for its strong orientation on matrix computing and capability for handling a large set of data. MATLAB's script was created with its own programming language for creating the envelope boundary condition. The script is handling all the obstacles discussed in the previous chapter. The runtime diagram is presented in Fig. 3.

The first step is a data input obtained from three measurements. Each measurement has different length and a moment when air starts heat the bar. Based on the shortest measurement, the other 2 are cropped to the same length and to have the same moment of heating. Their time values are rewritten. This assures that the moment of heating will be at same time point. The second step is data interpolations of every three temperatures from each set of measurements from the same thermocouple and same time. These interpolations make additional data at Z axis between planes of the measurements. The third step is interpolations of temperatures in each time in each plane along Z axis. These interpolations make additional data along  $\phi$  axis. All interpolations use the same method, an embedded cubic spline interpolation with a prescribed end slopes to enforce smooth distribution. Last step is storing all data on hard drive.

### 3.4. Calculation of heat flux and heat transfer coefficient

The heat transfer coefficient is calculated from the measured air and surface temperature and computed heat flux. Two APDL macros were used, the first one for automatic creation of geometry, mesh etc., and the second one for automatic calculation of the heat transfer coefficient at the specific points on the surface where the thermocouples are solder to the steel bar. Both macros read the lengths of data, the temperatures of hot air and time duration from the determined files produced by MATLAB script.

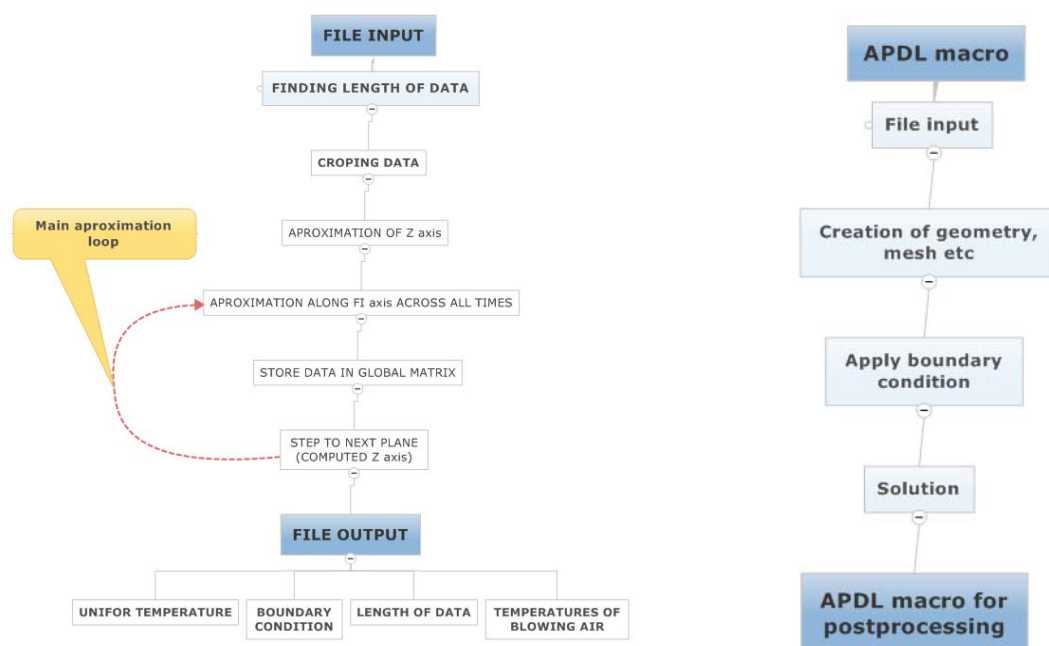


Fig. 3: The runtime diagrams of MATLAB script on the left side and ANSYS on the right side.



## 4. Conclusions

The algorithm for the calculation of the smooth envelope boundary condition has been provided. The algorithm requires only a manually filtered input data. The rest of the process is fully automatic and it doesn't require any special knowledge. The algorithm is fully adjustable for different computational demands.

Examples of results are shown in Figs. 4, 5. Fig. 4 shows the temperature distribution within the model at the end of calculation. The hottest area is above the nozzle outlet and the coldest one is in the area furthestmost from the nozzle outlet. Fig. 5 shows the heat flux distribution at the end of calculation. The right side of Fig. 5 shows heat flux trends of the thermocouples points in time.

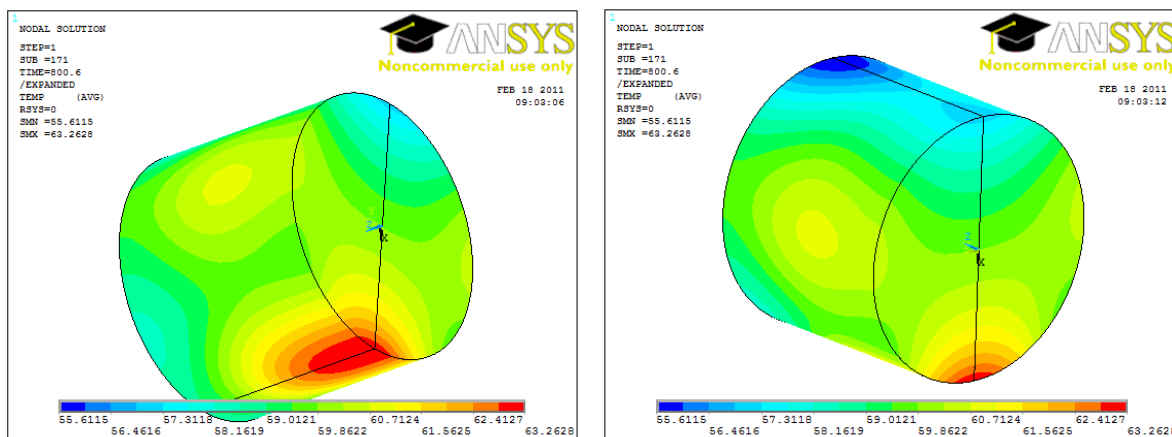


Fig. 4: The temperature distribution at the ANSYS model, isometric view of the hottest and the coldest area. Their locations are in expected places.

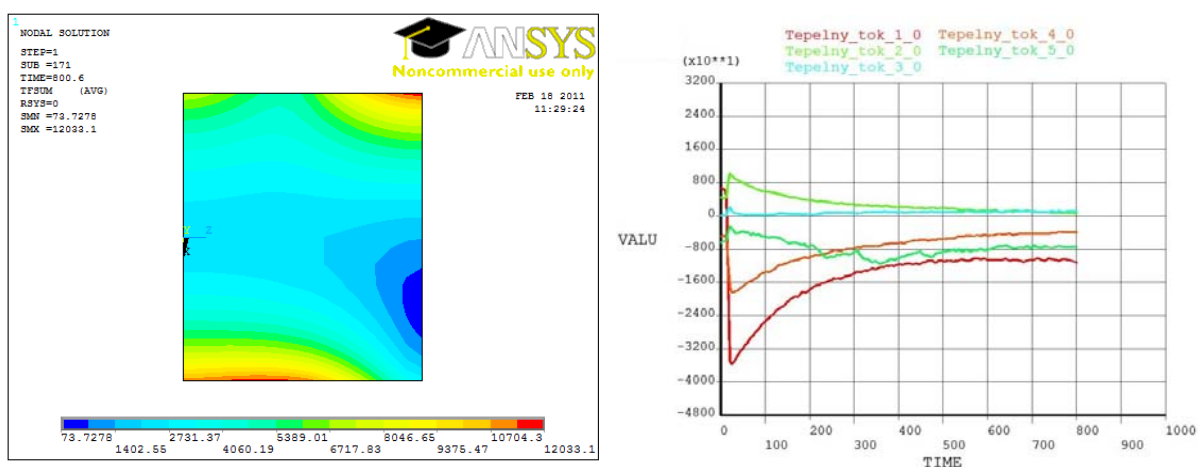


Fig. 5: Heat flux distribution in XZ plane on the left side and on the right side heat flux distribution  $[W \cdot m^{-2}]$  at surface points where thermocouples were attached.

## Acknowledgement

The paper was supported by the project Innovation Voucher 2011, No.: HS13045032. Authors would like to express his gratitude to Ing. Tomáš Luks for his advices concerning ANSYS and MATLAB software together with valuable suggestions.

## References

- Composite authors (2010) ANSYS Help, ANSYS, Inc.
- Composite authors (2010) MATLAB Help, Mathworks, Inc.

## **A COMPUTATIONAL ANALYSIS OF THE STEADY STATE LATERAL VIBRATION OF A FLEXIBLY SUPPORTED RIGID UNBALANCED ROTOR ATTENUATED BY SQUEEZING THE THIN FILMS OF CLASSICAL AND MAGNETORHEOLOGICAL LIQUIDS**

**J. Zapoměl<sup>\*</sup>, P. Ferfecki<sup>\*\*</sup>**

**Abstract:** *The vibration amplitude of rotors excited by imbalance can be significantly reduced if damping devices are inserted between the rotor and its stationary part. To achieve their optimum performance, the damping effect must be controllable. For this purpose a new semiactive damping element has been proposed. It works on the principle of squeezing two concentric lubricating films formed by classical and magnetorheological liquids. In the mathematical model they are represented by newtonian and Bingham materials respectively. The damping effect is controlled by the change of intensity of the magnetic field generated by electric current. The rotor is assumed to be absolutely rigid and is coupled with the stationary part by spring elements. Its vibration is governed by nonlinear equations of motion whose steady state solution is obtained by application of a collocation method. The newly proposed semiactive damping element minimizes amplitude of the rotor vibration by adapting the damping effect to the current operating conditions.*

**Keywords:** *Rotors, semiactive damping elements, magnetorheological fluid, steady state response.*

### **1. Introduction**

Amplitude of the lateral vibration of rotors can be significantly reduced if damping devices are inserted between their rotating and stationary parts. To achieve their optimum performance, the damping effect must be controllable. For this purpose a new semiactive coupling element working on the principle of squeezing two concentric films of classical and magnetorheological liquids has been proposed. The damping effect is controlled by changing induction of the magnetic field passing through the film of magnetorheological fluid.

In this paper there is investigated the steady state vibration of a flexibly supported rigid rotor that is excited by the unbalance forces and attenuated by the new damping element. The attention is focused on minimizing amplitude of the rotor vibration by means of adapting the damping effect to the current operating conditions.

### **2. Modelling of the new controllable damping element**

The rotor is supported by rolling-element bearings whose outer races are flexibly coupled through the squirrel springs with the stationary part. The proposed damping element consists of four rigid rings. Two rings are mounted with the stationary part directly and two ones with the squirrel springs carrying the bearings. The springs enable oscillation of the movable rings in the radial direction and prevent their rotation together with the shaft (Fig.1). The clearances between the fixed and flexibly supported rings are filled with classical (the inner clearances) and magnetorheological oils (the outer clearances). In the damper body there is imbedded an electric coil generating magnetic field. The magnetic flux passes through the layer of magnetorheological liquid and as resistance against its flow depends on magnetic induction, magnitude of the current can be used to control the damping effect.

---

<sup>\*</sup> prof. Ing. Jaroslav Zapoměl, DrSc.: Department of Mechanics, VŠB-Technical University of Ostrava, 17. listopadu 15, 708 33, Ostrava-Poruba; CZ, e-mail: jaroslav.zapomel@vsb.cz

<sup>\*\*</sup> Ing. Petr Ferfecki, Ph.D.: SIMD, VŠB-Technical University of Ostrava, 17. listopadu 15, 708 33, Ostrava-Poruba; CZ, e-mail: petr.ferfecki@vsb.cz

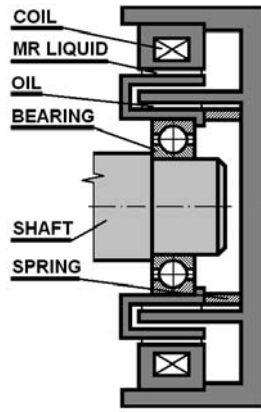


Fig. 1: Schema of the proposed damping element.

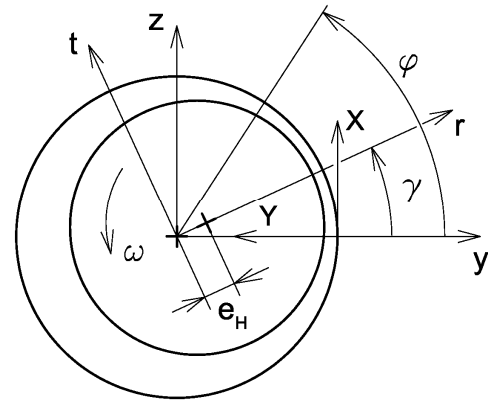


Fig. 2: The coordinate system.

The mathematical model of the proposed damping element originates from the assumptions of the classical theory of lubrication. The classical and magnetorheological oils are represented by newtonian and Bingham materials and the yield shear stress of the magnetorheological liquid depends on magnetic induction. The further attention is focused only on the dampers whose geometry and design make possible to consider them as short and on the dampers symmetric relative to their middle plane.

The thickness of the oil films depends on position of the rotor journal centre relative to the stationary part of the rotor system

$$h_{CO} = c_{CO} - e_H \cos(\varphi - \gamma), \quad h_{MR} = c_{MR} - e_H \cos(\varphi - \gamma). \quad (1)$$

$h_{CO}$ ,  $h_{MR}$  denote the thickness of the films of classical and magnetorheological oils,  $c_{CO}$ ,  $c_{MR}$  represent the width of the gaps between the rings filled with classical and magnetorheological lubricants,  $e_H$  is the rotor journal eccentricity,  $\varphi$  is the circumferential coordinate and  $\gamma$  denotes the position angle of the line of centres (Fig.2).

The pressure distribution in noncavitated parts of the lubricating films is governed by equations derived in Krämer (1993) and Zapoměl & Ferfecki (2009),

$$\frac{\partial^2 p_{CO}}{\partial Z^2} = \frac{12\eta}{h_{CO}^3} \dot{h}_{CO}, \quad (2)$$

$$h_{MR}^3 p_{MR}'^3 + 3(h_{MR}^2 \tau_y - 4\eta_B \dot{h}_{MR} Z) p_{MR}'^2 - 4\tau_y^3 = 0. \quad (3)$$

$p_{CO}$ ,  $p_{MR}$ ,  $p_{MR}'$  denote the pressure and the pressure gradient in the axial direction in the layers of the classical and magnetorheological liquids,  $\eta$  is the dynamical viscosity of the classical oil,  $\eta_B$  is the Bingham viscosity,  $Z$  is the axial coordinate,  $\tau_y$  is the yield shear stress and  $(\cdot)$  denotes the first derivative with respect to time. Equation (3) holds for the case when the pressure gradient in the axial direction is real (not complex), negative and satisfies the relation

$$p_{MR}' < -\frac{2\tau_y}{h_{MR}}. \quad (4)$$

The boundary conditions needed for solving equations (2) and (3) express that the pressure at the damper faces is equal to the pressure in the ambient space  $p_A$ .  $L$  is the length of the damping element

$$p_{CO} = p_A, \quad p_{MR} = p_A \quad \text{for} \quad Z = \frac{L}{2}. \quad (5)$$

In the simplest design case of the damping element, the rings, between which there is situated a layer of the magnetorheological liquid, can be considered as a divided core of an electromagnet. Then the dependence of the yield shear stress on magnetic induction can be approximately expressed

$$\tau_y = k_y \left( \frac{NI}{2h_{MR}} \right)^{n_y}. \quad (6)$$

$k_y$  and  $n_y$  are the material constants of the magnetorheological liquid,  $N$  is the number the coil turns and  $I$  is the electric current.

In the areas where the thickness of the lubricating films rises with time ( $\dot{h}_{CO} > 0, \dot{h}_{MR} > 0$ ) a cavitation is assumed. The pressure in these areas remains constant and is equal to the pressure in the ambient space. The damping force is given by integration of the pressure distributions  $p_{DCO}$ ,  $p_{DMR}$  in the cavitated and noncavitated regions around the circumference and along the length of the damping element

$$F_{dy} = -2 R_{CO} \int_0^{\frac{L}{2}} \int_0^{2\pi} p_{DCO} \cos \varphi dZ d\varphi - 2 R_{MR} \int_0^{\frac{L}{2}} \int_0^{2\pi} p_{DMR} \cos \varphi dZ d\varphi, \quad (7)$$

$$F_{dz} = -2 R_{CO} \int_0^{\frac{L}{2}} \int_0^{2\pi} p_{DCO} \sin \varphi dZ d\varphi - 2 R_{MR} \int_0^{\frac{L}{2}} \int_0^{2\pi} p_{DMR} \sin \varphi dZ d\varphi \quad (8)$$

$R_{CO}$  and  $R_{MR}$  are the radii of the layers of the classical and magnetorheological oils.

### 3. The equations of motion of the investigated rotor

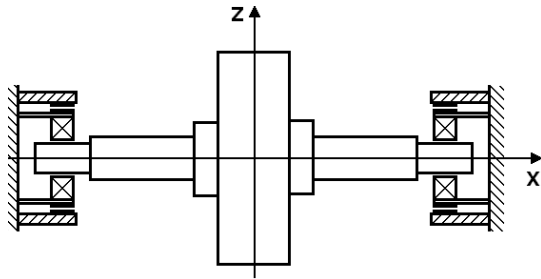


Fig. 3: Investigated rotor system.

The investigated rotor consists of a shaft carrying one disc (Fig.3). With the stationary part it is coupled by the squirrel springs and the new damping elements. The system is symmetric relative to the disc middle plane perpendicular to the shaft centreline. The rotor is loaded by its weight and is excited by the disc unbalance. The squirrel springs are prestressed to eliminate their deflection caused by the rotor weight.

Taking into account the system symmetry, the rotor lateral vibration is governed by two equations of motion that are nonlinear due to the damping forces

$$m_R \ddot{y} + b_p \dot{y} + 2k_D y = 2F_{dy}(y, z, \dot{y}, \dot{z}) + m_R e_T \omega^2 \cos(\omega t + \psi_o), \quad (9)$$

$$m_R \ddot{z} + b_p \dot{z} + 2k_D z = 2F_{dz}(y, z, \dot{y}, \dot{z}) + m_R e_T \omega^2 \sin(\omega t + \psi_o). \quad (10)$$

$m_R$  is the rotor mass,  $b_p$  is the external damping coefficient,  $k_D$  is the squirrel spring stiffness,  $\omega$  is the angular rotation speed,  $e_T$  is the eccentricity of the rotor unbalance,  $t$  is the time,  $\psi_o$  is the phase shift,  $y, z$  are displacements of the rotor centre and  $(\ddot{\phantom{x}})$  denote the second derivatives with respect to time.

Because of prestressing the spring elements, the steady state trajectory of the rotor centre is circular and therefore the steady state solution of (9) and (10) can be estimated as

$$y = r_C \cos \omega t - r_S \sin \omega t, \quad z = r_C \sin \omega t + r_S \cos \omega t. \quad (11)$$

To determine the unknown parameters  $r_C$  and  $r_S$  a collocation method is applied. Only one collocation moment of time is needed. Then substitution of relations (11) and their first and second derivatives with respect to time for  $t$  equal to zero yields a set of two nonlinear algebraic equations

$$(2k_D - m_R \omega^2) r_C - \omega b_p r_S - m_R e_T \omega^2 - 2F_{dy}(r_C, r_S) = 0, \quad (12)$$

$$\omega b_p r_C + (2k_D - m_R \omega^2) r_S - 2F_{dz}(r_C, r_S) = 0. \quad (13)$$

### 4. Results of the computational simulations

The task was to analyze amplitude of the excited vibration and magnitude of the force transmitted into the rotor stationary part.

The orbits of the rotor centre and time histories of the transmitted force in the vertical direction are drawn in Fig.4 and 5. They show that for the lower rotor revolutions the increase of the current rises the damping effect and reduces both the vibration and force amplitude. For higher rotor revolutions increase of the current decreases amplitude of the vibration only negligibly but magnitude of the transmitted force significantly rises. This confirms that the controllable damping effect makes possible to achieve the optimum rotor running by adapting the damping to the current operation conditions.

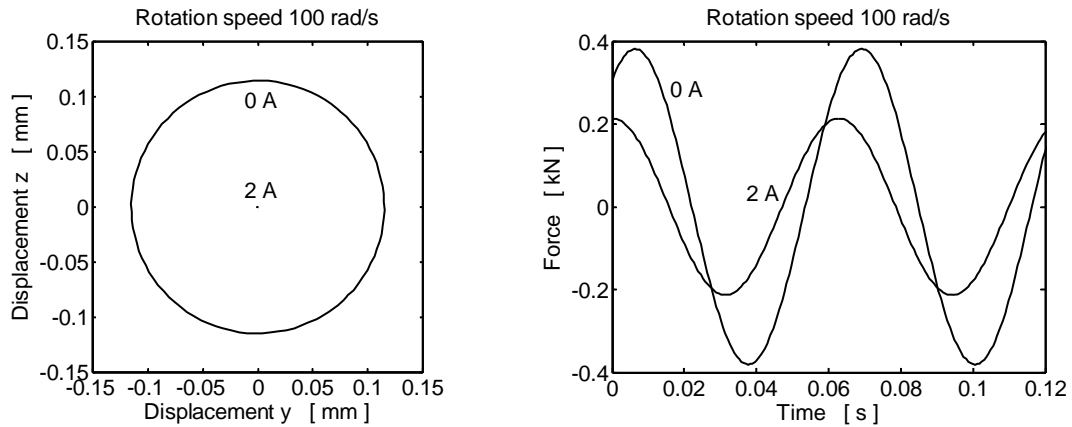


Fig. 4: The rotor centre orbits and the time history of the transmitted force (100 rad/s).

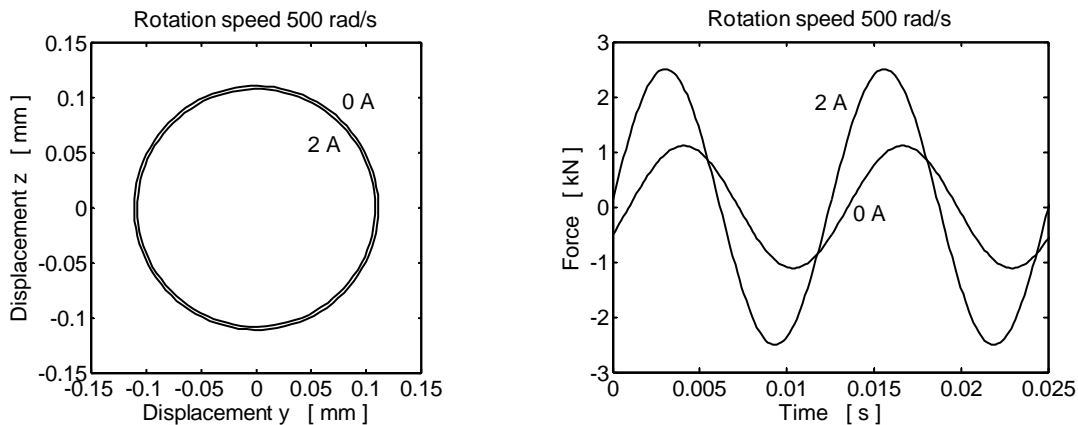


Fig. 5: The rotor centre orbits and the time history of the transmitted force (500 rad/s).

## 5. Conclusions

The developed procedure represents a tool for analysis of the steady state vibration of rigid rotors attenuated by the newly proposed semiactive damping elements working on the principle of squeezing two thin films of classical and magnetorheological oils. Advantage of the proposed damping device is that it does not require a complicated and expensive control system and makes possible to achieve the optimum performance of the rotating machine by means of adapting the damping to the current operating conditions.

## Acknowledgement

This work has been supported by the research projects P101/10/0209 and MSM 6198910027.

## References

- Krämer, E. (1993) Dynamics of Rotors and Foundations. Springer-Verlag, Berlin, New York.
- Zapoměl, J. & Ferfecki, P. (2009) Mathematical modelling of a short magnetorheological damper. Transactions of the VŠB – Technical University of Ostrava, Mechanical Series, LV, 1, pp. 289-294.

## SEAWATER DESALINATION PLANT – A CASE STUDY

E. Zeneli\*, F. Jirouš\*

**Abstract:** *This article is focused on two main methods of seawater desalination. Each method is analyzed separately. Municipal solid waste (MSW) is used as energy source. Coupling of waste to power and seawater desalination plant is discussed in this paper. The case study presents a touristic area where this process could be worthy. The main goal of this article is to calculate the unit product cost as main parameter in desalting plants.*

**Keywords:** *Desalination, MED, RO, energy, cost.*

### 1. Introduction

To live is to use water. Unfortunately, fresh water is becoming an ever-more precious commodity, again because the arid regions of the world appear to be expanding. This gap is expected to widen in the near future, due mainly to the high rate of population growth and the urbanization. Desalination of seawater is the logical or the only available solution to safe supplies of fresh water. This process consumes large amounts of energy while municipal solid waste (MSW) may be transformed to produce electricity and thermal energy (Dajnak et al., 2000). Waste treatment is an extraneous term in Albanian towns and their thermal utilization is encouraged. Seawater desalination can help to resolve local problems of water supply, which, especially in arid areas, can risk the development and the life of people. Since desalination involves high specific consumption of energy per m<sup>3</sup> of distilled water, the adoption of economic and efficient desalination technologies is desirable. The evaluation of unit product cost is considered in this paper.

### 2. Reverse Osmosis (RO)

Reverse osmosis is a membrane based desalination process. The membrane is capable of separating salt from water with a rejection of 98–99.5%. Reverse osmosis is based on a property of certain polymers called semi-permeability. While they are very permeable for water, their permeability for dissolved substances is low. By applying a pressure, difference across the membrane the water contained in the feed is forced to permeate through the membrane. In order to overcome the feed side osmotic pressure, fairly high feed pressure is required. In seawater desalination, it commonly ranges from 5.5 MPa to 7 MPa.

### 3. Multi-effect distillation (MED)

The MED process takes place in a series of vessels called effects and uses the principle of reducing the ambient pressure in the various effects. In a MED process the feed water enters the first effect and is raised to the boiling point after being preheated in tubes. The tubes are heated by steam from a boiler/turbine which is condensed on the opposite sides of the tubes. Only a portion of feed water applied to the tubes in the first effect is evaporated. The remaining feed water is fed to the second effect, where it is again applied to a tube series. The tubes are in turn being heated by the vapor created in the first effect. The vapor is condensed to distillate while giving up heat to evaporate a portion of remaining feed water in next effect. The main feature of the MED process is that it operates at low top brine temperature 60-70°C (Al-Salahi et al., 2006).

---

\* Ing. Edmond Zeneli and prof. Ing. František Jirouš, DrSc.: Department of Fluid Dynamics and Power Engineering. Czech Technical University in Prague, Technická 4, 166 07, Prague 6; CZ: e-mails: e\_zeneli@hotmail.com, frantisek.jirous@fs.cvut.cz

#### 4. The case study

An Albanian touristic area of 100 000 inhabitants is considered in our case. The typical present day per capita content of MSW is evaluated 450 – 550 kg/year. MSW calorific value is considerable, 8.5-13 MJ/kg (Reimann, 2006). For our calculations have accepted  $LHV_{waste}=11\,500\text{ kJ/kg}$ , from which results that nominal thermal power in boiler is  $Q_{boiler}=32.5\text{ MW}_{th}$  and electricity generated  $E=9\text{ MW}_{el}$ .

##### 4.1. Reverse Osmosis power by waste firing plant

First, we consider that the total energy production of  $9\text{ MW}_{el}$  is used to supply RO desalting plant. In order to calculate the unit product cost is necessary to make some assumptions:

- Steady state operation
- Isothermal operation. Therefore the temperatures of the feed, brine and permeate are equal.
- The membrane selectivity is constant and is equal for various types of salts.

In the scheme below is examined a  $2\,000\text{ m}^3/\text{d}$  desalination plant. This assumed value is much higher than last achievements in the membrane technology. The main design variables in RO systems are:

- the recovery rate,
- the salt rejection,  $S_R = 99\%$
- the operating pressure,
- the permeate flux, both in terms of overall product rate and specific rate.

For a given salt rejection of the membranes used, technical feasibility of single-stage systems for potable water production is expressed by the following condition:

$$TDS_p = (1 - S_R/100) * TDS_f \leq 500\text{ ppm} \quad (1)$$

$TDS_f$ - salinity of feed water,  $\approx 40\,000\text{ ppm}$  (typical value of Mediterranean seawater)

$TDS_p$ - salinity of product water, ppm

In order to decrease the power consumption a pressure exchanger is appropriate for energy recovery. These work exchangers directly transfer brine hydraulic energy to feed hydraulic energy. In any case, cost reduction rarely exceeds 10 % of water cost (Lamei, et al., 2007). A RO layout and with parameters is shown in Fig. 1. The results from the calculations are summarized in Tab. 2.

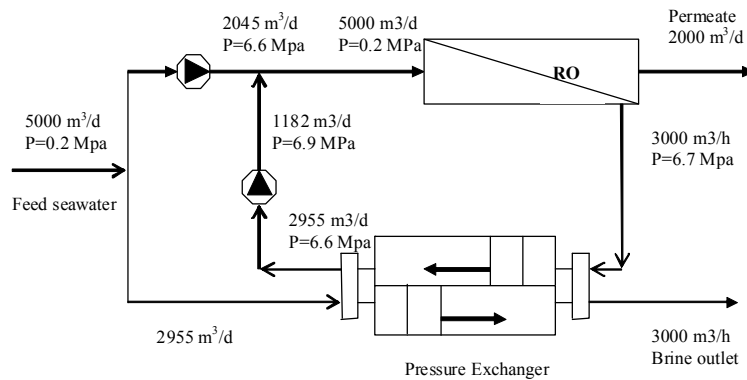


Fig. 1: Single RO desalination scheme.

##### 4.2. Multi-effect distillation process coupled with waste firing plant

Waste firing plant supplies with heat and electricity the MED plant. Desalting capacity is accepted  $2\,000\text{ m}^3/\text{d}$  with 6 effects. For our calculations is accepted specific heat consumption  $10\text{ kWh/m}^3$  distillate. Specific electric energy consumption is assumed  $2.5\text{ kWh/m}^3$ . Particularly for the MED section El-Dessouky et al., (1998) assume equal heat transfer area in each effect, and equal heat transfer coefficient. Equal temperature drop between effects as well equal specific heat for the brine, and feed water have been assumed.



The design of MED parameters starts with the definition of the temperature drop across all effects, which is obtained from equation (2).

$$\Delta T_{tot} = T_s - T_{bn} \quad (2)$$

Brine temperature in the first effect is obtained from the relation

$$T_{b1} = T_s - \Delta T_1 \quad (3)$$

Distillate flow rate in the first effect can be calculated from the evaporator energy balance (Jirouš, 2010) :

$$M_s \lambda_s = M_f c_p (T_{vi} - T_f) + D_i \lambda_i \quad (4)$$

Distillate flow rate in effects 2 to n:

$$D_{i-1} = \frac{M_f c_p (T_{vi} - T_f) + D_i \lambda_i}{\lambda_{i-1}} \quad (5)$$

Brine flow rate in effects 1 to n:

$$B_i = D_i \frac{X_f - X_d}{X_b - X_f} \quad (6)$$

The overall mass balance (Jirouš, 2010):

$$M_f = M_d + M_b \quad (7)$$

The evaporator heat transfer area, for the first and next effects are written as

$$A_e = \frac{M_s \lambda_s}{U_e (T_s - T_b)} \quad (8)$$

In Tab. 1, are shown the results for each effect of MED process. The enthalpies of brine and vapor are obtained from the formulas given in terms of the vapor and brine temperatures.

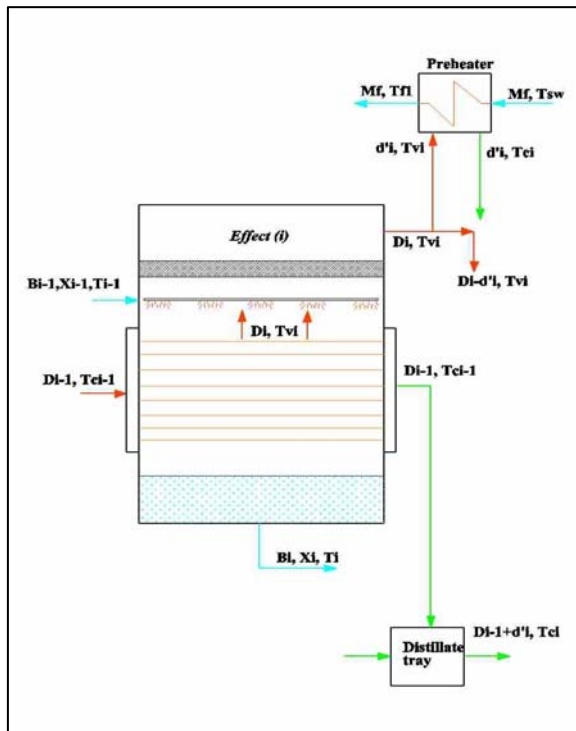


Fig. 2: Layout of the  $i^{th}$  effect of MED plant.

Tab. 1: Parameters of MED profile.

Effect	1	2	3	4	5	6
U (kW/m <sup>2</sup> K)	2	2	2	2	2	2
$\Delta T$ (°C)	4.16	4.16	4.16	4.16	4.16	4.16
$T_b$ (°C)	70.84	64.68	58.52	52.36	46.2	40
$T_v$ (°C)	68.84	62.68	56.52	50.36	44.2	38
$\lambda_v$ (kJ/kg)	2335.92	2350.6	2365.46	2380.51	2395.77	2411.28
D (kg/s)	3.039	2.262	1.618	1.1048	0.7196	0.46
A (m <sup>2</sup> )	902.04	902.04	902.04	902.04	902.04	902.04
B (kg/s)	8.201	8.978	9.622	10.1352	10.5204	10.78
F (kg/s)	11.24	11.24	11.24	11.24	11.24	11.24
$X_b$ (ppm)	64 000	64 000	64 000	64 000	64 000	64 000

In Tab. 2, are summarized the data of cost analysis for each desalination process. The economic analysis is based on cost equation of the total cost  $C_t$ ;

$$C_t = C_c + C_e + C_{ch} + C_l + C_m \quad (9)$$

Where,  $C_c$  is the yearly capital cost [€/year]:

$C_e$  - cost of energy [€/year];

$C_{ch}$  - cost of chemicals [€/year];

$C_l$  - the yearly cost of labor [€/year];

Tab. 2: Unit cost production of each desalination process.

	RO section		MED Section	
Plant capacity, m <sup>3</sup> /d		2 000		2000
Recovery rate (RO), % and conversion rate (MED), %		40		38
Direct capital cost, €/m <sup>3</sup> /d		1350		1400
Chemical consumption, kg/m <sup>3</sup>		0.28		0,1
Chemical cost, €/kg		0.18		0,18
Specific (labour +maintenance), €/m <sup>3</sup>		0.0645		0,022
Membrane replacement , €/m <sup>3</sup>		0.034		N/A
Specific thermal energy consumption, kWh/m <sup>3</sup>		N/A		10
Specific electric power consumption, kWh/m <sup>3</sup>		4.5		2,5
Specific electric energy cost, €/kWh		0.05		0,05
Interest rate	5%			5%
The annual fixed cost, €/year	209 637		168 000	
The annual chemical cost, €/year	32 256		11808	
The annual operation + maintenance, €/year	41 280		14432	
The annual membrane cost, €/year	21 760		N/A	
The annual energy cost €/year	144 000		410000	
Total	448 933		604 240	
<b>Unit product cost €/m<sup>3</sup></b>	<b>0.74</b>		<b>0.921</b>	

## 5. Conclusions

Two different methods of desalination have been discussed in this article. RO requires high pressures and the total electricity production of 9 MWel, is used for desalination plant. The second attempt is coupling power plant with MED section. Design parameters of MED, operating parameters and some data cost have been evaluated. Unit product cost of RO is slightly lower than thermal desalination unit product cost, due to higher energy requirement of MED. In the end, could say that results are interesting and encouraging mainly, when desalting plants are powered by a waste firing plant.

## Symbols

A - Area of evaporator, m <sup>2</sup>	T <sub>v</sub> - Vapour temperature in each effect, °C
B - Brine flow rate from each evaporation effect, kg/s	U - Heat transfer coefficient, kW/m <sup>2</sup> °C
λ - Latent heat for evaporation, kJ/kg	X - Salinity, ppm
PR - performance ratio, PR=Md/Ms,	D - Amount of vapour formed in each flashing stage or effect
T - Temperature, °C	F - Feed flow to each effect, kg/s
n - Number of effects,	M - Mass flow rate, kg/s

## References

- Al- Sahali, M. & Ettouney H. (2006) Developments in thermal desalination processes: Design, energy, and Costing aspects, Desalination, pp. 227-240.
- Dajnak, D. & Lockwood, F.C. (2000) Use of thermal energy from waste for seawater desalination.130, pp. 137-146.
- El-Dessouky, H., Alatiqi, I. & Ettouney, H. (1998) Steady-state analysis of the multiple-effect evaporationdesalination process, Chem.Eng. Technology, 21. pp. 437-451.
- Howe, E.D. (1974) Fundamentals of Water Desalination, Marcel Dekker, New York.
- Jirouš, F. (2010) Applied heat and mass transfer, CTU Press, Prague. ISBN 978-80-01-04514-5.
- Lamei, A. & Van der Zaag, P. & Von Munch, E. (2007) Basic cost equation to estimate unit production costs for RO desalination, Desalination 225, pp. 1-12.
- Reimann, D. O. (2006) Heat from combustion of waste, dirty business or clean resource? CEWEP, Germany.

## DEFLECTION OF REINFORCED CONCRETE STRUCTURES ACCORDING TO EC2: COMPARISON OF METHODS

R. Zídek\*, L. Brdečko\*

**Abstract:** *This paper compares two approaches to the analysis of deflections of reinforced concrete beam structures with consideration of creep. The first is based on simplified methods recommended in Eurocode 2. The second approach is more general and uses the incremental solution, the smeared crack model for modeling of material non-linearity and time discretization method for the assessment of rheology. The results of both analyses are similar. The general method also allows the influence of the erection process or stepwise loading to be taken into account.*

**Keywords:** *Creep, reinforced concrete, deflection, time discretization method, Eurocode.*

### 1. Introduction

Eurocode 2 for the analysis of reinforced concrete structures allows the use of a simplified approach to consider creep in the computation of displacements via the effective modulus of elasticity for concrete. The code also defines rules for the calculation of stiffness for a cross-section with cracks and states the possibility of using more accurate methods. The authors have assembled a program for the analysis of creep of reinforced concrete structures which is based on more general assumptions. The paper gives a short summary of the theoretical assumptions on which the Asteres computer program is built and the basic features of the method in (Eurocode 2). Consequently, a study of both approaches applied to practical structures is presented.

### 2. Analysis methods

Asteres software is designed for the analysis of planar beam structures. It is based on the finite element method. The program uses a special beam element which allows the behavior of concrete and groups of steel to be modeled separately. It is useful especially for the effective expression of concrete volume changes.

An iterative computation process with adaptive control of load level is implemented to consider the nonlinear behavior of reinforced concrete. For concrete in compression the nonlinear stress-strain diagram according to (Eurocode 2) is considered. The smeared cohesive crack model is used for concrete in tension. After the tension strength is reached the residual stiffness of the crack is considered. This stiffness depends on crack width and fracture energy  $G_f$ . The crack is smeared into a certain zone which for planar concrete structures is usually in relation to the size of finite elements. For reinforced structures in bending this model works only after reinforcement yielding occurs and one dominant crack has developed (Zídek, 2008). Before this limit is reached, the zone is considered as the real crack spacing calculated approximately according to (Eurocode 2). The redistribution of internal forces in the case of statically indeterminate structures and the redistributions of stresses between parts of the cross-section (especially between concrete and steel in compression) is ensured using incremental load solution and using the time discretization method.

Creep of concrete depends on the whole history of the stresses in the structure. Therefore, the method of time discretization was implemented. This method allows the observation of changes in the stresses in particular elements of the structure. The accuracy depends on the density of division of the considered time. Details about the theoretical background of the Asteres program are in (Zídek, 2008).

---

\* Ing. Rostislav Zídek, Ph.D. and Ing. Luděk Brdečko, Ph.D.: Institute of Structural Mechanics, Brno University of Technology, Veveří 97; 602 00, Brno; CZ, e-mails: zidek.r@fce.vutbr.cz, brdecko.l@fce.vutbr.cz

The method according to Eurocode 2, chapter 7.4, uses the stiffness of the not-fully-cracked cross-section based on another principle. The stress in the concrete crack is considered zero, but the stiffness of the steel is raised due to the concrete between the two cracks and its interaction with the steel. The change in stiffness is considered at one time and the redistribution of stresses is not allowed.

For the expression of creep the effective modulus of elasticity method is used. This method of analysis gives exact solutions only for structures where the redistribution of stresses is not assumed. In real structures, the redistribution is caused by a change in stiffness due to cracks in the case of statically indeterminate structures or by redistribution stresses between compressed concrete and steel.

According to the theory defined in (Eurocode 2) an Asteres software module was developed. The solution of linear FEM is common for both variants. Therefore, all examples mentioned below were analyzed with the same precision and with the same finite element division. The details of this implementation are in (Zídek & Brdečko, 2010).

### **3. Comparative study**

The goal of this study was to compare the methods used in the Asteres program with the simplified approach of the solution of displacements according to (Eurocode 2). Asteres also allows the observation of other quantities, for example stresses in concrete or reinforcement. The process of loading of the structures was considered simply to make it possible to analyze structures also using the simplified method according to (Eurocode 2). Because of the possibility of assessing a particular influence separately, shrinkage was not considered in any example. From all performed analyses three examples were chosen and presented: a continuous reinforced concrete beam, a one-storey one-span frame and a simply supported beam with reinforcement on one side. These examples best satisfied the conditions for the use of simplified methods.

Concrete C25/30 and reinforced steel ( $E = 200$  GPa,  $f_y = 500$  MPa) were considered for all examples. During the whole time of loading the yield strength was not reached for any of the examples. The erection progress proceeded as follows: After laying, the concrete structures were cured for 3 days and on the 28<sup>th</sup> day the temporary supports were removed and load was applied. The load didn't change for the whole observed time (10028 days from laying the concrete). The relative humidity of the ambient environment was 60%. The length of the finite elements was approx. 0.25 m and special elements were used for the concrete part of the cross-section and for top and bottom reinforcement.

The analysis of 40 time intervals with constant load was accomplished in Asteres. Particular time intervals were designed in line with the rule that the length of each following interval was to be 1.5 times larger than the previous one. The first, shortest interval was 39 seconds in length and the last had a length of 3333 days. For the analysis according to EC2 the considered time was divided into 13 time intervals to obtain a relatively smooth curve of deflection. The quality of the solution obtained by the time discretization method depends on the length of time intervals because the uniform distribution of stresses during the interval is assumed. Computation according to (Eurocode 2) - simplified method - is designed for structures where the stress does not significantly change. That criterion is approximately satisfied for these structures, and therefore the creep can be expressed en bloc for the whole considered time. The history of stress changes due to creep is not taken into account.

Note; The time 0 in all graphs means 28 days after placing the laying of concrete (removal of temporary supports).

#### **3.1. Continuous beam**

The first presented example is the two-span continuous beam. A scheme of the beam and reinforcement is shown in Fig. 1. The intensity of the transversal uniform load is 36.5 kN/m. This load continues for the whole considered time, which is 10028 days from the laying of the concrete.

#### **3.2. Frame**

The next solved structure was a one-storey one-span frame (Fig. 4) designed as a part of a building with a loading width of 6 m. The load is thus relatively high – 80.41 kN/m. The scheme of the structure – see Fig. 4; the deflection in the middle of the cross-beam – see Fig. 5.

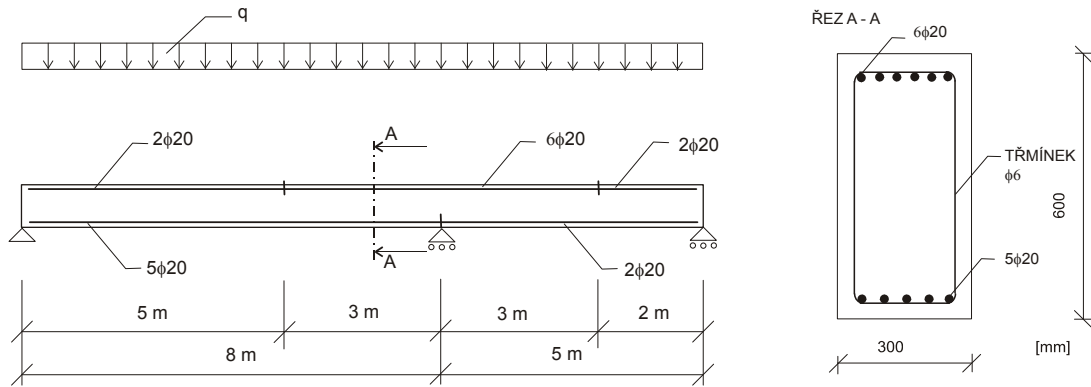


Fig. 1: Continuous beam – scheme of the structure.

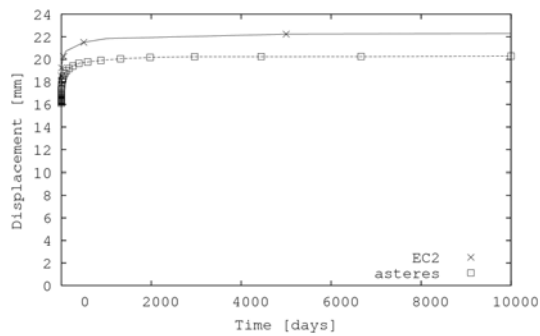


Fig. 2: Continuous beam – deflection in the middle of the span in time.

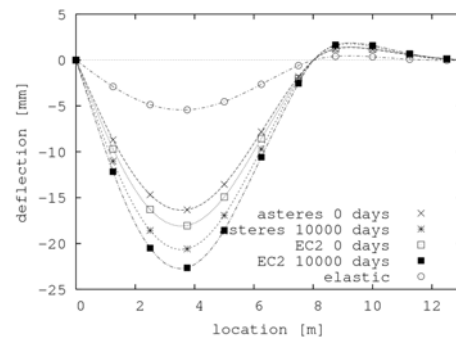


Fig. 3: Continuous beam – deflection along the length of the beam.

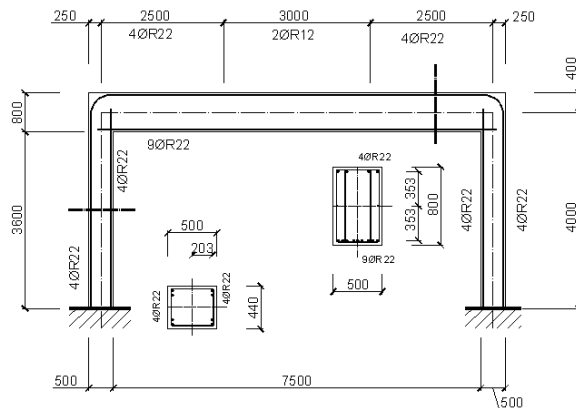


Fig. 4: Frame – scheme of the structure.

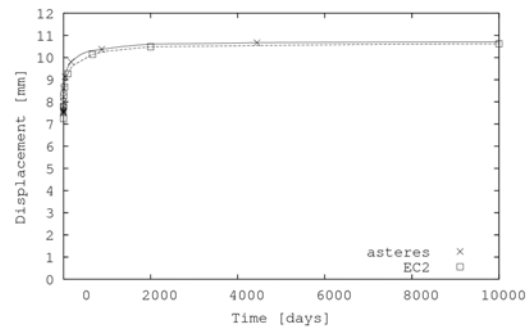
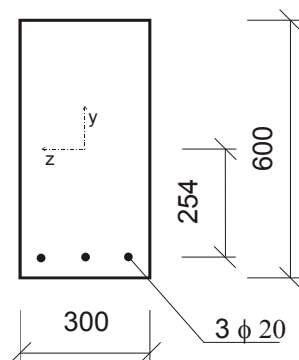


Fig. 5: Frame – deflection in the middle of the span of the cross-beam.

### 3.3. Simply supported beam

The third presented structure is a simply supported beam subjected only to bending moment and shear force. Internal force can not be redistributed because of its static determination. Reinforcement is only on one side, and because of the equilibrium between the forces in tension in the reinforcement and in compression in the concrete there is no redistribution of stresses between concrete and reinforcement (the tension force in cracked concrete is negligible).

The cross-section is shown in Fig. 6. Span is 8 m and intensity of uniformly distributed load is 26kN/m. Fig. 7 shows the dependency between time and the deflection in the middle of the span.



*Fig. 6: Simply supported beam – scheme of the structure.*

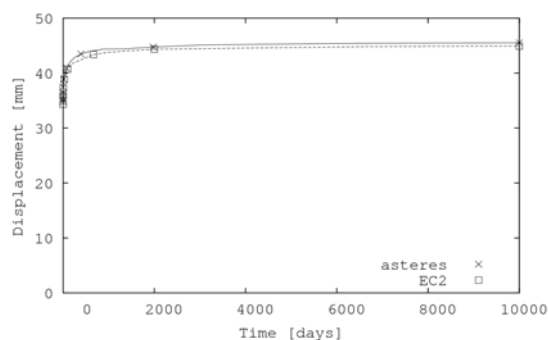


*Fig. 7: Simply supported beam – deflection in the middle of span in time.*

#### 4. Conclusions

The presented study compares the deflections of reinforced concrete structures solved using a method implemented in Asteres software and using the method recommended in (Eurocode 2), chapter 7.4. The influence of fracture energy (considered as 65 N/m) and crack spacing are not analyzed (Asteres input data). Earlier computations have shown the low influence of these parameters. Shrinkage was not considered in any of the models in order to achieve better separation of the particular influences.

Both approaches have shown good agreement in their results. Certain differences could be explained by the redistribution of internal forces and stresses, as the simplified approach is not able to deal with them.

The presented examples show acceptable agreement between the approach described in chapter 7.4 in (Eurocode 2) and Asteres. The theoretical background of Asteres satisfies general code requirements (Eurocode 2). This allows the use of approaches implemented in Asteres software for the assessment of the serviceability limit state of reinforced concrete beam structures. The main field of application of these methods is not only the improvement of deflection analysis of reinforced concrete structures but also the analysis of structures with a complicated history of building and loading. In these cases the use of simplified methods is problematic. If an appropriate erection process and loading is designed, it is possible to lower the deflections caused by rheology and design more slender or less reinforced structures.

#### Acknowledgement

This research has been sponsored by Grant Agency of the Czech Republic project P104/10/2359, and by the MSM0021630519 research fund of the Ministry of Education Youth and Sports.

#### References

- EN 1992-1-1 (Eurocode 2): Design of Concrete Structures, Part 1-1: General Rules and Rules for Buildings, (2005) ČNI, Prague, pp. 126-130.
- Zídek, R. - Brdečko, L. (2010) Alternativní řešení deformací železobetonových konstrukcí, Sborník abstraktů a CD příspěvků Mezinárodní konference Modelování v mechanice, Ostrava, pp. 51- 52.
- Zídek, R. (2008) Prediction of Rheology in Material Nonlinear Analysis of Concrete Reinforced Structures, Proceedings of Conference Life Cycle Assessment, Optimisation, Behaviour and Properties of Concrete and Concrete Structures, November 12-14, Brno, pp. 297-301.

## INFLUENCE OF INCREASING TEMPERATURE ON THE MECHANICAL PROPERTIES OF CEMENT PASTE MADE OF CEM I AND CEM II

O. Zobal\*, P. Padevět\*

**Abstract:** *Cement is still one of the most important materials in the building industry. The experimental investigation addressing the influence of temperature on the mechanical properties of cement paste is presented. In particular, the mixtures of Portland cement CEM I and CEM II are examined. The manufactured test samples are gradually heated to the required temperature and then subjected to the destructive uniaxial compression and three point bending tests to determine the compressive strength, the static modulus of elasticity and the tensile strength in bending.*

**Keywords:** *Cement paste, high temperature, compressive strength, tensile strength in bending, static modulus of elasticity.*

### 1. Introduction

Cement is the basic ingredient used in many mortars and concrete mixtures and is, obviously, one of the most important and widely used building materials. Despite the fact that cement is utilized in altered forms since middle ages, there are still the tendencies to examine and improve its properties. The various experimental tests are often supported by the numerical simulations for better understanding of material behavior, e.g. the numerical study of mechanical properties of cement - based composites was presented by (Kabele, 2010), (Sýkora et al., 2009) investigated transport processes in cement mortar, etc. On the other hand, the indispensable laboratory testing of cement based composites was introduced by many authors, e.g. (Padevět & Bittnar, 2009; Padevět & Zobal, 2009; Němeček et al., 2010) to cite a few. The main objective of this paper is to study the influence of increasing temperature on the mechanical properties of cement paste, particularly the compressive strength, the tensile strength in bending and the static modulus of elasticity.

### 2. Experimental test

In the exceptional conditions (e.g. in the fire conditions), the concrete structures are loaded by the high temperatures which can cause the destruction of mastic and consequently the decrease of concrete strength (Vystražil et al., 2010). For the experiments described herein, the normative samples marked CEM I and CEM II, respectively, are manufactured out of a cement paste. Afterwards, the above mentioned experimental tests are carried out on these samples.

#### 2.1. Manufacturing of test samples

Two different groups of samples for the experimental tests are fabricated.

- Cylinders with diameter 10 mm and length 100 mm are made in the mould, see Fig. 1, and later adjusted to the length 40 mm for the compression tests.
- Beams with the dimensions 20 x 20 x 100 mm are utilized for the three point bending tests.

The various coefficients of water – cement ratio  $w/c = 0.3; 0.4; 0.5$  are assumed for both CEM I and CEM II. To ensure better workability the plasticizer is added to the mixtures with coefficients equal to 0.3 and 0.4. After 48 hours, the specimens are taken out of the mould and placed into the water for

---

\* Ing. Ondřej Zobal and Ing. Pavel Padevět, Ph.D.: Faculty of Civil Engineering, CTU in Prague, Thákurova 7; 166 29, Prague; CZ, e-mails: [ondrej.zobal@fsv.cvut.cz](mailto:ondrej.zobal@fsv.cvut.cz), [pavel.padevet@fsv.cvut.cz](mailto:pavel.padevet@fsv.cvut.cz)



another 26 days. Note that the temperature of water is kept constant (20°C) during the whole period. Then the 28 days old samples are loaded by prescribed temperatures (Fig. 1) and the destructive tests are executed. Bear in mind that each examined group contains approximately five samples and all of them are measured and weighted to determine the volume weight (Zobal, 2009). All measurements are statistically evaluated and the resulting standard deviation does not exceed 5%.



*Fig. 1: The samples in the mould after 48 hours (left), after loading by temperature of 450 ° C with visible cracks (right).*

## 2.2. The methodology of the experiment

The experiment is designed in order to investigate the influence of temperature on mechanical properties and its relation with the value of w/c. The proposed experimental program involves the following temperatures: (i) 20°C – normal state; (ii) 200°C – water ejection; (iii) 450°C – clay decomposition; (iv) 600°C – portlandite decomposition; (v) 300°C – extra intermediate measurement. The heating rate set to 100°C/10 min and the required temperature is hold for constant two hours. Then the samples are slowly cooled down and measured. For the temperature 450°C and 600°C, respectively, the samples are remarkably damaged, see Fig. 1, and the measurement is very complicated or sometimes impossible.

The experiments are performed by means of the MTS Alliance RT-30 machine (Fig. 2) with the maximal loading force equal to 30 kN in compression and tension as well. As mentioned above, the cylindrical samples are subjected to compression and the strain gauges are attached if possible to estimate static modulus of elasticity. Three-point bending tests are carried out on the beams with span of supports 80 mm and the load applied in the mid-span.

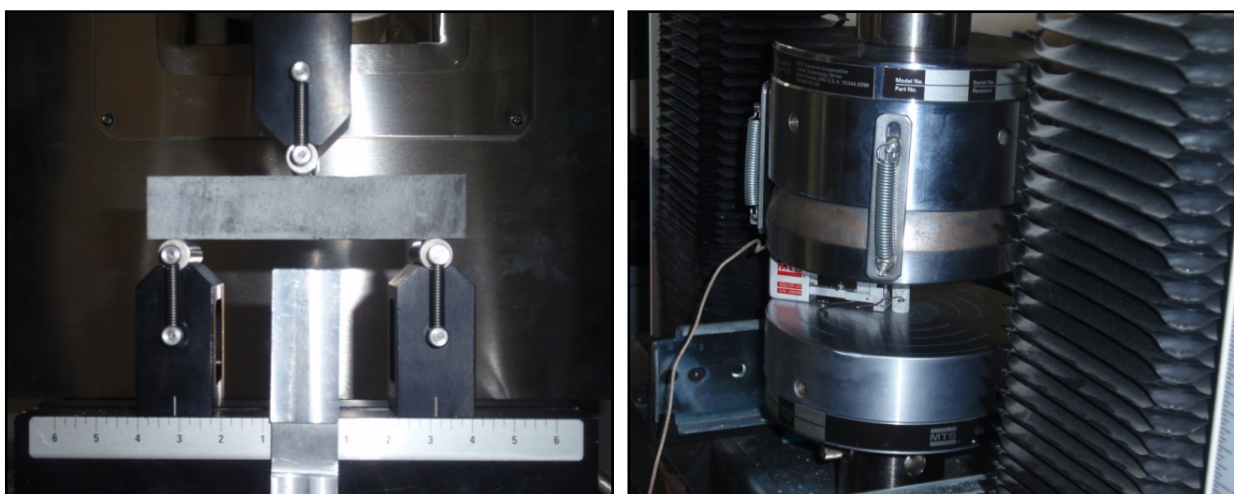


*Fig. 2: MTS Alliance RT-30 - three point bending tests (left) a uniaxial compression (right).*

### 2.3. Evaluation of the experiment

Fig. 3 shows the average values of compressive strength obtained from cylindrical samples after 28 days. The standard deviation for all results presented below did not exceed 5%. One can see that the compressive strength increased with the temperature up to 200 ° C for most of the samples and decreased at higher temperatures. The results demonstrate also the important role of the w/c. Its lower values induced higher compressive strength and vice versa. The highest value of compressive strength 147 MPa was obtained for samples manufactured out of cement CEM I with w/c = 0.3 at temperature 200 ° C and the lowest value (equal almost to zero) were measured for all samples with w/c equal to 0.4 and 0.5 at temperatures 450 ° C and 600 ° C.

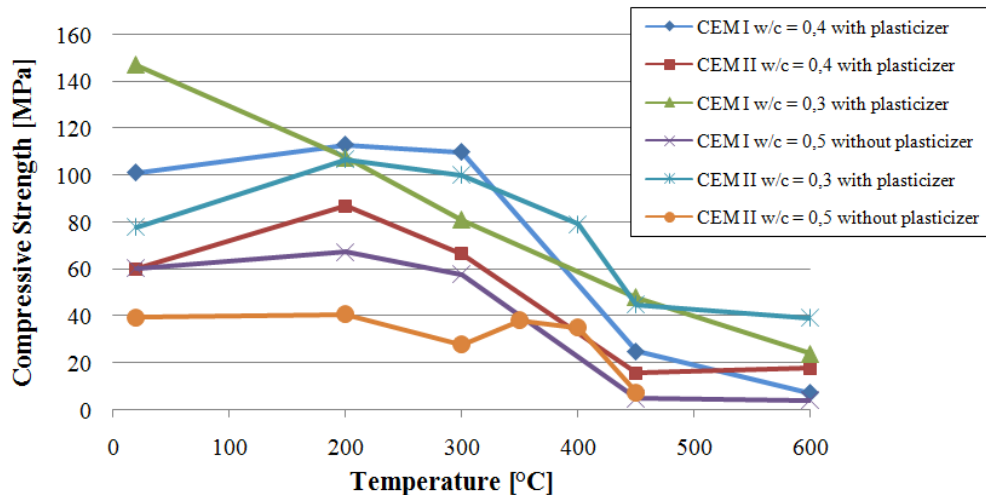


Fig. 3: Average compressive strength of cement paste after 28 days.

The average values of tensile strength in bending measured on beams are depicted in Fig. 4. The results show similar relation of tensile strength and the temperature as for the compressive strength. The highest value 9.5 MPa was obtained here for samples manufactured out of cement CEM II with w/c = 0.3 at temperature 200 ° C and the lowest value approached to zero at temperature 600 ° C for most of the samples.

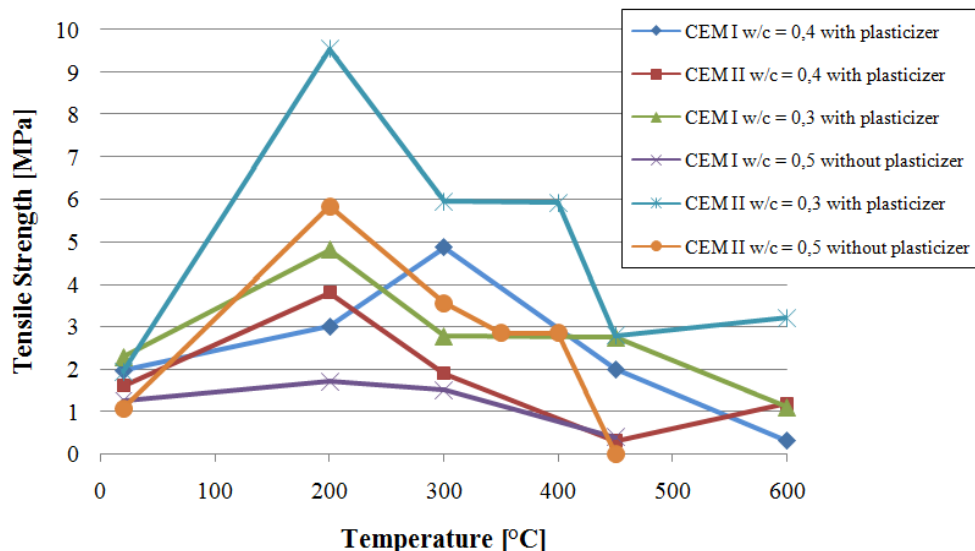


Fig. 4: Average tensile strength in bending of cement pastes after 28 days.

Using strain gauges, we measured the deformation of cylinders and we used it for computation of the static modulus of elasticity. The resulting average values decreases along with the increasing temperature for most of the samples, see Fig. 5. The only exception is the sample made of cement CEM I with w/c = 0.3. In contrast to quantities investigated above, the values of the elastic modulus decrease much more rapidly. The highest value 33.2 GPa was again obtained for samples with w/c = 0.3 at temperature 200 ° C.

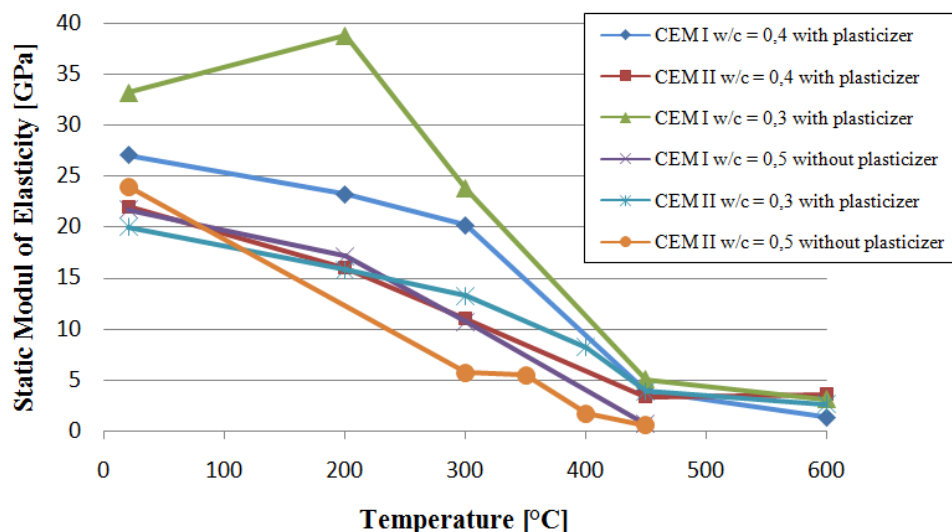


Fig. 5: Average static modulus of elasticity of cement pastes after 28 days.

### 3. Conclusions

The influence of high temperatures on mechanical parameters is significant for samples made of cement paste, and thus also for the concrete. It was shown that the w/c ratio has also an important impact to the results, while the increasing amount of water in cement paste reduces the values of investigated mechanical properties. Regarding the cement types, the variant CEM I attained higher values than the variant CEM II. The most important observation was the phenomenon of increasing values of studied properties along with the temperature up to 200 °C. For higher temperatures, nevertheless, their values started to decrease according to our presumptions. Therefore, we will study this phenomenon in our future experiments in more details.

### Acknowledgement

The financial support of this experiment by the Faculty of Civil Engineering, Czech Technical University in Prague (SGS project No. 10/136/OHK1/2W/11 „Advanced experimental methods“) is gratefully acknowledged.

### References

- Kabele, P. (2010) Stochastic finite element modeling of multiple cracking in fiber reinforced cementitious composites. in: *Fracture and Damage of Advanced Fibre-reinforced Cement-based Materials*. Freiburg: Aedificatio Publisher, pp. 155-163.
- Sýkora, J., Vorel, J., Krejčí, T., Šejnoha, M. & Šejnoha, J. (2009) Analysis of coupled heat and moisture transfer in masonry structures. *Materials and Structures*. 42, 8, pp. 1153-1167.
- Padevět, P. & Bittnar, P. (2009) Creep of cement paste with w/c ratio 0,5. in: *Experimental Stress Analysis 2009*. Liberec: Technical University, 2009, pp. 183-187.
- Padevět, P. & Zobal, O. (2009) Material Properties of Cement Paste at High Temperatures. in *Selected topics on Applied Mathematics, Circuits, Systems, and Signals*. Athens: WSEAS Press, 2009, pp. 39-42.
- Němeček, J., Pečová, P. & Němečková, J. (2010) Effect of Surface Treatment on the Microstructure of Cement Paste Assessed by AFM. in *Experimentální Analýza Napětí 2010*. Olomouc: Palacky University, 2010, pp. 269-276.
- Vyšvařil, M., Bayer, P., Rovníková, P. (2010) Properties of rehydrated cement paste under high temperatures (Vlastnosti rehydratovaných cementových past po expozici vysokými teplotami). in *Proc.: 17. Betonářské dny 2010*, pp. 479 – 483, Hradec Králové
- Zobal, O. (2009) Influence of temperature on the material properties of cement paste. Master Thesis, CTU in Prague, Prague.

## TESTING OF REHABILITATION DEVICE WITH INDUSTRIAL ROBOT

K. Židek<sup>\*</sup>, V. Maxim<sup>\*</sup>

**Abstract:** *The automatized rehabilitation area is currently in fast development together with rehabilitation robotics. After the device development is done, there is another important task to be accomplished - how to safely test device without patient injuries. This Article is describing one design in rehabilitation testing systems, based on industrial robot. The device is designated primarily for testing rehabilitation device with artificial muscle. The Construction based on artificial muscle is flexible, which enables to test reliability of the device before using it in practice. It is used for positioning articulated robot with 5 DOF Mitsubishi RV-2AJ. The robot is controlled from external C# application through serial port. Rehabilitation device is designed for upper arm rehabilitation and is connected to end of robot effector through coupling. We can reach any position in 3D robot workspace to define testing trajectory easily in draw area. Testing device can help check safety of rehabilitation device before testing with life patient.*

**Keywords:** *Automation, robotics, rehabilitation, artificial muscle.*

### 1. Introduction to rehabilitation systems

The coupling of several areas of the medical field with recent advances in robotic and automated systems have seen a paradigm shift in our approach to selected sectors of medical care, especially over the last decade. Rehabilitation medicine is one such area. Introduction was inspired by articles from (Kommu et al., 2007). Rehabilitation robotics is a special branch of Rehabilitation medicine focused on devices that can be used by people to recover from physical trauma. Rehabilitation robotics is nowadays in fast development in physical therapy. The first results in this area are described for example in these articles (Furusho et al., 2007; Pons et al., 2007; Sarakoglou et al., 2007). Within the area of rehabilitation robotics the machines are more likely to be used. They replace manual procedures as the possibility of autonomous help is increasing. There are three main areas of physical therapy: cardiopulmonary, neurological, and musculoskeletal. Though rehabilitation robotics has applications in all three areas of physical therapy, most of the work and development is focused on musculoskeletal uses of robotics. Musculoskeletal therapy assists in strengthening and restoring functionality in the muscle groups and the skeleton, and in improving coordination. In the current paradigm of physical therapy, many therapists often work with one patient, especially at the early stages of therapy. Automatized rehabilitation allows rehabilitation to occur with only one therapist, or none with adequate results. Automated systems allow more consistent training program with the robot tracking, patient's progress and shifting the stress level accordingly, or making recommendations to the human therapist. In the future rehabilitation robotics promises effective results. As the technology develops and prices decrease, rehabilitation systems will be available in everyday life.

### 2. Description of rehabilitation system

In this article, we are going to introduce rehabilitation device for upper arm rehabilitation based on artificial muscle, which will be tested with industrial robot testing device. Artificial muscles are suitable for these devices because of their flexibility especially in end positions. Presented automated rehabilitation device has three degrees of freedom: 2 DOF in arm and 1 DOF in elbow that provides

---

<sup>\*</sup> Ing. Kamil Židek, PhD. and assoc. prof. Ing. Vladislav Maxim, PhD.: Institute of Biomedical Engineering, Automation and Measuring, Technical University of Kosice, Letná 9; 042 00, Kosice; SK, e-mails: kamil.zidek@tuke.sk, vladislav.maxim@tuke.sk



almost all basic rehabilitation exercises as it was described by (Sara J. Cuccurullo, 2010). Artificial pneumatics muscles will be tested in connection with spring and antagonistic connection according design (Piteř J., Borřiková J., 2009). This system provides lifting and falling of arm construction. There is possibility to generate help force during rehabilitation or opposite load. Artificial muscles are controlled through pneumatics block terminals from micro computer based on MCU. Upper control system provides artificial intelligence based on neural network for prediction and change of load according sensor history values. Schematic and design of Rehabilitation device is showed in Fig. 1.

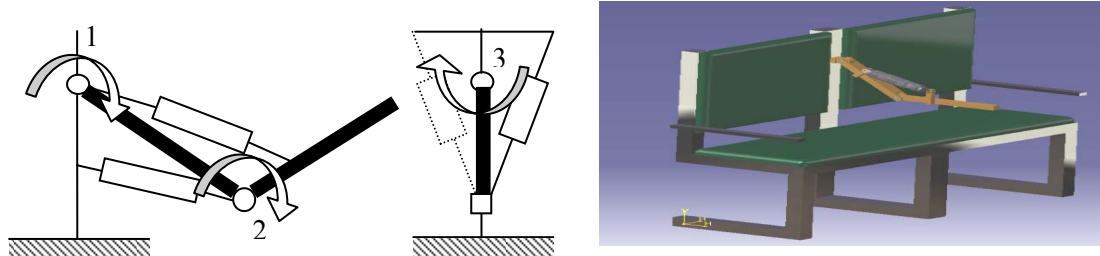


Fig. 1: Scheme of rehabilitation device, 3D design of rehabilitation device.

### 3. Description of testing device

This particular design of the device was applied because of its ability to be easily modified and used in other application. These special devices are used for short periods of time and therefore their ability to be modified is highly convenient. Another reason why we decided to use Assembly Industrial Robot Mitsubishi RV-2AJ (Mitsubishi, 2007) was that the robot has been easily accessible in our department and we did not need to develop new technology. In addition, the industrial robot is much more precise than rehabilitation device that is next reason for testing usability. Next advantage is auxiliary DOF in effector which can be used to setup angle and position of load. The system consists of industrial robot RV-2AJ, control system CR1, flexible coupling, communicating interface and external control application in programming language C#. Fig. 2 shows block communication scheme of device.

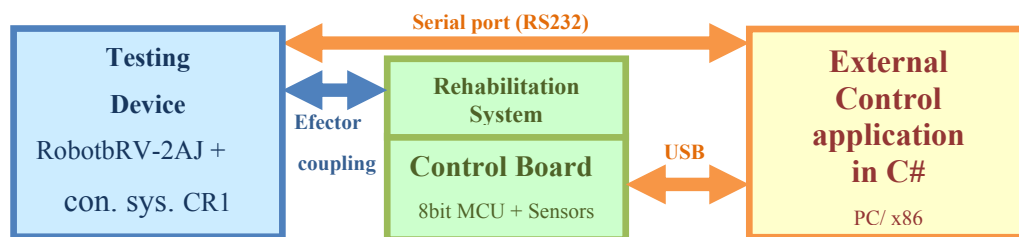


Fig. 2: Communication Block scheme of Testing Device and Rehabilitation Device.

Control Unit CR1 (Mitsubishi, 2007) provides serial port for communication with external application. Testing system is connected to rehabilitation device through coupling with flexible element. Control application is sending information about sequence start, end, ramp time and speed through USB/UART interface. Fig. 3 on the left shows simulated trajectories of testing device for 1 or 2 joint together, Fig. 3 right show first testing of generated trajectories on real device with drawing jig in scale 5:1 to real device. For successful testing and removing deviation from result there is disabled force sensor circuit in rehabilitation device. The speed of rehabilitation device is initialized straight from testing device. Precision of testing device is derived from industrial robot, repeatable precision is  $\pm 0.02$  mm.

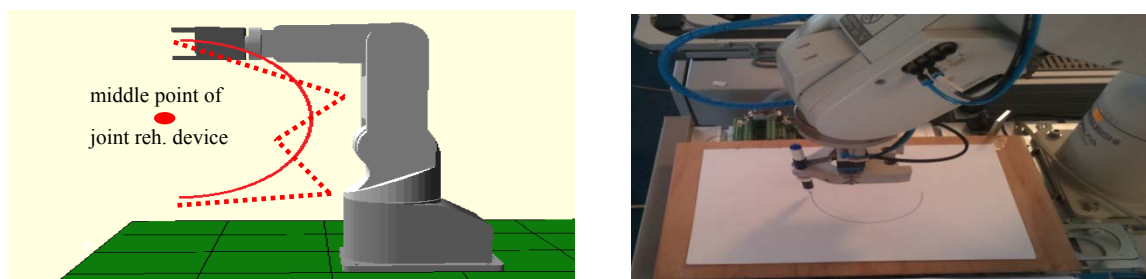


Fig. 3: Simulation of testing trajectories (circular interpolation one joint – red line, linear interpolation two joints together – dotted line), testing of trajectories draw jig.

Procedure of testing is divided to three tests:

1. Testing of one joint: First test of reliability is done on one joint, other two joint must be fixed and speed during whole trajectories will be same. This will be simulating movement of people arm for fluent rehabilitation. There is used circular interpolation.
2. Testing of two joints: We can test any movements in 2D space after successful first test. Two joint will be free and one fixed. Position of free joint is counted through goniometric function. There is used linear or circular interpolation. We can change speed of movement for any segment of linear interpolation.
3. Testing of emergency state: We can test instant stop, ramp start and movement in opposite direction. This test is suitable for testing unpredictable state of rehabilitation device, for example total stop reaction and test overload. This last test is checking states, which can cause injuries to patient during rehabilitation.

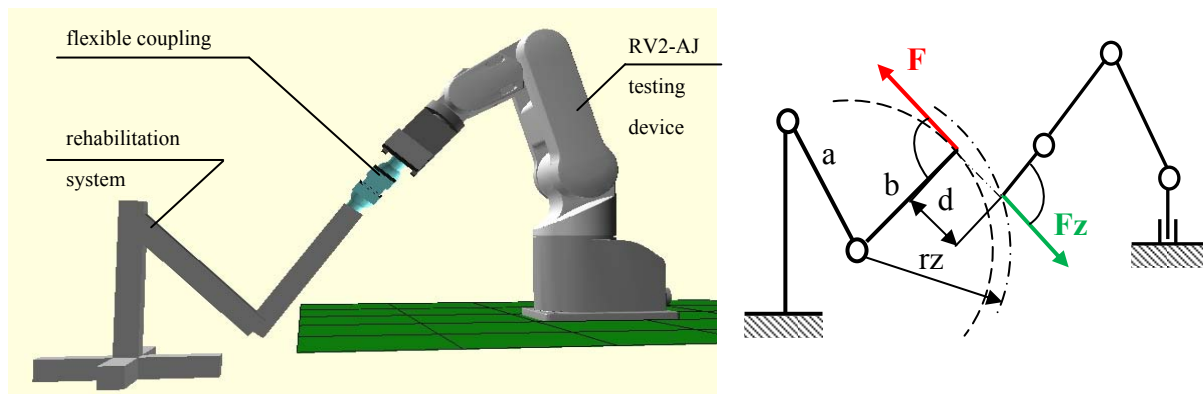


Fig. 4: Simulation of testing device and rehabilitation system, principle scheme of one joint testing.

Simulation of testing device with rehabilitation system showed in the Fig. 4 left. Principle of testing for one joint is showed in the Fig. 4 right. Initial load (force) is created thru flexible coupling element by changing dimension  $d$  according equation:

$$d = d1 \pm Fz/k \quad (1)$$

For circular interpolation we can easy acquire radius of testing device turning:

$$rz = \sqrt{d^2 + b^2} \quad (2)$$

#### 4. Software part of Solution

Principle of trajectory programming for Industrial robot is primarily based on before known number of Points (Positions). These points are stored to robot memory through teach pendant console. Program is created offline and is loaded to control system through serial port. We need faster and dynamic method for create Robot program and Points definition. That was a main reason for development of new external Robot control application. Our program provides dynamic robot programming. This possibility is defining trajectory by selecting Point in graphic area adapted to Robot workspace. There is possible dynamically change number of cycles. Principle of remote control Robot is using internal system command for control system and command for Robot. There is described minimal sequence for testing device: robot control system activation "1;1;CNTLON." and servomotor enable command "1;1;SRVON.". After the initial activation is done, we can use classical commands for robot programming MelfaBasic4, but with command prefix "EXEC", for example. "1;1;EXECMOV P1". The control program is working remote, that is reason why we must get periodically information about control and robot state, "1;1;STATE". Request for actual control system state is sent every 100 ms. The program is divided to three tests, which are described in last chapter. We create force (load) before of the program starts. The load is created by flexible coupling. Next step is communication with rehabilitation device. We sent data about testing angular speed to rehabilitation device thru UART. Then we start both devices in same time. Testing output is information about testing device written to text file with information about collision. On the end of cycle there is stored information that trajectories and cycle was successful done. The Fig. 5 shows control application for testing.

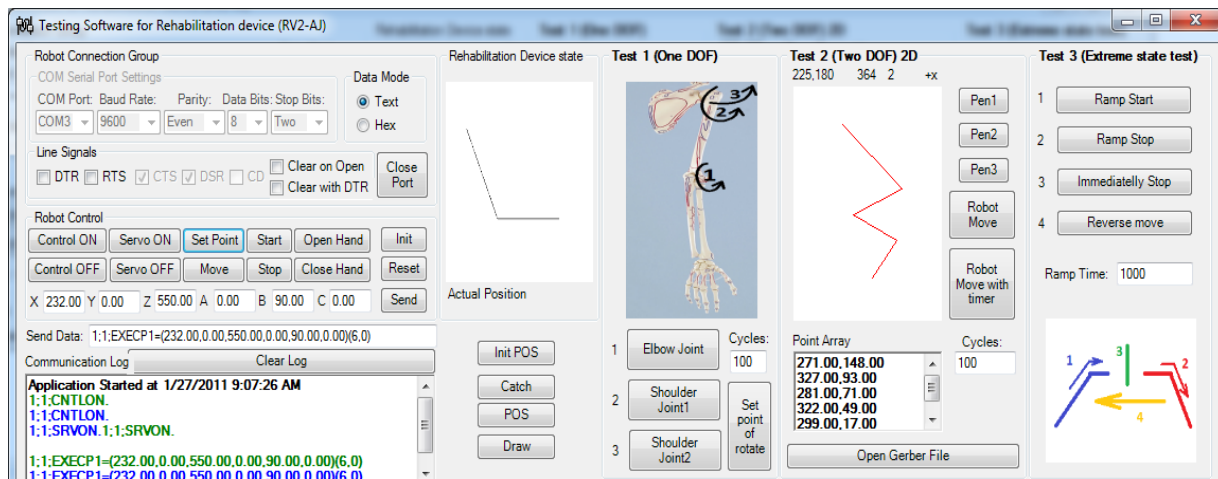


Fig. 5: C# application for testing rehabilitation device.

## 5. Conclusions

The introduced solution will be used for rehabilitation device testing. The Solution is based on industrial Robot Mitsubishi RV2-AJ. There are three level of testing, first for one joint testing, second for two joints together and third for unpredictable states testing (stop, start ramp, change direction of movement). There is possible to setup number of cycles for any movement. Software solution is using standardized programming language that means there is possibility to use same control application for many robots and control systems. Reliability check of testing system was done with simulation program and trajectories were checked with drawing jig scaled in XY plane. The Current solution only log robot state to text file during movement in fixed interval. Next works on the solution will be implementation database to store complex data (robot state, sensor data) from testing process for next result processing.

## Acknowledgement



The research work is supported by the Project of the Structural Funds of the EU, Operational Program Research and Development, Measure 2.2 Transfer of knowledge and technology from research and development into practice: Title of the project: Research and development of the intelligent non-conventional actuators based on artificial muscles ITMS code: 26220220103.

**We are support research activities in Slovakia / Project is cofounded from sources of ES.**

## References

- Furusho J., Kikuchi T., (2007) 3-D Rehabilitation System for Upper Limbs “EMUL”, and a 6-DOF Rehabilitation System “Robotherapist”, and Other Rehabilitation Systems with High Safety in: Rehabilitation Robotics, Osaka University, Japan, pp.115-136.
- Kommu I.S., et al., (2007) Rehabilitation Robotics, I-Tech Education and Publishing, Vienna, Austria, p638.
- Mitsubishi Industrial Robot (2007), RV-1A/2AJ Series, Robot Arm Setup & Maintenance, 2007, Tokyo, p462.
- Mitsubishi Industrial Robot (2007), CR1/CR2/CR3/CR4/CR7/CR8/CR9 Controller, Detailed explanations of functions and operations, 2007, Tokyo , p.72.
- Piteľ J., Boržiková J., (2009) Model of the pneumatic actuator based on artificial muscles, In: MMTT - 22. Tom 10. - Pskov : Pskovskij gosudarstvennyj politechničeskij institut, pp.102-104.
- Pons J.L., Rocon E., Ruiz A.F., Moreno J.C. (2007) Upper-Limb Robotic Rehabilitation Exoskeleton: Tremor Suppression, in: Rehabilitation Robotics, Bioengineering Group, Instituto de Automática Industrial – CSIC, Spain, pp.453-470.
- Sara J. Cuccurullo, (2010) Physical medicine and rehabilitation board review, Demos Medical Publishing, p.938.
- Sarakoglou I., Kousidou S., Nikolaos G., Tsagarakis, Caldwell, D. G. (2007) ItalyExoskeleton-Based Exercisers for the Disabilities of the Upper Arm and Hand in Rehabilitation Robotics, Italian Institute of Technology2, Genoa University of Salford1, Manchester, UK, pp.499-522.



## MODELING OF STRENGTH OF ELASTIC REINFORCED COMPOSITES BY FIBER INCLUSIONS

M. Žmindák<sup>\*</sup>, P. Novák<sup>\*</sup>, I. Eisner<sup>\*\*</sup>

**Abstract:** *In our contribution we will show how the Trefftz Radial Basis Functions (TRBF), i.e. RBF satisfying the governing equations can be used to increase the efficiency of modeling of such problems like composites reinforced by finite length fibres with large aspect ratio. Special attention will be given to application of the TRBF in the form of dipoles to the simulation of composite reinforced by fiber. The source functions (forces and dipoles) are continuously distributed along the fibre axis (i. e. outside of the domain, which is the domain of the matrix) and their intensities are modelled by 1D quadratic elements long the axis in order to satisfy continuity conditions between matrix and fibre. Obtained results are compared with FEM solutions obtained using own ICS FEM software.*

**Keywords:** *Elastic reinforced composites, finite length fibres, short Trefftz Radial Basis Functions.*

### 1. Introduction

The composites of the future reinforced by stiff particles or fibres are important materials possessing excellent mechanical and also thermal and electro-magnetic properties. Understanding the behaviour of composite materials and composite structures is essential for structural design (Kormaníková, 2007). Reinforced composites contain huge number of reinforcing elements with large gradients in all fields in small parts of the matrix (in micro scale) around the reinforcing elements and accurate computational models are important for homogenization of material properties in macro scale (adjustment of local stiffness of such material) and for evaluation of strength of material. Micromechanics is essentially multiscale theory: Although a "representative volume element (RVE) can be viewed as a material point at the macro scale, it is associated with specific microstructure at the micro scale. It is well known that using volume element approximation such as FEM hundreds of elements are necessary to achieve required accuracy even for simple problem ((Filip et al., 2005) where 50 000 to 100 000 trilinear elements were used for problem containing one spherical particle in the matrix). In this paper we study the interaction of matrix-fiber-fiber for regular distributed straight in a patch inside matrix.

### 2. Method of Continuous Source Functions

A composite material with micro/nano structure with regularly distributed reinforcing fibres of unique dimension is to be modelled. Due to very small dimension of particles the stress and strain field can be considered to be homogeneous in the whole domain and all stresses and strains can be imagined split into a constant part, which introduces the state of the matrix without the stiffening and the local part, due to stiffening effect by the fibres.

Let's consider that the cross sectional dimensions of a fibre are much smaller than its length, the tensional stiffness of the fibre is much higher than the stiffness of matrix, the fibre is straight and ideal cohesion forces are assumed in the present model. Then the action of the fibre can be introduced by zero strains in longitudinal direction of the fibre boundary and zero difference of displacements in

---

<sup>\*</sup> prof. Ing. Milan Žmindák, CSc. and Ing. Pavol Novák, PhD.: Faculty of Mechanical Engineering, Department of Applied Mechanics, University of Žilina, Univerzitná 1; 010 26, Žilina; SK, e-mails: milan.zmindak@fstroj.uniza.sk, pavol.novak@fstroj.uniza.sk

<sup>\*\*</sup> Igor Eisner: IPM Engineering, s.r.o.; Sokolská 12; 960 01, Zvolen; SK, e-mail: eisnerc@ipmeng.sk

directions perpendicular to the fibre axis. Aspect ratio (length to radius) of the fibre is considered to be very large (100:1, 1000:1 in examples used here).

The classical Eshelby solution (Eshelby, 1961) was obtained for an elastic isotropic inclusion in an infinite elastic matrix. The treatment of the RVE as an infinite space implies that the inclusion concentration is dilute, and therefore, a direct application of these results to the case of finite inclusion concentration is only approximate. An improved model was suggested by (Mori & Tanaka, 1973). Their method also assumes the absence of all inhomogenities but it includes certain effect of the inhomogeneity by taking average strain in the matrix phase when all inhomogenities are present. Modification of existing homogenization methods via finite Eshelby tensors (Qu & Cherkaoui, 2006) provides significant improvement in predicting the behaviour of composites. In particular, the Hashin-Shtrikman variational bounds are modified according to the prescribed boundary condition (Hashin & Shtrikman, 1963). Recently, (Sauer, et al.) solved the elastic field of an idealized, spherical, finite RVE embedded in an infinite, homogeneous, isotropic medium using Boundary Integral Equations (BIE).

Because of large aspect ratio, continuity of strains between a matrix and a fibre can be simulated by continuously distributed source functions (forces, dipoles, dislocations, etc. (Blok, 1964; Kachanov et al., 2003) as they are known from the potential theory) along the fibre axis (Fig. 1). The continuous source functions enable to simulate the continuity conditions with much reduced collocation points along the fibre boundary.

All displacement, strain and stress fields will be split into a homogeneous part corresponding to constant stress-strain in the matrix without the reinforcement. For simplicity an isotropic material properties are assumed in this paper.

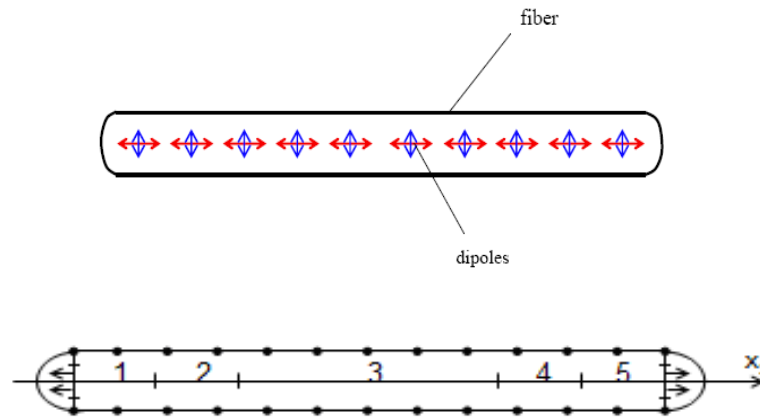


Fig. 1: Continuous force/dipole model for the fiber reinforcing element.

The field of displacements in an elastic continuum by a unit force acting in direction of the axis  $x_p$  is given by Kelvin solution

$$U_{pi}^{(F)} = \frac{1}{16\pi G(1-\nu)} \frac{1}{r} \left[ (3-4\nu)\delta_{ip} + r_{,i}r_{,p} \right] \quad (1)$$

where  $i$  denotes the  $x_i$  coordinate of the displacement,  $G$  and  $\nu$  are shear modulus and Poisson's ratio of the material of the matrix (isotropic material is considered here),  $r$  is the distance between the source point  $s$ , where the force is acting with a field point  $t$ , where the displacement is introduced, i. e.

$$r = \sqrt{r_i r_i}, \quad r_i = x_i(t) - x_i(s) \quad (2)$$

The summation convention over repeated indices acts and

$$r_{,i} = \partial r / \partial x_i(t) = r_i / r \quad (3)$$

is the directional derivative of radius vector  $r$ .

The displacement field of a dipole can be obtained from the displacement field of a force by differentiating it in the direction of the acting force, i.e.

$$U_{pi}^{(D)} = U_{pi,p}^{(F)} = -\frac{1}{16\pi G(1-\nu)} \frac{1}{r^2} [3r_{,i}r_{,p}^2 - r_{,i} + 2(1-\nu)r_{,p}\delta_{ip}] \quad (4)$$

The summation convention does not act over the repeated indices  $p$  here and in the following relations, too. Gradients of the displacement field are

$$U_{pi,j}^{(D)} = -\frac{1}{16\pi G(1-\nu)} \frac{1}{r^3} [-15r_{,i}r_{,j}r_{,p}^2 + 3r_{,i}r_{,j} + 2(1-2\nu)\delta_{ip}(\delta_{jp} - 3r_{,j}r_{,p}) + 6r_{,i}r_{,p}\delta_{jp} + \delta_{ip}(3r_{,p}^2 - 1)] \quad (5)$$

and corresponding strain and stress fields are

$$E_{pij}^{(D)} = \frac{1}{2}(U_{pi,j}^{(D)} + U_{pj,i}^{(D)}) = -\frac{1}{16\pi G(1-\nu)} \frac{1}{r^3} [-15r_{,i}r_{,j}r_{,p}^2 + 3r_{,i}r_{,j} + 2(1-2\nu)\delta_{ip}\delta_{jp} + 6\nu(\delta_{ip}r_{,j}r_{,p} + \delta_{jp}r_{,i}r_{,p}) + \delta_{ij}(3r_{,p}^2 - 1)] \quad (6)$$

$$S_{pij}^{(D)} = 2GE_{pij}^{(D)} + \frac{2G\nu}{1-2\nu}\delta_{ij}E_{pkk}^{(D)} = -\frac{1}{8\pi(1-\nu)} \frac{1}{r^3} [(1-2\nu)(2\delta_{ip}\delta_{jp} + 3r_{,p}^2\delta_{ij} - \delta_{ij}) + 6\nu r_{,p}(r_{,i}\delta_{jp} + r_{,j}\delta_{ip}) + 3(1-5r_{,p}^2)r_{,i}r_{,j}] \quad (7)$$

### 3. Fiber-Reinforced Composites

Two different problems were simulated in order to study the interaction of fibres with matrix and also the interaction of fibres: 1) a patch of non-overlapping rows of fibres as shown in Fig. 2 on the left and 2) a patch of overlaying rows of fibres according to the Fig. 2 on the right. In the examples the modulus of elasticity of the matrix was  $E = 1000$  and Poisson ratio  $\nu = 0.3$ . The matrix was reinforced by a patch of straight rigid cylindrical fibres. The length of fibres was  $L = 1000$  and  $L = 100$  and the radius  $R = 1$ . The distance between fibres was  $\Delta_1 = \Delta_2 = \Delta_3 = 16$  and for longer fibres also  $\Delta_3 = 200$  in the fibre direction. The fibres in the patch contain approximately 1% of the volume of the composite material.

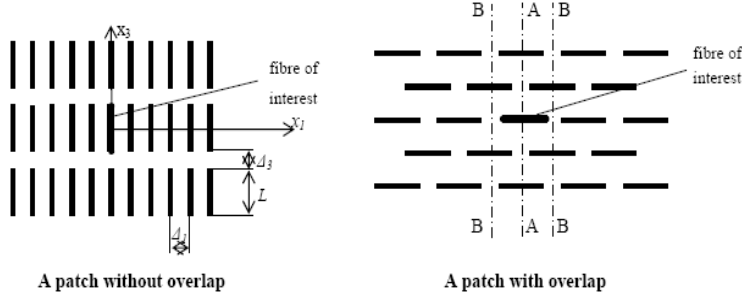


Fig. 2: 3D patches of regularly distributed fibres.

The patches of fibres consisted of  $5 \times 5 \times 7$  fibres in presented examples and "the fibre of interest" (FOI) were chosen in the middle to study the interaction of the fibre with matrix and with the other fibres as well. The domain is supposed to be loaded by far field stress  $\sigma_{33\infty} = 10$  in the direction ( $x_3$ ), which is also parallel to fibres' axes. The model of the fibre used in these examples contained less than 100 unknown parameters (intensities of the source functions) and about 200 collocation points. The problem is solved by LS method.

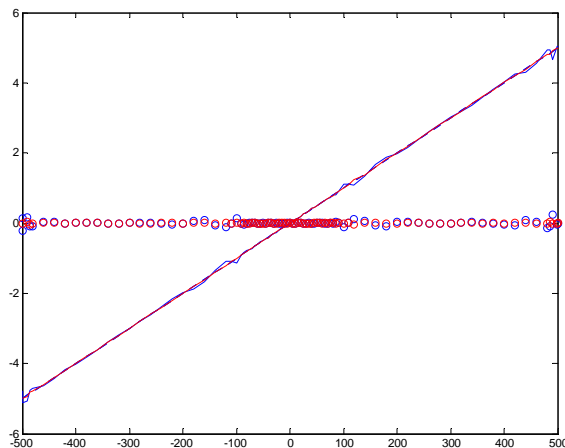


Fig. 3: Local displacements along a fibre.

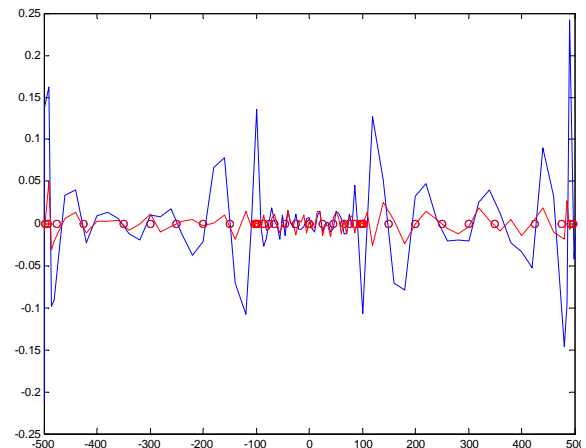


Fig. 4: Errors in local displacements along fibre.

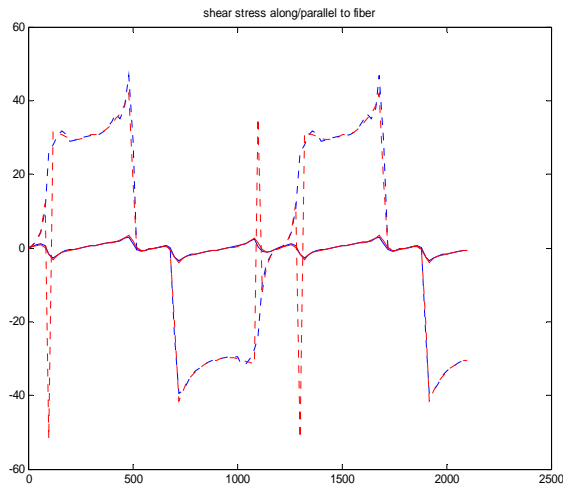


Fig. 5: Shear stress parallel to fibre axis.

#### 4. Conclusions

The MCSF enables to simulate both the interaction of matrix with stiff reinforcing fibres and the fibre with other fibres very effectively. Computational experiment have shown that very large gradients in all fields occur not only in the end parts of fibres, but also in the points close to the ends of neighbouring fibres, more precisely in points on the line perpendicular to the axis of the neighbouring fibre. The large gradients in the end parts of fibres influence also the numerical models. If polynomial interpolation of source functions is chosen in the models then finer division of the continuous function is to be defined in these parts.

#### Acknowledgement

The authors gratefully acknowledge the support by the Slovak Science and Technology Assistance Agency registered under number APVV-0169-07, the Slovak Grant Agency VEGA 1/0657/09.

#### References

- Blokh, V.I. (1964) Theory of Elasticity. University Press, Kharkov.
- Eshelby, J. D. (1961) Elastic inclusions and inhomogenities, in N. I. Sneddon and R. Hill, eds., Progress in Solid Mechanics, Vol. 2, North-Holland.
- Filip, C., Garnier, B. & Danes, F. (2005) Prediction of the effective thermal conductivity of composites with spherical particles of higher thermal conductivity than the one of the polymer matrix, in Proc. Of COMSOL Multiphysics User's Conference, Paris.
- Hashin, Z. & Shtrikman, S. (1963) A variational approach to the theory of the elastic behaviour of multiphase materials, J. Mech. Phys. Solids, 11, pp. 127-140.
- Kachanov, M., Shafiro, B. & Tsukrov, I. (2003) Handbook of Elasticity Solutions. Kluwer Academic Publishers, Dordrecht
- Kormaníková, E. (2007) Optimization of laminated circular cylindrical shell, in Proc. Computational Modeling and Experiments of the Composite materials with Micro- and Nano-Structure. Liptovský Mikuláš, Slovak Republic, CD ROM.
- Mori, T. & Tanaka, K. (1973) Average stressing matrix and average elastic energy of materials with misfitting inclusions, Acta Metall., 21, pp. 571-574.
- Qu, J. & Cherkaoui, M. (2006) Fundamentals of Micromechanics of Solids, John Wiley & Sons, Hoboken, New Jersey.
- Sauer, R. A., Wang, G. & Li, S. The composite Eshelby Tensors and their application to homogenization, Acta mechanica, 197, pp. 63-97.

Figs. 3 to 5 contain the local fields in the vicinity of the fibre of interest (coordinates origin is in the middle of the fibre) for length fiber ( $L = 1000 R$ ) with overlay and the distance  $\Delta_3 = 200 R$ . Displacement differences of the points on the fibre boundary were linear along the fibre (Fig. 3). As the LS method was used in the procedure the errors were examined as shown in Fig. 4. The circles denote nodal points in distributed source functions (fictive forces of the Kelvin functions and dipoles) along the fibre axis. Two different models were used: with discontinuities (A - red) by the ends of neighbour fibres where the fields have large gradients and with continuous distribution of source functions (B - blue) along whole fibre axis.

## DESIGN OF THE CONTROL SYSTEM FOR REHABILITATION DEVICE OF UPPER ARM

T. Župa<sup>\*</sup>, K. Židek<sup>\*</sup>, O. Líška<sup>\*</sup>

**Abstract:** *The article deals with a design of the control system for rehabilitation device of upper arm based on artificial muscles. The main part is devoted to a description of main control unit with MCU ATMEGA128L and its using with several input/output devices. The Control system is including different sensors and output switching elements for controlling pneumatic muscle system of a rehabilitation device. The sensorial system consists mainly from MEMS sensors, pressure and body temperature sensors. With small keypad and LCD display is possible to set several types of rehabilitation practices. Simply describes the algorithm for control of pneumatic muscles.*

**Keywords:** *Rehabilitation device, microcontroller, sensors.*

### 1. Introduction

For a rehabilitation of upper limb of the human body with the help of rehabilitation device is necessary that this device should to have reliable control system. This control system must perform three basic mainly functions as:

- a) regulate action of the pneumatic muscles on the basis of information from the sensors and the kind of practices,
- b) protect the patient's health in case of detection dangerous acceleration or other malfunctions,
- c) display information on a display of device with the option to select a different rehabilitation practices and possibility to connect control system with a PC (Pitel' & Balara, 2009).

The base is 8-bit microcontroller ATMEGA128L which using an algorithm and using information from sensors is capable to switch electromagnetic valves. Triggering of this valve is getting pressure to the pneumatic muscle and this muscle shrinks and then carries out the movement of rehabilitation arm. The control system should be controllable by the PC, where it would be possible to logging data about the practice on the rehabilitation of devices and on this basis, further modify and improve rehabilitation practices (Tao et al., 2009).

### 2. Design of the control part

Most commercially available sensors which are used for sensing are supplying from 3.3 V voltages, and from this is clear that the main control part (ATMEGA128L microcontroller) must be able to cooperate with these sensors. Therefore the supply voltage is equal to most sensors. It brings some limitations which microcontroller is able to operate at a frequency of only to 8 MHz, but for the control of pneumatic muscle it is enough.

On 10-bit analog/digital input of microcontroller is connected a pressure sensor in a pneumatic system, gyroscope and pressure sensor from limb (it senses pressure between limbs and rehabilitation arm), which by means of operational amplifier gives on the output voltage. Furthermore, on the I2C bus is connected to an accelerometer and temperature sensor of the human body. As the last sensor is connected incremental encoder to sense speed and position of arm and by means of a simple voltage divider, its output voltage is reduced from 5 to 3.3 V.

---

<sup>\*</sup> Ing. Tomáš Župa, Ing. Kamil Židek PhD. and assoc. prof. Ing. Ondrej Líška, CSc.: Technical University of Košice, Faculty of Mechanical engineering, Department of Biomedical Engineering, Automation and Measurement. Letná 9, 04200 Košice, e-mails: tomas.zupa@tuke.sk, kamil.zidek@tuke.sk, ondrej.liska@tuke.sk

The main output part for switching the electromagnetic valves is integrated transistor array, which is directly connected to the microcontroller output. For viewing process of the rehabilitation is necessary a display and for choosing the various practices in the rehabilitation, including buttons Start, Stop, Total stop is necessary a simple keypad. For communication Microcontroller with a PC is routed a serial link and by means of USART to USB converter is possible to connect device to any PC.

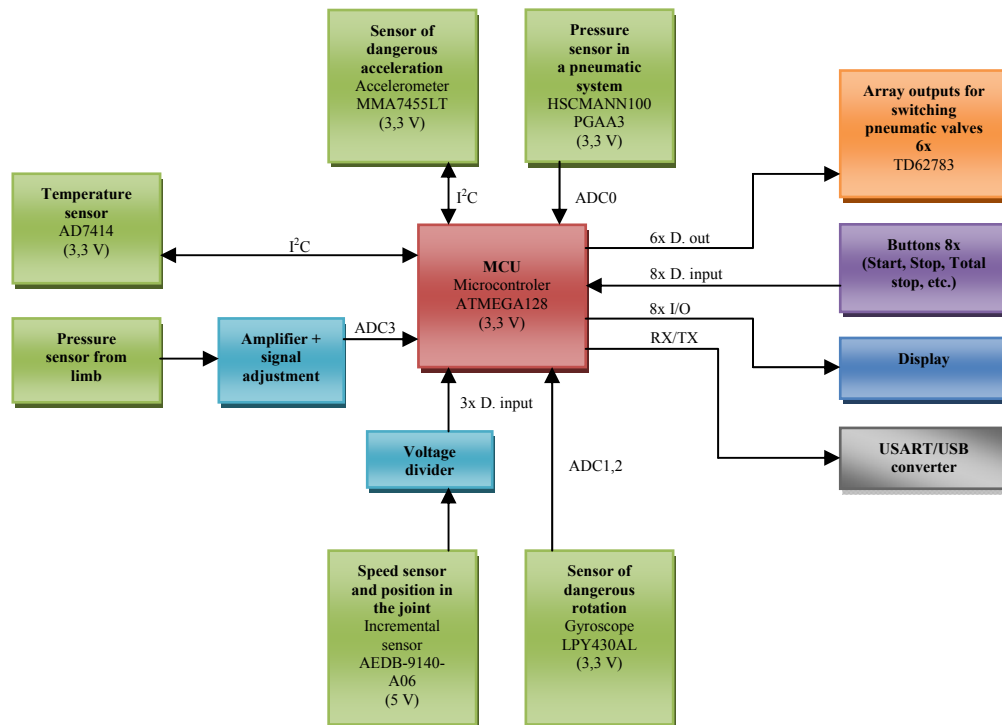


Fig. 1: Block diagram of control part.

### 3. Description of the control module

The schematic diagram is shown in Fig. 2 and is created in Eagle layout editor. Most of the sensors is placed on the printed circuit board, but by using connectors are attached to it. Two types of sensors to give output voltage without adjustment or have their output connected to the I<sup>2</sup>C bus. To obtain information from the incremental encoder is needed using a simple voltage divider to reduce output voltage because, to avoid damage to the microcontroller input (it is because of differences between the microcontroller supply voltage and incremental encoder). Therefore the pressure sensor from limb only works on the concept of change of electrical resistance relative to the pressure exerted on his surface, it must be connected with a simple converter including an amplifier. This feature provides an operational amplifier with non inverting input.

Change the program in the microcontroller is possible with using the ISP programming interface. It is possible to change the program through the serial link, because in the program of microcontroller is implemented a bootloader that makes this possible.

To supply individual components are needed three DC stabilized power supply voltages (+3.3 V, +5 V, +24 V). The microcontroller operates at a frequency of 7.3728 MHz, and because of the minimal errors of a serial link.

As the display unit is used a simple 16 character two line display, which displays information about the behavior and status of the rehabilitation process, as well as information from the sensors.



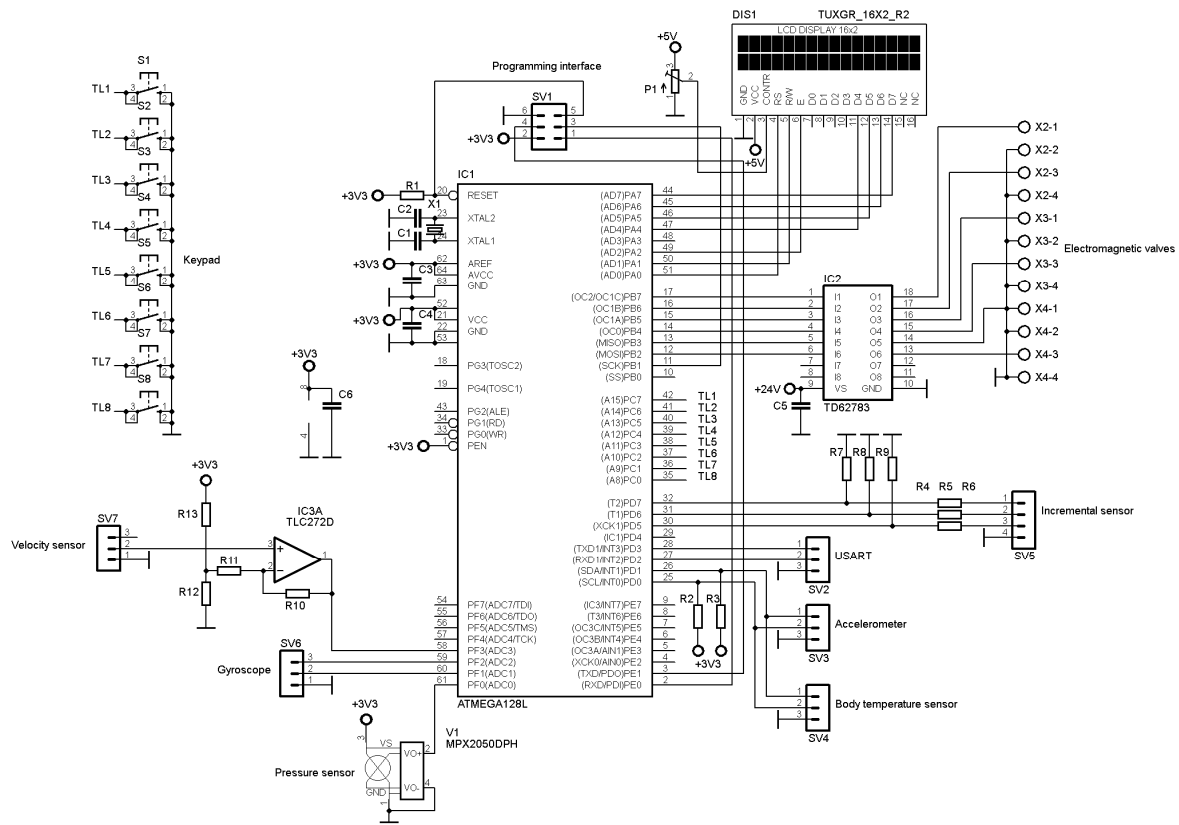


Fig. 2: Schematic diagram of the control module a rehabilitation device.

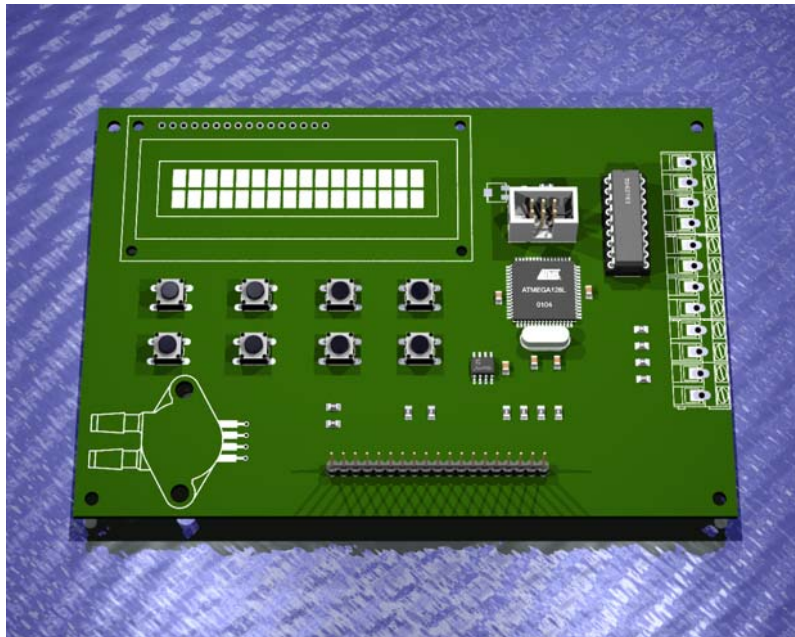


Fig. 3: Printed circuit board of control module rendered in Eagle 3D software.

#### 4. Basic algorithm for control of rehabilitation process

The basic control algorithm for the control of the rehabilitation process consists of three parts:

- regulatory part,
- protective part,
- user part.

The regulatory part of the algorithm ensures that the required rehabilitation practices conducted for the patient. An important feature for controlling the rehabilitation is pressure sensing of arm rehabilitation



from limbs. Based on this property we can achieve a suitable speed of shoulder rehabilitation practices in the prescribed mode.

The protective part of the algorithm is designed to ensure safety of the patient with rehabilitation practices, where for example: in detecting accelerations above a certain threshold to stop the movement of limbs rehabilitated within a few milliseconds. The important elements for detection is included acceleration sensor, gyroscope and temperature sensor of human body (to avoid overheating of the muscles during practice).

The user part of the algorithm ensures communication between the user and the microcontroller. By means of eight buttons you can choose several types of rehabilitation practices with various parameters. All data during practice are displayed on the display unit. Since the display that is not able to display all values at once, so individual information rotated cyclically in a time loop (Sun et al., 2007).

## 5. Conclusion

The main reason was to design the control electronics for control of artificial muscle of rehabilitation device. The base is ATMEGA128L microcontroller with control algorithm, which by means of a simple transistor array directly controls the electromagnetic valves and pneumatic muscles. Very important part is the sensorial system, without which it would be impossible to carry out control. The basic algorithm for control of the pneumatic artificial muscle consists of control, protection and user part, which is provided practically all the functionality of a rehabilitation device.

## Acknowledgement



The research work is supported by the Project of the Structural Funds of the EU, Operational Program Research and Development, Measure 2.2 Transfer of knowledge and technology from research and development into practice: Title of the project: Research and development of the intelligent non-conventional actuators based on artificial muscles ITMS code: 26220220103.

**We are support research activities in Slovakia / Project is cofounded from sources of ES.**

## References (EM 2011 Reference Chapter style)

- Piteľ J., Balara M. (2009) Pneumatický umelý sval – perspektívny prvok mechatroniky. in: AT&P journal 6, pp. 66-68.
- Pleros N., Kanellos G. T., Papaioannou G. (2009) Optical Fiber Sensors in Orthopedic Biomechanics and Rehabilitation. in: Proceedings of the 9th International Conference on Information Technology and Applications in Biomedicine.
- Salpavaara T., Verho J., Lekkala J. (2009) Capacitive Insole Sensor for Hip Surgery Rehabilitation. Institute of Measurement and Information Technology Tampere University of Technology, Finland.
- Sun J., Yu Y., Ge Y., Chen F. (2007) Research on the Multi-Sensors Perceptual System of a Wearable Power Assist Leg Based on CANBUS. in: Proceedings of the 2007 International Conference on Information Acquisition.
- Tao Y., Hu H., Zhou H. (2005) Integration of Vision and Inertial Sensors for Home-based Rehabilitation. in: ICRA'05, IEEE International Conference on Robotics and Automation.
- Zhou H., Hu H., Harris N. (2005) Wearable inertial sensors for arm motion tracking in home-based rehabilitation.

## Author Index

Bednář L.....	43, 671	Dušek D.....	123
Benčat J. ....	47	Dvořák J.....	127
Benkovský P.....	51		
Bílek M. ....	603	Eisner I.....	699
Bittnar P.....	447	Eliáš J. ....	131
Bittnar Z.....	667		
Blekta J.....	55	Ferfecki P.....	679
Borák L.....	380	Ficek F.....	251
Bouřil V. ....	59	Fischer C.....	135, 403
Brabenec L.....	407	Florian Z. ....	523, 635
Brdečko L.....	687	Foglar M. ....	139, 143, 555
Brouček M.....	63	Foldyna J. ....	291
Březina L.....	67	Forman M.....	663
Březina T.....	67	Frantík P.....	147, 360, 415
Burša J.....	25	Frydryšek K. ....	151
Byrtus M.....	71, 175	Fuis V. ....	155
Casha A. ....	527	Gottvald J. ....	159
Cech V. ....	75	Gultová E.....	199, 215
Cichański A.....	79, 627	Guran A. ....	17, 163
Cilia J.....	527		
Civín A.....	83, 391, 407	Had J. ....	111
		Hadas Z.....	167
Čada Z. ....	87, 91	Hájková A.....	171, 615
Čajka R.....	95, 335	Hajžman M.....	175, 475
Čečrdle J.....	99	Haluza M. ....	603
Čep R. ....	347	Haluzíková B. ....	348
		Harničárová M.....	291, 347, 579
Damborský P. ....	103	Havelka J. ....	179
Dančová P.....	107, 439	Havlík R.....	507
Dániel V.....	111	Heller L. ....	199
Darula R.....	567	Hladík O. ....	183
Doktor T.....	115, 356	Hlaváček P.....	187, 291, 347
Donát M.....	119	Hlavatý M.....	191

Horáček J. ....	507	Jonáš J. ....	251
Horák M. ....	195	Jung S. ....	627
Horný L. ....	199, 215	Juránová M. ....	415
Hortel M. ....	203	Jurenka J. ....	255, 351
Hotař V. ....	207	Jůza Z. ....	671
Houfek L. ....	319		
Houfek M. ....	319	Kabeláč J. ....	259
Hoznedl M. ....	671	Kadlec M. ....	263
Hradil P. ....	87, 91, 267, 431	Kala J. ....	87, 267, 271
Hrbáček J. ....	211, 515	Kala Z. ....	271
Hrbáček R. ....	211	Kanický V. ....	87
Hromádka D. ....	215	Kaplonek W. ....	347
Hubová O. ....	219	Karczmarzyk S. ....	275
Hůlka J. ....	339	Kawulok P. ....	579
Hyhlík T. ....	388	Keita I. ....	372
Hynek M. ....	223	Kellner J. ....	587
		Keršner Z. ....	595
Chalupa M. ....	227	Kharlamov A. A. ....	279
Chára Z. ....	279, 659	Kharlamova I. S. ....	279
Chavdarov I. ....	231	Kirchner J. ....	283
Chlup H. ....	199, 215	Klapka M. ....	287
Chmúrny R. ....	567	Klas R. ....	607
		Klich J. ....	291
Ilieva-Mitutsova L. ....	231	Klusák J. ....	491
		Knotek S. ....	295
Jamróz T. ....	111	Kohoutková A. ....	143, 555
Jandora R. ....	235	Kolařík F. ....	299
Janíček P. ....	25, 155, 235, 407	Koňár J. ....	47
Janouchová E. ....	239	Kopecký V. ....	303
Jašíková D. ....	303	Kotek M. ....	107, 303
Jevický J. ....	75	Kotoul M. ....	103, 491
Jícha M. ....	295, 663	Koudelka P. ....	307
Jirásek M. ....	195, 571	Král R. ....	483
Jirka L. ....	43	Králik J. ....	311
Jirouš F. ....	243, 683	Králik J. jr. ....	311
Jiroušek O. ....	115, 247, 356	Králik V. ....	315

Kratochvíl C.....	319	Manek F. ....	635
Kratochvíl O. ....	323	Marcián P. ....	380, 407, 523, 635
Krejsa J. ....	327, 515, 647	Matečková P. ....	95
Křižan J.....	323	Matějka L. ....	384
Kronek J.....	199, 215	Matějka M. ....	388
Krpalek D.....	380, 523, 635	Matug M. ....	83, 391, 407, 523
Krybus D. ....	331	Maxim V. ....	695
Křístek V. ....	139, 555	Mazůrek I. ....	287, 519
Křivý V.....	335	Mazurkiewicz A. ....	627
Kuběna V. ....	579	Mevald J.....	55
Kubík P.....	339	Miles J. ....	372
Kubis A.....	343	Mišun V.....	391
Kučerová A. ....	179, 239, 667	Mrkos J. ....	283, 395
Kuklík P. ....	63	Mrózek M. ....	91, 431
Kupsa V.....	243	Myšáková E. ....	399
Kušnerová M. ....	347		
Kuželka J.....	255, 351	Náprstek J.....	403, 483
Kvapil J. ....	675	Navrátil P.....	83, 235, 343, 380, 391, 407
Kvurt Y.....	372	Němcová H.....	411, 463
Kysela B.....	659	Němec I. ....	415, 419
Kytýř D.....	115, 356	Němec L. ....	423
		Němeček J.....	315
Laukkanen A. M.....	507	Nesládek M. ....	351, 427
Le J.-L. ....	131	Nevařil A.....	431
Lehký D. ....	360	Nikiforov A. ....	435
Lepš M.....	399	Novák P.....	699
Líška O. ....	651, 703	Novotný P.....	439
Lokaj A.....	364	Nowicki K. ....	627
Lošák P.....	368	Omes J.....	395
Lufinka A. ....	55	Omishore A.....	443
Lukerchenko N. ....	372		
		Padevět P. ....	171, 447, 691
Makovička D.....	376	Papán D.....	47
Makovička D. jr.....	376	Pásek M.....	451
Málek M. ....	155	Patzák B. ....	187, 299, 331
Malenovský E.....	368, 471	Pavlenko M. V. ....	455

Pečínka L.....	459	Sant Z. ....	527
Pěňčík J. ....	384	Sedlář M.....	495
Pešek L. ....	503	Seitl S.....	595
Petruška J.....	339	Sempruch J.....	531
Petříček J.....	55	Schmidová E.....	235
Pick P. ....	388	Sikora R. ....	479, 535, 583
Pirner M.....	403	Singule V.....	167
Plachý T.....	171, 411, 463, 615	Sitek L. ....	291
Podešva J.....	467	Skarolek A. ....	539
Pohanka L. ....	471	Skopintseva O. V.....	543
Pochylý F.....	547	Sládek J.....	563
Pokorný Z.....	251	Sládek V. ....	563
Polach P.....	475	Sloupenský Z. ....	547
Polák M. ....	411, 463	Sobotka J. ....	551
Pomp N.....	539	Sochorová E.....	143, 555
Poruba Z.....	479, 535, 583	Spano M.....	559
Pospíšil S.....	483	Spurný M.....	579
Potěšil A.....	487	Staňák P. ....	563
Profant T. ....	103, 491	Stara V. ....	559
Příhoda J. ....	495	Stárek K.....	243
Puklický L. ....	499	Starek L. ....	51, 191
Půst L.....	503	Stein G. J.....	567
Pustka M. ....	539	Stránský J.....	571
		Strecker Z. ....	287, 519
Radolf V. ....	507	Striz B.....	575
Rendlová Z.....	511	Strzelecki P. ....	531
Ripel T. ....	515	Svoboda R.....	33
Rokosz K. ....	579	Sýkora J. ....	179
Roupec J.....	519	Szarková V.....	579
Růžička J.....	351	Szweda J.....	479, 535, 583
		Šamánek O. ....	643
Řehák K.....	380, 391, 523, 635		
Řepka M.....	579	Šašek J.....	175, 587
		Šedek J. ....	591
Salač P. ....	207	Šejnoha M.....	59
Salajka V. ....	87, 91, 267	Ševčík I.....	415

Šimonová H. ....	595	Veverka J. ....	227
Šimurda J. ....	451	Vít T. ....	107, 439
Šklíba J. ....	33	Vítek K. ....	655
Škuderová A. ....	203	Vítkov V. ....	231
Šmilauer V. ....	187, 667	Vlach R. ....	227
Španiel M. ....	255, 351, 427	Vlasák P. ....	279, 659
Šperka O. ....	607	Vlk M. ....	83
Štěrbá P. ....	599	Vokoun D. ....	199
Štigler J. ....	603, 607	Volavý J. ....	663
Šulc J. ....	495	Vorel J. ....	59, 667
Švéda P. ....	319	Votapek P. ....	223
Švrček M. ....	459	Vrbka M. ....	643
		Vysanska M. ....	575
Tajč L. ....	43, 671		
Tesár A. ....	611	Weis L. ....	419
Tesárek P. ....	171, 411, 463, 615		
Tesař V. ....	619	Yaroshevsky V. ....	231
Tlustoš J. ....	623	Yun K. ....	671
Topoliński T. ....	627		
		Zahradník R. ....	675
Ťoupek R. ....	411	Zapletal L. ....	643
		Zapoměl J. ....	679
Uruba V. ....	183, 631	Zeleňák M. ....	347
		Zeman V. ....	175, 511, 587
Vahidi-Shams A. ....	163	Zeneli E. ....	683
Valach J. ....	115, 356	Zídek R. ....	687
Valášek J. ....	380, 523, 635	Zlámal P. ....	247
Valášek R. ....	639	Zobal O. ....	691
Valíček J. ....	291, 347, 579	Zubík P. ....	495
Vašek M. ....	391	Židek K. ....	651, 695, 703
Vaverka M. ....	643		
Vavrušová K. ....	364	Židlík P. ....	347
Věchet S. ....	211, 327, 647	Žitný R. ....	199, 215
Veseliny M. ....	651	Žmindák M. ....	699
Veselý J. ....	215	Župa T. ....	703
Veselý V. ....	147		